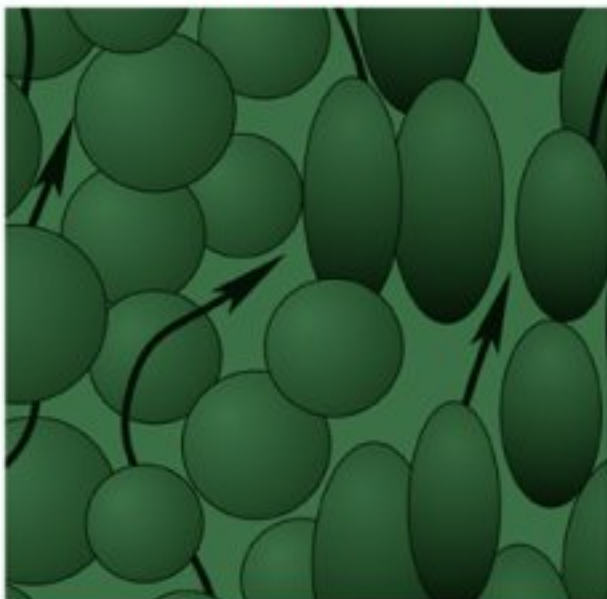


Handbook of POROUS MEDIA

Second Edition



Edited by
Kambiz Vafai



Taylor & Francis
Taylor & Francis Group

Handbook of POROUS MEDIA

Second Edition

Handbook of POROUS MEDIA

Second Edition

**Edited by
Kambiz Vafai**



Taylor & Francis
Taylor & Francis Group

Boca Raton London New York Singapore

A CRC title, part of the Taylor & Francis imprint, a member of the
Taylor & Francis Group, the academic division of T&F Informa plc.

Published in 2005 by
CRC Press
Taylor & Francis Group
6000 Broken Sound Parkway NW, Suite 300
Boca Raton, FL 33487-2742

© 2005 by Taylor & Francis Group, LLC
CRC Press is an imprint of Taylor & Francis Group

No claim to original U.S. Government works
Printed in the United States of America on acid-free paper
10 9 8 7 6 5 4 3 2 1

International Standard Book Number-10: 0-8247-2747-9 (Hardcover)
International Standard Book Number-13: 978-0-8247-2747-5 (Hardcover)

This book contains information obtained from authentic and highly regarded sources. Reprinted material is quoted with permission, and sources are indicated. A wide variety of references are listed. Reasonable efforts have been made to publish reliable data and information, but the author and the publisher cannot assume responsibility for the validity of all materials or for the consequences of their use.

No part of this book may be reprinted, reproduced, transmitted, or utilized in any form by any electronic, mechanical, or other means, now known or hereafter invented, including photocopying, microfilming, and recording, or in any information storage or retrieval system, without written permission from the publishers.

For permission to photocopy or use material electronically from this work, please access www.copyright.com (<http://www.copyright.com/>) or contact the Copyright Clearance Center, Inc. (CCC) 222 Rosewood Drive, Danvers, MA 01923, 978-750-8400. CCC is a not-for-profit organization that provides licenses and registration for a variety of users. For organizations that have been granted a photocopy license by the CCC, a separate system of payment has been arranged.

Trademark Notice: Product or corporate names may be trademarks or registered trademarks, and are used only for identification and explanation without intent to infringe.

Library of Congress Cataloging-in-Publication Data

Catalog record is available from the Library of Congress



Taylor & Francis Group
is the Academic Division of T&F Informa plc.

Visit the Taylor & Francis Web site at
<http://www.taylorandfrancis.com>

and the CRC Press Web site at
<http://www.crcpress.com>

Preface

Theoretical and applied research in flow, heat, and mass transfer in porous media has received increased attention during the past three decades. This is due to the importance of this research area in many engineering applications. Significant advances have been made in modeling fluid flow, heat, and mass transfer through a porous medium including clarification of several important physical phenomena. For example, the non-Darcy effects on momentum, energy, and mass transport in porous media have been studied in depth for various geometrical configurations and boundary conditions. Many of the research works in porous media for the past couple of decades utilize what is now commonly known as the Brinkman–Forchheimer-extended Darcy or the generalized model.

Important topics that have received significant interest include porosity variation, thermal dispersion, the effects of local thermal equilibrium between the fluid phase and the solid phase, partially filled porous configurations, and anisotropic porous media, among others. Advanced measurement techniques have also been developed including more efficient measurement of effective thermal conductivity, flow and heat transfer measurement, and flow visualization. The main objective of this handbook is to compile and present the pertinent recent research information related to heat and mass transfer including practical applications for analysis and the design of engineering devices and systems involving porous media. Both the first and the present editions of the *Handbook of Porous Media* are aimed at providing researchers with the most pertinent and up-to-date advances in modeling and analysis of flow, heat, and mass transfer in porous media. The second edition of the *Handbook of Porous Media*, which addresses a substantially different set of topics compared to the first edition includes recent studies related to current and future challenges and advances in fundamental aspects of porous media, viscous dissipation, forced and double diffusive convection in porous media, turbulent flow, dispersion, particle migration and deposition in porous media, dynamic modeling of convective transport through porous media, and a number of other important topics.

It is important to recognize that different models can be found in the literature and in the present handbook in the area of fluid flow, heat, and mass transfer in porous media. An in-depth analysis of these models is essential in resolving uncertainty in utilizing them (see Tien, C.L. and Vafai, K., 1989, Convective and radiative heat transfer in porous media, *Adv. Appl. Mech.*, 27, 225–282; Hadim, H. and Vafai, K., Overview of current computational

studies of heat transfer in porous media and their applications — forced convection and multiphase transport, in W. J. Minkowycz and E. M. Sparrow, eds, *Advances in Numerical Heat Transfer*, Taylor and Francis, Vol. 2, Chap. 9, pp. 291–330, Taylor & Francis, New York (2000); Vafai, K. and Hadim, H., Overview of current computational studies of heat transfer in porous media and their applications — natural convection and mixed convection, in W. J. Minkowycz and E. M. Sparrow, eds, *Advances in Numerical Heat Transfer*, Taylor and Francis, Vol. 2, Chap. 10, pp. 331–371, Taylor & Francis, New York (2000)). Additionally, competing models for multiphase transport models in porous media were analyzed in detail in Vafai and Sozen (Vafai, K. and Sozen, M., 1990, A comparative analysis of multiphase transport models in porous media, *Annu. Rev. Heat Transfer*, 3, 145–162). In that work, a critical analysis of various multiphase models including the phase change process was presented. These previous studies provide some clarification and insight for understanding several pertinent aspects of modeling of transport phenomena in porous media utilized in the literature and this handbook.

In another study, detailed analysis of variations among transport models for fluid flow and heat transfer in porous media was presented (see Alazmi, B. and Vafai, K., 2000, Analysis of variants within the porous media transport models, *ASME J. Heat Transfer*, 122, 303–326). In this work the pertinent models for fluid flow and heat transfer in porous media for four major categories were analyzed. Another important aspect of modeling in porous media relates to interface conditions between a porous medium and a fluid layer. As such, analysis of fluid flow and heat transfer in the neighborhood of an interface region for the pertinent interfacial models is presented in Alazmi and Vafai (Alazmi, B. and Vafai, K., 2000, Analysis of fluid flow and heat transfer interfacial conditions between a porous medium and a fluid layer, *Int. J. Heat Mass Transfer*, 44, 1735–1749). Determination of the appropriate thermal boundary conditions for the solid and fluid phases within a porous medium is also an important aspect of modeling in porous media. This type of modeling is necessary when prescribed wall heat flux boundary conditions and local thermal nonequilibrium effects are present. As such, Alazmi and Vafai (2000) presented and analyzed different pertinent forms of constant heat flux boundary conditions (see Alazmi, B. and Vafai, K., 2000, Constant wall heat flux boundary conditions in porous media under local thermal non-equilibrium conditions, *Int. J. Heat Mass Transfer*, 45, 3071–3087).

Developments in modeling transport phenomena in porous media have advanced several pertinent areas, such as biology (see Khaled, A. –R. A. and Vafai, K., 2003, The role of porous media in modeling flow and heat transfer in biological tissues, *Int. J. Heat Mass Transfer*, 46, 4989–5003). In this work, various biological areas such as diffusion in brain tissues, diffusion during tissue generation process, the use of Magnetic Resonance Imaging (MRI) to characterize tissue properties, blood perfusion in human tissues, blood flow in tumors, bioheat transfer in tissues, and bioconvection that utilize different transport models in porous media have been synthesized. Different turbulent models for transport through porous media were analyzed in detail by

Vafai et al. (Vafai et al., 2005, Synthesis of models for turbulent transport through porous media, in W. J. Minkowycz and E. M. Sparrow, eds, *Handbook of Numerical Heat Transfer*, John Wiley & Sons, New York). In this work, various features, strengths, and weaknesses of the pertinent turbulent models for flow through porous media have been analyzed and the formulation of a generalized model leading to a more promising model has been established and discussed. Further advances in porous media include modeling of the free surface fluid flow and heat transfer through porous media. This topic is important in a number of engineering applications such as geophysics, die filling, metal processing, agricultural and industrial water distribution, oil recovery techniques, and injection molding. Accordingly, a comprehensive analysis of the free surface fluid flow and heat transfer through porous media is presented in a recent work by Alazmi and Vafai (see Alazmi, B. and Vafai, K., 2004, Analysis of variable porosity, thermal dispersion and local thermal non-equilibrium effects on free surface flows through porous media, *J. Heat Transfer*, 126, 389–399).

This handbook is targeted at researchers, practicing engineers, as well as seasoned beginners in this field. A leading expert in the related subject area presents each topic. An attempt has been made to present the topics in a cohesive, concise yet complementary way with a common format. Nomenclature common to various sections was used as much as possible.

The Handbook of Porous Media, Second Edition, is arranged into seven sections with a total of 17 chapters. The material in [Part I](#) covers fundamental topics of transport in porous media including theoretical models of fluid flow, the local volume-averaging technique and viscous and dynamic modeling of convective heat transfer, and dispersion in porous media. [Part II](#) covers various aspects of forced convection in porous media including numerical modeling, thermally developing flows and three-dimensional flow, and heat transfer within highly anisotropic porous media. Natural convection, double diffusive convection and flows induced by both natural convection and vibrations in porous media are presented in [Part III](#). [Part IV](#) presents the effects of viscous dissipation in porous media for natural, mixed, and forced convection applications. [Part V](#) covers turbulence in porous media. Particle migration and deposition in porous media — composed of two parts — are discussed in [Part VI](#). The final part, [VII](#), covers several important applications of transport in porous media, including geothermal systems, liquid composite molding, combustion in inert porous media, and bioconvection applications in porous media. Also, the final part includes the application of Genetic Algorithms (GAs) for identification of the hydraulic properties of porous materials in the context of petroleum, civil, and mining engineering.

[Chapter 1](#) examines the general problem of coupled, nonlinear mass transfer with heterogeneous reaction in porous media. This situation occurs whenever the mole fraction of the diffusing species is not small compared to one. Under these conditions, the flux depends on both the mole fractions and the mole fraction gradients of all other species that are present. For most processes of diffusion and reaction in porous media, the governing equations

can be linearized over the averaging volume and this allows for the method of volume averaging to be applied in the traditional manner. The main conclusion of this work is that a single tortuosity tensor describes the influence of the porous medium on the diffusion process of all species present in the system.

In [Chapter 2](#), macroscopic descriptions of flows and convective heat transfer in porous media are obtained by averaging the microscopic Navier–Stokes and energy equations volumetrically over fluid and solid phases, respectively. This averaging procedure leads to the closure problem where new unknowns require modeling to relate the unknowns to the averaged flow quantities. Dynamic closure modeling for incompressible flows was constructed based on the first principle of microscopic heat convection over the solids. The coefficients in the closure relations, which depend only on the microstructure of solids, are evaluated experimentally and/or numerically for some special micro-geometries, such as the periodic media in two and three dimensions. The analogies of the flows and heat transfer in porous media to those of Hele-Shaw cells that represent laminated parallel-plates are examined. The characteristics of macroscopic convective heat transfer in porous media are demonstrated with the steady forced convections and the enhanced heat transfer by oscillating flows past a heated circular cylinder in Hele-Shaw cells.

[Chapter 3](#) starts with the general volume-averaged transport equations: fluid flow momentum equation, energy balance equation, and mass balance equation. In these equations, there is a common term that is absent for flow through a system where the porous matrix is not present, namely, the dispersion. Mathematically, the origin of the dispersion is due to the microscopic spatial velocity variation (special fluctuation). Physically, dispersion occurs because of constant joining and splitting of flow streams when the fluid is traversing through the porous structure. Discussion of the dispersion and its effect on single fluid (and multiple fluids) flow, heat transfer, and mass transfer is presented. Dispersion models are evaluated in this chapter.

[Chapter 4](#) deals with recent analytical studies of forced convection in channels or ducts. The studies fall under two headings, namely thermal development and transverse (cross-channel) heterogeneity. The extension to the case of local thermal nonequilibrium is also studied. Further, the extension to the case where axial conduction and viscous dissipation are not negligible is analyzed. In this chapter, the effect of transverse heterogeneity with respect to permeability or thermal conductivity (or both) is also discussed for the case of fully developed forced convection in a parallel-plate channel and a circular duct, with walls at uniform temperature or uniform heat flux.

[Chapter 5](#) presents a review of recent studies on the hydrodynamics and heat transfer effects of variable (with temperature) viscosity flows in a liquid saturated porous media channel. The Hydrodynamics section discusses in detail the fundamental modifications necessary to correct existing models, leading to the newly proposed Modified-HDD model. Influence of variable viscosity on the Nusselt number, the pump power, and other aspects

related to heat-transfer enhancements, are reviewed in the Heat Transfer section. A Perturbation Models section reviews alternative efforts to address the thermohydraulic problem analytically. Before concluding, a brief section is devoted on the experimental validation of the proposed models.

A numerical model for a three-dimensional heat and fluid flow through a bank of infinitely long cylinders in yaw has been proposed in [Chapter 6](#) to investigate complex flow and heat-transfer characteristics associated with man made anisotropic porous media, such as extended fins and plate fins in heat-transfer equipment. Upon exploiting the periodicity of the structure, one structural unit is found to represent the calculation domain. An economical quasi-three-dimensional calculation procedure has been proposed in this chapter to replace exhaustive three-dimensional numerical manipulations. Extensive numerical calculations were carried out in this chapter for various sets of the porosity, degree of anisotropy, Reynolds number, and macroscopic flow direction in a three-dimensional space. Upon examining the numerical data, a useful set of explicit expressions are established for the permeability tensor and directional interfacial heat-transfer coefficient to characterize flow and heat transfer through a bank of cylinders. The systematic modeling procedure proposed in this study can be utilized to conduct subscale modelings of manmade structures needed in the possible applications of a volume-averaging theory to investigate flow and heat transfer within complex heat and fluid flow equipment consisting of small elements.

[Chapter 7](#) contains substantially revised material on double-diffusive convection from the first version of the *Handbook of Porous Media*. Also, new updated material is included as well as new results concerning the Soret effect in double-diffusive convection in porous media.

[Chapter 8](#) presents a linear and weakly nonlinear stability analysis (analytical and numerical study) of the thermal diffusive regime under the action of mechanical harmonic vibrations. In this chapter, the influence of high frequencies and small amplitude vibrations on the onset of convection in an infinite horizontal porous layer and in rectangular cavity filled with a saturated porous medium is studied. The influence of the direction of vibration is also studied when the equilibrium or quasi-equilibrium solution exists. In this chapter, the so-called time-averaged formulation is utilized. The two horizontal walls, of the cell, are kept at different but uniform temperatures, while vertical walls are subject to adiabatic conditions.

[Chapter 9](#) reviews recent research progress related to the effect of viscous dissipation on steady free, forced, and mixed convection flows over a vertical plane surface embedded in a fluid saturated porous medium. The presence of viscous dissipation breaks the usual equivalence between the upward free convection flow from a heated vertical flat plate and from its downward cooled counterpart. In the latter case the opposing effect of the buoyancy forces due to heat release by viscous dissipation can give rise to a parallel flow. In the case of forced and mixed convection flows, the usual thermal asymptotic condition contradicts the energy equation when the viscous dissipation is taken into account. The asymptotic conditions that need to be substituted

in order to achieve consistency with the energy equation are set forth. It is shown that any local disturbance of the static equilibrium of a (resting) fluid leads to a local heat release due to viscous dissipation and in turn, owing to gravity, to a self-sustaining buoyant flow, even if the plate is kept at the constant ambient temperature of the fluid. With the aid of a uniform lateral suction of the fluid, this self-sustaining buoyant flow is shown to behave as a steady jet-like momentum and thermal boundary layer. This turns out to be a universal flow in the sense that its characteristics do not depend on the thermophysical properties of the fluid and the solid skeleton. These kinds of flows are discussed in detail in this chapter.

In [Chapter 10](#), the double-decomposition concept (Pedras, M.H.J. and de Lemos, M.J.S., *IJHMT*, 44(6), 1081–1093, 2001) is presented and thoroughly discussed prior to the derivation of macroscopic governing equations. Equations for turbulent momentum transport in porous media are listed showing detailed derivation for the mean and turbulent field quantities. The statistical $k-\varepsilon$ model for clear domains, used to model macroscopic turbulence effects, serves also as the basis for turbulent heat transport modeling. Also, this chapter discusses applications in Hybrid Media covering flow over wavy porous layers in channels and in cavities partially filled with porous material.

A microscopic phenomenological model and its simulation and experimental validation for fine particle migration and deposition in porous media is presented in [Chapter 11](#). The mathematical model of Gruesbeck and Collins (Gruesbeck, C. and Collins, R.E., 1982, Entrainment and deposition of fine particles in porous media, *SPEJ*, 22(6), 847–856) with the modifications and improvements proposed by Civan (Civan, F., 2000, *Reservoir Formation Damage — Fundamentals, Modeling, Assessment, and Mitigation*, Gulf Pub. Co. Houston, TX, and Butterworth-Heinemann, Woburn, MA) is utilized in this work. A bundle of plugging and nonplugging parallel capillary pathways is developed in order to represent the particle and fluid transfer processes associated with flow of a particle–fluid suspension through porous media. This model allows for particle transfer between the plugging (highly tortuous flow paths) and nonplugging (smoother flow paths) pathways by means of cross-flow, and attempts to simulate the porosity and permeability reduction, and the evolution of plugging and nonplugging pathways by particle deposition in porous media.

In [Chapter 12](#), rectilinear and radial macroscopic phenomenological models along with analytical solutions and applications for impairment of porous media by migration and deposition of fine particles are presented. The mechanism and kinetics of the fine-particle deposition in porous media for two different models are described. The two models are compared and a phenomenological approach is taken to represent the depositional source/sink term and to provide constitutive relationships. For these models, the coupled set of nonlinear equations are expressed in normalized variables and solved analytically by means of the method of characteristics for both rectilinear and radial flows in porous media. Analytical solutions are provided for both constant and variable deposition rates. The analysis in this chapter compares the

solutions and results of the two models with an eye toward the interpretation and representation of experimental data.

Chapter 13 describes the mathematical modeling process applied to physical systems where fluids move within heated porous ground structures. The parameters that are needed to describe the thermodynamic properties of the fluid and solid phases are listed and explained. Techniques for solving the nonlinear system of differential equations, which result from the formal modeling process are described, and some recent developments and foci of research in this area are discussed.

Chapter 14 deals with Liquid Composite Molding (LCM) processes such as Resin Transfer Molding (RTM), Vacuum Assisted Resin Transfer Molding (VARTM), CoInjection Resin Transfer Molding (CIRTM), and Structuring Reaction Injection Molding (SRIM). These processes are used for manufacturing advanced polymer composites. In such processes, the fiber preform is placed inside the mold cavity and a thermoset resin is injected into the mold to wet the fiber preform. The resin cures and cross-links to form a solid composite material. To understand the impregnation and the curing process during manufacturing of composites, research has been conducted to model the heat and flow phenomena in the LCM processes. The transport theories in porous media and the chemical reaction equations have been used to model the thermal and fluid behavior.

Chapter 15 of this handbook discusses premixed combustion of gaseous fuels and air, which react in porous inert media (PIM) that serve as “flame holders” for the burners. The intimate coupling of local chemical energy release during the reaction and heat transfer by conduction, convection, and radiation in the solid matrix results in recirculation of part of the heat of reaction and affects the flame speed, flame stability, the peak flame temperature, and pollutant emissions. The design, theory, modeling, and characteristics of selected combustion systems in which the reactants are preheated using heat recycled from beyond the flame zone, without mixing the two streams, are discussed in this chapter. Applications of devices that have the potential for high efficiencies, low pollutant emissions, and possibility of burning low calorific value gaseous fuels and combustion of lean hydrogen/air mixtures are discussed here.

Chapter 16 deals with bioconvection in porous media. This is an area that is related to a number of pertinent biological applications. One of the applications of porous media is in control and suppression of bioconvection. This problem is of importance, for example, in separation between living and dead cells in suspensions of upswimming mobile microorganisms. Since living microorganisms are heavier than water, their upswimming results in an increase in the density of the upper fluid layer. This leads to convection instability that induces convective motion in the fluid layer. This convective motion, called bioconvection, moves the dead cells from the lower part of the fluid layer and transports them to the upper part of the fluid layer, causing mixing between living and dead cells. By utilizing porous substrates it is possible to control or even completely suppress bioconvection. A large portion of

the chapter is devoted to derivation of the stability criteria for bioconvection in porous media. The effect of cell deposition and declogging as well as the effect of fouling of porous media on the critical permeability are investigated. Finally, this chapter also presents a theory of a bioconvection plume in a suspension of oxytactic bacteria in a deep chamber filled with a fluid saturated porous medium.

The last chapter in the handbook addresses the inverse problem of the identification of the hydraulic properties of porous materials in the context of petroleum, civil, and mining engineering. The application of GAs, which attempts to imitate the principles of biological evolution in the construction of optimization strategies and has led to the development of a powerful and efficient optimization tool, is investigated for such purposes. In this chapter, an inversion technique is formulated in order to retrieve homogeneous or spacewise dependent material property coefficients. Surface measurements by means of simulated ports along the sealed boundaries of the materials serve as information to the GA optimization procedure, thus enabling a modified least squares functional to minimize the difference between the observed and the numerically predicted boundary pressure and/or average hydraulic flux measurements under current hydraulic conductivity tensor and specific storage estimates. Composite anisotropic materials, that is, incorporating faults, are also investigated. Parameter identification in inverse problems is numerically investigated and the results are found to provide an accurate means of recovering the required material properties. A comparison on the performance of the inversion highlights the advantages of the GA optimization approach against a traditional gradient-based optimization procedure.

In each of these chapters whenever applicable pertinent aspects of experimental work or numerical techniques are discussed. Experts in the field reviewed each chapter of this handbook. Overall, there were many reviewers who were involved. The authors and I are very thankful for the valuable and constructive comments that were received.

Kambiz Vafai

List of Contributors

Suresh G. Advani

Department of Mechanical
Engineering
University of Delaware
Newark, Delaware

Marie Catherine Charrier-Mojtabi

Laboratoire d'Energétique E. A-UPS
Université Paul Sabatier
Allée du Pr. Camille Soula
Toulouse, France

Faruk Civan

Mewborne School of Petroleum and
Geological Engineering
University of Oklahoma
Sharkey's Energy Center
Norman, Oklahoma

Marcelo J.S. de Lemos

Departamento de Energia - IEME
Instituto Tecnologico de
Aeronautica - ITA
Sao Jose dos Campos - SP - Brazil

S.D. Harris

Rock Deformation Research Ltd,
School of Earth Sciences
University of Leeds
Leeds
United Kingdom

Kuang-Ting Hsiao

Department of Mechanical
Engineering
EGCB 212
University of South Alabama
Mobile, Alabama

C.T. Hsu

The Hong Kong University of
Science & Technology
Department of Mechanical
Engineering
One University Road
Clear Water Bay
Kowloon, Hong Kong

Derek B. Ingham

Department of Applied
Mathematics
University of Leeds, Leeds,
United Kingdom

B. Keller

Swiss Federal Institute of
Technology (ETH)
Wolfgang-Pauli- Str. 1, Ch-8093
Zurich, Switzerland

F. Kuwahara

Department of Mechanical
Engineering
Shizuoka University
3-5-1 Johoku, Hamamatsu 432
Japan

A.V. Kuznetsov

Department of Mechanical and
Aerospace Engineering
North Carolina State University
Raleigh, North Carolina

José L. Lage

Department of Mechanical
Engineering
Southern Methodist University
Dallas, Texas

Shijie Lui

Department of Chemical Engineering
University of Alberta
Edmonton, Alberta, Canada

E. Magyari

Swiss Federal Institute of
Technology (ETH)
Wolfgang-Pauli- Str. 1, Ch-8093
Zurich, Switzerland

Kittinan Maliwan

Institut de Mécanique des Fluides,
UMR CNRS-INP-UPS N 5502
Université Paul Sabatier
Allee du Pr. Camille Soula
Toulouse, France

Jacob H. Masliyah

Department of Chemical Engineering
University of Alberta
Edmonton, Alberta, Canada

Robert McKibbin

Institute of Information and
Mathematical Sciences
Massey University at Albany
Auckland, New Zealand

Abdelkader Mojtabi

Institut de Mécanique des Fluides
UMR CNRS-INP-UPS N 5502
Université Paul Sabatier
Allee du Pr. Camille Soula
Toulouse, France

Abdul-Khader Mojtabi

Laboratoire de Modelisation en
Mécanique des Fluides, U.F.R.
M.I.G.
Université Paul Sabatier
Allee du Pr. Camille Soula
Toulouse, France

Akira Nakayama

Department of Mechanical
Engineering
Shizuoka University
3-5-1 Johoku, Hamamatsu 432
Japan

Arunn Narasimhan

Department of Mechanical
Engineering
Indian Institute of Technology
Chennai
India

Vinh Nguyen

Poromechanics Institute, PMI
Mewborne School of Petroleum and
Geological Engineering
University of Oklahoma
T 301 Sarkeys Energy Center
Norman
Oklahoma

D.A. Nield

Department of Engineering
Science
University of Auckland
Auckland
New Zealand

Michel Quintard

Institut de Mecanique des Fluides de
Toulouse
Allee du Professeur Camille Soula
Toulouse
France

Maurice L. Rasmussen

School of Aerospace and Mechanical
Engineering
University of Oklahoma
Felgan Hall, Norman
Oklahoma

Yazdan Pedram Razi

Institut de Mécanique des Fluides
UMR CNRS-INP-UPS N 5502
Université Paul Sabatier
Allee du Pr. Camille Soula
Toulouse, France

D.A.S. Rees

School of Mechanical Engineering
University of Bath
Claverton Down, Bath
United Kingdom

Raymond Viskanta

School of Mechanical
Engineering
Purdue University
West Lafayette
Indiana

Stephen Whitaker

Department of Chemical
Engineering
University of California
Davis, California

Contents

I General Characteristics and Modeling of Porous Media	1
1 Coupled, Nonlinear Mass Transfer and Heterogeneous Reaction in Porous Media <i>Michel Quintard and Stephen Whitaker</i>	3
2 Dynamic Modeling of Convective Heat Transfer in Porous Media <i>Chin-Tsau Hsu</i>	39
3 Dispersion in Porous Media <i>Shijie Liu and Jacob H. Masliyah</i>	81
II Forced Convection	141
4 Forced Convection in Porous Media: Transverse Heterogeneity Effects and Thermal Development <i>D.A. Nield and A.V. Kuznetsov</i>	143
5 Variable Viscosity Forced Convection in Porous Medium Channels <i>Arunn Narasimhan and José L. Lage</i>	195
6 Three-Dimensional Flow and Heat Transfer within Highly Anisotropic Porous Media <i>F. Kuwahara and A. Nakayama</i>	235
III Flow Induced by Natural Convection and Vibration and Double Diffusive Convection in Porous Media	267
7 Double-Diffusive Convection in Porous Media <i>Abdelkader Mojtabi and Marie-Catherine Charrier-Mojtabi</i>	269
8 The Influence of Mechanical Vibrations on Buoyancy Induced Convection in Porous Media <i>Yazdan Pedram Razi, Kittinan Maliwan, Marie Catherine Charrier-Mojtabi, and Abdelkader Mojtabi</i>	321

IV	Viscous Dissipation in Porous Media	371
9	Effect of Viscous Dissipation on the Flow in Fluid Saturated Porous Media <i>E. Magyari, D.A.S. Rees, and B. Keller</i>	373
V	Turbulence in Porous Media	407
10	Mathematical Modeling and Applications of Turbulent Heat and Mass Transfer in Porous Media <i>Marcelo J.S. de Lemos</i>	409
VI	Particle Migration and Deposition in Porous Media	455
11	Modeling Particle Migration and Deposition in Porous Media by Parallel Pathways with Exchange <i>Faruk Civan and Vinh Nguyen</i>	457
12	Analytical Models for Porous Media Impairment by Particles in Rectilinear and Radial Flows <i>Faruk Civan and Maurice L. Rasmussen</i>	485
VII	Geothermal, Manufacturing, Combustion, and Bioconvection Applications in Porous Media	543
13	Modeling Heat and Mass Transport Processes in Geothermal Systems <i>Robert McKibbin</i>	545
14	Transport Phenomena in Liquid Composites Molding Processes and their Roles in Process Control and Optimization <i>Suresh G. Advani and Kuang-Ting Hsiao</i>	573
15	Combustion and Heat Transfer in Inert Porous Media <i>Raymond Viskanta</i>	607
16	Modeling Bioconvection in Porous Media <i>A.V. Kuznetsov</i>	645
17	Parameter Identification within a Porous Medium using Genetic Algorithms <i>S.D. Harris and D.B. Ingham</i>	687

Part I

General Characteristics and Modeling of Porous Media

1

Coupled, Nonlinear Mass Transfer and Heterogeneous Reaction in Porous Media

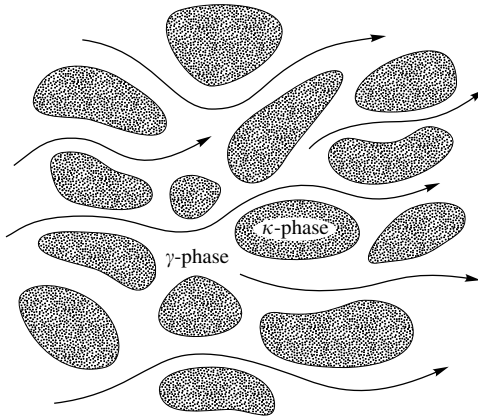
Michel Quintard and Stephen Whitaker

CONTENTS

1.1	Introduction	3
1.2	Mass Transfer	4
1.3	Diffusive Flux	9
1.4	Volume Averaging	11
1.5	Chemical Reactions	14
1.6	Convective and Diffusive Transport	15
1.7	Nondilute Diffusion	19
1.7.1	Constant Total Molar Concentration	19
1.7.2	Volume Average of the Diffusive Flux	20
1.8	Closure	21
1.8.1	Closed Form	29
1.9	Conclusions	33
	Nomenclature	34
	References	36

1.1 Introduction

This chapter deals with multicomponent mass transfer and heterogeneous reaction under conditions where temperature effects can be ignored. The process is illustrated in [Figure 1.1](#) where we have identified a flowing fluid as the γ -phase and an impermeable solid as the κ -phase. The chemical reaction takes place at the $\gamma-\kappa$ interface, and when convective transport is important this situation is often referred to as mass transfer with reaction at a nonporous catalyst. Such systems are commonly treated in texts on reactor design [1–4] and in many cases one must consider the effect of heat transfer on the reaction rate. When convective transport is negligible, the process illustrated in

**FIGURE 1.1**

Transport in a rigid porous medium.

Figure 1.1 represents a case of diffusion and reaction in a porous catalyst, and this is a major problem in the area of reactor design.

In texts on reactor design, problems of mass transfer and reaction are uniformly presented in terms of an uncoupled, linear convective-diffusion equation, or as an uncoupled, linear diffusion equation in the case of porous catalysts. This simplification is applicable when the reacting species is dilute and this requires that the mole fraction of the reacting species be small compared to one. When this is not the case, the diffusive transport becomes nonlinear, and what is often considered to be a routine transport problem becomes quite complex. Direct numerical solution of the nonlinear problem is possible; however, transport processes in porous media necessarily demand spatially smoothed equations [5] and this increases the complexity of the analysis.

1.2 Mass Transfer

Problems of isothermal mass transfer and reaction are usually based on the species continuity equation [6, 7] in the molar form given by

$$\frac{\partial c_{A\gamma}}{\partial t} + \nabla \cdot (c_{A\gamma} \mathbf{v}_{A\gamma}) = R_{A\gamma}, \quad A = 1, 2, \dots, N \quad (1.1)$$

along with the species mass jump condition at the $\gamma-\kappa$ interface. When surface transport [8] can be neglected, the jump condition takes the form

$$\frac{\partial c_{As}}{\partial t} = (c_{A\gamma} \mathbf{v}_{A\gamma}) \cdot \mathbf{n}_{\gamma\kappa} + R_{As}, \quad \text{at the } \gamma-\kappa \text{ interface}, \quad A = 1, 2, \dots, N \quad (1.2)$$

in which $\mathbf{n}_{\gamma\kappa}$ represents the unit normal vector directed from the γ -phase to the κ -phase. In Eq. (1.1) we have used $c_{A\gamma}$ to represent the bulk concentration of species A (moles per unit volume), while in Eq. (1.2) we have used c_{As} to represent the surface concentration of species A (moles per unit area). The nomenclature for the homogeneous reaction rate, $R_{A\gamma}$, and heterogeneous reaction rate, R_{As} , follows the same pattern. Both Eqs. (1.1) and (1.2) can be expressed in terms of the species mass density and the mass rate of reaction; however, most phase equilibrium data are given in terms of mole fractions and most chemical kinetic constitutive equations are given in terms of molar concentrations, thus we prefer to base our analysis on the molar forms given by Eqs. (1.1) and (1.2).

The independent homogeneous and heterogeneous chemical reaction rates [9] must be specified in terms of the molar concentrations of the N species by a chemical kinetic constitutive equation. A complete description of the mass transfer process requires a connection between the surface concentration, c_{As} , and the bulk concentration, $c_{A\gamma}$. One classic connection is based on the condition of local mass equilibrium, and for a linear equilibrium relation this concept takes the form

$$c_{As} = K_A c_{A\gamma}, \quad \text{at the } \gamma-\kappa \text{ interface}, \quad A = 1, 2, \dots, N \quad (1.3a)$$

The condition of local mass equilibrium can exist even when adsorption and chemical reaction are taking place [5, problem 1.3]. When local mass equilibrium is not valid, one must propose an interfacial flux constitutive equation. The classic linear form is given by [10, 11]

$$(c_{A\gamma} \mathbf{v}_{A\gamma}) \cdot \mathbf{n}_{\gamma\kappa} = k_{A1} c_{A\gamma} - k_{-A1} c_{As}, \quad \text{at the } \gamma-\kappa \text{ interface}, \quad A = 1, 2, \dots, N \quad (1.3b)$$

in which k_{A1} and k_{-A1} represent the adsorption and desorption rate coefficients for species A .

In addition to Eqs. (1.1) and (1.2), we need N momentum equations [12] that are used to determine the N species velocities represented by $\mathbf{v}_{A\gamma}$, $A = 1, 2, \dots, N$. There are certain problems for which the N momentum equations consist of the total, or mass average, momentum equation

$$\frac{\partial}{\partial t}(\rho_\gamma \mathbf{v}_\gamma) + \nabla \cdot (\rho_\gamma \mathbf{v}_\gamma \mathbf{v}_\gamma) = \rho_\gamma \mathbf{b}_\gamma + \nabla \cdot \mathbf{T}_\gamma \quad (1.4)$$

along with $N - 1$ Stefan–Maxwell equations that take the form

$$0 = -\nabla x_{A\gamma} + \sum_{\substack{E=1 \\ E \neq A}}^{E=N} \frac{x_{A\gamma} x_{E\gamma} (\mathbf{v}_{E\gamma} - \mathbf{v}_{A\gamma})}{\mathcal{D}_{AE}}, \quad A = 1, 2, \dots, N - 1 \quad (1.5)$$

The species velocity can be *decomposed* into an average velocity and a diffusion velocity in more than one way [6, 7, 13], and arguments are often given to justify a particular choice. In this work we prefer a decomposition in terms of the *mass average velocity* because governing equations, such as the Navier–Stokes equations, are available to determine this velocity. The mass average velocity in Eq. (1.4) is defined by

$$\mathbf{v}_\gamma = \sum_{A=1}^{A=N} \omega_{A\gamma} \mathbf{v}_{A\gamma} \quad (1.6)$$

and the associated *mass diffusion velocity* is defined by the decomposition

$$\mathbf{v}_{A\gamma} = \mathbf{v}_\gamma + \mathbf{u}_{A\gamma} \quad (1.7)$$

The mass diffusive flux has the *attractive characteristic* that the sum of the fluxes is zero, that is,

$$\sum_{A=1}^{A=N} \rho_{A\gamma} \mathbf{u}_{A\gamma} = 0 \quad (1.8)$$

As an alternative to Eqs. (1.6) through (1.8), we can define a molar average velocity by

$$\mathbf{v}_\gamma^* = \sum_{A=1}^{A=N} x_{A\gamma} \mathbf{v}_{A\gamma} \quad (1.9)$$

and the associated molar diffusion velocity is given by

$$\mathbf{v}_{A\gamma} = \mathbf{v}_\gamma^* + \mathbf{u}_{A\gamma}^* \quad (1.10)$$

In this case, the molar diffusive flux also has the *attractive characteristic* given by

$$\sum_{A=1}^{A=N} c_{A\gamma} \mathbf{u}_{A\gamma}^* = 0 \quad (1.11)$$

however, the use of the molar average velocity defined by Eq. (1.9) presents problems when Eq. (1.4) must be used as one of the N momentum equations.

If we make use of the *mass average velocity* and the *mass diffusion velocity* as indicated by Eqs. (1.6) and (1.7), the *molar flux* in Eq. (1.1) takes

the form

$$\underbrace{c_{A\gamma} \mathbf{v}_{A\gamma}}_{\text{total molar flux}} = \underbrace{c_{A\gamma} \mathbf{v}_\gamma}_{\text{molar convective flux}} + \underbrace{c_{A\gamma} \mathbf{u}_{A\gamma}}_{\text{mixed-mode diffusive flux}} \quad (1.12)$$

Here we have decomposed the total molar flux into what we want, the molar convective flux, and what remains, that is, a mixed-mode diffusive flux. Following Eq. (1.7), we indicate the *mixed-mode diffusive flux* as

$$\mathbf{J}_{A\gamma} = c_{A\gamma} \mathbf{u}_{A\gamma}, \quad A = 1, 2, \dots, N \quad (1.13)$$

so that Eq. (1.1) takes the form

$$\frac{\partial c_{A\gamma}}{\partial t} + \nabla \cdot (c_{A\gamma} \mathbf{v}_\gamma) = -\nabla \cdot \mathbf{J}_{A\gamma} + R_{A\gamma}, \quad A = 1, 2, \dots, N \quad (1.14)$$

The single drawback to this mixed-mode diffusive flux is that it does not satisfy a simple relation such as that given by either Eq. (1.8) or Eq. (1.11). Instead, we find that the mixed-mode diffusive fluxes are constrained by

$$\sum_{A=1}^{A=N} \mathbf{J}_{A\gamma} (M_A / \bar{M}) = 0 \quad (1.15)$$

in which M_A is the molecular mass of species A and \bar{M} is the mean molecular mass defined by

$$\bar{M} = \sum_{A=1}^{A=N} x_{A\gamma} M_A \quad (1.16)$$

There are many problems for which we wish to know the concentration, $c_{A\gamma}$, and the normal component of the molar flux of species A at a phase interface. The normal component of the molar flux at an interface will be related to the adsorption process and the heterogeneous reaction by means of the jump condition given by Eq. (1.2) and relations of the type given by Eq. (1.3), and this flux will be influenced by the convective, $c_{A\gamma} \mathbf{v}_\gamma$, and diffusive, $\mathbf{J}_{A\gamma}$, fluxes.

The governing equations for $c_{A\gamma}$ and \mathbf{v}_γ are available to us in terms of Eqs. (1.4) and (1.14), and here we consider the matter of determining $\mathbf{J}_{A\gamma}$. To determine the mixed-mode diffusive flux, we return to the Stefan–Maxwell equations and make use of Eq. (1.7) to obtain

$$0 = -\nabla x_{A\gamma} + \sum_{\substack{E=1 \\ E \neq A}}^{E=N} \frac{x_{A\gamma} x_{E\gamma} (\mathbf{u}_{E\gamma} - \mathbf{u}_{A\gamma})}{\mathcal{D}_{AE}}, \quad A = 1, 2, \dots, N-1 \quad (1.17)$$

This can be multiplied by the total molar concentration and rearranged in the form

$$0 = -c_\gamma \nabla x_{A\gamma} + x_{A\gamma} \sum_{\substack{E=1 \\ E \neq A}}^{E=N} \frac{c_{E\gamma} \mathbf{u}_{E\gamma}}{\mathcal{D}_{AE}} - \left\{ \sum_{\substack{E=1 \\ E \neq A}}^{E=N} \frac{x_{E\gamma}}{\mathcal{D}_{AE}} \right\} c_{A\gamma} \mathbf{u}_{A\gamma}, \quad A = 1, 2, \dots, N-1 \quad (1.18)$$

which can then be expressed in terms of Eq. (1.13) to obtain

$$0 = -c_\gamma \nabla x_{A\gamma} + x_{A\gamma} \sum_{\substack{E=1 \\ E \neq A}}^{E=N} \frac{\mathbf{J}_{E\gamma}}{\mathcal{D}_{AE}} - \left\{ \sum_{\substack{E=1 \\ E \neq A}}^{E=N} \frac{x_{E\gamma}}{\mathcal{D}_{AE}} \right\} \mathbf{J}_{A\gamma}, \quad A = 1, 2, \dots, N-1 \quad (1.19)$$

Here we can use the classic definition of the mixture diffusivity

$$\frac{1}{\mathcal{D}_{Am}} = \sum_{\substack{E=1 \\ E \neq A}}^{E=N} \frac{x_{E\gamma}}{\mathcal{D}_{AE}} \quad (1.20)$$

in order to express Eq. (1.19) as

$$\mathbf{J}_{A\gamma} - x_{A\gamma} \sum_{\substack{E=1 \\ E \neq A}}^{E=N} \frac{\mathcal{D}_{Am}}{\mathcal{D}_{AE}} \mathbf{J}_{E\gamma} = -c_\gamma \mathcal{D}_{Am} \nabla x_{A\gamma}, \quad A = 1, 2, \dots, N-1 \quad (1.21)$$

When the mole fraction of species A is smaller than one, we obtain the *dilute solution* representation for the diffusive flux

$$\mathbf{J}_{A\gamma} = -c_\gamma \mathcal{D}_{Am} \nabla x_{A\gamma}, \quad x_{A\gamma} \ll 1 \quad (1.22)$$

and the transport equation for species A takes the form

$$\frac{\partial c_{A\gamma}}{\partial t} + \nabla \cdot (c_{A\gamma} \mathbf{v}_\gamma) = \nabla \cdot (c_\gamma \mathcal{D}_{Am} \nabla x_{A\gamma}) + R_{A\gamma}, \quad x_{A\gamma} \ll 1 \quad (1.23)$$

Given the condition, $x_{A\gamma} \ll 1$, it is often plausible to impose the condition

$$x_{A\gamma} \nabla c_\gamma \ll c_\gamma \nabla x_{A\gamma} \quad (1.24)$$

and this leads to the following convective–diffusion equation that is ubiquitous in the reactor design literature:

$$\frac{\partial c_{A\gamma}}{\partial t} + \nabla \cdot (c_{A\gamma} \mathbf{v}_\gamma) = \nabla \cdot (\mathcal{D}_{Am} \nabla c_{A\gamma}) + R_{A\gamma}, \quad x_{A\gamma} \ll 1 \quad (1.25)$$

When the mole fraction of species A is not smaller than one, the *diffusive flux* in *this transport equation* will not be correct. If the diffusive flux plays an important role in the rate of heterogeneous reaction, Eq. (1.25) will not lead to a correct representation for the rate of reaction.

1.3 Diffusive Flux

We begin our analysis of the diffusive flux with Eq. (1.21) in the form

$$\mathbf{J}_{A\gamma} = -c_\gamma \mathcal{D}_{Am} \nabla x_{A\gamma} + x_{A\gamma} \sum_{\substack{E=1 \\ E \neq A}}^{E=N} \frac{\mathcal{D}_{Am}}{\mathcal{D}_{AE}} \mathbf{J}_{E\gamma}, \quad A = 1, 2, \dots, N-1 \quad (1.26)$$

and make use of Eq. (1.15) in an alternate form

$$\sum_{A=1}^{A=N} \mathbf{J}_{A\gamma} (M_A / M_N) = 0 \quad (1.27)$$

to obtain N equations relating the N diffusive fluxes. At this point we define a matrix $[R]$ according to

$$[R] = \begin{bmatrix} 1 & -\frac{x_{A\gamma} \mathcal{D}_{Am}}{\mathcal{D}_{AB}} & -\frac{x_{A\gamma} \mathcal{D}_{Am}}{\mathcal{D}_{AC}} & -\cdots & -\frac{x_{A\gamma} \mathcal{D}_{Am}}{\mathcal{D}_{AN}} \\ -\frac{x_{B\gamma} \mathcal{D}_{Bm}}{\mathcal{D}_{BA}} & +1 & -\frac{x_{B\gamma} \mathcal{D}_{Bm}}{\mathcal{D}_{BC}} & -\cdots & -\frac{x_{B\gamma} \mathcal{D}_{Bm}}{\mathcal{D}_{BN}} \\ -\frac{x_{C\gamma} \mathcal{D}_{Cm}}{\mathcal{D}_{CA}} & -\frac{x_{C\gamma} \mathcal{D}_{Cm}}{\mathcal{D}_{CB}} & +1 & -\cdots & -\frac{x_{C\gamma} \mathcal{D}_{Cm}}{\mathcal{D}_{CN}} \\ \vdots & \vdots & \vdots & \vdots & \vdots \\ \vdots & \vdots & \vdots & \vdots & \vdots \\ \frac{M_A}{M_N} & +\frac{M_B}{M_N} & +\frac{M_C}{M_N} & +\cdots & +1 \end{bmatrix} \quad (1.28)$$

and use Eqs. (1.26) and (1.27) to express the N diffusive fluxes according to

$$[R] \begin{bmatrix} J_{A\gamma} \\ J_{B\gamma} \\ J_{C\gamma} \\ \vdots \\ \vdots \\ J_{N\gamma} \end{bmatrix} = -c_\gamma \begin{bmatrix} \mathcal{D}_{Am} \nabla x_{A\gamma} \\ \mathcal{D}_{Bm} \nabla x_{B\gamma} \\ \mathcal{D}_{Cm} \nabla x_{C\gamma} \\ \vdots \\ \mathcal{D}_{(N-1)m} \nabla x_{(N-1)\gamma} \\ 0 \end{bmatrix} \quad (1.29)$$

We assume that the inverse of $[R]$ exists in order to express the column matrix of diffusive flux vectors in the form

$$\begin{bmatrix} J_{A\gamma} \\ J_{B\gamma} \\ J_{C\gamma} \\ \vdots \\ \vdots \\ J_{N\gamma} \end{bmatrix} = -c_\gamma [R]^{-1} \begin{bmatrix} \mathcal{D}_{Am} \nabla x_{A\gamma} \\ \mathcal{D}_{Bm} \nabla x_{B\gamma} \\ \mathcal{D}_{Cm} \nabla x_{C\gamma} \\ \vdots \\ \mathcal{D}_{(N-1)m} \nabla x_{(N-1)\gamma} \\ 0 \end{bmatrix} \quad (1.30)$$

in which the column matrix on the right-hand side of this result can be expressed as

$$\begin{bmatrix} \mathcal{D}_{Am} \nabla x_{A\gamma} \\ \mathcal{D}_{Bm} \nabla x_{B\gamma} \\ \mathcal{D}_{Cm} \nabla x_{C\gamma} \\ \vdots \\ \mathcal{D}_{(N-1)m} \nabla x_{(N-1)\gamma} \\ 0 \end{bmatrix} = \begin{bmatrix} \mathcal{D}_{Am} & 0 & 0 & \cdots & 0 & 0 \\ 0 & \mathcal{D}_{Bm} & 0 & \cdots & 0 & 0 \\ 0 & 0 & \mathcal{D}_{Cm} & \cdots & 0 & 0 \\ \vdots & \vdots & \vdots & \cdots & \vdots & \vdots \\ 0 & 0 & 0 & \cdots & \mathcal{D}_{(N-1)m} & 0 \\ 0 & 0 & 0 & \cdots & 0 & \mathcal{D}_{Nm} \end{bmatrix} \times \begin{bmatrix} \nabla x_{A\gamma} \\ \nabla x_{B\gamma} \\ \nabla x_{C\gamma} \\ \vdots \\ \nabla x_{(N-1)\gamma} \\ 0 \end{bmatrix} \quad (1.31)$$

The *diffusivity matrix* is now defined by

$$[D] = [R]^{-1} \begin{bmatrix} \mathcal{D}_{Am} & 0 & 0 & \cdots & 0 & 0 \\ 0 & \mathcal{D}_{Bm} & 0 & \cdots & 0 & 0 \\ 0 & 0 & \mathcal{D}_{Cm} & \cdots & 0 & 0 \\ \vdots & \vdots & \vdots & \cdots & \vdots & \vdots \\ 0 & 0 & 0 & \cdots & \mathcal{D}_{(N-1)m} & 0 \\ 0 & 0 & 0 & \cdots & 0 & \mathcal{D}_{Nm} \end{bmatrix} \quad (1.32)$$

so that Eq. (1.30) takes the form

$$\begin{bmatrix} \mathbf{J}_{A\gamma} \\ \mathbf{J}_{B\gamma} \\ \mathbf{J}_{C\gamma} \\ \vdots \\ \vdots \\ \mathbf{J}_{N\gamma} \end{bmatrix} = -c_\gamma [D] \begin{bmatrix} \nabla x_{A\gamma} \\ \nabla x_{B\gamma} \\ \nabla x_{C\gamma} \\ \vdots \\ \nabla x_{(N-1)\gamma} \\ 0 \end{bmatrix} \quad (1.33)$$

This result can be expressed in a form analogous to that given by Eq. (1.26) leading to

$$\mathbf{J}_{A\gamma} = -c_\gamma \sum_{E=1}^{E=N-1} D_{AE} \nabla x_{E\gamma}, \quad A = 1, 2, \dots, N \quad (1.34)$$

In the general case, the elements of the diffusivity matrix, D_{AE} , will depend on the mole fractions in a nontrivial manner. When this result is used in Eq. (1.14), we obtain the nonlinear, coupled governing differential equation for $c_{A\gamma}$ given by

$$\frac{\partial c_{A\gamma}}{\partial t} + \nabla \cdot (c_{A\gamma} \mathbf{v}_\gamma) = \nabla \cdot \left(c_\gamma \sum_{E=1}^{E=N-1} D_{AE} \nabla x_{E\gamma} \right) + R_{A\gamma}, \quad A = 1, 2, \dots, N \quad (1.35)$$

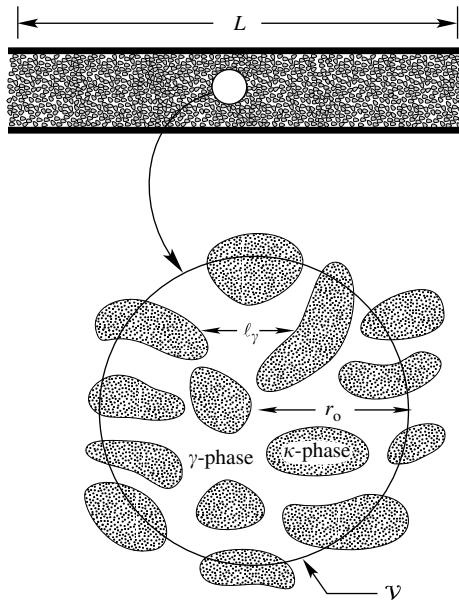
We seek a solution to this equation subject to the jump condition given by Eq. (1.2) and this requires knowledge of the concentration dependence of the homogeneous and heterogeneous reaction rates and information concerning the equilibrium adsorption isotherm. In general, a solution of Eq. (1.35) for the system shown in Figure 1.1 requires *upscaleing* from the point scale to the pore scale and this can be done by the method of volume averaging [5].

1.4 Volume Averaging

To obtain the volume-averaged form of Eq. (1.35), we first associate an averaging volume with every point in the $\gamma-\kappa$ system illustrated in Figure 1.1. One such averaging volume is illustrated in Figure 1.2, and it can be represented in terms of the volumes of the individual phases according to

$$\mathcal{V} = V_\gamma + V_\kappa \quad (1.36)$$

The radius of the averaging volume is r_o and the characteristic length scale associated with the γ -phase is indicated by ℓ_γ in Figure 1.2. In Figure 1.2 we

**FIGURE 1.2**

Averaging volume for a packed bed of nonporous catalyst.

have also illustrated a length L that is associated with the distance over which significant changes in averaged quantities occur. Throughout this analysis we will assume that the length scales are disparate, that is, the length scales are constrained by

$$\ell_\gamma \ll r_o \ll L \quad (1.37)$$

Elsewhere [5, chapter 1] it is shown that these constraints are overly severe; however, they are quite sufficient for the purposes of this presentation.

We will use the averaging volume \mathcal{V} to define two averages: the *superficial average* and the *intrinsic average*. Each of these averages is routinely used in the description of multiphase transport processes, and it is important to clearly define each one. We define the *superficial average* of some function ψ_γ according to

$$\langle \psi_\gamma \rangle = \frac{1}{\mathcal{V}} \int_{V_\gamma} \psi_\gamma \, dV \quad (1.38)$$

and we define the *intrinsic average* by

$$\langle \psi_\gamma \rangle^\gamma = \frac{1}{V_\gamma} \int_{V_\gamma} \psi_\gamma \, dV \quad (1.39)$$

These two averages are related according to

$$\langle \psi_\gamma \rangle = \varepsilon_\gamma \langle \psi_\gamma \rangle^\gamma \quad (1.40)$$

in which ε_γ is the volume fraction of the γ -phase defined explicitly as

$$\varepsilon_\gamma = V_\gamma / V \quad (1.41)$$

In this notation for the volume averages, a *Greek subscript* is used to identify the particular phase under consideration while a *Greek superscript* is used to identify an intrinsic average. Since the intrinsic and superficial averages differ by a factor of ε_γ , it is essential to make use of a notation that clearly distinguishes between the two averages.

When we form the volume average of any transport equation, we are immediately confronted with the average of a gradient (or divergence), and it is the gradient (or divergence) of the average that we are seeking. In order to interchange integration and differentiation, we will make use of the spatial averaging theorem [14–17]. For the two-phase system illustrated in Figure 1.2 this theorem can be expressed as

$$\langle \nabla \psi_\gamma \rangle = \nabla \langle \psi_\gamma \rangle + \frac{1}{V} \int_{A_{\gamma\kappa}} \mathbf{n}_{\gamma\kappa} \psi_\gamma \, dA \quad (1.42)$$

in which ψ_γ is any function associated with the γ -phase. Here $A_{\gamma\kappa}$ represents the interfacial area contained within the averaging volume, and we have used $\mathbf{n}_{\gamma\kappa}$ to represent the unit normal vector pointing from the γ -phase toward the κ -phase.

Even though Eq. (1.35) is considered to be the preferred form of the species continuity equation, it is best to begin the averaging procedure with Eq. (1.1) and we express the superficial average of that form as

$$\left\langle \frac{\partial c_{A\gamma}}{\partial t} \right\rangle + \langle \nabla \cdot (c_{A\gamma} \mathbf{v}_{A\gamma}) \rangle = \langle R_{A\gamma} \rangle, \quad A = 1, 2, \dots, N \quad (1.43)$$

For a rigid porous medium, one can use the transport theorem and the averaging theorem to express this result as

$$\frac{\partial \langle c_{A\gamma} \rangle}{\partial t} + \nabla \cdot \langle c_{A\gamma} \mathbf{v}_{A\gamma} \rangle + \frac{1}{V} \int_{A_{\gamma\kappa}} \mathbf{n}_{\gamma\kappa} \cdot (c_{A\gamma} \mathbf{v}_{A\gamma}) \, dA = \langle R_{A\gamma} \rangle \quad (1.44)$$

where it is understood that this applies to all N species. Since we seek a transport equation for the intrinsic average concentration, we make use of Eq. (1.40) to express Eq. (1.44) in the form

$$\varepsilon_\gamma \frac{\partial \langle c_{A\gamma} \rangle^\gamma}{\partial t} + \nabla \cdot \langle c_{A\gamma} \mathbf{v}_{A\gamma} \rangle + \frac{1}{V} \int_{A_{\gamma\kappa}} \mathbf{n}_{\gamma\kappa} \cdot (c_{A\gamma} \mathbf{v}_{A\gamma}) \, dA = \varepsilon_\gamma \langle R_{A\gamma} \rangle^\gamma \quad (1.45)$$

At this point, it is convenient to make use of the jump condition given by Eq. (1.2) in order to obtain

$$\varepsilon_\gamma \frac{\partial \langle c_{A\gamma} \rangle^\gamma}{\partial t} + \nabla \cdot \langle c_{A\gamma} \mathbf{v}_{A\gamma} \rangle = \varepsilon_\gamma \langle R_{A\gamma} \rangle^\gamma - \frac{1}{V} \int_{A_{\gamma\kappa}} \frac{\partial c_{As}}{\partial t} dA + \frac{1}{V} \int_{A_{\gamma\kappa}} R_{As} dA \quad (1.46)$$

We now define the *intrinsic interfacial area average* according to

$$\langle \psi_\gamma \rangle_{\gamma\kappa} = \frac{1}{A_{\gamma\kappa}} \int_{A_{\gamma\kappa}} \psi_\gamma dA \quad (1.47)$$

so that Eq. (1.46) takes the convenient form given by

$$\underbrace{\varepsilon_\gamma \frac{\partial \langle c_{A\gamma} \rangle^\gamma}{\partial t}}_{\text{accumulation}} + \underbrace{\nabla \cdot \langle c_{A\gamma} \mathbf{v}_{A\gamma} \rangle}_{\text{transport}} = \underbrace{\varepsilon_\gamma \langle R_{A\gamma} \rangle^\gamma}_{\text{homogeneous reaction}} - \underbrace{a_v \frac{\partial \langle c_{As} \rangle_{\gamma\kappa}}{\partial t}}_{\text{adsorption}} + \underbrace{a_v \langle R_{As} \rangle_{\gamma\kappa}}_{\text{heterogeneous reaction}} \quad (1.48)$$

One must keep in mind that this is a *general result* based on Eqs. (1.1) and (1.2); however, only the first term in Eq. (1.48) is in a form that is ready for application.

1.5 Chemical Reactions

To obtain a useful form for the homogeneous reaction rate, one needs a chemical kinetic constitutive equation that can be expressed as

$$R_{A\gamma} = R_{A\gamma}(c_{A\gamma}, c_{B\gamma}, \dots, c_{N\gamma}) \quad (1.49)$$

Even for nonlinear reaction rate mechanisms, the volume average of Eq. (1.49) can usually be expressed as

$$\langle R_{A\gamma} \rangle^\gamma = R_{A\gamma} (\langle c_{A\gamma} \rangle^\gamma, \langle c_{B\gamma} \rangle^\gamma, \dots, \langle c_{N\gamma} \rangle^\gamma) \quad (1.50)$$

This approximation requires that the concentration gradients be *small enough*, and what is meant by *small enough* has been explored by Wood and Whitaker [18, 19] for the case of biological reaction rate mechanisms. When Eq. (1.50) is valid, the treatment of *homogeneous* reactions in porous media becomes a routine matter and is not considered further in this chapter. When Eq. (1.50) is *not valid* the rate of homogeneous reaction will depend on $\nabla \langle c_{A\gamma} \rangle^\gamma, \nabla \langle c_{B\gamma} \rangle^\gamma$, etc., in addition to $\langle c_{A\gamma} \rangle^\gamma, \langle c_{B\gamma} \rangle^\gamma$, etc.

The chemical kinetic constitutive equation for the *heterogeneous* rate of reaction can be expressed as

$$R_{As} = R_{As}(c_{As}, c_{Bs}, \dots, c_{Ns}) \quad (1.51)$$

and here we see the need to relate the surface concentrations, $c_{As}, c_{Bs}, \dots, c_{Ns}$, to the bulk concentrations, $c_{A\gamma}, c_{B\gamma}, \dots, c_{N\gamma}$, and subsequently to the local volume-averaged concentrations, $\langle c_{A\gamma} \rangle^\gamma, \langle c_{B\gamma} \rangle^\gamma, \dots, \langle c_{N\gamma} \rangle^\gamma$. For heterogeneous reaction to occur, adsorption at the catalytic surface must also occur. However, there are many transient processes of mass transfer with heterogeneous reaction for which the catalytic surface can be treated as *quasi-steady* [20, 21]. When homogeneous reactions can be ignored and the catalytic surface can be treated as quasi-steady, the local volume-averaged transport equation simplifies to

$$\underbrace{\varepsilon_\gamma \frac{\partial \langle c_{A\gamma} \rangle^\gamma}{\partial t}}_{\text{accumulation}} + \underbrace{\nabla \cdot \langle c_{A\gamma} \mathbf{v}_{A\gamma} \rangle}_{\text{transport}} = \underbrace{a_v \langle R_{As} \rangle_{\gamma\kappa}}_{\text{heterogeneous reaction}} \quad (1.52)$$

and this result provides the basis for several special forms.

1.6 Convective and Diffusive Transport

Before examining the heterogeneous reaction rate in Eq. (1.52), we consider the transport term, $\langle c_{A\gamma} \mathbf{v}_{A\gamma} \rangle$. We begin with the mixed-mode decomposition given by Eq. (1.12) in order to obtain

$$\underbrace{\langle c_{A\gamma} \mathbf{v}_{A\gamma} \rangle}_{\substack{\text{total molar} \\ \text{flux}}} = \underbrace{\langle c_{A\gamma} \mathbf{v}_\gamma \rangle}_{\substack{\text{molar convective} \\ \text{flux}}} + \underbrace{\langle c_{A\gamma} \mathbf{u}_{A\gamma} \rangle}_{\substack{\text{mixed-mode} \\ \text{diffusive flux}}} \quad (1.53)$$

Here the convective flux is given in terms of the average of a product, and we want to express this flux in terms of the product of averages. As in the case of turbulent transport, this suggests the use of decompositions given by

$$c_{A\gamma} = \langle c_{A\gamma} \rangle^\gamma + \tilde{c}_{A\gamma}, \quad \mathbf{v}_\gamma = \langle \mathbf{v}_\gamma \rangle^\gamma + \tilde{\mathbf{v}}_\gamma \quad (1.54)$$

At this point one can follow a detailed analysis [5, chapter 3] of the convective transport to arrive at

$$\underbrace{\langle c_{A\gamma} \mathbf{v}_{A\gamma} \rangle}_{\substack{\text{total flux}}} = \underbrace{\varepsilon_\gamma \langle c_{A\gamma} \rangle^\gamma \langle \mathbf{v}_\gamma \rangle}_{\substack{\text{average convective} \\ \text{flux}}} + \underbrace{\langle \tilde{c}_{A\gamma} \tilde{\mathbf{v}}_\gamma \rangle}_{\substack{\text{dispersive} \\ \text{flux}}} + \underbrace{\langle \mathbf{J}_{A\gamma} \rangle}_{\substack{\text{mixed-mode} \\ \text{diffusive flux}}} \quad (1.55)$$

Here we have used the intrinsic average concentration since this is most closely related to the concentration in the fluid phase, and we have used the superficial average velocity since this is the quantity that normally appears in Darcy's law [5] or the Forchheimer equation [22]. Use of Eq. (1.55) in Eq. (1.52) leads to

$$\varepsilon_\gamma \frac{\partial \langle c_{A\gamma} \rangle^\gamma}{\partial t} + \nabla \cdot (\varepsilon_\gamma \langle c_{A\gamma} \rangle^\gamma \langle \mathbf{v}_\gamma \rangle) = - \underbrace{\nabla \cdot \langle \mathbf{J}_{A\gamma} \rangle}_{\text{diffusive transport}} - \underbrace{\nabla \cdot \langle \tilde{c}_{A\gamma} \tilde{\mathbf{v}}_\gamma \rangle}_{\text{dispersive transport}} + \underbrace{a_v \langle R_{As} \rangle_{\gamma\kappa}}_{\text{heterogeneous reaction}} \quad (1.56)$$

If we treat the catalytic surface as quasi-steady and make use of a simple first-order, irreversible representation for the heterogeneous reaction, one can show that R_{As} is given by [5, section 1.1]

$$R_{As} = -k_{As} c_{As} = - \left(\frac{k_{As} k_{A1}}{k_{As} + k_{-A1}} \right) c_{A\gamma}, \quad \text{at the } \gamma-\kappa \text{ interface} \quad (1.57)$$

when species A is *consumed* at the catalytic surface. Here we have used k_{As} to represent the *intrinsic surface reaction rate coefficient*, while k_{A1} and k_{-A1} are the adsorption and desorption rate coefficients that appear in Eq. (1.3b). Other more complex reaction mechanisms can be proposed; however, if a linear interfacial flux constitutive equation is valid, the heterogeneous reaction rates can be expressed in terms of the bulk concentration as indicated by Eq. (1.57). Under these circumstances the functional dependence indicated in Eq. (1.51) can be simplified to

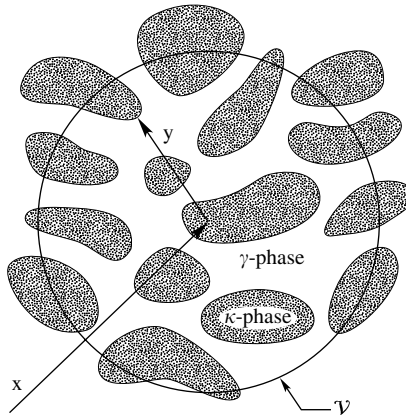
$$R_{As} = R_{As}(c_{A\gamma}, c_{B\gamma}, \dots, c_{N\gamma}), \quad \text{at the } \gamma-\kappa \text{ interface} \quad (1.58)$$

Given the type of constraints developed elsewhere [18, 19], the interfacial area average of the heterogeneous rate of reaction can be expressed as

$$\langle R_{As} \rangle_{\gamma\kappa} = \langle R_{As} \rangle_{\gamma\kappa}(\langle c_{A\gamma} \rangle_{\gamma\kappa}, \langle c_{B\gamma} \rangle_{\gamma\kappa}, \dots, \langle c_{N\gamma} \rangle_{\gamma\kappa}), \quad \text{at the } \gamma-\kappa \text{ interface} \quad (1.59)$$

Sometimes confusion exists concerning the idea of an *area averaged bulk concentration*, and to clarify this idea we consider the averaging volume illustrated in [Figure 1.3](#). There we have shown an averaging volume with the centroid located (arbitrarily) in the κ -phase. In this case, the area average of the bulk concentration is given explicitly by

$$\langle c_{A\gamma} \rangle_{\gamma\kappa}|_x = \frac{1}{A_{\gamma\kappa}(x)} \int_{A_{\gamma\kappa}(x)} c_{A\gamma}|_{x+y} dA \quad (1.60)$$

**FIGURE 1.3**

Position vectors associated with the area average over the $\gamma-\kappa$ interface.

in which \mathbf{x} locates the centroid of the averaging volume and \mathbf{y} locates points on the $\gamma-\kappa$ interface. We have used $A_{\gamma\kappa}(\mathbf{x})$ to represent the area of the $\gamma-\kappa$ interface contained within the averaging volume.

To complete our analysis of Eq. (1.59), we need to know how the area-averaged concentration, $\langle c_{A\gamma} \rangle_{\gamma\kappa}$, is related to the volume-averaged concentration, $\langle c_{A\gamma} \rangle^\gamma$. Here we consider two special cases; one in which convective transport dominates the system illustrated in Figure 1.1 and one in which diffusive transport dominates the system. The former case is associated with the analysis of a chemical reactor (see Figure 1.2) containing a nonporous catalyst, while the latter case is associated with analysis of diffusion and reaction in a porous catalyst. When the convective transport is *large enough* so that the area-averaged and volume-averaged concentrations are constrained by

$$\langle c_{A\gamma} \rangle^\gamma - \langle c_{A\gamma} \rangle_{\gamma\kappa} \ll \langle c_{A\gamma} \rangle^\gamma \quad (1.61)$$

and small causes give rise to small effects [23], we can express Eq. (1.56) as

$$\begin{aligned} \varepsilon_\gamma \frac{\partial \langle c_{A\gamma} \rangle^\gamma}{\partial t} + \nabla \cdot (\varepsilon_\gamma \langle c_{A\gamma} \rangle^\gamma \langle \mathbf{v}_\gamma \rangle) &= -\nabla \cdot \langle \mathbf{J}_{A\gamma} \rangle - \nabla \cdot \langle \tilde{c}_{A\gamma} \tilde{\mathbf{v}}_\gamma \rangle \\ &+ a_v (R_{As})_{\gamma\kappa} (\langle c_{A\gamma} \rangle^\gamma, \langle c_{B\gamma} \rangle^\gamma, \dots, \langle c_{N\gamma} \rangle^\gamma) \end{aligned} \quad (1.62)$$

When convective effects in an *isothermal reactor* are sufficiently large, both axial dispersion and axial diffusion can be neglected according to

$$\varepsilon_\gamma \langle c_{A\gamma} \rangle^\gamma \langle \mathbf{v}_\gamma \rangle \gg \langle \tilde{c}_{A\gamma} \tilde{\mathbf{v}}_\gamma \rangle \gg \langle \mathbf{J}_{A\gamma} \rangle \quad (1.63)$$

This leads to the special form of Eq. (1.62) given by

$$\varepsilon_\gamma \frac{\partial \langle c_{A\gamma} \rangle^\gamma}{\partial t} + \nabla \cdot (\varepsilon_\gamma \langle c_{A\gamma} \rangle^\gamma \langle \mathbf{v}_\gamma \rangle) = a_v \langle R_{As} \rangle_{\gamma\kappa} (\langle c_{A\gamma} \rangle^\gamma, \langle c_{B\gamma} \rangle^\gamma, \dots, \langle c_{N\gamma} \rangle^\gamma), \quad A = 1, 2, \dots, N \quad (1.64)$$

and the coupled set of volume-averaged transport equations can be solved directly to determine the rate of heterogeneous reaction. A complete analysis of this problem requires that constraints associated with the inequalities given by Eq. (1.63) be developed [24]. In addition, a complete analysis of Eq. (1.56) requires a detailed analysis of the dispersive flux, and that problem is left for a subsequent study.

When convective transport can be neglected, the inequalities given by Eq. (1.63) are reversed and we have

$$\langle \tilde{c}_{A\gamma} \tilde{\mathbf{v}}_\gamma \rangle \ll \varepsilon_\gamma \langle c_{A\gamma} \rangle^\gamma \langle \mathbf{v}_\gamma \rangle \ll \langle \mathbf{J}_{A\gamma} \rangle \quad (1.65)$$

The classic approach in this case is to assume that the inequality given by Eq. (1.61) is also satisfied and this leads to a transport equation that takes the form

$$\varepsilon_\gamma \frac{\partial \langle c_{A\gamma} \rangle^\gamma}{\partial t} = -\nabla \cdot \langle \mathbf{J}_{A\gamma} \rangle + a_v \langle R_{As} \rangle_{\gamma\kappa} (\langle c_{A\gamma} \rangle^\gamma, \langle c_{B\gamma} \rangle^\gamma, \dots, \langle c_{N\gamma} \rangle^\gamma), \\ A = 1, 2, \dots, N \quad (1.66)$$

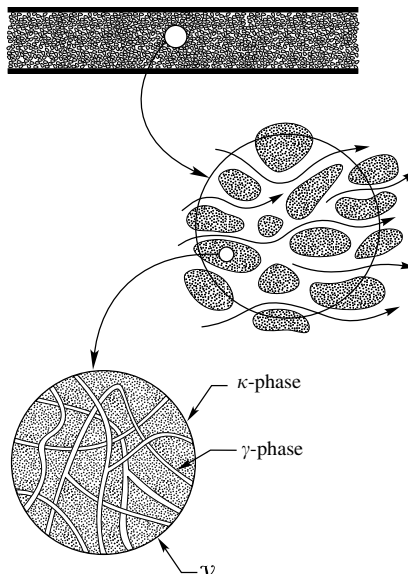


FIGURE 1.4

Diffusion and reaction in a porous catalyst.

Once again, the constraints associated with Eqs. (1.61) and (1.66) should be developed, and some of these are given elsewhere [12]. Equation (1.66) forms the basis for the classic problem of diffusion and reaction in a porous catalyst such as we have illustrated in [Figure 1.4](#). At this point we have not clearly identified how one goes from Eq. (1.51) to Eq. (1.59) for the nondilute solution described by Eqs. (1.1) and (1.2). That analysis will surely require a detailed treatment of the diffusive flux, and in the remainder of this chapter we direct our attention to the treatment of the process of diffusion and reaction in a porous catalyst for which Eq. (1.66) is applicable.

1.7 Nondilute Diffusion

We begin this part of our study with the use of Eq. (1.34) in Eq. (1.66) to obtain

$$\varepsilon_\gamma \frac{\partial \langle c_{A\gamma} \rangle^\gamma}{\partial t} = \nabla \cdot \left\langle c_\gamma \sum_{E=1}^{E=N-1} D_{AE} \nabla x_{E\gamma} \right\rangle + a_v \langle R_{AS} \rangle_{\gamma K} (\langle c_{A\gamma} \rangle^\gamma, \langle c_{B\gamma} \rangle^\gamma, \dots, \langle c_{N\gamma} \rangle^\gamma), \quad A = 1, 2, \dots, N \quad (1.67)$$

in which the diffusive flux is *nonlinear* because D_{AE} depends on the $N - 1$ mole fractions. This transport equation must be solved subject to the auxiliary conditions given by

$$c_\gamma = \sum_{E=1}^{E=N} c_{E\gamma}, \quad 1 = \sum_{E=1}^{E=N} x_{E\gamma} \quad (1.68)$$

and this suggests that numerical methods must be used. However, the diffusive flux must be arranged in terms of volume-averaged quantities before Eq. (1.67) can be solved, and any reasonable simplifications that can be made should be imposed on the analysis.

1.7.1 Constant Total Molar Concentration

Some nondilute solutions can be treated as having a constant total molar concentration and this simplification allows us to express Eq. (1.67) as

$$\varepsilon_\gamma \frac{\partial \langle c_{A\gamma} \rangle^\gamma}{\partial t} = \nabla \cdot \left\langle \sum_{E=1}^{E=N-1} D_{AE} \nabla c_{E\gamma} \right\rangle + a_v \langle R_{AS} \rangle_{\gamma K} (\langle c_{A\gamma} \rangle^\gamma, \langle c_{B\gamma} \rangle^\gamma, \dots, \langle c_{N\gamma} \rangle^\gamma), \quad A = 1, 2, \dots, N \quad (1.69)$$

The *restriction* associated with this simplification is given by

$$x_{A\gamma} \nabla c_\gamma \ll c_\gamma \nabla x_{A\gamma}, \quad A = 1, 2, \dots, N \quad (1.70)$$

and it is important to understand that the *mathematical consequence* of this restriction is given by

$$c_\gamma = \langle c_\gamma \rangle^\gamma = \text{constant} \quad (1.71)$$

Imposition of this condition means that there are only $N - 1$ independent transport equations of the form given by Eq. (1.69), and we shall impose this condition throughout the remainder of this chapter.

At this point we decompose the elements of the diffusion matrix according to

$$D_{AE} = \langle D_{AE} \rangle^\gamma + \tilde{D}_{AE} \quad (1.72)$$

If, for any particular system, we can neglect \tilde{D}_{AE} relative to $\langle D_{AE} \rangle^\gamma$, the transport equation given by Eq. (1.69) can be simplified to

$$\varepsilon_\gamma \frac{\partial \langle c_{A\gamma} \rangle^\gamma}{\partial t} = \nabla \cdot \sum_{E=1}^{E=N-1} \langle D_{AE} \rangle^\gamma \langle \nabla c_{E\gamma} \rangle + a_v \langle R_{As} \rangle_{\gamma\kappa} (\langle c_{A\gamma} \rangle^\gamma, \langle c_{B\gamma} \rangle^\gamma, \dots, \langle c_{(N-1)\gamma} \rangle^\gamma), \\ A = 1, 2, \dots, N - 1 \quad (1.73)$$

When the simplification given by

$$\tilde{D}_{AE} \ll \langle D_{AE} \rangle^\gamma \quad (1.74)$$

is *not satisfactory*, it may be possible to develop a *correction* based on the retention of the spatial deviation, \tilde{D}_{AE} ; however, it is not clear how this type of analysis would evolve and further study of this aspect of the diffusion process is in order.

1.7.2 Volume Average of the Diffusive Flux

The volume averaging theorem can be used with the average of the gradient in Eq. (1.73) in order to obtain

$$\langle \nabla c_{E\gamma} \rangle = \nabla \langle c_{E\gamma} \rangle + \frac{1}{V} \int_{A_{\gamma\kappa}} \mathbf{n}_{\gamma\kappa} c_{E\gamma} \, dA \quad (1.75)$$

and one can follow an established analysis [5, chapter 1] in order to express this result as

$$\langle \nabla c_{E\gamma} \rangle = \varepsilon_\gamma \nabla \langle c_{E\gamma} \rangle^\gamma + \frac{1}{V} \int_{A_{\gamma\kappa}} \mathbf{n}_{\gamma\kappa} \tilde{c}_{E\gamma} dA \quad (1.76)$$

Use of this result in Eq. (1.73) provides

$$\begin{aligned} \varepsilon_\gamma \frac{\partial \langle c_{A\gamma} \rangle^\gamma}{\partial t} &= \nabla \cdot \left[\sum_{E=1}^{E=N-1} \langle D_{AE} \rangle^\gamma \left(\underbrace{\varepsilon_\gamma \nabla \langle c_{E\gamma} \rangle^\gamma + \frac{1}{V} \int_{A_{\gamma\kappa}} \mathbf{n}_{\gamma\kappa} \tilde{c}_{E\gamma} dA}_{\text{filter}} \right) \right] \\ &\quad + a_V \langle R_{As} \rangle_{\gamma\kappa} \end{aligned} \quad (1.77)$$

in which the area integral of $\mathbf{n}_{\gamma\kappa} \tilde{c}_{E\gamma}$ has been identified as a *filter*. Not all the information available at the length scale associated with $\tilde{c}_{E\gamma}$ will pass through this filter to influence the transport equation for $\langle c_{A\gamma} \rangle^\gamma$, and the existence of filters of this type is a recurring theme in the method of volume averaging [5].

1.8 Closure

In order to obtain a closed form of Eq. (1.77), we need a representation for the spatial deviation concentration, $\tilde{c}_{A\gamma}$, and this requires the development of the *closure problem*. When convective transport is negligible and homogeneous reactions are ignored as being a trivial part of the analysis, Eq. (1.14) takes the form

$$\frac{\partial c_{A\gamma}}{\partial t} = -\nabla \cdot \mathbf{J}_{A\gamma}, \quad A = 1, 2, \dots, N-1 \quad (1.78)$$

Here one must remember that the total molar concentration is a specified constant, thus there are only $N-1$ independent species continuity equations. Use of Eq. (1.34) along with the restriction given by Eq. (1.70) allows us to express this result as

$$\frac{\partial c_{A\gamma}}{\partial t} = \nabla \cdot \sum_{E=1}^{E=N-1} D_{AE} \nabla c_{E\gamma}, \quad A = 1, 2, \dots, N-1 \quad (1.79)$$

and on the basis of Eqs. (1.72) and (1.74) this takes the form

$$\frac{\partial c_{A\gamma}}{\partial t} = \nabla \cdot \sum_{E=1}^{E=N-1} \langle D_{AE} \rangle^\gamma \nabla c_{E\gamma}, \quad A = 1, 2, \dots, N-1 \quad (1.80)$$

If we ignore variations in ε_γ and subtract Eq. (1.77) from Eq. (1.80), we can arrange the result as

$$\frac{\partial \tilde{c}_{A\gamma}}{\partial t} = \nabla \cdot \left[\sum_{E=1}^{E=N-1} \langle D_{AE} \rangle^\gamma \nabla \tilde{c}_{E\gamma} \right] - \nabla \cdot \left[\sum_{E=1}^{E=N-1} \frac{\langle D_{AE} \rangle^\gamma}{\varepsilon_\gamma} \frac{1}{\mathcal{V}} \int_{A_{\gamma\kappa}} \mathbf{n}_{\gamma\kappa} \tilde{c}_{E\gamma} \, dA \right] - \frac{a_v}{\varepsilon_\gamma} \langle R_{As} \rangle_{\gamma\kappa} \quad (1.81)$$

in which it is understood that this result applies to all $N - 1$ species. Equation (1.81) represents the governing differential equation for the spatial deviation concentration, and in order to keep the analysis relatively simple we consider only the first order, irreversible reaction described by Eq. (1.57) and expressed here in the form

$$R_{As} = -k_A c_{A\gamma}, \quad \text{at the } \gamma-\kappa \text{ interface} \quad (1.82)$$

Here one must remember that k_A is determined by the intrinsic surface reaction rate coefficient, the adsorption rate coefficient, and the desorption rate coefficient according to

$$k_A = \frac{k_{As} k_{A1}}{k_{As} + k_{-A1}} \quad (1.83)$$

One must also remember that this is a severe restriction in terms of realistic systems and more general forms for the heterogeneous rate of reaction need to be examined. Use of Eq. (1.82) in Eq. (1.81) leads to the following form

$$\frac{\partial \tilde{c}_{A\gamma}}{\partial t} = \nabla \cdot \left[\sum_{E=1}^{E=N-1} \langle D_{AE} \rangle^\gamma \nabla \tilde{c}_{E\gamma} \right] - \nabla \cdot \left[\sum_{E=1}^{E=N-1} \frac{\langle D_{AE} \rangle^\gamma}{\varepsilon_\gamma} \frac{1}{\mathcal{V}} \int_{A_{\gamma\kappa}} \mathbf{n}_{\gamma\kappa} \tilde{c}_{E\gamma} \, dA \right] + \frac{a_v k_A}{\varepsilon_\gamma} \langle c_{A\gamma} \rangle^\gamma \quad (1.84)$$

Here we have made use of the simplification

$$\langle c_{A\gamma} \rangle_{\gamma\kappa} = \langle c_{A\gamma} \rangle^\gamma \quad (1.85)$$

and the justification is given elsewhere [5, section 1.3.3]. In order to complete the problem statement for $\tilde{c}_{E\gamma}$, we need a boundary condition for $\tilde{c}_{E\gamma}$ at the $\gamma-\kappa$ interface. To develop this boundary condition, we again make use of the quasi-steady form of Eq. (1.2) to obtain

$$\mathbf{J}_{A\gamma} \cdot \mathbf{n}_{\gamma\kappa} = -R_{As}, \quad \text{at the } \gamma-\kappa \text{ interface} \quad (1.86)$$

where we have imposed the restriction given by

$$\mathbf{v}_\gamma \cdot \mathbf{n}_{\gamma\kappa} \ll \mathbf{u}_{A\gamma} \cdot \mathbf{n}_{\gamma\kappa}, \quad \text{at the } \gamma-\kappa \text{ interface} \quad (1.87)$$

This is certainly *consistent with* the inequalities given by Eq. (1.65); however, the neglect of $\mathbf{v}_\gamma \cdot \mathbf{n}_{\gamma\kappa}$ relative to $\mathbf{u}_{A\gamma} \cdot \mathbf{n}_{\gamma\kappa}$ is generally based on the *dilute solution* condition and the validity of Eq. (1.87) is another matter that needs to be carefully considered in a future study. On the basis of Eqs. (1.34), (1.70), (1.72), and Eq. (1.74) along with Eq. (1.82), the jump condition takes the form

$$- \sum_{E=1}^{E=N-1} \mathbf{n}_{\gamma\kappa} \cdot \langle D_{AE} \rangle^\gamma \nabla c_{E\gamma} = k_A c_{A\gamma}, \quad \text{at the } \gamma-\kappa \text{ interface} \quad (1.88)$$

In order to express this boundary condition in terms of the spatial deviation concentration, we make use of the decomposition given by the first of Eq. (1.54) to obtain

$$\begin{aligned} & - \sum_{E=1}^{E=N-1} \mathbf{n}_{\gamma\kappa} \cdot \langle D_{AE} \rangle^\gamma \nabla \tilde{c}_{E\gamma} - k_A \tilde{c}_{A\gamma} \\ &= \sum_{E=1}^{E=N-1} \mathbf{n}_{\gamma\kappa} \cdot \langle D_{AE} \rangle^\gamma \nabla \langle c_{E\gamma} \rangle^\gamma + k_A \langle c_{A\gamma} \rangle^\gamma, \quad \text{at the } \gamma-\kappa \text{ interface} \quad (1.89) \end{aligned}$$

With this result we can construct the following boundary value problem for $\tilde{c}_{A\gamma}$:

$$\underbrace{\frac{\partial \tilde{c}_{A\gamma}}{\partial t}}_{\text{accumulation}} = \underbrace{\nabla \cdot \left[\sum_{E=1}^{E=N-1} \langle D_{AE} \rangle^\gamma \nabla \tilde{c}_{E\gamma} \right]}_{\text{diffusion}} - \underbrace{\nabla \cdot \left[\sum_{E=1}^{E=N-1} \frac{\langle D_{AE} \rangle^\gamma}{\varepsilon_\gamma} \frac{1}{V} \int_{A_{\gamma\kappa}} \mathbf{n}_{\gamma\kappa} \tilde{c}_{E\gamma} dA \right]}_{\text{nonlocal diffusion}} + \underbrace{\frac{a_v k_A}{\varepsilon_\gamma} \langle c_{A\gamma} \rangle^\gamma}_{\text{reaction source}} \quad (1.90)$$

$$-\underbrace{\sum_{E=1}^{E=N-1} \mathbf{n}_{\gamma\kappa} \cdot (D_{AE})^\gamma \nabla \tilde{c}_{E\gamma}}_{\text{diffusive flux}} - \underbrace{k_A \tilde{c}_{A\gamma}}_{\text{heterogeneous reaction}}$$

BC.1

$$= \underbrace{\sum_{E=1}^{E=N-1} \mathbf{n}_{\gamma\kappa} \cdot (D_{AE})^\gamma \nabla \langle c_{E\gamma} \rangle^\gamma}_{\text{diffusive source}} + \underbrace{k_A \langle c_{A\gamma} \rangle^\gamma}_{\text{reaction source}}, \quad \text{at the } \gamma\text{-}\kappa \text{ interface} \quad (1.91)$$

BC.2 $\tilde{c}_{A\gamma} = \mathcal{F}(\mathbf{r}, t), \quad \text{at } \mathcal{A}_{\gamma e} \quad (1.92)$

IC. $\tilde{c}_{A\gamma} = \mathcal{F}(\mathbf{r}), \quad \text{at } t = 0 \quad (1.93)$

In addition to the flux boundary condition given by Eq. (1.91), we have added an unknown condition at the *macroscopic boundary* of the γ -phase, $\mathcal{A}_{\gamma e}$, and an unknown initial condition. Neither of these is important when the separation of length scales indicated by Eq. (1.37) is valid. Under these circumstances, the boundary condition imposed at $\mathcal{A}_{\gamma e}$ influences the $\tilde{c}_{A\gamma}$ -field only over a negligibly small region, and the initial condition given by Eq. (1.93) can be discarded because the closure problem is quasi-steady. Under these circumstances, the closure problem can be solved in some representative, local region [25–29].

In the governing differential equation for $\tilde{c}_{A\gamma}$, we have identified the accumulation term, the diffusion term, the so-called nonlocal diffusion term, and the nonhomogeneous term referred to as the *reaction source*. In the boundary condition imposed at the $\gamma\text{-}\kappa$ interface, we have identified the diffusive flux, the reaction term, and two nonhomogeneous terms that are referred to as the *diffusion source* and the *reaction source*. If the source terms in Eqs. (1.90) and (1.91) were zero, the $\tilde{c}_{A\gamma}$ -field would be generated only by the nonhomogeneous terms that might appear in the boundary condition imposed at $\mathcal{A}_{\gamma e}$ or in the initial condition given by Eq. (1.93). One can easily develop arguments indicating that the closure problem for $\tilde{c}_{A\gamma}$ is quasi-steady, thus the initial condition is of no importance [5, chapter 1]. In addition, one can develop arguments indicating that the boundary condition imposed at $\mathcal{A}_{\gamma e}$ will influence the $\tilde{c}_{A\gamma}$ -field over a negligibly small portion of the field of interest. Because of this, any useful solution to the closure problem must be developed for some *representative region* that is most often conveniently described in terms of a unit cell in a spatially periodic system. These ideas

lead to a closure problem of the form

$$\begin{aligned}
 0 = & \nabla \cdot \underbrace{\left[\sum_{E=1}^{E=N-1} \langle D_{AE} \rangle^\gamma \nabla \tilde{c}_{E\gamma} \right]}_{\text{diffusion}} - \nabla \cdot \underbrace{\left[\sum_{E=1}^{E=N-1} \frac{\langle D_{AE} \rangle^\gamma}{\varepsilon_\gamma \mathcal{V}} \int_{A_{\gamma\kappa}} \mathbf{n}_{\gamma\kappa} \tilde{c}_{E\gamma} dA \right]}_{\text{nonlocal diffusion}} \\
 & + \underbrace{\frac{a_v k_A}{\varepsilon_\gamma} \langle c_{A\gamma} \rangle^\gamma}_{\text{reaction source}} \\
 & - \underbrace{\sum_{E=1}^{E=N-1} \mathbf{n}_{\gamma\kappa} \cdot \langle D_{AE} \rangle^\gamma \nabla \tilde{c}_{E\gamma}}_{\text{diffusive flux}} - \underbrace{k_A \tilde{c}_{A\gamma}}_{\text{heterogeneous reaction}}
 \end{aligned} \tag{1.94}$$

BC.1

$$\begin{aligned}
 & = \sum_{E=1}^{E=N-1} \underbrace{\mathbf{n}_{\gamma\kappa} \cdot \langle D_{AE} \rangle^\gamma \nabla \langle c_{E\gamma} \rangle^\gamma}_{\text{diffusive source}} + \underbrace{k_A \langle c_{A\gamma} \rangle^\gamma}_{\text{reaction source}}, \quad \text{at the } \gamma-\kappa \text{ interface}
 \end{aligned} \tag{1.95}$$

BC.2

$$\tilde{c}_{A\gamma}(\mathbf{r} + \ell_i) = \tilde{c}_{A\gamma}(\mathbf{r}), \quad i = 1, 2, 3 \tag{1.96}$$

Here we have used ℓ_i to represent the three base vectors needed to characterize a spatially periodic system. The use of a spatially periodic system does not limit this analysis to simple systems since a periodic system can be an arbitrary complex [25–29]. However, the periodicity condition imposed by Eq. (1.96) can only be strictly justified when $\langle D_{AE} \rangle^\gamma$, $\langle c_{A\gamma} \rangle^\gamma$, and $\nabla \langle c_{A\gamma} \rangle^\gamma$ are constants and this does not occur for the types of systems under consideration. This matter has been examined elsewhere [5, 12] and the analysis suggests that the traditional separation of length scales allows one to treat $\langle D_{AE} \rangle^\gamma$, $\langle c_{A\gamma} \rangle^\gamma$, and $\nabla \langle c_{A\gamma} \rangle^\gamma$ as constants within the framework of the closure problem.

It is not obvious, but other studies [30] have shown that the reaction source in Eqs. (1.94) and (1.95) makes a negligible contribution to $\tilde{c}_{A\gamma}$. In addition, one can demonstrate [5] that the heterogeneous reaction, $k_A \tilde{c}_{A\gamma}$, can be neglected for all practical problems of diffusion and reaction in porous catalysts. Furthermore, the nonlocal diffusion term is negligible for traditional systems, and under these circumstances the boundary value problem for the spatial deviation concentration takes the form

$$0 = \nabla \cdot \left[\sum_{E=1}^{E=N-1} \langle D_{AE} \rangle^\gamma \nabla \tilde{c}_{E\gamma} \right] \tag{1.97}$$

$$\text{BC.1} \quad - \sum_{E=1}^{E=N-1} \mathbf{n}_{\gamma\kappa} \cdot \langle D_{AE} \rangle^\gamma \nabla \tilde{c}_{E\gamma} = \sum_{E=1}^{E=N-1} \mathbf{n}_{\gamma\kappa} \cdot \langle D_{AE} \rangle^\gamma \nabla \langle c_{E\gamma} \rangle^\gamma, \quad \text{at } A_{\gamma\kappa} \quad (1.98)$$

$$\text{BC.2} \quad \tilde{c}_{A\gamma}(\mathbf{r} + \ell_i) = \tilde{c}_{A\gamma}(\mathbf{r}), \quad i = 1, 2, 3 \quad (1.99)$$

Here one must remember that the subscript A represents species $A, B, C, \dots, N - 1$.

In this boundary value problem, there is only a single nonhomogeneous term represented by $\nabla \langle c_{E\gamma} \rangle^\gamma$ in the boundary condition imposed at the $\gamma-\kappa$ interface. If this source term were zero, the solution to this boundary value problem would be given by $\tilde{c}_{A\gamma} = \text{constant}$. Any constant associated with $\tilde{c}_{A\gamma}$ will not pass through the filter in Eq. (1.77), and this suggests that a solution can be expressed as a function of the gradients of the volume-averaged concentration. Since the system is linear in the $N - 1$ independent gradients of the average concentration, this leads to a solution of the form

$$\begin{aligned} \tilde{c}_{E\gamma} &= \mathbf{b}_{EA} \cdot \nabla \langle c_{A\gamma} \rangle^\gamma + \mathbf{b}_{EB} \cdot \nabla \langle c_{B\gamma} \rangle^\gamma + \mathbf{b}_{EC} \cdot \nabla \langle c_{C\gamma} \rangle^\gamma + \dots \\ &\quad + \mathbf{b}_{E,N-1} \cdot \nabla \langle c_{(N-1)\gamma} \rangle^\gamma \end{aligned} \quad (1.100)$$

If the gradients, $\nabla \langle c_{E\gamma} \rangle^\gamma$, and the diffusivities, $\langle D_{AE} \rangle^\gamma$, in Eq. (1.100) were constants, this representation for $\tilde{c}_{E\gamma}$ would be an *exact* application of the method of superposition [5, problems 1.20 and 2.4; 31]. Since these quantities undergo significant changes over the large length scale, L , illustrated in Figure 1.2, the representation given by Eq. (1.100) is an approximation based on the separation of length scales indicated in Eq. (1.37). The vectors, \mathbf{b}_{EA} , \mathbf{b}_{EB} , etc., in Eq. (1.100) are referred to as the *closure variables* or the *mapping variables* since they map the gradients of the volume-averaged concentrations onto the spatial deviation concentrations. In this representation for $\tilde{c}_{E\gamma}$, we can ignore the spatial variations of $\nabla \langle c_{A\gamma} \rangle^\gamma$, $\nabla \langle c_{B\gamma} \rangle^\gamma$, etc., within the framework of a local closure problem, and we can use Eq. (1.100) in Eq. (1.97) to obtain

$$0 = \nabla \cdot \left[\sum_{E=1}^{E=N-1} \langle D_{AE} \rangle^\gamma \sum_{D=1}^{D=N-1} \nabla \mathbf{b}_{ED} \cdot \nabla \langle c_{D\gamma} \rangle^\gamma \right] \quad (1.101)$$

$$\begin{aligned} \text{BC.1} \quad - \sum_{E=1}^{E=N-1} \mathbf{n}_{\gamma\kappa} \cdot \langle D_{AE} \rangle^\gamma \sum_{D=1}^{D=N-1} \nabla \mathbf{b}_{ED} \cdot \nabla \langle c_{D\gamma} \rangle^\gamma \\ = \sum_{E=1}^{E=N-1} \mathbf{n}_{\gamma\kappa} \cdot \langle D_{AE} \rangle^\gamma \nabla \langle c_{E\gamma} \rangle^\gamma, \quad \text{at } A_{\gamma\kappa} \end{aligned} \quad (1.102)$$

$$\text{BC.2} \quad \mathbf{b}_{AE}(\mathbf{r} + \ell_i) = \mathbf{b}_{AE}(\mathbf{r}), \quad i = 1, 2, 3, \quad A = 1, 2, \dots, N - 1 \quad (1.103)$$

The derivation of Eqs. (1.101) and (1.102) requires the use of simplifications of the form

$$\nabla (\mathbf{b}_{EA} \cdot \nabla \langle c_{A\gamma} \rangle^\gamma) = \nabla \mathbf{b}_{EA} \cdot \nabla \langle c_{A\gamma} \rangle^\gamma \quad (1.104)$$

which result from the inequality

$$\mathbf{b}_{EA} \cdot \nabla \nabla \langle c_{A\gamma} \rangle^\gamma \ll \nabla \mathbf{b}_{EA} \cdot \nabla \langle c_{A\gamma} \rangle^\gamma \quad (1.105)$$

The basis for this inequality is the separation of length scales indicated by Eq. (1.37), and a detailed discussion is available elsewhere [5]. One should keep in mind that the boundary value problem given by Eqs. (1.101) through (1.103) applies to all $N - 1$ species and that the $N - 1$ concentration gradients are independent. This latter condition allows us to obtain

$$0 = \nabla \cdot \left[\sum_{E=1}^{E=N-1} \langle D_{AE} \rangle^\gamma \nabla \mathbf{b}_{ED} \right], \quad D = 1, 2, \dots, N - 1 \quad (1.106)$$

BC.1

$$- \sum_{E=1}^{E=N-1} \mathbf{n}_{\gamma\kappa} \cdot \langle D_{AE} \rangle^\gamma \nabla \mathbf{b}_{ED} = \mathbf{n}_{\gamma\kappa} \langle D_{AD} \rangle^\gamma, \quad D = 1, 2, \dots, N - 1, \quad \text{at } A_{\gamma\kappa} \quad (1.107)$$

$$\text{Periodicity: } \mathbf{b}_{AD}(\mathbf{r} + \ell_i) = \mathbf{b}_{AD}(\mathbf{r}), \quad i = 1, 2, 3, \quad D = 1, 2, \dots, N - 1 \quad (1.108)$$

At this point it is convenient to expand the closure problem for species A in order to obtain

First Problem for Species A

$$0 = \nabla \cdot \left\{ \langle D_{AA} \rangle^\gamma \left[\nabla \mathbf{b}_{AA} + (\langle D_{AA} \rangle^\gamma)^{-1} \langle D_{AB} \rangle^\gamma \nabla \mathbf{b}_{BA} + (\langle D_{AA} \rangle^\gamma)^{-1} \times \langle D_{AC} \rangle^\gamma \nabla \mathbf{b}_{CA} + \dots + (\langle D_{AA} \rangle^\gamma)^{-1} \langle D_{A,N-1} \rangle^\gamma \nabla \mathbf{b}_{N-1,A} \right] \right\} \quad (1.109a)$$

$$\begin{aligned} & - \mathbf{n}_{\gamma\kappa} \cdot \nabla \mathbf{b}_{AA} - \mathbf{n}_{\gamma\kappa} \cdot (\langle D_{AA} \rangle^\gamma)^{-1} \langle D_{AB} \rangle^\gamma \nabla \mathbf{b}_{BA} - \mathbf{n}_{\gamma\kappa} \cdot (\langle D_{AA} \rangle^\gamma)^{-1} \\ & \quad \times \langle D_{AC} \rangle^\gamma \nabla \mathbf{b}_{CA} - \dots - \mathbf{n}_{\gamma\kappa} \cdot (\langle D_{AA} \rangle^\gamma)^{-1} \\ & \quad \times \langle D_{A,N-1} \rangle^\gamma \nabla \mathbf{b}_{N-1,A} = \mathbf{n}_{\gamma\kappa}, \quad \text{at } A_{\gamma\kappa} \end{aligned} \quad (1.109b)$$

$$\text{Periodicity: } \mathbf{b}_{DA}(\mathbf{r} + \ell_i) = \mathbf{b}_{DA}(\mathbf{r}), \quad i = 1, 2, 3, \quad D = 1, 2, \dots, N - 1 \quad (1.109c)$$

Second Problem for Species A

$$0 = \nabla \cdot \left\{ \langle D_{AB} \rangle^\gamma \left[(\langle D_{AB} \rangle^\gamma)^{-1} \langle D_{AA} \rangle^\gamma \nabla \mathbf{b}_{AB} + \nabla \mathbf{b}_{BB} + (\langle D_{AB} \rangle^\gamma)^{-1} \times \langle D_{AC} \rangle^\gamma \nabla \mathbf{b}_{CB} + \dots + (\langle D_{AB} \rangle^\gamma)^{-1} \langle D_{A,N-1} \rangle^\gamma \nabla \mathbf{b}_{N-1,B} \right] \right\} \\ (1.110a)$$

$$\text{BC. } -\mathbf{n}_{\gamma\kappa} \cdot \nabla \mathbf{b}_{AA} - \mathbf{n}_{\gamma\kappa} \cdot (\langle D_{AA} \rangle^\gamma)^{-1} \langle D_{AB} \rangle^\gamma \nabla \mathbf{b}_{BA} - \mathbf{n}_{\gamma\kappa} \cdot (\langle D_{AA} \rangle^\gamma)^{-1} \times \langle D_{AC} \rangle^\gamma \nabla \mathbf{b}_{CA} - \dots - \mathbf{n}_{\gamma\kappa} \cdot (\langle D_{AA} \rangle^\gamma)^{-1} \times \langle D_{A,N-1} \rangle^\gamma \nabla \mathbf{b}_{N-1,A} = \mathbf{n}_{\gamma\kappa}, \quad \text{at } A_{\gamma\kappa} \\ (1.110b)$$

$$\text{Periodicity: } \mathbf{b}_{DB}(\mathbf{r} + \ell_i) = \mathbf{b}_{DB}(\mathbf{r}), \quad i = 1, 2, 3, \quad D = 1, 2, \dots, N-1 \\ (1.110c)$$

Third Problem for Species A

An analogous boundary value problem involving

$$\mathbf{b}_{AC}, \mathbf{b}_{BC}, \mathbf{b}_{CC}, \dots, \mathbf{b}_{N-1,C} \quad (1.111)$$

N-1 Problem for Species A

An analogous boundary value problem involving

$$\mathbf{b}_{A,N-1}, \mathbf{b}_{B,N-1}, \mathbf{b}_{C,N-1}, \dots, \mathbf{b}_{N-1,N-1} \quad (1.112)$$

Here it is convenient to define a new set of *closure variables* or *mapping variables* according to

$$\mathbf{d}_{AA} = \mathbf{b}_{AA} + (\langle D_{AA} \rangle^\gamma)^{-1} \langle D_{AB} \rangle^\gamma \mathbf{b}_{BA} + (\langle D_{AA} \rangle^\gamma)^{-1} \langle D_{AC} \rangle^\gamma \mathbf{b}_{CA} \\ + \dots + (\langle D_{AA} \rangle^\gamma)^{-1} \langle D_{A,N-1} \rangle^\gamma \mathbf{b}_{N-1,A} \quad (1.113a)$$

$$\mathbf{d}_{AB} = (\langle D_{AB} \rangle^\gamma)^{-1} \langle D_{AA} \rangle^\gamma \mathbf{b}_{AB} + \mathbf{b}_{BB} + (\langle D_{AB} \rangle^\gamma)^{-1} \langle D_{AC} \rangle^\gamma \mathbf{b}_{CB} \\ + \dots + (\langle D_{AB} \rangle^\gamma)^{-1} \langle D_{A,N-1} \rangle^\gamma \mathbf{b}_{N-1,B} \quad (1.113b)$$

$$\mathbf{d}_{AC} = (\langle D_{AC} \rangle^\gamma)^{-1} \langle D_{AA} \rangle^\gamma \mathbf{b}_{AC} + (\langle D_{AC} \rangle^\gamma)^{-1} \langle D_{AB} \rangle^\gamma \mathbf{b}_{BC} \\ + \mathbf{b}_{CC} + \dots + (\langle D_{AC} \rangle^\gamma)^{-1} \langle D_{A,N-1} \rangle^\gamma \mathbf{b}_{N-1,C} \quad (1.113c) \\ \text{etc.} \quad (1.113n-1)$$

With these definitions, the closure problems take the following simplified forms:

First Problem for Species A

$$0 = \nabla^2 \mathbf{d}_{AA} \quad (1.114a)$$

$$\text{BC.} \quad -\mathbf{n}_{\gamma\kappa} \cdot \nabla \mathbf{d}_{AA} = \mathbf{n}_{\gamma\kappa}, \quad \text{at } A_{\gamma\kappa} \quad (1.114b)$$

$$\text{Periodicity:} \quad \mathbf{d}_{AA}(\mathbf{r} + \ell_i) = \mathbf{d}_{AA}(\mathbf{r}), \quad i = 1, 2, 3 \quad (1.114c)$$

Second Problem for Species A

$$0 = \nabla^2 \mathbf{d}_{AB} \quad (1.115a)$$

$$\text{BC.} \quad -\mathbf{n}_{\gamma\kappa} \cdot \nabla \mathbf{d}_{AB} = \mathbf{n}_{\gamma\kappa}, \quad \text{at } A_{\gamma\kappa} \quad (1.115b)$$

$$\text{Periodicity:} \quad \mathbf{d}_{AB}(\mathbf{r} + \ell_i) = \mathbf{d}_{AB}(\mathbf{r}), \quad i = 1, 2, 3 \quad (1.115c)$$

Third Problem for Species A

$$\text{An analogous boundary value problem for } \mathbf{d}_{AC} \quad (1.116)$$

N – 1 Problem for Species A

$$\text{An analogous boundary value problem for } \mathbf{d}_{A,N-1} \quad (1.117)$$

To obtain these simplified forms, one must make repeated use of inequalities of the form given by Eq. (1.105). Each one of these closure problems is identical to that obtained by Ryan et al. [30] and solutions have been developed by several researchers [30, 32–37]. In each case, the closure problem determines the *closure variable* to within an arbitrary constant, and this constant can be specified by imposing the condition

$$\langle \tilde{c}_{D\gamma} \rangle^\gamma = 0, \quad \text{or} \quad \langle \mathbf{d}_{GD} \rangle^\gamma = 0, \quad \begin{cases} G = 1, 2, \dots, N-1 \\ D = 1, 2, \dots, N-1 \end{cases} \quad (1.118)$$

However, any constant associated with a closure variable will not pass through the filter in Eq. (1.77), thus this constraint on the average is not necessary.

1.8.1 Closed Form

The closed form of Eq. (1.77) can be obtained by use of the representation for $\tilde{c}_{E\gamma}$ given by Eq. (1.100), along with the definitions represented by Eqs. (1.113).

After some algebraic manipulation, one obtains

$$\begin{aligned}
 \varepsilon_\gamma \frac{\partial \langle c_{A\gamma} \rangle^\gamma}{\partial t} = & \nabla \cdot \left[\varepsilon_\gamma \langle D_{AA} \rangle^\gamma \left(\mathbf{I} + \frac{1}{V_\gamma} \int_{A_{\gamma\kappa}} \mathbf{n}_{\gamma\kappa} \mathbf{d}_{AA} dA \right) \cdot \nabla \langle c_{A\gamma} \rangle^\gamma \right. \\
 & + \varepsilon_\gamma \langle D_{AB} \rangle^\gamma \left(\mathbf{I} + \frac{1}{V_\gamma} \int_{A_{\gamma\kappa}} \mathbf{n}_{\gamma\kappa} \mathbf{d}_{AB} dA \right) \cdot \nabla \langle c_{B\gamma} \rangle^\gamma \\
 & + \varepsilon_\gamma \langle D_{AC} \rangle^\gamma \left(\mathbf{I} + \frac{1}{V_\gamma} \int_{A_{\gamma\kappa}} \mathbf{n}_{\gamma\kappa} \mathbf{d}_{AC} dA \right) \cdot \nabla \langle c_{C\gamma} \rangle^\gamma + \dots \\
 & \dots + \varepsilon_\gamma \langle D_{A,N-1} \rangle^\gamma \left(\mathbf{I} + \frac{1}{V_\gamma} \int_{A_{\gamma\kappa}} \mathbf{n}_{\gamma\kappa} \mathbf{d}_{A,N-1} dA \right) \cdot \nabla \langle c_{N-1\gamma} \rangle^\gamma \left. \right] \\
 & + a_v k_A \langle c_{A\gamma} \rangle^\gamma
 \end{aligned} \tag{1.119}$$

Here one must remember that we have restricted the analysis to the simple, linear reaction rate expression given by Eq. (1.82), and one normally must work with more complex representations for R_{As} .

On the basis of the closure problems given by Eqs. (1.114) through (1.117), we conclude that there is a single tensor that describes the tortuosity for species A . This means that Eq. (1.119) can be expressed as

$$\begin{aligned}
 \varepsilon_\gamma \frac{\partial \langle c_{A\gamma} \rangle^\gamma}{\partial t} = & \nabla \cdot \left[\varepsilon_\gamma \mathbf{D}_{AA}^{\text{eff}} \cdot \nabla \langle c_{A\gamma} \rangle^\gamma + \varepsilon_\gamma \mathbf{D}_{AB}^{\text{eff}} \cdot \nabla \langle c_{B\gamma} \rangle^\gamma + \varepsilon_\gamma \mathbf{D}_{AC}^{\text{eff}} \cdot \nabla \langle c_{C\gamma} \rangle^\gamma \right. \\
 & + \dots + \varepsilon_\gamma \mathbf{D}_{A,N-1}^{\text{eff}} \cdot \nabla \langle c_{(N-1)\gamma} \rangle^\gamma \left. \right] + a_v k_A \langle c_{A\gamma} \rangle^\gamma
 \end{aligned} \tag{1.120}$$

in which the effective diffusivity tensors are related according to

$$\frac{\mathbf{D}_{AA}^{\text{eff}}}{\langle D_{AA} \rangle^\gamma} = \frac{\mathbf{D}_{AB}^{\text{eff}}}{\langle D_{AB} \rangle^\gamma} = \frac{\mathbf{D}_{AC}^{\text{eff}}}{\langle D_{AC} \rangle^\gamma} = \dots = \frac{\mathbf{D}_{A,N-1}^{\text{eff}}}{\langle D_{A,N-1} \rangle^\gamma} \tag{1.121}$$

The remaining diffusion equations for species $B, C, \dots, N - 1$ have precisely the same form as Eq. (1.120), and the various effective diffusivity tensors are related to each other in the manner indicated by Eq. (1.121). The generic closure problem can be expressed as:

Generic Closure Problem

$$0 = \nabla^2 \mathbf{d} \tag{1.122a}$$

$$\text{BC. } -\mathbf{n}_{\gamma\kappa} \cdot \nabla \mathbf{d} = \mathbf{n}_{\gamma\kappa}, \quad \text{at } A_{\gamma\kappa} \tag{1.122b}$$

$$\text{Periodicity: } \mathbf{d}(\mathbf{r} + \ell_i) = \mathbf{d}(\mathbf{r}), \quad i = 1, 2, 3 \tag{1.122c}$$

and the solution for this boundary value problem is relatively straightforward. The existence of a single, generic closure problem that allows for the determination of all the effective diffusivity tensors represents the main finding of this work. On the basis of this single closure problem, the tortuosity

tensor is defined according to

$$\boldsymbol{\tau} = \mathbf{I} + \frac{1}{V_\gamma} \int_{A_{\gamma\kappa}} \mathbf{n}_{\gamma\kappa} \mathbf{d} dA \quad (1.123)$$

and we can express Eq. (1.121) in the form

$$\mathbf{D}_{AA}^{\text{eff}} = \boldsymbol{\tau} \langle D_{AA} \rangle^\gamma, \mathbf{D}_{AB}^{\text{eff}} = \boldsymbol{\tau} \langle D_{AB} \rangle^\gamma, \dots, \mathbf{D}_{A,N-1}^{\text{eff}} = \boldsymbol{\tau} \langle D_{A,N-1} \rangle^\gamma \quad (1.124)$$

Substitution of these results into Eq. (1.120) allows us to represent the local volume-averaged diffusion-reaction equations as

$$\varepsilon_\gamma \frac{\partial \langle c_{A\gamma} \rangle^\gamma}{\partial t} = \nabla \cdot \left[\sum_{E=1}^{E=N-1} \varepsilon_\gamma \boldsymbol{\tau} \langle D_{AE} \rangle^\gamma \cdot \nabla \langle c_{E\gamma} \rangle^\gamma \right] + a_v k_A \langle c_{A\gamma} \rangle^\gamma, \\ A = 1, 2, \dots, N - 1 \quad (1.125)$$

It is important to remember that this analysis has been simplified on the basis of Eq. (1.70), which is equivalent to treating c_γ as a constant as indicated in Eq. (1.71). For a porous medium that is isotropic *in the volume-averaged sense*, the tortuosity tensor takes the classical form

$$\boldsymbol{\tau} = \mathbf{I} \tau^{-1} \quad (1.126)$$

in which \mathbf{I} is the unit tensor and τ is the tortuosity. For isotropic porous media, we can express Eq. (1.125) as

$$\varepsilon_\gamma \frac{\partial \langle c_{A\gamma} \rangle^\gamma}{\partial t} = \nabla \cdot \left[\sum_{E=1}^{E=N-1} (\varepsilon_\gamma / \tau) \langle D_{AE} \rangle^\gamma \nabla \langle c_{E\gamma} \rangle^\gamma \right] + a_v k_A \langle c_{A\gamma} \rangle^\gamma, \\ A = 1, 2, \dots, N - 1 \quad (1.127)$$

Often ε_γ and τ can be treated as constants; however, the diffusion coefficients in this transport equation will be functions of the local volume-averaged mole fractions and we are faced with a coupled, nonlinear diffusion and reaction problem.

The decoupling of the different closure problems is reminiscent of the classical results of the linearized theory proposed by Toor [38] or Stewart and Prober [39]. In that theory, variations of the coefficients in the diffusion matrix are assumed to be negligible. As a consequence, a special change of variable leads to a diagonal diffusion matrix and a set of uncoupled balance equations. Solving those equations directly for a spatially periodic porous medium would show that the pore scale geometry has the same influence on the resulting concentration fields, that is, the *tortuosity effects are the same for all constituents*. The question of the diagonalization of general diffusion matrices has been discussed in detail by Giovangigli [40]. If nonlinearities are

retained in the original formulation of the diffusion problem, the simplifications described by Giovangigli [40] are, in general, not available. However, we have achieved a similar simplification in the *closure problem* for the process of diffusion and reaction, and in the following paragraphs we wish to illustrate this idea in a more compact form than that given by Eqs. (1.97) through (1.125).

We begin a compact presentation of the theory with Eqs. (1.97) through (1.99) written in the form

$$0 = \nabla \cdot \{[\langle D \rangle^\gamma][\nabla \tilde{c}_\gamma]\} \quad (1.128a)$$

$$\text{BC.1} \quad -\mathbf{n}_{\gamma\kappa} \cdot [\langle D \rangle^\gamma][\nabla \tilde{c}_\gamma] = \mathbf{n}_{\gamma\kappa} \cdot [\langle D \rangle^\gamma][\nabla \langle c_\gamma \rangle^\gamma], \quad \text{at } A_{\gamma\kappa} \quad (1.128b)$$

$$\text{Periodicity: } [\tilde{c}_\gamma](\mathbf{r} + \ell_i) = [\tilde{c}_\gamma](\mathbf{r}), \quad i = 1, 2, 3 \quad (1.128c)$$

The nomenclature used in this formulation of the closure problem is given by

$$[\langle D \rangle^\gamma] = \begin{bmatrix} \langle D_{AA} \rangle^\gamma & \langle D_{AB} \rangle^\gamma & \langle D_{AC} \rangle^\gamma & \cdots & \langle D_{A(N-1)} \rangle^\gamma \\ \langle D_{BA} \rangle^\gamma & \cdots & \cdots & \cdots & \langle D_{B(N-1)} \rangle^\gamma \\ \langle D_{CA} \rangle^\gamma & \cdots & \cdots & \cdots & \langle D_{C(N-1)} \rangle^\gamma \\ \vdots & \cdots & \cdots & \cdots & \vdots \\ \langle D_{(N-1)A} \rangle^\gamma & \cdots & \cdots & \cdots & \langle D_{(N-1)(N-1)} \rangle^\gamma \end{bmatrix} \quad (1.129a)$$

$$[\nabla \tilde{c}_\gamma] = \begin{bmatrix} \nabla \tilde{c}_{A\gamma} \\ \nabla \tilde{c}_{B\gamma} \\ \nabla \tilde{c}_{C\gamma} \\ \vdots \\ \nabla \tilde{c}_{(N-1)\gamma} \end{bmatrix}, \quad [\nabla \langle c_\gamma \rangle^\gamma] = \begin{bmatrix} \nabla \langle c_{A\gamma} \rangle^\gamma \\ \nabla \langle c_{B\gamma} \rangle^\gamma \\ \nabla \langle c_{C\gamma} \rangle^\gamma \\ \vdots \\ \nabla \langle c_{(N-1)\gamma} \rangle^\gamma \end{bmatrix} \quad (1.129b)$$

Here one must be careful to note that \tilde{c}_γ does not represent the spatial deviation concentration for the total molar concentration and that $\langle c_\gamma \rangle^\gamma$ does not represent the volume average of the total molar concentration. Within the framework of the closure problem, the elements of $[\langle D \rangle^\gamma]$ are treated as constants, thus the change of variable leading to a diagonal diffusion matrix may be used. We denote the modal matrix by $[P]$ so that the diagonal version of $[\langle D \rangle^\gamma]$ is given by

$$[\langle D \rangle^\gamma]_{\text{diag}} = [P]^{-1}[\langle D \rangle^\gamma][P] \quad (1.130)$$

In addition, we introduce a new concentration deviation and a new average concentration defined by

$$[\tilde{C}_\gamma] = [P]^{-1}[\tilde{c}_\gamma], \quad [\langle C_\gamma \rangle^\gamma] = [P]^{-1}[\langle c_\gamma \rangle^\gamma] \quad (1.131)$$

so that the closure problem can be expressed as

$$0 = \nabla \cdot \{[\langle D \rangle^\gamma]_{\text{diag}}[\nabla \tilde{C}_\gamma]\} \quad (1.132a)$$

$$\text{BC.1} \quad -\mathbf{n}_{\gamma\kappa} \cdot \left\{ [\langle D \rangle^\gamma]_{\text{diag}} [\nabla \tilde{C}_\gamma] \right\} = \mathbf{n}_{\gamma\kappa} \cdot \left\{ [\langle D \rangle^\gamma]_{\text{diag}} [\nabla \langle C_\gamma \rangle^\gamma] \right\}, \quad \text{at } A_{\gamma\kappa} \quad (1.132\text{b})$$

$$\text{Periodicity:} \quad [\tilde{C}_\gamma](\mathbf{r} + \ell_i) = [\tilde{C}_\gamma](\mathbf{r}), \quad i = 1, 2, 3 \quad (1.132\text{c})$$

In this form of the closure problem we see that concentration deviations can be expressed as

$$[\tilde{C}_\gamma] = \mathbf{d} \cdot [\nabla \langle C_\gamma \rangle^\gamma] \quad (1.133)$$

in which \mathbf{d} is the generic *closure variable* determined by Eq. (1.122). We can now revert to the original concentration variable to obtain

$$[\tilde{c}_\gamma] = \mathbf{d} \cdot [\nabla \langle c_\gamma \rangle^\gamma] \quad (1.134)$$

and this indicates that all the gradients, $\nabla \langle c_{A\gamma} \rangle^\gamma$, $\nabla \langle c_{B\gamma} \rangle^\gamma$, etc., are mapped onto the spatial deviation concentrations, $\tilde{c}_{A\gamma}$, $\tilde{c}_{B\gamma}$, etc., in exactly the same manner. From this we conclude that the general expression for the effective diffusivity tensors is intimately related to the possibility of neglecting variations of the diffusion coefficients, $\langle D_{AB} \rangle^\gamma$, etc., at the closure level. When the length scale constraints given by Eq. (1.37) are satisfied, volume-averaged quantities such as $\langle D_{AB} \rangle^\gamma$ can be considered as constants over a unit cell [5, section 1.3] and the general result given by Eq. (1.134) is valid.

1.9 Conclusions

In this chapter we have shown how the coupled, nonlinear diffusion problem can be analyzed to produce volume-averaged transport equations containing effective diffusivity tensors. The original diffusion-reaction problem is described by

$$\frac{\partial c_{A\gamma}}{\partial t} = \nabla \cdot \sum_{E=1}^{E=N-1} D_{AE} \nabla c_{E\gamma}, \quad A = 1, 2, \dots, N-1 \quad (1.135\text{a})$$

$$\text{BC.} \quad - \sum_{E=1}^{E=N-1} \mathbf{n}_{\gamma\kappa} \cdot D_{AE} \nabla c_{E\gamma} = k_A c_{A\gamma}, \quad \text{at the } \gamma\text{-}\kappa \text{ interface} \quad (1.135\text{b})$$

$$c_\gamma = \langle c_\gamma \rangle^\gamma = \text{constant} \quad (1.135\text{c})$$

in which the D_{AE} are functions of the mole fractions. For a porous medium that is isotropic in the volume-averaged sense, the upscaled version of the

diffusion-reaction problem takes the form

$$\varepsilon_\gamma \frac{\partial \langle c_{A\gamma} \rangle^\gamma}{\partial t} = \nabla \cdot \left[\sum_{E=1}^{E=N-1} (\varepsilon_\gamma / \tau) \langle D_{AE} \rangle^\gamma \nabla \langle c_{E\gamma} \rangle^\gamma \right] + a_v k_A \langle c_{A\gamma} \rangle^\gamma, \quad A = 1, 2, \dots, N-1 \quad (1.136)$$

Here we have used the approximation that D_{AE} can be replaced by $\langle D_{AE} \rangle^\gamma$ and that variations of $\langle D_{AE} \rangle^\gamma$ can be ignored within the averaging volume. The fact that only a single tortuosity needs to be determined by Eqs. (1.122) and (1.123) represents the key contribution of this study. It is important to remember that this development is constrained by Eq. (1.61) along with the linear chemical kinetic constitutive equation given by Eq. (1.82). The process of diffusion in porous catalysts is normally associated with *slow* reactions and Eq. (1.61) is satisfactory; however, the first order, irreversible reaction represented by Eq. (1.82) is the exception rather than the rule, and this aspect of the analysis requires further investigation. When convective transport is important, we are normally dealing with *fast* reactions and Eq. (1.61) may not be a satisfactory simplification. An analysis of that case is reserved for a future study, which will also include a careful examination of the simplification indicated by Eq. (1.87).

Nomenclature

$A_{\gamma e}$	area of entrances and exits of the γ -phase contained in the macroscopic region, m^2
$A_{\gamma\kappa}$	area of the $\gamma-\kappa$ interface contained within the averaging volume, m^2
a_v	$A_{\gamma\kappa}/V$, area per unit volume, m^{-1}
\mathbf{b}_γ	body force vector, m/sec^2
$c_{A\gamma}$	bulk concentration of species A in the γ -phase, mol/m^3
$\langle c_{A\gamma} \rangle$	superficial average bulk concentration of species A in the γ -phase, mol/m^3
$\langle c_{A\gamma} \rangle^\gamma$	intrinsic average bulk concentration of species A in the γ -phase, mol/m^3
$\langle c_{A\gamma} \rangle_{\gamma\kappa}$	intrinsic area average bulk concentration of species A at the $\gamma-\kappa$ interface, mol/m^3
$\bar{c}_{A\gamma}$	$c_{A\gamma} - \langle c_{A\gamma} \rangle^\gamma$, spatial deviation concentration of species A , mol/m^3
c_γ	$\sum_{A=1}^{A=N} c_{A\gamma}$, total molar concentration, mol/m^3
c_{As}	surface concentration of species A associated with the $\gamma-\kappa$ interface, mol/m^2
\mathcal{D}_{AB}	binary diffusion coefficient for species A and B , m^2/sec
\mathcal{D}_{Am}	$\mathcal{D}_{Am}^{-1} = \sum_{\substack{E=1 \\ E \neq A}}^{E=N} x_{E\gamma} / \mathcal{D}_{AE}$, mixture diffusivity, m^2/sec

$[D]$	diffusivity matrix, m^2/sec
D_{AE}	element of the diffusivity matrix, m^2/sec
$\langle D_{AE} \rangle^\gamma$	intrinsic average element of the diffusivity matrix, m^2/sec
\tilde{D}_{AE}	$D_{AE} - \langle D_{AE} \rangle^\gamma$, spatial deviation of an element of the diffusivity matrix, m^2/sec
$\mathbf{J}_{A\gamma}$	$c_{A\gamma} \mathbf{u}_{A\gamma}$, mixed-mode diffusive flux, $\text{mol}/\text{m}^2\text{sec}$
K_A	adsorption equilibrium coefficient for species A , m
k_{A1}	adsorption rate coefficient for species A , m/sec
k_{-A1}	desorption rate coefficient for species A , sec^{-1}
k_{As}	intrinsic surface reaction rate coefficient, sec^{-1}
k_A	$k_{As}k_{A1}/(k_{As}+k_{-A1})$, pseudo surface reaction rate coefficient, m/sec
ℓ_γ	small length scale associated with the γ -phase, m
r_o	radius of the averaging volume, m
L	large length scale associated with the porous medium, m
M_A	molecular mass of species A , kg/kg mol
\bar{M}	$\sum_{A=1}^{A=N} x_{A\gamma} M_A$, mean molecular mass, kg/kg mol
$\mathbf{n}_{\gamma\kappa}$	unit normal vector directed from the γ -phase to the κ -phase
\mathbf{r}	position vector, m
$R_{A\gamma}$	rate of homogeneous reaction in the γ -phase, $\text{mol}/\text{m}^3\text{sec}$
R_{As}	rate of heterogeneous reaction associated with the $\gamma-\kappa$ interface, $\text{mol}/\text{m}^2\text{sec}$
$\langle R_{As} \rangle_{\gamma\kappa}$	area average heterogeneous reaction rate for species A , $\text{mol}/\text{m}^2\text{sec}$
t	time, sec
\mathbf{T}_γ	stress tensor for the γ -phase, N/m^2
$\mathbf{v}_{A\gamma}$	$\mathbf{v}_{A\gamma} - \mathbf{v}_\gamma$, mass diffusion velocity, m/sec
$\mathbf{u}_{A\gamma}^*$	$\mathbf{v}_{A\gamma} - \mathbf{v}_\gamma^*$, molar diffusion velocity, m/sec
$\mathbf{v}_{A\gamma}$	velocity of species A in the γ -phase, m/sec
\mathbf{v}_γ	$\sum_{A=1}^{A=N} \omega_{A\gamma} \mathbf{v}_{A\gamma}$, mass average velocity in the γ -phase, m/sec
\mathbf{v}_γ^*	$\sum_{A=1}^{A=N} x_{A\gamma} \mathbf{v}_{A\gamma}$, molar average velocity in the γ -phase, m/sec
$\langle \mathbf{v}_\gamma \rangle^\gamma$	intrinsic mass average velocity in the γ -phase, m/sec
$\langle \mathbf{v}_\gamma \rangle$	superficial mass average velocity in the γ -phase, m/sec
$\tilde{\mathbf{v}}_\gamma$	$\mathbf{v}_\gamma - \langle \mathbf{v}_\gamma \rangle^\gamma$, spatial deviation velocity, m/sec
V	averaging volume, m^3
V_γ	volume of the γ -phase contained within the averaging volume, m^3
V_κ	volume of the κ -phase contained within the averaging volume, m^3
$x_{A\gamma}$	$c_{A\gamma}/c_\gamma$, mole fraction of species A in the γ -phase
\mathbf{x}	position vector locating the center of the averaging volume, m
\mathbf{y}	position vector locating points on the $\gamma-\kappa$ interface relative to the center of the averaging volume, m

Greek Letters

ε_γ	volume fraction of the γ -phase (porosity)
$\rho_{A\gamma}$	mass density of species A in the γ -phase, kg/m^3
ρ_γ	mass density for the γ -phase, kg/m^3
$\omega_{A\gamma}$	$\rho_{A\gamma}/\rho_\gamma$, mass fraction of species A in the γ -phase

References

1. Carberry, J.J. *Chemical and Catalytic Reaction Engineering*. New York: McGraw-Hill Book Co., 1976.
2. Fogler, H.S. *Elements of Chemical Reaction Engineering*. Englewood Cliffs, NJ: Prentice Hall, 1992.
3. Schmidt, L.D. *The Engineering of Chemical Reactions*. Oxford: Oxford University Press, 1998.
4. Froment, G.F. and Bischoff, K.B. *Chemical Reactor Analysis and Design*. New York: John Wiley & Sons, 1979.
5. Whitaker, S. *The Method of Volume Averaging*. Dordrecht: Kluwer Academic Press, 1999.
6. Slattery, J.C. *Advanced Transport Phenomena*. Cambridge: Cambridge University Press, 1999.
7. Bird, R.B., Steward, W.E., and Lightfoot, E.N. *Transport Phenomena*, 2nd Edition. New York: John Wiley & Sons, 2002.
8. Ochoa-Tapia, J.A., del Río, J.A., and Whitaker, S. Bulk and surface diffusion in porous media: an application of the surface averaging theorem. *Chem. Eng. Sci.* 48: 2061–2082, 1993.
9. Higgins, B.G. and Whitaker, S. Stoichiometry. Submitted to *Chem. Eng. Sci.* 2005.
10. Langmuir, I. The constitution and fundamental properties of solids and liquids I: solids. *J. Amer. Chem. Soc.* 38: 2221–2295, 1916.
11. Langmuir, I. The constitution and fundamental properties of solids and liquids II: liquids. *J. Amer. Chem. Soc.* 39: 1848–1906, 1917.
12. Whitaker, S. Transport processes with heterogeneous reaction. In, S. Whitaker and A.E. Cassano, ed., *Concepts and Design of Chemical Reactors*. New York: Gordon and Breach Publishers, 1986, pp. 1–94.
13. Taylor, R. and Krishna, R. *Multicomponent Mass Transfer*. New York: John Wiley & Sons, 1993.
14. Anderson, T.B. and Jackson, R. A fluid mechanical description of fluidized beds. *Ind. Eng. Chem. Fundam.* 6: 527–538, 1967.
15. Marle, C.M. Ecoulements monophasique en milieu poreux. *Rev. Inst. Français du Pétrole* 22(10): 1471–1509, 1967.
16. Slattery, J.C. Flow of viscoelastic fluids through porous media. *AIChE J.* 13: 1066–1071, 1967.
17. Whitaker, S. Diffusion and dispersion in porous media. *AIChE J.* 13: 420–427, 1967.
18. Wood, B.D. and Whitaker, S. Diffusion and reaction in biofilms. *Chem. Eng. Sci.* 53: 397–425, 1998.
19. Wood, B.D. and Whitaker, S. Multi-species diffusion and reaction in biofilms and cellular media. *Chem. Eng. Sci.* 55: 3397–3418, 2000.
20. Carbonell, R.G. and Whitaker, S. Adsorption and reaction at a catalytic surface: the quasi-steady condition. *Chem. Eng. Sci.* 39: 1319–1321, 1984.
21. Whitaker, S. Transient diffusion, adsorption and reaction in porous catalysts: the reaction controlled, quasi-steady catalytic surface. *Chem. Eng. Sci.* 41: 3015–3022, 1986.

22. Whitaker, S. The Forchheimer equation: a theoretical development. *Transp. Porous Media* 25: 27–61, 1996.
23. Birkhoff, G. *Hydrodynamics: A Study in Logic, Fact, and Similitude*. Princeton: Princeton University Press, 1960.
24. Whitaker, S. Levels of simplification: the use of assumptions, restrictions, and constraints in engineering analysis. *Chem. Eng. Ed.* 22: 104–108, 1988.
25. Quintard, M. and Whitaker, S. Transport in ordered and disordered porous media I: the cellular average and the use of weighting functions. *Transp. Porous Media* 14: 163–177, 1994.
26. Quintard, M. and Whitaker, S. Transport in ordered and disordered porous media II: generalized volume averaging. *Transp. Porous Media* 14: 179–206, 1994.
27. Quintard, M. and Whitaker, S. Transport in ordered and disordered porous media III: closure and comparison between theory and experiment. *Transp. Porous Media* 15: 31–49, 1994.
28. Quintard, M. and Whitaker, S. Transport in ordered and disordered porous media IV: computer generated porous media. *Transp. Porous Media* 15: 51–70, 1994.
29. Quintard, M. and Whitaker, S. Transport in ordered and disordered porous media V: geometrical results for two-dimensional systems. *Transp. Porous Media* 15: 183–196, 1994.
30. Ryan, D., Carbonell, R.G., and Whitaker, S. A theory of diffusion and reaction in porous media. *AIChE Symp. Ser.* 202 71: 46–62, 1981.
31. Stakgold, I. *Boundary Value Problems of Mathematical Physics*, Vol. I. New York: The Macmillan Co., 1967.
32. Ochoa-Tapia, J.A., Stroeve, P., and Whitaker, S. Diffusive transport in two-phase media: spatially periodic models and Maxwell's theory for isotropic and anisotropic systems. *Chem. Eng. Sci.* 49: 709–726, 1994.
33. Chang, H.-C. Multiscale analysis of effective transport in periodic heterogeneous media. *Chem. Eng. Commun.* 15: 83–91, 1982.
34. Chang, H.-C. Effective diffusion and conduction in two-phase media: a unified approach. *AIChE J.* 29: 846–853, 1983.
35. Quintard, M. Diffusion in isotropic and anisotropic porous systems: three-dimensional calculations. *Transp. Porous Media* 11: 187–199, 1993.
36. Quintard, M. and Whitaker, S. Transport in ordered and disordered porous media: volume averaged equations, closure problems, and comparison with experiment. *Chem. Eng. Sci.* 48: 2537–2564, 1993.
37. Quintard, M. and Whitaker, S. One and two-equation models for transient diffusion processes in two-phase systems. In, J.P. Hartnett and T.F. Irvine, Jr, ed., *Advances in Heat Transfer*, Vol. 23. New York: Academic Press, 1993, pp. 369–465.
38. Toor, H.L. Solution of the linearized equations of multicomponent mass transfer. *AIChE J.* 10: 448–455, 460–465, 1964.
39. Stewart, W.E. and Prober, R. Matrix calculation of multicomponent mass transfer in isothermal systems. *Ind. Eng. Chem. Fundam.* 3: 224–235, 1964.
40. Giovangigli, V. *Multicomponent Flow Modeling*. Boston: Birkhauser, 1999.

2

Dynamic Modeling of Convective Heat Transfer in Porous Media

Chin-Tsau Hsu

CONTENTS

Summary	40
2.1 Introduction	40
2.1.1 Flows in Porous Media.....	41
2.1.2 Heat Transfer in Porous Media	42
2.2 Macroscopic Governing Equations	44
2.2.1 Scaling Law	45
2.2.2 Microscopic Transport Equations	45
2.2.3 Volumetric and Areal Averages	46
2.2.4 Macroscopic Transport Equations	49
2.2.4.1 Energy equations	50
2.3 Closure Modeling	51
2.3.1 Closure Relations for Momentum Dispersion and Interfacial Force	52
2.3.2 Closure Relations for Thermal Dispersion, Thermal Tortuosity, and Interfacial Heat Transfer	53
2.4 Superficial Flows and Heat Transfer.....	56
2.4.1 Governing Equations for Superficial Flows.....	57
2.4.2 Heat Transfer in Superficial Flows	58
2.5 Evaluation of Closure Coefficients	59
2.5.1 Hydrodynamic Experiments	59
2.5.1.1 Theory of oscillating flows in porous media	60
2.5.1.2 Experimental results	62
2.5.2 Heat Transfer Experiments	64
2.5.2.1 Thermal dispersion	64
2.5.2.2 Effective stagnant thermal conductivity and thermal tortuosity	65
2.5.2.3 Interfacial heat transfer.....	66
2.6 Flows and Heat Transfer in Hele-Shaw Cells	68
2.6.1 Steady Flows Past a Circular Cylinder in a Hele-Shaw Cell ..	72

2.6.2 Oscillating Flows Past a Heated Circular Cylinder in a Hele-Shaw Cell.....	73
2.7 Concluding Remarks	76
Acknowledgment.....	77
References	78

Summary

Flows and heat transfer through porous media had been the subject of investigations for centuries, because of their wide applications in mechanical, chemical, and civil engineering. A review of existing literatures shows that the current practices on describing the flow and the heat transfer in porous media remain piecewise. In this chapter, we attempt to formulate a complete set of macroscopic equations to describe these transport phenomena. The macroscopic transport equations were obtained by averaging the microscopic equations over a representative elementary volume (REV). The average procedure leads to the closure problem where the dispersion, the interfacial tortuosity, and the interfacial transfer become the new unknowns. The closure relations as constructed earlier by the author and others for the dispersion, tortuosity, and the interfacial transfer were summarized, reviewed, and adapted to close the equation system. However, several coefficients which appeared in the closure relations need to be determined experimentally (or numerically) *a priori*. Experiments conducted earlier for the determination of these coefficients were reviewed. These experimental results had basically confirmed the validity of the closure relations, but were insufficient for a complete evaluation of closure coefficients. More experiments are needed. An alternative method is to validate the closure relations and to determine the closure coefficients numerically. In view of the complexity of a random media, it is proposed to study the flows in Hele-Shaw cells. The analogy as well as difference between a Hele-Shaw cell and a porous medium is first discussed. The 3D steady and oscillating flows in Hele-Shaw cells past a heated circular cylinder were simulated by the direct numerical simulation (DNS) method. The results confirmed the basic theory of Hele-Shaw flows, but a complete determination of the closure coefficients requires further works.

2.1 Introduction

Matters with masses form naturally into porous structures. They occur almost over the entire world at different scales under considerations. One very good example is our human body. Materials with porous structures are called porous media. How the flows passing through the porous media with the

associated heat and mass transfer has been of great interest to scientists and engineers for centuries is because of its wide applications in materials, mechanical, chemical, civil, and biomedical engineering. In this context, we shall limit our discussions to the convective heat transfer through porous media, although the same physical concepts devoted here can also be applied to other disciplines.

2.1.1 Flows in Porous Media

Traditionally, the empirical Darcy's [1] law has been applied for flows through porous media when the Reynolds number based on the pore size (or particle diameter, d_p) is very small. Under this circumstance, the momentum equation for fluid flows passing through an isotropic media is described by

$$-\nabla P = \frac{\mu \mathbf{U}}{K} \quad (2.1)$$

where P is the pore pressure, μ the fluid viscosity, and \mathbf{U} the Darcy velocity. Here, Darcy velocity is taken as a superficial velocity by regarding the media as a continuum and ignoring the details of porous structures. In Eq. (2.1), the permeability, K , takes the well-known form of

$$K = \frac{\phi^3 d_p^2}{a(1 - \phi)^2} \quad (2.2)$$

where ϕ is the porosity of porous media and a is a constant to parameterize the microscopic geometry of the porous materials.

More lately, engineering practices require the operation of flows in porous media at high Reynolds number, such as those in packed-bed reactors. Experimental evidences showed that Eq. (2.1) was unable to describe the flows at high Reynolds number. By fitting to experimental data, a nonlinear term was added to Eq. (2.1) to correct for the advection inertia effect (Forchheimer [2]). Thus, Eq. (2.1) was modified empirically into

$$-\nabla P = \frac{\mu \mathbf{U}}{K} + \frac{F \rho |\mathbf{U}| \mathbf{U}}{\sqrt{K}} \quad (2.3)$$

where ρ is the fluid density. According to Ergun [3], the Forchheimer coefficient F is given by $F = b/\sqrt{a\phi^3}$ where b is again a constant to parameterize the microscopic geometry of the media. Although Eq. (2.3) had been used by researchers with some success in predicting flows in porous media, Hsu and Cheng [4] showed theoretically that in addition to the two terms on the right-hand side of Eq. (2.3), there is a need to include a term proportional to $|\mathbf{U}|^{1/2} \mathbf{U}$, to account for the viscous boundary layer effect at the intermediate

Reynolds number. As a result, Eq. (2.3) was then modified into

$$-\nabla P = \frac{\mu \mathbf{U}}{K} + \frac{H\sqrt{\rho\mu|\mathbf{U}|\mathbf{U}}}{K^{3/4}} + \frac{F\rho|\mathbf{U}|\mathbf{U}}{\sqrt{K}} \quad (2.4)$$

where the dimensionless coefficient H , like F , is a function of porosity and microscopic solid geometry. Equation (2.4) was confirmed by Hsu et al. [5] who performed experiments for flows through porous media over a wide range from low to high Reynolds numbers.

Equation (2.4) was constructed based on the experiments and theory for steady flows. Therefore, Eq. (2.4) is anticipated to apply only for steady flows over all range of Reynolds number. Unsteady flows in porous media have recently received great attention. One example is the oscillating flow in the regenerators used in Stirling engines and catalytic converters. Others are the transient processes in the start-up and shutdown of a capillary heat pipe in mechanical engineering, and the well-bore pumping in hydraulic and petroleum engineering. Because of the lack of adequate equations to describe the unsteady flows in porous media, Eq. (2.3) sometimes was used indiscriminately without justification. For coastal engineers to study the ocean waves acting on sand sea beds or porous breakwaters, the common practice is to incorporate into Eq. (2.1) the terms corresponding to transient inertia and viscous diffusion (Liu et al. [6]), based on the classical works of Biot [7] and Dagan [8]. The resultant equations had neglected the virtual mass and viscous-diffusion memory effects and are expected to be valid only for low Reynolds number flows of waves at long period. There remains the task to construct a model for unsteady flows through porous media, which to the first-order approximation is valid over the entire ranges of time scale and Reynolds number.

2.1.2 Heat Transfer in Porous Media

Heat transfer in porous media had been studied for more than a century. The simplest problem in heat transfer in porous media is the pure conduction when the fluid is not in motion (stagnant). Under the assumption of a local thermal equilibrium between fluid and solid phases, mixture models were used traditionally for heat conduction in porous media. By this the temperatures of solids and fluids are assumed the same locally and the heat conduction equations averaged over the solid and fluid phases are lumped into the following mixture equation,

$$(\rho c_p)_m \frac{\partial T}{\partial t} = \nabla \cdot [k_{st} \nabla T] \quad (2.5)$$

where T is the averaged temperature and k_{st} is the effective stagnant thermal conductivity. In Eq. (2.5), the effective heat capacity of the solid-fluid

mixture, $(\rho c_p)_m$, is defined as

$$(\rho c_p)_m = \phi \rho c_p + (1 - \phi) \rho_s c_{ps} \quad (2.6)$$

where ρc_p and $\rho_s c_{ps}$ are the heat capacities of fluid and solid, respectively, with ρ and ρ_s being their densities. As a result, the main task is to determine the effective stagnant thermal conductivity k_{st} as has appeared in the lumped mixture heat conduction equation.

The determination of effective stagnant thermal conductivity has been a subject of great effort for more than a century, beginning with the work by Maxwell [9]. A large number of experiments had been carried out to measure the effective stagnant thermal conductivity. Kunii and Smith [10], Krupiczka [11], and Crane and Vachon [12] have compiled these early experimental data. The experimental methods for determining k_{st} were also reviewed by Tsotsas and Martin [13]. Most of these measurements were carried out for materials with the solid to fluid thermal conductivity ratio $\sigma (= k_s/k)$ in the range of $1 < \sigma < 10^3$. Effective stagnant thermal conductivities of porous materials with higher value of σ were obtained experimentally by Swift [14] and Nozad et al. [15], while those with lower σ by Prasad et al. [16]. With the advances in computer technology, the effective stagnant thermal conductivities were determined numerically. Deissler and Boegli [17] were the first to calculate k_{st} for media with cubic-packing spheres on the basis of a finite-difference scheme, followed Wakao and Kato [18] and Wakao and Vortmeyer [19] for media of a periodic orthorhombic structure. More recently, Nozad et al. [15] and Sahraoui and Kaviany [20] had also obtained some numerical results for periodic media. It should be noted that all the numerical investigations were conducted for porous media with periodic structures to confine the computation domain to a unit cell. Since Maxwell [9], several analytical composite-layer models have been proposed for k_{st} (Kunii and Smith [10]; Zehner and Schlunder [21]). Recently, Hsu et al. [22] extended the model of Zehner and Schlunder [21] by introducing a particle touching parameter. The model of Kunii and Smith [10] was improved by Hsu et al. [23, 24], using the touching and nontouching geometry of Nozad et al. [15]; they found that the predicted results of k_{st} agree remarkably well with the experimental data of Nozad et al. [15]. Kaviany [25] and Cheng and Hsu [26] have reviewed the existing models of effective thermal conductivity in detail.

The validity of the assumption of local thermal equilibrium remains an open question, especially when the timescale of transient heat conduction is short and the thermal conductivity ratio between the fluid and solid is very much different from unity. If the solid and fluid are in thermally nonequilibrium state, the heat conductances in the fluid and solid phases have to be considered separately with a two-equation model. Closure modeling of the thermal tortuosity and the interfacial heat transfer becomes inevitable. Quintard and his coworkers [27, 28] had made considerable progresses on the two-equation model. Hsu [29] proposed a transient closure model with

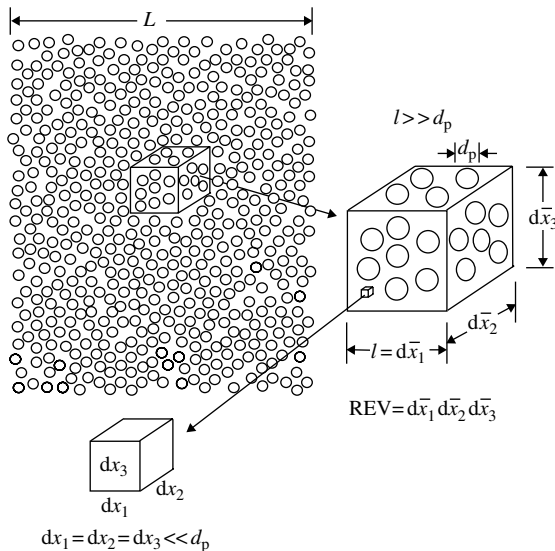
a method to evaluate the thermal tortuosity. The transient closure model also extended the model of Quintard and Whitaker [28] for interfacial heat transfer by taking into account the dependence on the thermal conductivity ratio of solid to fluid. A review of the transient heat conduction in porous media to assess the validity of local thermal equilibrium assumption was given by Hsu [30].

When the fluid in the porous media is in motion, a quantity due to thermal dispersion as has appeared in the averaged energy equation becomes a new unknown and requires closure modeling. Thermal dispersion bears considerable resemblance to mass dispersion that had received great attention for decades [31–41]. In contrary to mass dispersion, there exist only limited amount of works on thermal dispersion. Gunn and De Sousa [42], Gunn and Khalid [43], and Vortmeyer [44] represent some of the early works. More recently are those works by Levec and Carbonell [45, 46] and Hsu and Cheng [4]. The effect of fluid motion has also greatly enhanced the interfacial heat transfer as a result of convection. Considerable progresses were made on the modeling of the enhanced interfacial heat transfer. These can be traced back to the earlier works of Kunii and Suzuki [47], Nelson and Galloway [48], Martin [49], and Wakao et al. [50]. Wakao and Kaguei [51] provided a comprehensive summary on the interfacial heat transfer. They found a great scattering of the experimental data for low Reynolds number flows. Hsu [52] extended his earlier work of interfacial heat transfer for pure conduction [29] to incorporate the effect of forced convection for both low and high Reynolds number flows.

In this chapter, macroscopic equations governing the convective heat transfer in porous media are derived rigorously by the method of volumetric averaging [53], incorporated with an areal averaging procedure for the region near a macroscopic boundary. This procedure leads to the closure problem with new unknown terms as has appeared in the averaged equations where the closure modeling becomes inevitable. These unknowns are those associated with the momentum and thermal dispersions, the interfacial tortuosity, and the interfacial transfer. Closure relations as proposed by earlier works are summarized to form a closed equation system. The limitations on the closure relations are discussed to offer the possibility for further improvements. In order to verify some aspects of the closure relations, convection in Hele-Shaw cells in analog to flows and heat transfer in porous media is used. Flows and heat transfer in the Hele-Shaw cells are computed with a 3D code, with a direct numerical simulation method to assess the closure relations as well as their associated closure coefficients.

2.2 Macroscopic Governing Equations

In this section, we shall obtain the macroscopic governing equations for the transport of momentum and energy in porous media. The scaling law for

**FIGURE 2.1**

The schematic to illustrate the scaling law and the REV for the volumetric average scheme.

treating the porous media is first introduced, followed by a description of the transport equations at the microscopic scale. The volumetric and areal averaging procedures are then defined and applied to the microscopic transport equations to obtain the macroscopic transport equations. Here, we restrict our discussion to a rigid media where relative position of solids is fixed.

2.2.1 Scaling Law

As depicted in Figure 2.1, the macroscopic scale is defined by the coordinate system \bar{x}_i , $i = 1-3$, which has the global length scale of L for the problem under consideration. The increments of the macroscopic scale, $d\bar{x}_i$, are of the same order to the length l of an REV given by $V = \bar{d}_1 \bar{d}_2 \bar{d}_3$. The local microscopic coordinate system, x_i , also has the length scale l , which is assumed to be large compared to the characteristic length of the solid particles, d_p . Therefore, the increments of the microscopic coordinates, dx_i , are much smaller than d_p , but much larger than the molecular scale l_m . Hence, $L \gg l \gg d_p \gg l_m$, $d\bar{x}_i = l = O(x_i)$, and $d_p \gg dx_i \gg l_m$. With the last inequality, the concept of continuum mechanics can be applied directly at the microscopic scale.

2.2.2 Microscopic Transport Equations

For simplicity, we shall restrict our discussions to a rigid medium in which the solid structure is fixed in space. The properties of the fluid such as density,

viscosity, and thermal conductivity are assumed constant. Hence, the fluid is Newtonian and incompressible. The continuity, momentum, and energy equations of the fluids in pore space at the microscopic scale without body forces are described respectively by:

Continuity equation

$$\nabla \cdot \mathbf{u} = 0 \quad (2.7)$$

where \mathbf{u} is the fluid velocity and ∇ is the microscopic gradient operator.

Momentum equation

$$\rho \frac{\partial \mathbf{u}}{\partial t} + \rho \nabla \cdot (\mathbf{u} \mathbf{u}) = -\nabla p + \mu \nabla \mathbf{S} \quad (2.8)$$

where p is the pressure and \mathbf{S} is the strain rate tensor given by

$$\mathbf{S} = S_{ij} = \left(\frac{\partial u_i}{\partial x_j} + \frac{\partial u_j}{\partial x_i} \right) \quad (2.9)$$

Energy equation in fluid

$$\rho c_p \frac{\partial T}{\partial t} + \rho c_p \nabla \cdot (\mathbf{u} T) = k \nabla^2 T \quad (2.10)$$

where T is the temperature of the fluid, c_p is the specific heat capacity of fluid at constant pressure, k is the thermal conductivity of the fluid.

While the solid of the porous media is assumed to be rigid, that is, $\mathbf{u}_s = 0$, the conduction of heat in solids may occur. The energy equation for the solid phase can be obtained from Eq. (2.10) by subscripting the physical quantities with s for the solid phase and setting $\mathbf{u}_s = 0$ to yield:

Energy equation in solid

$$\rho_s c_{ps} \frac{\partial T_s}{\partial t} = k_s \nabla^2 T_s \quad (2.11)$$

where T_s is the temperature, ρ_s the density, c_{ps} the specific heat capacity, and k_s the thermal conductivity, of the solid.

2.2.3 Volumetric and Areal Averages

Volumetric averaging

The intrinsic average of a fluid quantity \mathbf{w} over the fluid phase is defined as

$$\bar{\mathbf{w}} = \frac{1}{V_f} \int_{V_f} \mathbf{w} dV \quad (2.12)$$

We now follow the procedure of Whitaker [53] to derive the volumetric average for the divergence of a flux \mathbf{w} . The divergence theorem reads

$$\int_{V_f} \nabla \cdot \mathbf{w} dV = \int_{S_f} \mathbf{w} \cdot d\mathbf{s} \quad (2.13)$$

where S_f is the surface enclosing the fluid volume V_f and $d\mathbf{s}$ is the surface areal increment vector which is represented by $\mathbf{n}dA$ with \mathbf{n} being the unit vector outward normal to S_f from fluid to solid and dA the scalar areal increment. For the REV depicted in Figure 2.1, the surface S_f consists of a fluid–solid interfacial surface A_{fs} and six flat fluid surfaces, two A_{fx_i} each at $\bar{x}_i \pm d\bar{x}_i/2$, $i = 1-3$. We should assume that the areal porosities in the x_i directions are identically equal to ϕ_a , that is, $A_{fx_i}/A_{x_i} = \phi_a$, and that A_{fx_i} and A_{x_i} are chosen sufficiently large, equal to A_f and A , respectively, to render ϕ_a being independent of the size of A . Therefore, Eq. (2.13) after being divided by V becomes

$$\frac{1}{V} \int_{V_f} \nabla \cdot \mathbf{w} dV = \bar{\nabla} \cdot \left(\frac{1}{A} \int_{A_f} \mathbf{w} dA \right) + \frac{1}{V} \int_{A_{fs}} \mathbf{w} \cdot d\mathbf{s} \quad (2.14)$$

where $\bar{\nabla}$ is the macroscopic gradient operator. The areal and volumetric averages can be taken as the same in the domain of a randomly packed porous medium where both are defined rigorously. As a result, Eq. (2.14) in terms of the intrinsic average quantity becomes

$$\phi \bar{\nabla} \cdot \bar{\mathbf{w}} = \bar{\nabla} \cdot (\phi \bar{\mathbf{w}}) + \frac{1}{V} \int_{A_{fs}} \mathbf{w} \cdot d\mathbf{s} \quad (2.15)$$

where the overhead bar represents the intrinsic average over the fluid phase, that is,

$$(\bar{\nabla} \cdot \bar{\mathbf{w}}, \bar{\mathbf{w}}) = \frac{1}{V_f} \int_{V_f} (\nabla \cdot \mathbf{w}, \mathbf{w}) dv \quad (2.16)$$

By applying the above divergence theorem to w_i , w_j , and w_k , respectively, and summing up the resultant expressions into a vector, the averaging procedure for a gradient reads

$$\phi \bar{\nabla} \bar{\mathbf{w}} = \bar{\nabla} (\phi \bar{\mathbf{w}}) + \frac{1}{V} \int_{A_{fs}} \mathbf{w} d\mathbf{s} \quad (2.17)$$

Note that the last terms in Eqs. (2.15) and (2.17) represent the interfacial transfer terms caused by the interaction between the fluid and solid. For the time derivatives of a quantity, the average over the REV leads to

$$\phi \frac{\partial \bar{\mathbf{w}}}{\partial t} = \frac{\partial (\phi \bar{\mathbf{w}})}{\partial t} - \frac{1}{V} \int_{A_{fs}} \mathbf{w} \mathbf{u} \cdot d\mathbf{s} \quad (2.18)$$

The above expressions are for the averages in fluid phase. Using the similar concept, it is easy to obtain the averages for solid phase. Then the quantity $\bar{\mathbf{w}}_s$ denotes the solid phase averaged results defined as

$$\bar{\mathbf{w}}_s = \frac{1}{V_s} \int_{V_s} \mathbf{w} dV \quad (2.19)$$

The expressions (2.15), (2.17), and (2.18) are then converted to

$$\phi_s \bar{\nabla} \cdot \bar{\mathbf{w}}_s = \bar{\nabla} \cdot (\phi_s \bar{\mathbf{w}}_s) - \frac{1}{V} \int_{A_{fs}} \mathbf{w}_s \cdot d\mathbf{s} \quad (2.20)$$

$$\phi_s \bar{\nabla} \bar{\mathbf{w}}_s = \bar{\nabla} (\phi_s \bar{\mathbf{w}}_s) - \frac{1}{V} \int_{A_{fs}} \mathbf{w}_s d\mathbf{s} \quad (2.21)$$

and

$$\phi_s \frac{\partial \bar{\mathbf{w}}_s}{\partial t} = \frac{\partial (\phi_s \bar{\mathbf{w}}_s)}{\partial t} + \frac{1}{V} \int_{A_{fs}} \mathbf{w}_s \mathbf{u}_s \cdot d\mathbf{s} \quad (2.22)$$

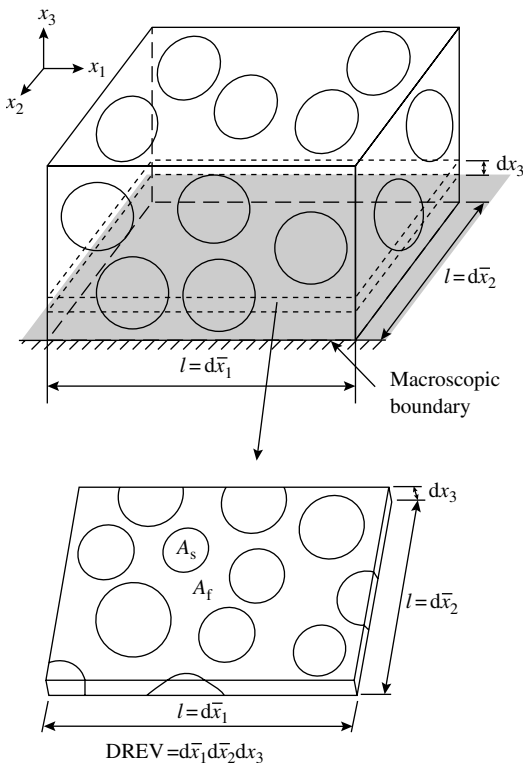
for the averages over solid phase, where $\phi_s = 1 - \phi$ is the volume ratio of solid phase. Note that the last terms in Eqs. (2.20) to (2.22) take a different sign from (2.15), (2.17), and (2.18) since $d\mathbf{s}$ is now inward into the solid. For rigid solid medium where $\mathbf{u} = \mathbf{u}_s = 0$ on A_{fs} , last terms in Eqs. (2.18) and (2.22) become zero.

Areal averaging

It should be noted that the volumetric average defined above fails to apply in the region near a macroscopic boundary. This problem becomes serious since most of the important transfer process occurs in a boundary layer near an impermeable wall. To circumvent this difficulty, we should degenerate the REV into a thin plate as shown in [Figure 2.2](#). Hence, $V = d\bar{x}_1 d\bar{x}_2 dx_3 = Adx_3$ where x_3 is measured in the normal direction from the macroscopic boundary. Note that x_3 remains at a microscopic scale, that is, $dx_3 \ll d_p$. The fluid volume in REV is given by $V_f = A_f dx_3$. Then, the porosity is defined by $V_f/V = A_f/A = \phi_a$. The intrinsic average of a fluid quantity \mathbf{w} over the fluid phase now becomes

$$\bar{\mathbf{w}} = \frac{1}{V_f} \int_{V_f} \mathbf{w} dV = \frac{1}{A_f} \int_{A_f} \mathbf{w} dA \quad (2.23)$$

For the degenerated REV (DREV), it can be easily shown that the relations given by Eqs. (2.15), (2.17), and (2.18) remain valid, except that the volumetric porosity ϕ is replaced by the areal porosity ϕ_a , that the overhead bar is interpreted as the areal average and that the macroscopic gradient $\bar{\nabla}$ is interpreted as $\bar{\nabla} = (\partial/\partial \bar{x}_1, \partial/\partial \bar{x}_2, \partial/\partial x_3)$. Expressions for the areal average

**FIGURE 2.2**

The schematic for the DREV for the areal average scheme near the macroscopic boundary wall.

over the solid phase similar to those of Eqs. (2.20) to (2.22) can be obtained, and the correspondent interpretations follow.

2.2.4 Macroscopic Transport Equations

By performing the volumetric averaging to the microscopic equations (2.7–2.11), invoking the relations (2.15–2.22) and decomposing the velocity, pressure, and temperatures into $\mathbf{u} = \bar{\mathbf{u}} + \mathbf{u}'$, $p = \bar{p} + p'$, $T = \bar{T} + T'$, and $T_s = \bar{T}_s + T'_s$, respectively, we find that

$$\bar{\nabla} \cdot (\phi \bar{\mathbf{u}}) = 0 \quad (2.24)$$

$$\rho \left[\frac{\partial}{\partial t} (\phi \bar{\mathbf{u}}) + \bar{\nabla} \cdot (\phi \bar{\mathbf{u}} \bar{\mathbf{u}}) \right] = -\bar{\nabla}(\phi \bar{p}) + \rho[\nu \bar{\nabla} \cdot (\phi \bar{\mathbf{S}}) + \bar{\nabla} \cdot (-\phi \bar{\mathbf{u}}' \bar{\mathbf{u}}')] + \bar{\mathbf{b}}_{fs} \quad (2.25)$$

where

$$\bar{\mathbf{S}} = \bar{S}_{ij} = \frac{1}{\phi} \left(\frac{\partial(\phi \bar{u}_i)}{\partial \bar{x}_j} + \frac{\partial(\phi \bar{u}_j)}{\partial \bar{x}_i} \right) \quad (2.26)$$

In Eq. (2.25),

$$\bar{\mathbf{b}}_{fs} = \frac{1}{V} \int_{A_{fs}} (-p\mathbf{I} + \mu\mathbf{S}) \cdot d\mathbf{s} = \frac{1}{V} \int_{A_{fs}} (-p'\mathbf{I} + \mu\mathbf{S}') \cdot d\mathbf{s} \quad (2.27)$$

represents the interfacial force per unit volume as exerted by the solids, with $\mathbf{I} = \delta_{ij}$ being the identity matrix. Note that the volumetric interfacial force is contributed from the pressure and the shear stresses acting on the solid surface. The quantities, $-\phi \bar{\mathbf{u}}' \bar{\mathbf{u}}'$, in Eq. (2.25) represent the additional stresses due to the correlation between the velocity variations over REV, called the *momentum dispersion*. Its occurrence may bear some resemblance to the Reynolds stresses appearing in turbulence.

2.2.4.1 Energy equations

Fluid phase

$$\rho c_p \frac{\partial(\phi \bar{T})}{\partial t} + \rho c_p \bar{\nabla} \cdot (\phi \bar{\mathbf{u}} \bar{T}) = k \bar{\nabla}^2(\phi \bar{T}) + \rho c_p \bar{\nabla} \cdot (-\phi \bar{\mathbf{u}}' \bar{T}') + k \bar{\nabla} \cdot \mathbf{\Lambda}_{fs} + q_{fs} \quad (2.28)$$

On the right-hand side of Eq. (2.28), the quantity $(-\bar{\mathbf{u}}' \bar{T}')$ represents the thermal dispersion, the quantity

$$\mathbf{\Lambda}_{fs} = \frac{1}{V} \int_{A_{fs}} T \cdot d\mathbf{s} = \frac{1}{V} \int_{A_{fs}} T' \cdot d\mathbf{s} \quad (2.29)$$

in the second last term represents the thermal tortuosity and the last term

$$q_{fs} = \frac{1}{V} \int_{A_{fs}} k \nabla T \cdot d\mathbf{s} \quad (2.30)$$

represents the interfacial heat transfer from solid into fluid per unit volume.

Solid phase

$$\rho_s c_{ps} \frac{\partial(\phi_s \bar{T}_s)}{\partial t} = k_s \bar{\nabla}^2(\phi_s \bar{T}_s) - k_s \bar{\nabla} \cdot \mathbf{\Lambda}_{fs} - q_{fs} \quad (2.31)$$

In Eq. (2.31), we have invoked the condition of the continuity of heat flux across the interface, that is,

$$k \nabla T = k_s \nabla T_s \quad \text{on } A_{fs} \quad (2.32)$$

so that the source term q_{fs} given by Eq. (2.28) for fluid phase becomes the sink term for solid phase, or vice versa. Because the surface increment ds is out-normal from fluid into solid, the second term on the right-hand side of Eq. (2.31) takes the negative sign as different from the corresponding term in Eq. (2.28).

The macroscopic transport equations given above with some prescribed boundary conditions cannot be solved directly because there are more unknowns than the number of equations. This leads to a so-called *closure problem*. These unknown terms are associated with the momentum and thermal dispersions, the thermal tortuosity, and the interfacial momentum and heat transfer. The interfacial momentum transfer appears as the resistant force on fluid by the solid structure and is also termed as the volumetric interfacial force. While the dispersions occur in the domain of fluid phase, the thermal tortuosity and the interfacial momentum and heat transfer occur at the solid–fluid interface. Constitutive relations need to be sought through closure modeling scheme to relate these new unknowns to the averaged macroscopic quantities.

2.3 Closure Modeling

The construction of closure relations associated with the dispersions, tortuosity, and the interfacial transfer now becomes the major task for the present treatise of the transport phenomena in porous medium. As the closure problem involves the microscopic deviation quantities, it is logical to examine the behaviors of \mathbf{u}' , p' , T' , and T'_s . This can be done by first obtaining the governing equations for the microscopic deviations, then normalizing the resultant equations to reveal the key nondimensional parameters such as Reynolds number, Péclet number, and Keulegan–Carpenter number that govern the behaviors of the microscopic transports. The closure relations applicable in different ranges of these key parameters then can be obtained based on the correlation between the microscopic deviations and the macroscopic quantities. The composite closure relations valid for all range of the parameters can then be constructed. This procedure of closure modeling scheme is quite standard and can be found in [4, 29, 30, 52, 53]. Here we shall not go into details of the closure modeling scheme, but only summarize the results of these closure relations as obtained earlier by others.

2.3.1 Closure Relations for Momentum Dispersion and Interfacial Force

Following the similar principle of Hsu and Cheng [4] for deriving the thermal dispersion, Hsu [52] obtained the closure relations for the momentum dispersion and interfacial force. The resultant composite closure relations that are valid for all Reynolds number, $Re_p = |\bar{\mathbf{u}}|d_p/\nu$, and all range of timescale are summarized as follows.

Momentum Dispersion

Following the Taylor series expansion, the velocity deviation \mathbf{u}' to the first-order approximation can be expressed into

$$\mathbf{u}' = c'_1 \bar{\mathbf{u}} + d_p c'_2 \cdot \bar{\mathbf{S}} \quad (2.33)$$

Therefore, the momentum dispersion becomes:

$$-\overline{\mathbf{u}'\mathbf{u}'} = -c \bar{\mathbf{u}} \bar{\mathbf{u}} + \varepsilon \bar{\mathbf{S}} \quad (2.34)$$

where ε is the dispersion viscosity given by

$$\varepsilon = c_1 \bar{l} |\bar{\mathbf{u}}| + c_2 \bar{l}^2 |\bar{\mathbf{S}}| \quad (2.35)$$

with \bar{l} being the mixing length of momentum dispersion and c_1 and c_2 being the correlation coefficients. The first term on the right-hand side of Eq. (2.35) resembles the Prandtl's third mixing length theory for turbulent eddy viscosity of a wake behind a sphere and that the second term resembles the eddy viscosity for turbulent boundary layer near a solid wall. However, the dispersion length for flows in porous media is assumed to scale with the particle diameter in the core region far away from an impermeable wall and then to become linearly proportional to the distance \bar{x}_3 measured from the impermeable wall. By adapting van Driest's damping factor A^+ , \bar{l} is expressed as

$$\bar{l} = c_3 d_p [1 - \exp(-A^+ \bar{x}_3 / d_p)] \quad (2.36)$$

Volumetric Interfacial Force

$$\begin{aligned} \bar{\mathbf{b}}_{fs} = & - \frac{\phi_s \mu c_S}{d_p^2} \bar{\mathbf{u}} - \frac{\phi_s c_B}{d_p^{3/2}} \sqrt{\rho \mu |\bar{\mathbf{u}}|} \bar{\mathbf{u}} - \frac{\rho \phi_s c_I}{d_p} |\bar{\mathbf{u}}| \bar{\mathbf{u}} \\ & - \frac{\phi_s c_G}{d_p} \sqrt{\frac{\rho \mu}{|\nabla \times (\phi \bar{\mathbf{u}})|}} \bar{\mathbf{u}} \times [\nabla \times (\phi \bar{\mathbf{u}})] \end{aligned}$$

$$\begin{aligned}
& - \rho \phi_s c_L \bar{\mathbf{u}} \times [\bar{\nabla} \times (\phi \bar{\mathbf{u}})] - \rho \phi_s c_V \frac{\bar{D}(\phi \bar{\mathbf{u}})}{\bar{D}t} \\
& - \sqrt{\frac{\rho \mu}{\pi}} \frac{\phi_s c_M}{d_p} \int_{-\infty}^t \frac{\partial(\phi \bar{\mathbf{u}})}{\partial \tau} \frac{d\tau}{\sqrt{t-\tau}}
\end{aligned} \tag{2.37}$$

where c_S is the drag coefficient due to Stokes flow, c_B and c_I are the viscous and inviscid drag coefficients due to fluid advection, c_G and c_L are the viscous and inviscid lift force coefficients due to mean vorticity, and c_V and c_M are the transient inertia drag coefficients due to the virtual mass and the Basset transient memory effects. Note that the form drag, the inviscid lift force, and the virtual mass force are independent of the viscosity, that is, they are associated mainly with the hydrodynamic pressure. The relation (2.37) bears considerable resemblance to that for the two-phase flows, although there are some differences in detail.

Macroscopic Momentum Transport Equations

By invoking Eq. (2.34) into Eq. (2.25), the macroscopic momentum transport equations with the aid of Eq. (2.26) now become

$$\rho \left[\frac{\partial}{\partial t} (\phi \bar{\mathbf{u}}) + \bar{\nabla} \cdot (\phi (1+c) \bar{\mathbf{u}} \bar{\mathbf{u}}) \right] = -\bar{\nabla}(\phi \bar{p}) + \rho \bar{\nabla} \cdot [(v + \varepsilon) \bar{\nabla}(\phi \bar{\mathbf{u}})] + \bar{\mathbf{b}}_{fs} \tag{2.38}$$

where $\bar{\mathbf{b}}_{fs}$ is given by Eq. (2.37). It is seen that the effects of momentum dispersion are to produce the excess mean momentum and the dispersion viscosity.

2.3.2 Closure Relations for Thermal Dispersion, Thermal Tortuosity, and Interfacial Heat Transfer

The closure for the thermal dispersion, thermal tortuosity, and interfacial heat transfer had been studied greatly for decades. Hsu and Cheng [4] proposed a closure model for the thermal dispersion. The early works on the closure modeling of thermal tortuosity were on the problem of stagnant heat conduction in porous media. Quintard and Whitaker [27, 28] gave a first comprehensive account of the thermal tortuosity, followed by the recent work of Hsu [29]. The early works on the interfacial heat transfer were highly experimental (Kunii and Suzuki [47]; Wakao et al. [50]). A more comprehensive theoretical treatment of the closure model for the interfacial heat transfer was given by Hsu [4, 52]. Here we should summarize the

closure relations as obtained by Hsu and Cheng [4], Hsu [29], and Hsu [52] as follows:

Thermal Dispersion

The thermal dispersion was modeled by Hsu and Cheng [4], who showed that

$$-\phi \bar{\mathbf{u}}' \bar{\mathbf{T}}' = \mathbf{A}_D \cdot \bar{\nabla} \bar{\mathbf{T}} \quad (2.39)$$

where \mathbf{A}_D is the dispersion thermal diffusivity tensor which for a homogeneous media can be expressed into

$$\mathbf{A}_D = \begin{bmatrix} \alpha_1 & 0 & 0 \\ 0 & \alpha_2 & 0 \\ 0 & 0 & \alpha_3 \end{bmatrix} \quad (2.40)$$

with α_1, α_2 , and α_3 being the dispersion thermal diffusivities in the longitudinal, transverse, and lateral directions, respectively. It is anticipated that the transverse and lateral dispersions are of the same order in core region of the porous media, but not in the region near the impermeable wall. According to Hsu and Cheng [4], the dispersion thermal diffusivities are linearly proportional to the Péclet number, $Pe_p = |\bar{\mathbf{u}}|d_p/\alpha$, when the Péclet number is large, and becomes proportional to the square of the Péclet number when the Péclet number is low. Therefore, the composite relations for the dispersion thermal diffusivities can be constructed as

$$\alpha_i = (1 - \phi)\alpha \frac{a_i Pe_p^2}{b_i + Pe_p} \quad (i = 1, 2, \text{and } 3) \quad (2.41)$$

where a_i and b_i are coefficients depending only on microscopic geometry of the media.

Thermal Tortuosity

According to the closure modeling of Hsu [29], the thermal tortuosity is expressed as

$$\Lambda_{fs} = G(\bar{\nabla} \bar{T} - \sigma \bar{\nabla} \bar{T}_s) \quad (2.42)$$

where G is the tortuosity parameter and $\sigma (= k_s/k)$ is the conductivity ratio between solid and fluid. The tortuosity parameter G can be determined from

$$G = \frac{[(k_{st}/k) - \phi - \sigma(1 - \phi)]}{(1 - \sigma)^2} \quad (2.43)$$

where k_{st} is the effective stagnant thermal conductivity of the porous media based on a mixture model under the condition of local thermal equilibrium.

A comprehensive review of the effective stagnant thermal conductivity of porous media was given in Cheng and Hsu [26].

Interfacial Heat Transfer

From Hsu [29], the closure relation for the interfacial transfer from solid to fluid is given by

$$q_{fs} = h_{fs}a_{fs}(\bar{T}_s - \bar{T}_f) \quad (2.44)$$

where $a_{fs}(= A_{fs}/V)$ is the specific interfacial area and h_{fs} is the interfacial heat transfer coefficient. From Hsu [52], the interfacial heat transfer coefficient takes the form of $h_{fs}^*(1 + c_4 Pr Re_p)$ at low Reynolds number where h_{fs}^* is the stagnant interfacial heat transfer coefficient when fluid is still (Hsu [29]); however, at large Reynolds number, it becomes proportional, $Pr^m Re_p^n$, where m and n depend on the ranges of Pr and Re_p of the microscopic flows. Therefore, the composite expressions for h_{fs} in terms of the interfacial Nusselt number becomes

$$Nu_{fs} = \frac{h_{fs}d_p}{k} = Nu_{fs}^* \left(1 + \frac{a Pr Re_p}{b + Nu_{fs}^* Pr^{1-m} Re_p^{1-n}} \right) \quad (2.45)$$

where Nu_{fs}^* is the stagnant interfacial Nusselt number and a and b are coefficients with $a/b = c_4$. From the classical theory of convective heat transfer, we have $n > 0.5$ for large Reynolds number. We also have $m = 1/2$ when $Pr \ll 1$ and $m = 1/3$ when $Pr \gg 1$. A quasi-steady model for Nu_{fs}^* as proposed by Hsu [29], on the basis of the parallel conduction layers on fluid and solid sides, respectively, is expressed as

$$Nu_{fs}^* = \frac{h_{fs}^* d_p}{k} = \frac{\sigma}{\alpha_A \sigma + \alpha_B} \quad (2.46)$$

where α_A and α_B represent the dimensionless conduction layer thickness in fluid and solid phases as normalized by the particle diameter, respectively.

Macroscopic Energy Equations

By substituting the closure relations for the thermal dispersion, thermal tortuosity, and interfacial heat transfer into (2.28) and (2.31), the macroscopic energy equations become:

Fluid phase

$$\begin{aligned} \rho c_p \frac{\partial(\phi \bar{T})}{\partial t} + \rho c_p \bar{\nabla} \cdot (\phi \bar{\mathbf{u}} \bar{T}) &= k \bar{\nabla}^2(\phi \bar{T}) + \rho c_p \bar{\nabla} \cdot (\mathbf{A}_D : \bar{\nabla} \bar{T}) \\ &\quad + k \bar{\nabla} \cdot [G(\bar{\nabla} \bar{T} - \sigma \bar{\nabla} \bar{T}_s)] + h_{fs} a_{fs} (\bar{T}_s - \bar{T}) \end{aligned} \quad (2.47)$$

Solid phase

$$\rho_s c_{ps} \frac{\partial(\phi_s \bar{T}_s)}{\partial t} = k_s \bar{\nabla}^2 (\phi_s \bar{T}_s) - k_s \bar{\nabla} \cdot [G(\bar{\nabla} \bar{T} - \sigma \bar{\nabla} \bar{T}_s)] - h_{fs} a_{fs} (\bar{T}_s - \bar{T}) \quad (2.48)$$

Equations (2.47) and (2.48) with the dispersion thermal diffusivity, the tortuosity, and the interfacial heat transfer coefficient given by Eqs. (2.39), (2.42), and (2.44), respectively, are the macroscopic governing equations for the unsteady convective heat transfer in porous media. The evaluation of the closure coefficients α_i , G , and h_{fs} then becomes one of the main tasks.

2.4 Superficial Flows and Heat Transfer

The above closure relations are derived in terms of the phase-averaged flow and heat transfer quantities that have their intrinsic physical meaning. For instance, for media with dispersed dilute spheres (limit case of $\phi \rightarrow 0$), \bar{u} is the incoming free stream velocity for the problem of flows past a sphere. Then the closure coefficients can be determined from the classical theory of fluid mechanics. However, in this study the porous media are made of densely packed particles or interlinked solids. The interference among solid particles is important and the closure coefficients depend strongly on the porosity. This dependence is hard to determine analytically; however, the evidences from the existing experimental data suggest that the proper scale to account for the contribution due to particle interference to the volumetric interfacial force should be the hydraulic diameter, defined by

$$d_h = \frac{\phi}{1-\phi} d_p \quad (2.49)$$

The flows through the porous media are then postulated as those passing through a series of capillary tubes of diameter d_h . To be inline with classical Darcy's formulation, we should express the equations in terms of the pore pressure, $P = \bar{p}$, and the Darcy velocity, $\mathbf{U} = \phi \bar{\mathbf{u}}$. Flows with velocity field \mathbf{U} are regarded as the superficial flows over the entire domain of porous media since the velocity \mathbf{U} does not represent the actual velocity in the media; however, for convenience \bar{T} and \bar{T}_s will remain to represent the averaged temperatures over the respective phases.

2.4.1 Governing Equations for Superficial Flows

In terms of Darcy velocity, pore pressure, and hydraulic diameter, the phase-averaged continuity and momentum equations, (2.24) and (2.38), become

$$\bar{\nabla} \cdot \mathbf{U} = 0 \quad (2.50)$$

and

$$\rho \left[\frac{\partial}{\partial t} (\mathbf{U}) + \bar{\nabla} \cdot ((1+c)\mathbf{U}\mathbf{U}/\phi) \right] = -\bar{\nabla}(\phi P) + \rho \bar{\nabla} \cdot [(v+\varepsilon)\bar{\nabla}(\mathbf{U})] + \bar{\mathbf{b}}_{fs} \quad (2.51)$$

where the dispersion viscosity in terms of the hydraulic diameter is rewritten as

$$\varepsilon = c_{h1} \bar{l}_h |\mathbf{U}| + c_{h2} \bar{l}_h^2 \left| \bar{\mathbf{S}}_h \right| \quad (2.52)$$

Here the strain rate tensor $\bar{\mathbf{S}}_h$ and the hydraulic dispersion length \bar{l}_h are redefined as

$$\bar{\mathbf{S}}_h = \phi \bar{\mathbf{S}} = \phi \bar{\mathbf{S}}_{ij} = \left(\frac{\partial U_i}{\partial \bar{x}_j} + \frac{\partial U_j}{\partial \bar{x}_i} \right) \quad (2.53)$$

and

$$\bar{l}_h = d_h [1 - \exp(-A_h^+ \bar{x}_3/d_h)] \quad (2.54)$$

Note that c_3 in Eq. (2.36) can be adjusted arbitrarily to render Eq. (2.54). The volumetric interfacial force in terms of Darcy velocity becomes

$$\begin{aligned} \bar{\mathbf{b}}_{fs} = & - \frac{\mu C_S}{d_h^2} \mathbf{U} - \frac{C_B}{d_h^{3/2}} \sqrt{\rho \mu |\mathbf{U}|} \mathbf{U} - \frac{\rho C_I}{d_h} |\mathbf{U}| \mathbf{U} - \frac{C_G}{d_h} \sqrt{\frac{\rho \mu}{|\bar{\nabla} \times \mathbf{U}|}} \mathbf{U} \times (\bar{\nabla} \times \mathbf{U}) \\ & - \rho C_L \mathbf{U} \times (\bar{\nabla} \times \mathbf{U}) - \rho C_V \frac{\bar{D}\mathbf{U}}{\bar{D}t} - \sqrt{\frac{\rho \mu}{\pi}} \frac{C_M}{d_h} \int_{-\infty}^t \frac{\partial \mathbf{U}}{\partial \tau} \frac{d\tau}{\sqrt{t-\tau}} \end{aligned} \quad (2.55)$$

Here, the dependence of the dispersion viscosity and the volumetric interfacial force on the porosity appears implicitly in the hydraulic diameter and the closure coefficients in Eqs. (2.52) and (2.55). These coefficients also depend strongly on the microscopic geometry of the solids; hence, they need to be determined experimentally.

Equations (2.50) to (2.55) form a closed set of equations that can be solved with proper macroscopic boundary conditions. They are the macroscopic governing equations for the superficial flows in porous media. These equations have taken account of the first-order leading terms over the entire ranges of Reynolds number and timescale. As seen from the right-hand side of Eq. (2.55), the first term represents the force due to Stokes drag, proportional to μ . It is contributed from both shear and pressure, and corresponds to creeping flows at low Reynolds number. The second, fourth, and seventh terms are proportional to $\mu^{1/2}$ corresponding to boundary layer flows at intermediate Reynolds number (lower-end of high Reynolds number) and intermediate timescale; the forces are solely contributed from shear. The third, fifth, and sixth terms are independent of μ corresponding to inviscid potential flows at very high Reynolds number and short timescale, and the forces are solely contributed from pressure.

The superficial flow in terms of Darcy velocity can be considered as being a continuum flow over the whole domain of the porous media. The details of the solid structure in the media are disregarded. This is equivalent to saying that the flows in porous media can be regarded macroscopically as the flows of a special type of fluids. We should call this fluid as "Darcy fluid." The flow of Darcy fluid has a mass flux $\rho\mathbf{U}$ but has a momentum flux $\rho(1+c)\mathbf{U}\mathbf{U}/\phi$; it also has a viscosity ($\nu + \varepsilon$) as if that of a non-Newtonian fluid and subject to a body force $\bar{\mathbf{b}}_{fs}$ associated with the resistance caused microscopically by the solids. The effective pressure to drive the Darcy fluid is ϕP . It is noted that the values of c , ε , and $\bar{\mathbf{b}}_{fs}$ depend strongly on the velocity and shear of the superficial flow. Particularly, $\bar{\mathbf{b}}_{fs}$ depends also on the transient acceleration of the superficial flow.

2.4.2 Heat Transfer in Superficial Flows

While the energy equation for the heat conduction in solid phase remains the same as given by Eq. (2.48), the energy equations governing the convective heat transfer of the Darcy fluid then become:

$$\rho c_p \frac{\partial(\phi \bar{T})}{\partial t} + \rho c_p \bar{\nabla} \cdot (\mathbf{U} \bar{T}) = k \bar{\nabla}^2(\phi \bar{T}) + \rho c_p \bar{\nabla} \cdot (\mathbf{A}_D \cdot \bar{\nabla} \bar{T}) \\ + k \bar{\nabla} \cdot [G(\bar{\nabla} \bar{T} - \sigma \bar{\nabla} \bar{T}_s)] + h_{fs} a_{fs} (\bar{T}_s - \bar{T}) \quad (2.56)$$

where the dispersion thermal diffusivities are given by

$$\alpha_i = \alpha \frac{a_{hi} Pe_h^2}{b_{hi} + Pe_h} \quad (i = 1, 2, \text{ and } 3) \quad (2.57)$$

with the Péclet number based on hydraulic diameter given by $Pe_h = |\mathbf{U}|d_h/\alpha$, and a_{hi} and b_{hi} being coefficients. The interfacial Nusselt number in terms of

the hydraulic diameter then becomes

$$Nu_{\text{hfs}} = \frac{h_{\text{fs}}d_{\text{h}}}{k} = Nu_{\text{hfs}}^* \left(1 + \frac{a_{\text{h}} Pr Re_{\text{h}}}{b_{\text{h}} + Nu_{\text{hfs}}^* Pr^{1-m} Re_{\text{h}}^{1-n}} \right) \quad (2.58)$$

where $Re_{\text{h}} = |\mathbf{U}|d_{\text{h}}/\nu$ is the Reynolds number based on Darcy velocity and hydraulic diameter, and Nu_{hfs}^* is stagnant Nusselt number given by

$$Nu_{\text{hfs}}^* = \frac{h_{\text{fs}}^* d_{\text{h}}}{k} = \frac{\sigma}{\alpha_{\text{hA}}\sigma + \alpha_{\text{hB}}} \quad (2.59)$$

If the solid and fluid phases are locally in thermal equilibrium, that is, $\bar{T}_s = \bar{T}$, we can lump Eqs. (2.48) and (2.56) together to yield:

$$(\rho c_p)_m \frac{\partial \bar{T}}{\partial t} + \rho c_p \bar{\nabla} \cdot (\mathbf{U} \bar{T}) = k_{\text{st}} \bar{\nabla}^2 \bar{T} + \rho c_p \bar{\nabla} \cdot (\mathbf{A}_D \cdot \bar{\nabla} \bar{T}) \quad (2.60)$$

where $(\rho c_p)_m = \phi \rho c_p + (1 - \phi) \rho_s c_{ps}$ is the heat capacity of the solid–fluid mixture.

2.5 Evaluation of Closure Coefficients

In this section, we shall review some of the experiments that are relevant for the determination of the closure coefficients that appear in the closure relations. They are summarized in the following sections.

2.5.1 Hydrodynamic Experiments

Most of the early experimental works on the flows in porous media were devoted to the determination of the coefficients in the interfacial force. To the author's knowledge, till date there exist no experimental data for the determination of the coefficients in the closure relation of momentum dispersion. The main difficulty lies on the fact that the Brinkman layer near an impermeable wall is too thin to be measurable. Even for the interfacial force, most of the early works were conducted on steady flows for determining the permeability to delineate the Darcy's law at very low Reynolds number and the Forchheimer inertia effect at very large Reynolds number. To delineate the transient effect, we need to study the unsteady flows. One of the simplest unsteady flows is the one-dimensional periodically oscillating flow. Recently, Hsu et al. [5] and Hsu and Fu [54] measured the velocity and the pressure-drop for both steady and oscillating flows across porous columns packed from wire screens. For better understanding of the experimental results,

a brief review of the theory of oscillating flows in porous media is given first. It should be noted that these experiments were only valid for flows in the core region of the porous media.

2.5.1.1 Theory of oscillating flows in porous media

We consider oscillating flows in a packed column. In the core region of the packed column, the superficial flow is one-dimensional, that is, $\mathbf{U} = (u, 0, 0)$ where u is a function of time only. Equation (2.51) with the substitution of (2.55) reduces to

$$\rho(1 + C_V) \frac{\partial u}{\partial t} = -\frac{\partial(\phi p)}{\partial x} - \frac{\mu C_S}{d_h^2} u - \frac{C_B}{d_h^{3/2}} \sqrt{\rho \mu |u|} u - \frac{\rho C_I}{d_h} |u| u - \sqrt{\frac{\rho \mu}{\pi}} \frac{C_M}{d_h} \int_{-\infty}^t \frac{\partial u}{\partial \tau} \frac{d\tau}{\sqrt{t-\tau}} \quad (2.61)$$

In Eq. (2.61), the terms with the coefficients C_S , C_B , C_I , C_V , and C_M are associated, respectively, with the Stokes drag force, the frictional force due to advection boundary layer, the inviscid form drag, the inviscid virtual mass force, and the Basset memory viscous force due to transient boundary layer.

In the limit of low frequency oscillating flows, Eq. (2.61) reduces further to the quasi-steady form of

$$-\frac{\partial(\phi p)}{\partial x} = \frac{\mu C_S}{d_h^2} u + \frac{C_B}{d_h^{3/2}} \sqrt{\rho \mu |u|} u + \frac{\rho C_I}{d_h} |u| u \quad (2.62)$$

which was proposed first by Hsu and Cheng [4]. Equation (2.62) indicates that the negative pressure gradient and the velocity are in-phase, that is, maximum pressure-drop occurs when the velocity is maximal. Taking the maximum of pressure and velocity oscillations, Eq. (2.62) becomes

$$f = \frac{C_S}{Re_h} + \frac{C_B}{Re_h^{1/2}} + C_I \quad (2.63)$$

where $f = \phi \Delta p_{\max} d_h / (\rho u_{\max}^2 L)$ is the pressure-drop coefficient with Δp_{\max} being the maximum pressure-drop across a distance L of the packed column, and $Re_h = u_{\max} d_h / \nu$ the Reynolds number with u_{\max} being the amplitude of a sinusoidal velocity, that is, $u = u_{\max} \cos \omega t$.

When the transient inertia force becomes important at high frequency, there will be a phase difference between velocity and pressure-gradient oscillations. A complete description of velocity and pressure-gradient correlation requires both the amplitude correlation and phase difference. The velocity and pressure gradient are assumed as the real part of the following complex

expressions,

$$U = \hat{u} e^{i\omega t} \quad \text{and} \quad -\frac{1}{\rho} \frac{\partial P}{\partial x} = \hat{\alpha} e^{i\omega t} + \text{harmonics} \quad (2.64\text{a,b})$$

where \hat{u} ($= u_{max}$) and $\hat{\alpha}$ represent the complex amplitudes of velocity and pressure gradient of the fundamental mode, respectively. The substitution of Eq. (2.64) into Eq. (2.61), and then collecting the fundamental mode of oscillation, leads to

$$\hat{\alpha} = \frac{1}{\phi} \left[\frac{v C_S}{d_h^2} + \frac{C_B}{d_h^{3/2}} \sqrt{\frac{2.64 v |\hat{u}|}{\pi}} + \frac{2.67 C_I |\hat{u}|}{\pi d_h} + \frac{C_M \sqrt{i\omega v}}{d_h} + (1 + C_V) i\omega \right] \hat{u} \quad (2.65)$$

From Eq. (2.65), it appears that the Basset memory force generates a pressure-gradient component of a 45° -phase difference from the velocity, while the virtual mass force generates a component of a 90° -phase difference. The quasi-steady state then represents the limit case of a 0° -phase difference when $\omega \rightarrow 0$. Taking the absolute value to Eq. (2.65) results in

$$\hat{f} = \left| \frac{C_S}{Re_h} + \frac{C_B}{Re_h^{1/2}} \sqrt{\frac{2.64}{\pi}} + \frac{2.67 C_I}{\pi} + \frac{C_M}{Re_h^{1/2}} \sqrt{\frac{id_h}{A}} + (1 + C_V) \frac{id_h}{A} \right| \quad (2.66)$$

where $\hat{f} = |\hat{\alpha}| \phi d_h / |\hat{u}|^2$ is the pressure-gradient coefficient based on the fundamental mode, $Re_h = |\hat{u}| d_h / v$ is the Reynolds number, and $A = |\hat{u}| / \omega$ is the amplitude of the fluid displacement of the superficial flow. Here we have $A = \phi \bar{A}$ with \bar{A} being the intrinsic average of fluid displacement in the pore. The phase angle between the pressure and velocity can be obtained by taking the argument to Eq. (2.65) to result in

$$\theta = \tan^{-1} \left[\frac{(1+C_V)(d_h/A) + (C_M/\sqrt{2Re_h})\sqrt{d_h/A}}{C_S/Re_h + (C_B/\sqrt{Re_h})\sqrt{2.64/\pi} + 2.67 C_I/\pi + (C_M/\sqrt{2Re_h})\sqrt{d_h/A}} \right] \quad (2.67)$$

Equations (2.66) and (2.67) indicate that the pressure gradient of an oscillating flow in a porous medium depends on two parameters, Re_h and d_h/A . The inverse of d_h/A is the Keulegan–Carpenter number commonly encountered in oscillating flows. In the limit of $d_h/A \rightarrow 0$ (i.e., $A \rightarrow \infty$ and $\omega \rightarrow 0$ while maintaining $|\hat{u}|$ as finite), Eq. (2.66) reduces to

$$\hat{f} = \frac{C_S}{Re_h} + \frac{C_B}{Re_h^{1/2}} \sqrt{\frac{2.64}{\pi}} + \frac{2.67 C_I}{\pi} \quad (2.68)$$

and the phase angle approaches zero. Note that Eq. (2.68) is different from Eq. (2.63) by the factors of $\sqrt{2.64/\pi}$ and $2.67/\pi$ in the last two terms because Eq. (2.68) uses the amplitude of fundamental mode rather than the maximum of the pressure gradient.

2.5.1.2 Experimental results

Figure 2.3 shows the experimental results of the pressure-drop coefficient varying with the Reynolds number for steady and low frequency oscillating flows across the packed column as obtained by Hsu et al. [5]. The most fascinating result is that the oscillating flow data collapses into the steady flow data. This implies that the oscillating flows in porous media in the low frequency limit are indeed quasi-steady. The most important feature in Figure 2.3 is that the experimental data covered a wide range of $0.27 < Re_h < 2600$ so that the constants C_S and C_I for the Darcy and the Forchheimer limits at low and high Reynolds numbers, respectively, can be determined with no ambiguity. As a result, C_B can also be determined accurately by fitting the experimental data to Eq. (2.63). The values of C_S , C_B , and C_I as obtained from the best curve-fit are 109, 5.0, and 1.0, respectively. For comparison, the curve for $C_B = 0$, which represents the two-term Darcy–Forchheimer correlation commonly used in the porous medium research community, is also plotted in Figure 2.3. It is seen that the exclusion of the term with $Re_h^{-1/2}$ on the

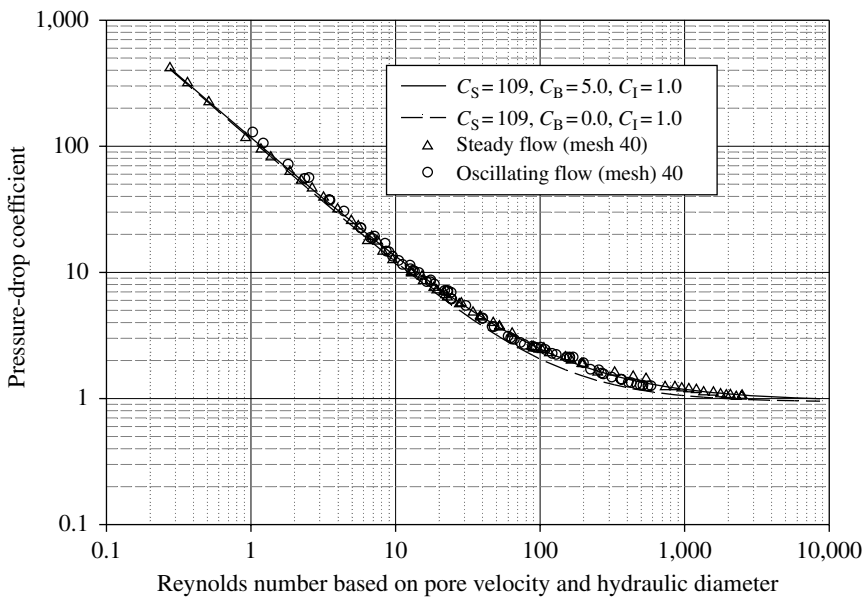
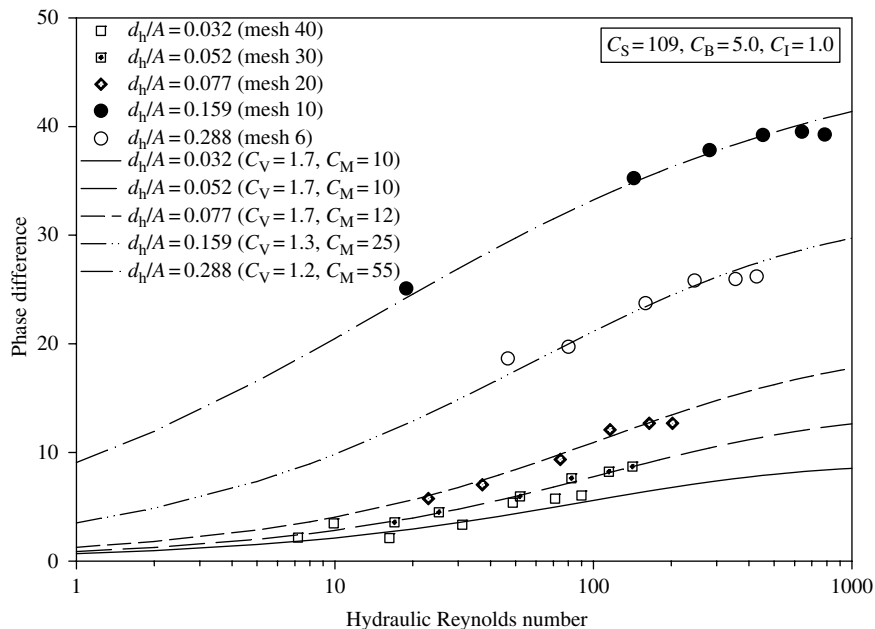


FIGURE 2.3

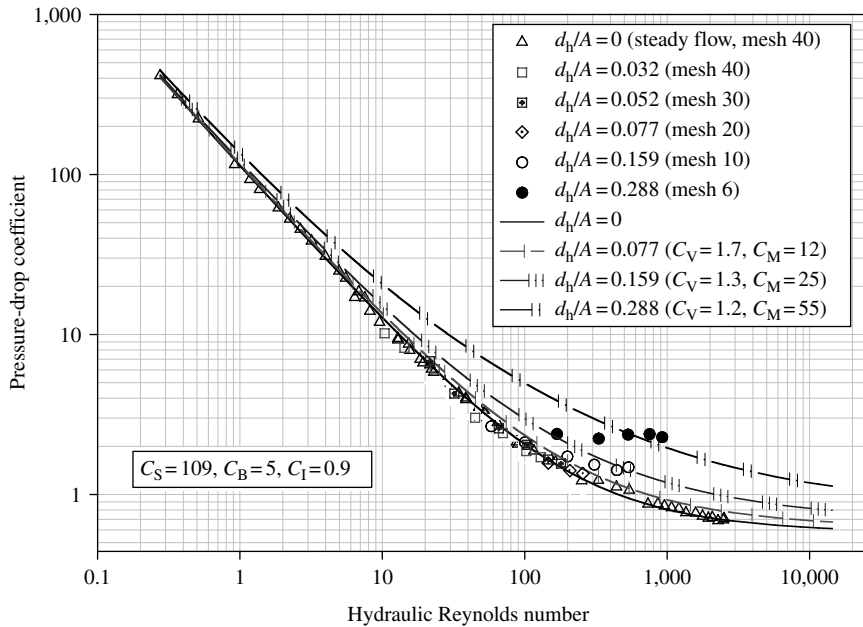
Correlation of pressure-drop coefficient with velocity of steady and oscillating flows through the packed porous column.

**FIGURE 2.4**

Phase difference between the fundamental mode oscillations of the velocity and the pressure-drop across packed columns made of different sizes of wire screens.

right-hand side of Eq. (2.63) underestimates the pressure-drop by 20–30% in the intermediate Reynolds number range of $40 < Re_h < 1000$.

The experimental results of pressure-drop and velocity correlation for high frequency oscillating flows in the packed column as given by Hsu and Fu [54] are shown in Figure 2.4 and Figure 2.5 for the phase angle and amplitude, respectively. We note that the amplitude data is not accurate enough to be used for the determination of the coefficients C_M and C_V . Instead, the phase angle data were used. From Figure 2.4, it is seen that the phase difference is as much as 40° at the Reynolds number of 780 when $d_h/A = 0.288$. This implies that the interfacial force due to transient inertia is of the same order in magnitude as that due to advection inertia. With the values of $C_S = 109$, $C_B = 5.0$, and $C_I = 1.0$ from Figure 2.3, the curves with the values of C_V and C_M obtained by best fit of the data to Eq. (2.67) are plotted in Figure 2.4. The agreement between the experimental results and the theoretical predictions is shown in Figure 2.4. This implies that the inclusion of the transient inertia force into the volumetric interfacial force due to solid resistance is crucial for a complete description of the unsteady flows in porous media. The predictions of amplitude correlation based on Eq. (2.66) using $C_S = 109$, $C_B = 5.0$, $C_I = 1.0$, and the fitted values of C_M and C_V for different d_h/A are plotted in Figure 2.5. For comparison, the steady flow data of Figure 2.3 (equivalent to $d_h/A = 0$) were first converted for Eq. (2.68) and plotted in Figure 2.5.

**FIGURE 2.5**

Correlation between the amplitudes of fundamental mode oscillations of velocity and pressure-drop across packed columns made of different sizes of wire screens.

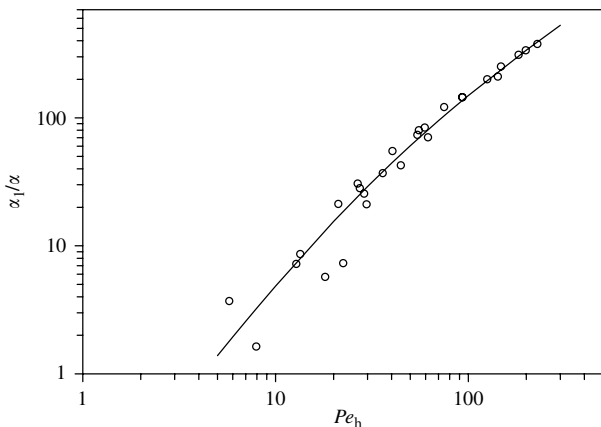
A good agreement is found between the experimental data and the theoretical predictions.

2.5.2 Heat Transfer Experiments

There exist considerable experiments on the heat transfer in porous media. Wakao and Kaguei [51] and Kaviany [25] had comprehensively compiled the early experimental results. Here we recapture those that are relevant to the thermal dispersion, thermal tortuosity, and interfacial heat transfer, incorporated with some results from recent experiments by Fu and Hsu [55].

2.5.2.1 Thermal dispersion

Under the low frequency condition, Fu and Hsu [55] measured the longitudinal thermal dispersion for oscillating flows through a porous column packed of wire screens. The oscillating flows at such low frequency are quasi-steady as demonstrated in Section 2.5.1. Figure 2.6 shows the variation of the effective longitudinal dispersion thermal diffusivity with the hydraulic Péclet number. As seen from Figure 2.6, α_1/α increases almost linearly with the Péclet number when $Pe_h \gg 10$. As Pe_h decreases toward $Pe_h \approx 10$, the value of

**FIGURE 2.6**

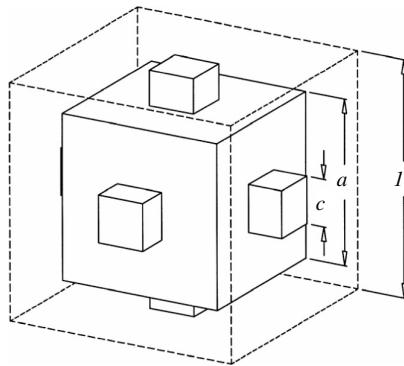
Comparison of the experimental results of dispersion thermal diffusivity (Fu and Hsu [55]) with the predictions based on the model of Hsu and Cheng. (Taken from C.T. Hsu and P. Cheng. *Int. J. Heat Transfer* 33:1587–1597, 1990. With permission.)

α_1/α decreases more rapidly to exhibit the trend of Pe_h^2 , although the data range of Pe_h is not low enough to provide a complete picture in the range of low Péclet number. Apparently, the data shown in Figure 2.6 are consistent with the quasi-steady closure model for thermal dispersion as given by Hsu and Cheng [4]. The composite expression as given by Eq. (2.57) was used by Fu and Hsu [55] to fit the data to obtain $a_{h1} = 1.94$ and $b_{h1} = 30$. The results of the best fit are given in Figure 2.6 as the solid curve. It should be noted that the value of b_{h1} may be subject to some uncertainty because of the lack of data in low Péclet number range; however, the value of $a_{h1} = 1.94$ should give better confidence.

2.5.2.2 Effective stagnant thermal conductivity and thermal tortuosity

As the tortuosity parameter G is related to the effective stagnant thermal conductivity k_{st} by Eq. (2.43), the main task becomes to experimentally determine k_{st} . A more complete experiment for the determination of k_{st} that covered a wide range of solid-to-fluid thermal conductivity ratio was the one conducted by Nozad et al. [15]. More recently, Hsu et al. [23] proposed the lumped parameter 2D and 3D models to predict the effective stagnant thermal conductivity. For the 3D model of in-line periodic arrays of cubes, the unit cell is shown as in Figure 2.7. The expression for the determination of k_{st}/k is then given as:

$$k_{st}/k = 1 - \gamma_a^2 - 2\gamma_c\gamma_a + 2\gamma_c\gamma_a^2 + \sigma\gamma_c^2\gamma_a^2 + \frac{\sigma\gamma_a^2(1 - \gamma_c^2)}{\sigma + \gamma_a(1 - \sigma)} + \frac{2\sigma\gamma_c\gamma_a(1 - \gamma_a)}{\sigma + \gamma_c\gamma_a(1 - \sigma)} \quad (2.69)$$

**FIGURE 2.7**

Unit cell of a 3D in-line array of cubes used in Hsu et al. (Taken from C.T. Hsu, P. Cheng, and K.W. Wong. *ASME J. Heat Transfer* 117:264–269, 1995. With permission.)

where the particle size parameter $\gamma_a (= a/l_e)$ and the solid-particle contact parameter $\gamma_c (= c/a)$, as shown in Figure 2.7, are related to the porosity by

$$1 - \phi = (1 - 3\gamma_c^2)\gamma_a^3 + 3\gamma_c^2\gamma_a^2 \quad (2.70)$$

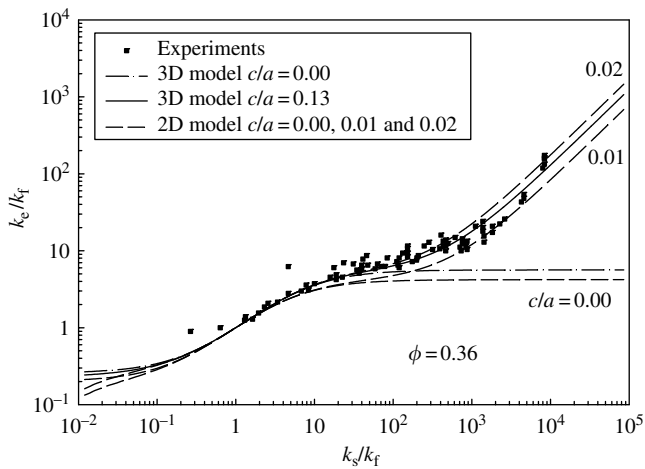
For nontouching cubes ($\gamma_c = 0$), $\gamma_a = (1 - \phi)^{1/3}$, and (2.84) reduces to

$$\frac{k_{st}}{k} = [1 - (1 - \phi)^{2/3}] + \frac{(1 - \phi)^{2/3}\sigma}{[1 - (1 - \phi)^{1/3}]\sigma + (1 - \phi)^{1/3}} \quad (2.71)$$

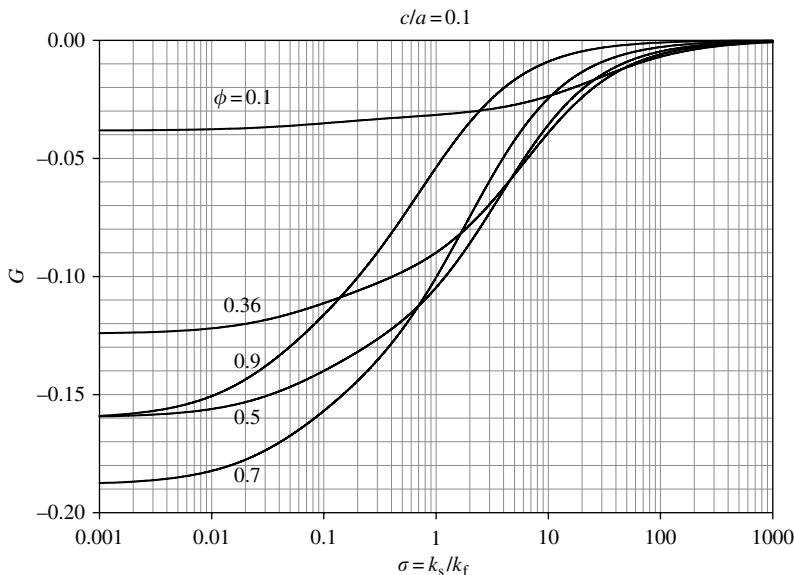
The predictions by the models of Hsu et al. [23] and the experimental results of Nozad et al. [15] are given in Figure 2.8. The comparison shows excellent agreement. Hsu [29] then used the above 3D model to calculate k_{st}/k and then evaluate the tortuosity parameter G by Eq. (2.43). The results of G as a function of σ are given in Figure 2.9 for different values of porosity when the solid-particle contact parameter takes a typical value of $\gamma_c = 0.1$.

2.5.2.3 Interfacial heat transfer

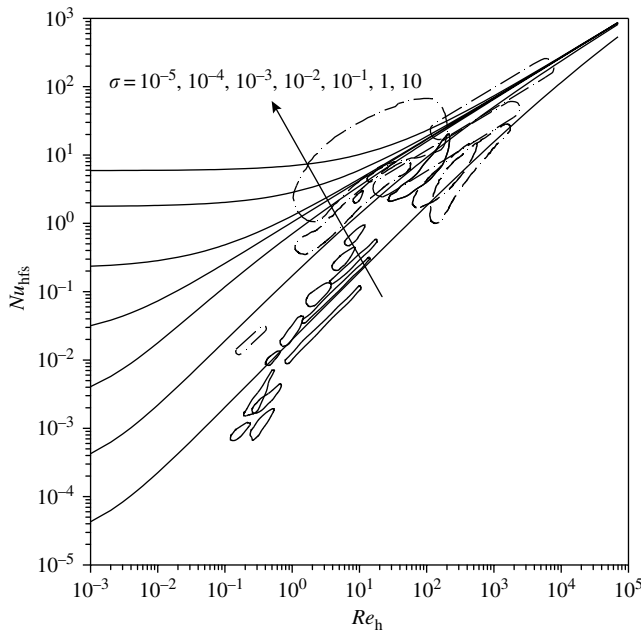
Unlike the thermal dispersion, considerable experimental works on the interfacial heat transfer were made in the past decades, because of important applications in chemical engineering. Figure 2.10 shows the data compiled by Kunii and Suzuki [47] in the range of low Reynolds number (areas enclosed by solid curves), and by Wakao and Kaguei [51] in the range of high Reynolds number (areas enclosed by dashed curves). The family of curves for different values of σ in Figure 2.10 is the prediction of Eqs. (2.58) and (2.59), with $m = 0.5$, $n = 0.6$, $a_h = 1.29$, and $b_h = 0.001$, $\alpha_{hA} = 0.125$, and $\alpha_{hB} = 0.443$ for air ($Pr = 0.7$). It appears that the model of Hsu [52] predicted the general

**FIGURE 2.8**

Comparison of the predictions of effective stagnant thermal conductivity based on the 3D cube and 2D square cylinder models of Hsu et al. [23] with the experimental results of Nozad et al. (Taken from S. Nozad, R.G. Carbonell, and S. Whitaker. *Chem. Eng. Sci.* 40:843–855, 1985. With permission.)

**FIGURE 2.9**

The interfacial thermal tortuosity parameter for different values of porosity with the particle-touching parameter fixed at 0.1.

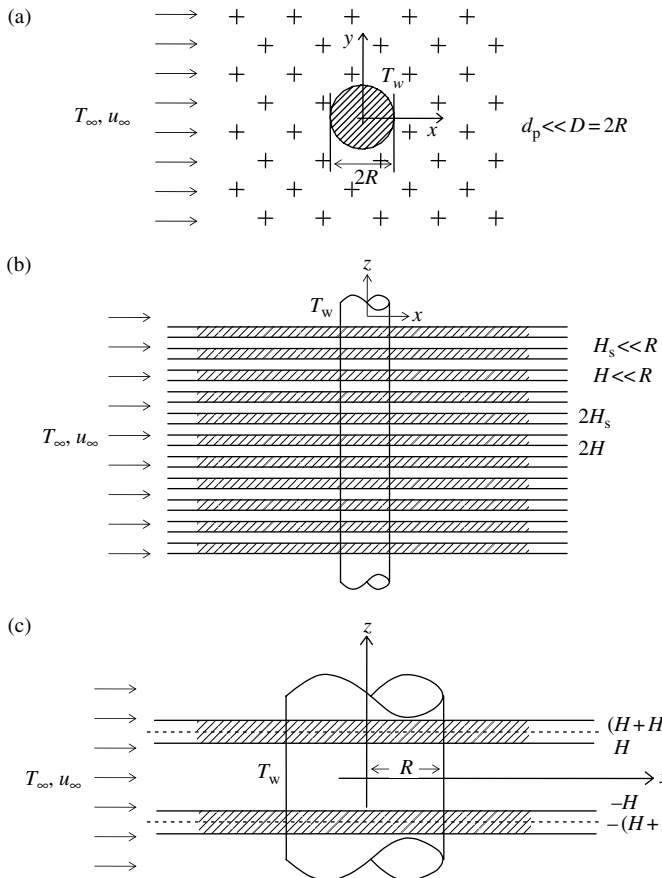
**FIGURE 2.10**

The predictions of the interfacial heat transfer coefficient based on the model of Hsu [52] and its comparison with the early experimental data compiled by Kunii and Suzuki [47] and by Wakao and Kaguei. (From N. Wakao and S. Kaguei. *Heat and Mass Transfer in Packed Beds*. New York: Gordon and Breach Science Pub. Inc., 1982. With permission.)

trend of experimental data with the correct magnitude. However, no solid conclusion can be drawn because of the high scattering in data range (Nu_{hfs} ranges from 10^{-4} to 10^3).

2.6 Flows and Heat Transfer in Hele-Shaw Cells

Flows in Hele-Shaw cells are usually regarded as flows in a thin gap bounded by two parallel plates. It has been widely used in analog by researchers for studying flows in porous media in two-dimensions [56–60]. However, the extent of Hele-Shaw flows in analog to the porous media flows and the limitation of such analog were not well understood. Here, we should closely examine the flows and heat transfer in Hele-Shaw cells using a heated circular cylinder imbedded in a porous medium as shown in Figure 2.11(a). For such problem a desegregated model is to simplify the medium by separating the fluid and solid phases in porous media into parallel layers. The characteristic length of the solid and fluid layers are d_p and d_h . As a result, the domain of the porous media consists of a series of parallel layers of solid and fluid as

**FIGURE 2.11**

(a) Schematic of the flows past a circular cylinder imbedded in porous media. (b) The media is simplified into a series of parallel layers of solid and fluid. (c) The unit cell represents a Hele-Shaw cell.

shown in Figure 2.11(b), with the unit cell depicted in Figure 2.11(c). Note that in Figure 2.11(b) and Figure 2.11(c) we have adopted the notation $d_p = 2H_s$ and $d_h = 2H$ for convenience. This unit cell is a Hele-Shaw cell. It becomes clear that

$$d_h + d_p = \frac{d_h}{\phi} = \frac{d_p}{1 - \phi} \quad (2.72)$$

which is consistent with Eq. (2.49). Flows and heat transfer in the Hele-Shaw cell microscopically is a 3D conjugate problem. They are governed by Eqs. (2.7) to (2.11) described in Section 2.2. For the case of constant temperature

T_w on the cylinder surface, the proper boundary conditions are:

On the cylinder surface, $r = R$:

$$\mathbf{u} = 0 \quad T = T_w \quad (2.73a)$$

On the solid–fluid interface (cell surface), $z = \pm H$:

$$\mathbf{u} = 0 \quad T = T_s \quad \text{and} \quad k\partial T/\partial z = k_s\partial T_s/\partial z \quad (2.73b)$$

On the mid-plane of solid layer, $z = \pm(H + H_s)$:

$$\partial T_s/\partial z = 0 \quad (2.73c)$$

At far away from the cylinder, $r = \infty$:

$$\mathbf{u} = \mathbf{u}_\infty \quad T = T_\infty \quad (2.73d)$$

where \mathbf{u}_∞ is a classical Hele-Shaw solution for fully developed channel flows.

The advantage of using Hele-Shaw cells is that the equation system (2.7) to (2.11) with the boundary conditions (2.73) is well defined. The system can be tackled much easier than dealing with random media, although obtaining the complete solution for a 3D Hele-Shaw flow remains as a challenge. To explore the analog between Hele-Shaw cells and porous media, the phase averages of a physical quantity over the thicknesses of the fluid and solid layers are defined, respectively, as:

$$\bar{W} = \frac{1}{2H} \int_{-H}^H W dz \quad \text{and} \quad \bar{W}_s = \frac{1}{2H_s} \int_H^{H+2H_s} W_s dz \quad (2.74a,b)$$

Performing the phase averages over the fluid and solid layers to Eqs. (2.7) to (2.11) leads to the following governing equations for the averaged 2D flow in parallel to the Hele-Shaw cell:

Fluid phase

$$\bar{\nabla} \cdot \bar{\mathbf{u}} = 0 \quad (2.75)$$

$$\rho \left[\frac{\partial \bar{\mathbf{u}}}{\partial t} + \bar{\nabla} \cdot (\bar{\mathbf{u}} \bar{\mathbf{u}}) \right] = -\bar{\nabla}(\bar{p}) + \rho \left[\nu \bar{\nabla} \cdot \bar{\mathbf{S}} + \bar{\nabla} \cdot (-\bar{\mathbf{u}}' \bar{\mathbf{u}}') \right] + \frac{\tau_w}{2H} \quad (2.76)$$

where

$$\bar{\mathbf{S}} = \bar{S}_{ij} = \left(\frac{\partial \bar{u}_i}{\partial \bar{x}_j} + \frac{\partial \bar{u}_j}{\partial \bar{x}_i} \right) \quad \text{with } i, j = 1, 2 \quad (2.77)$$

is the strain rate tensor and

$$\tau_w = \left(\mu \frac{\partial \mathbf{u}}{\partial z} \right)_{z=-H}^{z=H} \quad (2.78)$$

is the total wall shear stress. The averaged energy equation in the Hele-Shaw cell becomes:

$$\rho c_p \frac{\partial \bar{T}}{\partial t} + \rho c_p \bar{\nabla} \cdot (\bar{\mathbf{u}} \bar{T}) = k \bar{\nabla}^2(\bar{T}) + \rho c_p \bar{\nabla} \cdot (-\bar{\mathbf{u}}' \bar{T}') + \frac{q_w}{2H} \quad (2.79)$$

where $q_w = (k \nabla T)_{z=-H}^{z=H}$ is the heat source from the wall.

Solid phase

$$\rho_s c_{ps} \frac{\partial \bar{T}_s}{\partial t} = k_s \bar{\nabla}^2(\bar{T}_s) - \frac{q_w}{2H_s} \quad (2.80)$$

Under the local thermal equilibrium assumption, $\bar{T}_s = \bar{T}$. Equations (2.79) and (2.80), after being multiplied by $2H$ and $2H_s$ respectively, can be lumped into:

$$(\rho c_p)_m \frac{\partial \bar{T}}{\partial t} + \rho c_p \bar{\nabla} \cdot (\phi \bar{\mathbf{u}} \bar{T}) = k_{st} \bar{\nabla}^2(\bar{T}) + \rho c_p \bar{\nabla} \cdot (-\phi \bar{\mathbf{u}}' \bar{T}') \quad (2.81)$$

where $(\rho c_p)_m$ has been defined after Eq. (2.60) and $k_{st} = \phi k + (1 - \phi)k_s$ is the effective stagnant thermal conductivity based on parallel layers model. It is possible to construct a 2D thermal dispersion model for $(-\phi \bar{\mathbf{u}}' \bar{T}')$ that is similar to Eq. (2.39).

The comparison of the governing equations for the averaged flows and heat transfer in Hele-Shaw cells with those of porous media derived in Section 2.4 shows the following differences: (a) the averaged Hele-Shaw flow is 2D, (b) the interfacial force in the averaged Hele-Shaw flows is contributed solely from the shear force, and (c) there exists no thermal tortuosity for the averaged Hele-Shaw flows. As a result, a flow in Hele-Shaw cell can only be used as a good analog to a flow in porous medium, only when the volumetric averaged flow of porous media is 2D, viscous dominated, and thermal-tortuosity negligible. On the other hand, these simplified natures in Hele-Shaw flow render the flow as a good candidate for the verification of the closure modeling. In addition, a 3D numerical simulation of the convection heat transfer in Hele-Shaw cells may reveal some detailed physics of heat transfer in porous media that are impossible to tackle due to the randomness and the complexity of the microscopic solid geometry.

2.6.1 Steady Flows Past a Circular Cylinder in a Hele-Shaw Cell

For a steady flow past a circular cylinder (disc) in a Hele-Shaw cell, the 3D continuity and Navier-Stokes equations, normalized by using the mean velocity U_m far away from the cylinder as velocity scale and the cylinder radius R ($= D/2$ where D is the diameter of the cylinder) as length scale, subjected to the nonslip boundary condition given in Eq. (2.73) and the steady flow boundary condition at far away ($r = r_\infty$) as given by

$$u = 1.5 \times \left[1 - \frac{1}{r_\infty^2} \cos 2\theta \right] \times \left[1 - \frac{z^2}{H^2} \right] \quad (2.82a)$$

$$v = -1.5 \times \frac{1}{r_\infty^2} \sin 2\theta \times \left[1 - \frac{z^2}{H^2} \right] \quad (2.82b)$$

$$w = 0 \quad (2.82c)$$

were solved numerically by Kwan and Hsu [61] using the DNS method. Figure 2.12 shows the numerical results of the normalized wall shear stress τ_w (local friction coefficient) when $H/R = 0.02$ and $Re_D = U_m D/\nu = 100$. As a consequence of flow symmetry, the shear stress is symmetrical with respect to the x -axis, and antisymmetrical with respect to the y -axis. Far away from the cylinder, the computed stress is basically in the primary flow

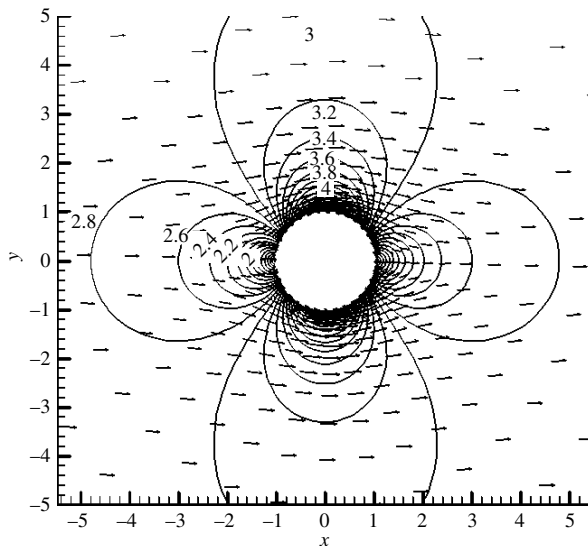
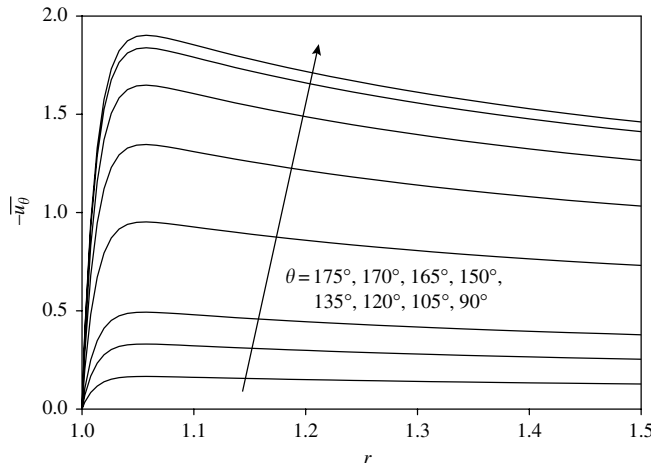


FIGURE 2.12

Direction and magnitude of normalized shear stress τ_w on the bottom wall of a Hele-Shaw cell. Arrows: direction; Curves and numbers: equal shear stress lines and magnitude. Max = 5.496 (at $\theta = 90^\circ$ and 270°), Min = 0.030 near stagnation points ($\theta = 0^\circ$ and 180°).

**FIGURE 2.13**

Comparison of the negative averaged circumferential velocity $-\bar{u}_\theta$ at the front of the cylinder.

direction and agrees with the Poiseuille solution for laminar channel flow $\tau_{wx}/\rho U_m^2 = 3/Re_H$ where $Re_H = U_m H/\nu = [Re_D(H/R)^2]/(2H/R) = 1$. Near the cylinder, the shear stress changes due to redirection of the flow. At the front and rear stagnation points ($\theta = 180^\circ$ and 0°), the velocity drops to zero and lowest shear stress is located at the stagnation point. On the other hand, at the upper and lower points ($\theta = 90^\circ$ and 270°), the flow converges to a higher velocity near the cylinder surface and creates the highest shear stress.

To demonstrate the behavior of the Brinkman boundary layer, the averaged circumferential velocity ($-\bar{u}_\theta$) at different θ is plotted in Figure 2.13. Figure 2.13 also illustrates the development of the boundary layer on the peripheral of the cylinder. With the flow symmetry, only the profiles on the upper side of the cylinder front face ($90^\circ < \theta < 180^\circ$) are shown in Figure 2.13. In the figure, when the fluid travels from the front stagnation point ($\theta = 180^\circ$) to the upper tip ($\theta = 90^\circ$) of the cylinder, the velocity increases but the boundary layer thickness is maintained at approximately $r \approx 1.05$. Hence, the present study confirms that the Brinkman boundary layer thickness along the peripheral is nearly constant, at the order of $2.5H$.

2.6.2 Oscillating Flows Past a Heated Circular Cylinder in a Hele-Shaw Cell

Here we consider the case when $H_s \ll H$ which corresponds to the limit case of $\phi \rightarrow 1$. Under this condition, the temperature in the solid can be approximated by its value at the solid–fluid interface and no heat flux condition $\partial T_s / \partial z = 0$ can be applied directly at the wall of the Hele-Shaw cell. The far away boundary condition of the oscillating flow is given by

the fully developed oscillating flow. Hence, $\mathbf{u}_\infty = (u_\infty, 0, 0)$ where $u_\infty = \frac{1}{2}[u_c(z, t) + \text{c.c.}]$ with $u_c(z, t)$ being a complex function and c.c. represents the complex conjugate. The analytical expression for $u_c(z, t)$ can easily be found as:

$$u_c(z, t) = \left[1 - \frac{\exp(\sqrt{\beta}(1+i)z) + \exp(-\sqrt{\beta}(1+i)z)}{\exp(\sqrt{\beta}(1+i)) + \exp(-\sqrt{\beta}(1+i))} \right] \exp\left(i \frac{\pi}{KC} t\right) \quad (2.83)$$

where $\beta = (\pi/4)(H/R)^2 Re_D / KC$ and $i = \sqrt{-1}$ is the imaginary. The Keulegan-Carpenter (KC) number is defined by $KC = 2\pi A/D$ where A is the displacement amplitude of fluid oscillation.

The results of the 3D oscillating flows in Hele-Shaw cell were obtained numerically by Kwan and Hsu [62]. Figure 2.14 shows the evolution of the z -vorticity (ω_z) in half cycle of oscillation, for the case of $Re_D = 3200$, $KC = 3$,

$Re_D = 3200$, $KC = 3$, $H/R = 0.1$, $Pr = 0.7$ and $R_o/R = 50$

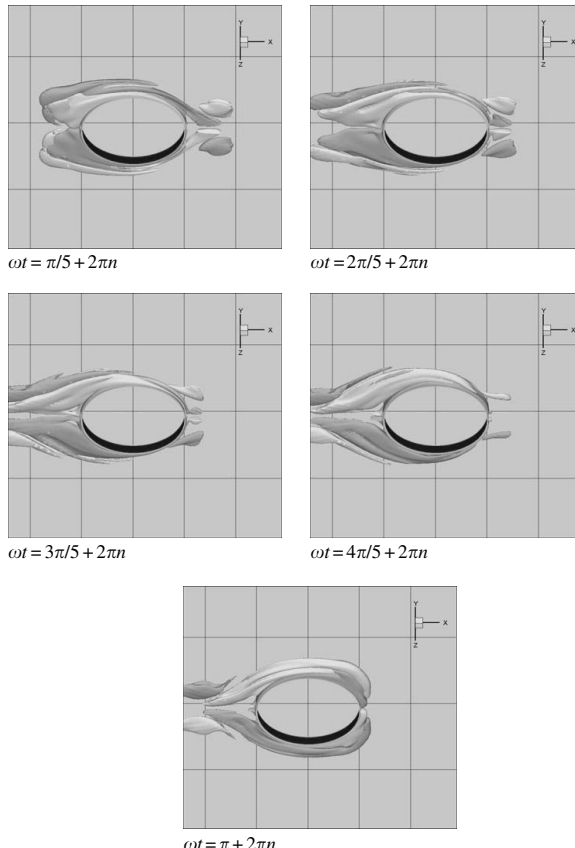


FIGURE 2.14

Variation of the z -vorticity (ω_z) field in a 3D view during the half cycle of oscillation when $Re_D = 3200$, $KC = 3$, and $H/R = 0.1$. The gray scales show the equal surfaces of vorticity generated at different cycle of oscillations. Note that vorticity is anti-symmetric with x -axis.

and $H/R = 0.1$. It is interesting to see that the flow separates periodically from the cylinder, even though the vorticity generated from flow separation does not shed from the cylinder. The occurrence of periodic flow separations also implies that the convective heat transfer in Hele-Shaw cell is confined to the narrow band in the wakes behind the cylinder. This is illustrated in Figure 2.15 which shows the variation during the half cycle of the temperature

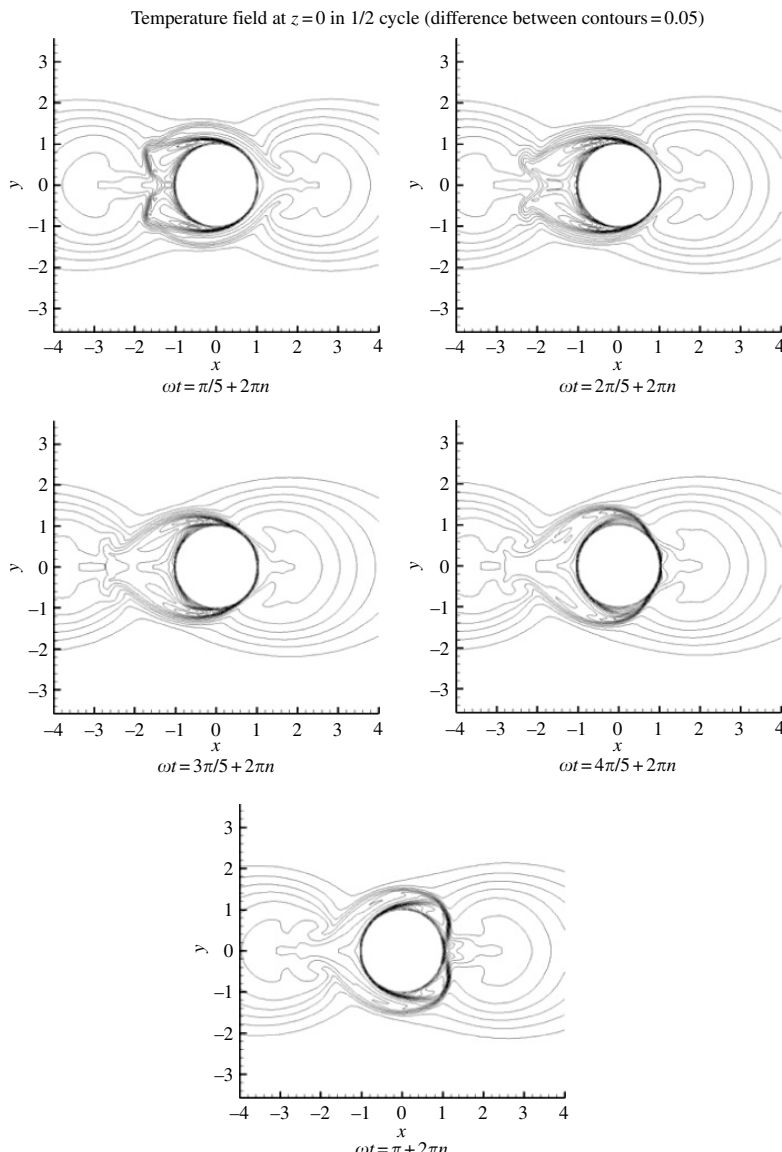


FIGURE 2.15

Distributions of isothermal lines on the mid-plane of the Hele-Shaw cell during the half cycle of flow oscillation, for the case of $Re_D = 3200$, $KC = 3$, and $H/R = 0.1$.

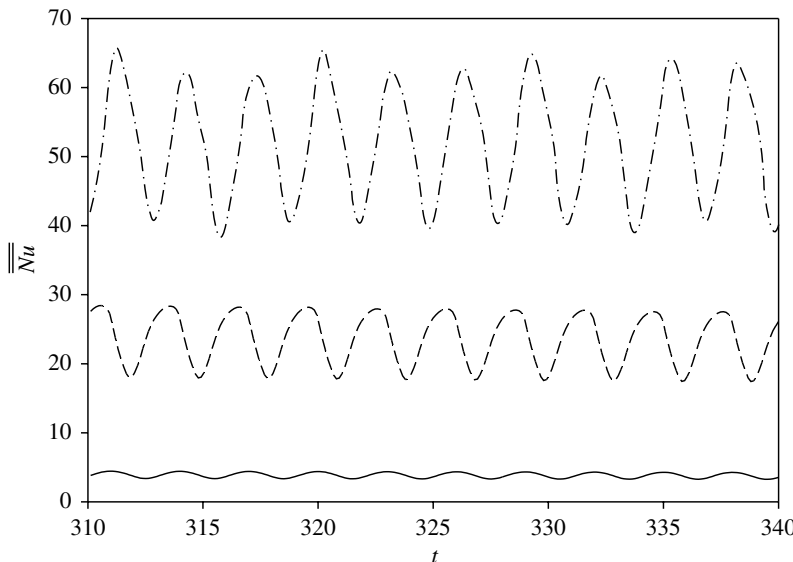


FIGURE 2.16

Time variations of heat transfer from the heated circular cylinder in Hele-Shaw cell for different Reynolds numbers, with fixed $KC = 3$ and $H/R = 0.1$. Solid line: $Re_D = 1000$; Dotted line: $Re_D = 3200$; Dashed-dotted line: $Re_D = 6500$. Note the amplification of the heat transfer as Re_D increases. The phase angles referenced to the free stream oscillation also change as Re_D increases.

distribution on the mid-plane of the Hele-Shaw cell. The convection heat transfer dominated by the periodic flow separation process is shown clearly in Figure 2.15. The variation of the total heat transfer from the heated circular cylinder as enhanced by the flow oscillations are shown in Figure 2.16 for different Reynolds numbers at $Re_D = 1,000, 32,000$, and $6,500$, with the Prandtl number fixed at $Pr = 0.7$ for air. Here, KC and H/R are also fixed at $KC = 3$ and $H/R = 0.1$. The increase in Reynolds number has greatly enhanced the heat transfer not only in overall mean value, but also the amplitude of oscillatory heat transfer (regeneration process). Interestingly, the phase of the oscillatory heat transfer shifts continuously as the Reynolds number increases.

2.7 Concluding Remarks

In this chapter, the macroscopic equations that govern the convective heat transfer in porous media are rigorously derived through the volumetric averaging procedure on the microscopic equations over a REV. The average procedure leads to the closure problem where the dispersion, the interfacial tortuosity, and the interfacial transfer become the new unknowns.

The dynamic closure models with relation to closing the equation system are composed by combining the earlier works by the author and others for the dispersion, tortuosity, and the interfacial transfer. The equation system plus proper boundary conditions then can be solved either analytically or numerically to predict the convective heat transfer in the porous media. However, there exist several coefficients in the closure relations that have to be determined experimentally (or numerically) *a priori*. Experiments conducted earlier for the determination of these coefficients were reviewed. These experimental results had basically confirmed the validity of the closure relations; however, they were insufficient. This leads to the conclusion that more experiments are needed for the determination of these coefficients.

It is noted that the momentum closure relation for the interfacial force as obtained by Hsu [52] contains all the components due to drag, lift, and transient inertia to the first-order approximation. The relative importance of these force components depend then on the ranges of Reynolds number and timescale involved in the process. Therefore, the macroscopic momentum equation is expected to be valid for all ranges of timescale and Reynolds number. This to some extent has clarified the recent debate on the validity as well as the limitations of the Brinkman–Forchheimer-extended Darcy equation [63, 64]. On the other hand, the closure relations for interfacial heat transfer as obtained by Hsu [52] were derived under the assumption of steady flows. Further investigations are needed to assess the suitability of such interfacial heat transfer model, particularly for unsteady flows.

In this chapter, flows and heat transfer in Hele-Shaw cells in analog to the convection heat transfer in porous media are explored in detail. In fact, the Hele-Shaw cells represent one category of the simplified porous structure. Although the averaged equations for Hele-Shaw flows bear great resemblance to the macroscopic equations for flows in porous media, several features such as form drag and thermal tortuosity are missing in the Hele-Shaw flow model. Nevertheless, the simplified Hele-Shaw model provides a viable way for the verification of the dynamic model through a DNS of the 3D flows in Hele-Shaw cells. The numerical results presented in this chapter as obtained from the DNS simulation of the 3D Hele-Shaw flows have shed light on a more complete understanding of the flows and heat transfer in porous media. The complexity of such flows and heat transfer remains a great challenge for the years to come.

Acknowledgment

This study is supported by the Hong Kong SAR Government under Grant No. HKUST6254/02E. The assistance on compiling and drawing the figures by Dr. M.K. Kwan and Mr. Ben S.W. Chiang is gratefully appreciated.

References

1. H. Darcy. *Les fontaines publiques de la ville de Dijon*. Paris: Victor Dalmont, 1856.
2. P.H. Forchheimer. *Z. Ver. Dtsch. Ing.* 45:1782–1788, 1901.
3. S. Ergun. Fluid flow through packed columns. *Chem. Eng. Prog.* 48:89–94, 1952.
4. C.T. Hsu and P. Cheng. Thermal dispersion in a porous medium. *Int. J. Heat Mass Transfer* 33:1587–1597, 1990.
5. C.T. Hsu, H.L. Fu, and P. Cheng. On pressure-velocity correlation of steady and oscillating flows in regenerators made of wire-screens. *ASME J. Fluids Eng.* 121:52–56, 1999.
6. L.F. Liu, M.H. Davis, and S. Downing. Wave-induced boundary layer flows above and in a permeable bed. *J. Fluid Mech.* 325:195–218, 1996.
7. M.A. Biot. General theory of three dimensional consolidation. *J. Appl. Phys.* 12:155–164, 1941.
8. G. Dagan. The generalization of Darcy's law for non-uniform flows. *Water Resour. Res.* 15:1–7, 1979.
9. J.C. Maxwell. *A Treatise on Electricity and Magnetism*. Oxford: Clarendon Press, 1873, p. 365.
10. D. Kunii and J.M. Smith. Heat transfer characteristics of porous rocks. *AIChE J.* 6:71–78, 1960.
11. R. Krupiczka. Analysis of thermal conductivity in granular materials. *Int. Chem. Eng.* 7:122–144, 1967.
12. R.A. Crane and R.I. Vachon. A prediction of the bounds on the effective thermal conductivity of granular materials. *Int. J. Heat Mass Transfer* 20:711–723, 1977.
13. E. Tsotsas and H. Martin. Thermal conductivity of packed beds: a review. *Chem. Eng. Prog.* 22:19–37, 1987.
14. D.L. Swift. The thermal conductivity of spherical metal powders including the effect of an oxide coating. *Int. J. Heat Mass Transfer* 9:1061–1073, 1966.
15. S. Nozad, R.G. Carbonell, and S. Whitaker. Heat conduction in multiphase systems. I: theory and experiments for two-phase systems. *Chem. Eng. Sci.* 40:843–855, 1985.
16. V. Prasad, N. Kladas, A. Bandyopadhyay, and Q. Tian. Evaluation of correlations for stagnant thermal conductivity of liquid-saturated porous beds of spheres. *Int. J. Heat Mass Transfer* 32:1793–1796, 1989.
17. R.G. Deissler and J.S. Boegli. An investigation of effective thermal conductivities of powders in various gases. *ASME Trans.* 80:1417–1425, 1958.
18. N. Wakao and K. Kato. Effective thermal conductivity of packed beds. *J. Chem. Eng. Japan* 2:24–32, 1969.
19. N. Wakao and D. Vortmeyer. Pressure dependency of effective thermal conductivity of packed beds. *Chem. Eng. Sci.* 26:1753–1765, 1971.
20. M. Sahraoui and M. Kaviany. Slip and non-slip temperature boundary conditions at interface of porous, plain media: conduction. *Int. J. Heat Mass Transfer* 36:1019–1033, 1993.
21. P. Zehner and E.U. Schlunder. Thermal conductivity of granular materials at moderate temperatures. *Chem. Ing.-Tech.* 42:933–941, 1970 (in German).
22. C.T. Hsu, P. Cheng, and K.W. Wong. Modified Zehner-Schlunder models for stagnant thermal conductivity of porous media. *Int. J. Heat Mass Transfer* 37:2751–2759, 1994.

23. C.T. Hsu, P. Cheng, and K.W. Wong. A lumped parameter model for stagnant thermal conductivity of spatially periodic porous media. *ASME J. Heat Transfer* 117:264–269, 1995.
24. C.T. Hsu, K.W. Wong, and P. Cheng. Effective thermal conductivity of wire screens. *AIAA J. Thermophys. Heat Transfer* 10:542–545, 1996.
25. M. Kaviany. *Principles of Heat Transfer in Porous Media*. New York: Springer-Verlag, 1991.
26. P. Cheng and C.T. Hsu. Heat conduction. In: D.B. Ingham and I. Pop, Eds. *Transport Phenomena in Porous Media*. Oxford: Pergamon Press, Elsevier Science, 1998, pp. 57–76.
27. M. Quintard and S. Whitaker. One- and two-equation models for transient diffusion processes in two-phase systems. *Adv. Heat Transfer* 23:369–367, 1993.
28. M. Quintard and S. Whitaker. Local thermal equilibrium for transient heat conduction: theory and comparison with numerical experiments. *Int. J. Heat Mass Transfer* 38:2779–2796, 1995.
29. C.T. Hsu. A closure model for transient heat conduction in porous media. *ASME J. Heat Transfer* 121:733–739, 1999.
30. C.T. Hsu. Heat conduction in porous media. In: K. Vafai, Ed. *Handbook of Porous Media*, 1st edn. New York: Marcel Dekker, 2000, pp. 171–199.
31. R. Aris and N.R. Amundson. Some remarks on longitudinal mixing or diffusion in fixed beds. *AIChE J.* 3:280–282, 1957.
32. P.G. Saffman. A theory of dispersion in a porous medium. *J. Fluid Mech.* 6:321–349, 1959.
33. P.G. Saffman. Dispersion due to molecular diffusion and macroscopic mixing in flow through a network of capillaries. *J. Fluid Mech.* 7:194–208, 1960.
34. D.R.F. Harleman and R.R. Rumer. Longitudinal and lateral dispersion in packed beds: effect of column length and particle size distribution. *J. Fluid Mech.* 16:385–394, 1963.
35. S. Whitaker. Diffusion and dispersion in porous medium. *AIChE J.* 13:420–427, 1967.
36. M.F. Edwards and J.E. Richardson. Gas dispersion in packed beds. *Chem. Eng. Sci.* 23:109–123, 1968.
37. R.G. Carbonell. Effect of pore distribution and flow segregation on dispersion in porous media. *Chem. Eng. Sci.* 34:1031–1039, 1979.
38. R.G. Carbonell. Flow nonuniformities in packed beds, effect on dispersion. *Chem. Eng. Sci.* 35:1347–1356, 1980.
39. D.L. Koch and J.F. Brady. Dispersion in fixed beds. *J. Fluid Mech.* 154:399–427, 1985.
40. D.L. Koch and J.F. Brady. A non-local description of advection–diffusion with application to dispersion in porous media. *J. Fluid Mech.* 180:387–403, 1987.
41. M. Quintard and S. Whitaker. Convection, dispersion, and interfacial transport of contaminants: homogeneous porous media. *Adv. Water Resour.* 17:221–239, 1994.
42. D.J. Gunn and J.F.C. de Sousa. Heat transfer and axial dispersion in packed beds. *Chem. Eng. Sci.* 29:1363–1371, 1974.
43. D.J. Gunn and M. Khalid. Thermal dispersion and wall transfer in packed beds. *Chem. Eng. Sci.* 30:261–267, 1975.
44. D. Vortmeyer. Axial heat dispersion in packed beds. *Chem. Eng. Sci.* 30:999–1001, 1975.

45. J. Levec and R.G. Carbonell. Longitudinal and lateral thermal dispersion in packed beds, I. *AIChE J.* 31:581–590, 1985.
46. J. Levec and R.G. Carbonell. Longitudinal and lateral thermal dispersion in packed beds, II. *AIChE J.* 31:591–602, 1985.
47. D. Kunii and M. Suzuki. Particle-to-fluid heat and mass transfer in packed beds of fine particles. *Int. J. Heat Mass Transfer* 10:845–852, 1967.
48. P.A. Nelson and T.R. Galloway. Particle-to-fluid heat and mass transfer in dense systems of fine particles. *Chem. Eng. Sci.* 30:1–6, 1975.
49. H. Martin. Low Peclet number particle-to-fluid heat and mass transfer in packed beds. *Chem. Eng. Sci.* 33:913–919, 1978.
50. N. Wakao, S. Kaguei, and T. Funazkri. Effect of fluid dispersion coefficients on particle-to-fluid heat transfer coefficients in packed beds. *Chem. Eng. Sci.* 34:325–336, 1979.
51. N. Wakao and S. Kaguei. *Heat and Mass Transfer in Packed Beds*. New York: Gordon and Breach Science Pub. Inc., 1982, p. 294.
52. C.T. Hsu. A unified closure model for convective heat and mass transfer in porous media, 2004 (in manuscript).
53. S. Whitaker. *The Method of Volumetric Averaging*. Dordrecht, Netherlands: Kluwer Academic Publishers, 1999.
54. C.T. Hsu and H. Fu. Measurements of pressure drop of high frequency oscillating flows through a packed column made of wire-screens, 2004 (in manuscript).
55. H. Fu and C.T. Hsu. Measurements of longitudinal thermal dispersion of oscillating flows through a packed column, 2004 (in manuscript).
56. J.S. Hele-Shaw. On the motion of a viscous fluid between two parallel plates. *Nature (London)* 58:34–42, 1898.
57. G.I. Taylor and P.G. Saffman. A note on the motion of bubbles in a Hele-Shaw cell and porous medium. *Q. J. Mech. Appl. Math.* 12:265–279, 1959.
58. C.W. Park and G.M. Homsy. Two-phase displacement in Hele-Shaw cells: theory. *J. Fluid Mech.* 139: 291–308, 1984.
59. C.W. Park, S. Gorell, and G.M. Homsy. Two-phase displacement in Hele-Shaw cells: experiments on viscously driven instabilities. *J. Fluid Mech.* 141: 257–287, 1984.
60. A.V. Gorin, D.P. Sikovsky, V.E. Nakoryakov, and V.D. Zhak. Two-dimensional turbulent jet in a Hele-Shaw cell. *The VII Proceeding of Conference on flow modeling and turbulence measurements*, Tainan, Taiwan, 1998, pp. 269–276.
61. M.K. Kwan and C.T. Hsu. A numerical study of steady flows past a circular cylinder in Hele-Shaw cells, 2004 (in manuscript).
62. M.K. Kwan and C.T. Hsu. Numerical simulation of oscillating flows past a heated circular cylinder in Hele-Shaw cells, 2004 (in manuscript).
63. D.A. Nield. The limitations of the Brinkman–Forchheimer equation in modeling flow in a saturated porous medium and at an interface. *Int. J. Heat Fluid Flow* 12:269–272, 1991.
64. K. Vafai and S.J. Kim. On the limitations of Brinkman–Forchheimer-extended Darcy equation. *Int. J. Heat Fluid Flow* 16:11–15, 1995.

3

Dispersion in Porous Media

Shijie Liu and Jacob H. Masliyah

CONTENTS

3.1	Definition of Dispersion	82
3.2	Volume Averaging	85
3.3	Volume Averaging of Transport Equation and Closures for Isotropic Porous Media	93
3.4	Tortuosity and Measurements	95
3.4.1	Volume Averaging of Electrical Conduction Equation	97
3.4.2	Propagation of Small Amplitude Low-Frequency Waves	99
3.4.3	Tortuosity Relations	100
3.5	Volume Averaged Navier–Stokes Equation for an Isotropic Porous Medium	106
3.6	Dispersion or Volume Averaged Advection–Diffusion Equation	112
3.7	Volume Averaged Heat Equation	114
3.8	Microscopic Inertia and Flow Induced Dispersion	118
3.9	Summary and Discussions	127
	Nomenclature	129
	References	132

Dispersion is a well-known phenomenon in porous media primarily for heat and mass transfer. Like viscosity in momentum transfer, heat conductivity in heat transfer, and diffusion coefficient in mass transfer, dispersion coefficient is a property valid only under continuum assumptions. Dispersion causes fluid (velocity, molecules, and temperature) to distribute evenly, which is directly analogous to mass diffusion (Fickian diffusion) and viscous stress. Fickian diffusion causes molecules to distribute evenly, whereas viscous stress causes flow velocity to be distributed evenly. However, dispersion is caused due to the fluctuations of bulk flow, whereas diffusion is caused due to random molecular motion.

3.1 Definition of Dispersion

To help us better understand dispersion, let us first examine the concept of diffusion. For the first instance, let us restrict ourselves to the transport of molecules. Diffusion is the spreading of “tracer molecules” among a “continuum of molecules.” Two ingredients must coexist for diffusion to occur: concentration gradient (“tracer molecules” are not evenly distributed) and random motion (all the molecules are moving about in relative positions). If there is no concentration gradient, diffusion loses meaning as there is no measure for the spreading (or the change of degree of mixedness) of the molecules. If the molecules remain steadily motionless relative to each other, spreading or mixing will not occur. Diffusion is a term reserved for the spreading or mixing in the molecular level, where the motion is random (or Brownian in fluids). To certain extent, dispersion is “identical” to diffusion. However, dispersion is a more general term but occurs when macroscopic motion (or flow) exists. In other words, dispersion is always associated with flow. Either there is a velocity fluctuation (or distribution) or there is flow stream splitting and rejoining along the path of the flow, it will cause dispersion to occur if a gradient exists. Dispersion is “convection” (or flow) induced spreading or mixing.

Dispersion occurs when convection exists. A well-known example is shown by Taylor [1], where the coupling of diffusion and velocity variation produces dispersion. Referring to Figure 3.1, when a pulse of tracer substance is injected into a smooth circular pipe within which fully developed laminar flow occurs, the concentration of the tracer will change from a near plug at the feeding point to a Gaussian distribution at a downstream observation location. This phenomenon can be exactly captured by convection and diffusion,

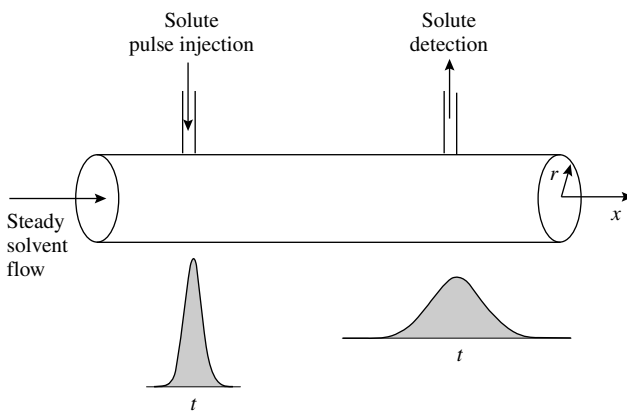


FIGURE 3.1
Taylor dispersion experiment set-up.

or mass transport, equation. For fully developed laminar flow in a circular pipe with a constant tracer diffusivity D_A , the mass transport equation is given by

$$\frac{\partial c_A^*}{\partial t} + 2U \left(1 - \frac{r^2}{R^2}\right) \frac{\partial c_A^*}{\partial x} - D_A \left(\frac{\partial^2 c_A^*}{\partial r^2} + \frac{1}{r} \frac{\partial c_A^*}{\partial r} + \frac{\partial^2 c_A^*}{\partial x^2}\right) = 0 \quad (3.1)$$

where c_A^* is the concentration of the tracer substance; t is time; U is the average discharge velocity in the pipe; r is the radial coordinate; R is the radius of the pipe; and x is the axial (longitudinal) coordinate. Equation (3.1) contains no dispersion term, only a diffusion term. The velocity distribution is accounted for by the parabolic velocity profile embedded in Eq. (3.1). If we were to simplify the equation by averaging out the radial variation, that is, using a constant velocity for the convection term, and averaging the concentration on the pipe cross-section or in the lateral (or radial) direction, then

$$\frac{\partial c_A}{\partial t} + U \frac{\partial c_A}{\partial x} - D_A(1 + K_{\parallel}) \frac{\partial^2 c_A}{\partial x^2} + D_A F_c (c_A - c_{As}) = 0 \quad (3.2)$$

where c_A is the cross-sectional averaged concentration, $c_A = (2/R^2) \int_0^R r c_A^* dr$; c_{As} is the tracer concentration on the pipe wall; the parameter K_{\parallel} is termed as the longitudinal dispersion coefficient; and $D_A F_c$ is the mass transfer coefficient. In so doing, we have effectively reduced the two-dimensional problem to a one-dimensional problem. The parameter F_c (or the product $D_A F_c$ term) accounts for the interaction between the pipe wall (solid) and the fluid. In most cases, the pipe wall is smooth (no immobile fluid being trapped that is in contact with the flowing fluid in the pipe), impermeable and not tracer releasing, the whole mass transfer term (or the solid–fluid interaction term) is zero. The longitudinal dispersion coefficient K_{\parallel} is used to account for the additional effects due to the original velocity variation in the radial direction. The value of K_{\parallel} can be determined by matching the solutions of Eq. (3.2) and (3.1), with the same boundary and initial conditions.

Since there is only one pulse of tracer injected into the pipe for the Taylor experiment, one can follow the movement of the isolated pulse downstream. Let $z = x - Ut$, then Eq. (3.2) is reduced to

$$\frac{\partial c_A}{\partial t} = K_T \frac{\partial^2 c_A}{\partial z^2} \quad (3.3)$$

where $K_T = D_A(1 + K_{\parallel})$ is the Taylor dispersion coefficient. By matching the solutions of Eqs. (3.3) and (3.1), Aris [2] has shown that the Taylor dispersion coefficient is given by

$$K_T = D_A + \frac{R^2 U^2}{48 D_A} \quad (3.4)$$

Taylor's work [1] has been extended by Aris [2] to other straight ducts of different shapes as well.

On comparing Eq. (3.3) with Eq. (3.1), one can infer the distinctive advantage of averaging. Equation (3.3) is much easier to solve than Eq. (3.1). However, as a result of averaging, we lose the ability to examine the radial variations. Owing to the averaging, additional closure parameters appear and these parameters bear physical meaning as well. Based on Eqs. (3.2) and (3.3), one can infer that dispersion is identical to diffusion, at least mathematically. Taylor dispersion shows that the coupling of diffusion and flow (or convection) can produce dispersion.

Dispersion occurs not only in mass transport (tracer dispersion), but in heat (thermal dispersion) and momentum (viscous dispersion) transports as well. Dispersion can be termed as flow-induced diffusion for mass transport, effective viscous dissipation for momentum transport, and effective thermal diffusion for heat transport. Because dispersion is an effective phenomenon occurring on a higher continuum level, where the velocity distributions or fluctuations on the continuum level of fluid are averaged out, averaging plays an important role in the study of dispersion. For porous media, the continuum approach by default involves the averaging above the continuum level of the fluid saturating the medium. Therefore, dispersion is always associated with porous media.

Dispersion can be caused by flow and geometrical obstruction as well. Even if the velocity variation and diffusion were absent at the level of fluid continuum (truly inviscid flow), the porous matrix would cause constant splitting and rejoining of the flow streams and thus create spreading (or dispersion) along the path of fluid traversing when the porous medium is being treated at continuum level. Figure 3.2 shows a sketch of such an example. In Figure 3.2,

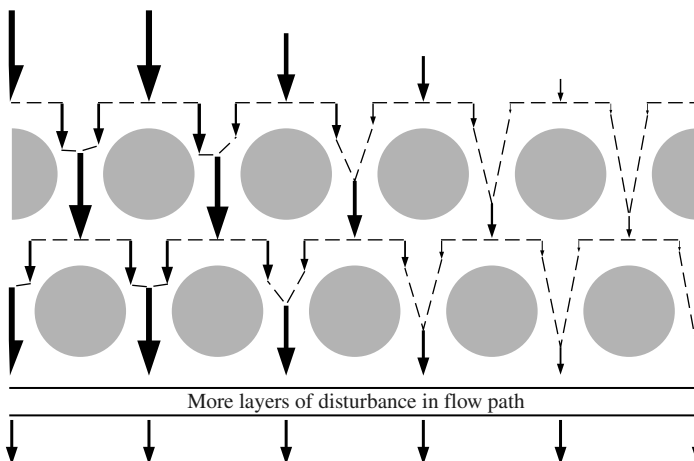


FIGURE 3.2

Flow and geometrical obstacle resulted dispersion.

the length of arrow represents the magnitude of the property (e.g., tracer concentration or temperature) under concern. Because of the splitting and rejoining of the streams, the property under concern gets mixed along the flow path and eventually resulted in an even distribution. This would occur in the absence of velocity distribution. However, owing to the presence of solid surfaces, the flow velocity distribution exists (zero on the solid wall). Therefore, dispersion is always part of flow in porous media.

3.2 Volume Averaging

A porous medium is a medium that is partially filled with solid material, which is interconnected and immobile. The portion of space that is not occupied by the solid material is also mostly interconnected. The solid material is normally called the solid matrix and the nonsolid portion is called pores or voids. Owing to the very complex and unknown nature of the geometry of a porous medium, the analysis of transport phenomena in porous media is difficult. It is for this reason that some averaging procedures have to be adopted in the analysis of fluid flow, heat, and mass transfer. The volume averaging concept of use today can be traced back to the continuum concept of fluid.

A possible approach for the study of fluid flow is to utilize the stochastic motion of the individual molecules of the fluid. In this approach, if one possesses a velocity probe whose size is smaller than or at most of comparable size to the dimension of the molecules, then at a given location in the flow field the measured or the "sensed point" velocity will fluctuate with time. The measured point velocity can take the variation as presented in Figure 3.3. The "sensed point" velocity can be taken to represent the individual motion of

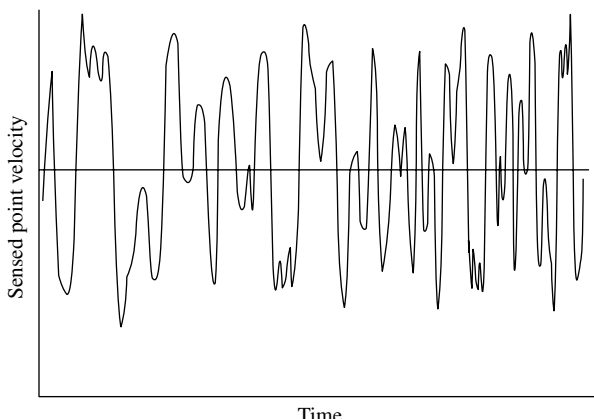


FIGURE 3.3

Local velocity readings with a probe of submolecular size.

the molecules. Here the size of the “point” is of a scale smaller than the size of the molecules themselves. Although the approach at this molecular scale is fundamental in its formulation, it is impractical in its application. This is simply due to the fact that the number of molecules in a gas or a liquid is so overwhelmingly large that it is not possible to accommodate such a large number of multibody interactions.

Similar to the case of a “point” velocity, other point fluid properties such as density and composition will also violently vary with time where the fluid at the molecular level is considered as being nonhomogeneous. However, in most instances, we are interested in the flow behavior on a larger scale, that is, on a macroscopic scale which is several orders of magnitude larger than the molecular dimension or the intermolecular distance. The macroscopic scale for the study of fluids and their motion implies that the physical quantities such as density, specific heat, and velocity associated with the matter contained within the macroscopic volume are regarded as being averaged out over the volume. Here, the macroscopic volume becomes the “point” within the fluid under consideration. Physically, the macroscopic volume can be very small, say of $O(10^3 \text{ nm}^3)$. Even at this small scale, the number of molecules it contains is very large. For the case of a gas under atmospheric pressure and room temperature, such a volume contains a large number of molecules of the order of 10^4 . As a consequence of this sweeping physical model, namely the continuum hypothesis, it becomes very convenient to study fluid motion. Due to the introduction of the continuum hypothesis, quantities such as fluid density, viscosity, thermal and electrical conductivities, and mass diffusivity are derived. These averaged quantities are essential in describing a fluid continuum. Here, the averaging is taken over the macroscopic volume that contains a large number of fluid molecules.

Mass conservation, momentum, and energy balance equations were developed to describe fluid motion using the continuum hypothesis. Experience has shown that the continuum hypothesis is valid under most conditions. Naturally, we would expect it to break down under a situation, where say, the free molecular path is of the same order of the magnitude as the flow channel dimension.

Fluid flow in porous media can be studied by solving the already developed flow equations for a continuous fluid. A difficulty arises in that the governing equations must be solved subject to the prevailing boundary conditions, for example, no-slip conditions at the solid surface of the porous medium matrix in contact with the flowing fluid. As the geometry of the porous medium channels is extremely complex and by-and-large not known, the situation becomes exceedingly difficult to obtain a flow solution even with the use of today's super-computers.

The approach outlined above will, of course, provide the local or the point fluid velocity on the continuum fluid scale. However, if one is willing to consider once again a continuum hypothesis, albeit on a much larger macroscopic scale whereby averaging is taken over a large enough volume that would embrace many pores and surfaces, then the second-order continuum

hypothesis will provide a description of the fluid motion in a porous medium in an “average sense.” Here, with this approach, one cannot provide the velocity profile between say two solid grains within the porous medium, however, the fluid velocity is provided on an averaged sense. While for the continuum hypothesis for a fluid, the macroscopic scale was very small, say $O(10^2)$ of the molecular dimension, the macroscopic scale as applied to the porous medium continuum hypothesis must also be, say $O(10)$ of the pore dimension.

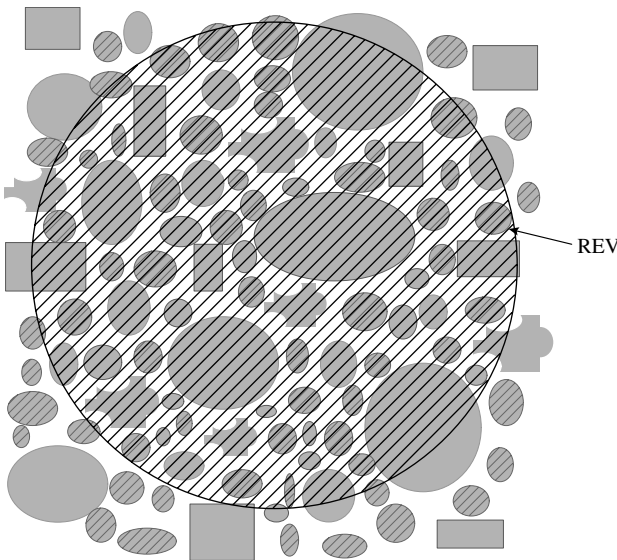
Averaging techniques are not unique either, all of which require certain closures. Notably, there are two main classes of averaging techniques, namely, ensemble averaging and volume averaging. While the ensemble average starts with one fixed particle in the space and collects the influences from the surrounding particles, that is, cluster of particles [3–14], the volume average starts with the continuum equations for a single phase [15–54]. Since the ensemble averaging technique is primarily for dispersed flow, only the volume average technique shall be discussed here. Whenever possible, mathematical rigorousness will be maintained. However, for practical applicability and simplicity, phenomenological approach on closures will precede mathematical extreme. Empirical parameters will be allowed to account for the unknown nature of porous structures. For more rigorous approaches on volume averaging, the reader is referred to, for example, Ref. [20].

Similar to the “mathematical point” concept in fluid continuum hypothesis, the Representative Elementary Volume, REV, concept was implicitly used by various authors such as Whitaker [15] and Slattery [22] and was formalized by Bear [24] for studies of transport in porous media. An REV is a conceptual space unit, which is the minimum volume that can be located anywhere inside the porous medium within which measurable characteristics of the porous medium become continuum quantities. An REV can be regarded as a macroscopic unit consisting of a large sum of microstructures. The sketch of an REV is shown in [Figure 3.4](#) for an unconsolidated porous medium (or solid particle packs).

To help us understand the concept of the REV, we shall now go back to the continuum treatment of fluids. When the motion of fluids or physical properties of a fluid is to be deduced, one often assumes an infinitesimal volume or a “point” size. For example, the fluid density at a given local position is the ratio of fluid mass over the volume when the volume approaches the volume of the assumed point with its centroid at the local position of concern. However, no one really cares what the size of the point is quantitatively. The fluid density is given as

$$\rho(P) = \lim_{\Delta V \rightarrow V_p} \frac{\Delta m}{\Delta V} \quad (3.5)$$

The characteristic volume V_p is called the *physical point* (or *material point*) of the fluid at the *mathematical point* P. The concept of the mathematical point is identical to an REV. When the volume of consideration is smaller than V_p , the

**FIGURE 3.4**

Planar section schematic of an REV.

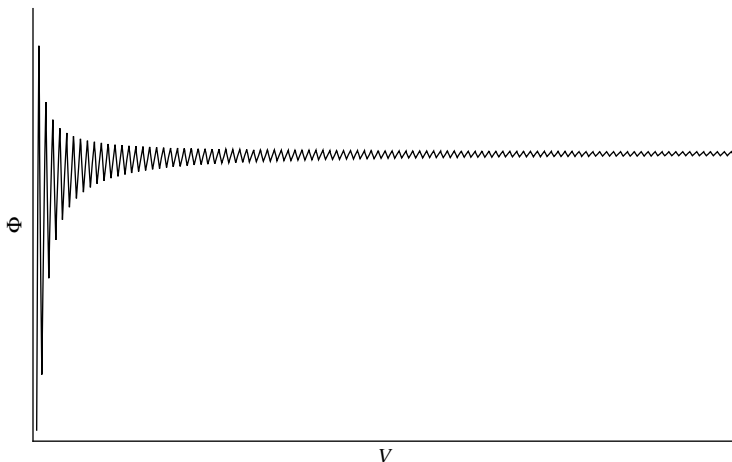
continuum concept breaks down. We plotted the fluid mass over the volume of sampling in Figure 3.5, where $\Phi = \rho$. The molecules are assumed to be uniformly placed in space. When the sampling volume is very small as it is suggested by the term *infinitesimal* used routinely in this connection in fluid mechanics texts, the fluid mass over volume ratio becomes undefined. When the sampling volume is at least of V_p , we obtain a fictitious smooth medium (instead of the molecules). Unlike the porous medium in which the solid matrix is immobile, the concept of fluid is also associated with time average as well since the molecules are moving about at any given instant even though the overall behavior is at a thermodynamic equilibrium. The time average is also to be implied for suspension systems where the exact location of a given particle is not to be tracked.

Knudsen [54] defines a dimensionless number, which is now known as the *Knudsen number* to test the validity of fluid continua

$$Kn = \frac{\lambda}{\rho} \frac{\partial \rho}{\partial l} \quad (3.6)$$

where λ is the mean free path of the fluid molecules and l is the minimum linear dimension of the system. When $Kn < 0.01$, the fluid can be considered as in continuum. When Kn is of order unity, the fluid exhibits *slip-flow* near a wall and when Kn is greater than unity, we have what is known as the *Knudsen flow*.

In addition, when the molecules are large (*macromolecules* or polymers) and the dimension between the confining walls is small, the continuum concept

**FIGURE 3.5**

Variation of a physical property Φ in a porous medium with a volume V .

also breaks down. Under this circumstance, *slip-flow* can occur, for example, flow of polymers in an ultra-fine capillary tube.

For porous media, the situation is slightly different. Since the solid matrix is immobile, the extent of error is reduced as compared with a fluid when continuum is imposed for systems near the border line of continua. The fact that the solid matrix is immobile and is rigid or can sustain pressure and stresses also makes a “point” in porous media different from the mathematical “point” in a pure fluid. The overall pressure and stresses for the fluid and solid matrix mixture are meaningless. However, the pressure and stresses for a fluid phase at a given point are still valid measures as long as that, within an REV, the void space is interconnected and there is no barrier to prevent the filling fluid from moving around.

For a porous medium system, one can refer to Figure 3.5 as well. The abscissa or sampling volume is of linear scale in the order of the grain size. The ordinate Φ can be any measurable physical property in a volume average sense, for example, the porosity. When the volume space is very small, the value of Φ is not defined, that is, Φ can assume any value depending on the location under consideration. As the sampling volume increases, Φ changes “periodically” for an orderly system and is randomly fluctuating for a random system. The amplitude of the oscillation decreases with increasing sampling volume. The volume of an REV is defined for such a sampling volume so that the amplitude of the oscillation is lower than certain acceptable degree when the sampling volume is further increased.

Figure 3.4 shows a special case of single fluid saturated medium. When multiple fluid phases each partially fill the open pores of a porous medium, more interfaces can be identified. In other words, interfaces between individual fluids will also enter into play.

In a multi-fluid system, the volume fraction, ε_i , of fluid i is defined as

$$\varepsilon_i = \frac{V_i}{V} = \varepsilon \frac{V_i}{V_o} \quad (3.7)$$

where V is the total volume of an REV, V_i is the volume occupied by fluid i , and V_o is the total open pore space in the REV. The porosity of the porous medium is a summation of the partial porosities, that is,

$$\sum \varepsilon_i = \varepsilon \quad (3.8)$$

The *intrinsic phase average* of a quantity, $\Phi_{\varepsilon i}$, is the average value of a quantity in terms of the partial volume of the phase (fluid) itself, that is,

$$\Phi_{\varepsilon i} = \frac{1}{V_i} \int_{V_i} \Phi_i^* dV_i \quad (3.9)$$

where Φ^* is the local (microscopic) quantity. The deviation of a quantity, $\hat{\Phi}_i$, is the difference between the local value and the intrinsic phase average value of that quantity,

$$\hat{\Phi}_i = \Phi_i^* - \Phi_{\varepsilon i} \quad (3.10)$$

Here Φ_i can be a scalar or a vector.

The volume average of a quantity for a fluid phase, Φ_i , is the average taken over the entire REV

$$\Phi_i = \frac{1}{V} \int_V \Phi_i^* dV \quad (3.11)$$

It can be shown that

$$\frac{1}{V} \int_V \mathbf{v}^* \Phi^* dV = \varepsilon \mathbf{v}_e \Phi_e + \frac{1}{V} \int_V \hat{\mathbf{v}} \hat{\Phi} dV \quad (3.12)$$

Therefore, when products are to be volume averaged, the resultants are not just direct products of their respective volume averages.

The relation between the volume average value and the intrinsic phase average values depends on the physical quantity itself. For the flow velocity, it is given by

$$\mathbf{v}_i = \varepsilon_i \mathbf{v}_e \quad (3.13)$$

However, for fluid density, pressure, viscosity, and concentration of a component, the strict definition by Eq. (3.13) loses its meaning. In other words, \mathbf{v}_i is not to be generalized by Φ_i in Eq. (3.13). As Liu et al. [51] and Liu and

Masliyah [55] pointed out, the average pressure must take into account the fact that the pressure inside the immobile solid material is not defined and is also irrelevant to the flow system. The solid matrix can sustain pressure and stresses. The fluids, on the other hand, will transmit the pressure and stresses to adjacent fluid elements or the solid matrix. When a stress is applied, the fluid will respond by flow and the solid matrix will deform according to its rigidity. When the solid matrix is rigid, immobile, and not supported by the fluid, it will not share the load with the saturated fluid. It is then logical to define an average pressure in a fluid phase by

$$p_i = p_{ei} \quad (3.14)$$

Equation (3.14) can be understood by considering the limiting case of no flow (static condition). Figure 3.6 shows a sketch of a fluid–solid system. When the solids are immobile and not supported by the fluid, the pressure due to a single fluid saturated medium at the bottom can be evaluated by the top pressure and the height between the bottom and the top, h , by

$$p_b = p_a + \rho_f gh \quad (3.15)$$

where ρ_f is the density of the fluid.

The total pressure is the same as the fluid pressure. In other words, the presence of the solids does not alter the pressure of the fluid system when the solids are connected and not suspended in the fluid phase as long as the fluid height is maintained the same. Referring to Figure 3.6, when the solid matrix is immobile, that is, not supported by the fluid,

$$(\Delta p)_f = (\Delta p)_T = p_b - p_a = \rho_f gh \quad (3.16)$$

where $(\Delta p)_f$ denotes the pressure difference contributed by the fluid phase to the total (or overall) pressure difference $(\Delta p)_T$. Hence, Eq. (3.14) applies.

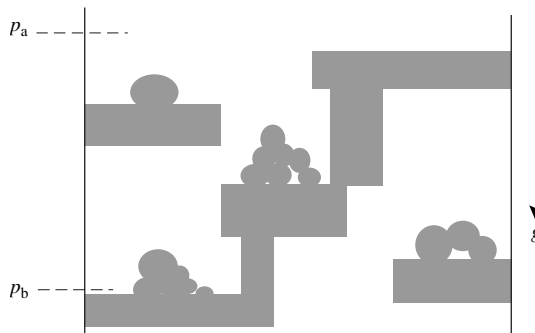


FIGURE 3.6
Evaluation of static pressure for fluid–solid systems.

However, when the solids are mobile, or in other words, the solids are suspended in the fluid. The solid phase is just like another fluid phase in the mixture, and the total pressure at the bottom becomes

$$p_b = p_a + [\rho_f \varepsilon + \rho_s(1 - \varepsilon)]gh \quad (3.17)$$

where ρ_s is the density of the suspended solids.

Equation (3.17) can also be interpreted as

$$(\Delta p)_T = p_b - p_a = (\Delta p)_f + (\Delta p)_s \quad (3.18a)$$

where $(\Delta p)_s$ is the part of the pressure difference due to the presence of the mobile solid phase. The contributions of the pressure difference can be readily split based on the density of the individual phases as

$$(\Delta p)_f = \varepsilon(\rho_f gh) \quad (3.18b)$$

$$(\Delta p)_s = (1 - \varepsilon)(\rho_s gh) \quad (3.18c)$$

Equation (3.18) implies that Eq. (3.13) is applicable for the pressure. When solids are suspended in the fluid phase(s), the collection of the solids is to be regarded as a “fluid phase” that is dispersed and hence similar treatments to a fluid phase are assumed. It is clear that the discontinuous nature of the “phase” needs to be accounted for when such a system is under consideration.

The relation, Eq. (3.14), is also used for the definition of the volume averaged pressure. It simply ignores the existence of the solid matrix since the pressure is not associated with the solid blockage that is not supported by the fluid as long as the fluid phase is connected. It should be noted that for an immiscible multiphase flow system, a finite pressure jump, like the flow velocities in different phases, is allowed between phases. As for the fluid viscosity, the same rule as that given by Eq. (3.14) can be used. For fluid density and concentration, the same rule as that given for velocity applies except that the intrinsic average should be used at all times since the volume averaged quantities lose their meaning.

On the other hand, the temperature is a different quantity. It is defined and it does not necessarily have to assume a fixed value (as that in a fluid phase) inside the solid material. Thermal energy can traverse through fluids as well as solids. Furthermore, when multiple fluid phases contact each other, a temperature jump between phases is less likely to occur. The same phenomenon may hold true for the concentration in a fixed bed reactor. In some situations, the continuity in the fluid and solid may allow for a single energy equation. Hence, the energy equation should be treated differently from the governing fluid flow (and mass transfer) equations.

It should be noted that the flow velocity is preferred in terms of a volume averaged value (superficial) in the governing equations since the average flow rate should remain continuous. The pressure and concentration

should be used in terms of their intrinsic values since no sudden increase in these quantities are allowed in one phase. For example, considering a free space–porous medium interface, the volume averaged flow velocity is expected to be continuous, that is, the flow in and out of the interface are equal. The pressure, electrical potential, and concentration in a phase must be continuous irrespective of the free space–porous medium interface.

3.3 Volume Averaging of Transport Equation and Closures for Isotropic Porous Media

The transport equation in a fluid phase can be represented by

$$\frac{\partial \Phi_i^*}{\partial t} + \nabla \cdot \mathbf{J}_i^* = S_{\Phi i}^* \quad (3.19)$$

with the flux \mathbf{J}_i^* being given by

$$\mathbf{J}_i^* = \mathbf{v}_i^* \Phi_i^* - D_{fi} \nabla \Phi_i^* \quad (3.20)$$

where D_{fi} is the diffusivity, Φ_i stands for the velocity field, concentration, and absolute temperature, and $S_{\Phi i}$ is the source term of the transport equation. For the momentum transfer, $S_{\Phi i} = \nabla p_i / \rho_i$ and for mass and heat transfer equations, $S_{\Phi i} = 0$ if no reaction occurs. When heat transfer is considered, we neglected the viscous dissipation besides assuming that the fluid properties remain constant. For the momentum equation, D_{fi} is to be replaced by the kinematic viscosity, $D_{fi} = \mu_i / \rho_i$. For heat transfer equation, the term D_{fi} is to be replaced by the thermal diffusivity, $D_{fi} = k_i / \rho_i c_{pi}$. For mass transfer (tracer displacement) equation, the diffusivity is given by $D_{fi} = D_i$, that is, the molecular diffusivity of the species.

For incompressible fluids with a constant diffusivity, the flux term in Eq. (3.19) can also be written as

$$\nabla \cdot \mathbf{J}_i^* = \mathbf{v}_i^* \cdot \nabla \Phi_i^* - D_{fi} \nabla^2 \Phi_i^* \quad (3.21)$$

Consider the volume average of Eq. (3.19) for incompressible flow in a porous medium of a nonconductive and nonsurface active solid matrix, which gives

$$\varepsilon_i \frac{\partial \Phi_{ei}}{\partial t} + \nabla \cdot \mathbf{J}_i = S_{\Phi i} \quad (3.22)$$

$$\begin{aligned} \nabla \cdot \mathbf{J}_i &= \frac{1}{V} \int_V \nabla \cdot \mathbf{J}_i^* dV = \frac{1}{V} \int_V \nabla \cdot (\mathbf{v}_i^* \Phi_i^* - D_{fi} \nabla \Phi_i^*) dV \\ &= -\frac{1}{V} \int_{S_i} (\mathbf{v}_i^* \Phi_i^* - D_{fi} \nabla \Phi_i^*) \cdot \mathbf{n}_i dS \end{aligned} \quad (3.23)$$

where S_i is the surface enclosing the i th fluid phase inside the REV and \mathbf{n}_i is normal to the surface S_i pointing out of the i th fluid phase. It should be noted that,

$$-\frac{1}{V} \int_{S_i} \mathbf{v}_i^* \Phi_i^* \cdot \mathbf{n}_i dS = \nabla \cdot (\mathbf{v}_i \Phi_{\varepsilon i}) + O(\varepsilon_i^2) \quad (3.24)$$

$$\begin{aligned} \frac{1}{V} \int_{S_i} D_{fi} \nabla \Phi_i^* \cdot \mathbf{n}_i dS &= \frac{\tau_i}{V} \int_{S_i} D_{fi} \nabla \Phi_{\varepsilon i} \cdot \mathbf{n}_i dS + O(\varepsilon_i^2) \\ &= -\tau_i \varepsilon_i D_{fi} \nabla^2 \Phi_{\varepsilon i} + O(\varepsilon_i^2) \end{aligned} \quad (3.25)$$

While Eq. (3.24) is straightforward as illustrated by Eq. (3.12), Eq. (3.25) needs further clarification. Inside the porous medium, transport does not occur directly from point to point on the shortest distance. Because of the solid matrix blockage, the transport passage is curved resulting in a longer path than the point to point straight line distance. The ratio of the straight line distance to the curved path length between the two points is termed tortuosity and is denoted by τ . Thus, the apparent gradient in Eq. (3.25) is reduced and a factor of τ is accessed to the overall gradient. Further clarification can be found in Section 3.4. Equations (3.24) and (3.25) are served as guidance to the closure of volume averaging. Higher order terms are not neglected completely and will be incorporated into closure parameters. Based on Eqs. (3.24) and (3.25), Eq. (3.23) can be reduced to

$$\nabla \cdot \mathbf{J}_i = \mathbf{v}_i \cdot \nabla \Phi_{\varepsilon i} - \tau_i \varepsilon_i D_{fi} \nabla^2 \Phi_{\varepsilon i} + II_i + OI_i \quad (3.26)$$

where

$$II_i = \frac{1}{V} \int_{S_{i-i}} (\mathbf{v}_i^* \Phi_i^* - \mathbf{v}_{\varepsilon i} \Phi_{\varepsilon i} - D_{fi} \nabla \hat{\Phi}_i) \cdot \mathbf{n}_i dS \quad (3.27)$$

$$OI_i = \frac{1}{V} \int_{S_{i-\emptyset}} (\mathbf{v}_i^* \Phi_i^* - \mathbf{v}_{\varepsilon i} \Phi_{\varepsilon i} - D_{fi} \nabla \Phi_i^*) \cdot \mathbf{n}_i dS \quad (3.28)$$

here S_{i-i} is the part of S_i with i th fluid to i th fluid contact and $S_{i-\emptyset}$ is the surface where fluid i is contacting other phases and solid matrix.

Closures are necessary in evaluating and expressing the results of the surface integrals: II_i and OI_i . It is understood that the interaction of fluid i with fluid i leads to a phenomenon similar to diffusion. Thus phenomenologically,

$$II_i = \frac{1}{V} \int_{S_{i-i}} (\mathbf{v}_i^* \Phi_i^* - \mathbf{v}_{\varepsilon i} \Phi_{\varepsilon i} - D_{fi} \nabla \hat{\Phi}_i) \cdot \mathbf{n}_i dS = \tau_i \nabla \cdot (D_{fi} \mathbf{K}_i \cdot \nabla \Phi_{\varepsilon i}) \quad (3.29)$$

The closure model in Eq. (3.29) has been widely used and perceived in dealing with fluid flow at turbulent conditions. For example, the term "eddy diffusivity" has been widely used although the fluctuations in turbulent flow

are usually assumed to be temporal. For transport in porous media, a more general term, dispersion coefficient tensor, \mathbf{K}_i , is used.

The closure for evaluating the interactions of the i -fluid phase with other phases and solid matrix can be given phenomenologically as

$$\begin{aligned} \text{OI}_i &= \frac{1}{V} \int_{S_{i-\emptyset}} (\mathbf{v}_i^* \Phi_i^* - \mathbf{v}_{\varepsilon i} \Phi_{\varepsilon i} - D_{fi} \nabla \Phi_i^*) \cdot \mathbf{n}_i dS \\ &= \sum_j F_{ij} (\Phi_{\varepsilon i} - \Phi_{\varepsilon j}) + D_{fi} F_{si} (\Phi_{\varepsilon i} - \Phi_{si}) \end{aligned} \quad (3.30)$$

where F_{si} is the surface interaction coefficient of fluid i (at the solid–fluid or flow–stagnant fluid interface), F_{ij} is the interface interaction coefficient for fluid j to fluid i and Φ_{si} is the average value of Φ_i^* at the i th fluid and solid matrix (or stagnant fluid) interface. The closure model, Eq. (3.30), is in direct analogy to mass transfer and heat transfer across interfaces (see transport phenomena texts, e.g. [56–60]). Transfers across interface occurs if there exists a driving force, $\Phi_{\varepsilon i} - \Phi_{\varepsilon j} \neq 0$.

Discrepancies can be found in earlier versions of the volume averaged equations where the fluid–solid interaction term in Eq. (3.30) has been recognized for the flow of fluid only and the dispersion term, Eq. (3.29), has been recognized for heat and mass transports only. It should be realized that all the terms in Eq. (3.26) have a pronounced effect on the fluid flow, that is, $\Phi = \mathbf{v}$, when the flow is strong. However, when the transport of mass or heat is of concern, the cross-phase interaction OI_i may be small since the concentration and temperature at the fluid–solid or flow–stagnant fluid interface can normally be assumed to be equal to that in the main flow stream if there is no significant amount of dead-end pores in the porous medium. Hence, for mass or heat equations, one can set

$$\Phi_{\varepsilon i} = \Phi_{si} \quad (3.31)$$

for simplicity. When the porous medium has a significant amount of dead-end pores, the flow–stagnant fluid interactions may become significant.

Further modeling is necessary in evaluating the dispersion coefficients and interaction coefficients for fluid flow, mass, and heat transports.

3.4 Tortuosity and Measurements

Tortuosity is a useful property of porous media. In the previous section, the tortuosity is introduced to the volume averaged transport equations in porous media through closure model, Eq. (3.25). Referring to Figure 3.7, one can draw an analogy of the passages or voids in a porous medium with a model curved

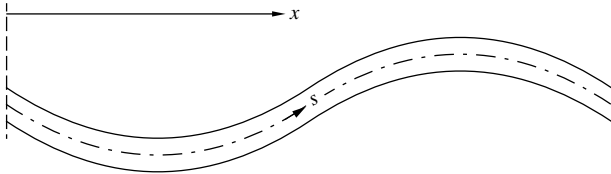


FIGURE 3.7
A curved passage.

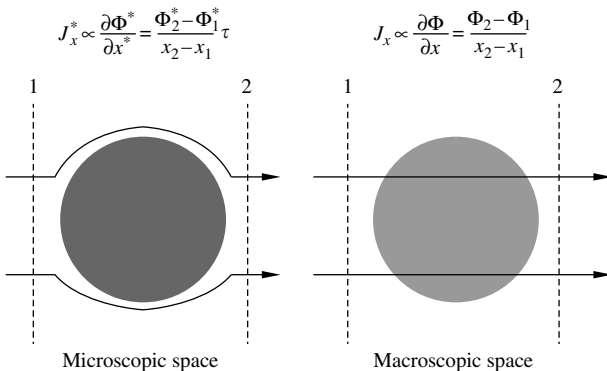


FIGURE 3.8
Relationship of diffusive fluxes in the microscopic space and in the macroscopic space.

passage. In deriving at Eq. (3.25), the tortuosity is defined as

$$\tau = \frac{dx}{ds} \quad (3.32)$$

The tortuosity is introduced into the volume averaged equation through the diffusive flux term as illustrated in Figure 3.8:

$$\frac{\partial \Phi^*}{\partial x} = \tau \frac{\partial \Phi_\varepsilon}{\partial x} + \frac{\partial \hat{\Phi}}{\partial x} \quad (3.33)$$

In this section, two additional transport processes: electrical conduction and wave propagation, will be discussed in light of the tortuosity measurements. In addition, the porous media are saturated with a single fluid. For these processes, we shall restrict ourselves in the linear regimes (i.e., linear flux-force relationships) and focus on the tortuosity relationships. The equations will be equally applicable if the system is a suspension rather than a porous medium. For example, in an electrical resistivity logging, the fluid movement is very weak and there is no induced particle movement for a suspension. In the case of a small amplitude wave propagation, the solid particles will not respond to the vibration and thus the displacement in solid matrix is negligible.

3.4.1 Volume Averaging of Electrical Conduction Equation

The electrical current density, \mathbf{i} , through an ionic solution is governed by

$$\mathbf{i}^* = e\mathbf{v}^* \sum_i z_i n_i^* - e \sum_i D_i z_i \nabla n_i^* - \frac{e^2 \sum_i D_i z_i^2 n_i^*}{k_B T} \nabla \psi^* \quad (3.34)$$

$$\nabla \cdot \mathbf{i}^* = 0 \quad (3.35)$$

where \mathbf{i} is the electric current density; e is the elementary charge of an electron, $e = 1.602 \times 10^{-19}$ C; z_i is the valency of the i th ionic species; n_i is the i th ionic species number concentration; D_i is the diffusivity of the i th ionic species; k_B is the Boltzmann constant, $k_B = 1.3806 \times 10^{-23}$ J/K; and ψ is the electric potential.

When the solution is electrically neutral and neither the solid matrix nor the containing wall is charged, we have

$$\sum_i n_i z_i = 0 \quad (3.36)$$

When the solution is homogeneous throughout the system, there is no concentration gradient. That is,

$$\nabla n_i = 0 \quad (3.37)$$

It should be noted that Eqs. (3.36) and (3.37) hold only under strict conditions in a porous medium. Equation (3.37) specifies that the fluid is homogeneous everywhere in the domain of concern. Equation (3.36) is a continuum equation in the microscopic space when a porous medium is present. If the porous medium is charged or conductive, it will cause the ionic species to distribute nonuniformly in the microscopic level and thus Eq. (3.36) will not apply. Equation (3.36) holds only if the counter ionic species are equally distributed at every “point” in the domain.

Substituting Eqs. (3.36) and (3.37) into Eq. (3.34), one obtains

$$\mathbf{i}^* = -\frac{e^2 \sum_i D_i z_i^2 n_i^*}{k_B T} \nabla \psi^* \quad (3.38)$$

Equation (3.38) is termed Ohm's law and is normally expressed as

$$\mathbf{i}^* = -\sigma_w^* \nabla \psi^* = -\nabla \psi^* / R_w \quad (3.39)$$

where σ_w is the electric conductivity and R_w is the electric resistivity of the pure fluid. They are defined as

$$\sigma_w^* = \frac{1}{R_w^*} = \frac{e^2 \sum_i D_i z_i^2 n_i^*}{k_B T} \quad (3.40)$$

Equation (3.39) describes the conduction of electricity in a pure fluid of ionic solution. When such a fluid is introduced to saturate a porous medium of a nonconducting and nonsurface active skeleton, Eq. (3.39) holds. Noting that the concentration of the electron carrying ions in the porous medium is affected by both the volume of the saturating fluid and the volume of the nonconducting and nonsurface active solid matrix, one has

$$\sigma_w = \frac{1}{R_w} = \frac{e^2 \sum_i D_i z_i^2 n_{ei}}{k_B T} \quad (3.41)$$

Averaging of Eq. (3.35) with the current density given by Eq. (3.38) or (3.39) is straightforward by following the same procedures as those for Eqs. (3.15) and (3.16). If the porous medium skeleton is nonconducting, one obtains

$$\begin{aligned} \frac{1}{V} \int_{S_i} \varepsilon \mathbf{i}_\varepsilon \cdot \mathbf{n}_i dS &= -\frac{1}{V} \int_V \nabla \cdot \mathbf{i}^* dV = -\frac{1}{V} \int_{S_i} \sigma_w^* \nabla \psi^* \cdot \mathbf{n}_i dS \\ &= -\frac{\tau \varepsilon}{V} \int_{S_i} \sigma_w \nabla \psi_\varepsilon \cdot \mathbf{n}_i dS - \frac{1}{V} \int_{S_i} (\sigma_w^* \nabla \psi^* - \sigma_w \nabla^* \psi_\varepsilon) \cdot \mathbf{n}_i dS \end{aligned} \quad (3.42)$$

Since the concentrations of the electrolyte ions are the same at solid–fluid interface as those inside the fluid medium and there are no convective fluxes contributing to the extra surface integral, it leads to a negligible extra surface integral. Therefore,

$$\frac{1}{V} \int_{S_i} \varepsilon \mathbf{i}_\varepsilon \cdot \mathbf{n}_i dS = -\frac{\tau \varepsilon}{V} \int_{S_i} \sigma_w \nabla \psi_\varepsilon \cdot \mathbf{n}_i dS \quad (3.43)$$

which leads to

$$\mathbf{i} = \varepsilon \mathbf{i}_\varepsilon = -\tau \varepsilon \sigma_w \nabla \psi_\varepsilon = -\tau \varepsilon \sigma_w \nabla \psi = -\tau \varepsilon \nabla \psi / R_w \quad (3.44)$$

Equation (3.44) is Ohm's law for a nonconducting and nonsurface active porous medium saturated with an ionic solution. Traditionally, Eq. (3.44) is given by

$$\mathbf{i} = -\sigma_0 \nabla \psi = -\nabla \psi / R_0 \quad (3.45)$$

where σ_0 and R_0 are the electric conductivity and the electric resistivity, respectively, of the porous medium saturated with an ionic solution. They are given by

$$\sigma_0 = \tau \varepsilon \sigma_w \quad \text{and} \quad R_0 = R_w / (\tau \varepsilon) \quad (3.46)$$

Since one can setup an experiment to measure the electric conductivity in the porous medium, the tortuosity is normally obtained through this means. Based on Eqs. (3.39) and (3.45), one can define a *formation* (electric resistivity) factor [61] as

$$F_\varepsilon = \frac{\sigma_w}{\sigma_0} = \frac{R_0}{R_w} \quad (3.47)$$

Using Eq. (3.46), we have

$$F_\varepsilon = \frac{1}{\tau_\varepsilon} \quad (3.48)$$

Equation (3.48) has been derived by, among others, Brown [62].

Hence, we have formally related the formation factor with the tortuosity through volume averaging. The tortuosity and the formation factor are inversely proportional. Equation (3.48) is valid for a porous medium of nonconductive and nonsurface active solid matrix. The tortuosity is the ratio of the apparent diffusion path length scale (i.e., in the volume averaged space) to the actual curved diffusion path length scale (i.e., in the microscopic space).

3.4.2 Propagation of Small Amplitude Low-Frequency Waves

In the small amplitude limit, the wave equation can be simplified as

$$\frac{\partial^2 \mathbf{u}^*}{\partial t^2} = c^2 \nabla^2 \mathbf{u}^* \quad (3.49)$$

where \mathbf{u} is the displacement vector of the propagating media and c is the speed of the wave in the propagating medium.

In the low-frequency limit, the propagation of waves in the porous medium skeleton (solid matrix) can be neglected. Hence, when a wave propagation is considered for a fluid-saturated porous medium under low frequency and small amplitude limit, Eq. (3.49) can be averaged without the complication of the porous medium skeleton. Under this limit, the porous medium can be considered rigid and nonconductive. Similar to averaging Eqs. (3.19) and (3.20), we have

$$\begin{aligned} \frac{1}{V} \int_V \frac{\partial^2 \mathbf{u}^*}{\partial t^2} dV &= \frac{1}{V} \int_V c^2 \nabla^2 \mathbf{u}^* dV = -\frac{1}{V} \int_{S_i} c^2 \nabla \mathbf{u}^* \cdot \mathbf{n}_i dS \\ &= -\frac{c^2 \tau_\varepsilon}{V} \int_{S_i} \nabla \mathbf{u}_\varepsilon \cdot \mathbf{n}_i dS - \frac{c^2}{V} \int_{S_i} \nabla^* \hat{\mathbf{u}} \cdot \mathbf{n}_i dS \end{aligned} \quad (3.50)$$

Since the propagation of the wave into the solid matrix is neglected, the displacement vector is similar to a concentration field that is defined only in the fluid. Owing to the absence of convection terms as well, we have

$$\int_{S_i} \nabla^* \hat{\mathbf{u}} \cdot \mathbf{n}_i dS \approx \mathbf{0} \quad (3.51)$$

Therefore, Eq. (3.50) is reduced to

$$\varepsilon \frac{\partial^2 \mathbf{u}_\varepsilon}{\partial t^2} = c^2 \tau \varepsilon \nabla^2 \mathbf{u}_\varepsilon \quad (3.52)$$

Equation (3.52) can be rearranged to yield

$$\frac{\partial^2 \mathbf{u}_\varepsilon}{\partial t^2} = c_0^2 \nabla^2 \mathbf{u}_\varepsilon \quad (3.53)$$

where c_0 is the apparent wave propagation speed in the porous medium with saturated fluid.

$$c_0 = \tau^{1/2} c \quad (3.54)$$

Owing to the difference in the wave propagation speed, one can define a reflection index for the porous medium. It is given by [63]

$$n = c_0/c \quad (3.55)$$

From Eq. (3.55), we obtain

$$\tau = n^2 \quad (3.56)$$

The relation between the reflection index and the formation factor can be obtained by substituting Eq. (3.56) into Eq. (3.48).

$$F_\varepsilon = \frac{1}{n^2 \varepsilon} \quad (3.57)$$

Although the relation was not formally established, Eq. (3.57) has been known as early as 1892 by Rayleigh [63].

3.4.3 Tortuosity Relations

In Sections 3.4.1 and 3.4.2, we have briefly discussed the electrical conduction and wave propagation in porous media. The electrical resistivity logging and sound logging are frequently applied to measure the tortuosity of a porous medium.

In the dilute limit, or when $\varepsilon \rightarrow 1$, Maxwell [64] derived a formula for the effective conductivity for the case in which both the fluid and the suspended spheres are conducting

$$\frac{\sigma_0/\sigma_w - 1}{\sigma_0/\sigma_w + 2} = (1 - \varepsilon) \frac{\sigma_s/\sigma_w - 1}{\sigma_s/\sigma_w + 2} \quad (3.58)$$

where σ_s is the conductivity of the solids. Hence, the formation factor for an isolated and fixed sphere can be deduced from Eqs. (3.58) and (3.47) assuming $\sigma_s = 0$,

$$F_\varepsilon = \frac{3 - \varepsilon}{2\varepsilon} \quad (3.59)$$

Equation (3.59) is now known as the Maxwell-Rayleigh equation and can be adapted to calculate the tortuosity for systems of high porosity. Equation (3.59) was also obtained by Rayleigh [63] for cubic array of spheres. Correspondingly, the tortuosity is given by

$$\tau = \frac{2}{3 - \varepsilon} \quad (3.60)$$

Another formula for the high porosity cases is given by Bacri and Salin [65] as

$$\tau = \frac{2\varepsilon}{1 + \varepsilon} \quad (3.61)$$

Bruggemann [66] employed a self-consistent treatment for a sphere immersed in the Maxwell field. Since the surroundings (i.e., the suspension itself) are considered to be uniform, the dilute limit is satisfied and the conductivity increase can be obtained for the addition of a sphere by

$$\frac{d\sigma_0}{d\varepsilon} = -\frac{3\sigma_0}{\varepsilon} \frac{\sigma_0 - \sigma_s}{2\sigma_0 + \sigma_s} \quad (3.62)$$

Solving Eq. (3.62) with the initial condition at $\varepsilon = 1$, one obtains

$$\frac{\sigma_0 - \sigma_s}{(\sigma_0/\sigma_w)^{1/3}(\sigma_w - \sigma_s)} = \varepsilon \quad (3.63)$$

In the limit of zero conductance for the spheres, the tortuosity equation can be deduced and is given by

$$\tau = \varepsilon^{1/2} \quad (3.64)$$

Equation (3.64) may be called the Bruggemann equation. The Bruggemann equation has been shown to be valid for a wide range of solid concentrations

and various particle shapes for suspensions by De la Rue and Tobias [67]. Equation (3.64) has also been shown to hold for fused glass beads [68–70]. For packed beds, Liu et al. [51] used geometrical arguments to arrive at Eq. (3.60). Sen et al. [66] and Wong et al. [70] constructed a percolation argument to arrive at a more general formula

$$\tau = a_\tau \varepsilon^m \quad (3.65)$$

where a_τ is an empirical constant and m is termed the cementation factor. Equation (3.65) was first proposed by Archie [61] and has also been known as the Archie's law. Based on Eq. (3.65), a correlation has been obtained for natural consolidated media and is given by

$$\tau = 1.61 \varepsilon^{1.15} \quad (3.66)$$

Equation (3.66) is known as the "Humble" formula [71].

Based on the formation factor data on fused glass beads, the tortuosity in the low porosity range is given by [70],

$$\tau = 2.8 \varepsilon^{5/4} \quad (3.67)$$

In the high porosity range, Eq. (3.64) is found to be satisfactory. Equation (3.64) and (3.67) may be combined asymptotically to give [55]

$$\tau = \left[\frac{(0.2 + 0.8\varepsilon)\varepsilon^{20}}{\varepsilon^{13} + 1.4 \times 10^{-8}(1 - \varepsilon)} \right]^{1/16} \quad (3.68)$$

Equation (3.68) can be used to estimate the tortuosity for suspensions, packed beds, and artificial consolidated porous media.

For natural consolidated media, the tortuosity is generally lower than that predicted by Eq. (3.68). Especially when the porosity is low, some of the pores may be blocked and hence not accessible to fluid flow and mass transfer. Depending on the degree of compaction, the tortuosity can be significantly different. The lower limit of the tortuosity for natural consolidated media is given by,

$$\tau = \varepsilon^{4/3} \quad (3.69)$$

When electrical conduction and wave propagation is considered, some of the very fine micropores may be involved in the transport processes. The micropores may increase the tortuosity and the following expression is constructed by [55]

$$\tau = b_\tau \varepsilon^{0.1} + (1 - b_\tau) \varepsilon^{4/3} \quad (3.70)$$

where b_τ is an empirical constant to account for the fraction of fine micropores in the total voids. The fine micropores may not be served as passages for the transport of fluids, in which case a slightly lower effective porosity is rendered and Eq. (3.69) applies.

Figure 3.9 shows the tortuosity variation with porosity for various model solid–fluid systems: suspensions, packed beds, and fused glass beads. Experimental data have been collected from various investigators. Among them, only Johnson et al. [69] obtained some data for fused glass beads by measuring the propagation of low-frequency sound waves (known as the fourth sound). The bulk of the data are based on electrical resistivity measurements. De la Rue and Tobias [67] measured the formation factor for various suspension systems by varying the suspended particle shape and sizes. Wyllie and Gregory [72] measured the formation factor for packed beds of various particle shapes. Sen et al. [68], Johnson et al. [69], and Wong et al. [70] measured the formation factor for fused glass beads of various bead sizes. One can observe that the Bruggemann equation, (3.64), predicts very well at least in the high-porosity range, $\varepsilon > 0.2$. One can observe that the Maxwell–Rayleigh equation, (3.60),

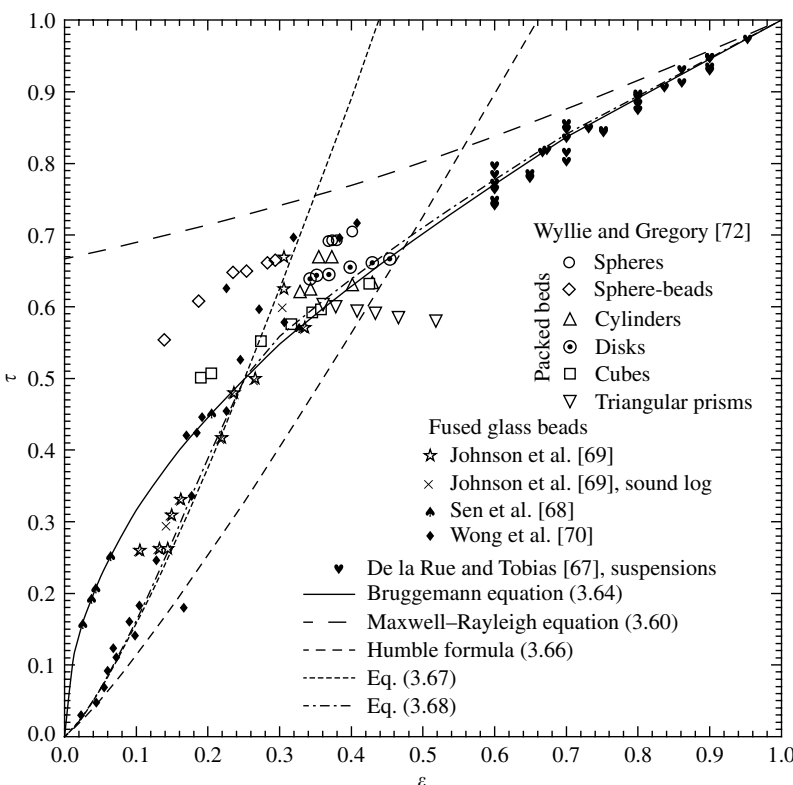


FIGURE 3.9

Tortuosity for various controlled systems: suspensions, packed beds, and fused glass beads.

and "Humble" formula (3.66) are not valid for the systems under consideration. To show more clearly the tortuosity variation at the lower spectrum of porosity, Figure 3.10 depicts the tortuosity versus porosity again on a log-log plane. One can observe that Eq. (3.67) fits the experimental data well when $\varepsilon < 0.2$. For the entire porosity range, Eq. (3.68) is a good alternative. Hence, Eqs. (3.64) for $\varepsilon > 0.2$, (3.67) for $\varepsilon < 0.2$, and (3.68) for all ε values can be used to estimate the tortuosity for model systems of no inaccessible pores: suspensions, packed beds, and artificial consolidated porous media (of minimum pore blocking) such as fibrous/metallic foams and structural packings.

For natural consolidated porous media, the variation of tortuosity with porosity is shown in Figure 3.11, where all the experimental data are based on the formation factor (or electrical conductivity) measurements. The experimental data of Wyllie and Spangler [73] and Dullien [74] were extracted from clean sandstone samples. Cornell and Katz [75] measured the formation factors for sandstones, dolomites, and limestones. Except for two off-trend data points, the experimental data show a definite trend of lower tortuosity for lower porosity. One can observe that the Bruggemann equation, (3.64),

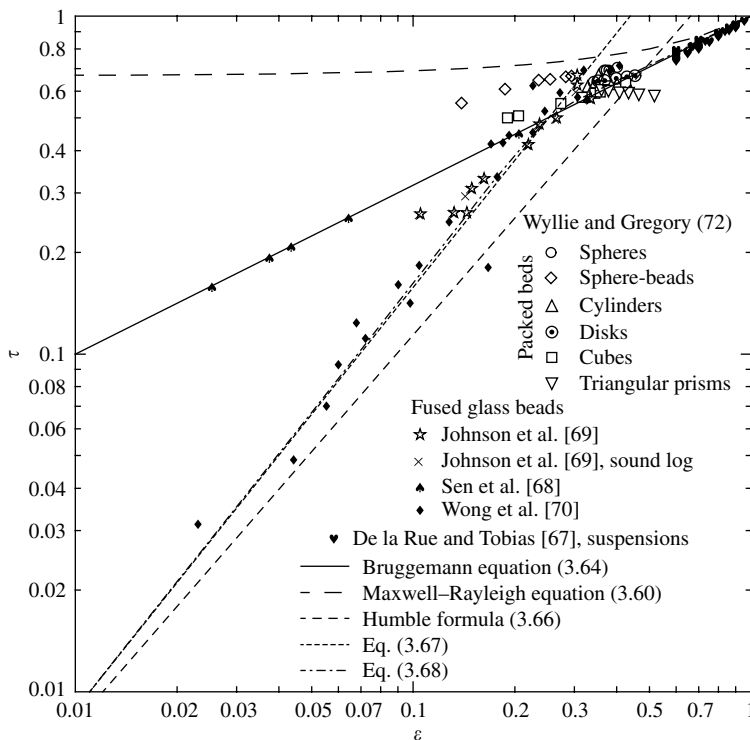
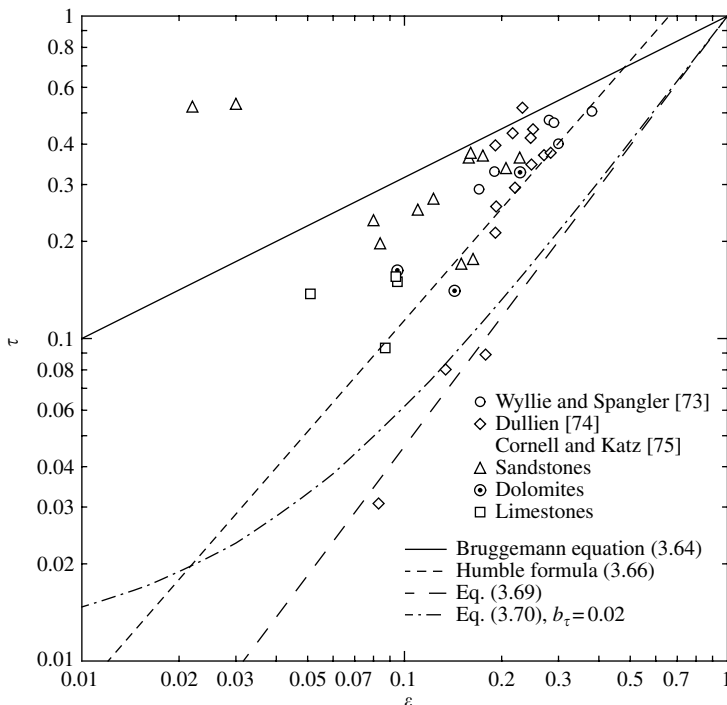


FIGURE 3.10

Variation of tortuosity with porosity for various model systems: suspensions, packed beds, and fused glass beads as compared with empirical correlations.

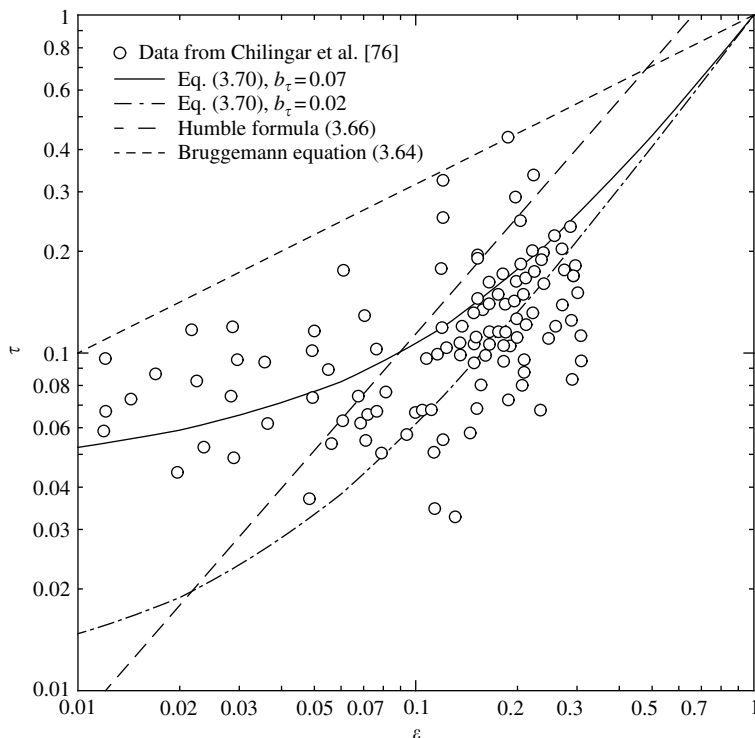
**FIGURE 3.11**

Variation of tortuosity with porosity for consolidated porous media.

over-predicts the experimental data on the tortuosity for natural porous media. The “Humble” formula (3.66), on the other hand, may be considered as a best fit to the experimental data, while Eq. (3.69) represents the low limit of the tortuosity data. This low-limit tortuosity may be useful when fluid flow is considered due to the inaccessibility of the very fine pores in the natural consolidated media.

Figure 3.12 shows more experimental data (formation factor) for limestone samples from Kuleshov deposit, Bashiriya, former USSR [76]. One can observe that the fraction of the micropores for the particular limestone samples is 7%, that is, $b_\tau = 0.07$. Equation (3.70) predicts the experimental data well. Although the “Humble” formula (3.66) is still a best fit to the experimental data in Figure 3.12, there is a definite trend deviation at the low-porosity range, $\varepsilon < 0.05$. Figure 3.12 strongly suggests the validity of Eq. (3.70), or the concept of very fine micropore existence in consolidated media.

Figure 3.11 and Figure 3.12 show that the tortuosity equation for unconsolidated media, the Bruggemann equation, (3.64), represents the upper bound for consolidated media. One can observe from Figures 3.9 through 3.12 that there are large scatters of the experimental data depending on the sources of the data and the porous material. There are many factors that

**FIGURE 3.12**

Variation of tortuosity with porosity for limestone samples from Kuleshov Deposit, Bashiriya, former USSR. (Data source G.V. Chilingar, R.W. Mannon, and H.H. Rieke, II. *Oil and Gas Production from Carbonate Rocks*. Elsevier: New York, 1972.)

cause experimental data scattering: difference in porous structure (from one sample to another); anisotropy of porous medium material; as well as the ability or degree of a particular substance (tracer molecules) and physical phenomenon (thermal or sound wave, etc.) to penetrate a given porous material, beside the experimental measurement errors. The diverse source and structural complexity of porous media have been the main reason for averaging and empiricism, whereby general trend behaviors are detected. However, an accurate prediction can be obtained by examining each individual medium.

3.5 Volume Averaged Navier–Stokes Equation for an Isotropic Porous Medium

For simplicity, we consider here that the fluid is Newtonian and the dynamic viscosity is constant, and that the gravity can be included into the pressure

term, that is, for the case of a constant fluid density. Furthermore, we confine ourselves to the case of continuous (fluid) phases only. When no porous medium is present, or the porosity is exactly unity, the flow for a phase is governed by the Navier–Stokes equation. The governing equations are referred to as the continuity and momentum equations. These equations are given in the following.

The continuity equation for free flow of the i -fluid phase is given by

$$\frac{\partial \rho_i^*}{\partial t} + \nabla \cdot (\rho_i^* \mathbf{v}_i^*) = \dot{m}_i^* \quad (3.71)$$

where \dot{m}_i^* is the net mass generation in the i -fluid phase due to mass transfer acquired from other fluid phases and solids, phase change and chemical reactions, etc. In general, with the absence of a nuclear reaction, there is no overall mass generation,

$$\sum_i \dot{m}_i^* = 0 \quad (3.72)$$

The momentum equation for free flow of the i th-fluid phase is given by

$$\frac{\partial (\rho_i^* \mathbf{v}_i^*)}{\partial t} + \nabla \cdot (\rho_i^* \mathbf{v}_i^* \mathbf{v}_i^*) + \nabla p_i^* - \mu_i^* \nabla^2 \mathbf{v}_i^* = \dot{M}_i^* \quad (3.73)$$

where \dot{M}_i^* is the momentum acquired from other phases. Although there is no difference between the intrinsic phase averaged value and its corresponding local value for flow in free space, the superscript * in the above equations is used to distinguish them from the properties in a porous medium system. The subscript i denotes the fluid phase under consideration and hence there is no summation applicable unless otherwise specifically mentioned.

For a rigid porous medium and with no volumetric change in the fluid phases, Eq. (3.71) is averaged to give

$$\varepsilon_i \frac{\partial \rho_i}{\partial t} + \nabla \cdot (\rho_i \mathbf{v}_i) = \varepsilon_i \dot{m}_i \quad (3.74)$$

For a rigid stationary solid porous medium and without nuclear reactions and net absorptions into or desorption from the solid matrix, the total accumulation of mass is zero.

$$\sum_i \varepsilon_i \dot{m}_i = 0 \quad (3.75)$$

For the case of no mass transfer between phases and no reactions, the continuity equation (3.74), is further reduced to

$$\varepsilon_i \frac{\partial \rho_i}{\partial t} + \nabla \cdot (\rho_i \mathbf{v}_i) = 0 \quad (3.76)$$

Owing to the fact that a convective flux carries a constant property, all the extra surface integral terms disappear. Hence, no dispersion, mass sink, or mass generation terms come into play in the final averaged continuity equation, when the fluid phase does not experience any volumetric change and the porous medium matrix is rigid.

The momentum equation can be obtained by averaging Eq. (3.73). Following the procedures for averaging Eqs. (3.19) and (3.20), we obtain

$$\begin{aligned} \frac{\partial(\rho_i \mathbf{v}_i)}{\partial t} + \nabla \cdot \frac{\rho_i \mathbf{v}_i \mathbf{v}_i}{\varepsilon_i} + \frac{\varepsilon_i}{\varepsilon} \nabla p_i + \mu_i \frac{F_i}{\varepsilon_i} \mathbf{v}_i - \tau_i \mu_i \nabla^2 \mathbf{v}_i \\ - \tau_i \mu_i \nabla \cdot \frac{\mathbf{K}_i}{\varepsilon_i} \cdot \nabla \mathbf{v}_i + \sum_j F_{ij} (\mathbf{v}_{\varepsilon i} - \mathbf{v}_{\varepsilon j}) = 0 \end{aligned} \quad (3.77)$$

It can be observed from Eq. (3.77) that any disturbance that is introduced into the system will decay much faster than that for a zero shear factor medium, that is, no solid matrix present. This is also an experimentally observed fact. However, it has been recognized that the decaying speed for flow in a porous medium is slower than that which would be predicted by the traditionally used volume averaged governing equations, see for example, Nield and Bejan [77]. Equation (3.77) does indicate a slower decaying speed than that based on the straight passage model. The decaying speed is still expected to be much faster than that for a medium free of solids. It is also this characteristic that makes the flow in a porous medium more stable than that in an infinitely permeable medium and delayed turbulence is expected.

Owing to the presence of the momentum dispersion, the effective viscosity of the fluid becomes larger when the flow in porous media is stronger. The momentum dispersion allows disturbances introduced by the boundary to carry more influence to the flow domain. The momentum dispersion does not allow a sharp change in the flow field, whereby decreasing the influence of the porous medium near the free fluid-porous medium and porous medium-solid wall interfaces. The momentum dispersion effects can extend into the free fluid in the vicinity of the interface due to the existence of velocity fluctuation near the interface [78].

The volume averaged equations can be summed up to yield one single set of governing equations for a fluid phase mixture. When conditions are appropriate, such an approach may be found very useful especially when some phases are dispersed. Fewer governing equations lead to less complexity

in solving the flow problem. The volume averaged equations become:
The continuity equation,

$$\varepsilon \frac{\partial \rho_m}{\partial t} + \nabla \cdot (\rho_m \mathbf{v}_m) = 0 \quad (3.78)$$

where

$$\rho_m = \frac{1}{\varepsilon} \sum_i \varepsilon_i \rho_i; \quad \mathbf{v}_m = \frac{1}{\rho_m} \sum_i \rho_i \mathbf{v}_i \quad (3.79)$$

Assuming that the intrinsic phase average velocity vector is nearly equivalent for all the phases and the phase interactions can be reorganized to be included in the internal shear loss term, the momentum equation can be written as

$$\begin{aligned} \frac{\partial(\rho_m \mathbf{v}_m)}{\partial t} + \nabla \cdot \frac{\rho_m \mathbf{v}_m \mathbf{v}_m}{\varepsilon} + \nabla p_m + \mu_m \frac{F_m}{\varepsilon} \mathbf{v}_m \\ - \tau \mu_m \nabla^2 \mathbf{v}_m - \tau \mu_m \nabla \cdot \frac{\mathbf{K}_m}{\varepsilon} \cdot \nabla \mathbf{v}_m = 0 \end{aligned} \quad (3.80)$$

where

$$\mu_m = \frac{1}{\tau \varepsilon} \sum_i \tau_i \varepsilon_i \mu_i; \quad F_m = \frac{1}{\mu_m} \sum_i \mu_i F_i \quad (3.81)$$

The most significant assumptions made to arrive at Eqs. (3.78) to (3.81) are that

$$\frac{\mathbf{v}_i}{\varepsilon_i} = \frac{\mathbf{v}_m}{\varepsilon}; \quad \tau \mu_m \mathbf{K}_m = \sum_i \tau_i \mu_i \mathbf{K}_i \quad (3.82)$$

Hence, the mixture (or homogeneous) model presented here is applicable to systems with negligible slip flow velocities between fluid phases and all the fluid phases are continuous, for example, stratified flow, with similar streamlines.

For the limiting case where the inertial and diffusion effects can be neglected, a different approach can be made on the mixture model. For example, Wang and Beckermann [79] used a phase relative permeability weighted pressure gradient to avoid the requirement of negligible slip velocity for a two phase flow. The model of Wang and Beckermann [79] can easily be generalized to multiphase flows as long as Darcy's law is valid for each phase.

For a single fluid flow, Eq. (3.77) is reduced to

$$\frac{\partial(\rho \mathbf{v})}{\partial t} + \nabla \cdot \frac{\rho \mathbf{v} \mathbf{v}}{\varepsilon} + \nabla p + \mu F \mathbf{v} - \tau \mu \nabla^2 \mathbf{v} - \tau \mu \nabla \cdot D_T \mathbf{K}_h \cdot \nabla \mathbf{v} = 0 \quad (3.83)$$

where D_T is the transverse dispersivity and \mathbf{K}_h is the normalized dispersion coefficient tensor. For isotropic porous media,

$$\mathbf{K}_h = \begin{bmatrix} \delta_L & 0 & 0 \\ 0 & 1 & 0 \\ 0 & 0 & 1 \end{bmatrix} \quad (3.84)$$

where δ_L is the normalized longitudinal dispersion coefficient. Although the porous medium is isotropic, the value of δ_L may not be unity due to different degree of mixing along the different directions. The existence of a main flow itself manifests anisotropy.

When inertial effects can be neglected (creeping flow); the flow is in a steady state, the volume averaged Navier–Stokes equation (3.83), is reduced to

$$\nabla p = -\mu F \mathbf{v} + \tau \mu \nabla^2 \mathbf{v} \quad (3.85)$$

Furthermore, if the tortuosity is near unity, Eq. (3.85) can be reduced to the Brinkman equation

$$\nabla p = -\frac{\mu}{k} \mathbf{v} + \mu \nabla^2 \mathbf{v} \quad (3.86a)$$

where k is the permeability and it is the reciprocal of the shear factor, F . It should be noted that, as a first estimation, the dispersion term has been dropped out from Eq. (3.85). Equation (3.86a) is the working version of the Brinkman equation where the viscosity associated with the viscous diffusion term is the same as the viscosity of the fluid.

In his original study, Brinkman [3] added the diffusion term simply to meet the boundary specifications and hence the viscosity was not defined. Brinkman's first version of the flow equation is given by

$$\nabla p = -\frac{\mu}{k} \mathbf{v} + \check{\mu} \nabla^2 \mathbf{v} \quad (3.86b)$$

where $\check{\mu}$ is a quantity having the dimension of viscosity and it was named the effective viscosity. One should acknowledge that Eq. (3.86b) is a general form of volume averaged Stokes equation. In general, the effective viscosity is not expected to be the same as the viscosity of the fluid owing to the effect of tortuosity and the dispersion of viscous diffusion flux.

Many investigators including Brinkman preferred the use of Eq. (3.86a) for weak flow in porous media [80]. Although it is a debatable point whether the viscosity is associated with the diffusion term or the effective viscosity, or is the same as the viscosity of the fluid or not, there is no definitive relation for the viscosity (or effective viscosity) when it is not treated the same as the fluid viscosity. Depending upon the type of porous media, numerical simulations showed that the effective viscosity may be

either smaller or greater than the viscosity of the fluid [25,80–90]. Through volume averaging of Navier–Stokes equation, Ochoa-Tapia and Whitaker [91] showed that $\bar{\mu}$ is identical to μ/ε . Other analyses [87–90] showed an effective viscosity more close to $\tau\mu$, which reinforces the validity of Eq. (3.85).

While citing Ochoa-Tapia and Whitaker's finding, Kuznetsov [92,93] reinstated the approach of Neale and Nader [94] by setting $\bar{\mu} = \gamma^2\mu$, with γ being a parameter. The inability in a model, such as the Brinkman equation, to account for the additional energy dissipation due to momentum dispersion lends itself to the effective viscosity that differs from the intrinsic viscosity. In other words, one can think of a difference between the effective viscosity and the intrinsic viscosity being due to the momentum dispersion. It has been generally accepted that $\bar{\mu}$ is strongly dependent on the type of porous media as well as the strength of the flow. When the medium is not isotropic, the flow behavior is different when viewed from different directions, which also contributes to the variations in the effective viscosity. It has been generally accepted that the effective viscosity in the Brinkman's equation should be taken to be the same as the viscosity of the flowing fluid for high porosity cases (e.g., see [94,95]). A more detailed discussion can be found in Masliyah et al. [78].

A study by Givler and Altobelli [96] attempted to settle the question of what is the effective viscosity through direct experimentation on the velocity profile for flow in a porous bed bounded by a solid wall. They carried out calculation on the effective viscosity using the measured velocity profile. They found that the effective viscosity is dependent on the flow rate, which is the first evidence of the momentum dispersion in porous media.

Originally, the Brinkman equation is a direct extension to the Darcy's law. Arbitration comes after the viscous diffusion term, which is an extension to the Darcy's law. The Darcy's law is given by

$$\nabla p = -\frac{\mu}{k}\mathbf{v} \quad (3.87)$$

Equation (3.87) can be directly obtained from Eq. (3.86) when the porous medium domain is very large and the boundary effects can be neglected. In other words, the Darcy's law can also be directly obtained under special conditions at which Eq. (3.87) is valid from the volume averaged Navier–Stokes equation. The Darcy's law, however, was obtained empirically and extended from the pressure-drop measurements for unidirectional flow by Darcy [97].

At this point, we should mention that the Brinkman–Forchheimer or Darcy–Brinkman–Forchheimer equation that has been employed by various investigators (e.g. [91,97–99]) in the literature have the following form,

$$-\nabla p = \frac{\mu}{k}\mathbf{v} + \frac{c_F\rho|\mathbf{v}|}{k^{1/2}}\mathbf{v} - \mu\nabla^2\mathbf{v} \quad (3.88)$$

where c_F is the form drag coefficient. Equation (3.88) is thought as an extension from the Brinkman's equation by accounting for the inertial effects on the internal shear loss term, however, the dispersion of momentum is not accounted for. Owing to the omission of the momentum dispersion, one should note that Eq. (3.88) is useful only for systems where the flow domain is large, that is, when Darcy's law is valid at creeping flow. Hence, strict restrictions apply to the use of the Brinkman–Forchheimer equation [100]. If the porous media domain is small, that is, free fluid-porous medium and solid-porous medium interfaces have a large role to play through the momentum dispersion, the form of Eq. (3.83) should be used.

When the diffusion term is dropped out, Eq. (3.88) becomes the Darcy–Forchheimer equation. That is,

$$-\nabla p = \frac{\mu}{k} \mathbf{v} + \frac{c_F \rho |\mathbf{v}|}{k^{1/2}} \mathbf{v} \quad (3.89)$$

Darcy–Forchheimer equation, (3.89), is strictly empirical and has been used by a large number of investigators. When an interface is encountered, an additional empirical model on the velocity jump condition needs to be provided in connection with the Darcy's law or Darcy–Forchheimer equation to account for the inconsistency of the governing equation and the physical description of the flow. For researchers who prefer the empirical treatment throughout, refer to Beavers and Joseph [101], Larson and Higdon [80], and Nield and Bejan [77]. However, one should note that the empirical treatments are case dependent, that is, different empirical coefficients should be used for different systems.

3.6 Dispersion or Volume Averaged Advection–Diffusion Equation

The advection–diffusion equation in a fluid phase i in the absence of the porous medium is given by the following mass balance equation

$$\frac{\partial c_{Ai}^*}{\partial t} + \nabla \cdot (c_{Ai}^* \mathbf{v}_i^* - D_{Ai} \nabla c_{Ai}^*) = R_{Ai}^* \quad (3.90)$$

where R_{Ai}^* is the mass generation of the component into the i -fluid phase. c_{Ai} is the concentration of component A in fluid phase i and D_{Ai} is the diffusivity.

Hence, the volume averaged advection–diffusion equation can be obtained by following the same procedures as outlined for averaging Eqs. (3.19)

and (3.20). The volume averaged species transport equation is given by

$$\begin{aligned} \varepsilon_i \frac{\partial c_{Ai}}{\partial t} + \nabla \cdot (\mathbf{v}_i c_{Ai} - \tau_i \varepsilon_i D_{Ai} \nabla c_{Ai}) - \tau_i \nabla \cdot (D_{Ai} \mathbf{K}_i \cdot \nabla c_{Ai}) \\ + D_{Ai} F_{ci} (c_{Ai} - c_{sA}) = \varepsilon_i R_{Ai} \end{aligned} \quad (3.91)$$

Here, we have assumed that the tortuosity are the same for all directions (isotropic). The term c_{sA} is the concentration c_{Ai} evaluated at the fluid–solid or flow–stagnant fluid interface. F_{ci} is the fluid–solid interaction factor, which is similar to the shear factor for fluid flow. For single phase flows, Eq. (3.91) can be simplified as

$$\varepsilon \frac{\partial c_A}{\partial t} + \nabla \cdot (\mathbf{v} c_A - \tau \varepsilon D_A \nabla c_A) - \tau \nabla \cdot (D_A \mathbf{K}_m \cdot \nabla c_A) + D_A F_c (c_A - c_{sA}) = R_A \quad (3.92)$$

It should be pointed out that we have also separated the diffusion term from the dispersion term, whereas they are traditionally treated together. Most dispersion theories are derived based on the same principles as diffusion in a medium, for example, the random walk theory [101], but mainly using heuristic arguments. Others studied the dispersion using direct numerical and theoretical simulations (e.g. [102–107]) based on certain porous medium models. The dispersion theories are summarized by, among others, [74, 108–112].

When no reaction and no adsorption or desorption occur in the system, the mass generation becomes zero. In this case, the single phase dispersion equation takes the following form,

$$\varepsilon \frac{\partial c_A}{\partial t} + \nabla \cdot (\mathbf{v} c_A - \tau \varepsilon D_A \nabla c_A) - \tau \nabla \cdot (D_A \mathbf{K}_m \cdot \nabla c_A) + D_A F_c (c_A - c_{sA}) = 0 \quad (3.93)$$

Normally, one can assume that at any local “point,” the concentration in the main flow stream is the same as that on the fluid–solid interface, that is,

$$c_A = c_{sA} \quad (3.94)$$

Then Eq. (3.93) becomes similar to the mass/tracer transport equation utilized in the earlier literature. However, if there are dead-end pores and stagnant fluid regions, or the solid matrix is slightly diffusive or surface active, the concentration at the flow–stagnant fluid interface cannot be treated the same as the concentration in the bulk flowing region. In this case, one more equation is needed to model the variation of c_{sA} . In the solid matrix, the volume averaged

transport equation can be written as

$$(1 - \varepsilon) \frac{\partial c_{sA}}{\partial t} = D_A F_c (c_A - c_{sA}) - \nabla \cdot (\mathbf{v}_s c_{sA} - \tau_s D_{sA} \nabla c_{sA}) \quad (3.95)$$

The term \mathbf{v}_s is the intrinsic average fluid flow velocity inside the solid matrix, it is identically zero if the solid matrix is not conductive. For a double porosity medium, the fine pores in the solid matrix can, however, be treated through this equation and hence a nonzero flow velocity prevails. The term $\tau_s D_{sA}$ is the effective diffusivity of the component inside the solid matrix. When the solid matrix is not diffusive and the fluid hold-ups in the medium are isolated, this term becomes identically zero. Hence, Eq. (3.95) is an expression such that the species acquired by transfer from the flowing stream is the only source of the species accumulation inside the solid matrix/stagnant fluid regions when the solid matrix is neither diffusive nor convective.

$$\frac{\partial c_{sA}}{\partial t} = \frac{D_A F_c}{1 - \varepsilon} (c_A - c_{sA}) \quad (3.96)$$

Now that Eqs. (3.93) and (3.96) are similar to the model of Coats and Smith [113], who assumed a trap zone in the porous media. The Coats-Smith model has been used widely to explain the trailing long tail of the concentration profile.

In a comprehensive review of earlier experimental studies, Perkins and Johnston [114] presented correlations for both longitudinal and transversal dispersion coefficients. Although early studies obtained a variety of dispersion coefficient dependence on the flow velocity [115], recent experimental treatments seem to converge on a linear dependence. The dispersion coefficient is proportional to the flow velocity when inertia is strong, see among others, Bear [24], Chang and Slattery [116], and Montillet et al. [117].

3.7 Volume Averaged Heat Equation

The differential heat or energy balance equation for a general case where the temperatures between phases do not reach equilibrium, that is, heat transfer between phases exists, can be written as

$$\frac{\partial(\rho_i c_{pi} T_i^*)}{\partial t} + \nabla \cdot (\rho_i c_{pi} \mathbf{v}_i^* T_i^* - k_i \nabla T_i^*) = R_i^* \quad (3.97)$$

where R_i^* is the heat generation in the i -fluid phase, c_{pi} is the specific heat or heat capacity for i -fluid phase at constant pressure, T_i^* is the absolute temperature of phase i , and k_i is the thermal conductivity.

In writing Eq. (3.97), we have assumed that viscous dissipation and the work done by pressure changes are negligible. Similar to the advection–diffusion equation, the volume averaged heat equation can be obtained as

$$\varepsilon_i \frac{\partial(\rho_i c_{pi} T_i)}{\partial t} + \nabla \cdot (\rho_i c_{pi} \mathbf{v} T_i - \tau_{hi} \varepsilon_i k_i \nabla T_i) - \tau_i \nabla \cdot (k_i \mathbf{K}_i \cdot \nabla T_i) = \varepsilon_i R_i + h_i \quad (3.98)$$

where τ_{hi} is the tortuosity for heat fluxes of the i -fluid phase and h_i is the net heat transfer into the i -fluid phase, which includes the fluid–fluid and fluid–solid interactions. In Eq. (3.98), the F -factor is included in the term h_i . Normally, the solid matrix is conductive to thermal energy, the fluid–solid interactions are not to be neglected.

We distinguish the heat flux tortuosity from the tortuosity of the porous medium because heat can travel through the void space as well as the solid matrix. Only the degree of difference in the conductivity exists, resulting in a tortuosity different from unity (free space) and the tortuosity of the porous medium. Hence, the tortuosity for heat flux can be related to the tortuosity of the porous medium and the thermal conductivity ratio of the solid material, k_s , to the i -fluid phase, k_i . When $k_s \ll k_i$, the solid material is virtually impenetrable to thermal energy, hence the exact advection–diffusion equation applies. That is,

$$\tau_{hi} = \tau_i \quad \text{when } k_s \ll k_i \quad (3.99)$$

On the other hand, when the thermal conductivity of the solid is greater than the thermal conductivity of the i -fluid phase, the thermal conduction path will appear to be shorter than the passages in the porous medium voids. Heat fluxes will tend to travel through the solid material instead of following the solid boundary. That is,

$$\tau_{hi} \geq 1 \quad \text{when } k_s \gg k_i \quad (3.100)$$

For the solid matrix, the energy balance equation is given by

$$\rho_s c_{ps} \frac{\partial T_s}{\partial t} + \nabla \cdot (k_s \nabla T_s) = R_s + h_s \quad (3.101)$$

where c_{ps} is the heat capacity of the solids, k_s is the thermal conductivity of the solid matrix, and h_s is the net heat transfer into the solid matrix.

For a homogeneous fluid flow in a nondiffusive (nonconvective) porous medium, Eqs. (3.98) and (3.101) reduce to

$$\varepsilon \rho_f c_{pf} \frac{\partial T}{\partial t} + \nabla \cdot (\rho_f c_{pf} \mathbf{v} T - \tau \varepsilon k_{mf} \nabla T) - \tau \nabla \cdot (k_f \mathbf{K}_t \cdot \nabla T) + k_f F_t (T - T_s) = R_f \quad (3.102)$$

$$(1 - \varepsilon) \rho_s c_{ps} \frac{\partial T_s}{\partial t} - \nabla \cdot (k_s \nabla T_s) - k_f F_t (T - T_s) = R_s \quad (3.103)$$

where the subscript f denotes the fluid phase, the subscript s denotes the solid phase, and k_{mf} is the effective thermal conductivity in the fluid phase. The term F_t is the F -factor for heat transfer. One should note that the convection in porous media is normally negligible, except for a double porosity porous medium. Hence, one is not to expect that the temperature be exactly governed by the same equation for both the solid and the fluid phases. Owing to the fluid–solid interaction, through the F_t term, the temperature may appear to behave as if one equation is governing both the fluid phase and the solid phase for pseudo-steady state at long times.

If the temperature can reach equilibrium between the phases instantaneously, then we can set

$$T_i = T_s = T \quad (3.104)$$

Summation of the governing equations over the fluid phases and the solid materials weighted by the volume fractions leads to

$$(\rho c_p)_m \frac{\partial T}{\partial t} + \nabla \cdot [(\rho c_p)_{fm} \mathbf{v}_m T - \tau \varepsilon k_m \nabla T] - \tau \nabla \cdot (k_f \mathbf{K}_t \cdot \nabla T) = R_m \quad (3.105)$$

where

$$(\rho c_p)_{fm} = \frac{1}{\varepsilon} \sum_i \varepsilon_i \rho_i c_{pi} \quad (3.106)$$

$$(\rho c_p)_m = (1 - \varepsilon) \rho_s c_{ps} + \varepsilon (\rho c_p)_{fm} \quad (3.107)$$

$$\mathbf{v}_m = \frac{\sum_i \rho_i c_{pi} \mathbf{v}_i}{(\rho c_p)_{fm}} \quad (3.108)$$

$$R_m = (1 - \varepsilon) R_s + \sum_i \varepsilon_i R_i \quad (3.109)$$

$$k_m = (1 - \varepsilon) k_s + \sum_i \varepsilon_i \tau_{hi} k_i \quad (3.110)$$

$$k_f = \frac{\sum_i \varepsilon_i k_i}{\varepsilon} \quad (3.111)$$

For single fluid flow in porous media, a one-equation model has been discussed among others [26,118–120]. Two-equation model has been discussed among others [26,37,121–123].

Carbonell and coworkers [37–39] showed that in the limit of long time or pseudo-steady state flows without internal heat generations, both the solid matrix and the fluid phase are governed by the same equation except that both can have their own averaged temperatures. Hence, either using a mixture model or using continuum model for both solid matrix and fluid phase, Eq. (3.105) is the volume averaged governing equation.

For the case of single phase convective heat transfer, the average heat conductivity k_m may be computed from the self-consistent electrical conductivity model, Eq. (3.64), of Bruggemann [66] for packed beds, or

$$\varepsilon = \frac{k_m - k_s}{(k_m/k_f)^{1/3}(k_f - k_s)} \quad (3.112)$$

where k_f is the fluid thermal conductivity. There are also some experimental results and correlations available for k_m , see for example [84,124–126]. However, owing to the difficulty in obtaining a true stagnant (zero or negligible) flow condition, the experimental values may not be fully reliable [77] especially for a high thermal conductivity ratio of the fluid to the solid.

It is generally accepted that the mixture (or effective) conductivity for single phase heat transfer is of the following form

$$k_m = \alpha \left(\frac{k_f}{k_s}, \varepsilon \right) k_s + \beta \left(\frac{k_f}{k_s}, \varepsilon \right) k_f \quad (3.113)$$

where $\alpha()$ and $\beta()$ are strong functions of porosity and the thermal conductivities. Models on the effective conductivity can be found in, for example, Hsu [126]. Equation (3.113) forms the basis for correlating the effective conductivity with other known physical properties for single phase heat conduction in packed beds.

The effective conductivity has been treated theoretically for suspensions by, among others [63,127–130]. Batchelor and O'Brien [127] found that the effective conductivity ratio is governed by

$$k_m/k_f = 4.0 \ln(k_s/k_f) - 11 \quad (3.114)$$

when the spheres are highly conductive and the spheres are touching each other with $\varepsilon \approx 0.37$, which is confirmed by Sangani and Acrivos [129].

For simplicity, we may assume the following quick estimation formula

$$\tau_{hi} = \frac{(1 - \tau_i)k_s^{1/2} + \tau_i k_i^{1/2}}{k_i^{1/2}} \quad (3.115)$$

Equation (3.115) can be used for estimating a mixture (effective) conductivity. At the extremes, Eq. (3.115) satisfies the conditions set by Eqs. (3.99) and (3.100).

The thermal dispersion coefficient has a predominant effect on the heat transfer in porous media, especially for strong convective heat transfer processes. It should be noted that most researchers use an expression that is similar to Eq. (3.105). Like the momentum and mass dispersivities, the thermal dispersivity is expected to be proportional to the flow strength. This behavior has been confirmed by experimental observations, see for example [130–137]. When the flow is very weak, the secondary flow is negligible. Hence, like the momentum dispersivity and dispersivity of species, the thermal dispersivity is expected to remain close to zero at low flow strengths. Only when the flow becomes strong, will the dispersivity be proportional to the flow strength.

3.8 Microscopic Inertia and Flow Induced Dispersion

Microscopic inertia and flow induced dispersion play a key role in the study of transport processes in porous media. In the simplest case of a single fluid flow in saturated porous media, the momentum dispersion governs the flow distribution [55]. When a tracer species is introduced to the system, the dispersion of species comes into play. For nonisothermal processes, additional dispersion of heat waves is encountered. The dispersion is also termed effective diffusivity. Hence, dispersion is a fundamental characteristic of transport phenomena in porous media as shown in the previous sections. In this section, we shall discuss the origin of these dispersions.

For simplicity, let us consider a porous medium saturated with a single fluid. The transport equation for the fluid phase is given by

$$\frac{\partial \Phi^*}{\partial t} + \nabla \cdot \mathbf{J}^* = S_\Phi^* \quad (3.116)$$

with the flux \mathbf{J}^* given by

$$\mathbf{J}^* = \mathbf{v}^* \Phi^* - D_f \nabla \Phi^* \quad (3.117)$$

For incompressible fluids with a constant diffusivity, the flux term in Eq. (3.116) can also be written as

$$\nabla \cdot \mathbf{J}^* = \mathbf{v}^* \cdot \nabla \Phi^* - D_f \nabla^2 \Phi^* \quad (3.118)$$

Taking a volume average of Eq. (3.116) for incompressible flow in a porous medium of a nonconductive and nonsurface active solid matrix,

one obtains

$$\varepsilon \frac{\partial \Phi_\varepsilon}{\partial t} + \nabla \cdot \mathbf{J} = S_\Phi \quad (3.119)$$

$$\begin{aligned} \nabla \cdot \mathbf{J} &= \mathbf{v} \cdot \nabla \Phi_\varepsilon - \tau D_f \nabla^2 \Phi_\varepsilon - \frac{1}{V} \int_{S_i} (\mathbf{v}^* \Phi^* - \mathbf{v}_\varepsilon \Phi_\varepsilon - D_f \nabla \hat{\Phi}) \cdot \mathbf{n}_i dS \\ &= \mathbf{v} \cdot \nabla \Phi_\varepsilon + \hat{\mathbf{v}} \cdot \nabla \hat{\Phi} - \tau D_f \nabla^2 \Phi_\varepsilon - D_f \nabla^2 \hat{\Phi} \end{aligned} \quad (3.120)$$

The relationship for the fluctuation or deviatoric property is obtained by subtracting Eq. (3.119) from Eq. (3.116),

$$\frac{\partial \hat{\Phi}}{\partial t} + \mathbf{v}^* \cdot \nabla \hat{\Phi} - D_f \nabla^2 \hat{\Phi} = \hat{\mathbf{v}} \cdot \nabla \Phi_\varepsilon \quad (3.121)$$

Here, we have written Eq. (3.121) in terms of the microscopic space. That is, the derivatives are not in terms of the averaging space. This treatment enables us to solve the problem using a unit cell approach, where the frame of reference is in the microscopic level.

Equation (3.121) indicates that, in general, the deviatoric quantity $\hat{\Phi}$ is a linear functional of the average quantity Φ_ε when $\Phi \neq \mathbf{v}$ and for $\Phi_s = \Phi_\varepsilon$. That is,

$$\hat{\Phi} = -\mathbf{B} \cdot \nabla \Phi_\varepsilon \quad (3.122)$$

where we have introduced the so-called “**B**-field” of Brenner [103], which is denoted as the “vector field **f**” by Carbonell and Whitaker [37, 138]. It should be mentioned here that we are using a negative sign before the **B**-field factor.

We assume that Eq. (3.122) is written in the microscopic space and is not to be interpreted in the volume averaged space. For clarity, a superscript * has been dropped out for the **B**-field factor. Since Eq. (3.122) is used for the convenience of evaluating the dispersion tensor when the microscopic velocity field can be obtained, using the microscopic space is a must.

In general, a deviatoric quantity is not a simple linear functional of its average quantity. Equation (3.122) does not apply for flow velocity field or $\Phi_s \neq \Phi_\varepsilon$. Hence, one must seek a more general solution (closure):

$$\hat{\mathbf{v}} \cdot \nabla \hat{\Phi} = \chi |\mathbf{v}| (\Phi_\varepsilon - \Phi_s) - \hat{\mathbf{v}} \cdot \nabla (\mathbf{B} \cdot \nabla \Phi_\varepsilon) \quad (3.123)$$

where χ is an inertial parameter or Forchheimer parameter. Equation (3.123) is written also in the microscopic space. In general, the inertial parameter χ should be a tensor. However, for our purpose, a scalar is sufficient for an isotropic random medium. The superscript * has also been dropped out from the inertial parameter χ for clarity.

The general form of the volume averaged transport equation can be written as

$$\varepsilon \frac{\partial \Phi_\varepsilon}{\partial t} + \mathbf{v} \cdot \nabla \Phi_\varepsilon - \tau D_f \nabla \cdot (\varepsilon + \mathbf{K}) \nabla \Phi_\varepsilon = S_\Phi - \tau D_f F_\Phi (\Phi_\varepsilon - \Phi_s) \quad (3.124)$$

where F is the shear factor/flow–stagnant fluid interaction factor and \mathbf{K} is the dispersion coefficient tensor. Assuming the medium under concern is isotropic, we set the dispersion coefficient tensor to be of the following form

$$\mathbf{K} = D_T \begin{bmatrix} \delta_L & 0 & 0 \\ 0 & 1 & 0 \\ 0 & 0 & 1 \end{bmatrix} \quad (3.125)$$

Here $D_T = K_\perp$ is the transverse dispersivity and δ_L is the normalized longitudinal dispersion coefficient, $\delta_L = K_\parallel/K_\perp$. Equation (3.125) is written in a set of orthogonal coordinates where the first axis corresponds to the direction of the average flow. Although the porous medium is isotropic, anisotropy appears in Eq. (3.125) due to the very fact that the existence of the main flow (with a direction) makes the system anisotropic.

Making use of Eq. (3.123), one can write the F -factor as

$$F_\Phi = F_{\Phi 0} + \frac{|\mathbf{v}|}{D_f} \frac{1}{V} \int_V \chi \, dV \quad (3.126)$$

For simplicity, we shall focus on the determination of the dispersivity alone. To avoid the complexity involving two unknowns: F -factor and dispersivity, $\Phi_\varepsilon = \Phi_s$ will be assumed when the dispersion properties are to be derived.

Substituting Eq. (3.122) into Eq. (3.119) and comparing the resulting equation with Eq. (3.124), one obtains the relationship between the \mathbf{B} -field and the dispersion coefficient tensor,

$$D_f \mathbf{K} = \frac{1}{V} \int_V \hat{\mathbf{v}} \mathbf{B} \, dV \quad (3.127)$$

Equation (3.127) indicates that the dispersivity is proportional to the magnitude of the deviatoric velocity or the velocity fluctuation. Since the velocity fluctuations are not expected to be sensitive in the direction of the flow or the direction of the reference for an isotropic media, the deviatoric velocity is expected to be proportional to the norm of the velocity in the inertial dominant flow. Hence, when the flow rate is high, or for inertial dominant flows, the dispersivity is expected to be proportional to the velocity norm.

For dispersion of mass and heat, substituting Eq. (3.122) into Eq. (3.121), one obtains

$$-\mathbf{v}^* \cdot \nabla \mathbf{B} + D_f \nabla^2 \mathbf{B} = \hat{\mathbf{v}} \quad (3.128)$$

As it is pointed out by Koch et al. [139], the **B**-field is time-independent. Like Eq. (3.121), Eq. (3.128) is written in the microscopic space. There have been a number of investigations that were set forth to model the tracer (mass) dispersion coefficient using the **B**-field or some similar concept [103–107,138–146]. These authors assumed a model unit cell structure for the porous media. In addition, they applied a creeping flow field, that is, there is no nonlinearity in the flow velocity field. Normally, a uniform overall (average) flow field is employed.

The equation for the flow velocity is much more complicated due to the microscopic inertial effects on the shear factor. If one considers the creeping flow velocity as a first estimate and applies Eq. (3.122) for the deviatoric velocity for the second estimation, then Eq. (3.128) still applies to the velocity field as well. Hence, one may use the transverse dispersion coefficient as an estimate for the momentum dispersion coefficient as that suggested by Liu and Masliyah [55]. A rigorous study of the inertial effects (shear factor and momentum dispersion) for a model structure requires numerical solutions. In addition, an overall (i.e., in a continuum sense) simple shear field may be applied in order to study the momentum dispersion.

To deduce the governing inertial group, we start with rendering the governing equations dimensionless. Using the norm of the velocity, $|\mathbf{v}|$, the characteristic length of the porous matrix, d_s , and the diffusivity, D_f , as the basic dimensions, Eq. (3.127) can be reduced to

$$\mathbf{K} = R_N \frac{1}{V} \int_V \frac{\hat{\mathbf{v}}}{|\mathbf{v}|} \frac{\mathbf{B}}{d_s} dV \quad (3.129)$$

where R_N is a governing dimensionless inertial group and is given by

$$R_N = \frac{d_s |\mathbf{v}|}{D_f} \quad (3.130)$$

Equation (3.128) can be written in dimensionless form as

$$-\frac{\mathbf{v}^*}{|\mathbf{v}|} \cdot d_s \nabla \frac{\mathbf{B}}{d_s} + \frac{1}{R_N} (d_s \nabla)^2 \frac{\mathbf{B}}{d_s} = \frac{\hat{\mathbf{v}}}{|\mathbf{v}|} \quad (3.131)$$

From Eq. (3.131), one can observe that the **B**-field is not a function of the governing inertial group R_N when $R_N \rightarrow \infty$. When this information is used for Eq. (3.129), one can draw the following conclusion

$$D_T = D_H R_N, \quad \text{when } R_N \rightarrow \infty \quad (3.132)$$

where D_H is a constant.

Owing to the linear relationship between the dispersion coefficients and the governing inertial group at high flow rates, it becomes convenient to define

a dispersivity based on the longitudinal dispersion coefficient

$$l_d = \frac{\tau K_{\parallel} D_f}{|\mathbf{v}|} = \frac{\delta_L \tau D_T D_f}{|\mathbf{v}|} \quad (3.133)$$

The dispersivity l_d as defined above has a length scale. Owing to the difficulty in obtaining a characteristic dimension for a natural consolidated porous medium, l_d becomes quite handy in dealing with transport phenomena in consolidated media.

The solution to Eqs. (3.129) and (3.131) with proper boundary conditions (zero flow and conduction inside solids) can be obtained at least for periodic porous media [103] or by using heuristic models such as the swarm model of Brinkman [3] and self-consistent models. The flow velocity field for creeping flow in terms of the swarm model was given by Brinkman [3] and more accurately by Acrivos et al. [147]. However, it becomes "technical" when one attempts to determine the dispersivity. Koch and Brady [104] found that there is no contribution to the transverse diffusivity from the one-particle (sphere), purely mechanical, analysis. Here, the term "mechanical" is an empirical description of the region of the dispersion where the effective diffusivity is not a function of the microscopic (molecular) diffusivity of the fluid. The null result occurs because of the integral of the transverse component of the velocity fluctuation along any streamline is zero, as it must be for streamlines bearing for-aft symmetry. Hence, particle interactions must be considered.

Although Koch and Brady [104] employed ensemble averaging to arrive at a macroscopic transport equation, there appears to be a difference by a factor of ε on the convection term between the macroscopic equation of Koch and Brady [104] and traditionally used empirical dispersion equation. Assuming that the discrepancy does not affect the general trend, the asymptotic solution of Koch and Brady [104] for tracer dispersion in beds of spheres may be cast as

$$D_T = \frac{(63\sqrt{2}/640)\varepsilon^{1/2}(1-\varepsilon)^{1/2}}{1 - (9\sqrt{2}/20)(1-\varepsilon)^{1/2}} R_N \quad \text{when } R_N \rightarrow \infty \quad (3.134)$$

where R_N is defined by Eq. (3.130) with d_s being the diameter of the spherical particles in the packed bed.

¹The dispersion equation traditionally used to derive dispersivity is given by (e.g. [115]):

$$\frac{\partial \Phi_\varepsilon}{\partial t} + \mathbf{v}_\varepsilon \cdot \nabla \Phi_\varepsilon - K' \nabla \cdot \nabla \Phi_\varepsilon = 0$$

where K' denotes the dispersion coefficient used in most experimental oriented studies. Compared with Eq. (3.124), the dispersion coefficient is given by

$$D_T = \frac{\varepsilon}{\tau} K'_\perp - D_f$$

Equation (3.134) is strictly valid for tracer dispersion and $\varepsilon \rightarrow 1$ in the analysis of Koch and Brady [104]. Owing to the analogies among these transport processes, the momentum dispersion, the thermal dispersion, and the dispersion of species should share the same transverse dispersivity based on the above discussions.

Although the order of the inertial group in the longitudinal dispersivity is higher than one when the tracer dispersion is dominated by inertial effects as predicted by Koch and Brady [104], there is no experimental evidence to support this behavior. Koch and Brady [104] used interparticle interaction (stagnant flow region hold-up), conductance of the particles (or particle hold-up), and the boundary layer distribution of concentration near particle surface to arrive at the higher order terms. These contributions are also termed the nonlocal, nonmechanical dispersion. Owing to the interrelation between the longitudinal and the transverse dispersivities, the higher order dependence should appear for transverse dispersion as well [148]. One situation where this analysis should prevail is the thermal dispersion since the particles are conductive, whereby a second-order dependence for high Péclet number flows would be expected. However, only a first-order dependence is observed [37,133,137]. Koch and Brady [106,107] explained that the nonappearance of the higher order dominant terms in dispersion is due to its long relaxation time. Normally, these higher order terms only manage to make their contribution in the transient behavior and cannot reach steady state (or pseudo-steady state) in experiments. If we go back to the general case where $\Phi_s \neq \Phi_\varepsilon$, Eq. (3.124), one can note that the stagnant flow region hold-up and particle hold-up are not contributing to the dispersion directly. The hold-ups act as buffers and are attributed to a nonlinear time variation, especially at long times. Owing to the resistance to change due to the hold-ups, a long trailing tail is expected. Hence when inertial effects are dominant, the linear relation for the dispersivity and the inertial group should hold.

Here K'_\perp is the transverse dispersion coefficient associated with the traditionally used dispersion equation.

The dispersion equation of Koch and Brady [104] is given by

$$\frac{\partial(\varepsilon\Phi_\varepsilon)}{\partial t} + \mathbf{v} \cdot \nabla(\varepsilon\Phi_\varepsilon) - \nabla \cdot \mathbf{D} \cdot \nabla(\varepsilon\Phi_\varepsilon) = 0$$

Ensemble averaging was utilized by Koch and Brady [104]. There is a factor of ε different on the convection term as the fluid velocity in the equation of Koch and Brady [104] was claimed to be volume averaged. Therefore, the dispersion equation of Koch and Brady [104] is incompatible with the traditionally used dispersion equation. It may be assumed that the velocity of the convection term in the dispersion equation of Koch and Brady [104] is the intrinsic phase averaged (not the volume averaged) velocity, and the velocity in their dispersion coefficient is the volume averaged velocity. When the mistake in Koch and Brady [104] is corrected, one would have

$$D_f \mathbf{K} = \frac{\varepsilon}{\tau} \mathbf{D} - \mathbf{1} D_f$$

which puts the dispersion tensor, \mathbf{D} , of Koch and Brady [104] to be the same as the traditionally used one.

For fluid flow, the governing inertial group R_N is replaced by the Reynolds number

$$Re_d = R_N|_{\text{Flow}} = \frac{d_s |\mathbf{v}| \rho}{\mu} \quad (3.135)$$

The inertial group for heat transfer is governed by the thermal Péclet number, that is

$$Pe_t = R_N|_{\text{Heat}} = \frac{d_s |\mathbf{v}| \rho c_p}{k_f} \quad (3.136)$$

and the inertial group for mass transfer is given by

$$Pe_m = R_N|_{\text{Mass}} = \frac{d_s |\mathbf{v}|}{D_i} \quad (3.137)$$

The variation of the F -factor at high flow rates can also be deduced through nondimensionalization of the closure equations. Rendering Eq. (3.124) into a dimensionless form, one obtains

$$\frac{\hat{\mathbf{v}}}{|\mathbf{v}|} \cdot (d_s \nabla) \frac{\Phi}{\bar{\Phi}} = (d_s \chi) \frac{\Phi^* - \Phi_s}{\bar{\Phi}} - \frac{\hat{\mathbf{v}}}{|\mathbf{v}|} \cdot \frac{\mathbf{B}}{d_s} \cdot (d_s \nabla) \frac{\Phi_\varepsilon}{\bar{\Phi}} \quad (3.138)$$

where $\bar{\Phi}$ is some average of Φ in the system.

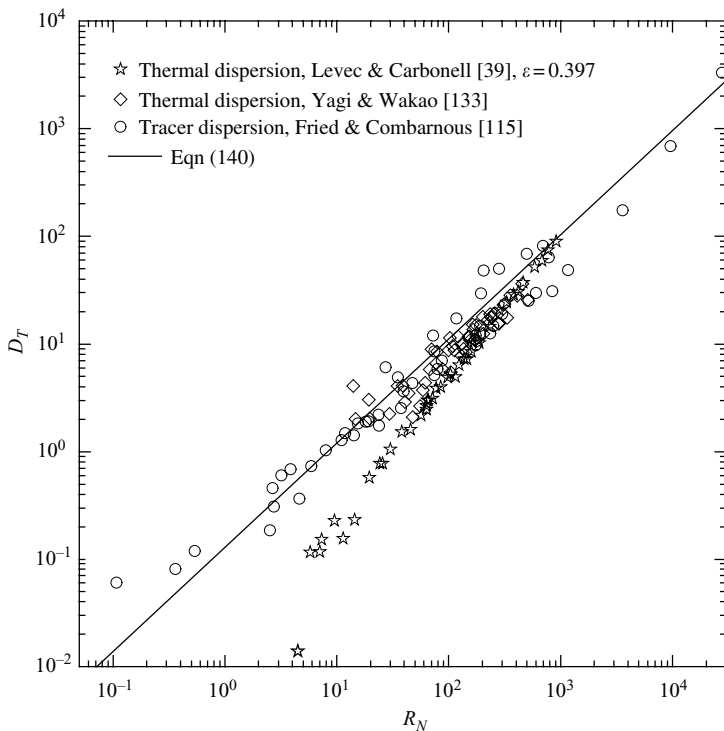
From Eq. (3.138), one can observe that the inertial parameter χ is not a function of the magnitude of the flow velocity when Reynolds number is high. The dimensionless F -factor can be written as

$$d_s^2 F_\Phi = d_s^2 F_{\Phi 0} + R_N \frac{1}{V} \int_V (d_s \chi) dV \quad (3.139)$$

Hence, the F -factor is also linearly proportional to the governing inertial group when $R_N \rightarrow \infty$.

In this section, we have arrived at the following conclusions: both the momentum dispersivity and the shear factor are proportional to the norm of the velocity or the Reynolds number when Re is large; when Pe_t is large, both the effective thermal dispersivity and the solid–fluid interaction factor F_t are proportional to Pe_t ; and both the effective tracer dispersivity and fluid–solid interaction factor F_c are proportional to Pe_m when Pe_m is large. In addition, all the dispersion coefficients should bear similar functional forms except for the difference in the governing inertial group.

Figure 3.13 shows the transverse dispersivity for packed beds, where $\varepsilon = 0.34$ is assumed if not specified. The experimental data are extracted from the thermal dispersion measurements [39,133] and the tracer dispersion data [115]. All the experimental data have been treated as being consistent with

**FIGURE 3.13**

Transverse dispersivity in packed beds.

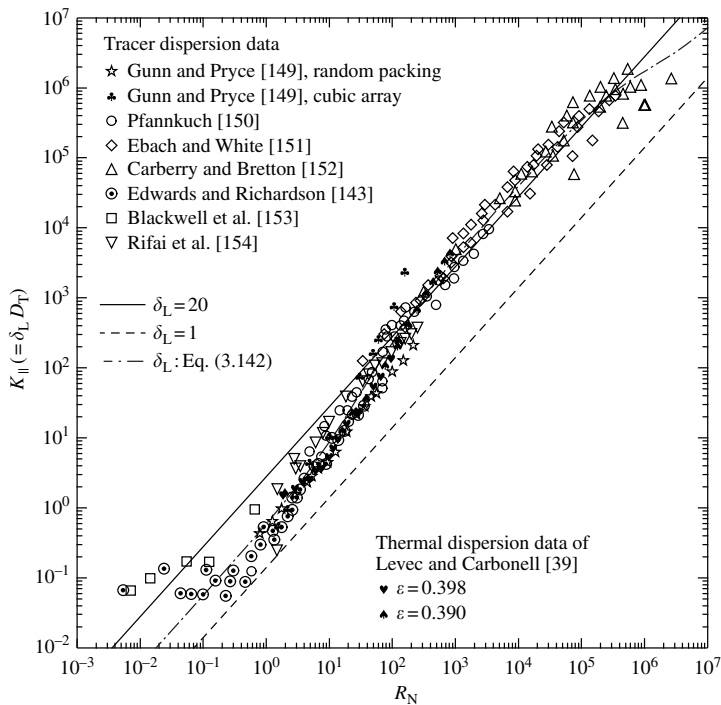
the governing equations we have seen earlier. One can observe that there is no significant difference between the thermal dispersion and the tracer dispersion. They can all be predicted by the following equation

$$D_T = 0.14R_N \quad (3.140)$$

One should note that the dispersion shown here is for inertia induced dispersion only. In particular, the thermal dispersion data shown in Figure 3.13 have subtracted the stagnant effective conductivity or diffusivity at zero flow condition. For the experimental data of Levec and Carbonell [39], the strength of convection is also corrected.

[Figure 3.14](#) shows the axial dispersivity, K_{\parallel}/R_N , for packed beds. The symbols represent the experimental data extracted for both the tracer dispersion measurements and the thermal dispersion measurements. The lines are predictions based on Eq. (3.140) for the transverse dispersivity. From Figure 3.14, one can note that

$$\delta_L = 20 \quad (3.141)$$

**FIGURE 3.14**

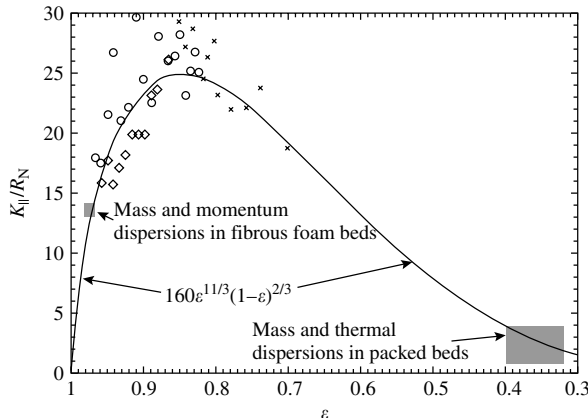
Axial dispersion in packed beds.

can represent the experimental data well for $50 < R_N < 5 \times 10^5$. As is in the current stage, the axial dispersion has to be determined by correlating with experimental data. For a wider range of applicability, the value of δ_L can be given by

$$\delta_L = 4 + \frac{25R_N}{(100 + R_N)(1 + 2 \times 10^{-6}R_N)} \quad (3.142)$$

Equation (3.142) can best represent the average trend of the experimental data in Figure 3.14. There are large scatters of experimental data in both Figure 3.13 and Figure 3.14. The source of the experimental data scattering is not solely the experimental observational error. Other sources, as mentioned previously when discussing the scattering of tortuosity data that is also evident here when R_N is very small, exist as well. The diversity of porous medium structure from sample to sample as well as the transport medium (fluid) have been regarded as the major sources of data scattering.

For fibrous beds and metallic foam beds, the dispersivity is much higher than that for a packed bed of spheres. Since Eq. (3.140) is derived based on the analysis of Koch and Brady [104] for media of spheres, one can fit other media with the same equation while treating the constant as a parameter of

**FIGURE 3.15**

Axial dispersion coefficient in packed beds and particle dispersion in fluidized beds. All the symbols are data points of Martin et al. for glass beads fluidized by glycerol–water corrected for velocity scales [155].

property of the media. Using the experimental data of Montillet et al. [117], one obtains the axial tracer dispersivity for a metallic foam bed

$$K_{\parallel} = \delta_L D_T = 14 R_N \quad (3.143)$$

The higher dispersivity for fibrous foam is due to its better pore connections.

Figure 3.15 shows the variation of longitudinal dispersivity with porosity for different transport processes: particle dispersion in fluidized beds (data of Martin et al. [155]); mass (or tracer, data of Montillet et al. [117]) and momentum (data of Givler and Altobelli [96]) dispersions of flow in porous fibrous foam beds; as well as the tracer and thermal dispersions in packed beds of spheres (data in Figure 3.14) as summarized by Liu [156]. One can observe that the longitudinal dispersivity may be represented by

$$K_{\parallel} = \delta_L D_T = 160\epsilon^{11/3}(1-\epsilon)^{2/3}R_N \quad (3.144)$$

Thus, the dispersion coefficient is a strong function of the porosity.

3.9 Summary and Discussions

The transport equation in porous media for the case of no internal generation can be obtained from Eq. (3.125),

$$\epsilon \frac{\partial \Phi_{\epsilon}}{\partial t} + \mathbf{v} \cdot \nabla \Phi_{\epsilon} - \tau D_f \nabla \cdot (\epsilon + \mathbf{K}) \nabla \Phi_{\epsilon} + \tau D_f F_{\Phi} (\Phi_{\epsilon} - \Phi_s) = 0 \quad (3.145)$$

where the value of the transporting quantity in the solid matrix is governed by Eq. (3.96) or in general,

$$(1 - \varepsilon) \frac{\partial \Phi_s}{\partial t} = D_f F_\Phi (\Phi_\varepsilon - \Phi_s) - \mathbf{v}_s \cdot \nabla \Phi_s + \tau_s D_s \nabla^2 \Phi_s \quad (3.146)$$

When the solid matrix is neither diffusive ($D_s = 0$) nor convective ($\mathbf{v}_s = 0$), then the right-hand side of Eq. (3.146) is left with one term only, the solid-flowing fluid interaction term. The traditional dispersion equation approach prevails only if the value of Φ_s is exactly the same as the value of Φ_ε .

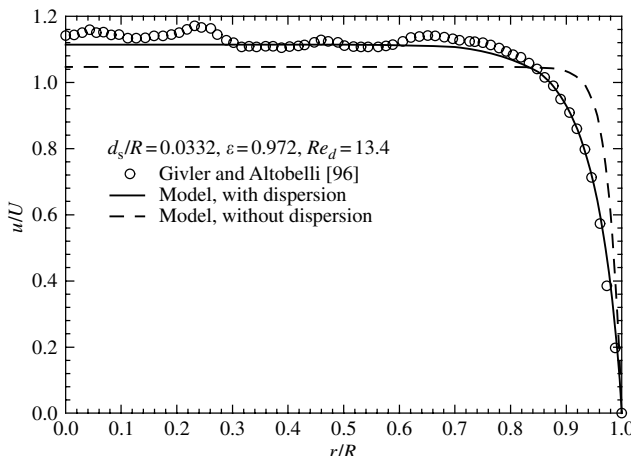
In general, for heat transfer, solid matrix-flowing fluid interaction is important as well as the flow-induced dispersion due to the thermal conductivity in the solid matrix. The coupling of the F -factor with the thermal dispersion can be used to explain the large deviations of the interpretation of the experimental data in dispersion. Owing to the fact that the F -factor is linearly dependent on the flow rate when the Péclet number is large, Eq. (3.139), the effective thermal dispersivity becomes much higher than its real value.

Owing to the coupling of the F -factor (solid matrix-flowing fluid interaction) and flow induced dispersion effects, the transport processes cannot normally be treated by the dispersion equation alone without losing accuracy.

For single fluid flow alone, the F -factor has a predominant effect on the flow behavior, whereas the dispersion effect is a clear secondary effect. In most applications, the dispersion can be neglected along with the other effects, such as the macroscopic viscous diffusion and the macroscopic inertial effects.

For mass transfer or displacement of fluids, the F -factor is normally not as large since in most cases the solid matrix can be considered as nondiffusive, that is, negligible concentration or thermal gradient on the solid surface. The F -factor effect enters into play because of the heterogeneity and stagnant fluid zones and closed stream lines in the media. When F -factor effect is significant, the transport of species differs from that described by the dispersion equation (i.e., assuming a zero F -factor) and the resultant behavior is normally termed anomalous dispersion. The solid matrix-flowing fluid interaction can be significant when the flow rate is high. The F -factor effect is normally observed in experiments through a nonsymmetrical breakthrough curve; especially, the long tail response to a pulse or step input. The asymmetrical breakthrough curve has been noted and studied since the 1950s, for example [113,157–161]. When equilibrium is reached the F -factor effect becomes minimal. The long tail breakthrough curve is observed in consolidated media [162,163], in unconsolidated media [148,164], and in double porosity media [165,166].

Modeling of flow in porous media relies on the closure models for the momentum dispersivity as well as shear factor. For shear factor models, please refer to Liu and Masliyah [55]. One should note that the shear factor models are commonly converted from pressure drop correlations. Therefore, attention should be paid on the form of the averaged equations used as the

**FIGURE 3.16**

The axial velocity profile in a fibrous bed. (Taken from S.Liu and J.H. Masliyah. *Chem. Eng. Commun.* 148–150: 653–732, 1996. With permission.)

volume averaged equation determines the exact forms of the shear factor and momentum dispersivity models, especially porosity dependence. To show the effect of momentum dispersion on single phase flow, Figure 3.16 shows the experimental data of the axial velocity profile (u is the volume averaged axial velocity and U is the average volumetric flux) variation with the radial distance (r is the radial coordinate and R is the bed radius) for flow in a porous foam bed. One can observe that the effect of momentum dispersion is significant as it affects the velocity distribution, especially near a bounding wall.

Mathematically, the origin of the dispersion is due to the microscopic spatial velocity variation. Physically, dispersion occurs because of constant joining and splitting of flow streams when the fluid is traversing through the porous structure. It is the blockage on the straight pass way of the solid matrix to fluid that leads to shear losses; curved streamlines for the fluid; as well as the dispersion or scattering of the fluid. The shear losses represent the fluid–solid matrix interaction. Curved streamlines are well characterized by the tortuosity of the porous media, which directly affects the strength of fluxes that are generic to microscopic flows. Dispersion causes extra fluxes to occur. The dispersion coefficient is a tensorial quantity with a higher dispersivity value in the general direction of flow.

Nomenclature

a_τ constant

B B-field of Brenner

b_τ	fraction of micropores
c	wave speed
c_A	concentration of A
c_p	heat capacity
c_0	apparent wave speed
c_F	drag coefficient factor, in Eq. (3.89)
D	diffusivity
D_H	constant
D_T	dimensionless transverse dispersivity
d_s	solid particle diameter
e	elementary charge
F	solid–fluid interaction coefficient or shear factor
F_ε	formation factor
g	gravitational acceleration
h	height
h_i	heat transfer into the i th phase
II	Intraphase interaction
\mathbf{i}	electric current vector
\mathbf{J}	flux
K	dispersivity
\mathbf{K}	dispersion coefficient tensor
Kn	Knudsen number
K_T	Taylor dispersion coefficient
K_{\parallel}	longitudinal dispersion coefficient
K_{\perp}	transversal dispersion coefficient
k	thermal conductivity, normally with a subscript indicating the phase
k	permeability
k_B	Boltzmann constant
l	minimum system length dimension
l_d	dispersivity, defined by Eq. (3.133)
M	momentum
n	reflective index
n_i	number concentration of ionic species i
\mathbf{n}_i	out normal of surface i (pointing out of phase i)
O	order of
OI	Interface interaction
P	point P
p	pressure
Pe_m	mass Péclet number
Pe_t	thermal Péclet number
R	radius of pipe
R_A	rate of generation for component A
R_i	heat generation in the i th phase
R_N	dimensionless inertia parameter
R_w	electric resistivity of pure fluid

R_0	apparent electric resistivity
r	radial coordinate
Re_d	Reynolds number, Eq. (3.135)
REV	Representative Elementary Volume
m	mass
S	Surface
s	principal coordinate in microscopic space
T	temperature
t	time
U	cross-sectional averaged velocity
u	volume averaged axial velocity
\mathbf{u}	displacement vector
V	volume
V_P	volume of "a point"
\mathbf{v}	velocity vector
x	axial coordinate, or x -coordinate
z	$z = x - Ut$
z_i	valency of ionic species i

Greek Symbols

$\alpha()$	a function of, Eq. (3.113)
$\beta()$	a function of, Eq. (3.113)
Δ	difference
δ_L	normalized longitudinal dispersivity
ε	porosity
λ	mean free path length
μ	viscosity
$\check{\mu}$	effective viscosity
ρ	density
σ_s	electric conductivity of the solid matrix
σ_w	electric conductivity of pure fluid
σ_0	apparent electric conductivity
τ	tortuosity
Φ	a property, normally stands for \mathbf{v} , T , or c_A
χ	Forchheimer parameter, Eq. (3.123)
ψ	electric potential
∇	gradient

Superscript or above

m	power law index
$*$	local value
\wedge	fluctuation or deviation from volume averaged value
\cdot	rate change of time

Subscript

A	component A
a	point a
b	point b
c	for mass transfer
f	fluid
h	for heat transfer
i	the <i>i</i> th fluid
<i>i</i> - <i>i</i>	the <i>i</i> th fluid with <i>i</i> th fluid interface
<i>i</i> -Ø	the interface between the <i>i</i> th fluid and other phases
<i>j</i>	the <i>j</i> th fluid
<i>ij</i>	interaction between the <i>i</i> th fluid and the <i>j</i> th fluid
m	overall; mixture
s	solid matrix or solid phase
T	overall; transversal
t	thermal
0	overall; apparent or mixture
ε	intrinsic average
Φ	for Φ
	longitudinal
⊥	transversal

References

1. G.I. Taylor. Dispersion of soluble matter in solvent flowing slowly through a tube. *Proc. R. Soc. A* 219: 186–203, 1953.
2. R. Aris. On the dispersion of a solute in a fluid flowing through a tube. *Proc. R. Soc. A* 235: 67–77, 1956.
3. H.C. Brinkman. A calculation of the viscous force exerted by a flowing fluid on a dense swarm of particles. *Appl. Sci. Res. A* 1: 27–34, 1949.
4. N. Zuber. On the dispersed two-phase flow in the laminar regime. *Chem. Eng. Sci.* 19: 897–917, 1964.
5. G.K. Batchelor. The stress system in a suspension of force-free particles. *J. Fluid Mech.* 41: 545–570, 1970.
6. G.K. Batchelor. Sedimentation in a dilute dispersion of spheres. *J. Fluid Mech.* 52: 245–268, 1972.
7. G.K. Batchelor. Transport properties of two-phase materials with random structure. *Ann. Rev. Fluid Mech.* 6: 227–255, 1974.
8. E.J. Hinch. An averaged-equation approach to particle interactions in a fluid suspension. *J. Fluid Mech.* 83: 695–720, 1977.
9. G.S. Arnold, D.A. Drew, and R.T. Lahey. Derivation of constitutive equations for interfacial force and Reynolds stress for a suspension of spheres using ensemble cell averaging. *Chem. Eng. Commun.* 86: 43–54, 1989.
10. D.D. Joseph and T.S. Lundgren. Ensemble average and mixture theory equations for incompressible fluid-particle suspensions. *Int. J. Multiphase Flow* 16: 35–42, 1990.

11. G.B. Wallis. The averaged Bernoulli equation and macroscopic equations of motion for the potential flow of a two-phase dispersion. *Int. J. Multiphase Flow* 17: 683–695, 1991.
12. D.A. Drew and G.B. Wallis. Fundamentals of two-phase flow modeling. In Proceedings of Third International Workshop on Two-Phase Flow Fundamentals. Imperial College: London, 1992.
13. C. Pauchon and P. Smereka. Momentum interactions in dispersed flow: an averaging and a variational approach. *Int. J. Multiphase Flow* 18: 65–87, 1992.
14. D.Z. Zhang and A. Prosperetti. Averaged equations for inviscid disperse two-phase flow. *J. Fluid Mech.* 267: 185–219, 1994.
15. S. Whitaker. The equations of motion in porous media. *Chem. Eng. Sci.* 21: 291–300, 1966.
16. S. Whitaker. Diffusion and dispersion in porous media. *AICHE J.* 13: 420–427, 1967.
17. S. Whitaker. Advances in the theory of fluid motion in porous media. *Ind. Eng. Chem.* 61: 14–28, 1969.
18. S. Whitaker. The transport equations for multi-phase systems. *Chem. Eng. Sci.* 28: 139–147, 1973.
19. S. Whitaker. Flow in porous media. *Transp. Porous Media* 1, I: theoretical derivation of Darcy's law, 3–26; II: the governing equations for immiscible two-phase flow, 105–125; and III: deformable media, 127–154, 1986.
20. S. Whitaker. *The Method of Averaging*. Kluwer: Dordrecht, 1999.
21. J.C. Slattery. Flow of viscoelastic fluid through porous media. *AICHE J.* 13: 1066–1077, 1967.
22. J.C. Slattery. Single-phase flow through porous media. *AICHE J.* 15: 866–872, 1969.
23. D.A. Drew. Averaged field equations for two-phase media. *Stud. Appl. Math.* 50: 133–166, 1971.
24. J. Bear. *Dynamics of Fluids in Porous Media*. Elsevier: New York, 1972.
25. T.S. Lundgren. Slow flow through stationary random beds and suspensions of spheres. *J. Fluid Mech.* 51: 273–299, 1972.
26. D. Vortmeyer. Axial heat dispersion in packed beds. *Chem. Eng. Sci.* 30: 999–1001, 1975.
27. W.G. Gray and K. O'Neill. On the general equations for flow in porous media and their reduction to Darcys law. *Water Resour. Res.* 12: 148–154, 1976.
28. W.G. Gray and P.C.Y. Lee. On the theorems of local volume averaging of multiphase systems. *Int. J. Multiphase Flow* 3: 333–340, 1977.
29. M. Hassanizadeh and W.G. Gray. General conservation equations for multiphase systems. *Adv. Water Resour.* 2, 1. Averaging procedure: 131–144; 2. Mass, momentum, energy and entropy equations: 191–20, 1979.
30. M. Hassanizadeh and W.G. Gray. General conservation equations for multiphase systems: constitutive theory for porous media flow. *Adv. Water Resour.* 3: 25–40, 1980.
31. M. Hassanizadeh and W.G. Gray. High velocity flow in porous media. *Transp. Porous Media* 2: 521–531 and 3: 319–321, 1987.
32. V. Veverka. Theorem for the local volume average of a gradient revisited. *Chem. Eng. Sci.* 36: 833–838, 1981.
33. K. Vafai and C.L. Tien. Boundary and inertial effects on flow and heat transfer in porous media. *Int. J. Heat Mass Transfer* 24: 195–20, 1981.

34. K. Vafai and C.L. Tien. Boundary and inertial effects on convective mass transfer in porous media. *Int. J. Heat Mass Transfer* 25: 1183–1190, 1982.
35. J.H. Cushman. Proofs of the volume averaging theorems for multiphase flow. *Adv. Water Resour.* 5: 248–253, 1982.
36. K. Vafai. Convective flow and heat transfer in variable-porosity media. *J. Fluid Mech.* 147: 233–259, 1984.
37. R.G. Carbonell and S. Whitaker. Heat and mass transfer in porous media. In, J. Bear and M.Y. Corapcioglu, eds., *Fundamentals of Transport Phenomena in Porous Media*. Martinus Nijhoff Publishers: Boston, 1984, pp. 121–199.
38. F. Zanotti and R.G. Carbonell. Development of transport equations for multiphase systems. *Chem. Eng. Sci.* 39, I: General development for two phase systems, 263–278; II: Application to one-dimensional axi-symmetric flows of two phases, 279–297; III: Application to heat transfer in packed beds, 299–311, 1984.
39. J. Levec and R.G. Carbonell. Longitudinal and lateral thermal dispersion in packed beds. *AIChE J.* 31: Part I: Theory, 581–590; Part II: Comparison between theory and experiment, 591–602, 1985.
40. V.D. Cvetkovic. A continuum approach to high velocity flow in porous media. *Transp. Porous Media* 1: 63–97, 1986.
41. Y. Bachmat and J. Bear. Macroscopic modelling of transport phenomena in porous media. *Transp. Porous Media* 1, 1: The continuum approach, 213–240; 2: Applications to mass, momentum and energy transport, 241–269, 1986.
42. O.A. Plumb and S. Whitaker. Dispersion in heterogeneous porous media 1. Local volume averaging and large-scale averaging. *Water Resour. Res.* 24: 913–926, 1988.
43. O.A. Plumb and S. Whitaker. Diffusion, adsorption and dispersion in porous media: small-scale averaging and local volume averaging. In J.H. Cushman, ed., *Dynamics of Fluids in Hierarchical Porous Media*. Academic Press: New York, ch. 5, pp. 97–108, 1990.
44. J.P. Du Plessis and J.H. Masliyah. Mathematical modelling of flow through consolidated isotropic porous media. *Transp. Porous Media* 3: 145–161, 1988.
45. J.P. Du Plessis and J.H. Masliyah. Flow through isotropic granular porous media. *Transp. Porous Media* 6: 207–221, 1991.
46. J. Bear and Y. Bachmat. *Introduction to Modeling of Transport Phenomena in Porous Media*. Kluwer Academic Publishers: New York, 1990.
47. M. Quintard and S. Whitaker. Two-phase flow in heterogeneous porous media: the method of large scale averaging. *Transp. Porous Media* 3: 357–41, 1988.
48. M. Quintard and S. Whitaker. Transport in ordered and disordered porous media. *Transp. Porous Media* 14, I: The cellular average and use of weighting functions, 163–177; II: Generalized volume averaging, 179–206, 1994.
49. M. Quintard and S. Whitaker. Theoretical analysis of transport in porous media. In K. Vafai, ed., *Handbook of Porous Media*, Marcel Dekker Inc.: New York, pp. 1–52, 2000.
50. C.Y. Wang and C. Beckermann. Single- vs dual-scale volume averaging for heterogeneous multiphase systems. *Int. J. Multiphase Flow* 19: 397–407, 1993.
51. S. Liu, A. Afacan, and J.H. Masliyah. Laminar flow through porous media. *Chem. Eng. Sci.* 49: 3565–3586, 1994.
52. S. Liu and J.H. Masliyah. Non-linear flows in porous media. *J. Non-Newt. Fluid Mech.* 86: 229–252, 1999.

53. S. Liu. A continuum model for gas–liquid flow in packed towers. *Chem. Eng. Sci.* 56: 5945–5953, 2001.
54. M. Knudsen. *The Kinetic Theory of Gases*. Mathen: London, 1934.
55. S. Liu and J.H. Masliyah. Single fluid flow in porous media. *Chem. Eng. Commun.* 148–150: 653–732, 1996.
56. R.B. Bird, W.E. Stewart, and E.N. Lightfoot. *Transport Phenomena*. John Wiley & Sons Inc.: New York, 1960.
57. R.E. Treybal. *Mass Transfer Operations*, 3rd edn. McGraw-Hill Book Company: Toronto, 1980.
58. F. Kreith and W.Z. Black. *Basic Heat Transfer*, 3rd edn. Harper & Row Publishers: New York, 1980.
59. E.L. Cussler. *Diffusion: Mass Transfer in Fluid Systems*, 2nd edn. Cambridge University Press: New York, 1997.
60. C.J. Geankoplis. *Transport Processes and Separation Process Principles*, 4th edn. Pearson Education Inc.: Upper Saddle River, NJ, 2003.
61. G.E. Archie. The electrical resistivity log as an aid in determining some reservoir characteristics. *Trans. A.I.M.E.* 146: 54–61, 1942.
62. R.J.S. Brown. Connection between formation factor for electrical resistivity and fluid–solid coupling factor in Biot's equations for acoustic waves in fluid-filled media. *Geophys.* 45: 1269–1275, 1980.
63. Lord Rayleigh (J.W. Strutt). On the influence of obstacles arranged in rectangular order upon the properties of a medium. *Philos. Mag.* 34: 481–502, 1892.
64. J.C. Maxwell. *A Treatise on Electricity and Magnetism*, 2nd edn., Vol. I. Oxford University Press: Oxford, 1881.
65. J.-C. Bacri and D. Salin. Characterization of fluids in porous media. In *von Karman Institute for Fluid Dynamics Lecture Series 1990–01: Modeling and Applications of Transport Phenomena in Porous Media*, February 05–09, Vol. 2, 1990.
66. D.A.G. Bruggemann. Berechnung verschiedener physikalischer Konstanten von heterogenen Substanzen. *Ann. Phys. (Leipzig)* 24: 636–679, 1935.
67. R.E. De la Rue and C.W. Tobias. On the conductivity of dispersions. *J. Electrochem. Soc.* 106: 827–883, 1959.
68. P.N. Sen, C. Scala, and M.H. Cohen. A self-similar model for sedimentary rocks with application to the dielectric constant of fused glass beads. *Geophys.* 46: 781–795, 1981.
69. D.L. Johnson, T.J. Plona, C. Scala, F. Pasierb, and H. Kojima. Tortuosity and acoustic slow waves. *Phys. Rev. Lett.* 49: 1840–1844, 1982.
70. P.-Z. Wong, J. Koplik, and J.P. Tomanic. Conductivity and permeability of rocks. *Phys. Rev. B* 30: 6606–6614, 1984.
71. W.O. Winsauer, H.M. Shearin, P.H. Masson and M. Williams. Resistivity of brine saturated sands in relation to pore geometry. *Bull. Amer. Ass. Petrol. Geol.* 36(2): 253–277, 1952.
72. M.R.J. Wyllie and A.R. Gregory. Fluid flow through unconsolidated porous aggregates: effect of porosity and particle shape on Kozeny–Carman constants. *Ind. Eng. Chem.* 47: 1379–1388, 1955.
73. M.R.J. Wyllie and M.B. Spangler. Application of electrical resistivity measurements to problems of fluid flow in porous media. *Bull. Amer. Ass. Petrol. Geol.* 36: 359–40, 1952.
74. F.A.L. Dullien. *Porous Media: Fluid Transport and Pore Structure*. Academic: Toronto, 1992.

75. D. Cornell and D. Katz. Flow of gases through consolidated porous media. *Ind. Eng. Chem.* 45: 2145–2152, 1953.
76. G.V. Chilingar, R.W. Mannon, and H.H. Rieke, II. *Oil and Gas Production from Carbonate Rocks*. Elsevier: New York, 1972.
77. D.A. Nield and A. Bejan. *Convection in Porous Media*. Springer-Verlag: New York, 1992.
78. J.H. Masliyah, A. Afacan, and S. Liu. Flow through a tube with an annual porous medium layer. *J. Porous Media*, in press.
79. C.Y. Wang and C. Beckermann. A two-phase mixture model of liquid–gas flow and heat transfer in capillary porous media. *Int. J. Heat Mass Transfer* 36, I: Formulation, 2747–2758; II: Application to pressure-driven boiling flow adjacent to a vertical heated plate, 2759–2768, 1993.
80. R.E. Larson and J.J.L. Higdon. Microscopic flow near the surface of two-dimensional porous media. Part 1. Axial flow. *J. Fluid Mech.* 166: 449–472, 1986.
81. J. Koplik, H. Levine, and A. Zee. Viscosity renormalizations in the Brinkman equation. *Phys. Fluids* 26: 2864–2870, 1983.
82. R.E. Larson and J.J.L. Higdon. Microscopic flow near the surface of two-dimensional porous media. Part 2. Transverse flow. *J. Fluid Mech.* 179: 119–136, 1987.
83. J.A. Kolodziej. Influence of the porosity of a porous medium on the effective viscosity in Brinkman's filtration equation. *Acta Mechanica* 75: 241–254, 1988.
84. D.A. Nield. Estimation of the stagnant thermal conductivity of saturated porous media. *Int. J. Heat Mass Transfer* 34: 1575–1576, 1991.
85. N. Kladias and V. Prasad. Experimental verification of Darcy–Brinkman–Forchheimer flow model for natural convection in porous media. *J. Thermophys. Heat Transfer* 5: 560–576, 1991.
86. N. Martys, D.P. Bentz, and E.J. Garboczi. Computer simulation study of the effective viscosity in Brinkman's equation. *Phys. Fluids* 6: 1434–1439, 1994.
87. H.L. Weissberg. Effective diffusion coefficients in porous media. *J. Appl. Phys.* 34: 2636–2639, 1963.
88. D. Ryan. The Theoretical Determination of Effective Diffusivities for Reactive, Spatially Periodic Porous Media. MS Thesis. University of California at Davis, 1983.
89. A.E. Sáez, J.C. Perfetti, and I. Rusinek. Prediction of effective diffusivities in porous media using spatially periodic models. *Transp. Porous Media* 6: 143–158, 1991.
90. M. Quintard. Diffusion in isotropic and anisotropic porous systems: three dimensional calculations. *Transp. Porous Media* 11: 187–199, 1993.
91. J.A. Ochoa-Tapia and S. Whitaker. Momentum transfer at the boundary between a porous medium and a homogeneous fluid — I. Theoretical development. *Int. J. Heat Mass Transfer* 38: 2647–2655, 1995.
92. A.V. Kuznetsov. Analytical study of fluid flow and heat transfer during forced convection in a composite channel partly filled with a Brinkman–Forchheimer porous medium. *Flow, Turbulence Combust.* 60: 173–192, 1998.
93. A.V. Kuznetsov. Analytical studies of forced convection in partly porous configurations. In K. Vafai, ed., *Handbook of Porous Media*. Marcel Dekker, Inc.: New York: pp. 269–312, 2000.
94. G.H. Neale and W.K. Nader. Practical significance of Brinkman's extension of Darcy's law: coupled parallel flows with a channel and a bounding porous medium. *Can. J. Chem. Eng.* 52: 475–478, 1974.

95. J. Rubinstein. Effective equations for flow in random porous media with a large number of scales. *J. Fluid Mech.* 170: 379–383, 1986.
96. R.C. Givler and S.A. Altobelli. A determination of the effective viscosity for the Brinkman–Forchheimer flow model. *J. Fluid Mech.* 258: 355–370, 1994.
97. H.P.G. Darcy. Les fontaines publique de la ville de Dijon, Victor Dalmount: Paris, 1856. English translation by M. Muskat, *Flow of Homogeneous Fluids Through Porous Media*. McGraw-Hill: New York, 1937.
98. K. Vafai and R. Thiyagaraja. Analysis of flow and heat transfer at the interface region of a porous medium. *Int. J. Heat Mass Transfer* 30: 1391–1405, 1987.
99. K. Vafai and S.J. Kim. On the limitations of the Brinkman–Forchheimer–extended Darcy equation. *Int. J. Heat Fluid Flow* 16: 11–15, 1995.
100. D.A. Nield. The limitations of the Brinkman–Forchheimer equation in modeling flow in a saturated porous medium and at an interface. *Int. J. Heat Fluid Flow* 12: 269–272, 1991.
101. G.S. Beavers and D.D. Joseph. Boundary condition at a naturally permeable wall. *J. Fluid Mech.* 30: 197–207, 1967.
102. P.G. Saffman. A theory of dispersion in a porous medium. *J. Fluid Mech.* 6: 321–349, 1959.
103. H. Brenner. Dispersion resulting from flow through spatially periodic porous media. *Phil. Trans. R. Soc. Lond. A* 297: 81–133, 1980.
104. D.L. Koch and J.F. Brady. Dispersion in fixed beds. *J. Fluid Mech.* 154: 399–427, 1985.
105. D.L. Koch and J.F. Brady. The symmetry properties of the effective diffusivity in anisotropic porous media. *Phys. Fluids* 30: 642–650, 1987.
106. D.L. Koch and J.F. Brady. A non-local description of advection–diffusion with application to dispersion in porous media. *J. Fluid Mech.* 180: 387–403, 1987.
107. D.L. Koch and J.F. Brady. Nonlocal description in porous media: non-mechanical effects. *Chem. Eng. Sci.* 42: 1377–1392, 1987.
108. C.G. Voigt. Modelling of Dispersion in Porous Media. MSc Thesis, University of Alberta, 1988.
109. R.A. Greenkorn. *Flow Phenomena in Porous Media: Fundamentals and Applications in Petroleum, Water, and Food Production*. Marcel Dekker Inc.: New York, 1983.
110. J.H. Cushman. *Dynamics of Fluids in Hierarchical Porous Media*. Academic: New York, 1990.
111. J. Salles, J.-F. Thovert, R. Delannay, L. Prevors, J.-L. Auriault, and P.M. Adler. Taylor dispersion in porous media — determination of the dispersion tensor. *Phys. Fluids A* 5: 2348–2376, 1993.
112. J.P. Hulin. Porous media: a model systems for the physics of disorder. *Adv. Colloid Interface Sci.* 49: 47–84, 1994.
113. K.H. Coats and B.D. Smith. Dead end pore volume and dispersion in porous media. *SPE J.* 4: 73–84, 1964.
114. T.K. Perkins and O.C. Johnston. A review of diffusion and dispersion in porous media. *SPE J.* 3: 70–84, 1963.
115. J.J. Fried and M.A. Combarous. Dispersion in porous media. *Adv. Hydrosci.* 7: 169–282, 1971.
116. S.H. Chang and J.C. Slattery. A new description for dispersion. *Transp. Porous Media* 3: 515–527, 1988.

117. A. Montillet, J. Comiti, and J. Legrand. Axial dispersion in liquid flow through packed reticulated metallic foams and fixed beds of different structures. *Chem. Eng. J.* 52: 63–71, 1993.
118. D. Vortmeyer and R.J. Schaefer. Equivalence of one- and two-phase models for heat transfer processes in packed beds: one-dimensional theory. *Chem. Eng. Sci.* 29: 485–491, 1974.
119. D. Vortmeyer and R.J. Schaefer. Evaluation of steady flow profiles in rectangular and circular packed-beds by a variational method. *Chem. Eng. Sci.* 38(10): 1691–1699, 1983.
120. E.U. Schlünder. Equivalence of one- and two-phase models for heat transfer processes in packed beds: one-dimensional theory. *Chem. Eng. Sci.* 30: 449–450, 1975.
121. D.W. Green, R.H. Perry, and R.E. Babcock. Longitudinal dispersion of thermal energy through porous media with a flowing fluid. *AIChE J.* 10: 645–651, 1964.
122. R.E. Babcock, D.W. Green, and R.H. Perry. Longitudinal dispersion mechanisms in packed beds. *AIChE J.* 12: 922–927, 1966.
123. A.G. Dixona and D.L. Creswell. Theoretical prediction of effective heat transfer parameters in packed beds. *AIChE J.* 25: 663–676, 1979.
124. V. Prasad, N. Kladias, A. Bandyopadhyaya, and Q. Tian. Evaluation of correlations for stagnant thermal conductivity of liquid-saturated porous beds of spheres. *Int. J. Heat Mass Transfer* 32: 1793–1796, 1989.
125. J. Rajaiah, G. Andrews, E. Ruckenstein, and R.K. Gupta. Thermal conductivity of concentrated, sterically stabilized suspensions. *Chem. Eng. Sci.* 47: 3863–3868, 1992.
126. C.T. Hsu. Heat conduction in porous media. In K. Vafai, ed., *Handbook of Porous Media*. Marcel Dekker Inc.: New York, pp. 1–52, 2000.
127. G.K. Batchelor and R.W. O'Brien. Thermal or electrical conduction through a granular material. *Proc. R. Soc. Lond. A* 355: 313–333, 1977.
128. M. Zuzovski and H. Brenner. Effective conductivities of composite materials composed of cubic arrangements of spherical particles embedded in an isotropic matrix. *J. Appl. Math. Phys. (ZAMP)* 28: 979–992, 1977.
129. A.S. Sangani and A. Acrivos. The effective conductivity of a periodic array of spheres. *Proc. R. Soc. Lond. A* 386: 263–275, 1983.
130. C.A. Coberly and W.R. Marshall, Jr. Temperature gradients in gas streams flowing through fixed granular beds. *Chem. Eng. Prog.* 47: 141–150, 1951.
131. D.A. Plautz and H.F. Johnstone. Heat and mass transfer in packed beds. *AIChE J.* 1: 193–199, 1955.
132. J.H. Quinton and J.A. Storrow. Heat transfer to air flowing through packed tubes. *Chem. Eng. Sci.* 5: 245–257, 1956.
133. S. Yagi and N. Wakao. Heat and mass transfer from wall to fluid in packed beds. *AIChE J.* 5: 79–85, 1959.
134. S. Yagi and D. Kunii. Studies on heat transfer near wall surface on packed beds. *AIChE J.* 6: 97–104, 1960.
135. D.J. Gunn and M. Khalid. Thermal dispersion and wall heat transfer in packed beds. *Chem. Eng. Sci.* 30: 261–267, 1975.
136. O. Kvernvold and P. Tyvand. Dispersion effects on thermal convection in porous media. *J. Fluid Mech.* 99: 673–686, 1980.
137. C.T. Hsu and P. Cheng. Thermal dispersion in a porous medium. *Int. J. Heat Mass Transfer* 33: 1587–1597, 1990.

138. R.G. Carbonell and S. Whitaker. Dispersion in pulsed systems — II: theoretical developments for passive dispersion in porous media. *Chem. Eng. Sci.* 38: 1795–1802, 1983.
139. D.L. Koch, R.G. Cox, H. Brenner, and J.F. Brady. The effect of order on dispersion in porous media. *J. Fluid Mech.* 200: 173–188, 1989.
140. H. Brenner and P.M. Adler. Dispersion resulting from flow through spatially periodic porous media: II. Surface and intraparticle transport. *Phil. Transp. R. Soc. Lond. A* 307: 149–200, 1982.
141. A. Eidsath, R.G. Carbonell, S. Whitaker, and L.R. Herrmann. Dispersion in pulsed systems — III: comparison between theory and experiments for packed beds. *Chem. Eng. Sci.* 38: 1803–1816, 1983.
142. D.L. Koch and J.F. Brady. Anomalous diffusion due to long-range velocity fluctuations in the absence of a mean flow. *Phys. Fluids A* 1: 47–51, 1989.
143. M.F. Edwards and J.F. Richardson. Gas dispersion in packed beds. *Chem. Eng. Sci.* 23: 109–112, 1968.
144. I. Frankel and H. Brenner. Taylor dispersion of orientable Brownian particles in unbounded homogeneous shear flows. *J. Fluid Mech.* 355: 129–156, 1993.
145. R. Mauri. Dispersion, convection and reaction in porous media. *Phys. Fluids A* 3: 743–756, 1991.
146. R. Mauri. Lagrangian self-diffusion of Brownian particles in periodic flow fields. *Phys. Fluids* 7: 275–284, 1995.
147. A. Acrivos, E.J. Hinch, and D.J. Jeffrey. Heat transfer to a slowly moving fluid from a dilute fixed bed of heated spheres. *J. Fluid Mech.* 101: 403–421, 1980.
148. C.G. Voigt, R.E. Hayes, and P.A. Tanguy. A study of two-dimensional dispersion in unconsolidated porous media. *Transp. Porous Media* 5: 269–286, 1990.
149. D.J. Gunn and C. Pryce. Dispersion in porous media. *Trans. Chem. Eng.* 47: T341–T350, 1969.
150. H.O. Pfannkuch. Contribution à l'étude des déplacements de fluides miscibles dans un milieu poreux. *Rev. Inst. Fr. Pétrole* 18(2): 1–54, 1963.
151. E.A. Ebach and R.R. White. Mixing of fluids flowing through beds of packed solids. *AIChE J.* 4: 161–164, 1958.
152. J.J. Carberry and R.H. Bretton. Axial dispersion of mass in flow through fixed beds. *AIChE J.* 4: 367–375, 1958.
153. R.J. Blackwell, J.R. Rayne, and W.M. Terry. Factors influencing the efficiency of miscible displacement. *Trans. AIME* 217: 1–8, 1959.
154. N.E. Rifai, W.J. Kaufman, and D.K. Todd. Dispersion phenomena in laminar flow through porous media. *Sanit. Engrg. Rept. Inst. Eng. Res. Ser.* 90, Berkeley, CA, 1956.
155. J. Martin, N. Rakotomalala, and D. Salin. Hydrodynamic dispersion of non-colloidal suspensions: measurement from Einstein's argument. *Phys. Rev. Lett.* 74: 1347–1350, 1995.
156. S. Liu. Particle dispersion for suspension flow. *Chem. Eng. Sci.* 54: 873–891, 1999.
157. G.A. Turner. The flow-structure in packed beds: a theoretical investigation utilizing frequency response. *Chem. Eng. Sci.* 7: 156–165, 1958.
158. K.B. Bischoff and O. Levenspiel. Fluid dispersion — generalization and comparison of mathematical models. *Chem. Eng. Sci.* 17, I. Generalization of models, 245–255; II. Comparison of models, 257–264, 1962.

159. H. Brenner. The diffusion model of longitudinal mixing in beds of finite length. Numerical values. *Chem. Eng. Sci.* 17: 229–24, 1962.
160. H.A. Deans. A mathematical model for dispersion in the direction of flow in porous media. *SPE J.* 3: 49–52, 1963.
161. C.F. Gottschlich. Axial dispersion in a packed bed. *AIChE J.* 9: 88–92, 1963.
162. E. Charlaix, J.P. Hulin, and T.J. Plona. Experimental study of tracer dispersion in sintered glass porous materials of variable compaction. *Phys. Fluids* 30: 1690–1698, 1987.
163. G.A. Gist, A.H. Thompson, A.J. Katz, and R.L. Higgins. Hydrodynamic dispersion and pore geometry in consolidated rock. *Phys. Fluids A* 2: 1533–1544, 1990.
164. J.-C. Bacri, N. Rakotomalala, and D. Salin. Anomalous dispersion and finite-size effects in hydrodynamic dispersion. *Phys. Fluids A* 2: 674–680, 1990.
165. P. Maloszewski and A. Zuber. On the theory of tracer experiments in fissured rocks with a porous matrix. *J. Hydrol.* 79: 33, 1985.
166. P. Magnico, C. Leroy, J.P. Bouchaud, C. Gauthier, and J.P. Hulin. Tracer dispersion in porous media with a double porosity. *Phys. Fluids A* 5: 46–57, 1993.

Part II

Forced Convection

4

Forced Convection in Porous Media: Transverse Heterogeneity Effects and Thermal Development

D.A. Nield and A.V. Kuznetsov

CONTENTS

Summary	144
4.1 Transverse Heterogeneity	144
4.1.1 Introduction	144
4.1.2 Parallel-Plate Channel.....	144
4.1.2.1 Darcy model	147
4.1.2.2 Brinkman model.....	156
4.1.2.3 Asymmetric heterogeneity	158
4.1.2.4 Interaction between the effects of conductivity heterogeneity and local thermal nonequilibrium ...	160
4.1.3 Circular Duct	161
4.1.3.1 Isoflux boundaries	163
4.1.3.2 Isotemperature boundaries	164
4.2 Thermal Development.....	164
4.2.1 Introduction	164
4.2.2 Walls at Uniform Temperature.....	165
4.2.2.1 Parallel-plate channel.....	165
4.2.2.2 Circular tube	168
4.2.3 Walls at Uniform Heat Flux	170
4.2.3.1 Parallel-plate channel.....	170
4.2.3.2 Circular tube	173
4.2.4 Local Thermal Nonequilibrium.....	175
4.2.5 Effects of Axial Conduction and Viscous Dissipation	183
Nomenclature	191
References	192

Summary

Recent analytical studies on thermal development and transverse heterogeneity effects on forced convection in channels and ducts are surveyed.

4.1 Transverse Heterogeneity

4.1.1 Introduction

Applications of the material in this chapter include the cooling of electronic equipment using devices made of compressed metallic foam material that is highly porous even after compression. The compression may not be uniform, and the channel length may be relatively short so that the thermal development effects are important.

In this section we survey analytical studies on the effect on forced convection, in channels and ducts, of the variation in the transverse direction of permeability and thermal conductivity. Both parallel-plate channels and circular ducts are considered, and walls at uniform temperature and uniform heat flux are treated in turn. Basic work using the Darcy model for thermal equilibrium is extended in some cases to the Brinkman equation and to the case of local thermal nonequilibrium. The standard work is for symmetric property variation and symmetric thermal boundary conditions, but some exceptions are also discussed.

4.1.2 Parallel-Plate Channel

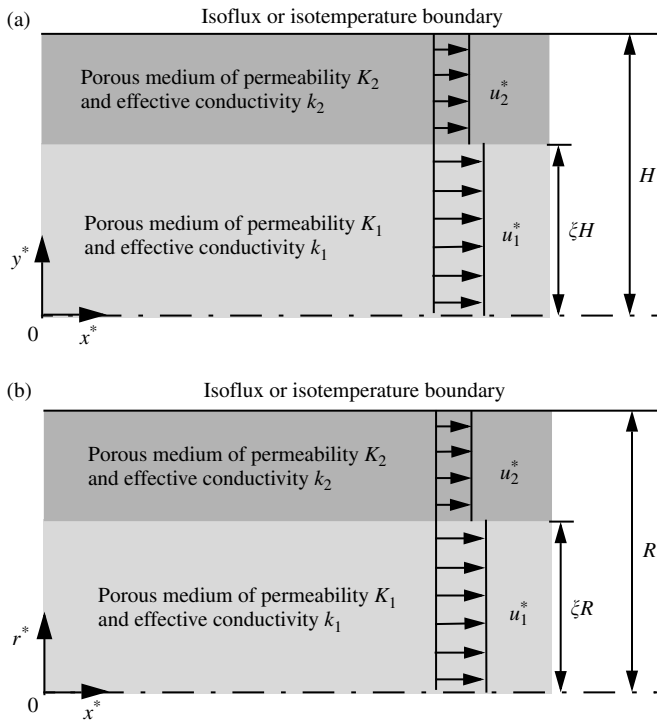
We allow the permeability K and the thermal conductivity k to be nonuniform in space, and define

$$\tilde{K} = \overline{\frac{K}{\bar{K}}}, \quad \tilde{k} = \frac{k}{\bar{k}} \quad (4.1)$$

where an overbar denotes a mean value taken over the volume occupied by the porous medium.

For the steady-state fully developed situation we have unidirectional flow in the x^* -direction between impermeable boundaries at $y^* = -H$ and $y^* = H$, as illustrated in [Figure 4.1\(a\)](#). The steady-state Darcy–Forchheimer–Brinkman equation is (for theoretical background and range of applicability, see [1])

$$G = \frac{\mu u^*}{K} + c_L \rho u^{*2} - \mu_{\text{eff}} \frac{d^2 u^*}{dy^{*2}} \quad (4.2)$$

**FIGURE 4.1**

Definition sketch: (a) parallel-plate channel, (b) circular duct.

where μ_{eff} is an effective viscosity, μ is the fluid viscosity, K is the permeability, and G is the applied pressure gradient and the coefficient c_L is related to the Forchheimer coefficient c_F used in Nield and Bejan [2] by

$$c_L = c_F K^{-1/2} \quad (4.3)$$

We define dimensionless variables

$$x = \frac{x^*}{H}, \quad y = \frac{y^*}{H}, \quad u = \frac{\mu u^*}{GH^2} \quad (4.4)$$

so that the dimensionless form of Eq. (4.2) is

$$M \frac{d^2 u}{dy^2} - \frac{u}{\tilde{K} Da} - \tilde{L} Fr u^2 + 1 = 0 \quad (4.5)$$

where the viscosity ratio M , the Darcy number Da , and the Forchheimer number Fr are defined by

$$M = \frac{\mu_{\text{eff}}}{\mu}, \quad Da = \frac{\bar{K}}{H^2}, \quad Fr = \frac{\bar{c}_L \rho G H^4}{\mu^2} \quad (4.6a,b,c)$$

while

$$\tilde{K} = \frac{K}{\bar{K}}, \quad \tilde{L} = \frac{c_L}{\bar{c}_L} \quad (4.7a,b)$$

where the bar denotes the mean value. If c_L can be taken as a constant, then

$$\tilde{L} = \tilde{K}^{-1/2} \quad (4.8)$$

and thus there is a simplification if this approximation is valid.

The mean velocity U^* and the bulk mean temperature T_m^* are defined by

$$U^* = \frac{1}{H} \int_0^H u^* dy^*, \quad T_m^* = \frac{1}{HU^*} \int_0^H u^* T^* dy^* \quad (4.9)$$

Further dimensionless variables are defined by

$$\hat{u} = \frac{u^*}{U^*}, \quad \hat{T} = \frac{T^* - T_w^*}{T_m^* - T_w^*} \quad (4.10)$$

This implies that

$$\hat{u} = \frac{u}{\int_0^1 u dy} \quad (4.11)$$

The Nusselt number Nu is defined as

$$Nu = \frac{2Hq''}{k(T_w^* - T_m^*)} \quad (4.12)$$

The Nusselt number is the traditional nondimensional measure of the rate of heat transfer from the boundaries into the bulk of the fluid. The thermal energy equation for the case of local thermal equilibrium, with axial conduction and viscous dissipation ignored, is

$$u^* \frac{\partial T^*}{\partial x^*} = \frac{k}{\rho c_p} \frac{\partial^2 T^*}{\partial y^{*2}} \quad (4.13)$$

The reader should note that in the weak variation case considered below $(dk/dy)(\partial T^*/\partial y^*)$ is negligible in comparison with $k(\partial^2 T^*/\partial y^{*2})$, and for the piecewise constant layered case considered below it is zero in each layer.

4.1.2.1 Darcy model

In the Darcy flow case, corresponding to $Fr \rightarrow 0, Da \rightarrow 0$ we have

$$\hat{u} = \tilde{K} \quad (4.14)$$

(For the Forchheimer model, the problem reduces to the Darcy case but with a different distribution of permeability.)

4.1.2.1.1 Isoflux boundaries

Before proceeding, we note that the analysis for the case considered in this section has been extended, to include the effect of a viscosity varying in the transverse direction, by Sundaravadivelu and Tso [3]. However, here we ignore this effect.

The first law of thermodynamics leads to

$$\frac{\partial T^*}{\partial x^*} = \frac{dT_m^*}{dx^*} = \frac{q''}{\rho c_p H U^*} = \text{constant} \quad (4.15)$$

In this case the thermal energy equation may be written as

$$\frac{d^2\hat{T}}{dy^2} = -\frac{1}{2\tilde{k}} Nu \hat{u} \quad (4.16)$$

For the Darcy flow case this becomes

$$\frac{d^2\hat{T}}{dy^2} = -\frac{1}{2\tilde{k}} Nu \tilde{K} \quad (4.17)$$

The boundary conditions on $\hat{T}(y)$ are

$$\frac{d\hat{T}}{dy}(0) = 0, \quad \hat{T}(1) = 0 \quad (4.18a,b)$$

4.1.2.1.1.1 Continuous weak variation — We first consider the case where the permeability and thermal conductivity distributions are given by

$$\begin{aligned} K &= K_0 \left\{ 1 + \varepsilon_K \left(\frac{|y^*|}{H} - \frac{1}{2} \right) \right\} \\ k &= k_0 \left\{ 1 + \varepsilon_k \left(\frac{|y^*|}{H} - \frac{1}{2} \right) \right\} \end{aligned} \quad (4.19a,b)$$

The coefficients ε_K and ε_k are each assumed to be small compared with unity.

The mean values of K, k are thus K_0, k_0 , respectively, and so

$$\begin{aligned}\tilde{K} &= 1 + \varepsilon_K \left(|y| - \frac{1}{2} \right) \\ \tilde{k} &= 1 + \varepsilon_k \left(|y| - \frac{1}{2} \right)\end{aligned}\quad (4.20a,b)$$

The velocity distribution is given by

$$\hat{u} = \tilde{K} = 1 + \varepsilon_K \left(|y| - \frac{1}{2} \right) \quad (4.21)$$

and Eq. (4.17) gives, to first order in small quantities,

$$\frac{d^2\hat{T}}{dy^2} = -\frac{1}{2}Nu \left\{ 1 + (\varepsilon_K - \varepsilon_k) \left(y - \frac{1}{2} \right) \right\} \quad (4.22)$$

The solution of Eq. (4.22) subject to the boundary conditions in Eq. (4.18) is

$$\hat{T} = -\frac{1}{24}Nu \{ 6(y^2 - 1) + (\varepsilon_K - \varepsilon_k)(2y^3 - 3y^2 + 1) \} \quad (4.23)$$

The compatibility condition (an identity required by the definitions of \hat{u} and \hat{T}) is

$$\int_0^1 \hat{u} \hat{T} dy = 1 \quad (4.24)$$

Substitution of the expressions (4.21) and (4.23) into (4.24) leads, to first order, to

$$Nu = 6 \left(1 + \frac{1}{4}\varepsilon_K - \frac{1}{8}\varepsilon_k \right) \quad (4.25)$$

4.1.2.1.1.2 Stepwise variation (double layer) — Suppose that

$$K = K_1 \quad \text{and} \quad k = k_1 \quad \text{for } 0 < |y^*| < \xi H \quad (4.26a)$$

$$K = K_2 \quad \text{and} \quad k = k_2 \quad \text{for } \xi H < |y^*| < H \quad (4.26b)$$

The mean values are given by

$$\begin{aligned}\bar{K} &= \xi K_1 + (1 - \xi)K_2 \\ \bar{k} &= \xi k_1 + (1 - \xi)k_2\end{aligned}\quad (4.27a,b)$$

We write

$$\tilde{K}_i = \frac{K_i}{\bar{K}} \quad \text{and} \quad \tilde{k}_i = \frac{k_i}{\bar{k}} \quad \text{for } i = 1, 2 \quad (4.28)$$

The velocity distribution is given by

$$\begin{aligned}\hat{u}_1 &= \tilde{K}_1 && \text{for } 0 < y < \xi \\ \hat{u}_2 &= \tilde{K}_2 && \text{for } \xi < y < 1\end{aligned} \quad (4.29a,b)$$

We have now to solve the differential equations

$$\begin{aligned}\frac{d^2\hat{T}_1}{dy^2} &= -\frac{Nu\tilde{K}_1}{2\tilde{k}_1} && \text{for } 0 < y < \xi \\ \frac{d^2\hat{T}_2}{dy^2} &= -\frac{Nu\tilde{K}_2}{2\tilde{k}_2} && \text{for } \xi < y < 1\end{aligned} \quad (4.30a,b)$$

subject to the symmetry and boundary conditions

$$\frac{d\hat{T}_1}{dy}(0) = 0, \quad \hat{T}_2(1) = 0 \quad (4.31)$$

and the matching conditions (for temperature and heat flux, which are assumed to be continuous)

$$\hat{T}_1(\xi) = \hat{T}_2(\xi), \quad \tilde{k}_1 \frac{d\hat{T}_1}{dy}(\xi) = \tilde{k}_2 \frac{d\hat{T}_2}{dy}(\xi) \quad (4.32)$$

The solution is

$$\begin{aligned}\hat{T}_1 &= \frac{Nu}{4} \left\{ \frac{\tilde{K}_1}{\tilde{k}_1} (\xi^2 - y^2) + \frac{\tilde{K}_1}{\tilde{k}_2} (2\xi - 2\xi^2) + \frac{\tilde{K}_2}{\tilde{k}_2} (\xi^2 - 2\xi + 1) \right\} \\ \hat{T}_2 &= \frac{Nu}{4} \left\{ \frac{\tilde{K}_2}{\tilde{k}_2} (1 - 2\xi + 2\xi y - y^2) + \frac{\tilde{K}_1}{\tilde{k}_2} (2\xi - 2\xi y) \right\}\end{aligned} \quad (4.33a,b)$$

Substitution into the integral compatibility condition

$$\int_0^1 \hat{u} \hat{T} dy = \int_0^\xi \hat{u}_1 \hat{T}_1 dy + \int_\xi^1 \hat{u}_2 \hat{T}_2 dy = 1 \quad (4.34)$$

then yields the Nusselt number expression,

$$Nu = 6 \left/ \left\{ \xi^3 \frac{\tilde{K}_1^2}{\tilde{k}_1} + 3\xi^2(1-\xi) \frac{\tilde{K}_1^2}{\tilde{k}_2} + 3\xi(1-\xi)^2 \frac{\tilde{K}_1 \tilde{K}_2}{\tilde{k}_2} + (1-\xi)^3 \frac{\tilde{K}_2^2}{\tilde{k}_2} \right\} \right. \quad (4.35)$$

For the homogeneous case, $\tilde{K}_1 = \tilde{K}_2 = \tilde{k}_1 = \tilde{k}_2 = 1$, this expression reduces to $Nu = 6$, independent of the value of ξ , as expected.

4.1.2.1.1.3 Stepwise variation (triple layer) — The analysis has been extended to three layers (one of which may be solid, so that one has a conjugate conduction–convection problem) by Kuznetsov and Nield [4].

Suppose that

$$\begin{aligned} K &= K_1 \quad \text{and} \quad k = k_1 \quad \text{for } 0 < |y^*| < \xi H \\ K &= K_2 \quad \text{and} \quad k = k_2 \quad \text{for } \xi H < |y^*| < \eta H \\ K &= K_3 \quad \text{and} \quad k = k_3 \quad \text{for } \eta H < |y^*| < H \end{aligned} \quad (4.36a,b,c)$$

Then, corresponding to Eq. (4.35), one finds that

$$\begin{aligned} Nu = 6 \left/ \left\{ \right. \right. &\xi^3 \frac{\tilde{K}_1^2}{\tilde{k}_1} + 3\xi^2(\eta - \xi) \frac{\tilde{K}_1^2}{\tilde{k}_2} + 3\xi^2(1 - \eta) \frac{\tilde{K}_1^2}{\tilde{k}_3} + 3\xi(\eta - \xi)^2 \frac{\tilde{K}_1 \tilde{K}_2}{\tilde{k}_2} \\ &+ 6\xi(\eta - \xi)(1 - \eta) \frac{\tilde{K}_1 \tilde{K}_2}{\tilde{k}_3} + 3\xi(1 - \eta)^2 \frac{\tilde{K}_1 \tilde{K}_3}{\tilde{k}_3} + (\eta - \xi)^3 \frac{\tilde{K}_2^2}{\tilde{k}_2} \\ &+ 3(\eta - \xi)^2(1 - \eta) \frac{\tilde{K}_2^2}{\tilde{k}_3} + 3(\eta - \xi)(1 - \eta)^2 \frac{\tilde{K}_2 \tilde{K}_3}{\tilde{k}_3} + (1 - \eta)^3 \frac{\tilde{K}_3^2}{\tilde{k}_3} \left. \left. \right\} \right. \end{aligned} \quad (4.37)$$

For the expressions for \hat{T}_1 , \hat{T}_2 , and \hat{T}_3 the reader is referred to [4]. The expression for the conjugate problem is obtained by putting $\tilde{K}_3 = 0$. (In order to conform with the usual definition of the Nusselt number for the conjugate problem, it is necessary to alter the temperature scale in the definition, and this means rescaling Nu . For details, see Kuznetsov and Nield [4].)

Kuznetsov and Nield [4] have hypothesized that, in the case of N layers, with interfaces at $y = \xi_1, \xi_2, \dots, \xi_{N-1}$, that

$$Nu = 6 \left/ \sum c_{PQR} z_P z_Q z_R \tilde{K}_P \tilde{K}_Q / \tilde{k}_R \right. \quad (4.38)$$

where

$$z_j = \xi_j - \xi_{j-1} \quad \text{for } j = 1, 2, \dots, N; \quad \xi_0 = 0 \text{ and } \xi_N = 1 \quad (4.39)$$

and the coefficients c_{PQR} are those that appear in the trinomial expansion

$$(z_1 + z_2 + \cdots + z_N)^3 = \sum c_{PQR} z_P z_Q z_R \quad (4.40)$$

If this hypothesis is correct (and it is certainly true for $N = 2$ and $N = 3$), then one can immediately deduce, using some elementary inequalities, bounds on the value of the Nusselt number for a general transversely heterogeneous porous medium. Let $\tilde{K}_{\max}, \tilde{K}_{\min}, \tilde{k}_{\max}, \tilde{k}_{\min}$ be the maximum, minimum values of \tilde{K}, \tilde{k} , respectively, within the porous medium. Then

$$6\tilde{k}_{\min}/\tilde{K}_{\max}^2 \leq Nu \leq 6\tilde{k}_{\max}/\tilde{K}_{\min}^2 \quad (4.41)$$

4.1.2.1.2 Isotemperature boundaries

For the case where the wall temperature T_w^* is held constant, Eq. (4.16) is replaced by

$$\frac{d^2\hat{T}}{dy^2} = -\frac{1}{2\tilde{k}} Nu \hat{u} \hat{T} \quad (4.42)$$

The extra factor \hat{T} on the right-hand side arises because now the excess temperature decays exponentially in the axial direction, and so the axial excess temperature gradient is proportional to the excess temperature. The boundary conditions, Eq. (4.18a,b), remain unchanged, but the integral compatibility condition is replaced by the differential compatibility condition

$$Nu = -2 \frac{d\hat{T}}{dy}(1) \quad (4.43)$$

This condition is also an identity arising from the definition of \hat{T} . We believe that our publications are the first in which the integral and differential compatibility conditions are explicitly discussed. In the case of isotemperature boundaries the first condition is satisfied automatically and the second must be imposed, while in the isoflux case the roles of the two conditions are reversed.

4.1.2.1.2.1 Continuous weak variation — Equations (4.19) through (4.21) are pertinent. In place of Eq. (4.22) we now have

$$\frac{d^2\hat{T}}{dy^2} = -\frac{1}{2} Nu \left\{ 1 + (\varepsilon_K - \varepsilon_k) \left(y - \frac{1}{2} \right) \right\} \hat{T} \quad (4.44)$$

This is to be solved subject to the boundary conditions (4.18a,b). A perturbation expansion in terms of the small parameter $\varepsilon = \varepsilon_K - \varepsilon_k$ leads to

$$Nu = \frac{\pi^2}{2} \left\{ 1 + \frac{2}{\pi^2} (\varepsilon_K - \varepsilon_k) \right\} \quad (4.45)$$

4.1.2.1.2.2 Stepwise variation (double layer) — Equations (4.26) through (4.29) are still pertinent, but instead of Eq. (4.30) we now have

$$\begin{aligned} \frac{d^2 \hat{T}_1}{dy^2} &= -\lambda_1^2 \hat{T}_1 && \text{for } 0 < y < \xi \\ \frac{d^2 \hat{T}_2}{dy^2} &= -\lambda_2^2 \hat{T}_2 && \text{for } \xi < y < 1 \end{aligned} \quad (4.46a,b)$$

where

$$\lambda_i = \left(\frac{Nu \tilde{K}_i}{2 \tilde{k}_i} \right)^{1/2}, \quad \text{for } i = 1, 2 \quad (4.47)$$

The solutions of Eqs. (4.46a,b) satisfying the boundary conditions (4.18a,b) are

$$\begin{aligned} \hat{T}_1 &= A_1 \cos \lambda_1 y \\ \hat{T}_2 &= A_2 \sin \lambda_2 (1 - y) \end{aligned} \quad (4.48a,b)$$

The continuity of temperature and heat flux at the interface $y = \xi$ then implies the matching conditions

$$\begin{aligned} A_1 \cos \lambda_1 \xi &= A_2 \sin \lambda_2 (1 - \xi) \\ \tilde{k}_1 \lambda_1 A_1 \sin \lambda_1 \xi &= \tilde{k}_2 \lambda_2 A_2 \cos \lambda_2 (1 - \xi) \end{aligned} \quad (4.49a,b)$$

The condition that Eqs. (4.49a,b) have a nontrivial solution is that

$$\tan \lambda_1 \xi \tan \lambda_2 (1 - \xi) = \frac{\tilde{k}_2 \lambda_2}{\tilde{k}_1 \lambda_1} \quad (4.50)$$

In view of Eq. (4.47), this equation may be regarded as an eigenvalue equation for Nu . As soon as the value of Nu has been found, the compatibility

condition gives

$$A_2 = \frac{Nu}{2\lambda_2} \quad (4.51)$$

and then either (4.49a) or (4.49b) gives A_1 to complete the solution.

In general, Eq. (4.50) must be solved numerically. For the homogeneous case, $\tilde{K}_1 = \tilde{K}_2 = \tilde{k}_1 = \tilde{k}_2 = 1$, one can check that $\lambda_1 = \lambda_2 = \pi/2$ makes Eq. (4.50) an identity in ξ , so that $Nu = \pi^2/2$ and $A_1 = A_2 = \pi/2$, and so

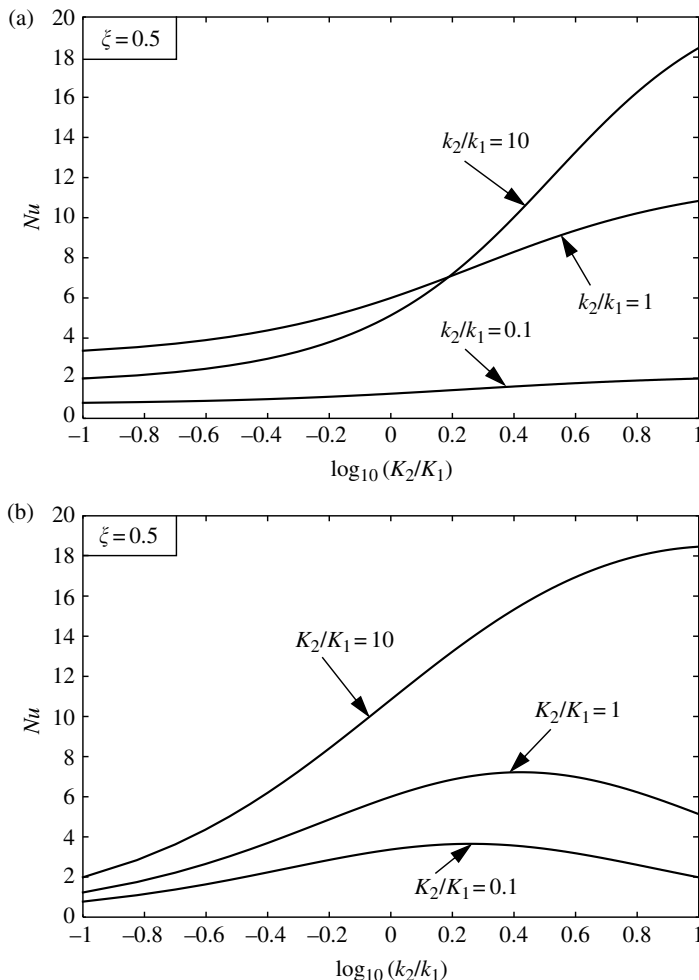
$$\hat{T} = \frac{\pi}{2} \cos \frac{\pi y}{2} \quad (4.52)$$

as expected.

Immediately from Eqs. (4.25) and (4.45), we can see the prime effects of permeability variation and conductivity on the Nusselt number. If the permeability is above average in the region adjacent to the wall (and consequently is below average in the mid-channel region), so that ε_K is positive, then the Nusselt number is thereby increased. Also from Eqs. (4.25) and (4.45) we see that the prime effect of thermal conductivity variation is in the opposite direction to that of permeability variation. An above average conductivity near the wall leads to a reduction in Nu .

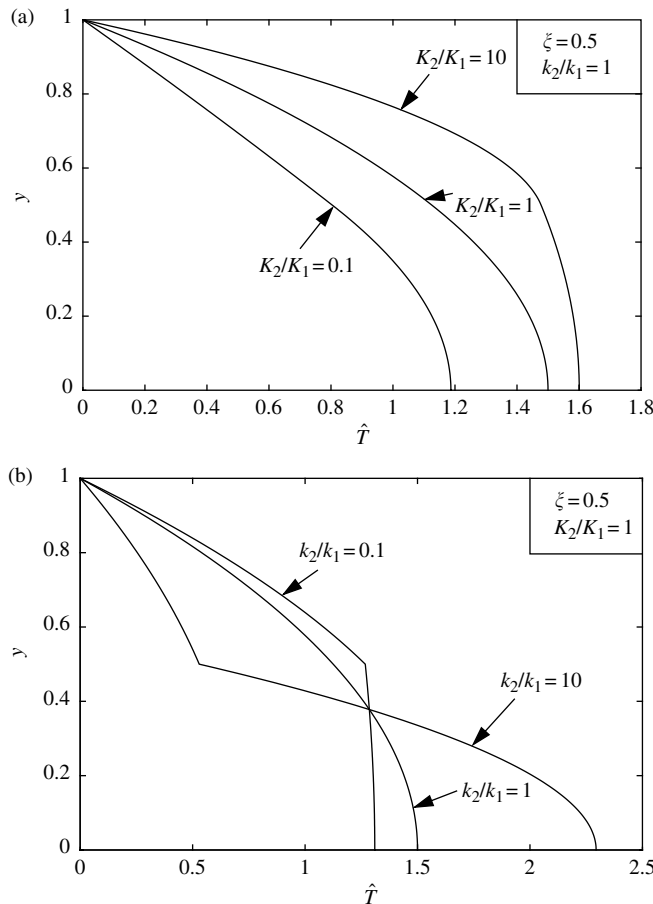
We now consider the stepwise variation situation. For the case of isoflux boundaries, and for the case where $\xi = 0.5$ so that each medium occupies half the channel, plots of the Nusselt number Nu are displayed in [Figure 4.2](#). In accordance with the trend noted in Section 4.1.2.1.1.1, Nu increases as K_2/K_1 increases, because above average permeability and hence above average velocity near the wall leads to a smaller difference between the bulk mean temperature and the wall temperature. In contrast, the way in which Nu varies with k_2/k_1 is more complex. As k_2/k_1 increases, Nu at first increases but then goes through a maximum. It is only at large values of k_2/k_1 that Nu decreases as k_2/k_1 increases in line with the trend observed for the case of continuous variation. Besides the effect of thermal conductivity on curvature of the temperature profile, there is an effect resulting from the change in slope of that profile at the interface.

The difference between the effects of permeability variation and conductivity variation is strikingly shown in the plots of temperature profiles presented in [Figure 4.3](#). [Figure 4.3\(a\)](#) shows that in the absence of conductivity variation, the effect of increase of permeability near the wall leads to profiles with larger mean values but with continuously varying slopes. On the other hand, the effect of conductivity variation leads to profiles having a discontinuity in slope, and whether this leads to an increase or decrease in the value of the mean temperature depends on the relative magnitudes of slope increment and curvature variation.

**FIGURE 4.2**

Nusselt number for the parallel-plate channel with isoflux boundaries: (a) effect of permeability variation, (b) effect of thermal conductivity variation.

The corresponding results for the case of isotemperature boundaries are presented in Figure 4.4 and Figure 4.5. Compared with the isoflux case, the major change is that, for most values of the permeability and conductivity parameters, the Nusselt number is reduced (and the temperature profiles become more peaked) as expected. The exception is when conductivity near the wall is much less than average, and in this case the Nusselt number is already small. The trends relating to permeability and conductivity variation are similar for the two types of thermal boundary conditions.

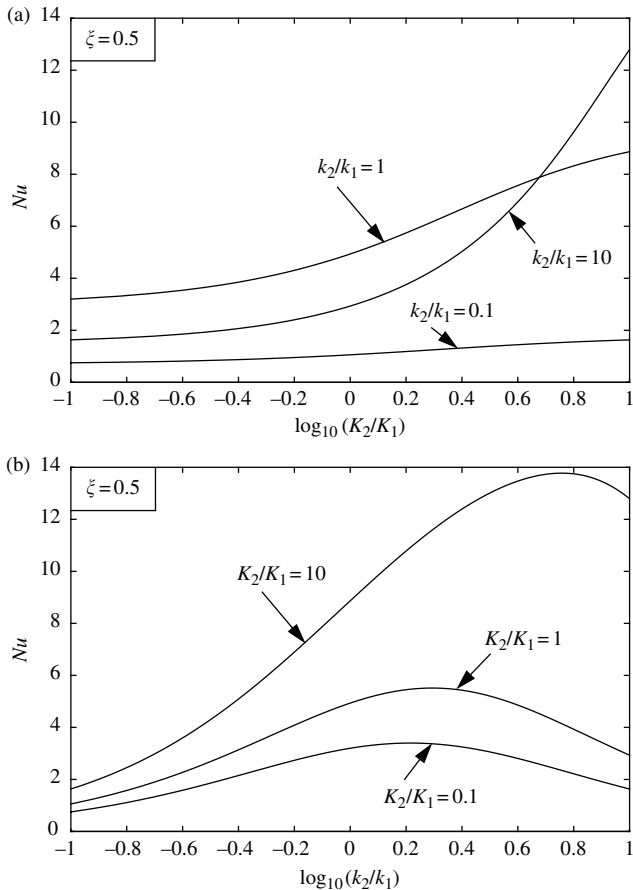
**FIGURE 4.3**

Temperature profiles for the parallel-plate channel with isoflux boundaries: (a) effect of permeability variation, (b) effect of thermal conductivity variation.

4.1.2.1.2.3 Stepwise variation (triple layer) — For the three layer case, Eq. (4.50) generalizes to

$$\det \begin{bmatrix} \cos \lambda_1 \xi & -\cos \lambda_2 \xi & -\sin \lambda_2 \xi & 0 \\ \tilde{k}_1 \lambda_1 \sin \lambda_1 \xi & -\tilde{k}_2 \lambda_2 \sin \lambda_2 \xi & \tilde{k}_2 \lambda_2 \cos \lambda_2 \xi & 0 \\ 0 & \cos \lambda_2 \eta & \sin \lambda_2 \eta & -\sin \lambda_3 (1 - \eta) \\ 0 & -\tilde{k}_2 \lambda_2 \sin \lambda_2 \eta & \tilde{k}_2 \lambda_2 \cos \lambda_2 \eta & \tilde{k}_3 \lambda_3 \cos \lambda_3 (1 - \eta) \end{bmatrix} = 0 \quad (4.53)$$

For details see Kuznetsov and Nield [4].

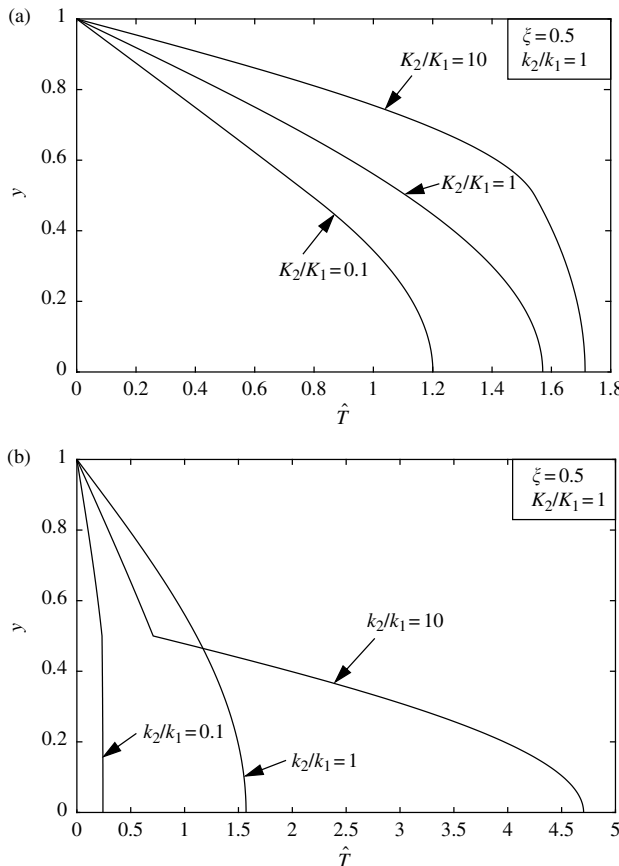
**FIGURE 4.4**

Nusselt number for the parallel-plate channel with isothermal boundaries: (a) effect of permeability variation, (b) effect of thermal conductivity variation.

This last result has been exploited by Nield and Kuznetsov [5] to model a situation in which there is gross heterogeneity and anisotropy, namely, the experimental work reported by Paek et al. [6].

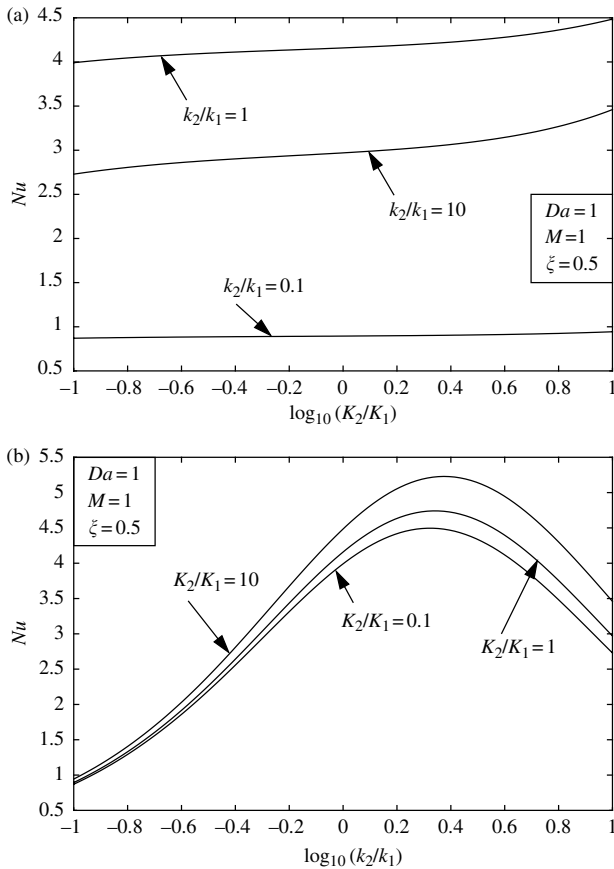
4.1.2.2 Brinkman model

The analysis is similar to that for the Darcy model, but the algebra is more complicated and has been carried out just for the case of uniform flux boundaries. For details refer to Nield and Kuznetsov [7]. Some results are presented in Figure 4.6 and Figure 4.7. These are for the case of $Da = 1$, and so are representative of a hyperporous medium. These figures may be compared with Figure 4.2 and Figure 4.3 that apply to the Darcy model, that is, the limiting case Da tends to zero. For the hyperporous case, as for the near Darcy case, the

**FIGURE 4.5**

Temperature profiles for the parallel-plate channel with isotemperature boundaries: (a) effect of permeability variation, (b) effect of thermal conductivity variation.

Nusselt number increases monotonically with K_2/K_1 , but now the increase is only gradual. This gradual change is as expected, because now the velocity profile is strongly influenced by the Laplacian viscous term as well as the Darcy term in the momentum equation (4.2), and the velocity profiles are more parabolic than slug-like. Again the Nusselt number goes through a maximum as the conductivity ratio k_2/k_1 increases. The temperature profiles are shown in Figure 4.8. It is noteworthy that the temperature profile changes little with variation of the permeability ratio but a lot with variation of the conductivity ratio. In fact, the trends shown in Figure 4.8(b) are very similar to those shown in Figure 4.3(b). This illustrates the obvious fact that the variation of the Darcy number is essentially a hydrodynamic change rather than a thermal one, and so the temperature profiles should be qualitatively independent of Da .

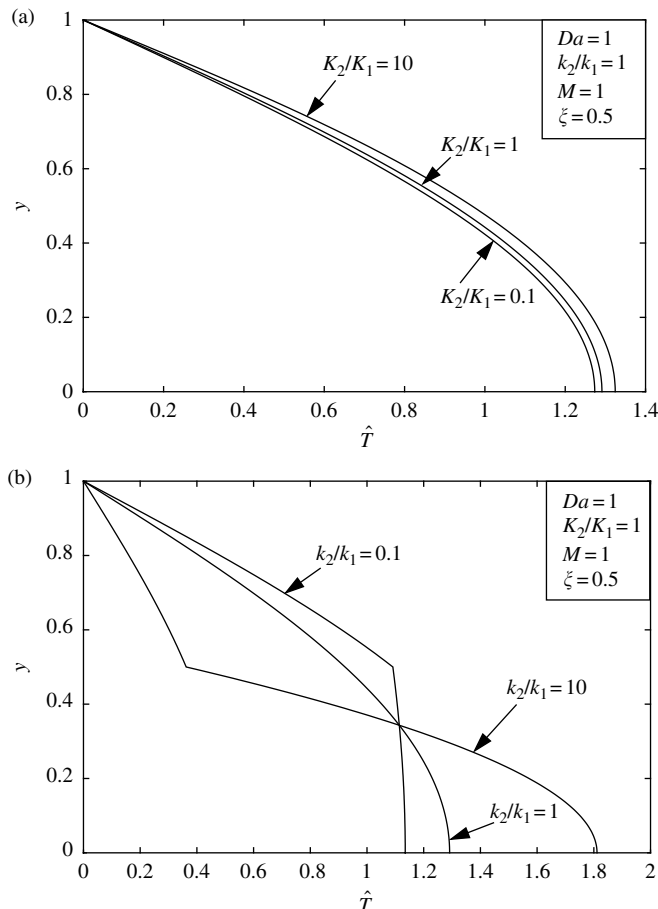
**FIGURE 4.6**

Nusselt number for a hyperporous case, $Da = 1$: (a) effect of permeability variation, (b) effect of thermal conductivity variation ($M = 1, \xi = 0.5$).

In Figure 4.9 we present the variation of Nusselt number with the Darcy number. As Da increases there is a change from the Darcy flow situation, in which permeability variation plays a dramatic role, to the hyperporous situation in which permeability variation is not important, and for which the value of Nu is smaller than for the Darcy case. In the case where there is no conductivity variation, Nu tends to the clear-fluid value 4.12 as Da tends to infinity, independent of the permeability variation, as expected. The effect of conductivity variation is just as important for the hyperporous case as it is for the Darcy case, again as expected.

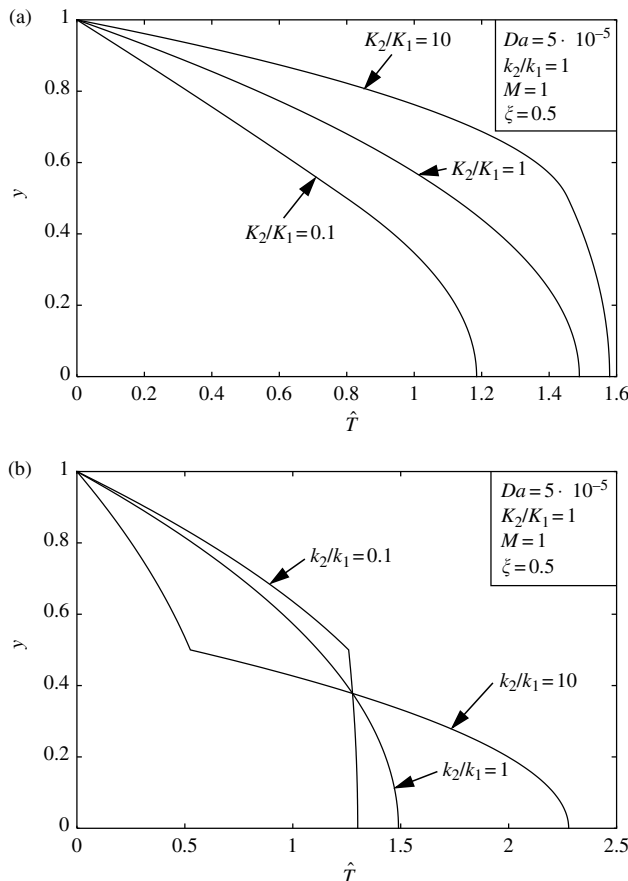
4.1.2.3 Asymmetric heterogeneity

So far we have been considering the case of symmetric heterogeneity, which is the most interesting case (when one swaps the core and sheath there is

**FIGURE 4.7**

Temperature profiles for the case of isoflux boundaries and for a hyperporous case, $Da = 1$:
 (a) effect of permeability variation, (b) effect of thermal conductivity variation ($M = 1, \xi = 0.5$).

obviously a significant change). However, the case of asymmetric heterogeneity is of interest when coupled with asymmetric heating. This situation has been studied by Nield and Kuznetsov [8]. They found that for the case of uniform heat flux boundaries, both permeability variation and conductivity variation lead to a reduction in the value of the Nusselt number Nu , but for the uniform temperature case the situation is more complicated. For the isoflux case and permeability variation alone, Nu is independent of the degree of asymmetric heating as represented by a flux ratio τ , but in the case of conductivity variation Nu is strongly dependent on τ and the degree of conductivity variation. In the case of uniform temperature boundary conditions no fully developed solution exists when both the property variation and the heating are asymmetric.

**FIGURE 4.8**

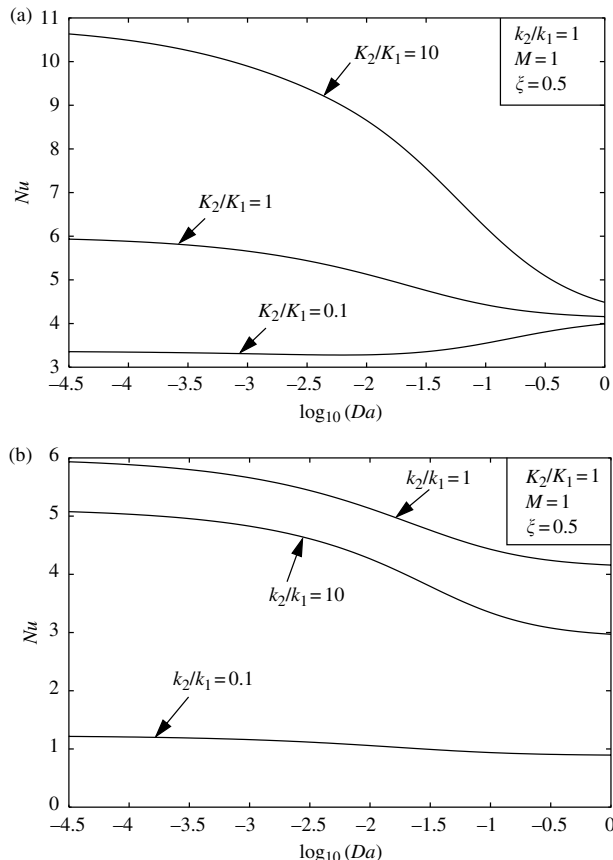
Temperature profiles for the case of isoflux boundaries and for the near Darcy limit, $Da = 5 \times 10^{-5}$.
 (a) effect of permeability variation, (b) effect of thermal conductivity variation ($M = 1, \xi = 0.5$).

4.1.2.4 Interaction between the effects of conductivity heterogeneity and local thermal nonequilibrium

Nield and Kuznetsov [9] have considered the case of a parallel-plate channel divided into core and sheath layers occupied respectively by two porous media, of the same porosity ϕ and permeability K , and saturated by the same fluid of thermal conductivity k_f , but with the solid thermal conductivity k_s being given by

$$\begin{aligned} k_s &= k_{s1} && \text{for } 0 < |y^*| < \xi H \\ k_s &= k_{s2} && \text{for } \xi H < |y^*| < H \end{aligned} \quad (4.54a)$$

Some results are shown in Figure 4.10.

**FIGURE 4.9**

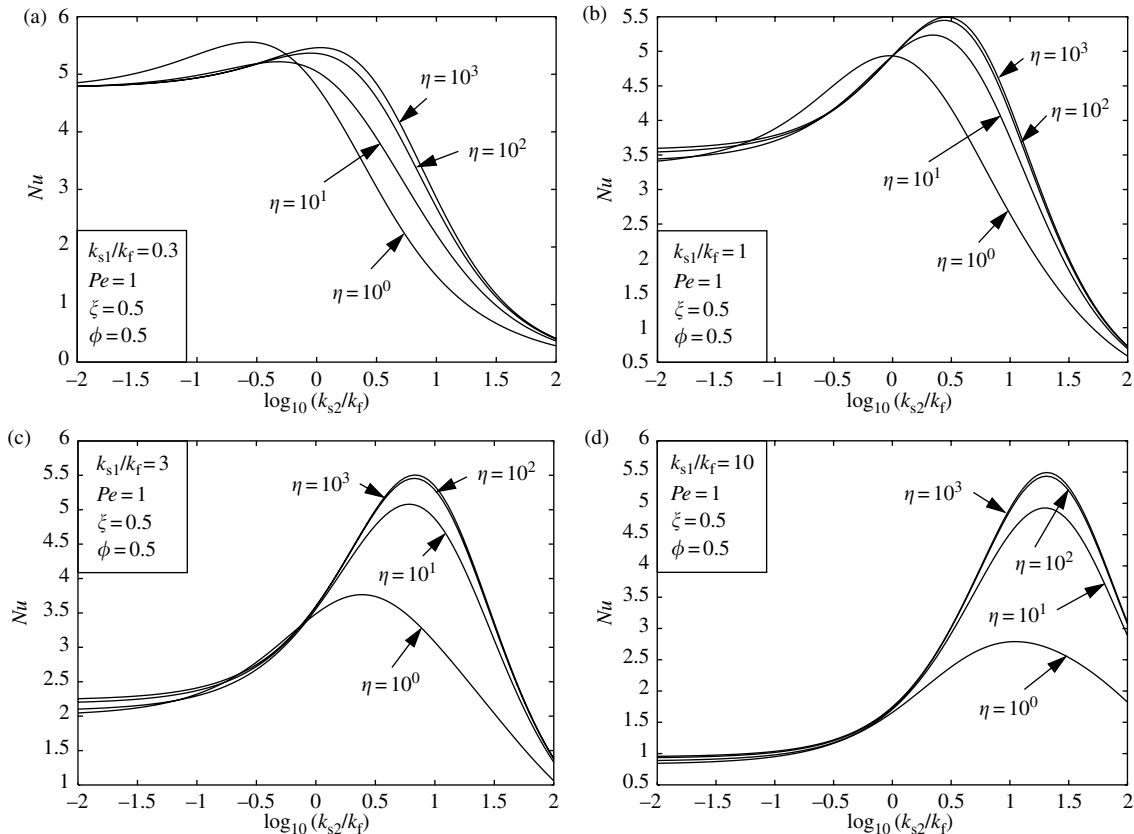
Variation of Nusselt number with Darcy number: (a) effect of permeability variation, (b) effect of thermal conductivity variation ($M = 1, \xi = 0.5$).

4.1.3 Circular Duct

The analysis for the case of a circular duct (for symmetric property variation) closely follows that for a parallel-plate channel, so we can omit most of the details. Figure 4.1(b) is applicable. The boundary is now at $r^* = R$, and R replaces H as the length scale used in dimensionless quantities. For example, the Nusselt number is now defined as

$$Nu = \frac{2Rq''}{\bar{k}(T_w^* - T_m^*)} \quad (4.54b)$$

The results in the following sections are all for the Darcy model.

**FIGURE 4.10**

Plots of Nusselt number versus solid-to-fluid conductivity ratio k_{s2}/k_f for various values of the solid-to-fluid heat transfer number η for (a) $k_{s1}/k_f = 0.3$, (b) $k_{s1}/k_f = 1$, (c) $k_{s1}/k_f = 3$, (d) $k_{s1}/k_f = 10$ ($\xi = 0.5, \phi = 0.5$).

4.1.3.1 Isoflux boundaries

4.1.3.1.1 Continuous weak variation

We now consider the case where the permeability and thermal conductivity distributions are given by

$$\begin{aligned} K &= K_0 \left\{ 1 + \varepsilon_K \left(\frac{r^*}{R} - \frac{2}{3} \right) \right\} \\ k &= k_0 \left\{ 1 + \varepsilon_k \left(\frac{r^*}{R} - \frac{2}{3} \right) \right\} \end{aligned} \quad (4.55a,b)$$

The velocity and temperature distributions, and the Nusselt number, are given by

$$\hat{u} = \tilde{K} = 1 + \varepsilon_K \left(r - \frac{2}{3} \right) \quad (4.55)$$

$$\hat{T} = -\frac{1}{36} Nu \{ 9(r^2 - 1) + (\varepsilon_K - \varepsilon_k)(4r^3 - 6r^2 + 2) \} \quad (4.56)$$

$$Nu = 8 \left(1 + \frac{4}{15} \varepsilon_K - \frac{2}{15} \varepsilon_k \right) \quad (4.57)$$

4.1.3.1.2 Stepwise variation

Suppose that

$$K = K_1 \quad \text{and} \quad k = k_1 \quad \text{for } 0 < |y| < \xi R \quad (4.58a)$$

$$K = K_2 \quad \text{and} \quad k = k_2 \quad \text{for } \xi R < |y| < R \quad (4.58b)$$

The velocity and temperature distributions, and the Nusselt number, are given by

$$\begin{aligned} \hat{u}_1 &= \tilde{K}_1 \quad \text{for } 0 < r < \xi \\ \hat{u}_2 &= \tilde{K}_2 \quad \text{for } \xi < r < 1 \end{aligned} \quad (4.60a,b)$$

$$\begin{aligned} \hat{T}_1 &= \frac{Nu}{4} \left\{ \frac{\tilde{K}_1}{\tilde{k}_1} (\xi^2 - r^2) + \frac{\tilde{K}_1}{\tilde{k}_2} (-2\xi^2 \ln \xi) + \frac{\tilde{K}_2}{\tilde{k}_2} (-\xi^2 + 2\xi^2 \ln \xi + 1) \right\} \\ \hat{T}_2 &= \frac{Nu}{4} \left\{ \frac{\tilde{K}_2}{\tilde{k}_2} (1 + 2\xi^2 \ln r - r^2) - \frac{\tilde{K}_1}{\tilde{k}_2} (2\xi^2 \ln r) \right\} \end{aligned} \quad (4.61a,b)$$

$$Nu = 8 \left/ \left\{ \xi^4 \frac{\tilde{K}_1^2}{\tilde{k}_1} - 4\xi^4 \ln \xi \frac{\tilde{K}_1^2}{\tilde{k}_2} + (4\xi^2 - 4\xi^4 + 8\xi^4 \ln \xi) \frac{\tilde{K}_1 \tilde{K}_2}{\tilde{k}_2} + (1 - 4\xi^2 + 3\xi^4 - 4\xi^4 \ln \xi) \frac{\tilde{K}_2^2}{\tilde{k}_2} \right\} \right. \quad (4.62)$$

For the homogeneous case, $\tilde{K}_1 = \tilde{K}_2 = \tilde{k}_1 = \tilde{k}_2 = 1$, this expression reduces to $Nu = 8$, independent of the value of ξ , as expected.

4.1.3.2 Isotemperature boundaries

For the case of continuous weak variation

$$Nu = 5.783 \{1 + 0.243(\varepsilon_K - \varepsilon_k)\} \quad (4.63)$$

For the case of stepwise variation, the eigenvalue equation for Nu is found to be

$$\frac{J_1(\lambda_1 \xi)}{J_0(\lambda_1 \xi)} \left[\frac{Y_0(\lambda_2) J_0(\lambda_2 \xi) - J_0(\lambda_2) Y_0(\lambda_2 \xi)}{Y_0(\lambda_2) J_1(\lambda_2 \xi) - J_0(\lambda_2) Y_1(\lambda_2 \xi)} \right] = \frac{\tilde{k}_2 \lambda_2}{\tilde{k}_1 \lambda_1} \quad (4.64)$$

where

$$\lambda_i = \left(\frac{Nu \tilde{K}_i}{\tilde{k}_i} \right)^{1/2}, \quad \text{for } i = 1, 2 \quad (4.65)$$

For the homogeneous case, $\tilde{K}_1 = \tilde{K}_2 = \tilde{k}_1 = \tilde{k}_2 = 1$, one can check that $\lambda_1 = \lambda_2 = 2.40483 = \tilde{\lambda}$ (the smallest positive zero of $J_0(x)$) makes Eq. (4.64) an identity in ξ , so that $Nu = (2.40483)^2 = 5.783$ and

$$\hat{T} = \frac{\tilde{\lambda} J_0(\tilde{\lambda} r)}{2 J_1(\tilde{\lambda})} \quad (4.66)$$

The results for the circular duct are closely similar to those for the parallel-plate channel, the most prominent difference being that the Nusselt numbers for the circular duct are higher than those for the parallel-plate channel. This arises because of the additional weighting factor r involved in averages for the case of circular geometry. For detailed results, see [10].

4.2 Thermal Development

4.2.1 Introduction

In forced convection in a porous medium, hydrodynamic development is not normally of importance. This is because the hydrodynamic development

length is readily shown to be of order of magnitude $(K/\phi)^{1/2}$ and usually this is very small compared with the channel width. In contrast, the thermal development length can be much greater.

For the Darcy model one has slug flow and the classical Graetz solution for thermal development is applicable. The following analysis is for the Brinkman model. The additional effect of a Forchheimer term has not yet been treated. The addition would involve an extra parameter but nothing fundamental would be changed. An increase in Forchheimer number would produce a more slug-like flow, and thus have an effect similar to that produced by a reduction in Darcy number.

4.2.2 Walls at Uniform Temperature

4.2.2.1 Parallel-plate channel

For the steady-state hydrodynamically developed situation we have unidirectional flow in the x^* -direction between impermeable boundaries at $y^* = -H$ and $y^* = H$. The temperature on each boundary is held constant at the uniform value T_w^* . At $x^* = 0$ the inlet temperature T_{IN}^* is assumed constant and uniform.

We now scale the longitudinal coordinate as

$$\tilde{x} = \frac{x^*}{PeH} \quad (4.67)$$

where the Péclet number Pe is defined as

$$Pe = \frac{\rho c_p H U^*}{k} \quad (4.68)$$

The dimensionless form of the momentum equation (see Eq. (4.5)) is in this case

$$M \frac{d^2 u}{dy^2} - \frac{u}{Da} + 1 = 0 \quad (4.69)$$

The solution of Eq. (4.69) subject to the boundary condition $u = 0$ at $y = 1$, and the symmetry condition $du/dy = 0$ at $y = 0$ is

$$u = Da \left(1 - \frac{\cosh Sy}{\cosh S} \right) \quad (4.70)$$

where

$$S = \left(\frac{1}{MDa} \right)^{1/2} \quad (4.71)$$

Further dimensionless variables are now defined by

$$\hat{u} = \frac{u^*}{U^*}, \quad \theta = \frac{T^* - T_w^*}{T_{IN}^* - T_w^*} \quad (4.72)$$

This implies that

$$\hat{u} = \frac{S}{S - \tanh S} \left(1 - \frac{\cosh Sy}{\cosh S} \right) \quad (4.73)$$

For the moment we assume local thermal equilibrium and that the Péclet number is sufficiently large for axial conduction to be neglected. The steady-state thermal energy equation then becomes

$$\hat{u} \frac{\partial \theta}{\partial \tilde{x}} = \frac{\partial^2 \theta}{\partial y^2} \quad (4.74)$$

Equation (4.15) holds with the heat transfer coefficient related by

$$q'' = h(T_w^* - T_m^*) \quad (4.75)$$

Since here the wall temperature T_w^* is held uniform, it follows that

$$T_w^* - T_m^* = (T_w^* - T_{IN}^*) e^{-\beta \tilde{x}} \quad (4.76)$$

where T_{IN}^* is the inlet temperature and the Biot number β is defined as

$$\beta = \frac{hH}{k} \quad (4.77)$$

The problem now is to solve Eq. (4.74) subject to the conditions

$$\theta = 1 \text{ at } \tilde{x} = 0, \quad \theta = 0 \text{ at } y = 1, \quad d\theta/dy = 0 \text{ at } y = 0 \quad (4.78a,b,c)$$

Separation of variables, following the assumption that

$$\theta = \Xi(\tilde{x})Y(y) \quad (4.79)$$

leads to two linear and homogeneous equations for Ξ and Y ,

$$\Xi' + \lambda^2 \Xi = 0 \quad (4.80)$$

$$Y'' + \lambda^2 \hat{u} Y = 0 \quad (4.81)$$

Equation (4.81) together with the homogeneous boundary conditions

$$Y'(0) = Y(1) = 0 \quad (4.82)$$

defines an eigenvalue problem of Sturm–Liouville type with eigenvalues λ_n and corresponding eigenfunctions $Y_n(y)$ for $n = 1, 2, 3, \dots$. In particular,

$$Y_n'' + \lambda_n^2 \hat{u} Y_n = 0 \quad (4.83)$$

The general solution of Eqs. (4.79) to (4.82) is the series

$$\theta = \sum_{n=1}^{\infty} C_n Y_n(y) \exp(-\lambda_n^2 \tilde{x}) \quad (4.84)$$

where the constants C_n are determined by the condition (4.78a). Since the eigenfunctions satisfy the orthogonality condition

$$\int_0^1 \hat{u} Y_m Y_n dy = 0 \quad \text{if } m \neq n \quad (4.85)$$

it follows that

$$C_n = \frac{\int_0^1 \hat{u} Y_n dy}{\int_0^1 \hat{u} Y_n^2 dy} \quad (4.86)$$

If θ_m is defined by

$$\theta_m = \frac{T_m^* - T_w^*}{T_{IN}^* - T_w^*} \quad (4.87)$$

then it follows that

$$\theta_m = \int_0^1 \hat{u} \theta dy = \sum_{n=1}^{\infty} \frac{G_n}{\lambda_n^2} \exp(-\lambda_n^2 \tilde{x}) \quad (4.88)$$

where

$$G_n = \int_0^1 C_n \lambda_n^2 \hat{u} Y_n dy = -C_n Y'_n(1) \quad (4.89)$$

In obtaining the last equality the differential equation (4.81) and one of the boundary conditions satisfied by Y_n have been used.

Equation (4.75) leads to

$$Nu = \left. \frac{-2}{\theta_m} \frac{\partial \theta}{\partial y} \right|_{y=1} = \frac{2 \sum_{n=1}^{\infty} G_n \exp(-\lambda_n^2 \tilde{x})}{\sum_{n=1}^{\infty} (G_n / \lambda_n^2) \exp(-\lambda_n^2 \tilde{x})} \quad (4.90)$$

This gives the local Nusselt number. The mean Nusselt number, averaged over a length \tilde{x} , is

$$\overline{Nu} = \frac{1}{\tilde{x}} \int_0^{\tilde{x}} Nu \, d\tilde{x} = -\frac{2}{\tilde{x}} \ln \left(\frac{1}{\theta_m} \right) \quad (4.91)$$

This mean Nusselt number can be expressed as

$$\overline{Nu} = \frac{2Hq''}{k\Delta T_{ml}} \quad (4.92)$$

where ΔT_{ml} is the log-mean temperature difference given by

$$\Delta T_{ml} = \frac{1}{x^*} \int_0^{x^*} (T_m^* - T_w^*) \, dx^* = \frac{(T_w^* - T_{IN}^*) - (T_w^* - T_m^*)}{\ln[(T_w^* - T_{IN}^*)/(T_w^* - T_m^*)]} \quad (4.93)$$

Equation (4.76) has been used to derive the last equality.

The eigenvalues and eigenfunctions can be obtained by a shooting method (see [11]) and then the coefficients C_n and G_n can be obtained by simple numerical integration of the integrals that are involved, and the solution is readily completed. Results are presented in Figure 4.11. A careful inspection of the figure reveals that the thermal entry length (the value of the longitudinal coordinate at which the Nusselt number differs from its asymptotic value by a given small amount) decreases slightly as Da increases. The results show that the curves for $Da = 1$ or larger are effectively coincident with those for infinite Da . We also see that the flow becomes fully developed thermally when the dimensionless coordinate \tilde{x} becomes of order unity, that is when $x^*/H = O(Pe)$, as expected. (Strictly speaking, the figure indicates that the flow becomes fully developed when $(\tilde{x}/16)^{1/2} = 0.1$.)

4.2.2.2 Circular tube

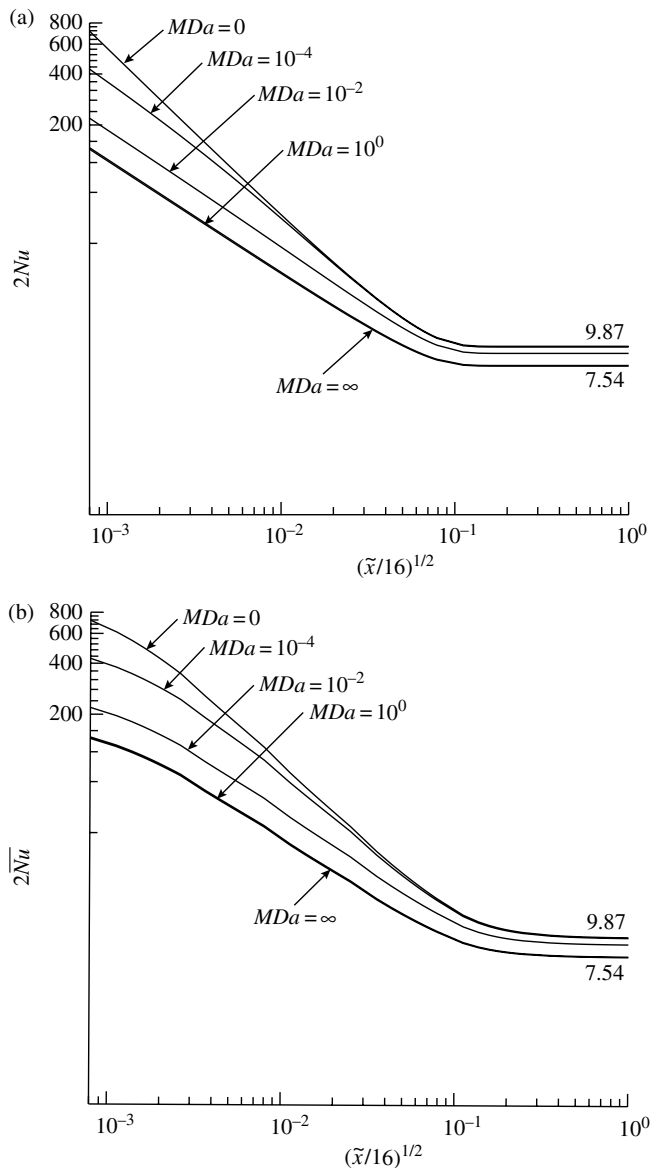
The analysis is much the same as that for the parallel-plate channel, so we briefly note the changes. The boundary is now at $r^* = r_0$.

We define dimensionless variables

$$\tilde{x} = \frac{x^*}{Pe r_0}, \quad r = \frac{r^*}{r_0}, \quad u = \frac{\mu u^*}{Gr_0^2} \quad (4.94)$$

The Péclet number Pe is now defined as

$$Pe = \frac{\rho c_P r_0 U^*}{k} \quad (4.95)$$

**FIGURE 4.11**

Plots of (a) local Nusselt number, and (b) average Nusselt number, versus longitudinal coordinate, for the parallel-plate channel problem, uniform temperature boundaries. The values displayed on the right-hand side of the figure are the fully developed values (attained asymptotically as $\tilde{x} \rightarrow \infty$) for the limiting cases of $Da \rightarrow 0$ (slug flow) and $Da \rightarrow \infty$ (plane Poiseuille flow).

Now the dimensionless velocity (with unit mean) is

$$\hat{u} = \frac{S\{I_0(S) - I_0(Sr)\}}{SI_0(S) - 2I_1(S)} \quad (4.96)$$

and the Nusselt number Nu is defined as

$$Nu = \frac{2r_0 q''}{k(T_w^* - T_m^*)} \quad (4.97)$$

The Biot number β is defined as

$$\beta = \frac{2hr_0}{k} \quad (4.98)$$

[Figure 4.12](#) presents the results found by Nield et al. [11].

4.2.3 Walls at Uniform Heat Flux

In the case of walls held at constant heat flux the wall boundary conditions on the temperature deviation are not homogeneous, and this means that the analysis has to proceed in two steps: first, the fully developed solution to the problem must be found, and then the problem involving the perturbation temperature can be tackled using the method of separation of variables.

Thus we now assume that the heat flux takes a constant value q'' on the walls. We use the subscript FD to distinguish the solution of the full-developed problem.

4.2.3.1 Parallel-plate channel

The dimensionless thermal energy equation is

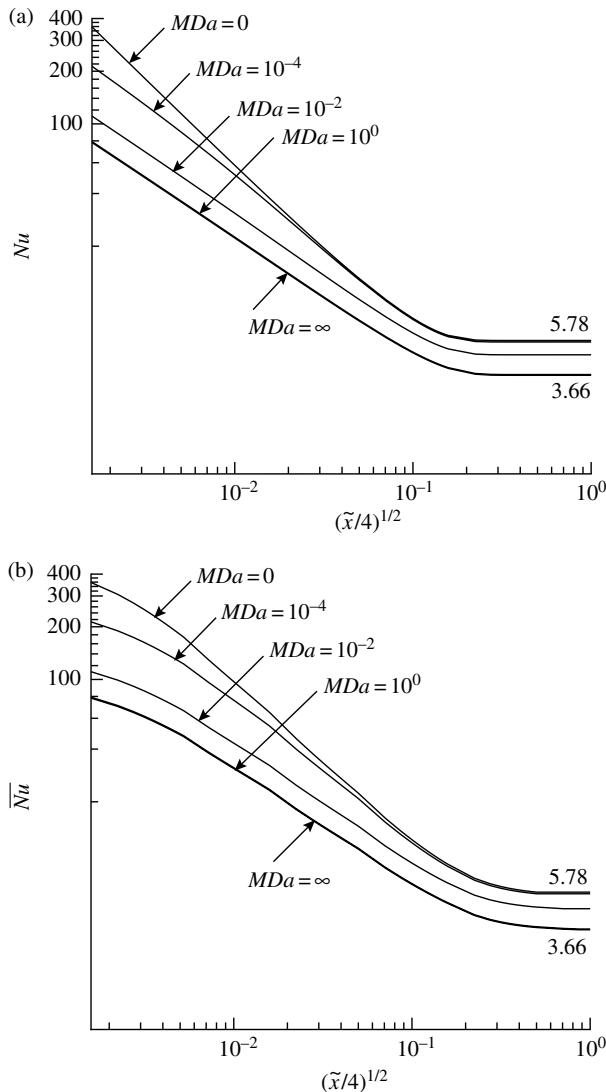
$$\frac{d^2\theta_{FD}}{dy^2} = -\frac{1}{2}Nu_{FD}\hat{u} \quad (4.99)$$

The solution of this equation subject to the boundary conditions

$$\frac{d\theta_{FD}}{dy}(0) = 0, \quad \theta_{FD}(1) = 0 \quad (4.100)$$

is

$$\theta_{FD} = \frac{SNu_{FD}}{S - \tanh S} \left\{ \frac{1}{4}(1 - y^2) - \frac{\cosh S - \cosh Sy}{2S^2 \cosh S} \right\} \quad (4.101)$$

**FIGURE 4.12**

Plots of (a) local Nusselt number, and (b) average Nusselt number, versus longitudinal coordinate, for the circular tube problem, uniform temperature boundaries. The values displayed on the right-hand side of the figure are the fully developed values (attained asymptotically as $\tilde{x} \rightarrow \infty$) for the limiting cases of $Da \rightarrow 0$ (slug flow) and $Da \rightarrow \infty$ (Poiseuille flow).

Substitution in the integral compatibility condition yields

$$Nu_{FD} = \frac{12S(S - \tanh S)^2}{2S^3 - 15S + 15 \tanh S + 3S \tanh^2 S} \quad (4.102)$$

In order to tackle the thermally developing problem, it is convenient to work in terms of a new dimensionless temperature θ , now defined by

$$\frac{T^* - T_m}{Hq''/k} = \frac{2(1 - \theta)}{Nu} \quad (4.103)$$

From integration of Eq. (4.15), one finds that

$$\frac{T_m - T_{IN}}{Hq''/k} = \tilde{x} \quad (4.104)$$

From Eqs. (4.103) and (4.104), by addition, and specification to the fully developed case, one has

$$\frac{T_{FD}^* - T_{IN}}{Hq''/k} = \tilde{x} + \frac{2(1 - \theta_{FD})}{Nu_{FD}} \quad (4.105)$$

Here T_{FD}^* is the dimensional temperature corresponding to the fully developed case.

We now introduce a perturbation temperature defined by

$$T^+ = T^* - T_{FD}^* \quad (4.106)$$

and define

$$\theta^+ = \frac{T^+}{Hq''/k} \quad (4.107)$$

Since T^+ also satisfies Eq. (4.13), it follows that

$$\hat{u} \frac{\partial \theta^+}{\partial \tilde{x}} = \frac{\partial^2 \theta^+}{\partial y^2} \quad (4.108)$$

Moreover, we have the boundary conditions

$$\frac{\partial \theta^+}{\partial y}(\tilde{x}, 0) = 0, \quad \frac{\partial \theta^+}{\partial y}(\tilde{x}, 1) = 0 \quad (4.109)$$

and the initial condition

$$\theta^+(0, y) = \frac{2(\theta_{FD} - 1)}{Nu_{FD}} \equiv -f(y) \quad (4.110)$$

We can now proceed as above, but with the boundary conditions (4.82) for the eigenvalue problem now replaced by

$$Y'(0) = Y'(1) = 0 \quad (4.111)$$

We obtain a solution of the form

$$\theta^+ = \sum_{n=1}^{\infty} C_n Y_n(y) \exp(-\lambda_n^2 \tilde{x}) \quad (4.112)$$

where now the constants C_n are determined by the condition (4.110).

At the wall,

$$\frac{T_w^* - T_{IN}}{Hq''/k} = \tilde{x} + f(1) + \sum_{n=1}^{\infty} C_n Y_n(1) \exp(-\lambda_n^2 \tilde{x}) \quad (4.113)$$

It follows that the local Nusselt number is given by

$$Nu = \frac{2}{f(1) + \sum_{n=1}^{\infty} C_n Y_n(1) \exp(-\lambda_n^2 \tilde{x})} \quad (4.114)$$

Results obtained by Nield et al. [12] are presented in [Figure 4.13](#).

4.2.3.2 Circular tube

The analysis is much the same as that for the parallel-plate channel, so we briefly list the main changes.

In place of Eq. (4.99) one has

$$\frac{d^2\theta_{FD}}{dr^2} + \frac{1}{r} \frac{d\theta_{FD}}{dr} = -Nu_{FD}\hat{u} \quad (4.115)$$

The solution of this equation subject to the boundary conditions

$$\frac{d\theta_{FD}}{dr}(0) = 0, \quad \theta_{FD}(1) = 0 \quad (4.116)$$

is

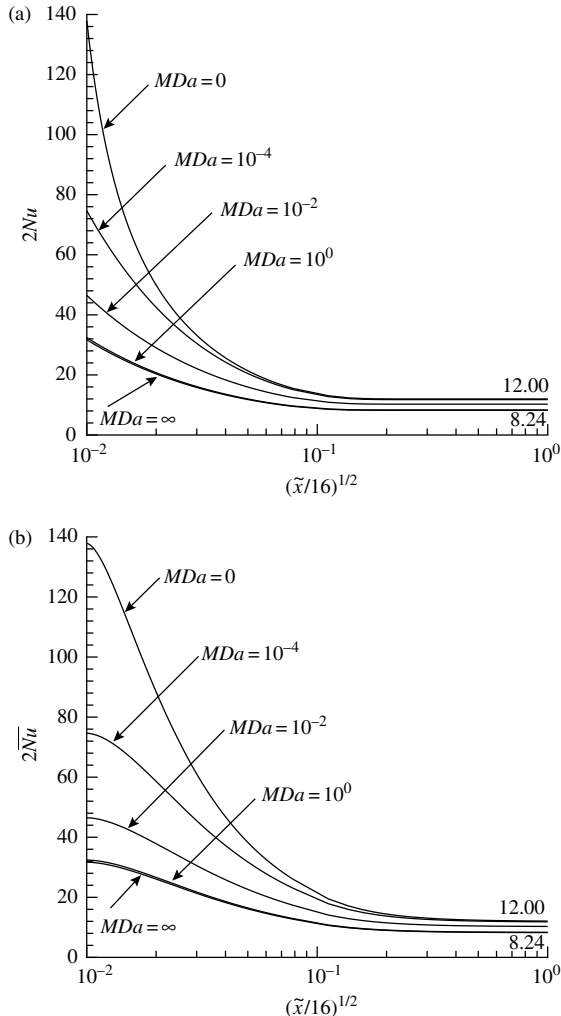
$$\theta_{FD} = \frac{SNu_{FD}}{SI_0(S) - 2I_1(S)} \left\{ \frac{I_0(S)}{4}(1 - r^2) - \frac{I_0(S) - I_0(Sr)}{S^2} \right\} \quad (4.117)$$

Substitution in the compatibility condition

$$2 \int_0^1 r \hat{u} \theta_{FD} dr = 1 \quad (4.118)$$

yields

$$Nu_{FD} = \frac{8S(SI_0(S) - 2I_1(S))^2}{(S^3 - 24S)[I_0(S)]^2 + 48I_0(S)I_1(S) + 8S[I_1(S)]^2} \quad (4.119)$$

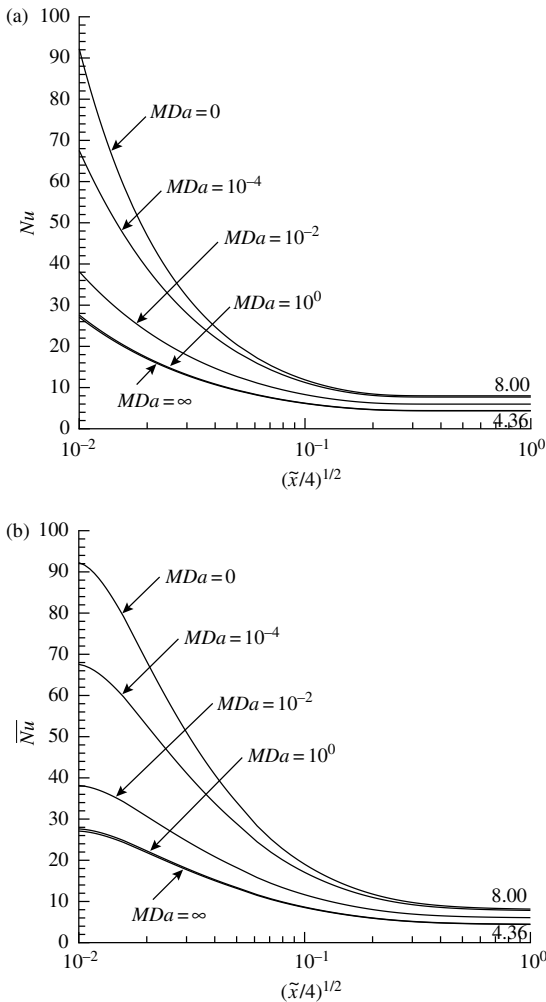
**FIGURE 4.13**

Plots of (a) local Nusselt number, and (b) average Nusselt number, versus longitudinal coordinate, for the parallel-plate channel problem, uniform heat flux boundaries. The values displayed on the right-hand side of the figure are the fully developed values (attained asymptotically as $\tilde{x} \rightarrow \infty$) for the limiting cases of $Da = 0$ (slug flow) and $Da = \infty$ (plane Poiseuille flow).

For the thermally developing flow one finds that the Nusselt number is now given by Eq. (4.114) with Y_n replaced by R_n , the eigenfunctions of the eigenvalue problem

$$R'' + (1/r)R' + \lambda^2 \hat{u}R = 0, \quad R'(0) = R'(1) = 0 \quad (4.120)$$

Results obtained by Nield et al. [12] are presented in [Figure 4.14](#).

**FIGURE 4.14**

Plots of (a) local Nusselt number, and (b) average Nusselt number, versus longitudinal coordinate, for the circular tube problem, uniform heat flux boundaries. The values displayed on the right-hand side of the figure are the fully developed values (attained asymptotically as $\tilde{x} \rightarrow \infty$) for the limiting cases of $Da = 0$ (slug flow) and $Da = \infty$ (Poiseuille flow).

4.2.4 Local Thermal Nonequilibrium

We now consider the more general situation when there is no longer local thermal equilibrium, for the case of a parallel-plate channel with uniform temperature on the boundary walls. We assume that the Péclet number is sufficiently large for axial conduction to be neglected. We also assume that T_s^* and T_f^* are governed by the steady-state heat transfer (energy) equations

$$(1 - \phi) \nabla \cdot (k_s \nabla T_s^*) + h_{fs}(T_f^* - T_s^*) = 0 \quad (4.121)$$

$$\phi \nabla \cdot (k_f \nabla T_f^*) + h_{fs}(T_s^* - T_f^*) = (\rho c_P)_f \mathbf{v}^* \cdot \nabla T_f^* \quad (4.122)$$

Here h_{fs} is a fluid–solid heat transfer coefficient. We define

$$\theta_f^* = T_f^* - T_w, \quad \theta_s^* = T_s^* - T_w \quad (4.123)$$

For the case of unidirectional flow in the axial direction, where the Darcy velocity \mathbf{v}^* has the value u^* in the axial direction, and when axial conduction is neglected, Eqs. (4.121) and (4.122) reduce to

$$\left[(1 - \phi) k_s \frac{\partial^2}{\partial y^{*2}} - h_{fs} \right] \theta_s^* + h_{fs} \theta_f^* = 0 \quad (4.124)$$

$$\left[\phi k_f \frac{\partial^2}{\partial y^{*2}} - h_{fs} - (\rho c_P)_f u^* \frac{\partial}{\partial x^*} \right] \theta_f^* + h_{fs} \theta_s^* = 0 \quad (4.125)$$

Equations (4.124) and (4.125) must be solved subject to the wall boundary conditions

$$\theta_f^* = \theta_s^* = 0 \quad \text{at } y^* = H \quad (4.126)$$

the symmetry conditions

$$\frac{\partial \theta_f^*}{\partial y^*} = \frac{\partial \theta_s^*}{\partial y^*} = 0 \quad \text{at } y^* = 0 \quad (4.127)$$

and the inlet condition

$$\theta_f^* = \theta_{IN} \quad \text{at } x^* = 0 \quad (4.128)$$

We now introduce dimensionless variables. We take H as length scale and θ_{IN} as the temperature scale. We will present our results in terms of a Nusselt number, the porosity ϕ , and four other dimensionless parameters, namely a Péclet number, Pe , a porous medium conductivity ratio, k_r , and a solid–fluid heat exchange parameter, η , defined as follows:

$$Pe = U^* H (\rho c_P)_f / k_f, \quad k_r = k_s / k_f, \quad \eta = h_{fs} H^2 / k_{eff} \quad (4.129)$$

where

$$k_{eff} = \phi k_f + (1 - \phi) k_s \quad (4.130)$$

For convenience, we perform the algebra in terms of the parameters

$$N_f = \phi / Pe, \quad N_s = (1 - \phi) k_r / Pe, \quad N_h = \eta [\phi + (1 - \phi) k_r] / Pe \quad (4.131)$$

We let

$$x = x^*/PeH, \quad y = y^*/H, \quad \theta_f = \theta_f^*/\theta_{IN}, \quad \theta_s = \theta_s^*/\theta_{IN} \quad (4.132)$$

We then get

$$[N_s \partial^2/\partial y^2 - N_h] \theta_s + N_h \theta_f = 0 \quad (4.133)$$

$$N_h \theta_s + [N_f \partial^2/\partial y^2 - N_h - \hat{u} \partial/\partial x] \theta_f = 0 \quad (4.134)$$

$$\theta_f = 0 \quad \text{and} \quad \theta_s = 0 \quad \text{at } y = 1 \quad (4.135)$$

$$\partial \theta_f / \partial y = 0, \quad \partial \theta_s / \partial y = 0 \quad \text{at } y = 0 \quad (4.136)$$

$$\theta_f = 1 \quad \text{at } x = 0 \quad (4.137)$$

Since the differential equations (4.133) and (4.134) and the boundary conditions (4.135) and (4.136) are all homogeneous, we can immediately separate the variables. We write

$$\theta_f = F(y) e^{-\lambda^2 x}, \quad \theta_s = S(y) e^{-\lambda^2 x} \quad (4.138)$$

Then we have an eigenvalue problem constituted by

$$N_s S'' - N_h S + N_h F = 0 \quad (4.139)$$

$$N_f F'' - N_h F + \lambda^2 \hat{u} F + N_h S = 0 \quad (4.140)$$

$$F'(0) = 0, \quad S'(0) = 0, \quad F(1) = 0, \quad S(1) = 0 \quad (4.141)$$

Here the primes denote derivatives with respect to y .

We denote the eigenvalues by λ_n and the corresponding eigenfunction pairs by $F_n(y), S_n(y)$ for $n = 1, 2, 3, \dots$. In particular,

$$N_s S_n'' - N_h S_n + N_h F_n = 0 \quad (4.142)$$

$$N_f F_n'' - N_h F_n + \lambda_n^2 \hat{u} F_n + N_h S_n = 0 \quad (4.143)$$

For the local thermal nonequilibrium (LTNE) case we no longer have a Sturm–Liouville system to deal with, but from Eqs. (4.142) and (4.143), and the corresponding boundary conditions, it is still easy to establish the orthogonality result

$$\int_0^1 \hat{u} F_m F_n dy = 0 \quad \text{if } m \neq n \quad (4.144)$$

It is noteworthy that the S_n are not involved in this condition.

The general solution of Eqs. (4.133) to (4.136) is the pair of series

$$\theta_f = \sum_{n=1}^{\infty} C_n F_n(y) \exp(-\lambda_n^2 x) \quad (4.145)$$

$$\theta_s = \sum_{n=1}^{\infty} D_n S_n(y) \exp(-\lambda_n^2 x) \quad (4.146)$$

where the constants C_n are determined by the entrance condition (4.137). Using the orthogonality condition (4.144) it follows that

$$C_n = \frac{\int_0^1 \hat{u} F_n dy}{\int_0^1 \hat{u} F_n^2 dy} \quad (4.147)$$

With the solution for θ_f completed, one can obtain θ_s from Eq. (4.134). One quickly finds that

$$D_n = C_n \quad (4.148)$$

With the temperature distribution completely found, one can then compute the heat transfer. Matching the heat flux at the channel wall gives

$$q'' = \phi k_f (\partial T_f^* / \partial y^*)_{y^*=H} + (1 - \phi) k_s (\partial T_s^* / \partial y^*)_{y^*=H} \quad (4.149)$$

The Nusselt number is defined by

$$Nu = 2Hh/k_{eff} \quad (4.150a)$$

where, in turn,

$$h = q'' / (T_w - T_{b,eff}) \quad (4.150b)$$

where the effective bulk temperature

$$T_{b,eff} = \frac{1}{U^* H} \int_0^H u^* \{ \phi T_f^* + (1 - \phi) T_s^* \} dy^* = \frac{1}{H} \int_0^H \hat{u} \{ \phi T_f^* + (1 - \phi) T_s^* \} dy^* \quad (4.151)$$

It follows that

$$\begin{aligned} Nu &= \frac{2\{\phi k_f (\partial \theta_f / \partial y)_{y=1} + (1-\phi) k_s (\partial \theta_s / \partial y)_{y=1}\}}{k_{\text{eff}} \int_0^1 \hat{u} [\phi \theta_f + (1-\phi) \theta_s] dy} \\ &= \frac{2 \sum_{n=1}^{\infty} C_n \{\phi k_f F'_n(1) + (1-\phi) k_s S'_n(1)\} e^{-\lambda_n^2 x}}{k_{\text{eff}} \sum_{n=1}^{\infty} C_n [\int_0^1 \hat{u} \{\phi F_n + (1-\phi) S_n\} dy] e^{-\lambda_n^2 x}} \end{aligned} \quad (4.152)$$

where, from Eqs. (4.142) and (4.143),

$$\begin{aligned} F'_n(1) &= \frac{1}{N_f} \left\{ N_h \int_0^1 (F_n - S_n) dy + \int_0^1 \lambda_n^2 \hat{u} F_n dy \right\} \\ S'_n(1) &= \frac{-N_h}{N_s} \int_0^1 (F_n - S_n) dy \end{aligned} \quad (4.153a,b)$$

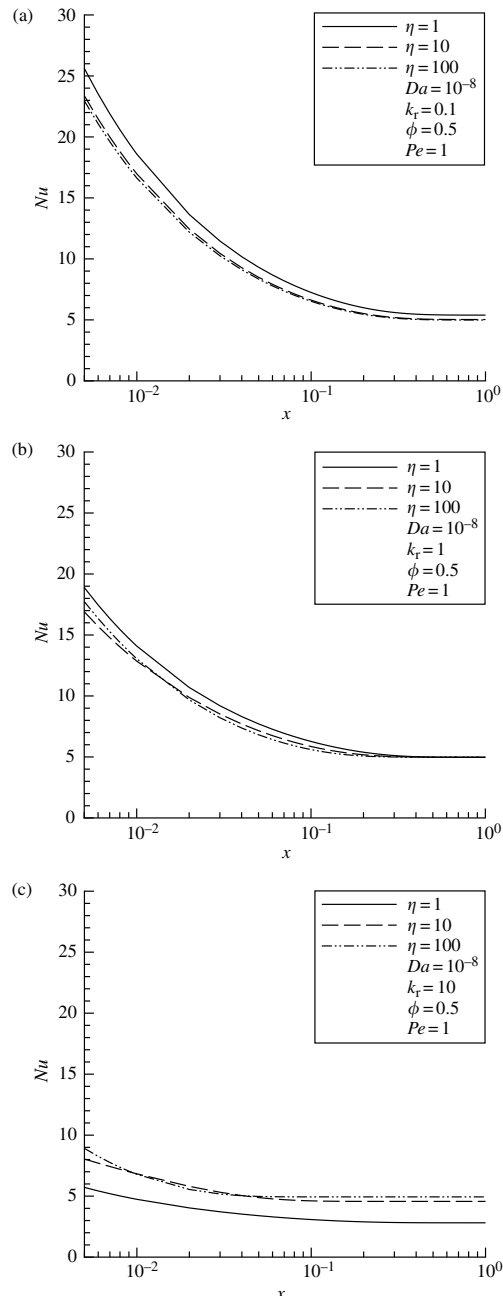
In order to express our results in terms of k_r we can also use

$$k_f/k_{\text{eff}} = 1/\{\phi + (1-\phi)k_r\}, \quad k_s/k_{\text{eff}} = k_r/\{\phi + (1-\phi)k_r\} \quad (4.154)$$

Nield et al. [13] solved the system of Eqs. (4.142) and (4.143), subject to the appropriate boundary conditions (4.141), by reduction to a system of first-order equations and shooting.

Some of their results are presented in Figures 4.15, 4.16, and 4.17. All these results are for a porous medium of porosity $\phi = 0.5$. In Figure 4.15 and Figure 4.16 the value of $Pe (=1)$ is fixed and there are presented, first for a relatively dense porous medium ($Da = 10^{-8}$) and then for a relatively sparse one ($Da = 10^{-3}$), plots of the local Nusselt number versus the longitudinal coordinate for representative values of the solid/fluid conductivity ratio k_r and the solid–fluid heat exchange parameter η . In the case of fully developed convection, the special cases $k_r = 1$ and very large η each correspond to local thermal equilibrium. One can observe that for the developing convection situation there is a small LTNE effect apparent even when $k_r = 1$. The most prominent features shown in Figure 4.15 and Figure 4.16 are: (a) a variation in the Darcy number has little effect on the Nusselt number, (b) the effect of the variation of heat exchange parameter is small, and the direction of change depends on the value of k_r ; as η decreases from large values; the trend is for Nu to decrease if k_r is small and for Nu to increase if k_r is not small, and (c) the Nusselt number decreases markedly as the solid/fluid conductivity ratio increases.

In Figure 4.17 we present the effect of variation of the Péclet number. In the case of local thermal equilibrium, the dependence on Pe is confined to the scaling of the horizontal coordinate, but in the case of LTNE there is a further substantial effect. For a given value of $x = x^*/PeH$, the local Nusselt number increases as Pe increases, and this effect is particularly large if the solid/fluid conductivity ratio is small.

**FIGURE 4.15**

Plots of local Nusselt number Nu versus longitudinal coordinate x for various values of the fluid–solid heat exchange parameter η , and conductivity ratios (a) $k_r = 0.1$, (b) $k_r = 1$, (c) $k_r = 10$. All results are for porosity $\phi = 0.5$, Péclet number $Pe = 1$, and Darcy number $Da = 10^{-8}$.

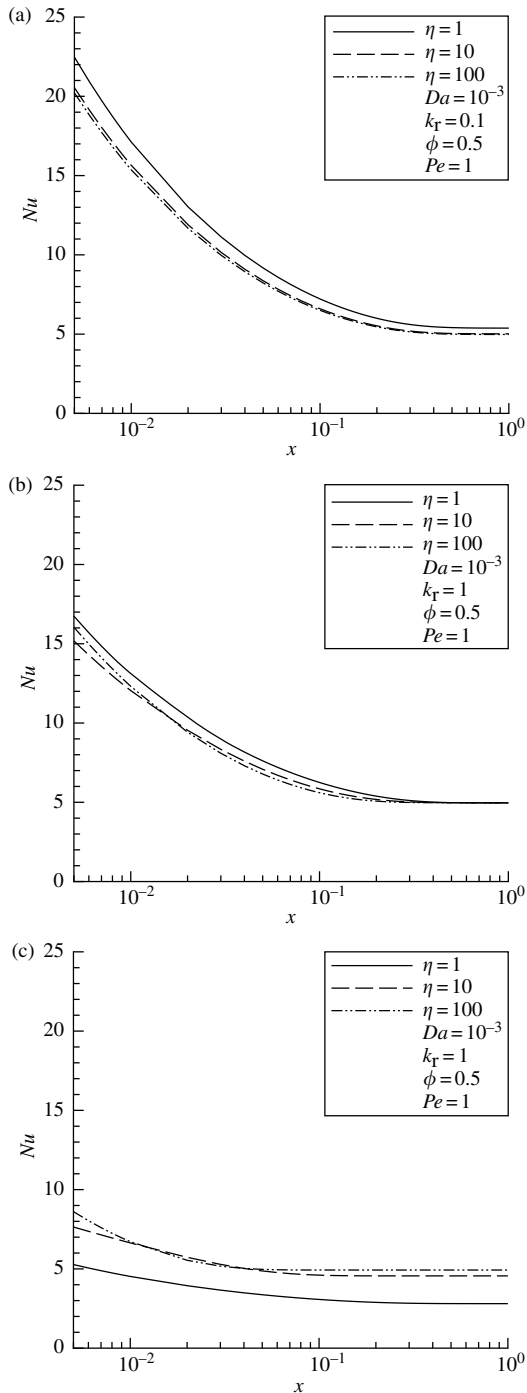
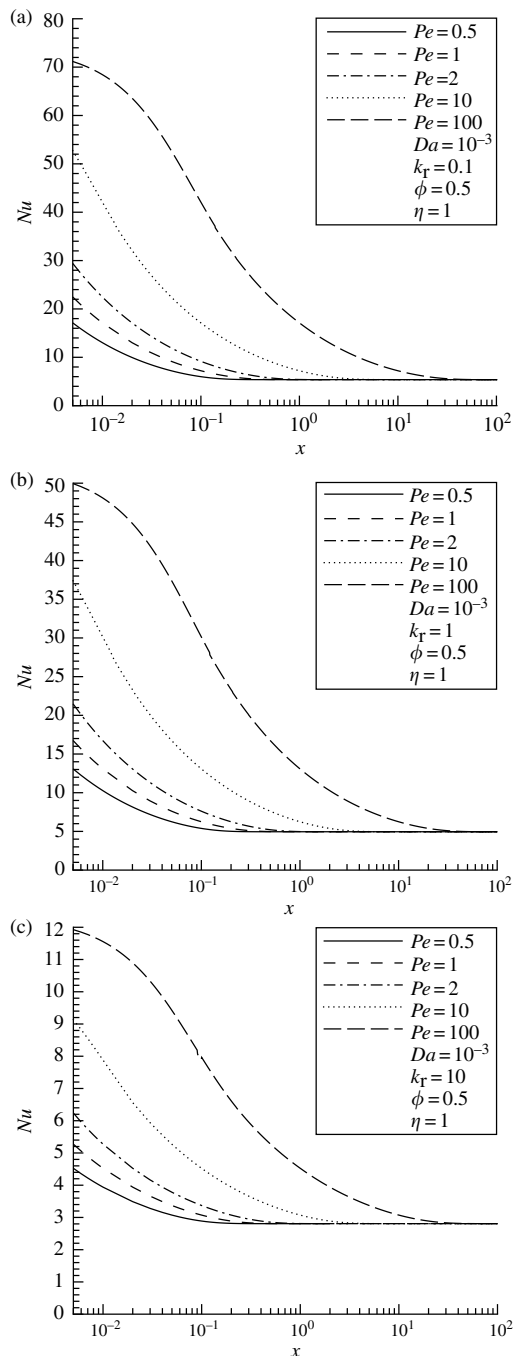


FIGURE 4.16
As for [Figure 4.15](#), but for $Da = 10^{-3}$.

**FIGURE 4.17**

Plots of local Nusselt number Nu versus longitudinal coordinate x for various values of the Péclet number Pe , and conductivity ratios (a) $k_r = 0.1$, (b) $k_r = 1$, (c) $k_r = 10$. All results are for porosity $\phi = 0.5$, fluid–solid heat exchange parameter $\eta = 1$, and Darcy number $Da = 10^{-3}$.

4.2.5 Effects of Axial Conduction and Viscous Dissipation

The incorporation of the effect of axial conduction requires a major change in approach (because of the upstream propagation of temperature changes). However, once this change has been made it is also comparatively simple to incorporate the effect of viscous dissipation.

For the steady-state hydrodynamically developed situation we have unidirectional flow in the x^* -direction between impermeable boundaries at $y^* = -H$ and $y^* = H$, as illustrated in Figure 4.18. For $x^* > 0$ the (downstream) temperature on each boundary is held constant at the value T_w^* . For $x^* < 0$ the inlet (upstream) wall temperature T_{IN}^* is assumed constant on each boundary. We now use the notation

$$\xi = \frac{x^*}{PeH}, \quad \eta = \frac{y^*}{H}, \quad u = \frac{\mu u^*}{GH^2} \quad (4.155)$$

Local thermal equilibrium is now assumed. The steady-state thermal energy equation is then

$$\rho c_p u^* \frac{\partial T^*}{\partial x^*} = k \left(\frac{\partial^2 T^*}{\partial x^{*2}} + \frac{\partial^2 T^*}{\partial y^{*2}} \right) + \Phi \quad (4.156)$$

where Φ is the contribution due to viscous dissipation. The modeling of this viscous term is controversial. The simplest expression, which is appropriate to the Darcy equation, in the present case is

$$\Phi = \frac{\mu u^{*2}}{K} \quad (4.157a)$$

Nield [1,14] argued that the viscous dissipation should remain equal to the power of the drag force when the Brinkman equation is considered, and in the present case this implies that

$$\Phi = \frac{\mu u^{*2}}{K} - \mu_{eff} u^* \frac{d^2 u^*}{dy^{*2}} \quad (4.157b)$$

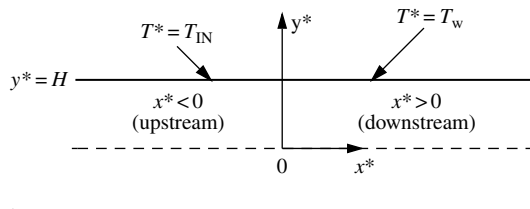


FIGURE 4.18
Definition sketch.

On the other hand, Al-Hadrami et al. [15] proposed a form that is compatible with an expression derived from the Navier–Stokes equation for a fluid clear of solid material, in the case of a large Darcy number, and in this case we have

$$\Phi = \frac{\mu u^*}{K} + \mu \left(\frac{du^*}{dy^*} \right)^2 \quad (4.157c)$$

In each case the added Brinkman term is $O(Da)$ in comparison with the Darcy term. Consequently, in the case of small Da the three models are effectively equivalent to each other. In this survey the form (4.157a) alone is treated, for simplicity. The other cases are discussed by Nield et al. [16].

In nondimensional form Eq. (4.156) becomes

$$\hat{u} \frac{\partial \theta}{\partial \xi} = \frac{1}{Pe^2} \frac{\partial^2 \theta}{\partial \xi^2} + \frac{\partial^2 \theta}{\partial \eta^2} + BrD(S, \eta) \quad (4.158)$$

where the Brinkman number Br is defined as

$$Br = \frac{\mu U^{*2} H^2}{k(T_{IN}^* - T_w^*)K} \quad (4.159)$$

$$D(S, \eta) = \left[\frac{S \cosh S - S \cosh S \eta}{S \cosh S - \sinh S} \right]^2 \quad (4.160)$$

The problem now is to solve Eq. (4.158) subject to the conditions

$$\begin{aligned} \theta_1 &= 1 && \text{at } \eta = 1 \text{ for } \xi < 0 \\ \theta_2 &= 0 && \text{at } \eta = 1 \text{ for } \xi > 0 \\ \frac{\partial \theta_i}{\partial \eta} &= 0 && \text{at } \eta = 0 \text{ for all } \xi \quad (i = 1, 2) \\ \theta_1 &= \theta_2 && \text{at } \xi = 0 \text{ for } 0 < \eta < 1 \\ \frac{\partial \theta_1}{\partial \xi} &= \frac{\partial \theta_2}{\partial \xi} && \text{at } \xi = 0 \text{ for } 0 < \eta < 1 \end{aligned} \quad (4.161a,b,c,d,e)$$

Equations (4.161d) and (4.161e) express the continuities of the temperature and the heat flux at the entrance section $\xi = 0$. For infinitely large values of $|\xi|$, the dimensionless temperature is the particular solution of the equation

$$\frac{\partial^2 \theta_i}{\partial \eta^2} = -BrD(S, \eta) \quad (4.162)$$

Following Lahjomri et al. [17], one can use a separation of variables method to generate the general solution of Eq. (4.158) in the upstream and downstream

regions satisfying the conditions (4.161a,b,c) and (4.162). This solution can be represented by

$$\theta_1(\xi, \eta) = 1 + \sum_{n=1}^{\infty} A_n f_n(\eta) \exp(\lambda_n^2 \xi) + BrF(S, \eta) \quad \text{for } \xi < 0 \quad (4.163a,b)$$

$$\theta_2(\xi, \eta) = \sum_{n=1}^{\infty} B_n g_n(\eta) \exp(-\beta_n^2 \xi) + BrF(S, \eta) \quad \text{for } \xi > 0$$

where,

$$F(S, \eta) = \frac{(1/4)S^2(1 + 2 \cosh^2 S)(1 - \eta^2) + 2 \cosh S(\cosh S\eta - \cosh S) - (1/8)(\cosh 2S\eta - \cosh 2S)}{(S \cosh S - \sinh S)^2} \quad (4.164)$$

The λ_n and β_n are eigenvalues associated with the eigenfunctions f_n and g_n , respectively, and the A_n and B_n are coefficients to be determined from the matching condition (4.161d,e) (see below). The eigenfunctions f_n and g_n are the solutions of the following differential equations:

$$\begin{aligned} \frac{d^2 f_n}{d\eta^2} + \lambda_n^2 \left[\frac{\lambda_n^2}{Pe^2} - \hat{u}(\eta) \right] f_n &= 0 \\ \frac{d^2 g_n}{d\eta^2} + \beta_n^2 \left[\frac{\beta_n^2}{Pe^2} + \hat{u}(\eta) \right] g_n &= 0 \end{aligned} \quad (4.165a,b)$$

satisfying the boundary conditions

$$\begin{aligned} f'_n(0) &= 0 \quad \text{and} \quad f_n(1) = 0 \\ g'_n(0) &= 0 \quad \text{and} \quad g_n(1) = 0 \end{aligned} \quad (4.166a,b)$$

From the matching conditions (4.161d,e), one obtains the following equations determining the coefficients A_n and B_n :

$$\begin{aligned} 1 + \sum_{n=1}^{\infty} A_n f_n(\eta) &= \sum_{n=1}^{\infty} B_n g_n(\eta) \\ \sum_{n=1}^{\infty} \lambda_n^2 A_n f_n(\eta) &= - \sum_{n=1}^{\infty} \beta_n^2 B_n g_n(\eta) \end{aligned} \quad (4.167a,b)$$

The eigenvalue problem constituted by Eqs. (4.165) and (4.166) is not of the classical Sturm-Liouville type and so the usual orthogonality formula is not

valid. However, as Lahjomri et al. [17] showed, the coefficients can still be isolated from each other, and are given by the formulas

$$\begin{aligned} A_n &= \frac{-\int_0^1 [(\lambda_n^2/Pe^2) - \hat{u}(\eta)] f_n d\eta}{\int_0^1 [(2\lambda_n^2/Pe^2) - \hat{u}(\eta)] f_n^2 d\eta} \\ B_n &= \frac{\int_0^1 [(\beta_n^2/Pe^2) + \hat{u}(\eta)] g_n d\eta}{\int_0^1 [(2\beta_n^2/Pe^2) + \hat{u}(\eta)] g_n^2 d\eta} \end{aligned} \quad (4.168a,b)$$

For large values of the Péclet number ($Pe \rightarrow \infty$) and when $S = 0$ and $Br = 0$, the solution tends to the classical Graetz problem without axial conduction, and one finds that $\theta_1(\xi, \eta)$ tends to 1 (a uniform temperature profile in the upstream region), as expected.

The dimensionless bulk temperature $\theta_{b,i}(\xi)$ and the local Nusselt number $Nu_i(\xi, \eta)$ (based on the gap width $2H$ rather than the hydraulic diameter) for the upstream and downstream regions are given by

$$\theta_{b,i}(\xi) = \int_0^1 \hat{u}(\eta) \theta_i d\eta \quad (4.169)$$

$$Nu_i = -\frac{2[\partial\theta_i/\partial\eta]_{\eta=1}}{\theta_{b,i} - [\theta_i]_{\eta=1}} \quad (i = 1, 2) \quad (4.170)$$

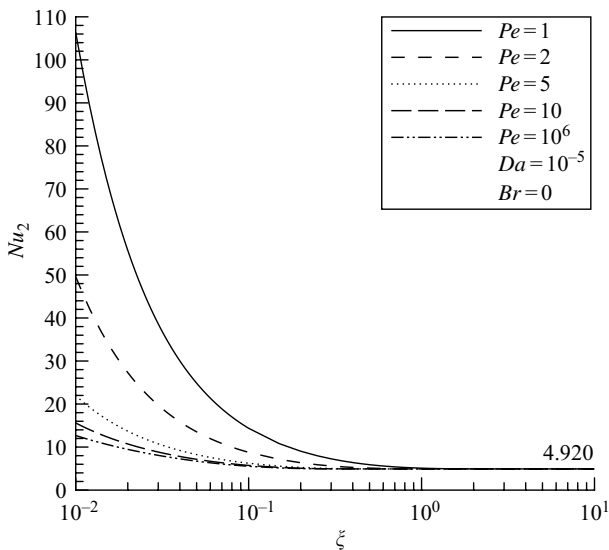
In particular, from Eqs. (4.169), (4.170), (4.165b), and (4.166b), the local Nusselt number for the downstream region ($\xi > 0$) is given by

$$Nu_2(\xi) = \frac{2 \sum_{n=1}^{\infty} B_n g'_n(1) \exp(-\beta_n^2 \xi) + 2BrF'(S, 1)}{\sum_{n=1}^{\infty} B_n \exp(-\beta_n^2 \xi) \left[(g'_n(1)/\beta_n^2) + (\beta_n^2/Pe^2) \int_0^1 g_n(\eta) d\eta \right] - Br \int_0^1 \hat{u}(\eta) F(S, \eta) d\eta} \quad (4.171)$$

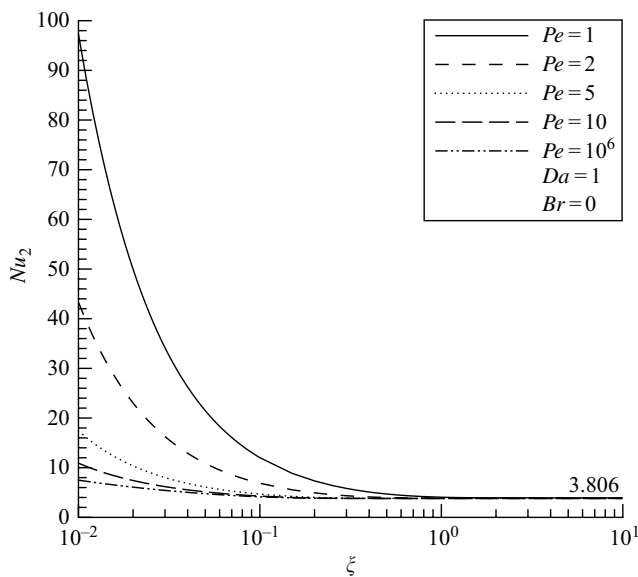
where

$$F'(S, 1) = \frac{3S \sinh S \cosh S - S^2 - 2S^2 \cosh^2 S}{2(S \cosh S - \sinh S)^2} \quad (4.172)$$

Again one can solve the eigenvalue system by reduction to first-order equations and shooting. By this means Nield et al. [16] obtained results for the downstream Nusselt number. First we consider the case in which viscous dissipation is negligible ($Br = 0$). Plots of the downstream Nusselt number are presented in [Figure 4.19](#) and [Figure 4.20](#). It is clear that an increase in Da results in an increase of the thermally developing Nusselt number by a comparatively small amount. (The increase is not surprising, since one would

**FIGURE 4.19**

Plots of downstream local Nusselt number versus dimensionless axial coordinate, for the case of negligible viscous dissipation and for small Darcy number, for various values of the Péclet number.

**FIGURE 4.20**

Plots of downstream local Nusselt number versus dimensionless axial coordinate, for the case of negligible viscous dissipation and for large Darcy number, for various values of the Péclet number.

expect that a less restrictive medium would lead to greater convection.) The Nusselt number for large ξ is the fully developed value. The value 4.920 for the case $Da = 10^{-5}$ is close to the known value $4.935 (\pi^2/2)$ for the Darcy flow (slug flow) limit. The value 3.806 for the case $Da = 1$ is close to the known value 3.770 for the plane Poiseuille flow limit.

In contrast, the developing Nusselt number is strongly dependent on the value of the Péclet number Pe . The case of the large Pe number ($Pe = 10^6$) illustrates the situation where the axial conduction term is negligible. As one would expect, our results for this case agree with results based on our previous analysis. In [Figure 4.19](#) and [Figure 4.20](#) the plot for $Pe = 10$ is not far from that for $Pe = 10^6$, but for smaller values of Pe the increase in the value of the developing Nu (for a fixed value of ξ) is quite dramatic, the value varying with $1/Pe$ approximately.

We now move on to consider the effect of viscous dissipation. Figure 4.21 and [Figure 4.22](#) are for the case of very large Pe , where the effect of axial conduction is negligible (and again for the small Da and large Da cases, respectively). A feature of considerable interest is that even a small amount of viscous dissipation (nonzero Br) leads to a jump in the fully developed Nu_2 to a value that is then independent of Br , and this effect is especially noticeable in the case of the small Darcy number. (The jump is not too surprising when one observes that the change from zero Br to nonzero Br changes Eq. (4.158) from a homogeneous equation into a nonhomogeneous equation, and this

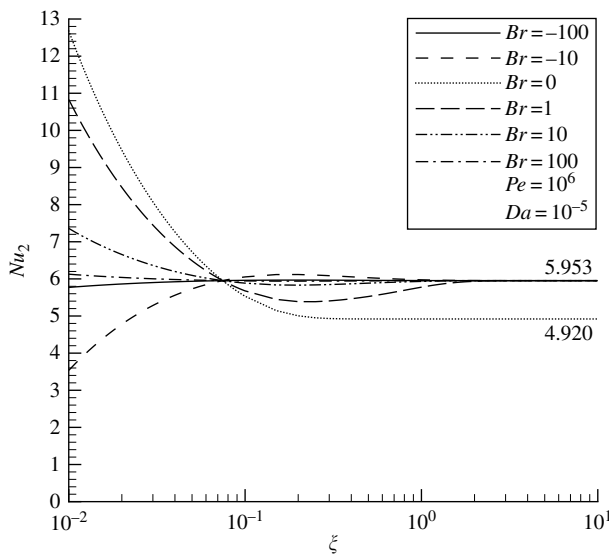
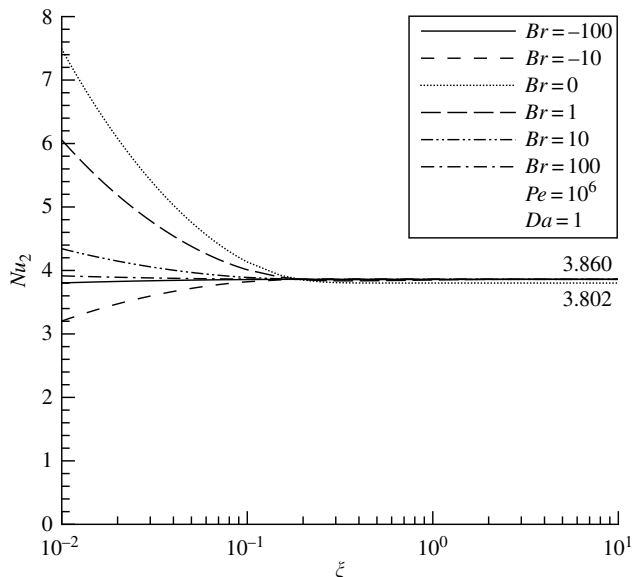


FIGURE 4.21

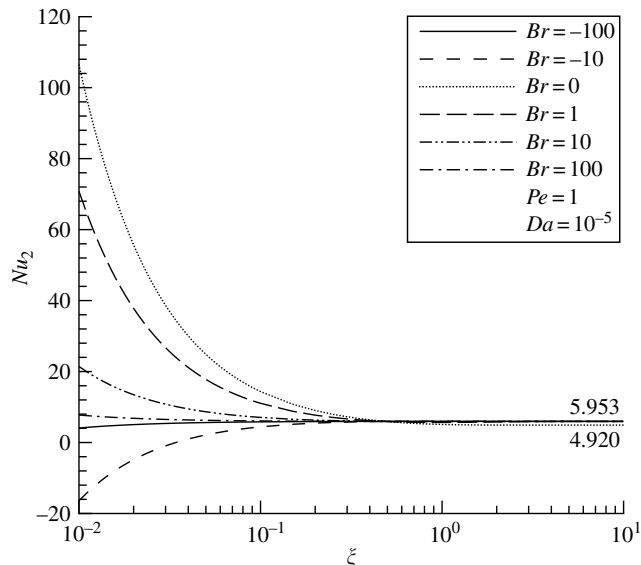
Plots of downstream local Nusselt number versus dimensionless axial coordinate, for the case of negligible axial conduction (large Péclet number) and for small Darcy number, for various values of the Brinkman number.

**FIGURE 4.22**

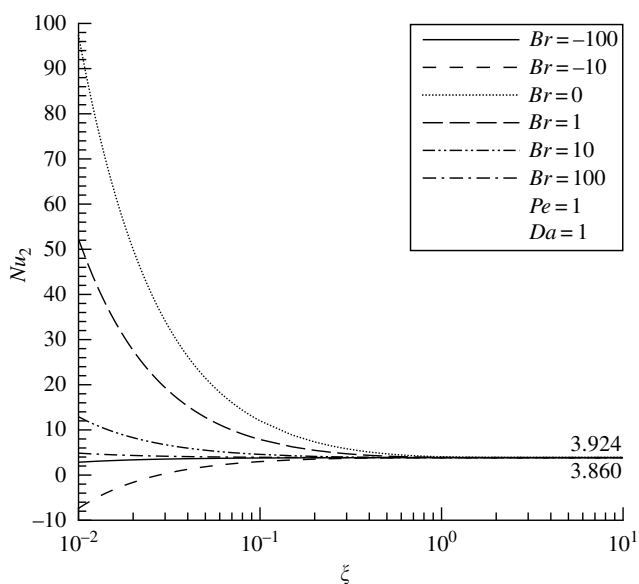
Plots of downstream local Nusselt number versus dimensionless axial coordinate, for the case of negligible axial conduction (large Péclet number) and for large Darcy number, for various values of the Brinkman number.

is analogous to changing a free oscillation problem into a forced oscillation problem. Viscous dissipation provides a heat source distribution that persists downstream [unlike the heat flux at walls subject to a constant-temperature boundary condition, which decays downstream] and changes the nature of the fully developed temperature distribution.) We also see a dramatic difference between the effect of positive Br and the effect of negative Br . The case $Br > 0$ corresponds to incoming fluid being heated at the walls. The viscous dissipation produces a (generally nonuniform) distribution of positive heat sources, and this reinforces the heating effect as the fluid moves downstream. As ξ increases the value of the Nusselt number passes through a minimum. For very large values of Br the value of Nu changes only slowly with ξ . The case $Br < 0$ corresponds to incoming fluid being cooled at the walls, and this cooling at the walls is opposed by the heating due to viscous dissipation in the bulk of the fluid. This opposition is particularly dramatic for the case $Br = -1$, for which the difference between the wall temperature and the bulk temperature changes sign at some value of ξ . This means that the Nusselt number based on that difference becomes quantitatively meaningless, and for that reason we have not plotted in our figures any curve for that value of Br . For $Br = -10$ or less, the plots for Nu_2 are regular and exhibit a maximum value at some value of ξ .

In Figure 4.23 and Figure 4.24 we present companions to Figure 4.21 and Figure 4.22, for the cases of $Pe = 1$. When $Pe = 1$, the effect of axial conduction

**FIGURE 4.23**

As for Figure 4.21, but with $Pe = 1$.

**FIGURE 4.24**

As for Figure 4.22, but with $Pe = 1$.

is more dramatic. It results in a significant increase in the variation of Nu_2 as the flow develops. In particular, it results in Nu_2 becoming negative for small values of ξ when Br is moderately large and negative. In the circumstance of Figure 4.24 ($Pe = 1$, $Da = 1$) the jump in the value of the fully developed Nusselt number as Br goes from zero to a nonzero value is very small.

The analysis just described has an important limitation. The ansatz assumed in writing down Eq. (4.163) implies that the temperature at a great distance downstream is independent of the axial coordinate. This assumption is a sensible one for a discussion of thermally developing flow. It is also a sensible assumption to apply at the exit cross-section when using numerical modeling. However, it is not a good assumption when considering the limit as the thermal convection becomes fully developed. In fact, it violates the First Law of Thermodynamics when the viscous dissipation is not zero. Thus the jump in the value of the fully developed Nusselt number as Br goes from zero to a nonzero value should be regarded as an artifact of mathematical modeling. Likewise, not much should be read into the fact that the fully developed Nusselt number for nonzero Br is independent of Pe (compare Figure 4.21 and Figure 4.23 with Figure 4.22 and Figure 4.24).

The foregoing analysis for a parallel-plate channel has been repeated for the case of a circular tube by Kuznetsov et al. [18].

Nomenclature

A_n, B_n	coefficients
c_F	Forchheimer coefficient
c_P	specific heat at constant pressure
C_n	coefficients
Da	Darcy number, K/H^2 for a channel and K/r_0^2 for a circular tube
Fr	Forchheimer number
G	applied pressure gradient ($-dp^*/dx^*$)
G_n	functions
h	heat transfer coefficient
H	half channel width
I_0	modified Bessel function of zero order
I_1	modified Bessel function of first order
k	fluid thermal conductivity
\bar{k}	mean value of k
\tilde{k}	k/\bar{k}
K	permeability
\bar{K}	mean value of K
\tilde{K}	K/\bar{K}
M	μ_{eff}/μ
Nu	local Nusselt number
\bar{Nu}	mean Nusselt number
p^*	pressure
Pe	Péclet number

q''	wall heat flux
r_0	tube radius
R_n	eigenfunctions for a circular tube
S	$(MDa)^{-1/2}$
T^*	temperature
T_{IN}^*	inlet temperature
T_m^*	bulk mean temperature
T_w^*	wall temperature
\hat{T}	$(T^* - T_w^*)/(T_{IN}^* - T_w^*)$
u	$\mu u^*/GH^2$ for a channel and $\mu u^*/Gr_0^2$ for a circular tube
u^*	filtration velocity
\hat{u}	u^*/U^*
U^*	mean velocity
x^*	longitudinal coordinate
\tilde{x}	x/Pe
y	y^*/H
y^*	transverse coordinate
Y_n	eigenfunctions for a channel

Greek symbols

β	Biot number
$\varepsilon_k, \varepsilon_K$	coefficients
ξ	dimensionless coordinate for the layer interface (Section 4.1)
ξ	dimensionless axial coordinate (Section 4.2)
η	interphase heat exchange parameter
θ	$(T^* - T_w^*)/(T_{IN}^* - T_w^*)$
θ_m	$(T_m^* - T_w^*)/(T_{IN}^* - T_w^*)$
λ_n	eigenvalues
μ	fluid viscosity
μ_{eff}	effective viscosity in the Brinkman term
ρ	fluid density
ϕ	porosity

References

1. D.A. Nield. Modelling fluid flow in saturated porous media and at interfaces. In: D.B. Ingham and I. Pop, eds., *Transport Phenomena in Porous Media II*. Oxford: Elsevier, 2002 pp. 1–19.
2. D.A. Nield and A. Bejan. *Convection in Porous Media*. 2nd edn. New York: Springer, 1999.
3. K. Sundaravadivelu and C.P. Tso. Influence of viscosity variations on the forced convection flow through two types of heterogeneous porous media with isoflux boundary condition. *Int. J. Heat Mass Transfer* 46: 2329–2339, 2003.

4. A.V. Kuznetsov and D.A. Nield. Effects of heterogeneity in forced convection in a porous medium: parallel plate channel or circular duct: triple layer or conjugate problem. *Numerical Heat Transfer A* 40: 363–385, 2001.
5. D.A. Nield and A.V. Kuznetsov. Effects of gross heterogeneity and anisotropy in forced convection in a porous medium: layered medium analysis. *J. Porous Media* 6: 51–57, 2003.
6. J.W. Paek, S.Y. Kim, B.H. Kang, and J.M. Hyun. Forced convective heat transfer from aluminum foam in a channel flow, in *Proceedings of the 33rd National Heat Transfer Conference*, Paper NHTC99-158, 1999, pp. 1–8.
7. D.A. Nield and A.V. Kuznetsov. Effects of heterogeneity in forced convection in a porous medium: parallel plate channel, Brinkman model. *J. Porous Media* 6: 257–266, 2003.
8. D.A. Nield and A.V. Kuznetsov. Effects of heterogeneity in forced convection in a porous medium: parallel plate channel, asymmetric property variation and asymmetric heating. *J. Porous Media* 4: 137–148, 2001.
9. D.A. Nield and A.V. Kuznetsov. The interaction of thermal nonequilibrium and heterogeneous conductivity effects in forced convection in layered porous channels. *Int. J. Heat Mass Transfer* 44: 4375–4379, 2001.
10. D.A. Nield and A.V. Kuznetsov. Effects of heterogeneity in forced convection in a porous medium: parallel plate channel or circular duct. *Int. J. Heat Mass Transfer* 43: 4119–4134, 2000.
11. D.A. Nield, A.V. Kuznetsov, and M. Xiong. Thermally developing forced convection in a porous medium: parallel plate channel or circular tube with isothermal walls. *J. Porous Media* 7: 19–27, 2004.
12. D.A. Nield, A.V. Kuznetsov, and M. Xiong. Thermally developing forced convection in a porous medium: parallel plate channel or circular tube with walls at constant heat flux. *J. Porous Media* 6: 203–212, 2003.
13. D.A. Nield, A.V. Kuznetsov, and M. Xiong. Effect of local thermal non-equilibrium on thermally developing forced convection in a porous medium. *Int. J. Heat Mass Transfer* 45: 4949–4955, 2002.
14. D.A. Nield. Resolution of a paradox involving viscous dissipation and nonlinear drag in a porous medium. *Transp. Porous Media* 41: 349–357, 2000.
15. A.K. Al-Hadhami, L. Elliott, and D.B. Ingham. A new model for viscous dissipation in porous media across a range of permeability values. *Transp. Porous Media* 53: 117–122, 2003.
16. D.A. Nield, A.V. Kuznetsov, and M. Xiong. Thermally developing forced convection in a porous medium: parallel plate channel with walls at constant temperature, with longitudinal conduction and viscous dissipation effects. *Int. J. Heat Mass Transfer* 46: 643–651, 2003.
17. J. Lahjomri, A. Oubarra, and A. Alemany. Heat transfer by laminar Hartmann flow in thermal entrance region with a step change in wall temperature: the Graetz problem extended. *Int. J. Heat Mass Transfer* 45: 1127–1148, 2002.
18. A.V. Kuznetsov, M. Xiong, and D.A. Nield. Thermally developing forced convection in a porous medium: circular duct with walls at constant temperature, with longitudinal conduction and viscous dissipation effects. *Transp. Porous Media* 53: 331–345, 2003.

5

Variable Viscosity Forced Convection in Porous Medium Channels

Arunn Narasimhan and José L. Lage

CONTENTS

Summary	196
5.1 Introduction	196
5.2 Hydrodynamics	197
5.2.1 HDD Model and Temperature-Dependent Viscosity	197
5.2.2 The HDD Model and Velocity Profiles for Temperature-Dependent Viscosity	199
5.2.3 Limiting Case of the HDD Model	201
5.2.4 Modified-HDD Model for Temperature-Dependent Viscosity Flows	201
5.2.5 M-HDD Model Coefficients	204
5.2.6 Hydrodynamics of Temperature-Dependent Viscosity Channel Flows	205
5.2.7 Transition from Darcy Flow	206
5.2.8 Prediction of Transition in Temperature-Dependent Viscosity Flows	210
5.3 Heat Transfer	211
5.3.1 Nusselt Number	211
5.3.2 Temperature Profiles for $\mu(T)$ in Porous Media	212
5.3.3 Nusselt Number and $\mu(T)$ in Porous Media	214
5.3.4 Temperature-Dependent Viscosity and Pump Power	216
5.4 Perturbation Models	218
5.4.1 Physical Model and the Zero-Order Perturbation Solution ..	218
5.4.2 First- and Second-Order Perturbation Solution	220
5.4.3 Pressure-Drop Results and Velocity Profiles	222
5.4.4 Temperature Profiles and Nusselt Numbers	226
5.5 Experimental Validation	228
5.6 Conclusions	230
Nomenclature	231
References	232

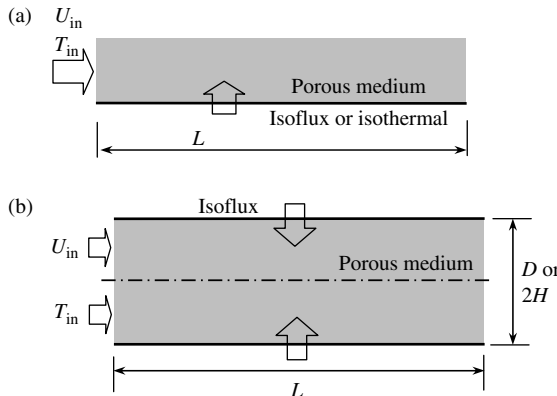
Summary

A review of recent studies on the hydrodynamics and heat-transfer effects of variable viscosity flows in saturated porous media is presented in the restricted context of a liquid, whose viscosity variation is strongly dependent on the temperature variation, flowing through porous media bounded by solid wall(s) on one (flat plate) or two sides (parallel-plates channel). Section 5.2 on Hydrodynamics unravels the effects of temperature-dependent viscosity on the Hazen–Dupuit–Darcy (HDD) model, and on the departure from Darcy flow. This section also presents the need for fundamental modifications necessary to correct both the viscous- and form-drag effects, leading to the introduction of the Modified-HDD (M-HDD) model. Also, the inlet temperature effects on the variable viscosity-affected transition parameter are explained in detail. Influence of variable viscosity on the Nusselt number, defined suitably for the chosen porous medium configuration, the power gain in the pump used to maintain flow in a heated porous configuration, and other aspects related to heat-transfer enhancements, are reviewed in Section 5.3. Substantial effects on the local velocity variation but surprisingly small effects on the heat transfer (Nusselt numbers) are the noteworthy outcomes of previous studies. Section 5.4 reviews the analytical efforts to address the problem of both hydrodynamics and heat transfer in porous medium channels with temperature-dependent viscosity flows. Before concluding, a brief section is devoted on the experimental validation of the proposed models.

5.1 Introduction

What are the hydrodynamics and heat-transfer effects of variable viscosity flows in saturated porous media? In this chapter, this question is answered in the restricted context of a liquid, whose viscosity variation is strongly dependent on the temperature variation, flowing through porous media bounded by solid wall(s) on one (flat plate, [Figure 5.1\[a\]](#)) or two sides (parallel-plates channel, [Figure 5.1\[b\]](#)). The pressure-dependency of a liquid's viscosity is usually negligible and is not considered here.

The chapter is divided into three major sections. Section 5.2 enunciates recent studies on the effects of temperature-dependent viscosity on the Hazen–Dupuit–Darcy (HDD) model (also referred to as the Darcy–Forchheimer model), and on the departure from Darcy flow. Here the review of porous medium channel flows with temperature-dependent viscosity is done in line with the historical development of the present-day HDD model, from Darcy's experiments (1856) to the ad hoc generalization to three dimensions by Stanek and Szekely (1973) — which were all done essentially, with porous channels. Section 5.3, titled Heat Transfer reports on the effects of

**FIGURE 5.1**

Schematic of (a) flat-plate bounded porous medium flow; (b) parallel-plates channel sandwiching porous medium flows.

temperature-dependent viscosity on the Nusselt number suitably defined for flat-plates and parallel-plates channel, bounding porous medium flows. Section 5.4 explains the analytical perturbation models addressing the problem of both hydrodynamics and heat transfer in porous medium channels with temperature-dependent viscosity flows. Before the conclusion, there is a brief section on the experimental validation of the proposed models.

5.2 Hydrodynamics

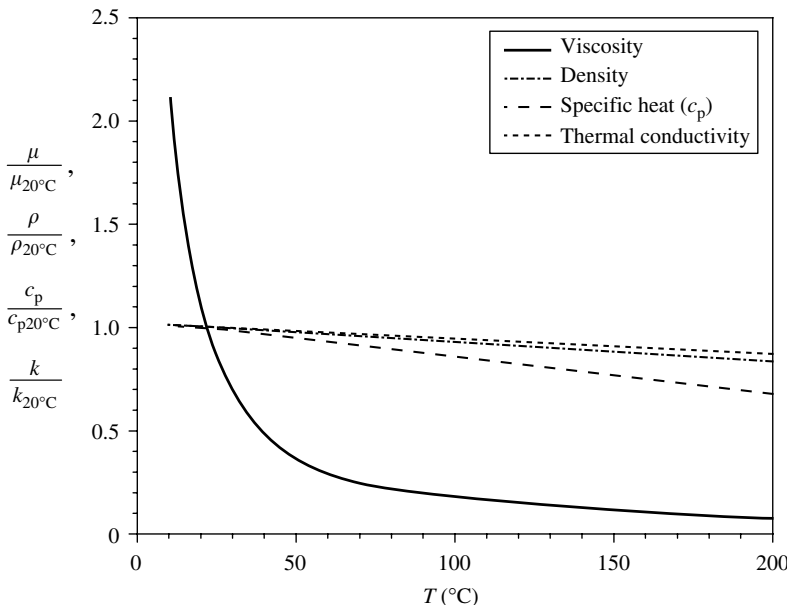
5.2.1 HDD Model and Temperature-Dependent Viscosity

The presently accepted global HDD model (see Kaviany, 1991; Nield and Bejan, 1992 and 1999) normally used to predict the global pressure-drop across the channel of Figure 5.1(b), if it were to be filled with a porous medium is

$$\frac{\Delta P}{L} = \frac{\mu(T)}{K_0} U + C_0 \rho U^2 \quad (5.1)$$

The subscript "0" in K and C signifies that these properties of the porous medium are obtained from the results of isothermal flow experiments, where the fluid viscosity is uniform throughout the channel, $\mu(T) = \mu(T_{in}) = \mu_{in}$. Observe that the choice of T_{in} value is irrelevant as long as the fluid is neither heated nor cooled during the flow experiment.

To test the validity of the HDD model, Eq. (5.1), as such, in capturing the temperature-dependent viscosity effects, we can perform a forced convection experiment through the channel shown in Figure 5.1(b), sandwiching a low-permeability, high form-coefficient porous medium. Forced convection

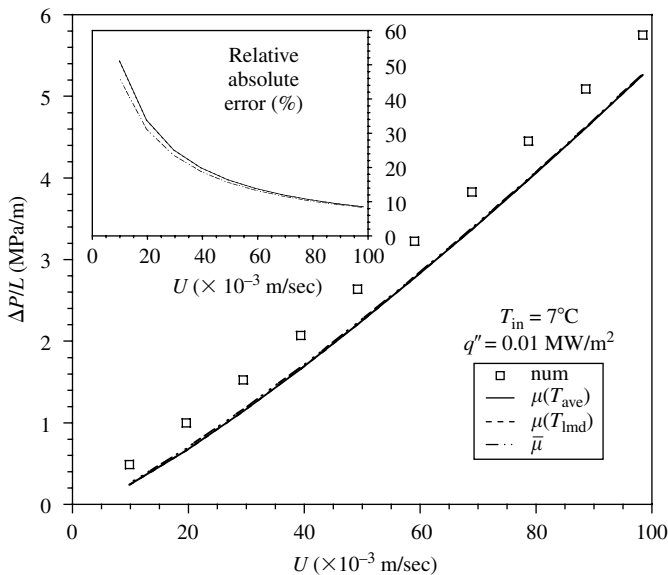
**FIGURE 5.2**

Thermo-physical properties of PAO with temperature, from Chevron (1981): *y*-axis numbers represent values, which are normalized with respective properties at 20°C.

of a fluid with temperature-dependent viscosity $\mu(T)$, entering the channel with uniform temperature T_0 and uniform longitudinal speed U_0 , is achieved through isoflux heating from the walls. The convecting fluid with strong temperature-dependent viscosity is chosen to be the organic liquid PAO, whose properties are given in Figure 5.2. In addition, as required by Eq. (5.1), the permeability and form coefficient of the porous medium filling the channel is assumed to be known. These values are obtained by using the same Eq. (5.1) but with pressure-drop versus velocity data obtained from isothermal experiments in which case, the viscosity is a constant. We use here and in the rest of the chapter, $K_0 = 4.1 \times 10^{-10} \text{ m}^2$, $C_0 = 1.2 \times 10^5 \text{ m}^{-1}$.

Results from the forced convection “numerical” experiment with this coolant at $T_{in} = 7^\circ\text{C}$, flowing through the porous channel of Figure 5.1(b), are shown in Figure 5.3, for the heat flux $q'' = 0.01 \text{ MW/m}^2$. The performance of Eq. (5.1) in predicting these experimental results, for what is essentially a nonisothermal flow, is also shown in Figure 5.3. The relative absolute error, $|(\Delta P/L)_{\text{num}} - (\Delta P/L)_{\text{eq.(5.1)}}| / (\Delta P/L)_{\text{num}}$, between the experimental data and the various predictions from Eq. (5.1) is also shown as in the inset.

All the results obtained by using Eq. (5.1), with an averaged viscosity (obtained by various viscosity evaluation options involving the bulk temperature of the channel — see Narasimhan and Lage, 2001a, for details), evidently fail to predict the experimental results. Hence a suitable modification to the HDD model, Eq. (5.1), is required for nonisothermal porous

**FIGURE 5.3**

Longitudinal pressure-drop versus cross-section averaged velocity: comparison of numerical results with predictions by Eq. (5.1) for various viscosity alternatives.

medium flow situations to include the variable viscosity effects in the accurate determination of the global pressure-drop.

5.2.2 The HDD Model and Velocity Profiles for Temperature-Dependent Viscosity

To better understand why the HDD model, Eq. (5.1), fails for temperature-dependent viscosity, let us retrace its evolution from the differential counterpart and in the process, try to suggest modification of Eq. (5.1) that incorporates the temperature-dependent viscosity effects into it. The general macroscopic differential mass, momentum, and energy conservation statements for the porous channel flow of Figure 5.2 are, respectively,

$$\nabla \cdot \mathbf{u} = 0 \quad (5.2)$$

$$0 = -\nabla p - \left[\frac{\mu(T)}{K_0} \right] \mathbf{u} - \rho C_0 |\mathbf{u}| \mathbf{u} \quad (5.3)$$

$$\rho c_p \mathbf{u} \cdot \nabla T = k_e \nabla^2 T \quad (5.4)$$

The absence of the convective inertia and Brinkman terms in the momentum equation, Eq. (5.3), is in accordance with the low-permeability (K_0) and high form-coefficient (C_0) porous medium assumption made earlier.

For isothermal porous medium channel flows, the velocity profile (local velocity variation along y -direction, $u(y)$, in Figure 5.1[b]) mimics a slug flow profile. Hence, barring the *entrance effects* that normally subside well within a short channel length, the local velocity $u(y)$ everywhere inside the channel is identical to U , the channel cross-section averaged longitudinal velocity. This fact allows us to integrate the differential HDD model, Eq. (5.3), easily for the entire channel, resulting in the global HDD model, Eq. (5.1). However, while doing so, we have assumed the local viscosity to be uniform everywhere inside the channel. In other words, the viscosity in Eqs. (5.1) and (5.3) are the same, evaluated at a suitable reference temperature, usually the inlet temperature. However, when the channel is heated/cooled, the spatial variation of fluid viscosity distribution distorts the velocity profile in the x -direction as the fluid flows along the channel, thus affecting the energy transport equation. The resulting altered temperature profile from the energy equation affects in turn, the local fluid viscosity, owing to the coupling between energy and momentum transport equations.

Using PAO as the convecting liquid through the channel, upon heating, the viscosity of PAO flowing near the heated channel wall will reduce markedly than the centerline (see Figure 5.4). For holding the same pressure-drop across the heated channel, since the viscosity is reduced everywhere (the average viscosity of the heated channel is less than the isothermal constant viscosity), we can expect an increase in the average velocity of the channel (as the local

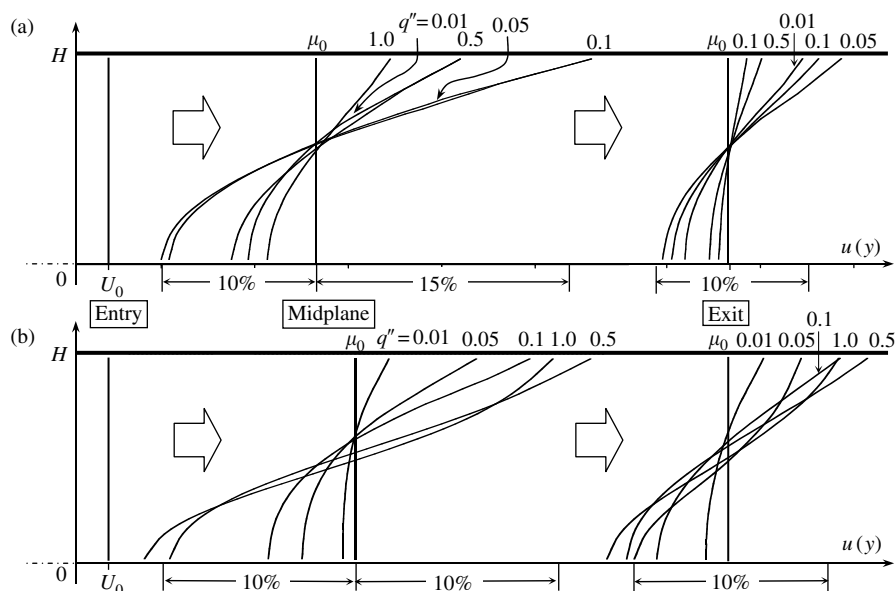


FIGURE 5.4

Channel velocity profiles for several heat fluxes (q'' values in MW/m^2): (a) low ($U_0 = 1 \times 10^{-3} \text{ m/sec}$) and (b) high ($U_0 = 1 \times 10^{-2} \text{ m/sec}$) velocities.

velocity would have increased everywhere). In other words, for the same longitudinal pressure-drop, we expect an increased discharge for viscosity reduction.

In the numerical experiment, constant average velocity (same mass flow rate) is imposed (see Narasimhan and Lage, 2001a), and hence the velocity profile behaves in the fashion shown in Figure 5.4 (i.e., vary about a mean velocity value), with a consequent reduction in the longitudinal pressure-drop. Notice also the *stretch* and *shrink* in the velocity profile, along the length of the channel. As the fluid progressively gets hotter along the length of the channel, the viscosity reduces and hence velocity profiles distort (from slug flow) continuously with a resulting stretch in the distorted velocity profiles. However, when the local viscosity has reduced to a very low (limiting) value, further heating would result in the complete obliteration of the global viscous-drag and Eq. (5.1) will be governed more by the form-drag term alone. These result in a shrink in the profile, an indication of the approach back to the slug-flow profile. Notice, this effect can be achieved either by heating sufficiently a local cross-section in the channel or by having a sufficiently long channel heated with a constant heat flux, with the stretch and shrink resulting *along* the channel. The velocity profiles in Figure 5.4 amply portray both of these effects (see also Narasimhan et al., 2001b).

5.2.3 Limiting Case of the HDD Model

Notice in Eq. (5.1), viscosity is present only in the linear term. With the forced convection experiments that led to Figure 5.4, for further higher heating, we would expect the viscosity variation to affect only this linear viscous-drag term. Therefore, for liquids like PAO, we may infer, when $q'' \rightarrow \infty$, viscosity $\mu \rightarrow 0$ and hence the viscous-drag term in Eq. (5.1) may be neglected to read

$$\frac{\Delta P}{L} = \rho C_0 U^2 \quad (5.5)$$

Equation (5.5) is for a *limiting case*. The physical situation akin to this model is a flow with small, nonzero positive local viscosity that renders, in Eq. (5.1), the *global* viscous-drag term negligible *in comparison* with the *global* form-drag. It is important to remember that when viscosity is zero ($\mu = 0$), there is *no drag* on the flow because of the porous medium. The fluid is ideal, and hence the flow is *inviscid* (recall, inviscid flow requires $(\mu \nabla^2 u) = 0$; this can happen even for $\mu \neq 0$, with $\nabla^2 u = 0$) and should not experience *any* drag, form or otherwise.

5.2.4 Modified-HDD Model for Temperature-Dependent Viscosity Flows

Obviously, the local viscous-drag term, second term in the RHS of Eq. (5.3), is affected when the fluid is heated and the velocity profile is no longer flat.

Moreover, the local velocity influenced by the local viscosity alters also the local form drag as it depends on the local velocity. Particularly, when u is only a function of y , the unidirectional differential equation (5.3), written with uniform viscous- and form-coefficients $\alpha_0 = \mu_0/K_0$ and $\beta_0 = \rho C_0$, becomes

$$-\frac{\partial p(y)}{\partial x} = \left(\frac{\mu(T)}{\mu_0} \right) \alpha_0 u(y) + \beta_0 u(y)^2 \quad (5.6)$$

with μ_0 being the fluid dynamic viscosity evaluated at the inlet temperature T_0 . An algebraic representation is obtained by the cross-section averaging of Eq. (5.6), that is,

$$\left(\frac{1}{H} \int_0^H -\frac{\partial p(y)}{\partial x} dy \right) = \alpha_0 \left(\frac{1}{H} \int_0^H \frac{\mu(T)}{\mu_0} u(y) dy \right) + \beta_0 \left(\frac{1}{H} \int_0^H u(y)^2 dy \right) \quad (5.7)$$

The first term of Eq. (5.7) can be replaced by the cross-section averaged quantity $\partial P/\partial x$. In the second term, since $\mu(T)$ is also a function of y , similar averaging is not that simple while for the third term it cannot be done as the integral of $u(y)^2$ does not equal HU^2 when u is function of y . This last observation is interesting because, it yields the quadratic term indirectly dependent on the fluid viscosity, something not anticipated by the form of Eq. (5.1).

Proceeding to obtain an algebraic representation of Eq. (5.6) we now average Eq. (5.7) along the channel length L to obtain

$$\begin{aligned} \frac{1}{L} \int_0^L -\frac{\partial P}{\partial x} dx &= \alpha_0 \frac{1}{L} \int_0^L \left(\frac{1}{H} \int_0^H \frac{\mu(T)}{\mu_0} u(y) dy \right) dx \\ &\quad + \beta_0 \frac{1}{L} \int_0^L \left(\frac{1}{H} \int_0^H u(y)^2 dy \right) dx \end{aligned} \quad (5.8)$$

Integrating the first term of Eq. (5.8) leads to $\Delta P/L$. The second and third integrals cannot be resolved because the integrands are functions of x , and we cannot resolve the integrals unless we know the temperature and velocity variations in x and y . Equation (5.8) has to be suitably altered to fulfill the experimental need for an algebraic representation of the pressure-drop versus the fluid speed in terms of global, cross-section averaged quantities, which can be easily measured in experiments. This is done by the introduction of two new coefficients, namely ζ_μ and ζ_C , defined as

$$\begin{aligned} \zeta_\mu &= \frac{(1/L) \int_0^L ((1/H) \int_0^H (\mu(T)/\mu_0) u(y) dy) dx}{U} \\ \zeta_C &= \frac{(1/L) \int_0^L ((1/H) \int_0^H u(y)^2 dy) dx}{U^2} \end{aligned} \quad (5.9)$$

allowing us to rewrite Eq. (5.8) as

$$\frac{\Delta P}{L} = \zeta_\mu \left(\frac{\mu_0}{K_0} \right) U + \zeta_C (\rho C_0) U^2 \quad (5.10)$$

The algebraic model presented in Eq. (5.10) retains the same form of Eq. (5.1) describing the transport of fluids with temperature-dependent viscosity through porous media. The coefficients ζ_μ and ζ_C represent the lumped local effect of temperature-dependent viscosity and the effect of viscosity on the fluid velocity profile, respectively. Obviously, for uniform viscosity (no heating), $\zeta_\mu = \zeta_C = 1$ and Eq. (5.1) is recovered. Comparing Eq. (5.10) with Eq. (5.1), it is apparent that the inappropriateness of the global HDD model, Eq. (5.1), is because it is unable to capture the indirect viscosity effect on the global form-drag term, a term originally believed to be viscosity-independent.

In Figure 5.5, the M-HDD model, Eq. (5.10), is tested using the numerical results for various heat flux values. In the first situation envisioned, the form-coefficient correcting factor ζ_C equals unity, and curve-fit the numerical results with the corresponding Eq. (5.10) determining the value of ζ_μ that yields the best curve-fit. The result is presented as the dashed curves in Figure 5.5. This first trial is done to isolate the temperature effect on the fluid viscosity (the effect responsible for ζ_μ). Then, we consider a curve-fit to the numerical results allowing both ζ_μ and ζ_C to vary. The results are also shown in Figure 5.5 as the continuous-line curves. It is evident from Figure 5.5 that model (5.10), with ζ_μ and ζ_C different from unity, satisfactorily correlates the

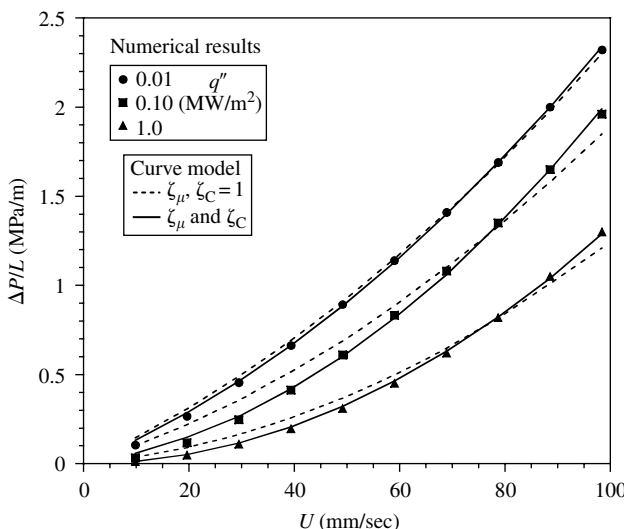


FIGURE 5.5

Verification of one ($\zeta_\mu, \zeta_C = 1$) and two (ζ_μ, ζ_C) coefficients model, Eq. (2.22).

numerical results. Setting $\zeta_C = 1$, does not yield good curve-fitting result. Moreover, the curve-fit using $\zeta_C = 1$ deteriorates when the heat flux is between 0.01 and 1.0 MW/m². The maximum deviation is found to be as high as 20% when using the model with $\zeta_C = 1$, and only 3.8% when using ζ_μ and ζ_C (see Narasimhan and Lage, 2001a, for more details).

5.2.5 M-HDD Model Coefficients

Figure 5.6 presents ζ_μ and ζ_C , for several heat flux values, leading to the best curve-fit results of Figure 5.5. Observe by following the circles, for increasing heat flux, ζ_μ reaches zero asymptotically, beyond $q'' \sim 0.5$ MW/m² (circles). The region beyond this heat flux values, where $\zeta_\mu \sim 0$, is referred as the *null global viscous-drag regime*, as shown in Figure 5.6. As it is difficult to precisely identify the switch by ζ_μ , from nonzero (positive) to zero value, it is presented as a transition region. Based on these results, predictive empirical relations for correcting the viscous- and form-drag terms, complementing the algebraic global (M-HDD) model, were obtained by Narasimhan and Lage (2001a), as functions of the surface heat flux,

$$\zeta_\mu = \left[1 - \left(\frac{Q''}{1 + Q''} \right)^{0.325} \right] \left(\frac{1}{1 + Q''} \right)^{18.2} \quad \zeta_C = 2 + Q''^{0.11} - \zeta_\mu^{-0.06} \quad (5.11)$$

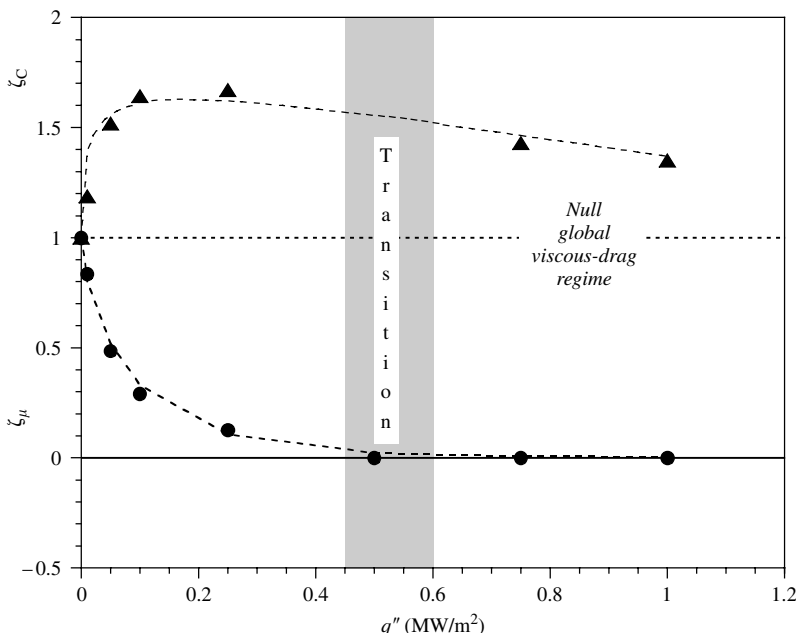


FIGURE 5.6
 ζ_μ and ζ_C for several heat fluxes.

with the nondimensional Q'' given by

$$Q'' = \frac{q''}{(k_e/K_0 C_0) \mu_0} \left| \frac{d\mu}{dT} \right|_{T_0} \quad (5.12)$$

Notice in Eq. (5.12) that the viscosity, μ_0 , and its derivative are evaluated at the inlet temperature T_0 . In other words, the parameters necessary to estimate the dimensionless group in Eq. (5.11), using Eq. (5.12), are already known, once we perform the isothermal pressure-drop experiment to determine K_0 and C_0 . Therefore, for a heat flux input q'' , by using Eqs. (5.11) and (5.12), we can estimate the viscosity variation effects from the M-HDD model, Eq. (5.10), on the total pressure-drop along the channel.

5.2.6 Hydrodynamics of Temperature-Dependent Viscosity Channel Flows

A summary of the fundamental implications of temperature-dependent viscosity effects on the global porous media flow models is presented in Figure 5.7. The uppermost curve is for a nonheating (uniform viscosity) configuration, where the HDD model, Eq. (5.1), is fully valid. When the heat flux is progressively increased (following the block arrow) we immediately get into a viscous-drag and form-drag regime. Here, due to the nonuniformity of the velocity profile (a result of spatially varying local viscosity), both the global viscous- and form-drag terms are affected. That is, the coefficients ζ_μ and ζ_C of the M-HDD model, Eq. (5.10), take nonzero positive values ($\zeta_\mu < 1$ and $\zeta_C > 1$).

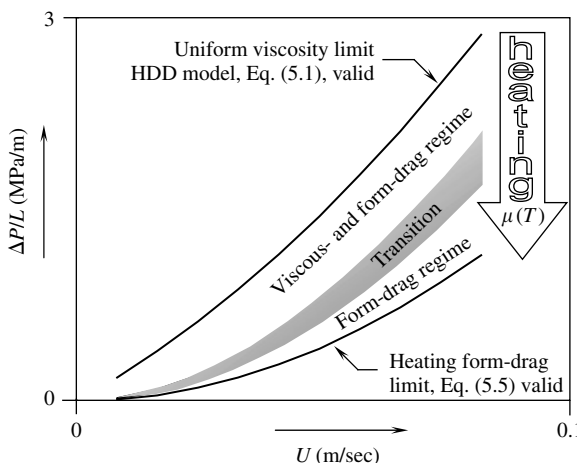


FIGURE 5.7

Summary of the hydrodynamics of temperature-dependent viscosity flows through heated porous medium channels.

This regime is then followed by a transition beyond which a form-drag regime is achieved where only the form-drag term is affected by the viscosity variation. Notice the interesting aspect of this transition, which is similar but not identical to the transition from Darcy flow achieved even in unheated flows (constant viscosity) by merely increasing the flow speed. Both these transitions make the flow form-drag dominant, that is, the pressure-drop is balanced (more) by global form-drag. However, the transition by heating makes it even more so, because it almost entirely nullifies the viscous-drag term. Recall, in the constant viscosity case, we simply neglect the viscous-drag term (but is always present) in comparison with the form-drag term that gains magnitude for higher velocities.

Moreover, transition by heating can happen for a particular velocity (notice in [Figure 5.7](#), the curve drops vertically) even well within the Darcy flow limit of the constant viscosity flow. This suggests that a Darcy flow can be made to become form-drag dominant at practically any speed, by merely sufficiently heating the fluid. This gives an interesting new perspective on the departure from Darcy flow in light of temperature-dependent viscosity effects, discussed in Section 5.2.7.

Proceeding with [Figure 5.7](#), finally, when the heat flux is large enough, the viscosity effect on the form drag becomes negligible and the fluid velocity profile becomes uniform again. At this limit, the flow becomes essentially independent of viscosity effects and the plot of global pressure-drop versus average fluid speed reaches a minimum. Further heating will have no hydrodynamic effect through viscosity. This limit (at which $\zeta_C = 1$ and $\zeta_\mu = 0$) is termed the *heating form-drag limit*, as the global form-drag becomes independent of the viscosity effect. For this limiting case, the longitudinal pressure-drop will be equal to the form drag when the channel is not heated. In other words, this limit can be predicted by the simple equation, Eq. (5.5). Notice that this result, as shown earlier, can be obtained from the HDD model, Eq. (5.1), itself. Moreover, this result is fundamental in nature — true for all fluids with viscosity inversely dependent on temperature — and of great practical importance, as it sets an upper bound for the magnitude of the reduction in the global pressure-drop achievable by heating a fluid with temperature-dependent viscosity.

The last assertion, Eq. (5.5), sets a limitation on the analogy between Hagen–Poiseuille flow through capillary beds and flow through porous media, for flows with temperature-dependent viscosity. In Hagen–Poiseuille flow, the pressure-drop decreases without limit, with an increase in the heat flux. In porous medium flow, the decrease in pressure-drop by increasing the heat flux is limited by the ever-existing pressure-drop caused by the form drag.

5.2.7 Transition from Darcy Flow

For an isothermal flow through the porous channel of [Figure 5.1](#), with $D_{C_0} = \rho C_0 U^2$ representing the global form-drag and $D_{\mu_0} = \mu_0 U / K_0$, the global

viscous-drag (with viscosity evaluated at the inlet fluid temperature, that is, $\mu_0 = \mu(T_0 = T_{\text{in}})$) acting within the porous medium, the global HDD model, Eq. (5.1), reads

$$\frac{\Delta P}{L} \Big|_0 = \frac{\mu(T_{\text{in}})}{K_0} U + \rho C_0 U^2 = D_{\mu_0} + D_{C_0} \quad (5.13)$$

Here $\Delta P/L|_0$ refers to the pressure-drop across the channel for isothermal flows.

It is widely understood that the flow through porous media is characterized by two distinct regimes (see Dullien [1979] and Nield and Bejan [1992] for further details). The transition from linear Darcy flow (i.e., $\Delta P/L|_0 \sim D_{\mu_0}$) to the nonlinear flow (i.e., $\Delta P/L|_0 \sim D_{C_0}$), is estimated using the parameter λ , the ratio of global form-drag and global viscous-drag forces along a porous channel with uniform cross-section, defined using scaling arguments in Lage (1998). It is given by

$$\lambda = \frac{\text{form drag}}{\text{viscous drag}} = \frac{D_{C_0}}{D_{\mu_0}} = \left(\frac{\rho C_0 K_0}{\mu_0} \right) U \quad (5.14)$$

where K_0 and C_0 are the permeability and form coefficient of the porous medium obtained from isothermal experiments and U is the cross-section averaged Darcy (or seepage) fluid speed. The parameter λ should not be confused with the Reynolds number, as the latter is dependent upon a single length scale independent of the hydraulic properties (K_0 and C_0) of the porous medium.

From Eqs. (5.13) and (5.14), when $\lambda > 1$, the flow is said to have departed from Darcy flow, into the quadratic-flow regime. The tacit assumption behind the use of λ parameter for establishing the transition criterion is that the global HDD model, Eq. (5.13), is fundamentally valid for the flow configuration considered.

The increase in λ is prompted by the increase in U , the flow velocity. However, λ can be increased by another means as well. Decreasing the viscosity by heating the channel flow would result in the increase of λ for a liquid whose viscosity decreases with increasing temperature. However, as seen in Section 5.2.6, in this situation the HDD model is no longer valid. Hence, it is imperative we study the transition from Darcy flow, utilizing the M-HDD model, Eq. (5.10). Using the drag terminology introduced earlier with Eq. (5.13), the M-HDD model reads

$$\frac{\Delta P}{L} = \zeta_\mu \left(\frac{\mu_0}{K_0} \right) U + \zeta_C (\rho C_0) U^2 = \zeta_\mu D_{\mu_0} + \zeta_C D_{C_0} = D_\mu + D_C \quad (5.15)$$

The global pressure-drop results of Eqs. (5.13) and (5.15) are for the constant (and uniform) viscosity and variable viscosity cases, respectively. We can

define a nondimensional pressure-drop through the ratio between them,

$$\Phi = \frac{(\Delta P/L)}{(\Delta P/L)|_0} = \frac{D_\mu}{(D_{\mu_0} + D_{C_0})} + \frac{D_C}{(D_{\mu_0} + D_{C_0})} = \Phi_\mu + \Phi_C \quad (5.16)$$

This nondimensional pressure-drop quintessentially highlights the viscosity variation effect, as it compares the pressure-drop obtained by considering viscosity variation, Eq. (5.15), to that of uniform viscosity, Eq. (5.13). For the case of a fluid flowing with uniform viscosity then $\zeta_\mu = \zeta_C = 1$, and, from Eq. (5.15), $\Delta P/L$ equals $\Delta P/L|_0$, thus yielding $\Phi = 1$ from Eq. (5.16). Using Eqs. (5.14) to (5.16), we can recast Eqs. (5.13) and (5.15), respectively, as

$$\Phi_0 = \frac{1}{(1 + \lambda)} + \frac{\lambda}{(1 + \lambda)} = 1 \quad (5.17)$$

and

$$\Phi = \zeta_\mu \left(\frac{1}{1 + \lambda} \right) + \zeta_C \left(\frac{\lambda}{1 + \lambda} \right) \quad (5.18)$$

Figure 5.8 displays the viscosity effects on the transition with increasing heat flux (for 0 and 0.10 MW/m^2), for an inlet temperature of 21°C . The continuous line that starts from close to zero on the y -axis and increases for higher λ values, represent the corresponding global form-drag value (Φ_{C_0}). This pair portrays the gaining dominance of the nonlinear, form-drag effect as λ increases. Furthermore, the curves cross for $\lambda = 1(\lambda_T)$, marked in Figure 5.8 with a square, representing the equivalence in strength of the drags. Beyond

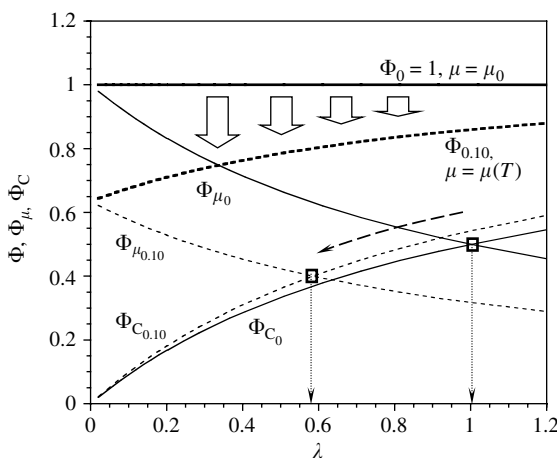


FIGURE 5.8

Shift due to heating ($q'' = 0.01 \text{ MW/m}^2$) in the transition point for $T_{\text{in}} = 21^\circ\text{C}$.

this point (i.e., for all higher velocities) the global form-drag predominates. For any velocity (λ), the sum of these corresponding drag values ($\Phi_{\mu_0} + \Phi_{C_0}$) will give the total nondimensional pressure-drop experienced by the flow across the channel ($\Phi = 1$) for the no heating, constant viscosity case, represented by the horizontal continuous thick line at unity, in the y -axis. This result, a direct consequence of the scaling used in Eq. (5.17), clearly suggests that there is no viscosity variation effect on the total pressure-drop.

The dash-lined curves represent cases for $q'' = 0.1 \text{ MW/m}^2$. For heating with $q'' = 0.1 \text{ MW/m}^2$, ($\mu = \mu(T)$), the global viscous-drag reduces from its no heating value (continuous curve, Φ_{μ_0}) to the dashed curve $\Phi_{\mu_{0.10}}$, and a corresponding increase takes place in the form drag (compare curve Φ_{C_0} to $\Phi_{C_{0.10}}$). Similar to the explanation given for the constant viscosity case, in the previous paragraph, the sum of the viscosity influenced drags ($\Phi_{\mu_{0.10}} + \Phi_{C_{0.10}}$) give the total pressure-drop ($\Phi_{0.10} < 1$), represented by the dash-lined curve $\Phi_{0.10}$ just below the top horizontal line, marked with $\mu = \mu(T)$. In other words, following the vertical block arrows, the net result of variable viscosity is to reduce the pressure-drop, as expected.

Some important observations that are relevant to the above events of heating with $q'' = 0.1 \text{ MW/m}^2$ are: (1) in contrast to the global form-drag, the global viscous-drag starts reducing immediately, even for low velocities; (2) the global form-drag slowly increases; and (3) the viscosity influenced drag curve pairs meet at an *earlier* point (in terms of λ) when compared to the constant viscosity case ($\lambda = 1$). Specific to the results displayed in Figure 5.8, the location of the transition for $q'' = 0.10 \text{ MW/m}^2$ happens around $\lambda \sim 0.57$.

Clearly, observation (1) is a direct consequence of the presence of the viscosity in the global viscous-drag term. Since it is getting reduced because of heating, the global viscous-drag starts to decrease immediately. The increase in the form drag, as noted in observation (2), is unexpected. It is caused primarily because of the nonuniformity of the velocity profile, a consequence of the variation in the local viscosity everywhere inside the channel. These two observations are promptly captured in the correction coefficients of the M-HDD model, Eq. (5.15) (i.e., $\zeta_\mu < 1$ and $\zeta_C > 1$).

In observation (3), the shift in the transition point, is of particular interest to us. It results as a combination of the two earlier observations of the direct influence of viscosity reduction with temperature and of the change in the global form-drag. It is worthwhile at this point to note that the use of a Reynolds number, as explained in connection with Eq. (5.14), will invariably fail to provide us with correct information about the transition point. The transition point for fluids with viscosity decreasing with temperature occurs at lesser and lesser velocity values as the heat flux increases. As the local viscosity decreases further, for sufficiently higher heat fluxes, the effect of the global viscous-drag would become so negligible that the flow practically is always form-drag dominant.

In general, for a particular heat flux crossing the channel wall, for a chosen velocity (λ , in the figure) the fluid can be in linear (viscous-drag dominant) or

nonlinear (form-drag dominant) regime based on the fluid inlet temperature (see Narasimhan and Lage, 2002). Further, as the heat flux increases, the transition, for fluids with viscosity decreasing with temperature, occurs at lesser and lesser velocity values. As the local viscosity decreases further, for sufficiently higher heat fluxes, the effect of the global viscous-drag would become so negligible that the flow practically is always form-drag dominant. This conclusion is particularly useful from an engineering standpoint.

5.2.8 Prediction of Transition in Temperature-Dependent Viscosity Flows

From the definition given in Eq. (5.14), it is clear that λ assumes the validity of the HDD model, which in turn requires uniform viscosity flow. However, when the HDD model is superseded by the more general M-HDD model, Eq. (5.15), which accounts for temperature-dependent viscosity effects, it follows that the transition point happens only when the global drag terms of Eq. (5.15) are comparable. In other words, we must use the balance of the two drag terms on the RHS of Eq. (5.15) instead of Eq. (5.13). Doing so

$$\zeta_\mu D_{\mu_0} \sim \zeta_C D_C \quad (5.19)$$

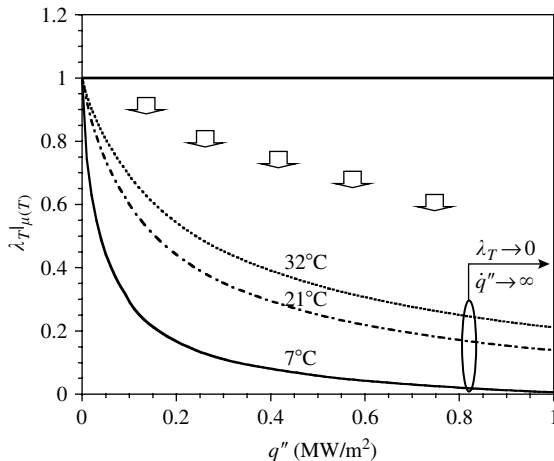
would result in

$$\lambda_T|_{\mu(T)} = \frac{\zeta_\mu}{\zeta_C} \quad (5.20)$$

Equation (5.20) gives the $\lambda_T|_{\mu(T)}$, beyond which the flow becomes form-drag dominant for flows with temperature-dependent viscosity effects. Since $\zeta_\mu < 1$ and $\zeta_C > 1$ always (see Eqs. [5.11] and [5.12]), the transition point for temperature-dependent viscosity flows, as predicted by Eq. (5.20), is always less than that for the constant viscosity case (i.e., $\lambda_T = 1$).

In addition, for uniform viscosity, that is, when we do not heat the channel ($q'' = 0$), ζ_μ and ζ_C are identically equal to unity, as seen earlier. This makes the prediction of Eq. (5.20) consistent with the previous result, that is, $\lambda_T|_{\mu(T)} = \lambda_T = 1$. Recall that the previous result (of $\lambda \sim 1$ for transition to begin) is obtained by using the equivalence of drags in the HDD model, Eq. (5.13).

Figure 5.9 depicts the variation of $\lambda_T|_{\mu(T)}$ with heat flux, for different inlet temperatures. The curves show how for increasing heat flux the transition point is shifted (from 1, for constant viscosity — no heating — case) to values less than 1, when temperature-dependent viscosity effects are included. It is worth noting that irrespective of the inlet temperature of the flow, if we assume viscosity is constant, $\lambda_T|_{\mu(T)}$ is always equal to unity. Immaterial of the amount of heating, once the properties (here, viscosity) are assumed constant, the HDD model (momentum equation) gets de-coupled from the energy transport equation. However, for heating, with a particular heat flux, we can observe from Figure 5.9 that the flow with $T_{in} = 7^\circ\text{C}$ becomes form-drag dominant earlier than for other higher inlet temperatures. In addition, the flow

**FIGURE 5.9**

Transition parameter versus heat flux.

with $T_{in} = 7^\circ\text{C}$ asymptotically reaches zero for $q'' > 1.0 \text{ MW/m}^2$. This means temperature-dependent viscosity effects on the viscous-drag term makes it practically equal to zero (i.e., in Eq. [5.20], $\lambda_T|_{\mu(T)} \rightarrow 0$ as the numerator $\zeta_\mu \rightarrow 0$). This makes the flow purely form-drag dependent (notice the use of the word "dependent" as against the original "dominant") for all higher heat fluxes. Moreover, this assertion, as shown in the figure, is theoretically true for $q'' \rightarrow \infty$ immaterial of the inlet temperature, once we assume throughout the heating the flow remains in the liquid phase.

Further, although the temperature-dependent viscosity effect cannot affect the global viscous-drag term anymore, it is not restricted in influencing the global form-drag. The global form-drag can still be influenced by the velocity profile variation caused by the local viscosity variation (i.e., ζ_C can still be a nonzero positive number). This effect, as we saw in the earlier sections, is the main claim of the M-HDD model. It can be viewed as a fundamental signature to the physics of flow through porous media, by fluids with temperature-dependent viscosity.

5.3 Heat Transfer

5.3.1 Nusselt Number

Reconsider the problem of PAO, with temperature-dependent viscosity $\mu(T)$, flowing through a channel of length L formed by two parallel isoflux surfaces, spaced by a distance $2H$ (or D), and filled with a low-permeability porous medium, as was shown in Figure 5.1(b). PAO enters the channel with

uniform temperature T_0 and uniform longitudinal speed U_0 . We define two nondimensional heat-transfer coefficients, one the local (can vary along the channel) Nu , and the other, Nu_L , as an overall heat-transfer coefficient that represents the heat transfer in the entire channel, respectively,

$$Nu = \frac{2Hq''}{k_e[T_w(x) - T_b(x)]} \quad (5.21)$$

$$Nu_L = \frac{2Hq''}{k_e [\bar{T}_w - T_{b_{in}}]} \quad (5.22)$$

In Eqs. (5.21) and (5.22), q'' is the constant heat flux from the surfaces of the channel (Figure 5.1[b]); \bar{T}_w in Eq. (5.22) is the wall temperature averaged over the length L of the channel and k_e is the effective thermal conductivity, which based on the chosen porous medium, is suitably evaluated using one of the existing models (see Kaviany, 1991).

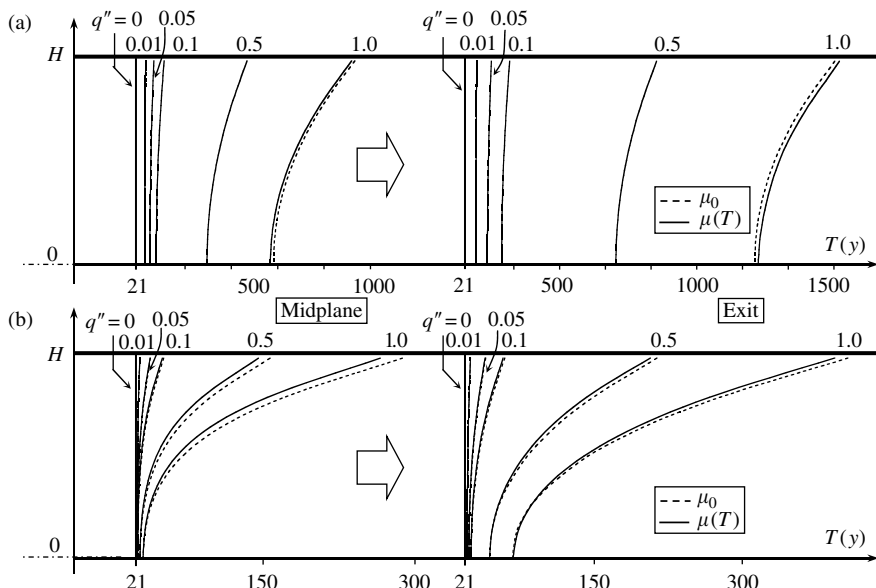
For fully developed (see discussion of Nield and Bejan, 1992, p. 57), Darcy flow with constant viscosity, the Nusselt number in Eq. (5.21) can be obtained from Rohsenow and Hartnett (1973) for parallel-plates porous channel as equal to 4.93, when the wall temperature T_w is constant and equal to 6, when the heat flux q'' is constant. Even though it is commonly used, observe that the local Nusselt number, Nu , Eq. (5.21), is defined in terms of the local wall temperature and the local fluid bulk temperature — a value, as pointed out earlier, difficult to measure accurately. By implicitly assuming fully developed flow, and applying the First Law of Thermodynamics for the channel of Figure 5.1(b) to find the channel length averaged bulk temperature, we can find a useful relation between Nu and Nu_L as

$$Nu_L = \frac{1}{(1/Nu) + (L/4H^2\lambda Pr_e)} \quad (5.23)$$

5.3.2 Temperature Profiles for $\mu(T)$ in Porous Media

Before proceeding to check how the Nusselt numbers defined in Section 5.3.1 behave for temperature-dependent viscosity flows, we will first study the temperature profiles. We discussed earlier, in Section 5.2.3, the effect of increasing the wall heat flux on the local (at mid-channel, i.e., $x = L/2$, and at the end of the heated section of the channel, i.e., $x = L$) longitudinal fluid speed, u , profile, for a chosen minimum and maximum inlet fluid speed (see Figure 5.4). The temperature profiles corresponding to these velocity profiles are shown in Figure 5.10.

Interestingly, for heating the PAO flow, Figure 5.10 reveals a very modest effect of temperature-dependent viscosity on the temperature distribution along the channel, even though the velocity profile is dramatically altered as shown in Figure 5.4. In fact, the shapes of the fluid temperature profiles

**FIGURE 5.10**

Channel temperature profiles for several heat fluxes (q'' values in MW/m^2): (a) low ($U_0 = 1 \times 10^{-3} \text{ m/sec}$) and (b) high ($U_0 = 1 \times 10^{-2} \text{ m/sec}$) velocities.

obtained by heating the fluid with uniform viscosity (shown with dashed line, for $\mu = \mu_0$) are preserved along the channel. Particularly in Figure 5.10(a), deviations from the no heating results are observable only when the wall heat flux equals $1.0 \text{ MW}/\text{m}^2$. Results for the maximum inlet fluid speed, Figure 5.10(b), show a slower increase of the fluid temperature along the channel, than the temperature profile for the uniform viscosity case. This effect is apparent at wall heat flux values of $0.1 \text{ MW}/\text{m}^2$ or higher.

When combined with the velocity profiles of Figure 5.4, we can infer more on the stretch and shrink effect discussed in Section 5.2.3. Recall that the inlet velocity profile remains unchanged (slug-flow profile) throughout the entire channel when the viscosity is assumed uniform and equal to μ_0 . Even in this case of uniform viscosity, the temperature of the channel will vary because of forced convection. The higher temperature can be verified in Figure 5.10(a) and (b), when the fluid temperature near the center of the channel is, in most cases, in fact higher than the inlet fluid temperature ($T_0 = T_{in} = 21^\circ\text{C}$).

However, the increase in the fluid velocity near the heated surface (at $y = H$, in Figure 5.4), caused by the increase in the fluid temperature and corresponding decrease in the viscosity, is compensated by a corresponding decrease in the velocity near the center of the channel (at $y = 0$). Because the fluid is convecting (being heated) over the entire cross-section of the channel, we might expect the resulting viscosity decrease to cause an increase in the fluid velocity, everywhere. However, this would violate the conservation of mass

principle. A consequence of this cross-section mass-flow conservation, which must be satisfied along the channel, is observed in Figure 5.4 as a decrease in velocity near the center of the channel, even when the fluid is heated in this region.

5.3.3 Nusselt Number and $\mu(T)$ in Porous Media

Figure 5.11 shows the local Nusselt number, Nu , calculated for the maximum inlet fluid speed ($U = 1 \times 10^{-2}$ m/sec). It shows a very small effect of temperature-dependent viscosity, with the effect pronounced only when the heat flux is high ($q'' = 1.0 \text{ MW/m}^2$), and only near the entrance of the channel. By comparing Figure 5.11 (for $q'' = 1.0 \text{ MW/m}^2$) and Figure 5.4 (exit profile, for $q'' = 1.0 \text{ MW/m}^2$) we can infer that the local Nusselt number, Nu , is insensitive to the local velocity profile. Even though the velocity profile is not yet fully developed (not slug, see Figure 5.4) the local Nusselt number has already achieved almost the value predicted for the slug-flow configuration (i.e., $Nu = 6$) of a fluid with uniform viscosity.

For increasing heat flux, there will be a stronger variation on the viscosity value along the channel. With minimum inlet fluid speed, this viscosity variation will be even stronger (as the fluid resides more inside the channel to get its viscosity affected by the heat seepage), a result of the relatively weak convection (heat transport, as against heat storage) effect. This aspect influences the heat-transfer process, as it induces upstream conduction. The fluid flow being weak allows the fluid temperature near the inlet to change drastically.

As the fluid temperature just outside the inlet (i.e., about to enter the channel) is a constant, a large temperature gradient appears near the inlet boundary. Hence, heat energy can be transferred by conduction out of the

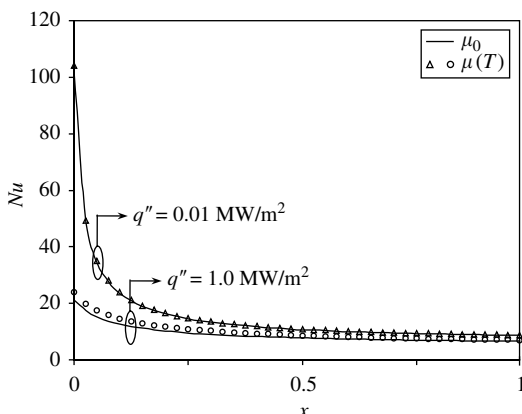
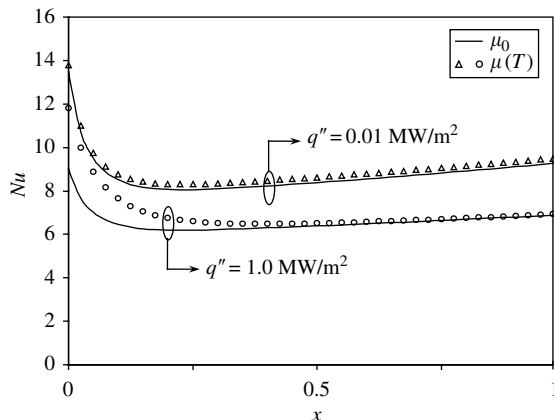


FIGURE 5.11

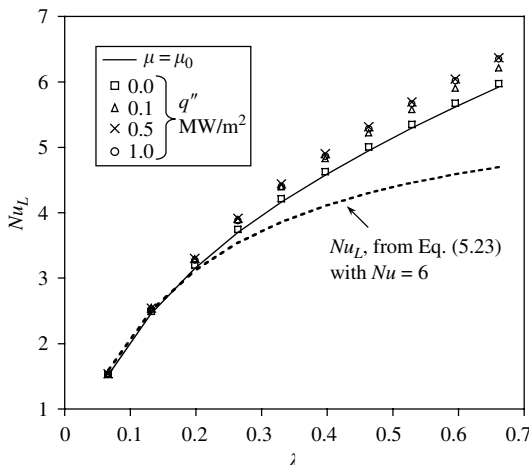
Evolution of Nu along the length (L) of the channel for $U_{\max} = 10^{-2}$ m/sec.

**FIGURE 5.12**

Evolution of Nu along the length (L) of the channel for $U_{\min} = 10^{-3}$ m/sec.

channel through the inlet boundary. This phenomenon, termed *back-diffusion*, has been observed experimentally and discussed in detail in Porneala (1998). It is nevertheless, independent of the fluid having a temperature-dependent viscosity. One particular effect of back-diffusion is the reduction of the local temperature difference between the wall-temperature and bulk-temperature, causing the local Nusselt number, Eq. (5.21), to appear higher than normal. This is seen in Figure 5.12, for $q'' = 0.01 \text{ MW/m}^2$. As the heat flux increases, the back-diffusion effect becomes relatively weaker because the variation in the bulk fluid temperature (from channel inlet to outlet) becomes stronger. This also is captured in Figure 5.12, for $q'' = 1.0 \text{ MW/m}^2$. Observe in this case that the local Nusselt number tends to the known value, $Nu = 6$, which is valid for fully developed profile, Darcy flow, and uniform properties, as stated in Section 5.3.2.

Figure 5.13 presents Nu_L , defined in Eq. (5.23). The overall effect of temperature-dependent viscosity is to increase the surface-averaged heat transfer by as much as 10% when compared with the Nusselt number obtained by heating a fluid with uniform viscosity. A further increase in the wall heat flux would decrease Nu_L towards the value obtained for the uniform viscosity case. From Eq. (5.23), we can infer that when $4H^2\lambda Pr_e \gg 6L$, Nu_L tends to the uniform (fully developed) value of the local Nusselt number, that is, $Nu = 6$. Evaluating PAO (fluid used) properties at 21°C and considering the channel geometry ($L = 1 \text{ m}$; $H = 10 \text{ cm}$) that is used to generate Figure 5.13, this requirement translates into: $\lambda \gg 0.18$. This is confirmed by the results shown in Figure 5.13. Included in Figure 5.13 are results using Eq. (5.23) with $Nu = 6$, the Nu_L for fully developed flow. The deviation of the numerical results when λ increases is due to the longer developing length necessary to achieve fully developed flow (see Narasimhan and Lage, 2001d).

**FIGURE 5.13**

Nu_L versus λ , for temperature-dependent viscosity channel flows.

Ling and Dybbs (1987, 1992) investigated theoretically, the temperature-dependent fluid viscosity influence on the forced convection through a semi-infinite porous medium bounded by an isothermal flat plate. The fluid viscosity was modeled as an inverse linear function of the fluid temperature, which is a very good model for many liquids, including water and crude oil. Their study, with fluid flow governed by the Darcy equation was restricted to heat-transfer analysis. It showed a strong influence of temperature-dependent viscosity on the heat transfer from the flat plate.

For a similar flat-plate configuration, Postelnicu et al. (2001) considered the effect of heat generation as well. For non-Darcy flow in the same flat-plate porous medium flow configuration, Kumari (2001a, 2001b), provided similar solutions for mixed convection with variable viscosity, under constant and variable wall heat flux. When compared with the constant viscosity case, increased heat transfer for liquids while a decreased heat transfer for gases is observed in both of these works.

5.3.4 Temperature-Dependent Viscosity and Pump Power

For sustaining a desired flow rate in a thermo-hydraulic engineering system (channels, ducts, etc.), the required pressure-drop is achieved by means of a pump. Reduction in the power required by this pump, without adversely affecting the pressure-drop value, is obviously an important issue, which is given careful thought by the design engineer. Heating the channel for liquid flow reduces the viscosity, and the M-HDD model predicts the resulting pressure-drop. Obviously, we might then consider the benefit of heating the flow as a means to reduce the pumping power. In what follows, we present the findings of Narasimhan and Lage (2004).

Taking into consideration that we are forced to spend energy in one form (heating of the channel) to achieve savings in another form (pump power reduction), we can define a figure of merit R to establish the energy efficiency of the entire thermo-hydraulic process as

$$R = \frac{\dot{W}_{\mu_0} - \dot{W}_h}{\dot{Q}} \quad (5.24)$$

where \dot{W}_{μ_0} is the power necessary to pump the fluid without heating, and \dot{W}_h is the power necessary to pump the fluid when heating the fluid with a certain amount of energy \dot{Q} . In terms of nondimensional quantities, Φ and λ , given by Eqs. (5.18) and (5.14), respectively, Eq. (5.24) becomes

$$R = H(1 - \Phi)(\lambda + 1)A \quad (5.25)$$

with

$$A = \frac{D_\mu U}{q''} \quad (5.26)$$

Figure 5.14 is obtained by calculating R for several heat fluxes and plotting the results versus λ . The process of heating the fluid to reduce the pump power becomes increasingly more efficient as λ increases, or equivalently, when the fluid speed increases. In addition, for the same λ value, the increase in heat flux reduces the energy efficiency of the process. This is because of the nonlinearity of the degree of viscosity reduction with temperature (or with heat flux). As the heat flux progressively increases by a fixed amount, the corresponding reduction in fluid viscosity becomes smaller and smaller.

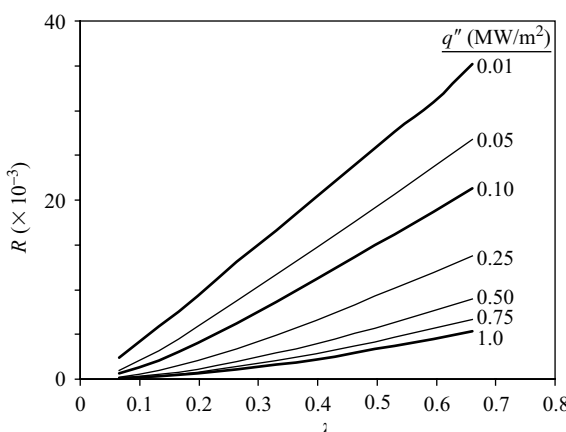


FIGURE 5.14

Overall energy gain due to $\mu(T)$ versus fluid speed (λ).

Hotter the fluid becomes; more heat energy is necessary to keep reducing the viscosity by the same amount. As a result, the reduction in pumping power, numerator of Eq. (5.24), becomes smaller and smaller for the same increase in heat flux, denominator of Eq. (5.24). Moreover, hotter the fluid becomes smaller is the impact (reduction) on the viscous drag. When the fluid temperature is high enough to render the effect of viscous drag negligible, an increase in the heating will have no effect on the pump power, whatsoever.

5.4 Perturbation Models

In this section, we will exposit for the same heated porous channel flow problem, perturbation analysis based predictive models, as presented in Nield (1999) and Narasimhan et al. (2001a). In essence, these analyses result in series type modifications to the HDD model, Eq. (5.1), to account for temperature-dependent viscosity effects. As will be seen, heat-transfer effects (i.e., $\mu(T)$ influence on Nusselt number) also evolve simultaneously, along with the hydrodynamic effects. While Nield et al. (1999) considered only the viscous-drag effects (i.e., the macroscopic form of Eq. [5.1], with $C_0 = 0$, is the starting point for the analysis), Narasimhan et al. (2001a) included the form-drag effects (i.e., macroscopic form of Eq. [5.1], the HDD model, is the starting point of the analysis). We proceed to explain here, the more general analysis from Narasimhan et al. (2001a), done with the HDD model, Eq. (5.1).

5.4.1 Physical Model and the Zero-Order Perturbation Solution

Reconsider the unidirectional, parallel-plate porous channel flow of PAO, being heated by a constant heat flux, q'' , at the top and bottom walls (as depicted in [Figure 5.1\[b\]](#)). Owing to the symmetry of the configuration, we limit our attention to the top half of the channel, with half-channel distance, H and length L . Assuming fully developed flow, that is, $\partial u / \partial x = 0$, and combining it with the continuity equation, Eq. (5.2), and the impermeable boundary condition at the channel surface, would yield $v = 0$. The momentum equation, Eq. (5.3), written with $G = -\partial p / \partial x$, hence becomes

$$C_0 \rho K_0 u^2 + \mu(T)u - GK_0 = 0 \quad (5.27)$$

The energy equation, Eq. (5.4), with the assumption of negligible longitudinal conduction (or high Péclet number) is,

$$\frac{\partial^2 T}{\partial y^2} = \frac{\rho c_p}{k_e} u \frac{\partial T}{\partial x} \quad (5.28)$$

For thermally fully developed flow, the temperature variation along the channel, $\partial T / \partial x$ in the RHS of Eq. (5.28), can be related to the bulk-temperature variation as $\partial T / \partial x = \partial T_b / \partial x$ (see section 3.4 of Bejan, 1995). Applying the First Law of Thermodynamics for the channel shown in [Figure 5.1\(b\)](#), to express $\partial T_b / \partial x$ in terms of the constant heat flux q'' and using the result in Eq. (5.28) yields

$$\frac{\partial^2 T}{\partial y^2} = \left(\frac{u}{U} \right) \frac{q''}{k_e H} \quad (5.29)$$

Solving Eq. (5.29) would need us to determine the ratio u/U , where U is the channel cross-section averaged fluid speed. The quadratic equation given by Eq. (5.27) when solved for u will result in a positive root, which will be a function of $\mu(T)$. The solution would resemble

$$u = F(\mu(T)) \quad (5.30)$$

To learn more from this equation, we have to somehow represent, in general, the temperature dependency of the dynamic viscosity of the fluid. This is done as an approximation through the second-order Taylor series expansion, enabling us to express the RHS of Eq. (5.30) as,

$$F(\mu(T)) = F(\mu_r) + F'(\mu_r)(\mu - \mu_r) + \frac{1}{2}F''(\mu_r)(\mu - \mu_r)^2 \quad (5.31)$$

where μ_r is the reference viscosity value, evaluated at $T = T_r$, a suitable reference temperature (for the channel flow configuration) that is yet to be defined. Expanding the individual terms in Eq. (5.31) as functions of temperature, we get

$$F(\mu(T)) = F(\mu_r) + F'(\mu_r)\mu'_r(T - T_r) + \frac{1}{2} \left[F'(\mu_r)\mu''_r + F''(\mu_r)\mu'^2_r \right] (T - T_r)^2 \quad (5.32)$$

By substituting for $F(\mu(T))$ in Eq. (5.30), we can get progressively, the zero-, first-, and second-order solutions for u when we use, respectively, the first, the first and second, or all the terms of Eq. (5.32). The zero-order result, that is, substituting $F(\mu(T)) = F(\mu_r)$ in Eq. (5.30), corresponds to the uniform viscosity case where $u = U_0$. Hence, from Eq. (5.27),

$$G = \frac{\mu_r}{K_0} U_0 + C_0 \rho U_0^2 \quad (5.33)$$

Moreover, simplifying the energy equation using $u = U_0$ and integrating it in y , with $\partial T / \partial y = 0$ at $y = 0$ and $T = T_w$ at $y = H$ as boundary conditions,

we get the zero-order temperature distribution

$$T_0 = T_w - \frac{q''H}{2k_e} \left[1 - \left(\frac{y}{H} \right)^2 \right] \quad (5.34)$$

Using the result for T from Eq. (5.34) to rewrite the bulk temperature in terms of T_w , and substituting the result in the definition of the local Nusselt number Nu , Eq. (5.21), we can show that $Nu = 6$, the expected result for isoflux parallel-plate channel. Clearly, this value remains unchanged along the channel for fluids with constant and uniform viscosity.

5.4.2 First- and Second-Order Perturbation Solution

Proceeding further to determine the first-order solution, we need to find a suitable expression for $(T - T_r)$ in the second term of Eq. (5.32). Implicit in the way Eq. (5.32) is written, is the assumption that the reference temperature T_r is always higher than T . Therefore, a natural candidate for T_r is the wall temperature T_w , which is higher than T , the fluid temperature inside the channel. Using the zero-order solution for T , Eq. (5.31), and T_w for T_r in Eq. (5.32), allows us to evaluate u in Eq. (5.30) as

$$u_1 = a_1 + \frac{a_2 N}{2} \left[1 - \left(\frac{y}{H} \right)^2 \right] \quad (5.35)$$

where a_1 , a_2 , and N are defined as

$$\begin{aligned} a_1 &= \frac{GK_0}{2\mu_w} \left[\frac{-1 + \sqrt{1 + 4\zeta}}{\zeta} \right], & a_2 &= \frac{GK_0}{2\mu_w \zeta} \left[1 - \frac{1}{\sqrt{1 + 4\zeta}} \right] \\ N &= \frac{q''H}{k_e} \frac{1}{\mu_w} \left(\frac{d\mu}{dT} \right)_{T_w} \end{aligned} \quad (5.36)$$

with

$$\zeta = \frac{\rho C_0 K_0^2 G}{\mu_w^2} \quad (5.37)$$

The local (defined on the macroscopic porous continuum) u , derived in Eq. (5.35), can be integrated along y , to find the global, cross-section averaged fluid speed,

$$U_1 = a_1 + \frac{a_2 N}{3} \quad (5.38)$$

Using Eqs. (5.35) and (5.38) in Eq. (5.29), we find the first-order temperature distribution as

$$T_1 = T_w - \frac{q''H}{k_e} \left\{ \frac{1}{2} \left(1 - \frac{y^2}{H^2} \right) + \frac{a_2 N}{a_1} \left[\frac{1}{12} \left(1 - \frac{y^2}{H^2} \right) - \frac{1}{24} \left(1 - \frac{y^4}{H^4} \right) \right] \right\} \quad (5.39)$$

Upon similar use of Eq. (5.39), we get from Eq. (5.30) the second-order solutions as

$$u_2 = a_1 + \frac{a_2 N}{2} \left[1 - \left(\frac{y}{H} \right)^2 \right] + \left[\frac{a_2^2 N^2}{24 a_1} + \frac{1}{8} (a_3 N^2 - a_2 M) \right] \left[1 - \left(\frac{y}{H} \right)^2 \right]^2 \quad (5.40)$$

$$U_2 = a_1 + \frac{a_2 N}{3} + \frac{a_2^2 N^2}{45 a_1} - \frac{a_2 M}{15} + \frac{a_3 N^2}{15} \quad (5.41)$$

$$T_2 = T_w - \frac{a_1}{U_2} \Omega_1(y) - \frac{a_1 q'' H}{U_2 k_e} \left[\frac{1}{24} \left(\frac{a_2 N}{a_1} \right)^2 - \frac{a_2 M}{8 a_1} + \frac{a_3 N^2}{8 a_1} \right] \Omega_2(y) \quad (5.42)$$

where the Ω_1 and Ω_2 of Eq. (5.42) are

$$\begin{aligned} \Omega_1(y) &= T_w - \frac{q'' H}{k_e} \left\{ \frac{1}{2} \left(1 - \frac{y^2}{H^2} \right) + \frac{a_2 N}{a_1} \left[\frac{1}{4} \left(1 - \frac{y^2}{H^2} \right) - \frac{1}{24} \left(1 - \frac{y^4}{H^4} \right) \right] \right\} \\ \Omega_2(y) &= \left[\frac{1}{2} \left(1 - \frac{y^2}{H^2} \right) - \frac{1}{6} \left(1 - \frac{y^4}{H^4} \right) + \frac{1}{30} \left(1 - \frac{y^6}{H^6} \right) \right] \end{aligned} \quad (5.43)$$

and a_3 and M are defined as

$$a_3 = \frac{2 G K_0}{\mu_w (1 + 4\zeta)^{3/2}}, \quad M = \left(\frac{q'' H}{k_e} \right)^2 \frac{1}{\mu_w} \left[\frac{d^2 \mu}{dT^2} \right]_{T_w} \quad (5.44)$$

The corresponding first- and second-order Nusselt numbers, upon using Eq. (5.30), are given, respectively, by

$$Nu_1 = 6 \left[1 - \frac{2 a_2 N}{15 a_1} \right] \quad (5.45)$$

and

$$Nu_2 = Nu_1 + 6 \left[\frac{68 a_2^2 N^2}{1575 a_1^2} + \frac{4}{105 a_1} (a_2 M - a_3 N^2) \right] \quad (5.46)$$

Finally, to complete the solution, one must find a proper value for the wall temperature T_w for calculating the viscosity and its derivatives in Eqs. (5.36), (5.37), and (5.44). Accounting for the fact that the chosen T_w must be higher than the maximum fluid temperature anywhere in the channel, we must use the wall temperature at $x = L$, $T_w(L) = T_{\max}$, given as

$$T_w(L) = q'' \left(\frac{L}{\rho c_p U H} + \frac{H}{3k_e} \right) + T_0 \quad (5.47)$$

Moreover, as an immediate validation of the higher order solutions, notice when the form-drag coefficient C_0 is negligible then from Eq. (5.37), $\zeta \rightarrow 0$. In this case, from Eq. (5.36), $a_1 = a_2 \rightarrow GK_0/\mu_w$ and the first-order solutions of Eqs. (5.38) and (5.45), reduce to

$$U = \left(\frac{\Delta P}{L} \right) \frac{K_0}{\mu(T_{\max})} \left[1 + \frac{N}{3} \right] \quad (5.48)$$

$$Nu = 6 \left(1 - \frac{2}{15} N \right) \quad (5.49)$$

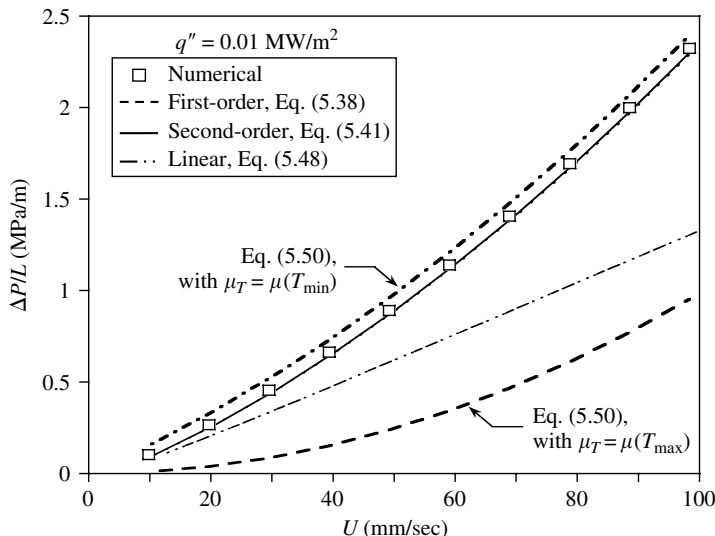
These results are identical to the results reported in Nield et al. (1999), who developed a similar predictive theory for a fluid with temperature-dependent viscosity, but starting with the linear Darcy flow regime, that is, Eq. (5.27) replaced by $u = [K_0/\mu(T)]G$, as stated in the beginning of this section.

5.4.3 Pressure-Drop Results and Velocity Profiles

Again, to facilitate easy understanding and useful comparison, the numerical simulations details and results used here, are identical to those that were used in the previous sections, in discussing the M-HDD model. [Figure 5.15](#) shows a comparison between the theoretical predictions and the results from the numerical simulations for $q'' = 0.01 \text{ MW/m}^2$. The simplest theoretical predictions are obtained first from the HDD model, restated here as

$$\frac{\Delta P}{L} = \frac{\mu(T_r)}{K_0} U + C_0 \rho U^2 \quad (5.50)$$

assuming: (1) $\mu(T_r) = \mu_r = \mu(T_{\min})$ and (2) $\mu(T_r) = \mu_r = \mu(T_w(L)) = \mu(T_{\max})$. These two options are plotted in Figure 5.15. They are, respectively, the lower-bound and upper-bound limits for the fluid speed U , with a fixed pressure-drop $\Delta P/L$ along the channel, because they are calculated using the minimum, T_{\min} , and maximum, $T_w(L)$, temperatures attained by the fluid along the channel. Any other temperature chosen will fall between these two limits. Observe that the result from the HDD model using a viscosity evaluated at the minimum temperature (inlet), is independent of the heat

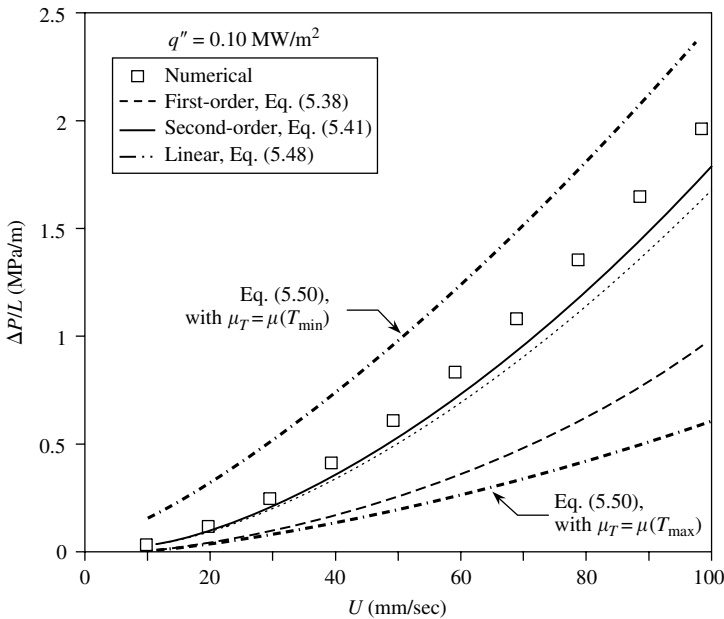
**FIGURE 5.15**

Comparison of theoretical and numerical pressure-drop versus fluid speed results for $q'' = 0.01 \text{ MW/m}^2$ (Narasimhan et al., 2001a).

flux (thereby, of variation in temperature inside the channel) thus representing both no heating and uniform viscosity situations.

The analyses performed in this section, on the unidirectional, differential HDD model, Eq. (5.27), leads to a theory that improves on the lower-bound velocity results predicted by Eq. (5.50). From Figure 5.15, we can observe that the first- and second-order solutions, Eqs. (5.38) and (5.41), predict velocities that compare extremely well with the numerical results. Also plotted in the same figure is the theoretical prediction of the linear model, from Eq. (5.48). Observe that the predicted pressure-drop, for a given fluid speed, is smaller than the pressure-drop predicted from Eqs. (5.38) and (5.41). This is expected from a model that does not include the form-drag effects.

Figure 5.16 presents similar results, but for $q'' = 0.10 \text{ MW/m}^2$. Comparison of Figure 5.15 and Figure 5.16 indicates that the curve obtained from Eq. (5.50) with $\mu(T_r) = \mu(T_{\max})$ is unchanged when the heat flux increases. This is surprising because T_{\max} certainly changes (increases) with the heat flux. However, the results show that the fluid temperature is irrelevant to the fluid speed versus pressure-drop relation Eq. (5.50). This, as we know, happens only when the viscous-drag effect is negligible as compared with the form-drag effect. Hence we can conclude that T_{\max} , even for the low heat flux considered in Figure 5.15, is already high enough to yield a negligible viscous drag. In this regard, the curves for $\mu(T_r) = \mu(T_{\max})$ from Eq. (5.50), presented in Figure 5.15 and Figure 5.16, are the lower-bound curves for pressure-drop versus fluid speed. Keep in mind, however, that this is true only when we account for the form-drag effect.

**FIGURE 5.16**

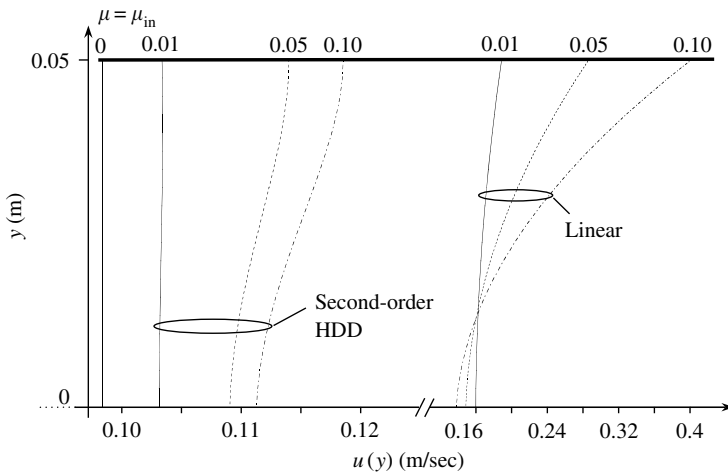
Comparison of theoretical and numerical pressure-drop versus fluid speed results for $q'' = 0.10 \text{ MW/m}^2$ (Narasimhan et al., 2001a).

When the form-drag effect is ignored, as in the linear model based on the Darcy equation, Eq. (5.48), the decrease in pressure-drop with heat flux has no limit. Observe, for instance in Figure 5.16, how the curve obtained from Eq. (5.48) lies even below the curve obtained by Eq. (5.50) with $\mu(T_r) = \mu(T_{\max})$! This situation is analogous to the Hagen–Poiseuille flow configuration or to flow through a porous medium with zero form coefficient ($C_0 = 0$).

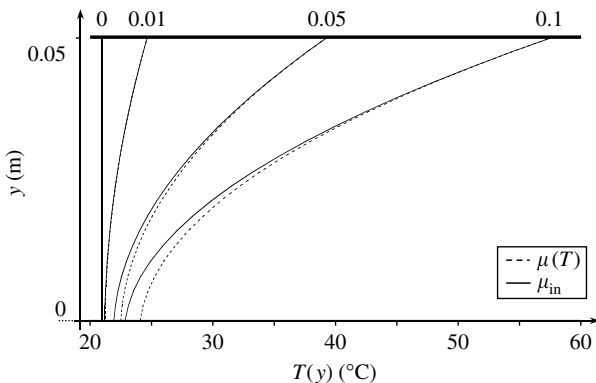
In contrast to Figure 5.15, the agreement between first-order, second-order, and numerical results is not so good in Figure 5.16. We can now see the improvement in going from first-order to second-order analysis. The deviation between first-order results and the numerical results is either because of the inaccuracy of the first-order truncation or from the fully developed flow assumption.

Figure 5.17 shows the local velocity variation $u(y)$ predicted by the linear model (from Nield et al. 1999), and the second-order HDD model, Eq. (5.40), results for $q'' = 0.01, 0.05$, and 0.10 MW/m^2 , respectively. Also shown is the velocity profile for no heating ($q'' = 0$), labeled $\mu = \mu_{in}$. All curves are obtained with the same pressure-drop G , equivalent to $U = 1 \times 10^{-1} \text{ m/sec}$ when the channel is not heated. Increased fluid speed is expected when heating the channel.

Compare this situation with the discussion under the M-HDD model section. There, the imposition of constant cross-section averaged speed U

**FIGURE 5.17**

Velocity profiles $u(y)$ from second-order HDD theory (left side profiles) and linear theory (right side profiles) for several heat fluxes.

**FIGURE 5.18**

Comparison of temperature profiles from second-order HDD theory with those of uniform viscosity case, for several heat fluxes.

(mass conservation) yielded from the numerical simulations, velocity profiles shown in Figure 5.4, which vary about the mean speed value. However, a decrease in the global pressure-drop G was observed.

The linear model neglects the influence of the form-drag term, the fluid velocity profile is expected to follow the temperature profile, having a maximum velocity at the wall (where the viscosity is minimum because the temperature is maximum) and decreasing progressively toward the axis of the channel. This is observed in Figure 5.17 (also, compare this figure with the next one for temperature profiles, Figure 5.18).

The second-order HDD result for $q'' = 0.01 \text{ MW/m}^2$, however, indicates a slug-flow profile, with a reduction in the fluid speed (as compared to the linear fluid speed) caused by the form-drag effect. This makes the curvature of the velocity profile (as predicted by the linear theory) to flatten near the walls, as indicated in the right side profiles of Figure 5.17. When the heat flux is increased, the second-order HDD results indicate a pronounced velocity increase of the fluid near the channel surface. This aspect is due to the influence of viscosity variation on the viscous drag. The variation in viscosity reduces the viscous drag to a greater extent near the wall, where the reduction in viscosity, because of the higher temperature, is more dramatic. This is ably captured by the second-order HDD theory, as evident from Figure 5.17.

5.4.4 Temperature Profiles and Nusselt Numbers

Temperature profiles, similar in style and corresponding to the second-order velocity profiles in Figure 5.17, are shown in Figure 5.18, obtained from Eq. (5.42). For the flow of a fluid with decreasing viscosity for increasing temperature, we deduced from Figure 5.17, that increasing the heat flux increases the local velocity near the wall relative to that at the axis. This results in an increase in the curvature of the temperature profile near the wall and a corresponding decrease toward the axis, resulting in a net flattening of the entire profile, as shown in Figure 5.18.

Nusselt numbers from the linear model, Eq. (5.49), and from the second-order HDD model Eq. (5.46), are compared in Figure 5.19. Also shown in the figure is the curve $Nu = 6$, the uniform viscosity μ_{in} result. Recall that the fluid bulk temperature T_b and the reference (maximum wall) temperature T_{max} , on which Eqs. (5.46) and (5.49) are based, are both functions of the fluid speed.

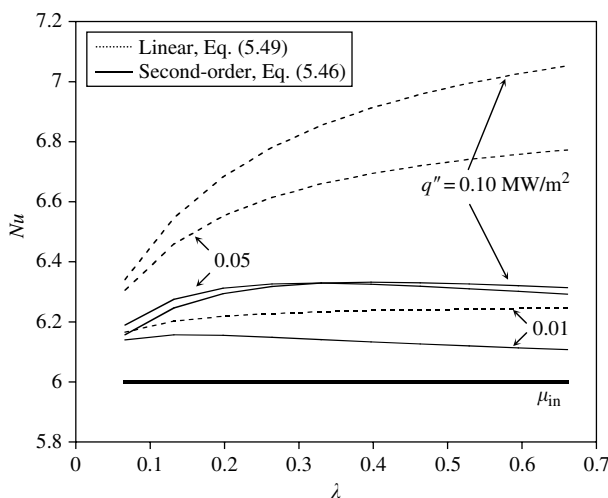


FIGURE 5.19

Nusselt numbers obtained by the two theories as a function of λ .

From Figure 5.19, the linear model yields a Nusselt number that increases with the fluid speed (represented by λ) and the heat flux. This is a consequence of the increased fluid bulk temperature estimated by this model as the fluid speed and/or the heat flux increase. As noticed earlier from Figure 5.17 and Figure 5.18, for the linear model, the predicted velocity distribution parallels the temperature distribution. Therefore, the high fluid temperature adjacent of the heated surface (wall) has more significance in the computation of the bulk temperature than the low temperature near the center of the channel. In addition, the Nusselt number predicted by the linear model, Eq. (5.49), is higher than the Nusselt number predicted by the second-order HDD model, Eq. (5.46). This is a consequence of the inclusion of the form-drag effect by the second-order HDD model, which leads to a smaller fluid speed and bulk temperature.

In general, as the fluid speed increases, the viscous drag decreases in importance as compared with the form drag. Hence, we can expect Nu to evolve toward $Nu = 6$. This decrease in the Nu as the fluid speed increases, can also be seen from the results of the second-order model, Eq. (5.46), shown in Figure 5.19. Even for fully developed flow assumption, the theory presented here predicts a Nu dependent on the fluid speed still invariant in x . However, a real situation with undeveloped flow has local Nusselt number varying in x . This fact makes the comparison between these two Nusselt numbers less effective and cumbersome, as the comparison in principle should be done for all fluid speeds considered.

As seen earlier, the alternative global Nusselt number, Nu_L , Eq. (5.22) and related to the previous Nusselt number, Nu , through Eq. (5.23), subsumes the x -dependency of Nu , therefore making the comparison with results from developing flow configurations straightforward. The results plotted in Figure 5.20 demonstrate that the theoretical results are very accurate for λ

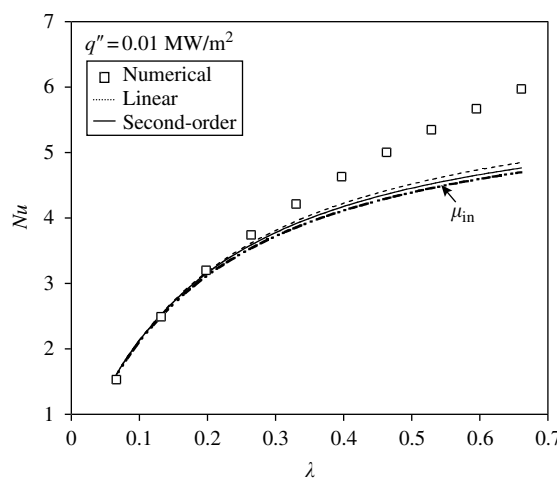


FIGURE 5.20

Comparison of Nu_L from theoretical result with the numerical result.

smaller than 0.3. Observe that Nu_L is relatively insensitive to the inclusion of the form-drag effect (linear or second-order HDD) as opposed to what happens in the pressure-drop versus fluid speed, [Figure 5.15](#). Moreover, the results of [Figure 5.20](#) demonstrate that the fully developed assumption behind the second-order HDD model affects the accuracy of the thermal results much more than it affects the accuracy of the hydraulic results ([Figure 5.15](#) and [Figure 5.16](#)).

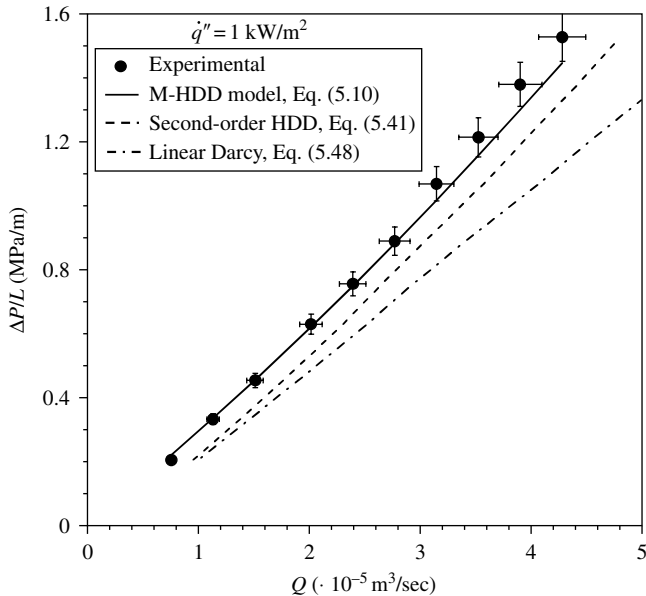
It is important to note the implicit assumption of a rigid porous matrix, one in which the temperature change does not affect (by volumetric expansion or contraction) the structure of the medium vis-à-vis porosity, topology, etc.

5.5 Experimental Validation

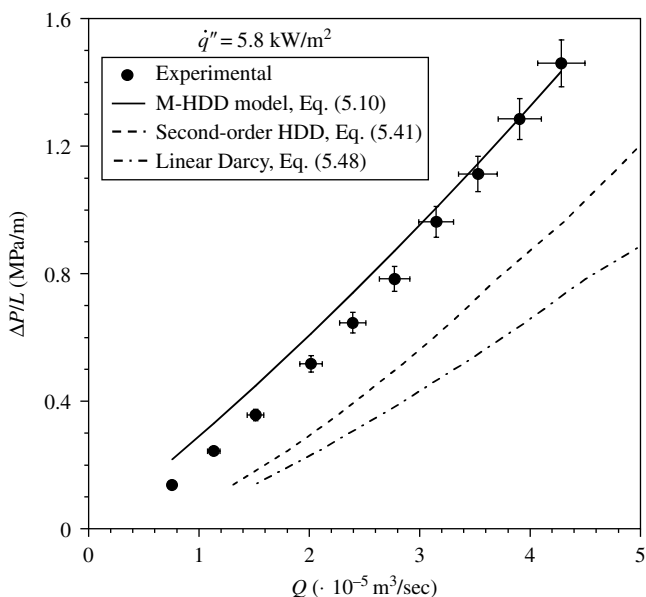
We now briefly focus on the experimental validation of the hydraulic performance (i.e., pressure-drop versus fluid speed relationship) of the models, in lieu of the minimal temperature-dependent viscosity effect on the heat-transfer aspects. A micro-porous cold plate with a porous insert made of compressed aluminium-alloy porous foam sandwiched (brazed) between rectangular (102×508 mm) plate sections was designed and manufactured for cooling a phased-array radar slat. For detailed explanation of this design, see Lage et al. (1998, 2004). It is sufficient to realize at present that this cold plate, using PAO as the coolant flow through the porous insert resembles the parallel plate isoflux channel of [Figure 5.1\(b\)](#). This makes it appropriate for the hydraulic results from this cold plate to be used for appraising our theoretical models.

The effective permeability K_0 and the form coefficient C_0 of the porous insert were determined (by fitting the experimental no heating results in the HDD model, Eq. [5.1]) to be $K_0 = 4.01 \times 10^{-10} \text{ m}^2$ and $C_0 = 33.458 \times 10^3 \text{ m}^{-1}$, respectively. This low permeability and high form-factor of the chosen porous medium make it particularly suitable for verifying the theoretical models, because of their negligible convective inertia and viscous diffusion effects. Further details of the experimental apparatus and procedure are documented in Porneala (1998). By heating the cold plate with electric heaters generating a constant heat flux, the volumetric flow rate and the total PAO pressure-drop across the cold plate are measured.

The results for two heat flux values are presented in [Figure 5.21](#) and [Figure 5.22](#). Figure 5.21 compares the experimental pressure-drop results with that predicted by the second-order perturbation model, Eq. (5.41), and the M-HDD model, Eq. (5.10), for a reference coolant temperature $T_0 = 21^\circ\text{C}$, and $q'' = 1 \text{ kW/m}^2$. To highlight the influence of form-drag effects, predictions by the linear-Darcy model, Eq. (5.48) is also shown. The comparison for a higher heat flux, $q'' = 5.8 \text{ kW/m}^2$, is shown in [Figure 5.21](#). From [Figure 5.21](#)

**FIGURE 5.21**

Pressure-drop versus volumetric PAO flow rate for $T_{in}=21^\circ\text{C}$ and $\dot{q}''=1 \text{ kW/m}^2$ (Uncertainties: $U_{\Delta P}/\Delta P=3\%$ and $U_Q/Q=5\%$).

**FIGURE 5.22**

Pressure-drop versus volumetric PAO flow rate for $T_{in}=21^\circ\text{C}$ and $\dot{q}''=5.8 \text{ kW/m}^2$ (Uncertainties: $U_{\Delta P}/\Delta P=3\%$ and $U_Q/Q=5\%$).

we see, for lower velocities ($Q < 2 \times 10^{-5} \text{ m}^3/\text{sec}$), both the perturbation theories, Eqs. (5.48) and (5.41), agree well in their predictions. However, for higher velocities ($Q > 2 \times 10^{-5} \text{ m}^3/\text{sec}$), with the gaining strength of the form drag, the linear-Darcy model, Eq. (5.48) deviates, as expected.

The results validate the two theoretical models, subject to their respective limitations. The second-order HDD model, Eq. (5.41), due to the inclusion of the form-drag effects, is better than the earlier model, Eq. (5.48), based on the simpler Darcy equation. However, Eq. (5.41) is accurate only for fully developed (hydrodynamic and thermal) flow situations with very small temperature variation along the channel. For higher heat fluxes (such as in [Figure 5.22](#)), the temperature distribution along the channel grows in strength making the perturbation model assumption of small temperature variation along the channel invalid. This prompts a systematic deviation of the second-order HDD model from the experimental results. The M-HDD model, Eq. (5.10), agrees well with the experimental results for both heat fluxes ([Figure 5.21](#) and [Figure 5.22](#)). However, note that the high-heat flux correlation for ζ_μ and ζ_C , the null-global viscous-drag regime has not been tested.

5.6 Conclusions

The M-HDD hydrodynamic model proposed by Narasimhan and Lage (2001a) is believed to be valid universally for all porous medium configurations, that is, independent of the fluid and the porous medium used. However, the empirical correlations predicting the correction coefficients, ζ_μ and ζ_C , to be used in the M-HDD model, has some restrictions. These correlations are proposed with simulation results for PAO. Hence, they can be recommended only for liquids that show similar viscosity functional dependency on temperature. Further, the analysis assumes the structure of the porous medium to be rigid (incompressible), and other thermo-physical properties such as the density of the liquid to be constant. Relaxing the constant density assumption can lead to an alternate study in which the form drag will directly be affected by the density variation, apart from being indirectly influenced by the viscosity via the velocity. Suitable experimental configurations (with different geometry, porous medium characteristics) can be used to test the full range of validity of the correlations proposed. A parametric study of the results should give proper information necessary for further experiments and alterations in the correlation functions, while generalizing them to include other fluids. In association with existing advanced CFD software for simulation and design, these suggestions, once implemented, should allow consistent prediction of the thermal-hydraulic performance of a large number of porous media based systems and devices, including cold plates and self-lubricating bearings.

Nomenclature

A	heat-transfer area, m^2
A_f	flow cross-section area, m^2
c_F	Forchheimer coefficient
c_P	specific heat capacity at constant pressure, J kg/K
C	form coefficient ($= c_F K^{-1/2}$), per m
D	global drag, Pa/m
D_e	average particle diameter, m
G	pressure-drop across a length of the channel, Eq. (5.27)
H	half-channel spacing, m
HDD	Hazen-Dupuit-Darcy
k	thermal conductivity, W/K/m
k_e	effective thermal conductivity ($= \phi k_f + (1 - \phi)k_s$), W/K/m
K	permeability, m^2
L	channel length, heated section, m
M-HDD	modified-Hazen-Dupuit-Darcy
Nu	local Nusselt number, Eq. (5.21)
Nu_L	channel average Nusselt number, Eq. (5.22)
p	macroscopic pressure, Pa
P	global (cross-section averaged) pressure, Pa
Pe	Péclet number ($= QL/A_f \alpha_e$)
Pr_e	effective Prandtl number ($= \mu_{in} c_P / k_e$)
q''	heat flux, W/m^2
Q	volumetric flow rate, m^3/sec
Q''	nondimensional heat flux, Eq. (5.12)
R	figure of merit, Eq. (5.24)
T	temperature, $^\circ\text{C}$
\bar{T}_w	average wall temperature, $^\circ\text{C}$, Eq. (5.22)
u	x -component, seepage macroscopic velocity, m/sec
U	global (cross-section averaged) longitudinal velocity, m/sec
$U_{\Delta P}/\Delta P$	experimental pressure-drop uncertainty
U_Q/Q	experimental volumetric flow rate uncertainty
\mathbf{u}	seepage macroscopic velocity vector
v	y -component, seepage macroscopic velocity, m/sec
V	voltage supplied to the heating strips of the cold plate, V
\dot{W}	pump power (as work per unit time), Eq. (5.24)

Greek Symbols

α_e	effective thermal diffusivity ($= k_e / \rho c_P$), m^2/sec
η	relative pressure-drop error ($= (\Delta P_{HDD} - \Delta P_{num}) / \Delta P_{num}$), Figure (5.3)
ϕ	porosity

Φ	nondimensional pressure-drop ratio, Eq. (5.16)
λ	transition parameter, form- and viscous-drag ratio, Eq. (5.14)
$\lambda_T _{\mu(T)}$	transition parameter for $\mu(T)$ flows, Eq. (5.20)
μ	dynamic viscosity, Nsec/m ²
ρ	density, kg/m ³
ζ	drag correction factor, Eq. (5.11)

Subscripts

b	bulk
C	form
e	effective
f	fluid
in	inlet
max	maximum value
min	minimum value
num	numerical simulation result
r, ref	reference
s	solid
w	wall
μ	viscous
ζ	drag correction factor based result
0	inlet

Superscripts

'	first derivative of a variable
''	flux of a variable

Other Symbols

	absolute value
_w	evaluated at wall conditions
₀	evaluated at inlet conditions

References

- A. Bejan. *Heat Transfer*. New York: John Wiley and Sons, Inc., 1993, p. 231.
- A. Bejan. *Convection Heat Transfer*. 2nd edn., New York: John Wiley and Sons, Inc., 1995, p. 104.
- Chevron. *Synfluid Synthetic Fluids*. Physical Property Data, 1981.
- F.A.L. Dullien. *Porous Media: Fluid Transport and Pore Structure*. 2nd edn. San Diego: Academic Press, 1992.
- M. Kaviany. *Principles of Heat Transfer in Porous Media*. New York: Springer-Verlag, 1991.

- M. Kumari. Effect of variable viscosity on non-Darcy free or mixed convection flow on a horizontal surface in a saturated porous medium. *Int. Commun. Heat Mass Transfer* 28:723–732, 2001a.
- M. Kumari. Variable viscosity effects on free and mixed convection boundary-layer flow from a horizontal surface in a saturated porous medium — variable heat flux. *Mech. Res. Commun.* 28:339–348, 2001b.
- J.L. Lage. The fundamental theory of flow through permeable media: from Darcy to turbulence. In: D.B. Ingham and I. Pop, eds. *Transport Phenomena in Porous Media*. New York: Pergamon, 1998, pp. 1–30.
- J.L. Lage, A. Narasimhan, D.C. Porneala, and D.C. Price. Experimental study of forced convection through microporous enhanced heat sinks: enhanced heat sinks for cooling airborne microwave phased-array radar antennas. In: D.B. Ingham and I. Pop, eds. NATO Advanced Study Institute. New York: Kluwer Academic Publishers, Netherlands, 28:433–452, 2004.
- J.X. Ling and A. Dybbs. Forced convection over a flat plate submersed in a porous medium, variable viscosity case. *ASME*, Paper No. 87-WA-HT-23, 1987.
- J.X. Ling and A. Dybbs. The effect of variable viscosity on forced convection over a flat plate submersed in a porous medium. *ASME J. Heat Transfer* 114:1063–1065, 1992.
- A. Narasimhan and J.L. Lage. Modified Hazen–Dupuit–Darcy model for forced convection of a fluid with temperature-dependent viscosity. *ASME J. Heat Transfer* 123:31–38, 2001a.
- A. Narasimhan and J.L. Lage. Forced convection of a fluid with temperature-dependent viscosity through a porous medium channel. *Numer. Heat Transfer A* 40:801–820, 2001b.
- A. Narasimhan and J.L. Lage. Inlet temperature influence on the departure from Darcy flow by fluids with variable viscosity. *Int. J. Heat Mass Transfer* 45:2419–2422, 2002.
- A. Narasimhan and J.L. Lage. Pump power gain for heated porous medium channel flows. *ASME J. Fluids Eng.* 126:494–497, 2004.
- A. Narasimhan, J.L. Lage, and D.A. Nield. New theory for forced convection through porous media by fluids with temperature-dependent viscosity. *ASME J. Heat Transfer* 123:1045–1051, 2001a.
- A. Narasimhan, J.L. Lage, D.A. Nield, and D.C. Porneala. Experimental verification of two new theories for predicting the temperature-dependent viscosity effects on the forced convection through a porous medium channel. *ASME J. Fluids Eng.* 123:948–951, 2001b.
- D.A. Nield and A. Bejan. *Convection in Porous Media*. New York: Springer-Verlag, 1992.
- D.A. Nield and A. Bejan. *Convection in Porous Media*. 2nd edn. New York: Springer-Verlag, 1999.
- D.A. Nield, D.C. Porneala, and J.L. Lage. A theoretical study, with experimental verification of the viscosity effect on the forced convection through a porous medium channel. *ASME J. Heat Transfer* 121:500–503, 1999.
- D.C. Porneala. *Experimental tests of microporous enhanced cold plates for cooling high frequency microwave antennas*. Ph.D. Dissertation, SMU, Dallas, Texas, 1998.
- A. Postelnicu, T. Grosan, and I. Pop. The effect of variable viscosity on forced convection flow past a horizontal flat plate in a porous medium with internal heat generation. *Mech. Res. Commun.* 28:331–337, 2001.
- W.M. Rohsenow and J.P. Hartnett. *Handbook of Heat Transfer*. New York: McGraw Hill Pub., 1973.

6

Three-Dimensional Flow and Heat Transfer within Highly Anisotropic Porous Media

*Numerical Determination of Permeability Tensor, Inertial
Tensor, and Interfacial Heat Transfer Coefficient*

F. Kuwahara and A. Nakayama

CONTENTS

6.1	Introduction	235
6.2	Volume-Averaged Governing Equations	238
6.3	Preliminary Consideration of Macroscopically Uniform Flow Through an Isothermal Porous Medium	239
6.4	Periodic Boundary Conditions for Three-Dimensional Periodic Structure	241
6.5	Quasi-Three-Dimensional Numerical Calculation Procedure	244
6.6	Method of Computation and Preliminary Numerical Consideration	246
6.7	Validation of Quasi-Three-Dimensional Calculation Procedure	248
6.8	Determination of Permeability Tensor	249
6.9	Determination of Forchheimer Tensor	252
6.10	Determination of Interfacial Heat Transfer Coefficient	256
6.11	Conclusions	262
	Nomenclature	262
	References	263

6.1 Introduction

In order to design efficient heat transfer equipment, one must know the details of both flow and temperature fields within the equipment. Such detailed flow and temperature fields within a manmade assembly may be investigated numerically by solving the set of governing equations based on the first

principles (i.e., continuity, momentum, and energy balance equations), so as to resolve all scales of flow and heat transfer in the system. However, in reality, it would hardly be possible to reveal such details even with the most powerful super computer available today. For example, a grid system, designed for a comparatively large scale of heat exchanger systems, would not be fine enough to describe the details of flow and heat transfer around a fin in a heat transfer element.

It has been recently pointed out by DesJardin (personal communication, 2001) and many others [1,2] that the concept of local volume-averaging theory, namely, VAT, widely used in the study of porous media [3–5] may be exploited to investigate the flow and heat transfer within such a complex heat and fluid flow equipment. These complex assemblies usually consist of small-scale elements, such as a bundle of tubes and fins, which one does not want to grid. Under such a difficult situation, one may resort to the concept of VAT instead, so as to establish a macroscopic model, in which these collections of small-scale elements are treated as highly anisotropic porous media. There are a number of situations in which one has to introduce macroscopic models to describe complex fluid flow and heat transfer systems.

Nakayama and Kuwahara [6] appealed to VAT and derived a set of macroscopic governing equations for turbulent heat and fluid flow through an isotropic porous medium in local thermal equilibrium. The resulting set of governing equations was generalized by Nakayama et al. [7], to treat highly anisotropic porous media by integrating the microscopic governing equations, namely, the Reynolds averaged versions of continuity, Navier–Stokes, and energy equations. One can conveniently use these macroscopic equations designed for highly anisotropic porous media, to investigate the flow and heat transfer within complex equipment, since a single set of the volume-averaged governing equations can be applied to the entire calculation domain within the complex heat transfer equipment consisting of both large- and small-scale elements. All that one has to do is to specify the spatial distributions of macroscopic model parameters such as porosity and permeability. The clear fluid flow region without small-scale obstructions, for example, will be treated as a special case, as one sets the porosity for unity with an infinitely large permeability.

In order to utilize these macroscopic equations for such large-scale numerical computations, one must close the macroscopic equations by modeling the flow resistance associated with individual subscale solid elements and also the heat transfer rate between the flowing fluid and the subscale elements, in terms of the macroscopic velocity vector and relevant geometrical parameters. Such subscale models can be established by carrying out direct numerical experiments at a pore scale for individual subscale elements. Since the subscale structure is often periodic, the numerical experiment can be performed economically, focusing on one structural unit and utilizing periodic boundary conditions there. The microscopic results, thus obtained, are processed to extract the macroscopic hydrodynamic and

thermal characteristics, and eventually to determine the unknown model constants of the subscale models associated with permeability tensor, inertial (Forchheimer) tensor, and interfacial heat transfer coefficient. Kuwahara et al. [8], Nakayama and Kuwahara [9], Nakayama et al. [10], and De Lemos and Pedras [11,12] have conducted such microscopic computations successfully. The unknown model constants including the interfacial heat transfer coefficient, permeability, and Forchheimer constants were determined by carrying out exhaustive numerical experiments using a periodic array of square and circular cylinders. A review on the research towards this endeavor may be found in [chapter 10](#) of the first edition of the handbook [13].

All these investigations, however, were limited to the cases of the cross-flows over two-dimensional structures. In reality, all manmade elements such as those in plate fin heat exchangers are three-dimensional in nature. Naturally, the macroscopic velocity vector is not always perpendicular to the axis of the cylinder. The deviating angle between the velocity vector and the plane perpendicular to the axis of the cylinder is called "yaw" angle. Thus, the three-dimensional yaw effects on the permeability tensor, inertial tensor, and interfacial heat transfer coefficient must be elucidated beforehand, in order to design such heat transfer elements and systems. Nakayama et al. [14] used a bundle of rectangular cylinders to describe such three-dimensional anisotropic porous media, and showed that, under macroscopically uniform flow, the three-dimensional governing equations reduce to quasi-three-dimensional forms, in which all derivatives associated with the axis of the cylinder can be either eliminated or replaced by other determinable expressions. Thus, only two-dimensional storages are required for the dependent variables. This quasi-three-dimensional numerical calculation procedure has been exploited to investigate the three-dimensional effects on the permeability tensor, inertial tensor, and interfacial heat transfer coefficient, which are needed to close the proposed set of the macroscopic governing equations.

In what follows, we shall review a series of extensive investigations on three-dimensional flow and heat transfer within highly anisotropic porous media. A bank of long cylinders is considered as one of fundamental geometrical configurations often found in heat exchangers and many other manmade anisotropic porous media. Numerical determination of the important subscale model parameters, such as permeability tensor, inertial tensor, and interfacial heat transfer coefficient, will be described in detail, so as to elucidate the three-dimensional yaw effects on these macroscopic hydrodynamic and thermal parameters. The results are compared with available experimental data to substantiate the validity of the present modeling strategy for three-dimensional flow and heat transfer within highly anisotropic porous media. Upon correlating these macroscopic results, a useful set of explicit expressions will be established for the permeability tensor, inertial Forchheimer tensor, and interfacial heat transfer coefficient, so as to characterize three-dimensional flow and heat transfer through a bank of infinitely long cylinders in yaw.

6.2 Volume-Averaged Governing Equations

According to Nakayama et al. [2,15], the set of the macroscopic equations based on VAT for the case of laminar flow through an anisotropic porous medium runs as

$$\frac{\partial \langle u_j \rangle^f}{\partial x_j} = 0 \quad (6.1)$$

$$\begin{aligned} \rho_f \left(\frac{\partial \langle u_i \rangle^f}{\partial t} + \frac{\partial}{\partial x_j} \langle u_j \rangle^f \langle u_i \rangle^f \right) &= - \frac{\partial \langle p \rangle^f}{\partial x_i} + \frac{\partial}{\partial x_j} \left[\mu_f \left(\frac{\partial \langle u_i \rangle^f}{\partial x_j} + \frac{\partial \langle u_j \rangle^f}{\partial x_i} \right) \right] \\ &\quad - \phi \left(\mu_f K_{ij}^{-1} + \phi \rho_f b_{fij} (\langle u_k \rangle^f \langle u_k \rangle^f)^{1/2} \right) \langle u_j \rangle^f \end{aligned} \quad (6.2)$$

$$\begin{aligned} \rho_f c_{pf} \left(\frac{\partial \langle T \rangle^f}{\partial t} + \frac{\partial}{\partial x_j} \langle u_j \rangle^f \langle T \rangle^f \right) &= \frac{\partial}{\partial x_j} \left[k_f \frac{\partial \langle T \rangle^f}{\partial x_j} + \frac{1}{V_f} \int_{A_{int}} k_f T n_j dA - \rho_f c_{pf} \langle u'_j T' \rangle^f \right] \\ &\quad + h_f a_f (\langle T \rangle^s - \langle T \rangle^f) \end{aligned} \quad (6.3)$$

where

$$a = \langle a \rangle^f + a' \quad (6.4a)$$

and

$$\langle a \rangle^f = \frac{1}{V_f} \int_{V_f} a dV \quad (6.4b)$$

in general denotes the intrinsic averaged value of a over the volume space V_f occupied by the fluid, whereas a' denotes its spatial deviation. In fact, the idea of VAT is quite near to that of the representative elementary volume. However, the size of the elementary volume V should be large enough to cover the microscopic structure, but, at the same time, much smaller than the macroscopic scale. The sub- and superscripts f and s stand for the fluid and solid phases, respectively. In the foregoing momentum and energy equations, the terms associated with the microscopic structure are modeled according to

$$\begin{aligned} \frac{1}{V_f} \int_{A_{int}} \mu_f \left(\frac{\partial u_i}{\partial x_j} + \frac{\partial u_j}{\partial x_i} \right) n_j dA - \rho_f \frac{\partial}{\partial x_j} \langle u'_j u'_i \rangle^f \\ \equiv -\phi \left(\mu_f K_{ij}^{-1} + \phi \rho_f b_{fij} (\langle u_k \rangle^f \langle u_k \rangle^f)^{1/2} \right) \langle u_j \rangle^f \end{aligned} \quad (6.5)$$

and

$$\frac{1}{V} \int_{A_{\text{int}}} k_f \frac{\partial T}{\partial x_j} n_j dA \equiv h_f a_f (\langle T \rangle^s - \langle T \rangle^f) \quad (6.6)$$

where $\phi = V_f/V$ is the porosity, and n_j is the unit vector normal to the interface pointing from the fluid side to solid side. Equation (6.5) is a generalized form of Forchheimer-extended-Darcy's law. The net heat transfer between the fluid and solid is given by $h_f a_f (\langle T \rangle^f - \langle T \rangle^s)$ upon introducing the interfacial heat transfer coefficient h_f , where $a_f = A_{\text{int}}/V$ is the specific interfacial area.

In order to close the foregoing set of the macroscopic governing equations, we must determine the permeability tensor K_{fij} and Forchheimer tensor b_{fij} appearing in Eq. (6.5) and also the interfacial heat transfer coefficient h_f appearing in Eq. (6.6), for a given microscopic structure. As will be demonstrated later, such subscale models can be established by conducting microscopic numerical experiments for individual subscale elements. Then, the microscopic results are fed into the LHS terms of Eqs. (6.5) and (6.6) to determine these unknown tensors and coefficient as functions of the macroscopic quantities. When the structure is geometrically periodic, only one structural unit may be taken as a calculation domain.

6.3 Preliminary Consideration of Macroscopically Uniform Flow Through an Isothermal Porous Medium

In order to appreciate the foregoing macroscopic governing equations, we consider one of the most fundamental flows through a manmade structure, namely, a macroscopically uniform steady flow through an isothermal three-dimensional periodic structure of infinite extent as shown in Figure 6.1. The body shape of the structural element is arbitrary, and its arrangement can be aligned as in Figure 6.1 or staggered in an arbitrary fashion. Let us find the macroscopic pressure and temperature solutions using the foregoing macroscopic momentum and energy equations.

Upon referring to the orthogonal unit vectors $(\vec{l}, \vec{m}, \vec{n})$ as shown in Figure 6.1, the macroscopically steady and uniform velocity field may be presented by

$$\langle \vec{u} \rangle = |\langle \vec{u} \rangle| (\cos \alpha \vec{l} + \cos \beta \vec{m} + \cos \gamma \vec{n}) \quad (6.7)$$

where

$$\langle \vec{u} \rangle = \frac{1}{V} \int_V \vec{u} dV \quad (6.8)$$

is the Darcian velocity, which differs from the intrinsic average velocity (given by Eq. 6.4[b]) by the factor ϕ , such that $\langle \vec{u} \rangle = \phi \langle \vec{u} \rangle^f$. The local volume V for

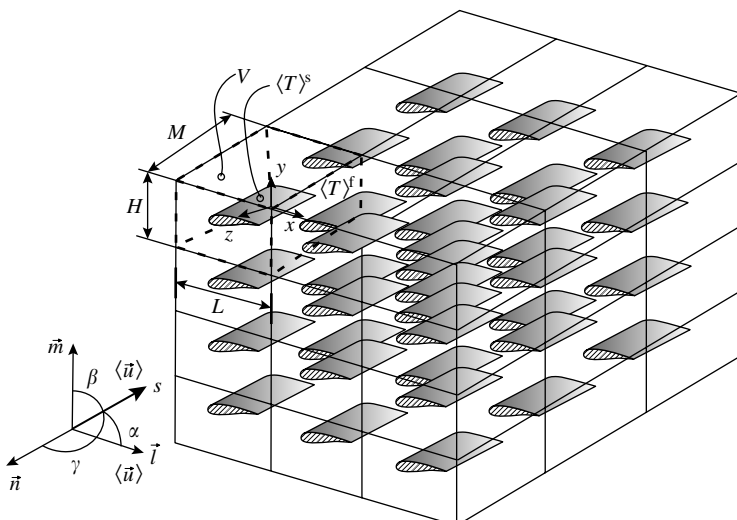


FIGURE 6.1
Three-dimensional periodic structure.

integration may be taken as the structural volume element as indicated by dashed lines in the figure. The directional cosines of the volume-averaged macroscopic velocity vector satisfy the obvious relationship, namely,

$$\cos^2 \alpha + \cos^2 \beta + \cos^2 \gamma = 1 \quad (6.9)$$

This relation may be rewritten equivalently using the cross-flow angle α' projected onto the $x-y$ plane as

$$\cos \alpha = \sin \gamma \cos \alpha' \quad \text{and} \quad \cos \beta = \sin \gamma \sin \alpha' \quad (6.10)$$

Under the macroscopically uniform velocity as given by Eq. (6.7), the volume-averaged momentum equation (6.2) reduces to

$$-\frac{\partial \langle p \rangle^f}{\partial x_i} = (\mu_f K_{fij}^{-1} + \rho_f b_{fij} |\langle \vec{u} \rangle|) \langle u_j \rangle \quad (6.11)$$

where

$$\langle u_k \rangle \langle u_k \rangle = |\langle \vec{u} \rangle|^2 \quad (6.12)$$

Thus, the macroscopic momentum equation leads to the Forchheimer extended Darcy's law [16], generalized for the case of anisotropic porous media.

We shall assume that the wall surfaces of the structure are maintained at a constant temperature. Then, the microscopic temperature field, when

averaged spatially within a local structural control volume V , should lead to the macroscopic temperature field whose gradient aligns with the macroscopic velocity vector in the s direction, such that the volume-averaged energy equation (6.3), under the macroscopically steady and uniform velocity field with negligible macroscopic longitudinal conduction reduces to

$$\rho_f c_{pf} |\langle \vec{u} \rangle| \frac{d\langle T \rangle^f}{ds} = -h_f a_f (\langle T \rangle^f - \langle T \rangle^s) \quad (6.13)$$

where

$$ds = \cos \alpha dx + \cos \beta dy + \cos \gamma dz \quad (6.14)$$

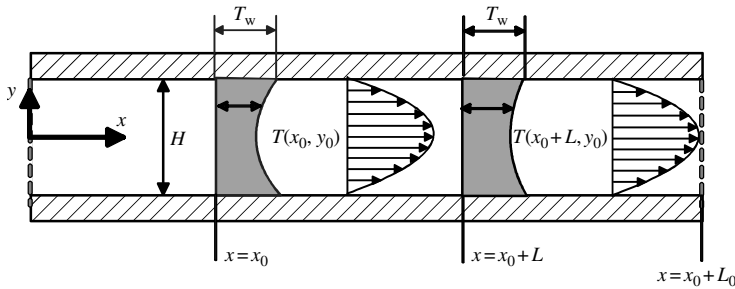
Since the surface temperature of the structure $\langle T \rangle^s$ is constant, Eq. (6.13) naturally yields the macroscopic temperature field as

$$\langle T \rangle^f - \langle T \rangle^s = (\langle T \rangle^f - \langle T \rangle^s)_{ref} \exp \left(-\frac{a_f h_f}{\rho_f c_{pf} |\langle \vec{u} \rangle|} (s - s_{ref}) \right) \quad (6.15)$$

Note that the interfacial heat transfer coefficient h_f is expected to be constant for the periodically fully developed heat and fluid flow, as in the cases of thermally fully developed tube and channel flows. The correct set of the periodic boundary conditions should lead to the microscopic temperature field compatible with the macroscopic temperature field as given by Eq. (6.15). (In other words, the resulting microscopic temperature field, when averaged spatially, must yield the macroscopic temperature field given by Eq. [6.15].)

6.4 Periodic Boundary Conditions for Three-Dimensional Periodic Structure

The periodic boundary conditions needed to conduct microscopic numerical experiments for manmade structures must be compatible with the foregoing macroscopic solutions for the macroscopically uniform flow. The prescription of the periodic boundary conditions for the velocity field (or pressure field instead) is rather straightforward, since the profiles at both upstream and downstream boundaries must be identical. Patankar et al. [17] prescribed the pressure drop over one structural unit to attack the problem of fully developed flow and heat transfer in ducts having streamwise-periodic variations of cross-sectional area, while Nakayama et al. [18] and Kuwahara et al. [19] chose to prescribe the mass flow rate (rather than the pressure drop) to obtain the fully developed velocity and temperature fields within two-dimensional periodic arrays. However, the prescription of the periodic temperature field requires some consideration, when the surface wall temperature is kept constant. Naturally, the temperature difference between the fluid and solid wall

**FIGURE 6.2**

Fully developed channel flow.

becomes vanishingly small at the fully developed stage, as in the case of thermally fully developed tube flow with uniform surface temperature.

In what follows, we shall seek an appropriate set of the periodic boundary conditions to impose along such periodic boundaries of the structure. Let us consider one of the simplest temperature fields, namely, the fully developed temperature field for the case of forced convection from isothermal parallel plates with a channel height H , as shown in Figure 6.2.

The thermally fully developed flow of this kind may be regarded as one of the special periodically fully developed flows, since the temperature profile at $x = x_0$ is similar to that at $x = x_0 + L$, such that

$$\frac{T(x_0 + L, y) - T_w}{T_B(x_0 + L) - T_w} = \frac{T(x_0, y) - T_w}{T_B(x_0) - T_w} \quad (6.16)$$

where L is any axial distance of arbitrary size (which may be unlimitedly large or small), and T_B is the bulk mean temperature. This can be rearranged as

$$\frac{T(x_0 + L, y) - T_w}{T(x_0, y) - T_w} = \frac{T_B(x_0 + L) - T_w}{T_B(x_0) - T_w} = \exp\left(-\frac{2h_f L}{\rho_f c_{pf} u_B H}\right) \quad (6.17)$$

where u_B is the bulk mean velocity. The last expression in the RHS comes from the macroscopic temperature solution given by Eq. (6.15), as we note that $|\langle \vec{u} \rangle| = u_B$, $\langle T \rangle^f = T_B$, $\langle T \rangle^s = T_w$, and $a_f = 2/H$ for this case. Selecting a reference axial distance L_0 along an arbitrary level at $y = y_0$ gives

$$\frac{T(x_0 + L_0, y_0) - T_w}{T(x_0, y_0) - T_w} = \exp\left(-\frac{2h_f L_0}{\rho_f c_{pf} u_B H}\right) \quad (6.18)$$

Upon combining Eqs. (6.17) and (6.18), we obtain

$$T(x_0 + L, y) - T_w = (T(x_0, y) - T_w) \tau^{L/L_0} \quad (6.19)$$

where

$$\tau \equiv \frac{T(x_0 + L_0, y_0) - T_w}{T(x_0, y_0) - T_w} \quad (6.20)$$

Hence, Eq. (6.19) is one of the many possible expressions for the thermally periodic boundary condition for this simple case, which guarantees us to provide the microscopic temperature field compatible with the macroscopic temperature field as given by Eq. (6.15). It is straightforward to extend the case to an infinite series of flat plates of finite length, to the two-dimensional periodic structure of arbitrary shape, and finally to a general three-dimensional periodic structure, as shown in [Figure 6.1](#), as done by Nakayama et al. [14].

Thus, the steady-state microscopic governing equations and their correct set of the boundary conditions for periodically fully developed heat and fluid flow through a three-dimensional periodic structure are given as follows:

$$\nabla \cdot \vec{u} = 0 \quad (6.21)$$

$$\rho_f(\nabla \cdot \vec{u})\vec{u} = -\nabla p + \mu_f\nabla^2\vec{u} \quad (6.22)$$

$$\rho_f c_p f \nabla \cdot (\vec{u} T) = k_f \nabla^2 T \quad (6.23)$$

On the solid walls:

$$\vec{u} = \vec{0} \quad (6.24a)$$

$$T = T_w (= \langle T \rangle^s) \quad (6.24b)$$

On the periodic boundaries:

$$\vec{u}|_{x=-L/2} = \vec{u}|_{x=L/2} \quad (6.25a)$$

$$\vec{u}|_{y=-H/2} = \vec{u}|_{y=H/2} \quad (6.25b)$$

$$\vec{u}|_{z=-M/2} = \vec{u}|_{z=M/2} \quad (6.25c)$$

where the origin of the Cartesian coordinates (x, y, z) is set in the center of the structural unit $(-L/2 \leq x \leq L/2, -H/2 \leq y \leq H/2, -M/2 \leq z \leq M/2)$, as indicated in [Figure 6.1](#). The mass flow rate constraints based on Eq. (6.7) are given by:

$$\int_{-M/2}^{M/2} \int_{-H/2}^{H/2} u \, dy \, dz|_{x=-L/2} = \int_{-M/2}^{M/2} \int_{-H/2}^{H/2} u \, dy \, dz|_{x=L/2} = HM \cos \alpha \langle |\vec{u}| \rangle \quad (6.26a)$$

$$\int_{-M/2}^{M/2} \int_{-L/2}^{L/2} v \, dx \, dz|_{y=-H/2} = \int_{-M/2}^{M/2} \int_{-L/2}^{L/2} v \, dx \, dz|_{y=H/2} = LM \cos \beta \langle |\vec{u}| \rangle \quad (6.26b)$$

$$\int_{-H/2}^{H/2} \int_{-L/2}^{L/2} w \, dx \, dy|_{z=-M/2} = \int_{-H/2}^{H/2} \int_{-L/2}^{L/2} w \, dy \, dx|_{z=M/2} = LH \cos \gamma \langle |\vec{u}| \rangle \quad (6.26c)$$

Finally, the thermal boundary conditions for the periodic boundaries are given by

$$(T - T_w)|_{x=L/2} = \tau^{(L \cos \alpha)/(L \cos \alpha + H \cos \beta + M \cos \gamma)} (T - T_w)|_{x=-L/2} \quad (6.27a)$$

$$(T - T_w)|_{y=H/2} = \tau^{(H \cos \beta)/(L \cos \alpha + H \cos \beta + M \cos \gamma)} (T - T_w)|_{y=-H/2} \quad (6.27b)$$

$$(T - T_w)|_{z=M/2} = \tau^{(M \cos \gamma)/(L \cos \alpha + H \cos \beta + M \cos \gamma)} (T - T_w)|_{z=-M/2} \quad (6.27c)$$

where

$$\tau = \frac{(T - T_w)|_{x=L/2, y=H/2, z=M/2}}{(T - T_w)|_{x=-L/2, y=-H/2, z=-M/2}} \quad (6.28)$$

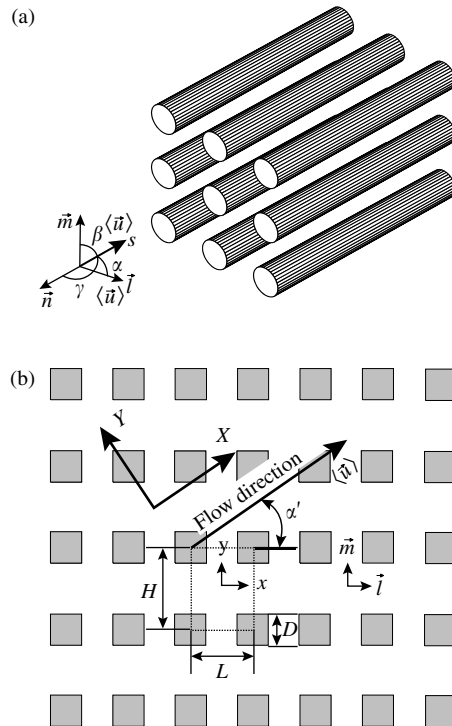
The literature survey [14] has revealed that no explicit periodic thermal boundary conditions (such as given by Eqs. [6.27]) have been reported before for three-dimensional periodic heat and fluid flows of this kind.

6.5 Quasi-Three-Dimensional Numerical Calculation Procedure

The foregoing set of governing equations and corresponding boundary conditions may greatly be simplified for the case of the three-dimensional heat and fluid flow through a two-dimensional periodic structure such as a bank of cylinders in yaw, as illustrated in Figure 6.3(a) and more specifically in Figure 6.3(b) to show the cross-sectional plane of the square cylinder bank subject to the present numerical experiment. All square cylinders in the figure, which may be regarded as heat sinks (or sources), are maintained at a constant temperature $T_w (= \langle T \rangle^s)$, which is lower (or higher) than the temperature of the flowing fluid. Since the cylinders are infinitely long, the set of the governing equations (6.21) to (6.23) reduces to a quasi-three-dimensional form, in consideration of the limiting case, namely, $M \rightarrow 0$:

$$\frac{\partial u}{\partial x} + \frac{\partial v}{\partial y} = 0 \quad (6.29)$$

$$\frac{\partial}{\partial x} \left(u^2 - v \frac{\partial u}{\partial x} \right) + \frac{\partial}{\partial y} \left(vu - v \frac{\partial u}{\partial y} \right) = -\frac{1}{\rho} \frac{\partial p}{\partial x} \quad (6.30)$$

**FIGURE 6.3**

Two-dimensional periodic structure; (a) bank of circular cylinders, (b) bank of square cylinders (cross-sectional view).

$$\frac{\partial}{\partial x} \left(uv - v \frac{\partial v}{\partial x} \right) + \frac{\partial}{\partial y} \left(v^2 - v \frac{\partial v}{\partial y} \right) = -\frac{1}{\rho} \frac{\partial p}{\partial y} \quad (6.31)$$

$$\frac{\partial}{\partial x} \left(uw - v \frac{\partial w}{\partial x} \right) + \frac{\partial}{\partial y} \left(vw - v \frac{\partial w}{\partial y} \right) = \frac{v}{A_{\text{fluid}}} \oint_{P_{\text{int}}} \frac{\partial w}{\partial n} dP \quad (6.32)$$

$$\frac{\partial}{\partial x} \left(uT - \frac{v}{Pr_f} \frac{\partial T}{\partial x} \right) + \frac{\partial}{\partial y} \left(vT - \frac{v}{Pr_f} \frac{\partial T}{\partial y} \right) = S_w \quad (6.33)$$

where P is the coordinate along the wetted periphery, whereas n is the coordinate normal to P pointing inward from the peripheral wall to fluid side. A_{fluid} is the passage area of the fluid, and

$$S_w = -\frac{\partial}{\partial z} \left(wT - \frac{v}{Pr_f} \frac{\partial T}{\partial z} \right) \\ = - \left(w - \frac{v}{Pr_f} \frac{\cos \gamma \ln \tau_0}{L \cos \alpha + H \cos \beta} \right) \frac{\cos \gamma \ln \tau_0}{L \cos \alpha + H \cos \beta} (T - T_w)|_{z=0} \quad (6.34)$$

since

$$\begin{aligned}\frac{\partial T}{\partial z} &= (T - T_w)|_{z=0} \lim_{M \rightarrow 0} \frac{\tau^{(M \cos \gamma)/(L \cos \alpha + H \cos \beta + M \cos \gamma)} - 1}{M} \\ &= \frac{(T(x, y, 0) - T_w) \cos \gamma}{L \cos \alpha + H \cos \beta} \ln \tau_0\end{aligned}\quad (6.35)$$

where

$$\tau_0 \equiv \tau|_{z=0} = \frac{(T - T_w)|_{x=L/2, y=H/2, z=0}}{(T - T_w)|_{x=-L/2, y=-H/2, z=0}} \quad (6.36)$$

The boundary and compatibility conditions for the periodic planes are given by

$$\vec{u}|_{x=-L/2} = \vec{u}|_{x=L/2} \quad (6.37a)$$

$$\vec{u}|_{y=-H/2} = \vec{u}|_{y=H/2} \quad (6.37b)$$

$$\int_{-H/2}^{H/2} u \, dy \Big|_{x=-L/2} = \int_{-H/2}^{H/2} u \, dy \Big|_{x=L/2} = H \cos \alpha \langle |\vec{u}| \rangle \quad (6.38a)$$

$$\int_{-L/2}^{L/2} v \, dx \Big|_{y=-H/2} = \int_{-L/2}^{L/2} v \, dx \Big|_{y=H/2} = L \cos \beta \langle |\vec{u}| \rangle \quad (6.38b)$$

$$\int_{-H/2}^{H/2} \int_{-L/2}^{L/2} w \, dx \, dy = LH \cos \gamma \langle |\vec{u}| \rangle \quad (6.38c)$$

$$(T - T_w)|_{x=L/2} = \tau_0^{(L \cos \alpha)/(L \cos \alpha + H \cos \beta)} (T - T_w)|_{x=-L/2} \quad (6.39a)$$

$$(T - T_w)|_{y=H/2} = \tau_0^{(H \cos \beta)/(L \cos \alpha + H \cos \beta)} (T - T_w)|_{y=-H/2} \quad (6.39b)$$

In this way, all derivatives associated with z can be eliminated. Thus, only two-dimensional storages are required to solve Eqs. (6.29) to (6.33). (Note that both Eqs. (6.32) and (6.33) may be treated as two-dimensional scalar transport equation.)

6.6 Method of Computation and Preliminary Numerical Consideration

The governing equations (6.29) to (6.31) subject to the foregoing boundary and compatibility conditions (6.37a), (6.37b), (6.38a), and (6.38b) were numerically

solved using SIMPLE algorithm proposed by Patankar and Spalding [20]. As the u and v velocity fields were established, the remaining equations (6.32) and (6.33) subject to the boundary conditions (6.37c), (6.38c), (6.39a), and (6.39b) were solved to find w and T . Convergence was measured in terms of the maximum change in each variable during an iteration. The maximum change allowed for the convergence check was set to 10^{-5} , as the variables are normalized by appropriate references. The hybrid scheme has been adopted for the advection terms. Further details on this numerical procedure can be found in Patankar [21] and Nakayama et al. [22]. For the cases of square cylinder banks, all computations have been carried out for a one structural unit $L \times H$, as indicated by dashed lines in Figure 6.3(b), using nonuniform grid arrangements with 91×91 , after comparing the results against those obtained with 181×181 for some selected cases, and confirming that the results are independent of the grid system. All computations were performed using the computer system at Shizuoka University Computer Center.

In order to confirm the validity of the present numerical procedure based on the periodic boundary conditions, preliminary computations were also conducted for the case of forced convection from isothermal parallel plates with a channel height H , as shown in Figure 6.2. Since $\alpha = 0$, $\beta = \gamma = \pi/2$ for this case, we find $w = S_w = 0$, and

$$Nu_{2H} = \frac{h_f(2H)}{k_f} = \frac{\rho c_p f u_B H^2}{L k_f} \ln \left(\frac{1}{\tau_0} \right) \quad (6.40)$$

from Eqs. (6.18) and (6.39a). The computations were made for $10 \leq Re_{2H} \leq 10^3$ and $Pr = 1$, and the numerical results for Nu_{2H} are presented in Figure 6.4. The predicted Nusselt number attains its fully developed value, namely, $Nu_{2H} = 7.54$, which coincides with the exact solution.

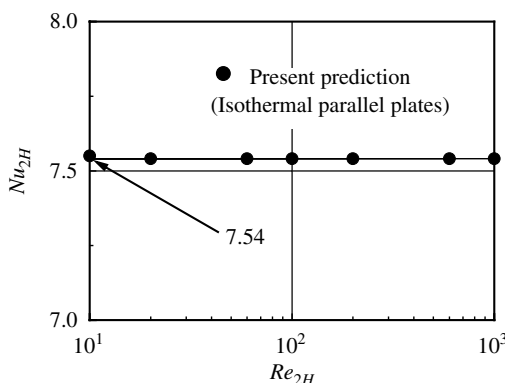


FIGURE 6.4

Fully developed Nusselt number in a channel.

6.7 Validation of Quasi-Three-Dimensional Calculation Procedure

The efficiency and accuracy of the quasi-three-dimensional calculation procedure, proposed for the two-dimensional structure, may be examined by comparing the results based on the procedure with those based on the full three-dimensional calculation procedure. Extensive calculations have been carried out using the full three-dimensional governing equations (6.21) to (6.23) for macroscopically uniform flow through a bank of square cylinders in yaw, as illustrated in [Figure 6.3\(b\)](#).

Computations may be made using the dimensionless equations based on the absolute value of the Darcian velocity vector $|\langle \vec{u} \rangle|$, and the longitudinal center-to-center distance L as reference scales. For carrying out a series of numerical calculations, it may be convenient to use the Reynolds number based on L as $Re_L = |\langle \vec{u} \rangle|L/v_f$, which can readily be translated into the Reynolds number based on the size of square rod D as follows:

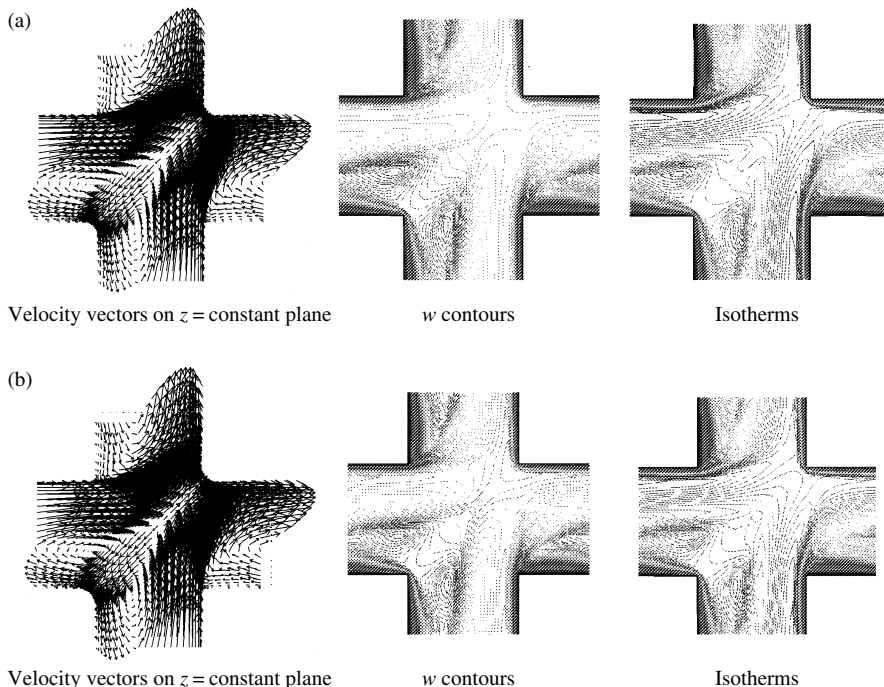
$$Re_D = |\langle \vec{u} \rangle|D/v_f = \left((1 - \phi) \frac{H}{L} \right)^{1/2} Re_L \quad (6.41)$$

where the porosity is given by

$$\phi = 1 - (D^2/HL) \quad (6.42)$$

In this numerical experiment, the Reynolds number is varied from 10^{-2} to 6×10^3 , as in the study for the cross-flows (i.e., with $\gamma = \pi/2$) [10]. For this time, both cross-flow angle α' and yaw angle γ are varied from 0 to $\pi/2$ with an increment $\pi/36$ to cover all possible macroscopic flow directions in the three-dimensional space, such that entire solution surfaces may be constructed over the domain $0 \leq \alpha' \leq \pi/2$ and $0 \leq \gamma \leq \pi/2$. Moreover, the ratio H/L is set to 1, $\frac{3}{2}$, and 2 to investigate the effects of the degree of the anisotropy, whereas the ratio D/L is fixed to $\frac{1}{2}$ for all calculations.

In [Figures 6.5](#), the resulting velocity and temperature fields obtained for the case of $H/L = 1$, $\alpha' = 45^\circ$, $\gamma = 45^\circ$, $Re_L = 600$, and $Pr = 1$ using the full three-dimensional calculation procedure ([Figure 6.5\[a\]](#)) are compared with those based on the quasi-three-dimensional calculation procedure based on the simplified governing equations (6.29) to (6.33) ([Figure 6.5\[b\]](#)). Excellent agreement between the two sets of the results can be seen, which verifies the accuracy and efficiency of the proposed quasi-three-dimensional calculation procedure. The CPU time required for the convergence using the full three-dimensional calculation turned out to be roughly 3 h, 6 times more than that using the quasi-three-dimensional calculation. This proves the effectiveness of the quasi-three-dimensional calculation procedure.

**FIGURE 6.5**

Comparison of two distinct three-dimensional calculation procedures ($H/L = 1$, $\alpha' = 45^\circ$, $\gamma = 45^\circ$, $Re_L = 600$, $Pr = 1$). (a) Results based on the full three-dimensional calculation procedure. (b) Results based on the quasi-three-dimensional calculation procedure.

This economical quasi-three-dimensional calculation procedure has been used to conduct a numerical experiment for macroscopically uniform flow through a bank of square cylinders in yaw over a wide range of the Reynolds number and flow angle.

6.8 Determination of Permeability Tensor

The gradient of the intrinsic average pressure may readily be evaluated using the microscopic results as

$$\begin{aligned}
 -\frac{\partial \langle p \rangle^f}{\partial s} &= \frac{\cos \alpha}{L(H-D)} \int_{-(H-D)/2}^{(H-D)/2} (p|_{x=-L/2} - p|_{x=L/2}) dy \\
 &+ \frac{\cos \beta}{H(L-D)} \int_{-(L-D)/2}^{(L-D)/2} (p|_{y=-H/2} - p|_{y=H/2}) dy + \frac{\mu \cos \gamma}{(HL-D^2)} \oint_{P_f} \frac{\partial w}{\partial n} dP
 \end{aligned} \quad (6.43)$$

When the velocity (i.e., Reynolds number) is low, the proposed model equation (6.11) reduces to Darcy's law as

$$-\frac{\partial \langle p \rangle^f}{\partial x_i} = \left(\mu_f K_{fij}^{-1} + \rho_f b_{fij} |\langle \vec{u} \rangle| \right) \langle u_j \rangle \cong \mu_f K_{fij}^{-1} \langle u_j \rangle \quad (6.44)$$

For the orthotropic media, the permeability tensor may be modeled following Dullien [23] as

$$K_{fij}^{-1} = (l_i l_j) / K_{f1} + (m_i m_j) / K_{f2} + (n_i n_j) / K_{f3} \quad (6.45)$$

such that

$$-\frac{\partial \langle p \rangle^f}{\partial x_i} \cong \mu_f K_{fij}^{-1} \langle u_j \rangle = \left(\frac{\cos \alpha}{K_{f1}} l_i + \frac{\cos \beta}{K_{f2}} m_i + \frac{\cos \gamma}{K_{f3}} n_i \right) |\langle \vec{u} \rangle| \quad (6.46)$$

where

$$\cos \alpha = \frac{l_j \langle u_j \rangle}{|\langle \vec{u} \rangle|}, \quad \cos \beta = \frac{m_j \langle u_j \rangle}{|\langle \vec{u} \rangle|}, \quad \cos \gamma = \frac{n_j \langle u_j \rangle}{|\langle \vec{u} \rangle|} \quad (6.47)$$

Thus, the directional permeability measured along the macroscopic flow direction s is given by

$$\frac{1}{K_{fn}} = \frac{\cos^2 \alpha}{K_{f1}} + \frac{\cos^2 \beta}{K_{f2}} + \frac{\cos^2 \gamma}{K_{f3}} \quad (6.48)$$

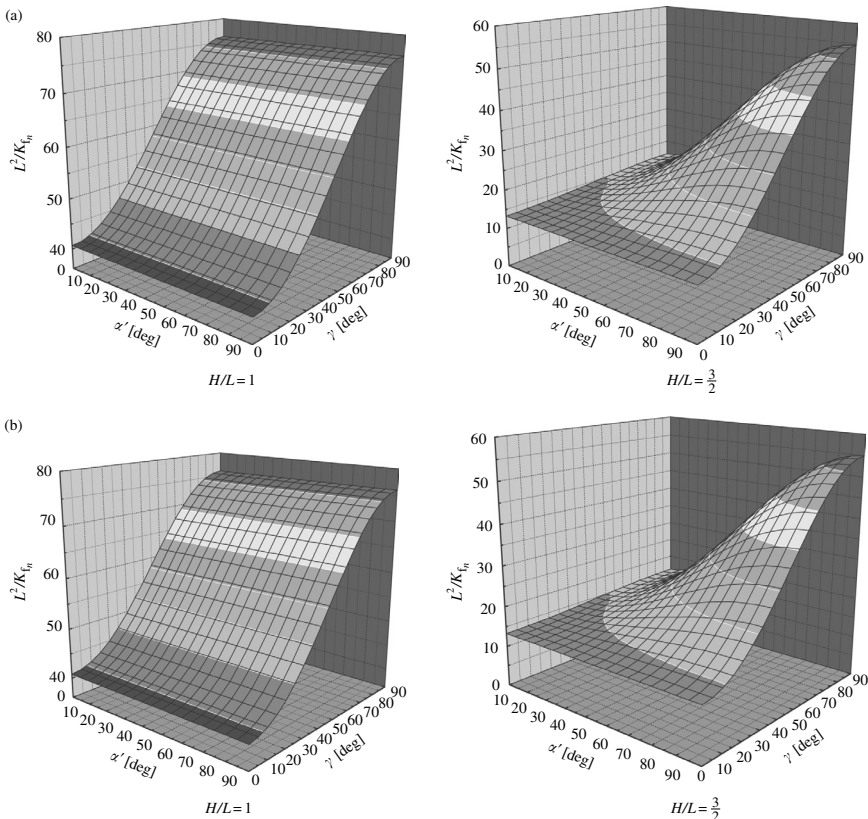
such that

$$-\frac{\partial \langle p \rangle^f}{\partial s} = \frac{\mu_f}{K_{fn}} |\langle \vec{u} \rangle| \quad (6.49)$$

or, in dimensionless form, as

$$-\frac{\partial \langle p \rangle^f}{\partial s} \frac{L^2}{\mu_f |\langle \vec{u} \rangle|} = \frac{L^2}{K_{fn}} \quad (6.50)$$

Thus, the directional permeability K_{fn} may readily be determined by reading the intercept of the ordinate variable, as we plot $-(\partial \langle p \rangle^f / \partial s) (L^2 / \mu_f |\langle \vec{u} \rangle|)$ against Re_L , as done in the study on the cross-flow case [10]. The solution surfaces of the directional permeability are constructed using the numerical values and presented in terms of L^2 / K_{fn} against the projected angle α' and the yaw angle γ for the cases of $H/L = 1$ and $\frac{3}{2}$ in Figure 6.6(a). The solution surface changes drastically as the ratio H/L departs from unity. It is interesting to note that the effect of the projected angle α' on the directional permeability is

**FIGURE 6.6**

Solution surfaces for directional permeability; (a) numerical experiments, $H/L = 1$, $H/L = \frac{3}{2}$, (b) correlations, $H/L = 1$, $H/L = \frac{3}{2}$.

TABLE 6.1

Coefficients for Macroscopic Pressure Gradient

$H/L (\phi)$	L^2/K_{f_1}	L^2/K_{f_2}	L^2/K_{f_3}	$b_{f_1}L$	$b_{f_2}L$	$bb_{f_1}L$
1 (0.750)	76	76	41	0.2	0.2	8.2
$\frac{3}{2}$ (0.833)	16	55	13	0.1	0.6	3.2
2 (0.875)	7	42	6	0.05	0.8	1.2

totally absent for the arrangement $H/L = 1$. The coefficients K_{f_1} , K_{f_2} , and K_{f_3} in the proposed expression (6.48) may be determined by fitting the numerical results against the solution surfaces based on Eq. (6.48). Such solution surfaces generated by the proposed Eq. (6.48) are presented in Figure 6.6(b) for comparison. The numerical values of K_{f_1} , K_{f_2} , and K_{f_3} determined in this manner are listed in Table 6.1. The validity of the proposed Eq. (6.48) with

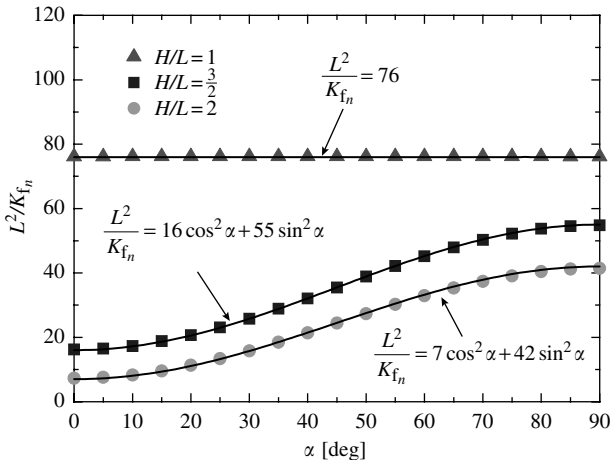


FIGURE 6.7
Directional permeability at $\gamma = \pi/2$.

the values listed in Table 6.1 can be examined further by plotting L^2/K_{f_n} as shown in Figure 6.7 for the case of $\gamma = \pi/2$, where the fluid flows perpendicularly to the rods. It is seen that the numerical results closely follow the curves generated from Eq. (6.48).

6.9 Determination of Forchheimer Tensor

When the velocity (i.e., Reynolds number) is sufficiently high, the inertial Forchheimer term describing the form drag predominates over the Darcy term such that

$$-\frac{\partial \langle p \rangle^f}{\partial x_i} = \left(\mu_f K_{fij}^{-1} + \rho_f b_{fij} |\langle \vec{u} \rangle| \right) \langle u_j \rangle \cong \rho_f b_{fij} |\langle \vec{u} \rangle| \langle u_j \rangle \quad (6.51)$$

Usually, the principal axes of the permeability tensor K_{fij}^{-1} do not coincide with those of the inertial Forchheimer tensor b_{fij} . For the orthotropic media in consideration, however, the tensors b_{fij} should be symmetric, and hence, they must satisfy the following symmetric conditions:

$$\frac{\partial b_{f_n}}{\partial \alpha} \Big|_{\alpha=0, \pi/2} = \frac{\partial b_{f_n}}{\partial \beta} \Big|_{\beta=0, \pi/2} = \frac{\partial b_{f_n}}{\partial \gamma} \Big|_{\gamma=0, \pi/2} = 0 \quad (6.52)$$

where

$$b_{f_n} \equiv b_{f_{ij}} \frac{\langle u_i \rangle \langle u_j \rangle}{|\langle \vec{u} \rangle|^2} \quad (6.53)$$

is the directional Forchheimer coefficient measured along the macroscopic flow direction s . One of the simplest functions that satisfy these conditions may be:

$$\begin{aligned} b_{f_{ij}} = & b_{f_1}(l_i l_j) + b_{f_2}(m_i m_j) + b_{f_3}(n_i n_j) + b b_{f1} \cos \alpha \cos \beta ((l_i m_j) + (l_j m_i)) \\ & + b b_{f2} \cos \beta \cos \gamma ((m_i n_j) + (m_j n_i)) + b b_{f3} \cos \gamma \cos \alpha ((n_i l_j) + (n_j l_i)) \end{aligned} \quad (6.54)$$

which results in

$$\begin{aligned} b_{f_n} = & b_{f_1} \cos^2 \alpha + b_{f_2} \cos^2 \beta + b_{f_3} \cos^2 \gamma + 2 b b_{f1} \cos^2 \alpha \cos^2 \beta \\ & + 2 b b_{f2} \cos^2 \beta \cos^2 \gamma + 2 b b_{f3} \cos^2 \gamma \cos^2 \alpha \end{aligned} \quad (6.55)$$

such that

$$-\frac{\partial \langle p \rangle^f}{\partial s} = \frac{\mu_f}{K_{f_n}} |\langle \vec{u} \rangle| + \rho_f b_{f_n} |\langle \vec{u} \rangle|^2 \quad (6.56)$$

or, in dimensionless form, as

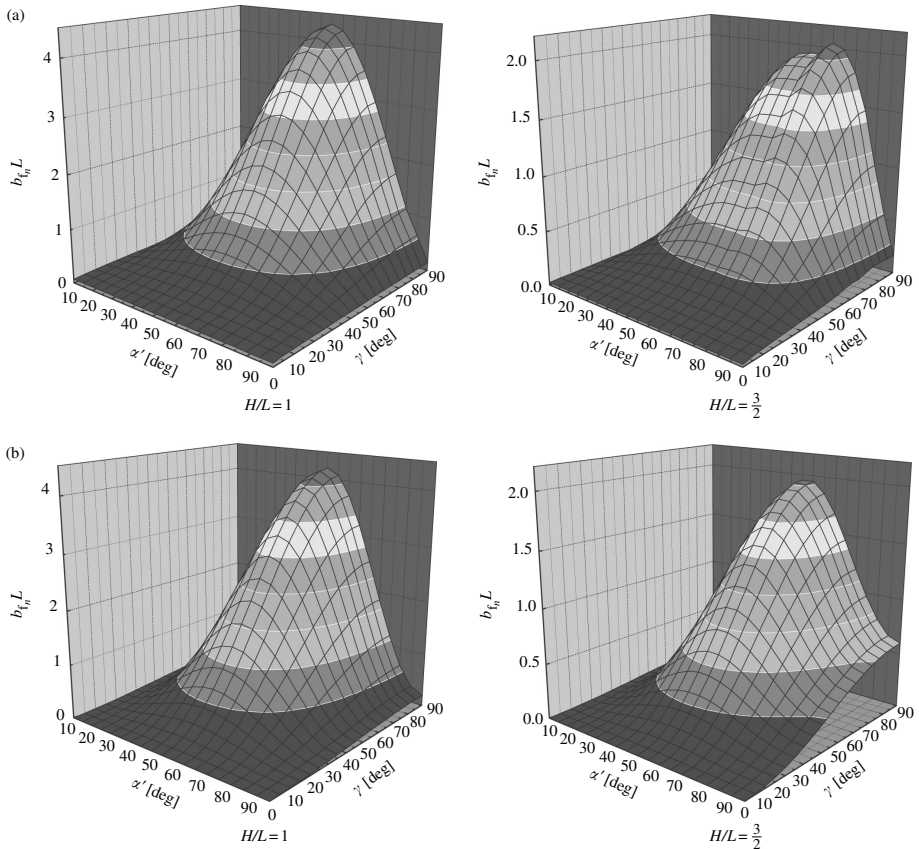
$$-\frac{\partial \langle p \rangle^f}{\partial s} \frac{L}{\rho_f |\langle \vec{u} \rangle|^2} = \frac{L^2}{K_{f_n} Re_L} + b_{f_n} L \quad (6.57)$$

Plotting the results of macroscopic pressure gradient in terms of $-(\partial \langle p \rangle^f / \partial s)(L / \rho_f |\langle \vec{u} \rangle|^2)$ and reading the horizontal asymptotes, we can readily determine the directional Forchheimer constant.

The numerical values of the directional Forchheimer constant for the cases of $H/L = 1$ and $\frac{3}{2}$ are shown in terms of the solution surfaces of $b_{f_n} L$ in [Figure 6.8\(a\)](#). These figures clearly show that, for fixed γ , the directional Forchheimer constant attains its peak around $\alpha' = \pi/2$, while, for fixed α' , it decreases monotonically from $\gamma = \pi/2$ to 0.

From this observation, we find that the coefficients and $b b_{f1}$ is nonzero while b_{f_3} , $b b_{f2}$, and $b b_{f3}$ in Eq. (6.55) should vanish for the bank of cylinders, such that

$$\begin{aligned} b_{f_n} = & b_{f_1} \cos^2 \alpha + b_{f_2} \cos^2 \beta + 2 b b_{f1} \cos^2 \alpha \cos^2 \beta \\ = & (b_{f_1} \cos^2 \alpha' + b_{f_2} \sin^2 \alpha' + 2 b b_{f1} \cos^2 \alpha' \sin^2 \alpha' \sin^2 \gamma) \sin^2 \gamma \end{aligned} \quad (6.58)$$

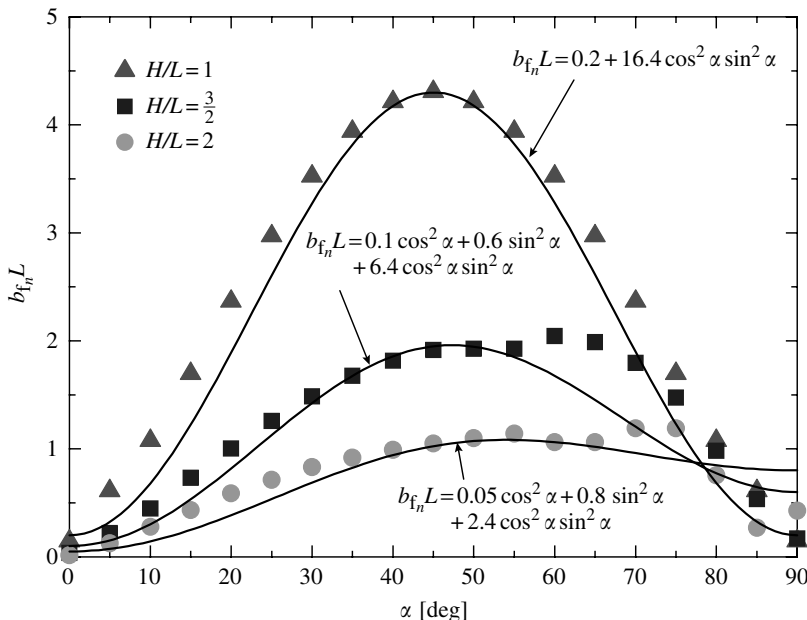
**FIGURE 6.8**

Solution surfaces for directional Forchheimer coefficient; (a) numerical experiments, $H/L = 1$, $H/L = \frac{3}{2}$, (b) correlations, $H/L = 1$, $H/L = \frac{3}{2}$.

The corresponding $b_{f_n}L$ surfaces based on the proposed expression (6.58) with the values of b_{f_1} , b_{f_2} , and bb_{f_1} as listed in Table 6.1 are presented in Figure 6.8(b) for comparison. Furthermore, the numerical results of the directional Forchheimer constant obtained with $\gamma = \pi/2$ for $H/L = 1$, $\frac{3}{2}$, and 2 are presented in Figure 6.9 as a function of the cross-flow angle $\alpha (= \alpha')$. In the same figure, the solid curves generated from the proposed Eq. (6.58) are presented to elucidate the validity of the proposed expression. Note that, for this case of $\gamma = \pi/2$, the foregoing equation reduces to

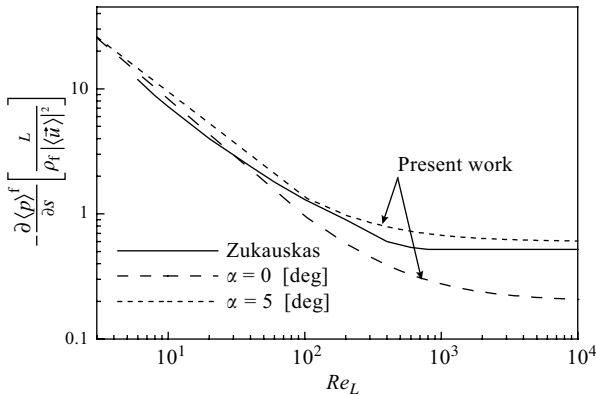
$$b_{f_n} = b_{f_1} \cos^2 \alpha + b_{f_2} \sin^2 \alpha + 2bb_{f_1} \cos^2 \alpha \sin^2 \alpha \quad (6.59)$$

It is interesting to note that the numerical results for the cases $H/L = \frac{3}{2}$ and 2 show two consecutive peaks, while the model Eq. (6.59) yields only one

**FIGURE 6.9**Directional Forchheimer coefficient at $\gamma = \pi/2$.

peak (the first peak). The second peak appears when the macroscopic flow angle, α , reaches roughly $\tan^{-1}(H/L)$. Note that, for the case of $H/L = 1$, this second peak coincides with the first one. Unfortunately, the model equation is incapable of describing the second peak.

Zukauskas [24] assembled the experimental data for the fully developed pressure drop across the tube banks in both inline-square and staggered-triangle arrangements, and presented a chart for the Euler number (i.e., the dimensionless macroscopic pressure drop over a unit). His inline-square arrangement corresponds to the present arrangement with $\alpha = 0$, $\gamma = \pi/2$, and $L/D = 2$. However, it is noted that, in reality, the macroscopic flow direction rarely coincides with the principal axes, since even small disturbances at a sufficiently high Reynolds number deviate the flow from the axis. Thus, it is understood that the chart provided by Zukauskas gives only the average level of the pressure drop within a range of small α (say $0^\circ < \alpha < 5^\circ$). The dimensionless macroscopic pressure gradient $-(\partial \langle p \rangle^f / \partial s)(L/\rho_f |\langle \vec{u} \rangle|^2)$ for the case of $\gamma = \pi/2$ and $L/D = 2$ is plotted against Re_L in Figure 6.10, where the curves generated from the model Eq. (6.57) with the numerical values taken from Table 6.1 and Figure 6.9 (note that $b_{f_n}L = 0.2$ and 0.6, for $\alpha = 0^\circ$ and 5° , respectively) are drawn together with the empirical chart provided by Zukauskas for the inline-square arrangement. The agreement between these curves appears fairly good.

**FIGURE 6.10**

Dimensionless macroscopic pressure gradient.

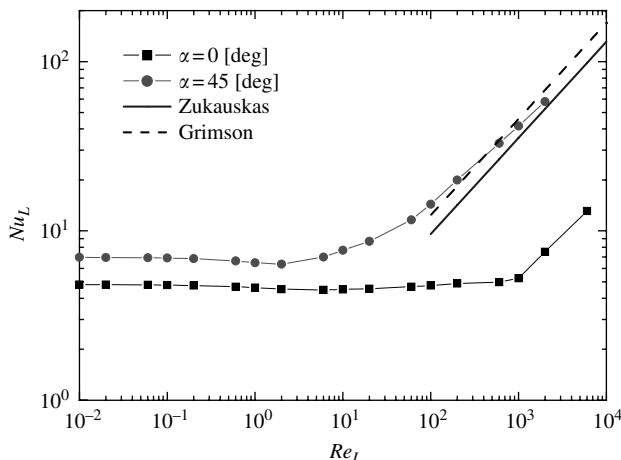
6.10 Determination of Interfacial Heat Transfer Coefficient

The interfacial heat transfer coefficient as defined by Eq. (6.6) may be obtained by substituting the microscopic temperature results into the following equation:

$$h_f \equiv \frac{(1/V) \int_{A_{\text{int}}} k_f \nabla T \cdot d\vec{A}}{(\langle T \rangle^s - \langle T \rangle^f)} = \frac{\frac{1}{A_{\text{fluid}}} \oint_{P_{\text{int}}} (-k_f (\partial T / \partial n)) dP}{(\langle T \rangle^s - \langle T \rangle^f)} \quad (6.60)$$

where A_{int} is the total interface between the fluid and solid, while $d\vec{A}$ is its vector element pointing outward from the fluid to solid side. In Figure 6.11, the heat transfer results obtained at $\alpha = 0$ and $\pi/4$ for the cross-flows (i.e., $\gamma = \pi/2$) are presented in terms of the interfacial Nusselt number $Nu_L = h_f L / k_f$ against the Reynolds number Re_L . The figure suggests that the lower and higher Reynolds number data follow two distinct limiting lines for the case of nonzero α , namely, $\alpha = \pi/4$. The lower Reynolds number data stay constant for the given array and flow angle, whereas the high Reynolds number data vary in proportion to $Re_L^{0.6}$.

Another series of computations changing the Prandtl number, conducted following Kuwahara et al. [19], revealed that the exponents associated with the Reynolds and Prandtl numbers are the same as those Wakao and Kaguei [25] observed as collecting and scrutinizing reliable experimental data on interfacial convective heat transfer coefficients in packed beds. The similarity, albeit the difference in the Reynolds number dependence, between the Nusselt number Nu_L and the macroscopic pressure gradient as given by Eq. (6.56) is noteworthy, which prompts us to model the directional Nusselt

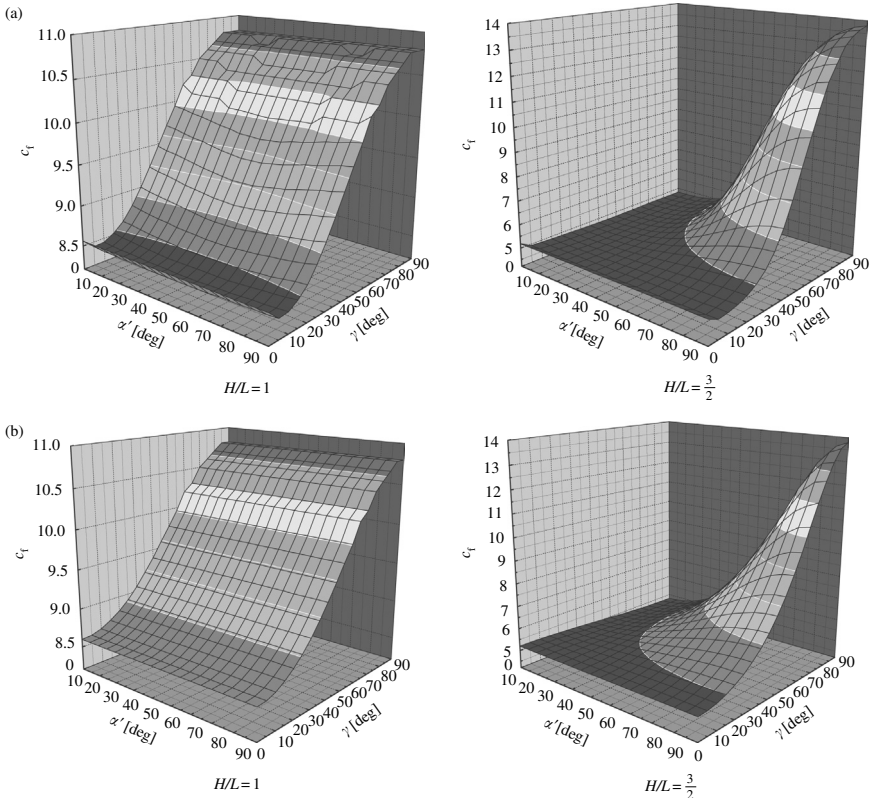
**FIGURE 6.11**Effect of Reynolds number on directional Nusselt number ($Pr = 1$).

number as follows:

$$Nu_L \equiv \frac{h_f L}{k_f} = c_f + d_f Re_L^{0.6} Pr_f^{1/3} \quad (6.61)$$

In the figure, the experimental correlation proposed by Zukauskas [26] for the heat transfer from the circular tubes in staggered banks is compared with the present results obtained for the case of $\alpha = \pi/4$, $\gamma = \pi/2$, and $H/L = 1$. (Note $Nu_f \cong Nu_L/2$ and $Re_f \cong Re_L$ in Eq. (6.39) of Zukauskas since $D/L = \frac{1}{2}$.) The present results follow closely along the experimental correlation of Zukauskas as increasing the Reynolds number. Grimson [27] carried out an exhaustive experiment to investigate heat transfer from tube rows of a bank in both staggered and aligned arrangements with respect to the direction of the macroscopic flow. His case, in which the ratio of the transverse pitch to tube diameter and that of the longitudinal pitch to tube diameter are 3 and 1.5, respectively, gives a configuration close to the present orthogonal configuration with $\alpha = \pi/4$, $\gamma = \pi/2$, and $H/L = 1$. Thus, the experimental correlation established by Grimson for the case is also presented in the figure, which agrees very well with the present numerical results. These correlations are believed to hold for a comparatively wide Reynolds number range, covering from a predominantly laminar flow regime to turbulent flow regime.

Following the procedure similar to the one adopted for determining the directional permeability, the coefficient $c_f \equiv Nu_L|_{Re_L \rightarrow 0}$ for each macroscopic flow angle is evaluated and plotted in terms of the solution surfaces in Figure 6.12(a), using the low Reynolds number data. It is noted that the effect of the projected angle α' on the interfacial heat transfer coefficient is totally absent for the arrangement $H/L = 1$.

**FIGURE 6.12**

Solution surfaces for directional heat transfer coefficient at small Reynolds number; (a) numerical experiments, $H/L = 1$, $H/L = \frac{3}{2}$, (b) correlations, $H/L = 1$, $H/L = \frac{3}{2}$.

The similarity between the solution surfaces of c_f and those of L^2/K_{f_n} is obvious, which leads us to introduce a functional form as follows:

$$c_f = \left(c_{f_1}^{n_c} \cos^2 \alpha + c_{f_2}^{n_c} \cos^2 \beta + c_{f_3}^{n_c} \cos^2 \gamma \right)^{1/n_c} \quad (6.62)$$

such that c_f reduces to c_{f_1} , c_{f_2} , and c_{f_3} for $\alpha = 0$, $\beta = 0$, and $\gamma = 0$, respectively, as it should.

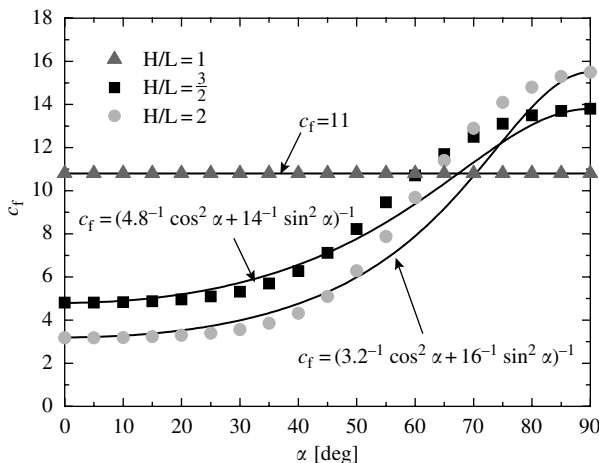
Careful examination of the numerical results over the whole domain within $0 \leq \alpha' \leq \pi/2$ and $0 \leq \gamma \leq \pi/2$ suggests that n_c is close to minus one, which leads us to a harmonic mean expression as

$$\frac{1}{c_f} = \frac{\cos^2 \alpha}{c_{f_1}} + \frac{\cos^2 \beta}{c_{f_2}} + \frac{\cos^2 \gamma}{c_{f_3}} \quad (6.63)$$

TABLE 6.2

Coefficients for Directional Nusselt Number

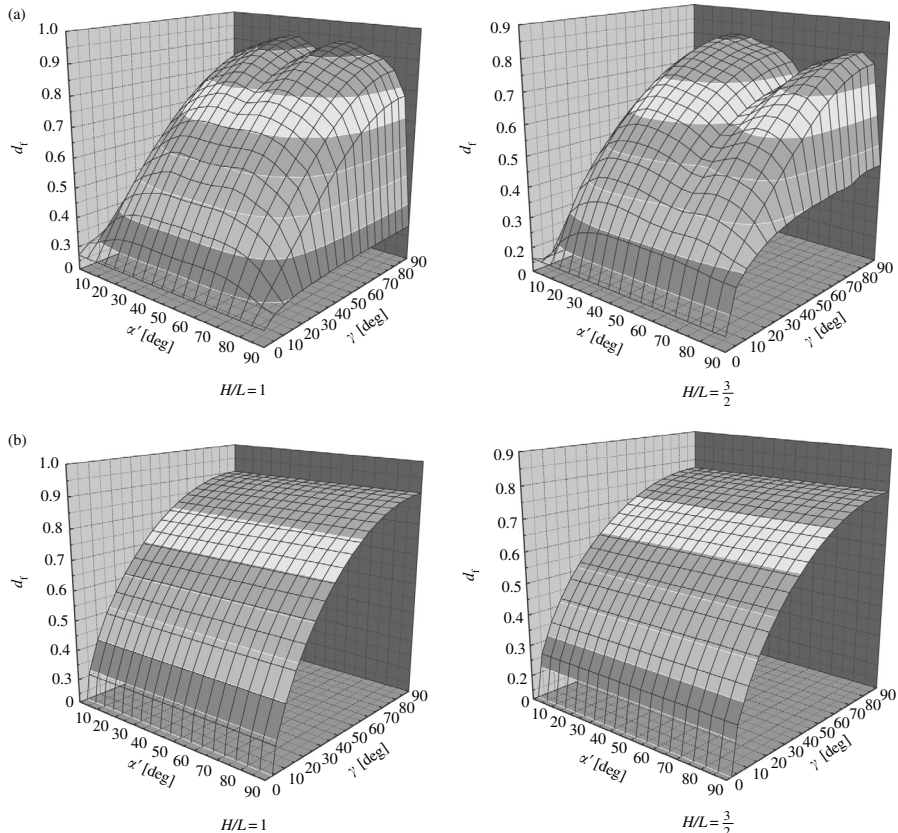
$H/L (\phi)$	c_{f_1}	c_{f_2}	c_{f_3}	n_c	$d_{f_1} = d_{f_2}$	n_d
1 (0.750)	11	11	8.6	-1.0	0.90	4.5
$\frac{3}{2}$ (0.833)	4.8	14	5.2	-1.0	0.77	4.5
2 (0.875)	3.2	16	3.6	-1.0	0.67	4.5

**FIGURE 6.13**Effect of the cross-flow angle α on the coefficient c_f at $\gamma = \pi/2$.

The values of c_{f_1} , c_{f_2} , and c_{f_3} listed in Table 6.2 have been determined by fitting the numerical results against the foregoing equation. The resulting surfaces based on the proposed expression (6.63) are presented in Figure 6.12(b) for their comparison with the surfaces based on the numerical experiments shown in Figure 6.12(a). Furthermore, Figure 6.13 shows the numerical results of c_f obtained at $\gamma = \pi/2$ for the three distinct arrangements, namely, $H/L = 1, \frac{3}{2}$, and 2. The solid curves in the figure are generated from the proposed Eq. (6.63) with the values of c_{f_1} and c_{f_2} as listed in Table 6.2.

The second coefficient d_f may be determined using the data $Nu_L/Re_L^{0.6} Pr_f^{1/3}$ in the high Reynolds number range. The resulting solution surfaces of d_f are presented in Figure 6.14 for $H/L = 1$ and $\frac{3}{2}$. Unlike the Forchheimer coefficient b_{f_n} , the coefficient d_f stays roughly constant for a fixed yaw angle γ .

More careful observation on the solution surfaces reveals that the coefficient d_f drops abruptly as the projected angle α' reaches close to either 0 or $\pi/2$ (in which the fluid flows along the principal axis of the structure). However, as already pointed out, it is quite unlikely to have the macroscopic flow align perfectly with the principal axes. Thus, we may assume that d_f is the function

**FIGURE 6.14**

Solution surfaces for directional heat transfer coefficient at large Reynolds number; (a) numerical experiments, $H/L = 1$, $H/L = \frac{3}{2}$, (b) correlations, $H/L = 1$, $H/L = \frac{3}{2}$.

of the yaw angle γ alone, namely, $d_f = d_f(\gamma)$. It is interesting to note that $d_f = d_f(\gamma)$ is consistent with the idea of the effective velocity $u_{\text{eff}} = |\langle \vec{u} \rangle| \sin \gamma$ used in the hot-wire anemometry. Thus, we may model d_f as

$$d_f = \left(d_{f_1}^{n_d} \sin^2 \gamma + d_{f_3}^{n_d} \cos^2 \gamma \right)^{1/n_d} \quad (6.64)$$

A careful observation on the solution surfaces leads us to $d_{f_3} \cong 0$, and also reveals the values of d_{f_1} and n_d as listed in Table 6.2. Thus, we propose the expression as follows:

$$Nu_L = \left(c_{f_1}^{n_c} \cos^2 \alpha + c_{f_2}^{n_c} \cos^2 \beta + c_{f_3}^{n_c} \cos^2 \gamma \right)^{1/n_c} + d_{f_1} \sin^{2/n_d} \gamma Re_L^{0.6} Pr_f^{1/3} \quad (6.65a)$$

or

$$Nu_D = \frac{1}{2} \left(c_{f_1}^{n_c} \cos^2 \alpha + c_{f_2}^{n_c} \cos^2 \beta + c_{f_3}^{n_c} \cos^2 \gamma \right)^{1/n_c} + \frac{d_{f_1}}{20.4} \sin^{2/n_d} \gamma Re_D^{0.6} Pr_f^{1/3} \quad (6.65b)$$

Note that the exponents $n_c = -1$ and $n_d = \frac{9}{2}$ irrespectively of the value of H/L , while the coefficients $c_{f_1}, c_{f_2}, c_{f_3}$, and d_{f_1} depend on that particular geometrical configuration.

Zukauskas [24] investigated the effect of the yaw angle on the interfacial heat transfer rate. He varied the yaw angle γ for both staggered and aligned arrangements, and compared the corresponding heat transfer rates for the same Reynolds number. He pointed out that the data when normalized by the value obtained at $\gamma = \pi/2$ for all staggered and inline arrangements, namely, $Nu_D/Nu_D|_{\gamma=\pi/2}$, can be approximated by a single curve irrespective of the Reynolds number. His data for both staggered and inline arrangements are plotted in Figure 6.15 together with the expression based on the model Eq. (6.65b), namely,

$$\frac{Nu_D}{Nu_D|_{\gamma=\pi/2}} \cong \sin^{2/n_d} \gamma = \sin^{4/9} \gamma \quad (6.66)$$

for the case of sufficiently high Reynolds number. The agreement between the experimental data and the curve based on Eq. (6.66) is fairly good, which indicates the validity of the model Eq. (6.65b). It should also be noted that the staggered arrangement corresponds to the case of $\alpha' = \pi/4$ while the inline arrangement to the case in which α' is close to zero (but $\alpha' \neq 0$ since the macroscopic flow direction never coincides with the principal axis of the

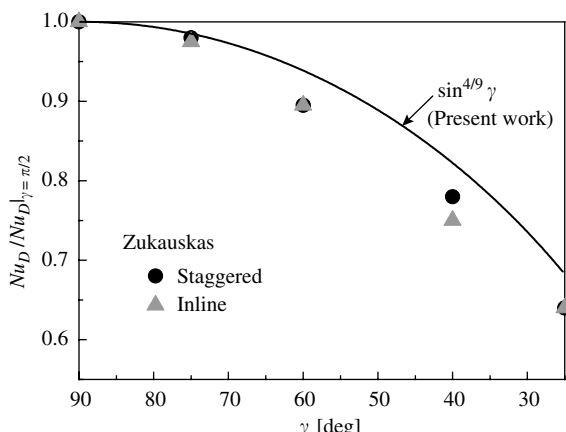


FIGURE 6.15

Effect of the yaw angle γ on the interfacial Nusselt number.

structure). Thus, these experimental data substantiates our finding based on the numerical experiment, namely, that the multiplicative constant for the interfacial Nusselt number d_f stays virtually constant (irrespective of α') for a fixed yaw angle, as illustrated by the solution surfaces in [Figure 6.14](#).

6.11 Conclusions

A numerical modeling strategy for dealing with three-dimensional flow and heat transfer within highly anisotropic porous media has been proposed to attack complex fluid flow and heat transfer associated with heat transfer equipment. An appropriate set of the periodic boundary conditions has been derived appealing to the concept of VAT, and applying it to a macroscopically uniform flow through an isothermal porous medium of infinite extent. For three-dimensional heat and fluid flow through a two-dimensional structure, a quasi-three-dimensional calculation procedure is found possible. The procedure can be exploited to investigate three-dimensional heat and fluid flow through a bank of cylinders in yaw, which represents a numerical model for manmade structures such as plate-fin heat exchangers. Only one structural unit was taken as a calculation domain, noting the periodicity of the structure. This inexpensive and yet efficient numerical calculation procedure based on one structural unit along with periodic boundary conditions was employed to conduct extensive three-dimensional calculations for a number of sets of the porosity, degree of anisotropy, Reynolds number, Prandtl number, and macroscopic flow direction. The numerical results, thus obtained at the pore level, were integrated over a structural unit to determine the permeability tensor, Forchheimer tensor, and interfacial heat transfer coefficient, so as to elucidate the effects of yaw angle on these macroscopic flow and heat transfer characteristics. Upon examining these numerical experimental data, a useful set of explicit expressions for the permeability tensor, Forchheimer tensor, and interfacial heat transfer coefficient have been established for the first time, such that one can easily evaluate the pressure drop and heat transfer rate from the bank of cylinders in yaw. The systematic modeling procedure proposed in this study can be utilized to conduct subscale modeling of manmade structures needed in the possible applications of a VAT to investigate flow and heat transfer within complex heat and fluid flow equipment consisting of small elements.

Nomenclature

- \vec{A} surface area vector
 A_{int} total interface between the fluid and solid

$b_{f_{ij}}, b_{f_n}$	Forchheimer coefficient tensor, directional Forchheimer coefficient
c_p	specific heat capacity at constant pressure
c_f, d_f	coefficients associated with directional Nusselt number
D	size of square rod
H, L	size of structural unit
h_f	interfacial convective heat transfer coefficient
k_f	thermal conductivity
$K_{f_{ij}}, K_{f_n}$	permeability tensor, directional permeability
Pr_f	Prandtl number
u, v, w	microscopic velocity components in the x, y , and z directions
T	microscopic temperature
p	microscopic pressure
Re_L	Reynolds number based on L and the Darcian velocity
Re_D	Reynolds number based on D and the Darcian velocity
V	elementary representative volume
x, y, z	Cartesian coordinates
α, β, γ	angles between the macroscopic velocity vector and principal axes
α'	projected angle, cross-flow angle
ν_f	kinematic viscosity
ρ_f	density
μ_f	viscosity
ϕ	porosity

Subscripts and superscripts

f	fluid
s	solid

Special symbols

$\langle \rangle$	volume-average
$\langle \rangle^{f,s}$	intrinsic average

References

1. A. Nakayama, F. Kuwahara, A. Naoki, and G. Xu. A volume averaging theory and its sub-control-volume model for analyzing heat and fluid flow within complex heat transfer equipment. *Proceedings of 12th International Heat Transfer Conference*, Grenoble, 2002, pp. 851–856.
2. V.S. Travkin and I. Catton. Transport phenomena in heterogeneous media based on volume averaging theory. *Adv. Heat Transfer*, 34: 1–133, 2001.
3. P. Cheng. Heat transfer in geothermal systems. *Adv. Heat Transfer*, 14: 1–105, 1978.

4. K. Vafai and C.L. Tien. Boundary and inertia effects on flow and heat transfer in porous media. *Int. J. Heat Mass Transfer*, 24: 195–203, 1981.
5. A. Nakayama. *PC-Aided Numerical Heat Transfer and Convective Flow*. Boca Raton, FL: CRC Press, 1995, pp. 103–176.
6. A. Nakayama and F. Kuwahara. A macroscopic turbulence model for flow in a porous medium. *J. Fluids Eng.*, 121: 427–433, 1999.
7. A. Nakayama, F. Kuwahara, A. Naoki, and G. Xu. A three-energy equation model based on a volume averaging theory for analyzing complex heat and fluid flow in heat exchangers. *Proceedings of International Conference on Energy Conversion and Application*, Wuhan, China, 2001, pp. 506–512.
8. F. Kuwahara, A. Nakayama, and H. Koyama. Numerical modeling of heat and fluid flow in a porous medium. *Proceedings of 10th International Heat Transfer Conference*, Brighton, 1994, Vol. 5, pp. 309–314.
9. A. Nakayama and F. Kuwahara. Convective flow and heat transfer in porous media. *Recent Res. Dev. Chem. Eng.*, 3: 121–177, 1999.
10. A. Nakayama, F. Kuwahara, T. Umemoto, and T. Hayashi. Heat and fluid flow within an anisotropic porous medium. *J. Heat Transfer*, 124: 746–753, 2002.
11. M.J.S. De Lemos and M.H.J. Pedras. Recent mathematical models for turbulent flow in saturated rigid porous media. *J. Fluids Eng.*, 123: 935–940, 2001.
12. M.H.J. Pedras and M.J.S. De Lemos. On the mathematical description and simulation of turbulent flow in a porous medium formed by an array of elliptic rods. *J. Fluids Eng.*, 123: 941–947, 2001.
13. A. Nakayama and F. Kuwahara. Numerical modeling of convective heat transfer in porous media using microscopic structures. In: K. Vafai, ed., *Handbook of Porous Media*. New York: Marcel Dekker, 2000, pp. 441–488.
14. A. Nakayama, F. Kuwahara, and T. Hayashi. Numerical modeling for three-dimensional heat and fluid flow through a bank of cylinders in yaw. *J. Fluid Mech.*, 498: 139–195, 2004.
15. A. Nakayama, F. Kuwahara, and G. Xu. A two-energy equation model in porous media. *Int. J. Heat Mass Transfer*, 44: 4375–4379, 2001.
16. P.H. Forchheimer. Wasserbewegung durch Boden. *Z. Ver. Dtsch. Ing.*, 45: 1782–1788, 1901.
17. S.V. Patankar, C.H. Liu, and E.M. Sparrow. Fully developed flow and heat transfer in ducts having streamwise-periodic variations of cross-sectional area. *J. Heat Transfer*, 99: 180–186, 1977.
18. A. Nakayama, F. Kuwahara, Y. Kawamura, and H. Koyama. Three-dimensional numerical simulation of flow through a microscopic porous structure. *Proceedings of ASME/JSME Thermal Engineering Conference*, Hawaii, 1995, Vol. 3, pp. 313–318.
19. F. Kuwahara, M. Shirota, and A. Nakayama. A numerical study of interfacial convective heat transfer coefficient in two-energy equation model for convection in porous media. *Int. J. Heat Mass Transfer*, 44: 1153–1159, 2001.
20. S.V. Patankar and D.B. Spalding. A calculation procedure for heat, mass and momentum transfer in three-dimensional parabolic flows. *Int. J. Heat Mass Transfer*, 15: 1787–1806, 1972.
21. S.V. Patankar. *Numerical Heat Transfer and Fluid Flow*. Washington, D.C.: Hemisphere, 1980.
22. A. Nakayama, W.L. Chow, and D. Sharma. Calculation of fully developed turbulent flows of ducts of arbitrary cross-section. *J. Fluid Mech.*, 128: 199–217, 1983.

23. F.A.L. Dullien. *Porous Media: Fluid Transport and Pore Structure*. San Diego, CA: Academic Press, 1979.
24. A. Zukauskas. *Convective Transfer in Heat Exchangers*. Moscow: Nauka, 1982, p. 472.
25. N. Wakao and S. Kaguei. *Heat and Mass Transfer in Packed Beds*. New York: Gordon and Breach Science Publishers, 1982, pp. 243–295.
26. A. Zukauskas. Heat transfer from tubes in crossflow. *Adv. Heat Transfer*, 18: 87–159, 1987.
27. E.D. Grimison. Correlation and utilization of new data on flow resistance and heat transfer for cross flow of gases over tube banks. *Trans. ASME*, 59: 583–594, 1937.

Part III

Flow Induced by Natural Convection and Vibration and Double Diffusive Convection in Porous Media

7

Double-Diffusive Convection in Porous Media

Abdelkader Mojtabi and Marie-Catherine Charrier-Mojtabi

CONTENTS

7.1	Introduction	270
7.1.1	Definitions	270
7.1.2	Experimental Studies.....	271
7.1.3	Linear Stability Analysis	272
7.1.4	Numerical and Analytical Studies	274
7.1.4.1	Type I.....	274
7.1.4.2	Type II.....	275
7.1.4.3	Type III.....	277
7.1.5	Other Geometrical Configurations	279
7.1.6	Other Formulations and Physical Problems	281
7.1.6.1	Brinkmann and Brinkmann–Forchheimer model ...	281
7.1.6.2	Double-diffusive convection in an anisotropic or multidomain porous medium	283
7.2	Mathematical Formulation.....	284
7.2.1	Governing Equations Describing the Conservation Laws....	284
7.2.1.1	Momentum equation	284
7.2.1.2	Continuity equation	285
7.2.1.3	Energy equation	285
7.2.1.4	Mass transfer equation	286
7.2.1.5	Combined heat and mass transfer	286
7.2.2	Nondimensional Equations (Case of Darcy Model)	287
7.3	Onset of Double-Diffusive Convection in a Tilted Cavity.....	288
7.3.1	Linear Stability Analysis	288
7.3.1.1	Linear stability analysis for an infinite horizontal cell	290
7.3.1.2	Linear stability analysis for a general case	292
7.3.1.3	Comparisons between fluid and porous medium...	295
7.3.2	Weakly Nonlinear Analysis	296

7.3.3	Numerical Results	302
7.3.3.1	Numerical procedure	302
7.3.3.2	Numerical determination of the critical Rayleigh number Ra_c for different values of the Lewis number.....	302
7.3.4	Scale Analysis	306
7.3.4.1	Boundary layer flow	306
7.3.4.2	Effect of the buoyancy ratio N on the heat and mass transfer regimes in a vertical porous enclosure	306
7.4	Soret Effect and Thermogravitational Diffusion in Multicomponent Systems	308
7.4.1	Soret Effect	308
7.4.2	Thermogravitational Diffusion	310
7.5	Conclusions and Outlook	312
	Nomenclature	313
	References	314

7.1 Introduction

7.1.1 Definitions

Natural convection flow in porous media, due to thermal buoyancy alone, has been widely studied (Combarous and Bories, 1975) and well-documented in the literature (Cheng, 1978; Bejan, 1984; Nield and Bejan, 1992, 1998) while only a few works have been devoted to double-diffusive convection in porous media. This type of convection concerns the processes of combined (simultaneous) heat and mass transfer which are driven by buoyancy forces. Such phenomena are usually referred to as thermohaline, thermosalutal, double-diffusive, or combined heat and mass transfer natural convection, in this case the mass fraction gradient and the temperature gradient are independent (no coupling between the two). Double-diffusive convection frequently occurs in seawater flow and mantle flow in the earth's crust, as well as in many engineering applications.

Soret-driven thermosalutal convection results from the tendency of solute to diffuse under the influence of a temperature gradient. The concentration gradient is created by the temperature field and is not the result of a boundary condition (see De Groot and Mazur, 1961; Patil and Rudraiah, 1980). For saturated porous media, the phenomenon of cross-diffusion is further complicated due to the interaction between fluid and porous matrix, and accurate values of cross-diffusion coefficients are not available. This makes it impossible to proceed to a practical quantitative study of cross-diffusion

effects in porous media. The Dufour coefficient is an order of magnitude smaller than the Soret coefficient in liquids, and the corresponding contribution to the heat flux can be ignored. Knobloch (1980) and Taslim and Narusawa (1986), demonstrated in a fluid medium and a porous medium, respectively, that there exists a close relationship between cross-diffusion problems (taking into account the Dufour effect and Soret effect) and double-diffusion problems.

Recent interest in double-diffusive convection through porous media has been motivated by its importance in many natural and industrial problems. Some examples of thermosolutal convection can be found in astrophysics, metallurgy, electrochemistry, and geophysics. Double-diffusive flows are also of interest with respect to contaminant transport in groundwater and exploitation of geothermal reservoirs.

Two regimes of double-diffusive convection are commonly distinguished. When the faster diffusing component is destabilizing, as it is when stably stratified saltwater is heated from below in a horizontal cell, the system is in the diffusive regime. When the slower diffusing component is destabilizing, as is the case when cold fresh water is overlain by hot salty water, the system is in the fingering regime.

In such binary fluids, the diffusivity of heat is usually much higher than diffusivity of salt; thus, a displaced particle of fluid loses any excess heat more rapidly than any excess solute. The resulting buoyancy force may tend to increase the displacement of the particle from its original position causing instability. The same effect may cause overstability involving oscillatory motions of large amplitudes since heat and solute diffuse widely at different rates.

The current state of knowledge concerning double-diffusive convection in a saturated porous medium is summarized in the overviews by Nield and Bejan (1998) and recent developments and reviews are given by Ingham and Pop (2000, 2002).

The double-diffusion problem is interesting and exhibits quite complicated nonlinear phenomena, which depend on the boundary layer thickness. In general, three kinds of boundary layers are associated with the double-diffusion process: hydrodynamic, thermal, and species concentration boundary layers. The relative thickness of those boundary layers defines the rate of the heat and mass transfer process and the dynamics of the flow. Also, the local density of the fluid depends on the temperature and species concentration. Accordingly the dynamics of the flow can be complicated due to density reversal.

7.1.2 Experimental Studies

We consider, here, the most significant experimental studies in thermosolutal convection in porous media. The first was carried out by Griffith (1981). He used both a Hele-Shaw cell and a sand-tank model with salt and sugar or heat

and salt as the diffusing components and porous medium of glass spheres to study the "diffusive" configuration (a thin diffusive interface). He measured salt-sugar and heat-salt fluxes through two-layer convection systems and compared the results with predictions from a model. This was applied to the Wairakei geothermal system, and the observed values were consistent with those found in laboratory experiments.

The second work was carried out by Imhoff and Green (1988). They studied double-diffusive groundwater fingers, using a sand-tank model and a salt-sugar system. They observed that double-diffusive groundwater fingers can transport solutes at rates of, as much as, two orders of magnitude larger than those associated with molecular diffusion in motionless groundwater. This could play a major role in the vertical transport of near-surface pollutants in groundwater.

The third experimental work, by Murray and Chen (1989), is closer to our study, Charrier-Mojtabi et al. (1997), and concerns the onset of double-diffusive convection in a finite box filled with porous medium. The experiments were performed in a horizontal layer consisting of 3 mm diameter glass beads contained in a box $24 \times 12 \times 4 \text{ cm}^3$ high. The rigid top and bottom walls of the box provide a linear basic-state temperature profile but only allow a nonlinear time-dependent basic-state profile for salinity. They observed that when a porous medium is saturated with a fluid having a stabilizing salinity gradient, the onset of convection was marked by dramatic increase in heat flux at the critical ΔT , and the convection pattern was three-dimensional, while two-dimensional rolls are observed for single-component convection in the same apparatus. They also observed a hysteresis loop reducing the temperature difference from supercritical to subcritical values.

7.1.3 Linear Stability Analysis

Concerning the theoretical studies, various modes of double-diffusive convection can be developed depending not only on how both thermal and solutal gradients are imposed relative to each other but also on the numerous nondimensional parameters involved.

Many of the published works regarding double-diffusive convection in porous media concern linear stability analysis. The linear stability characteristics of the flow in horizontal layers with imposed vertical temperature and concentration gradients have been the subject of many studies. The onset of thermosolutal convection was predicted by Nield (1968), on the basis of linear stability analysis. This flow configuration was later studied by many investigators. Tanton et al. (1972) extended Nield's analysis and considered salt-fingering convection in a porous layer. Trevisan and Bejan (1985) studied mass transfer in the case where buoyancy is entirely due to temperature gradients. Rudraiah et al. (1986) applied linear and nonlinear stability analysis and showed that subcritical instabilities are possible in the case of two-component

fluids. Brand et al. (1983) obtained amplitude equations for the convective instability of a binary fluid mixture in a porous medium. They found an experimentally feasible example of a codimension-two bifurcation (intersection of stationary and oscillatory bifurcation lines).

With regard to porous layers heated from the side, the focus has been on the double-diffusive instability of double boundary-layer structures that form near a vertical wall immersed in a temperature and concentration stratified porous medium. The stability of this problem was studied by Gershuni et al. (1976) and independently by Khan and Zebib (1981). The occurrence of both monotonic and oscillatory instability was predicted. Raptis et al. (1981) constructed similar solutions for the boundary layer near a vertical wall immersed in a porous medium with constant temperature and concentration. Nield et al. (1981) analyzed the convection induced by inclined thermal and solutal gradients in a shallow horizontal layer of a porous medium.

Recently, Mahidjiba et al. (2003) have examined the effect of mixed thermal and solutal boundary conditions (constant temperatures and mass fluxes, or vice versa, prescribed on the horizontal boundaries). The thresholds for oscillatory and stationary convection are obtained. It is also demonstrated that, when the thermal and solute effects oppose each other, the flow patterns become much different from the classical Benard convective flows. Amahmid et al. (2000) developed analytical and numerical linear stability studies for double-diffusive flow in a horizontal Brinkmann porous layer subjected to constant heat and mass fluxes. Considering the work of Mamou and Vasseur (1999a), Kalla et al. (2001b) have studied the effect of lateral heating on the bifurcation phenomena present in double-diffusive convection within a horizontal enclosure and found that the lateral heating acts as an imperfection superimposed on the bifurcation curves.

The case of vertical or inclined enclosures subjected to opposing and equal buoyancy forces ($N = -1$) has been extensively studied during the last decade. For this situation, on the basis of both linear and nonlinear stability analysis, Charrier-Mojtabi et al. (1997), Mamou et al. (1997, 1998a, 1998b), Marcoux et al. (1998), Karimi-Fard et al. (1999), and Mojtabi and Charrier-Mojtabi (2000) have demonstrated that there exists a threshold for the onset of oscillatory or stationary convection. Different convective regimes such as subcritical, overstable, and stationary convective modes were delineated in terms of the governing parameters (Lewis number, enclosure aspect ratio, normalized porosity of the porous medium, inclination angle, and thermal and solutal boundary conditions). Subcritical convection was found to occur in a wide range of Lewis numbers.

However, the overstable regime was found to occur in a narrow range of Lewis number (close to 1, as in the case of many gases) depending on the normalized porosity. In an infinite layer, the wavelength at the onset of stationary convection was found to be independent of the Lewis number and this has been verified by Mamou (2002) but it is not the case at the onset of overstability. It has also been demonstrated, when the Lewis number is

close to unity, that the system remains conditionally stable, provided that the normalized porosity is lower than unity.

Considering vertical enclosure subject to constant fluxes of heat and solute, Amahmid et al. (2000) have studied the situation where the buoyancy forces are nearly equal: $N = -1 + \varepsilon$ where $\varepsilon \ll 1$ is a very small positive number. As expected, multiple unicellular convective flows were predicted.

The present chapter is devoted to a two-dimensional study of double-diffusive convective flows within tilted porous enclosures subject to opposing thermal and solutal gradients. The situation where the thermal and solutal buoyancy forces are equal and opposing each other ($N = -1$) is considered. The case of an arbitrary buoyancy ratio is introduced for a horizontal enclosure, subject to vertical gradients of heat and solute. Similar and mixed thermal and solutal boundary conditions are considered. A reliable numerical technique is developed for determining the critical parameters for the onset of convection and, for comparison, a finite element solution of the full governing equations is obtained and the effects of the governing parameters on the convective flow behavior are studied.

7.1.4 Numerical and Analytical Studies

As far as the relation between thermal and concentration buoyancy forces is concerned, the problem of double diffusion can be classified into the following categories (Mohamad, 2003; Mohamad et al., 2004):

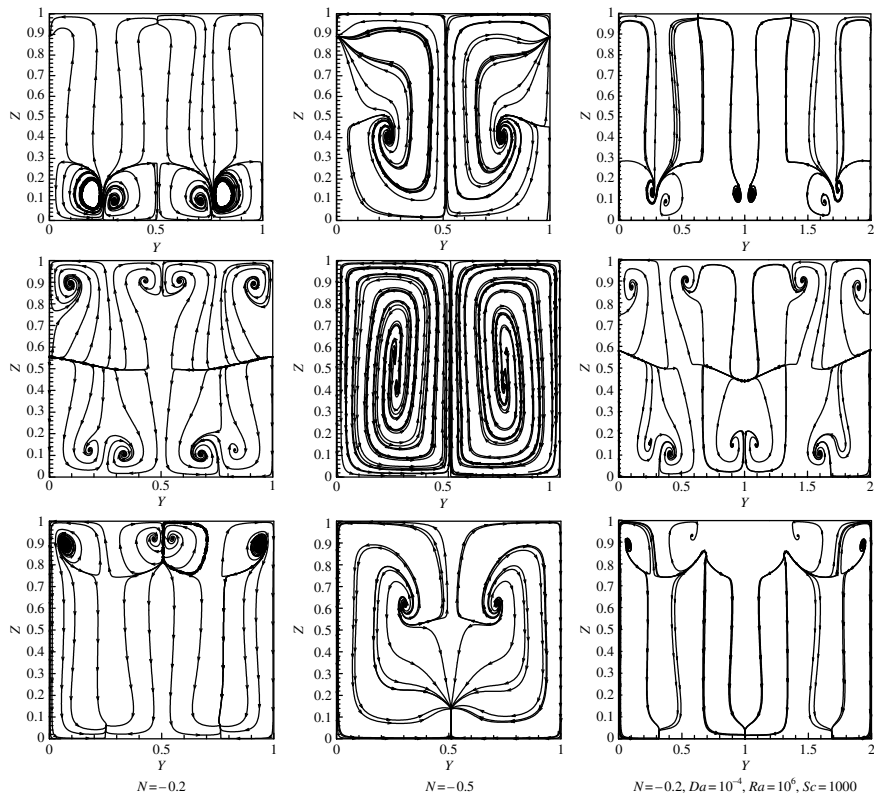
Type I — Temperature and species concentration or their gradients are imposed horizontally along the enclosure, either aiding or opposing each other.

Type II — Temperature and species or their gradients are imposed vertically, again either aiding or opposing each other (modified Rayleigh–Benard convection; stratified medium).

Type III — Temperature (or species concentration) or their gradient is imposed vertically and species concentration (or temperature) or their gradient imposed horizontally. It is important to note that most of these works are theoretical.

7.1.4.1 Type I

Horizontally imposed gradients. Sezai and Mohamad (1999) presented results for three-dimensional flow in a cubic cavity filled with porous medium and subjected to opposing a horizontal thermal and concentration gradients. Their results revealed that, for a certain range of the controlling parameters, the flow becomes three-dimensional and multiple solutions are possible within this range. In the following paragraphs a few results will be shown to illustrate the flow pattern and their effects on heat and mass transfer.

**FIGURE 7.1**

Stream functions at $X = 0.25$ (upper), $X = 0.5$ (middle), and $X = 0.75$ (bottom) for aspect ratio of unity (left) with $N = -0.2$ and $N = -0.5$ (middle) and aspect ratio of two (right) with $N = -0.2$. $Ra = 10^6$, $Da = 10^{-4}$, $Sc = 1000$. (Taken from I. Sezai and A.A. Mohamad. *J. Fluid Mech.* 400: 333–353, 1999. With permission.)

Figure 7.1 compares flow patterns for $N = -0.2$ and $N = -0.5$, for aspect ratios of 1.0 and 2.0. The results at different lateral planes $X = 0.25, 0.5$, and 0.75 , are illustrated in this figure. The flow is complex for $N = -0.2$ and the complexity decreases for $N = -0.5$.

7.1.4.2 Type II

Vertical and inclined porous layer subjected to constant heat and mass fluxes. Although the most basic geometry for the study of simultaneous heat and mass transfer from the side is the vertical wall, most of the available studies dealing with double-diffusion convection are in confined porous media and concern rectangular cavities subjected to constant heat and mass fluxes at their vertical walls.

For a vertical wall immersed in an infinite porous medium, Bejan and Khair (1985) studied the vertical natural convective flows due to the combined buoyancy effects of thermal and species diffusion. They presented an order of magnitude analysis of boundary layer equations, which yields functional relations for the Nusselt and Sherwood numbers in limiting cases. This fundamental problem was reexamined by Lai and Kulacki (1991). Their solutions cover a wide range of governing parameters. The similar approach employed by Bejan and Khair (1985) was generalized by Jang and Chang (1988a, 1988b) to consider the effect of wall inclination on a two-layer structure. Recently, Nakayama and Hossain (1995) obtained an integral solution for aiding-flow adjacent to vertical surfaces. Rastogi and Poulikakos (1995) considered non-Newtonian fluid saturated porous media and presented similar solutions for aiding-flows with constant wall temperature and concentration as well as constant wall flux conditions. Benhadji and Vasseur (2001) also studied the double-diffusive convection in a shallow porous cavity filled with non-Newtonian fluid.

Rectangular cavities with imposed uniform heat and mass fluxes have been the subject of numerous works. Trevisan and Bejan (1986) developed an analytical Oseen-linearized solution for boundary-layer regimes for $Le = 1$, and proposed a similarity solution for heat transfer driving flows for $Le > 1$. They also performed an extensive series of numerical experiments that validate the analytical results and provide heat and mass transfer data in the domain not covered by analytical study. The same configuration was considered by Alavyoon (1993) for cooperative ($N > 0$) buoyancy forces and Alavyoon et al. (1994) for opposing ($N < 0$) buoyancy forces. They presented an analytical solution valid for stratified flow in slender enclosures ($A \gg 1$) and scale analysis that agrees with the heat driven and solute driven limits, using numerical and analytical methods and scale analysis. Comparisons between fully numerical and analytical solutions are presented for a wide range of parameters. They also show the existence of oscillatory convection with opposing buoyancy forces. Transient heat and mass transfer in a square porous enclosure has been studied numerically by Lin (1993). He showed that an increase of the buoyancy ratio N improves heat and mass transfer and causes the flow to approach steady-state conditions in a short time. An extension of these studies to the case of the inclined porous layer subjected to transverse gradients of heat and solute was carried out by Mamou et al. (1995a). Their results are presented for $10^{-3} \leq Le \leq 10^3$, $0.1 \leq Ra_T \leq 10^4$, $-10^4 \leq N \leq 10^4$, $2 \leq A \leq 15$, and $-180^\circ \leq \phi \leq 180^\circ$ where ϕ corresponds to the inclination of the enclosure. They obtained an analytical solution by assuming parallel flow in the core region of the tilted cavity. The existence of multiple steady-state solutions, for opposing buoyancy forces, has been demonstrated numerically. Mamou et al. (1995b) have also numerically shown that, in square cavities where the thermal and solutal buoyancy forces counteract each other ($N = -1$), a purely diffusive (motionless) solution is possible even for Lewis numbers different from unity.

Recently Amahmid et al. (2000) analyzed the transition between aiding and opposing double-diffusive flows in vertical porous matrix.

Vertical and horizontal cavities with imposed temperature and concentration. The configuration of a vertical cavity with imposed temperature and concentration along the vertical sidewalls was considered by Trevisan and Bejan (1985, 1990), Charrier-Mojtabi et al. (1997) and by Angiraza et al. (1997). Trevisan and Bejan (1985) considered a square cavity submitted to horizontal temperature and concentration gradients. Their numerical simulations are compared to scaling analysis. They found that the onset of the convective regime depends on the cell aspect ratio, A , the Lewis number, the thermal and solutal Rayleigh number Ra_T and Ra_S or the buoyancy ratio N . Their numerical simulations were carried out for the range $0.01 \leq Le \leq 100$, $50 \leq Ra_T \leq 10^4$, and $-5 \leq N \leq +3$ for $A = 1$. Angiraza et al. (1997), without making approximations of boundary layer character, numerically solved the Darcy type equation. They found that for high Rayleigh number aiding-flows, the numerical solutions match the similar solutions very closely. However, they differ substantially for opposing flows and for low Rayleigh numbers. Flow and transport follow complex patterns depending on the interaction between the diffusion coefficients and the buoyancy ratio $N = Ra_S/Ra_T$. The Nusselt and Sherwood numbers reflect this complex interaction.

7.1.4.3 Type III

The first analytical solution for this configuration has been proposed by Kalla et al. (1999), for the case of shallow cavity subjected to cross fluxes of heat. This was followed by the analytical and numerical studies for double-diffusive convection by Kalla et al. (2001a).

This problem has also been recently considered by Mohamad and Bennacer (2001, 2002) and Bennacer et al. (2001). They assume that the flow is two- and three-dimensional and analysis is performed for an enclosure of aspect ratio two, $Pr = 0.71$, $Le = 10$, $Gr_T = 10^6\text{--}10^8$, $Da = 10^{-4}\text{--}10^{-6}$ and for buoyancy ratio, $0.25 \leq N \leq 2.0$. Flow bifurcation is predicted for N values in the range of about 0.8 to 1.0. The bifurcation occurs when the concentration buoyancy force starts to overcome the thermally induced flow. One main circulation observed for thermally driven flow is suppressed and flow breaks into two thermally driven circulations. These circulations appear at the near horizontal boundaries. With further increase to a strong stable concentration gradient (N), the flow is totally suppressed. Also, Bennacer et al. (2001) explore the stability of the same problem, where oscillatory flow is predicted for a limited range of buoyancy ratios. The oscillatory flow is attributed to interaction between concentration plume and thermal cells. The difference between two- and three-dimensional results is not that significant as far as the rate of heat and mass transfer is concerned, even though the flow structure is different. This suggests that the lateral flow is not that significant compared with axial and vertical flows. Despite the fact that the flow patterns are complex and

three-dimensionality of the flow is obvious, the average Nu and Sh numbers for two- and three-dimensional simulations are almost the same. Figure 7.2 shows the effect of the buoyancy ratio on the average rate of heat and mass transfer. For absolute N greater than or equal to one, the heat transfer is diffusive, while the rate of mass transfer is enhanced by advection of the momentum induced by thermal buoyancy.

The effects of Rayleigh and Lewis number of the average heat and mass transfer is illustrated in Figure 7.3 and Figure 7.4, respectively, for $N = -0.5$, $Pr = 10$, $Da = 10^{-3}$. There is clear evidence from these figures that the difference between predictions of two- and three-dimensional simulations is not that significant as far as average heat and mass transfer are concerned. For more detailed analysis and discussion, the reader should consult the paper by Mohamad and Bennacer (2002).

Furthermore, Mohamad et al. (2004) examined the effect of lateral aspect ratio on the flow development and heat transfer in three-dimensional enclosures filled with binary fluids. The effect of thermal Ra , Sc , aspect ratio, and buoyancy ratio on the heat and mass transfer and flow structure were addressed. Using particular initial conditions, they found, that the flow may duplicate itself if the aspect ratio increased by an integer number for a certain range of the controlling parameters. In other words, longitudinal rolls form similar to Rayleigh–Benard but with different local structures.

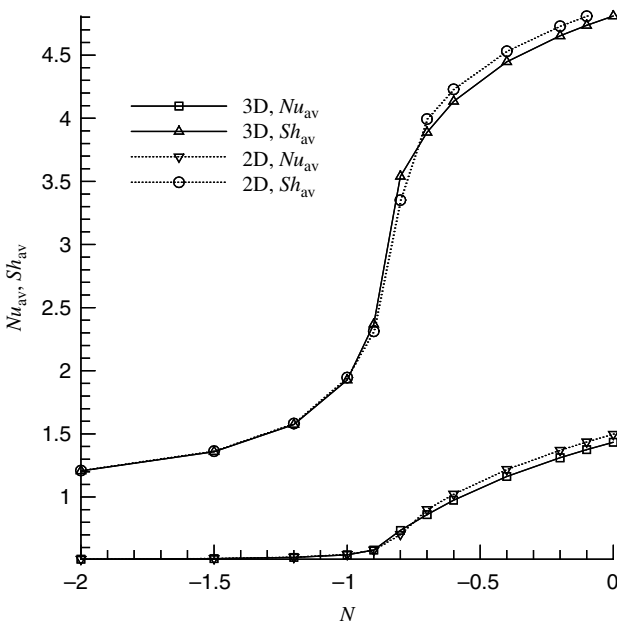
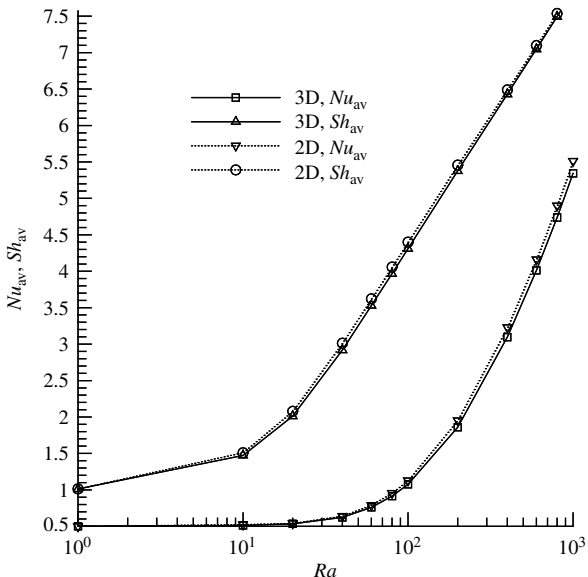
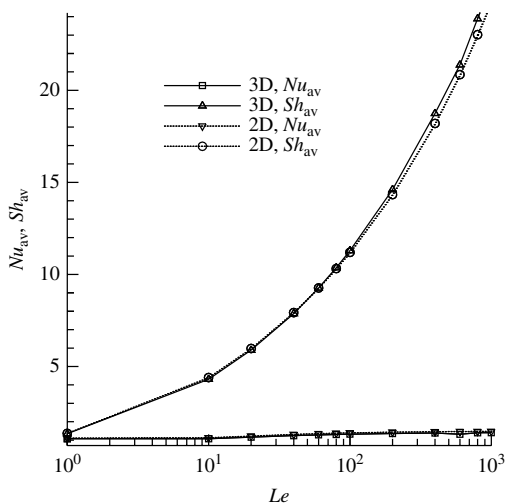


FIGURE 7.2

The effect of N on Nu and Sh , $Ra = 10^5$, $Pr = 10$, $Le = 10$, $Da = 10^{-3}$.

**FIGURE 7.3**

The effect of Ra on Nu and Sh , $N = -0.5$, $Pr = 10$, $Da = 10^{-3}$.

**FIGURE 7.4**

The effect of Le on Nu and Sh , $N = -0.5$, $Pr = 10$, $Da = 10^{-3}$.

7.1.5 Other Geometrical Configurations

The double diffusive case of natural convection in a vertical annular porous layer under the condition of constant heat and mass fluxes at the vertical boundaries was analyzed by Marcoux et al. (1999). The system of governing

equations was solved numerically to obtain a detailed description of the velocity, temperature, and concentration within the cavity in order to emphasize the influence of the dimensionless parameters Ra_T , Le , N , and curvature on steady and unsteady convective flows. For the case of high

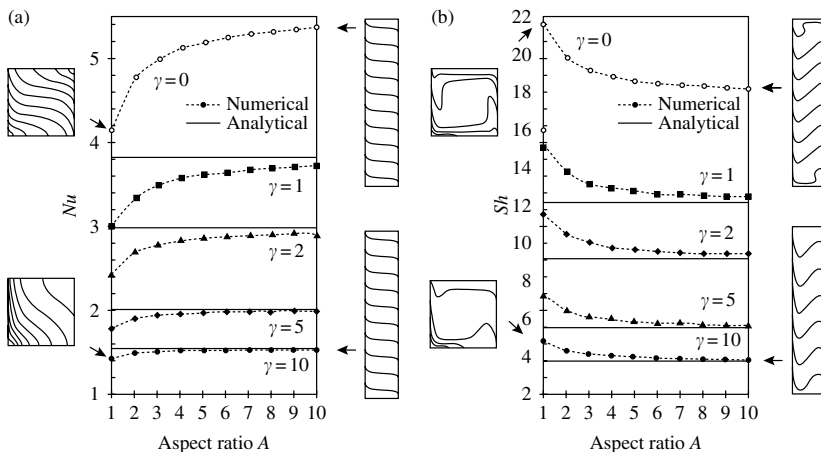


FIGURE 7.5

Influence of the aspect ratio A on the Nu_i (a) and Sh_i (b) numbers for different values of γ isotherms (a) and isohalines (b) at steady state for $Ra_T = 100$, $Le = 10$, $A = 1$ and 10 , $\gamma = 0$ and 10 . (Taken from M. Marcoux, M.C. Charrier-Mojtabi and M. Azaiez. *Int. J. Heat Mass Transfer*, 2313–2325, 1999. With permission.)

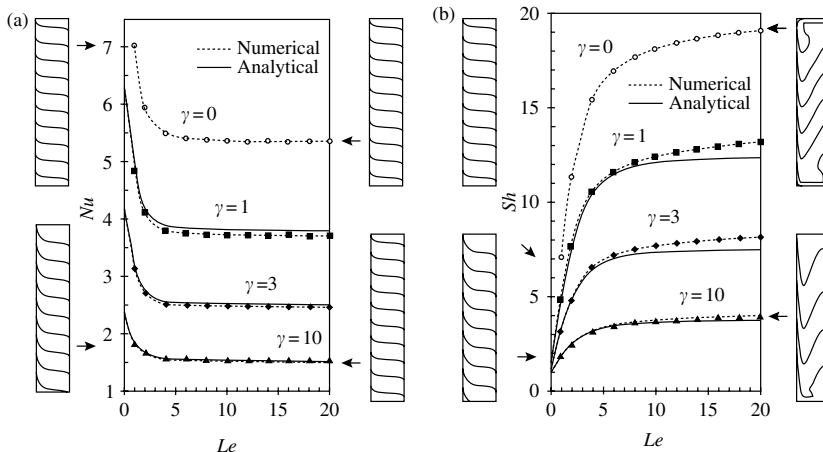


FIGURE 7.6

Influence of the Lewis number on the Nu_i (a) and Sh_i (b) numbers for different values of γ isotherms (a) and isohalines (b) at steady state for $Ra_T = 100$, $N = 1$, $A = 10$, $Le = 1$ and 20 , $\gamma = 0$ and 10 . (Taken from M. Marcoux, M.C. Charrier-Mojtabi and M. Azaiez. *Int. J. Heat Mass Transfer*, 2313–2325, 1999. With permission.)

aspect ratios ($A \gg 5$), an analytical solution is proposed on the basis of a parallel flow model. The good agreement of this solution with numerical results shows that the analytical model can be faithfully used to obtain a concise description of the problem for these cases as seen in [Figure 7.5](#) and [Figure 7.6](#).

Double-diffusive convection over a sphere was analyzed by Lai and Kulacki (1990), while Yucel (1990) similarly treated the flow over a vertical cylinder. Flow over a horizontal cylinder, with the concentration gradient being produced by transpiration, was studied by Hassan and Mujumdar (1985). All the above studies (Sections 7.1.3, 7.1.4, 7.1.5) describe the momentum conservation in the porous medium using the Darcy model.

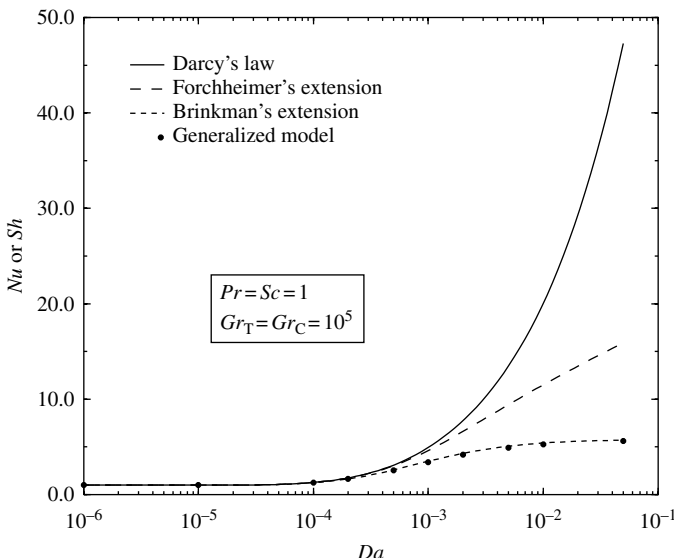
The effect of the curvature on the necessary N value to pass from the clockwise to the anticlockwise rolls was analyzed by Beji et al. (1999) and by Bennacer et al. (2001).

7.1.6 Other Formulations and Physical Problems

7.1.6.1 Brinkmann and Brinkmann–Forchheimer model

Poulikakos (1986) studied the criterion of onset of double-diffusive convection using the Darcy–Brinkmann model to describe momentum conservation in the porous medium: the results clearly show the influence of Darcy number. F. Chen and C.F. Chen (1993) also used the Brinkmann and Forchheimer terms to consider nonlinear two-dimensional horizontally periodic, double-diffusive fingering convection. The stability boundaries, which separate regions from different regimes of convection, are identified. The Darcy–Brinkmann formulation was adopted recently by Goyeau et al. (1996) for a vertical cavity with imposed temperature and concentration along the vertical sidewalls. This study deals with natural convection driven by cooperating thermal and solutal buoyancy forces. The numerical simulations presented span a wide range of the main parameters (Ra and Darcy number, Da) in the domain of positive buoyancy numbers, N and $Le > 1$. This contribution completes certain observations on the Darcy regime already mentioned in the previous studies. It is shown that the numerical results for mass transfer are in excellent agreement with scaling analysis over a very wide range of parameters. Recently, the Darcy–Brinkmann model was also analyzed for thermosolutal convection in a vertical annular porous layer by Bennacer et al. (2000).

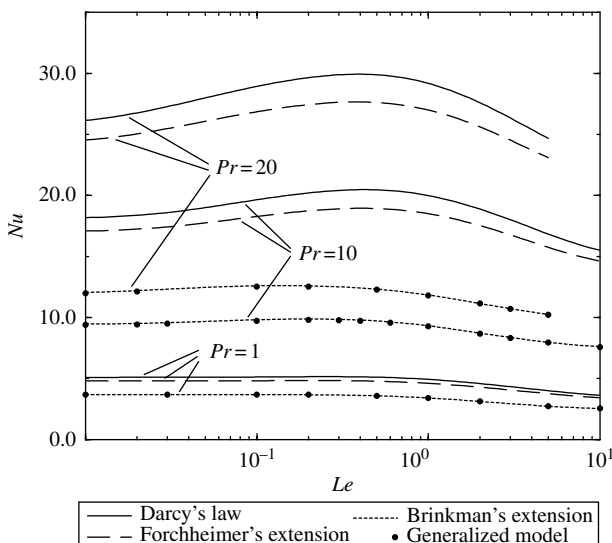
Multiphase transport is another aspect of double-diffusive convection. Vafai and Tien (1989) and Tien and Vafai (1990) studied phase change effects and multiphase transport in porous materials. They used the Darcy law for flow motion without the Boussinesq approximation. The problem was modeled by a system of transient intercoupled equations governing the two-dimensional multiphase transport process in porous media. It should be noted that (aside from non-Darcian effects) the problem of double-diffusive convection within a porous medium will then be a special case of multiphase transport in porous media as analyzed in Vafai and Tien (1989) and

**FIGURE 7.7**

Variations of Nusselt or Sherwood number as a function of Darcy number for different flow models. (Taken from M. Karimi-Fard, M.C. Charrier-Mojtabi, and K. Vafai. *Numer. Heat Transfer, part A* 31: 837–852, 1997. With permission.)

Tien and Vafai (1990). The more recent work by Karimi-Fard et al. (1997) studied double-diffusive convection in a square cavity filled with a porous medium. Several different flow models for porous media, such as Darcy flow, Forchheimer's extension, Brinkmann's extension, and generalized flow are considered. The influence of boundary and inertial effects on heat and mass transfer is analyzed to determine the validity of Darcy's law in this configuration. It is shown that the inertial and boundary conditions have a profound effect on the double-diffusive convection.

A comparison between different models is presented in Figure 7.7. The plots clearly show that the difference between the models increases with an increase in Da . Figure 7.8 shows the influence of Le on heat transfer for $Pr = 1$, 10, and 20. Boundary and inertial effects are also shown in Figure 7.4. It can be seen that the use of the Darcy results induces an overestimation for Nu compared to models based on Forchheimer extension and Brinkmann extension. The essential non-Darcian effect is the boundary effect. The plots clearly show that the generalized model and Brinkmann extension of the Darcy model give almost the same Nu . An interesting effect is observed for double-diffusive convection. As seen in Figure 7.8, heat transfer is maximized for a critical value of the Lewis number. This behavior exists for all models but is more significant for the Darcy model and Forchheimer's extension of the Darcy model than for Brinkmann's extension and the generalized models.

**FIGURE 7.8**

Variations of Nusselt number as a function of Lewis and Prandtl numbers for $Gr_T = Gr_C = 10^{-5}$, $Da = 10^{-3}$, and $\Lambda = 2.34$.

7.1.6.2 Double-diffusive convection in an anisotropic or multidomain porous medium

Tyvand (1980) was the first to study double-diffusive convection in an anisotropic porous medium. He considered a horizontal layer, which retains horizontal isotropy with respect to permeability, thermal diffusivity, and solute diffusivity. It was shown that for porous media, with a thermally insulating solid matrix, the stability diagram has the same shape as in the case of isotropy. The onset of double-diffusive convection in a rotating porous layer of infinite horizontal extent was investigated numerically by Patil et al. (1989) for anisotropic permeability and horizontal isotropy. Double-diffusive convection in layered anisotropic porous media was studied numerically by Nguyen et al. (1994). A rectangular enclosure, consisting of two anisotropic porous layers with dissimilar hydraulic and transport properties, was considered. The problem was solved numerically. Four different sets of boundary constraints were imposed on the system, including aiding diffusion, opposing diffusion, and the two modes of cross diffusion. The results show that each set of boundary conditions produces distinct flow, temperature, and concentration fields. The overall heat transfer rates may or may not be sensitive to the Rayleigh numbers, depending on the orientation of the boundary conditions of the temperature and concentration fields. Recently, double-diffusive convection in dual permeability, dual porosity media was studied by Saghir and Islam (1999). The Brinkmann model is used as the momentum balance equation and solved simultaneously with mass and energy balance equations in the two-dimensional domain. Special emphasis is given to the

study of double-diffusive phenomena in layered porous bed with contrasting permeabilities. The study is completed for a wide range of permeability contrasts. A numerical and analytical approach (scale analysis) are also used by Bennacer et al. (2001) to take into account the thermal and hydrodynamic anisotropy using the Darcy and Darcy–Brinkmann models. The effect of permeability and buoyancy ratios on mass transfer (comparison between the numerical and analytical results) is studied by these authors. Double-diffusive convection in a vertical multilayer saturated porous medium has been recently studied by Bennacer et al. (2003a).

7.2 Mathematical Formulation

7.2.1 Governing Equations Describing the Conservation Laws

7.2.1.1 Momentum equation

The basic dynamic equations for the description of the flow in porous media have been the subject of controversial discussion for several decades. Most of the analytical and numerical work presented in the literature is based on the Darcy–Oberbeck–Boussinesq formulation. Darcy's law is valid only when the pore Reynolds number, Re , is of the order of 1. Lage (1992, 1998) studied the effect of the convective inertia term for Bénard convection in porous media. He concluded that the convective term, included in the general momentum equation, has no significant effect on the calculation of overall heat transfer. Chan et al. (1970) utilized Brinkmann's extension to study natural convection in porous media with rectangular impermeable boundaries. However, they essentially concluded that non-Darcian effects have very little influence on heat transfer results. For many practical applications, however, Darcy's law is not valid, and boundary and inertial effects need to be accounted for. A fundamental study of boundary and inertial effects can be found in the work of Vafai and Tien (1981) and Hsu and Cheng (1985). A systematic study of the non-Darcian effects in natural convection is presented in the work of Ettefagh et al. (1991). These authors report a formal derivation of a general equation for fluid flow through an isotropic, rigid, and homogeneous porous medium. The general final equation for an incompressible fluid is:

$$\rho \left[\frac{\partial \vec{V}'}{\varepsilon \partial t'} + \frac{1}{\varepsilon^2} \vec{V}' \cdot \nabla \vec{V}' \right] = -\nabla P' + \rho \vec{g} + \mu_e \nabla^2 \vec{V}' - \frac{\mu}{K} \vec{V}' - \frac{b\rho}{K^{1/2}} \|\vec{V}'\| \vec{V}' \quad (7.1)$$

where ρ , μ , μ_e , K , b , and ε are fluid density, dynamic viscosity, effective viscosity, permeability, form coefficient, and porosity respectively.

We suppose that the medium is homogeneous and spatially invariant and the viscosity is taken as a constant. Double-diffusive convection is often studied using the Darcy formulation and Boussinesq approximation, provided the fluid moves slowly so that the inertial effects are negligible

and one can usually drop the time derivative term completely based on the analysis given by Nield and Bejan (1992, 1998), as:

$$\vec{V}' = \frac{K}{\mu}(-\nabla P' - \rho g \vec{k}) \quad (7.2)$$

where $\vec{V}' = (u', v', w')$ and P' are the seepage (Darcy) velocity and pressure respectively. $\vec{k} = -\sin(\varphi)\vec{x} + \cos(\varphi)\vec{y}$ defines the tilt of the cavity.

7.2.1.2 Continuity equation

Conservation of fluid mass, assuming that an incompressible fluid and no sources or sinks, can be expressed as:

$$\nabla \cdot \vec{V}' = 0 \quad (7.3)$$

7.2.1.3 Energy equation

The macroscopic description of heat transfer in porous media by a single energy equation implies the assumption of local thermal equilibrium between the moving fluid phase and the solid phase ($T'_s = T'_f = T'$). This hypothesis has been investigated by several authors (Sözen and Vafai, 1990; Gobbe and Quintard, 1994; Kaviany, 1995; and Quintard and Whitaker, 1996a, 1996b). For situations in which local thermal equilibrium is not valid, models have been proposed based on the concept of two macroscopic continua, one for the fluid phase and the other for the solid phase; see Quintard et al. (1997).

The temperature differences imposed across the boundaries are small, and consequently the Boussinesq approximation is valid. The single-energy equation is:

$$\frac{(\rho c)_m}{(\rho c)_f} \frac{\partial T'}{\partial t'} + \vec{V}' \cdot \nabla T' = \alpha_e \nabla^2 T' \quad (7.4)$$

where c is the specific heat, α_e is the effective thermal conductivity of saturated porous medium divided by the specific heat capacity of the fluid. Subscript f refers to fluid properties while subscript m refers to the fluid–solid mixture and s to the solid matrix, where

$$(\rho c)_m = \varepsilon(\rho c)_f + (1 - \varepsilon)(\rho c)_s \quad (7.5)$$

$$\alpha_e = \varepsilon \frac{k_f}{(\rho c)_f} + (1 - \varepsilon) \frac{k_s}{(\rho c)_f} = \varepsilon \alpha_f + (1 - \varepsilon) \frac{k_s}{(\rho c)_f} \quad (7.6)$$

which corresponds to effective thermal conductivity obtained as weighted arithmetic mean of the conductivities k_s and k_f . In general, the effective thermal conductivity depends, in a complex fashion, on the geometry of the

medium. Many others expressions given k^* do exist like geometric mean $k^* = k_s^\varepsilon k_f^{1-\varepsilon}$ and many others listed in the book of Kaviany (1995).

7.2.1.4 Mass transfer equation

For a porous solid matrix saturated by a fluid mixture we have:

$$\varepsilon \frac{\partial C'}{\partial t'} + \vec{V}' \cdot \nabla C' = D_m \nabla^2 C' \quad (7.7)$$

Parameter D_m represents the diffusivity of a constituent through the fluid-saturated porous matrix. One finds several expressions in the literature (Bear, 1972; de Marsily, 1986; Nield and Bejan, 1992, 1998) for the link between diffusion coefficients in free layers and in porous medium, like $D^* = \varepsilon D$ or $D^* = D/\tau^2$ where ε is the porosity and τ the tortuosity of the porous medium. Sometimes more complex expressions based on homogenization theory are proposed by Adler (1992), but are not always of practical application.

7.2.1.5 Combined heat and mass transfer

Generally, the transport of heat and mass are not directly coupled and Eqs. (7.4) and (7.6) hold without change. In thermosolutal convection, coupling takes place because the density of the binary fluid depends on both temperature T' and mass fraction C' . For small density variations due to temperature and mass fraction changes at constant pressure, the density variations can be expressed as:

$$\rho(T', C') = \rho_r(1 - \beta_T(T' - T_r) - \beta_C(C' - C_r)) \quad (7.8)$$

where T_r and C_r are taken as the reference state, and the coefficients of volumetric expansion with temperature $\beta_T = -(1/\rho_r)(\partial\rho/\partial T')_{C'}$ or with concentration $\beta_C = -(1/\rho_r)(\partial\rho/\partial C')_{T'}$ are assumed constant. It is noted that the expansion coefficient β_T is usually positive and the expansion coefficient β_C is negative if C corresponds to the mass fraction of the denser component.

In some circumstances there is direct coupling. This occurs when cross diffusion (Soret and Dufour effects) is not negligible. The Soret effect refers to the mass flux produced by temperature gradients, and the Dufour effect refers to the heat flux produced by a concentration gradient. With no heat or mass sources, instead of Eqs. (7.4) and (7.6), we have:

$$\frac{(\rho c)_m}{(\rho c)_f} \frac{\partial T'}{\partial t'} + \vec{V}' \cdot \nabla T' = \alpha_e \left(\nabla^2 T' + \frac{\alpha_m}{\alpha_e} \nabla^2 C' \right) \quad (7.9)$$

$$\varepsilon \frac{\partial C'}{\partial t'} + \vec{V}' \cdot \nabla C' = D_m \left(\nabla^2 C' + \frac{D_T}{D_m} \nabla^2 T' \right) \quad (7.10)$$

where $(\alpha_m/\alpha_e) = D_d$ and $(D_T/D_m) = S_T$ are, respectively, the Dufour and Soret dimensional coefficient of the porous medium. Independent of which expression is used, the value of the thermodiffusion coefficient D_T is also affected by the solid matrix. One finds in the literature (Jamet et al., 1992) the statement that the Soret coefficient should have the same value in a porous medium and in a free liquid layer, based on the argument that since both coefficients D_T and D_m are of the same nature, the corrections should be the same and therefore their ratio should be unaffected by the porous medium. This argument seems intuitively correct at first sight and could be true, but on the other hand could be incorrect owing to the fact that the thermodiffusion coefficient could also depend on the ratio of the thermal conductivity of the liquid mixture to that of the solid matrix see, Platten and Costeseque (2004).

7.2.2 Nondimensional Equations (Case of Darcy Model)

The fluid flow within the porous medium is assumed to be incompressible and governed by Darcy's law. The contribution to the heat flux by Dufour effect is assumed negligible in liquids. The Oberbeck–Boussinesq approximation is applicable in the range of temperatures and concentrations expected. We introduce nondimensional variables with the help of the following scales: L for distance, $L^2(\rho c)_m/k_e$ for time, α_e/L for velocity, ΔT for temperature, ΔC for concentration, $k_e \mu / K(\rho c_p)_f$ for pressure. Thus we obtain the system of governing equations for nondimensional variables:

$$\begin{aligned} \nabla \cdot \vec{V} &= 0 \\ \vec{V} &= -\nabla P + (Ra_T T + Ra_S C) \vec{k} \\ \frac{\partial T}{\partial t} + \vec{V} \cdot \nabla T &= \nabla^2 T \\ \varepsilon \frac{\partial C}{\partial t} + \vec{V} \cdot \nabla C &= \frac{1}{Le} (\nabla^2 C + S_T^* \nabla^2 T) \end{aligned} \quad (7.11)$$

$\vec{k} = -\sin(\varphi)\vec{x} + \cos(\varphi)\vec{y}$ defines the tilt of the cavity.

The problem formulated involves the following nondimensional parameters: the thermal Rayleigh number, Ra_T , the solutal Rayleigh number, Ra_S , the Lewis number, Le , the parameter of Soret effect, S_T^* , the normalized porosity, these five dimensionless parameters governing the convective dynamics are defined by:

$$\begin{aligned} Ra_T &= \frac{Kg\beta_T(\rho c)_f \Delta TL}{k^* \nu}, & Ra_S &= \frac{Kg\beta_C(\rho c)_f \Delta CL}{k^* \nu} \\ Le &= \frac{a}{D'}, & S_T^* &= \frac{D_T}{D} \Delta T_r, & \varepsilon &= \varepsilon^* \frac{(\rho c)_f}{(\rho c)_m} \end{aligned}$$

If we introduce the buoyancy ratio

$$N = \frac{Ra_S}{Ra_T} = \frac{\beta_C \Delta C_r}{\beta_T \Delta T_r}$$

N is positive for cooperative buoyancy forces and negative for opposing buoyancy forces.

The Darcy equation becomes:

$$\vec{V} = -\nabla P + Ra_T(T + NC)\vec{k} \quad (7.12)$$

7.3 Onset of Double-Diffusive Convection in a Tilted Cavity

7.3.1 Linear Stability Analysis

The purpose of this paragraph is to analyze the linear stability of a purely diffusive solution, in a tilted rectangular or infinite box with porous medium saturated by binary fluid. We complete the previous results obtained for horizontal layers by Nield (1968), Charrier-Mojtabi et al. (1997), Mamou et al. (1999a), and Mahidjiba et al. (2000). The influence of the tilt of the cavity on the bifurcation points is analyzed. We show the existence of oscillatory instability even for the case where $Le = 1$, and for various tilts of the cavity.

With reference to Figure 7.9, we consider a Cartesian frame with an angle of tilt φ with respect to the vertical axis. We assume that the rectangular porous cavity (height H , width L , aspect ratio $A = H/L$) is bounded by two walls at different, but uniform temperatures and concentrations, respectively, T'_1 and T'_2 (C'_1 and C'_2); the other two walls are impermeable and adiabatic. We assume that the medium is homogeneous and isotropic, that Darcy's law is valid, and that the Oberbeck–Boussinesq approximation is applicable. The Soret and Dufour effects are assumed to be negligible (see Section 7.4).

The dimensionless thermal, species, and velocity boundary conditions are given by the equations:

$$\begin{aligned} \frac{\partial C}{\partial y} &= \frac{\partial T}{\partial y} = V = 0 && \text{for } y = 0, A \quad \forall x \\ T = C &= U = 0 && \text{for } x = 0 \quad \forall y \\ T = C &= 1; U = 0 && \text{for } x = 1 \quad \forall y \end{aligned} \quad (7.13)$$

The motionless double-diffusive solution ($\vec{V}_0 = 0, T_0 = x, C_0 = x$) is a particular solution of the set of Eqs. (7.11) and (7.13) for horizontal cell. To study the stability of this solution we introduce infinitesimal three-dimensional perturbations (\vec{v}, θ, c) defined by: $\vec{v} = \vec{V}^* - \vec{V}_0$; $\theta = T^* - T_0$; $c = C^* - C_0$, where \vec{V}^*, T^*, C^* indicate the disturbed flow and \vec{V}_0, T_0, C_0 indicate the basic

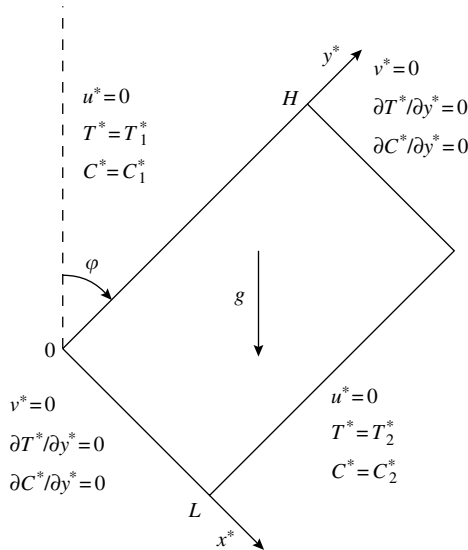


FIGURE 7.9
Definition sketch.

flow. We assume that the perturbation quantities (\vec{v} , θ , c) are small and we ignore the smaller second-order quantities and after linearization we obtain the following system of equations for small disturbances:

$$\begin{aligned}\vec{v} &= -\nabla p + Ra_T(\theta + Nc)\vec{k} \\ \frac{\partial \theta}{\partial t} &= \nabla^2 \theta - u \\ \varepsilon \frac{\partial c}{\partial t} &= \frac{\nabla^2 c}{Le} - u\end{aligned}\tag{7.14}$$

Operating first on Eq. (7.14) twice with curl, using the continuity equation and taking only the x component of the resulting equation, we obtain:

$$\nabla^2 u = -Ra_T \left(\frac{\partial^2(\theta + Nc)}{\partial x \partial y} \cos(\varphi) + \left(\frac{\partial^2(\theta + Nc)}{\partial y^2} + \frac{\partial^2(\theta + Nc)}{\partial z^2} \right) \sin(\varphi) \right)\tag{7.15}$$

with the following boundary conditions:

$$\begin{aligned}\frac{\partial u}{\partial y} &= \frac{\partial c}{\partial y} = \frac{\partial \theta}{\partial y} = 0; \quad \text{for } y = 0, A \quad \forall x, \forall z, \forall t \\ u &= c = \theta = 0; \quad \text{for } x = 0, 1 \quad \forall y, \forall z, \forall t\end{aligned}\tag{7.16}$$

7.3.1.1 Linear stability analysis for an infinite horizontal cell

We first consider the two limit cases of horizontal cells ($\varphi = \pm(\pi/2)$). In this situation the cross-derivative term in Eq. (7.15) is simplified. The problem can be solved by direct calculation and no numerical approximation is needed. Equations (7.14) and (7.15) become

$$\begin{aligned}\nabla^2 u &= -JRa_T \left(\frac{\partial^2(\theta + Nc)}{\partial y^2} + \frac{\partial^2(\theta + Nc)}{\partial z^2} \right) \\ \frac{\partial \theta}{\partial t} &= \nabla^2 \theta - u \\ \varepsilon \frac{\partial c}{\partial t} &= \frac{\nabla^2 c}{Le} - u\end{aligned}\tag{7.17}$$

where J is defined by
$$\begin{cases} \varphi = +\frac{\pi}{2} \rightarrow J = 1 \\ \varphi = -\frac{\pi}{2} \rightarrow J = -1 \end{cases}$$

The boundary conditions associated with this problem are:

$$\begin{aligned}\frac{\partial u}{\partial y} = \frac{\partial c}{\partial y} = \frac{\partial \theta}{\partial y} &= 0; \quad \text{for } y = 0, A \quad \forall x, \forall z, \forall t \\ u = c = \theta &= 0; \quad \text{for } x = 0, 1 \quad \forall y, \forall z, \forall t\end{aligned}\tag{7.18}$$

When we consider a cell of infinite extension in directions y and z , the perturbation functions are written as follows:

$$(u(x, y, z, t), \theta(x, y, z, t), c(x, y, z, t)) = (u(x), \theta(x), c(x))e^{\sigma t + I(ky + \ell z)}\tag{7.19}$$

where $u(x)$, $\theta(x)$, and $c(x)$ are the amplitude, k and ℓ are the wave numbers in directions y and z , respectively, I is the imaginary unit and σ defined by: $\sigma = \sigma_r + I\omega$. The marginal state corresponds to $\sigma_r = 0$.

We substitute expansion (7.19) into (7.17) and then obtain the following linear differential equations for amplitude:

$$\begin{aligned}(D^2 - \alpha^2)u &= JRa_T \alpha^2 (\theta + Nc) \\ (D^2 - \alpha^2 - \sigma)\theta - u &= 0 \\ (D^2 - \alpha^2 - \varepsilon\sigma Le)c - Le u &= 0\end{aligned}\tag{7.20}$$

where D is the operator: $D = d/dx$ and $\alpha^2 = k^2 + \ell^2$.

In these equations α is an overall horizontal wave number. System of Eqs. (7.20) must be solved subject to the boundary conditions:

$$u(x) = c(x) = \theta(x) = 0 \quad \text{for } x = 0 \text{ and } x = 1 \quad (7.21)$$

Solutions of the form:

$$(u, c, \theta) = (u_0, c_0, \theta_0) \sin(i\pi x) \quad (7.22)$$

are possible if:

$$B(B + \sigma)(B + \sigma\varepsilon Le) - JRa_T\alpha^2(NLe(B + \sigma) + B + \varepsilon\sigma Le) \quad (7.23)$$

where $B = (i\pi)^2 + \alpha^2$.

At marginal stability, $\sigma = i\omega$ where ω is real. The real and imaginary parts of Eq. (7.23) become:

$$\begin{aligned} (B^2 - \varepsilon Le\omega^2) - JRa_T\alpha^2(NLe + 1) &= 0 \\ \omega[(1 + \varepsilon Le)B^2 - JRa_T\alpha^2 Le(N + \varepsilon)] &= 0 \end{aligned} \quad (7.24)$$

Two solutions are possible

$$\begin{cases} \omega = 0 \\ Ra_T = \frac{JB^2}{\alpha^2(NLe + 1)} \end{cases} \quad \text{and} \quad \begin{cases} Ra_T = \frac{JB^2(1 + \varepsilon Le)}{\alpha^2 Le(N + \varepsilon)} \\ \omega^2 = -\frac{B^2(1 + \varepsilon NLe^2)}{\varepsilon Le^2(N + \varepsilon)} \end{cases} \quad (7.25)$$

since B^2/α^2 has the minimum value $4\pi^2$, attained when $i = 1$ and $\alpha = \pi$.

1. Case $\varphi = +\pi/2$ ($J = 1$). The saturated porous medium is heated from below where the highest concentration is imposed. The two critical solutions are:

$$\begin{cases} \omega = 0 \\ Ra_{Tc} = \frac{4\pi^2}{NLe + 1} \end{cases} \quad \text{and} \quad \begin{cases} Ra_{Tc} = \frac{4\pi^2(1 + \varepsilon Le)}{Le(N + \varepsilon)} \\ \omega_c^2 = -\frac{4(1 + \varepsilon NLe^2)\pi^4}{\varepsilon Le^2(N + \varepsilon)} \end{cases} \quad (7.26)$$

For cooperative buoyancy forces ($N > 0$), $\omega_c^2 < 0$, then the motionless solution loses its stability via stationary bifurcation with $Ra_{Tc} = 4\pi^2/(NLe + 1)$.

For opposing buoyancy forces ($N < 0$) stationary bifurcation is possible if $N > -(1/Le)$ and Hopf bifurcation is possible if $N \in]-\varepsilon, -1/(\varepsilon Le^2)[$. The pulsation ω_c must be positive, this latter relation is acceptable for $Le > 10$, that is, for liquids. We can verify that if the Hopf bifurcation occurs it will appear

before the stationary bifurcation. For $N < -\varepsilon$, the motionless double-diffusive solution is infinitely linearly stable for all values of ε and Le .

2. Case $\varphi = -\pi/2$ ($J = -1$). The saturated porous medium is now heated from the top where the highest concentration is imposed.

For cooperative buoyancy forces ($N > 0$), $\omega_c^2 < 0$, the motionless double-diffusive solution is infinitely linearly stable for all values of ε and Le .

For opposing buoyancy forces ($N < 0$), the stationary bifurcation is possible if $N < -(1/Le)$ and Hopf bifurcation is possible only if $N \in]-\varepsilon, -1/(\varepsilon Le^2)[$. The pulsation ω_c must be positive, this latter relation is acceptable for $Le > 10$, that is, for liquids. In this case if the Hopf bifurcation occurs it will appear after the stationary bifurcation.

It was also demonstrated by Mamou et al. (1999a) and Bahloul et al. (2003) that the rest flow yields to the supercritical Rayleigh number R^{supac} , the overstable Rayleigh number R^{overac} and the oscillating Rayleigh number R^{oscac} given by:

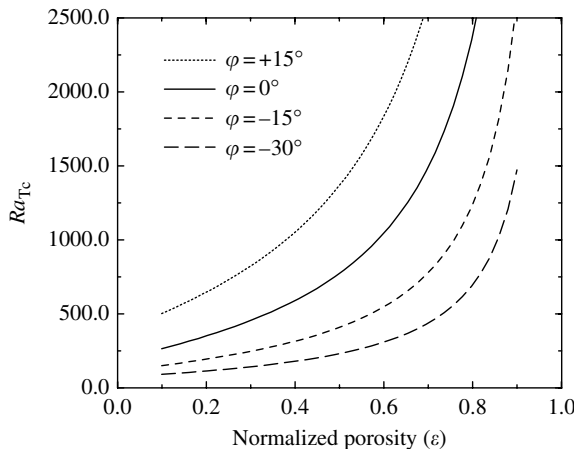
$$R^{oscac} = \frac{(\varepsilon Le + 1)}{Le(\varepsilon + N)^2} - [(\varepsilon - N) + 2\sqrt{-\varepsilon N}] R^{supac}$$

The value of the constant R^{supac} depends upon the types of boundary conditions (Dirichlet or Newman) and the aspect ratio of the layer. For infinite layer it is found that $R^{supac} = 4\pi^2$ for Dirichlet conditions and $R^{supac} = 12$ for Neumann conditions. The onset of convection in horizontal cell subject to mixed boundary conditions has been investigated by Bahloul et al. (2003). The resulting expressions for R^{supac} , R^{overac} , R^{oscac} are function of the aspect ratio A of the layer and parameters N , Le , and ε . The linear stability analysis can also be used to investigate the stability of steady convective flow in order to predict the onset of oscillating flow (Hopf bifurcation R^{Hopfac}). Such an analysis was carried out by Mamou et al. (1999a) and Bahloul et al. (2003) and numerical results were obtained for $R^{Hopfac} = f(A, \varepsilon, N, Le)$.

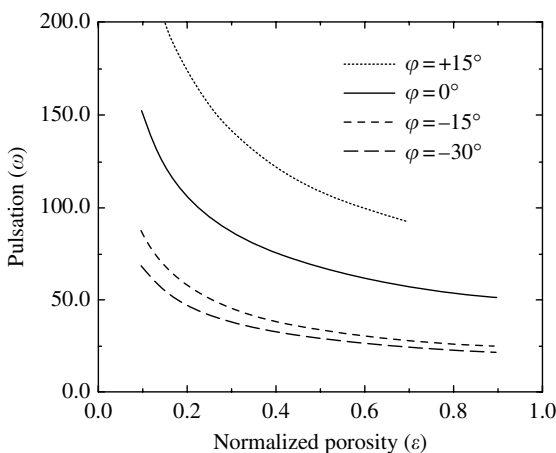
7.3.1.2 Linear stability analysis for a general case

In the general case, for any tilt, the motionless double-diffusive steady-state linear distribution ($\vec{V}_0 = 0$, $T_0 = x$, $C_0 = x$) is not a solution of Eq. (7.11) with $S_T^* = 0$. When the thermal and solutal buoyancy forces are of the same order but have opposite signs ($Ra_T = -Ra_S \iff N = -1$), the steady linear distribution ($\vec{V}_0 = 0$, $T_0 = x$, $C_0 = x$) is a particular solution of Eq. (7.11) for any aspect ratio and for any tilt. To study the stability of this solution, we use a numerical approach based on the Galerkin method, analytical resolution of the stability problem is not possible. Three situations are considered, $Le = 1$, $Le > 1$, and $Le < 1$.

Case $Le = 1$. A complete analysis of this situation shows that the motionless solution can lose its stability via a Hopf bifurcation. Figure 7.10 and Figure 7.11 show the influence of normalized porosity on the critical Rayleigh number and the pulsation corresponding to the Hopf bifurcation for a

**FIGURE 7.10**

Influence of the normalized porosity ε on the critical Rayleigh number Ra_{Tc} of the Hopf bifurcation for $A = 1$ and $Le = 1$. (Taken from M. Karimi-Fard, M.C. Charrier-Mojtabi, and A. Mojtabi. *Phys. Fluids* 11(6): 1346–1358, 1999. With permission.)

**FIGURE 7.11**

Influence of the normalized porosity ε on the pulsation ω_c for $A = 1$ and $Le = 1$. (Taken from M. Karimi-Fard, M.C. Charrier-Mojtabi, and A. Mojtabi. *Phys. Fluids* 11(6): 1346–1358, 1999. With permission.)

square cavity and $Le = 1$. We can see that the critical Rayleigh number increases with the normalized porosity. This means that ε has a stabilizing effect. In this case, the mass and thermal diffusion coefficients are identical and they do not cause instability. The cause of instability is the difference between the unsteady temperature and concentration profiles. The difference increases when ε decreases, which is consistent with the results presented in Figure 7.10. Moreover, for $\varepsilon = 1$, the temperature and concentration profiles

are identical and there are no sources of instability. The motionless double diffusive-solution is then infinitely linearly stable.

$Le > 1$. In this case the thermal diffusivity is higher than the mass diffusivity, which means that the concentration perturbations has the most destabilizing effect. Thus, the stability of the motionless solution depends directly on the destabilizing effects of the concentration. Karimi-Fard et al. (1999) have shown that the lowest critical parameter is obtained for $\varphi = -\pi/2$ (the upper wall is maintained at the highest concentration) which corresponds to the case where the concentration field is the most destabilizing. This destabilizing effect decreases with φ which induces the increase of the critical parameter. These authors demonstrated that the first primary bifurcation creates either branches of steady solutions or time-dependent solutions via Hopf bifurcation. They identified two types of steady bifurcation: transcritical or pitchfork bifurcations depending on the aspect ratio of the box as seen in Figure 7.12. The nature of bifurcation depends on ε , Le , and A . The porosity of the porous medium was found to have a strong influence on the nature of the first bifurcation and there exists a threshold for convective motion even when $Le = 1$. These results agree with those obtained by Mamou et al. (1999a) for a vertical cavity subjected to constant fluxes of heat and solute on the vertical walls when the two horizontal walls are impermeable and adiabatic. Trevisan and Bejan (1985) however found that convection was strongly attenuated in the vicinity of $N = -1$ and that the flow disappeared completely if $Le = 1$ and $N = -1$.

The numerical resolution of the perturbation equations shows the existence of two zones in the (Le, ε) parameter space separated by the curve $\varepsilon Le^2 = 1$. When $\varepsilon Le^2 > 1$, the first primary bifurcation creates steady-state branches of solution and for $\varepsilon Le^2 < 1$, the first bifurcation is a Hopf bifurcation. It is

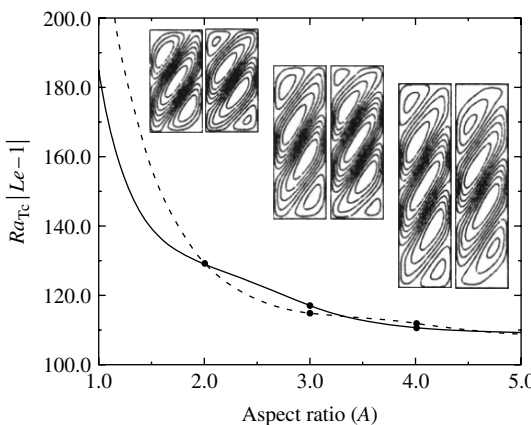
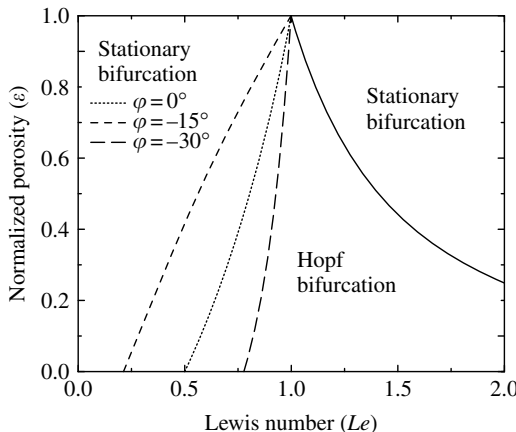


FIGURE 7.12

Evolution of transcritical (solid line) and pitchfork (dashed line) bifurcations with respect to the aspect ratio for $\varphi = 0$. The streamfunctions associated to the first bifurcation are drawn on the left side ($A = 2, 3$, and 4).

**FIGURE 7.13**

Domains of the existence of stationary and Hopf bifurcation in (Le, α) parameter space for $A = 1$. (Taken from M. Karimi-Fard, M.C. Charrier-Mojtabi, and A. Mojtabi. *Phys. Fluids* 11(6): 1346–1358, 1999. With permission.)

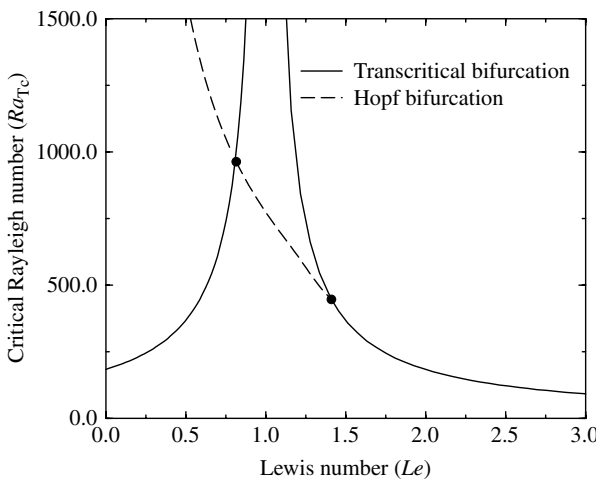
important to observe that these results do not depend on either the aspect ratio or the tilt of the cavity. As can be observed in Figure 7.13, the same curve (solid line) was obtained for all tested angles of tilt.

$Le < 1$. For Lewis numbers lower than one, the stability of the solution will depend on the destabilizing effect of the temperature. In this case the situation is more complicated. There are still two zones in the (Le, ε) parameter space, but they are separated by a curve depending on both the angle of tilt and the aspect ratio. Figure 7.13 shows the results obtained for a square cavity and for three angles of tilt ($\varphi = -15^\circ$, $\varphi = 0^\circ$, and $\varphi = 15^\circ$). Each discontinuous line represents a codimension-two bifurcation curve and delimits with the curve defined by $\varepsilon Le^2 - 1 = 0$ the zone where the first bifurcation occurs is a Hopf one. A section of Figure 7.13 for $\varepsilon = 0.5$ is presented in Figure 7.14. This figure shows the evolution of critical Rayleigh numbers associated to transcritical and Hopf bifurcation as a function of Lewis number for $A = 1$ and $\varphi = 0^\circ$. The curve of Hopf bifurcation crosses the transcritical curve at a codimension-two bifurcation point.

Mamou et al. (1998a) analyzed the linear stability in a vertical Brinkmann porous layer. Critical Rayleigh number is obtained in terms of the aspect ratio of the cavity and the Darcy number of the porous medium. Both Dirichlet and Neumann conditions are considered.

7.3.1.3 Comparisons between fluid and porous medium

Three recent papers have been published in *Physics of Fluids* (Gobin and Bennacer, 1997; Ghorayeb and Mojtabi, 1997; and Xin et al., 1998) on the same problem in a fluid medium with the same boundary conditions and

**FIGURE 7.14**

Critical Rayleigh number versus Lewis number, for $A = 1$, $\varphi = 0$, and $\varepsilon = 0.5$. (Taken from M. Karimi-Fard, M.C. Charrier-Mojtabi, and A. Mojtabi. *Phys. Fluids* 11(6): 1346–1358, 1999. With permission.)

for $N = -1$. In a fluid medium, the first primary bifurcation is never a Hopf one.

The existence of a Hopf bifurcation in a porous medium may be explained through normalized porosity. This parameter induces different evolution in time between the temperature and the concentration. The difference is enhanced when the normalized porosity decreases. Indeed, diffusion and advection of concentration can only be carried out in space occupied by fluid and thus both diffusion and advection are magnified by ε^{-1} , compared to diffusion and advection of heat.

On the contrary, results concerning the bifurcations which lead to steady states are very similar to the ones obtained in a fluid medium: the bifurcations are transcritical or pitchfork depending on the aspect ratio A and the tilt of the cavity. The perturbation equations also have centro-symmetry.

Mamou et al. (1998a) discussed the transition between porous medium and fluid medium. The critical Rayleigh number is predicted in terms of Da for which $Da \rightarrow 0$ corresponds to Darcy law and $Da \rightarrow \infty$ to pure fluid situation.

7.3.2 Weakly Nonlinear Analysis

The purpose of this paragraph is to get the normal form of the amplitude equation and to determine the characteristics of supercritical solutions (stream function, Nusselt number, and Sherwood number) near the bifurcation point for square vertical cavity. The weakly nonlinear analysis that we are going to carry out is based on the multiscale technique. The nonlinear stability problem

formulated in terms of (ψ, θ, c) , for $N = -1$, gives:

$$\begin{aligned} 0 &= \nabla^2 \psi - Ra \left(\frac{\partial c}{\partial x} - \frac{\partial \theta}{\partial x} \right) \\ \frac{\partial \theta}{\partial t} &= \nabla^2 \theta - \frac{\partial \psi}{\partial y} - \frac{\partial \psi}{\partial y} \frac{\partial \theta}{\partial x} + \frac{\partial \psi}{\partial x} \frac{\partial \theta}{\partial y} \\ \varepsilon \frac{\partial c}{\partial t} &= \frac{\nabla^2 c}{Le} - \frac{\partial \psi}{\partial y} - \frac{\partial \psi}{\partial y} \frac{\partial c}{\partial x} + \frac{\partial \psi}{\partial x} \frac{\partial c}{\partial y} \end{aligned} \quad (7.27)$$

Let us rewrite Eq. (7.27) in the form:

$$\frac{\partial \tilde{\vec{u}}}{\partial t} = L(\vec{u}) - N(\vec{u}, \vec{u}) \quad (7.28)$$

where $\vec{u} = (\psi, \theta, c)$, $\tilde{\vec{u}} = (0, \theta, \varepsilon c)$,

$$L = \begin{bmatrix} \nabla^2 & Ra \partial / \partial x & -Ra \partial / \partial x \\ -\partial / \partial y & \nabla^2 & 0 \\ -\partial / \partial y & 0 & \nabla^2 / Le \end{bmatrix} \quad (7.29)$$

and

$$N(\vec{u}, \vec{u}) = \left(0, \frac{\partial \psi}{\partial y} \frac{\partial \theta}{\partial x} - \frac{\partial \psi}{\partial x} \frac{\partial \theta}{\partial y}, \frac{\partial \psi}{\partial y} \frac{\partial c}{\partial x} - \frac{\partial \psi}{\partial x} \frac{\partial c}{\partial y} \right)$$

L and N represent the linear and nonlinear parts of the evolution operator, respectively.

In order to study the onset of convection near the critical Rayleigh number, we expand the linear operator and the solution into power series of the positive parameter η defined by:

$$\eta = \frac{Ra - Ra_c}{Ra_c} \Rightarrow Ra = Ra_c(1 + \eta) \quad \text{with } \eta \ll 1 \quad (7.30)$$

Thus:

$$L = L_0 + \eta L_1 \quad (7.31)$$

$$\vec{u} = \eta \vec{u}_1 + \eta^2 \vec{u}_2$$

where:

$$L_0 = \begin{bmatrix} \nabla^2 & Ra_c \partial / \partial x & -Ra_c \partial / \partial x \\ -\partial / \partial y & \nabla^2 & 0 \\ -\partial / \partial y & 0 & \nabla^2 / Le \end{bmatrix} \quad \text{and} \quad L_1 = \begin{bmatrix} 0 & Ra_c \partial / \partial x & -Ra_c \partial / \partial x \\ 0 & 0 & 0 \\ 0 & 0 & 0 \end{bmatrix}$$

It can be noted that L_0 is the operator which governs the linear stability.

By introducing Eqs. (7.30) and (7.31) into (7.28), with the classical transformation of time $\tau = \eta t$, we obtain after equating like powers of η , the sequential system of equations:

$$\begin{aligned} 0 &= L_0(\vec{u}_1) \quad \text{at order } \eta \\ \frac{\partial \tilde{\vec{u}}_1}{\partial \tau} &= L_0(\vec{u}_2) + L_1(\vec{u}_1) - N(\vec{u}_1, \vec{u}_1) \quad \text{at order } \eta^2 \\ \frac{\partial \tilde{\vec{u}}_2}{\partial \tau} &= L_0(\vec{u}_3) + L_1(\vec{u}_2) - N(\vec{u}_1, \vec{u}_2) - N(\vec{u}_2, \vec{u}_1) \quad \text{at order } \eta^3 \end{aligned} \quad (7.32)$$

etc.

The first-order equation leads us to solve the linear system:

$$\begin{aligned} 0 &= \nabla^2 \psi_1 - Ra_c \left(\frac{\partial c_1}{\partial x} - \frac{\partial \theta_1}{\partial x} \right) \\ 0 &= \nabla^2 \theta_1 - \frac{\partial \psi_1}{\partial y} \\ 0 &= \frac{\nabla^2 c_1}{Le} - \frac{\partial \psi_1}{\partial y} \end{aligned} \quad (7.33)$$

Taking into account the boundary conditions (7.18), Eq. (7.33) yields: $c_1 = Le\theta_1$ such that we have:

$$\vec{u}_1 = \mathcal{A}(\tau)(\psi_1, \theta_1, c_1 = Le\theta_1) = \mathcal{A}(\tau)\vec{\phi}$$

where $\vec{\phi}$ is the eigenmode of the linear stability problem and \mathcal{A} its amplitude. The solution of system (7.33) at the first-order of approximation, does not allow us to determine the amplitude (\mathcal{A}). Only the minimum value of Ra_c is found. The eigenmode $\vec{\phi}$ may be written for square cavity:

$$\begin{aligned} \psi_1 &= \sum_{i=1} \sum_{j=1} a_{i,j}^1 \sin(i\pi x) \sin(j\pi y) \\ \theta_1 &= \sum_{i=1} \sum_{j=0} b_{i,j}^1 \sin(i\pi x) \cos(j\pi y) \quad \text{and} \quad c_1 = Le\theta_1 \end{aligned} \quad (7.34)$$

Substituting Eq. (7.34) into Eq. (7.33) we obtain, by direct identification: $b_{n,0}^1 = 0 \forall n$.

The amplitude $\mathcal{A}(t)$ of the first-order solution is known by using the solvability of the Fredholm alternative or compatibility condition. Before solving the problem for each \vec{u}_i , it is necessary to determine the eigenmode of the

adjoint operator L_0^* of L_0 defined by:

$$L_0^* = \begin{bmatrix} \nabla^2 & \frac{\partial}{\partial y} & \frac{\partial}{\partial y} \\ -Ra_c \frac{\partial}{\partial x} & \nabla^2 & 0 \\ Ra_c \frac{\partial}{\partial x} & 0 & \nabla^2/Le \end{bmatrix}$$

The second equation of system (7.32) leads to:

$$\frac{d(\mathcal{A}(\tau))}{d\tau} \vec{\phi} = L_0(\vec{u}_2) + \mathcal{A}(\tau)L_1(\vec{\phi}) - \mathcal{A}^2(\tau)N(\vec{\phi}, \vec{\phi}) \quad (7.35)$$

The existence of a solution for Eq. (7.35) requires the compatibility equation to be satisfied such that:

$$\frac{d(\mathcal{A}(\tau))}{d\tau} \langle \vec{\phi}^*, \tilde{\phi} \rangle = \mathcal{A}(\tau) \langle \vec{\phi}^*, L_1(\vec{\phi}) \rangle - \mathcal{A}^2(\tau) \langle \vec{\phi}^*, N(\vec{\phi}, \vec{\phi}) \rangle \quad (7.36)$$

where $\vec{\phi}^*$ is the eigenvector of L_0^* adjoint of L_0 and the inner product is defined as:

$$\langle \psi, \theta \rangle = \int_0^1 \int_0^1 \psi \theta \, dx \, dy$$

To determine the coefficients of amplitude Eq. (7.36), we must first solve the adjoint linear problem:

$$\begin{aligned} 0 &= \nabla^2 \psi_1^* + \left(\frac{\partial c_1^*}{\partial y} + \frac{\partial \theta_1^*}{\partial y} \right) \\ 0 &= \nabla^2 \theta_1^* - Ra_c \frac{\partial \psi_1^*}{\partial x} \\ 0 &= \frac{\nabla^2 c_1^*}{Le} + Ra_c \frac{\partial \psi_1^*}{\partial x} \end{aligned} \quad (7.37)$$

Taking into account the boundary condition relative to the adjoint problem we obtain $c_1^* = -Le\theta_1^*$.

The eigenmode $\vec{\phi}^*$ for the adjoint problem may be written as:

$$\begin{aligned} \psi_1^* &= \sum_{i=1} \sum_{j=1} a_{i,j}^{1*} \sin(i\pi x) \sin(j\pi y) \\ \theta_1^* &= \sum_{i=1} \sum_{j=0} b_{i,j}^{1*} \sin(i\pi x) \cos(j\pi y) \quad \text{and} \quad c_1^* = -Le\theta_1^* \end{aligned} \quad (7.38)$$

After introducing the expression of the two eigenmodes $\vec{\phi}$ and $\vec{\phi}^*$ into (7.36) one obtains:

$$\langle \vec{\phi}^*, N(\vec{\phi}, \vec{\phi}) \rangle \neq 0 \quad \text{and} \quad \langle \vec{\phi}^*, L_1(\vec{\phi}) \rangle \neq 0$$

When $d\mathcal{A}(\tau)/d\tau = 0$, the two steady solutions for the square cavity are:

$$\mathcal{A} = 0 \quad \text{and} \quad \mathcal{A} = \frac{\langle \vec{\phi}^*, L_1(\vec{\phi}) \rangle}{\langle \vec{\phi}^*, N(\vec{\phi}, \vec{\phi}) \rangle}$$

The stationary bifurcation is then transcritical. If we consider that: $\theta_1^* = [\bar{\theta}_1/(Le - 1)]$ and after some algebraic manipulations, we obtain the amplitude \mathcal{A} :

$$\mathcal{A} = \frac{\langle \vec{\phi}^*, L_1(\vec{\phi}) \rangle}{\langle \vec{\phi}^*, N(\vec{\phi}, \vec{\phi}) \rangle} = \frac{Ra_c(Le - 1)}{(Le + 1)} \frac{\left\langle \psi_1^*, \frac{\partial \theta_1}{\partial x} \right\rangle}{\left\langle \bar{\theta}_1, \left(\frac{\partial \theta_1}{\partial x} \frac{\partial \psi_1}{\partial y} - \frac{\partial \theta_1}{\partial y} \frac{\partial \psi_1}{\partial x} \right) \right\rangle}$$

We verify that near the bifurcation point the stream function and temperature are proportional to the following: $(Ra - Ra_c)[(Le - 1)/(Le + 1)]$ which is in good agreement with the numerical results ([Figure 7.15\[a\]](#)).

The importance of thermal and mass exchange are given by the overall Nusselt and Sherwood numbers respectively at the vertical walls. The dimensionless Nu and Sh numbers are defined in a square cavity by:

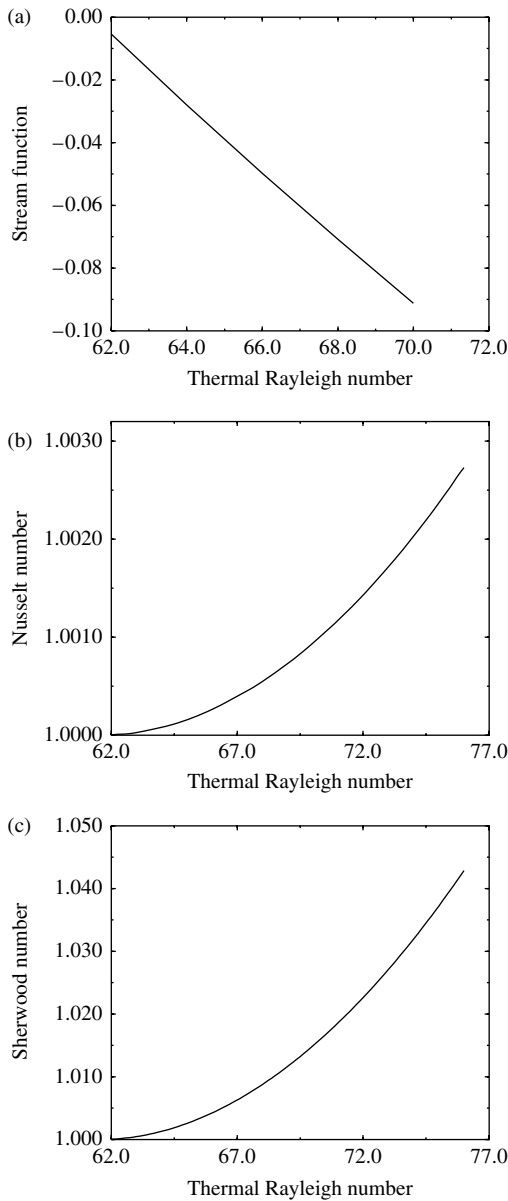
$$Nu = \int_0^1 -\frac{\partial T}{\partial x} \Big|_{x=0 \text{ or } 1} dy \quad \text{and} \quad Sh = \int_0^1 -\frac{\partial C}{\partial x} \Big|_{x=0 \text{ or } 1} dy \quad (7.39)$$

Substituting T and C by their expressions into Eq. (7.39), we obtain:

$$\begin{aligned} Nu &= 1 + \eta \int_0^1 -\frac{\partial \theta_1}{\partial x} \Big|_{x=0,1} dy + \eta^2 \int_0^1 -\frac{\partial \theta_2}{\partial x} \Big|_{x=0,1} dy + \dots \\ Sh &= 1 + \eta \int_0^1 -\frac{\partial c_1}{\partial x} \Big|_{x=0,1} dy + \eta^2 \int_0^1 -\frac{\partial c_2}{\partial x} \Big|_{x=0,1} dy + \dots \end{aligned} \quad (7.40)$$

If we now introduce θ_1 and c_1 given by (7.34) into (7.40) we verify that:

$$\int_0^1 \frac{\partial \theta_1}{\partial x} \Big|_{x=0,1} = \frac{1}{Le} \int_0^1 \frac{\partial c_1}{\partial x} \Big|_{x=0,1} = \sum_{n=1} b_{n,0}^1 = 0 \quad \text{since: } b_{n,0}^1 = 0 \quad \forall n$$

**FIGURE 7.15** $Le = 4, N = -1, A = 1$ (a) Stream function at the center of the cavity versus Ra , near Ra_c (b) Average Nusselt number versus Ra , near Ra_c (c) Average Sherwood number versus Ra , near Ra_c .(Taken from M.C. Charrier-Mojtabi, M. Karimi-Fard, M. Azaiez, and A. Mojtabi. *J. Porous Media* 1: 104–118, 1997. With permission.)

The final expressions of Nu and Sh are then:

$$\begin{aligned} Nu &= 1 + \eta^2 \int_0^1 -\frac{\partial \theta_2}{\partial x} \Big|_{x=0,1} dy + \dots \\ Sh &= 1 + \eta^2 \int_0^1 -\frac{\partial c_2}{\partial x} \Big|_{x=0,1} dy + \dots \end{aligned} \quad (7.41)$$

These results show that the $(Nu - 1)$ and $(Sh - 1)$ are proportional to η^2 . The numerical simulation performed in this study confirms this analytical result ([Figure 7.15\[b\]](#) and [Figure 7.15\[c\]](#)).

7.3.3 Numerical Results

7.3.3.1 Numerical procedure

Two numerical models, based on formulation with primitive variables, first one with a spectral collocation method and the second one with a finite volume method have been performed, Charrier-Mojtabi et al. (1997).

The validity of the two codes was first established by comparing our results to those obtained by Goyeau et al. (1996) and Trevisan and Bejan (1985). For fluxes of heat and mass prescribed at vertical walls, we also compared our results to those obtained by Alavyoon et al. (1994). We found, like these authors, that oscillatory flows occur for sufficiently large values of the Rayleigh number.

7.3.3.2 Numerical determination of the critical Rayleigh number Ra_c for different values of the Lewis number

For the present case (constant temperatures and concentrations imposed at the vertical walls) the study of the transition between the purely diffusive regime and the thermosolutal convective regime, obtained for $N = -1$, was carried out for $Le = 0.1, 0.2, 0.3, 2, 3, 4, 7, 11$, in a square cavity ($A = 1$) and for $\varphi = 0^\circ$.

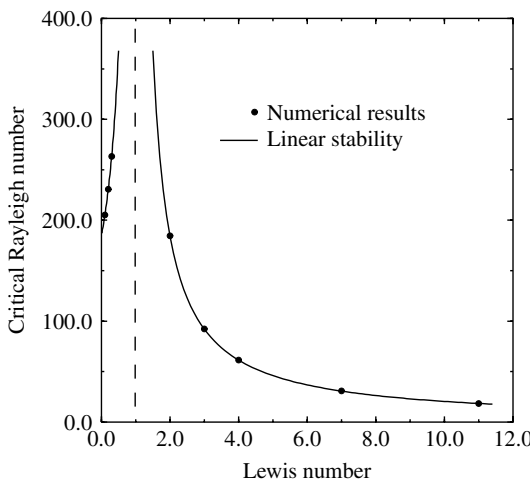
The transition between the equilibrium solution and the convective regime systematically occurs for a critical thermal Rayleigh number satisfying the relation:

$$Ra_c |Le - 1| = 184.06$$

This is in very good agreement with the stability analysis performed in Section 7.3.1 as indicated in [Table 7.1](#) and [Figure 7.16](#). The thermosolutal supercritical convective regime obtained just after the transition is symmetrical with respect to the center of the cavity as shown in [Figure 7.17](#). For $Le = 4, A = 1, N = -1$, the stream function at the center of the cavity, the global Nusselt number, and the Sherwood number are plotted as functions

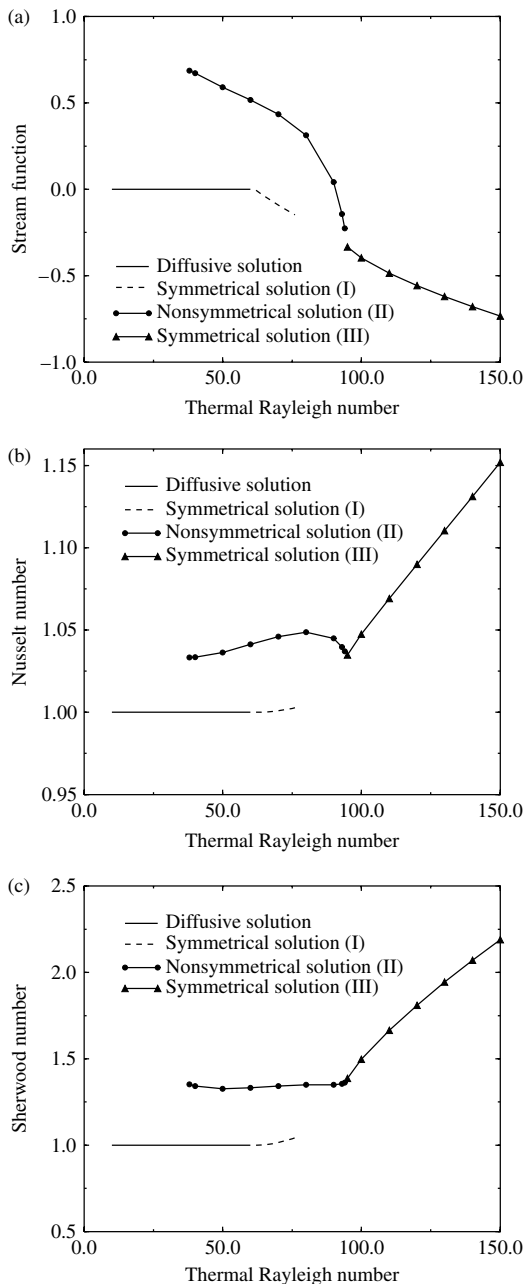
TABLE 7.1 $Ra_c|Le - 1|$ as Function of the Aspect Ratio A

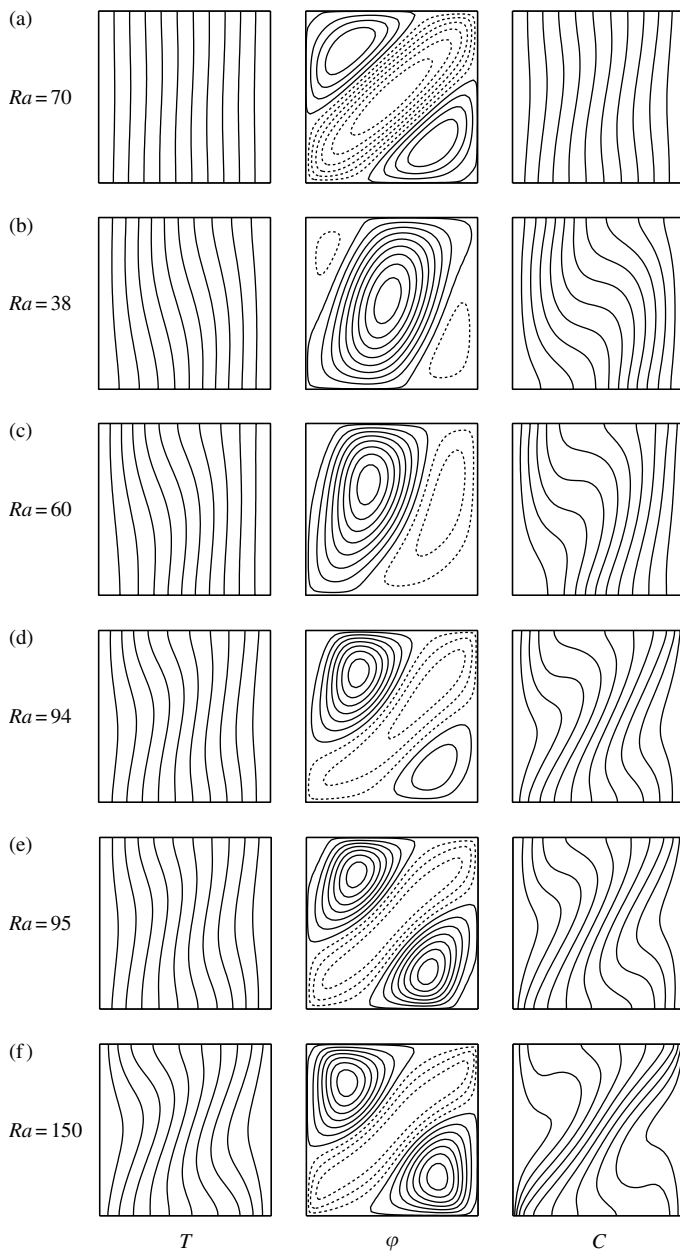
$A = 0.5$	$N \times M$	6×6	7×7	8×8	20×10	40×20
	$Ra_c Le - 1 $	517.36	517.12	517.01	516.87	516.85
$A = 1$	$N \times M$	6×6	7×7	8×8	20×20	30×30
	$Ra_c Le - 1 $	184.33	184.15	184.13	184.06	184.06
$A = 2$	$N \times M$	6×6	7×7	8×8	8×16	20×40
	$Ra_c Le - 1 $	129.34	129.38	129.25	129.22	129.21
$A = 5$	$N \times M$	6×6	7×7	8×8	5×25	14×70
	$Ra_c Le - 1 $	109.71	109.55	109.31	109.21	109.16
$A = 10$	$N \times M$	7×7	8×8	3×30	6×60	10×100
	$Ra_c Le - 1 $	117.75	111.01	106.77	106.37	106.35

**FIGURE 7.16**

$Ra_c = f(Le)$ for $A = 1$, $\varphi = 0$: analytical and numerical results. (Taken from M.C. Charrier-Mojtabi, M. Karimi-Fard, M. Azaiez, and A. Mojtabi. *J. Porous Media* 1: 104–118, 1997. With permission.)

of the Rayleigh number (Figure 7.15) near the bifurcation point. We observe that the stream function depends linearly on the Rayleigh number while the global Nusselt number and Sherwood number vary quadratically with the Rayleigh number. These variations are in good agreement with the results obtained by nonlinear stability analysis (Eq. 7.41). The bifurcation diagrams for the value of the stream function in the center of the cavity, the global Nusselt, and Sherwood number are presented in Figures 7.17(a) to 7.17(c), respectively, for $Le = 4$, $N = -1$, and $A = 1$. One can observe the presence of two other branches of solution (branch I and III), different to the one corresponding to the transition described in the previous sections (branch I), see Figure 7.18.

**FIGURE 7.17**Diagrams bifurcation for $Le = 4, N = -1, A = 1$:(a) Stream function = $f(Ra)$, at the center of the cavity(b) Nusselt number = $f(Ra)$ (c) Sherwood number = $f(Ra)$.(Taken from M.C. Charrier-Mojtabi, M. Karimi-Fard, M. Azaiez, and A. Mojtabi. *J. Porous Media* 1: 104–118, 1997. With permission.)

**FIGURE 7.18**

Isotherms, streamlines, and isoconcentrations for $Le = 4, N = -1, A = 1$

branch I: (a) $Ra = 70$

branch II: (b) $Ra = 38$, (c) $Ra = 60$, (d) $Ra = 94$

branch III: (e) $Ra = 95$, (f) $Ra = 150$

(dashed lines correspond to clockwise rotations).

(Taken from M.C. Charrier-Mojtabi, M. Karimi-Fard, M. Azaiez, and A. Mojtabi. *J. Porous Media* 1: 104–118, 1997. With permission.)

7.3.4 Scale Analysis

Scale analysis was applied to double-diffusive convection in order to determine the heat and mass transfer at the wall.

7.3.4.1 Boundary layer flow

Bejan and Khair (1985) studied the phenomenon of naturally convective heat and mass transfer near a vertical surface embedded in a fluid saturated porous medium. The vertical surface is maintained at a constant temperature T_0 and constant concentration C_0 different than the porous medium temperature T_∞ and concentration C_∞ observed sufficiently far from the wall. The scale of the flow, temperature, and concentration fields near the vertical wall are determined, based on order-of-magnitude analysis.

This study shows that the vertical boundary-layer flux is driven by heat transfer when ($|\beta_T \Delta T| \gg |\beta_C \Delta C| \iff |N| \ll 1$) or by mass transfer when ($|\beta_C \Delta C| \gg |\beta_T \Delta T| \iff |N| \gg 1$), or by a combination of heat and mass transfer effects.

These authors have distinguished four limiting regimes depending on N and Le numbers:

1. For heat transfer driven flow ($|N| \ll 1$) they found for $Le \gg 1$: $Nu \approx Ra^{1/2}$ and $Sh \approx (Ra Le)^{1/2}$; and for $Le \ll 1$: $Nu \approx Ra^{1/2}$ and $Sh \approx Ra^{1/2}Le$.
2. For mass transfer driven flow ($|N| \gg 1$) they found for $Le \gg 1$: $Nu \approx (Ra|N|/Le)^{1/2}$ and $Sh \approx (Ra Le|N|)^{1/2}$ and for $Le \ll 1$: $Nu \approx (Ra|N|)^{1/2}$ and $Sh \approx (Ra Le|N|)^{1/2}$.

7.3.4.2 Effect of the buoyancy ratio N on the heat and mass transfer regimes in a vertical porous enclosure

Previous works have dealt with vertical boxes with either imposed temperatures and concentrations along the vertical side-walls (Trevisan and Bejan, 1985; Charrier-Mojtabi et al., 1997; and Karimi-Fard et al., 1999), or prescribed heat and mass fluxes across the vertical side walls (Trevisan and Bejan, 1986; Alavyoon et al., 1994; Mamou et al., 1995b, 1998b). For both of these boundary conditions, when the ratio of the solutal to thermal buoyancy forces, N , is equal to (-1) , a purely diffusive state (equilibrium solution) can be obtained at low thermal Rayleigh numbers and any Lewis number (Karimi-Fard et al., 1999).

In general, flow and transport follow complex patterns depending on the aspect ratio of the cell, the interaction between the diffusion coefficients (Le) and the buoyancy ratio (N). These groups account for the many distinct heat and mass transfer regimes that can exist. Trevisan and Bejan (1985) identified these regimes on the basis of scale analysis and numerical experiments.

For heat driven flows ($|N| \ll 1$) there are five distinct regimes and in each subdomain of the two-dimensional domain ($Le, Ra_T/A^2$) they give the overall

heat and mass transfer rates as follows:

$$\text{subdomain 1: } Sh \approx \frac{1}{A} (Ra_T Le)^{1/2}, \quad Nu \approx \frac{1}{A} (Ra_T)^{1/2}.$$

In the case $N = 0$ and $A = 1$, the numerical simulations conducted by Goyeau et al. (1996) show that the Nusselt number does not depend on the Lewis number for given Ra_T , since the flow is totally driven by the thermal buoyancy force. On the other hand, the Sherwood number increases with Le and Ra_T . The power law deduced from the computed values of the Sherwood number gives: $Sh = 0.40(Ra_T Le)^{0.51}$ which is in close agreement with the precedent scaling law.

$$\text{subdomain 2: } Sh \approx \frac{1}{A} (Le Ra_T)^{1/2}, \quad Nu \approx \frac{1}{A} Ra_T^{1/2}$$

$$\text{subdomain 3: } Sh \approx 1, \quad Nu \approx \frac{1}{A} Ra_T^{1/2}$$

$$\text{subdomain 4: } Sh \approx 1, \quad Nu \approx 1$$

$$\text{subdomain 5: } Sh \approx \frac{1}{A} (Ra_T Le)^{1/2}, \quad Nu \approx 1$$

For mass driven flows ($|N| \gg 1$) five distinct regimes are also possible and in each subdomain of the two-dimensional domain ($Le, Ra_T |N| / A^2$) the authors give the overall heat and mass transfer rates as:

$$1. \quad Sh \approx \frac{1}{A} (Ra_T |N| Le)^{1/2}, \quad Nu \approx \frac{1}{ALe^{1/2}} (Ra_T |N|)^{1/2}$$

A regression of numerical results obtained by Goyeau et al. (1996) for higher values of N and $A = 1$ leads to the following correlation: $Sh = 0.75(Ra_T Le N)^{0.46}$ where the exponent is in fairly good agreement with the value 0.5 assessed by the scale analysis.

$$2. \quad Sh \approx \frac{1}{A} (Ra_T |N| Le)^{1/2}, \quad Nu \approx \frac{1}{A} (Ra_T |N|)^{1/2}$$

$$3. \quad Sh \approx 1, \quad Nu \approx \frac{1}{A} (Ra_T |N|)^{1/2}$$

$$4. \quad Sh \approx 1, \quad Nu \approx 1$$

$$5. \quad Sh \approx \frac{1}{A} (Ra_T |N| Le)^{1/2}, \quad Nu \approx 1$$

It is shown by Goyeau et al. (1996) that numerical results for mass transfer are in good agreement with the scaling analysis over the wide range of parameters. As a conclusion of the analysis presented by these authors, it is clear that more investigations are required in order to derive the appropriate scaling laws in the domains where the flow is neither fully dominated by the thermal nor by the solutal component of the buoyancy force.

The vertical cavity subject to heat and mass fluxes across the vertical side walls was discussed by Mamou et al. (1995b) and by Amahmid et al. (1999). For this boundary conditions analytical models are presented for Nu and Sh such that the range of validity of asymptotic expressions (obtained for $Ra \rightarrow \infty, N \rightarrow 0, N \rightarrow \infty, Le \rightarrow 0, Le \rightarrow \infty, \dots$ etc.) can be identified through the complete solution. It is noted by Amahmid et al. (1999) that

boundary-layer regime is obtained for $N < 0$ which is quite different from that found for $N > 0$.

7.4 Soret Effect and Thermogravitational Diffusion in Multicomponent Systems

7.4.1 Soret Effect

A review of these studies may be found in the monograph by Platten and Legros (1984) and Turner (1985). Binary fluids in a horizontal porous cell, initially homogeneous in composition, heated from below, will, in the steady state, display a concentration gradient due to the so-called thermal diffusion or Soret effect. Therefore, depending on the sign of the Soret coefficient, the onset of convection can be delayed or anticipated. The Soret coefficient is strongly dependent on composition of the binary fluids. In the last decade, a renewed interest was given to this problem due to the rich dynamic behavior involved in the stabilizing concentration gradient. The first instability sets in as oscillations of increasing amplitude, while the first bifurcation is stationary in horizontal cells saturated by a pure fluid in the Rayleigh–Bénard configuration. Finite amplitude convection is characterized by traveling waves, and sometimes by localized traveling waves, etc. Next, by increasing the Rayleigh number, there is a bifurcation towards steady overturning convection.

The critical Rayleigh number, deduced from the linear stability theory, for the marginal state of stationary instability, in the absence of an imposed solutal gradient, is given by:

$$Ra_c = \frac{4\pi^2}{1 + S_T^*(1 + Le)} \quad (7.42)$$

We find for free, permeable, and conductive boundaries in a fluid medium a similar relation:

$$Ra_c = \frac{27\pi^4/4}{1 + S_T^*(1 + Le)}$$

where Ra_c is the critical Rayleigh number corresponding to exchange of stability. Marginal oscillatory instability occurs for:

$$Ra_c = \frac{4\pi^2(\sigma + \varepsilon^*Le)}{Le(\varepsilon^* + \sigma S_T^*)} \quad (7.43)$$

The general situation, with both cross diffusion and double diffusion (thermal and solutal gradients imposed), was studied by Patil and Rudraiah (1980).

Brand and Steinberg (1983) pointed out that with the Soret effect it is possible to have oscillatory convection induced by heating from above.

Generally, the mass and heat fluxes are given, respectively, by:

$$\vec{J}_c = -\rho D \nabla C' - \rho C'_0 (1 - C'_0) D_T \nabla T' \quad (7.44)$$

$$\vec{J}_T = -\lambda \nabla T' - \rho C' T' D_T \frac{\partial \mu}{\partial C} \nabla C' \quad (7.45)$$

where μ is chemical potential of the solute.

The two contributions to the mass flux are of opposite sign: the temperature gradient is responsible for thermo-migration, thus molecular separation, while isothermal diffusion tends to homogenize the solution. There exists a convectionless steady state where these two contributions are of equal intensity ($\vec{J}_c = 0$) and the resulting mass fraction gradient is then proportional to the temperature gradient

$$\nabla C' = -\frac{D_T}{D} C'_0 (1 - C'_0) \nabla T'$$

The ratio $S_T = D_T/D$ (thermal diffusion coefficient/isothermal diffusion coefficient) is commonly referred to as the Soret coefficient (in K^{-1}). Its magnitude and sign, usually in the 10^{-3} to $10^{-2} K^{-1}$ range, may vary to a large extent from one chemical to another and, for a given chemical; S_T is a complicated function of state variables.

Recently, Platten et al. (2004), obtained experimentally, for a particular namely the system 1, 2, 3, 4-tetrahydronaphthalene-dodecane (THN-C12), 50wt% in each component around room temperature (mean temperature: 25°C), that the Soret coefficient is the same in a free fluid and in a porous medium, since the two values found experimentally are identical but there are experimental errors, discussed in details in a recent Ph.D. thesis (Dutrieux, 2002). They are estimated to be of the order of 5% both for D and for D_T . The same should be true in a porous medium. Thus the error on the Soret coefficient could be as high as 10% (by the way, when looking at the literature, this is not too bad for cross effect). Thus the extraordinary agreement between S_T and S_T^* is certainly fortuitous. If for any theoretical reason there is a difference (e.g., due to the difference in the thermal conductivities of the solid matrix and the fluid), then this difference should be smaller than 10%. This error that we have today on the Soret coefficient is due to the strategy adopted; measuring independently D and D_T . An alternative way would be to measure directly the ratio D_T/D in a horizontal layer. Research in this direction is now undertaken in Toulouse.

When we impose a concentration gradient ($C = 0$ at $x = 0$ and $C = 1$ at $x = 1$) in the dimensionless form, it is common to ignore the Soret effect (i.e., the concentration gradient induced by the temperature gradient). This is due to the low values of the Soret coefficient, for the classical binary mixtures

S_T is between 10^{-4} and 10^{-2} K^{-1} . We have what is called the thermosolutal problem. In this case the concentration gradient exists even in the absence of a thermal gradient.

Bahloul et al. (2003) studied the stability of a horizontal layer for both double diffusive and Soret effects. They found general analytical relations covering these two cases. This work includes an analytical model for finite amplitude convection yielding an expression for subcritical Rayleigh number and numerical results for critical Hopf bifurcation. For finite amplitude convection a comparison is made to illustrate the difference between double-diffusive convection and Soret induced convection in terms of ψ_{\max} , Nu , and Sh .

Soret instability in a vertical Brinkmann porous layer ($N = -1$) has been considered by Joly et al. (2001). Analytical model is proposed for finite amplitude convection. Both the supercritical and subcritical Rayleigh numbers are obtained in term of Darcy number. Also, a comparison between Soret-driven and double-diffusive convection has been discussed by Boutana et al. (2004) for convection in a vertical cavity.

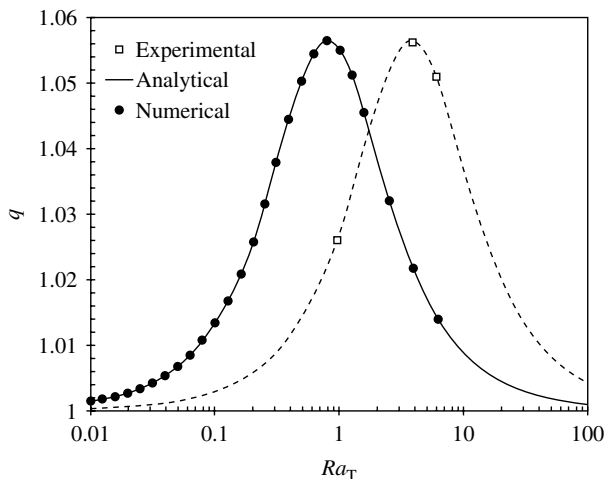
The existence of multiple solutions and the influence of Soret effect on convection in a horizontal porous domain under cross temperature and concentration gradients is discussed by Bennacer et al. (2003b).

Knobloch (1980) and Taslim and Narusawa (1986) demonstrated in a fluid medium and porous medium respectively that a close relationship exists between cross-diffusion problems (taking into account the Dufour effect and Soret effect) and double-diffusion problems. In fact, they demonstrated that these two problems are mathematically identical.

7.4.2 Thermogravitational Diffusion

Thermogravitational is a physical process occurring when a thermal gradient is applied on a fluid mixture. It might contribute to large number of natural physical processes. A fluid mixture saturating a vertical porous cavity under a gravity field, and exposed to a uniform horizontal thermal gradient, is subject not only to convective transfer, but also to thermodiffusion, corresponding to a concentration gradient associated to the Soret effect. The coupling of these two phenomena is called thermogravitational diffusion and leads to species separation. The convective steady state obtained in this case is characterized by large concentration contrast between the top and the bottom of the cell. This contrast is measured by the separation factor, which is defined as the ratio of the mass fraction of the denser component at the bottom of the cell to its mass fraction at the top ($q = C_{\text{bottom}}/C_{\text{top}}$).

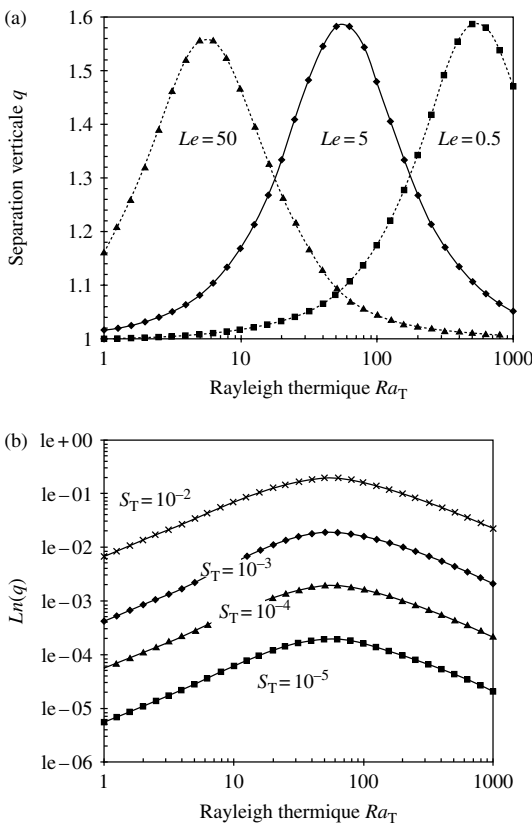
This phenomenon, well known for more than a hundred years, has been lately under investigation owing to its involvement in several natural physical processes in geophysics and mineralogy, where a fluid saturates a porous medium (Jamet et al., 1992). Industrial projects using this thermogravitational

**FIGURE 7.19**

Vertical separation versus Rayleigh number. (Taken from P. Jamet, D. Fargue, and P. Costesque. *Transp. Porous Media* 30(3): 323–344, 1998. With permission.)

diffusion phenomenon coupled to convection in order to separate or to concentrate species have been developed.

The different analytical studies by Fury et al. (1939) and by Estebe and Schott (1970) into this phenomenon have shown the existence of a maximum separation ratio obtained for the corresponding optimum permeability. Marcoux and Charrier-Mojtabi (1998) consider a thermogravitational cell bounded by temperature-imposed vertical walls and adiabatic horizontal walls and filled with homogeneous isotropic porous medium saturated by a two-component incompressible fluid. The dimensionless form of the equations considered, in that work, lead to five parameters: the thermal Rayleigh number, the buoyancy ratio N , the normalized porosity, the Lewis number, and the dimensionless Soret number. These authors have numerically studied the influence of each of these parameters in species separation. The numerical results show the expected existence of a maximum separation corresponding to an optimal Rayleigh number. But till now there is no agreement between numerical and experimental results, already observed by Jamet et al. (1992) and Marcoux et al. (1996), and as seen in Figure 7.19 and this remains an open question still to be solved. The numerical curves in Figure 7.20 shows the influence, on the optimal Ra number, of vertical separation of the Lewis number, the Soret number. They confirmed, rather simple, previous analytical results established by Estebe and Schott (1970) who evaluated the maximum separation ratio and the corresponding optimum permeability as functions of the different physical parameters. Recently, Platten et al. (2002), have clearly demonstrated that when a thermogravitational column is inclined, the molecular separation increases.

**FIGURE 7.20**

Vertical separation versus Rayleigh number, for various values of (a) Lewis number and (b) Soret number. (Taken from P. Jamet, D. Fargue, and P. Costesque. *Transp. Porous Media* 30(3): 323–344, 1998. With permission.)

7.5 Conclusions and Outlook

Several modern engineering processes can benefit from a better understanding of double-diffusive convection in saturated porous medium where the flow and transport follow complex patterns that depend on the interaction between diffusion coefficients and buoyancy ratio.

In geophysics, recent effort are focused more on heat and mass transfer flows in regions below geothermal reservoirs in order to provide better understanding of the processes which transfer heat and chemicals from deep magmatic sources to the base of reservoirs and to surface discharge features (McKibbin, 1998).

Another important area of practical interest is one in materials science, namely in the casting and solidification of metal alloy where double-diffusive convection in mushy zone, characterized by high variation of porosity, can have important effect on the quality of the final product (Sinha and Sundararajan, 1992; Gobin et al., 1998).

The double-diffusive convection phenomena described in this chapter depend essentially on the gravity field, but they can also be observed in the case of pure weightlessness in a cavity filled with a saturated porous medium subjected to vibrations (Khalilouf et al., 1995). It is the coupling between these two external force field (gravity and inertia) and the diffusion that organizes the flow into a form which permits its control (Gershuni and Lyubimov, 1998).

In microgravity conditions, the surface tension effect can induce stable convective motions when the conductive situation becomes instable. A linear and nonlinear stability analysis of Marangoni double-diffusive convection in binary mixtures, saturated porous media, subjected to the Soret effect, are needed for a better understanding and better control of fluid motions in microgravity.

Comprehensive predictions made possible by means of the thermogravitational diffusion model require experimental values of the Soret coefficient. For most binary mixtures the Soret coefficient is unknown. Till date, quantitative experimental data suitable for model validation are quite scarce and, thus, coordinated efforts between modeling and experimentation are needed to provide an ultimate understanding of double-diffusive convection in porous media.

Nomenclature

Roman Letters

A	aspect ratio of the cell H/L
a	thermal diffusivity
C	mass fraction
C_1 (C_2)	mass fraction at cold (hot) vertical wall, $\Delta C = C_2 - C_1$
C_r	reference mass fraction = C_1
c	disturbance concentration
H	height of the cavity
L	width of the cavity
Le	Lewis number; $Le = a/D$
D	mass diffusivity of the constituent through the fluid mixture
g	intensity of gravity ($\vec{g} = -\vec{g}_e \hat{e}_y$)
k	wavenumber
k_c	critical wavenumber

k^*	effective thermal conductivity of the porous medium
I	$\sqrt{-1}$
M, N	orders of approximation
N	Buoyancy ratio ($N = Ra_S/Ra_T$)
Nu	average Nusselt number
q	vertical separation
Ra_S	solutal Rayleigh number based on L ; $Ra_S = (Kg\beta_C(\rho c)_f \Delta CL/k^* v)$
Ra_T	thermal Rayleigh number based on L ; $Ra_T = (Kg\beta_T(\rho c)_f \Delta TL/k^* v)$
Ra_c	critical thermal Rayleigh number
r_i	inner cylinder radius
r_o	outer cylinder radius
S_T	dimensionless Soret number
Sh	average Sherwood number
T	dimensionless temperature
$T'_1 (T'_2)$	temperature at cold (hot) vertical wall, $\Delta T = T'_2 - T'_1$
T_r	reference temperature = T'_1
U	dimensionless horizontal component of the velocity
V	dimensionless vertical component of the velocity

Greek Letters

α	wavenumber
α_e	effective thermal diffusivity of the porous medium
β_T	coefficient of volumetric expansion with respect to the temperature
β_c	coefficient of volumetric expansion with respect to the concentration
γ	curvature parameter = $(r_o - r_i)/r_i$
ε	normalized porosity, $\varepsilon = \varepsilon^*(\rho c)_f / (\rho c)^*$
σ	heat capacity ratio, $\sigma = (\rho c)_f / (\rho c)^*$
ε^*	porosity of the porous matrix
ν	kinematic viscosity of fluid
$(\rho c)_f$	heat capacity of fluid
$(\rho c)^*$	heat capacity of saturated porous medium
θ	disturbance temperature
ψ	disturbance stream function

References

- Adler P.M. *Porous Media: Geometry and Transport*. Stoneham, MA: Butterworth-Heinemann, 1992.
- Alavyoon F. On natural convection in vertical porous enclosures due to prescribed fluxes of heat and mass at the vertical boundaries. *Int. J. Heat Mass Transfer* 36(10): 2479–2498, 1993.

- Alavyoon F., Masuda Y., and Kimura S. On natural convection in vertical porous enclosures due to opposing fluxes of heat and mass prescribed at the vertical walls. *Int. J. Heat Mass Transfer* 37(2): 195–206, 1994.
- Amahmid A., Hasnaoui M., Mamou M., and Vasseur P. Double-diffusive parallel flow induced in a horizontal Brinkmann porous layer subjected to constant heat and mass fluxes: analytical and numerical studies. *Heat Mass Transfer* 35: 409–421, 1999.
- Amahmid A., Hasnaoui M., Mamou M., and Vasseur P. On the transition between aiding and opposing double diffusive flows in a vertical porous matrix. *J. Porous Media* 3: 123–137, 2000.
- Angirasa D., Peterson G.P., and Pop I. Combined heat and mass transfer by natural convection with opposing buoyancy effects in a fluid saturated porous medium. *Int. J. Heat Mass Transfer* 40: 2755–2773, 1997.
- Bahloul A., Boutana N., and Vasseur P. Double-diffusive and Soret induced convection in a shallow horizontal porous layer. *J. Fluid Mech.* 491: 325–352, 2003.
- Bear J. *Dynamics of Fluid in Porous Media*. Amsterdam: Elsevier, 1972.
- Bejan A. *Convection Heat Transfer*. New York: Wiley, 1984 (2nd edn., 1995).
- Bejan A. and Khair K.R. Heat and mass transfer by natural convection in a porous medium. *Int. J. Heat Mass Transfer* 28: 909–918, 1985.
- Beji H., Bennacer R., Duval R., and Vasseur P. Double diffusive natural convection in a vertical porous annulus. *Numer. Heat Transfer*, part A 36: 153–170, 1999.
- Benhadji K. and Vasseur P. Double diffusive convection in a shallow porous cavity filled with no-Newtonian fluid. *Int. Commun. Heat Mass Transfer* 28(6): 763–772, 2001.
- Bennacer R., Beji H., Duval R., and Vasseur P. The Brinkmann model for thermosolutal convection in a vertical annular porous layer. *Int. Commun. Heat Mass Transfer* 27(1): 69–80, 2000.
- Bennacer R., Mohamad A.A., and Akrou D. Transient natural convection in an enclosure with horizontal temperature and vertical solutal gradients. *Int. J. Thermal Sci.* 40: 899–910, 2001.
- Bennacer R., Beji H., and Mohamad A.A. Double diffusive natural convection in a vertical multilayer saturated porous media. *Int. J. Thermal Sci.* 42: 141–151, 2003a.
- Bennacer R., Mahidjiba A., Vasseur P., Beji H., and Duval R. The Soret effect on convection in a horizontal porous domain under cross temperature and concentration gradient. *Int. J. Numer. Meth. Heat Fluid Flow* 13(2): 199–215, 2003b.
- Boutana N., Bahloul A., Vasseur P., and Joly F. Soret driven and double diffusive natural convection in a vertical porous cavity. *J. Porous Media* 7: 1–50, 2004.
- Brand H. and Steinberg V. Convective instabilities in binary mixtures in a porous medium. *Physica A* 119: 327–338, 1983.
- Brand H.R., Hohenberg P.C., and Steinberg V. Amplitude equation near a polycritical point for the convective instability of binary fluid mixture in a porous medium. *Phys. Rev. A* 27: 591–593, 1983.
- Chan B.K.C., Ivey C.M., and Arry J.M. Natural convection in enclosed porous media with rectangular boundaries. *J. Heat Transfer* 92: 21–27, 1970.
- Charrier-Mojtabi M.C., Karimi-Fard M., Azaiez M., and Mojtabi A. Onset of a double diffusive convective regime in a rectangular porous cavity. *J. Porous Media* 1: 104–118, 1997.

- Chen F. and Chen C.F. Double-diffusive fingering convection in porous medium. *Int. J. Heat Mass Transfer* 36: 793–807, 1993.
- Cheng P. Heat transfer in geothermal systems. *Adv. Heat Transfer* 14: 1–105, 1978.
- Combarious M. and Bories S. Hydrothermal convection in saturated porous media. *Advances in Hydroscience*. Academic Press, pp. 231–307, 1975.
- De Groot S.R. and Mazur P. *Nonequilibrium Thermodynamics*. Amsterdam: North-Holland Pub. Co., 1961.
- de Marsily G. *Quantitative Hydrogeology, Groundwater Hydrology for Engineers*. Academic Press, 1986.
- Dutrieux J.F. *Contributions à la métrologie du coefficient Soret*. Ph.D. Université Mons Hainault Belgique, 2002.
- Estebe J. and Schott J. Concentration saline et cristallisation dans un milieu poreux par effet thermogravitationnel. *C. R. Acad. Sci. (Paris)* 271: 805–807, 1970.
- Ettefagh J., Vafai K., and Kim S.J. Non-Darcian effects in open-ended cavities filled with a porous medium. *J. Heat Transfer* 113: 747–756, 1991.
- Fury W.H., Jones R.C., and Onsager L. On the theory of isotropic separation by thermal diffusion. *Phys. Rev.* 55: 1083–1095, 1939.
- Gershuni D.Z., Zhukhovskii E.M., and Lyubimov D.V. Thermal concentration instability of a mixture in a porous medium. *Sov. Phys. Dokl.* 21: 375–377, 1976.
- Gershuni D.Z. and Lyubimov D.V. *Thermal Vibrational Convection*. New York: John Wiley and Sons, 1998.
- Ghorayeb K. and Mojtabi A. Double-diffusive convection in vertical rectangular cavity. *Phys. Fluids* 9: 2339–2348, 1997.
- Gobbé C. and Quintard M. Macroscopic description of unsteady heat transfer in heterogeneous media. *High Temp.-High Pressures* 26: 1–14, 1994.
- Gobin D. and Bennacer R. Double diffusion in a vertical fluid layer: onset of the convective regime. *Phys. Fluids* 6(1): 59–67, 1997.
- Gobin D., Goyeau B., and Songbe J.P. Double diffusive convection in a composite fluid-porous layer. *J. Heat Transfer* 120: 234–242, 1998.
- Goyeau B., Songbe J.P., and Gobin D. Numerical study of double-diffusive natural convection in a porous cavity using the Darcy–Brinkman formulation. *Int. J. Heat Mass Transfer* 39(7): 1363–1378, 1996.
- Griffith R.W. Layered double-diffusive convection, in porous media. *J. Fluid Mech.* 102: 221–248, 1981.
- Hassan M. and Mujumdar A.S. Transpiration-induced buoyancy effect around a horizontal cylinder embedded in porous medium. *Int. J. Energy Res.* 9: 151–163, 1985.
- Hsu C.T. and Cheng P. The Brinkmann model for natural convection about a semi-infinite vertical flat plate in porous medium. *Int. J. Heat Mass Transfer* 28: 683–697, 1985.
- Imhoff B.T. and Green T. Experimental investigation in a porous medium. *J. Fluid Mech.* 188: 363–382, 1988.
- Ingham D.B. and Pop I. *Transport Phenomena in Porous Media I and II*. GB, UK: Pergamon/Elsevier Science, 2000/2002.
- Jamet P., Fargue D., Costesèque P., de Marsily G., and Cernes A. The thermogravitational effect in porous media: a modelling approach. *Transp. Porous Media* 9: 223–240, 1992.
- Jang J.Y. and Chang W.J. Buoyancy-induced inclined boundary layer flows in a porous medium resulting from combined heat and mass buoyancy effects. *Int. Commun. Heat Mass Transfer* 15: 17–30, 1988a.

- Jang J.Y. and Chang W.J. The flow and vortex instability of horizontal natural convection in a porous medium resulting from combined heat and mass buoyancy effects. *Int. J. Heat Mass Transfer* 31: 769–777, 1988b.
- Joly F., Vasseur P., and Labrosse G. Soret instability in a vertical Brinkmann porous enclosure. *Numer. Heat Transfer-part A-Appl.* 39(4): 339–359, 2001.
- Kalla L., Mamou M., Vasseur P., and Robillard L. Multiple steady states for natural convection in a shallow porous cavity subject to uniform heat fluxes. *Int. Commun. Heat Mass Transfer* 26: 761–770, 1999.
- Kalla L., Vasseur P., Bennacer R., Beji H., and Duval R. Double diffusive convection in a horizontal porous layer salted from the bottom and heated horizontally. *Int. Commun. Heat Mass Transfer* 28(1): 1–10, 2001a.
- Kalla L., Mamou M., Vasseur P., and Robillard L. Multiple solutions for double diffusive convection in a shallow porous cavity with vertical fluxes of heat and mass. *Int. J. Heat Mass Transfer* 44: 4493–4504, 2001b.
- Karimi-Fard M., Charrier-Mojtabi M.C., and Vafai K. Non-Darcian effects on double-diffusive convection within a porous medium. *Numer. Heat Transfer, part A* 31: 837–852, 1997.
- Karimi-Fard M., Charrier-Mojtabi M.C., and Mojtabi A. Onset of stationary and oscillatory convection in a tilted porous cavity saturated with a binary fluid. *Phys. Fluids* 11(6): 1346–1358, 1999.
- Kaviany M. *Principles of Convective Heat Transfer in Porous Media*, 2nd edn. New York: Springer, 1995.
- Khalouf H., Gershuni G.Z., and Mojtabi A. Numerical study of two-dimensional thermovibrational convection in rectangular cavities. *Numer. Heat Transfer, part A* 27: 297–305, 1995.
- Khan A.A. and Zebib A. Double-diffusive instability in a vertical layer of a porous medium. *J. Heat Transfer* 103: 179–181, 1981.
- Knobloch E. Convection in binary fluids. *Phys. Fluids* 23(9): 1918–1920, 1980.
- Lage J.L. Effect of the convective inertia term on Bénard convection in a porous medium. *Numer. Heat Transfer, part A* 22: 469–485, 1992.
- Lage J.L. The fundamental theory of flow through permeable media from Darcy to turbulence. *Transport Phenomena in Porous Media*. Ingham D.B. and Pop I. eds., Oxford: Pergamon/Elsevier Science, pp. 1–30, 1998.
- Lai F.C. and Kulacki F.A. Coupled heat and mass transfer from a sphere buried in an infinite porous medium. *Int. J. Heat Mass Transfer* 33: 209–215, 1990.
- Lai F.C. and Kulacki F.A. Coupled heat and mass transfer by natural convection from vertical surfaces in porous medium. *Int. Heat Mass Transfer* 34: 1189–1194, 1991.
- Lin K.W. Unsteady natural convection heat and mass transfer in saturated porous enclosure. *wärm- und Stoffübertragung* 28: 49–56, 1993.
- Mahidjiba A., Mamou M., and Vasseur P. Onset of double-diffusive convection in a rectangular porous cavity subject to mixed boundary conditions. *Int. J. Heat Mass Transfer* 43: 1505–1522, 2003.
- Mamou M. Stability analysis of thermosolutal convection in a vertical packed porous enclosure. *Phys. Fluids* 14: 4301–4314, 2002.
- Mamou M. Stability analysis of the perturbed rest state and of the finite amplitude steady double-diffusive convection in a shallow porous enclosure. *Int. J. Heat Mass Transfer* 46(12): 2263–2277, 2003.
- Mamou M. and Vasseur P. Thermosolutal bifurcation phenomena in porous enclosures subject to vertical temperature and concentration gradients. *J. Fluid Mech.* 395: 61–87, 1999a.

- Mamou M. and Vasseur P. Hysterisis effect on thermosolutal convection with opposed buoyancy forces in inclined enclosures. *Int. Commun. Heat Mass Transfer* 26: 421–430, 1999b.
- Mamou M., Vasseur P., Bilgen E., and Gobin D. Double-diffusive convection in an inclined slot filled with porous medium. *Eur. J. Mech. B/Fluids* 14(5): 629–652, 1995a.
- Mamou M., Vasseur P., and Bilgen E. Multiple solutions for double-diffusive convection in a vertical porous enclosure. *Int. J. Heat Mass Transfer* 38(10): 1787–1798, 1995b.
- Mamou M., Vasseur P., and Bilgen E. A Galerkin finite-element study of the onset of double-diffusive convection in an inclined porous enclosure. *Int. J. Heat Mass Transfer* 41: 1513–1529, 1997.
- Mamou M., Mahidjiba A., Vasseur P., and Robillard L. Onset of convection in an anisotropic porous medium heated from below by a constant heat flux. *Int. Commun. Heat Mass Transfer* 25: 799–808, 1998a.
- Mamou M., Vasseur P., and Bilgen E. Double-diffusive convection instability in a vertical porous enclosure. *J. Fluid Mech.* 368: 263–289, 1998b.
- Mamou M., Vasseur P., and Hasnaoui M. On numerical stability analysis of double-diffusive convection in confined enclosures. *J. Fluid Mech.* 433: 209–250, 2001.
- Marcoux M., Platten J.K., Chavepeyer G., and Charrier-Mojtabi M.C. Diffusion thermogravitationnelle entre deux cylindres coaxiaux; effets de la courbure. *Entropie* 198(1): 89–96, 1996.
- Marcoux M. and Charrier-Mojtabi M.C. Etude paramétrique de la thermogravitation en milieu poreux. *Comptes Rendus de l'Académie des Sciences* 326: 539–546, 1998.
- Marcoux M., Charrier-Mojtabi M.C., and Azaiez M. Double-diffusive convection in an annular vertical porous layer. *Int. J. Heat Mass Transfer* 42: 2313–2325, 1999.
- McKibbin R. Mathematical models for heat and mass in geothermal systems. *Transport Phenomena in Porous Media*. Ingham D.B. and Pop I. eds., Oxford: Pergamon/Elsevier Science, pp. 131–154, 1998.
- Mojtabi A. and Charrier-Mojtabi M.C. Double diffusive convection in porous media, in *Hand-Book of Porous Media*. Vafai K. and Hadim, H. eds., Basel, NY: Marcel Dekker, 2000.
- Mohamad A.A. Double diffusion, natural convection in three-dimensional enclosures filled with porous media, in *Current Issues on Heat and Mass Transfer in Porous Media*, Proceedings of the NATO Advanced Study Institute on Porous Media, 9–20 June 2003, Neptun-Olimp, Romania, pp. 368–377, 2003.
- Mohamad A.A. and Bennacer R. Natural convection in a confined saturated porous medium with horizontal temperature and vertical solutal gradients. *Int. J. Thermal Sci.* 40: 82–93, 2001.
- Mohamad A.A. and Bennacer R. Double diffusion, natural convection in an enclosure filled with saturated porous medium subjected to cross gradients, stably stratified fluid. *Int. J. Heat Mass Transfer* 45: 3725–3740, 2002.
- Mohamad A.A., Bennacer R., and Azaiez J. Double diffusive natural convection in a rectangular enclosure filled with binary fluid saturated porous media; the effect of lateral aspect ratio, *Phys. Fluids* 16(1): 184–199, 2004.
- Murray B.J. and Chen C.F. Double-diffusive convection in a porous medium. *J. Fluid Mech.* 201: 147–166, 1989.
- Nakayama A. and Hossain M.A. An integral treatment for combined heat and mass transfer by natural convection in a porous medium. *Int. J. Heat Mass Transfer* 38: 761–765, 1995.

- Nguyen H.D., Paik S., and Douglass R.W. Study of double diffusion convection in layered anisotropic porous media. *Numer. Heat Transfer B* 26: 489–505, 1994.
- Nield D.A. Onset of thermohaline convection in a porous medium. *Water Resour. Res.* 4: 553–560, 1968.
- Nield D.A. and Bejan A. *Convection in Porous Medium*. New York, Berlin, Heidelberg: Springer-Verlag, 1992 (2nd edn., 1998).
- Nield D.A., Manole D.M., and Lage J.L. Convection induced by inclined thermal and solutal gradients in a shallow horizontal layer of porous medium. *J. Fluid Mech.* 257: 559–574, 1981.
- Patil P. and Rudraiah N. Linear convective stability and thermal diffusion of a horizontal quiescent layer of two-component fluid in a porous medium. *Int. J. Eng. Sci.* 18: 1055–1059, 1980.
- Patil P., Paravathy C.P., and Venkatakrishnan K.S. Thermohaline instability in a rotating anisotropic porous medium. *Appl. Sci. Res.* 46: 73–88, 1989.
- Platten J.K. and Legros J.C. *Convection in Liquids*. Berlin, Heidelberg, New York, Tokyo: Springer-Verlag, 1984.
- Platten J.K. and Costeseque P. The Soret coefficient in porous media. *J. Porous Media* 2004 (in press).
- Platten J.K., Dutrieux J.F., and Bou-Ali M.M. Enhanced molecular separation in inclined thermogravitational columns. *Phil. Mag.* 2004 (in press).
- Poulikakos D. Double-diffusive convection in a horizontally sparsely packed porous layer. *Int. Commun. Heat Mass Transfer* 13: 587–598, 1986.
- Quintard M. and Whitaker S. Transport in chemically and mechanically heterogeneous porous media I: theoretical development of region averaged equations for slightly compressible single-phase flow. *Adv. Water Resour.* 19: 2779–2796, 1996a.
- Quintard M. and Whitaker S. Transport in chemically and mechanically heterogeneous porous media II: theoretical development of region averaged equations for slightly compressible single-phase flow. *Adv. Water Resour.* 19: 49–60, 1996b.
- Quintard M., Kaviany M., and Whitaker S. Two-medium treatment of heat transfer in porous media: numerical results for effective properties. *Adv. Water Resour.* 20(2–3): 77–94, 1997.
- Raptis A., Tzivanidis G., and Kafousias N. Free convection and mass transfer flow through a porous medium bounded by infinite vertical limiting surface with constant suction. *Lett. Heat Mass Transfer* 8: 417–424, 1981.
- Rastogi S.K. and Poulikakos D. Double-diffusion from a vertical surface in a porous region saturated with a non-Newtonian fluid. *Int. J. Heat Mass Transfer* 38: 935–946, 1995.
- Rudraiah N., Srimani P.K., and Friedrich R. Amplitude convection in a two-component fluid porous layer. *Int. Commun. Heat Mass Transfer* 3: 587–598, 1986.
- Saghir M.Z. and Islam M.R. Double-diffusive convection in dual-permeability, dual-porosity porous media. *Int. J. Heat Mass Transfer* 42: 437–454, 1999.
- Sezai I. and Mohamad A.A. Three-dimensional double-diffusive convection in a porous cubic enclosure due to opposing gradients of temperature and concentration. *J. Fluid Mech.* 400: 333–353, 1999.
- Sinha S.K. and Sundararajan T. A variable property analysis of alloy solidification using the anisotropic porous approach. *Int. J. Heat Mass Transfer* 35: 2865–2877, 1992.

- Sözen M. and Vafai K. Analysis of the non-thermal equilibrium condensing flow of gas through a packed bed. *Int. J. Heat Mass Transfer* 33: 1247–1261, 1990.
- Tanton J.W., Lighfoot E.N., and Green T. Thermohaline instability and salt fingers in a porous medium. *Phys. Fluids* 15: 748–753, 1972.
- Taslim M.E. and Narusawa U. Binary fluid convection and double-diffusive convection in a porous medium. *J. Heat Transfer* 108: 221–224, 1986.
- Tien H.C. and Vafai K. Pressure stratification effects on multiphase transport across a vertical slot porous insulation. *J. Heat Transfer* 112: 1023–1031, 1990.
- Trevisan O. and Bejan A. Natural convection with combined heat and mass transfer buoyancy effects in a porous medium. *Int. J. Heat Mass Transfer* 28(8): 1597–1611, 1985.
- Trevisan O. and Bejan A. Mass and heat transfer by natural convection in a vertical slot filled with porous medium. *Int. J. Heat Mass Transfer* 29(3): 403–415, 1986.
- Trevisan O. and Bejan A. Combined heat and mass transfer by natural convection in porous medium. *Adv. Heat Transfer* 20: 315–352, 1990.
- Turner J.S. Multicomponent convection. *Ann. Rev. Fluid Mech.* 17: 11–44, 1985.
- Tyvand P.A. Thermohaline instability in anisotropic porous media. *Water Resour. Res.* 16: 325–330, 1980.
- Vafai K. and Tien H.C. A numerical investigation of phase change effects in porous materials. *Int. J. Heat Mass Transfer* 32: 195–203, 1981.
- Vafai K. and Tien H.C. Boundary and inertia effects on flow and heat transfer in porous media. *Int. J. Heat Mass Transfer* 24: 1261–1277, 1989.
- Xin S., Le Quéré P., and Tuckerman L. Bifurcation analysis of double-diffusive convection with opposing horizontal thermal and solutal gradients. *Phys. Fluids* 10(4): 850–857, 1998.
- Yucel A. Natural convection heat and mass transfer along a vertical cylinder in porous layer heated from below. *Int. J. Heat Mass Transfer* 33: 2265–2274, 1990.

8

The Influence of Mechanical Vibrations on Buoyancy Induced Convection in Porous Media

**Yazdan Pedram Razi, Kittinan Maliwan, Marie Catherine
Charrier-Mojtabi, and Abdelkader Mojtabi**

CONTENTS

8.1	Introduction	322
8.1.1	Definition	322
8.1.2	Linear Stability Analysis	323
8.1.3	Other Geometries	326
8.2	Influence of Vibration on a Porous Layer Saturated by a Pure Fluid	331
8.2.1	Infinite Porous Layer	331
8.2.1.1	Introduction	331
8.2.1.2	Governing equations	331
8.2.1.3	Time-averaged formulation.....	332
8.2.1.4	Scale analysis method	333
8.2.1.5	Time-averaged system of equations	335
8.2.1.6	Stability analysis.....	336
8.2.1.7	Comparison of the two methods.....	345
8.2.1.8	Effect of the direction of vibration	348
8.2.2	Confined Cavity.....	350
8.2.2.1	Introduction	350
8.2.2.2	Stability analysis.....	350
8.2.2.3	Numerical results	352
8.2.2.4	Conclusions	353
8.3	Influence of Vibration on a Porous Layer Saturated by a Binary Fluid	354
8.3.1	Infinite Horizontal Layer	354
8.3.1.1	Introduction	354
8.3.1.2	Governing equations	355
8.3.1.3	The time-averaged formulation	356
8.3.1.4	Stability analysis.....	357

8.3.1.5	Limiting case of the long-wave mode	360
8.3.2	Confined Cavity.....	361
8.3.2.1	Introduction	361
8.3.2.2	Governing equation.....	361
8.3.2.3	Stability analysis.....	362
8.3.2.4	Numerical results	364
8.4	Conclusions and Outlook	366
	Nomenclature	367
	References	368

8.1 Introduction

8.1.1 Definition

Natural convection is a fluid flow mechanism in which the convective motion is produced by the density difference in a fluid subjected to a body force. This difference is usually caused by thermal and/or chemical species diffusion. Consequently, to obtain natural convection, two necessary conditions should be satisfied; the existence of a density variation within a fluid and the existence of a body force. Some common examples of body forces include gravitational, centrifugal, and electromagnetic forces, which may be constant, like gravitational force or may exhibit spatial variation as in centrifugal force. It should be noted that the existence of the body force and the density variation do not guarantee the appearance of convective motion. The relative orientation of the density gradient to the body force provides the sufficient condition for the onset of convection.

The possibility of controlling the hydrodynamic stability of flows by modulation has attracted the attention of researchers for many years [1]. Two types of modulations have been extensively studied; the temperature modulation and the gravity modulation. It is shown that by proper selection of the modulation parameters, dramatic modification in the stability behavior of the dynamic system can be observed [2].

In some applications, it may be desirable to operate at Rayleigh numbers higher than the critical one at which the convection occurs and yet have no convection. Also it is advantageous to suppress undesired chaotic motions in order to remove temperature oscillations which may exceed safe operational conditions. In the context of the temperature or heat flux modulation in porous media, we may mention the study of Caltagirone [3] and of Rees [4], Rudariah and Malashetty [5] in the Rayleigh–Bénard configuration by temperature modulation and Antohe and Lage [6] in a square cavity heated laterally by flux modulation. Thermo-vibrational convection belongs to a special class of periodic flows in which the buoyancy force is time dependent. In this class, which is different from the problems concerning spatial variations of body forces [7–9], the action of external force field

(namely, mechanical vibration) in the presence of a nonhomogeneous scalar field (e.g., temperature or concentration) may be used to control the onset of convective motion. Under microgravity conditions, the gravitational force will be reduced drastically and consequently the buoyancy induced convection. However this situation may cause other forces, which under normal conditions are of secondary importance, to become significant.

Therefore, residual vibration, which naturally exists in a spacecraft, may be used to increase the rate of heat or mass transfer. In its simplest form, the imposed vibration can be considered as a harmonic oscillation having zero average over a vibration period. As with any subject concerning thermo-fluid science, the study of the effects of a vibration mechanism on convective motion has been motivated by practical considerations. It is a known fact that, in the presence of gravitational field, the temperature and concentration gradients may produce natural flows. This, in turn, drastically affects material processing; for example, the rate of crystal growth, etc. With the progress of the space industry, there is an opportunity to grow perfect crystals aboard a spacecraft where there exists a highly reduced gravitational environment. Further, it was thought that the unfavorable effects of natural convection would be eliminated. Therefore, many crystal growth experiments were conducted aboard Skylab and the Mir space station. However the results were surprisingly much less interesting than expected [10]. It was confirmed experimentally that the space station did not represent an acceleration-free environment; there are transient disturbances due to space station maneuvers, impulsive crew movement, and operation of life supporting systems. These residual accelerations are referred to as g-jitter, which can be modeled as harmonic oscillations [11–14]. The theory of thermo-vibrational convection in the fluid medium is summarized in the book written by Gershuni and Lyubimov [15] which reports the Russian studies in this field.

In contrast to the thermo-vibrational problem in fluid media, work on the vibrational problem in porous media is quite recent. We can classify these studies according to geometry, direction of vibration, range of frequency, the number of saturating fluids (mono-component or multi-component), type of boundary conditions, and transport modeling.

8.1.2 Linear Stability Analysis

Most studies concerning thermo-vibrational convection in porous media are theoretical and are focused on the linear stability analysis. The preferred method is the time-averaged method [16]. For porous media saturated by pure fluid, Zenkovskaya [17] studies the effect of vertical vibration (parallel to the temperature gradient) on the thermal stability of the conductive solution. The geometry considered is an infinite horizontal porous layer. A momentum equation is used where the macroscopic nonlinear convective terms are included. The influence of various directions of vibration for the same geometry is described in Zenkovskaya and Rogovenko [18]. The results of their linear stability analysis show that only the vertical vibration

always has a stabilizing effect. These authors find that, for other directions of vibration, depending on the vibrational parameter and the angle of vibration, stabilizing and destabilizing effects are possible.

The effect of low frequency vibration is analyzed by Malashetty and Padmavathi [19]. They use the Brinkman–Forchheimer model in their momentum equation. It has been found that the low frequency g-jitter has a significant effect on the stability of the system and that the effect of gravity modulation can be used to stabilize the conductive solution.

In a confined porous cavity heated from below, Bardan and Mojtabi [20] discuss the effect of vertical vibration. The vibration is in the limiting case of high frequency and small amplitude, which justifies their use of the time-averaged method. The transient Darcy model is used in their momentum equation. It is shown that vibration reduces the number of convective rolls, Figure 8.1. Their results show that, in order to apply the time-averaged formulation effectively, the transient Darcy model should be used. Further, they find that vibration increases the stability threshold. They also perform a weakly nonlinear stability analysis which indicates that primary bifurcations are of a special type of symmetry-breaking pitch-fork bifurcation.

The influence of vibration is extended to the thermohaline problem in porous media by Jounet and Bardan [21]. They find that, based on the values of $\varepsilon^* Le$ (ε^* is the normalized porosity and Le is the Lewis number) and the sign of N/ε^* (N is the ratio of solutal to thermal forces), the solution may bifurcate toward a stationary or Hopf bifurcation. The vibration delays the onset of stationary convection (stabilizing effect) when $N/\varepsilon^* + 1 > 0$. They perform

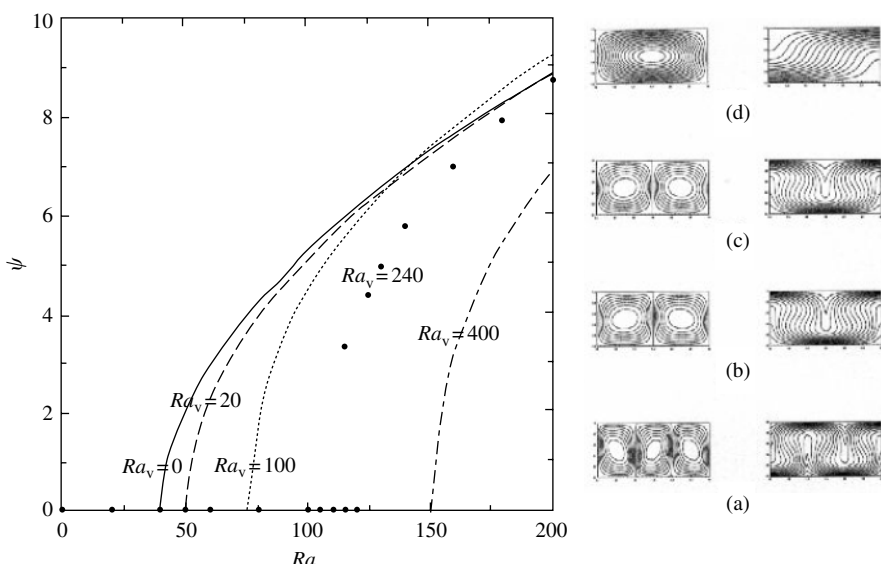


FIGURE 8.1

Bifurcation diagram in the ψ - Ra plane for different values of vibrational Rayleigh number. (From G. Bardan and A. Mojtabi. *Phys. Fluids* 12: 1–9, 2000. With permission.)

a weakly nonlinear analysis which shows that the bifurcation is of pitch-fork type, Figure 8.2. Sovran et al. [22] include the Soret effect in vibro-convective problem in an enclosure saturated by a binary mixture. For negative separation factor they find Hopf bifurcation, Figure 8.3; the direction of vibration is vertical. For various directions of vibration Maliwan et al. [23] study the same problem and find that, generally, when direction of vibration is not parallel to the temperature gradient, vibration reduces the domain of stability.

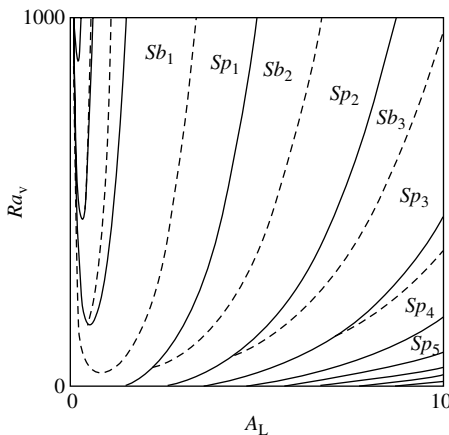


FIGURE 8.2

Map of the regions where the pitch-fork bifurcation is supercritical or subcritical for ($\varepsilon = 1$, $Le = 0.5$, and $N = 0.5$). Sp_i and Sb_i denote supercritical and subcritical branches respectively. (From A. Jounet and G. Bardan. *Phys. Fluids* 13: 1–3, 2001. With permission.)

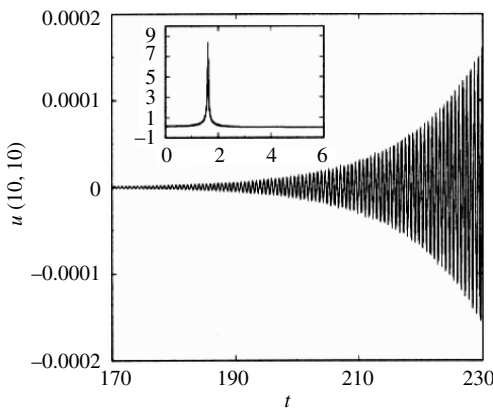


FIGURE 8.3

Onset of oscillatory convection for $Le = 2$, $\varepsilon^* = 0.5$, $\psi = -0.2$, and $R_v = 100$. Horizontal velocity component time evolution is plotted at one point. Inset represents Fourier transform. (From O. Sovran, M.C. Charrier-Mojtabi, M. Azaiez, and A. Mojtabi. International Heat Transfer Conference, IHTC12, Grenoble, 2002. With permission.)

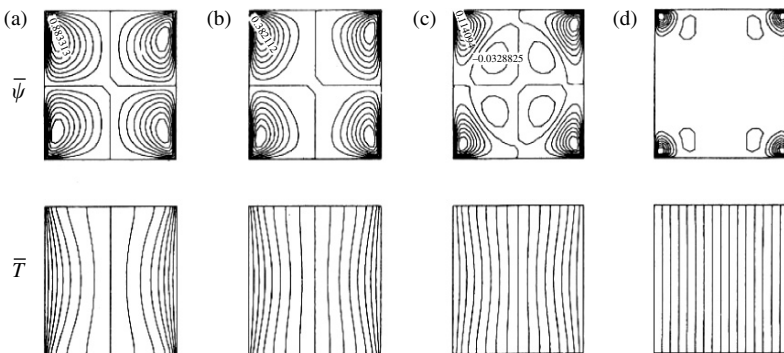
The problem of the onset of thermohaline convection in an infinite horizontal layer under the action of vertical vibration is examined by Maliwan et al. [24]. They find analytical relationships for the onset of convection for both stationary and Hopf bifurcation. Charrier-Mojtabi et al. [25] consider the effect of vibration on fluid flow structure under microgravity conditions. Interesting structures typical of thermo-vibrational convection are found. Razi et al. [26] and Charrier-Mojtabi et al. [27] discuss the validity of the time-averaged formulation in the Horton-Rogers-Lapwood problem using two different approaches; the time-averaged and the so-called direct method. They also explain, from a physical point of view, the necessary assumptions for performing the time-averaged method. From the direct method the thermal stability of the problem is sought by solving the Mathieu equation.

8.1.3 Other Geometries

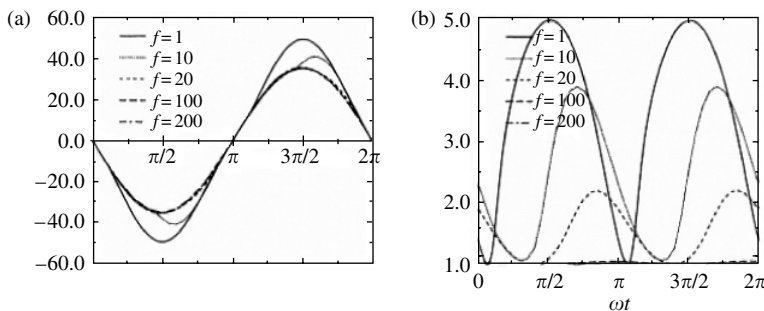
Due to its numerous industrial applications, the differentially heated cavity under constant gravitational acceleration has been studied extensively in the literature; for example, see Nield and Bejan [28].

The thermo-convective motion in a differentially heated square cavity, under the effect of mechanical vibration, is investigated by Khalouf et al. [29]. The direction of vibration is perpendicular to the temperature gradient. The formulation is based on the Darcy-Boussinesq model and the nondimensional system of equations depends on thermal Rayleigh number, vibrational Rayleigh number, and the frequency of vibration. The numerical method used in this research is based on the spectral method. The study is limited to relatively small values of Rayleigh ($Ra_T < 200$) and vibrational Rayleigh numbers ($R_v < 500$). Two different physical cases have been considered, namely convection under microgravity conditions ($Ra_T = 0$) and thermo-vibrational convection in the presence of gravity. They find that, at low frequencies, the diffusion mechanism dominates the heat transfer and a four-roll convective structure characterizes the fluid flow, [Figure 8.4](#) and [Figure 8.5](#). For the case of vibration in presence of gravity in which the two instability mechanisms are involved, the results show that for $\tilde{R} > 2$ (\tilde{R} being acceleration ratio), vibration has a strong effect on fluid flow.

The effect of g-jitter on the boundary layer problems has received particular attention in recent years. Rees and Pop [30] consider the boundary layer induced flow around a vertical isothermal plate embedded in a porous medium. They show that the variations in gravitational acceleration modify the thermal characteristics of the problem. It should be noted that these authors consider the case in which the amplitude of the modulation is small compared with mean gravitational acceleration. An amplitude expansion is used to determine the detailed effect of such g-jitter. The expansion is carried out to the fourth order. They find nonsimilar boundary layer equations for heat and momentum transfer. It is shown that the effect of g-jitter is confined to the leading edge of the plate and decays further down stream,

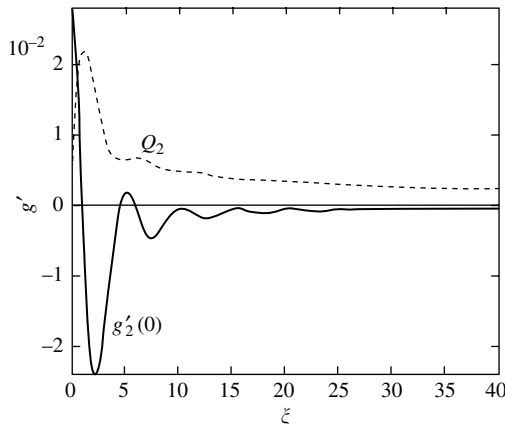
**FIGURE 8.4**

Structures of the stream functions and isotherms at $R_v = 200$, $Ra = 0$ for frequencies (a) 10, (b) 20, (c) 100, and (d) 400. (From H. Khalilov, G.Z. Gershuni, and A. Mojtabi. *Numer Heat Transfer Part A* 30: 605–618, 1996. With permission.)

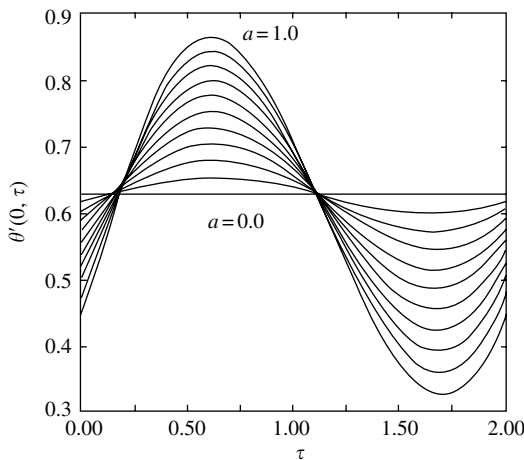
**FIGURE 8.5**

Periodic oscillation of (a) ψ in the center of cavity and (b) Nu at $R_v = 200$ and $Ra = 0$ for different values of frequency. (From H. Khalilov, G.Z. Gershuni, and A. Mojtabi. *Numer Heat Transfer Part A* 30: 605–618, 1996. With permission.)

Figure 8.6. Following the same procedure, Rees and Pop [31] study the effect of g-jitter on free convection near a stagnation point of a uniformly heated cylinder in a porous medium. They examine the response of the system for different vibrational frequencies. The boundary layer system of equations is obtained and numerically solved by the Keller-Box method. The numerical results show that the flow is unaffected by the g-jitter and the averaged heat transfer rate is reduced when the frequency is increased, [Figure 8.7](#). Finally Rees and Pop [32] study the effect of large amplitude g-jitter on a uniformly heated vertical plate embedded in a porous medium. Their results indicate that the effect of large amplitude g-jitter is confined mainly to the region near the leading edge and decays further away from it, [Figure 8.8](#). It is suggested that the overall effect of g-jitter is to diminish the magnitude of the mean flow rate of the heat transfer. It should be emphasized that, in these

**FIGURE 8.6**

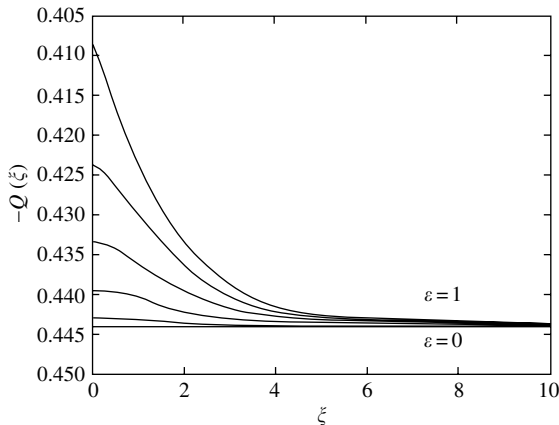
Local rate of heat transfer $g'_2(0)$ (solid line) and global rate of heat transfer, Q_2 (dashed line), as function of ξ ($\xi = \omega x$). (From D.A.S. Rees and I. Pop. *Int. Commun Heat Mass Transfer* 27: 415–424, 2000. With permission.)

**FIGURE 8.7**

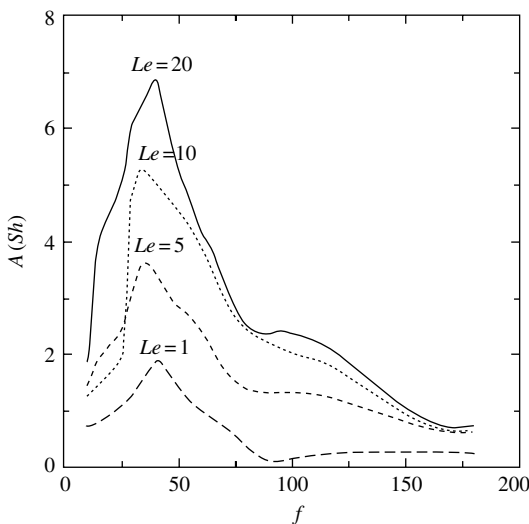
Rate of heat transfer, $\theta'(0, \tau)$, for ω (frequency) = 0.2 with a (amplitude) = 0.0, 0.1, . . . , 1.0. (From D.A.S. Rees and I. Pop. *Int. J. Heat Mass Transfer* 44: 877–883, 2001. With permission.)

three works, Rees and Pop [30–32] used the Darcy model in the momentum equation.

Sovran et al. [33] provide a numerical study for the thermo-vibrational problem in a double-diffusive convection. Darcy–Forchheimer–Brinkman model has been used in the momentum equation. They investigate the square cavity filled with a binary fluid, which is heated differentially. Under finite

**FIGURE 8.8**

Variation of the mean global heat transfer rate $Q(\xi)$ for ε (amplitude of modulation) = 0, 0.2, 0.4, 0.6, 0.8, and 1.0. (From D.A.A. Rees and I. Pop. *Int. J. Heat Mass Transfer* 46: 1097–1102, 2003. With permission.)

**FIGURE 8.9**

Amplitude of the Sherwood number (Sh) versus the vibration frequency for different values of the Lewis number (Le). Set of parameters: $Da = 10$, $Rat_T = 10^5$, $Pr = 0.71$, and $\tilde{R} = 1/5$. (From O. Sovran, G. Bardan, M.C. Charrier-Mojtabi, and A. Mojtabi. *Numer Heat Transfer Part A* 37: 877–896, 2000. With permission.)

frequency of vibration, the case where the solutal and thermal buoyancy forces reinforce each other is considered. The case of resonance is observed for $\tilde{R} < 10$, Figure 8.9. However, it is shown that the maximum amplitude of Sherwood number at resonance smoothes in a highly diffusive porous

medium, Figure 8.10. In the cases studied in this work, they showed that the resonance frequency is independent of Le number. When $\tilde{R} > 1$, significant modifications of fluid flow structures can be observed at low frequencies, Figure 8.11.

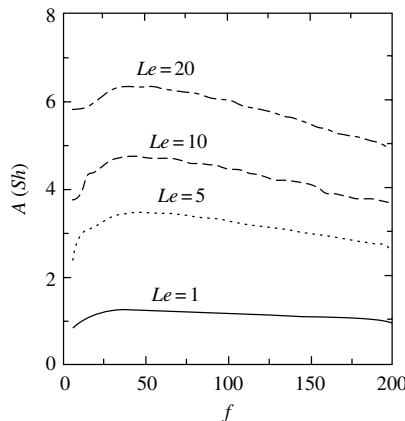


FIGURE 8.10

Amplitude of Sherwood number (Sh), versus the frequency (f) for different Lewis (Le) numbers. For $Da = 10^{-4}$, $Ra = 10^5$, $Pr = 0.71$, and $\tilde{R} = \frac{1}{5}$. (From O. Sovran, G. Bardan, M.C. Charrier-Mojtabi, and A. Mojtabi. *Numer Heat Transfer Part A* 37: 877–896, 2000. With permission.)

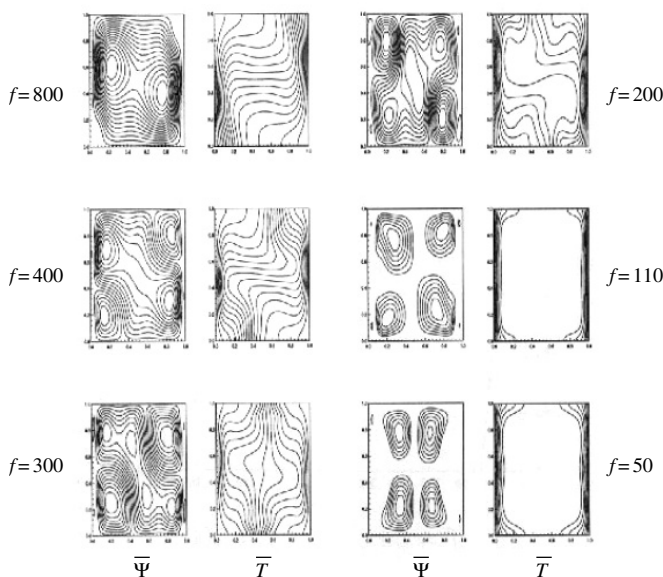


FIGURE 8.11

Mean streamlines and mean isotherms for different frequencies for $Ra_T = 10^4$, $\tilde{R} = 100$, $Da = 10^{-4}$, $Pr = 0.71$, and $Le = 1$. (From O. Sovran, G. Bardan, M.C. Charrier-Mojtabi, and A. Mojtabi. *Numer Heat Transfer Part A* 37: 877–896, 2000. With permission.)

8.2 Influence of Vibration on a Porous Layer Saturated by a Pure Fluid

8.2.1 Infinite Porous Layer

8.2.1.1 Introduction

This section is devoted to the thermal stability of Horton–Rogers–Lapwood problem under the effect of mechanical vibrations. The Horton–Rogers–Lapwood problem is the equivalent of Rayleigh–Bénard problem in porous media, for historical terminology [28]. The layer can be heated from below or from above. Charrier-Mojtabi et al. [27] and Razi et al. [26] use both the direct and the time-averaged methods. The case of vertical vibration is considered; the direction of vibration is parallel to the temperature gradient. Zenkovskaya and Rogovenko [18] extend the same problem to arbitrary direction of vibrations.

8.2.1.2 Governing equations

Two horizontal parallel plates with infinite extension characterize the geometry of the problem. The plates are kept at two constant but different temperatures T_1 and T_2 . The porosity and permeability of the porous material filling the layer are ε and K , respectively. The system is subjected to a mechanical harmonic vibration. As the objective is to study the onset of convection, the Darcy model can be used in the momentum equation. In addition, the porous medium is considered homogenous and isotropic. The fluid which saturates the porous media is assumed to be Newtonian and to satisfy the Oberbeck–Boussinesq approximation. The thermophysical properties are considered constant except for the density of fluid in the buoyancy term which depends linearly on the local temperature:

$$\rho(T) = \rho_0 [1 - \beta_T(T - T_{\text{ref}})] \quad (8.1)$$

where T_{ref} represents the reference temperature; the coefficient of volumetric expansion β_T is assumed to be constant ($\beta_T > 0$). In a reference frame linked to the layer, the gravitational field is replaced by the sum of the gravitational and vibrational accelerations $\mathbf{g} \rightarrow -g\mathbf{k} + b\omega^2 \sin(\omega t)\mathbf{e}$. In this transformation \mathbf{e} is the unit vector along the axis of vibration, b is the displacement amplitude, and ω is the angular frequency of vibration. After making standard assumptions (local thermal equilibrium, negligible viscous heating dissipations, . . .), the governing equations may be written as:

$$\nabla \cdot \mathbf{V} = 0$$

$$\begin{aligned} \frac{\rho_0}{\varepsilon} \frac{\partial \mathbf{V}}{\partial t} &= -\nabla P + \rho_0[\beta_T(T - T_{\text{ref}})](-g\mathbf{k} + b\omega^2 \sin \omega t \mathbf{e}) - \frac{\mu_f}{K} \mathbf{V} \\ &+ (\rho c)_* \frac{\partial T}{\partial t} + (\rho c)_f \mathbf{V} \cdot \nabla T = \lambda_* \nabla^2 T \end{aligned} \quad (8.2)$$

The boundary conditions corresponding to this system are written as:

$$\begin{aligned} V_z(x, z=0) &= 0 & T(x, z=0) &= T_1 \\ V_z(x, z=H) &= 0 & T(x, z=H) &= T_2 \end{aligned} \quad (8.3)$$

In (8.2), μ_f is the dynamic viscosity of fluid, $(\rho c)_*$ represents the effective volumic heat capacity, $(\rho c)_f$ is the volumic heat capacity of fluid, and λ_* is the effective thermal conductivity of saturated porous media.

8.2.1.3 Time-averaged formulation

In order to study the mean behavior of the thermal system, Eqs. (8.2) and (8.3), the time-averaged method is used. This method is adopted under the condition of high frequency and small amplitude of vibration. Under these conditions, it is shown that two different timescales exist, which make it possible to subdivide the fields into two different parts. The first part varies slowly with time (i.e., the characteristic time is large with respect to vibration period) while the second part varies rapidly with time and is periodic with period $\tau = 2\pi/\omega$. Simonenko and Zenkovskaya [16] used this procedure in the fluid system under the action of vibration and the mathematical justification for this method is given in Simonenko [34]. So we may write:

$$\begin{aligned} \mathbf{V}(M, t) &= \bar{\mathbf{V}}(M, t) + \mathbf{V}'(M, \omega t) \\ T(M, t) &= \bar{T}(M, t) + T'(M, \omega t) \\ P(M, t) &= \bar{P}(M, t) + P'(M, \omega t) \end{aligned} \quad (8.4)$$

In the above transformations $(\bar{\mathbf{V}}, \bar{T}, \bar{P})$ represent the averaged fields (for a given function $f(M, t)$, the average is defined as $\bar{f}(M, t) = (1/\tau) \int_{t-\tau/2}^{t+\tau/2} f(M, s) ds$).

On replacing (8.4) in system (8.2), we obtain two-coupled systems of equations:

For the mean flow we obtain:

$$\nabla \cdot \bar{\mathbf{V}} = 0$$

$$\begin{aligned} \frac{\rho_0}{\varepsilon} \frac{\partial \bar{\mathbf{V}}}{\partial t} &= -\nabla \bar{P} + \rho_0 \beta_T (\bar{T} - T_{ref}) g \mathbf{k} + \overline{\rho_0 \beta_T T' b \omega^2 \sin \omega t} \mathbf{e} - \frac{\mu_f}{K} \bar{\mathbf{V}} \\ (\rho c)_* \frac{\partial \bar{T}}{\partial t} + (\rho c)_f \bar{\mathbf{V}} \cdot \nabla \bar{T} + (\rho c)_f \bar{\mathbf{V}}' \cdot \nabla T' &= \lambda_* \nabla^2 \bar{T} \end{aligned} \quad (8.5a)$$

and for the oscillatory flow:

$$\begin{aligned}
 \nabla \cdot \mathbf{V}' &= 0 \\
 \frac{\rho_0}{\varepsilon} \frac{\partial \mathbf{V}'}{\partial t} &= -\nabla P' + \rho_0 \beta_T (\bar{T} - T_{\text{ref}}) b \omega^2 \sin \omega t \mathbf{e} \\
 &\quad + \rho_0 \beta_T T' (g \mathbf{k} + b \omega^2 \sin \omega t \mathbf{e}) - \overline{\rho_0 \beta_T T' b \omega^2 \sin \omega t} \mathbf{e} - \frac{\mu_f}{K} \mathbf{V}' \\
 (\rho c)_* \frac{\partial T'}{\partial t} + (\rho c)_f \mathbf{V}' \cdot \nabla \bar{T} + (\rho c)_f \mathbf{V}' \cdot \nabla T' + (\rho c)_f \bar{\nabla} \cdot \nabla T' - (\rho c)_f \bar{\nabla} \cdot \nabla T' \\
 &= \lambda_* \nabla^2 T'
 \end{aligned} \tag{8.5b}$$

Our objective of applying the scale analysis method is to establish connections between these two-coupled systems of equations which enable us to obtain a closed set of equations for time-averaged fields.

8.2.1.4 Scale analysis method

Let us find how we can resolve the closure problem, that is, how the oscillatory fields can be expressed in terms of the averaged ones. To do this, we use the scale analysis method. This method has been successfully used in predicting the boundary layer approximations, obtaining optimal geometries and predicting critical parameters [35,36]. It should be mentioned that Davis [1] gives an interesting discussion on the importance of relevant scales in the time-modulated problems. Razi et al. [26] and Charrier-Mojtabi et al. [27] use the following scales in the oscillatory system of equations in the porous layer of horizontal infinite extension:

$$O(\bar{T} - T_{\text{ref}}) \approx T_1 - T_2 = \Delta T \quad O\left(\frac{\partial(\cdot)}{\partial t}\right) \approx \omega(\cdot) \quad O\left(\frac{\partial(\cdot)}{\partial z}\right) \approx \frac{1}{H} \tag{8.6}$$

Replacing these scales in the oscillating momentum equation (8.5b) and assuming that $T' \ll \Delta T$ allows them to neglect the buoyancy terms involving T' (the condition for this assumption is validated later). The order magnitude of important terms are as follows:

$$\text{Inertia: } O\left(\frac{\rho_0}{\varepsilon} \frac{\partial \mathbf{V}'}{\partial t}\right) \approx \frac{\rho_0 v' \omega}{\varepsilon}$$

$$\text{Buoyancy: } O(\rho_0 \beta_T (\bar{T} - T_{\text{ref}}) b \omega^2 \sin \omega t) \approx \rho_0 \beta_T \Delta T b \omega^2$$

$$\text{Friction: } O\left(\frac{\mu_f}{K} \mathbf{V}'\right) \approx \frac{\mu_f}{K} v'$$

In order to study the possibility of convective motion, the following case is considered:

$$\text{Buoyancy} \approx \text{Inertia} \quad (8.7\text{a})$$

$$\text{Inertia} \gg \text{Friction} \quad (8.7\text{b})$$

Replacing the order magnitudes of corresponding terms in (8.7a) gives:

$$v' \approx \varepsilon \beta_T \Delta T b \omega \quad (8.8)$$

Furthermore, from (8.7b) one obtains:

$$\frac{\varepsilon v_f}{K\omega} \ll 1 \quad \text{or} \quad \tau_{\text{vib}} \ll \tau_{\text{hyd}} \quad (8.9)$$

In relation (8.9) $\tau_{\text{vib}} = 1/\omega$ and $\tau_{\text{hyd}} = K/\varepsilon v_f$ represent vibrational and hydrodynamic timescales, respectively. Assumption (8.9) allows us to neglect the viscous term in the oscillating momentum equation.

Following the same procedure in the oscillatory energy equation (8.5b), the order magnitude of important terms may be obtained. Due to the assumption $T' \ll \Delta T$ only the convective term involving ΔT is kept:

$$\text{Transient: } (\rho c)_* \frac{\partial T'}{\partial t} \approx (\rho c)_* T' \omega$$

$$\text{Convection: } (\rho c)_f \mathbf{V}' \cdot \nabla \bar{T} \approx (\rho c)_f v' \frac{\Delta T}{H}$$

$$\text{Diffusion: } \lambda_* \nabla^2 T' \approx \lambda_* \frac{T'}{H^2}$$

To study the possibility of oscillatory convective motion, the following case is considered:

$$\text{Convection} \approx \text{Transient} \quad (8.10\text{a})$$

$$\text{Inertia} \gg \text{Diffusion} \quad (8.10\text{b})$$

Imposing the velocity scale (8.8) in (8.10a) and defining heat capacity ratio $\sigma (\sigma = (\rho c)_*/(\rho c)_f)$ results in:

$$T' \approx \frac{\varepsilon}{\sigma} \beta_T \Delta T^2 \frac{b}{H} \quad \text{or} \quad b \ll \frac{H}{(\varepsilon/\sigma) \beta_T \Delta T} \quad (8.11)$$

Inequality (8.11) gives the criteria for small-amplitude vibration. Also, from (8.10b) we obtain:

$$\frac{a_*}{\sigma H^2 \omega} \ll 1 \quad \text{or} \quad \tau_{\text{vib}} \ll \tau_{\text{ther}} \quad \left(a_* = \frac{\lambda_*}{(\rho c)_f} \right) \quad (8.12)$$

In relation (8.12) $\tau_{\text{ther}} = \sigma H^2/a_*$ represents the thermal timescale. Relation (8.12) allows us to neglect the diffusive term in the energy equation.

The final step is to validate assumptions in the oscillatory momentum equation; in other words we should show under which condition $\rho_0 \beta_T \Delta T b \omega^2$ is the dominant buoyancy force. Close examination of different buoyancy forces in the scaled form reveals that under the following condition:

$$\omega^2 \gg \frac{g}{H} \cdot \frac{\varepsilon \beta_T \Delta T}{\sigma} \quad \text{or} \quad \tau_{\text{vib}} \ll \tau_{\text{buoy}} \quad (8.13)$$

$\rho_0 \beta_T \Delta T b \omega^2$ is the dominant buoyancy force in the oscillatory momentum equation. Inequality (8.13) determines another frequency range for achieving high-frequency vibration ($\tau_{\text{buoy}} = (\sigma H / (\varepsilon g \beta_T \Delta T))^{1/2}$).

8.2.1.5 Time-averaged system of equations

To obtain the exact oscillating velocity and temperature, assumptions (8.9), and (8.11) to (8.13) may be applied to (8.5b). In addition, by using the Helmholtz decomposition, defined as

$$(\bar{T} - T_{\text{ref}})\mathbf{e} = \mathbf{W} + \nabla \vartheta \quad (8.14)$$

($\mathbf{W}, \nabla \vartheta$ are solenoidal and irrotational parts); the oscillatory pressure can be eliminated which leads us to:

$$\mathbf{V}' = -(\varepsilon \beta_T b \omega \cos \omega t) \mathbf{W} \quad (8.15)$$

$$T' = \left(\frac{\varepsilon}{\sigma} \beta_T b \sin \omega t \right) \mathbf{W} \cdot \nabla \bar{T} \quad (8.16)$$

By substituting (8.15) and (8.16) in (8.5a), we find the averaged system and, by introducing the reference parameter, $T_1 - T_2$ for temperature, H for height, $\sigma H^2/a_*$ for time, $(a_* = \lambda_*/(\rho c)_f$ is the effective thermal diffusivity), a_*/H for velocity, $\beta_T \Delta T$ for W , and $\mu_f a_*/K$ for pressure, we obtain the resulting averaged system in dimensionless form:

$$\begin{aligned} \nabla \cdot \bar{\mathbf{V}}^* &= 0 \\ B \frac{\partial \bar{\mathbf{V}}^*}{\partial t} &= -\nabla \bar{P}^* + Ra_T \bar{T}^* \mathbf{k} + Ra_v (\mathbf{W}^* \cdot \nabla) \bar{T}^* \mathbf{e} - \bar{\mathbf{V}}^* \\ \frac{\partial \bar{T}^*}{\partial t} + \bar{\mathbf{V}}^* \cdot \nabla \bar{T}^* &= \nabla^2 \bar{T}^* \\ \nabla \cdot \mathbf{W}^* &= 0 \\ \nabla \times \mathbf{W}^* &= \nabla \bar{T}^* \times \mathbf{e} \end{aligned} \quad (8.17)$$

The corresponding boundary conditions for this system are:

$$\begin{aligned} \forall x^*, \text{ for } z^* = 0 & \quad \bar{V}_z^* = 0 \quad \bar{T}^* = 1 \quad W_z^* = 0 \\ \forall x^*, \text{ for } z^* = 1 & \quad \bar{V}_z^* = 0 \quad \bar{T}^* = 0 \quad W_z^* = 0 \end{aligned} \quad (8.18)$$

where:

$$\begin{aligned} Ra_T &= \frac{Kg\beta_T \Delta TH}{v_f a_*} \quad Ra_v = \frac{(\delta^* Fr_F Ra_T \omega^*)^2}{2B} \\ \left(\delta^* = \frac{b}{H} \quad Fr_F = \frac{a_*^2}{gH^3 \sigma^2} \quad \omega^* = \omega \frac{\sigma H^2}{a_*} \quad B = \frac{a_* K}{\varepsilon v_f \sigma H^2} = \frac{\tau_{hyd}}{\tau_{ther}} \right) \end{aligned}$$

In above relations Ra_T is the thermal Rayleigh number, Ra_v is the vibrational Rayleigh number, ω^* is the dimensionless pulsation, B is the transient coefficient, Fr_F is the filtration Froude number, and δ^* is the dimensionless amplitude.

8.2.1.6 Stability analysis

8.2.1.6.1 Linear stability analysis of the time-averaged system of equations

In the presence of vertical vibration, mechanical equilibrium is possible. In order to find the necessary condition for stability in our problem, we set velocity equal to zero in Eqs. (8.17) and (8.18) and the steady-state distribution of fields are sought.

The equilibrium state corresponds to:

$$\bar{T}_0^* = 1 - z^* \quad \mathbf{W}_0^* = \mathbf{0} \quad (8.19)$$

For stability analysis, the fields are perturbed around the equilibrium state (for simplicity bars are omitted):

$$\mathbf{V}^* = \mathbf{0} + \mathbf{v}' \quad T^* = T_0^* + \theta \quad P^* = P_0^* + p' \quad W^* = W_0^* + w'$$

Replacing the above equations in system (8.17) and (8.18), and after linearization we obtain:

$$\begin{aligned} \nabla \cdot \mathbf{v}' &= 0 \\ B \frac{\partial \mathbf{v}'}{\partial t^*} &= -\nabla p' + Ra_T \theta \mathbf{k} + Ra_v (\mathbf{w}' \cdot \nabla T_0^* + \mathbf{W}_0^* \cdot \nabla \theta) \mathbf{k} - \mathbf{v}' \\ \frac{\partial \theta}{\partial t^*} + \mathbf{v}' \cdot \nabla T_0^* &= \nabla^2 \theta \\ \nabla \cdot \mathbf{w}' &= 0 \\ \nabla \times \mathbf{w}' &= \nabla \theta \times \mathbf{k} \end{aligned} \quad (8.20)$$

with corresponding boundary conditions:

$$\begin{aligned} v'_z(x^*, z^* = 0) &= 0 & \theta(x^*, z^* = 0) &= 0 & w'_z(x^*, z^* = 0) &= 0 \\ v'_z(x^*, z^* = 1) &= 0 & \theta(x^*, z^* = 1) &= 0 & w'_z(x^*, z^* = 1) &= 0 \end{aligned} \quad (8.21)$$

Introducing the stream functions ϕ, φ_T , one can write:

$$v'_x = \frac{\partial \phi}{\partial z^*} \quad v'_z = -\frac{\partial \phi}{\partial x^*} \quad w'_x = \frac{\partial \varphi_T}{\partial z^*} \quad w'_z = -\frac{\partial \varphi_T}{\partial x^*} \quad (8.22)$$

We consider the 2D disturbances which are developed in normal modes:

$$(\phi, \theta, \varphi_T) = (\phi(z^*), \theta(z^*), \varphi_T(z^*)) \exp(-\lambda t^* + ikx^*) \quad (8.23)$$

where k is the wave number. Replacing (8.23) in (8.20) and (8.21), and eliminating pressure leads one to:

$$\begin{aligned} (-\lambda B + 1) \left(\frac{d^2 \phi(z^*)}{dz^{*2}} - k^2 \phi(z^*) \right) &= -ikRa_T \theta(z^*) + k^2 Ra_v \varphi_T(z^*) \\ -\lambda \theta(z^*) + ik\phi(z^*) &= \frac{d^2 \theta(z^*)}{dz^{*2}} - k^2 \theta(z^*) \\ -k^2 \varphi_T(z^*) + \frac{d^2 \varphi_T(z^*)}{dz^{*2}} &= -ik\theta(z^*) \end{aligned} \quad (8.24a)$$

The boundary conditions are:

$$\begin{aligned} \phi(z^* = 0) &= \theta(z^* = 0) = \varphi_T(z^* = 0) = 0 \\ \phi(z^* = 1) &= \theta(z^* = 1) = \varphi_T(z^* = 1) = 0 \end{aligned} \quad (8.24b)$$

System (8.24a) is a spectral amplitude problem where λ is the eigenvalue of the system, which depends on:

$$\lambda = \lambda(Ra_T, Ra_v, k, B)$$

Generally, λ is a complex number ($\lambda = \lambda_r + i\lambda_i$).

The system (8.24), admits exact solutions of the form:

$$(\phi(z^*), \theta(z^*), \varphi_T(z^*)) = \sum_{n=1}^N (\phi_n, \theta_n, \varphi_{Tn}) \sin n\pi z^* \quad (8.25)$$

Replacing the above equations in (8.24a), we obtain for marginal stability ($\lambda = 0$):

$$Ra_T = \frac{(\pi^2 + k^2)^2}{k^2} + Ra_v \frac{k^2}{\pi^2 + k^2} \quad (N = 1) \quad (8.26)$$

One can understand from the above equation that, under micro gravity ($Ra_T = 0$), the system is always stable.

Under the condition of vibration in presence of gravity, we can replace Ra_v with $(\delta^* Fr_F \omega^* Ra_T)^2 / 2B$. From (8.26), we get:

$$Ra_T = \frac{B}{\delta^{*2} Fr_F^2 \omega^{*2}} \frac{k^2}{k^2 + \pi^2} \left[1 - \sqrt{1 - 2 \frac{\delta^{*2} Fr_F^2 \omega^{*2}}{B} (k^2 + \pi^2)} \right] \quad (8.27)$$

Another interesting feature of this equation is that it gives additional information:

$$\omega_{\max}^* = \frac{\sqrt{B/2}}{\delta^* Fr_F \pi} \quad (k_c \rightarrow 0) \quad (8.28)$$

Relation (8.28) gives the maximum frequency for achieving absolute stabilization for high-frequency and small-amplitude vibration. For example, for a porous medium of 1 cm in height consisting of glass spheres of 1 mm diameter saturated by methanol, an external velocity of 1.78 m/sec may stop convective motion ($K = 3.1 \times 10^{-10}$, $\sigma = 0.8$, and $\varepsilon = 0.3$).

8.2.1.6.2 Weakly nonlinear stability analysis of the time-averaged system of equations

In this subsection, the normal form of the amplitude equation can be obtained, which determines the characteristics of solutions near the bifurcation point. The method is based on the multiscale approach. The nonlinear stability problem of the time-averaged formulation is expressed in terms of $(\phi, \theta, \varphi_T)$ as follows:

$$\underbrace{\frac{\partial}{\partial t^*} \begin{bmatrix} B \nabla^2 \phi \\ \theta \\ 0 \end{bmatrix}}_L = \begin{bmatrix} -\nabla^2 & -Ra_T \frac{\partial}{\partial x^*} & -Ra_v \frac{\partial^2}{\partial x^{*2}} \\ -\frac{\partial}{\partial x^*} & \nabla^2 & 0 \\ 0 & \frac{\partial}{\partial x^*} & \nabla^2 \end{bmatrix} \begin{bmatrix} \phi \\ \theta \\ \varphi_T \end{bmatrix} + \begin{bmatrix} N_1 \\ N_2 \\ 0 \end{bmatrix} \quad (8.29)$$

in which \mathbf{L} represents a linear operator whereas N_1 and N_2 are nonlinear operators:

$$\begin{aligned} N_1 &= -Ra_v \left[\frac{\partial^2 \theta}{\partial x^{*2}} \frac{\partial \varphi_T}{\partial z^*} + \frac{\partial \theta}{\partial x^*} \frac{\partial^2 \varphi_T}{\partial x^* \partial z^*} - \frac{\partial^2 \varphi_T}{\partial x^{*2}} \frac{\partial \theta}{\partial z^*} - \frac{\partial \varphi_T}{\partial x^*} \frac{\partial^2 \theta}{\partial x^* \partial z^*} \right] \\ N_2 &= \frac{\partial \phi}{\partial x^*} \frac{\partial \theta}{\partial z^*} - \frac{\partial \phi}{\partial z^*} \frac{\partial \theta}{\partial x^*} \end{aligned}$$

In order to study the onset of thermo-vibrational convection near the critical thermal Rayleigh number, the linear operator and the solution are expanded into power series of the positive small parameter η , defined by:

$$Ra_T = Ra_{Tc} + \eta Ra_{T1} + \eta^2 Ra_{T2} + \dots \quad (8.30)$$

Thus:

$$\begin{aligned} [\phi, \theta, \varphi_T] &= \eta [\phi_1, \theta_1, \varphi_{T1}] + \eta^2 [\phi_2, \theta_2, \varphi_{T2}] + \dots \\ \mathbf{L} &= \mathbf{L}_0 + \eta \mathbf{L}_1 + \eta^2 \mathbf{L}_2 + \dots \end{aligned} \quad (8.31)$$

(\mathbf{L}_0 is the operator which governs the linear stability.) It should be noted that, in the operators, Ra_v is also expanded:

$$Ra_v = \frac{(\delta^* Fr_F \omega^*)^2}{2B} \left[Ra_{Tc}^2 + 2\eta Ra_{T1} Ra_{Tc} + \eta^2 (2Ra_{Tc} Ra_{T2} + Ra_{T1}^2) + \dots \right] \quad (8.32)$$

By replacing (8.30) to (8.32) in (8.29), and after introducing the classical time transformation:

$$\frac{\partial}{\partial t^*} = \eta \frac{\partial}{\partial t_1^*} + \eta^2 \frac{\partial}{\partial t_2^*} + \dots$$

on equating the same power of η we obtain a sequential system of equations.

At each order of η , a linear eigenvalue problem is found. At the first order (η) the perturbation is written in the following form:

$$\begin{bmatrix} \phi_1 \\ \theta_1 \\ \varphi_{T1} \end{bmatrix} = A(t_1^*, t_2^*, \dots) \begin{bmatrix} (\pi^2 + k^2)/k^2 \sin \pi z^* \sin kx^* \\ -(\pi^2 + k^2)/k \sin \pi z^* \cos kx^* \\ \sin \pi z^* \sin kx^* \end{bmatrix}$$

The amplitude A depends on slow time evolutions (t_1^*, t_2^*, \dots) .

At the second order η^2 , the existence of a convective solution requires that the solvability lemma be satisfied, in other words there must be a nonzero

solution for the adjoint of \mathbf{L}_0 associated with identical boundary conditions. From the adjoint operator, we obtain:

$$Ra_{Tc}^* = Ra_{Tc}$$

(Ra_{Tc}^* is the critical Rayleigh number corresponding to adjoint system.) Also, we find $Ra_{T1} = 0$ and amplitude A does not depend on timescale t_1^* .

At the third order η^3 by invoking the solvability condition and the Fredholm alternative we obtain the amplitude equation:

$$\frac{dA}{dt_2^*} = \alpha(A - \beta A^3) \quad (8.33)$$

in which α and β are defined as:

$$\begin{aligned} \alpha &= \frac{k^2}{(k^2 + \pi^2)^2} \left[(k^2 + \pi^2) - \frac{(\delta^* Fr_F \omega^*)^2}{B} k^2 Ra_{Tc} \right] Ra_{T2} \\ \beta &= \frac{(\pi^2 + k^2)^2 [1 - (k^4 (\delta^* Fr_F \omega^*)^2 / B (\pi^2 + k^2)^3) Ra_{Tc}^2]}{8 Ra_{T2} [\pi^2 + k^2 - ((\delta^* Fr_F \omega^*)^2 / B) k^2 Ra_{Tc}]} \end{aligned}$$

In α and β , Ra_{T2} is defined as $Ra_{T2} = (Ra_T - Ra_{Tc})/\eta^2$ which is the control parameter.

When there is no vibrational effect, the amplitude of thermo-convective flow near the bifurcation point is proportional to:

$$A \approx \sqrt{Ra_T - Ra_{Tc}}$$

which is in agreement with Palm et al. [37].

Under the effect of vibration α and β are both positive, which results in a supercritical pitch-fork bifurcation.

8.2.1.6.3 Linear stability analysis from direct formulation

The stability of the solution corresponding to the governing equations in the original form is examined in this section. When the direction of vibration is parallel to gravitational acceleration, mechanical stability is possible, which is characterized by a linear temperature and parabolic pressure distribution. In order to study linear stability, the field variables (velocity, pressure, and temperature) are infinitesimally perturbed around the motionless equilibrium

state. The perturbed system becomes:

$$\nabla \cdot \tilde{\mathbf{v}} = 0$$

$$\begin{aligned} \frac{\rho_0}{\varepsilon} \frac{\partial \tilde{\mathbf{v}}}{\partial t} &= -\nabla \tilde{p} + \rho_0 \beta_T \tilde{\theta} (g + b\omega^2 \sin \omega t) \mathbf{k} - \frac{\mu_f}{K} \tilde{\mathbf{v}} \\ \sigma \frac{\partial \tilde{\theta}}{\partial t} + \tilde{\mathbf{v}} \cdot \nabla T_0 &= a_* \nabla^2 \tilde{\theta} \end{aligned} \quad (8.34)$$

By eliminating the pressure in the momentum equation and introducing the normal modes as:

$$\tilde{v}_z = X(t) e^{ik(x/H)} \sin \frac{z}{H} \pi \quad \tilde{\theta} = Y(t) e^{ik(x/H)} \sin \frac{z}{H} \pi \quad (8.35)$$

and on replacing the above relations in system (8.34), we obtain:

$$\begin{aligned} \frac{\rho_0}{\varepsilon} \frac{dX(t)}{dt} + \frac{\mu_f}{K} X(t) &= \rho_0 \beta_T \frac{k^2}{k^2 + \pi^2} (g + b\omega^2 \sin \omega t) Y(t) \\ X(t) &= \frac{H}{\Delta T} \left[\sigma \frac{dY(t)}{dt} + a_* \left[\left(\frac{k}{H} \right)^2 + \left(\frac{\pi}{H} \right)^2 \right] Y(t) \right] \end{aligned} \quad (8.36)$$

Elimination of $X(t)$ in system (8.36) gives:

$$\begin{aligned} \frac{d^2Y}{dt^2} + \left[\frac{a_*}{\sigma H^2} (k^2 + \pi^2) + \frac{\varepsilon v_f}{K} \right] \frac{dY}{dt} \\ + \left[\frac{\varepsilon v_f a_*}{KH^2 \sigma} (k^2 + \pi^2) - \frac{\varepsilon \beta_T \Delta T}{\sigma H} \frac{k^2}{k^2 + \pi^2} (g + b\omega^2 \sin \omega t) \right] Y = 0 \end{aligned} \quad (8.37)$$

The above equation is similar to a mechanical pendulum with an oscillating support:

$$\ddot{\Theta} + 2\xi \omega_n \dot{\Theta} \pm \left(\omega_n^2 - \omega^2 \frac{\delta}{\ell} \sin \omega t \right) \Theta = 0 \quad (8.38)$$

in which ω_n represents the natural frequency, ξ damping ratio, ω vibrational frequency, ℓ pendulum length, and finally δ the amplitude of vibration. The plus sign in (8.43) corresponds to a normal hanging pendulum while the negative sign corresponds to an inverted pendulum. Equalizing the vibrational effect in the two systems gives:

$$\ell_{\text{eff}} \approx \frac{H}{(\varepsilon/\sigma) \beta_T \Delta T} \quad (8.39)$$

which is the effective length of the equivalent system. In addition it is clear that this effective length is quite long ($\beta_T \Delta T \ll 1$).

Equation (8.37) can be written in dimensionless form:

$$B \frac{d^2 Y^*}{dt^{*2}} + [B(k^2 + \pi^2) + 1] \frac{dY^*}{dt^*} + \left[(k^2 + \pi^2) - Ra_T \frac{k^2}{k^2 + \pi^2} (1 + \tilde{R} \sin \omega^* t^*) \right] Y^* = 0 \quad (8.40)$$

where B , Ra_T , ω^* are defined as in Section 8.2.1.6.2. Also we can define \tilde{R} as $\delta^* Fr_F \omega^{*2}$. For the above equation two different cases are distinguished:

1. $B\omega^* \ll 1$. In this case, the governing equation is written as:

$$\frac{dY^*}{dt^*} + \left[(\pi^2 + k^2) - Ra_T \frac{k^2}{k^2 + \pi^2} (1 + \delta^* Fr_F \omega^{*2} \sin \omega^* t^*) \right] Y^* = 0 \quad (8.41)$$

The solution of this first-order differential equation with periodic coefficient is:

$$Y^* = Y_0^* \exp - \left[(\pi^2 + k^2) - \frac{k^2}{k^2 + \pi^2} Ra_T \right] t^* \times \exp \left(2\delta^* Fr_F \omega^* \frac{k^2}{k^2 + \pi^2} Ra_T \sin^2 \frac{\omega^* t^*}{2} \right) \quad (8.42)$$

$$Y^*(0) = Y_0^*$$

When there is no vibration ($\delta^* Fr_F \omega^* = 0$), from (8.42) the classical result of $Ra_{Tc} = 4\pi^2$ for marginal stability may be deduced. In the presence of vibration, if the layer is heated from above ($Ra_T < 0$) the solution is always stable. This is true because, in this situation, the arguments in exponential functions (8.42) are always positive. When the layer is heated from below ($Ra_T > 0$), the solution is composed of two parts, see (8.42) the second part of which can be considered as a positive bounded periodic function. Therefore, for marginal stability, the first part is important and gives $Ra_{Tc} = 4\pi^2$. In other words, vibration has no effect on stability threshold. Physically from the mechanical analogy, this case corresponds to a pendulum in which the viscous damping is much larger than angular acceleration. Strong damping is able to destroy the oscillatory movements.

2. $B\omega^* \gg 1$. Using transformation $h^*(t^*) = e^{-mt^*} M(t^*)$, Eq. (8.42) is cast into Mathieu's equation m being $(\pi^2 + k^2 + 1/B)/2$:

$$\frac{d^2M(\tau)}{d\tau^2} + (A - 2Q \cos 2\tau)M(\tau) = 0 \quad \left(\omega^* t^* = 2\tau - \frac{\pi}{2} \right) \quad (8.43)$$

in which A and Q are:

$$A = \frac{\pi^2 + k^2}{B} - m^2 - \frac{k^2}{B(\pi^2 + k^2)} Ra_T \quad Q = \frac{2k^2}{B(\pi^2 + k^2)} \delta^* Fr_F Ra_T \quad (8.44)$$

Detailed analysis of the stable regions for this equation can be found elsewhere (see [38–40]). They divide the domain into alternate stable and unstable regions. In order to solve Eq. (8.43), the Floquet theory is used, which considers the solution as:

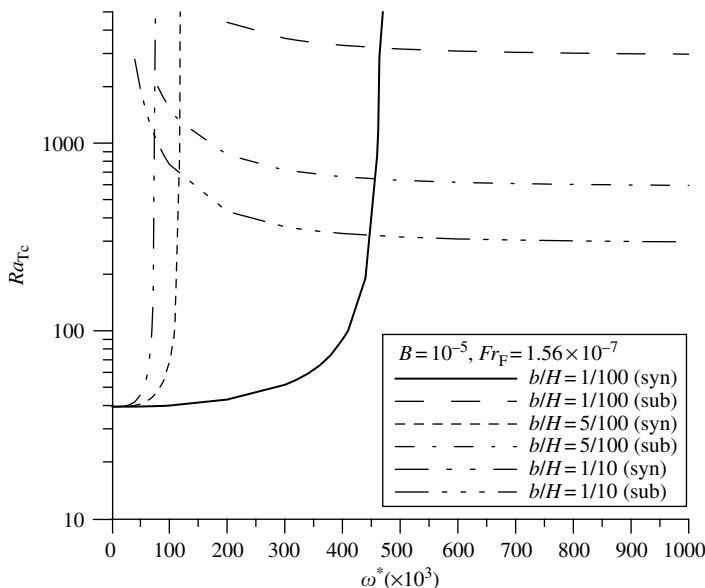
$$M = R(\tau)e^{\mu\tau}$$

in which $R(\tau)$ is a periodic function having period π or 2π , the parameter μ is the Floquet exponent, and the marginal stability condition is $m = \mu\omega^*/2$. The details of this method can be found elsewhere (see [41]).

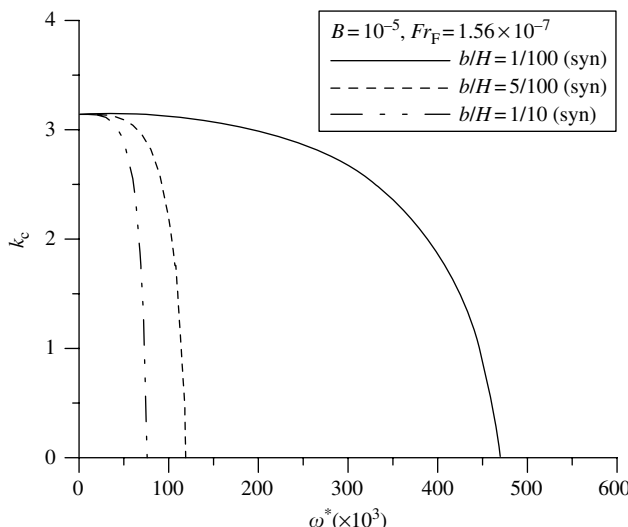
To obtain the critical thermal Rayleigh and wave numbers for marginal stability, working parameters ($B, \omega^*, \delta^*, Fr_F$) are fixed except Ra_T and k . Then we search for the minimum Ra_T versus k . The results are shown in Figure 8.12 to Figure 8.14. From these figures it can be concluded that, for given dimensionless amplitude δ^* and dimensionless frequency of vibration ω^* , there are two modes of convection onset, namely harmonic (with dimensionless frequency ω^*) and subharmonic (with dimensionless frequency $\omega^*/2$). In order to interpret the results, two different thermal cases are considered: heating from below ($Ra_T > 0$) and heating from above ($Ra_T < 0$).

For heating from below (which corresponds to $Ra_T < 0$), two different behaviors for harmonic and subharmonic modes are distinguished: for harmonic mode with increasing ω^* , thermal Rayleigh number Ra_{Tc} increases. This means that vibration has a stabilizing effect, which depends significantly on the choice of dimensionless amplitude δ^* . Figure 8.12 shows that by decreasing δ^* , the stable region with harmonic response widens. If the frequency is increased, the critical wave number for this mode decreases, Figure 8.13. For the subharmonic mode we have a different scenario, the vibration has a destabilizing effect, in other words Ra_{Tc} decreases and ultimately reaches a limiting value. It should be emphasized that our reference here is “the intersection” of the two curves corresponding to harmonic and subharmonic. The critical wave number in this mode increases with increasing dimensionless frequency, Figure 8.14. It should be noted that the intersection of harmonic and subharmonic modes corresponds to different values of wave number.

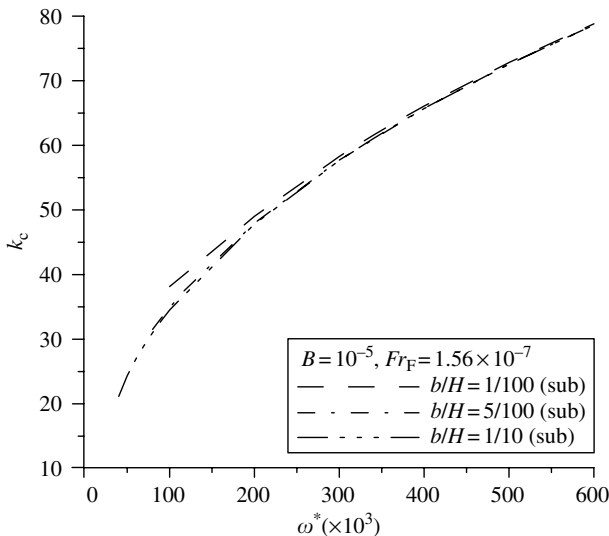
For heating from above, in both harmonic and subharmonic modes, the onset of convection is possible. This is in contrast to the classical terrestrial

**FIGURE 8.12**

The effect of vibrations on the critical Rayleigh number Ra_{Tc} for the layer heated from below as a function of the dimensionless ω^* for $B = 10^{-5}$ and different values of dimensionless amplitude b/H for harmonic and subharmonic modes (direct method).

**FIGURE 8.13**

The effect of vibration on the critical wave number (k_c) as a function of dimensionless frequency ω^* for harmonic (synchronous) solutions for different dimensionless amplitudes with direct formulation (the layer is heated from below).

**FIGURE 8.14**

The effect of vibration on the critical wave number (k_c) as a function of dimensionless frequency ω^* for the subharmonic solutions for different dimensionless amplitudes with direct formulation (heated from above).

case where, on heating from above, the conducive solution is always stable. In both of these modes, with increasing dimensionless frequency, the thermal Rayleigh numbers begin at high values and then sharply reduce and finally tend to asymptotic values. The critical wave number k_c of harmonic mode for this case increases rapidly and then tends to a limiting value. This is in severe contrast to the behavior of the wave number for the harmonic mode heated from below. The transition to subharmonic mode accompanies a drastic and discontinuous drop in the critical wave number: after a sharp increase the slope changes and increases slowly. Our results are in good qualitative agreement with those found for a modulated fluid layer heated from below or above (see [42]).

8.2.1.7 Comparison of the two methods

We compare the two approaches of stability analysis in the thermo-vibrational problem, namely, the time-averaged and the direct methods. The time-averaged method under high-frequency and small-amplitude vibration is considered in Section 8.2.1.6.3. This limiting case permits us to subdivide the temperature, velocity, and pressure fields into two parts. The question is under which condition we can find this characteristic of solution (subdivision of fields) by adopting the direct method. Let us examine what will happen if we apply the assumptions needed for finding the criteria of high frequency and small amplitude to the coefficients of Mathieu's equation.

We write Mathieu's equation and its coefficients A and Q as:

$$\begin{aligned} \frac{d^2M(\tau)}{d\tau^2} + (A - 2Q \cos 2\tau)M(\tau) &= 0 \\ A = -\left[\frac{a_*}{\sigma H^2 \omega}(k^2 + \pi^2) + \frac{\varepsilon v_f}{K\omega}\right]^2 + 4\left(\frac{\varepsilon v_f}{K\omega}\right)\left(\frac{a_*}{\omega \sigma H^2}\right)(k^2 + \pi^2) \\ &\quad - 4\left(\frac{\varepsilon \beta_T \Delta T g}{\sigma H \omega^2}\right) \frac{k^2}{k^2 + \pi^2} \\ Q = 2\left(\frac{\varepsilon}{\sigma} \beta_T \Delta T \frac{b}{H}\right) \frac{k^2}{k^2 + \pi^2} \end{aligned} \tag{8.45}$$

Close examination of A and Q reveals the following facts:

The first and second terms in A involve the two assumptions on thermal and hydrodynamic timescales with respect to frequency (8.9), (8.11), while the third term involves the assumption on frequency (8.13).

Q involves the hypothesis of small amplitude (8.11). Based on our hypothesis of high frequency and small amplitude all these terms are very small so A and Q tend to zero. We use a regular perturbation method in which Q is considered as a small parameter

$$\begin{aligned} M(\tau) &= M_0(\tau) + QM_1(\tau) + Q^2M_2(\tau) + \dots \\ A &= A_0 + QA_1 + Q^2A_2 + \dots \end{aligned} \tag{8.46}$$

Replacing the above expansions in Mathieu's equation results in the following systems:

$$Q^0 : \frac{d^2M_0}{d\tau^2} + A_0 M_0 = 0 \tag{8.47a}$$

$$Q^1 : \frac{d^2M_1}{d\tau^2} + A_0 M_1 = -A_1 M_0 + 2M_0 \cos 2\tau \tag{8.47b}$$

$$Q^2 : \frac{d^2M_0}{d\tau^2} + A_0 M_2 = -A_2 M_0 + 2M_1 \cos 2\tau - A_1 M_1 \tag{8.47c}$$

We search for a stable solution

$$A_0 = 0 \Rightarrow M_0 = \text{const.}$$

$$A_1 = 0 \Rightarrow M_1 = -\frac{a_0}{2} \cos 2\tau$$

where a_0 is an arbitrary constant. By substituting the above relation in (8.47c), we get:

$$\frac{d^2M_2}{d\tau^2} = -a_0 \left(\frac{1}{2} + A_2 \right) - \frac{a_0}{2} \cos 4\tau \quad (8.48)$$

The necessary condition for obtaining a stable solution in (8.47) is to consider:

$$A_2 = -\frac{1}{2}$$

On replacing A_0, A_1, A_2 in (8.46) we obtain:

$$A = -\frac{Q^2}{2} \quad (8.49a)$$

$$M = a_0 - \frac{a_0}{2} \cos 2\tau \quad (8.49b)$$

On replacing A and Q in Eq. (8.49a) and using the fact that $\mu = [a_*(k^2 + \pi^2)/\sigma H^2 \omega + (\varepsilon v/K \omega)] = 0$, we find:

$$Ra_T = \frac{(\pi^2 + k^2)^2}{k^2} + Ra_v \frac{k^2}{k^2 + \pi^2} \quad \left(Ra_v = \frac{(\delta^* Fr_F \omega^* Ra_T)^2}{2B} \right)$$

which means that imposing the assumptions needed for the averaging method on Mathieu's equation gives identical results to the time-averaged formulation. The most interesting thing about this fact is that the time-averaged method gives only harmonic (with dimensionless frequency ω^*) mode and is not able to give subharmonic mode. As can be seen from the results of the Direct method for subharmonic and harmonic cases, we find some asymptotic values. This is not surprising because the special case of $\mu = 0$ results in a class of solutions called Mathieu functions (see [38]), for each of which there exists a unique relation between A and Q . For example, for the case of the subharmonic solution (with dimensionless frequency $\omega^*/2$) in which the layer is heated from below we find that $A = 0$ and $Q \rightarrow 0.9$ which gives the following asymptotic relation (for $k_c^2/(k_c^2 + \pi^2) \rightarrow 1$):

$$Ra_{Tc} \approx 0.445 \frac{B}{\delta^* Fr_F} \quad (8.50)$$

Relation (8.50) clearly shows that increasing the dimensionless amplitude reduces the critical Rayleigh number. For other cases corresponding to harmonic or subharmonic modes similar relations are found ($k_c^2/(k_c^2 + \pi^2) \rightarrow 1$):

$$Ra_{Tc} \approx -3.75 \frac{B}{\delta^* Fr_F} \text{ (harmonic response, the layer heated from above)} \quad (8.51a)$$

$$Ra_{Tc} \approx -0.445 \frac{B}{\delta^* Fr_F} \text{ (subharmonic response, the layer heated from above)} \quad (8.51b)$$

Also it should be emphasized that if we choose $(B, \omega^*, Fr_F, \delta^*)$ properly we are able to predict the possibility of convective motion for the layer heated from above. However, the time-averaged method predicts that with heating from above the layer is infinitely stable.

8.2.1.8 Effect of the direction of vibration

The effect of the direction of vibration on the onset of convection is described by Zenkovskaya and Rogovenko [18]. They use the time-averaged formulation and discuss several physical situations. When the direction of vibration is not parallel to the temperature gradient, there is a quasi-equilibrium; that is, the mean velocity is zero but the oscillating velocity is not zero (see [43]). The equilibrium solution is characterized by:

$$\mathbf{V}_0^* = \mathbf{0}, \quad T_0^* = 1 - z^* \quad \text{and} \quad W_{0x}^* = \left(\frac{1}{2} - z^* \right) \cos \alpha \quad (8.52)$$

The following cases are studied:

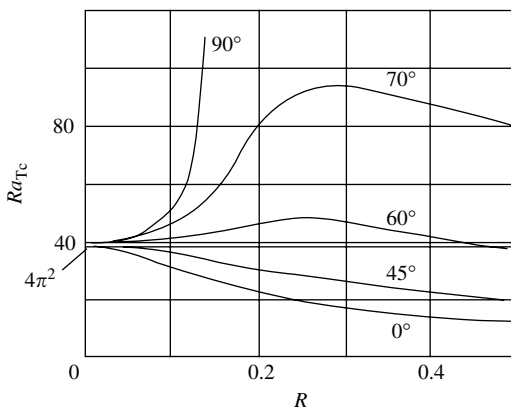
1. *The onset of convection under microgravity ($Ra_T = 0$)*. One of the most interesting results reported by Zenkovskaya and Rogovenko [18] is that, if the direction of vibration is not parallel to the temperature gradient, there is a possibility of convective motion under microgravity conditions. Table 8.1 shows the critical values of the vibrational Rayleigh number (Ra_v) and the critical values of wave number (k_c) as a function of α (the direction of vibration with respect to the heated plate). It can be observed that, with increasing direction of vibration α , the domain of stability increases. At the same time, the wave number decreases with increasing direction of vibration. It should be emphasized that for $\alpha = \pi/2$, that is, the vertical vibration, the equilibrium solution is infinitely linearly stable.

2. *The onset of thermo-vibrational convection in the presence of gravity ($Ra_T \neq 0$ and $R \neq 0$)*. In this case, the two controlling mechanisms, namely, the vibrational and gravitational, are present. Figure 8.15 shows that, based on

TABLE 8.1

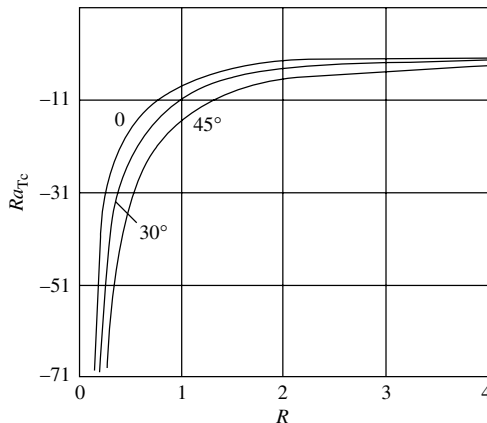
The Critical Vibrational Rayleigh Ra_{vc} and Wave Numbers for Different Directions of Vibration

α	k_c	Ra_{vc}
0	2.87	140.56
$\pi/16$	2.75	156.22
$\pi/8$	2.40	217.8
$3\pi/16$	1.92	391.41
$\pi/4$	1.42	916.50
$5\pi/16$	0.98	2,905.53
$3\pi/8$	0.62	14,908.16
$7\pi/16$	0.3	24,1063.52
$\pi/2$	—	∞

**FIGURE 8.15**

Critical Rayleigh number Ra_{Tc} as a function of R for different values of α . (From S.M. Zenkovskaya and T.N. Ragovenko. *J. Appl. Mech. Tech. Phys.* 40: 379–385, 1999. With permission.)

the values of R (vibrational parameter which does not depend on temperature difference) and α , stabilizing or destabilizing effects may be found. For the direction of vibrations $5\pi/16 < \alpha < \pi/2$, there are some values of R for which maximum stability may be obtained. Another interesting feature of the effect of direction of vibration is that for the layer heated from above, we may obtain convective motions. This is in severe contrast to the classical Horton–Rogers–Lapwood problem in which, for the case of the layer heated from above, the layer is infinitely stable. The results for the layer heated from above are illustrated in Figure 8.16 showing that for $\alpha \neq \pi/2$, on increasing the vibrational parameter the stability domain decreases.

**FIGURE 8.16**

Critical Rayleigh number, Ra_{Tc} , as a function of R for different values of α . (From S.M. Zenkovskaya and T.N. Ragovenko. *J. Appl. Mech. Tech. Phys.* 40: 379–385, 1999. With permission.)

8.2.2 Confined Cavity

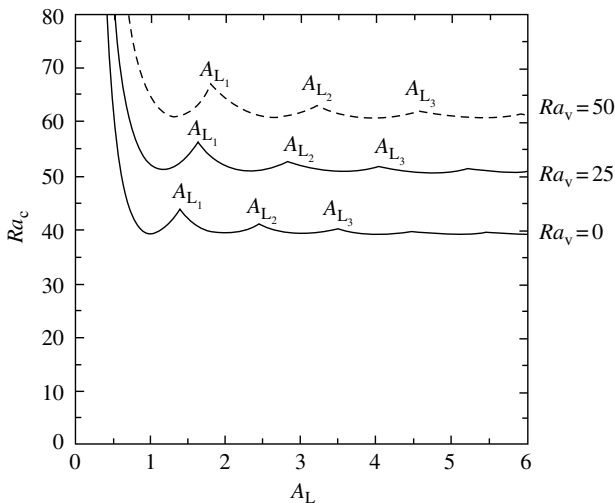
8.2.2.1 Introduction

A numerical and an analytical study of convective motion in a rectangular porous cavity saturated by a pure fluid and subjected to a high-frequency and small-amplitude vibration is presented by Bardan and Mojtabi [20]. The Darcy formulation is adopted in the momentum equation. As vibration has high frequency and small amplitude, the relevant equations are solved by the time-averaged method.

8.2.2.2 Stability analysis

1. *Linear stability analysis.* In (8.20), the attention is focused on the case of vertical vibration, that is, $\alpha = \pi/2$. It is shown that the problem admits an equilibrium solution given by $V_0^* = 0$, $T_0^* = 1 - z^*$, and $W_0^* = 0$, Figure 8.17. The linear stability of this equilibrium solution is sought by means of the Galerkin method using the following expansions:

$$\begin{aligned} \phi &= \sum_{n=1}^P \sum_{m=1}^Q \phi_{nm} \sin(n\pi z^*) \sin\left(\frac{m\pi x^*}{A_L}\right) e^{\lambda t^*} \\ \theta &= \sum_{n=1}^P \sum_{m=1}^Q \theta_{nm} \sin(n\pi z^*) \cos\left(\frac{m\pi x^*}{A_L}\right) e^{\lambda t^*} \\ \varphi_T &= \sum_{n=1}^P \sum_{m=1}^Q \varphi_{Tnm} \sin(n\pi z^*) \cos\left(\frac{m\pi x^*}{A_L}\right) e^{\lambda t^*} \end{aligned} \quad (8.53)$$

**FIGURE 8.17**

Critical Rayleigh number Ra_{Tc} of the first primary bifurcation point as a function of the aspect ratio A_L . (From G. Bardan and A. Mojtabi. *Phys. Fluids* 12: 1–9, 2000. With permission.)

The bifurcation points are obtained by solving the linear algebraic system obtained when we substitute expression (8.53) into system (8.20). The thermal Rayleigh number, which determines the limit of the even and odd solutions, can be studied analytically:

$$Ra_T = \frac{\pi^2(n^2 + m^2 A_L^2)^3 + n^4 A_L^2 Ra_v}{n^2 A_L^2(n^2 + m^2 A_L^2)} \quad (8.54)$$

In (8.54) A_L represents aspect ratio and Ra_v is vibrational Rayleigh number. Figure 8.17 shows the analytical prediction of the critical thermal Rayleigh number for different values of Ra_v . As can be observed clearly from the figure, vibration increases the domain of stability in the bifurcation diagram.

2. *Weakly nonlinear stability analysis.* A weakly nonlinear analysis is carried out to obtain the canonical form of the amplitude equation and to determine the characteristics of solutions (stream function and temperature) near the bifurcation point. The analysis is based on the multiscale approach. The procedure is the same as in Section 8.2 and will not be repeated. The amplitude equation can be written as:

$$a \frac{\partial A}{\partial t} = bA(\mu + cA^2) \quad (8.55)$$

and $Ra_{T2} = (Ra_T - Ra_{Tc})/\eta^2$ represents the bifurcation parameter. This amplitude equation applies for $A_{L(n-1)} < A_L < A_{L(n)}$ and the coefficients a , b , and c are evaluated analytically from the following relations ($m = 1$):

$$\begin{aligned} a &= \frac{\pi^4(n^2 + A_L^2)^3 + \pi^2 A_L(n^2 + A_L^2)^2}{4n^2 A_L^2} \quad b = \frac{n^2 + A_L^2}{4A_L} \\ c &= \pi^6 \frac{(n^2 + A_L^2)^2}{8A_L^4} Ra_v - \pi^8 \frac{(n^2 + A_L^2)^5}{8A_L^6 n^4} \end{aligned} \quad (8.56)$$

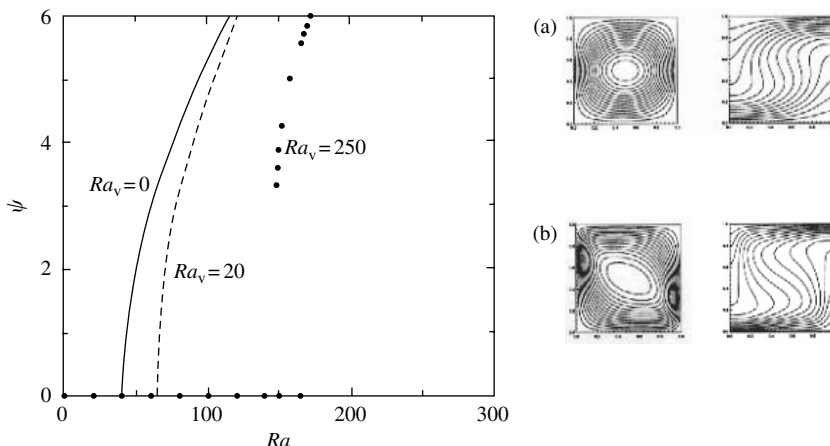
The sign of these coefficients (a , b , and c) are functions of Ra_v and A_L . We distinguish two different cases:

- $c > 0$ and $-b\mu/a < 0 \Rightarrow$ bifurcation is stable supercritical pitch-fork
- $c < 0$ and $-b\mu/a > 0 \Rightarrow$ bifurcation is unstable subcritical pitch-fork

It is interesting to note that for $A_L = A_{L(n)}$, a codimension two bifurcation results from the interaction between the centro-symmetrical and symmetrical modes.

8.2.2.3 Numerical results

Bardan and Mojtabi [20] study this problem from a numerical point of view. The numerical method used in this work is based on a spectral method, the details of which are described in Khallouf et al. [29]. The numerical study is concentrated on $A_L = 1$ and $A_L = 3$ in order to investigate the cases in which there are substantial effects of vibration. The computations are done in the interval of $0 < Ra_T < 300$ and $0 < Ra_v < 400$. The results for $A_L = 1$ are presented in Figure 8.18. In the case of static gravitational acceleration, the pitch-fork bifurcation point occurs at $Ra_T \approx 4\pi^2$. The emerging branch is supercritical and stable. Along this branch the solution is in the form of one-cell flow structure. By increasing the vibrational Rayleigh number, the onset of convection is delayed and the pitch-fork bifurcation remains supercritical up to $Ra_v = 80$. For $Ra_v > 80$, it is found that vibration destabilizes the pitch-fork branch which becomes subcritical or unstable. The bifurcation diagram for $A_L = 3$ is presented in Figure 8.1. For the static case, the onset of convection is centro-symmetric which is characterized by a three-cell flow structure. For a fixed value of thermal Rayleigh number, by increasing vibrational Rayleigh number up to $Ra_v = 40$ it is shown that the conductive solution remains stable. The emerging branch is supercritical pitch-fork along which the solutions have a three-cell structure that is S_0 symmetric. For vibrational Rayleigh number in the interval of $40 < Ra_v < 160$, the emerging branch remains a supercritical pitch-fork; however solutions have a two-cell structure. In the interval of $160 < Ra_v < 350$, the pitch-fork bifurcation becomes subcritical

**FIGURE 8.18**

Bifurcation diagram in the ψ - Ra plane for different values of Ra_v when $A_L = 1$. The insets represents iso-streamlines and isotherms for mean fields at ($Ra_T = 165, Ra_v = 0$) and ($Ra_T = 165, Ra_v = 250$). (From G. Bardan and A. Mojtabi. *Phys. Fluids* 12: 1–9, 2000. With permission.)

and the emerging branch is unstable. Along this stable branch, the solution consists of two-cell flow structures. For $Ra_v > 350$, the first primary bifurcation becomes supercritical along which the branch has a one-cell structure. For $Ra_v > 1250$ the pitch-fork bifurcation becomes subcritical. In summary, they conclude that it is possible to obtain a one-cell flow structure at the onset of convection provided that the vibration intensity is properly chosen.

8.2.2.4 Conclusions

In this section, the stability analysis of a porous layer under the effect of mechanical vibration is presented. The layer can be heated uniformly from below or from above. As found earlier in problems concerning fluid systems, vibration can also influence the onset of convective motion in porous media. The change of threshold depends on direction, amplitude, and frequency of vibration. For the case of mechanical vibration parallel to the temperature gradient (vertical vibration), mechanical equilibrium exists. For this case, under different heating conditions (heating from above or below), there is a possibility of convective motion that largely depends on the chosen values of amplitude and frequency of vibration. The response of the system shows harmonic or subharmonic behavior. For heating from below, the harmonic mode exhibits a stabilizing behavior whereas the subharmonic mode exhibits a destabilizing one. When the frequency is increased, for heating from above the response is predominantly subharmonic and there is a jump in critical wave number for the intersection of harmonic and subharmonic

modes, both of these modes show that vibration has a destabilizing effect.

For heating from below the results indicate that, under the condition of high frequency and small amplitude of vibration, the harmonic part shows a strong stabilizing effect. Under this limiting situation, the time-averaged formulation can be adopted. A weakly nonlinear stability analysis is performed for this averaged system revealing that bifurcation is of supercritical pitch-fork type. It is interesting to note that, near the transition, the Darcy model leads us to the same physical results as obtained from Navier-Stokes equations.

For the case of other directions of vibration ($\alpha \neq \pi/2$) under high frequency and small amplitude, it is shown that, in the presence of gravitational acceleration for the layer heated from below, vibration may produce stabilizing or destabilizing effects. These depend largely on the choice of vibrational parameter and the direction of vibration. For the layer heated from above, decreasing the direction of vibration from $\alpha = \pi/2$ to $\alpha = 0$ reduces the stability domain (Ra_{Tc} decreases). For the case of convection under microgravity conditions, it is shown that there is a possibility of thermo-vibrational convection for all directions of vibration except vertical vibration ($\alpha \neq \pi/2$).

8.3 Influence of Vibration on a Porous Layer Saturated by a Binary Fluid

8.3.1 Infinite Horizontal Layer

8.3.1.1 Introduction

The onset of convection in binary fluids is of practical importance because it may help us in producing materials of improved quality. It can be also used as a method for measuring the transport coefficients. A configuration that has received special attention is a horizontal layer filled with a binary mixture. Typically this system can be heated from below or from above in the terrestrial gravitational field. It is interesting to note that the stability behavior of a binary mixture is quite different from that of a pure fluid. Soret or Dufour effects can strongly modify the onset of convection and the resulting fluid flow structures [44]. Due to importance of material processing in space conditions (weightlessness), Gershuni et al. [45,46] analyzed the stability of conductive solution of a thermosolutal problem with Soret effect in a fluid system under mechanical vibration. They found that total equilibrium was only possible under vertical vibration [46] while, for the horizontal vibration, the state of quasi-equilibrium was possible [45]. They emphasized that high-frequency and small-amplitude vibration could drastically change the stability threshold of conductive solution in the stability diagram.

These important and interesting results, which have direct applications in solidification processes, and measurement of the Soret effect, motivated the study of the analog problem in porous media [22].

8.3.1.2 Governing equations

The geometry consists of an infinite horizontal porous layer containing binary mixtures. The boundaries of the layer are assumed rigid and impermeable, and are kept at different but constant temperatures. Under the Soret effect, the temperature gradient induces a concentration gradient. The geometry undergoes a harmonic oscillation which is characterized by the amplitude b , the dimensional frequency ω , and the direction of vibration α . The transient Darcy model in the framework of the Boussinesq approximation is selected and a linear dependence of density upon temperature and mass fraction is considered:

$$\rho = \rho_0(1 - \beta_T(T - T_{\text{ref}}) - \beta_c(C - C_{\text{ref}})) \quad (8.57)$$

The reference frame is connected to the layer, which allows us to replace the gravitational acceleration \mathbf{g} by $\mathbf{g} - b\omega^2 \sin(\omega t)\mathbf{e}$, where \mathbf{e} is the direction of vibration.

By introducing the reference scales: H for the length, $H^2/(\lambda_*/(\rho c)_*)$ for the time, a_*/H for the velocity ($a_* = \lambda_*/(\rho c)_f$), $\Delta T = T_1 - T_2$ for the temperature and $\Delta C = \Delta T C_i(1 - C_i)D_T/D^*$ for the mass fraction, the dimensionless governing conservation equations for mass, momentum, energy, and chemical species when the Soret effect is taken into account can be written as:

$$\begin{aligned} \nabla \cdot \mathbf{V}^* &= 0 \\ B \frac{\partial \mathbf{V}^*}{\partial t^*} &= -\nabla P^* + Ra_T(T^* + \Psi C^*)(\mathbf{k} + \tilde{R} \sin(\omega^* t^*) \mathbf{e}) - \mathbf{V}^* \\ &\quad \frac{\partial T^*}{\partial t^*} + \mathbf{V}^* \cdot \nabla T^* = \nabla^2 T^* \\ \varepsilon^* \frac{\partial C^*}{\partial t^*} + \mathbf{V}^* \cdot \nabla T^* &= \frac{1}{Le} (\nabla^2 C^* - \nabla^2 T^*) \end{aligned} \quad (8.58)$$

where $B = Da(\rho c)_f/((\rho c)_* \varepsilon Pr^*)$, $\tilde{R} = b\omega^2/g$, and $Da = K/H^2$ is the Darcy number.

The dimensionless boundary conditions are:

$$\begin{aligned} T^* &= 1 & \text{for } z^* = 0; & \quad T^* = 0 & \text{for } z^* = 1 \\ \nabla C^* \cdot \mathbf{n} &= \nabla T^* \cdot \mathbf{n} & \text{for } z^* = 0, 1; & \quad \mathbf{V}^* \cdot \mathbf{n} = 0 & \forall M \in \partial\Omega \end{aligned} \quad (8.59)$$

The problem depends on the following nondimensional parameters: the thermal Rayleigh number Ra_T , the vibrational Rayleigh number $R_v = Ra_T \tilde{R}$, the separation ratio $\Psi = -(\beta_c/\beta_T)(D_T/D^*)C_i(1 - C_i)$, the Lewis number $Le = a/D^*$, the dimensionless pulsation ω^* , the normalized porosity $\varepsilon^* = \varepsilon(\rho c)_f/(\rho c)_*$, the factor B , and the angle of vibration α .

As was explained in Section 8.2, for the problems related to high frequency vibrations, we should keep the term $B \partial \mathbf{V} / \partial t$.

8.3.1.3 The time-averaged formulation

In the limiting case of high-frequency and small-amplitude vibrations, the method of time averaging is applied to study the phenomena of vibrational convection [15]. The details of this method are explained in Section 8.2

$$\begin{aligned} \mathbf{V}^*(M, t^*) &= \bar{\mathbf{V}}^*(M, t^*) + \mathbf{V}'(M, \omega^* t^*) & P^*(M, t^*) &= \bar{P}^*(M, t^*) + P'(M, \omega^* t^*) \\ T^*(M, t^*) &= \bar{T}^*(M, t^*) + T'(M, \omega^* t^*) & C^*(M, t^*) &= \bar{C}^*(M, t^*) + C'(M, \omega^* t^*) \end{aligned} \quad (8.60)$$

where $\bar{\mathbf{V}}, \bar{P}, \bar{T}, \bar{C}$ are the average fields (i.e., the mean value of the field calculated over the period $\tau = 2\pi/\omega$) of the velocity, the pressure, the temperature, and the mass fraction. Also, \mathbf{V}', P', T', C' represent the oscillating fields with zero average over the vibration period. By adopting the procedure explained in Section 8.2 and applying the following hypotheses:

$$\begin{aligned} \tau_{\text{vib}} &\ll \min \left(\frac{K}{\varepsilon \nu_f}, \frac{\sigma H^2}{a_*}, \frac{\varepsilon H^2}{D^*} \right) & \omega &\gg \frac{g}{H} \left(\frac{\varepsilon}{\sigma} \beta_T \Delta T + \beta_C \Delta C \right) \\ b &\ll H / \left(\frac{\varepsilon}{\sigma} \beta_T \Delta T + \beta_C \Delta C \right) \end{aligned}$$

we may obtain the linearized equations for the oscillatory momentum, energy, and concentration. This linearization of the momentum equation justifies the use of Helmholtz decomposition to eliminate pressure:

$$\bar{T}^* \mathbf{e} = \mathbf{W}_T^* + \nabla \vartheta_T^* \quad \bar{C}^* \mathbf{e} = \mathbf{W}_C^* + \nabla \vartheta_C^*$$

where \mathbf{W}_T^* and \mathbf{W}_C^* are the solenoidal parts of the temperature and concentration mean fields. From the definition of solenoidal vectors $\nabla \cdot \mathbf{W}_T^* = \nabla \cdot \mathbf{W}_C^* = 0$, closed form relations for oscillating fields are found. Replacing these

oscillating fields in the averaged system of equations leads to the following system:

$$\begin{aligned}
 \nabla \cdot \bar{\mathbf{V}}^* &= 0 \\
 B \frac{\partial \bar{\mathbf{V}}^*}{\partial t} &= -\nabla \bar{P}^* + Ra_T (\bar{T}^* + \Psi \bar{C}^*) \mathbf{k} + Ra_v (\mathbf{W}_T^* + \Psi \mathbf{W}_C^*) \\
 &\times \nabla \left(\bar{T}^* + \frac{\Psi}{\varepsilon^*} \bar{C}^* \right) (\cos \alpha \mathbf{i} + \sin \alpha \mathbf{k}) - \bar{\mathbf{V}}^* \\
 \frac{\partial \bar{T}^*}{\partial t} + \bar{\mathbf{V}}^* \cdot \nabla \bar{T}^* &= \nabla^2 \bar{T}^* \\
 \varepsilon^* \frac{\partial \bar{C}^*}{\partial t} + \bar{\mathbf{V}}^* \cdot \nabla \bar{C}^* &= \frac{1}{Le} (\nabla^2 \bar{C}^* - \nabla^2 \bar{T}^*) \\
 \nabla \cdot \mathbf{W}_T^* = 0 &\quad \nabla \times \mathbf{W}_T^* = \nabla \bar{T}^* \times (\cos \alpha \mathbf{i} + \sin \alpha \mathbf{k}) \\
 \nabla \cdot \mathbf{W}_C^* = 0 &\quad \nabla \times \mathbf{W}_C^* = \nabla \bar{C}^* \times (\cos \alpha \mathbf{i} + \sin \alpha \mathbf{k})
 \end{aligned} \tag{8.61}$$

In addition to boundary conditions (8.59) applied to the mean fields, we have: $\mathbf{W}_T^* \cdot \mathbf{n} = \mathbf{W}_C^* \cdot \mathbf{n} = 0$. The dimensionless number $Ra_v = R^2 Ra_T^2 = (\tilde{R}^2 Ra_T^2 B)/(2(B^2 \omega^{*2} + 1))$ characterizes the intensity of the vibrations. Unlike the oscillating system, in the averaged system of Eqs. (8.61), we may neglect the term $B \partial \mathbf{V}^* / \partial t$.

8.3.1.4 Stability analysis

If the axis of vibration is not vertical, a mechanical quasi-equilibrium solution exists (the average velocity field is zero but the oscillating velocity field is not zero). This solution is characterized by:

$$\begin{aligned}
 \bar{\mathbf{V}}_0^* &= \mathbf{0}; & \bar{T}_0^* &= 1 - z^*; & \bar{C}_0^* &= c_1 - z^* \\
 W_{T0x}^* &= c_2 - z^* \cos \alpha & W_{T0z}^* &= 0 & W_{C0x}^* &= c_3 - z^* \cos \alpha & W_{C0z}^* &= 0
 \end{aligned} \tag{8.62}$$

In the above equations c_1 , c_2 , and c_3 are constants.

The solution is perturbed around the equilibrium state to analyze the stability of the quasi-equilibrium solution. We introduce the stream function perturbation ϕ , the temperature perturbation θ , and the concentration perturbation c . The stream function perturbations associated with \mathbf{W}_T^* and \mathbf{W}_C^* are φ_T and φ_C respectively. Two new functions $\eta = c - \theta$ and $\varphi_\eta = \varphi_C - \varphi_T$ are introduced to satisfy the zero flux at the boundaries. A Galerkin method is used to solve the resulting linear stability analysis system. The perturbations

are chosen as follows:

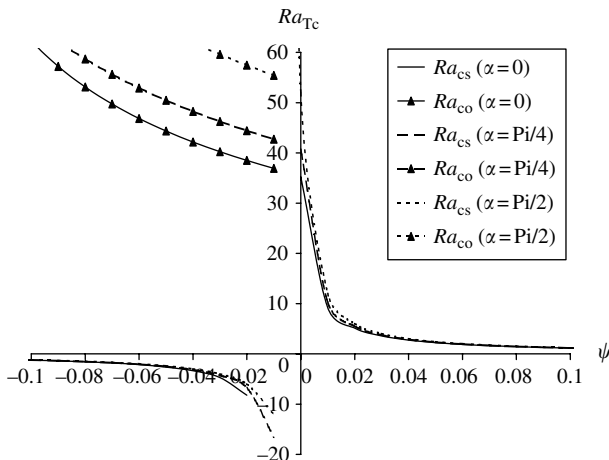
$$\begin{aligned}\phi &= \sum_{n=1}^N \phi_n \sin(n\pi z^*) \exp(\lambda t^* + ikx^*) & \theta &= \sum_{n=1}^N \theta_n \sin(n\pi z^*) \exp(\lambda t^* + ikx^*) \\ \eta &= \sum_{n=1}^N \eta_n \sin(n\pi z^*) \exp(\lambda t^* + ikx^*) & \varphi_T &= \sum_{n=1}^N \varphi_{Tn} \sin(n\pi z^*) \exp(\lambda t^* + ikx^*) \\ \varphi_\eta &= \sum_{n=1}^N \varphi_{\eta n} \sin(n\pi z^*) \exp(\lambda t^* + ikx^*)\end{aligned}\tag{8.63}$$

where k is the wave number in the horizontal direction Ox and $i^2 = 1$.

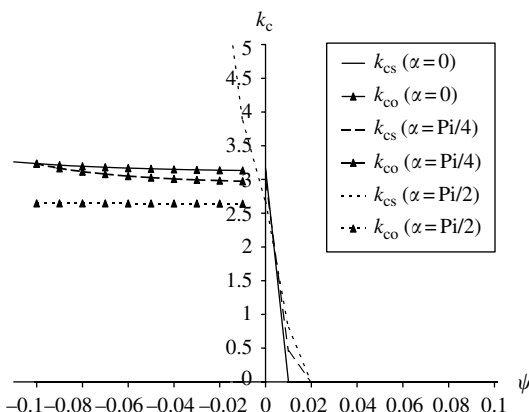
1. Stationary bifurcation. If we assume the principle of exchange of stability to be valid (i.e., $\lambda \in \Re$), then the marginal stability can be obtained ($\lambda = 0$). For different sets of parameters, $R = 0.1$, $\varepsilon^* = 0.3$, $Le = 100$, and for different directions of vibration ($\alpha = 0, \pi/4, \pi/2$), the bifurcation diagrams are determined ($Ra_{cs} = f(\psi)$ and $k_{cs} = f(\psi)$, where Ra_{cs} and k_{cs} are the critical thermal Rayleigh number and the critical wave number respectively).

- (i) Effect of Lewis number: in all separation ratios, positive or negative, increasing the Le number decreases the region of stability. For a given Lewis number, the wave number has the interesting feature that, for the layer heated from above, the mono-cellular regime is dominant (k_c tends to zero). But for the layer heated from below, in positive separation ratios, the wave number decreases with increasing Lewis (Le) number. For the negative separation ratios $\psi < -1$, the mono-cellular regime is dominant (this is only a mathematical prediction, in reality $\psi < -1$ is very hard to achieve).
- (ii) Influence of the direction of vibration: generally, increasing the direction of vibration with respect to the heated layer has a stabilizing effect. This is true for the situation in which the layer is heated from below or above under all separation ratios, [Figure 8.19](#). At the same time, for the layer heated from below, decreasing the vibration angle reduces the wave number. This effect is more noticeable for larger Lewis numbers, [Figure 8.20](#).

2. Oscillatory bifurcation. In this part, the existence of unsteady Hopf bifurcation is sought (i.e., $\lambda = \lambda_r + i\lambda_i$); the marginal state corresponds to $\lambda_r = 0$. In the classical case of thermo-solutal convection in the presence of Soret-effect ($Ra_v = 0$), when the layer is heated from below for the negative separation ratio $\psi \in (-1, 0)$, the first primary bifurcation is a Hopf one. In this case the denser component migrates towards the lower hot plate, which produces an opposing stabilizing effect. More precisely, it is shown elsewhere

**FIGURE 8.19**

The effect of direction of vibrational α on critical Rayleigh number for $Le = 100, \varepsilon^* = 0.3, R = 0.1$. (From K. Maliwan, Y.P. Razi, M.C. Charrier-Mojtabi, M. Azaiez, and A. Mojtabi. *Proceeding of 1st International Conference on Applications of Porous Media*, Tunisia, 2002, pp. 489–497. With permission.)

**FIGURE 8.20**

The effect of vibrational direction α on wave number for $Le = 100, \varepsilon^* = 0.3, R = 0.1$. (From K. Maliwan, Y.P. Razi, M.C. Charrier-Mojtabi, M. Azaiez, and A. Mojtabi. *Proceeding of 1st International Conference on Applications of Porous Media*, Tunisia, 2002, pp. 489–497. With permission.)

(see [22]) that, if ψ is lower than a limiting value which is expressed as $\psi_0 = \psi_0(Le, \varepsilon^*)$, the first primary bifurcation is always a Hopf one. In addition, with increasing Le number or normalized porosity, this limiting separation ratio tends to zero ($\psi_0 \rightarrow 0^-$). The left side of Figure 8.19 illustrates the effect of

vibrational direction on the Hopf bifurcations. It can be observed that increasing vibration direction contributes to the stability which causes the critical Rayleigh number (Ra_{co}) to increase. In this case, increasing the vibration angle slightly reduces the wave number, [Figure 8.20](#).

8.3.1.5 Limiting case of the long-wave mode

The numerical results of the last section show that the long-wave mode ($k = 0$) is the preferred type of thermo-solutal flow under the influence of vibration. For this reason the special case of long-wave mode ($k = 0$) is studied theoretically. In some research work (see [45–47]), it is shown that this analysis leads to closed form relations for marginal stability. A regular perturbation method, with the wave number considered as a small parameter, is used to obtain such a relation:

$$\begin{aligned}\phi &= \sum_{n=0}^N k^n \phi_n & \theta &= \sum_{n=0}^N k^n \theta_n & \eta &= \sum_{n=0}^N k^n \eta_n \\ \varphi_T &= \sum_{n=0}^N k^n \varphi_{Tn} & \varphi_\eta &= \sum_{n=0}^N k^n \varphi_{\eta n} & \lambda &= \sum_{n=0}^N k^n \lambda_n\end{aligned}\quad (8.64)$$

By replacing the above relations in the resulting linear stability system, we find for the zeroth term:

$$\phi_0 = 0 \quad \theta_0 = 0 \quad \eta_0 = \text{const.} \quad \varphi_{T0} = 0 \quad \varphi_{\eta 0} = 0 \quad \lambda_0 = 0$$

For the first-order term:

$$\begin{aligned}\phi_1 &= -\frac{i\eta_0}{2} \Psi \left[Ra_T - Ra_v \frac{d}{dy} (W_{T0x}^* + \Psi W_{C0x}^*) \cos \alpha \right] z^*(1-z^*) \\ \theta_1 &= 0; \quad \eta_1 = \text{const.}; \quad \varphi_{T1} = 0; \quad \varphi_{\eta 1} = 0; \quad \lambda_1 = 0\end{aligned}$$

Finally, for the second-order term after integration:

$$\lambda_2 = \frac{1}{\varepsilon^*} \left[\frac{1}{Le} - \frac{1}{12} \left(Ra_T \Psi + Ra_v (1 + \Psi) \frac{\Psi}{\varepsilon^*} \cos^2 \alpha \right) \right]$$

We note that $\lambda_2 \in \Re$, which means instability is of a stationary type. For the marginal stability ($\lambda_2 = 0$) we obtain:

$$Ra_T + \frac{1 + \Psi}{\varepsilon^*} Ra_v \cos^2 \alpha = \frac{12}{Le \Psi} \quad (Ra_v = R^2 Ra_T^2) \quad (8.65)$$

From this relation, we distinguish several physical cases:

1. Absence of vibration ($Ra_v = 0$): In this situation we find the result of thermosolutal convection with Soret effect (Sovran et al. [48]).
2. Microgravity ($Ra_T = 0$): In this case, the vibrational Rayleigh number is expressed as:

$$Ra_v = \frac{12\varepsilon^*}{\Psi(1 + \Psi)L e \cos^2\alpha} \quad (8.66)$$

The instability in this case is caused by the vibrational mechanism only.

We see that, when α varies from zero to $\pi/2$, the stability region increases. In the interval of $\psi \in [-1, 0]$, it is impossible to have a unicellular regime because, by definition, Ra_v is always positive. It is clear that increasing the Le number has a destabilizing effect.

3. Vibration in presence of gravitational acceleration: At $\alpha = \pi/2$, the vibration has no effect on critical values. For $\alpha \neq \pi/2$ increasing the angle of vibration generally increases the stable regions.

8.3.2 Confined Cavity

8.3.2.1 Introduction

The confined cavity saturated with two-component fluid is examined by Jounet and Bardan [21]. In this study the concentration and the temperature gradients are independent and parallel. Thermosolutal convection in porous media in Rayleigh–Bénard configuration can give rise to different flow patterns and phenomena, which are quite different from those found in porous media saturated only by a pure fluid. The stability analysis of the conductive solution under vertical vibration is performed and the effect of mechanical vibration on the flow structure is studied. The presence of the additional driving mechanism; namely the solutal force, may dramatically alter the onset of convection. Both stationary and Hopf bifurcations are analyzed. It is shown that, when the solutal and thermal buoyancy forces are opposing, there is a possibility of Hopf bifurcation. The weakly nonlinear analysis shows that the stationary bifurcation is of the pitch-fork type. The selection of the vibrational parameter to obtain subcritical or supercritical vibration is explained. Their numerical simulations confirm the theoretical results obtained from the stability analysis.

8.3.2.2 Governing equation

Under the same hypotheses and assumptions which were explained in Section 8.2, the governing equations under high frequency and small

amplitude are written as:

$$\begin{aligned}
 \nabla \cdot \bar{\mathbf{V}}^* &= 0 \\
 B \frac{\partial \bar{\mathbf{V}}^*}{\partial t} + \bar{\mathbf{V}}^* &= -\nabla \bar{P}^* + Ra_T (\bar{T}^* - N \bar{C}^*) \mathbf{k} \\
 &\quad + Ra_v (\mathbf{W}_T^* - N \mathbf{W}_C^*) \cdot \nabla \left(\bar{T}^* - \frac{N}{\varepsilon^*} \bar{C}^* \right) \mathbf{k} \\
 \frac{\partial \bar{T}^*}{\partial t} + (\bar{\mathbf{V}}^* \cdot \nabla) \bar{T}^* &= \nabla^2 \bar{T}^* \\
 \varepsilon^* \frac{\partial \bar{C}^*}{\partial t} + (\bar{\mathbf{V}}^* \cdot \nabla) \bar{C}^* &= \frac{1}{Le} \nabla^2 \bar{C}^* \\
 \nabla \cdot \mathbf{W}_T^* &= 0 \quad \nabla \times \mathbf{W}_T^* = \nabla \bar{T}^* \times \mathbf{k} \\
 \nabla \cdot \mathbf{W}_C^* &= 0 \quad \nabla \times \mathbf{W}_C^* = \nabla \bar{C}^* \times \mathbf{k}
 \end{aligned} \tag{8.67}$$

The corresponding boundary conditions are:

$$\begin{aligned}
 \bar{\mathbf{V}}^* \cdot \mathbf{n} &= 0 \quad \begin{cases} \text{at } z^* = 0 \ \forall x^* \Rightarrow \bar{T}^* = 1 \text{ and } \bar{C}^* = 0 \\ \text{at } z^* = 1 \ \forall x^* \Rightarrow \bar{T}^* = 0 \text{ and } \bar{C}^* = 1 \end{cases} \\
 \frac{\partial \bar{T}^*}{\partial x^*} &= \frac{\partial \bar{C}^*}{\partial x^*} = 0 \quad \text{for } x^* = 0 \text{ and } A_L, \ \forall z^* \\
 \mathbf{W}_T^* \cdot \mathbf{n} &= \mathbf{W}_C^* \cdot \mathbf{n} = 0
 \end{aligned} \tag{8.68}$$

8.3.2.3 Stability analysis

1. *Linear stability analysis.* The problem admits a conductive solution which is characterized by:

$$\bar{T}_0 = 1 - z^*, \quad \bar{C}_0 = z^*, \quad \mathbf{W}_{T0}^* = \mathbf{W}_{C0}^* = 0 \tag{8.69}$$

In this case, there is a strict mechanical equilibrium, that is, the oscillatory components of velocity vanish as well. The stability equations are obtained by adding small perturbations (\mathbf{v}' , p' , T' , c' , \mathbf{w}'_T , \mathbf{w}'_C) to the equilibrium solution. For facility, the stream functions are introduced as follows:

$$\begin{aligned}
 v'_x &= -\partial \phi / \partial z^* & v'_z &= \partial \phi / \partial x^* \\
 w'_{Tx} &= -\partial \varphi_T / \partial z^* & w'_{Tz} &= \partial \varphi_T / \partial x^* \\
 w'_{Cx} &= -\partial \varphi_C / \partial z^* & w'_{Cz} &= \partial \varphi_C / \partial x^*
 \end{aligned}$$

The marginal stability of the resulting perturbation problem is studied by means of a Galerkin method. Perturbations can be expanded as follows:

$$\begin{aligned}\phi(x^*, z^*) &= \sum_{n=1}^N \sum_{m=1}^M \phi_{nm} \sin(n\pi x^*/A_L) \sin(m\pi z^*) e^{i\lambda_i t^*} \\ \theta(x^*, z^*) &= \sum_{n=1}^N \sum_{m=1}^M \theta_{nm} \cos(n\pi x^*/A_L) \sin(m\pi z^*) e^{i\lambda_i t^*} \\ c(x^*, z^*) &= \sum_{n=1}^N \sum_{m=1}^M c_{nm} \cos(n\pi x^*/A_L) \sin(m\pi z^*) e^{i\lambda_i t^*} \\ \varphi_T(x^*, z^*) &= \sum_{n=1}^N \sum_{m=1}^M \varphi_{Tnm} \sin(n\pi x^*/A_L) \sin(m\pi z^*) e^{i\lambda_i t^*} \\ \varphi_C(x^*, z^*) &= \sum_{n=1}^N \sum_{m=1}^M \varphi_{Cnm} \sin(n\pi x^*/A_L) \sin(m\pi z^*) e^{i\lambda_i t^*}\end{aligned}$$

where λ_i is a real number, $i = \sqrt{-1}$ and $(n, m) \in N^2$. For stationary and oscillatory bifurcations, the following relations are found:

$$\begin{aligned}Ra_T = Ra_{Snm} &= \frac{\Gamma_{nm}^2}{\delta_n^2(1 + NLe)} + (\varepsilon^* + N) \frac{\delta_n^2}{\varepsilon^* \Gamma_{nm}} Ra_v \quad \lambda_i = 0 \\ Ra_T = Ra_{0nm} &= \frac{\Gamma_{nm}^2(\varepsilon^* Le + 1)}{\delta_n^2(\varepsilon^* + N)Le} + (\varepsilon^* + N) \frac{\delta_n^2}{\varepsilon^* \Gamma_{nm}} Ra_v \\ \lambda_i^2 = \lambda_{inn}^2 &= -\Gamma_{nm}^2 \frac{1 + \varepsilon^* Le^2 N}{\varepsilon^* Le^2 (\varepsilon^* + N)} > 0 \\ \Gamma_{nm} &= (n\pi/A_L)^2 + (m\pi)^2 \quad \delta_n = (n\pi/A_L)\end{aligned}\tag{8.70}$$

For the classical case of thermo-solutal convection under static acceleration ($Ra_v = 0$) their analytical results are the same as the classical results cited in Nield and Bejan [28].

2. *Weakly nonlinear stability analysis.* To study the stability of different branches of the solution near the stationary convective bifurcation point, a weakly nonlinear stability analysis is performed. The procedure is similar to what was explained in Section 8.2. The field perturbations, the Rayleigh number, and the temporal derivatives are expanded in powers of a small

parameter η :

$$\begin{aligned}\phi &= \eta\phi_1 + \eta^2\phi_2 + \dots & \varphi_T &= \eta\varphi_{T1} + \eta^2\varphi_{T2} + \dots \\ \varphi_C &= \eta\varphi_{C1} + \eta^2\varphi_{C2} + \dots & \theta &= \eta\theta_1 + \eta^2\theta_2 + \dots \\ \frac{\partial}{\partial t} &= \eta \frac{\partial}{\partial t^{(1)}} + \eta^2 \frac{\partial}{\partial t^{(2)}} + \dots & Ra_T &= Ra_{Tc} + \eta Ra_{T1} + \eta^2 Ra_{T2} + \dots\end{aligned}$$

Replacing these developments in the governing system of equations and using the solvability lemma, the following amplitude equation is found:

$$a \frac{\partial A}{\partial t^{(2)}} = A(\mu + cA^2) \quad (8.71)$$

The coefficients a , μ , and c are defined as:

$$\begin{aligned}a &= 8\Gamma_{nm}^3\varepsilon^*(1+N\varepsilon^*Le^2)/\delta_n^2 & \mu &= 8Ra_T^{(2)}\Gamma_{nm}^2\varepsilon^*(1+NLe)^2 \\ c &= \alpha Ra_v - \beta \quad (\alpha = \delta_{nm}^4(1+NLe)^2(\varepsilon^* + NLe^2), \beta = \Gamma_{nm}^3\varepsilon^*(1+NLe^3))\end{aligned}$$

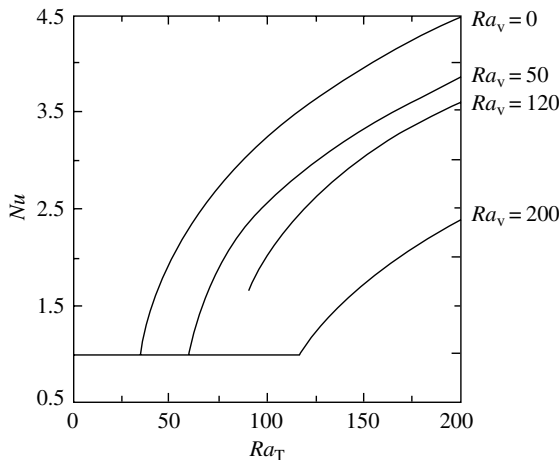
Under the action of vibration, their analysis shows that the type of bifurcation can change depending on the sign of N/ε^* and $-1/Le^2$ and the intensity of vibration.

8.3.2.4 Numerical results

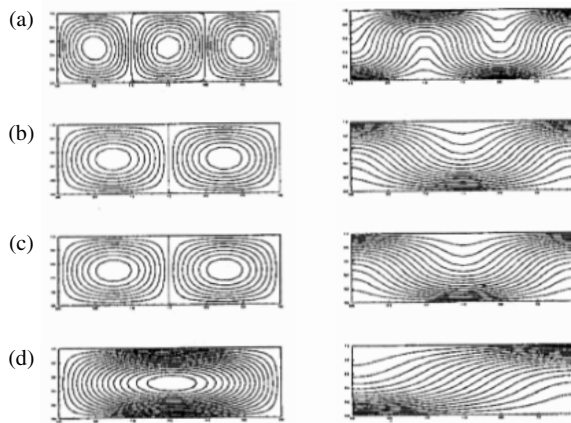
System (8.67) and (8.68) is solved numerically using a spectral method. The values of $(\varepsilon^*, Le, N, A_L, Ra_v)$ are so chosen to illustrate the variety of the possible flows at the onset of convection. The simulation is restricted to positive Rayleigh numbers (heating from below) for the stationary bifurcations. The bifurcation diagrams are presented in the (Nu, Ra_T) , where Nu is defined as:

$$Nu = \frac{1}{A_L} \int_0^{A_L} \left(\frac{\partial \bar{T}^*}{\partial z^*} \right)_{z=0,1} dx^*$$

In [Figure 8.21](#) the evolution of Nu versus Ra_T is presented for aspect ratio $A_L = 3$. The results show that in this region vibration has stabilizing effect and reduces the heat transfer rate. The corresponding fluid flow structures are illustrated in [Figure 8.22](#). Generally, in this region the same results as

**FIGURE 8.21**

Bifurcation diagrams in the $Nu - Ra_T$ plane for $\varepsilon^* = 1, Le = 0.5, N = 0.5$, and $A_L = 3$. (From A. Jounet and G. Bardan. *Phys. Fluids* 13: 1–13, 2001. With permission.)

**FIGURE 8.22**

Streamlines and isotherms corresponding to vibrational parameters of Figure 8.21; (a) $Ra_v = 0$, (b) $Ra_v = 50$, (c) $Ra_v = 120$, (d) $Ra_v = 200$. (From A. Jounet and G. Bardan. *Phys. Fluids* 13: 1–13, 2001. With permission.)

for a porous medium filled with pure fluid are obtained. Increasing the intensity of vibration, increases the domain of stability which is characterized by reduction of Nu number and number of convective rolls.

For $A_L = 1$, in the region with negative N , the numerical simulation is done for $\varepsilon^* = 1, Le = 0.5, N = -1.5$. It is interesting to note that for this case vibration has a destabilizing effect.

8.4 Conclusions and Outlook

The majority of the studies related to thermo-vibrational problem in porous media are addressed in this chapter. We conclude that thermo-vibrational problem in porous media offers many opportunities for research areas and industrial application. Here we propose several research fields which are essential for progress in thermo-vibrational problem:

1. *Effect of boundary conditions.* It is shown in this chapter that only the isothermal boundary condition (Dirichlet type) has received special attention. From a physical point of view, it corresponds to cases in which the heat conductivities of the boundaries are much higher than that of the fluid. However, when the conductivities of the fluid and boundaries have the same-order magnitude, one should consider this effect. Also, we may investigate the constant heat flux which provides us with another practical applications in space industry.

2. *Different types of transport modeling.* We observe from the studies devoted to thermo-vibrational problem that linear stability analysis has a special place. Hence, the Darcy model or transient Darcy model are well fitted for these studies. But, if our objective is to study the convective problems other models in momentum equation should be used, such as Forchheimer. In addition, we should consider the Brinkman model when the porosity of the porous media is relatively high (of the order 0.8). In this case, the viscous effect of friction force on walls cannot be neglected.

3. *Vibration modeling.* Periodic accelerations are commonly used for the problems involving thermo-vibration. However, the experimental measurements in microgravity have shown that the behavior of residual accelerations may be well characterized by stochastic nature. So, it is interesting to study the effect of this kind of vibration for bridging the gap between theory and reality.

4. *Numerical simulation.* Numerical methods described here dealt with two-dimensional problems. Extension to three-dimensional problems is equally important. This can motivate the development of robust algorithms for solving the governing equations.

5. *Geometric optimization.* Another field that should be addressed in future research in vibration-induced convection problem is geometric-optimization. By proper selection of geometric parameters and appropriate use of the driving mechanism, we may increase the heat transfer rate. As vibrations are characteristics of any space station, their utilization along with proper geometries adapted for space station environment may result in construction of energy-saving devices. Developing heat transfer correlations in this case provides a challenge for researchers.

6. *Experimental studies.* A close look at the publications related to thermo-vibrational problem in porous media reveals that, there is no comprehensive experiment regarding the effect of vibration on convective

motion in porous media. In order to justify the porous media modeling, well-planned experiments are necessary.

Nomenclature

Roman Letters

a_*	effective thermal diffusivity, m^2/sec
b	vibration amplitude, m
B	ratio of hydrodynamic timescale to thermal timescale
C_i	initial mass fraction
C	perturbation of concentration
D^*	mass diffusion coefficient
D_T	thermodiffusion coefficient
Da	Darcy number (K/H^2)
e	direction of vibration
F_{rF}	filtration Froude number
g	gravitational acceleration, m/sec^2
H	height, m
\mathbf{k}	unit vector in z direction
k	wave number
K	permeability, m^2
Le	Lewis number (a/D^*)
N	buoyancy ratio ($\beta_c \Delta C / \beta_T \Delta T$)
P	pressure, N/m^2
Pr^*	Prandtl number (ν/a_*)
\Re	real numbers
\tilde{R}	acceleration ratio ($b\omega^2/g$)
R	vibrational parameter independent of temperature difference ($Ra_v^{1/2}/Ra_T$)
R_v	vibrational parameter ($Ra_T \tilde{R}$)
Ra_T	Rayleigh number
Ra_v	vibrational Rayleigh number
Sh	Sherwood number
T	temperature
t	time
\mathbf{V}	velocity, m/sec
\mathbf{W}	solenoidal vector

Greek Letters

α	direction of vibration
β_C	coefficient of mass expansion

β_T	coefficient of thermal expansion
δ^*	dimensionless amplitude (b/H)
ΔT	temperature difference ($T_1 - T_2$)
ε	porosity
ε^*	normalized porosity
θ	perturbation of temperature
λ	eigenvalue of the system
λ_*	effective thermal conductivity
μ_f	dynamic viscosity of fluid, Pa sec
ν_f	kinematic viscosity, m ² /sec
ρ	density, kg/m ³
$(\rho c)_*$	volumic heat capacity of medium
σ	dimensionless volumic heat capacity ratio
τ	vibration period
ϕ	steam function perturbation
Ψ	separation ratio
ω	vibrational frequency

References

1. S.H. Davis. The stability of time-periodic flows. *Ann. Rev. Fluid Mech.* 8: 57–74, 1976.
2. S. Ostrach. Low gravity fluid flows. *Ann. Rev. Fluid Mech.* 14: 313–345, 1982.
3. J.P. Caltagirone. Stabilité d'une couche poreuse horizontale soumise à des conditions aux limites périodiques. *Int. J. Heat Mass Transfer* 19: 815–820, 1976.
4. D.A. Rees. The effect of long-wavelength thermal modulations on the onset of convection in an infinite porous layer heated from below. *Q. J. Appl. Math.* 43: 189–213, 1990.
5. N. Rudariah and M.S. Malashetty. Effect of modulation on the onset of convection in a sparsely packed porous layer. *ASME J. Heat Transfer* 122: 685–689, 1990.
6. B.V. Antohe and J.L. Lage. The Prandtl number effect on the optimum heating frequency of an enclosure filled with fluid or with a saturated porous medium. *Int. J. Heat Mass Transfer* 40: 1313–1323, 1997.
7. S.M. Alex and R. Patil. Effect of variable gravity field on Soret driven thermosolutal convection in a porous medium. *Int. Comm. Heat Mass Transfer* 28: 509–518, 2001.
8. S.M. Alex and R. Patil. Effect of a variable gravity field on convection in an anisotropic porous medium with internal heat source and inclined temperature gradient. *ASME J. Heat Transfer* 124: 144–150, 2002.
9. S.M. Alex, P.R. Patil, and K.S. Venkatakrishnan. Variable gravity effects on thermal instability in a porous medium with internal heat source and inclined temperature gradient. *Fluid Dyn. Res.* 29: 1–6, 2001.
10. Y. Kamotani, A. Prasad, and S. Ostrach. Thermal convection in an enclosure due to vibrations aboard spacecraft. *AIAA J.* 19: 511–516, 1981.

11. J.I.D. Alexander. Residual gravity jitter effects on fluid processes. *Microgravity Sci. Tech.* 7: 131–136, 1994.
12. J.I.D. Alexander. Low-gravity experiment sensitivity to residual acceleration: a review. *Microgravity Sci. Tech.* 3: 52–68, 1990.
13. E.S. Nelson. An examination of anticipated g-jitter on space station and its effect on material processing. NASA TM 103775, 1994.
14. E.S. Nelson and M. Kassemi. The effects of residual acceleration on concentration fields in directional solidification. *AIAA J.* 97–1002, 1997.
15. G.Z. Gershuni and D.U. Lyubimov. *Thermal Vibrational Convection*. Wiley: New York, 1998.
16. I.B. Simonenko and S.M. Zenkovskaya. On the effect of high frequency vibration on the origin of convection. *Izv. Akad. Nauk SSSR, Mekh. Zhidk. Gaza* 5: 51, 1966.
17. S.M. Zenkovskaya. Action of high-frequency vibration on filtration convection. *J. Appl. Mech. Tech. Phys.* 32: 83–86, 1992.
18. S.M. Zenkovskaya and T.N. Rogovenko. Filtration convection in a high frequency vibration field. *J. Appl. Mech. Tech. Phys.* 40: 379–385, 1999.
19. M.S. Malashetty and V. Padmavathi. Effect of gravity modulation on the onset of convection in a fluid and porous layer. *Int. J. Eng. Sci.* 35: 829–840, 1997.
20. G. Bardan and A. Mojtabi. On the Horton–Rogers–Lapwood convective instability with vertical vibration. *Phys. Fluids* 12: 1–9, 2000.
21. A. Jounet and G. Bardan. Onset of thermohaline convection in a rectangular porous cavity in the presence of vertical vibration. *Phys. Fluids* 13: 1–13, 2001.
22. O. Sovran, M.C. Charrier-Mojtabi, M. Azaiez, and A. Mojtabi. Onset of Soret driven convection in porous medium under vertical vibration. *International Heat Transfer Conference*, IHTC12, Grenoble, 2002.
23. K. Maliwan, Y.P. Razi, M.C. Charrier-Mojtabi, M. Azaiez, and A. Mojtabi. Influence of direction of vibration on onset of Soret-driven convection in porous medium. *Proceeding of 1st International Conference on Applications of Porous Media*, Tunisia, 2002, pp. 489–497 (Eds. R. Bennacer and A.A. Mohamed).
24. K. Maliwan, Y.P. Razi, G. Bardan, and A. Mojtabi. Onset of double diffusive convection in a porous medium due to vibration under micro-gravity. *Proceeding of the Fifth Euromech Fluid Mechanics Conference*, Toulouse, 2003, p. 506.
25. M.C. Charrier-Mojtabi, K. Maliwan, Y.P. Razi., M. Azaiez and A. Mojtabi. Influence of vibrational directions on Soret driven flows in a confined porous cavity. *The Fifth Euromech Fluid Mechanics Conference*, 2003, Toulouse, p. 505.
26. Y.P. Razi, K. Maliwan, and A. Mojtabi. Two different approaches for studying the stability of the Horton–Rogers–Lapwood problem under the effect of vertical vibration. *The First International Conference in Applications of Porous Media*, Tunisia, 2002, pp. 479–488 (Eds. R. Bennacer and A.A. Mohamed).
27. M.C. Charrier-Mojtabi, K. Maliwan, Y.P. Razi, G. Bardan, and A. Mojtabi. Contrôle des écoulements thermoconvectifs par vibration. *Mécanique et Industrie* 4: 545–549, 2003.
28. D. Nield and A. Bejan. *Convection in Porous Media*, 2nd edn. Springer: Berlin, 1999.
29. H. Khallouf, G.Z. Gershuni, and A. Mojtabi. Some properties of convective oscillations in porous medium. *Numer. Heat Transfer Part A* 30: 605–618, 1996.
30. D.A.S. Rees and I. Pop. The effect of G-jitter on vertical free convection boundary layer flow in porous media. *Int. Commun. Heat Mass Transfer* 27: 415–424, 2000.

31. D.A.S. Rees and I. Pop. The effect of g-jitter on free convection near a stagnation point in a porous medium. *Int. J. Heat Mass Transfer* 44: 877–883, 2001.
32. D.A.S. Rees and I. Pop. The effect of large amplitude g-jitter vertical free convection boundary layer-flow in porous media. *Int. J. Heat Mass Transfer* 46: 1097–1102, 2003.
33. O. Sovran, G. Bardan, M.C. Charrier-Mojtabi, and A. Mojtabi. Finite frequency external modulation in doubly diffusive convection. *Numer. Heat Transfer Part A* 37: 877–896, 2000.
34. I.B. Simonenko. A justification of the averaging method for a problem of convection in a field of rapidly oscillating forces and other parabolic equations. *Mat. Sb.* 129: 245–263, 1972.
35. A. Bejan. *Convection Heat Transfer*, 2nd edn. Wiley: New York, 1994.
36. A. Bejan and R.A. Nelson. Constructual optimization of internal flow geometry in convection. *ASME J. Heat Transfer* 120: 357–364, 1998.
37. E. Palm, J.E. Weber, and O. Kvernvold. On steady convection in a porous medium. *J. Fluid Mech.* 54: 153–161, 1972.
38. N.W. Mc Lachlan. *Theory and Application of Mathieu Functions*. Dover: New York, 1964.
39. W.J. Cunningham. *Introduction to Nonlinear Analysis*. McGraw-Hill: New York, 1958.
40. D.W. Jordan and P. Smith. *Nonlinear Ordinary Differential Equation: An Introduction to Dynamical Systems*. Oxford University Press: New York, 1987.
41. A. Aniss, M. Souhar, and M. Belhaq. Asymptotic study of the convective parametric instability in Hele-Shaw cell. *Phys. Fluids* 12: 262–268, 2000.
42. P.M. Gresho and R.L. Sani. The effects of gravity modulation on the stability of heated fluid layer *J. Fluid Mech.* 40: 783–806, 1970.
43. G.Z. Gershuni and Y.E.M. Zhukhovitskiy. Vibration-induced thermal convection in weightlessness. *Fluid Mech.-Sov. Res.* 15: 63–84, 1986.
44. J.K. Platten and J.C. Legros. *Convection in Liquids*. Springer-Verlag: Berlin, 1984.
45. G.Z. Gershuni, A.K. Kolesnikov, J.C. Legros, and B.L. Myznikova. On the vibrational convective instability of a horizontal binary-mixture layer with Soret effect. *J. Fluid Mech.* 330: 251–269, 1997.
46. G.Z. Gershuni, A.K. Kolesnikov, J.C. Legros, and B.L. Myznikova. On the convective instability of a horizontal binary mixture layer with Soret effect under transversal high frequency vibration. *Int. J. Heat Mass Transfer* 42: 547–553, 1999.
47. E. Knobloch and D.R. Moore. Linear stability of experimental Soret convection. *Phys. Rev. A* 37(3): 860–870, 1988.
48. O. Sovran, M.C. Charrier-Mojtabi, and A. Mojtabi. Naissance de la convection thermosolutale en couche poreuse infinie avec effect Soret. *C.R. Acad. Sci. Paris serie IIb* 329: 287–293, 2001.

Part IV

Viscous Dissipation in Porous Media

9

Effect of Viscous Dissipation on the Flow in Fluid Saturated Porous Media

E. Magyari, D.A.S. Rees, and B. Keller

CONTENTS

9.1	Introduction	374
9.2	Basic Thermal Energy Equations.....	376
9.2.1	Darcy Terms	376
9.2.2	Forchheimer Terms	377
9.2.3	Brinkman Terms	377
9.2.4	Order-of-Magnitude Estimates	378
9.3	Free Convective Boundary Layers	379
9.3.1	Equations of Motion.....	379
9.3.2	Breaking the Upflow/Downflow Equivalence	381
9.3.3	The Asymptotic Dissipation Profile	382
9.3.4	Flow Development Toward the ADP	384
9.3.5	Other Free Convective Flows	387
9.4	Forced Convection with Examples	387
9.4.1	Boundary-Layer Analysis	387
9.4.2	Channel Flows	392
9.5	Mixed Convection	393
9.5.1	The Darcy–Forchheimer Flow	393
9.5.2	Perturbation Approach for Small Gebhart Number	396
9.5.3	The Aiding Up- and Downflows	397
9.5.4	Channel Flows	400
9.6	Stability Considerations	400
9.7	Research Opportunities	402
	Nomenclature	402
	References	404

9.1 Introduction

The viscous dissipation effect, which is a local production of thermal energy through the mechanism of viscous stresses, is a ubiquitous phenomenon and it is encountered in both the viscous flow of clear fluids and the fluid flow within porous media. When compared with other thermal influences on fluid motion (i.e., by means of buoyancy forces induced by heated or cooled walls, and by localized heat sources or sinks) the effect of the heat released by viscous dissipation covers a wide range of magnitudes from being negligible to being significant. Gebhart [1] discussed this range at length and stated that "a significant viscous dissipation may occur in natural convection in various devices which are subject to large decelerations or which operate at high rotational speeds. In addition, important viscous dissipation effects may also be present in stronger gravitational fields and in processes wherein the scale of the process is very large, e.g., on larger planets, in large masses of gas in space, and in geological processes in fluids internal to various bodies." In contrast to such situations, many free convection processes are not sufficiently vigorous to result in a significant quantitative effect, although viscous dissipation sometimes serves to alter the qualitative nature of the flow.

Although viscous dissipation is generally regarded as a weak effect, a property it shares with relativistic and quantum mechanical effects in everyday life, it too has played a seminal role in history of physics. It was precisely this "weak" physical effect that allowed James Prescott Joule in 1843 to determine the mechanical equivalent of heat using his celebrated paddle-wheel experiments, and thereby to set in place one of the most important milestones toward the formulation of the first principle of thermodynamics. Curiously enough, the Royal Society declined to publish Joule's work in the famous *Transactions* (the *Physical Review Letters* of that time) and thus the paper appeared only two years later in a more liberal journal, the *Philosophical Magazine*. Today, papers on viscous dissipation frequently suffer a similar fate as Joule's first paper, and it is often neglected. One of the aims of the present review is to assess the quantitative and qualitative changes brought about by the presence of viscous dissipation.

From a mathematical point of view the effect of viscous dissipation arises as an additional term in the energy equation. It expresses the rate of volumetric heat generation, q''' , by internal friction in the presence of a fluid flow. For a plane boundary-layer flow or a unidirectional flow, q''' takes the following forms for clear fluids and for Darcy flow through a porous medium,

$$q_{\text{clear}}''' \equiv \mu \left(\frac{\partial u}{\partial y} \right)^2 \quad \text{and} \quad q_{\text{Darcy}}''' \equiv \frac{\mu}{K} u^2 \quad (9.1a,b)$$

respectively, where μ is the dynamic viscosity and K is the permeability. It would appear that the above expression for q_{Darcy}''' was deduced for the first

time by Ene and Sanchez-Palencia [2] and Bejan [3] in independent works. Other early applications of this “ u^2 -model” for viscous dissipation in porous media are those of Nakayama and Pop [4], which discusses the external free convection from nonisothermal bodies, and of Ingham et al. [5], which deals with the mixed convection problem between two vertical walls.

From a physical point of view, the difference between the two expressions in Eqs. (9.1a) and (9.1b) originates from the fact that u denotes the actual fluid velocity for a clear fluid flow, but denotes the fluid seepage velocity (i.e., the bulk velocity divided by porosity) for a porous medium flow. At microscopic levels within a porous medium, the fluid is “extruded” through the pores of the solid matrix, and local flows are typically three dimensional even though the overall macroscopic flow is uniform and unidirectional. This microscopic process considerably enhances the rate of heat generation by viscous dissipation. Thus, as can be seen immediately for uniform forced convection flows in clear fluids ($u = \text{const.} \equiv u_\infty$), no heat is released by viscous dissipation, at least by the agency of internal frictional forces. However, in porous media the heat generation rate increases quadratically with u . In the context of boundary-layer flows it has been shown recently [6] that this fact has important consequences for far-field thermal boundary conditions for both forced and mixed convection in extended porous media. For free convection boundary-layer flows, expressions (9.1a) and (9.1b) are both compatible with the uniform asymptotic condition for the temperature, that is, $T(x, y \rightarrow \infty) = \text{const.} = T_\infty$. This condition is usually imposed on the temperature field since $u \rightarrow 0$ as $y \rightarrow \infty$. But in forced and mixed convection flows in extended porous media, this asymptotic thermal condition contradicts the corresponding energy equation because the term $q''_{\text{Darcy}} = (\mu/K)u_\infty^2$ is nonvanishing as $y \rightarrow \infty$. Accordingly, some recent results pertaining to mixed convection flows in extended porous media [7,8] should be reconsidered (see Magyari et al. [9] and responses by Tashtoush [10] and Nield [11]) by taking into account suitably modified boundary conditions on T in the far field ([6] and Sections 9.4 and 9.5).

Even if the quantitative effect of viscous dissipation is negligible in some cases (see exceptions cited by Gebhart [1], Gebhart and Mollendorf [12], and Nield [13], which include situations where high accelerations exist such as in rapidly rotating systems) its qualitative effect may become significant. One interesting effect of the presence of viscous dissipation, to be discussed in more detail later, is the breaking of both the physical and mathematical equivalence that usually exists between a free convective boundary-layer flow ascending from a hot plate ($T_w > T_\infty$) and its counterpart, descending from a cold plate ($T_w < T_\infty$). For the latter case the resulting flow is strictly a parallel boundary-layer flow of constant thickness, which has been named the “asymptotic dissipation profile” or ADP (see Magyari and Keller [14] and Section 9.3). A second qualitative difference arises when viscous dissipation is included in a stability analysis of the Darcy–Benard problem — a porous layer heated from below. For a Boussinesq fluid in a Darcian medium with uniform steady temperatures on the boundaries, the basic no-flow state is

first destabilized by two-dimensional roll patterns. The presence of viscous dissipation causes a hexagonal pattern to appear at Rayleigh numbers close to the critical value (see Rees et al. [15]).

This chapter begins with a presentation of the precise mathematical formulae to be used for modeling viscous dissipation, with an emphasis on the very recent debate on the correct form to use when the Brinkman terms are significant in the momentum equations. This is followed by an overview of the current state of the art in free, mixed, and forced convective boundary-layer flows, and some first tentative steps toward the application of stability theory to certain free convective flows.

9.2 Basic Thermal Energy Equations

The thermal energy equation for steady convection in a porous medium may be stated as:

$$\rho c_p \underline{v} \cdot \nabla T = \nabla \cdot (k \nabla T) + \Phi \quad (9.2)$$

where ρ is the density of the saturating fluid, c_p its specific heat, and k the thermal conductivity of the saturated porous medium. In Eq. (9.2) it is also assumed that the fluid and the porous material are in local thermal equilibrium. The last term Φ in (9.2) is the viscous dissipation term, previously denoted by q''_{Darcy} . The purpose of this section is to present the various forms that this term may take when the momentum equations are modeled in different ways.

9.2.1 Darcy Terms

When the flow in an isotropic porous medium satisfies Darcy's law, the appropriate heat-source term that models viscous dissipation in the thermal energy equation is given by (9.1), but only when the flow is undirectional, or when it is predominantly in one direction, such as in a boundary-layer flow. More generally, the full expression for Φ is

$$\Phi = \frac{\mu}{K} (u^2 + v^2 + w^2) \quad (9.3)$$

This form should be used for isotropic media and is independent of the orientation of the coordinate axes. Nield [16] has stated that this form for Φ is obtained by taking

$$\Phi = \underline{v} \cdot \underline{F} \quad (9.4)$$

where \underline{F} is the drag force on the porous medium. Thus, if Darcy's law is valid and the permeability is isotropic, then $\underline{F} = (\mu/K)\underline{v}$. If the drag force argument is used in such circumstances where the porous medium is anisotropic with permeability tensor, $\underline{\underline{K}}$, then (9.3) may be replaced by

$$\Phi = \mu \underline{v} \cdot \underline{\underline{K}}^{-1} \cdot \underline{v} \quad (9.5)$$

9.2.2 Forchheimer Terms

When the microscopic Reynolds number is approximately greater than unity, then the momentum equation is usually supplemented by a quadratic nonlinear term corresponding to form drag within the medium, and the extra term is known as the Forchheimer term. Initially it was thought that the presence of form drag does not affect viscous dissipation because the coefficient of $|\underline{v}| \underline{v}$, which is $c_{fp} K^{-1/2}$, does not involve viscosity [17]. (Here, the value c_{fp} is a nondimensional parameter that is dependent on the geometry of the porous medium.) Recently, Nield [16] used the drag force argument to state that Eq. (9.3) should now read

$$\Phi = \frac{\mu}{K} \underline{v} \cdot \underline{v} + \frac{c_f \rho}{K^{1/2}} |\underline{v}| \underline{v} \cdot \underline{v} \quad (9.6)$$

The apparent paradox that a term that is independent of the viscosity may contribute to the viscous dissipation was resolved in an earlier paper by Nield [13]. Under such conditions, the advective inertia terms in the Navier–Stokes equations are not negligible and therefore wake formation and boundary-layer separation takes place at pore/particle length-scales. This, in turn, means that microscopic velocities are altered and thereby the heat generated by viscous dissipation is increased.

Other versions of the momentum equation exist that have cubic terms; see, for example, Mei and Auriault [18] and Lage et al. [19]. To date such terms have not been included in the expression for Φ using (9.4).

9.2.3 Brinkman Terms

While the form for Φ that is given by (9.6) is widely accepted for Darcy–Forchheimer flow, the same cannot be said for flows where boundary effects, as modeled by the Brinkman terms, are significant. Nield's [16] drag force formula yields the form

$$\Phi = \frac{\mu}{K} \underline{v} \cdot \underline{v} - \tilde{\mu} \underline{v} \cdot \nabla^2 \underline{v} \quad (9.7)$$

where $\tilde{\mu}$ is an effective viscosity, while Al-Hadhrami et al. [20] use an argument based on the work done by frictional forces to obtain,

$$\Phi = \frac{\mu}{K}(u^2 + v^2 + w^2) + \tilde{\mu} \left[2 \left(\frac{\partial u}{\partial x} \right)^2 + 2 \left(\frac{\partial v}{\partial y} \right)^2 + 2 \left(\frac{\partial w}{\partial z} \right)^2 + \left(\frac{\partial u}{\partial y} + \frac{\partial v}{\partial x} \right)^2 + \left(\frac{\partial u}{\partial z} + \frac{\partial w}{\partial x} \right)^2 + \left(\frac{\partial v}{\partial z} + \frac{\partial w}{\partial y} \right)^2 \right] \quad (9.8)$$

Both formulae yield the correct form for Φ in the limit of small permeability, but when the porosity increases toward unity then only the formula of Al-Hadhrami et al. [20] matches that for a clear fluid. While Al-Hadhrami et al. [20] argue further that Nield's [13] formula can in some circumstances yield negative values for Φ , which is physically unacceptable, Nield [16] has countered by questioning the use of the stress tensor in an identical manner to the way it is used in clear fluids. Moreover, he also questions the often indiscriminate use of the Brinkman term, even though it appears to give a smooth transition between Darcy flow and the flow of a clear fluid. However, both Al-Hadhrami et al. [20] and Nield [16] agree that further studies in this area are essential to resolve the present conflict.

9.2.4 Order-of-Magnitude Estimates

Here, we repeat Nield's [13] analysis of the situations in which one might expect viscous dissipation to be significant. This is done by simply comparing the orders of magnitude of the dissipation terms with the thermal diffusion terms in the thermal energy equation. We concentrate on the form of Φ corresponding to Darcy's law, as given in (9.3).

If the quantities, U , L , and ΔT are used to denote representative values of velocity, length, and temperature drop within a system, then the orders of magnitude of the thermal diffusion and viscous dissipation terms in (9.3) are, respectively,

$$\frac{k\Delta T}{L^2} \quad \text{and} \quad \frac{\mu U^2}{K} \quad (9.9)$$

In mixed and forced convective flows there exists a given velocity scale, and therefore viscous dissipation effects are negligible when

$$\left(\frac{\mu U^2}{k\Delta T} \right) \frac{L^2}{K} = \frac{Br}{Da} \ll 1 \quad (9.10)$$

Here Br and Da are the Brinkman and Darcy numbers where the Brinkman number is the term in brackets in (9.10).

On the other hand, there is no natural length-scale in free convection, but a simple scaling analysis (or even a full vertical thermal boundary-layer analysis along the lines of that undertaken by Cheng and Minkowycz [21]) yields the velocity scale,

$$U \propto \left(\frac{\alpha}{L}\right) Ra^{1/2} \quad (9.11)$$

where

$$Ra = \frac{\rho g \beta K L \Delta T}{\alpha \mu} \quad \text{and} \quad \alpha = k / \rho c_p \quad (9.12)$$

are the Darcy–Rayleigh number and the thermal diffusivity of the medium, respectively. Substitution of the above expression for U into (9.10) yields

$$Ge = \frac{g \beta L}{c_p} \ll 1 \quad (9.13)$$

as the condition for viscous dissipation to be negligible. The quantity Ge is the Gebhart number.

Given the forms of expressions (9.10) and (9.12) it is clear that viscous dissipation is more likely to be significant when velocities are high and length-scales are large. Thus vigorous flows or flows within geologically sized regions are more likely to display significant viscous dissipative effects. Nield [13] also quotes particle bed nuclear reactors as one other possible area of application where viscous dissipation should not be neglected.

9.3 Free Convective Boundary Layers

9.3.1 Equations of Motion

In this subsection the basic equations (continuity, Darcy, and energy equation) and boundary conditions are written down in the form they apply to the case of free convection over a vertical semi-infinite plate of uniform temperature. Later they are amended according to the physical requirements of forced and mixed convection problems. On applying the boundary-layer approximation ($x \gg y$) and the Boussinesq approximation, the basic equations are (e.g., see Nield and Bejan [17]),

$$\frac{\partial u}{\partial x} + \frac{\partial v}{\partial y} = 0 \quad (9.14)$$

$$\frac{\partial u}{\partial y} = -s_g \frac{g\beta K}{v} \frac{\partial T}{\partial y} \quad (9.15)$$

$$u \frac{\partial T}{\partial x} + v \frac{\partial T}{\partial y} = \alpha \frac{\partial^2 T}{\partial y^2} + \frac{v}{Kc_p} u^2 \quad (9.16)$$

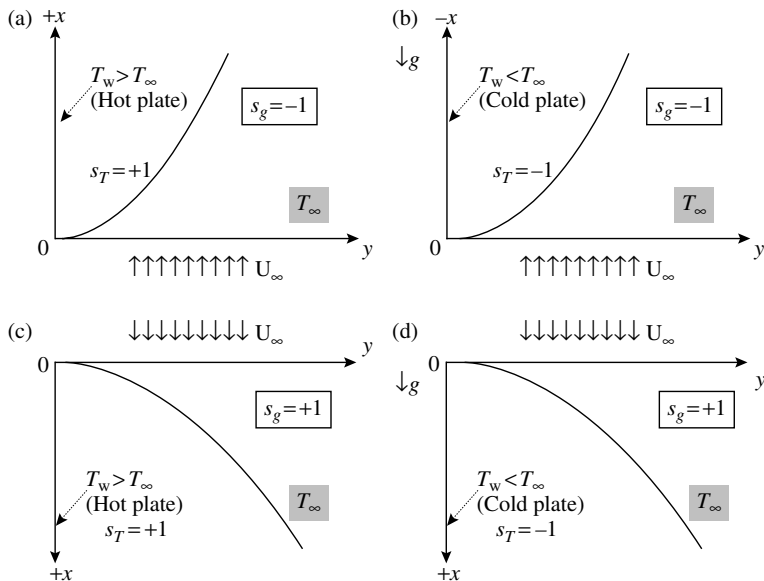
and the boundary conditions read

$$v = 0, \quad T = \text{const.} = T_w \quad \text{on } y = 0 \quad (9.17a)$$

$$u \rightarrow 0, \quad T \rightarrow T_\infty \quad \text{as } y \rightarrow \infty \quad (9.17b)$$

Here x and y are the Cartesian coordinates along and normal to the heated surface, respectively, while u and v are the respective velocity components. T is the fluid temperature, K is the permeability of the porous medium, g is the acceleration due to gravity, c_p is the specific heat at constant pressure, α , β , and $v = \mu/\rho$ are the effective thermal diffusivity, thermal expansion coefficient, and kinematic viscosity, respectively. The second term on the right-hand side of Eq. (9.16) is proportional to the volumetric heat generation rate $\Phi = \mu u^2/K$ by viscous dissipation. The origin of the coordinate system is placed on the definite edge of the plate and the positive x -axis is directed along the plate toward its indefinite edge at $x = +\infty$.

For a vertical surface in the presence of viscous dissipation, four physical situations must be distinguished, as depicted schematically in Figure 9.1(a)–(d). The different situations correspond to surfaces that are either upward or downward projecting and are either hot or cold. Mathematically these cases are specified by the signs s_T and s_g where $s_T = \text{sgn}(T_w - T_\infty)$ and where s_g denotes the projection on the positive x -axis of $g/|g|$. Thus $s_g = +1$ when the positive x -axis points in the direction of g (i.e., vertically downwards) and $s_g = -1$ when it points in the direction opposite to g . According to the nomenclature introduced by Goldstein [22] only the “forward” (i.e., the usual) boundary-layer flows will be considered here. These correspond to the cases in which the definite edge of the plate, $x = 0$, represents its leading edge. Their “backward” counterparts, where the definite edge of the plate is a trailing edge, are not considered here. In the case of free convection this means that the backward boundary-layer flows arising in the situations shown in Figure 9.1(b) and (c) will not be discussed in this chapter. Likewise, in the case of forced and mixed convection, it will be assumed that the uniform stream of velocity U_∞ always comes from $x = -\infty$. Thus, in the presence of viscous dissipation, both “aiding” and “opposing” mixed flow regimes can be distinguished. They correspond to Figure 9.1(a) and (d) and 9.1(b) and (c), respectively.

**FIGURE 9.1**

Representations of the four different mixed convection situations involving either heated or cooled surfaces, and either forward or backward boundary layers. In the absence of viscous dissipation situations (a) and (d) are mathematically identical as are (b) and (c). In the presence of viscous dissipation, the four situations (a), (b), (c), and (d) become physically distinct.

9.3.2 Breaking the Upflow/Downflow Equivalence

In the case of free convection, Eqs. (9.15) and (9.17b) yield

$$u = -s_g \frac{g\beta K}{v} (T - T_\infty) \quad (9.18)$$

After the substitution of,

$$T = T_\infty + s_T |T_w - T_\infty| \cdot \theta \quad (9.19)$$

Equations (9.18), (9.16), and (9.17) become

$$u = -s_g s_T \frac{g\beta K |T_w - T_\infty|}{v} \theta \quad (9.20)$$

$$u \frac{\partial \theta}{\partial x} + v \frac{\partial \theta}{\partial y} = \alpha \frac{\partial^2 \theta}{\partial y^2} + \frac{s_T v}{K c_p |T_w - T_\infty|} u^2 \quad (9.21)$$

$$v = 0, \quad \theta = 1 \quad \text{on } y = 0 \quad (9.22\text{a})$$

$$u \rightarrow 0, \quad \theta \rightarrow 0 \quad \text{as } y \rightarrow \infty \quad (9.22\text{b})$$

As mentioned in Section 9.3.1, the forward (or usual) free convection boundary-layer flows, which we are interested in, correspond to the situations shown in Figure 9.1(a) and (d). In both of these cases $s_g s_T = -1$, which, according to Eq. (9.20), implies the same relationship between u and θ . The boundary conditions (9.22), on the other hand, are independent of the signs s_g and s_T . Now, if the viscous dissipation is neglected, Eq. (9.21) also becomes independent of s_T and thus we immediately recover the well-known textbook result concerning the physical equivalence of the free convection flow over an upward projecting hot plate ($s_T = +1$, Figure 9.1[a]) and over its downward projecting cold counterpart ($s_T = -1$, Figure 9.1[d]). If, however, in Eq. (9.21) the viscous dissipation is taken into account, then due to the sign $s_T = \pm 1$ in front of u^2 this physical equivalence gets broken. This means that the free convection flow over the upward projecting hot plate ("upflow," Figure 9.1[a]) and over its downward projecting cold counterpart ("downflow," Figure 9.1[d]) become physically distinct. As reported recently [14, 23] one of the dramatic consequences of this broken equivalence is the existence of a strictly parallel free convection flow, the so called ADP, which can only occur over the downward projecting cold plate of Figure 9.1(d) but not over its upward projecting hot counterpart of Figure 9.1(a).

9.3.3 The Asymptotic Dissipation Profile

Introducing the stream function ψ by the usual definition $u = \partial\psi/\partial y$, $v = -\partial\psi/\partial x$ and the dimensionless quantities ξ , Y , and Ψ according to the definitions

$$x = L\xi, \quad y = LR^{-1/2}Y, \quad \psi = \alpha R^{+1/2}\Psi \quad (9.23)$$

where the reference length L and the Darcy–Rayleigh number R are defined as

$$L = \frac{c_p}{g\beta}, \quad R = \frac{g\beta K|T_w - T_\infty|L}{\nu\alpha} \quad (9.24)$$

we obtain the quantities θ , u , and v in terms of Ψ as follows

$$\theta = -s_g s_T \frac{\partial\Psi}{\partial Y}, \quad u = \frac{\alpha}{L} R \frac{\partial\Psi}{\partial Y}, \quad v = -\frac{\alpha}{L} R^{1/2} \frac{\partial\Psi}{\partial\xi} \quad (9.25)$$

Here, for the forward boundary-layer flows of Figure 9.1(a) and (d) $s_g s_T = -1$ holds. Thus, we are left with a single unknown function, Ψ , which satisfies

the energy equation

$$\frac{\partial \Psi}{\partial Y} \frac{\partial^2 \Psi}{\partial Y \partial \xi} - \frac{\partial \Psi}{\partial \xi} \frac{\partial^2 \Psi}{\partial Y^2} = \frac{\partial^3 \Psi}{\partial Y^3} - s_g \left(\frac{\partial \Psi}{\partial Y} \right)^2 \quad (9.26)$$

along with the boundary conditions

$$\frac{\partial \Psi}{\partial \xi} = 0 \quad \text{and} \quad \frac{\partial \Psi}{\partial Y} = -s_g s_T = +1 \quad \text{on } Y = 0 \quad (9.27a)$$

$$\frac{\partial \Psi}{\partial Y} \rightarrow 0 \quad \text{as } Y \rightarrow \infty \quad (9.27b)$$

In these dimensionless variables the “broken equivalence” described above becomes manifest again. Indeed, in both the situations shown in Figure 9.1(a) and (d) the boundary conditions (9.27) are the same but due to the presence of s_g in the basic Eq. (9.26) the upward/downward equivalence gets broken.

Our interest in this subsection is in the existence of a strictly parallel-flow solution to the boundary-value problem (9.26), (9.27), that is, on a solution Ψ that depends only on the normal coordinate Y , $\Psi = \Psi(Y)$. Such a solution, if any, satisfies the equation

$$\frac{d^3 \Psi}{dY^3} - s_g \left(\frac{d\Psi}{dY} \right)^2 = 0 \quad (9.28)$$

along with the boundary conditions (9.28). As shown by Magyari and Keller [14] these requirements can only be satisfied for $s_g = +1$ (downflow, Figure 9.1[d]), the corresponding solution being the ADP:

$$\Psi = -\frac{6}{Y + \sqrt{6}}, \quad \theta = \frac{6}{(Y + \sqrt{6})^2}, \quad u = \frac{\alpha}{L} R \theta, \quad v = 0 \quad (9.29)$$

Therefore, the ADP is an algebraically decaying parallel-flow solution of the basic Eq. (9.14) to (9.16) of the free convection over a (cold, downward projecting) vertical plate. Its (dimensionless) surface heat flux is given by

$$Q_0 = -\left. \frac{\partial \theta}{\partial Y} \right|_{Y=0} = +\sqrt{\frac{2}{3}} \quad (9.30)$$

and its 1% thickness (i.e., the value Y_δ of Y for which $\theta(Y_\delta) = 0.01$) is $Y_\delta = 9\sqrt{6}$.

The existence of the ADP is quite surprising, since in the absence of viscous dissipation the boundary-value problem (9.14) to (9.17) does not admit

solutions with vanishing transversal component $v = 0$; compared with the parallel component u , the transversal velocity component v is small but always nonvanishing (e.g., see the classical Cheng–Minkowycz solution [21]). The existence of the ADP, however, shows that the (small) buoyancy forces due to heat release by viscous dissipation are able to cancel the (small) transversal component v of the free convection velocity field, thus giving rise to a strictly parallel flow. Such “self-parallelization” of the velocity field in the presence of viscous dissipation can only happen in a free convection flow that descends over a cold plate (downflow), but never in its ascending counterpart over a hot plate (upflow). The reason is that in the latter case, the buoyancy forces due to heat release by viscous dissipation assist the “main” buoyancy forces sustained by the wall temperature gradient, while in the former case of the cold plate, they oppose them.

9.3.4 Flow Development Toward the ADP

The main concern of this section is to discuss the question of whether the ADP solution (9.16) of the boundary-value problem (9.14) to (9.17) represents a physically realizable state of the descending free convection flow or not. The answer, which has been given recently by Rees et al. [23], is that it is realizable. The starting point of the proof given by Rees et al. [23] is the following simple physical reasoning.

In the neighborhood of the leading edge, where the effect of viscous dissipation is negligible, the steady flow has the character of the classical Cheng–Minkowycz boundary-layer solution [21] whose thickness increases with the wall coordinate as $x^{1/2}$. Thus, if the viscous dissipation term in the energy equation is neglected, the boundary-layer thickness grows indefinitely according to the Cheng–Minkowycz similarity solution. This holds both for an ascending free convection flow from a hot plate as well as one descending from a cold plate. But the heat released by viscous dissipation warms up the moving fluid. This in turn accelerates the growth of the ascending boundary layer but decelerates that of the descending one. It is therefore expected that far enough from the leading edge, the thickness of the cold boundary layer will be limited by the warming effect of viscous dissipation to a constant asymptotic value. The limiting state of this boundary-layer flow, which is approached at some distance x_* from the leading edge, should be precisely the ADP which is described by Eq. (9.29).

The numerical experiment of Rees et al. [23] proceeded by first introducing the usual Cheng–Minkowycz similarity variable for boundary-layer flow from a uniform temperature surface in order to describe the beginning stages of the evolution of the flow. Then Eq. (9.26), with $s_g = +1$, were used further downstream. Therefore, the following transformations

$$\eta = \xi^{-1/2} Y, \quad \Psi = \xi^{+1/2} f(\eta, \xi), \quad \theta = \theta(\eta, \xi) \quad (9.31)$$

were substituted into Eq. (9.26) to obtain,

$$f''' + \frac{1}{2}ff'' - \xi f'^2 = \xi \left(f' \frac{\partial f'}{\partial \xi} - f'' \frac{\partial f}{\partial \xi} \right), \quad \theta = f' \quad (9.32)$$

where the primes denote differentiation with respect to η . In this form of the basic equations it may be seen explicitly that the viscous dissipation term, $\xi f'^2$, disappears at the origin, where $\xi = 0$.

In numerical simulation, Eq. (9.32) is solved in the range $0 \leq \xi \leq 1$, and Eq. (9.26) in the range $\xi \geq 1$. This means that the developing boundary-layer flow is well approximated near the leading edge, but that the approach to the constant thickness ADP arises naturally within the context of Eq. (9.26). When $\xi \leq 1$, Eq. (9.32) is solved subject to the boundary conditions

$$\eta = 0: f = 0, f' = 1; \quad \eta \rightarrow \infty: f' \rightarrow 0 \quad (9.33)$$

but when $\xi > 1$, Eq. (9.26) is solved subject to

$$Y = 0: \Psi = 0, \frac{\partial \Psi}{\partial Y} = 1; \quad Y \rightarrow \infty: \frac{\partial \Psi}{\partial Y} \rightarrow 0 \quad (9.34)$$

The respective pairs of equations were solved by a straightforward application of the well-known Keller box method. The solution at the leading edge ($\xi = 0$) is readily seen to satisfy a pair of ordinary differential equations, and the solutions there are the same as those presented by Cheng and Minkowycz [21]. The leading edge profiles were then marched forward in ξ . The accuracy of our numerical scheme is such that the steady value of Q_0 is 0.816454, which has a relative error of 0.00005 on comparison with Eq. (9.30).

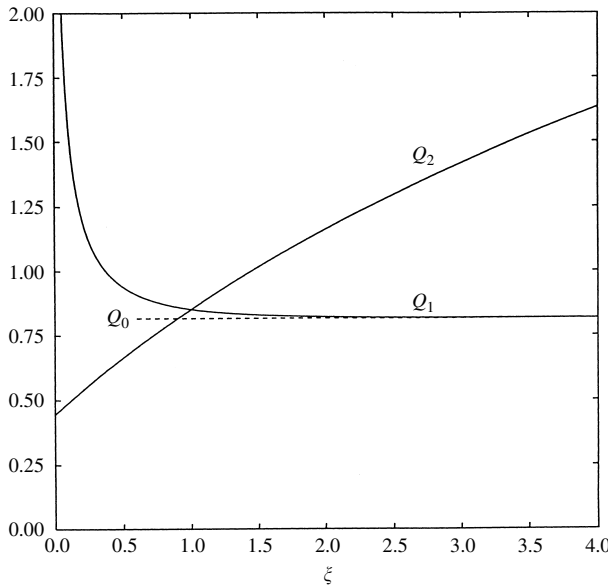
Figure 9.2 shows the surface rate of heat transfer in two forms as functions of ξ . More specifically the figure depicts

$$Q_1 = -\xi^{-1/2} \frac{\partial \theta}{\partial \eta} \Big|_{\eta=0} \quad \text{for } \xi \leq 1, \quad Q_1 = -\frac{\partial \theta}{\partial Y} \Big|_{Y=0} \quad \text{for } \xi \geq 1 \quad (9.35)$$

and

$$Q_2 = -\frac{\partial \theta}{\partial \eta} \Big|_{\eta=0} \quad \text{for } \xi \leq 1, \quad Q_2 = -\xi^{+1/2} \frac{\partial \theta}{\partial Y} \Big|_{Y=0} \quad \text{for } \xi \geq 1 \quad (9.36)$$

The value Q_1 shows how the surface rate of heat transfer evolves compared with that of the uniform thickness ADP to which the flow tends as $\xi \rightarrow \infty$. Near the leading edge the heat transfer is large simply because the boundary layer is thin relative to the ADP. On the other hand, Q_2 represents a rate of heat transfer that is scaled in the same way as for free convection in the absence of viscous dissipation. In this context, the rate of heat transfer increases because the boundary layer becomes relatively thin as ξ increases.

**FIGURE 9.2**

Variation with ξ of the rate of the heat transfer as represented by Q_1 and Q_2 , as defined in Eqs. (9.35) and (9.36), respectively. The Cheng–Minkowycz value of Q_2 is 0.44376 which corresponds to $\xi = 0$. Also shown as a dashed line is the value (9.30) of Q_0 corresponding to the ADP.

From the data from which Figure 9.2 was generated, the curve Q_1 is found to be within 1% of the ADP value of $Q_0 = +\sqrt{2/3} = 0.816496$, when $x = 1.79$, and therefore this value may be chosen as being the appropriate value for x_* . In dimensional terms, this is equivalent to

$$x \equiv x_* = 1.79L = 1.79 \frac{c_p}{g\beta} \quad (9.37)$$

which is the distance from the leading edge beyond which the uniform thickness ADP solution applies. The dependence of this “self-parallelization length” of the flow on the parameters β and c_p corresponds to physical expectation. Indeed, the stronger the buoyancy forces, which are proportional to $\rho g \beta \Delta T$, the stronger the self-parallelization effect and accordingly the shorter must be the distance x_* . This explains why both β and g appear in the denominator of Eq. (9.37). Furthermore, the smaller the heat capacity c_p , the larger is the temperature increase due to the heat being released by viscous dissipation, which again shortens the distance x_* at which the growth of the cold boundary-layer ends. This explains the place of c_p in the numerator of Eq. (9.37). It should be underlined here that in usual applications the order of magnitude of x_* amounts to several kilometers so that self-parallelization of free convection flows due to dissipative effects is likely to occur only in geologically sized applications.

9.3.5 Other Free Convective Flows

We now discuss briefly other works on free convection boundary-layer flows where viscous dissipation has been included in the thermal energy equation.

A rather early paper by Nakayama and Pop [4] discusses free convection induced by a heated surface of arbitrary shape, of which a flat plate and a horizontal cylinder are but two special cases. Their analysis proceeds by expanding the governing nonsimilar boundary-layer equations as a series solution in εx , where ε is the Gebhart number, and solving the resulting systems of ordinary differential equations using the Karman–Pohlhausen integral technique. It was found that the presence of viscous dissipation reduces the heat flux from the heated surface, in general. They also obtained similarity solutions for certain special variations in the surface temperature when the heated surface is vertical.

Murthy and Singh [24] and Murthy [25] also used a small- ε expansion in their study of Darcy–Forchheimer convection from a vertical surface. In addition these authors used a velocity-dependent thermal diffusivity. Once more it was found that the surface rate of heat transfer decreases as the Gebhart number increases from zero.

The vertical plate was also considered by Takhar et al. [26] using the Darcy–Brinkman model for the momentum equations. However, the formula for viscous dissipation which was used by those authors corresponds to that for a clear fluid, rather than one of the forms given by Eqs. (9.7) or (9.8). Unfortunately, a similar use of the clear fluid model may be found in the papers by Kumari and Nath [27], Yih [28], El-Amin [29], and Israel-Cookey et al. [30], who study boundary-layer flows in the presence of a magnetic field, and in the mixed convection paper by Kumari et al. [31].

Sections 9.3.3 and 9.3.4 reported the situation for Darcy flow over a downward projecting cold plate. When the plate is upward and hot (i.e., it corresponds to [Figure 9.1\(a\)](#)), then the flow may be computed by solving Eq. (9.32) but with the viscous dissipation term having the opposite sign. Preliminary studies by the authors show that the boundary layer becomes exponentially thin as ξ increases, and the temperature becomes exponentially large due to the positive feedback between buoyancy and viscous dissipation; this will be reported in due course.

9.4 Forced Convection with Examples

9.4.1 Boundary-Layer Analysis

In this section, we consider a uniform forced convection flow of an incompressible fluid with imposed velocity $\mathbf{v} = (u, 0, 0)$, where $u = \text{const.} \equiv U_\infty$ within a porous medium extending to $x \geq 0, y \geq 0$, as shown in [Figure 9.1\(a\)](#). Thus fluid enters the porous domain at $x = 0$. The only governing

equation is the energy equation (9.16) which in this case reduces to

$$U_{\infty} \frac{\partial T}{\partial x} = \alpha \frac{\partial^2 T}{\partial y^2} + \frac{\nu}{Kc_p} U_{\infty}^2 \quad (9.38)$$

where it has been assumed that streamwise diffusion is negligible (i.e., that the boundary-layer approximation applies). The temperature of the porous boundary at $x = 0$ (termed the entrance boundary) coincides with the constant temperature T_{∞} of the entering fluid,

$$T(0, y \geq 0) = T_{\infty} \quad (9.39)$$

and the temperature of the impermeable plane surface $y = 0$ adjacent to the porous medium (termed the adjacent surface) is now a given function of the coordinate x ,

$$T(x \leq 0, 0) = T_{\infty}, \quad T(x > 0, 0) = T_w(x) \quad (9.40)$$

The general physical requirement that no heat “disappears” at infinity reads:

$$\frac{\partial T}{\partial y}(x \geq 0, \infty) = 0 \quad (9.41)$$

Now, it is immediately seen that in such a forced convection problem the “usual” far-field condition, namely, $T(x > 0, \infty) = \text{const.} = T_{\infty}$ is inconsistent with the energy equation (9.38); since it implies that $U_{\infty} = 0$, which is contrary to the assumption. Instead, Eqs. (9.38) and (9.41) imply in this case

$$\frac{\partial T}{\partial x}(x \geq 0, \infty) = \frac{\nu U_{\infty}}{Kc_p} \quad (9.42)$$

which further yields

$$T(x \geq 0, \infty) = T_{\infty} + \frac{\nu U_{\infty}}{Kc_p} x \quad (9.43)$$

Hence the only far-field condition which is consistent with the energy equation is given by Eq. (9.43). It specifies an asymptotic temperature that is not a constant, but a linear function of the wall coordinate x . This condition applies both for the forced and the mixed convection problems in extended porous media when the effect of viscous dissipation is taken into account [6].

We may conclude, then, that it is not possible to set a far-field temperature profile when considering mixed or forced convection in the presence of viscous dissipation. This result is in full agreement with physical expectation. Indeed, in contrast to free convection where the flow velocity goes to

zero as $y \rightarrow \infty$, in the forced and mixed convection boundary-layer flows where $U_\infty = \text{const.} \neq 0$, the mechanical power needed to extrude the fluid through the pores continues to generate frictional heat in the asymptotic region $y \rightarrow \infty$. Practically, the correct numerical solutions may be obtained by applying either Eq. (9.41) or Eq. (9.43) as $y \rightarrow \infty$. It may also be seen that Eq. (9.38) is mathematically equivalent to Fourier's equation for heat conduction in a semi-infinite homogeneous solid with uniform volumetric heat generation (where x is regarded as the time variable). Thus, after an infinitely long time (i.e., as $x \rightarrow \infty$), the whole solid must become infinitely hot in accordance with Eq. (9.43).

For more transparency, it is convenient to introduce a reference length L , a reference temperature $T_{\text{ref}} > T_\infty$, and define the Eckert, Prandtl, Darcy, and Péclet numbers in terms of these quantities as follows:

$$Ec = \frac{U_\infty^2}{c_p(T_{\text{ref}} - T_\infty)}, \quad Pr = \frac{\mu}{\rho\alpha}, \quad Da = \frac{K}{L^2}, \quad Pe = \frac{U_\infty L}{\alpha} \quad (9.44)$$

Thus, the asymptotic condition (9.43) becomes

$$T(x \geq 0, \infty) = T_\infty + (T_{\text{ref}} - T_\infty) \tilde{Ec} \frac{x}{L} \quad (9.45)$$

where \tilde{Ec} is a "modified Eckert number" defined as

$$\tilde{Ec} = \frac{Ec \cdot Pr}{Da \cdot Pe} = \frac{\mu U_\infty L}{K \rho c_p (T_{\text{ref}} - T_\infty)} \quad (9.46)$$

Alternatively, it is convenient to use the "local" counterparts of these quantities, which can be obtained by substituting L in Da and Pe simply by x . Thus the "local modified Eckert number" \tilde{Ec}_x , the counterpart of \tilde{Ec} , is

$$\tilde{Ec}_x = \frac{Ec \cdot Pr}{Da_x \cdot Pe_x} = \tilde{Ec} \frac{x}{L} \quad (9.47)$$

Now, the analytical solution of Eq. (9.38) for some realistic temperature distributions $T_w = T_w(x)$ of the adjacent surface $y = 0$ will be given. To this end, we first make the change of variables

$$T(x, y) = T_\infty + (T_{\text{ref}} - T_\infty) \frac{U_\infty \cdot \tilde{Ec}}{L} \tau + \theta(\tau, y), \quad \tau = \frac{x}{U_\infty} \quad (9.48)$$

and Eq. (9.38) becomes:

$$\frac{\partial \theta}{\partial \tau} = \alpha \frac{\partial^2 \theta}{\partial y^2} \quad (9.49)$$

on taking into account that

$$T(x, y) = T_\infty + (T_{\text{ref}} - T_\infty) \tilde{E}c \frac{x}{L} \quad (9.50)$$

represents the exact solution of Eq. (9.38) corresponding to $\alpha = 0$. Equation (9.48) implies that the quantity $\theta(\tau, y)$ describes precisely the contribution of heat diffusion in the y -direction to the temperature field $T(x, y)$ in addition to the effect of viscous dissipation and convection. Accordingly, Eq. (9.49) coincides formally with Fourier's equation of heat conduction in a homogeneous solid of thermal diffusivity α , where the role of time variable is played by $\tau = x/U_\infty$ and where now the above-mentioned uniform heat generation has been removed by transformation (9.48). In this way, our forced convection heat transfer problem reduces to one of a transient heat conduction problem in a semi-infinite solid occupying the region $y > 0$ and subject to the initial condition,

$$\theta(0, y \geq 0) = 0 \quad (9.51)$$

As a consequence of Eqs. (9.48) and (9.40) the temperature at the boundary at $y = 0$ is given by

$$\theta(\tau > 0, 0) = T_w(x) - T_\infty - (T_{\text{ref}} - T_\infty) \frac{U_\infty \cdot \tilde{E}c}{L} \tau \equiv \theta_w(\tau) \quad (9.52)$$

The solution of the heat conduction problem (9.49), (9.51), (9.52) is well known (e.g., see Carslaw and Jaeger [32], section 9.2.5) and reads:

$$\theta(\tau, y) = \frac{2}{\sqrt{\pi}} \int_{\eta}^{\infty} \theta_w \left(\tau - \frac{y^2}{4\alpha\xi^2} \right) e^{-\xi^2} d\xi \quad (9.53)$$

where

$$\eta = \sqrt{Pe} \frac{y}{2\sqrt{Lx}} = \sqrt{Pe_x} \frac{y}{2x} \quad (9.54)$$

In this way, the temperature profiles $\theta = \theta(\tau, y)$ of the solid at different "instants" $\tau = x/U_\infty$ determine the temperature profiles of the uniformly moving fluid in our porous body at different distances x from the entrance boundary $x = 0$. This analogy allows us to transcribe easily the exact solution of several well-known heat conduction problems listed, for example, in Carslaw and Jaeger [32] for the case of the present forced convection problem.

A part of the integrations in (9.53) with $\theta_w(\tau)$ given by Eq. (9.52) can be performed without the need to specify the surface temperature distribution

$T_w(x)$ explicitly. Thus we obtain the following general expression for the temperature field:

$$\begin{aligned} \frac{T(x, y) - T_{\text{ref}}}{T_{\text{ref}} - T_{\infty}} &= \tilde{E}c_x(1 - 4t^2 \operatorname{erfc} \eta) - \operatorname{erf} \eta \\ &- \frac{1}{T_{\text{ref}} - T_{\infty}} \left(T_{\text{ref}} \operatorname{erfc} \eta - \frac{2}{\sqrt{\pi}} \int_{\eta}^{\infty} T_w \left(x - \frac{x\eta^2}{\xi^2} \right) e^{-\xi^2} d\xi \right) \end{aligned} \quad (9.55)$$

Here, $\operatorname{erf} \eta$ and $\operatorname{erfc} \eta = 1 - \operatorname{erf} \eta$ denote the error and complementary error functions respectively, where $t^n \operatorname{erfc} \eta$ stands for the n th repeated integrals of the error function (see Carslaw and Jaeger [32], appendix II).

The remainder of this section is devoted to two explicit examples. The quantities of physical interest will be the temperature field $T(x, y)$ and the wall heat flux

$$q_w(x) = -k \frac{\partial T}{\partial y}(x, 0) = -k \frac{\partial \theta}{\partial y}(\tau, 0) \quad (9.56)$$

corresponding to a prescribed temperature distribution $T_w(x)$ of the adjacent plane surface $y = 0$. The local Nusselt number related to (9.33) will be defined in this chapter as follows

$$Nu_x = \frac{q_w(x) \cdot x}{k(T_{\text{ref}} - T_{\infty})} \quad (9.57)$$

Note that in the denominator the same temperature difference has been included as in the definition (9.44) of the Eckert number.

Example 1. The most simple mathematical example is obtained for $\theta_w(\tau) \equiv 0$ when the integral (9.53) is vanishing and thus $\theta(\tau, y) \equiv 0$. According to Eq. (9.52), this case corresponds to the temperature distribution

$$T_w(x) = T_{\infty} + (T_{\text{ref}} - T_{\infty}) \tilde{E}c_x \quad (9.58)$$

of the adjacent surface, which as $\theta(\tau, y) \equiv 0$, becomes identical with the solution (9.48) for the problem, $T_w(x) = T(x, y)$. This coincides further with the temperature field (9.50) found in the purely convective case ($\alpha = 0$). Accordingly, the linear heating law (9.58) of the adjacent surface has the consequence that (a) the wall heat flow is identically vanishing, $q_w(x) \equiv 0$, and (b) nowhere in the bulk of the fluid does heat diffusion occur.

Example 2. As a second simple example, we consider the case $\theta_w(x) = \text{const.} \equiv T_{\text{ref}} - T_{\infty} \equiv T_0 - T_{\infty} > 0$, which corresponds to the wall temperature distribution

$$T_w(x) = T_0 + (T_0 - T_{\infty}) \tilde{E}c_x \quad (9.59)$$

In this case, the integral (9.53) yields $\theta(\tau, y) = (T_0 - T_\infty)\operatorname{erfc} \eta$ and the solution (9.48) becomes

$$T(x, y) = T_0 + (T_0 - T_\infty)(\tilde{E}c_x - \operatorname{erf} \eta) \quad (9.60)$$

When $y \rightarrow \infty$, we easily recover the far-field relationship (9.45). For $\mu = 0$, that is, in the absence of viscous dissipation, Eq. (9.59) reduces to $T_w(x) = T_0$ and in Eq. (9.60) we immediately recover Bejan's classical result [3,17]:

$$T(x, y) = T_0 - (T_0 - T_\infty)\operatorname{erf} \eta \quad (9.61)$$

The wall heat flux and the local Nusselt number corresponding to the temperature field (9.60) are given by

$$q_w(x) = \frac{k(T_0 - T_\infty)}{x} \sqrt{\frac{Pe_x}{\pi}} \quad (9.62)$$

$$Nu_x = \sqrt{\frac{Pe_x}{\pi}} \quad (9.63)$$

Note that Bejan's solution (9.61) for the forced convection flow over the adjacent plane surface of constant temperature T_0 without viscous dissipation also leads to the same expressions (9.62) and (9.63) that have been obtained from the present result (9.60). In the present case, however the surface temperature is not a constant but a linear function of x , being given by Eq. (9.59). Hence, compared to the constant surface temperature without viscous dissipation, the linear increase of $T_w(x)$ according to Eq. (9.59) represents the surface temperature distribution that exactly removes the effect of the viscous dissipation on the surface heat flow.

Finally, it is worth underlining again that for a consistent description of the forced and mixed convection problems in fluid saturated porous media in the presence of viscous dissipation the usual far-field condition must be substituted by

$$T(x \geq 0, \infty) = T_\infty + (T_{\text{ref}} - T_\infty)\tilde{E}\frac{x}{L} = T_\infty + (T_{\text{ref}} - T_\infty)\tilde{E}c_x \quad (9.64)$$

As a consequence, several recent publications concerning the mixed convection problems in the presence of viscous dissipation must basically be revised (for more details see the next section).

9.4.2 Channel Flows

At present only two papers exist that deal with forced convective flows in channels in the presence of viscous dissipation. The papers by Nield et al. [33]

and Kuznetsov et al. [34] are two in a series of papers by the same authors that consider porous medium versions of the classical Graetz problem. In this problem fully developed flow exists in a uniform channel that points in the x -direction where the boundary temperature is set at T_0 when $x < 0$, and where the temperature of one or both surfaces (or the surface in the case of a circular pipe) is raised to T_1 when $x > 0$. The strength of the flow is measured in terms of the Péclet number, Pe , and the classical Graetz problem analyses the thin thermal boundary layer that exists downstream of $x = 0$ when the Péclet number is large. The strength of the viscous dissipation effect is measured by the size of the Brinkman number, Br .

In the above-quoted papers these authors study cases where Pe is not large using a series expansion method. Nield et al. [33] consider a plane channel while Kuznetsov et al. [34] apply the same methodology to a circular pipe flow. In both cases, the authors found that variations in the value of Br affect the surface rates of heat transfer very considerably. The authors also investigated the differences in the results obtained by each of the three models of viscous dissipation given by Eqs. (9.3), (9.7), and (9.8). It was found that the corresponding far downstream values of the Nusselt number differ appreciably only when the Darcy number is of magnitude unity or higher, that is, in cases where the porous medium is very highly porous.

9.5 Mixed Convection

9.5.1 The Darcy–Forchheimer Flow

In this section and in Sections 9.5.2 and 9.5.3, we consider the mixed convection case of a Darcy–Forchheimer steady-boundary-layer flow over an isothermal vertical flat plate in the physical situations depicted in Figure 9.1(a)–(d). Following Murthy [8] and the notation used in Eqs. (9.1) to (9.3), we write the mass, momentum, and energy balance equations (subject to both the boundary layer and Boussinesq approximations) in the form

$$\frac{\partial u}{\partial x} + \frac{\partial v}{\partial y} = 0 \quad (9.65)$$

$$\frac{\partial}{\partial y} \left(u + \frac{C\sqrt{K}}{v} u^2 \right) = -s_g \frac{Kg\beta}{v} \frac{\partial}{\partial y} (T - T_\infty) \quad (9.66)$$

$$u \frac{\partial T}{\partial x} + v \frac{\partial T}{\partial y} = \alpha \frac{\partial^2 T}{\partial y^2} + \frac{v}{Kc_p} u \cdot \left(u + \frac{C\sqrt{K}}{v} u^2 \right) \quad (9.67)$$

and the corresponding boundary conditions in the form [8]

$$y = 0: v = 0, \quad T = \text{const.} \equiv T_w \quad (9.68a,b)$$

$$y \rightarrow \infty: u \rightarrow U_\infty, \quad T \rightarrow T_\infty \quad (9.69\text{a,b})$$

where C denotes the Forchheimer form drag coefficient.

Now, it is immediately seen that the thermal far-field condition (9.69b) is not suitable since, as discussed in Section 9.4, it is inconsistent with the energy equation. Indeed, having in mind Eq. (9.41), the energy equation (9.67) requires

$$\lim_{y \rightarrow \infty} \frac{\partial T}{\partial x} = \frac{\nu U_\infty}{Kc_p} (1 + Re) \quad (9.70)$$

where

$$Re = \frac{C U_\infty \sqrt{K}}{\nu} \quad (9.71)$$

denotes the modified Reynolds number. Thus, integrating Eq. (9.70) once and taking into account condition (9.39) at the entrance boundary we obtain

$$T(x, \infty) = T_\infty + \frac{\nu U_\infty}{Kc_p} (1 + Re)x \quad (9.72)$$

Therefore, a consistent description of the present mixed convection problem requires us to replace the (unsuitable) boundary condition (9.69b) by the condition (9.72), that is

$$y \rightarrow \infty: u \rightarrow U_\infty, T \rightarrow T_\infty + \frac{\nu U_\infty}{Kc_p} (1 + Re)x \quad (9.73\text{a,b})$$

With the aid of the pseudo-similarity transformation [8]

$$\begin{aligned} \eta &= \frac{y}{x} \sqrt{Pe_x} \\ \psi &= \alpha \sqrt{Pe_x} \cdot f(x, \eta) \\ T &= T_\infty + s_T \cdot |T_w - T_\infty| \theta(x, \eta), \quad s_T = \operatorname{sgn}(T_w - T_\infty) \end{aligned} \quad (9.74)$$

and the usual definition of the stream function, $u = \partial \psi / \partial y$ and $v = -\partial \psi / \partial x$, we transform Eqs. (9.66) and (9.67) in

$$f'' + 2Re \cdot f' \cdot f'' = -s_g s_T \frac{R_x}{Pe_x} \theta' \quad (9.75)$$

$$\theta'' + \frac{1}{2} f \theta' + s_T \frac{Pe_x}{R_x} \varepsilon f'^2 (1 + Re \cdot f') = \varepsilon \left(f' \frac{\partial \theta}{\partial \varepsilon} - \theta' \frac{\partial f}{\partial \varepsilon} \right) \quad (9.76)$$

and the boundary conditions (9.68) and (9.73) in

$$\eta = 0: f(x, 0) + 2x \frac{\partial f}{\partial x}(x, 0) = 0, \quad \theta(x, 0) = 1 \quad (9.77a,b)$$

$$\eta \rightarrow \infty: f'(x, \infty) = 1, \quad \theta(x, \infty) = s_T \frac{Pe_x}{R_x} (1 + Re) \varepsilon \quad (9.78a,b)$$

where the prime denotes derivatives with respect to the similarity variable η . The local Darcy-Rayleigh number R_x that occurs in the above equations is obtained by substituting in Eq. (9.24) the reference length L by the wall coordinate x while ε stands for the local Gebhart number

$$Ge_x = \frac{\beta g x}{c_p} \equiv \varepsilon \quad (9.79)$$

Thus, the ratio Pe_x/R_x is in fact independent of x . Now, integrating Eq. (9.75) once and determining the (ε -dependent) integration constant by taking into account the boundary condition (9.78) we obtain

$$f' \cdot (1 + Re \cdot f') = (1 + Re)(1 + s_g \varepsilon) - s_g s_T \frac{R_x}{Pe_x} \theta \quad (9.80)$$

which when substituted in Eq. (9.76) results in

$$\theta'' + \frac{1}{2} f \theta' - \varepsilon f' \left[s_g \theta - s_T \frac{Pe_x}{R_x} (1 + Re)(1 + s_g \varepsilon) \right] = \varepsilon \left(f' \frac{\partial \theta}{\partial \varepsilon} - \theta' \frac{\partial f}{\partial \varepsilon} \right) \quad (9.81)$$

We note that the boundary condition (9.77a) can be reduced to $f(x, 0) = 0$ by assuming that $f(0, 0) = 0$. Indeed, a formal integration of Eq. (9.77a) yields $f(x, 0) = \text{const.} \cdot x^{-1/2}$, which results precisely in $f(x, 0) = 0$ if one assumes $f(0, 0) = 0$. Hence, for a consistent solution of the present mixed convection problem we must consider Eq. (9.81) and Eq. (9.75), or the first integral of Eq. (9.75) given by Eq. (9.80), along with the boundary conditions

$$\eta = 0: f(x, 0) = 0, \quad \theta(x, 0) = 1 \quad (9.82a,b)$$

$$\eta \rightarrow \infty: f'(x, \infty) = 1, \quad \theta(x, \infty) = s_T \frac{Pe_x}{R_x} (1 + Re) \varepsilon \quad (9.83a,b)$$

In this way, the main difference compared with the work of earlier authors are (a) of the boundary condition (9.83b), instead of $\theta(x, \infty) = 0$

and (b) of the second term occurring in the square bracket of Eq. (9.81).

9.5.2 Perturbation Approach for Small Gebhart Number

For small values of the local Gebhart number $\varepsilon = g\beta x/c_p$, the above boundary-value problem can be solved by a perturbation approach based on the series expansions [8].

$$\begin{aligned} f(x, \eta) &= \sum_{m=0}^{\infty} (-1)^m \varepsilon^m f_m(\eta) \\ \theta(x, \eta) &= \sum_{m=0}^{\infty} (-1)^m \varepsilon^m t_m(\eta) \end{aligned} \quad (9.84)$$

with which we proceed here up to order ε^2 , that is,

$$\begin{aligned} f(x, \eta) &= f_0(\eta) - \varepsilon f_1(\eta) + \varepsilon^2 f_2(\eta) \\ \theta(x, \eta) &= t_0(\eta) - \varepsilon t_1(\eta) + \varepsilon^2 t_2(\eta) \end{aligned} \quad (9.85)$$

Thus, after some algebra we obtain, to orders 0, 1, and 2 in ε , the following systems of ordinary differential equations and boundary conditions.

To order ε^0 :

$$\begin{aligned} f'_0 + Re f_0'^2 + s_g s_T \frac{R_x}{Pe_x} t_0 &= 1 + Re \\ t''_0 + \frac{1}{2} f_0 t'_0 &= 0 \\ f_0(0) = 0, \quad f'_0(\infty) = 1, \quad t_0(0) = 1, \quad t_0(\infty) = 0 \end{aligned} \quad (9.86)$$

To order ε^1 :

$$\begin{aligned} f'_1 + 2Re f'_0 f'_1 + s_g s_T \frac{R_x}{Pe_x} t_1 &= -s_g (1 + Re) \\ t''_1 + \frac{1}{2} (f_0 t'_1 + t'_0 f_1) + s_g f'_0 t_0 + f_1 t'_0 - f'_0 t_1 &= s_T \frac{Pe_x}{R_x} (1 + Re) f'_0 \\ f_1(0) = 0, \quad f'_1(\infty) = 0, \quad t_1(0) = 0, \quad t_1(\infty) &= -s_T \frac{Pe_x}{R_x} (1 + Re) \end{aligned} \quad (9.87)$$

To order ε^2 :

$$\begin{aligned}
 & f'_2 + Re \left(2f'_0 f'_2 + f'^2_1 \right) + s_g s_T \frac{R_x}{Pe_x} t_2 = 0 \\
 & t''_2 + \frac{1}{2} (f_0 t'_2 + f_1 t'_1 + t'_0 f_2) + s_g (f'_0 t_1 + f'_1 t_0) + f_1 t'_1 - f'_1 t_1 + 2 (t'_0 f_2 - f'_0 t_2) \\
 & = s_T \frac{Pe_x}{R_x} (1 + Re) (f'_1 - s_g f'_0) \\
 & f_2(0) = 0, \quad f'_2(\infty) = 0, \quad t_2(0) = 0, \quad t_2(\infty) = 0
 \end{aligned} \tag{9.88}$$

On comparing these system of equations with the corresponding equations of earlier authors, one sees that the essential difference between the present analysis and others comes from the nonvanishing right-hand sides of the equations for t in (9.87) and (9.88) and in the asymptotic condition in (9.87) for $t_1(\infty)$.

9.5.3 The Aiding Up- and Downflows

In order to be more specific we restrict the discussion to the Darcy mixed convection flows ($Re=0$) for the two “aiding” cases corresponding to the physical situations shown in Figure 9.1(a) (upward projecting hot plate in assisting stream) and 9.1(d) (downward projecting cold plate in assisting stream), respectively. In both of these cases we have $s_T \cdot s_g = -1$. In addition, we chose $R_x/Pe_x = 1$.

For these parameter values the following simple relationships hold:

$$f'(x, \eta) = 1 + s_g \varepsilon + \theta(x, \eta), \quad f'(x, 0) = 2 + s_g \varepsilon \tag{9.89a}$$

$$f'_0(\eta) = 1 + t_0(\eta), \quad f'_0(0) = 2 \tag{9.89b}$$

$$f'_1(\eta) = -s_g + t_1(\eta), \quad f'_1(0) = -s_g \tag{9.89c}$$

$$f'_2(\eta) = t_2(\eta), \quad f'_2(0) = 0 \tag{9.89d}$$

$$f''(x, \eta) = \theta'(x, \eta) \tag{9.90}$$

Equation (9.89a) represents a modified form of the Reynolds analogy known from the viscous flow of clear fluids.

We first solved the boundary-value problems (9.86) to (9.88) corresponding to the case of the hot plate (Figure 9.1[a], $s_T = +1, s_g = -1$) with the aid of the familiar shooting method, obtaining for the missing “initial values” the numerical results,

$$\begin{aligned}
 t'_0(0) &= -0.7205853 \\
 t'_1(0) &= -2.41893785 \quad (\text{hot plate}, s_T = +1, s_g = -1) \\
 t'_2(0) &= -0.794596877
 \end{aligned} \tag{9.91}$$

It is worth mentioning that the numerical calculations becomes more and more sensitive with increasing order of the approximation.

Owing to some simple symmetry considerations, the case of the cold plate ([Figure 9.1\[d\]](#), $s_T = -1$, $s_g = +1$) does not require new numerical effort. Indeed, all our basic equations and boundary conditions (9.80) to (9.83) are invariant under the sign-change transformation $(s_T, s_g, \varepsilon) \rightarrow (-s_T, -s_g, -\varepsilon)$. As a consequence, all the perturbation equations and boundary conditions (9.86) to (9.88) are invariant under the transformation

$$(s_T, s_g, f_1, t_1) \rightarrow (-s_T, -s_g, -f_1, -t_1) \quad (9.92)$$

This means that in the case of the cold plate ([Figure 9.1\[d\]](#), $s_T = -1, s_g = +1$) the missing “initial values” can be obtained from Eqs. (9.91) by only changing the sign of $t'_1(0)$:

$$\begin{aligned} t'_0(0) &= -0.7205853 \\ t'_1(0) &= +2.41893785 \quad (\text{cold plate}, s_T = -1, s_g = +1) \\ t'_2(0) &= -0.794596877 \end{aligned} \quad (9.93)$$

The local Nusselt number, defined according to Eq. (9.57) with $T_{\text{ref}} \equiv T_w$, can thus be calculated to order ε^2 as

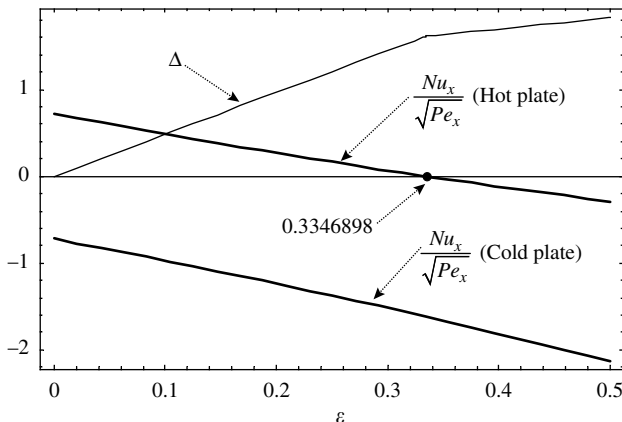
$$\frac{Nu_x}{\sqrt{Pe_x}} = -\theta'(x, 0) = s_T \cdot \left[-t'_0(0) + \varepsilon t'_1(0) - \varepsilon^2 t'_2(0) \right] \quad (9.94)$$

In [Figure 9.3](#), $Nu_x/\sqrt{Pe_x}$ is plotted for the two mixed convection flows as a function Gebhart number ε . The difference Δ of the absolute values of the amount of heat transferred in these two cases as given by

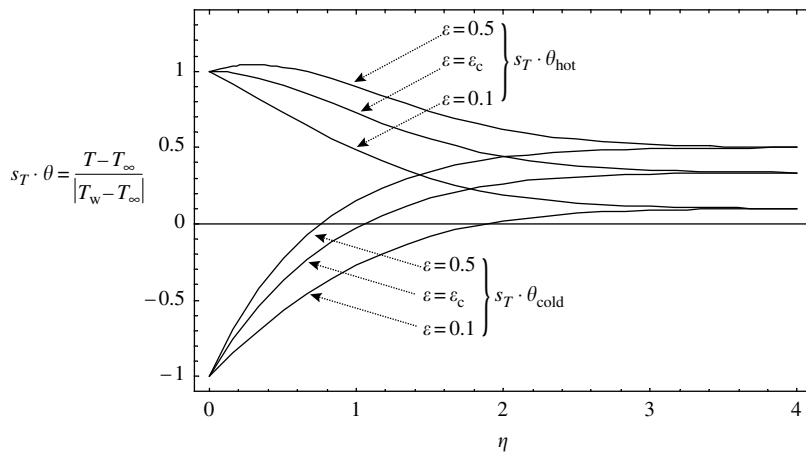
$$\Delta = \left| \frac{Nu_x}{\sqrt{Pe_x}} \right| (\text{cold plate}) - \left| \frac{Nu_x}{\sqrt{Pe_x}} \right| (\text{hot plate}) \quad (9.95)$$

is also shown in Figure 9.3.

As expected, in the case of the cold plate the heat transfer coefficient is negative, that is, heat is always transferred from the fluid to the wall. This amount of heat increases with increasing value of the local Gebhart number ε (from 0.72058 if the viscous dissipation is neglected, $\varepsilon = 0$, to 2.128703 for $\varepsilon = 0.5$). In the case of the hot plate, the heat transfer coefficient is positive (i.e., heat is transferred from the wall to the fluid) as long as the effect of viscous dissipation is weak enough which means $\varepsilon < 0.3346898$. When ε exceeds this critical value $\varepsilon_c = 0.3346898$ the heat released by viscous dissipation overcomes the effect of the hot wall and the wall heat flux becomes reversed. For $\varepsilon = \varepsilon_c$ the wall becomes adiabatic. As the thin curve of Figure 9.3 shows, for the same value of ε , the amount of heat transferred to the cold plate always exceeds the amount of heat transferred from, as well as, to the hot plate.

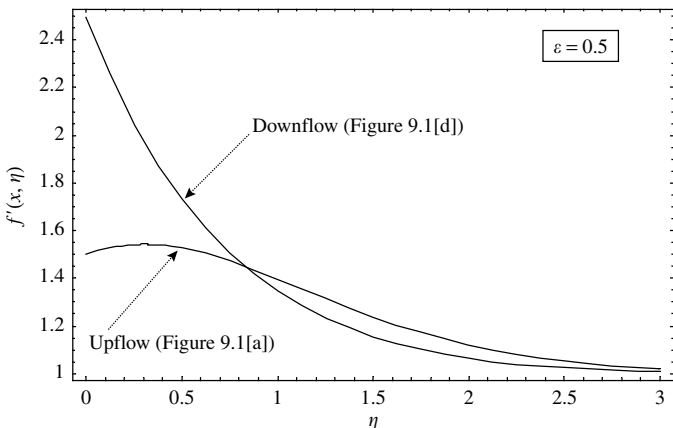
**FIGURE 9.3**

Heat-transfer coefficients (9.94) for two types of aided mixed convection flows along an upward projecting hot plate (Figure 9.1[a]) and a downward projecting cold plate (Figure 9.1[d]). The thin curve represents the difference Δ between the absolute values of the amount of heat transferred in these two cases, as given by Eq. (9.95).

**FIGURE 9.4**

Dimensionless temperature profiles $s_T \cdot \theta_{\text{hot}} = +\theta_{\text{hot}}$ and $s_T \cdot \theta_{\text{cold}} = -\theta_{\text{cold}}$ corresponding to the two cases of aided Darcy mixed convection flow (Figures 9.1[a] and [d], respectively). The critical value $\varepsilon_c = 0.3346898$ corresponds to the adiabatic case of the hot plate.

In Figure 9.4 the dimensionless temperature profiles $s_T \cdot \theta = (T - T_\infty)/|T_w - T_\infty|$ are shown for $s_T = +1$ and -1 and a couple of values of ε . The change from the direct to reversed wall heat flux at the critical Gebhart number $\varepsilon_c = 0.3346898$ in the case of the hot plate is immediately seen in this figure. It is also clearly seen that, according to the boundary condition (9.83b), both the dimensionless temperature profiles $s_T \cdot \theta_{\text{hot}} = +\theta_{\text{hot}}$ and $s_T \cdot \theta_{\text{cold}} = -\theta_{\text{cold}}$ approach the same asymptotic value $s_T \cdot \theta(x, \infty) = \varepsilon$ as $\eta \rightarrow \infty$. This is in

**FIGURE 9.5**

Dimensionless downstream velocity profiles corresponding to two cases of aided Darcy mixed convection flow (Figures 9.1[a] and [d], respectively).

whole agreement with the special case $\{Re = 0, R_x/Pe_x = 1\}$ of the boundary condition (9.73b).

Finally in Figure 9.5 the dimensionless downstream velocity profiles $f'(x, \eta)$ are shown for $\varepsilon = 0.5$. Figure 9.4 and Figure 9.5 are related to each other by Eq. (9.89a), which may be checked easily.

9.5.4 Channel Flows

Ingham et al. [5] and Al-Hadhrami et al. [35] have both considered mixed convection in a vertical porous channel in the presence of viscous dissipation. In both cases the bounding surfaces have a temperature that is a linear decreasing function of height, that is, the channel is unstably stratified, and there is a fixed local temperature difference across the channel. Ingham et al. [5] used the Darcy flow model and determined the basic flow and temperature fields. In the absence of viscous dissipation the governing equations yield singular solutions when the Rayleigh number, Ra , is such that $Ra^{1/2}$ is an odd multiple of π . When viscous dissipation is included, then the singularity disappears, and is replaced by a pair of solutions, one of which corresponds to the limit as Ra tends upward toward a critical value, and the other as Ra tends downward toward the same value. Al-Hadhrami et al. [35] extended the analysis to cases where the Darcy–Brinkman model apply. The same qualitative results appear here too, but they also show that multiple solutions arise in general.

9.6 Stability Considerations

The study of viscous dissipation in porous media cannot yet be considered to be a mature realm of science for a variety of reasons, not the least of which

is the uncertainty as to how it should be modeled when the Brinkman terms are significant in the momentum equations. It might therefore seem a little premature to consider whether or not the flows discussed herein are realizable in practice, should they suffer small perturbations. Given that there appears to be general agreement in the published literature over the form that the viscous dissipation terms take when the flow obeys Darcy's law, it is important that some studies are undertaken to assess the stability characteristics of some flows. At present only two such studies have been undertaken. Rees et al. [35] analyzed the linear stability of the ADP from an inclined surface, while Rees et al. [15] reworked the standard weakly nonlinear analysis for the case of Darcy–Benard convection given in Rees [36]. This section briefly summarizes the chief features of these analyses because the details are beyond the space available.

When a cold downward-projected surface is rotated so that it is inclined away from the vertical, and in such a way that the normal vector to the cold surface has a downward component, then the ADP analysis described earlier still applies but the parallel-flow boundary layer is thicker because buoyancy is less effective. The expression for θ is given by Eq. (9.29), but with Y replaced by $Y \cos \alpha$, where α is the inclination of the surface from the vertical. In such situations it is possible to introduce disturbances of the form of streamwise vortices. A straightforward linearized stability theory yields a curve relating the Rayleigh number to the wavelength of the disturbance, and this has the same shape as the Darcy–Benard problem, namely that it has one well-defined minimum and that Ra tends to infinity as the wavelength of the vortex tends either to zero or to infinity; for details see Rees et al. [37]. The critical Rayleigh number and wavenumber are given by

$$Ra^{1/2} \tan \alpha = 16.8469 \quad k_c = 0.5166 \quad (9.96)$$

From this we see that the critical Rayleigh number becomes infinite as the surface approaches the vertical, and therefore we conclude that the ADP conditions described in Section 9.3 are also realizable in practice from the point of view of stability. Some fully nonlinear computations are also presented in Rees et al. [37].

A very detailed analysis of the weakly nonlinear convection in a Darcy–Benard problem is given in Rees et al. [15]. When viscous dissipation is absent then convection arises when the Darcy–Rayleigh number exceeds $4\pi^2$. Initially, convection sets in as a set of parallel rolls when the layer is of infinite horizontal extent. When viscous dissipation is present the temperature profile within the layer loses its up/down symmetry when convection occurs, and this causes hexagonal cells to arise. This is because the lack of symmetry allows two rolls, whose axes are at 60° to one another, to interact and reinforce a roll at 60° to each of them, thus providing the hexagonal pattern. Hexagonal convection is subcritical and appears at Rayleigh numbers below $4\pi^2$. However, when Ra is sufficiently above $4\pi^2$, the rolls are re-established as the preferred pattern of convection. When Forchheimer terms are included,

then the range of Rayleigh numbers over which hexagons exist and are stable decreases, and they are eventually extinguished. A similar qualitative result has been shown when the layer is tilted at increasing angles from the horizontal, although there are two main orientations of hexagonal solutions in this case. The rolls that form when hexagons are destabilized are longitudinal rolls and may be regarded as streamwise vortices like those considered in Rees et al. [37].

9.7 Research Opportunities

We close this chapter with some proposals for research opportunities.

- While the form of the viscous dissipation term for Darcy and Darcy–Forchheimer flows are well established, there remain some differences over the correct form when boundary effects are significant. At present there exists no REV model of viscous dissipation, nor are there any detailed computations in periodically structured porous media at small length-scales.
 - As far as we are aware, free, forced, and mixed convective backward boundary-layer flows, where the edge ($x = 0$) of the semi-infinite vertical plate is (not a leading edge but) a trailing edge, has not yet been investigated in the literature.
 - Numerical (perturbation) solutions to the mixed convection problem for small values of the Gebhart number have only been discussed here for the two “aiding” cases of Darcy flow. The discussion of the Darcy–Forchheimer case is still open. In addition, the investigation of the two “opposing cases,” and for both the Darcy and the Darcy–Forchheimer cases, is also an open problem.
 - Currently no published studies on strongly nonlinear free convection in cavities and in the presence of viscous dissipation exist. Given our observations, here, regarding the manner in which up/down symmetry is broken, it is very likely that novel qualitative phenomena arise in cavities with heating from below or from sidewall.
-

Nomenclature

ADP	asymptotic dissipation profile
Br	Brinkman number
c_{fp}	coefficient of Forchheimer term
C	Forchheimer coefficient
c_p	specific heat

Da	Darcy number
Ec	Eckert number
f	reduced streamfunction
F	drag force
g	gravity
Ge	Gebhart number
k	thermal conductivity of the porous medium
K	permeability
L	representative length
Nu	Nusselt number
$\underline{\underline{K}}$	permeability tensor
\overline{Pe}	Péclet number
Pr	Prandtl number
q'''	volumetric rate of heat production
Q	dimensionless heat flux
Ra, R	Darcy–Rayleigh number
Re	Reynolds number
REV	representative elementary volume
s_g	projection of $g/ g $ on the x -axis
s_T	$\text{sgn}(T_w - T_\infty)$
T	temperature
u, v, w	velocities in the x -, y -, and z -directions, respectively
U	representative velocity
x, y, z	Cartesian coordinates
Y	dimensionless y -coordinate

Greek letters

α	thermal diffusivity/inclination angle
β	thermal expansion coefficient
ΔT	representative temperature difference
ε	local Gebhart number
η	similarity variable
θ	scaled temperature
μ	dynamic viscosity
$\tilde{\mu}$	effective viscosity
ν	kinematic viscosity
ξ	dimensionless x -coordinate
ρ	fluid density
τ	scaled x -coordinate
Φ	heat source term
ψ	streamfunction

Subscripts

clear	clear fluid
Darcy	porous medium

ref	reference conditions
w	wall or surface condition
x	local quantity
∞	ambient conditions
δ	boundary-layer thickness

References

1. B. Gebhart. Effects of viscous dissipation in natural convection. *J. Fluid Mech.* 14: 225–232, 1962.
2. H.I. Ene and E. Sanchez-Palencia. On thermal equation for flow in porous media. *Int. J. Eng. Sci.* 20: 623–630, 1982.
3. A. Bejan. *Convection Heat Transfer*, 2nd edn. New York: John Wiley & Sons, 1995.
4. A. Nakayama and I. Pop. Free convection over a non-isothermal body in a porous medium with viscous dissipation. *Int. Comm. Heat Mass Transfer* 16: 173–180, 1989.
5. D.B. Ingham, I. Pop, and P. Cheng. Combined free and forced convection in a porous medium between two vertical walls with viscous dissipation. *Transp. Porous Media* 5: 381–398, 1990.
6. E. Magyari, I. Pop, and B. Keller. Effect of viscous dissipation on the Darcy forced convection flow past a plane surface. *J. Porous Media* 6: 111–112, 2003.
7. B. Tashtoush. Analytical solution for the effect of viscous dissipation on mixed convection in saturated porous media. *Transp. Porous Media* 41: 197–209, 2000.
8. P.V.S.N. Murthy. Effect of viscous dissipation on mixed convection in a non-Darcy porous medium. *J. Porous Media* 4: 23–32, 2001.
9. E. Magyari, I. Pop, and B. Keller. Comment on “analytical solution for the effect of viscous dissipation on mixed convection in saturated porous media.” *Transp. Porous Media* 53: 367–369, 2003.
10. B. Tashtoush. Reply to comments on “analytical solution for the effect of viscous dissipation on mixed convection in saturated porous media.” *Transp. Porous Media* 41: 197–209, 2000 and 53: 371–372, 2003.
11. D.A. Nield. Comments on “Comments on ‘analytical solution for the effect of viscous dissipation on mixed convection in saturated porous media’.” *Transp. Porous Media* 55: 117–118, 2004.
12. B. Gebhart and J. Mollendorf. Viscous dissipation in external natural convection flows. *J. Fluid Mech.* 38: 97–107, 1969.
13. D.A. Nield. Resolution of a paradox involving viscous dissipation and nonlinear drag in a porous medium. *Transp. Porous Media* 41: 349–357, 2000.
14. E. Magyari and B. Keller. The opposing effect of viscous dissipation allows for a parallel free convection boundary-layer flow along a cold vertical flat plate. *Transp. Porous Media* 51: 227–230, 2003.
15. D.A.S. Rees, E. Magyari, and B. Keller. Hexagonal cell formation in a Darcy–Benard convection with viscous dissipation and its modification by form drag and layer inclination. Submitted for publication, 2004.
16. D.A. Nield. Modelling fluid flow in saturated porous media and at interfaces. In: D.B. Ingham and I. Pop, eds., *Transport Phenomena in Porous Media II*. London: Pergamon, 2002, pp. 1–19.

17. D.A. Nield and A. Bejan. *Convection in Porous Media*, 2nd edn. New York: Springer-Verlag, 1999.
18. C.C. Mei and J.L. Auriault. The effect of weak inertia on flow through a porous medium. *J. Fluid Mech.* 222: 647–663, 1991.
19. J.L. Lage, B.V. Antohe, and D.A. Nield. Two types of nonlinear pressure-drop versus flow-rate relation observed for saturated porous media. *ASME J. Fluids Eng.* 119: 701–706, 1997.
20. A.K. Al-Hadrami, L. Elliott, and D.B. Ingham. A new model for viscous dissipation across a range of permeability values. *Transp. Porous Media* 53: 117–122, 2003.
21. P. Cheng and W.J. Minkowycz. Free convection about a vertical flat plate embedded in a porous medium with application to heat transfer from a dike. *J. Geophys. Res.* 82: 2040–2044, 1977.
22. S. Goldstein. On backward boundary layers and flow in converging passages. *J. Fluid Mech.* 21: 33–45, 1965.
23. D.A.S. Rees, E. Magyari, and B. Keller. The development of the asymptotic viscous dissipation profile in a vertical free convective boundary layer flow in a porous medium. *Transp. Porous Media* 53: 347–355, 2003.
24. P.V.S.N. Murthy and P. Singh. Effect of viscous dissipation on a non-Darcy natural convection regime. *Int. J. Heat Mass Transfer* 40: 1251–1260, 1997.
25. P.V.S.N. Murthy. Thermal dispersion and viscous dissipation effects on non-Darcy mixed convection in a fluid saturated porous medium. *Heat Mass Transfer* 33: 295–300, 1998.
26. H.S. Takhar, V.M. Soundalgekar, and A.S. Gupta. Mixed convection of an incompressible viscous fluid in a porous medium past a hot vertical plate. *Int. J. Non-linear Mech.* 25: 723–728, 1990.
27. M. Kumari and G. Nath. Simultaneous heat and mass transfer under unsteady mixed convection along a vertical slender cylinder embedded in a porous medium. *Wärme Stoffübertragung* 28: 97–105, 1993.
28. K.A. Yih. Viscous and Joule heating effects on non-Darcy MHS natural convection flow over a permeable sphere in porous media with internal heat generation. *Int. Comm. Heat Mass Transfer* 27: 591–600, 2000.
29. M.F. El-Amin. Combined effect of viscous dissipation and Joule heating on MHD forced convection over a non-isothermal horizontal cylinder embedded in a fluid saturated porous medium. *J. Magnetism Magn. Mater.* 263: 337–343, 2003.
30. C. Israel-Cookey, A. Ogulu, and V.B. Omubo-Pepple. Influence of viscous dissipation and radiation on unsteady MHD free-convection flow past an infinite heated vertical plate in a porous medium with time-dependent suction. *Int. J. Heat Mass Transfer* 46: 2305–2311, 2003.
31. M. Kumari, H.S. Takhar, and G. Nath. Mixed convection flow over a vertical wedge embedded in a highly porous medium. *Heat Mass Transfer* 37: 139–146, 2001.
32. H.S. Carslaw and J.C. Jaeger. *Conduction of Heat in Solids*. Oxford: Clarendon Press, 1995.
33. D.A. Nield, A.V. Kuznetsov and Ming Xiong. Thermally developing forced convection in a porous medium: parallel plate with walls at uniform temperature, with axial conduction and viscous dissipation effects. *Int. J. Heat Mass Transfer* 46: 643–651, 2003.

34. A.V. Kuznetsov, Ming Xiong, and D.A. Nield. Thermally developing forced convection in a porous medium: circular duct with walls at uniform temperature, with axial conduction and viscous dissipation effects. *Transp. Porous Media* 53: 331–345, 2003.
35. A.K. Al-Hadrami, L. Elliott, and D.B. Ingham. Combined free and forced convection in vertical channels of porous media. *Transp. Porous Media* 49: 265–289, 2002.
36. D.A.S. Rees. Stability analysis of Darcy–Benard convection. Lecture notes from *Summer School on Porous Media, Neptun, Constanta, Romania, July 2001*. (Notes available from the author.)
37. D.A.S. Rees, E. Magyari, and B. Keller. Vortex instability of the asymptotic dissipation profile in a porous medium. Submitted for publication, 2004.

Part V

Turbulence in Porous Media

10

Mathematical Modeling and Applications of Turbulent Heat and Mass Transfer in Porous Media

Marcelo J.S. de Lemos

CONTENTS

Summary	410
10.1 Introduction	411
10.2 Local Instantaneous Governing Equations	411
10.3 Volume and Time Average Operators	413
10.4 Time-Averaged Transport Equations	415
10.5 The Double-Decomposition Concept	416
10.5.1 Basic Relationships	416
10.6 Turbulent Momentum Transport in Porous Media	419
10.6.1 Mean Flow Equations	419
10.6.1.1 Continuity	419
10.6.1.2 Momentum — one average operator	419
10.6.1.3 Momentum equation — two average operators ..	420
10.6.1.4 Inertia term — space and time (double) decomposition	421
10.6.2 Equations for Fluctuating Velocity	424
10.6.3 Turbulent Kinetic Energy	426
10.6.3.1 Equation for $\langle k \rangle^i = \langle \bar{u}' \cdot \bar{u}' \rangle^i / 2$	428
10.6.3.2 Comparison of macroscopic transport equations ..	430
10.7 Turbulent Heat Transport	431
10.7.1 Governing Equations	431
10.7.1.1 Time average followed by volume average	431
10.7.1.2 Volume average followed by time average	432
10.7.2 Turbulent Thermal Dispersion	434
10.7.3 Local Thermal Equilibrium Hypothesis	436
10.7.4 Macroscopic Buoyancy Effects	437
10.7.4.1 Mean flow	437
10.7.4.2 Turbulent field	438

10.8	Turbulent Mass Transport	440
10.8.1	Mean and Turbulent Fields	440
10.8.2	Turbulent Mass Dispersion	442
10.9	Applications in Hybrid Media	444
10.9.1	The Stress Jump Conditions at Interface	444
10.9.2	Buoyant Flows in Cavities Partially Filled with Porous Inserts	446
10.9.3	Flow Around a Sinusoidal Interface in a Channel	447
10.10	Concluding Remarks	447
	Acknowledgments	448
	Nomenclature	448
	References	449

Summary

Engineering equipment design and environmental impact analyses can benefit from appropriate modeling of turbulent flow in porous media. Accordingly, a number of natural and engineering systems can be characterized by some sort of porous structure through which a working fluid permeates. Turbulence models proposed for such flows depend on the order of application of time and volume-average operators. Two developed methodologies, following the two orders of integration, lead to different governing equations for the statistical quantities. This chapter reviews recently published methodologies to mathematically characterize turbulent transport in porous media.

For hybrid media, involving both a porous structure and a clear flow region, difficulties arise due to the proper mathematical treatment given at the interface. This chapter also presents and discusses numerical solutions for such hybrid media, here considering a channel partially filled with a wavy porous layer through which fluid flows in turbulent regime. In addition, macroscopic forms of buoyancy terms are also considered in both the mean and the turbulent fields. Cases reviewed include heat transfer in cavities partially filled with porous material.

In summary, within this chapter local instantaneous governing equations are reviewed for clear flow before volume and time-average operators are applied to them. The double-decomposition concept is presented and thoroughly discussed prior to the derivation of macroscopic governing equations. Equations for turbulent momentum transport in porous media follow showing detailed derivation for the mean and turbulent field quantities. The statistical $k-e$ model for clear domains, used to model macroscopic turbulence effects, also serves as the basis for turbulent heat transport modeling. Turbulent mass transport in porous matrices is further reviewed in the light of the double-decomposition concept. A section on applications in hybrid media

covers flow over porous layers in channels and in cavities partially filled with porous material.

10.1 Introduction

Customarily, modeling of macroscopic transport for incompressible flows in porous media has been based on the volume-average methodology (Whitaker, 1999; Vafai and Tien, 1981) for either heat (Hsu and Cheng, 1990), or mass transfer (Whitaker, 1966, 1967; Bear and Bachmat, 1967; Bear, 1972). If time fluctuations of the flow properties are also considered, in addition to spatial deviations, there are two possible methodologies to follow in order to obtain macroscopic equations: (a) application of time-average operator followed by volume-averaging (Kuwahara et al., 1966; Masuoka and Takatsu, 1996; Kuwahara and Nakayama, 1998; Nakayama and Kuwahara, 1999), or (b) use of volume-averaging before time-averaging is applied (Lee and Howell, 1987; Wang and Takle, 1995; Antohe and Lage, 1997; Getachewa et al., 2000). In fact, these two sets of macroscopic transport equations are equivalent when examined under the recently established *double-decomposition* concept (Pedras and de Lemos, 1999a, 2000a, 2001a, 2001b, 2001c, 2003). This methodology, initially developed for the flow variables, has been extended to nonbuoyant heat transfer in porous media where both time fluctuations and spatial deviations were considered for velocity and temperature (Rocamora and de Lemos, 2000a; de Lemos and Rocamora, 2002). Recently, studies on natural convection (de Lemos and Braga, 2003; Braga and de Lemos, 2004), flow over a porous layer (de Lemos and Silva, 2003; Silva and de Lemos, 2003a, 2003b), double-diffusive convection (de Lemos and Tofaneli, 2004) and a general classification of all proposed models for turbulent flow and heat transfer in porous media have been published (de Lemos and Pedras, 2001). Here, new developments in applying the double-decomposition theory to buoyant flows (de Lemos and Braga, 2003) and to mass transfer (de Lemos and Mesquita, 2003) are reviewed. Some numerical results are also included.

10.2 Local Instantaneous Governing Equations

The steady-state local or microscopic instantaneous transport equations for an incompressible fluid with constant properties are given by:

$$\nabla \cdot \mathbf{u} = 0 \quad (10.1)$$

$$\rho \nabla \cdot (\mathbf{u} \mathbf{u}) = -\nabla p + \mu \nabla^2 \mathbf{u} + \rho \mathbf{g} \quad (10.2)$$

$$(\rho c_p) \nabla \cdot (\mathbf{u} T) = \nabla \cdot (\lambda \nabla T) \quad (10.3)$$

where \mathbf{u} is the velocity vector, ρ is the density, p is the pressure, μ is the fluid viscosity, \mathbf{g} is the gravity acceleration vector, c_p is the specific heat, T is the temperature, and λ is the fluid thermal conductivity.

In addition, the mass fraction distribution for the chemical species ℓ is governed by the following transport equation,

$$\nabla \cdot (\rho \mathbf{u} m_\ell + \mathbf{J}_\ell) = \rho R_\ell \quad (10.4)$$

where m_ℓ is the mass fraction of component ℓ , \mathbf{u} is the mass-averaged velocity of the mixture, $\mathbf{u} = \sum_\ell m_\ell \mathbf{u}_\ell$, and \mathbf{u}_ℓ is the velocity of species ℓ . Further, the mass diffusion flux \mathbf{J}_ℓ in Eq. (10.4) is due to the velocity slip of species ℓ and is given by,

$$\mathbf{J}_\ell = \rho_\ell (\mathbf{u}_\ell - \mathbf{u}) = -\rho D_\ell \nabla m_\ell \quad (10.5)$$

where D_ℓ is the diffusion coefficient of species ℓ into the mixture. The second equality in Eq. (10.5) is known as Fick's law. The generation rate of species ℓ per unit of mixture mass is given in Eq. (10.4) by R_ℓ . It is interesting to point out that Eqs. (10.1) to (10.4) are written for steady-state problems to be consistent with this section's purpose. Transient formulations will be presented later when turbulence is considered.

If one considers that the density in the last term of (10.2) varies with temperature, for natural convection flow, the Boussinesq hypothesis reads, after renaming this density ρ_T ,

$$\rho_T \cong \rho [1 - \beta(T - T_{\text{ref}})] \quad (10.6)$$

where the subscript ref indicates a reference value and β is the thermal expansion coefficient defined by,

$$\beta = -\left. \frac{1}{\rho} \frac{\partial \rho}{\partial T} \right|_p \quad (10.7)$$

Equation (10.6) is an approximation of (10.7) and shows how density varies with temperature in the body force term of the momentum equation.

Further, substituting (10.6) into (10.2), one has,

$$\rho \nabla \cdot (\mathbf{u} \mathbf{u}) = -(\nabla p)^* + \mu \nabla^2 \mathbf{u} - \rho \mathbf{g} \beta (T - T_{\text{ref}}) \quad (10.8)$$

where $(\nabla p)^* = \nabla p - \rho \mathbf{g}$ is a modified pressure gradient.

When (10.3) is written for the fluid and solid phases with heat sources it becomes,

– Fluid

$$(\rho c_p)_f \nabla \cdot (\mathbf{u} T_f) = \nabla \cdot (\lambda_f \nabla T_f) + S_f \quad (10.9)$$

- Solid (Porous Matrix)

$$0 = \nabla \cdot (\lambda_s \nabla T_s) + S_s \quad (10.10)$$

where the subscripts f and s refer to each phase, respectively. If there is no heat generation either in the solid or in the fluid phase, one has further,

$$S_f = S_s = 0 \quad (10.11)$$

As mentioned, there are, in principle, two ways that one can follow in order to treat turbulent flow in porous media. The first method applies a time-average operator to the governing equations set (10.1) to (10.4) before the volume-average procedure is applied. In the second approach, the order of application of the two average operators is reversed. Both techniques aim at derivation of suitable macroscopic transport equations.

Volume-averaging in a porous medium, described in detail in Slattery (1967), Whitaker (1969, 1999), and Gray and Lee (1977) makes use of the concept of a representative elementary volume (REV) over which local equations are integrated. In a similar fashion, statistical analysis of turbulent flow leads to time mean properties. Transport equations for statistical values are considered in lieu of instantaneous information on the flow.

For the sake of clarity, before undertaking the task of developing macroscopic equations, it is convenient to recall the definitions of time and volume average and review the proposal of double decomposing the dependent variables.

10.3 Volume and Time Average Operators

The volume average of a general property φ taken over a REV, in a porous medium can be written (see Slattery, 1967; Whitaker, 1969, 1999; Gray and Lee, 1977)

$$\langle \varphi \rangle^v = \frac{1}{\Delta V} \int_{\Delta V} \varphi \, dV \quad (10.12)$$

The value $\langle \varphi \rangle^v$ is defined for any point x surrounded by a REV of size ΔV . This average is related to the intrinsic average for the fluid phase as follows:

$$\langle \varphi_f \rangle^v = \phi \langle \varphi_f \rangle^i \quad (10.13)$$

where $\phi = \Delta V_f / \Delta V$ is the local medium porosity and ΔV_f is the volume occupied by the fluid in a REV. Furthermore, one can write,

$$\varphi = \langle \varphi \rangle^i + {}^i\varphi \quad (10.14)$$

with $\langle {}^i\varphi \rangle^i = 0$. In Eq. (10.14), ${}^i\varphi$ is the spatial deviation of φ with respect to the intrinsic average $\langle \varphi \rangle^i$.

For deriving the flow governing equations, it is necessary to know the relationship between the volumetric average of derivatives and the derivatives of the volumetric average. These relationships are presented in a number of works, namely Slattery (1967), Whitaker (1969, 1999), and Gray and Lee (1977) and others, being known as the Theorem of local volumetric average. They are written as:

$$\langle \nabla \varphi \rangle^v = \nabla (\phi \langle \varphi \rangle^i) + \frac{1}{\Delta V} \int_{A_i} \mathbf{n} \varphi \, dS \quad (10.15)$$

$$\langle \nabla \cdot \varphi \rangle^v = \nabla \cdot (\phi \langle \varphi \rangle^i) + \frac{1}{\Delta V} \int_{A_i} \mathbf{n} \cdot \varphi \, dS \quad (10.16)$$

and

$$\left\langle \frac{\partial \varphi}{\partial t} \right\rangle^v = \frac{\partial}{\partial t} (\phi \langle \varphi \rangle^i) - \frac{1}{\Delta V} \int_{A_i} \mathbf{n} \cdot (\mathbf{u}_i \varphi) \, dS \quad (10.17)$$

where A_i , \mathbf{u}_i and \mathbf{n} are the interfacial area, the interfacial velocity of phase f and the unity vector normal to A_i , respectively.

The area A_i should not be confused with the surface area surrounding volume ΔV . For single-phase flow, phase f is the fluid itself and $\mathbf{u}_i = 0$ if the porous substrate is assumed to be fixed. In developing Eqs. (10.15) to (10.17) the only restriction applied is the independence of ΔV in relation to time and space. If the medium is further assumed to be rigid and heterogeneous, then ΔV_f is dependent on space and is not time-dependent (Gray and Lee, 1977).

Further, the time average of a general quantity φ is defined as follows,

$$\bar{\varphi} = \frac{1}{\Delta t} \int_t^{t+\Delta t} \varphi \, dt \quad (10.18)$$

where the time interval Δt is small compared to the fluctuations of the average value, $\bar{\varphi}$, but large enough to capture turbulent fluctuations of φ .

Time decomposition can then be written as follows,

$$\varphi = \bar{\varphi} + \varphi' \quad (10.19)$$

with $\bar{\varphi}' = 0$, where φ' is the time fluctuation of φ around its average value $\bar{\varphi}$.

10.4 Time-Averaged Transport Equations

In order to apply the time-average operator to Eqs. (10.1), (10.2), and (10.8), one considers:

$$\mathbf{u} = \bar{\mathbf{u}} + \mathbf{u}' \quad T = \bar{T} + T' \quad p = \bar{p} + p' \quad (10.20)$$

Substituting (10.20) into (10.1), (10.2), and (10.8), respectively, one has after considering constant property flow,

$$\nabla \cdot \bar{\mathbf{u}} = 0 \quad (10.21)$$

$$\rho \nabla \cdot (\bar{\mathbf{u}} \bar{\mathbf{u}}) = -(\nabla \bar{p})^* + \mu \nabla^2 \bar{\mathbf{u}} + \nabla \cdot (-\rho \bar{\mathbf{u}}' \bar{\mathbf{u}}') - \rho \mathbf{g} \beta (\bar{T} - T_{\text{ref}}) \quad (10.22)$$

$$(\rho c_p) \nabla \cdot (\bar{\mathbf{u}} \bar{T}) = \nabla \cdot (k \nabla \bar{T}) + \nabla \cdot (-\rho c_p \bar{\mathbf{u}}' \bar{T}') \quad (10.23)$$

For clear fluid, the use of the eddy-diffusivity concept for expressing the stress-rate of strain relationship for the Reynolds stress appearing in (10.22) gives,

$$-\rho \bar{\mathbf{u}}' \bar{\mathbf{u}}' = \mu_t \bar{\mathbf{D}} - \frac{2}{3} \rho k \mathbf{I} \quad (10.24)$$

where $\bar{\mathbf{D}} = [\nabla \bar{\mathbf{u}} + (\nabla \bar{\mathbf{u}})^T]/2$ is the mean deformation tensor, $k = \bar{\mathbf{u}}' \cdot \bar{\mathbf{u}}'/2$ is the turbulent kinetic energy per unit mass, μ_t is the turbulent viscosity, and \mathbf{I} is the unity tensor. Similarly, for the turbulent heat flux on the right-hand side of (10.23) the eddy-diffusivity concept reads,

$$-\rho c_p \bar{\mathbf{u}}' \bar{T}' = c_p \frac{\mu_t}{\sigma_T} \nabla \bar{T} \quad (10.25)$$

where σ_T is known as the turbulent Prandtl number.

The transport equation for the turbulent kinetic energy is obtained by first multiplying the difference between the instantaneous and the time-averaged momentum equations by \mathbf{u}' . Thus, further applying the time-average operator to the resulting product, one has,

$$\rho \nabla \cdot (\bar{\mathbf{u}} k) = -\rho \nabla \cdot \left[\bar{\mathbf{u}}' \left(\frac{p'}{\rho} + q \right) \right] + \mu \nabla^2 k + P_k + G_k - \rho \varepsilon \quad (10.26)$$

where $P_k = -\rho \overline{\mathbf{u}' \mathbf{u}'} : \nabla \bar{\mathbf{u}}$ is the generation rate of k due to gradients of the mean velocity and

$$G_k = -\rho \beta \mathbf{g} \cdot \overline{\mathbf{u}' T'} \quad (10.27)$$

is the buoyancy generation rate of k . Also, $q = (\mathbf{u}' \cdot \mathbf{u}')/2$.

10.5 The Double-Decomposition Concept

The double-decomposition idea, herein used for obtaining macroscopic equations, has been detailed in Pedras and de Lemos (1999a, 2001a, 2001b, 2001c, 2003), so that only a brief overview is presented here. Further, the resulting equations using this concept for the flow (Pedras and de Lemos, 2001a) and nonbuoyant thermal fields (Rocamora and de Lemos, 2000a; de Lemos and Rocamora, 2002) are already available in the literature and for this reason they are not repeated here. Extensions of the double-decomposition methodology to buoyant flows (de Lemos and Braga, 2003; Braga and de Lemos, 2004) to mass transport (de Lemos and Mesquita, 2003) and to double-diffusive convection (de Lemos and Tofaneli, 2004) have also been presented in the literature.

Basically, for porous media analysis, a macroscopic form of the governing equations is obtained by taking the volumetric average of the entire equation set. In that development, the porous medium is considered to be rigid and saturated by an incompressible fluid.

10.5.1 Basic Relationships

From the work in Pedras and de Lemos (2000a) and Rocamora and de Lemos (2000a), one can write for any flow property φ combining decompositions (10.14) and (10.19),

$$\langle \varphi \rangle^i = \langle \bar{\varphi} \rangle^i + \langle \varphi' \rangle^i \quad (10.28)$$

$$\bar{\varphi} = \langle \bar{\varphi} \rangle^i + {}^i \bar{\varphi} \quad (10.29)$$

$${}^i \varphi = {}^i \bar{\varphi} + {}^i \varphi' \quad (10.30)$$

$$\varphi' = \langle \varphi' \rangle^i + {}^i \varphi' \quad (10.31)$$

or further

$$\varphi' = \langle \varphi \rangle^{i'} + {}^i \varphi' = \langle \varphi' \rangle^i + {}^i \varphi' \quad (10.32)$$

where ${}^i\varphi'$ can be understood as either the *time fluctuation of the spatial deviation* or the *spatial deviation of the time fluctuation*. After some manipulation, one can prove that (Pedras and de Lemos, 2001a)

$$\begin{aligned}\overline{\langle \varphi \rangle^v} &= \langle \bar{\varphi} \rangle^v \quad \text{or} \quad \overline{\langle \varphi \rangle^i} = \langle \bar{\varphi} \rangle^i \\ \overline{\langle \varphi \rangle^i} &= \langle \bar{\varphi} \rangle^i\end{aligned}\quad (10.33)$$

that is, the time and volume averages commute. Also,

$$\begin{aligned}{}^i\bar{\varphi} &= \bar{{}^i\varphi} \\ \langle \varphi' \rangle^i &= \langle \varphi \rangle^{i'}\end{aligned}\quad (10.34)$$

or say,

$$\langle \varphi \rangle^i = \frac{1}{\Delta V_f} \int_{\Delta V_f} \varphi dV = \frac{1}{\Delta V_f} \int_{\Delta V_f} (\bar{\varphi} + \varphi') dV = \langle \bar{\varphi} \rangle^i + \langle \varphi' \rangle^i \quad (10.35)$$

$${}^i\varphi = {}^i\bar{\varphi} + {}^i\varphi' = \bar{{}^i\varphi} + {}^i\varphi' \quad (10.36)$$

so that,

$$\left. \begin{aligned}\varphi' &= \langle \varphi' \rangle^i + {}^i\varphi' \\ {}^i\varphi &= {}^i\bar{\varphi} + {}^i\varphi'\end{aligned}\right\} \quad \text{where} \quad {}^i\varphi' = \varphi' - \langle \varphi' \rangle^i = {}^i\varphi - \bar{{}^i\varphi} \quad (10.37)$$

Finally, one can have a full variable decomposition as:

$$\begin{aligned}\varphi &= \langle \bar{\varphi} \rangle^i + \langle \varphi' \rangle^i + {}^i\bar{\varphi} + {}^i\varphi' \\ &= \overline{\langle \varphi \rangle^i} + \langle \varphi \rangle^{i'} + \bar{{}^i\varphi} + {}^i\varphi'\end{aligned}\quad (10.38)$$

or further,

$$\varphi = \underbrace{\langle \bar{\varphi} \rangle^i + \langle \varphi' \rangle^i}_{\langle \varphi \rangle^i} + \underbrace{{}^i\bar{\varphi} + {}^i\varphi'}_{\bar{\varphi}} = \underbrace{\overline{\langle \varphi \rangle^i} + \bar{{}^i\varphi}}_{\bar{\varphi}} + \underbrace{\langle \varphi \rangle^{i'} + {}^i\varphi'}_{\varphi'} \quad (10.39)$$

Equation (10.38) comprises the *double decomposition* concept. A significance of the four terms in (10.39) can be reviewed as: (a) $\langle \bar{\varphi} \rangle^i$, is the intrinsic average of the time mean value of φ . Or say, we compute first the time-averaged values of all points composing the REV, and then we find their volumetric mean to get $\langle \bar{\varphi} \rangle^i$. Instead, we could also consider a certain point x surrounded by the REV and take the volumetric average, at different time steps. Thus, we calculate the average over such different values in time. We get $\langle \varphi \rangle^i$ and, according to (10.33), $\langle \bar{\varphi} \rangle^i = \overline{\langle \varphi \rangle^i}$, or say, volumetric and time

average commute. (b) If we now take the volume average of all fluctuating components of φ , which compose the REV, we end up with $\langle \varphi' \rangle^i$. Instead, with the volumetric average around point x taken at different time steps we can determine the difference between the instantaneous and a time-averaged value. This will be $\langle \varphi \rangle^i'$ that, according to (10.34), equals $\langle \varphi' \rangle^i$. Further, performing first a time-averaging operation over all points that contribute with their local values to the REV, we get a distribution of $\bar{\varphi}$ within this volume. If now we calculate the intrinsic average of this distribution of $\bar{\varphi}$, we get $\langle \bar{\varphi} \rangle^i$. The difference or deviation between these two values is $\bar{\varphi} - \langle \bar{\varphi} \rangle^i$. Now, using the same space decomposition approach we can find for any instant of time t the deviation $i\varphi$. This value also fluctuates with time, and as such a time mean can be calculated as $i\bar{\varphi}$. Again the use of (10.34) gives $i\bar{\varphi} = i\varphi'$. Finally, it is interesting to note the meaning of the last term on each side of (10.39). The first term, $i\langle \varphi' \rangle^i$, is the time fluctuation of the spatial component whereas $(i\varphi')^i$ means the spatial component of the time varying term. If, however, one makes use of relationships (10.33) and (10.34) to simplify (10.39), one finally concludes,

$$i\varphi' = i\varphi' \quad (10.40)$$

and, for simplicity of notation, one can write both superscripts at the same level in the format: $i\varphi'$. Also, $\langle i\varphi' \rangle^i = \bar{i}\varphi' = 0$.

With the help of Figure 10.1 taken from Rocamora and de Lemos (2000a), the concept of *double-decomposition* can be better understood. The figure shows a three-dimensional diagram for a general vector variable φ . For a scalar, all the quantities shown would be drawn on a single line.

The basic advantage of the double-decomposition concept is to serve as a mathematical framework for analysis of flows where within the fluid phase there is enough room for turbulence to be established. As such, the double-decomposition methodology would be useful in situations where a solid phase is existent in the domain under analysis so that a macroscopic

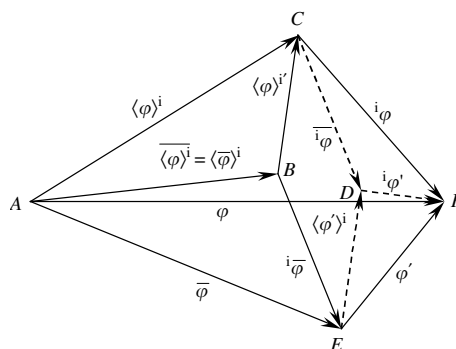


FIGURE 10.1

General three-dimensional vector diagram for a quantity φ . (Taken from Rocamora Jr., F.D. and de Lemos, M.J.S., *Int. Commun. Heat Transfer*, 27(6), 825–834. With permission.)

view is appropriate. At the same time, properties in the fluid phase are subjected to the turbulent regime, and a statistical approach becomes convenient. Examples of possible applications of such methodology can be found in engineering systems such as heat exchangers, porous combustors, nuclear reactor cores, etc. Natural systems include atmospheric boundary layer over forests and crops.

10.6 Turbulent Momentum Transport in Porous Media

10.6.1 Mean Flow Equations

The development to follow assumes single-phase flow in a saturated, rigid porous medium (ΔV_f independent of time) for which, in accordance with (10.33), time-average operation on variable φ commutes with space average. Application of the double-decomposition idea in Eq. (10.39) to the inertia term in the momentum equation leads to four different terms. Not all these terms are considered in the same analysis in the literature.

10.6.1.1 Continuity

The microscopic continuity equation for an incompressible fluid flowing in a clean (nonporous) domain was given by (10.1). Expanding \mathbf{u} in (10.1) using the double-decomposition idea of (10.39) gives,

$$\nabla \cdot \mathbf{u} = \nabla \cdot (\langle \bar{\mathbf{u}} \rangle^i + \langle \mathbf{u}' \rangle^i + i\bar{\mathbf{u}} + i\mathbf{u}') = 0 \quad (10.41)$$

Applying both volume and time-average to (10.41) gives,

$$\nabla \cdot (\varphi \langle \bar{\mathbf{u}} \rangle^i) = 0 \quad (10.42)$$

For the continuity equation, the averaging order is immaterial with regard to the final result.

10.6.1.2 Momentum — one average operator

The transient form of the microscopic momentum equation (10.2) for a fluid with constant properties is given by the Navier–Stokes equation as

$$\rho \left[\frac{\partial \mathbf{u}}{\partial t} + \nabla \cdot (\mathbf{u} \mathbf{u}) \right] = -\nabla p + \mu \nabla^2 \mathbf{u} + \rho \mathbf{g} \quad (10.43)$$

Its time average using $\mathbf{u} = \bar{\mathbf{u}} + \mathbf{u}'$ gives

$$\rho \left[\frac{\partial \bar{\mathbf{u}}}{\partial t} + \nabla \cdot (\bar{\mathbf{u}} \bar{\mathbf{u}}) \right] = -\nabla \bar{p} + \mu \nabla^2 \bar{\mathbf{u}} + \nabla \cdot (-\rho \bar{\mathbf{u}}' \mathbf{u}') + \rho \mathbf{g} \quad (10.44)$$

where the stresses, $-\rho\overline{\mathbf{u}'\mathbf{u}'}$, are the well-known Reynolds stresses. On the other hand, the volumetric average of (10.43) using the Theorem of local volumetric average (Eqs. [10.15] to [10.17]), results in

$$\rho \left[\frac{\partial}{\partial t} (\phi \langle \mathbf{u} \rangle^i) + \nabla \cdot [\phi \langle \mathbf{u} \mathbf{u} \rangle^i] \right] = -\nabla(\phi \langle p \rangle^i) + \mu \nabla^2(\phi \langle \mathbf{u} \rangle^i) + \phi \rho \mathbf{g} + \mathbf{R} \quad (10.45)$$

where

$$\mathbf{R} = \frac{\mu}{\Delta V} \int_{A_i} \mathbf{n} \cdot (\nabla \mathbf{u}) dS - \frac{1}{\Delta V} \int_{A_i} \mathbf{n} p dS \quad (10.46)$$

represents the total drag force per unit volume due to the presence of the porous matrix, being composed of both viscous drag and form (pressure) drag. Further, using spatial decomposition to write $\mathbf{u} = \langle \mathbf{u} \rangle^i + {}^i \mathbf{u}$ in the inertia term,

$$\begin{aligned} & \rho \left[\frac{\partial}{\partial t} (\phi \langle \mathbf{u} \rangle^i) + \nabla \cdot [\phi \langle \mathbf{u} \rangle^i \langle \mathbf{u} \rangle^i] \right] \\ &= -\nabla(\phi \langle p \rangle^i) + \mu \nabla^2(\phi \langle \mathbf{u} \rangle^i) - \nabla \cdot [\phi \langle {}^i \mathbf{u} {}^i \mathbf{u} \rangle^i] + \phi \rho \mathbf{g} + \mathbf{R} \end{aligned} \quad (10.47)$$

Hsu and Cheng (1990) point out that the third term on the right of (10.47), $\nabla \cdot (\phi \langle {}^i \mathbf{u} {}^i \mathbf{u} \rangle^i)$, represents the hydrodynamic dispersion due to spatial deviations. Note that Eq. (10.47) models typical porous media flow for $Re_p < 150-200$. When extending the analysis to turbulent flow, time varying quantities have to be considered.

10.6.1.3 Momentum equation — two average operators

The set of Eqs. (10.44) and (10.47) are used when treating turbulent flow in clear fluid or low Re_p porous media flow, respectively. In each one of those equations only one averaging operator was applied, either time or volume, respectively. In this work, an investigation on the use of both operators is now conducted with the objective of modeling turbulent flow in porous media.

The volume average of (10.44) for the time mean flow in a porous medium, becomes:

$$\begin{aligned} & \rho \left[\frac{\partial}{\partial t} (\phi \langle \bar{\mathbf{u}} \rangle^i) + \nabla \cdot (\phi \langle \bar{\mathbf{u}} \bar{\mathbf{u}} \rangle^i) \right] \\ &= -\nabla(\phi \langle \bar{p} \rangle^i) + \mu \nabla^2(\phi \langle \bar{\mathbf{u}} \rangle^i) + \nabla \cdot (-\rho \phi \langle \overline{\mathbf{u}'\mathbf{u}'} \rangle^i) + \phi \rho \mathbf{g} + \bar{\mathbf{R}} \end{aligned} \quad (10.48)$$

where

$$\bar{\mathbf{R}} = \frac{\mu}{\Delta V} \int_{A_i} \mathbf{n} \cdot (\nabla \bar{\mathbf{u}}) dS - \frac{1}{\Delta V} \int_{A_i} \mathbf{n} \bar{p} dS \quad (10.49)$$

is the time-averaged total drag force per unit volume (“body force”), due to solid particles, composed of both viscous and form (pressure) drags.

Likewise, we now apply the time-average operation to (10.45), to get:

$$\begin{aligned} \rho & \left[\frac{\partial}{\partial t} \overline{(\phi(\bar{\mathbf{u}} + \mathbf{u}')^i)} + \nabla \cdot \overline{(\phi((\bar{\mathbf{u}} + \mathbf{u}')(\bar{\mathbf{u}} + \mathbf{u}'))^i)} \right] \\ & = -\nabla \overline{(\phi(\bar{p} + p')^i)} + \mu \nabla^2 \overline{(\phi(\bar{\mathbf{u}} + \mathbf{u}')^i)} + \phi \rho \mathbf{g} + \bar{\mathbf{R}} \end{aligned} \quad (10.50)$$

Dropping terms containing only one fluctuating quantity results in,

$$\begin{aligned} \rho & \left[\frac{\partial}{\partial t} (\phi \overline{\langle \mathbf{u} \rangle^i}) + \nabla \cdot (\phi \overline{\langle \mathbf{u} \rangle^i \mathbf{u}}^i) \right] \\ & = -\nabla (\phi \overline{\langle \bar{p} \rangle^i}) + \mu \nabla^2 (\phi \overline{\langle \mathbf{u} \rangle^i}) + \nabla \cdot (-\rho \phi \overline{\langle \mathbf{u}' \mathbf{u}' \rangle^i}) + \phi \rho \mathbf{g} + \bar{\mathbf{R}} \end{aligned} \quad (10.51)$$

where

$$\begin{aligned} \bar{\mathbf{R}} & = \frac{\mu}{\Delta V} \int_{A_i} \mathbf{n} \cdot [\nabla \overline{(\bar{\mathbf{u}} + \mathbf{u}')}^i] dS - \frac{1}{\Delta V} \int_{A_i} \mathbf{n} \overline{(\bar{p} + p')}^i dS \\ & = \frac{\mu}{\Delta V} \int_{A_i} \mathbf{n} \cdot (\nabla \bar{\mathbf{u}})^i dS - \frac{1}{\Delta V} \int_{A_i} \mathbf{n} \bar{p}^i dS \end{aligned} \quad (10.52)$$

Comparing (10.48) and (10.51) one can see that for the momentum equation also the order of the application of both averaging operators is immaterial.

It is interesting to emphasize that both views in the literature use the same final form for the momentum equation. The term $\bar{\mathbf{R}}$ is modeled by the Darcy–Forcheimer (Dupuit) expression after either order of application of the average operators. Since both orders of integration lead to the same equation, namely, expression (10.49) or (10.52), there would be no reason to model them in a different form. Had the outcome of both integration processes been distinct, the use of a different model for each case would have been consistent. In fact, it has been pointed out by Pedras and de Lemos (2000), that the major difference between those two paths lies in the definition of a suitable turbulent kinetic energy for the flow. Accordingly, the source of controversies comes from the inertia term, as seen below.

10.6.1.4 Inertia term — space and time (double) decomposition

Applying the double-decomposition idea seen before for velocity (Eq. [10.39]), to the inertia term of (10.43) will lead to different sets of terms. In the literature, not all of them are used in the same analysis.

Starting with time decomposition and applying both average operators (see Eq. [10.48]) gives,

$$\begin{aligned}\nabla \cdot \overline{(\phi \langle \mathbf{u} \mathbf{u} \rangle^i)} &= \nabla \cdot \overline{(\phi \langle (\bar{\mathbf{u}} + \mathbf{u}')(\bar{\mathbf{u}} + \mathbf{u}') \rangle^i)} \\ &= \nabla \cdot [\phi \langle \bar{\mathbf{u}} \bar{\mathbf{u}} \rangle^i + \langle \bar{\mathbf{u}}' \bar{\mathbf{u}}' \rangle^i]\end{aligned}\quad (10.53)$$

Using spatial decomposition to write $\bar{\mathbf{u}} = \langle \bar{\mathbf{u}} \rangle^i + {}^i\bar{\mathbf{u}}$ and plugging it into (10.53) gives,

$$\begin{aligned}\nabla \cdot [\phi \langle \bar{\mathbf{u}} \bar{\mathbf{u}} \rangle^i + \langle \bar{\mathbf{u}}' \bar{\mathbf{u}}' \rangle^i] &= \nabla \cdot \left\{ \phi \left[\langle (\langle \bar{\mathbf{u}} \rangle^i + {}^i\bar{\mathbf{u}})(\langle \bar{\mathbf{u}} \rangle^i + {}^i\bar{\mathbf{u}}) \rangle^i + \langle \bar{\mathbf{u}}' \bar{\mathbf{u}}' \rangle^i \right] \right\} \\ &= \nabla \cdot \left\{ \phi \left[\langle \bar{\mathbf{u}} \rangle^i \langle \bar{\mathbf{u}} \rangle^i + \langle {}^i\bar{\mathbf{u}} {}^i\bar{\mathbf{u}} \rangle^i + \langle \bar{\mathbf{u}}' \bar{\mathbf{u}}' \rangle^i \right] \right\}\end{aligned}\quad (10.54)$$

Now, applying Eq. (10.32) to write $\mathbf{u}' = \langle \mathbf{u}' \rangle^i + {}^i\mathbf{u}'$ and substituting it into (10.54) gives,

$$\begin{aligned}\nabla \cdot \left\{ \phi \left[\langle \bar{\mathbf{u}} \rangle^i \langle \bar{\mathbf{u}} \rangle^i + \langle {}^i\bar{\mathbf{u}} {}^i\bar{\mathbf{u}} \rangle^i + \langle \bar{\mathbf{u}}' \bar{\mathbf{u}}' \rangle^i \right] \right\} \\ &= \nabla \cdot \left\{ \phi \left[\langle \bar{\mathbf{u}} \rangle^i \langle \bar{\mathbf{u}} \rangle^i + \langle {}^i\bar{\mathbf{u}} {}^i\bar{\mathbf{u}} \rangle^i + \overline{\langle (\langle \mathbf{u}' \rangle^i + {}^i\mathbf{u}')(\langle \mathbf{u}' \rangle^i + {}^i\mathbf{u}') \rangle^i} \right] \right\} \\ &= \nabla \cdot \left\{ \phi \left[\langle \bar{\mathbf{u}} \rangle^i \langle \bar{\mathbf{u}} \rangle^i + \langle {}^i\bar{\mathbf{u}} {}^i\bar{\mathbf{u}} \rangle^i + \overline{\langle (\langle \mathbf{u}' \rangle^i \langle \mathbf{u}' \rangle^i + \langle \mathbf{u}' \rangle^i {}^i\mathbf{u}' + {}^i\mathbf{u}' \langle \mathbf{u}' \rangle^i + {}^i\mathbf{u}' {}^i\mathbf{u}') \rangle^i} \right] \right\} \\ &= \nabla \cdot \left\{ \phi \left[\langle \bar{\mathbf{u}} \rangle^i \langle \bar{\mathbf{u}} \rangle^i + \langle {}^i\bar{\mathbf{u}} {}^i\bar{\mathbf{u}} \rangle^i + \overline{\langle \mathbf{u}' \rangle^i \langle \mathbf{u}' \rangle^i} + \overline{\langle \mathbf{u}' \rangle^i {}^i\mathbf{u}' \rangle^i} + \overline{\langle {}^i\mathbf{u}' \langle \mathbf{u}' \rangle^i \rangle^i} + \overline{\langle {}^i\mathbf{u}' {}^i\mathbf{u}' \rangle^i} \right] \right\}\end{aligned}\quad (10.55)$$

The fourth and fifth terms on the right of (10.55) contain only one space varying quantity and will vanish under the application of volume integration. Equation (10.55) will then be reduced to,

$$\nabla \cdot \overline{(\phi \langle \mathbf{u} \mathbf{u} \rangle^i)} = \nabla \cdot \left\{ \phi \left[\langle \bar{\mathbf{u}} \rangle^i \langle \bar{\mathbf{u}} \rangle^i + \overline{\langle \mathbf{u}' \rangle^i \langle \mathbf{u}' \rangle^i} + \langle {}^i\bar{\mathbf{u}} {}^i\bar{\mathbf{u}} \rangle^i + \langle \bar{\mathbf{u}}' \bar{\mathbf{u}}' \rangle^i \right] \right\} \quad (10.56)$$

Using the equivalence (10.33) to (10.35), Eq. (10.56) can be further rewritten as,

$$\nabla \cdot \overline{(\phi \langle \mathbf{u} \mathbf{u} \rangle^i)} = \nabla \cdot \left\{ \phi \left[\overline{\langle \mathbf{u} \rangle^i} \overline{\langle \mathbf{u} \rangle^i} + \overline{\langle \mathbf{u} \rangle^i} \overline{\langle \mathbf{u}' \rangle^i} + \overline{\langle \bar{\mathbf{u}} \rangle^i} \overline{\langle \bar{\mathbf{u}} \rangle^i} + \overline{\langle \bar{\mathbf{u}}' \rangle^i} \overline{\langle \bar{\mathbf{u}}' \rangle^i} \right] \right\} \quad (10.57)$$

with an interpretation of the terms in (10.56) given later.

Another route to follow to reach the same results is to start out with the application of the space decomposition in the inertia term, as usually done in classical mathematical treatment of porous media flow analysis. Then one has

$$\nabla \cdot \overline{(\phi \langle \mathbf{u} \mathbf{u} \rangle^i)} = \nabla \cdot \overline{(\phi \langle (\langle \mathbf{u} \rangle^i + {}^i\mathbf{u})(\langle \mathbf{u} \rangle^i + {}^i\mathbf{u}) \rangle^i)} = \nabla \cdot \overline{[\phi \langle (\langle \mathbf{u} \rangle^i \langle \mathbf{u} \rangle^i + \langle {}^i\mathbf{u} {}^i\mathbf{u} \rangle^i) \rangle^i]} \quad (10.58)$$

The time average of the right-hand side of (10.58), using Eq. (10.35) to express $\langle \mathbf{u} \rangle^i = \langle \bar{\mathbf{u}} \rangle^i + \langle \mathbf{u}' \rangle^i$, becomes,

$$\begin{aligned}\nabla \cdot \overline{[\phi(\langle \mathbf{u} \rangle^i \langle \mathbf{u} \rangle^i + \langle i \mathbf{u}^i \mathbf{u} \rangle^i)]} &= \nabla \cdot \left\{ \overline{\phi[(\langle \bar{\mathbf{u}} \rangle^i + \langle \mathbf{u}' \rangle^i)(\langle \bar{\mathbf{u}} \rangle^i + \langle \mathbf{u}' \rangle^i) + \langle i \mathbf{u}^i \mathbf{u} \rangle^i]} \right\} \\ &= \nabla \cdot \left\{ \overline{\phi[\langle \bar{\mathbf{u}} \rangle^i \langle \bar{\mathbf{u}} \rangle^i + \langle \mathbf{u}' \rangle^i \langle \mathbf{u}' \rangle^i + \langle i \mathbf{u}^i \mathbf{u} \rangle^i]} \right\} \end{aligned} \quad (10.59)$$

With the help of Eq. (10.36) one can write $i \mathbf{u} = i \bar{\mathbf{u}} + i \mathbf{u}'$ which, inserted into (10.59), gives,

$$\begin{aligned}\nabla \cdot \left\{ \overline{\phi[\langle \bar{\mathbf{u}} \rangle^i \langle \bar{\mathbf{u}} \rangle^i + \langle \mathbf{u}' \rangle^i \langle \mathbf{u}' \rangle^i + \langle i \bar{\mathbf{u}}^i \mathbf{u} \rangle^i]} \right\} \\ &= \nabla \cdot \left\{ \overline{\phi[\langle \bar{\mathbf{u}} \rangle^i \langle \bar{\mathbf{u}} \rangle^i + \langle \mathbf{u}' \rangle^i \langle \mathbf{u}' \rangle^i + \langle (i \bar{\mathbf{u}} + i \mathbf{u}') (i \bar{\mathbf{u}} + i \mathbf{u}') \rangle^i]} \right\} \\ &= \nabla \cdot \left\{ \overline{\phi[\langle \bar{\mathbf{u}} \rangle^i \langle \bar{\mathbf{u}} \rangle^i + \langle \mathbf{u}' \rangle^i \langle \mathbf{u}' \rangle^i + \langle i \bar{\mathbf{u}}^i \bar{\mathbf{u}} + i \bar{\mathbf{u}}^i \mathbf{u}' + i \mathbf{u}'^i \bar{\mathbf{u}} + i \mathbf{u}'^i \mathbf{u}' \rangle^i]} \right\} \end{aligned} \quad (10.60)$$

Application of the time-average operator to the fourth and fifth terms on the right of (10.60), containing only one fluctuating component, vanishes it. In addition, recalling that with (10.34) there is the equivalence $\langle \mathbf{u}' \rangle^i = \langle \mathbf{u} \rangle^{i'}$, with (10.33) one can write $\langle \mathbf{u} \rangle^i = \langle \bar{\mathbf{u}} \rangle^i$ and using (10.34) one has $i \bar{\mathbf{u}} = i \mathbf{u}$, then Eq. (10.60) becomes,

$$\nabla \cdot \overline{[\phi(\langle \mathbf{u} \rangle^i \langle \mathbf{u} \rangle^i + \langle i \mathbf{u}^i \mathbf{u} \rangle^i)]} = \nabla \cdot \left\{ \underbrace{\overline{\phi[\langle \bar{\mathbf{u}} \rangle^i \langle \bar{\mathbf{u}} \rangle^i]}}_{I} + \underbrace{\overline{\phi[\langle \mathbf{u}' \rangle^i \langle \mathbf{u}' \rangle^i]}}_{II} + \underbrace{\overline{\phi[i \bar{\mathbf{u}}^i \bar{\mathbf{u}}]}}_{III} + \underbrace{\overline{\phi[i \mathbf{u}'^i \mathbf{u}']}_{IV}}_{IV} \right\} \quad (10.61)$$

which is the same as (10.56).

A physical significance of all four terms on the right of (10.61) can be discussed as follows: I — convective term of macroscopic mean velocity, II — turbulent (Reynolds) stresses divided by density ρ due to the fluctuating component of the macroscopic velocity, III — dispersion associated with spatial fluctuations of microscopic time mean velocity. Note that this term is also present in laminar flow, or say, when $Re_p < 150$, and IV — turbulent dispersion in a porous medium due to both time and spatial fluctuations of the microscopic velocity.

Further, the *macroscopic Reynolds stress tensor* (MRST) is given in Pedras and de Lemos (2001a) based on Eq. (10.24) as,

$$-\rho \phi \overline{\langle \mathbf{u}' \mathbf{u}' \rangle^i} = \mu_{t_\phi} 2 \overline{\langle \bar{\mathbf{D}} \rangle^v} - \frac{2}{3} \phi \rho \langle k \rangle^i \mathbf{I} \quad (10.62)$$

where

$$\langle \bar{\mathbf{D}} \rangle^v = \frac{1}{2} \{ \nabla(\phi \langle \bar{\mathbf{u}} \rangle^i) + [\nabla(\phi \langle \bar{\mathbf{u}} \rangle^i)]^T \} \quad (10.63)$$

is the macroscopic deformation tensor, $\langle k \rangle^i$ is the intrinsic average for k and μ_{t_ϕ} is the macroscopic turbulent viscosity assumed to be (Fox and McDonald [1998])

$$\mu_{t_\phi} = \rho c_\mu \frac{\langle k \rangle^i}{\langle \varepsilon \rangle^i} \quad (10.64)$$

10.6.2 Equations for Fluctuating Velocity

The starting point of an equation for flow turbulent kinetic energy is the microscopic velocity fluctuation \mathbf{u}' . Such a relationship can be written after subtracting the equation for the mean velocity $\bar{\mathbf{u}}$ from the instantaneous momentum equation, resulting in (Hinze, 1959; Warsi, 1998):

$$\rho \left\{ \frac{\partial \mathbf{u}'}{\partial t} + \nabla \cdot [\bar{\mathbf{u}} \mathbf{u}' + \mathbf{u}' \bar{\mathbf{u}} + \mathbf{u}' \mathbf{u}' - \overline{\mathbf{u}' \mathbf{u}'}] \right\} = -\nabla p' + \mu \nabla^2 \mathbf{u}' \quad (10.65)$$

Now, the volumetric average of (10.65) using the Theorem of local volumetric average will give,

$$\begin{aligned} & \rho \frac{\partial}{\partial t} (\phi \langle \mathbf{u}' \rangle^i) + \rho \nabla \cdot \left\{ \phi [\langle \bar{\mathbf{u}} \mathbf{u}' \rangle^i + \langle \mathbf{u}' \bar{\mathbf{u}} \rangle^i + \langle \mathbf{u}' \mathbf{u}' \rangle^i - \overline{\langle \mathbf{u}' \mathbf{u}' \rangle^i}] \right\} \\ &= -\nabla(\phi \langle p' \rangle^i) + \mu \nabla^2(\phi \langle \mathbf{u}' \rangle^i) + \mathbf{R}' \end{aligned} \quad (10.66)$$

where,

$$\mathbf{R}' = \frac{\mu}{\Delta V} \int_{A_i} \mathbf{n} \cdot (\nabla \mathbf{u}') dS - \frac{1}{\Delta V} \int_{A_i} \mathbf{n} p' dS \quad (10.67)$$

is the fluctuating part of the total drag due to the porous structure.

Further expanding the divergent operators in Eq. (10.66) by means of Eqs. (10.29) and (10.31), one ends up with an equation for $\langle \mathbf{u}' \rangle^i$ as,

$$\begin{aligned} & \rho \frac{\partial}{\partial t} (\phi \langle \mathbf{u}' \rangle^i) + \rho \nabla \cdot \left\{ \phi [\langle \bar{\mathbf{u}} \rangle^i \langle \mathbf{u}' \rangle^i + \langle \mathbf{u}' \rangle^i \langle \bar{\mathbf{u}} \rangle^i + \langle \mathbf{u}' \rangle^i \langle \mathbf{u}' \rangle^i \right. \\ & \quad \left. + \langle^i \bar{\mathbf{u}}^i \mathbf{u}' \rangle^i + \langle^i \mathbf{u}'^i \bar{\mathbf{u}} \rangle^i + \langle^i \mathbf{u}'^i \mathbf{u}' \rangle^i - \overline{\langle \mathbf{u}' \rangle^i \langle \mathbf{u}' \rangle^i} - \langle \overline{\langle \mathbf{u}'^i \mathbf{u}' \rangle^i} \rangle^i] \right\} \\ &= -\nabla(\phi \langle p' \rangle^i) + \mu \nabla^2(\phi \langle \mathbf{u}' \rangle^i) + \mathbf{R}' \end{aligned} \quad (10.68)$$

Another route to follow in order to obtain the same Eq. (10.68) is to start out with the macroscopic instantaneous momentum equation for an incompressible fluid given by Hsu and Cheng (1990), as

$$\rho \left[\frac{\partial}{\partial t} (\phi \langle \mathbf{u} \rangle^i) + \nabla \cdot (\phi \langle \mathbf{u} \mathbf{u} \rangle^i) \right] = -\nabla(\phi \langle p \rangle^i) + \mu \nabla^2(\phi \langle \mathbf{u} \rangle^i) + \phi \rho \mathbf{g} + \mathbf{R} \quad (10.69)$$

or

$$\begin{aligned} \rho \left\{ \frac{\partial}{\partial t} (\phi \langle \mathbf{u} \rangle^i + \nabla \cdot (\phi \langle \mathbf{u} \rangle^i \langle \mathbf{u} \rangle^i)) \right\} \\ = -\nabla[\phi(\langle p \rangle^i)] + \mu \nabla^2(\phi \langle \mathbf{u} \rangle^i) + \phi \rho \mathbf{g} - \nabla \cdot (\phi \langle \mathbf{u}^i \mathbf{u}^i \rangle^i) + \mathbf{R} \end{aligned} \quad (10.70)$$

where again \mathbf{R} is given by (10.46) and the term $\langle \mathbf{u}^i \mathbf{u}^i \rangle^i$ is known as *dispersion*. The fluctuating component of (10.46) was given earlier by Eq. (10.67). The mathematical meaning of dispersion can be seen as a correlation between spatial deviations of velocity components.

Making use of the double-decomposition concept given by Eq. (10.38), expression (10.70) can be expanded as,

$$\begin{aligned} \rho \left\{ \frac{\partial}{\partial t} [\phi(\langle \bar{\mathbf{u}} \rangle^i + \langle \mathbf{u}' \rangle^i)] + \nabla \cdot \left[\phi \left\langle [\langle \bar{\mathbf{u}} \rangle^i + \langle \mathbf{u}' \rangle^i + \langle \bar{\mathbf{u}} \rangle^i \mathbf{u}' + \mathbf{u}' \bar{\mathbf{u}}]^i [\langle \bar{\mathbf{u}} \rangle^i + \langle \mathbf{u}' \rangle^i + \langle \bar{\mathbf{u}} \rangle^i \mathbf{u}' + \mathbf{u}' \bar{\mathbf{u}}]^i \right\rangle^i \right] \right\} \\ = -\nabla[\phi(\langle \bar{p} \rangle^i + \langle p' \rangle^i)] + \mu \nabla^2[\phi(\langle \bar{\mathbf{u}} \rangle^i + \langle \mathbf{u}' \rangle^i)] + \phi \rho \mathbf{g} + \mathbf{R} \end{aligned} \quad (10.71)$$

which results after some manipulation in,

$$\begin{aligned} \rho \left\{ \frac{\partial}{\partial t} [\phi(\langle \bar{\mathbf{u}} \rangle^i + \langle \mathbf{u}' \rangle^i)] + \nabla \cdot \left[\phi \left\langle [\langle \bar{\mathbf{u}} \rangle^i \langle \bar{\mathbf{u}} \rangle^i + \langle \bar{\mathbf{u}} \rangle^i \langle \mathbf{u}' \rangle^i + \langle \mathbf{u}' \rangle^i \langle \bar{\mathbf{u}} \rangle^i + \langle \mathbf{u}' \rangle^i \langle \mathbf{u}' \rangle^i] \right\rangle^i \right. \right. \\ \left. \left. + \langle \bar{\mathbf{u}}^i \bar{\mathbf{u}}^i \rangle^i + \langle \bar{\mathbf{u}}^i \mathbf{u}'^i \rangle^i + \langle \mathbf{u}'^i \bar{\mathbf{u}}^i \rangle^i + \langle \mathbf{u}'^i \mathbf{u}'^i \rangle^i \right] \right\} \\ = -\nabla[\phi(\langle \bar{p} \rangle^i + \langle p' \rangle^i)] + \mu \nabla^2[\phi(\langle \bar{\mathbf{u}} \rangle^i + \langle \mathbf{u}' \rangle^i)] + \phi \rho \mathbf{g} + \mathbf{R} \end{aligned} \quad (10.72)$$

Taking the time average of (10.72) results in

$$\begin{aligned} \rho \left\{ \frac{\partial}{\partial t} (\phi \langle \bar{\mathbf{u}} \rangle^i) + \nabla \cdot \left\{ \phi \left[\langle \bar{\mathbf{u}} \rangle^i \langle \bar{\mathbf{u}} \rangle^i + \overline{\langle \mathbf{u}' \rangle^i \langle \mathbf{u}' \rangle^i} + \langle \bar{\mathbf{u}}^i \bar{\mathbf{u}}^i \rangle^i + \overline{\langle \mathbf{u}'^i \bar{\mathbf{u}}^i \rangle^i} \right] \right\} \right\} \\ = -\nabla(\phi \langle \bar{p} \rangle^i) + \mu \nabla^2(\phi \langle \bar{\mathbf{u}} \rangle^i) + \phi \rho \mathbf{g} + \overline{\mathbf{R}} \end{aligned} \quad (10.73)$$

where

$$\bar{\mathbf{R}} = \frac{\mu}{\Delta V} \int_{A_i} \mathbf{n} \cdot (\nabla \bar{\mathbf{u}}) dS - \frac{1}{\Delta V} \int_{A_i} \mathbf{n} \bar{p} dS \quad (10.74)$$

represents the time-averaged value of the instantaneous total drag given by (10.46).

An equation for the fluctuating macroscopic velocity is then obtained by subtracting Eq. (10.73) from (10.72) resulting in,

$$\begin{aligned} \rho \frac{\partial}{\partial t} (\phi \langle \mathbf{u}' \rangle^i) + \rho \nabla \cdot \left\{ \phi [\langle \bar{\mathbf{u}} \rangle^i \langle \mathbf{u}' \rangle^i + \langle \mathbf{u}' \rangle^i \langle \bar{\mathbf{u}} \rangle^i + \langle \mathbf{u}' \rangle^i \langle \mathbf{u}' \rangle^i \right. \\ \left. + \langle \bar{\mathbf{u}}^i \mathbf{u}' \rangle^i + \langle \mathbf{u}'^i \bar{\mathbf{u}} \rangle^i + \langle \mathbf{u}'^i \mathbf{u}' \rangle^i - \overline{\langle \mathbf{u}' \rangle^i \langle \mathbf{u}' \rangle^i} - \overline{\langle \mathbf{u}'^i \mathbf{u}' \rangle^i}] \right\} \\ = -\nabla(\phi \langle p' \rangle^i) + \mu \nabla^2(\phi \langle \mathbf{u}' \rangle^i) + \mathbf{R}' \end{aligned} \quad (10.75)$$

Here \mathbf{R}' is also given by (10.67) such that Eq. (10.75) is the same as Eq. (10.68).

10.6.3 Turbulent Kinetic Energy

As mentioned, the determination of the flow macroscopic turbulent kinetic energy follows two different paths in the literature. In the models of Lee and Howell (1987), Wang and Takle (1995), Antohe and Lage (1997), and Getachewa et al. (2000), their turbulence kinetic energy was based on $k_m = \langle \mathbf{u}'^i \cdot \mathbf{u}'^i \rangle / 2$. They started with a simplified form of Eq. (10.68) neglecting the 5th, 6th, 7th, and 9th terms (dispersions). Then they took the scalar product of it by $\langle \mathbf{u}' \rangle^i$ and applied the time-average operator. On the other hand, if one starts out with Eq. (10.65) and proceeds with time-averaging first, one ends up, after volume-averaging, with $\langle k \rangle^i = \langle \mathbf{u}' \cdot \mathbf{u}' \rangle^i / 2$. This was the path followed by Masuoka and Takatsu (1996), Kuwahara et al. (1998), Kuwahara and Nakayama (1998), Takatsu and Masuoka (1998), and Nakayama and Kuwahara (1999).

The objective of this section is to derive both transport equations for k_m and $\langle k \rangle^i$ in order to compare similar terms.

The equation for $k_m = \langle \mathbf{u}'^i \cdot \mathbf{u}'^i \rangle / 2$. From the instantaneous microscopic continuity equation for a constant property fluid one has,

$$\nabla \cdot (\phi \langle \mathbf{u} \rangle^i) = 0 \Rightarrow \nabla \cdot [\phi (\langle \bar{\mathbf{u}} \rangle^i + \langle \mathbf{u}' \rangle^i)] = 0 \quad (10.76)$$

with time average,

$$\nabla \cdot (\phi \langle \bar{\mathbf{u}} \rangle^i) = 0 \quad (10.77)$$

From (10.76) and (10.77) one verifies that,

$$\nabla \cdot (\phi \langle \mathbf{u}' \rangle^i) = 0 \quad (10.78)$$

Taking the scalar product of (10.66) by $\langle \mathbf{u}' \rangle^i$, making use of Eqs. (10.76) to (10.78) and time-averaging it, an equation for k_m will have for each of its terms (note that ϕ is here considered as independent of time):

$$\rho \overline{\langle \mathbf{u}' \rangle^i \cdot \frac{\partial}{\partial t} (\phi \langle \mathbf{u}' \rangle^i)} = \rho \frac{\partial (\phi k_m)}{\partial t} \quad (10.79)$$

$$\begin{aligned} \rho \overline{\langle \mathbf{u}' \rangle^i \cdot \{ \nabla \cdot (\phi \langle \bar{\mathbf{u}} \mathbf{u}' \rangle^i) \}} &= \rho \overline{\langle \mathbf{u}' \rangle^i \cdot \{ \nabla \cdot [\phi \langle \bar{\mathbf{u}} \rangle^i \langle \mathbf{u}' \rangle^i + \phi \langle^i \bar{\mathbf{u}}^i \mathbf{u}' \rangle^i] \}} \\ &= \rho \nabla \cdot [\phi \langle \bar{\mathbf{u}} \rangle^i k_m] + \rho \overline{\langle \mathbf{u}' \rangle^i \cdot \{ \nabla \cdot [\phi \langle^i \bar{\mathbf{u}}^i \mathbf{u}' \rangle^i] \}} \end{aligned} \quad (10.80)$$

$$\begin{aligned} \rho \overline{\langle \mathbf{u}' \rangle^i \cdot \{ \nabla \cdot (\phi \langle \mathbf{u}' \bar{\mathbf{u}} \rangle^i) \}} &= \rho \overline{\langle \mathbf{u}' \rangle^i \cdot \{ \nabla \cdot [\phi \langle \mathbf{u}' \rangle^i \langle \bar{\mathbf{u}} \rangle^i + \phi \langle^i \mathbf{u}'^i \bar{\mathbf{u}} \rangle^i] \}} \\ &= \rho \phi \overline{\langle \mathbf{u}' \rangle^i \langle \mathbf{u}' \rangle^i : \nabla \cdot \langle \bar{\mathbf{u}} \rangle^i} + \rho \overline{\langle \mathbf{u}' \rangle^i \cdot \{ \nabla \cdot [\phi \langle^i \mathbf{u}'^i \bar{\mathbf{u}} \rangle^i] \}} \end{aligned} \quad (10.81)$$

$$\begin{aligned} \rho \overline{\langle \mathbf{u}' \rangle^i \cdot \{ \nabla \cdot (\phi \langle \mathbf{u}' \mathbf{u}' \rangle^i) \}} &= \rho \overline{\langle \mathbf{u}' \rangle^i \cdot \{ \nabla \cdot [\phi \langle \mathbf{u}' \rangle^i \langle \mathbf{u}' \rangle^i + \phi \langle^i \mathbf{u}'^i \mathbf{u}' \rangle^i] \}} \\ &= \rho \nabla \cdot \left[\phi \overline{\langle \mathbf{u}' \rangle^i \langle \mathbf{u}' \rangle^i} \frac{\langle \mathbf{u}' \rangle^i \cdot \langle \mathbf{u}' \rangle^i}{2} \right] + \rho \overline{\langle \mathbf{u}' \rangle^i \cdot \{ \nabla \cdot [\phi \langle^i \mathbf{u}'^i \mathbf{u}' \rangle^i] \}} \end{aligned} \quad (10.82)$$

$$\rho \overline{\langle \mathbf{u}' \rangle^i \cdot \{ \nabla \cdot (-\phi \overline{\langle \mathbf{u}' \mathbf{u}' \rangle^i}) \}} = 0 \quad (10.83)$$

$$-\overline{\langle \mathbf{u}' \rangle^i \cdot \nabla (\phi \langle p' \rangle^i)} = -\nabla \cdot \overline{[\phi \langle \mathbf{u}' \rangle^i \langle p' \rangle^i]} \quad (10.84)$$

$$\mu \overline{\langle \mathbf{u}' \rangle^i \cdot \nabla^2 (\phi \langle \mathbf{u}' \rangle^i)} = \mu \nabla^2 (\phi k_m) - \rho \phi \varepsilon_m \quad (10.85)$$

$$\overline{\langle \mathbf{u}' \rangle^i \cdot \mathbf{R}'} \equiv 0 \quad (10.86)$$

where $\varepsilon_m = \nu \overline{\nabla \langle \mathbf{u}' \rangle^i : (\nabla \langle \mathbf{u}' \rangle^i)^T}$. In handling (10.84) the porosity ϕ was assumed to be constant only for simplifying the manipulation to be shown next. This procedure, however, does not represent a limitation in deriving a general form of transport equation for k_m since term (10.84) will require further modeling.

Another important point is the treatment given to the scalar product shown in (10.86). Here, a different view from the work in Lee and Howell (1987), Wang and Takle (1995), Antohe and Lage (1997), and Getachew et al. (2000), is considered. The fluctuating drag form \mathbf{R}' acts through the solid–fluid interfacial area and, as such, on fluid particles at rest. The fluctuating mechanical energy represented by the operation in Eq. (10.86) is not associated with any fluid particle movement and, as a result, is here considered to be of null value. This point shall be further discussed later in this chapter.

A final equation for k_m gives,

$$\begin{aligned} \rho \frac{\partial(\phi k_m)}{\partial t} + \rho \nabla \cdot [\phi \langle \bar{\mathbf{u}} \rangle^i k_m] &= -\rho \nabla \cdot \left\{ \overline{\phi \langle \mathbf{u}' \rangle^i \left[\frac{\langle p' \rangle^i}{\rho} + \frac{\langle \mathbf{u}' \rangle^i \cdot \langle \mathbf{u}' \rangle^i}{2} \right]} \right\} \\ &\quad + \mu \nabla^2 (\phi k_m) - \rho \phi \overline{\langle \mathbf{u}' \rangle^i \langle \mathbf{u}' \rangle^i} : \nabla \langle \bar{\mathbf{u}} \rangle^i - \rho \phi \varepsilon_m - D_m \end{aligned} \quad (10.87)$$

where

$$D_m = \rho \overline{\langle \mathbf{u}' \rangle^i \cdot \{ \nabla \cdot [\phi (\langle \bar{\mathbf{u}}^i \mathbf{u}' \rangle^i + \langle \bar{\mathbf{u}}^i \mathbf{u}' \rangle^i + \langle \mathbf{u}'^i \mathbf{u}' \rangle^i)] \}} \quad (10.88)$$

represents the dispersion of k_m given by the last terms on the right of Eqs. (10.80), (10.81), and (10.82), respectively. It is interesting to point out that this term can be both negative and positive.

The first term on the right of (10.87) represents the turbulent diffusion of k_m and is normally modeled via a diffusion-like expression resulting for the transport equation for k_m (Antohe and Lage, 1997; Getachewa et al., 2000),

$$\rho \frac{\partial(\phi k_m)}{\partial t} + \rho \nabla \cdot [\phi \langle \bar{\mathbf{u}} \rangle^i k_m] = \nabla \cdot \left[\mu + \frac{\mu_{t_m}}{\sigma_{k_m}} \nabla (\phi k_m) \right] + P_m - \rho \phi \varepsilon_m - D_m \quad (10.89)$$

where

$$P_m = -\rho \phi \overline{\langle \mathbf{u}' \rangle^i \langle \mathbf{u}' \rangle^i} : \nabla \langle \bar{\mathbf{u}} \rangle^i \quad (10.90)$$

is the production rate of k_m due to the gradients of the macroscopic time-mean velocity $\langle \bar{\mathbf{u}} \rangle^i$.

Lee and Howell (1987), Wang and Takle (1995), Antohe and Lage (1997), and Getachewa et al. (2000), made use of the above equation for k_m considering for \mathbf{R}' (10.67) the Darcy–Forchheimer extended model with macroscopic time-fluctuation velocities $\langle \mathbf{u}' \rangle^i$. They have also neglected all dispersion terms that were here grouped into D_m (10.88). Note also that the order of application of both volume- and time-average operators in this case cannot be changed. The quantity k_m is defined by applying first the volume operator to the fluctuating velocity field.

10.6.3.1 Equation for $\langle k \rangle^i = \langle \overline{\mathbf{u}' \cdot \mathbf{u}'} \rangle^i / 2$

The other procedure for composing the flow turbulent kinetic energy is to take the scalar product of (10.65) by the microscopic fluctuating velocity \mathbf{u}' . Then apply both time and volume operators for obtaining an equation for $\langle k \rangle^i = \langle \overline{\mathbf{u}' \cdot \mathbf{u}'} \rangle^i / 2$. It is worth noting that in this case the order of application

of both operations is immaterial since no additional mathematical operation (the scalar product) is conducted in between the averaging processes. Therefore, this is the same as applying the volume operator to an equation for the microscopic k .

The volumetric average of a transport equation for k has been carried out in detail by de Lemos and Pedras (2000a), and Pedras and de Lemos (2001a), and for that only the final resulting equation is presented here. It reads,

$$\rho \left[\frac{\partial}{\partial t} (\phi \langle k \rangle^i) + \nabla \cdot (\bar{\mathbf{u}}_D \langle k \rangle^i) \right] = \nabla \cdot \left[\left(\mu + \frac{\mu_{t\phi}}{\sigma_k} \right) \nabla (\phi \langle k \rangle^i) \right] + P_i + G_i - \rho \phi \langle \varepsilon \rangle^i \quad (10.91)$$

where

$$P_i = -\rho \langle \bar{\mathbf{u}}' \bar{\mathbf{u}}' \rangle^i : \nabla \bar{\mathbf{u}}_D \quad (10.92)$$

$$G_i = c_k \rho \phi \frac{\langle k \rangle^i |\bar{\mathbf{u}}_D|}{\sqrt{K}} \quad (10.93)$$

are the production rate of $\langle k \rangle^i$ due to mean gradients of the seepage velocity and the generation rate of intrinsic k due the presence of the porous matrix. As mentioned, Eq. (10.91) has been proposed by Pedras and de Lemos (2001a), where more details on its derivation can be found. Nevertheless, for the sake of completeness, a few steps of such derivation are reproduced here. Application of the volume-average theorem to the transport equation for the turbulence kinetic energy k gives:

$$\begin{aligned} \rho \left[\frac{\partial}{\partial t} (\phi \langle k \rangle^i) + \nabla \cdot (\phi \langle \bar{\mathbf{u}} k \rangle^i) \right] &= -\rho \nabla \cdot \left\{ \phi \sqrt{\mathbf{u}' \left(\frac{p'}{\rho} + k \right)} \right\}^i + \mu \nabla^2 (\phi \langle k \rangle^i) \\ &\quad - \rho \phi \langle \bar{\mathbf{u}}' \bar{\mathbf{u}}' : \nabla \bar{\mathbf{u}} \rangle^i - \rho \phi \langle \varepsilon \rangle^i \end{aligned} \quad (10.94)$$

where the divergent on the right of (10.94) can be expanded as,

$$\nabla \cdot (\phi \langle \bar{\mathbf{u}} k \rangle^i) = \nabla \cdot [\phi (\langle \bar{\mathbf{u}} \rangle^i \langle k \rangle^i + \langle \bar{\mathbf{u}}^i k \rangle^i)] \quad (10.95)$$

The first term on the right of (10.95) is the convection of $\langle k \rangle^i$ due to the macroscopic velocity whereas the second one is the convective transport due to spatial deviations of both k and \mathbf{u} . Likewise, the production term on the right of (10.94) can be expanded as,

$$-\rho \phi \langle \bar{\mathbf{u}}' \bar{\mathbf{u}}' : \nabla \bar{\mathbf{u}} \rangle^i = -\rho \phi [\langle \bar{\mathbf{u}}' \bar{\mathbf{u}}' \rangle^i : \langle \nabla \bar{\mathbf{u}} \rangle^i + \langle \bar{\mathbf{u}}^i \bar{\mathbf{u}}' \rangle^i : \langle \nabla \bar{\mathbf{u}} \rangle^i] \quad (10.96)$$

Similarly, the first term on the right of (10.96) is the production of $\langle k \rangle^i$ due to the mean macroscopic flow and the second one is the $\langle k \rangle^i$ production associated with spatial deviations of flow quantities k and \mathbf{u} .

The extra terms appearing in Eqs. (10.95) and (10.96), respectively, represent extra transport/production of $\langle k \rangle^i$ due to the presence of solid material inside the integration volume. They should be null for the limiting case of clear fluid flow, or say, when $\phi \rightarrow 1 \Rightarrow K \rightarrow \infty$. Also, they should be proportional to the macroscopic velocity and to $\langle k \rangle^i$ itself.

In Pedras and de Lemos (2001a), a proposal for those two extra transport/production rates of $\langle k \rangle^i$ was made as:

$$\nabla \cdot (\phi \langle i \bar{\mathbf{u}}^i k^i \rangle) - \rho \phi \langle i \overline{(\mathbf{u}' \mathbf{u}') :^i} \rangle = G_k = c_k \rho \phi \frac{\langle k \rangle^i |\bar{\mathbf{u}}_D|}{\sqrt{K}} \quad (10.97)$$

where c_k is a constant, which was numerically determined by fine flow computations considering the medium to be formed by circular rods (Pedras and de Lemos, 2001b), as well as longitudinal (Pedras and de Lemos, 2001c) and transversal rods (Pedras and de Lemos, 2003). In spite of the variation in the medium morphology and the use of a wide range of porosity and the Reynolds number, a value of 0.28 was found to be suitable for most calculations.

10.6.3.2 Comparison of macroscopic transport equations

A comparison between terms in the transport equation for k_m and $\langle k \rangle^i$ can now be conducted. Pedras and de Lemos (2000), have already showed the connection between these two quantities as being,

$$\langle k \rangle^i = \frac{\langle \overline{\mathbf{u}' \cdot \mathbf{u}'}^i \rangle}{2} = \frac{\langle \overline{(\mathbf{u}')^i \cdot (\mathbf{u}')^i} \rangle}{2} + \frac{\langle \overline{i \mathbf{u}' \cdot i \mathbf{u}'}^i \rangle}{2} = k_m + \frac{\langle \overline{i \mathbf{u}' \cdot i \mathbf{u}'}^i \rangle}{2} \quad (10.98)$$

Expanding the correlation forming the production term P_i by means of Eq. (10.14), a connection between the two generation rates can also be written as,

$$\begin{aligned} P_i &= -\rho \langle \overline{\mathbf{u}' \mathbf{u}'}^i : \nabla \bar{\mathbf{u}}_D \rangle = -\rho \left(\langle \overline{(\mathbf{u}')^i (\mathbf{u}')^i} : \nabla \bar{\mathbf{u}}_D \rangle + \langle \overline{i \mathbf{u}' \cdot i \mathbf{u}'}^i : \nabla \bar{\mathbf{u}}_D \rangle \right) \\ &= P_m - \rho \langle \overline{i \mathbf{u}' \cdot i \mathbf{u}'}^i : \nabla \bar{\mathbf{u}}_D \rangle \end{aligned} \quad (10.99)$$

One can note that all production rate of k_m due to the mean flow constitutes only part of the general production rate responsible for maintaining the overall level of $\langle k \rangle^i$.

The dissipation rates also carry a correspondence if one expands

$$\begin{aligned}\langle \varepsilon \rangle^i &= \nu \overline{\langle \nabla \mathbf{u}' : (\nabla \mathbf{u}')^T \rangle^i} \\ &= \nu \overline{\langle \nabla \mathbf{u}' \rangle^i : [\langle \nabla \mathbf{u}' \rangle^i]^T} + \nu \overline{i' \langle \nabla \mathbf{u}' \rangle : i \langle \nabla \mathbf{u}' \rangle^T}^i \\ &= \frac{\nu}{\phi^2} \overline{\nabla(\phi \langle \mathbf{u}' \rangle^i) : [\nabla(\phi \langle \mathbf{u}' \rangle^i)]^T} + \nu \overline{i' \langle \nabla \mathbf{u}' \rangle : i \langle \nabla \mathbf{u}' \rangle^T}^i\end{aligned}\quad (10.100)$$

Considering further constant porosity,

$$\langle \varepsilon \rangle^i = \varepsilon_m + \nu \overline{i' \langle \nabla \mathbf{u}' \rangle : i \langle \nabla \mathbf{u}' \rangle^T}^i \quad (10.101)$$

Equation (10.101) indicates that an additional dissipation rate is necessary to fully account for the energy decay process inside the REV.

10.7 Turbulent Heat Transport

10.7.1 Governing Equations

10.7.1.1 Time average followed by volume average

In order to apply the time-average operator to Eqs. (10.9) and (10.10), one considers,

$$T = \bar{T} + T' \quad (10.102)$$

$$\mathbf{u} = \bar{\mathbf{u}} + \mathbf{u}' \quad (10.103)$$

Substituting (10.102) and (10.103) into (10.9) and (10.10), respectively, one has:

$$(\rho c_p)_f \nabla \cdot (\bar{\mathbf{u}} \bar{T}_f + \bar{\mathbf{u}}' T'_f + \mathbf{u}' \bar{T}_f + \mathbf{u}' T'_f) = \nabla \cdot (k_f \nabla (\bar{T}_f + T'_f)) \quad (10.104)$$

$$0 = \nabla \cdot (k_s \nabla (\bar{T}_s + T'_s)) \quad (10.105)$$

Applying time average to (10.104) and (10.105), one obtains:

$$(\rho c_p)_f \nabla \cdot (\bar{\mathbf{u}} \bar{T}_f + \bar{\mathbf{u}}' T'_f) = \nabla \cdot (k_f \nabla \bar{T}_f) \quad (10.106)$$

$$0 = \nabla \cdot (k_s \nabla \bar{T}_s) \quad (10.107)$$

The second term on the left of (10.106) is known as *turbulent heat flux*. It requires a model for closure of the mathematical problem. Also, in order to apply the volume average to (10.106) and (10.107), one must first define the

spatial deviations with respect to the time averages, given by:

$$\bar{T} = \langle \bar{T} \rangle^i + {}^i\bar{T} \quad (10.108)$$

$$\bar{\mathbf{u}} = \langle \bar{\mathbf{u}} \rangle^i + {}^i\bar{\mathbf{u}} \quad (10.109)$$

Now substituting (10.108) and (10.109) into (10.104) and (10.105), respectively, and performing the volume-average operation, one has:

$$\begin{aligned} & (\rho c_p)_f \nabla \cdot \{ \phi (\langle \bar{\mathbf{u}} \rangle^i \langle \bar{T}_f \rangle^i + \langle {}^i\bar{\mathbf{u}} \rangle^i \langle \bar{T}_f \rangle^i + \langle \bar{\mathbf{u}}' \bar{T}_f \rangle^i) \} \\ &= \nabla \cdot [k_f \nabla (\phi \langle \bar{T}_f \rangle^i)] + \nabla \cdot \left[\frac{1}{\Delta V} \int_{A_i} \mathbf{n} k_f \bar{T}_f dS \right] + \frac{1}{\Delta V} \int_{A_i} \mathbf{n} \cdot k_f \nabla \bar{T}_f dS \end{aligned} \quad (10.110)$$

$$\nabla \cdot \left\{ k_s \nabla [(1 - \phi) \langle \bar{T}_s \rangle^i] \right\} - \nabla \cdot \left[\frac{1}{\Delta V} \int_{A_i} \mathbf{n} k_s \bar{T}_s dS \right] - \frac{1}{\Delta V} \int_{A_i} \mathbf{n} \cdot k_s \nabla \bar{T}_s dS = 0 \quad (10.111)$$

Equations (10.110) and (10.111) are the macroscopic energy equations for the fluid and the porous matrix (solid) taking first the *time average* followed by the *volume average* operator.

10.7.1.2 Volume average followed by time average

To apply the volume average to (10.9) and (10.10) one has:

$$T = \langle T \rangle^i + {}^iT \quad (10.112)$$

$$\mathbf{u} = \langle \mathbf{u} \rangle^i + {}^i\mathbf{u} \quad (10.113)$$

in addition,

$$\begin{cases} \langle T \rangle^v = \gamma \langle T \rangle^i \\ \langle \mathbf{u} \rangle^v = \gamma \langle \mathbf{u} \rangle^i \end{cases} \quad \text{where } \gamma = \begin{cases} \phi & \text{for the fluid} \\ (1 - \phi) & \text{for the solid} \end{cases} \quad (10.114)$$

Substituting (10.112) and (10.113) into (10.9) and (10.10), one obtains:

$$(\rho c_p)_f \nabla \cdot (\langle \mathbf{u} \rangle^i \langle T_f \rangle^i + \langle \mathbf{u} \rangle^i {}^iT_f + {}^i\mathbf{u} \langle T_f \rangle^i + {}^i\mathbf{u} {}^iT_f) = \nabla \cdot [k_f \nabla (\langle T_f \rangle^i + {}^iT_f)] \quad (10.115)$$

$$0 = \nabla \cdot [k_s \nabla (\langle T_s \rangle^i + {}^iT_s)] \quad (10.116)$$

Taking the volume average of (10.115) and (10.116), one has:

$$\begin{aligned} (\rho c_p)_f \nabla \cdot \left[\phi (\langle \mathbf{u} \rangle^i \langle T_f \rangle^i + \langle \mathbf{u}^i T_f \rangle^i) \right] \\ = \nabla \cdot \left[k_f \nabla (\phi \langle T_f \rangle^i) \right] + \nabla \cdot \left[\frac{1}{\Delta V} \int_{A_i} \mathbf{n} k_f T_f dS \right] + \frac{1}{\Delta V} \int_{A_i} \mathbf{n} \cdot k_f \nabla T_f dS \end{aligned} \quad (10.117)$$

$$\nabla \cdot \left\{ k_s \nabla [(1 - \phi) \langle T_s \rangle^i] \right\} - \nabla \cdot \left[\frac{1}{\Delta V} \int_{A_i} \mathbf{n} k_s T_s dS \right] - \frac{1}{\Delta V} \int_{A_i} \mathbf{n} \cdot k_s \nabla T_s dS = 0 \quad (10.118)$$

The second term on the left of Eq. (10.117) appears in classical analysis of convection in porous media (e.g., Hsu and Cheng, 1990) and is known as *thermal dispersion*. In order to apply the time average to (10.117) and (10.118), one defines the intrinsic volume average as:

$$\langle T \rangle^i = \overline{\langle T \rangle^i} + \langle T \rangle^{i'} \quad (10.119)$$

$$\langle \mathbf{u} \rangle^i = \overline{\langle \mathbf{u} \rangle^i} + \langle \mathbf{u} \rangle^{i'} \quad (10.120)$$

Substituting (10.119) and (10.120) in (10.117) and (10.118) and taking the time average, we obtain:

$$\begin{aligned} (\rho c_p)_f \nabla \cdot \left[\phi \left(\overline{\langle \mathbf{u} \rangle^i} \overline{\langle T_f \rangle^i} + \overline{\langle \mathbf{u} \rangle^{i'} \langle T_f \rangle^{i'}} + \overline{\langle \mathbf{u}^i T_f \rangle^i} \right) \right] \\ = \nabla \cdot \left[k_f \nabla (\phi \overline{\langle T_f \rangle^i}) \right] + \nabla \cdot \left[\frac{1}{\Delta V} \int_{A_i} \mathbf{n} k_f \overline{T_f} dS \right] + \frac{1}{\Delta V} \int_{A_i} \mathbf{n} \cdot k_f \nabla \overline{T_f} dS \end{aligned} \quad (10.121)$$

$$\nabla \cdot \left\{ k_s \nabla [(1 - \phi) \overline{\langle T_s \rangle^i}] \right\} - \nabla \cdot \left[\frac{1}{\Delta V} \int_{A_i} \mathbf{n} k_s \overline{T_s} dS \right] - \frac{1}{\Delta V} \int_{A_i} \mathbf{n} \cdot k_s \nabla \overline{T_s} dS = 0 \quad (10.122)$$

Equations (10.121) and (10.122) are the macroscopic energy equations for the fluid and the porous matrix (solid) taking first the volume average followed by the time average.

It is interesting to observe that (10.110) and (10.111), obtained through the first procedure (time–volume average) are similar to (10.121) and (10.122), respectively, obtained through the second method (volume–time average). To show their equivalence is the purpose of next section.

10.7.2 Turbulent Thermal Dispersion

Now using (10.34) to (10.37), the third terms on the left-hand side of (10.110) and (10.121) can be expanded as:

$$\langle \overline{\mathbf{u}' T'_f} \rangle^i = \langle (\langle \mathbf{u}' \rangle^i + i\mathbf{u}') (\langle T_f^i \rangle^i + iT') \rangle^i = \langle \overline{\mathbf{u}'} \rangle^i \langle \overline{T'_f} \rangle^i + \langle \overline{i\mathbf{u}'^i T'_f} \rangle^i \quad (10.123)$$

$$\langle \overline{i\mathbf{u}'^i T_f} \rangle^i = \langle (i\overline{\mathbf{u}} + i\mathbf{u}') (i\overline{T_f} + iT') \rangle^i = \langle \overline{i\mathbf{u}^i} \rangle^i \langle \overline{T_f} \rangle^i + \langle \overline{i\mathbf{u}'^i T_f} \rangle^i \quad (10.124)$$

Substituting (10.123) into (10.110), the convection term will read,

$$(\rho c_p)_f \nabla \cdot (\overline{\phi \langle \mathbf{u} T \rangle^i}) = (\rho c_p)_f \nabla \cdot \left\{ \phi (\langle \overline{\mathbf{u}} \rangle^i \langle \overline{T_f} \rangle^i + \langle \overline{i\mathbf{u}^i} \rangle^i \langle \overline{T_f} \rangle^i + \langle \overline{\mathbf{u}'} \rangle^i \langle \overline{T'_f} \rangle^i + \langle \overline{i\mathbf{u}'^i T'_f} \rangle^i) \right\} \quad (10.125)$$

Also, plugging (10.124) into (10.121) will give for the same convection term,

$$(\rho c_p)_f \nabla \cdot (\overline{\phi \langle \mathbf{u} T \rangle^i}) = (\rho c_p)_f \nabla \cdot \left\{ \phi (\overline{\langle \mathbf{u} \rangle^i} \overline{\langle T_f \rangle^i} + \overline{\langle \mathbf{u} \rangle^i} \overline{\langle T_f \rangle^i} + \langle \overline{i\mathbf{u}^i} \rangle^i \langle \overline{T_f} \rangle^i + \langle \overline{i\mathbf{u}'^i T_f} \rangle^i) \right\}$$

↑ ↑ ↑ ↑
I II III IV

(10.126)

Comparing (10.125) with (10.126), in light of (10.33) and (10.34), one can conclude that (10.110) and (10.111) are, in fact, equal to (10.121) and (10.122), respectively. This demonstrates that the final expanded form of the macroscopic energy equation for a rigid, homogeneous porous medium saturated with an incompressible fluid, does not depend on the averaging order, that is, both procedures lead to the same results.

Further, the four terms on the right of (10.126) could be given the following physical significance:

- I. *Convective heat flux* based on macroscopic time mean velocity and temperature.
- II. *Turbulent heat flux* due to the fluctuating components of macroscopic velocity and temperature.
- III. *Thermal dispersion* associated with deviations of microscopic time mean velocity and temperature. Note that this term is also present when analyzing laminar convective heat transfer in porous media.
- IV. *Turbulent thermal dispersion* in a porous medium due to both time fluctuations and spatial deviations of both microscopic velocity and temperature.

Thus, the macroscopic energy equations for an incompressible flow in a rigid, homogeneous and saturated porous medium can be

written as:

- Fluid

$$\begin{aligned} & (\rho c_p)_f \nabla \cdot [\phi(\langle \bar{\mathbf{u}} \rangle^i \langle \bar{T}_f \rangle^i + \langle \bar{\mathbf{u}}^i \bar{T}_f \rangle^i + \langle \bar{\mathbf{u}}' \rangle^i \langle \bar{T}'_f \rangle^i + \langle \bar{\mathbf{u}}'^i \bar{T}'_f \rangle^i)] \\ &= \nabla \cdot [k_f \nabla(\phi \langle \bar{T}_f \rangle^i)] + \nabla \cdot \left[\frac{1}{\Delta V} \int_{A_i} \mathbf{n} k_f \bar{T}_f dS \right] + \frac{1}{\Delta V} \int_{A_i} \mathbf{n} \cdot k_f \nabla \bar{T}_f dS \end{aligned} \quad (10.127)$$

- Solid (Porous Matrix)

$$\nabla \cdot \left\{ k_s \nabla[(1-\phi) \langle \bar{T}_s \rangle^i] \right\} - \nabla \cdot \left[\frac{1}{\Delta V} \int_{A_i} \mathbf{n} k_s \bar{T}_s dS \right] - \frac{1}{\Delta V} \int_{A_i} \mathbf{n} \cdot k_s \nabla \bar{T}_s dS = 0 \quad (10.128)$$

Further, adding Eqs. (10.127) and (10.128), a global macroscopic energy equation can be obtained:

$$\begin{aligned} & (\rho c_p)_f \nabla \cdot [\phi(\langle \bar{\mathbf{u}} \rangle^i \langle \bar{T}_f \rangle^i + \langle \bar{\mathbf{u}}^i \bar{T}_f \rangle^i + \langle \bar{\mathbf{u}}' \rangle^i \langle \bar{T}'_f \rangle^i + \langle \bar{\mathbf{u}}'^i \bar{T}'_f \rangle^i)] \\ &= \nabla \cdot \left\{ k_f \nabla(\phi \langle \bar{T}_f \rangle^i) + k_s \nabla[(1-\phi) \langle \bar{T}_s \rangle^i] \right\} + \nabla \cdot \left[\frac{1}{\Delta V} \int_{A_i} \mathbf{n} (k_f \bar{T}_f - k_s \bar{T}_s) dS \right] \\ &+ \frac{1}{\Delta V} \int_{A_i} \mathbf{n} \cdot (k_f \nabla \bar{T}_f - k_s \nabla \bar{T}_s) dS \end{aligned} \quad (10.129)$$

where the applicable boundary conditions on the surface A_i are given by:

$$\left. \begin{array}{l} T_f = T_s \\ \mathbf{n} \cdot (k_f \nabla T_f) = \mathbf{n} \cdot (k_s \nabla T_s) \end{array} \right\} \quad \text{in } A_i \quad (10.130)$$

In view of the boundary conditions expressed by (10.130), one verifies that the last term on the right-hand side of (10.129) vanishes (due to the heat flux continuity at the fluid–solid interface). Thus, one can write:

$$\begin{aligned} & (\rho c_p)_f \nabla \cdot [\phi(\langle \bar{\mathbf{u}} \rangle^i \langle \bar{T}_f \rangle^i + \langle \bar{\mathbf{u}}^i \bar{T}_f \rangle^i + \langle \bar{\mathbf{u}}' \rangle^i \langle \bar{T}'_f \rangle^i + \langle \bar{\mathbf{u}}'^i \bar{T}'_f \rangle^i)] \\ &= \nabla \cdot \{k_f \nabla[\phi \langle \bar{T}_f \rangle^i] + k_s \nabla[(1-\phi) \langle \bar{T}_s \rangle^i]\} + \nabla \cdot \left[\frac{1}{\Delta V} \int_{A_i} \mathbf{n} (k_f \bar{T}_f - k_s \bar{T}_s) dS \right] \end{aligned} \quad (10.131)$$

The model proposed by de Lemos and Rocamora (2002) for the macroscopic turbulent heat flux follows the eddy-diffusivity concept embodied in (10.25)

and reads,

$$-(\rho c_p)_f \langle \overline{\mathbf{u}' T'_f} \rangle^i = c_{pf} \frac{\mu_{t\phi}}{\sigma_{T_\phi}} \nabla \langle \overline{T_f} \rangle^i \quad (10.132)$$

where $\mu_{t\phi}$ is given by (10.64), σ_{T_ϕ} is a constant, and the subscript f, as before, identifies fluid phase properties. According to Eq. (10.132), the macroscopic turbulent heat flux is taken as the sum of the turbulent heat flux and the turbulent thermal dispersion, as proposed by Rocamora and de Lemos (2000a). These two terms were related there to the components of the conductivity tensor, \mathbf{K}_t and $\mathbf{K}_{\text{disp},t}$, respectively, by the expression,

$$\mathbf{K}_t + \mathbf{K}_{\text{disp},t} = \phi c_{pf} \frac{\mu_{t\phi}}{\sigma_{T_\phi}} \mathbf{I} \quad (10.133)$$

10.7.3 Local Thermal Equilibrium Hypothesis

The local thermal equilibrium hypothesis assumes that the intrinsic average of the time-mean temperature for fluid and solid phases are equal, or say,

$$\langle \overline{T_f} \rangle^i = \langle \overline{T_s} \rangle^i = \langle \overline{T} \rangle^i \quad (10.134)$$

Thus, applying (10.134) in (10.131) one gets,

$$\begin{aligned} (\rho c_p)_f \nabla \cdot (\phi \langle \overline{\mathbf{u}} \rangle^i \langle \overline{T} \rangle^i) &= \nabla \cdot \left\{ [k_f \phi + k_s (1 - \phi)] \nabla \langle \overline{T} \rangle^i \right\} \\ &\quad + \nabla \cdot \left[\frac{1}{\Delta V} \int_{A_i} \mathbf{n} (k_f \overline{T_f} - k_s \overline{T_s}) dS \right] \\ &\quad - (\rho c_p)_f \nabla \cdot \left\{ \phi \left(\langle \overline{\mathbf{u}}^i \overline{T_f} \rangle^i + \overline{\langle \mathbf{u}' \rangle^i \langle T'_f \rangle^i} + \overline{\langle i \mathbf{u}'^i T'_f \rangle^i} \right) \right\} \end{aligned} \quad (10.135)$$

Using further the Dupuit–Forchheimer relationship $\mathbf{u}_D = \langle \overline{\mathbf{u}} \rangle^v = \phi \langle \overline{\mathbf{u}} \rangle^i$, one can rewrite (10.135) as:

$$\begin{aligned} (\rho c_p)_f \nabla \cdot (\mathbf{u}_D \langle \overline{T} \rangle^i) &= \nabla \cdot \left\{ [k_f \phi + k_s (1 - \phi)] \nabla \langle \overline{T} \rangle^i \right\} \\ &\quad + \nabla \cdot \left[\frac{1}{\Delta V} \int_{A_i} \mathbf{n} (k_f \overline{T_f} - k_s \overline{T_s}) dS \right] \\ &\quad - (\rho c_p)_f \nabla \cdot \left[\phi \left(\langle \overline{\mathbf{u}}^i \overline{T_f} \rangle^i + \overline{\langle \mathbf{u}' \rangle^i \langle T'_f \rangle^i} + \overline{\langle i \mathbf{u}'^i T'_f \rangle^i} \right) \right] \end{aligned} \quad (10.136)$$

The last three terms in (10.136) are additional unknowns coming from application of both processes of averaging, namely, time and volume averaging. As mentioned above, they represent *dispersion* due to the *spatial deviations*, *turbulent heat flux* due to *time fluctuations* and *turbulent dispersion* due to both *time fluctuations* and *spatial deviations*. Models for thermal dispersion and for turbulent heat flux have been applied on separate flows through clear and porous domains, respectively. To the best of the author's knowledge, no work in the literature has proposed a general model encompassing all terms in (10.136).

10.7.4 Macroscopic Buoyancy Effects

10.7.4.1 Mean flow

Now focusing attention to buoyancy effects only, application of the volume-average procedure to the last term of (10.22) leads to,

$$\langle \rho \mathbf{g} \beta (\bar{T} - T_{\text{ref}}) \rangle^V = \frac{\Delta V_f}{\Delta V} \frac{1}{\Delta V_f} \int_{\Delta V_f} \rho \mathbf{g} \beta (\bar{T} - T_{\text{ref}}) dV \quad (10.137)$$

Expanding the left-hand side of (10.137) in light of (10.14), the buoyancy term becomes,

$$\langle \rho \mathbf{g} \beta (\bar{T} - T_{\text{ref}}) \rangle^V = \rho \beta_\phi \mathbf{g} \phi (\langle \bar{T} \rangle^i - T_{\text{ref}}) + \underbrace{\rho \mathbf{g} \beta \phi \overline{\langle \bar{T} \rangle^i}}_{=0} \quad (10.138)$$

where the second term on the right-hand side is null since $\langle \bar{\varphi} \rangle^i = 0$. Here, the coefficient β_ϕ is the macroscopic thermal expansion coefficient. Assuming that gravity is constant over the REV, an expression for it based on (10.138) is given as,

$$\beta_\phi = \frac{\langle \rho \beta (\bar{T} - T_{\text{ref}}) \rangle^V}{\rho \phi (\langle \bar{T} \rangle^i - T_{\text{ref}})} \quad (10.139)$$

Including (10.138) into the formulation of Pedras and de Lemos (2001a), the macroscopic time-mean Navier-Stokes (NS) equation for an incompressible fluid with constant properties is given as,

$$\begin{aligned} \rho \nabla \cdot \left(\frac{\bar{\mathbf{u}}_D \bar{\mathbf{u}}_D}{\phi} \right) &= -\nabla(\phi \langle \bar{p} \rangle^i) + \mu \nabla^2 \bar{\mathbf{u}}_D + \nabla \cdot (-\rho \phi \langle \bar{\mathbf{u}}' \bar{\mathbf{u}}' \rangle^i) \\ &\quad - \rho \beta_\phi \mathbf{g} \phi (\langle \bar{T} \rangle^i - T_{\text{ref}}) - \left[\frac{\mu \phi}{K} \bar{\mathbf{u}}_D + \frac{c_F \phi \rho |\bar{\mathbf{u}}_D| \bar{\mathbf{u}}_D}{\sqrt{K}} \right] \end{aligned} \quad (10.140)$$

10.7.4.2 Turbulent field

As mentioned, this work extends the development in Pedras and de Lemos' (2001a) work to include the buoyancy production rate term in the turbulence model equations. For clear flows, the buoyancy contribution to the k equation is given in Eq. (10.27). Applying the volume-average operator to that term, one has,

$$\langle G_k \rangle^v = G_\beta^i = \langle -\rho \beta \mathbf{g} \cdot \overline{\mathbf{u}' T'_f} \rangle^v = -\rho \beta_\phi^k \phi \mathbf{g} \cdot \langle \overline{\mathbf{u}' T'_f} \rangle^i \quad (10.141)$$

where the coefficient β_ϕ^k , for a constant value of \mathbf{g} within the REV, is given by $\beta_\phi^k = \langle \beta \overline{\mathbf{u}' T'_f} \rangle^v / \phi \langle \overline{\mathbf{u}' T'_f} \rangle^i$, which, in turn, is not necessarily equal to β_ϕ given by (10.139). However, for the sake of simplicity and in the absence of better information, one can make use of the assumption $\beta_\phi^k = \beta_\phi = \beta$. Further, expanding the right-hand side of (10.141) in light of (10.14) and (10.34), one has

$$\begin{aligned} -\rho \beta_\phi^k \phi \mathbf{g} \cdot \langle \overline{\mathbf{u}' T'_f} \rangle^i &= -\rho \beta_\phi^k \phi \mathbf{g} \cdot \langle (\langle \mathbf{u}' \rangle^i + \overline{i \mathbf{u}'}) (\langle T'_f \rangle^i + \overline{i T'_f}) \rangle^i \\ &= -\rho \beta_\phi^k \phi \mathbf{g} \cdot \left(\langle \langle \mathbf{u}' \rangle^i \langle T'_f \rangle^i \rangle^i + \langle \overline{i \mathbf{u}' \langle T'_f \rangle^i} \rangle^i \right. \\ &\quad \left. + \langle \overline{\langle \mathbf{u}' \rangle^i \overline{i T'_f}} \rangle^i + \langle \overline{i \mathbf{u}' \langle T'_f \rangle^i} \rangle^i \right) \\ &= -\rho \beta_\phi^k \phi \mathbf{g} \cdot \left(\underbrace{\langle \overline{\langle \mathbf{u}' \rangle^i \langle T'_f \rangle^i} \rangle^i}_I + \underbrace{\langle \overline{i \mathbf{u}' \langle T'_f \rangle^i} \rangle^i}_{II} + \underbrace{\langle \overline{\langle \mathbf{u}' \rangle^i \langle i T'_f \rangle^i} \rangle^i}_{=0} + \underbrace{\langle \overline{i \mathbf{u}' \langle T'_f \rangle^i} \rangle^i}_{=0} \right) \end{aligned} \quad (10.142)$$

The last two terms on the right of (10.142) are null since $\langle \overline{i T'_f} \rangle^i = 0$ and $\langle \overline{i \mathbf{u}'} \rangle^i = 0$. In addition, the following physical significance can be inferred to the two remaining terms on the right-hand side of (10.142):

- I. *Generation/destruction rate due to macroscopic time fluctuations.* Buoyancy generation/destruction rate of $\langle k \rangle$ due to time fluctuations of macroscopic velocity and temperature. This term is also present in turbulent flow in clear (nonobstructed) domains and represents an exchange between the energy associated with the macroscopic turbulent motion and potential energy. In stable stratification, this term damps turbulence by being of negative value whereas the potential energy of the system is increased. On the other hand, in unstable stratification, it enhances $\langle k \rangle^i$ at the expense of potential energy.
- II. *Generation/destruction rate due to turbulent buoyant dispersion.* Buoyancy generation/destruction rate of $\langle k \rangle^i$ in a porous medium due to time fluctuations and spatial deviations of both microscopic velocity and temperature. This term might be interpreted as an additional

source/sink of turbulent kinetic energy due to the fact that time fluctuations of local velocities and temperatures present a spatial deviation in relation to their macroscopic value. Then, additional exchange between turbulent kinetic energy and potential energy in systems may occur due to the presence of a porous matrix.

A model for (10.142) is still necessary in order to solve an equation for $\langle k \rangle^i$, which information is necessary when computing $\mu_{t\phi}$ using (10.64). As such, terms I and II above have to be modeled as a function of average temperature, $\langle \bar{T} \rangle^i$. To accomplish this, a gradient type diffusion model is used, in the form,

- Buoyancy generation of $\langle k \rangle^i$ due to *turbulent fluctuations*:

$$-\rho\beta_\phi^k\phi\mathbf{g} \cdot \overline{\langle \mathbf{u} \rangle^i \langle T_f \rangle^i} = \rho\mathbf{B}_t \cdot \nabla \langle \bar{T} \rangle^i \quad (10.143)$$

- Buoyancy generation of $\langle k \rangle^i$ due to *turbulent buoyant dispersion*:

$$-\rho\beta_\phi^k\phi\mathbf{g} \cdot \overline{\langle \mathbf{u}'^i T_f' \rangle^i} = \rho\mathbf{B}_{\text{disp},t} \cdot \nabla \langle \bar{T} \rangle^i \quad (10.144)$$

The buoyancy coefficients shown above, namely \mathbf{B}_t and $\mathbf{B}_{\text{disp},t}$, are modeled here through the eddy-diffusivity concept, similar to the work of Nakayama and Kuwahara (1999). It should be noticed that these terms arise only if the flow is turbulent and if buoyancy is of importance.

Using an expression similar to (10.132), the macroscopic buoyancy generation of k can then be modeled as,

$$G_\beta^i = -\rho\beta_\phi^k\phi\mathbf{g} \cdot \overline{\langle \mathbf{u}' T_f' \rangle^i} = \beta_\phi^k\phi \frac{\mu_{t\phi}}{\sigma_{T_\phi}} \mathbf{g} \cdot \nabla \langle \bar{T} \rangle^i = \mathbf{B}_{\text{eff}} \cdot \nabla \langle \bar{T} \rangle^i \quad (10.145)$$

where $\mu_{t\phi}$ and σ_{T_ϕ} have been defined before and the two coefficients \mathbf{B}_t and $\mathbf{B}_{\text{disp},t}$ are expressed as,

$$\mathbf{B}_t + \mathbf{B}_{\text{disp},t} = \mathbf{B}_{\text{eff}} = \beta_\phi^k\phi \frac{\mu_{t\phi}}{\sigma_{T_\phi}} \mathbf{g} \quad (10.146)$$

Final transport equations for $\langle k \rangle^i = \langle \overline{\mathbf{u}' \cdot \mathbf{u}'} \rangle^i / 2$ and $\langle \varepsilon \rangle^i = \mu \langle \nabla \mathbf{u}' : (\nabla \mathbf{u}')^\top \rangle^i / \rho$, in their so-called High Reynolds number form, as proposed in Pedras and de Lemos (2001a), can now include the buoyancy generation terms seen above, in the form,

$$\rho \nabla \cdot (\overline{\mathbf{u}_D} \langle k \rangle^i) = \nabla \cdot \left[\left(\mu + \frac{\mu_{t\phi}}{\sigma_k} \right) \nabla (\phi \langle k \rangle^i) \right] + P^i + G^i + G_\beta^i - \rho \phi \langle \varepsilon \rangle^i \quad (10.147)$$

$$\begin{aligned} \rho \nabla \cdot (\bar{\mathbf{u}}_D \langle \varepsilon \rangle^i) &= \nabla \cdot \left[\left(\mu + \frac{\mu_{t_\phi}}{\sigma_\varepsilon} \right) \nabla (\phi \langle \varepsilon \rangle^i) \right] \\ &\quad + \frac{\langle \varepsilon \rangle^i}{\langle k \rangle^i} [c_1 P^i + c_2 G^i + c_1 c_3 G_\beta^i - c_2 \rho \phi \langle \varepsilon \rangle^i] \end{aligned} \quad (10.148)$$

where c_1, c_2, c_3 , and c_k are constants, $P^i = -\rho \langle \bar{\mathbf{u}}' \bar{\mathbf{u}}' \rangle^i : \nabla \bar{\mathbf{u}}_D$ is the production rate of $\langle k \rangle^i$ due to gradients of $\bar{\mathbf{u}}_D$, $G^i = c_k \rho (\phi \langle k \rangle^i | \bar{\mathbf{u}}_D | / \sqrt{K})$ is the generation rate of the intrinsic average of $\langle k \rangle^i$ due to the action of the porous matrix and $G_\beta^i = \mathbf{B}_{\text{eff}} \cdot \nabla \langle \bar{T} \rangle^i$ is the generation of $\langle k \rangle^i$ due to buoyancy.

10.8 Turbulent Mass Transport

10.8.1 Mean and Turbulent Fields

Mass transport analysis follows similar steps taken in Section 10.7 for heat transfer. First, to apply the volume average to (10.4), one has:

$$m_\ell = \langle m_\ell \rangle^i + {}^i m_\ell \quad (10.150)$$

$$\mathbf{u} = \langle \mathbf{u} \rangle^i + {}^i \mathbf{u} \quad (10.151)$$

Substituting (10.150) and (10.151) into (10.4), one obtains:

$$\frac{\partial (\langle m_\ell \rangle^i + {}^i m_\ell)}{\partial t} + \nabla \cdot [(\langle \mathbf{u} \rangle^i + {}^i \mathbf{u})(\langle m_\ell \rangle^i + {}^i m_\ell)] = \langle R_\ell \rangle^i + {}^i R_\ell + D_\ell \nabla^2 (\langle m_\ell \rangle^i + {}^i m_\ell) \quad (10.152)$$

where the mixture density ρ and the coefficient D_ℓ in (10.5) have been assumed to be constant. Expanding the convection term and taking the volume average of (10.152) with the help of (10.15) to (10.17), one has:

$$\begin{aligned} &\frac{\partial \phi (\langle m_\ell \rangle^i + {}^i m_\ell)^i}{\partial t} + \nabla \cdot [\phi (\langle \mathbf{u} \rangle^i \langle m_\ell \rangle^i + {}^i \mathbf{u} \langle m_\ell \rangle^i + \langle \mathbf{u} \rangle^i {}^i m_\ell + {}^i \mathbf{u} {}^i m_\ell)^i] \\ &= \phi (\langle R_\ell \rangle^i + {}^i R_\ell)^i + D_\ell \nabla^2 \phi (\langle m_\ell \rangle^i + {}^i m_\ell)^i \end{aligned} \quad (10.153)$$

or

$$\frac{\partial \phi \langle m_\ell \rangle^i}{\partial t} + \nabla \cdot [\phi (\langle \mathbf{u} \rangle^i \langle m_\ell \rangle^i + {}^i \mathbf{u} {}^i m_\ell)^i] = \phi \langle R_\ell \rangle^i + D_\ell \nabla^2 (\phi \langle m_\ell \rangle^i) \quad (10.154)$$

The third term on the left of (10.154) appears in classical analysis of mass transport in porous media (e.g. Hsu and Cheng, 1990; Whitaker, 1967) and is known as *mass dispersion*.

In order to apply the time average to (10.154), one defines the intrinsic volume average as:

$$\langle m_\ell \rangle^i = \overline{\langle m_\ell \rangle^i} + \langle m_\ell \rangle^{i'} \quad (10.155)$$

$$\langle \mathbf{u} \rangle^i = \overline{\langle \mathbf{u} \rangle^i} + \langle \mathbf{u} \rangle^{i'} \quad (10.156)$$

Substituting Eqs. (10.151) and (10.156) in (10.154) and taking the time average, we obtain:

$$\frac{\partial \phi \overline{\langle m_\ell \rangle^i}}{\partial t} + \nabla \cdot \phi (\overline{\langle \mathbf{u} \rangle^i} \overline{\langle m_\ell \rangle^i} + \overline{\langle \mathbf{u} \rangle^{i'} \langle m_\ell \rangle^{i'}} + \overline{\langle \mathbf{u}^i m_\ell \rangle^i}) = \phi \overline{\langle R_\ell \rangle^i} + D_\ell \nabla^2 (\phi \overline{\langle m_\ell \rangle^i}) \quad (10.157)$$

Equation (10.157) is the macroscopic mass transfer equation for the species ℓ in the porous matrix taking first the *volume average* followed by the *time average*.

Another route to reach a macroscopic transport equation for turbulent flow, is to invert the order of application of the same average operators applied to Eq. (10.4). Therefore, starting now with the time average, one needs to consider the time decompositions,

$$m_\ell = \overline{m}_\ell + m'_\ell \quad (10.158)$$

$$\mathbf{u} = \overline{\mathbf{u}} + \mathbf{u}' \quad (10.159)$$

Substituting Eqs. (10.158) and (10.159) into (10.4) one has:

$$\frac{\partial (\overline{m}_\ell + m'_\ell)}{\partial t} + \nabla \cdot [(\overline{\mathbf{u}} + \mathbf{u}')(\overline{m}_\ell + m'_\ell)] = \overline{R_\ell} + R'_\ell + D_\ell \nabla^2 (\overline{m}_\ell + m'_\ell) \quad (10.160)$$

where again the mixture density ρ and the diffusion coefficient D_ℓ were kept constants. Applying time average to (10.160) one obtains,

$$\frac{\partial \overline{(\overline{m}_\ell + m'_\ell)}}{\partial t} + \nabla \cdot (\overline{\mathbf{u}} \overline{m}_\ell + \overline{\mathbf{u}} m'_\ell + \mathbf{u}' \overline{m}_\ell + \mathbf{u}' m'_\ell) = \overline{\overline{R_\ell} + R'_\ell} + D_\ell \nabla^2 \overline{(\overline{m}_\ell + m'_\ell)} \quad (10.161)$$

or

$$\frac{\partial \overline{m}_\ell}{\partial t} + \nabla \cdot (\overline{\mathbf{u}} \overline{m}_\ell + \overline{\mathbf{u}' m'_\ell}) = \overline{R_\ell} + D_\ell \nabla^2 \overline{m}_\ell \quad (10.162)$$

The second term on the left of Eq. (10.162) is known as *turbulent mass flux* (divided by ρ). It requires a model for closure of the mathematical problem.

Further, in order to apply the volume average to Eq. (10.162), one must first define the spatial deviations with respect to the volume averages, given by:

$$\bar{m}_\ell = \langle \bar{m}_\ell \rangle^i + {}^i\bar{m}_\ell \quad (10.163)$$

$$\bar{\mathbf{u}} = \langle \bar{\mathbf{u}} \rangle^i + {}^i\bar{\mathbf{u}} \quad (10.164)$$

Now substituting Eqs. (10.163) and (10.164) into (10.162) and performing the volume-average operation, one has:

$$\frac{\partial \phi \langle \bar{m}_\ell \rangle^i}{\partial t} + \nabla \cdot \phi (\langle \bar{\mathbf{u}} \rangle^i \langle \bar{m}_\ell \rangle^i + \langle {}^i\bar{\mathbf{u}} {}^i\bar{m}_\ell \rangle^i + \langle \bar{\mathbf{u}}' \bar{m}'_\ell \rangle^i) = \phi \langle \bar{R}_\ell \rangle^i + D_\ell \nabla^2 \phi \langle \bar{m}_\ell \rangle^i \quad (10.165)$$

Equation (10.165) is the macroscopic mass diffusion equation for taking first the time average followed by the volume-average operator.

It is interesting to observe that Eq. (10.157), obtained through the first procedure (volume-time average), is equivalent to Eq. (10.165) as will be shown in the next section.

10.8.2 Turbulent Mass Dispersion

Now using Eqs. (10.34) to (10.38), the fourth term on the left-hand side of (10.157) can be expanded as:

$$\overline{{}^i\mathbf{u}{}^i m_\ell}^i = \overline{({}^i\bar{\mathbf{u}} + {}^i\mathbf{u}')({}^i\bar{m}_\ell + {}^i m'_\ell)}^i = \langle {}^i\bar{\mathbf{u}} {}^i\bar{m}_\ell \rangle^i + \overline{{}^i\mathbf{u}' {}^i m'_\ell}^i \quad (10.166)$$

Substituting Eq. (10.166) into Eq. (10.157), the convection term will read,

$$\nabla \cdot (\overline{\phi \langle \mathbf{u} m_\ell \rangle^i}) = \nabla \cdot \left\{ \phi \left(\overline{(\mathbf{u})^i \langle \bar{m}_\ell \rangle^i} + \langle {}^i\bar{\mathbf{u}} {}^i\bar{m}_\ell \rangle^i + \overline{\langle \mathbf{u} \rangle^{i'} \langle m_\ell \rangle^{i'}} + \langle {}^i\bar{\mathbf{u}}' {}^i m'_\ell \rangle^i \right) \right\}$$

↑ ↑ ↑ ↑
 I II III IV

$$(10.167)$$

Likewise, applying again Eq. (10.34) to (10.38) to the fourth term on the left-hand side of (10.165), one gets,

$$\overline{\langle \mathbf{u}' m'_\ell \rangle^i} = \overline{((\mathbf{u}')^i + {}^i\mathbf{u}')(\langle m'_\ell \rangle^i + {}^i m'_\ell)}^i = \overline{\langle \mathbf{u}' \rangle^i \langle m'_\ell \rangle^i} + \overline{{}^i\mathbf{u}' {}^i m'_\ell}^i \quad (10.168)$$

Also, plugging Eq. (10.168) into (10.165) will give for the same convection term,

$$\nabla \cdot (\overline{\phi \langle \mathbf{u} m_\ell \rangle^i}) = \nabla \cdot \left\{ \phi (\langle \bar{\mathbf{u}} \rangle^i \langle \bar{m}_\ell \rangle^i + \langle \bar{\mathbf{u}}^i \bar{m}_\ell \rangle^i + \overline{\langle \mathbf{u}' \rangle^i \langle m'_\ell \rangle^i} + \overline{\langle \bar{\mathbf{u}}' \rangle^i \langle \bar{m}'_\ell \rangle^i}) \right\}$$

↑ ↑ ↑ ↑
I II III IV

(10.169)

Comparing Eq. (10.169) with (10.167), in light of Eq. (10.34), one can conclude that Eq. (10.165) is, in fact, equal to Eq. (10.157). This demonstrates that the final expanded form of the macroscopic mass transfer equation for a rigid, homogeneous porous medium saturated with an incompressible fluid does not depend on the averaging order and both procedures lead to equivalent results.

Further, the four terms on the right of either Eq. (10.167) or (10.169) could be given the following physical significance (multiplied by ρ):

- I. *Convective Mass Flux* based on macroscopic time-mean velocity and mass fraction.
- II. *Mass Dispersion* associated with deviations of microscopic time-mean velocity and mass fraction. Note that this term is also present when analyzing laminar mass transfer in porous media, but it does not exist if a volume average is not performed.
- III. *Turbulent Mass Flux* due to the fluctuating components of both macroscopic velocity and mass fraction. This term is also present in turbulent flow in clear (nonporous) domains. It is not defined for laminar flow in porous media where time fluctuations do not exist.
- IV. *Turbulent Mass Dispersion* in a porous medium due to both *time fluctuations* and *spatial deviations* of both microscopic velocity and mass fraction.

Thus, the macroscopic mass transport equation for an incompressible flow in a rigid, homogeneous and saturated porous medium can be written as:

$$\begin{aligned} & \frac{\partial \phi \langle \bar{m}_\ell \rangle^i}{\partial t} + \nabla \cdot \phi (\langle \bar{\mathbf{u}} \rangle^i \langle \bar{m}_\ell \rangle^i + \langle \bar{\mathbf{u}}^i \bar{m}_\ell \rangle^i + \overline{\langle \mathbf{u}' \rangle^i \langle m'_\ell \rangle^i} + \overline{\langle \bar{\mathbf{u}}' \rangle^i \langle \bar{m}'_\ell \rangle^i}) \\ &= \phi \langle \bar{R}_\ell \rangle^i + D_\ell \nabla^2 (\phi \langle \bar{m}_\ell \rangle^i) \end{aligned} \quad (10.170)$$

or in its equivalent form (see de Lemos and Mesquita, 2003),

$$\begin{aligned} & \frac{\partial \phi \overline{\langle m_\ell \rangle^i}}{\partial t} + \nabla \cdot \phi (\overline{\langle \mathbf{u} \rangle^i \langle m_\ell \rangle^i} + \langle \bar{\mathbf{u}}^i \bar{m}_\ell \rangle^i + \overline{\langle \mathbf{u}' \rangle^{i'} \langle m_\ell \rangle^{i'}} + \overline{\langle \bar{\mathbf{u}}' \rangle^{i'} \langle \bar{m}_\ell \rangle^{i'}}) \\ &= \phi \overline{\langle R_\ell \rangle^i} + D_\ell \nabla^2 (\phi \overline{\langle m_\ell \rangle^i}) \end{aligned} \quad (10.171)$$

10.9 Applications in Hybrid Media

Detailed information on the numerical treatment used in the examples below is found in Pedras and de Lemos (2001a, 2001b, 2001c, 2003). For this reason, they are not repeated here. Also, in the numerical results to follow, standard wall functions have been employed to calculate the flow in the proximity of channel walls. Justification for using such simple treatment is twofold: (a) final velocity values close to the interface will be a function not only of the inertia and viscous effects in the full Navier–Stokes equation, but also due to the Darcy–Forchheimer resistance terms. Therefore, eventual errors occurring from inaccurate use of a more appropriate boundary condition will have little influence on the final value for the velocity close to the wall since drag forces, caused by the porous structure, will also play an important role in determining the final value for the wall velocity; (b) logarithm wall laws are simple and can be incorporated when simulating flow over rigid surfaces and for that they have been modified to include surface roughness and to simulate flows over irregular surfaces at the bottom of rivers (Lane and Hardy, 2002).

In addition, it is interesting to emphasize that the class of flows under consideration is akin to having a sequence of closely spaced grids in a flow with a flat macroscopic Darcy velocity profile. Mechanical energy is transformed into turbulent kinetic energy as the flow crosses and is perturbed by the porous matrix. This interpretation of the model used here has been detailed in de Lemos and Pedras (2001a).

10.9.1 The Stress Jump Conditions at Interface

The equation proposed in Ochoa-Tapia and Whitaker (1995a, 1995b) for describing the stress jump at the interface between the clear flow region and the porous structure is given by,

$$\mu_{\text{eff}} \frac{\partial u_{D_p}}{\partial \eta} \Big|_{\text{Porous Medium}} - \mu \frac{\partial u_{D_p}}{\partial \eta} \Big|_{\text{Clear Fluid}} = \beta \frac{\mu}{\sqrt{K}} u_{D_p} \Big|_{\text{Interface}} \quad (10.172)$$

where u_{D_p} is the Darcy velocity component parallel to the interface, μ_{eff} is the effective viscosity for the porous region, and β an adjustable coefficient that accounts for the stress jump at the interface (do not confuse with the thermal expansion coefficient β defined in equation 10.7). A justification for using (10.172) lies in the fact that simpler analyses of flow around interfaces consider the permeability of the porous medium to be constant, even within the interface region. This assumption, however, does not correspond to reality since the closer the interface the more permeable the medium becomes.

It is important to emphasize that the macroscopic model for the interface employed here makes no assumption about the topology of the surface, nor is this interface the one existing in transpired solid walls. Although the

microscopic interfacial area surrounding the irregular geometry of solid particles facing the clear medium may be characterized by statistical values, such as an average thickness or roughness, in the present macroscopic view no such thickness or roughness is associated with the interface. In fact, in Kaviany (1995, p. 71), the order of magnitude of the roughness of the interface is of order of d (pore/particle diameter), which is much higher than \sqrt{K} , another length associated with permeable media. Had the interface roughness been considered, it would be of the order of d , the mean particle/pore diameter. Here, irregular or rough boundaries between the porous medium and the clear fluid are treated under the macroscopic view and, as such, no statistical value of interface thickness is attributed to the modeled surface separating the two media. Likewise, transpired walls made of a porous substrate with extremely small porous sizes are not treated here. Also, the macroscopic velocity at the interface and on its surroundings is assumed to be of sufficient value such that a viscous sublayer similar to the one existing over impermeable surfaces is not present in the context herein.

In addition to Eq. (10.172), continuity of velocity, pressure, statistical variables, and their fluxes across the interface is given by,

$$\bar{\mathbf{u}}_D|_{0 < \phi < 1} = \bar{\mathbf{u}}_D|_{\phi=1} \quad (10.173)$$

$$\langle \bar{p} \rangle^i \Big|_{0 < \phi < 1} = \langle \bar{p} \rangle^i \Big|_{\phi=1} \quad (10.174)$$

$$\langle k \rangle^v \Big|_{0 < \phi < 1} = \langle k \rangle^v \Big|_{\phi=1} \quad (10.175)$$

$$\left(\mu + \frac{\mu_{t\phi}}{\sigma_k} \right) \frac{\partial \langle k \rangle^v}{\partial y} \Big|_{0 < \phi < 1} = \left(\mu + \frac{\mu_t}{\sigma_k} \right) \frac{\partial \langle k \rangle^v}{\partial y} \Big|_{\phi=1} \quad (10.176)$$

$$\langle \varepsilon \rangle^v \Big|_{0 < \phi < 1} = \langle \varepsilon \rangle^v \Big|_{\phi=1} \quad (10.177)$$

$$\left(\mu + \frac{\mu_{t\phi}}{\sigma_\varepsilon} \right) \frac{\partial \langle \varepsilon \rangle^v}{\partial y} \Big|_{0 < \phi < 1} = \left(\mu + \frac{\mu_t}{\sigma_\varepsilon} \right) \frac{\partial \langle \varepsilon \rangle^v}{\partial y} \Big|_{\phi=1} \quad (10.178)$$

Further, the extension of Eq. (10.172) to the case of turbulent flow can be given as,

$$(\mu_{eff} + \mu_{t\phi}) \frac{\partial \bar{u}_{D_p}}{\partial y} \Big|_{0 < \phi < 1} - (\mu + \mu_t) \frac{\partial \bar{u}_{D_p}}{\partial y} \Big|_{\phi=1} = (\mu + \mu_t) \frac{\beta}{\sqrt{K}} \bar{u}_{D_i} \Big|_{\text{Interface}} \quad (10.179)$$

Equations (10.173) and (10.174) were also proposed by Ochoa-Tapia and Whitaker (1995a, 1995b) whereas relationships (10.175) through (10.179) were used by Lee and Howell (1987). Laminar (Silva and de Lemos, 2003a) and turbulent (Silva and de Lemos, 2003b) flow solutions using the above interface conditions applied to channel flows have been presented. Further, one should point out that condition (10.179) is valid along the macroscopic surface area dividing the clear and the porous regions. Application of the volume-average

operators to a representative elementary volume (Whitaker, 1969; Gray and Lee, 1977) gives rise to terms such as the Darcy and Forchheimer flow resistances (Kuznetsov, 1996, 1999; Ochoa-Tapia and Whitaker, 1995a, 1995b), which are not presented here when analyzing macroscopic interfacial areas.

10.9.2 Buoyant Flows in Cavities Partially Filled with Porous Inserts

The problem considered is a horizontal two-dimensional square cavity with a porous plate positioned at the cavity at mid height. The cavity is isothermally heated from the bottom and cooled on the top surface. The side walls are kept insulated. For laminar flow the no-slip condition is applied to the velocity field at the walls. For the turbulent regime, the wall function approach is used. The Rayleigh number is calculated as in the case of a clear cavity.

Calculations for turbulent flow were performed for all cases using a 50×50 regular grid. From left to right Figure 10.2 shows the isotherms, streamlines, and isolines of turbulent kinetic energy, respectively, for Ra ranging from 4×10^4 to 10^7 . For $Ra = 10^2$ (results not shown here), the isotherms are stratified and the main mechanism of heat transfer is conduction. For $Ra = 4 \times 10^4$, Figure 10.2 (top), a plume rises from the bottom of the heated wall impinging onto the porous plate. The flow is divided into four vortices, two on each side of the porous obstruction and the generation rates of turbulent kinetic energy remain small, except close to the walls. Increasing Ra to 10^6 , Figure 10.2 (middle), the plume becomes stronger, impinging through the

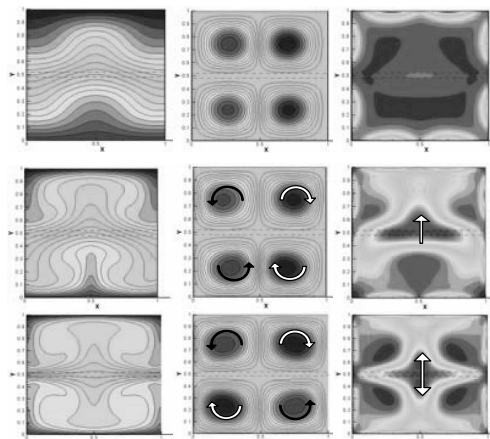
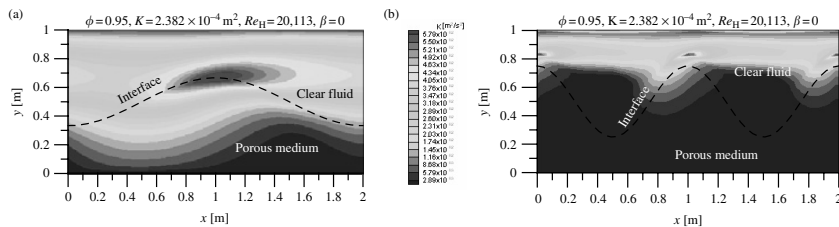


FIGURE 10.2

Turbulent isotherms, streamlines, and isolines of k for a square cavity with a porous obstruction, Rayleigh number $Ra = 4 \times 10^4$ (top), 10^6 (middle), and 10^7 (bottom); $\phi = 0.95$ and $K = 0.2382 \times 10^{-5} \text{ m}^2$. (Compiled from Braga, E. J. and de Lemos, M. J.S., 2003, Turbulent Heat Transfer in a Horizontal Enclosure with a thin Porous Obstruction in the Middle, Paper IMECE2003-41463, Proc. of IMECE'03–2003 ASME International Mechanical Engineering Congress. With permission.)

**FIGURE 10.3**

Turbulent kinetic energy around a wavy interface: (a) $a = 1/3, n = 1$, (b) $a = 2/3, n = 2$, where a is the amplitude and n the wave number. (Taken from de Lemos and Silva, 2003, Turbulent Flow Around a Wavy Interface Between a Porous Medium and a Clear Domain, Paper FEDSM2003-45457, Proc. of ASME-FEDSM 2003 4th ASME/JSME Joint Fluids Engineering Conference. With Permission.)

porous obstruction more intensively. The vortices turn a little faster than before (not seen in the figure) and high generation rates of turbulent kinetic energy are clearly detected, mainly inside and in the vicinity of the porous obstruction. The porous matrix contributes to the overall levels of $\langle k \rangle^i$ through the two terms added to Eq. (10.147), namely G^i and G_β^i , proposed in Pedras and de Lemos (2001a) and de Lemos and Braga (2003), respectively. For $Ra = 10^7$, Figure 10.2 (bottom), computations show that two plumes arise from the porous obstruction, and move in opposite directions toward the heated walls. Further investigation is necessary to determine whether the observed pattern is due to the physics of the problem, or else is the sole outcome of numerical sensitivity to the computational parameters used.

10.9.3 Flow Around a Sinusoidal Interface in a Channel

Finally, Figure 10.3 presents numerical solutions for the turbulent kinetic energy of the flow around a wavy interface in a channel. We can see that at positions corresponding to peaks of the interface, the values of k are higher. In these positions, the velocity at the clear region is accelerated further increasing velocity gradients within the clear passage. This, in turn, promotes higher k generation rates through the P^i term in Eq. (10.147). On the other hand, within the porous matrix, and around the same peaks, higher velocities promote additional generation rates for k , here considered via the G^i term in Eq. (10.147). Thus, either by gradients of the mean velocity in the clear fluid or by higher mass fluxes in the porous layer, a greater portion of the available mechanical energy around the peaks is converted into turbulence. These results might benefit studies of flow around irregular interfaces between a porous matrix and a clear fluid region.

10.10 Concluding Remarks

This chapter described a new methodology for analysis of turbulent flow in permeable media. A novel concept called the *double-decomposition* idea was

detailed showing how a variable can be decomposed in both time and volume in order to simultaneously account for fluctuations (in time) and deviations (in space) around mean values. Transport equations for the mean and turbulence flow were presented, including consideration of heat transfer with buoyancy and mass transport.

The usefulness of this research might be better appreciated when studying transport over highly permeable media where the turbulence flow regime occurs in the fluid phase. Analyses of important environmental and engineering flows can benefit from the derivations herein and, ultimately, it is expected that additional research on this new subject will be stimulated by the work presented here.

Acknowledgments

The author thanks CNPq and FAPESP, Brazil, for their financial support during the preparation of this work. Thanks are also due to the authors' former and current graduate students who conducted their graduate programs with the topic discussed here.

Nomenclature

A_i	interfacial area
c_k	constant in the extra production term for k -equation
D	rod diameter
H	height of periodic cell
k	turbulence kinetic energy (TKE), $k = \overline{\mathbf{u}' \cdot \mathbf{u}'} / 2$
$\langle k \rangle^i$	intrinsic (fluid) average for k , $\langle k \rangle^i = \overline{\langle \mathbf{u}' \cdot \mathbf{u}' \rangle^i} / 2$
k_m	TKE based on the fluctuation of $\langle \bar{\mathbf{u}} \rangle^i$, $k_m = \langle \mathbf{u}'^i \cdot \langle \mathbf{u}' \rangle^i \rangle / 2$
k_ϕ	fully developed value of $\langle k \rangle^i$
K	medium permeability
p	pressure
Re_p	pore Reynolds number
Re_H	Reynolds number based on H
S	length of periodic cell, $S = 2H$
T	temperature
\mathbf{u}	microscopic velocity vector
$\bar{\mathbf{u}}_D$	Darcy velocity vector
$\langle \bar{\mathbf{u}} \rangle^i$	intrinsic velocity vector

u_{D_n}, u_{D_p}	components of Darcy velocity at interface along η (normal) and ξ (parallel) directions, respectively
u_{D_x}, v_{D_y}	components of Darcy velocity at interface along x and y , respectively

Greek Letters

β	interface stress jump coefficient
ε	dissipation rate of k , $\varepsilon = \mu \overline{\nabla \mathbf{u}' : (\nabla \mathbf{u}')^T} / \rho$
$\langle \varepsilon \rangle^i$	intrinsic (fluid) average for ε
ε_ϕ	fully developed value of $\langle \varepsilon \rangle^i$
λ	thermal conductivity
ΔV	representative elementary volume
ΔV_f	volume of fluid inside ΔV
φ	general variable
ϕ	porosity
$\langle \varphi \rangle^i$	intrinsic (fluid) average of φ
$i\varphi$	spatial deviation from intrinsic average of φ
$\mu_{t\phi}$	macroscopic coefficient of exchange for porous media
μ	fluid viscosity
μ_{eff}	effective viscosity for a porous medium
σ_k	turbulent Prandtl number for $\langle k \rangle^i$
σ_ε	turbulent Prandtl number for $\langle \varepsilon \rangle^i$
ρ	fluid density

References

- Abe, K., Nagano, Y., and Kondoh, T., 1992, An improved $k-\varepsilon$ model for prediction of turbulent flows with separation and reattachment, *Trans. JSME, Ser. B.*, **58** (554), 3003–3010.
- Antohe, B.V. and Lage, J.L., 1997, A general two-equation macroscopic turbulence model for incompressible flow in porous media, *Int. J. Heat Mass Transfer*, **40**, 3013–3024.
- Awartani, M. and Hamdan, M.H., 1999, Non-reactive gas-particle models of flow through porous media, *Appl. Math. Comput.*, **100**, 93–102.
- Bear, J., 1972, *Dynamics of Fluids in Porous Media*, American Elsevier Pub. Co., New York.
- Bear, J. and Bachmat, Y., 1967, A Generalized Theory on Hydrodynamic Dispersion in Porous Media, *I.A.S.H. Symp. Artificial Recharge and Management of Aquifers*, Haifa, Israel, P.N. 72, 7–16, I.A.S.H.
- Bird, R.B., Stewart, W.E., and Lightfoot, E.N., 1960, *Transport Phenomena*, John Wiley & Sons, New York.

- Braga, E.J. and de Lemos, M.J.S., 2003, Turbulent Heat Transfer in a Horizontal Enclosure with a Thin Porous Obstruction in the Middle, *Proc. of IMECE'03—2003 ASME International Mechanical Engineering Congress* (on CD-ROM), Paper IMECE2003-41463, Washington, D.C., USA, November 16–21.
- Braga, E.J. and de Lemos, M.J.S., 2004, Turbulent Natural Convection in a Porous Square Cavity Computed with a Macroscopic k-e Model, *Intern. J. Heat and Mass Transfer*, Vol. 47, n°26, pp. 5635–5646.
- Brinkman, H.C., 1947, A calculation of the viscous force exerted by a flowing fluid on a dense swarm of particles, *Appl. Sci. Res. A*, **1**, 27–34.
- Chan, E.C., Lien, F.-S., and Yovanovich, M.M., 2000, Numerical Study of Forced Flow in a Back-Step Channel Through Porous Layer, *Proc. 34th ASME-Natl. Heat Transfer Conf.* (on CD-ROM), ASME-HTD-I463CD, Paper NHTC2000-12118, ISBN: 0-7918-1997-3, Pittsburgh, PA, August 20–22.
- Darcy, H., 1856, *Les Fontaines Publiques de la Ville de Dijon*, Victor Dalmond, Paris.
- de Lemos, M.J.S. and Braga, E.J., 2003, *Int. Commun. Heat Mass Transfer*, **30**(5), 615–624.
- de Lemos, M.J.S. and Mesquita, M.S., 2003, *Int. Commun. Heat Mass Transfer*, **30**, 105–113.
- de Lemos, M.J.S. and Pedras, M.H.J., 2000a, Modeling Turbulence Phenomena in Incompressible Flow Through Saturated Porous Media, *Proc. 34th ASME-Natl. Heat Transfer Conf.* (on CD-ROM), ASME-HTD-I463CD, Paper NHTC2000-12120, ISBN: 0-7918-1997-3, Pittsburgh, PA, August 20–22.
- de Lemos, M.J.S. and Pedras, M.H.J., 2000b, Simulation of Turbulent Flow Through Hybrid Porous Medium-Clear Fluid Domains, *Proc. IMECE2000 — ASME — Intern. Mech. Eng. Congr.*, ASME-HTD-366-5, pp. 113–122, ISBN: 0-7918-1908-6, Orlando, FL, November 5–10.
- de Lemos, M.J.S. and Pedras, M.H.J., 2001, Recent mathematical models for turbulent flow in saturated rigid porous media, *ASME J. Fluids Eng.* **123**(4), 935–940.
- de Lemos, M.J.S. and Rocamora, F.D., 2002, Turbulent transport modeling for heated flow in rigid porous media, *Proc. 12th Intern. Heat Transfer Conf.* **4**, 791–796.
- de Lemos, M.J.S. and Silva, R.A., 2002, Numerical Treatment of the Stress Jump Interface Condition for Laminar Flow in a Channel Partially Filled with a Porous Material, *Proc. ASME Fluids Eng. Div. Summer Meeting*, Paper ASME-FEDSM2002-31126, Montreal, Quebec, Canada.
- de Lemos, M.J.S. and Silva, R.A., 2003, Turbulent Flow Around a Wavy Interface Between a Porous Medium and a Clear Domain, *Proc. of ASME-FEDSM2003 4th ASME/JSME Joint Fluids Engineering Conference* (on CD-ROM), Paper FEDSM2003-45457, Honolulu, Hawaii, USA, July 6–11.
- de Lemos, M.J.S. and Tofaneli, L.A., 2004, Modeling of Double-Diffusive Turbulent Natural Convection in Porous Media, *International Journal of Heat Mass Transfer*, Vol. 47, n° 19–20, pp. 4233–4241.
- Forchheimer, P., 1901, Wasserbewegung durch Boden, *Z. Ver. Deutsch. Ing.*, **45**, 1782–1788.
- Fox, R.W. and McDonald, A.T., 1998, *Introduction to Fluids Mechanics*, John Wiley & Sons, New York, 5th edn, p. 156.
- Getachewa, D., Minkowycz, W.J., and Lage, J.L., 2000, A modified form of the $k-\varepsilon$ model for turbulent flow of an incompressible fluid in porous media, *Int. J. Heat Mass Transfer*, **43**, 2909–2915.
- Gratton, L., Travkin, V.S., and Catton, I., 1994, Numerical solution of turbulent heat and mass transfer in a stratified geostatistical porous layer for high permeability media, *ASME Proc. HTD* **41**, 1–14.

- Gray, W.G. and Lee, P.C.Y., 1977, On the theorems for local volume averaging of multiphase system, *Int. J. Multiphase Flow*, **3**, 333–340.
- Hinze, J.O., 1959, *Turbulence*, McGraw-Hill, New York.
- Hsu, C.T. and Cheng, P., 1990, Thermal dispersion in a porous medium, *Int. J. Heat Mass Transfer*, **33**, 1587–1597.
- Kaviany, M., 1995 *Principles of Heat Transfer in Porous Media*, Springer, New York.
- Kuwahara, F. and Nakayama, A., 1998, Numerical Modeling of Non-Darcy Convective Flow in a Porous Medium, *Proc. 11th Int. Heat Transf. Conf.*, Kyongyu, Korea, August 23–28.
- Kuwahara, F., Nakayama, A., and Koyama, H., 1996, *J. Heat Transfer*, **118**, 756–761.
- Kuwahara, F., Kameyama, Y., Yamashita, S., and Nakayama, A., 1998, Numerical modeling of turbulent flow in porous media using a spatially periodic array, *J. Porous Media*, **1**, 47–55.
- Kuznetsov, A.V., 1996, Analytical investigation of the fluid flow in the interface region between a porous medium and a clear fluid in channels partially filled with a porous medium, *Int. J. Heat Fluid Flow*, **12**, 269–272.
- Kuznetsov, A.V., 1997, Influence of the stresses jump condition at the porous-medium/clear-fluid interface on a flow at a porous wall, *Int. Commun. Heat Mass Transfer*, **24**, 401–410.
- Kuznetsov, A.V., 1999, Fluid mechanics and heat transfer in the interface region between a porous medium and a fluid layer: a boundary layer solution, *J. Porous Media*, **2**(3), 309–321.
- Kuznetsov, A.V., Cheng, L., and Xiong, M., 2002, Effects of thermal dispersion and turbulence in forced convection in a composite parallel-plate channel: investigation of constant wall heat flux and constant wall temperature cases, *Numer. Heat Transfer: Part A Appl.*, **42**(4), 365–383.
- Kuznetsov, A.V., Cheng, L., and Xiong, M., 2003, Investigation of turbulence effects on forced convection in a composite porous/fluid duct: constant wall flux and constant wall temperature cases, *J. Heat Mass Transfer*, **39**(7), 613–623.
- Lage, J.L., 1998, The fundamental theory of flow through permeable media from Darcy to turbulence, In *Transport Phenomena in Porous Media*, Eds. D.B. Ingham and I. Pop, Elsevier Science Ltd., ISBN: 0-08-042843-6, pp. 446.
- Lage, J.L., de Lemos, M.J.S., and Nield, D.A., 2002, Modeling turbulence in porous media. In *Transport Phenomena in Porous Media*, vol. 2, Eds. D.B. Ingham and I. Pop, pp. 198–230, Kidlington, UK.
- Lane, S.N. and Hardy, R.J., 2002, Porous rivers: A new way of conceptualising and modelling river and Flooplain flows? In *Transport Phenomena in Porous Media II*, eds. D. Ingham and I. Pop, 1st edn, pp. 425–449, Pergamon Press, Kidlington, UK.
- Lee, K. and Howell, J.R., 1987, Forced convective and radiative transfer within a highly porous layer exposed to a turbulent external flow field, *Proc. 1987 ASME-JSME Thermal Eng. Joint Conf.*, **2**, 377–386.
- Lim, I.G. and Matthews, R.D., 1993, Development of a model for turbulent combustion within porous inert media, *Transport Phenomena in Thermal Engineering* vol. 1, Eds. J.S. Lee, S.H. Chung, and K.Y. Kim, pp. 631–636, Begell House, New York.
- Masuoka, T. and Takatsu, Y., 1996, Turbulence model for flow through porous media, *Int. J. Heat Mass Transfer*, **39**(13), 2803–2809.
- Mickley, H.S., Smith, K.A., and Korchak, E.I., 1965, Fluid flow in packed beds, *Chem. Eng. Sci.*, **20**, 237–246.

- Nakayama, A. and Kuwahara, F., 1999, A macroscopic turbulence model for flow in a porous medium, *ASME J. Fluids Eng.*, **121**, 427–433.
- Ochoa-Tapia, J.A. and Whitaker, S., 1995a, Momentum transfer at the boundary between a porous medium and a homogeneous fluid — I. Theoretical development, *Int. J. Heat Mass Transfer*, **38**, 2635–2646.
- Ochoa-Tapia, J.A. and Whitaker, S., 1995b, Momentum transfer at the boundary between a porous medium and a homogeneous fluid — II. Comparison with experiment, *Int. J. Heat Mass Transfer*, **38**, 2647–2655.
- Pedras, M.H.J. and de Lemos, M.J.S., 1998, Results for Macroscopic Turbulence Modeling for Porous Media, *Proc. ENCIT98-7th Braz. Congr. Eng. Th. Sci.*, vol. 2, pp. 1272–1277, Rio de Janeiro, Brazil, November 3–6 (in Portuguese).
- Pedras, M.H.J. and de Lemos, M.J.S., 1999a, On Volume and Time Averaging of Transport Equations for Turbulent Flow in Porous Media, *Proc. 3rd ASME/JSME Joint Fluids Eng. Conf.* (on CDROM), ASME-FED-248, Paper FEDSM99-7273, ISBN 0-7918-1961-2, San Francisco, CA, July 18–23.
- Pedras, M.H.J. and de Lemos, M.J.S., 1999b, Macroscopic Turbulence Modeling for Saturated Porous Media, *Proc. COBEM99 — 15th Braz. Congr. Mech. Eng.* (on CD-ROM), ISBN: 85-85769-03-3, Águas de Lindóia, São Paulo, Brazil, November 22–26 (in Portuguese).
- Pedras, M.H.J. and de Lemos, M.J.S., 2000a, On the definition of turbulent kinetic energy for flow in porous media, *Int. Commun. Heat Mass Transfer*, **27**(2), 211–220.
- Pedras, M.H.J. and de Lemos, M.J.S., 2000b, Numerical Solution of Turbulent Flow in Porous Media using a Spatially Periodic Cell and the Low Reynolds $k-\varepsilon$ Model, *Proc. CONEM2000—Natl Mechanical Eng. Congr.* (on CD-ROM), Natal, Rio Grande do Norte, Brazil, August 7–11 (in Portuguese).
- Pedras, M.H.J. and de Lemos, M.J.S., 2001a, Macroscopic turbulence modeling for incompressible flow through undeformable porous media, *Int. J. Heat Mass Transfer*, **44**(6), 1081–1093.
- Pedras, M.H.J. and de Lemos, M.J.S., 2001b, Simulation of turbulent flow in porous media using a spatially periodic array and a low Re two-equation closure, *Numer. Heat Transfer: Part A Appl.*, **39**(1), 35–59.
- Pedras, M.H.J. and de Lemos, M.J.S., 2001c, On mathematical description and simulation of turbulent flow in a porous medium formed by an array of elliptic rods, *ASME J. Fluids Eng.*, **123**(4), 941–947.
- Pedras, M.H.J. and de Lemos, M.J.S., 2003, Computation of turbulent flow in porous media using a low Reynolds k -epsilon model and an infinite array of transversally-displaced elliptic rods. *Numer. Heat Transfer: Part A Appl.*, **43**(6), 585–602.
- Prausnitz, J.M. and Wilhelm, R.H., 1957, Turbulent concentrations fluctuations in a packed bed, *Industrial Eng. Chem.*, **49**, 237–246.
- Prescott, P.J. and Incropera, F.P., 1995, The effect of turbulence on solidification of a binary metal alloy with electromagnetic stirring, *ASME J. Heat Transfer*, **117**, 716–724.
- Rocamora Jr., F.D. and de Lemos, M.J.S., 1998, Numerical Solution of Turbulent Flow in Porous Media using a Spatially Periodic Array and the $k-\varepsilon$ Model, *Proc. ENCIT98-7th. Braz. Congr. Eng. Th. Sci.*, vol. 2, pp. 1265–1271, Rio de Janeiro, RJ, Brazil, November 3–6.
- Rocamora Jr., F.D. and de Lemos, M.J.S., 1999, Simulation of Turbulent Heat Transfer in Porous Media Using a Spatially Periodic Cell and the $k-\varepsilon$ Model, *Proc. of*

- COBEM99 — 15th Braz. Congr. Mech. Eng. (on CD-ROM), ISBN: 85-85769-03-3, Águas de Lindóia, São Paulo, Brazil, November 22–26.
- Rocamora Jr., F.D. and de Lemos, M.J.S., 2000a, Analysis of convective heat transfer for turbulent flow in saturated porous media, *Int. Commun. Heat Mass Transfer*, **27**(6), 825–834.
- Rocamora Jr., F.D. and de Lemos, M.J.S., 2000b, Laminar Recirculating Flow and Heat Transfer in Hybrid Porous Medium-Clear Fluid Computational Domains, *Proc. 34th ASME — Natl Heat Transfer Conf.* (on CD-ROM), ASME-HTD-I463CD, Paper NHTC2000-12317, ISBN 0-7918-1997-3, Pittsburgh, PA.
- Rocamora Jr., F.D. and de Lemos, M.J.S., 2000c, Heat Transfer in Suddenly Expanded Flow in a Channel with Porous Inserts, *Proc. IMECE200 — ASME — Intern. Mech. Eng. Congr.*, ASME-HTD-366-5, pp. 191–195, ISBN: 0-7918-1908-6, Orlando, FL.
- Rocamora Jr., F.D. and de Lemos, M.J.S., 2000d, Prediction of Velocity and Temperature Profiles for Hybrid Porous Medium-Clean Fluid Domains, *Proc. CONEM2000 — Natl Mechanical Eng. Cong.* (on CD-ROM), Natal, Rio Grande do Norte, Brazil, August 7–11.
- Rudraiah, N., 1988, Turbulent convection in porous media with non-Darcy effects, *ASME-HTD* **96**(1), 747–754.
- Rudraiah, N., Siddheshwar, G., and Masuoka, T. 1995, Turbulent convection in a high porosity porous medium with convective acceleration, *J. Math. Phys. Sci.*, **19**, 93–117.
- Silva, R.A. and de Lemos, M.J.S., 2002, Laminar Flow in a Channel With a Layer of Porous Material Considering the Non-Linear Forchheimer Term (in Portuguese). *II National Congr. Mechanical Eng.*, João Pessoa-PB, Brazil.
- Silva, R.A. and de Lemos, M.J.S., 2003a, Numerical analysis of the stress jump interface condition for laminar flow over a porous layer, *Numer. Heat Transfer: Part A Appl.*, **43**(6), 603–617.
- Silva, R.A. and de Lemos, M.J.S., 2003b, Turbulent flow in a channel occupied by a porous layer considering the stress jump at the interface, *Int. J. Heat Mass Transfer*, **46**(26), 5113–5121.
- Slattery, J.C., 1967, Flow of viscoelastic fluids through porous media, *A.I.Ch.E.J.*, **13**, 1066–1071.
- Takatsu, Y. and Masuoka, T., 1998, Turbulent phenomena in flow through porous media, *J. Porous Media*, **1**(3), 243–251.
- Travkin, V.S. and Catton, I., 1992, Models of turbulent thermal diffusivity and transfer coefficients for a regular packed bed of spheres, *Proc. 28th Natl Heat Transfer Conf.*, San Diego, C-4, ASME-HTD-193, pp. 15–23.
- Travkin, V.S. and Catton, I., 1995, A two temperature model for turbulent flow and heat transfer in a porous layer, *J. Fluid Eng.*, **117**, 181–188.
- Travkin, V.S. and Catton, I., 1998, Porous media transport descriptions — non-local, linear and non-linear against effective thermal/fluid properties, *Adv. Colloid Interface Sci.*, **76–77**, 389–443.
- Travkin, V.S., Catton, I., and Gratton, L., 1993, Single-phase turbulent transport in prescribed non-isotropic and stochastic porous media, *Heat Transfer Porous Media*, ASME-HTD-240, 43–48.
- Travkin, V.S., Hu, K., and Catton, I., 1999, Turbulent Kinetic Energy and Dissipation Rate Equation Models for Momentum Transport in Porous Media, *Proc. 3rd ASME/JSME Joint Fluids Eng. Conf.* (on CD-ROM), Paper FEDSM99-7275, San Francisco, CA, July 18–23.

- Vafai, K. and Tien, C.L., 1981, Boundary and inertia effects on flow and heat transfer in porous media, *Int. J. Heat Mass Transfer*, **24**, 195–203.
- Wang, H. and Takle, E.S., 1995, Boundary-layer flow and turbulence near porous obstacles, *Boundary Layer Meteorol.*, **74**, 73–88.
- Ward, J.C., 1964, Turbulent flow in porous media, *J. Hydraul. Div. ASCE.*, **90**(HY5), 1–12.
- Warsi, Z.U.A., 1998, *Fluid Dynamics — Theoretical and Computational Approaches*, 2nd. edn., CRC Press, Boca Raton.
- Whitaker, S., 1966, Equations of Motion in Porous Media, *Chem. Eng. Sci.*, **21**, 291–300.
- Whitaker, S., 1967, Diffusion and Dispersion in Porous Media, *J. Am. Inst. Chem. Eng.*, **13**(3), 420–427.
- Whitaker, S., 1969, Advances in theory of fluid motion in porous media, *Ind. Eng. Chem.*, **61**, 14–28.
- Whitaker, S., 1999, *The Method of Volume Averaging*, Kluwer Academic Publishers, Dordrecht.

Part VI

Particle Migration and Deposition in Porous Media

11

Modeling Particle Migration and Deposition in Porous Media by Parallel Pathways with Exchange

Faruk Civan and Vinh Nguyen

CONTENTS

Summary	458
11.1 Introduction	458
11.2 Improved Plugging–Nonplugging Parallel Pathways	
Model	460
11.2.1 Plugging and Nonplugging Pathways with Exchange	
Model of Porous Media	460
11.2.2 Porosity	461
11.2.3 Fractions of Porous Media Containing the Plugging and	
Nonplugging Pathways	461
11.2.4 Permeability	462
11.2.5 Volumetric Flux of the Particle–Carrier Fluid Suspension ..	462
11.2.6 Particle Deposition Kinetics	463
11.2.7 Particle Transport	466
11.2.8 Average Particle Deposition and Overall Pressure	
Difference in a Core Plug	467
11.3 Numerical Solution	468
11.4 Experimental Validation	469
11.5 Discussion	477
11.6 Conclusions	479
11.7 Acknowledgment	479
Nomenclature	479
Appendix — Evaluation of Spatial Derivatives and Integrals	481
References	483

Summary

An improved microscopic phenomenological model and its numerical solution, and experimental validation for fine particle migration and deposition in porous media are presented. The mathematical model of Gruesbeck and Collins ("Entrainment and Deposition of Fine Particles in Porous Media," *SPEJ*, 22(6), 847–856, 1982) with the modifications and improvements made here and proposed by Civan (*Reservoir Formation Damage — Fundamentals, Modeling, Assessment, and Mitigation*, Gulf Pub. Co., Houston, TX, and Butterworth-Heinemann, Woburn, MA, 742 pp. 2000) is facilitated and applied.

A bundle of plugging and nonplugging parallel capillary pathways with exchange model of porous media is developed in order to represent the particle and fluid transfer processes associated with the flow of a particle–fluid suspension through porous media. Relatively smoother flow paths having larger cross-sectional areas are classified as the nonplugging pathways, which primarily undergo surface deposition and sweeping processes. Highly tortuous flow paths having significantly varying cross-sectional areas are called the plugging pathways, along which the particle bridges formed across the pore throats may interrupt the particle migration and limit the flow of the carrier fluid. Simultaneously, particle transfer between the plugging and nonplugging pathways is allowed by means of cross-flow. This model is used to simulate the porosity and permeability reduction, and the evolution of the plugging and nonplugging pathways by particle deposition in porous media.

The model is solved numerically by means of the method of lines approach and the results are shown to compare favorably with experimental data involving typical laboratory core tests undergoing suspension injection. The values of the various phenomenological parameters are determined by matching the simulation results to the measured data. The improved model provides an accurate representation of the phenomena resulting from the fine particle deposition and provides valuable insights into the consequences of fine particle migration through the plugging and nonplugging pathways in porous media.

11.1 Introduction

Impairment of porous media due to migration and deposition of particles has long been known to have a profound effect on the performance of the production and injection wells. Particle migration and deposition are the primary culprits for porous formation damage measured as permeability reduction during petroleum reservoir exploitation [1]. Formation damage may occur as a result of various types of particulate processes involving

drilling mud invasion, oil and gas production from petroleum reservoirs, injection of particle containing fluids into porous media, hydraulic fracturing of wells completed into subsurface reservoirs, and work-over operations applied to wells [1]. Therefore, appropriate considerations should be given to the modeling of the effects of the various particulate phenomena in the prediction of the porous media impairment and reduction of well performance.

There are various mechanisms causing permeability impairment and formation damage processes involving the flow of particulate suspension through porous media, such as surface deposition and sweeping, pore-throat plugging, and internal pore-filling. Previous studies have shown that formation damage can be a result of one of these mechanisms or a combination of them. Gruesbeck and Collins [2] developed a partial differential equation type model based on the concept of parallel flow of suspension of particles through the plugging and nonplugging pathways as illustrated in Figure 11.1. The porous media depicted in Figure 11.1 has a bimodal pore structure incorporating the attributes of the plugging and nonplugging pathways. A typical measured data of the pore and pore-throat size distributions of geological porous formations indicate bimodal distributions including a coarse grains region containing the nonplugging pathways and a fine grains region containing the plugging pathways [1]. However, Gruesbeck and Collins [2] provide only an incomplete set of input data as to the actual values of the various parameters used in their simulation studies. Thus, it is impossible to verify the validity of their model and reproduce their simulation results.

The parallel pathways model originally presented by Gruesbeck and Collins [2] has several shortcomings. They assumed that the plugging and nonplugging pathways are interconnected and therefore hydraulically

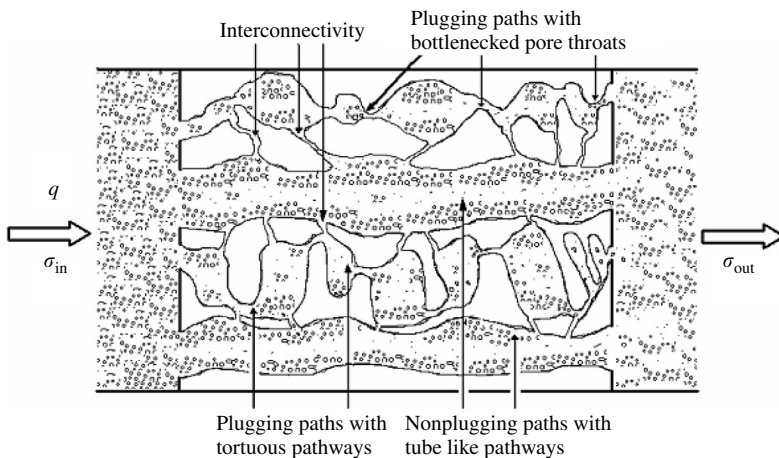


FIGURE 11.1

Realization of plugging and nonplugging parallel pathways with exchange for particle migration and deposition in porous media.

communicating. However, they did not allow for particle exchange between these pathways. The most limiting assumption is the consideration of the same particle concentrations in both the plugging and nonplugging pathways. They also assumed the fractions of the plugging and nonplugging pathways to remain constant, which is not a true representation of the porous media undergoing an alteration. As demonstrated here, the bulk volume fractions of the porous medium containing such pathways generally vary as the simultaneous entrainment and deposition of particles progress. Further, some of their formulations required corrections as pointed out by Civan [1,3] and here. Civan [3] made some improvements and generalizations to the model but he did not provide any numerical results for this modified model and a verification of it with experimental data.

Here, we develop a numerical solution scheme for the improved plugging–nonplugging parallel pathways model of Civan [1,3] after further minor improvements made here, and validate it against the experimental data of Gruesbeck and Collins [2]. First, the formulation for the phenomenological model and the methodology for determination of the model parameters are presented. Then a method of lines numerical scheme implementing the finite difference formulae for algebraic approximations of the spatial derivatives is developed to solve the problem. The applications of the model and the parameter estimation method are demonstrated using several examples. Finally, the testing and validation of the improved model with experimental data for impairment of porous media by particle migration and deposition is presented. The values of the various phenomenological parameters and comparison of the simulation results with experimental data are also provided.

11.2 Improved Plugging–Nonplugging Parallel Pathways Model

The porous medium is assumed incompressible, homogenous, and isotropic. The fluid is considered incompressible and Newtonian. The flow is single-phase, one-dimensional rectilinear, horizontal, and Darcian. The overall system is isothermal. The fine particles involving the various particulate processes are relatively smaller than the pore size, incompressible, and rigid. The physical properties of the particles and the carrier fluid are constant.

11.2.1 Plugging and Nonplugging Pathways with Exchange Model of Porous Media

The central and unique concept of the present model is the visualization of the flow paths in the form of a bundle of capillary parallel pathways interacting with each other through cross-flow as depicted in [Figure 11.1](#).

Two different types of pathways are distinguished in porous media depending on the involved mechanisms of fines retention. Smoother flow paths having larger cross-sectional areas can undergo surface deposition and sweeping processes. Surface deposition narrows the flow tubes without obstructing the fluid flow. These paths are called nonplugging. The nonplugging pathways cannot be completely clogged with particles because as the pore diameter is reduced by surface deposition, the interstitial fluid velocity increases to attain the critical particle mobilization condition necessary for sweeping of the pore surface deposits. On the other hand, the highly tortuous flow paths having significantly varying cross-sectional areas are called the plugging pathways. The particles approaching the constrictions, called the pore throats, may interrupt the flow along such paths by forming particle bridges across the pore throats. Then, the fluid is diverted to other flow paths. The particle concentrations of the fluids flowing through the plugging and nonplugging pathways are different because of the different particle deposition mechanisms involved along such paths and the cross-flow particle transfer occurring across these paths [1,3].

11.2.2 Porosity

Following Civan [1,3], ϕ_{po} and ϕ_{npo} indicate the initial pore volume fractions of the plugging and nonplugging pathways in porous media. The symbols ε_p and ε_{np} denote the bulk volume fractions occupied by the particle deposits in the respective flow paths. The instantaneous porosities in the plugging and nonplugging flow pathways and the total porosity of the porous medium are given, respectively, by:

$$\phi_p = \phi_{po} - \varepsilon_p \quad (11.1)$$

$$\phi_{np} = \phi_{npo} - \varepsilon_{np} \quad (11.2)$$

$$\phi = \phi_p + \phi_{np} \quad (11.3)$$

Hence, the overall porosity decreases as the porosity of the plugging and nonplugging pathways decrease by particle deposition.

11.2.3 Fractions of Porous Media Containing the Plugging and Nonplugging Pathways

The bulk volume fractions f_p and f_{np} of porous media containing the plugging and nonplugging pathways, respectively, vary due to the net deposition of particles. The plugging and nonplugging pathways volume fractions of the porous medium are approximated, respectively, as [3]:

$$f_p \cong \frac{\phi_p}{\phi} \quad (11.4)$$

$$f_{np} \cong \frac{\phi_{np}}{\phi} \quad (11.5)$$

Equations (11.3) to (11.5) yield:

$$f_p + f_{np} = 1 \quad (11.6)$$

11.2.4 Permeability

The permeability of the plugging and nonplugging pathways is given, respectively, by [4–7]:

$$K_p = K_{po} \exp \left[-\alpha \varepsilon_p^{n_1} \right] \quad (11.7)$$

$$K_{np} = K_{npo} \left[1 - \frac{\varepsilon_{np}}{\phi_{npo}} \right]^{n_2} \quad (11.8)$$

where n_1 and n_2 are empirical parameters. Equation (11.7) expresses the rapid permeability reduction by particle accumulation behind the obstructed pore throats. Equation (11.8) expresses the gradual permeability reduction by pore narrowing due to particle deposition over the pore surface. Then the fractional plugging and nonplugging pathways' weighted average permeability of the porous medium is given by [4,8]:

$$K = f_p K_p + f_{np} K_{np} \quad (11.9)$$

The arithmetic weighted average as described here is appropriate in the present case dealing with a cross-sectional area of a bulk porous medium which is normal to the flow associated with the plugging and nonplugging type pathways, through which the flows are parallel to each other. The validity of this approach has been proven independently by Civan [4] and Schechter [8] by applying Darcy's law for parallel flow. Had different property of porous media in series been considered in the flow direction, a harmonic average permeability would have to be resorted.

Combining Eqs. (11.7) to (11.9) yields [4–7]:

$$K = f_p K_{po} \exp \left[-\alpha \varepsilon_p^{n_1} \right] + f_{np} K_{npo} \left[1 - \frac{\varepsilon_{np}}{\phi_{npo}} \right]^{n_2} \quad (11.10)$$

11.2.5 Volumetric Flux of the Particle-Carrier Fluid Suspension

Assuming that the plugging and nonplugging pathways may interact with each other, the fluid fluxes through these pathways are expressed over the bulk cross-sectional area of porous media, respectively, by the following

expressions modified after Gruesbeck and Collins [2]:

$$u_p = f_p \frac{K_p}{K} u \quad (11.11)$$

$$u_{np} = f_{np} \frac{K_{np}}{K} u \quad (11.12)$$

Applying Eqs. (11.6), (11.9), (11.11), and (11.12), it can be shown that the total volumetric flux through porous media is given by:

$$u = u_p + u_{np} \quad (11.13)$$

Note that Gruesbeck and Collins [2] expressed the fluid fluxes through the individual cross-sectional areas of the plugging and nonplugging regions of the porous media instead of expressing them over the total cross-sectional area of the bulk porous media. Therefore, Eqs. (11.11) through (11.13) are different than those presented by Gruesbeck and Collins [2]. The present approach provides an expression for the total volume flux consistent with the usual convention for porous media flow formulation based on the total bulk porous cross-sectional area normal to the flow.

11.2.6 Particle Deposition Kinetics

Different kinetic laws govern the rate of fine particle deposition in different pathways. The rate of particle deposition in the plugging pathways is given by, considering that the pores will be filled following the particle bridging of the pore throats:

$$\frac{\partial \varepsilon_p}{\partial t} = (\delta + k_p \phi_p) u_p \sigma_p \quad (11.14)$$

$$\varepsilon_p = \varepsilon_{po} \quad \text{at } t = 0 \quad (11.15)$$

where σ_p is the volume fraction of particles in the fluid flowing through the plugging pathways, δ the pore-throat plugging constant, and k_p the pore-filling rate constant given by:

$$\begin{aligned} k_p &\neq 0, & \text{for } t > t_{cr} \quad \text{when } \beta < \beta_{cr}, \\ k_p &= 0, & \text{otherwise} \end{aligned} \quad (11.16)$$

where t_{cr} is a critical time, representing the instant that the pore throats are first obstructed by particles. The parameter $\beta = D_{pt}/D_p$ denoting the ratio of the pore-throat diameter D_{pt} to particle diameter D_p is given by [9]:

$$\frac{1}{\beta} \cong \frac{D_p(\mu m)}{30.0 \sqrt{K(\text{Darcy})}} \quad (11.17)$$

The critical value β_{cr} of β required for obstruction of the pore throats is determined by the following dimensionless correlation [1]:

$$\beta_{\text{cr}} = A(Re_p)^B + C \quad (11.18)$$

where A, B, C are some empirical constants and Re_p is the particle Reynolds number given as:

$$Re_p = \rho_p \sigma_p D_p \tau u_p / (\mu \phi_p) \quad (11.19)$$

where ρ_p is the particle density, μ is the particle-carrier fluid suspension viscosity, D_p is the mean particle diameter, and τ denotes the tortuosity of the flow path defined as the ratio of the hydraulic flow tube length to the porous media length. Thus, pore-throat obstruction does not occur when the value of β is greater than its critical value β_{cr} determined by Eq. (11.18).

Note that Eq. (11.14) is slightly different than the original equation of Civan [1] in that it introduces a pore-throat plugging constant δ . This constant accounts for the gradual particle buildup at the pore throat in a manner to reduce its diameter gradually until the initiation of the pore-throat obstruction by particle bridging. This process continues as long as β is less than β_{cr} . Thereafter, the pore throat is completely obstructed by particles. Then, the particles pile up in the pore space behind the clogged pore throats in the plugging pathways as long as the carrier fluid can filter through the space in between the deposited particles.

The rate of deposition in the nonplugging pathways is expressed by [1,3,5–7]:

$$\frac{\partial \varepsilon_{\text{np}}}{\partial t} = k_d u_{\text{np}} \sigma_{\text{np}} \phi_{\text{np}}^{2/3} - k_e \varepsilon_{\text{np}} \phi_{\text{np}}^{2/3} \eta_e (\tau_{\text{np}} - \tau_{\text{cr}}) \quad (11.20)$$

$$\varepsilon_{\text{np}} = \varepsilon_{\text{npo}} \quad \text{at } t = 0 \quad (11.21)$$

The first term on the right side of Eq. (11.20) accounts for the surface deposition and the second term accounts for the mobilization and sweeping of particles attached to the surface. Here, k_d and k_e denote the surface deposition and mobilization rate constants, respectively. The mobilization rate constant is assigned the values of

$$\begin{aligned} k_e &\neq 0 & \text{for } \tau_{\text{np}} \geq \tau_{\text{cr}} \\ k_e &= 0 & \text{for } \tau_{\text{np}} < \tau_{\text{cr}} \end{aligned} \quad (11.22)$$

where τ_{np} is the wall shear stress and τ_{cr} is the critical shear stress required for sweeping of particles from the surface deposits.

Assuming a Newtonian fluid behavior, the parameter τ_{np} is the wall shear stress estimated according to the equation, given by:

$$\tau_{\text{np}} = 8\mu v_{\text{np}}/D_{\text{np}} \quad (11.23)$$

where μ is the suspension viscosity. v_{np} is the interstitial velocity, expressed by the Dupuit relationship as:

$$v_{\text{np}} = \tau u_{\text{np}}/\phi_{\text{np}} \quad (11.24)$$

where τ denotes the tortuosity of the flow path defined as the ratio of the hydraulic flow tube length to the porous media length. D_{np} is the mean pore diameter in the nonplugging pathways given by [9]:

$$D_{\text{np}} \cong C_1 4\sqrt{2\tau} \sqrt{\frac{K_{\text{np}}}{\phi_{\text{np}}}} \quad (11.25)$$

where C_1 is an empirical shape factor. Equation (11.23) can only provide a macroscopic average value of the shear stress over the representative volume element of porous media, in which the shear stress vary by position due to the local differences in the pore space attributes and interstitial fluid velocity.

The critical shear stress τ_{cr} is a characteristic value essentially depending on the interaction forces between the particles and the pore surface. It can be predicted theoretically using the following expression [10]:

$$\tau_{\text{cr}} = H/(24D_p l^2) \quad (11.26)$$

where D_p is the average particle diameter, l is the separation distance between the particles present at the pore surface, and $H = 3.0 \times 10^{-13}$ erg is the Hamaker coefficient. However, this equation may only provide a first-order accurate estimate value because the ideal theory omits the effect of surface roughness and particle stickiness on the critical shear stress required for particle sweeping from the pore surface [11,12]. The critical shear stress or critical interstitial fluid velocity can be determined more accurately by experimental methods as demonstrated by Gruesbeck and Collins [2].

A fraction of the particles attached to the pore surface may have been covered by a multilayer particle deposition and therefore prevented from entrainment by the flowing suspension. The fraction η_e of the uncovered deposits available for sweeping from the pore surface is estimated by [13]:

$$\eta_e \cong \exp(-k\varepsilon_{\text{np}}) \quad (11.27)$$

where k denotes an empirical factor.

11.2.7 Particle Transport

Considering different particle concentrations in the plugging and nonplugging pathways, and neglecting the particle transport by dispersion, the one-dimensional total volumetric balances of the particles are expressed separately in the plugging and nonplugging paths [1,3]. The volumetric balance equations for the water (flowing carrier fluid) and fine particles (migrating plus deposited particles) in the plugging pathways are given, respectively, by [1]:

$$\frac{\partial}{\partial t}(\phi_p \sigma_{wp}) + \frac{\partial}{\partial x}(u_p \sigma_{wp}) = \dot{q}_{wp} \quad (11.28)$$

$$\frac{\partial}{\partial t}(\phi_p \sigma_p + \varepsilon_p) + \frac{\partial}{\partial x}(u_p \sigma_p) = \dot{q}_p \quad (11.29)$$

The water and particle fractions in the flowing fluid add up to one:

$$\sigma_{wp} + \sigma_p = 1 \quad (11.30)$$

Combining Eqs. (11.28) to (11.30) yields the volumetric balance equation for the particles in the suspension flowing through the plugging pathways, as:

$$\phi_p \frac{\partial \sigma_p}{\partial t} + u_p \frac{\partial \sigma_p}{\partial x} + (1 - \sigma_p) \frac{\partial \varepsilon_p}{\partial t} = (1 - \sigma_p) \dot{q}_p - \sigma_p \dot{q}_{wp} \equiv \dot{q}_{ep} \quad (11.31)$$

where \dot{q}_{ep} represents the rate of the effective particle transfer from the plugging to nonplugging pathways. Similarly, the volumetric balance equation for the particles in the fluid flowing through the nonplugging pathways can be expressed by:

$$\phi_{np} \frac{\partial \sigma_{np}}{\partial t} + u_{np} \frac{\partial \sigma_{np}}{\partial x} + (1 - \sigma_{np}) \frac{\partial \varepsilon_{np}}{\partial t} = (1 - \sigma_{np}) \dot{q}_{np} - \sigma_{np} \dot{q}_{wnp} \equiv \dot{q}_{enp} \quad (11.32)$$

where \dot{q}_{enp} represents the rate of the effective particle transfer from the nonplugging to plugging pathways. The rate of particle exchange between the plugging and nonplugging pathways is expressed by:

$$\dot{q}_{ep} = -\dot{q}_{enp} = \kappa(\sigma_p - \sigma_{np}) \quad (11.33)$$

where κ is the effective particle transfer coefficient. Combining Eqs. (11.31) to (11.33) yields the following expressions for particle transport in different pathways:

$$\phi_p \frac{\partial \sigma_p}{\partial t} + u_p \frac{\partial \sigma_p}{\partial x} + (1 - \sigma_p) \frac{\partial \varepsilon_p}{\partial t} = \kappa(\sigma_p - \sigma_{np}) \quad (11.34)$$

$$\sigma_{\text{np}} \frac{\partial \sigma_{\text{np}}}{\partial t} + u_{\text{np}} \frac{\partial \sigma_{\text{np}}}{\partial x} + (1 - \sigma_{\text{np}}) \frac{\partial \varepsilon_{\text{np}}}{\partial t} = -\kappa (\sigma_p - \sigma_{\text{np}}) \quad (11.35)$$

The initial and boundary conditions are given by:

$$\sigma_p = \sigma_{\text{np}} = 0, \quad 0 \leq x \leq L, \quad t = 0 \quad (11.36)$$

$$\sigma_p = \sigma_{\text{np}} = \sigma_{\text{in}}, \quad x = 0, \quad t > 0 \quad (11.37)$$

where σ_{in} denotes the particle volume concentration in the injection fluid.

11.2.8 Average Particle Deposition and Overall Pressure Difference in a Core Plug

In experimental studies using core plugs, usually the net amount of particle deposition is determined by the difference in particle concentrations between the injected and the effluent solutions. However, the overall pressure drop across the core plug is directly measured. For validation of the model, it is necessary to compare the model predictions with the experimental measurements on the same basis.

The core-length average cumulative volume of particles deposited per unit volume of porous media is given by:

$$\bar{\varepsilon}(t) = \bar{\varepsilon}_p(t) + \bar{\varepsilon}_{\text{np}}(t) \equiv \frac{1}{L} \int_0^L [\varepsilon_p(t) + \varepsilon_{\text{np}}(t)] dx \quad (11.38)$$

Gruesbeck and Collins [2] report their particle deposition data in core plugs based on the initial pore volume ($\bar{\varepsilon}/\phi_0$), whereas the above formulation considers particle deposition per unit bulk volume basis ($\bar{\varepsilon}$). Therefore, the difference between them is a factor of the initial porosity ϕ_0 .

The pressure drop across a core plug can be calculated readily using Darcy's law given as:

$$u = \frac{q}{A} = -\frac{K(x,t)}{\mu} \frac{\partial P(x,t)}{\partial x} \quad (11.39)$$

Therefore, integrating Eq. (11.39) over the core length for constant rate flow yields [14]:

$$\Delta P(t) = P_{\text{out}} - P_{\text{in}} = \int_{P_{\text{in}}}^{P_{\text{out}}} \partial P(x,t) = -\mu u \int_0^L \frac{dx}{K(x,t)} \quad (11.40)$$

The initial pressure drop for homogeneous porous media with constant permeability K_0 is given by:

$$\Delta P_o = \Delta P(0) = -\mu u \frac{L}{K_0} \quad (11.41)$$

Hence, using Eqs. (11.40) and (11.41), the overall pressure drop ratio over the core length is expressed by:

$$\frac{\Delta P(t)}{\Delta P_o} = \frac{K_0}{L} \int_0^L \frac{dx}{K(x,t)} \quad (11.42)$$

11.3 Numerical Solution

For a prescribed set of values of the various phenomenological parameters Eqs. (11.14), (11.15), (11.20), (11.21), (11.34), and (11.37) can be solved simultaneously to obtain the quantities ε_p , ε_{np} , σ_p , and σ_{np} as a function of time (or in number of pore volumes) and distance along the core length. Other useful quantities such as the cumulative particle deposition over the core length ($\bar{\varepsilon}$) and the overall pressure drop across the core (ΔP) can be deduced by appropriate integration according to Eqs. (11.38) and (11.42). Solutions to these equations yield the net amount of particle deposition in different pathways of the formation and reveal various other information including the instantaneous fractions of the plugging and nonplugging pathways, hydraulic resistance buildup, porosity reduction, and permeability impairment.

The numerical simulation of the particle migration and deposition in porous media using the present mathematical model was carried out over a uniform linear grid system, depicted in Figure 11.2, by implementing

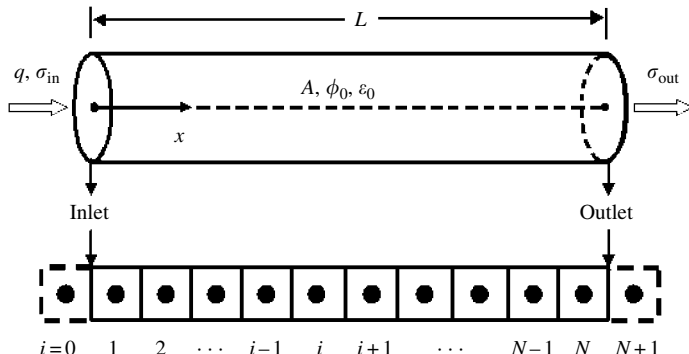


FIGURE 11.2

Spatial discretization of core plug or sand pack for numerical solution.

the discretized set of algebraic equations presented in the appendix. The governing equations are nonlinear, coupled, and first-order type partial differential equations (PDEs). For convenient numerical solution, the method of lines is applied here. This method reduces the nonlinear PDEs to a convenient set of first-order ordinary differential equations (ODEs). For this purpose, the central-finite difference formulae are substituted for algebraic representation of the spatial derivatives. The resulting system of first-order ODEs can then be solved readily by an appropriate numerical method, such as the Runge–Kutta method. As a computational tool, the “ND Solve” built-in function of *Mathematica* 4.2® [15] version 4.2.1.0 is used to solve the resulting system of ODEs. NDSolve provides a numerical solution to the ODEs, conveniently, through the application of various numerical schemes. In the simulation, the NDSolve is forced to use the Runge–Kutta method as an option to solve the system of ODEs. The integral terms appearing in Eqs. (11.38) and (11.42) are evaluated using the Gaussian quadrature rule.

11.4 Experimental Validation

To verify the validity of the model, the governing equations are solved numerically by assuming trial values for the various phenomenological parameters until a match is obtained to the experimental data of Gruesbeck and Collins [2]. In their experimental studies, they injected suspensions of glass beads and water into the columns of sand packs. The effluent glass beads concentration and cumulative glass beads deposited in the sand pack were measured as a function of the number of pore volumes of suspension of glass beads (in the unit of initial pore volume) injected at a constant rate. [Table 11.1](#) provides the experimental data on the preparation of the sand pack and the suspensions of glass beads.

The tortuosity of cubic packing of equal-sized spheres is estimated as $\tau = \sqrt{2}$ according to Carman [16]. The viscosity of the hard sphere particle suspension is predicted by the Brinkman’s [17] extension of Einstein’s equation given as follows:

$$\mu = \mu_0 / (1 - \sigma)^{2.5} \quad (11.43)$$

where μ_0 denotes the carrier liquid viscosity and σ is the volume concentration or fraction of suspended particles. Gruesbeck and Collins [2] do not provide any information about the temperature and the carrier fluid used for the suspension of spherical glass particles. We considered water at 20°C as the carrier fluid.

The number of grid blocks was chosen to be 20 for simulation purposes considering that the grid size is sufficiently small (0.762 cm). *Mathematica* 4.2® [15] automatically determines and uses an optimum time step size. The relative

TABLE 11.1

Experimental Input Data

Quantities	Values	Units
L	15.3 ^a	cm
d	3.81 ^a	cm
ϕ	0.30 ^a	Fraction
$PV_0 = AL\phi_0$	52.1	cm ³
τ	$\sqrt{2}$ ^b	cm/cm
$\varepsilon_{p,i}$	0.0	Fraction
$\varepsilon_{np,i}$	0.0	Fraction
D_p	7.5 ^a	μm
D_g	274.0 ^a	μm
D_{ps}	42.0 ^a	μm
ρ_p	2.85	g/cm ³
q	1.7 ^a and 5.1 ^a	cm ³ /sec
σ_{in}	9.5×10^{-4} ^a	cm ³ /cm ³
K	1.0 ^a	Darcy
μ	1.0 ^c	cP

^a Modified from Gruesbeck, C. and Collins, R.E., *SPEJ*, 22(6): 847–856, 1982.

^b Provided by Carman, P.C., *Trans. Inst. Chem. Eng. (London)*, 15: 150–167, 1937.

^c Calculated by the Brinkman's [17] extension of Einstein's equation considering water as the carrier fluid at 20°C.

deviation between the numerical solutions at consecutive iteration steps, denoted by the superscripts of s and $(s + 1)$, is defined as:

$$E_r^{(s+1)} = \frac{F^{(s+1)} - F^{(s)}}{F^{(s+1)}} \quad (11.44)$$

where $F \in (\varepsilon_p, \varepsilon_{np}, \sigma_p, \sigma_{np})$ represents the solution array. The solution of the nonlinear system of ODEs is carried out iteratively until the solution satisfactorily converges to a relative error of 1.0×10^{-6} or less.

The values of the various phenomenological parameters have been adjusted in order to match the measured data. In view of the initial porosity and flow rate, a set of parameters is guessed to start with. The most sensitive parameters are the deposition and entrainment (mobilization or sweeping) rate constants, such as δ , k_p , k_d , and k_e . All of these parameters are flow rate dependent [1]. For higher flow rates, we expect a lower deposition rate constant and higher entrainment rate constant, and vice versa. The trial process is carried out mostly by adjusting these four rate constants.

Table 11.2 shows the values of the parameters yielding a successful match to the experimental data of Gruesbeck and Collins [2]. Because the model is nonlinear, there is no guarantee about the uniqueness of the parameter values yielding matches to the experimental data. Gruesbeck and Collins [2]

TABLE 11.2
Adjustable Parameter Values

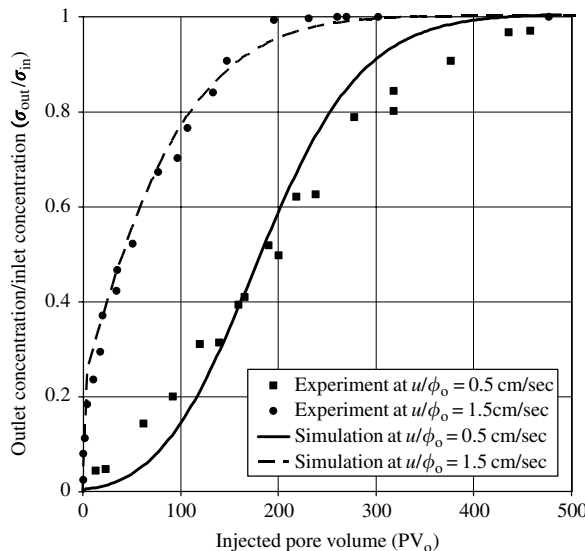
Parameters	Values ^a		Units cm/sec
	$u/\phi_0 = 0.5$	$u/\phi_0 = 1.5$	
$K_{p,i}$	1.0	1.0	Darcy
$K_{np,i}$	25.0	25.0	Darcy
α	10.0	10.0	Dimensionless
n_1	0.55	0.25	Dimensionless
n_2	4.0	6.0	Dimensionless
f_{po}	0.34	0.34	Fraction
δ	0.1	0.1	per cm
k_p	1.0	10.0	per cm
k_d	1.28	0.58	per cm
k_e	0.001	0.002	per Pa
τ_{cr}	20.0	20.0	Pa
κ	0.0001	0.0001	per sec
k	13.0	1.0	Dimensionless
C_1	0.083	0.083	Fraction
A^b	4.5	4.5	Dimensionless
B^b	0.05	0.05	Dimensionless
C^b	1.62	1.62	Dimensionless

^a All data were obtained by history matching unless otherwise noted.

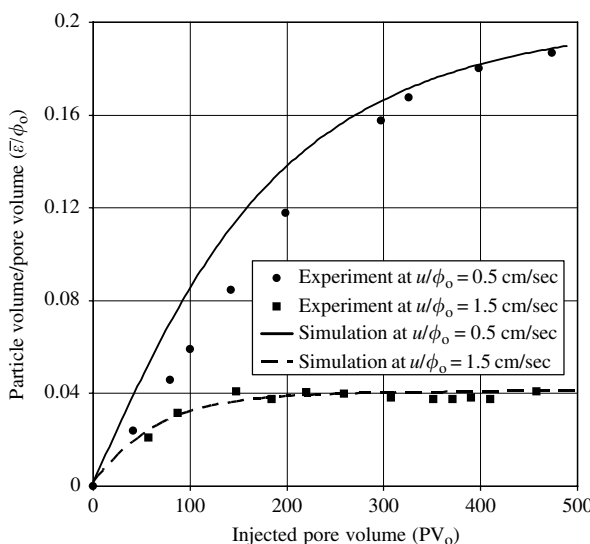
^b Adapted from the correlation of Civan, F., *Reservoir Formation Damage—Fundamentals, Modeling, Assessment, and Mitigation*, Gulf Publ. Co., Houston, TX, and Butterworth-Heinemann, Woburn, MA, p. 742, 2000.

demonstrated that some of these parameters could be determined directly by conducting experiments under properly designed special conditions. However, they only provide an incomplete set of data for the actual values of the various parameters. Nevertheless, the probability of unique determination of the parameter values improves when the model response is matched simultaneously to different types of measurements made during a prescribed core plug testing. Here, the measurements of the effluent particle concentration, the volume of particles deposited per unit pore volume, and the overall pressure difference across the core plug versus the number of injected pore volume were matched simultaneously. Consequently, the attainability of uniqueness in the estimated parameter values is favorably better in the present exercise.

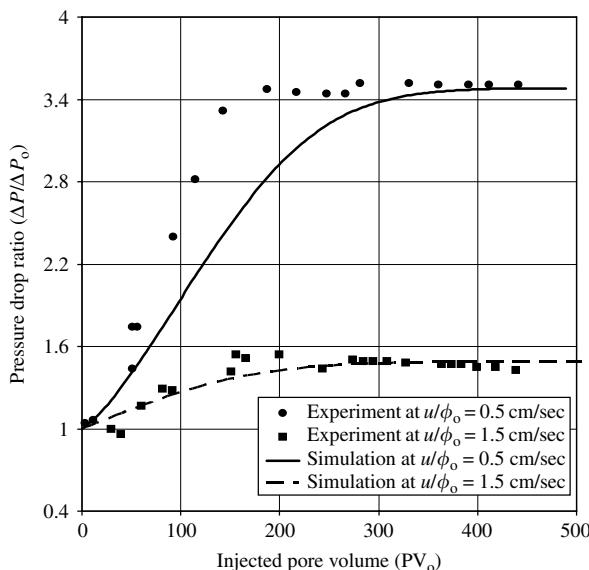
The simulation results are shown in Figures 11.3, 11.4, and 11.5. The satisfactory prediction of the experimental observations indicates that the model based on the plugging and nonplugging pathways concept is valid for this experimental system. The results of Figure 11.3 and Figure 11.4 indicate that equilibrium is reached after a certain time. This can be explained from the deposition rate laws. When the plugging pathways are eliminated by pore-throat plugging, the flow will be diverted to the nonplugging pathways. Particle detainment can still happen in the plugging pathways but with

**FIGURE 11.3**

Suspension of particle concentration in the effluent versus injected pore volume of suspension during deposition and entrainment of 5–10 μm diameter (7.5 μm average) glass beads in a sand pack of 250–297 μm diameter (274 μm average) grains using a 9.5×10^{-4} injection suspension volume fraction and interstitial velocity of 0.5 and 1.5 cm/sec.

**FIGURE 11.4**

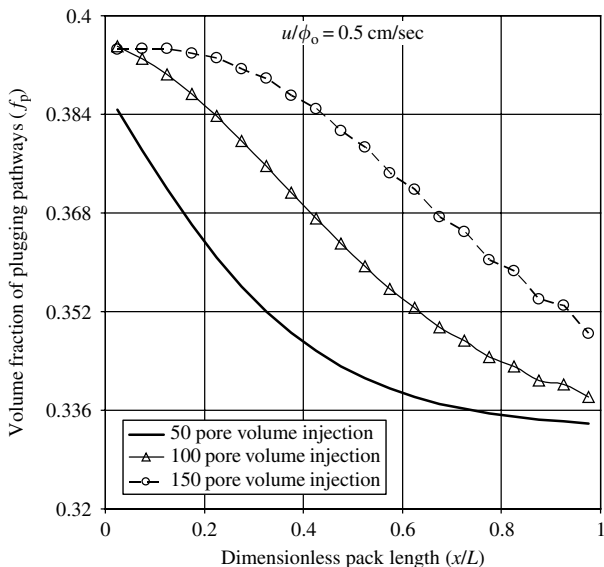
Volume fraction of fine particles retained versus injected pore volume of suspension during deposition and entrainment of 5–10 μm diameter (7.5 μm average) glass beads in a sand pack of 250–297 μm diameter (274 μm average) grains using a 9.5×10^{-4} injection suspension volume and interstitial velocity of 0.5 and 1.5 cm/sec.

**FIGURE 11.5**

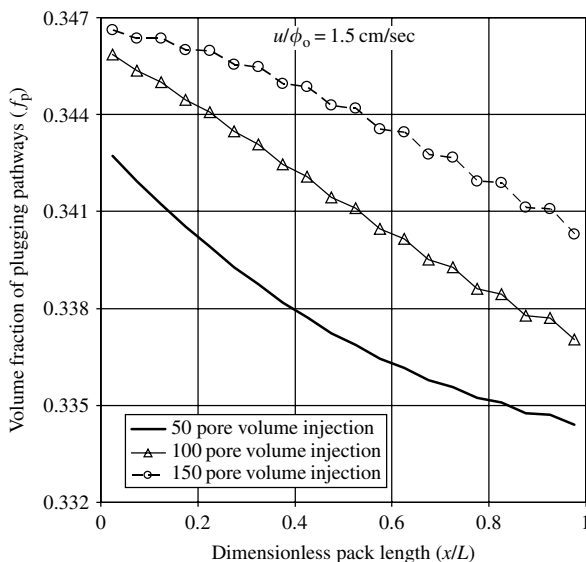
Pressure drop across the sand pack versus injected pore volume of suspension during deposition and entrainment of 5–10 μm diameter (7.5 μm average) glass beads in a sand pack of 250–297 μm diameter (274 μm average) grains using a 9.5×10^{-4} injection suspension volume fraction and interstitial velocity of 0.5 and 1.5 cm/sec.

reduced magnitude because the flow rate through the plugging pathways is much lowered. Then all the flow is diverted into the nonplugging pathways. The plateaus depicted in Figures 11.3, 11.4, and 11.5 are attained when a dynamic equilibrium is established between the surface deposition and entrainment processes. This reveals that the nonplugging pathways will never be clogged by surface deposition of the very small particles considered in the present case compared to the mean-hydraulic diameter, even though the mean-hydraulic diameter decreased to below the initial tube diameter. However, for suspensions with large-diameter particles, the nonplugging pathways could eventually transform into the types of the plugging pathways, which could be clogged by large particles under favorable conditions. Using the above formulation and Eq. (11.18), it is possible to calculate the pore-throat to particle diameter ratio required in order for such transformation to take place. Figure 11.6 and Figure 11.7 show the variation of the bulk volume fraction of the plugging pathways along the core length at various times. It is observed that the volume fraction of the plugging pathways is actually increasing. This is because the decrease rate of the total pore volume is greater than the decrease rate of the plugging pathways volume fraction.

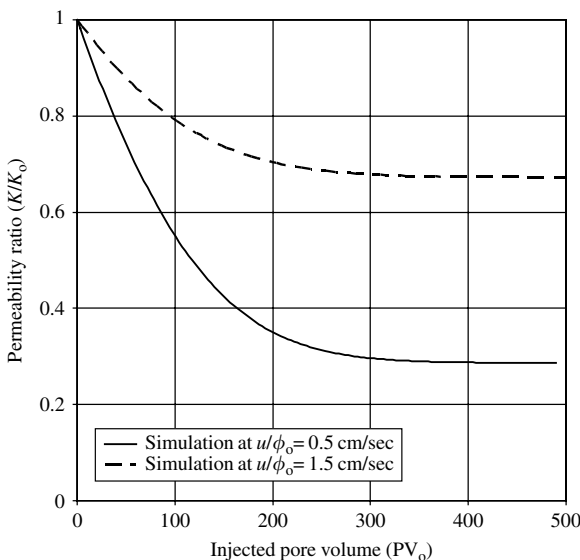
Next, we turn our attention to the permeability impairment in the sand pack due to the deposition and entrainment processes. Figure 11.8 shows the permeability reduction with respect to the pore volume of suspension

**FIGURE 11.6**

Volume fraction of plugging pathways along the sand pack versus distance from the injection port for various pore volume of suspension injected during deposition and entrainment of 5–10 μm diameter (7.5 μm average) glass beads in a sand pack of 250–297 μm diameter (274 μm average) grains using a 9.5×10^{-4} injection suspension volume fraction and interstitial velocity of 0.5 cm/sec.

**FIGURE 11.7**

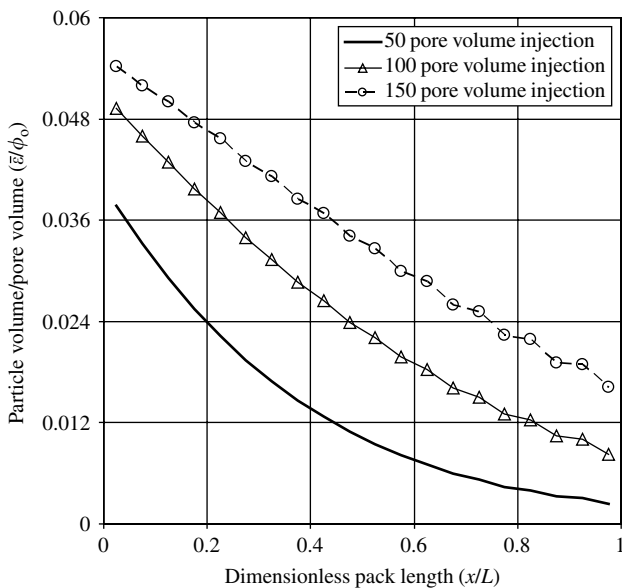
Volume fraction of plugging pathways along the sand pack versus distance from the injection port for various pore volume of suspension injected during deposition and entrainment of 5–10 μm diameter (7.5 μm average) glass beads in a sand pack of 250–297 μm diameter (274 μm average) grains using a 9.5×10^{-4} injection suspension volume fraction and interstitial velocity of 1.5 cm/sec.

**FIGURE 11.8**

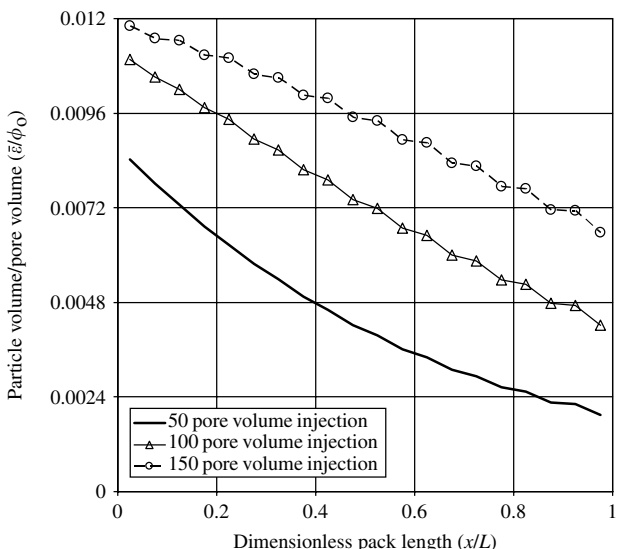
Permeability reduction versus injected pore volume of suspension during deposition and entrainment of $5\text{--}10\mu\text{m}$ diameter ($7.5\mu\text{m}$ average) glass beads in a sand pack of $250\text{--}297\mu\text{m}$ diameter ($274\mu\text{m}$ average) grains using a 9.5×10^{-4} injection suspension volume fraction and interstitial velocity of 0.5 and 1.5 cm/sec .

injected. The lower injection velocity of $u/\phi_0 = 0.5\text{ cm/sec}$ creates more damage to the pack than the higher velocity. This makes sense because the lower the flow rate, the longer the retention time of the particle inside the sand pack. Thus, at low flow rates, the particles are less mobile and tend to attach to the pore surface readily. Also, a low flow rate may not create sufficient shear stress to mobilize the uncovered surface deposits. [Figure 11.9](#) and [Figure 11.10](#) show the amount of particle deposition along the pack length with respect to time. It is obvious that the low flow rate is associated with more particle deposition than the high flow rate.

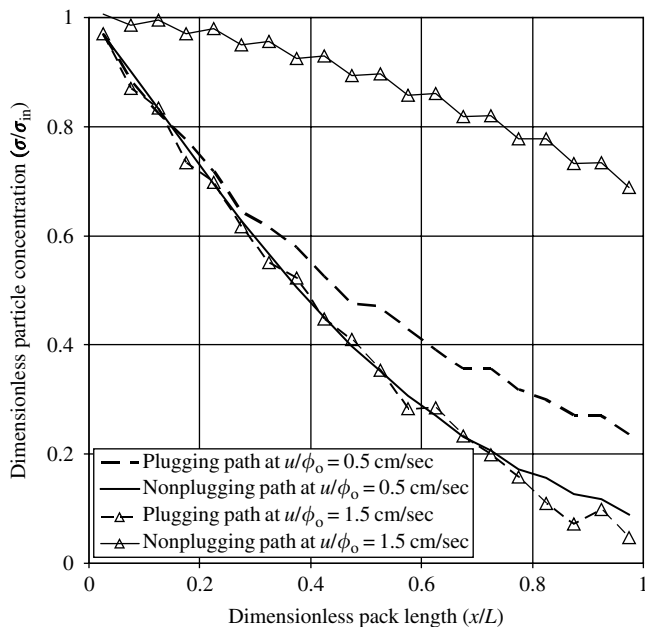
To better illustrate the capability of the present microscopic phenomenological model, we examine the behavior of particles in each flow path. [Figure 11.11](#) shows the changes in suspension volume concentration along the sand pack in the plugging and nonplugging pathways at 50 pore volumes injection for injection fluid velocities of 0.5 and 1.5 cm/sec . First, as suggested by Civan [1,3], the plot shows that the particle concentrations of the flowing suspension in both pathways would not be equal to each other. In contrast, Gruesbeck and Collins [2] make the assumption of equal particle concentrations for both the plugging and nonplugging pathways. At the 0.5 cm/sec injection velocity, the suspension concentration in the plugging pathways is higher than in the nonplugging pathways. This implies that more deposition occurs in the nonplugging pathway than in the plugging

**FIGURE 11.9**

Volume fraction of fine particles retained along the sand pack versus distance from the injection port for various pore volumes of suspension injected during deposition and entrainment of 5–10 μm diameter (7.5 μm average) glass beads in a sand pack of 250–297 μm diameter (274 μm average) grains using a 9.5×10^{-4} injection suspension volume fraction and interstitial velocity of 0.5 cm/sec.

**FIGURE 11.10**

Volume fraction of fine particles retained along the sand pack versus distance from the injection port for various pore volumes of suspension injected during deposition and entrainment of 5–10 μm diameter (7.5 μm average) glass beads in a sand pack of 250–297 μm diameter (274 μm average) grains using a 9.5×10^{-4} injection suspension volume fraction and interstitial velocity of 1.5 cm/sec.

**FIGURE 11.11**

Suspension particle concentrations in plugging and nonplugging pathways along the sand pack versus distance from the injection port for 50 pore volume of suspension injected during deposition and entrainment of $5\text{--}10\ \mu\text{m}$ diameter ($7.5\ \mu\text{m}$ average) glass beads in a sand pack of $250\text{--}297\ \mu\text{m}$ diameter ($274\ \mu\text{m}$ average) grains using a 9.5×10^{-4} injection suspension volume fraction and interstitial velocity of 0.5 and 1.5 cm/sec.

pathway. Thus, at low flow rates, the deposition may be more significant in the nonplugging pathways than in the plugging pathways. At the 1.5 cm/sec injection velocity, the difference between the concentrations in the two pathways is much more pronounced. The suspension concentration in the plugging pathways now is much lower than in the nonplugging pathways. One possible explanation is that, at high flow rates, the plugging pathways are clogged much rapidly and more particles fill up the pores behind the obstructed pore throats, which allows the carrier fluid flow but prevents particle migration. In the nonplugging pathways, the high flow rate induces more mobilization of the uncovered particles present at the surface. Therefore, the decrease in suspension concentration is not as much pronounced.

11.5 Discussion

The plugging–nonplugging parallel pathways with exchange model presented here with modifications after Gruesbeck and Collins [2] distinguishes

between the bundles of capillary flow paths with regard to the mechanism of particle deposition and the evolution of the bundle of capillary flow paths as a result of particle deposition. This description provides valuable information about the internal detail concerning the particle deposition phenomena which could not be obtained from a macroscopic model in a convenient manner. However, the model involves a set of 17 parameters, which have been determined by adjusting their values to match the numerical solution of the model to experimental data. Because the model is a consistent representation of the governing mechanisms, it is possible to fit any set of experimental data. This course had to be taken here because of the lack of sufficient experimental data on the parameter values from Gruesbeck and Collins [2]. In fact, to the best of the authors' knowledge, there is no one complete set of measured data available till date in the literature which can be used with the present model.

In order for the model to be predictive, experiments should be carefully designed and conducted for *a priori* determination of the model parameters. For example, Gruesbeck and Collins [2] determined the critical shear stress or critical interstitial fluid velocity accurately by conducting experimental studies under sufficiently rapid flow conditions which would allow only particle sweeping and not any particle deposition for all practical purposes. By measuring the amount of particles entering and leaving a core sample at various times, Čerňanský and Široký [18] were able to determine the empirical relationships for permeability impairment by particle deposition and the values of the particle deposition and sweeping rate constants. It was also possible to determine the ratio of these rate constants by means of the measurements at the equilibrium condition when the rate of deposition equalized to the rate of sweeping. Further, Civan [1] pointed out that Čerňanský and Široký [18] permeability–porosity data actually showed two distinct regions which could be attributed to the plugging and nonplugging pathways, and the weighting coefficient appearing in their empirical correlation of the permeability versus porosity could be interpreted as the fraction of the plugging pathways. Wojtanowicz et al. [19] derived special algebraic relationships for the various particle deposition mechanisms allowing the direct determination of the values of the model parameters under certain prevailing conditions. The application of their equations, however, required the conduction of experiments at conditions under which the individual expressions were applicable. Other data, such as the initial fraction of the plugging and nonplugging pathways, and the porosity of the porous media regions containing these pathways can be readily measured by means of petrographical analysis of thin porous media sections.

The majority of the particles present in natural sandstone formations are the clays of various types. The mechanism of retention of the submicrometer clay particles involves transport by Brownian diffusion toward the pore surface. Whereas, the fine particles used in the particulate suspension by Gruesbeck and Collins [2] involving the experimental data used here are the glass, which behaves differently than the clay minerals. The retention mechanism of the relatively large glass particles involves interception and settling. However, the

present model can adequately represent the overall surface and pore-throat particulate deposition phenomena at the macroscopic scale in terms of the particle deposition and mobilization rate constants determined as average values defined over the representative volume element of porous media. A comprehensive review and discussion of the relevant interaction forces between particles and pore surface, and the potential mechanisms of formation damage resulting from particulate processes are provided elsewhere by Khilar and Fogler [20].

By the evidence provided here, it is possible to carry out specially designed experiments in order to measure the values of the various model parameters instead of determining their values by matching the model to core flow data. However, the aforementioned techniques offered in the literature are usually tedious and time consuming. Nevertheless, the advantage of determining the values of the model parameters *a priori* in this way is that the model can then be used as a predictive tool.

11.6 Conclusions

The mathematical model of Gruesbeck and Collins [2], with the modifications and improvements proposed by Civan [1,3] and here, was shown to simulate the consequences of the particulate processes in porous media successfully. The numerical scheme developed for the improved model yielded stable and practical numerical solutions and the results compared favorably with the experimental data. It has been demonstrated that the improved model yields an accurate representation of the phenomena resulting from particle deposition in porous media and provides valuable insights into the mechanism of partitioning of the particles between the plugging and nonplugging pathways in porous media.

11.7 Acknowledgment

The support by the PoroMechanics Institute at the University of Oklahoma is gratefully acknowledged. We also wish to express our appreciation to Younane Abousleiman for his assistance and discussion during the numerical solution of the mathematical model.

Nomenclature

A area, cm^2

d core diameter, cm

D_g	average porous media grain diameter, μm
D_p	average suspended particle diameter, μm
D_{ps}	average pore size diameter, μm
D_{pt}	average pore-throat diameter, μm
f	fraction of porous media containing the corresponding pathways
H	the Hamaker coefficient, $H = 3.0 \times 10^{-13}$ erg
k	dimensionless constant
k_d	deposition rate constant, per cm
k_e	entrainment rate constant, per Pa
k_p	surface deposition rate constant, per cm
K	permeability, Darcy
l	separation distance between particles, cm
L	sand pack length, cm
n_1	dimensionless constant
n_2	dimensionless constant
PV	initial pore volume ($\text{LA}\phi_0$), cm^3
q	injection rate, cm^3/sec
t	time, sec
u	superficial velocity, cm/sec
v	interstitial velocity, cm/sec
x	distance along the pack, cm

Greek letters

α	dimensionless constant
β	pore throat to particle diameter ratio, dimensionless
δ	deposition rate constant for plugging pathways, per cm
ε	bulk volume fraction of solid deposits, fraction
ϕ	porosity, fraction
κ	coefficient for particle transfer between the plugging and nonplugging pathways, per sec
σ	suspension particle volume fraction, cm^3/cm^3
τ	tortuosity, dimensionless
τ_{np}	nonplugging pathways wall shear stress, Pa
ρ	particle density, kg/m^3
μ	suspension viscosity, cP
μ_o	carrier liquid viscosity, cP

Subscripts

cr	critical
i	finite difference grid point
in	inlet condition
np	nonplugging
o	initial condition
p	plugging
w	water

Appendix — Evaluation of Spatial Derivatives and Integrals

The grid system depicted in Figure 11.2 is implemented here for formulation of a numerical solution scheme. The spatial grid points are located in the center of each block and denoted by the subscript indices $i = 0, 1, 2, \dots, N, N + 1$. The points $i = 0$ and $i = N + 1$ are the fictitious points located beyond the inlet and outlet ends of a core plug. Applying the quadrature central-finite difference scheme to the governing equations yields the following set of ordinary differential equations:

$$\frac{d\varepsilon_{p,i}}{dt} = (\delta + k_{p,i}\phi_{p,i})u_{p,i}\sigma_{p,i} \quad (11.A1)$$

$$\frac{d\varepsilon_{np,i}}{dt} = k_d u_{np,i}\sigma_{np,i}\phi_{np,i}^{2/3} - k_e i \varepsilon_{np,i}\phi_{np,i}^{2/3}\eta_{e,i}(\tau_{np,i} - \tau_{cr}) \quad (11.A2)$$

$$\phi_{p,i} \frac{d\sigma_{p,i}}{dt} + (1 - \sigma_{p,i}) \frac{d\varepsilon_{p,i}}{dt} = -u_{p,i} \frac{(\sigma_{p,i+1} - \sigma_{p,i-1})}{2\Delta x} + \kappa(\sigma_{p,i} - \sigma_{np,i}) \quad (11.A3)$$

$$\phi_{np,i} \frac{d\sigma_{np,i}}{dt} + (1 - \sigma_{np,i}) \frac{d\varepsilon_{np,i}}{dt} = -u_{np,i} \frac{(\sigma_{np,i+1} - \sigma_{np,i-1})}{2\Delta x} - \kappa(\sigma_{p,i} - \sigma_{np,i}) \quad (11.A4)$$

These equations are valid for the interior points $i = 1, 2, 3, \dots, N$ with the initial conditions given, respectively, as:

$$\varepsilon_{p,i} = \varepsilon_{po}, \quad t = 0 \quad (11.A5)$$

$$\varepsilon_{np,i} = \varepsilon_{npo}, \quad t = 0 \quad (11.A6)$$

$$\sigma_{p,i} = \sigma_{po}, \quad t = 0 \quad (11.A7)$$

$$\sigma_{np,i} = \sigma_{npo}, \quad t = 0 \quad (11.A8)$$

The initial values defined by Eqs. (11.A5) to (11.A8) are usually taken as zero.

For convenience, Eqs. (11.A1) to (11.A4) can be rewritten in compact forms, respectively, as:

$$\frac{d\varepsilon_{p,i}}{dt} = A_{p,i} \quad (11.A9)$$

$$\frac{d\varepsilon_{np,i}}{dt} = A_{np,i} \quad (11.A10)$$

$$B_{p,i} \frac{d\sigma_{p,i}}{dt} + C_{p,i} \frac{d\varepsilon_{p,i}}{dt} = D_{p,i} \quad (11.A11)$$

$$B_{np,i} \frac{d\sigma_{np,i}}{dt} + C_{np,i} \frac{d\varepsilon_{np,i}}{dt} = D_{np,i} \quad (11.A12)$$

where $A_{p,i}$, $A_{np,i}$, $B_{p,i}$, $B_{np,i}$, $C_{p,i}$, $C_{np,i}$, $D_{p,i}$, and $D_{np,i}$ are the coefficients defined, respectively, as:

$$A_{p,i} = (\delta + k_{p,i}\phi_{p,i})u_{p,i}\sigma_{p,i}$$

$$A_{np,i} = k_d u_{np,i}\sigma_{np,i}\phi_{np,i}^{2/3} - k_{e,i}\varepsilon_{np,i}\phi_{np,i}^{2/3}\eta_{e,i}(\tau_{np,i} - \tau_{cr}) \quad (11.A13)$$

$$B_{p,i} = \phi_{p,i} \quad (11.A14)$$

$$B_{np,i} = \phi_{np,i} \quad (11.A15)$$

$$C_{p,i} = (1 - \sigma_{p,i}) \quad (11.A16)$$

$$C_{np,i} = (1 - \sigma_{np,i}) \quad (11.A17)$$

$$D_{p,i} = -u_{p,i} \frac{(\sigma_{p,i+1} - \sigma_{p,i-1})}{2\Delta x} + \kappa(\sigma_{p,i} - \sigma_{np,i}) \quad (11.A18)$$

$$D_{np,i} = -u_{np,i} \frac{(\sigma_{np,i+1} - \sigma_{np,i-1})}{2\Delta x} - \kappa(\sigma_{p,i} - \sigma_{np,i}) \quad (11.A19)$$

The solution of Eqs. (11.A5) to (11.A12) requires the incorporation of the boundary conditions at the inlet and outlet ends of the core plug in order to circumvent the fictitious point values. For this purpose, the fictitious point particle concentrations near the inlet boundary are estimated by the following arithmetic averages:

$$\sigma_{p,1-1/2} = \sigma_{in} = \frac{\sigma_{p,0} + \sigma_{p,1}}{2} \quad (11.A20)$$

$$\sigma_{np,1-1/2} = \sigma_{in} = \frac{\sigma_{np,0} + \sigma_{np,1}}{2} \quad (11.A21)$$

Thus, substituting Eqs. (11.A20) and (11.A21) into Eqs. (11.A18) and (11.A19) at the core inlet point $i = 1$ yields:

$$D_{p,1} = -u_{p,1} \frac{(\sigma_{p,2} - 2\sigma_{in} + \sigma_{p,1})}{2\Delta x} + \kappa(\sigma_{p,1} - \sigma_{np,1}) \quad (11.A22)$$

$$D_{np,1} = -u_{np,1} \frac{(\sigma_{np,2} - 2\sigma_{in} + \sigma_{np,1})}{2\Delta x} - \kappa(\sigma_{p,1} - \sigma_{np,1}) \quad (11.A23)$$

Hence, at the grid point of $i = 1$, Eqs. (11.A9) to (11.A12) become:

$$\frac{d\varepsilon_{p,1}}{dt} = A_{p,1} \quad (11.A24)$$

$$\frac{d\varepsilon_{np,1}}{dt} = A_{np,1} \quad (11.A25)$$

$$B_{p,1} \frac{d\sigma_{p,1}}{dt} + C_{p,1} \frac{d\varepsilon_{p,1}}{dt} = D_{p,1} \quad (11.A26)$$

$$B_{\text{np},1} \frac{d\sigma_{\text{np},1}}{dt} + C_{\text{np},1} \frac{d\varepsilon_{\text{np},1}}{dt} = D_{\text{np},1} \quad (11.\text{A}27)$$

The concentration at the fictitious point near the outlet boundary ($N + 1$) is estimated by:

$$\sigma_{\text{p},N+1} = \sigma_{\text{p},N} \quad (11.\text{A}28)$$

$$\sigma_{\text{np},N+1} = \sigma_{\text{np},N} \quad (11.\text{A}29)$$

Thus, substituting Eqs. (11.A28) and (11.A29) into Eqs. (11.A18) and (11.A19) at the core outlet point $i = N$ yields:

$$D_{\text{p},N} = -u_{\text{p},N} \frac{(\sigma_{\text{p},N} - \sigma_{\text{p},N-1})}{2\Delta x} + \kappa (\sigma_{\text{p},N} - \sigma_{\text{np},N}) \quad (11.\text{A}30)$$

$$D_{\text{np},N} = -u_{\text{np},N} \frac{(\sigma_{\text{np},N} - \sigma_{\text{np},N-1})}{2\Delta x} - \kappa (\sigma_{\text{p},N} - \sigma_{\text{np},N}) \quad (11.\text{A}31)$$

Hence, at the grid point of $i = N$, Eqs. (11.A9) to (11.A12) become:

$$\frac{d\varepsilon_{\text{p},N}}{dt} = A_{\text{p},N} \quad (11.\text{A}32)$$

$$\frac{d\varepsilon_{\text{np},N}}{dt} = A_{\text{np},N} \quad (11.\text{A}33)$$

$$B_{\text{p},N} \frac{d\sigma_{\text{p},N}}{dt} + C_{\text{p},N} \frac{d\varepsilon_{\text{p},N}}{dt} = D_{\text{p},N} \quad (11.\text{A}34)$$

$$B_{\text{np},N} \frac{d\sigma_{\text{np},N}}{dt} + C_{\text{np},N} \frac{d\varepsilon_{\text{np},N}}{dt} = D_{\text{np},N} \quad (11.\text{A}35)$$

Equations (11.A24) to (11.A27) for $i = 1$, Eqs. (11.A5) to (11.A12) for $i = 2, 3, 4, \dots, N - 1$, and Eqs. (11.A32) to (11.A35) for $i = N$ together with the initial conditions given by Eqs. (11.A5) to (11.A8) form a complete set of ODEs equations with prescribed conditions of solutions that can be readily solved numerically using the Runge–Kutta fourth-order algorithm. The quantities ε_{p} , ε_{np} , σ_{p} , and σ_{np} are calculated at every grid point as a function of time.

References

1. Civan, F., *Reservoir Formation Damage — Fundamentals, Modeling, Assessment, and Mitigation*, Gulf Publ. Co., Houston, TX, and Butterworth-Heinemann, Woburn, MA, p. 742, 2000.
2. Gruesbeck, C. and Collins, R.E., Entrainment and deposition of fine particles in porous media, *SPEJ*, 22(6): 847–856, 1982.

3. Civan, F., Modeling and simulation of formation damage by organic deposition, *Proceedings of the First International Symposium on Colloid Chemistry in Oil Production: Asphaltene and Wax Deposition*, ISCOP '95, Rio de Janeiro, Brazil, pp. 102–107, November 26–29, 1995.
4. Civan, F., Evaluation and comparison of the formation damage models, paper SPE 23787, *Proceedings of the SPE International Symposium on Formation Damage Control*, Lafayette, Louisiana, pp. 219–236, February 26–27, 1992.
5. Civan, F., Predictability of formation damage: an assessment study and generalized models, *Final Report*, U.S. DOE Contract No. DE-AC22-90BC14658, April 1994.
6. Civan, F., A multi-phase mud filtrate invasion and well bore filter cake formation model, paper SPE 28709, *Proceedings of the SPE International Petroleum Conference and Exhibition of Mexico*, Veracruz, Mexico, pp. 399–412, October 10–13, 1994.
7. Civan, F., A multi-purpose formation damage model, paper SPE 31101, *The SPE Formation Damage Control Symposium*, Lafayette, Louisiana, pp. 311–326, February 14–15, 1996.
8. Schechter, R.S., *Oil Well Stimulation*, Prentice Hall, Englewood Cliffs, NJ, p. 602, 1992.
9. Dullien, F.A.L., *Porous Media Fluid Transport and Pore Structure*, Academic Press, London, p. 396, 1979.
10. Potanin, A.A. and Uriev, N.B., Micro-rheological models of aggregated suspensions in shear flow, *J. Coll. Int. Sci.*, 142(2): 385–395, 1991.
11. Civan, F., Incompressive cake filtration: mechanism, parameters, and modeling, *AICHE J.*, 44(11): 2379–2387, 1998.
12. Civan, F., Practical model for compressive cake filtration including fine particle invasion, *AICHE J.*, 44(11): 2388–2398, 1998.
13. Ohen, H.A. and Civan, F., Simulation of formation damage in petroleum reservoirs, *SPE Adv. Technol. Ser.*, 1(1): 27–35, 1993.
14. Civan, F., Quadrature solution for waterflooding of naturally fractured reservoirs, *SPE Reservoir Evaluation Eng. J.*, 1(2): 141–147, 1998.
15. *Mathematica 4.2®*, Wolfram Research, Inc., 100 Trade Center Drive, Champaign, IL 61820-7237, USA, 2004.
16. Carman, P.C., Fluid flow through a granular bed, *Trans. Inst. Chem. Eng. (London)*, 15: 150–167, 1937.
17. Brinkman, H.C., The viscosity of concentrated suspensions and solutions, *J. Chem. Phys.*, 20: 571, 1952.
18. Černanský, A. and Široký, R., Deep-bed filtration on filament layers on particle polydispersed in liquids, *Int. Chem. Eng.*, 25(2): 364–375, 1985.
19. Wojtanowicz, A.K., Krilov, Z., and Langlinais, J.P., Experimental determination of formation damage pore blocking mechanisms, *Trans. of the ASME, J. Energ. Resour. Technol.*, 110: 34–42, 1988.
20. Khilar, K.C. and Fogler, H.S., *Migration of Fines in Porous Media (Theory and Applications of Transport in Porous Media*, Vol. 12), Kluwer Academic Publishers, Norwell, MA, p. 171, 2000.

12

Analytical Models for Porous Media Impairment by Particles in Rectilinear and Radial Flows

Faruk Civan and Maurice L. Rasmussen

CONTENTS

Summary	486
12.1 Introduction	487
12.2 Formulation	489
12.2.1 Basic Transport Equation	489
12.2.2 Modeling for Rate of Deposition Function.....	492
12.2.2.1 Present model.....	492
12.2.2.2 The Model by Herzig et al.	495
12.2.2.3 Discussion of the models.....	496
12.2.3 Permeability Impairment, Injectivity Ratio, and Impedance Index	497
12.2.3.1 One-dimensional rectilinear case	498
12.2.3.2 Radial case.....	498
12.3 One-Dimensional Rectilinear Problem with Constant Injection Rate.....	499
12.3.1 Transport Equation	499
12.3.2 Constant-Rate Coefficient	499
12.3.2.1 Nondimensional variables	500
12.3.2.2 Characteristic equations.....	502
12.3.3 Variable-Rate Coefficient	509
12.3.3.1 Present model.....	510
12.3.3.2 Solution for the model by Herzig et al.	512
12.3.3.3 Comparison and discussion	514
12.3.3.4 Average permeability and impedance index.....	518
12.4 One-Dimensional Rectilinear Problem with Time-Dependent Injection Rate	522

12.5 Radial Problem with Constant Injection Rate	523
12.5.1 Transport Equation	523
12.5.2 Constant-Rate Coefficient	524
12.5.2.1 Nondimensional variables	524
12.5.2.2 Characteristic equations	525
12.5.3 Variable-Rate Coefficient	528
12.5.3.1 Solution for present model.....	528
12.5.3.2 Partial solution for model by Herzig et al.	532
12.6 Radial Problem with Time-Dependent Injection Rate	533
12.7 Applications and Validation of Analytic Solutions.....	533
12.7.1 One-Dimensional Rectilinear Case	533
12.7.1.1 Case 1	534
12.7.1.2 Case 2	535
12.7.1.3 Case 3	535
12.7.2 Radial Case	536
12.8 Concluding Remarks	538
Nomenclature	539
Conversion Factors.....	541
References	541

Summary

One-dimensional rectilinear and radial macroscopic phenomenological models along with analytical solutions and applications for impairment of porous media by migration and deposition of fine particles, and effects on the injectivity decline during flow of particle–fluid suspensions, are presented in this chapter. The mechanism and kinetics of the fine particle deposition in porous medium for two different models are described and compared. The present approach considers the rate of deposition at a given location to be proportional to the particle flux, with the proportionality factor being a function of the cumulative particles passing by the location per unit volume. The popular model by Herzig et al. [Herzig, J.P., Leclerc, D.M., and Le Goff, P., Flow of suspensions through porous media — application to deep filtration, *Industrial Eng. Chem.*, 62(5), 8–35, 1970.] stems from the assumption that the proportionality factor, called the filtration coefficient, is a variable depending on the deposition function itself. The present new system of equations has a similar appearance to that developed by Herzig et al., but the equivalent constitutive relations are subtly different.

The formulation and analytic solution for the constant and time-dependent injection-rate cases are carried out. A methodology for determination of the parameters of the deep-bed filtration process is provided. Typical scenarios

are simulated, illustrating the parametric sensitivity and application of the present analytical solutions.

12.1 Introduction

Frequently, the water produced from oil-field reservoirs and the seawater contain various particulate matters, such as sand, clay, and bacteria. When these waters are used for flooding the petroleum reservoirs in order to achieve a secondary recovery, the fine particles migrating in sufficient concentrations through porous reservoir rock may clog the pore throats and reduce the permeability near the well-bore petroleum-bearing porous rock formations. Consequently, the water injection performance of the wells, expressed by the injectivity or impedance indices, declines due to the increase of the hydraulic resistance of the rock to fluid flow. This adverse phenomenon is a well-known deep-bed filtration problem that causes formation damage [1] in petroleum reservoirs. Its mitigation can be accomplished more effectively, based on the predictability of the permeability impairment near the well-bore by using appropriate phenomenological models. Such models are of significant importance in developing optimal strategies to avoid or delay formation damage and to estimate the time required for formation damage remediation.

Comprehensive reviews of the efforts for modeling deep-bed filtration phenomenon for this purpose have been presented in the literature, including those by Civan [1], Wennberg [2], and Bedrikovetsky et al. [3], and therefore, are not repeated here. However, it is sufficient to draw attention to the fact that the majority of the previous modeling efforts were focused on rectilinear one-dimensional filtration problems assuming a constant particle deposition rate coefficient, whereas the flow around the well-bores is predominantly radial (cylindrically symmetric) and the particle deposition rate coefficient has been proven as being dependent on the impairment of porous rock by particle deposition. In addition, the previous modeling efforts generally assumed a constant injection rate. In reality, the injection rate declines naturally as the permeability of the porous media is impaired by particle deposition. Therefore, the analytical solutions implementing time-dependent injection rates are of significant practical importance.

In this chapter, one-dimensional rectilinear and radial macroscopic phenomenological deep-bed filtration models along with analytical solutions and applications for impairment of porous media by migration and deposition of fine particles, and effects on the injectivity decline during the flow of particle-fluid suspensions, are presented. The mechanism and kinetics of the fine particle deposition in porous media for two different models, namely the present model and the popular model by Herzig et al. [4], are

described and compared. A phenomenological approach is taken to represent the depositional source/sink term and provide constitutive relations. The present system of equations has a similar appearance to that developed by Herzig et al. [4], but the equivalent constitutive relations are subtly different. In the present approach, the rate of deposition function is taken as a field function and expressed in terms of plausible flow variables, leading to sets of constitutive relations corresponding to the particular assumptions made. For the present model, the rate of deposition at a given location is proportional to the particle mass or number flux, with the proportionality factor being a function of the cumulative mass or number of particles passing through the location, per unit volume. On the other hand, the model by Herzig et al. stems from the assumption that the proportionality factor, often referred to as the filtration coefficient, is a variable depending on the deposition function itself. The two models are thus a contrast between the explicit constitutive relations of the present model versus the implicit constitutive relations of the model by Herzig et al. The analysis herein compares the solutions and the results of the two models with an eye toward the interpretation and representation of experimental data.

For each model, the coupled set of nonlinear equations is expressed in terms of normalized variables and solved analytically by the method of characteristics, or by the use of characteristic coordinates, for both rectilinear and radial flows in porous media. Analytical solutions are provided for both the cases of constant and variable deposition rate coefficients, but only the present model yields an exact analytic solution for the variable-coefficient radial-flow case. The results are then used to generate a number of new useful formulas of practical importance, including the variation of the injectivity ratio, impedance index, porosity, and permeability; and fine particle concentration in the suspension and porous media by fine particle retention. The solutions for the rectilinear flow case are applied for the core tests and the radial flow case for the well impairment.

The analytical solutions are provided for both the constant and variable deposition rate coefficients. The profiles are illustrated for the particle concentration in the particle–fluid suspension and the amount of particles deposited in porous media as a function of the dimensionless time. Scenarios are simulated in order to demonstrate the parametric sensitivity of the evolution of the outgoing wave front and disturbances generated by the wave front. A methodology for determination of the parameters of the deep-bed filtration process, by fitting the large time portion of the experimental data, is proposed and validated. Applications are illustrated for interpretation and evaluation of the various laboratory tests involving the injection of particle–fluid suspensions into core plugs and field observations concerning deep-bed filtration near the well-bore formation resulting from the injection of a fluid containing fine particles into completed wells in petroleum reservoirs. This chapter provides the analytical solutions to this problem for one-dimensional rectilinear and radial geometry involving the cases of constant and time-dependent injection rates.

12.2 Formulation

The equations governing the migration and deposition of particles in porous media, and the porous-media impairment at isothermal conditions are derived in this section. One-dimensional rectilinear and radial flows through a horizontal porous medium are considered. The properties of the porous medium, particles, and carrier fluid are assumed constant and therefore, they are incompressible. Thus, the material density of the particles, ρ_p^* , and carrier fluid, ρ_f^* , are assumed constant. The gravity effect is neglected. The particles are considered sufficiently small compared to the pore size so that an external filter cake would not form until the porous medium is fully saturated with the particles.

12.2.1 Basic Transport Equation

Particle transport through porous media is described here. Let ρ_p be the mass concentration of the particulate matter and \mathbf{u}_p the volumetric flux (Darcy velocity) of the particles. Then the macroscopic equation of change for the particulate mass in a representative volume element of a porous medium [5] is given by:

$$\frac{\partial(\phi\rho_p)}{\partial t} + \nabla \cdot (\mathbf{u}_p\rho_p) = -\dot{\mu}_s \quad (12.1)$$

where $\dot{\mu}_s$ is a particle mass per unit bulk volume of porous media per unit time-sink term that represents the withdrawal of particulates from the streaming flow which causes the clogging of the pores. Further, we introduce the particulate number density n_p such that $\rho_p = n_p m_p$, where m_p is the average mass per particle. We also introduce the material density $\rho_p^* = m_p/V_p^*$ of an average particle, where V_p^* is the volume of an average particle. The particle volume concentration can now be defined such that

$$c_p \equiv \frac{\rho_p}{\rho_p^*} = n_p V_p^* \quad (12.2)$$

Thus, c_p is also a volume fraction, that is, the fraction of volume occupied by the particles in a unit volume of the particle–fluid suspension. It is also a measure of the number of particles contained within that fraction of volume. As such, c_p is typically measured in parts per million (ppm) bulk volume of porous medium. Consequently, we have $\rho_p = c_p \rho_p^*$, and Eq. (12.1) can be written as:

$$\frac{\partial(\phi c_p)}{\partial t} + \nabla \cdot (\mathbf{u}_p c_p) = -\dot{\sigma}_s \quad (12.3)$$

where

$$\dot{\sigma}_s \equiv \frac{\dot{\mu}_s}{\rho_p^*} \quad (12.4)$$

is called the *volumetric rate of deposition function* and has the units of ppm per unit time. Similarly, the equation of change for the carrier fluid (water phase) in porous media is given by:

$$\frac{\partial(\phi c_f)}{\partial t} + \nabla \cdot (\mathbf{u}_f c_f) = -\dot{\sigma}_f = 0 \quad (12.5)$$

in which \mathbf{u}_f is the volumetric flux (Darcy velocity) of the carrier fluid, taken as the water here. Note that we assume that the porous medium does not absorb any water; that is, $\dot{\sigma}_f = 0$. In addition, the volume fractions of the particles and the water phase add up to one in the particulate suspension; that is,

$$c_p + c_f = 1 \quad (12.6)$$

Therefore, combining Eqs. (12.3) and (12.5) in view of Eq. (12.6) yields the volumetric equation of change for the particulate suspension as:

$$\frac{\partial \phi}{\partial t} + \nabla \cdot \mathbf{u} = -\dot{\sigma}_s \quad (12.7)$$

in which \mathbf{u} denotes the volumetric-weighted average flux of the suspension, given by:

$$\mathbf{u} = \mathbf{u}_p c_p + \mathbf{u}_f c_f \quad (12.8)$$

Note that the volumetric fluxes of the particles and the carrier fluid (water) can be expressed, respectively, as:

$$\mathbf{u}_p c_p = \mathbf{u} c_p + \mathbf{j}_p \quad (12.9)$$

$$\mathbf{u}_f c_f = \mathbf{u} c_f + \mathbf{j}_f \quad (12.10)$$

in which the volumetric diffusion flux vectors of the particles \mathbf{j}_p and the carrier fluid (water) \mathbf{j}_f can be expressed, respectively, as:

$$\mathbf{j}_p \equiv (\mathbf{u}_p - \mathbf{u}) c_p \quad (12.11)$$

$$\mathbf{j}_f \equiv (\mathbf{u}_f - \mathbf{u}) c_f \quad (12.12)$$

Hence, substituting Eq. (12.9) into Eq. (12.3) yields:

$$\frac{\partial(\phi c_p)}{\partial t} + \nabla \cdot (\mathbf{u} c_p) = -\dot{\sigma}_s - \nabla \cdot \mathbf{j}_p \quad (12.13)$$

Similarly, substituting Eq. (12.10) into Eq. (12.5) yields:

$$\frac{\partial(\phi c_f)}{\partial t} + \nabla \cdot (\mathbf{u} c_f) = -\nabla \cdot \mathbf{j}_f \quad (12.14)$$

When the left-hand side of Eqs. (12.13) and (12.14) are expanded and simplified by means of the volume-mean balance equation given by Eq. (12.7), we get

$$\phi \frac{\partial c_p}{\partial t} + \mathbf{u} \cdot \nabla c_p = -c_f \dot{\sigma}_s - \nabla \cdot \mathbf{j}_p \quad (12.15)$$

$$\phi \frac{\partial c_f}{\partial t} + \mathbf{u} \cdot \nabla c_f = c_f \dot{\sigma}_s - \nabla \cdot \mathbf{j}_f \quad (12.16)$$

The sum of these two equations vanishes identically. Note that the porosity ϕ appears outside the time derivative even though no restriction has been made regarding its variation with time.

At this point, we introduce several simplifying assumptions for convenience in the following derivation. For the applications considered in this chapter, the volumetric concentration of the particles in the dilute particle suspensions is very small and in the order of ppm; that is, $c_p \ll 1$ and therefore $c_f \cong 1$. We neglect the transport of particles by diffusion and, therefore, consider that

$$\mathbf{u} \cong \mathbf{u}_p \cong \mathbf{u}_f \quad (12.17)$$

The implication of this consideration is that the smooth variation of particle concentration in the progressing front is replaced by a sharp discontinuity front. This changes the diffusion equation to a wave equation.

We assume the porosity to remain approximately constant for all practical purposes, because the quantity of particles deposited from such dilute solutions occupies a negligible space in the pores. However, a small amount of deposition may be sufficient to clog the relatively narrow pore throats and cause significant permeability impairment.

Based on the above-described assumptions, the volumetric equation of change for the particulate suspension, Eq. (12.7), simplifies as:

$$\nabla \cdot \mathbf{u} \cong 0 \quad (12.18)$$

Consequently, when we suppress the subscript p denoting the particles, then Eq. (12.3) can be simplified as:

$$\phi \frac{\partial c}{\partial t} + \mathbf{u} \cdot \nabla c \cong -\dot{\sigma}_s \quad (12.19)$$

Equation (12.19) is a fundamental expression used by Herzig et al. [4] and many others for the description of the volumetric balance of particulate matter in suspensions flowing through porous media.

The interstitial or actual pore fluid velocity \mathbf{v} can be estimated by the Dupuit [6] relationship, given by:

$$\mathbf{v} = \tau_a \mathbf{u} / \phi \quad (12.20)$$

in which the macroscopic average tortuosity τ_a of the flow paths in porous media is defined as the ratio of the length of the flow paths to the length of porous media.

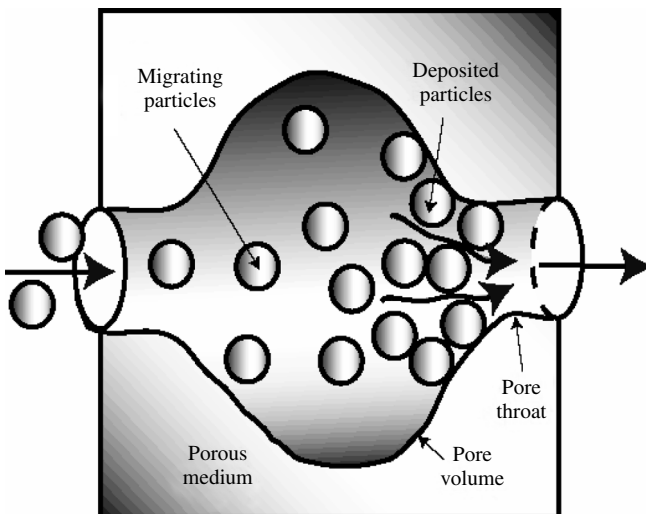
12.2.2 Modeling for Rate of Deposition Function

The mechanism and kinetics of fine particle deposition in porous media are described here. Consider the schematic of fine particle migration and deposition in a typical pore volume in porous media as depicted in Figure 12.1. The particles approaching the pore throat can form a bridge across it, which allows the carrier fluid flow through it but limits the particle migration. Consequently, the particles accumulate behind the bridge and increase the resistance of porous media to fluid flow. Here, we take the phenomenological approach that $\dot{\sigma}_s$ is a source term (or sink term, actually) and provide constitutive relations. Our system of equations has a similar appearance to that developed by Herzig et al. [4], but the equivalent constitutive relations are subtly different as described in the following section.

12.2.2.1 Present model

The rate of deposition function is, basically, a field function $\dot{\sigma}_s(\mathbf{x}, t)$, but we wish to express it on physical grounds in terms of plausible well-defined functions by what amounts to constitutive relations. Different approaches and assumptions lead to different formulas. Ultimately, the final merit of a given model depends on how well its results agree with experiment.

The rate of deposition at a given location should depend on the mass flux, or equivalently the number flux, that is, the particle-number migration rate

**FIGURE 12.1**

Fine particle migration and deposition in a typical pore volume.

per unit area, given by:

$$\frac{\partial N}{\partial t} \equiv u n_p = \frac{uc}{V_p^*} \quad (12.21)$$

where $u \equiv |\mathbf{u}|$. Equation (12.21) can be used to define the function N as the total number of particles that cross a unit area at a given location in the time t , that is,

$$N(x, t) = \int_0^t \frac{uc(x, \tilde{t})}{V_p^*} d\tilde{t} \quad (12.22)$$

We suppose that in general the rate of deposition $\dot{\sigma}_s$ is a function of at least N and $\partial N / \partial t$, that is,

$$\dot{\sigma}_s = fn \left(N, \frac{\partial N}{\partial t} \right) \quad (12.23)$$

Now, suppose that the particle suspension is sufficiently dilute so that the number N is considerably small so as to be inconsequential. Then it is plausible to assume that the rate at which particles are withdrawn from a location in

the flow and then deposited is proportional to the number of particles flowing through unit area per unit time, that is, in consideration of Eq. (12.22),

$$\dot{\sigma}_s = k_o V_p^* \frac{\partial N}{\partial t} = k_o u c \quad (12.24)$$

where k_o is an empirical constant, called the *filtration coefficient* that must be determined from experiment. Now define a new variable σ in consideration of Eq. (12.22) as:

$$\sigma \equiv k_o V_p^* N = \int_0^t k_o u c(x, \tilde{t}) d\tilde{t} \quad (12.25)$$

and therefore

$$\frac{\partial \sigma}{\partial t} \equiv k_o u c \quad (12.26)$$

Comparing Eqs. (12.24) and (12.25), the rate of deposition then becomes:

$$\dot{\sigma}_s = \frac{\partial \sigma}{\partial t} \equiv k_o u c \quad (12.27)$$

When expression (12.27) is substituted back into Eq. (12.3), a single first-order linear partial differential equation for c results. The solution for c allows for σ being determined, which in this case is also equal to σ_s , as inferred by Eq. (12.27). This basic, but primitive, formulation and solution for c are predicated on the rate term $\partial \sigma / \partial t$, which is proportional to the number-flux term $\partial N / \partial t$. The term $\partial \sigma / \partial t$ can be interpreted as a measure of the number of particles per unit time that are filtered out of the main flow and are available for deposition in the matrix of the porous medium. It is thus referred to as the *basic filtration rate*. Correspondingly, the term σ can be interpreted as the measure of the number of particles filtered out in the time t , and referred to as the *basic filtration number*. When the formulation is done in terms of σ instead of N , the factor V_p^* drops out. The variable σ is dimensionless, but is typically measured in ppm by volume, as is the variable c . The empirical filtration coefficient k_o has the units of per unit length.

Consider now a generalization of Eq. (12.27) to allow for large values of σ . In view of Eq. (12.25), the general functional equation (12.23) can be expressed alternatively as:

$$\dot{\sigma}_s = fn \left(\sigma, \frac{\partial \sigma}{\partial t} \right) \quad (12.28)$$

Now, instead of assuming, when σ is small, that $\dot{\sigma}_s$ is effectively *equal* to $\partial\sigma/\partial t$ as defined by Eq. (12.26), we assume more generally that it is *proportional* to $\partial\sigma/\partial t$ with the proportionality factor being a function of σ , that is,

$$\dot{\sigma}_s = F(\sigma) \frac{\partial\sigma}{\partial t} = F(\sigma) k_0 u c \quad (12.29)$$

In particular, we will be interested in the case when

$$F(\sigma) = 1 + b\sigma \quad (12.30)$$

where b is an empirical constant that must be determined by experiment. For this case, the constitutive relations become

$$\dot{\sigma}_s = (1 + b\sigma) \frac{\partial\sigma}{\partial t} = (1 + b\sigma) k_0 u c \quad (12.31)$$

$$\frac{\partial\sigma}{\partial t} = k_0 u c \quad (12.32)$$

When expression (12.31) is used to eliminate $\dot{\sigma}_s$ in Eq. (12.3), then the resulting equation together with Eq. (12.32) constitute a pair of coupled nonlinear first-order partial differential equations for c and σ . Observe that Eq. (12.31) could have been obtained directly from Eq. (12.27) by replacing the constant filtration coefficient with a variable coefficient, that is, by letting $k_0 \rightarrow (1 + b\sigma)k_0$, while at the same time keeping k_0 a constant in the basic definition for $\partial\sigma/\partial t$ given by Eq. (12.26). In this sense, the Eqs. (12.31) and (12.32) can be classified as a variable-rate-coefficient model.

12.2.2.2 The Model by Herzog et al.

The analysis of Herzog et al. [4] starts with Eqs. (12.27) and (12.26) in the constant filtration coefficient analysis, but allows for the filtration coefficient to be a variable, $k_0 \rightarrow k$, in both equations:

$$\dot{\sigma}_s = \frac{\partial\sigma_1}{\partial t} \quad (12.33)$$

$$\frac{\partial\sigma_1}{\partial t} = k u c \quad (12.34)$$

It is now further assumed that

$$k = k_0 F(\sigma_1) \quad (12.35)$$

where $\sigma_1 \equiv \sigma_s$ is equal to the deposition function itself. Let us adopt the symbol σ_1 to represent the basic filtration rate defined by Eq. (12.29). Then we have

$$\dot{\sigma}_s \equiv \frac{\partial \sigma_1}{\partial t} = F(\sigma_1) \frac{\partial \sigma}{\partial t} = F(\sigma_1) k_o u c \quad (12.36)$$

For $F(\sigma_1)$ specified analogous to the previous case, we have

$$F(\sigma_1) = 1 + b_1 \sigma_1 \quad (12.37)$$

where b_1 is an empirical constant, and the constitutive equations for the rate of deposition become:

$$\dot{\sigma}_s = \frac{\partial \sigma_1}{\partial t} \quad (12.38)$$

$$\frac{\partial \sigma_1}{\partial t} = (1 + b_1 \sigma_1) \frac{\partial \sigma}{\partial t} = (1 + b_1 \sigma_1) k_o u c \quad (12.39)$$

In the present notation, these are the equations for the model of Herzog et al. [4], and are the counterparts to Eqs. (12.31) and (12.32) for the present model. They lead to a pair of coupled nonlinear first-order partial differential equations for c and σ_1 when considered with Eq. (12.3).

12.2.2.3 Discussion of the models

Superficially, the constitutive equations for the present model and for the model by Herzog et al. [4] are very similar. The difference stems from the way the functions σ and σ_1 are defined. Essentially, the present model represents $\dot{\sigma}_s$ as an *explicit* function of σ according to Eq. (12.28), whereas the model by Herzog et al. [4] amounts to an *implicit* representation in terms of the variable $\sigma_1 \equiv \sigma_s$ via a functional relation of the form

$$\dot{\sigma}_s = fn \left(\sigma_s, \frac{\partial \sigma}{\partial t} \right) \quad (12.40)$$

The merit of each model depends on how well it represents experimental data. In the following analysis, the results stemming from each model will be compared with each other with an eye toward the analysis of experimental data when it is available.

12.2.3 Permeability Impairment, Injectivity Ratio, and Impedance Index

The reduction of local permeability by particle deposition in porous media is given by the following semi-empirical equation [7]:

$$\frac{K}{K_0} = \frac{1}{1 + \beta\sigma_s} \quad (12.41)$$

where β is a damage factor. Equation (12.41) can be used to derive the formulae for calculation of the permeability impairment, and the injectivity and impedance indices for one-dimensional rectilinear- and radial-flow cases, respectively Figure 12.2 and Figure 12.3, as described in the following sections.

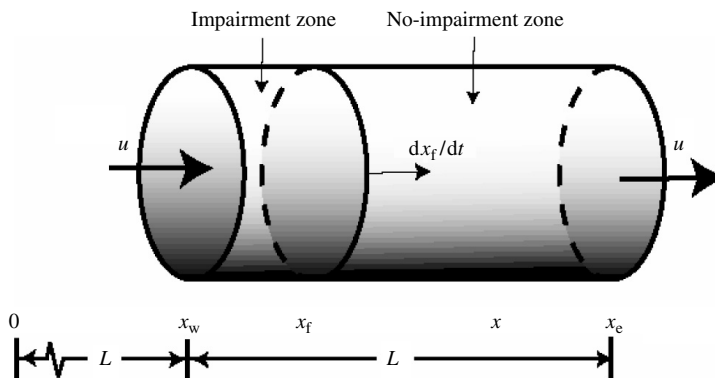


FIGURE 12.2

Impairment and no-impairment zones formed during one-dimensional flow of a suspension of fine particles in a core plug.

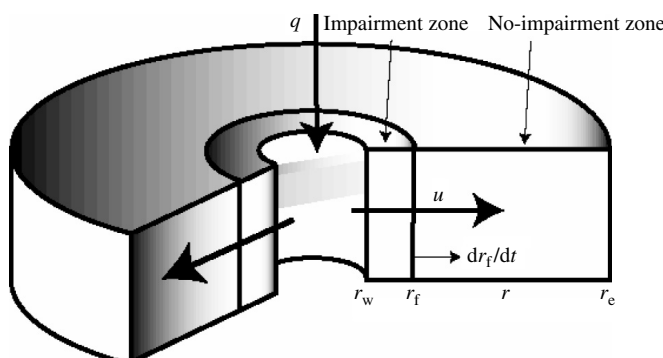


FIGURE 12.3

Impairment and no-impairment zones formed during radial flow of a suspension of fine particles in a near well-bore region in a reservoir.

12.2.3.1 One-dimensional rectilinear case

Consider Figure 12.2 describing the impairment and no-impairment zones distinguished during one-dimensional flow of a suspension of fine particles in a core plug. The harmonic average permeability of the deposit or impairment region is given by:

$$\bar{K}(t) = \frac{x_f(t) - x_w}{\int_{x_w}^{x_f(t)} dx / K(x, t)} \quad (12.42)$$

where $x_f(t)$ denotes the location of the front position ahead of which there is no deposition.

The impedance index J is given by the reciprocal of the injectivity ratio α as:

$$\begin{aligned} J(t) \equiv \frac{1}{\alpha(t)} &= \frac{(x_f(t) - x_w)/\bar{K}(t) + (x_e - x_f(t))/K_o}{(x_e - x_w)/K_o} \\ &= 1 + \frac{x_f(t) - x_w}{x_e - x_w} \left(\frac{K_o}{\bar{K}(t)} - 1 \right) \end{aligned} \quad (12.43)$$

in which $x_e - x_w \equiv L$ denotes the distance of influence from the face of the injection location, or the length of core plug. The location of the injection port is denoted by x_w .

12.2.3.2 Radial case

Consider Figure 12.3 describing the impairment and no-impairment zones identified during radial flow of a suspension of fine particles near a well-bore region in a reservoir. The harmonic average permeability of the deposit or impairment region is given by:

$$\bar{K}(t) = \frac{\ln(r_f(t)/r_w)}{\int_{r_w}^{r_f(t)} dr / r K(r, t)} \quad (12.44)$$

where $r_f(t)$ denotes the radius of the front position ahead of which there is no deposition.

The impedance index J is given by the reciprocal of the injectivity ratio α as:

$$\begin{aligned} J(t) \equiv \frac{1}{\alpha(t)} &= \frac{(1/\bar{K}(t)) \ln(r_f(t)/r_w) + (1/K_o) \ln(r_e/r_f(t))}{(1/K_o) \ln(r_e/r_w)} \\ &= 1 + \frac{\ln(r_f(t)/r_w)}{\ln(r_e/r_w)} \left(\frac{K_o}{\bar{K}(t)} - 1 \right) \end{aligned} \quad (12.45)$$

in which r_e denotes the radius of influence of the injection well.

12.3 One-Dimensional Rectilinear Problem with Constant Injection Rate

The above-presented equations are solved analytically for constant- and variable-rate coefficients in the one-dimensional rectilinear-flow case described in [Figure 12.2](#).

12.3.1 Transport Equation

The formulation considers a constant volumetric injection rate q_0 . For one-dimensional flows, the volumetric flux of the flowing suspension is given by:

$$u = \frac{q_0}{A_0} = u_0 = \text{const.} \quad (12.46)$$

where A_0 denotes the constant cross-sectional area of the porous formation or a core plug. We therefore have for the mass-average velocity of the particulate suspension:

$$\mathbf{u} = u_0 \mathbf{e}_x \quad (12.47)$$

where \mathbf{e}_x is the unit vector in the rectilinear-flow direction, and \mathbf{u} satisfies the incompressibility condition (12.18). Consequently, substituting Eq. (12.46) into Eq. (12.3) gives the volumetric balance of suspended particles in a near injection location of a porous medium in the Cartesian form [4]:

$$\phi \frac{\partial c}{\partial t} + u_0 \frac{\partial c}{\partial x} = -\dot{\sigma}_s, \quad x > x_w, \quad t > 0 \quad (12.48)$$

Note that x_w is the location of the injection port.

The initial and boundary conditions are given, respectively, by:

$$c = 0, \quad \sigma_s = 0, \quad x > x_w, \quad t = 0 \quad (12.49)$$

$$c = c_w, \quad x = x_w, \quad t > 0 \quad (12.50)$$

12.3.2 Constant-Rate Coefficient

The sink term, expressing the loss of particles from the flowing suspension by deposition of particles at a rate proportional to the suspended particle flux, is given by Eq. (12.27):

$$\dot{\sigma}_s = k_o u_0 c \quad (12.51)$$

where k_o is a constant filtration coefficient. Thus, substituting Eq. (12.51) into Eq. (12.48) yields:

$$\phi \frac{\partial c}{\partial t} + u_o \frac{\partial c}{\partial x} = -k_o u_o c, \quad x > x_w, \quad t > 0 \quad (12.52)$$

12.3.2.1 Nondimensional variables

Introduce the following nondimensional variables for the flowing suspension particle concentration, distance, and time:

$$C \equiv \frac{c}{c_w}, \quad X \equiv \frac{x}{x_w}, \quad \tau \equiv \frac{u_o}{\phi x_w} t \quad (12.53)$$

where $x_w = L$. For the semiinfinite one-dimensional problem, the reference length L is arbitrary. Here, it is taken equal to the core length, which implies $x_e = 2L$. Its utility, as a characteristic length, will be realized when comparisons are made with the cylindrical problem.

Equation (12.52) can thus be written in the nondimensional variables as:

$$\frac{\partial C}{\partial \tau} + \frac{\partial C}{\partial X} + \lambda C = 0 \quad (12.54)$$

where $\lambda \equiv k_o x_w$. The initial and boundary conditions become

$$\begin{aligned} C(X > 1, 0^+) &= 0 \\ C(X = 1, \tau > 0) &= 1 \end{aligned} \quad (12.55)$$

The nondimensional time can be considered as the ratio

$$\tau = t/t_c \quad (12.56)$$

where

$$t_c \equiv L\phi/u_o \quad (12.57)$$

is a pertinent characteristic time for a given problem, determined by some characteristic length L , the porosity ϕ , and the injection velocity u_o . As an example representing typical laboratory tests shown in Table 12.1, we can take in round numbers $L = 0.1$ m, $\phi = 0.25$, and $u_o = 0.0025$ m/sec, which yield the characteristic time to be $t_c = 10$ sec = 0.167 min = 0.00278 h = 0.000116 days. For this example, a nondimensional time of $\tau = 10,000$ would represent about 1.16 days. If the characteristic velocity is one-tenth as big (with L and ϕ the same) as it is approximately for the situations shown in Table 12.2, then the characteristic time is ten times as big, and a nondimensional time of $\tau = 1,000$ represents about 1.16 days. Also the nondimensional time τ is

TABLE 12.1

Parameter Values for Rectilinear Case

Parameters	Case 1: van den Broek et al. [10]	Case 2: Al-Abduwani et al. [11]	Case 3: Bedrikovetsky et al. [3]
Rock type	Bentheimer sandstone	Bentheimer sandstone	Bentheimer sandstone
Particles	Grounded rock	Grounded rock	Hematite
Carrier fluid	Water	Water	Water
$c_{\text{inj}} = c_w$, ppm by volume	24.0	60.0	3.8 (20 ppm by weight)
$K_o, \text{ m}^2$	1.04×10^{-12} (1055 mD)	1.56×10^{-12} (1582 mD)	1.38×10^{-12} (1.4 D)
ϕ , volume fraction	0.225	0.225	0.22
$L, \text{ m}$	0.075	0.075	0.127
$q_{\text{inj}} = q_w, \text{ m}^3/\text{sec}$	1.11×10^{-6} (4.0 l/h)	1.11×10^{-6} (4.0 l/h)	1.5×10^{-6} (5.4 l/h)
$u_{\text{inj}} = u_w = q_{\text{inj}}/\pi D^2/4, \text{ m/sec}$	2.3×10^{-3} (2.3 mm/sec)	2.3×10^{-3} (2.3 mm/sec)	2.9×10^{-3}
$t_c = L\phi/u_{\text{inj}}, \text{ sec}$	7.34	7.34	9.64
D , core plug diameter, m	0.025	0.025	0.02566
b_o , present, dimensionless	—	—	—
b_{1o} , Herzig et al. dimensionless	1.0	1.0	1.0
B , dimensionless			
Herzig et al.	2.4×10^5	15.2	397.0
Present	—	—	—
λ , dimensionless			
Herzig et al.	1.0×10^{-8}	1.0×10^{-3}	1.0×10^{-5}
Present	—	—	—
$\beta = B/(\phi c_w)$, 1/ppm			
Herzig et al.	4.44×10^{10}	2.82×10^6	4.75×10^8
Present	—	—	—
$k_o = \lambda/L, 1/\text{m}$			
Herzig et al.	1.33×10^{-7}	1.33×10^{-2}	1.05×10^{-3}
Present	—	—	—
$b = b_o/(\phi c_w)$, present, dimensionless	—	—	—
$b_1 = b_{1o}/(\phi c_w)$, Herzig et al., dimensionless	1.85×10^5	7.41×10^4	1.20×10^6
			4.90×10^6

TABLE 12.2

Parameter Values for Radial Case

Parameters	Wennberg [2]
Rock type	Well A42
Particles	Bacteria and microorganisms
Carrier fluid	Sea water
$c_{\text{inj}} = c_w$, ppm by volume	1.0 vol/vol (should be ppm)
K_o , m ²	1.02×10^{-12} (1035 mD)
ϕ , volume fraction	0.33
$q_{\text{inj}} = q_w$, m ³ /sec	$q_w(t) = q_\infty + (q_0 - q_\infty)e^{-\delta t}$ $\delta = 2.22 \times 10^{-7}$ per sec (0.0192 per day), $q_0 = 6.44 \times 10^{-3}$ (3500 bbl/d), and $q_\infty = 9.75 \times 10^{-4}$ (530 bbl/d)
$u_o = u_{wo} = q_0/(2\pi r_w h)$, m/sec	2.36×10^{-4}
$t_c = r_w \phi / u_{\text{inj}}$, sec	197.0
h , m	30.8 (101 ft)
r_w , m	0.141 (5.54 in.)
r_e , m	536.0 (1760 ft)
λ	70.0
B	1.32×10^{-3}
$\beta = B/(\phi c_w)$, dimensionless	4.0×10^3
$k_o = \lambda/r_w$, 1/m	490

equal to the number of pore volumes injected in the time t , usually measured in terms of the initial pore volume, and is given by:

$$\tau = \frac{Q}{PV_o} = \frac{q_w t}{AL\phi_o} = \frac{u_w At}{AL\phi_o} = \frac{u_w t}{L\phi_o} \quad (12.58)$$

where Q denotes the cumulative volume of suspension injected, A is the cross-sectional area of core, L is the core length, PV_o is the initial pore volume, ϕ_o is the initial porosity, q_w and u_w denote the suspension injection volumetric flow rate and flux at the injection port of the porous medium, and t is time.

12.3.2.2 Characteristic equations

According to the theory of characteristics [8], a quasi-linear first-order partial differential equation can be expressed as a total (or ordinary) differential equation written along certain curves in space called *characteristic* curves or *base characteristics*. The characteristic equations for Eq. (12.54) are

$$\frac{dC}{dX} = -\lambda C \quad \text{on } \frac{d\tau}{dX} = 1 \quad (12.59)$$

The second of Eqs. (12.59) describes the base characteristics. They are a family of parallel straight lines all having the same slope on a τ versus X diagram.

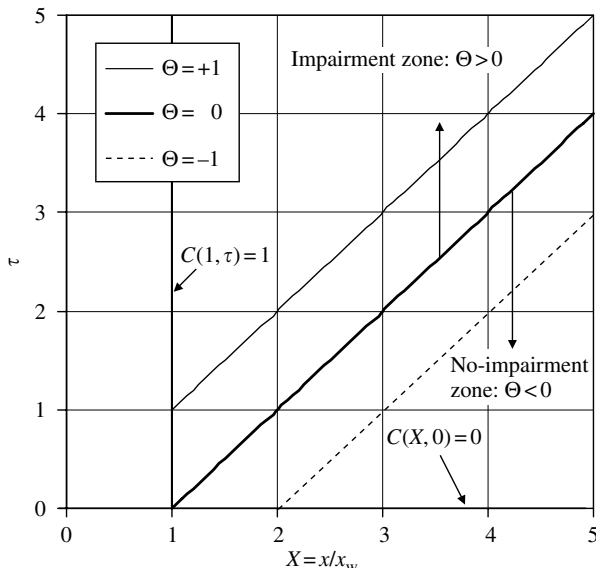


FIGURE 12.4
 τ -X diagram for rectilinear problem.

The integrated form is

$$\tau - X + 1 \equiv \Theta = \text{const.} \quad (12.60)$$

The constant of integration is denoted by Θ , and each member of the family of parallel straight lines is designated by its value of Θ (see Figure 12.4). The constant of integration has been selected arbitrarily so that $\Theta = 0$ represents the curve that passes through the point of initial disturbance, $\tau = 0$ and $X = 1$.

Integration of the first of Eqs. (12.59) gives:

$$C(X, \tau) = A(\Theta)e^{-\lambda X} \quad \text{on } \Theta \equiv \tau - X + 1 = \text{const.} \quad (12.61)$$

where $A(\Theta)$ is a function of integration that is a constant along a prescribed base characteristic, but possibly a different constant along a different characteristic. Enforcing the initial and boundary conditions described by Eq. (12.61) gives:

$$\begin{aligned} A(\tau) &= e^\lambda, \quad \tau > 0 \\ A(-X + 1) &= 0, \quad X > 1 \end{aligned} \quad (12.62)$$

In terms of the unit Heaviside step function $H(u)$, defined as

$$H(u) = \begin{cases} 0, & u < 0 \\ 1, & u > 0 \end{cases} \quad (12.63)$$

the function of integration becomes

$$A(\Theta) = H(\Theta)e^\lambda \quad (12.64)$$

and the solution (12.61) becomes:

$$C(X, \tau) = e^{-\lambda(X-1)}H(\Theta), \quad \text{where } \Theta \equiv \tau - X + 1 \quad (12.65)$$

These results show that a wave front travels along the base characteristic $\Theta = 0$. The function C is discontinuous across the wave front, being zero ahead of it, $\Theta < 0$, and nonzero positive behind it, $\Theta > 0$. Along the discontinuity wave, $\Theta = 0^+$ or $\tau = (X - 1)^+$, the volume fraction of particles decreases exponentially,

$$C = \exp[-\lambda(X - 1)] \quad (12.66)$$

A plot of C versus X for various times τ is shown in Figure 12.5. For a fixed location X , as shown in Figure 12.6 there is no variation in C with time except for the jump across the discontinuity wave front when it passes by. The region

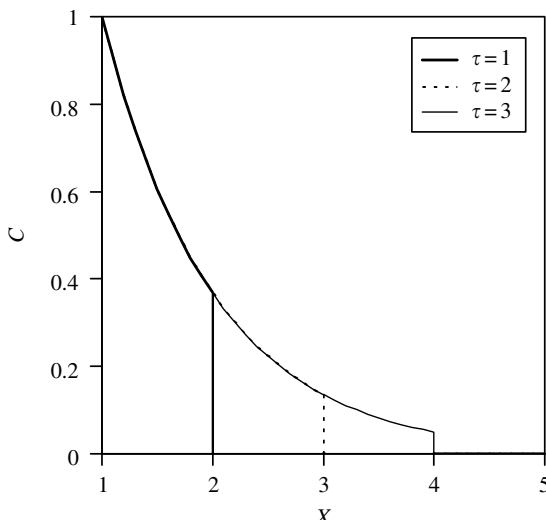
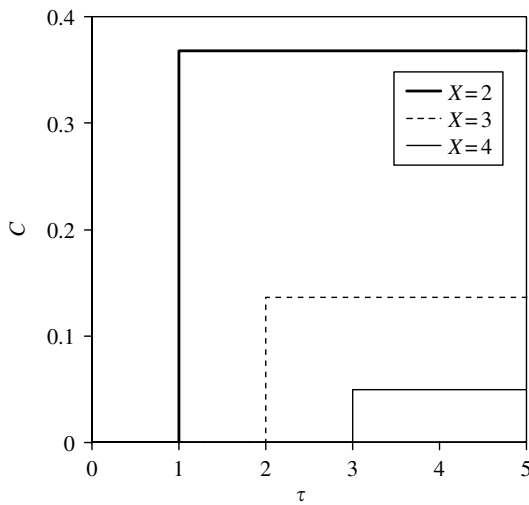


FIGURE 12.5

Particle volumetric fraction C versus X for $\tau = 1, 2$, and 3, and constant-rate coefficient for $\lambda = 1$.

**FIGURE 12.6**

Particle volumetric fraction C versus τ for $X = 2, 3, 4$, and constant-rate coefficient for $\lambda = 1$.

ahead of the discontinuity wave front is called the *no-impairment zone*, and the region behind the wave front is called the *impairment zone* (see [Figure 12.2](#) and [Figure 12.4](#)).

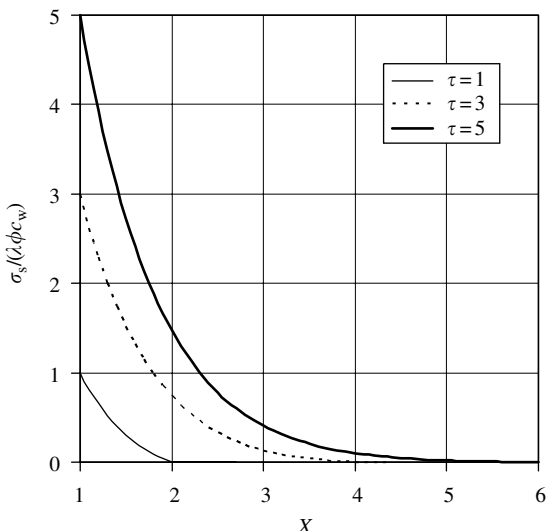
Consider the total deposition at a given position x as a function of time t according to Eq. (12.27):

$$\begin{aligned} \sigma_s &= \int_0^t \dot{\sigma}_s dt = \frac{\phi x_w}{u_o} \int_0^\tau \dot{\sigma}_s d\tau \\ &= 0 \quad \text{for } \tau < X - 1, \text{ or } \Theta < 0 \\ &= \frac{\phi x_w}{u_o} \int_{X-1}^\tau \dot{\sigma}_s d\tau \quad \text{for } \tau \geq X - 1, \text{ or } \Theta \geq 0 \end{aligned} \quad (12.67)$$

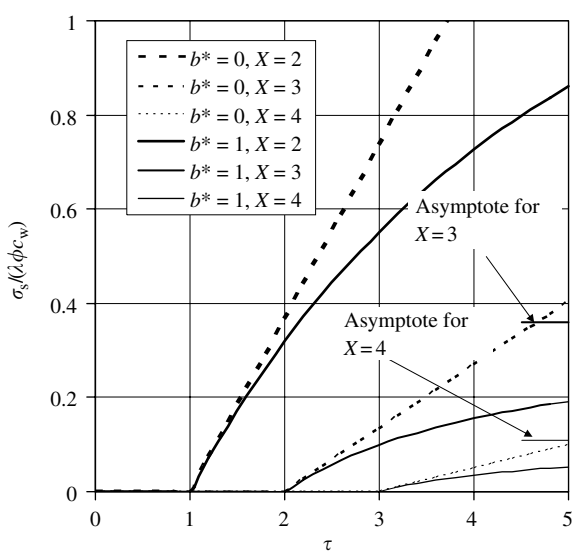
We then calculate

$$\sigma_s(X, \tau) = \sigma(X, \tau) = \lambda \phi c_w \Theta e^{-\lambda(X-1)} H(\Theta) \quad (12.68)$$

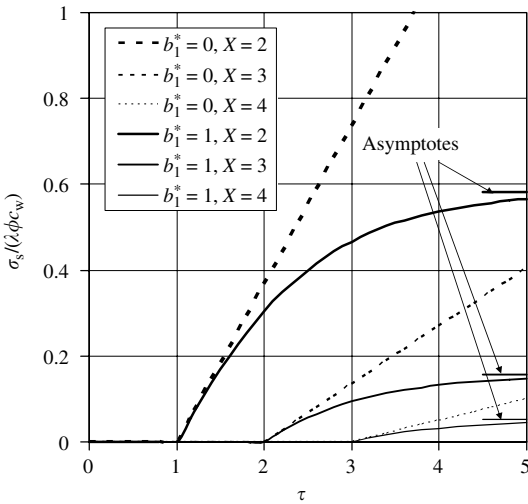
The deposition function σ_s , as well as the function σ , is continuous at the wave front and equal to zero there. The X -derivative is also continuous and equal to zero, $\partial\sigma/\partial X = 0$, along the wave front, but the τ -derivative is discontinuous at any given location. A plot of σ versus X for various values of τ is shown in [Figure 12.7](#). After the wave front passes a given location X , the deposition function grows linearly with time, as is indicated in [Figure 12.8](#) and [Figure 12.9](#) in comparison with variable-rate results. The latter are described in a subsequent section.

**FIGURE 12.7**

Normalized particle deposition $\sigma_s / (\lambda\phi c_w)$ versus X for $\tau = 1, 3, 5$, and constant-rate coefficient for $\lambda = 1$.

**FIGURE 12.8**

Normalized particle deposition $\sigma_s / (\lambda\phi c_w)$ versus τ for $X = 2, 3, 4$, and variable-rate coefficient (present model) and constant-rate coefficient for $\lambda = 1$.

**FIGURE 12.9**

Normalized particle deposition $\sigma_s/(\lambda\phi c_w)$ versus τ for $X = 2, 3, 4$, and variable-rate coefficient (model by Herzig et al.) and constant-rate coefficient for $\lambda = 1$.

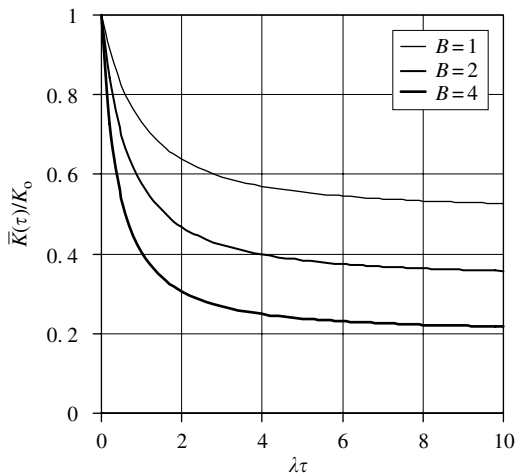
The average permeability, according to Eq. (12.42), is expressed as:

$$\begin{aligned} \frac{\bar{K}(\tau)}{K_o} &= \frac{1}{1 + \beta\phi c_w [1 - (1/(\lambda\tau))(1 - e^{-\lambda\tau})]} \\ &\sim 1 - \frac{B\lambda}{2}\tau + O(\tau^2), \quad \tau \rightarrow 0 \\ &\sim \frac{1}{1 + B} + O\left(\frac{1}{\tau}\right), \quad \tau \rightarrow \infty \end{aligned} \quad (12.69)$$

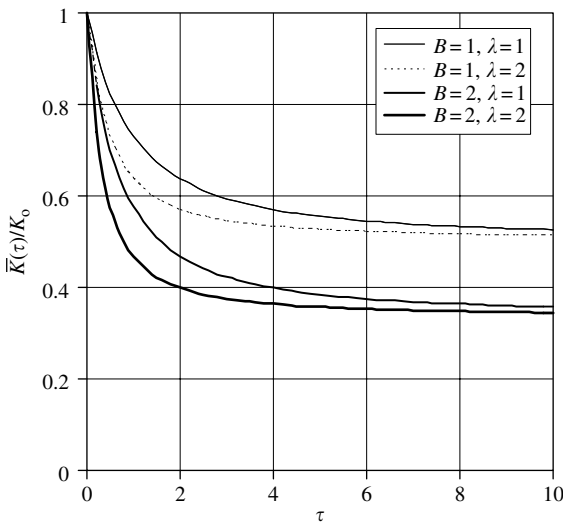
where $B \equiv \beta\phi c_w$. The average permeability is plotted as a function of the combination $\lambda\tau$ in Figure 12.10 for $B = 1, 2$, and 4 . The curves are asymptotic to $1/(1 + B)$ when $\lambda\tau$ becomes very large. Figure 12.11 shows the average permeability as a function of $B = 1$ and 2 and for $\lambda = 1$ and 2 .

The corresponding impedance index J , according to Eq. (12.43), is given for the case of injection occurring at $X = 1$ by:

$$\begin{aligned} J(t) \equiv \frac{1}{\alpha(t)} &= 1 + B \frac{\tau}{L/x_w} \left[1 - \frac{1}{\lambda\tau} (1 - e^{-\lambda\tau}) \right] \\ &\sim 1 + \frac{B\lambda}{L/x_w} \frac{\tau^2}{2} + O(\tau^3), \quad \tau \rightarrow 0 \\ &\sim \left\{ 1 - \frac{B}{L/x_w} \left(\frac{1}{\lambda} \right) \right\} + \frac{B}{L/x_w} \tau + O\left(\frac{1}{\tau}\right), \quad \tau \rightarrow \infty \end{aligned} \quad (12.70)$$

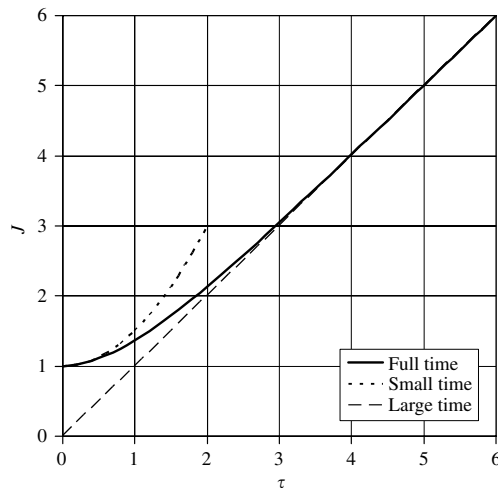
**FIGURE 12.10**

Normalized harmonic average permeability $\bar{K}(\tau)/K_0$ versus $\lambda\tau$ for $B = \beta\phi c_w = 1, 2, 4$, and constant-rate coefficient.

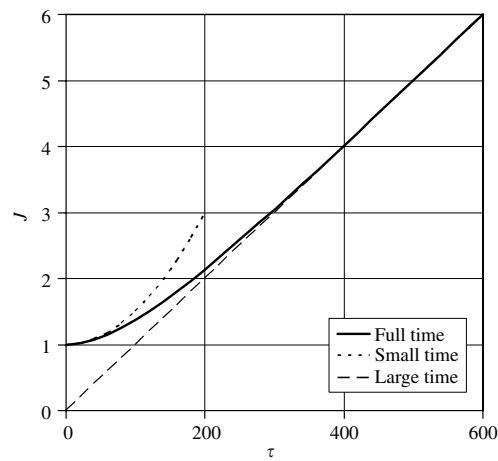
**FIGURE 12.11**

Normalized harmonic average permeability $\bar{K}(\tau)/K_0$ versus τ for $(B, \lambda) = (1, 1), (1, 2), (2, 1)$, and $(2, 2)$, and constant-rate coefficient where $B \equiv \beta\phi c_w$.

[Figure 12.12](#) and [Figure 12.13](#) show examples for the impedance index J versus τ , for B and λ of order unity and for smaller values, together with the small- and large-time asymptotic curves. These representations are relevant to the interpretation of experimental data and the extraction of the empirical

**FIGURE 12.12**

Example of impedance index J versus τ , for $L/x_w = 1$ and $B = \lambda = 1$, showing asymptotic behavior.

**FIGURE 12.13**

Example of impedance index J versus τ , for $L/x_w = 1$ and $B = \lambda = 0.01$, showing asymptotic behavior.

constants λ and B there from by fitting the theoretical curves to the data. This will be discussed further in a later section.

12.3.3 Variable-Rate Coefficient

In this section, solutions for the present model and for the model by Herzig et al. [4] are obtained, and the results are compared.

12.3.3.1 Present model

The constitutive equations (12.31) and (12.32) together with the equation of change (12.3) combine to give the following coupled equations for c and σ :

$$\phi \frac{\partial c}{\partial t} + u_o \frac{\partial c}{\partial x} = -(1 + b\sigma) \frac{\partial \sigma}{\partial t} \quad (12.71)$$

$$\frac{\partial \sigma}{\partial t} = k_o u_o c \quad (12.72)$$

After these have been solved, the deposition function $\dot{\sigma}_s$ can be obtained from Eq. (12.31) using

$$\dot{\sigma}_s \equiv (1 + b\sigma) \frac{\partial \sigma}{\partial t} \quad (12.73)$$

When rewritten in terms of the nondimensional variables defined by Eqs. (12.53), Eqs. (12.71) and (12.72) become:

$$\frac{\partial C}{\partial \tau} + \frac{\partial C}{\partial \bar{X}} = -\frac{1}{\phi c_w} (1 + b\sigma) \frac{\partial \sigma}{\partial \tau} \quad (12.74)$$

$$\frac{\partial \sigma}{\partial \tau} = \lambda \phi c_w C \quad (12.75)$$

where $\lambda \equiv k_o x_w$ as before. Equations (12.74) and (12.75) are controlled by the same base characteristic equation (12.60) that controls Eq. (12.54). However, for the present problem, it is more convenient to take a different approach and change to a characteristic-based set of independent coordinates, \bar{X} and θ , based on the following transformation:

$$\begin{aligned} F(X, \tau) &= \bar{F}(\bar{X}, \theta) \\ \bar{X} &= X \quad \text{and} \quad \theta = \tau - (X - 1) \\ \frac{\partial F}{\partial X} &= \frac{\partial \bar{F}}{\partial \bar{X}} \frac{\partial \bar{X}}{\partial X} + \frac{\partial \bar{F}}{\partial \theta} \frac{\partial \theta}{\partial X} = \frac{\partial \bar{F}}{\partial \bar{X}} - \frac{\partial \bar{F}}{\partial \theta} \\ \frac{\partial F}{\partial \tau} &= \frac{\partial \bar{F}}{\partial \bar{X}} \frac{\partial \bar{X}}{\partial \tau} + \frac{\partial \bar{F}}{\partial \theta} \frac{\partial \theta}{\partial \tau} = \frac{\partial \bar{F}}{\partial \theta} \end{aligned} \quad (12.76)$$

In terms of the over-bar variables, Eqs. (12.74) and (12.75) become:

$$\frac{\partial \bar{C}}{\partial \bar{X}} = -\frac{1}{\phi c_w} (1 + b\bar{\sigma}) \frac{\partial \bar{\sigma}}{\partial \theta} \quad (12.77)$$

$$\frac{\partial \bar{\sigma}}{\partial \theta} = \lambda \phi c_w \bar{C} \quad (12.78)$$

The coordinate θ is sometimes called the delay time. It is the time measured from zero after the initial discontinuity wave front passes a given location X . Equations (12.77) and (12.78) are equivalent to the characteristics equations (12.59) and (12.60) for the constant-rate-coefficient case, that is, for $b = 0$. For the rest of this analysis, we will suppress the over bar notation and take X and θ as the independent variables.

The boundary condition is that $C = 1$ for $X = 1$ (or for $X = 0$, say, by a simple shift along the X -axis) by Eq. (12.55). Thus $C(1, \theta) = 1$. Also, originally and before the disturbance wave arrives, we have $C = 0$ and $\sigma = 0$. Because the location of the initial disturbance wave that starts at $X = 1$ is denoted by $\theta = 0$, we have $C(X, \theta < 0) = 0$ and $\sigma(X, \theta \leq 0) = 0$.

Eliminate C from Eq. (12.77) by means of Eq. (12.78) and obtain a single second-order equation for σ as:

$$\begin{aligned}\frac{\partial^2 \sigma}{\partial X \partial \theta} &= -\lambda(1 + b\sigma) \frac{\partial \sigma}{\partial \theta} \\ &= -\lambda \frac{\partial}{\partial \theta} \left(\sigma + \frac{b}{2} \sigma^2 \right)\end{aligned}\quad (12.79)$$

Interchange the order of derivatives on the left-hand side and then integrate with respect to θ :

$$\frac{\partial \sigma}{\partial X} = -\lambda \sigma \left(1 + \frac{b}{2} \sigma \right) + f(X) \quad (12.80)$$

Here, $f(X)$ is an arbitrary function of integration. Because $\sigma = 0$ on $\theta = 0$ for all X , then it follows that $\partial \sigma / \partial X = 0$ on $\theta = 0$, and thus that $f(X) = 0$. Consequently, Eq. (12.80) reduces to

$$\frac{\partial \sigma}{\partial X} = -\lambda \sigma \left(1 + \frac{b}{2} \sigma \right) \quad (12.81)$$

In this equation, the variable θ does not appear explicitly, and thus it can be treated as an ordinary differential equation. The variables can now be separated as:

$$\lambda dX = -\frac{d\sigma}{\sigma(1 + (b/2)\sigma)} \quad (12.82)$$

After this equation has been integrated, σ can be solved for explicitly and the result written as:

$$\sigma(X, \theta) = \frac{g(\theta)e^{-\lambda(X-1)}}{1 - (b/2)g(\theta)e^{-\lambda(X-1)}} \quad (12.83)$$

where $g(\theta)$ is arbitrary constant (or function) of integration.

The function $C(X, \theta)$ is now determined by means of Eq. (12.78):

$$C(X, \theta) = \frac{1}{\lambda \phi c_w} \frac{(dg/d\theta)e^{-\lambda(X-1)}}{[1 - (b/2)g(\theta)e^{-\lambda(X-1)}]^2} \quad (12.84)$$

The initial and boundary conditions are satisfied when $g(0) = 0$ and when

$$\lambda \phi c_w = \frac{dg/d\theta}{[1 - (b/2)g(\theta)]^2} \quad (12.85)$$

This is a differential equation for $g(\theta)$ which, when solved, gives the result of

$$g(\theta) = \frac{\lambda \phi c_w \theta}{1 + (b/2)\lambda \phi c_w \theta} \quad (12.86)$$

The derivative is

$$\frac{dg}{d\theta} = \frac{\lambda \phi c_w}{[1 + (b/2)\lambda \phi c_w \theta]^2} \quad (12.87)$$

The above results hold when $\theta \geq 0$. When $\theta < 0$, both σ and C vanish.

For the deposition function, integration of Eq. (12.73) leads to the result

$$\sigma_s = \sigma \left(1 + \frac{b}{2} \sigma \right) H(\theta) = \frac{g(\theta)e^{-\lambda(X-1)}}{[1 - (b/2)g(\theta)e^{-\lambda(X-1)}]^2} H(\theta) \quad (12.88)$$

12.3.3.2 Solution for the model by Herzig et al.

When the constitutive equations (12.38) and (12.39) are combined with the equation of change (12.3), then the two coupled equations for c and σ_1 are:

$$\phi \frac{\partial c}{\partial t} + u_o \frac{\partial c}{\partial x} = -\frac{\partial \sigma_1}{\partial t} \quad (12.89)$$

$$\frac{\partial \sigma_1}{\partial t} = (1 + b_1 \sigma_1) k_o u_o c \quad (12.90)$$

where the subscript 1 delineates those variables associated with the formulation of Herzig et al. [4]. After these have been solved, then the deposition function $\dot{\sigma}_s$ can be obtained from

$$\dot{\sigma}_s \equiv \frac{\partial \sigma_1}{\partial t} \quad (12.91)$$

When the nondimensional variables (12.53) are introduced together with the transformation (12.76) to the characteristic coordinates, then Eqs. (12.89)

and (12.90) can be rewritten as:

$$\frac{\partial C}{\partial X} = -\frac{1}{\phi c_w} \frac{\partial \sigma_1}{\partial \theta} \quad (12.92)$$

$$\frac{\partial \sigma_1}{\partial \theta} = \lambda \phi c_w (1 + b_1 \sigma_1) C \quad (12.93)$$

These are the counterparts to Eqs. (12.77) and (12.78) for the present analysis model. The apparent difference is that the factor $(1+b\sigma) \rightarrow (1+b_1\sigma_1)$ has been shifted from one equation to the other. The initial and boundary conditions are the same as for the previous problem, with only σ replaced by σ_1 .

We now proceed to finding a single equation for σ_1 . First, solve for C from Eq. (12.93):

$$C = \frac{1}{\lambda \phi c_w b_1} \frac{\partial}{\partial \theta} \ln(1 + b_1 \sigma_1) \quad (12.94)$$

Substitute this into the left-hand side of Eq. (12.92) and obtain the following second-order equation for σ_1 :

$$\frac{1}{b_1} \frac{\partial^2 \ln(1 + b_1 \sigma_1)}{\partial X \partial \theta} = -\lambda \frac{\partial \sigma_1}{\partial \theta} \quad (12.95)$$

Interchange the order of integration on the left-hand side and then integrate with respect to θ . Set the function of integration equal to zero by virtue of the conditions $\sigma_1 = 0$ and $\partial \sigma_1 / \partial X = 0$ on $\theta = 0$, and finally obtain

$$\frac{\partial \sigma_1}{\partial X} = -\lambda \sigma_1 (1 + b_1 \sigma_1) \quad (12.96)$$

Herzig et al. [4] obtained this equation by a different approach.

Equation (12.96) is the same as our counterpart Eq. (12.81) except that the factor b_1 appears in place of $b/2$. The solution is therefore

$$\sigma_1(X, \theta) = \frac{g_1(\theta) e^{-\lambda(X-1)}}{1 - b_1 g_1(\theta) e^{-\lambda(X-1)}} \quad (12.97)$$

where $g_1(\theta)$ is an arbitrary function of integration. The function $C(X, \theta)$ is determined from Eq. (12.94):

$$C(X, \theta) = \frac{1}{\lambda \phi c_w} \frac{(d g_1 / d \theta) e^{-\lambda(X-1)}}{1 - b_1 g_1(\theta) e^{-\lambda(X-1)}} \quad (12.98)$$

Satisfying the boundary condition $C(1, \theta) = 1$ gives

$$\lambda\phi c_w = \frac{dg_1/d\theta}{1 - b_1 g_1(\theta)} \quad (12.99)$$

The solution to this differential equation subject to the initial condition $g_1(0) = 0$ is:

$$g_1(\theta) = \frac{1}{b_1} [1 - \exp(-b_1 \lambda \phi c_w \theta)] \quad (12.100)$$

The above results hold when $\theta \geq 0$. When $\theta < 0$, then both σ_1 and C vanish.

For the deposition function, integration of Eq. (12.91) yields the result

$$\sigma_s(X, \theta) = \sigma_1(X, \theta)H(\theta) = \frac{g_1(\theta)e^{-\lambda(X-1)}}{1 - b_1 g_1(\theta)e^{-\lambda(X-1)}} H(\theta) \quad (12.101)$$

These results are the same as obtained by Herzig et al. [4], only expressed in our current notation.

12.3.3.3 Comparison and discussion

The function $g(\theta)$ for the present model, given by Eq. (12.86), is algebraic in character, whereas the function $g_1(\theta)$ for the model by Herzig et al., given by Eq. (12.100), is exponential in character. As $\theta \rightarrow \infty$, $g(\theta)$ approaches its asymptote $2/b$, and $g_1(\theta)$ approaches its asymptote $1/b_1$. The variations $(b/2)g(\theta)$ versus θ^* and $b_1 g_1(\theta)$ versus θ_1^* , where $\theta^* \equiv (b/2)\lambda\phi c_w \theta$ and $\theta_1^* \equiv b_1 \lambda \phi c_w \theta$, are compared in Figure 12.14. As θ increases, the function $g_1(\theta)$ approaches its asymptote much more rapidly than the function $g(\theta)$.

Along the discontinuity wave, $\theta = 0^+$ or $\tau = (X - 1)^+$, the volume fraction of particles C decreases exponentially, the same as that for the present model, the model by Herzig et al. [4], and the constant-rate-coefficient model, that is, $C = \exp(-\lambda(X - 1))$, given by Eq. (12.66). On the other hand, unlike the constant-rate-coefficient model, the two variable-rate-coefficient models for C do vary with τ in the impairment zone for fixed locations of X .

The variations of C with X for the fixed time periods of $\tau = 1, 2$, and 3 are shown in Figure 12.15 and Figure 12.16 for the present model and for the model by Herzig et al. The calculations are for $\lambda = 1$, $b^* \equiv b\lambda\phi c_w = 1$, and $b_1^* \equiv b_1 \lambda \phi c_w = 1$, which correspond to $b = b_1$ for comparison purposes of the two models. For both models for a given τ , the curves start at the same value $C = 1$ at $X = 1$ and end with the same value at the discontinuity wave front $X = \tau + 1$. The curves for the model by Herzig et al., however, drop off much more rapidly than those for the present model, in a manner consistent with the variations shown in Figure 12.14.

The corresponding variations of C with τ for the fixed locations $X = 2, 3$, and 4 are shown in Figure 12.17 and Figure 12.18. At a given location

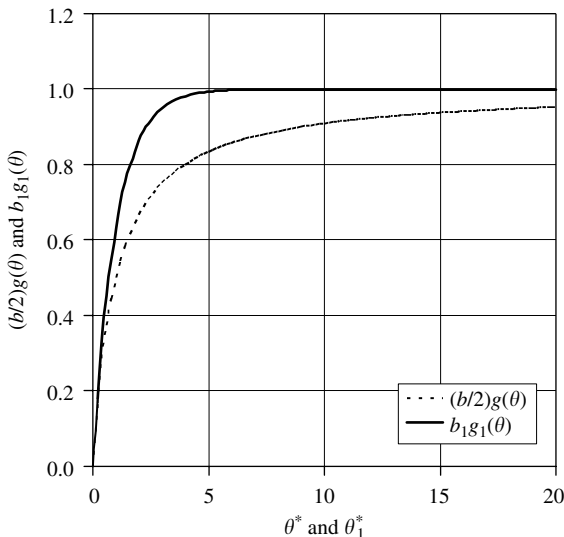


FIGURE 12.14
Comparison of the functions $g(\theta)$ and $g_1(\theta)$.

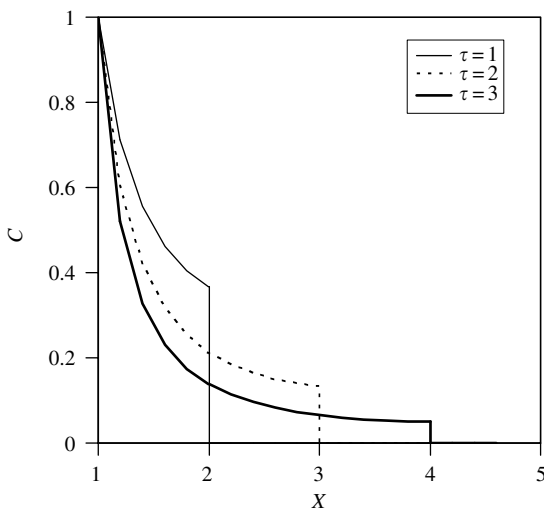
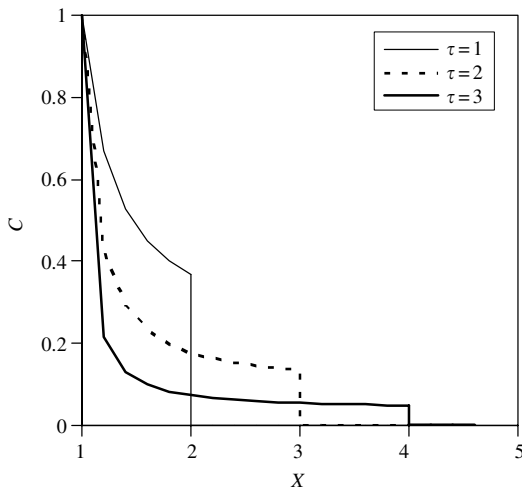
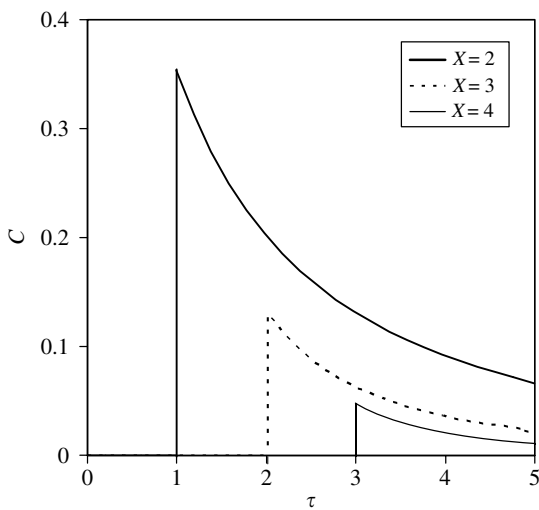


FIGURE 12.15
Particle volumetric fraction C versus X for $\tau = 1, 2, 3$ and $\lambda = 1$, $b^* = b\lambda\phi c_w = 1$, and variable-rate coefficient (present model).

X , after the jump across the discontinuity wave front at time $\tau = X - 1$, the curves for both the models start at the same value of C and then subsequently decrease with time. The model by Herzig et al. shows a stronger decrease with time, again consistent with the variations shown in Figure 12.14.

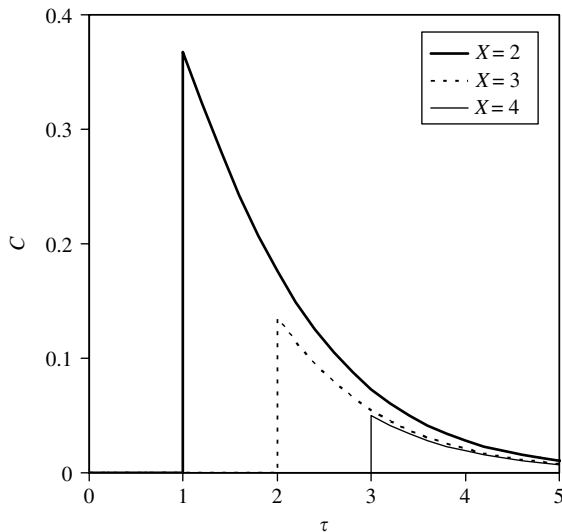
**FIGURE 12.16**

Particle volumetric fraction C versus X for $\tau = 1, 2, 3$ and $\lambda = 1, b_1^* = b_1\lambda\phi c_w = 1$, and variable-rate coefficient (model by Herzig et al.).

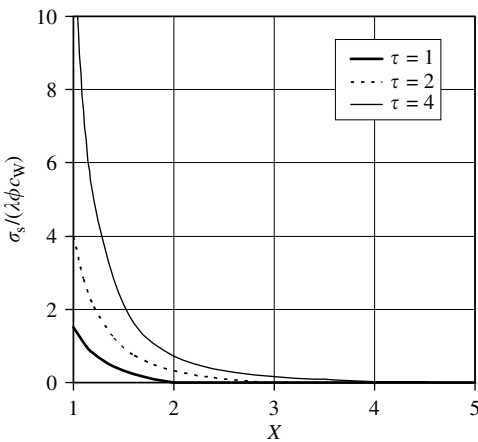
**FIGURE 12.17**

Particle volumetric fraction C versus τ for $X = 2, 3, 4, \lambda = 1, b^* = 1$, and variable-rate coefficient (present model).

[Figure 12.19](#) and [Figure 12.20](#) show the variations of the normalized particle deposition function $\sigma_s/\lambda\phi c_w$ with position X at time periods, $\tau = 1, 2$, and 4 for the two models. At the injection interface $X = 1$, the particle deposition function σ_s is greater for the model by Herzig et al. than for the present model,

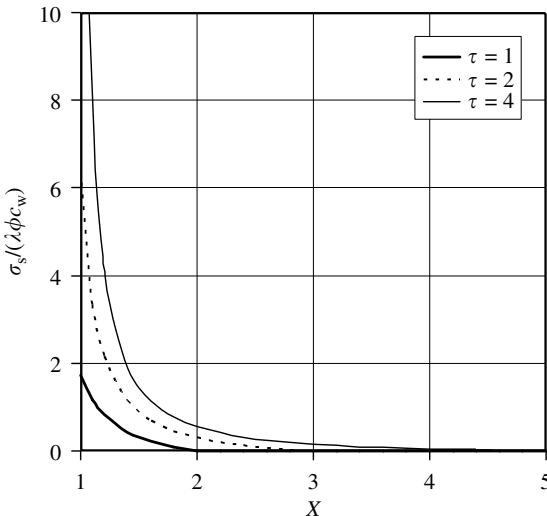
**FIGURE 12.18**

Particle volumetric fraction C versus τ for $X = 2, 3, 4, \lambda = 1, b_1^* = 1$, and variable-rate coefficient (model by Herzig et al.).

**FIGURE 12.19**

Normalized particle deposition $\sigma_s / (\lambda \phi c_w)$ versus X for $\tau = 1, 2, 4, \lambda = 1, b^* = 1$, and variable-rate coefficient (present model).

which in turn is greater than the basic model of a constant-rate coefficient (see Figure 12.7) for which $b = b_1 = 0$. All the curves decrease to zero at the wave-front location $X = \tau + 1$, where the slope also vanishes $\partial\sigma_s/\partial X = 0$. The model by Herzig et al. shows the steepest decrease.

**FIGURE 12.20**

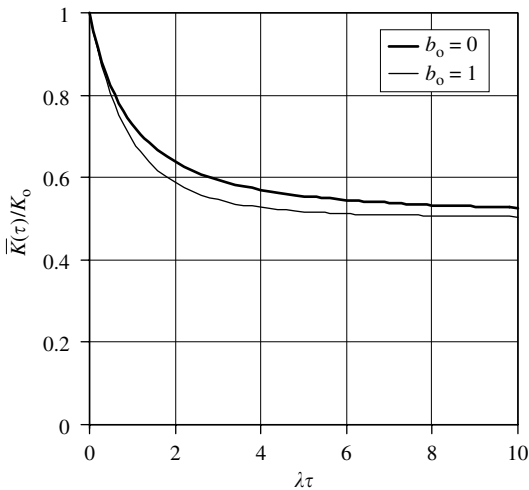
Normalized particle deposition $\sigma_s / (\lambda \phi c_w)$ versus X for $\tau = 1, 2, 4$, $\lambda = 1$, $b_1^* = 1$, and variable-rate coefficient (model by Herzig et al.).

The variations of the deposition function with the time τ are shown in Figure 12.8 and Figure 12.9 at the locations $X = 2, 3$, and 4 for the two models. The curves for the basic constant-rate-coefficient model ($b = b_1 = 0$) are also shown. At a given position X , all the curves start at the value zero when the wave front passes at the time $\tau = X - 1$, and then increase as the time increases subsequently. The curves for the constant-rate coefficient increase linearly and become unbounded, whereas the curves for the two models of variable-rate coefficients are bounded and approach asymptotes. For the present model, shown in Figure 12.8, the asymptotes are approached slowly and are $\sigma_s / \lambda \phi c_w = 1.833, 0.361$, and 0.110 for the locations designated by $X = 2, 3$, and 4 . For the model by Herzig et al., shown in Figure 12.9, the asymptotes are approached much more rapidly and are $\sigma_s / \lambda \phi c_w = 0.582, 0.157$, and 0.052 for the same locations.

12.3.3.4 Average permeability and impedance index

For the present model, the average permeability as defined by Eq. (12.42) can be expressed as:

$$\frac{\bar{K}(\tau)}{K_o} = \frac{1}{1 + BI(\lambda\tau, b_o)} \quad (12.102)$$

**FIGURE 12.21**

Normalized harmonic average permeability $\bar{K}(\tau)/K_o$ versus $\lambda\tau$ for $B \equiv \beta\phi c_w = 1$ and $b_o = 1$ (present model) and $b_o = 0$ (constant-rate coefficient).

where $B \equiv \beta\phi c_w$, $b_o \equiv b\phi c_w$, and $I(T, b)$ is the quadrature function defined by:

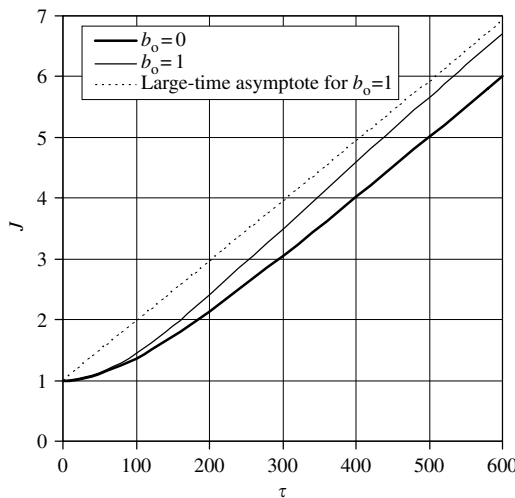
$$I(T, b) \equiv \frac{1}{T} \int_0^T \frac{2(T-u)\{2+b(T-u)\}e^{-u}}{[2+b(T-u)(1-e^{-u})]^2} du \quad (12.103)$$

These reduce to the constant-rate results when $b_o = 0$. A plot of the average permeability versus $T \equiv \lambda\tau$ is shown in Figure 12.21 for $B = 1$ and for $b_o = 1$ and 0. The curve for the variable-rate approaches the same asymptote but at a faster rate. The impedance index as determined by Eq. (12.43) with $L/x_w = 1$ is given by:

$$J(\tau) = 1 + B\tau I(\lambda\tau, b_o) \quad (12.104)$$

An example of J versus τ for the present model is shown in Figure 12.22 for $B = 0.01$, $\lambda = 0.01$, and $b_o = 1$, and compared with the constant-rate model $b_o = 0$. For small time periods, the two curves share the same asymptote, which is indicated in Figure 12.13. For large time periods, the present variable-rate curve departs from the constant-rate curve and swerves upward, slowly approaching its own straight-line asymptote. These curves are reminiscent of a set of data that will be analyzed in a later section.

For the model by Herzog et al., the formulas (12.102) and (12.104) still hold but with the quadrature $I(\lambda\tau, b_o)$ is replaced by $I_1(\lambda\tau, b_{1o})$, where

**FIGURE 12.22**

Example of impedance index J versus τ , for $L/x_w = 1$ and $B = \lambda = 0.01$, comparing variable-rate results (present model) with constant-rate results.

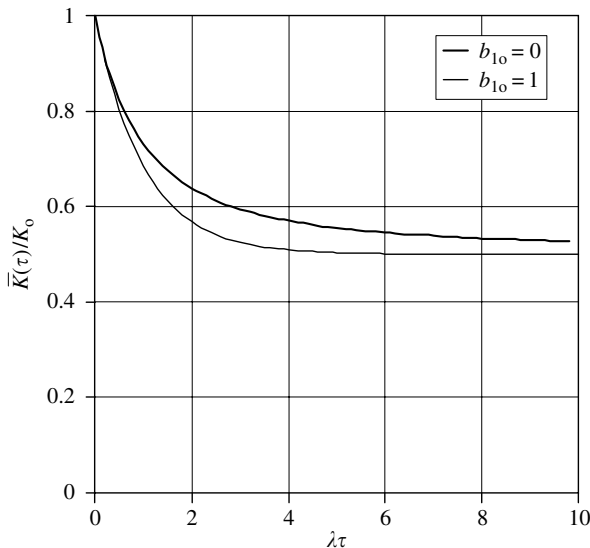
$b_{10} \equiv b_1 \phi c_w$ and

$$I_1(T, b) = \frac{1}{bT} \int_0^T \frac{(1 - e^{-b(T-u)})e^{-u}}{1 - (1 - e^{-b(T-u)})e^{-u}} du \quad (12.105)$$

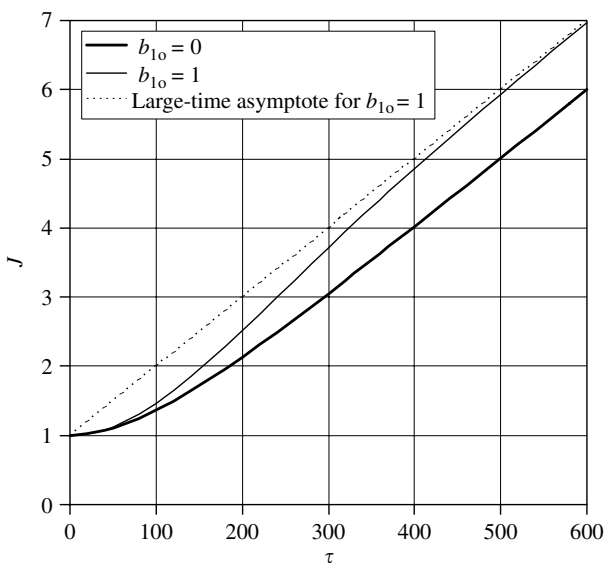
These reduce to the constant-rate results when $b_{10} = 0$. When $b_{10} = 1$, this quadrature can be evaluated explicitly:

$$I_1(T, b = 1) = \frac{1 - e^{-T}}{1 + e^{-T}} \quad (12.106)$$

This special case is suggestive of the overall exponential behavior of the quadrature. A plot of the average permeability versus $T \equiv \lambda\tau$ is shown in Figure 12.23 for $B = 1$ and for $b_{10} = 1$ and 0. The curve for the variable-rate case, owing to its strong exponential behavior, decreases much more rapidly toward the common asymptote shared by the constant-rate case. It also decreases more rapidly than the curve for the present model shown in Figure 12.21. An example of J versus τ for the model of Herzig et al. is shown in Figure 12.24 for $B = 0.01, \lambda = 0.01$, and $b_{10} = 1$, and compared with the constant-rate model $b_{10} = 0$. For small time periods, all the curves share the same asymptote. For large time periods, the Herzig et al. variable-rate curve departs from the constant-rate curve and swerves upward, rapidly approaching its own straight-line asymptote, which is parallel to the large-time asymptote for the constant-rate curve.

**FIGURE 12.23**

Normalized harmonic average permeability $\bar{K}(\tau)/K_0$ versus $\lambda\tau$ for $B \equiv \beta\phi c_w = 1$ and $b_{10} = 1$ (model by Herzig et al.) and $b_{10} = 0$ (constant-rate coefficient).

**FIGURE 12.24**

Example of impedance index J versus τ , for $L/x_w = 1$ and $B = \lambda = 0.01$, comparing variable-rate results (model by Herzig et al.) with constant-rate results.

12.4 One-Dimensional Rectilinear Problem with Time-Dependent Injection Rate

Suppose that the injection flow rate is time dependent according to the relation

$$q(t) = q_0 W(t) \quad (12.107)$$

Then the injection velocity is given by

$$u(t) = u_0 W(t) \quad (12.108)$$

Now consider the transport Eq. (12.52), for example. Because the velocity appears in the x -derivative term and the deposition term only, we can divide by the factor $W(t)$ and write the transport equation as:

$$\frac{\phi}{W(t)} \frac{\partial c}{\partial t} + u_0 \frac{\partial c}{\partial x} = -k_0 u_0 c \quad (12.109)$$

In all the cases treated so far in this analysis, the factor will appear in front of the time derivative as it does in Eq. (12.109). This suggests that we introduce the following time transformation:

$$t^*(t) = \int_0^t W(\tilde{t}) d\tilde{t} \quad \text{or} \quad \tau^*(\tau) = \int_0^\tau W(t_c \tilde{\tau}) d\tilde{\tau} \quad (12.110)$$

Now Eq. (12.109) can be written as:

$$\phi \frac{\partial c}{\partial \tau^*} + u_0 \frac{\partial c}{\partial x} = -k_0 u_0 c \quad (12.111)$$

This equation has the same form as for the steady injection-rate problem. The initial and boundary conditions are also invariant. Consequently, any solution that is known for the steady-injection problem can be readily converted to a solution for the time-dependent injection problem, specified by Eq. (12.107), by letting $\tau \rightarrow \tau^*(\tau)$.

For example, consider the following exponential decline function for the injection flow rate given by Donaldson and Chernoglazov [9], but modified as following in order to account for the limiting flow rate q_∞ :

$$q(t) = q_\infty + (q_0 - q_\infty) e^{-\delta t} \quad (12.112)$$

where δ is the reciprocal characteristic time. The validity of Eq. (12.112) is demonstrated later by correlating typical experimental data. Applying

Eq. (12.112), Eq. (12.107) can be written as:

$$W(\tau) = \frac{q_\infty}{q_0} + \left(1 - \frac{q_\infty}{q_0}\right) e^{-\delta^* \tau} \quad (12.113)$$

where $\delta^* \equiv \delta t_c$. Upon integration, we get

$$\begin{aligned} \tau^*(\tau) &= \frac{q_\infty}{q_0} \tau + \left(1 - \frac{q_\infty}{q_0}\right) \frac{1 - e^{-\delta^* \tau}}{\delta^*} \\ &\sim \frac{q_\infty}{q_0} \tau + \frac{1}{\delta^*} \left(1 - \frac{q_\infty}{q_0}\right), \quad \tau \rightarrow \infty \end{aligned} \quad (12.114)$$

If a large-time straight-line asymptote in the steady-injection case is denoted by $b + m\tau^*$, then in the time-dependent injection case it becomes:

$$b + m\tau^* = \left\{ b + \frac{m}{\delta^*} \left(1 - \frac{q_\infty}{q_0}\right) \right\} + \left(m \frac{q_\infty}{q_0}\right) \tau, \quad \tau \rightarrow \infty \quad (12.115)$$

Because q_∞/q_0 is less than unity for a decreasing rate of injection, the slope of the straight-line asymptote is less and the y -axis intercept is greater for the time-dependent injection case. An example is discussed in a later section.

12.5 Radial Problem with Constant Injection Rate

A corresponding analysis is carried out for constant- and variable-rate coefficients in the radial-flow case described in Figure 12.3. It is reasonable to consider a cylindrical radial flow around the wells completed into petroleum reservoirs because the thickness of typical petroleum reservoirs is significantly smaller compared to the lateral extent. Hence, the flow geometry is commonly assumed to be radially symmetrical in cylindrical coordinates and not in spherical coordinates in isotropic porous media.

12.5.1 Transport Equation

For radial flows, the volumetric flux for the particles in the flowing suspension is given by:

$$u = \frac{q_0}{2\pi rh} \quad (12.116)$$

where the parameters q_o and h denote the constant injection rate and reservoir formation thickness. We thus have

$$u(r) = u_w \frac{r_w}{r} = \frac{\text{const.}}{r} \quad (12.117)$$

where $u_w = q_o/2\pi r_w h$ is the injection velocity at the well-bore. Thus, in radial cylindrical coordinates we have

$$\mathbf{u} = u(r)\mathbf{e}_r \quad (12.118)$$

where \mathbf{e}_r is the unit basis vector in the flow direction, and \mathbf{u} satisfies the incompressibility condition (12.18). Therefore, substituting Eq. (12.118) into Eq. (12.3) yields the volumetric balance of suspended particles in terms of radial cylindrical coordinates:

$$\phi \frac{\partial c}{\partial t} + u(r) \frac{\partial c}{\partial r} = -\dot{\sigma}_s, \quad r > r_w, \quad t > 0 \quad (12.119)$$

The initial and boundary conditions are

$$c = 0, \quad \sigma_s = 0, \quad r > r_w, \quad t = 0 \quad (12.120)$$

$$c = c_w, \quad r = r_w, \quad t > 0 \quad (12.121)$$

12.5.2 Constant-Rate Coefficient

The sink term, expressing the loss of particles from the flowing suspension by deposition of particles at a rate proportional to the suspended-particle flux, is

$$\dot{\sigma}_s = k_o u(r) c \quad (12.122)$$

where k_o is the constant filtration coefficient. Use of Eqs. (12.117) and (12.122) now leads to the following first-order linear partial differential equation, with variable coefficients:

$$\phi \frac{\partial c}{\partial t} + \frac{u_w r_w}{r} \frac{\partial c}{\partial r} = -\frac{k_o u_w r_w}{r} c, \quad r > r_w, \quad t > 0 \quad (12.123)$$

This is the counterpart to Eq. (12.52) for the rectilinear-flow problem.

12.5.2.1 Nondimensional variables

Now change variables such that

$$C \equiv \frac{c}{c_w}, \quad Z \equiv \left(\frac{r}{r_w} \right)^2, \quad \tau \equiv \frac{u_w}{\phi r_w} t \quad (12.124)$$

Then we have

$$\frac{\partial C}{\partial \tau} + 2 \frac{\partial C}{\partial Z} = -\lambda \frac{C}{\sqrt{Z}}, \quad Z > 1, \quad \tau > 0 \quad (12.125)$$

where $\lambda \equiv k_0 r_w$. This is the counterpart to Eq. (12.54). The initial and boundary conditions become

$$C(Z > 1, 0^+) = 0 \quad (12.126)$$

$$C(1, \tau > 0) = 1 \quad (12.127)$$

12.5.2.2 Characteristic equations

Akin to the analysis leading to the characteristic equations (12.59) for the rectilinear-flow problem, the characteristic equations for Eq. (12.125) are found to be

$$\frac{dC}{dZ} = -\frac{\lambda}{2} \frac{C}{\sqrt{Z}} \quad \text{on} \quad \frac{d\tau}{dZ} = \frac{1}{2} \quad (12.128)$$

The integrated form of the base characteristic can be expressed as:

$$\tau - \frac{Z-1}{2} \equiv \Phi = \text{const.} \quad \text{or} \quad \tau - \frac{R^2-1}{2} \equiv \Phi = \text{const.} \quad (12.129)$$

where $Z = R^2$ and $R \equiv r/r_w$. The constant of integration is denoted by Φ . In the $\tau-R$ diagram shown in Figure 12.25, the base characteristics constitute a family of parabolas, each member of which is designated by its value of Φ . The constant of integration has been selected arbitrarily so that $\Phi = 0$ represents the curve that passes through the point of initial disturbance, $\tau = 0$ and $R = 1$.

Integration of the first of Eqs. (12.128) gives:

$$C(Z, \tau) = A(\Phi) e^{-\lambda \sqrt{Z}} \quad \text{on} \quad \Phi \equiv \tau - \frac{Z-1}{2} = \text{const.} \quad (12.130)$$

where $A(\Phi)$ is a function of integration that is a constant along a given base characteristic. When the initial and boundary conditions are enforced, the function of integration is found to be the same as Eq. (12.64) for the rectilinear-flow case, and the solution for the radial-flow case becomes

$$C(Z, \tau) = e^{-\lambda(\sqrt{Z}-1)} H(\Phi) \quad (12.131)$$

where $H(\Phi)$ is the unit Heaviside step function.

These results show that a wave front travels along the base characteristic $\Phi = 0$. The function C is discontinuous across the wave front, being zero ahead of it, $\Phi < 0$, and nonzero positive behind it, $\Phi > 0$. The trajectory of

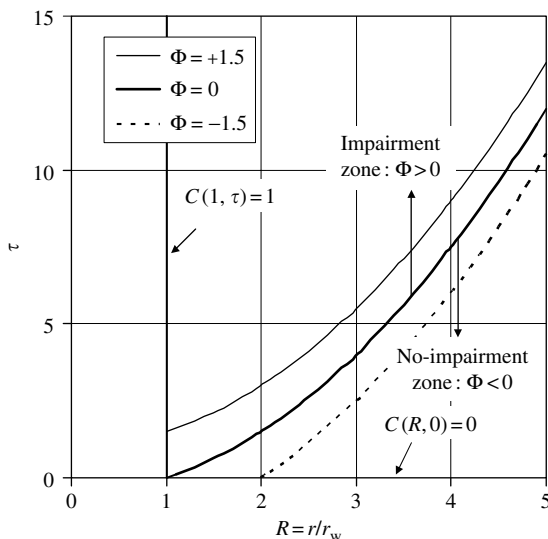


FIGURE 12.25
 τ - R diagram for radial problem.

the discontinuity wave is a parabola, described by $\Phi = 0$, or $\tau = (R^2 - 1)/2$, or $R = \sqrt{1 + 2\tau}$. Immediately downstream of the wave front, the volume fraction of particles decreases exponentially with distance,

$$C = \exp[-\lambda(R - 1)] \quad (12.132)$$

which is the same as for the rectilinear flow, Eq. (12.66). The variation with time, however, is different. For a fixed location R , there is no variation in C with time except for the jump across the discontinuity wave front when it passes by.

The deposition function can be determined by means of Eqs. (12.27) and (12.67). We find that

$$\sigma_s(Z, \tau) = \sigma(Z, \tau) = \lambda \phi c_w \Phi \frac{e^{-\lambda(\sqrt{Z}-1)}}{\sqrt{Z}} H(\Phi) \quad (12.133)$$

The deposition function decreases faster with distance than for the rectilinear-flow case, Eq. (12.68). It is zero along the wave front and continuous across it. The Z -derivative is zero and continuous along the wave front, but the time derivative at a given position is discontinuous. As for the rectilinear-flow case, the deposition function is zero at a given location until the wave front passes, and then it grows linearly with time.

The average permeability, according to Eq. (12.44), is

$$\frac{\bar{K}(\tau)}{K_o} = \frac{\ln(\sqrt{1+2\tau})}{\ln(\sqrt{1+2\tau}) + BI_r(\lambda, \tau)} \quad (12.134)$$

where $B \equiv \beta\phi c_w$ and

$$\begin{aligned} I_r(\lambda, \tau) &\equiv \frac{\lambda e^\lambda}{2} \int_1^{\sqrt{1+2\tau}} e^{-\lambda u} \left(\frac{1+2\tau}{u^2} - 1 \right) du \\ &= \frac{\lambda e^\lambda}{2} (1+2\tau) \left[E_2(\lambda) - \frac{E_2(\lambda\sqrt{1+2\tau})}{\sqrt{1+2\tau}} \right] - \frac{1 - e^{-\lambda(\sqrt{1+2\tau}-1)}}{2} \end{aligned} \quad (12.135)$$

and where

$$E_2(x) \equiv \int_1^\infty \frac{e^{-xu}}{u^2} du \quad (12.136)$$

is the exponential integral of order 2. The average permeability is plotted in Figure 12.26 for $B = 1$ and 2 , and $\lambda = 1$. The average permeability does not tend to a finite limiting value as for the rectilinear case, but slowly vanishes as $\tau \rightarrow \infty$.

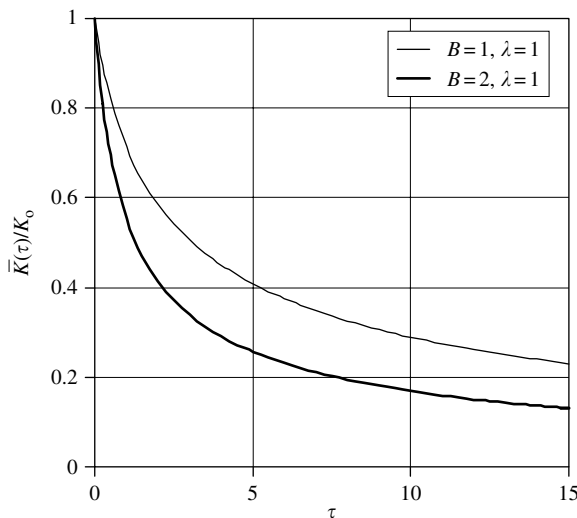
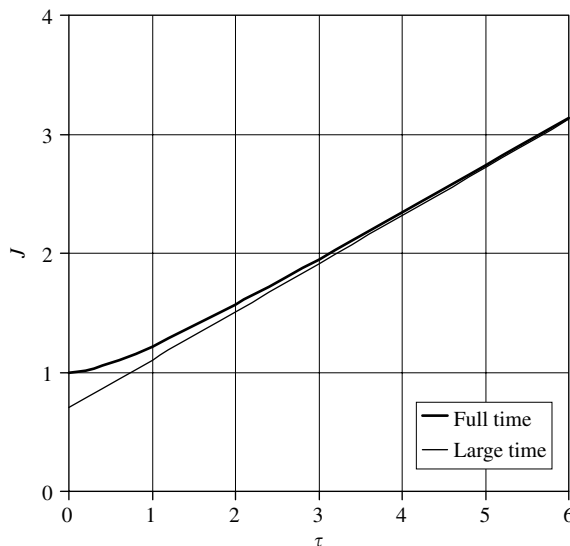


FIGURE 12.26

Example of normalized harmonic average permeability $\bar{K}(\tau)/K_o$ versus τ for radial flow, $\lambda = 1$, and constant-rate coefficient.

**FIGURE 12.27**

Example of impedance index J versus τ , for $R_e = e^1 = 2.7 \dots$ and $B = \lambda = 0.01$, for radial flow and constant-rate coefficient, showing asymptotic behavior.

The impedance index J , according to Eq. (12.45), is

$$\begin{aligned} J(\tau) &= 1 + \frac{B}{\ln(R_e)} I_r(\lambda, \tau) \\ &\sim \left\{ 1 - \frac{B}{2 \ln(R_e)} (1 - \Lambda(\lambda)) \right\} + \frac{B \Lambda(\lambda)}{\ln(R_e)} \tau, \quad \tau \rightarrow \infty \end{aligned} \quad (12.137)$$

where $\Lambda(\lambda) \equiv \lambda e^\lambda E_2(\lambda)$ and $R_e \equiv r_e/r_w$. Figure 12.27 shows J versus τ for $B = 1$ and $\lambda = 1$.

12.5.3 Variable-Rate Coefficient

For the present model, the solution for a variable-rate coefficient is derived for radial flow. No analytical solution has been found previously for the case of a variable-rate coefficient. Although Wennberg [2] mentions having a simulator developed for this case, no details as to the nature of the numerical solution method is provided.

12.5.3.1 Solution for present model

In terms of the nondimensional variables specified by Eqs. (12.124), the transport equation and constitutive relations for the radial-flow problem

become:

$$\frac{\partial C}{\partial \tau} + 2 \frac{\partial C}{\partial Z} = - \frac{r_w}{u_w c_w} \dot{\sigma}_s \quad (12.138)$$

$$\dot{\sigma}_s = \frac{u_w}{\phi r_w} (1 + b\sigma) \frac{\partial \sigma}{\partial \tau} \quad (12.139)$$

$$\frac{\partial \sigma}{\partial \tau} \equiv \frac{\lambda \phi c_w}{\sqrt{Z}} C \quad (12.140)$$

Eliminate $\dot{\sigma}_s$ between Eqs. (12.138) and (12.139), and obtain

$$\frac{\partial C}{\partial \tau} + 2 \frac{\partial C}{\partial Z} = - \frac{1}{\phi c_w} (1 + b\sigma) \frac{\partial \sigma}{\partial \tau} \quad (12.141)$$

Equations (12.140) and (12.141) constitute two coupled equations for C and σ .

Now transform to characteristic coordinates, Z and Φ , in a fashion similar to Eqs. (12.76):

$$\begin{aligned} F(Z, \tau) &= \bar{F}(\bar{Z}, \Phi) \\ \bar{Z} = Z \quad \text{and} \quad \Phi &= \tau - \frac{Z - 1}{2} \\ \frac{\partial F}{\partial Z} &= \frac{\partial \bar{F}}{\partial \bar{Z}} - \frac{1}{2} \frac{\partial \bar{F}}{\partial \Phi} \\ \frac{\partial F}{\partial \tau} &= \frac{\partial \bar{F}}{\partial \Phi} \end{aligned} \quad (12.142)$$

The discontinuity wave front is defined by $\Phi = 0$, the impairment zone by $\Phi > 0$, and the no-impairment zone by $\Phi < 0$.

Suppress the over-bar notation and obtain the counterparts to Eqs. (12.77) and (12.78):

$$2 \frac{\partial C}{\partial Z} = - \frac{1}{\phi c_w} (1 + b\sigma) \frac{\partial \sigma}{\partial \Phi} \quad (12.143)$$

$$\frac{\partial \sigma}{\partial \Phi} = \frac{\lambda \phi c_w}{\sqrt{Z}} C \quad (12.144)$$

Substitute for C into Eq. (12.143):

$$2 \frac{\partial}{\partial Z} \frac{\partial}{\partial \Phi} (\sqrt{Z} \sigma) = -\lambda (1 + b\sigma) \frac{\partial \sigma}{\partial \Phi} \quad (12.145)$$

Integrate with respect to Φ and obtain

$$2 \frac{\partial}{\partial Z} (\sqrt{Z}\sigma) = -\lambda \left(1 + \frac{b}{2}\sigma\right)\sigma + F(Z) \quad (12.146)$$

or

$$2\sqrt{Z} \frac{\partial\sigma}{\partial Z} = -\lambda \left(1 + \frac{b}{2}\sigma\right)\sigma - \frac{\sigma}{\sqrt{Z}} + F(Z) \quad (12.147)$$

where $F(Z)$ is an arbitrary function of integration. The initial and boundary conditions are

$$\sigma(Z, \Phi = 0) = 0 \quad \text{and} \quad C(Z = 1, \Phi) = 1 \quad (12.148)$$

It can now be established that $\partial\sigma/\partial Z = 0$ on $\Phi = 0$ and $\sigma = 0$, and thus that we must have $F(Z) = 0$, which was found to be true for the previous problems also. Consequently, Eq. (12.147) becomes

$$2\sqrt{Z} \frac{\partial\sigma}{\partial Z} = -\lambda \left(1 + \frac{b}{2}\sigma\right)\sigma - \frac{\sigma}{\sqrt{Z}} \quad (12.149)$$

Based on the form of solution (12.83) for the rectilinear problem, we assume that the solution for σ in this case has the form

$$\sigma = \frac{w_0}{1 - (b/2)w_1} \quad (12.150)$$

where w_0 and w_1 are functions to be determined. Because we have assumed two unknown functions to describe one, we have an arbitrary condition at our disposal. Substituting Eq. (12.150) into (12.149) yields:

$$[2(w_0\sqrt{Z})' + \lambda w_0] + \frac{b}{2}[-2(w_0\sqrt{Z})'w_1 + 2(w_0\sqrt{Z})w_1' + \lambda w_0[(w_0 - w_1)]] = 0 \quad (12.151)$$

Because the parameter b is arbitrary, set the collected terms inside the brackets separately equal to zero. This implies that the functions w_0 and w_1 , aside from the functions of integration do not depend explicitly on the parameter b :

$$2(w_0\sqrt{Z})' + \lambda w_0 = 0 \quad (12.152)$$

$$-\{2(w_0\sqrt{Z})' + \lambda w_0\}w_1 + 2(w_0\sqrt{Z})w_1' = -\lambda w_0^2 \quad (12.153)$$

or

$$2(w_0\sqrt{Z})w_1' = -\lambda w_0^2 \quad (12.154)$$

The solution to (12.152) is given by:

$$w_o = g(\Phi) \frac{e^{-\lambda(\sqrt{Z}-1)}}{\sqrt{Z}} \quad (12.155)$$

where $g(\Phi)$ is an arbitrary function of integration. Equation (12.155) is the counterpart of Eq. (12.133) for the constant-rate case. We can now treat Eq. (12.154):

$$w'_1 = -\frac{\lambda w_o}{2\sqrt{Z}} = \frac{(w_o\sqrt{Z})'}{\sqrt{Z}} = w'_o + \frac{w_o}{2Z} \quad (12.156)$$

Integration of Eq. (12.156) gives:

$$w_1 = w_o + \int_1^Z \frac{w_o}{2Z} dZ \quad (12.157)$$

Explicitly, we have

$$w_1 = g(\Phi) \left\{ \frac{e^{-\lambda(\sqrt{Z}-1)}}{\sqrt{Z}} + \int_1^Z \frac{e^{-\lambda(\sqrt{Z}-1)}}{2Z^{3/2}} dZ \right\} \quad (12.158)$$

or, after integrating by parts,

$$w_1 = g(\Phi) \left[1 - \lambda \int_1^Z \frac{e^{-\lambda(\sqrt{Z}-1)}}{2Z} dZ \right] \quad (12.159)$$

In Eq. (12.157) an arbitrary function of integration was set to zero order to accomplish the result $w_1(1, \Phi) = w_o(1, \Phi)$ and thus to have only one arbitrary function to deal with.

The function C is determined by means of Eq. (12.144), that is,

$$C(Z, \Phi) = \frac{\sqrt{Z}}{\lambda \phi c_w} \frac{\partial \sigma}{\partial \Phi} = \frac{1}{\lambda \phi c_w} \frac{\{dg/d\Phi\} e^{-\lambda(\sqrt{Z}-1)}}{[1 - (b/2)w_1]^2} \quad (12.160)$$

When the initial and boundary conditions (12.148) are enforced, it is found that the function $g(\Phi)$ is the same as Eq. (12.86) for the rectilinear-flow case, that is,

$$g(\Phi) = \frac{\lambda \phi c_w \Phi}{1 + (b/2)\lambda \phi c_w \Phi} \quad (12.161)$$

The above results are exact. They hold when $\Phi \geq 0$. When $\Phi < 0$, then both σ and C vanish.

The deposition function is found to be

$$\sigma_s = \sigma \left(1 + \frac{b}{2} \sigma \right) \quad (12.162)$$

$$\sigma_s = \frac{w_o [1 + (b/2)(w_o - w_1)]}{(1 - (b/2)w_1)^2} H(\Phi) \quad (12.163)$$

12.5.3.2 Partial solution for model by Herzog et al.

For the Herzog et al. [4] problem in the nondimensional coordinates, the transport equation (12.138) remains the same, but the constitutive equations are:

$$\dot{\sigma}_s = \frac{u_w}{\phi r_w} \frac{\partial \sigma_1}{\partial \tau} \quad (12.164)$$

$$\begin{aligned} \frac{\partial \sigma_1}{\partial \tau} &= (1 + b_1 \sigma_1) \frac{\partial \sigma}{\partial \tau} \\ &= \lambda \phi c_w (1 + b_1 \sigma_1) \frac{C}{\sqrt{Z}} \end{aligned} \quad (12.165)$$

Note that Eq. (12.140) still holds, but becomes inconsequential after it is used to get the second of Eqs. (12.165). Now after Eq. (12.164) is used to eliminate $\dot{\sigma}_s$ from the transport equation (12.138) the problem reduces to the following two coupled equations for C and σ_1 :

$$\frac{\partial C}{\partial \tau} + 2 \frac{\partial C}{\partial Z} = - \frac{1}{\phi c_w} \frac{\partial \sigma_1}{\partial \tau} \quad (12.166)$$

$$\frac{\partial \sigma_1}{\partial \tau} = \lambda \phi c_w (1 + b_1 \sigma_1) \frac{C}{\sqrt{Z}} \quad (12.167)$$

When these are written in terms of the characteristic coordinates, we have

$$2 \frac{\partial C}{\partial Z} = - \frac{1}{\phi c_w} \frac{\partial \sigma_1}{\partial \Phi} \quad (12.168)$$

$$\frac{\partial \sigma_1}{\partial \Phi} = \frac{\lambda \phi c_w}{\sqrt{Z}} (1 + b_1 \sigma_1) C \quad (12.169)$$

Solve for C from Eq. (12.169) and substitute into Eq. (12.168):

$$2 \frac{\partial}{\partial Z} \frac{\partial}{\partial \Phi} (\sqrt{Z} \ln(1 + b_1 \sigma_1)) = -\lambda b_1 \frac{\partial \sigma_1}{\partial \Phi} \quad (12.170)$$

Integrate with respect to Φ and obtain

$$2 \frac{\partial}{\partial Z} (\sqrt{Z} \ln(1 + b_1 \sigma_1)) = -\lambda b_1 \sigma_1 \quad (12.171)$$

where the function of integration was set equal to zero. Equation (12.171) can be written alternatively as:

$$2\sqrt{Z}\frac{\partial\sigma_1}{\partial Z} = -\lambda\sigma_1(1+b_1\sigma_1) - \frac{(1+b_1\sigma_1)\ln(1+b_1\sigma_1)}{b_1\sqrt{Z}} \quad (12.172)$$

Compare this equation with Eq. (12.149) for the present model.

Equation (12.172) does not lend itself to an exact solution. On the other hand, a perturbation analysis is possible. Factor out the linear term from the second term on the right-hand side of Eq. (12.172) and rewrite the equation as follows:

$$2\sqrt{Z}\sigma'_1 = -k_o r_w \sigma_1(1+b_1\sigma_1) - \frac{\sigma_1}{\sqrt{Z}} - \frac{P(b_1\sigma_1)}{b_1\sqrt{Z}} \quad (12.173)$$

where

$$P(b_1\sigma_1) \equiv (1+b_1\sigma_1)\ln(1+b_1\sigma_1) - b_1\sigma_1 \quad (12.174)$$

Except for the factor that contains $P(b_1\sigma_1)$, Eq. (12.173) has the same form as Eq. (12.149). Thus when $P(b_1\sigma_1)$ is sufficiently small, the solution for σ_1 is nearly the same as for σ with $b \rightarrow 2b_1$. Thus, a perturbation or a successive-approximation scheme appears feasible. Such a course of action will not be pursued further here.

12.6 Radial Problem with Time-Dependent Injection Rate

The procedure described in Section 12.4 for the one-dimensional rectilinear-flow case also holds for the radial-flow case. Therefore, it is not repeated here, but applied in the next section.

12.7 Applications and Validation of Analytic Solutions

The analytical solutions of the one-dimensional rectilinear and radial macroscopic phenomenological models are applied for analysis of the impairment of porous media by migration and deposition of fine particles and its effect on the injectivity decline during flow of particle–fluid suspensions.

12.7.1 One-Dimensional Rectilinear Case

The one-dimensional rectilinear-flow experiments were carried out by injecting particle–water suspensions into core plugs at constant rates ([Figure 12.2](#)).

Here, we analyze the experimental data of van den Broek et al. [10], Bedrikovetsky et al. [3], and Al-Abduwani et al. [11]. These studies report the data of the overall permeability reduction or the impedance index variation as a function of the number of pore volumes of fluid injected into laboratory core plugs, measured in terms of the initial pore volume, given by Eq. (12.58). The relationship given by Eq. (12.58) also expresses the dimensionless time used in the present formulation.

12.7.1.1 Case 1

van den Broek et al. [10] injected a suspension of grounded Bentheimer sandstone particles and water into the Bentheimer sandstone cores. The conditions of their two separate experiments carried out using the 24- and 60-ppm concentration suspensions are described by the second and third columns in Table 12.1. Both the present model and the model by Herzig et al. [4] yield about the same quality representation of the experimental data. Therefore, only the results obtained with the model by Herzig et al. [4] are compared with experimental data in Figure 12.28. The model represents both injection tests satisfactorily during the early period. However, the measured permeability decline during the late period is more pronounced than the simulated results, probably because of the explanations offered in Section 12.8. The columns two and three of Table 12.1 also present the best-estimate parameter values obtained by least-squares regression and the values of the permeability impairment parameter, the filtration rate coefficient, and the deposition coefficient calculated there from.

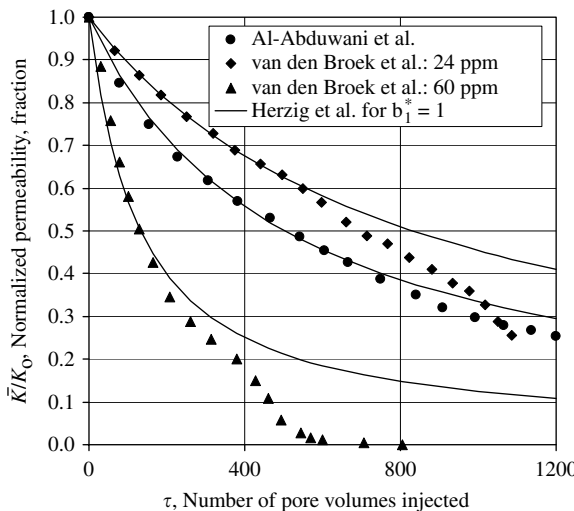


FIGURE 12.28

Normalized harmonic average permeability versus number of pore volume injected: comparison of the analytic solution of Herzig et al. for $b_1^* = 1$ with experimental data for rectilinear case.

12.7.1.2 Case 2

Al-Abduwani et al. [11] injected a suspension of grounded Hematite particles and water into a Bentheim sandstone core. The conditions of their experiment are described by the fourth column in [Table 12.1](#). Both the present model and the model by Herzog et al. [4] yield about the same quality representation of their experimental data. Therefore, only the results with the model by Herzog et al. [4] are compared with the experimental data in [Figure 12.28](#). It is observed that the model generally represents the experimental data satisfactorily over the full test period. However, the measured permeability decline during the late period is slightly faster than the simulated results probably because of the explanations offered in Section 12.8, but not as fast as the decline observed in Case 1. Column four of Table 12.1 presents the best-estimate parameter values obtained by least-squares regression and the values of the permeability impairment parameter, the filtration rate coefficient, and the deposition coefficient calculated there from.

12.7.1.3 Case 3

Bedrikovetsky et al. [3] injected seawater into a core taken from a Brazilian deep-water offshore reservoir formation. The conditions of their experiments are described in column five of Table 12.1. Their experimental data are compared with the fitted curves according to the model by Herzog et al. and the present model in [Figure 12.29](#) and [Figure 12.30](#). Both the present model and

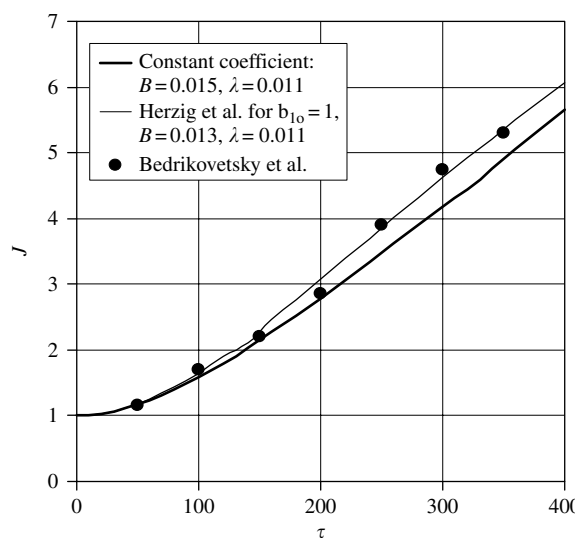
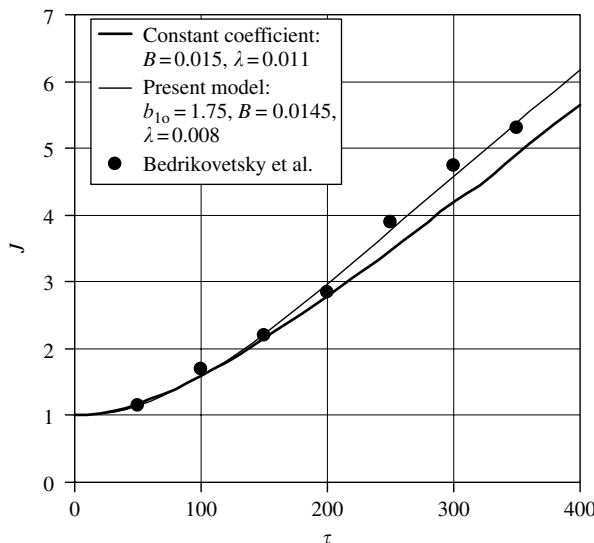


FIGURE 12.29

Correlation of data with theory: impedance index J versus τ , variable-coefficient (model by Herzog et al.) versus constant-coefficient model for $L/x_w = 1$.

**FIGURE 12.30**

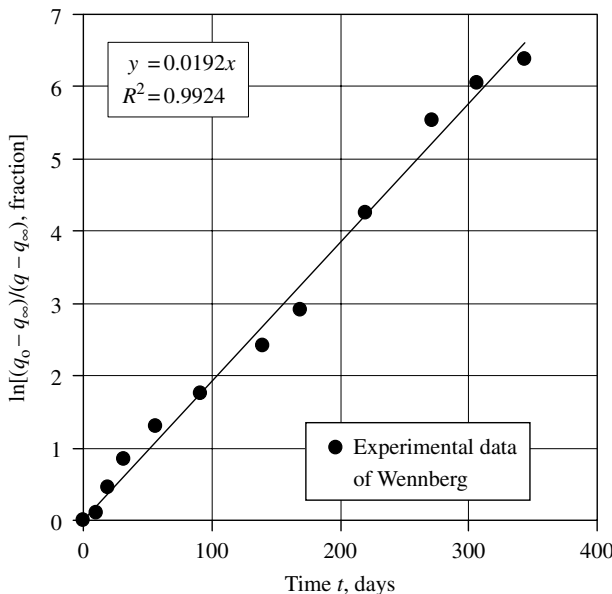
Correlation of data with theory: impedance index J versus τ , present model for variable-coefficient versus constant-coefficient model for $L/x_w = 1$.

the model by Herzog et al. [4] accurately represent their experimental data, similar to Cases 1 and 2. Column five of Table 12.1 presents the best-estimate parameter values obtained by least-squares regression and the values of the permeability impairment parameter, the filtration rate coefficient, and the deposition coefficient calculated there from.

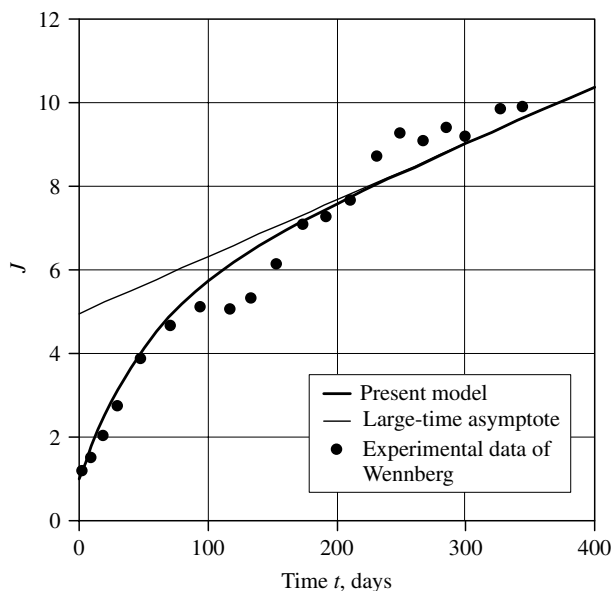
12.7.2 Radial Case

The one-dimensional radial-flow field experiment was carried out by the injection of a particle–water suspension into a reservoir as described in Figure 12.3. Here, we analyze the experimental data of Wennberg [2], who conducted a test at a variable injection rate. The data were reported as a function of the actual time instead of the number of pore volumes of fluid injected.

Wennberg [2] injected seawater into Well A42 at a variable rate. The type of the rock formation was not described. The conditions of this experiment are described in Table 12.2. The validity of Eq. (12.112) is demonstrated by Figure 12.31 showing a successful least-squares linear regression of this equation to typical decline rate data of Wennberg [2] with a coefficient of regression $R^2 = 0.99$, very close to 1.0. Table 12.2 also presents the best-estimate parameter values (q_∞, λ) obtained by least-squares linear regression

**FIGURE 12.31**

Correlation of the experimental time-dependent injection rate data of Wennberg for radial case for Well A42 after filter change.

**FIGURE 12.32**

Correlation of data of Wennberg for Well A42 after filter change with theory: impedance index J versus time t , radial flow with time-dependent injection and constant-rate coefficient for $\lambda = 70$ and $B/\ln(Re) = 0.00021$.

on a semi-logarithmic scale. The experimental measurements of Wennberg [2] on the impairment of the porous medium are compared with the fitted curves according to the present time-dependent injection rate model using a constant-rate coefficient in [Figure 12.32](#). Column two in [Table 12.2](#) presents the best-estimate parameter values obtained by least-squares regression and the values of the permeability impairment parameter, the filtration rate coefficient, and the deposition coefficient calculated there from. The present model represents the experimental data with reasonable accuracy.

12.8 Concluding Remarks

The mechanism and kinetics of fine particle deposition in porous media were described by two different approaches and compared. A new phenomenological approach was taken here in order to represent the source/sink term with constitutive relations. The present approach expressed the rate of deposition function as a function of the particle mass or number flux, with the proportionality factor being a function of the mass or number of particles per unit volume, whereas Herzig et al. [4] simply allow the filtration coefficient to be a variable with the deposition function itself. Although the present system of equations has a similar appearance to that developed by Herzig et al. [4], the equivalent constitutive relations are subtly different and more rigorous.

The resulting equations were expressed in normalized variables and solved analytically for rectilinear and radial flows in porous media. The analytical solutions were provided for both the constant and variable deposition rate coefficients. The results were used to generate a number of new useful formula of practical importance, including the variation of the injectivity ratio, impedance index, porosity, and permeability, and fine particle concentration in the suspension and porous media by fine particle retention. Besides the variable-rate coefficient, we have also dealt with the formulation and analytic solution for the time-dependent injection rate case. Further, the profiles were illustrated for the particle concentration in the particle–fluid suspension and the cumulative particle deposition in porous media as a function of the dimensionless time. Typical scenarios simulated demonstrated the parametric sensitivity of the evolution of the outgoing wave front and disturbances generated by the wave front. A methodology for determination of the parameters of the deep-bed filtration process by fitting the large-time portion of the experimental data was proposed and shown to be valid. Applications were illustrated for interpretation and evaluation of the various laboratory tests involving the injection of particle–fluid suspensions into core plugs and the field observations concerning the deep-bed filtration near the well-bore formation resulting from the injection of a fluid containing fine particles into completed wells in petroleum reservoirs.

The analytical solution of the deep-bed filtration model can only represent the experimental data until the initiation of a possible external filter cake buildup over the injection face of the porous medium. As stated at the beginning of the model formulation, here the particles are considered sufficiently small compared to the pore size so that an external filter cake would not form until the porous medium is fully saturated with the particles. Nevertheless, the effect of the external filter cake can be taken into account by using a suitable external cake buildup model as described by Civan [1]. However, this is beyond the focus of the present chapter. It is also possible that the filtration coefficient significantly varies when the pore-volume conditions approach the maximum particle-packing limit of porous medium as the pore volume is saturated by the deposited particles. The charge effects (zeta-potential) and rapid change of the fluid velocity (convective acceleration/deceleration) inversely with radial distance also play an important role. These effects should be taken into account when analyzing the late-time data. Application of complicated correlations such as given by Tien [12] may require a numerical solution. This suggests that further theory and experiments are necessary in order to investigate and understand the underlying phenomena.

Nomenclature

A_o	constant cross-sectional surface area of the porous formation or a core plug, m^2
A	cross-sectional surface area, m^2
c, c_p	particle volume concentration or volume fraction occupied by the particles in a particle–fluid suspension, ppm
c_f	carrier fluid volume concentration or volume fraction occupied by the carrier fluid in a particle–fluid suspension, ppm
c_w	value of c at the injection port, ppm
\mathbf{e}_x	unit vector in the rectilinear-flow direction
\mathbf{e}_r	unit vector in the radial-flow direction
$f(X)$	an arbitrary function of integration
$g_1(\theta)$	an arbitrary function of integration
h	reservoir formation thickness, m
$H(u)$	the unit Heaviside step function
J	impedance index, dimensionless
\mathbf{j}_w	volumetric diffusion flux vector of the carrier fluid (water), $\text{m}^3/\text{m}^2/\text{sec}$
\mathbf{j}_p	volumetric diffusion flux vector of the particles, $\text{m}^3/\text{m}^2/\text{sec}$
k_o	filtration coefficient, per sec
K	permeability, m^2
\bar{K}	harmonic-average permeability, m^2
L	core length, m
m_p	average mass per particle, kg/number

N	total number of particles that cross a unit area at a given location in the time t , number/m ² /sec
p	pressure, Pa
PV_0	initial pore volume, m ³
q_o	constant or initial volumetric injection rate, m ³ /sec
q	volumetric rate of flow, m ³ /sec
q_w	volumetric injection rate, m ³ /sec
q_∞	limiting injection rate, m ³ /sec
Q	cumulative volume of suspension injected, m ³
r	distance in the radial coordinate direction, m
r_e	radius of influence of the injection well, m
r_f	radius of the front position ahead of which there is no deposition, m
r_w	radius of the injection well-bore, m
\mathbf{u}, u	volumetric flux, superficial velocity, or Darcy velocity of the particulate suspension, m ³ /m ² /sec
\mathbf{v}	interstitial or actual pore space velocity of the particulate suspension, m/sec
V_p^*	volume of an average particle, m ³
x	distance in the Cartesian coordinate direction, m
x_e	distance of influence of the injection well, m
x_f	location of the front position ahead of which there is no deposition, m
x_w	location of the injection well-bore, m
X	dimensionless distance in the Cartesian coordinate direction, dimensionless
Z	square of dimensionless distance in the radial coordinate direction, dimensionless
α	injectivity ratio, dimensionless
ϕ	porosity, fraction
λ	$k_o L$ or $k_o r_w$, dimensionless
ρ	density, kg/m ³
ρ_p	mass density of the particulate matter, kg/m ³
ρ_p^*	material density of an average particle, kg/m ³
ρ_f	mass density of the carrier fluid phase, kg/m ³
ρ_f^*	material density of the carrier fluid phase, kg/m ³
δ	reciprocal characteristic time, per sec
τ	dimensionless time or number of injected pore volumes, dimensionless
τ_a	macroscopic average tortuosity of the flow paths in porous media, dimensionless
$\dot{\mu}_s$	a particle mass per unit bulk volume of porous media per unit time sink term, kg/m ³ /sec
σ	number of particles filtered out in the time t , and referred to as the basic filtration number, ppm
σ_1	basic filtration rate defined by Eq. (12.29), ppm per unit time
$\dot{\sigma}_s$	volumetric rate of deposition function, ppm per unit time

Subscripts

- e external or effluent-end boundary
f front position
o initial state
w well-bore
 ∞ long-time condition
-

Conversion Factors

- 1 in. = 0.0254 m
1 ft = 0.3048 m
1 d = 86,400 sec
1 ml = 10^{-6} m³
1 D = $0.9869233 \times 10^{-12}$ m²
1 bbl/d = 1.84×10^{-6} m³/sec
1 l/h = 2.778×10^{-7} m³/sec
-

References

1. Civan, F., *Reservoir Formation Damage — Fundamentals, Modeling, Assessment, and Mitigation*, Gulf Pub. Co, Houston, TX, and Butterworth-Heinemann, Woburn, MA, p. 742, 2000.
2. Wennberg, K.E., Particle Retention in Porous Media: Applications to Water Injectivity Decline, Ph.D. Dissertation, the Norwegian University of Science and Technology, Trondheim, February 1998, p. 177.
3. Bedrikovetsky, P., Marchesin, D., Shecaira, F., Souza, A.L., Milanez, P.V., and Rezende, E., Characterization of deep bed filtration system from laboratory pressure drop measurements, *J. Pet. Sci. Eng.*, 32, 167–177, 2001.
4. Herzig, J.P., Leclerc, D.M., and Le Goff, P., Flow of suspensions through porous media—application to deep filtration, *Industrial Eng. Chem.*, 62(5), 8–35, 1970.
5. Slattery, J.C., *Advanced Transport Phenomena*, Cambridge, UK: Cambridge University Press, p. 734, 1999.
6. Dupuit, J., *Etudes Theoriques et Pratiques sur le Mouvement des Eaux dans les Canaux Decouverts et a Travers les Terrains Permeables*, 2nd edn., Dunod, Paris, 1863.
7. Payatakes, A.C., Rajagopalan, R., and Tien, C., Application of porous media models to the study of deep bed filtration, *The Canadian J. Chem. Eng.*, 52, No. 6, 722–731, 1974.
8. Hildebrand, F.B., *Advanced Calculus for Applications*, Englewood Cliffs, New Jersey: Prentice-Hall Inc., pp. 379–389, 1962.
9. Donaldson, E.C. and Chernoglazov, V., Drilling mud fluid invasion model, *J. Pet. Sci. Eng.*, 1(1), 3–13, 1987.

10. van den Broek, W.M.G.T., Bruin, J.N., Tran, T.K., van der Zande, M.J., and van der Meulen, H., Core-Flow Experiments with Oil and Solids Containing Water, SPE paper 54769, Presented at the 1999 SPE European Formation Damage Control Conference, the Hague, 31 May–1 June 1999, p. 8.
11. Al-Abduwani, F.A.H., Shirzadi, A., van den Broek, W.M.G.T., and Currie, P.K., Formation Damage vs. Solid Particles Deposition Profile During Laboratory Simulated PWRI, SPE paper 82235, Presented at the 2003 SPE European Formation Damage Control Conference, the Hague, 13–14 May 2003, 10 p.
12. Tien, C., *Granular Filtration of Aerosols and Hydrosols*, Butterworth-Heinemann, Woburn, MA, p. 365, 1989.

Part VII

Geothermal, Manufacturing, Combustion, and Bioconvection Applications in Porous Media

13

Modeling Heat and Mass Transport Processes in Geothermal Systems

Robert McKibbin

CONTENTS

13.1 Introduction	546
13.2 Physical Processes	547
13.3 Conservation Equations	548
13.3.1 Conservation of Mass	549
13.3.2 Conservation of Linear Momentum (Darcy's Law).....	550
13.3.3 Conservation of Energy	551
13.3.4 Formation Parameters.....	552
13.3.5 Fluid Parameters	555
13.3.6 Distribution Laws.....	559
13.3.6.1 Molecular diffusion	559
13.3.6.2 Dalton's law	560
13.3.6.3 Henry's law	560
13.3.7 Boundary Conditions	561
13.4 Steady One-Dimensional Flows	561
13.4.1 Horizontal Flows: Total Viscosity and Flowing Enthalpy ..	561
13.4.1.1 Total, or effective viscosity	561
13.4.1.2 Flowing enthalpy.....	562
13.4.2 Steady Vertical Flows: Heat Pipes	563
13.5 Numerical Simulation	565
13.6 Some Current Research Efforts	568
13.7 Summary	569
References	570

13.1 Introduction

Historically, geothermal systems have been an important energy source in those countries lucky enough to have them. Hot groundwater has been used for many centuries for cooking, bathing, therapeutic, heating, and chemical processes. Modern industrial developments have expanded these uses to extensive space-heating for buildings and to the usage of higher enthalpy fluids for electricity generation; see, for example, Lund and Freeston [1] and Huttner [2]. While the former uses involved tapping the surface outflows in the form of hot springs and fumaroles, the usage of the latter had to wait for the suitable drilling, piping, machinery, and materials technology of the last century.

The mathematical modeling of heat and mass flows has introduced a powerful tool to aid virtual exploitation of underground geothermal systems. The relatively high cost of drilling wells into geothermal aquifers, especially those that are either overpressured with respect to hydrostatic gradients or those that are boiling, has made the use of modeling and computational simulation attractive. Computing the effects of exploitation of such resources on a large scale and predicting how systems would react locally to proposed usage are done without large-scale engineering resources. The predictive capabilities of quantitative models led to their being used in the engineering design process; they also play an essential role in planning new energy developments and in improving current ones.

Several decades of experience and testing of the models and computations mean that the relatively near-surface regions are now better understood. Most of the geothermal systems that are being exploited now have well-developed numerical models, which are continually updated and adjusted as more data becomes available. Current attention is being focused on the deeper zones that underlie geothermal reservoirs, and that provide a link between their bases and the magmatic heat sources further below. The dialogue between volcanologists and geothermal scientists and engineers is being strengthened by the interaction of the geological, geophysical, and geochemical groups with reservoir engineers and modelers.

This chapter describes the mathematical modeling processes that are applied to physical systems, where fluids move within heated porous underground structures, and the differential equations that describe the mass and energy transport processes. The various parameters that are needed to describe the thermodynamic properties of the fluid and solid phases are listed and explained. Some of the techniques for solving the nonlinear systems of differential equations that result from the formal modeling process are described, and some recent developments and foci of research attention are mentioned. There is, naturally, a generic overlap with quantitative descriptions of other such phenomena; it is the medium-scale estimates of structural and fluid properties that are important in geothermal modeling, and it is

precisely these estimates that are difficult to make because of the “invisibility” of most of the systems that are being simulated.

Many of the finer details of laboratory-scale porous media investigations are not important in geothermal system modeling. As noted above, the matrix structures of the underground systems are unable to be described exactly because of their inaccessibility. Hot water can pervade geological matrices of different types, including sediments (some of which may be partly cemented by chemical deposits), rock fractures formed through cooling of volcanic magma flows, double-porosity structures where fractures link permeable blocks, and combinations of these. Many, if not most, geothermal systems are composed of layers of different rock materials laid down through a succession of geological events over thousands of years. Clearly defined boundaries cannot be placed exactly, other than at a few points where they are intersected by boreholes. So the effort in geothermal modeling is on broad-scale approaches, and the current thinking on useful models is the focus of this chapter.

Other chapters in this Handbook of Porous Media cover some related aspects. The derivation of the fundamental conservation equations is discussed in [Chapter 1](#), the porosity structure in fractured porous media is characterized in [Chapter 3](#), while mechanical dispersion models are evaluated in [Chapter 5](#). The effects on the fluid density of temperature and salinity are discussed in [Chapter 8](#) on double-diffusive convection. Some of these areas of investigation are directly relevant to geothermal systems, while others apply to phenomena that are overwhelmed by the length scales and/or the heat and mass fluxes of the geophysical situation.

13.2 Physical Processes

Models of flow processes in geothermal systems have to take into account the strong coupling between heat and mass transport. The usual conceptual models on which such quantitative mathematical models are based involve motion of a single-phase fluid (liquid or gas) or a flow of two fluid phases that are in thermodynamic equilibrium, within a stationary porous rock matrix. The dominant fluid component is water, with solutes and gases in relatively small concentrations. Because geothermal systems evolve slowly over long periods of time, the assumption that rock and fluid have the same temperature in an undisturbed system is a good one. Even when exploitation or fluid injection takes place, the time constant for temperature equilibration over pore sizes is usually much shorter than over the intermediate scale used for averages, and local thermal equilibrium is assumed.

The fluid-filled rock structure is thermally conductive and serves to transport heat from high-temperature regions near the base of the Earth’s crust to

the surface. However, it is the internal energy that is contained within the rock matrix that contributes most significantly to the energy reserve. For typical geothermal system porosities of less than 5%, more than 90% of the internal energy is contained in the rock matrix. In contrast to the flow of hydrocarbons within an oil reservoir that is tapped through wells, the flowing fluid in a geothermal structure serves mainly as a medium to transport the thermal energy contained within the rock matrix, rather than as the main container of energy in the system. It is this feature of geothermal systems that must be reflected correctly in good physical models.

The earliest models of geothermal systems were based on pure water as the saturating fluid and the focus was on the thermodynamics of pure water substance. The determination of suitable correlations for its properties, in forms easily converted for use in computer subroutines, was essential to the quantification of mass and heat flows by numerical simulation. Early computer subroutines used interpolations within lookup tables of thermodynamic properties; the design of those computational subroutines reflected differences of opinion as to which were the most favorable primary thermodynamic state parameters to use.

Development of further sophistication through consideration of chemicals dissolved in the liquid phase, and of various gas components contributing to the total gas pressure, has recently led to more complicated formulations, and also to interest in modeling the transport of minerals and the leaching and/or deposition within the rock matrix of the solid phases of solutes. Some of these aspects are mentioned below.

The porous matrix has received attention, too, with more detail being placed on the fractured nature of geothermal rocks, in contrast to the early models, which were based on typical groundwater aquifers, and which were considered to be homogeneous, but not necessarily isotropic, sedimentary structures. Chapter 3 of this handbook discusses fractured media in some detail. On the length scales of geothermal systems, the porosity and permeability are usually considered as smoothly varying spatially in regions between discontinuities such as faults or strata interfaces, whatever the pore structure. However, bedding induces anisotropy in the permeability and this is reflected in the structure of the permeability tensor (see below and, e.g., Bear [3], Bear and Bachmat [4], and Nield and Bejan [5]).

13.3 Conservation Equations

The description of a geothermal system is largely based on the continuum hypothesis, using a representative elementary volume (REV) formulation. It is assumed that the scale of description is large enough for volume-averaged quantities to be statistically valid, while being small compared with the macroscopic dimensions of the large geophysical structure (e.g., see Refs. [3–5]).

System descriptions are based on locally averaged quantities that may vary spatially and temporally.

The distribution of phases is calculated using volume fractions, while the phase properties are based on mass units. The volume fraction of the system that may be occupied by geothermal fluid is called the effective porosity ϕ ; it is a local measure of the interconnected pore space available to the geothermal fluid and may vary according to rock type and position (as well as time, if deposition and/or dissolution are taking place). The remaining volume fraction, $1 - \phi$, is occupied by the rock matrix and possibly some, usually small, unconnected pores. These latter pores contribute to the total porosity, the space not occupied by solid rock. The distinction between the values of the total and effective porosities is usually neglected in geothermal modeling. The volume fractions of the interconnected pore space occupied by the liquid and gas phases are denoted S_ℓ and S_g respectively (called the liquid and gas saturations) with $S_\ell + S_g = 1$.

13.3.1 Conservation of Mass

Equations derived from the principle of mass conservation for each of the system fluid components i (i = water, solute, noncondensable gas, etc.), which may be distributed within both liquid and gas phases, are usually written in the following form, see, for example, Ref. [4]:

$$\frac{\partial A_m^{(i)}}{\partial t} + \nabla \cdot \mathbf{Q}_m^{(i)} = q_m^{(i)} \quad (13.1)$$

Here the mass per unit formation volume for component i is given by

$$A_m^{(i)} = \phi \left[X_\ell^{(i)} S_\ell \rho_\ell + X_g^{(i)} S_g \rho_g \right] \quad (13.2)$$

where ρ_ℓ and ρ_g are the densities of the liquid and gas phases respectively, while $X_\ell^{(i)}$ and $X_g^{(i)}$ are the mass fractions of component i present in each of the separate fluid phases. The specific mass flux, or mass flux of component i per unit cross-sectional area of the formation, is $\mathbf{Q}_m^{(i)}$, defined in Eqs. (13.6), (13.7) below, while $q_m^{(i)}$ is a source term for component i in units of mass per unit time and per unit formation volume. This last term can be used to model extraction or injection of fluid via boreholes, and to model precipitation and/or dissolution of chemicals contained in the fluid onto/from the pore surfaces of the rock matrix.

Summation of the mass conservation equations (13.1), (13.2) over all fluid components gives:

$$\frac{\partial A_m}{\partial t} + \nabla \cdot \mathbf{Q}_m = q_m \quad (13.3)$$

where the total fluid mass per unit formation volume is given by

$$A_m = \phi [S_\ell \rho_\ell + S_g \rho_g] \quad (13.4)$$

while \mathbf{Q}_m is the total specific mass flux and q_m is the total mass source term.

13.3.2 Conservation of Linear Momentum (Darcy's Law)

Known as Darcy's law, the simplest model for fluid flow in a porous medium is derived by considering, because fluid velocities are small, that terms representing inertial forces in the momentum conservation equation are negligible compared with those for pressure, body and viscous forces (i.e., $Re \ll 1$); see Ref. [5]. This approximation is reasonable for geothermal flows, except perhaps near boreholes; the latter, while important as point sinks or sources in simulations, form only very small regions of the total formation volumes considered. The question of whether Darcy's law is appropriate or should be extended with other nonlinear terms is debated in Ref. [5].

When only one fluid phase is present in the pores, one momentum equation is used, but for a general two-phase formulation, separate equations are required for the liquid and gas phase mass fluxes per unit cross-sectional formation area, $\mathbf{Q}_{m\ell}$ and \mathbf{Q}_{mg} , given respectively by:

$$\mathbf{Q}_{m\ell} = \rho_\ell \mathbf{v}_\ell = \rho_\ell \frac{k_{r\ell}}{\mu_\ell} \mathbf{k} \otimes [-\nabla p_\ell + \rho_\ell \mathbf{g}] \quad (13.5a)$$

$$\mathbf{Q}_{mg} = \rho_g \mathbf{v}_g = \rho_g \frac{k_{rg}}{\mu_g} \mathbf{k} \otimes [-\nabla p_g + \rho_g \mathbf{g}] \quad (13.5b)$$

where \otimes is the tensor product operator, and \mathbf{v}_ℓ and \mathbf{v}_g are the specific volume fluxes (volume flux per unit cross-sectional formation area) for the liquid and gas phases, respectively. These are also known as the Darcy velocities of the separate phases. The mass fluxes for component i in the liquid and gas phases are given by

$$\mathbf{Q}_{m\ell}^{(i)} = X_\ell^{(i)} \mathbf{Q}_{m\ell} \quad (13.6a)$$

$$\mathbf{Q}_{mg}^{(i)} = X_g^{(i)} \mathbf{Q}_{mg} + D_w^{(i)} \rho_g [-\nabla X_g^{(i)}] \quad (13.6b)$$

The total mass flux for component i (as used in Eq. [13.1]) is then given by:

$$\mathbf{Q}_m^{(i)} = \mathbf{Q}_{m\ell}^{(i)} + \mathbf{Q}_{mg}^{(i)} \quad (13.7)$$

The last term in Eq. (13.6b) represents the transport of mass in the gas phase by diffusion as well as advection. Diffusive fluxes of components in the liquid phase are regarded as very small compared with their advected mass fluxes,

and are usually neglected in geothermal simulations. Further comment is made in the section on distribution laws.

Other parameters not already defined include the following: \mathbf{k} is the formation intrinsic permeability tensor; k_{rl} and k_{rg} are permeability reduction factors (or relative permeabilities) that depend on the liquid saturation S_ℓ ; μ_ℓ and μ_g are the dynamic viscosity of each phase; p_ℓ and p_g are the liquid and gas phase pressures; $D_w^{(i)}$ is the mass diffusion coefficient for component i in water vapor in the gas phase. Further definitions and comments about these parameters will be given below.

When only one fluid phase is present, a single equation can be retrieved by setting to zero either all the $X_\ell^{(i)}$ (for gas phase only) or all the $X_g^{(i)}$ (for liquid phase only).

13.3.3 Conservation of Energy

As already mentioned, geothermal fluid flow speeds are small. It is then usual to assume that all components and phases are in local thermodynamic equilibrium, and in particular are at the same temperature. The equation that reflects conservation of energy may be written as follows, see, for example, Ref. [4]:

$$\frac{\partial A_e}{\partial t} + \nabla \cdot \mathbf{Q}_e = q_e \quad (13.8)$$

where the energy per unit formation volume is

$$A_e = (1 - \phi)\rho_r u_r + \phi[S_\ell \rho_\ell u_\ell + S_g \rho_g u_g] \quad (13.9)$$

and the specific energy flux (flux per unit cross-sectional formation area) is

$$\mathbf{Q}_e = \sum_i \left[h_\ell^{(i)} \mathbf{Q}_{m\ell}^{(i)} + h_g^{(i)} \mathbf{Q}_{mg}^{(i)} \right] + \mathbf{K} \otimes (-\nabla T) \quad (13.10)$$

Equation (13.10) reflects the transport of heat by both advection and thermal conduction. Cross-diffusion (Soret and Dufour) effects are neglected since they are unable to be measured *in situ* and are also unlikely to be significant because density gradients in natural geothermal systems are small, having evolved over millennia, and temperature gradients produce gravitational buoyancy forces, the effect of which will dominate in advection.

In these equations, q_e is a source term in units of energy per unit time and per unit formation volume, while ρ_r and u_r are the density and specific internal energy of the rock particles; u_ℓ and u_g are the specific internal energies and $h_\ell^{(i)}$ and $h_g^{(i)}$ are the component specific enthalpies of the liquid and gas fluid phases respectively. The local temperature of all components and phases is T , while \mathbf{K} is the effective thermal conductivity tensor of the rock–fluid mixture.

Because the porosity in geothermal systems is small (typically less than 5%), the rock matrix contains the majority of the internal energy; also, the thermodynamic properties of the matrix dominate rock–fluid mixture values of the thermal conductivity (see Section 13.3.4 for further discussion).

13.3.4 Formation Parameters

As mentioned above, early models of geothermal reservoirs regarded the formations as essentially consisting of (maybe several) isotropic sedimentary-type layers, with anisotropy arising from the layering itself. More recent modeling recognizes that thermal fracturing of the volcanic rocks that form most of such reservoirs have an inherent anisotropy. The rock material between the fractures may also have a secondary permeability, with flow into and out of the surrounding fractures.

The parameters used in the conservation equations above are discussed in more detail here. The discussion relates only to the application of the more general theory of flow in porous media to geothermal modeling, and represents approximations that are necessarily made to model large-scale systems about which very little detailed data is available.

Effective porosity ϕ . This is the local fraction of the formation, which consists of connected pore space that is available to fluid. Isolated pore space, assumed relatively small, is not taken into account. While the pointwise porosity may vary from zero in a rock particle to 100% in a pore, ϕ is the spatially averaged value over a REV; it may vary with position in a reservoir, but is more commonly assumed to be of uniform value within specified subregions of the formation being considered. The quantity ϕ is dimensionless.

Effective thermal conductivity tensor \mathbf{K} . The effective or overall thermal conductivity of the rock–fluid mixture is a combination of the rock and fluid values, and also depends in a complicated way on the geometry of the matrix structure. If conduction in the rock and fluid phases occurs in parallel, then the averaged thermal conductivity is the weighted arithmetic mean of the rock and fluid values, given by $K = (1 - \phi)K_r + \phi K_f$. If heat conduction takes place in series, the averaged value is the porosity-weighted harmonic mean. A weighted geometric mean has also been proposed [5]. In all cases, since the porosity ϕ is usually small, the rock value dominates.

A commonly used approximation for the thermal conductivity in geothermal systems that takes some account of the presence of solid and fluid phases, is given by the isotropic tensor \mathbf{K} with $K_{ii} = K$ ($i = 1, 2, 3$), where

$$K = (1 - \phi)K_r + \phi K_f \quad (13.11)$$

with the rock value K_r typically in the range 2.0 to 2.5 W/m/K for solid rock material, while the fluid thermal conductivity, which varies with the fluid phase composition in the pores, is taken to be the volume-weighted average of the liquid and gas values, given by $K_f = S_\ell K_\ell + S_g K_g$. If

any gas phase (which has low density and low thermal conductivity) is present, K_f is about an order of magnitude less than K_r , so, in most cases, $K = K_r$ is a close approximation. A more detailed discussion is given in Ref. [5].

Rock density ρ_r and specific internal energy u_r . The density of the solid rock particles is usually taken to lie in the range 2000 to 3000 kg/m³, depending on the rock type. Appropriate data is readily available in the geological literature, or see Ref. [6]. A variety of values used in simulations may be seen in Refs. [7–16]. The specific heat c_r of rock varies very little with either temperature or pressure, so the specific internal energy of the rock particles may be written:

$$u_r = c_r T \quad (13.12)$$

where c_r has a constant value of around 1000 kJ/kg/K and T is measured in °C. (Note that the zero datum for energy values in geothermal systems is usually taken to be 0°C.)

Intrinsic permeability tensor \mathbf{k} . The permeability is a measure of how easily a single phase fluid moves in a porous medium under the influence of a dynamic pressure gradient (absolute pressure gradient adjusted for gravitational effects). It is a property of the porous matrix only; fluid property effects are incorporated in Darcy's law through the fluid density and dynamic viscosity (see Eqs. [13.5a,b]). The principal axes of \mathbf{k} are influenced mostly by the bedding or fracturing of the porous matrix. For a system with a horizontal bedding structure, there is little variation in the horizontal plane, and in most cases a significantly smaller value of permeability in the vertical direction. With respect to a Cartesian coordinate system with position vector components (x, y, z) where the gravitational acceleration vector is represented by $\mathbf{g} = (0, 0, -g)$, the principal components of \mathbf{k} can be written (k_h, k_h, k_v), where the vertical permeability k_v is smaller, by up to an order of magnitude, than the horizontal value k_h . Typical values of the components of \mathbf{k} for fractured geothermal systems lie in the range 10^{-15} to 10^{-12} m² (i.e., 1 millidarcy to 1 darcy, where 1 darcy $\approx 1.0 \times 10^{-12}$ m²) with values up to two orders of magnitude larger for sedimentary (low-temperature) systems. The horizontal permeability of geothermal systems is usually estimated from well-testing procedures as for petroleum reservoirs, but with more difficulty, because of the high compressibility of boiling mixtures. A variety of case studies are discussed in Refs. [7–16]. Discussions about the relationship between porosity and permeability may be found in, for example, Refs. [5] and [17]; however, the detailed correlations for granular-type matrix structures is largely not useful for fractured rocks.

Relative permeabilities k_{rl}, k_{rg} . Also known as permeability reduction factors, these parameters allow for modeling the way that one fluid phase interferes with the motion of the other when two phases are present in the pores. Each reduction factor is a function of the liquid saturation S_ℓ . Most models reflect various experimental evidence that, if one of the phases is present in only relatively small amounts ($S_\ell < S_{\ell r}$ or $S_g < S_{gr}$, where $S_{\ell r}$ and S_{gr} are called the

residual liquid and gas saturations, respectively), movement of that phase is almost completely inhibited by the other and the corresponding permeability reduction factor is effectively zero.

While there are a number of specific formulations of the relationship between the relative permeabilities and liquid or gas saturation, most follow a common structure. Typically, the functions are of the form $k_{rl}(S_\ell)$ and $k_{rg}(S_\ell)$, where both are continuous and monotonic, with,

$$\text{for } S_\ell \leq S_{\ell r}, \quad k_{rl} = 0, \quad k_{rg} = 1 \quad (13.13a)$$

$$\text{for } S_{\ell r} < S_\ell < 1 - S_{gr}, \quad k_{rl} = f(S_\ell), \quad k_{rg} = g(S_\ell) \quad (13.13b)$$

$$\text{for } S_\ell \geq 1 - S_{gr} \text{ (or } S_g \leq S_{gr}), \quad k_{rl} = 1, \quad k_{rg} = 0 \quad (13.13c)$$

where f and g are monotonic functions of S_ℓ . The simplest formulation uses straight line functions:

$$f(S_\ell) = S_\ell^* = \frac{S_\ell - S_{\ell r}}{1 - S_{gr} - S_{\ell r}} \quad g(S_\ell) = 1 - S_\ell^* \quad (13.14a)$$

while another commonly used set of formulae is that first derived by Corey [18]:

$$f(S_\ell) = (S_\ell^*)^4 \quad g(S_\ell) = (1 - S_\ell^*)^2 \left[1 - (S_\ell^*)^2 \right] \quad (13.14b)$$

where S_ℓ^* is defined in Eq. (13.14a). Typical values of $S_{\ell r}$ and S_{gr} lie in the ranges 0–0.4 and 0–0.1, respectively. The two sets of relative permeability curves defined above are illustrated in Figure 13.1 for the case $S_{\ell r} = 0.2$, $S_{gr} = 0.1$.

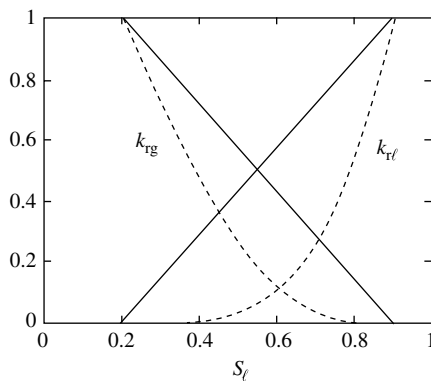


FIGURE 13.1

Relative permeability functions $k_{rl}(S_\ell)$ and $k_{rg}(S_\ell)$ for $S_{\ell r} = 0.2$, $S_{gr} = 0.1$: ——— straight line functions (Eq. [13.14a]), - - - - - Corey curves (Eq. [13.14b]).

Voidage ε . Deposition of solid precipitates from the fluid onto the walls of the rock pore spaces decreases the pore volume available for the fluid. This may be measured by the voidage ε , the volume fraction of the rock pore space available for fluid. Equations (13.1) to (13.4), (13.8), and (13.9) above take $\varepsilon = 1$, but any consideration of the solid precipitate's contribution to mass and energy balances would need another parameter such as ε to account for it, while specific properties for the solid precipitate phase would also be required.

Large amounts of such deposition would inevitably alter the permeability by sealing pore connections, perhaps completely. For small amounts of deposition, the effect on permeability is usually neglected. As will be described below, recent developments in modeling deep high-pressure high-temperature brines, where solid salt precipitate may exist in equilibrium with solute-saturated fluids, explicitly include the solid precipitate fraction in mass and energy balances, see McKibbin and McNabb [19,20]. Quartz deposition and dissolution in a geothermal system owing to field development is discussed in Ref. [21].

The timescale for deposition depends on the geochemical processes at work. Rejection of geothermal waste liquid from power generation plants is becoming common; if the fluid is cooled and becomes saturated with respect to one or more of the solutes, rapid sealing may occur. For naturally developed systems, the process is slower, and self-adjustment of the formation by refracturing may take place; see comments in Ref. [20].

13.3.5 Fluid Parameters

Because water is the predominant fluid component in geothermal systems, accurate modeling of its thermodynamic properties is essential. Tables of the thermodynamic properties of water substance are readily available, usually given in terms of the independent state variable pair (p, T) , with pressure p in bars absolute ($1 \text{ bar} = 10^5 \text{ Pa}$) and temperature T in $^\circ\text{C}$ ($0^\circ\text{C} = 273.15 \text{ K}$); for an example of such tables, see Ref. [22].

For any given reservoir temperature $T < 374.15^\circ\text{C}$ (the so-called critical temperature), a boiling or saturation pressure exists, denoted by $p = p_{\text{sat}}(T)$, at which, under ideal conditions, both the liquid and gas (steam, or water vapor) phases of water can coexist; conditions are then said to be saturated. At the critical temperature, $p_{\text{crit}} = p_{\text{sat}}(374.15^\circ\text{C}) = 221.2$ bars absolute. The inverse function, which gives the saturation temperature in terms of pressure, is written $T = T_{\text{sat}}(p)$. For $T > 374.15^\circ\text{C}$, or $p > 221.2$ bars absolute, the conditions are said to be supercritical, and there is no pressure at which the two phases become distinguishable.

For a fluid that is composed mainly of water, but with some disassociated salts and noncondensable gases dissolved in it, the boiling or saturation relationship will be slightly different from that for pure water. In general, the

boiling pressure will be given by $p = p_{\text{sat}}(T, X_\ell^{(1)}, X_\ell^{(2)}, \dots, X_\ell^{(N)})$, where N is the total number of components, and $i = 1$ corresponds to water.

Generally, two thermodynamic variables determine the state of a system for a pure substance; at saturated conditions, the pressure p and temperature T are functionally related and so are no longer independent. The liquid saturation S_ℓ may be used as a replacement for either T or p ; then either (p, S_ℓ) or (T, S_ℓ) is used as an independent state variable pair (together with concentrations of other components, if present in large enough mass fractions $X_\ell^{(i)}$ to cause significant effects). For $p < p_{\text{sat}}(T, X_\ell^{(i)})$ [or $T > T_{\text{sat}}(p, X_\ell^{(i)})$], superheated vapor forms the only phase (gas), while single-phase compressed liquid conditions prevail for $p > p_{\text{sat}}(T, X_\ell^{(i)})$ [or $T < T_{\text{sat}}(p, X_\ell^{(i)})$]. Generally, the presence of dissolved salts increases the boiling temperature, while noncondensable gases cause boiling-temperature depression; see O'Sullivan et al. [23].

The thermodynamic properties of a brine that has a significant content of NaCl (common salt) were investigated by Palliser and McKibbin [24–26] while the presence of (noncondensable) CO₂ gas was considered in Refs. [20,27]. Insofar as these (NaCl, CO₂) components are representative of solutes and noncondensable gases in general, the properties of a geothermal fluid that contains total equivalents of salt or gases can be approximated by the correlations set out in those works. The difficulties of accurately estimating all the cross-correlations for diffusion, etc., in multicomponent mixtures makes this equivalent-type model attractive for many systems where NaCl and CO₂ are the main solute and noncondensable gas components.

Surface tension and adsorption effects may balance a small difference in liquid and gas phase pressures, p_ℓ and p_g in two-phase fluids in porous systems; this is called vapor pressure lowering, and is discussed further below. Such effects are usually small under natural geothermal two-phase conditions, and the assumption that the pressures in the liquid and gas phases are the same produces little error. However, injection of colder water into a two-phase vapor-dominated system may produce significant effects, as shown through numerical simulation by Pruess [28].

Liquid saturation S_ℓ . For conditions corresponding to single-phase (compressed) liquid, where $p > p_{\text{sat}}(T)$, the liquid saturation $S_\ell = 1$, while the gas saturation $S_g = 0$. Similarly, for $T > T_{\text{sat}}(p)$, $S_\ell = 0$ while $S_g = 1$. Note that these are volume fractions, unlike the quantity known as the quality or dryness used in thermomechanical process calculations; that parameter, commonly denoted by X , is the mass fraction of steam (water vapor) in a two-phase mixture. Problems associated with determining suitable values of the saturations when conditions are supercritical have been addressed by Kissling [29].

Fluid phase pressures p_ℓ, p_g . The phenomenon of vapor pressure lowering occurs when surface tension effects at the fluid phase interfaces balance a difference in the separate phase pressures. The thermodynamic properties of

the fluid phases are then altered inside the porous medium by capillary forces and by adsorption of liquid on mineral phases. For pure water, the pressure difference may be expressed by

$$p_\ell - p_g = p_{\text{suc}}(S_\ell) \quad (13.15)$$

where p_{suc} , a function of the liquid saturation S_ℓ , is termed the suction (or capillary) pressure; see Ref. [28]. Vapor pressure above a liquid phase held by capillary or adsorptive forces is reduced in comparison to the saturation vapor pressure above the flat surface of a bulk liquid. The reduction is expressed in terms of a vapor pressure lowering factor, $f = p_g/p_{\text{sat}}(T)$, given by Kelvin's equation:

$$f = \exp \left[\frac{M_w p_{\text{suc}}}{\rho_\ell R(T + 273.15)} \right] \quad (13.16)$$

where M_w is the molecular weight of water, R is the universal gas constant; and all the other parameters have previously been defined.

Fluid phase densities ρ_ℓ, ρ_g . For pure water, these properties are well known and are tabulated over a wide range of pressures and temperatures [22]. Reliable correlation formulae are also available; computer calculations are faster using such correlations rather than table lookups and interpolation.

When other components are present in the fluid, the pure water densities must be modified. Components other than water may be divided into two groups: chemical solutes and noncondensable gases. The former reside mainly in the liquid phase, while noncondensable gases have the greatest effect in the gas phase. Over the normal range of conditions prevailing in a geothermal system, it is usual to assume that the liquid density is unaltered by the presence of noncondensable gases, but ρ_ℓ must be modified to take account of any solutes present. For NaCl solutions, see Ref. [25].

In the gas phase, modifications are made for the noncondensable gas components, density $\rho_g^{(i)}$, which also each contribute a partial pressure $p_g^{(i)}$ to the total gas pressure p_g . The total gas phase density is expressed in terms of the component densities by Dalton's law. The mass fraction of each dissolved noncondensable gas component in the liquid phase may be related to an equivalent gas partial pressure through Henry's law. Both distribution laws are discussed further below. Density units are kg/m^3 .

Fluid phase specific enthalpies h_ℓ, h_g . As for densities, the specific enthalpies for pure water may be calculated from correlation formulae, or from tables, for example, Ref. [22]. In a two-phase fluid mixture, the difference between the gas and liquid values is called the latent heat of vaporization $h_{\ell g}$, given by

$$h_{\ell g} = h_g - h_\ell \quad (13.17)$$

This is the amount of heat that is required to boil a unit mass of liquid to gas at a given pressure (or temperature, since conditions are saturated, see above);

because of the change in specific volume, work is required as well as internal energy, and both are included in the enthalpy. Again, the specific enthalpy values for water are altered by the presence of other components. The overall gas specific enthalpy is calculated as a linear combination of the separate gas component values, weighted by their mass fractions:

$$h_g = \sum_j X_g^{(j)} h_g^{(j)} \quad (13.18)$$

The specific enthalpy of each of the dissolved noncondensable gases in the liquid phase is expressed in terms of its gas value plus its heat of solution (the amount of energy required to dissolve the gas into the liquid):

$$h_\ell^{(j)} = h_g^{(j)} + h_{\text{sol}}^{(j)} \quad (13.19)$$

The overall liquid specific enthalpy is then given by a linear combination of the water value ($i = 1$), the contributions from the solutes and those from the noncondensable gas fractions (Eq. [13.19]), as follows:

$$h_\ell = X_\ell^{(1)} h_\ell^{(1)} + \sum_{\text{solutes}} X_\ell^{(i)} h_\ell^{(i)} + \sum_{\text{gases}} X_\ell^{(j)} \left[h_g^{(j)} + h_{\text{sol}}^{(j)} \right] \quad (13.20)$$

Specific enthalpy values have units kJ/kg.

Fluid phase dynamic viscosities μ_ℓ, μ_g . Again, pure water values are readily available from correlation formulae over a wide range of (p, T) values; see Ref. [22]. It is usually assumed that the liquid value μ_ℓ is altered negligibly from the pure water value due to dissolved noncondensable gases. However, large concentrations of chemical solutes do affect the liquid viscosity; in particular, very saline liquids are significantly more viscous than water at the same (p, T) conditions. Correlations are available for such “pure” solutions, but are reliable only over limited ranges of ($p, T, X_\ell^{(i)}$) values (for NaCl solutions, see Ref. [26]).

The overall mixture viscosity for the gas phase may be approximated by a linear combination of the separate noncondensable gas component values:

$$\mu_g = \sum_j X_g^{(j)} \mu_g^{(j)} \quad (13.21)$$

This formula is an extension of that used in Ref. [23] for water + CO₂. As mentioned above, if the mass fractions of noncondensable gas components is small, then the value of μ_g may be taken to be that of pure water (steam) for the given temperature. Dynamic viscosity measurement units are kg/m.s.

Kinematic viscosities ν_ℓ , ν_g . These are defined for each phase in terms of the respective dynamic viscosities and densities by

$$\nu_\ell = \frac{\mu_\ell}{\rho_\ell} \quad \text{and} \quad \nu_g = \frac{\mu_g}{\rho_g} \quad (13.22)$$

with units m^2/s . As will be shown in the section on one-dimensional flows below, for horizontal two-phase flows a total, or effective, kinematic viscosity can be defined, based on the separate phase viscosities being suitably weighted by relative permeabilities.

13.3.6 Distribution Laws

In two-phase conditions, the components are distributed within both phases. Usually salt concentrations within the gas phase are small, but noncondensable gases may dissolve in the liquid phase.

13.3.6.1 Molecular diffusion

If a gas phase is present, molecular diffusion of different gas molecules is taken into account through the last term in Eq. (13.6b). The net transport of a particular component is proportional to the gradient of its concentration expressed as a mass fraction of the total gas mixture. Since water vapor is the dominant gas component, the transport of a minor component may be regarded as controlled predominantly by its binary diffusion rate in water vapor and is quantified by $D_w^{(i)}$, the mass diffusion coefficient of component i , $i = 2, \dots, N$ in pure water vapor ($i = 1$). The coefficient for minor component i may be expressed in the form:

$$D_w^{(i)}(p, T) = \tau_c \phi S_g \frac{D_w^{(i)}(p_0, T_0)}{p/p_0} \left[\frac{T + 273.15}{273.15} \right]^\theta \quad (13.23)$$

Here, τ_c is the coefficient of tortuosity of the porous matrix ($\tau_c = 1/\tau < 1$ where the tortuosity $\tau > 1$), and $D_w^{(i)}(p_0, T_0)$ is the mass diffusion coefficient at some defined standard conditions; for example, the values $(p_0, T_0) = (1 \text{ bar}, 0^\circ\text{C})$ are used in Ref. [30]; θ is usually taken to be about 1.8. The diffusion is reduced by the tortuosity of the paths followed by particles that diffuse in the porous matrix.

As previously mentioned, diffusive fluxes of components in the liquid phase are regarded as negligible compared with the advected component transport by the liquid, and are usually neglected in geothermal systems.

13.3.6.2 Dalton's law

Standard models of gas mixtures assume that each component is uniformly distributed throughout the mixtures, and that the total density is the sum of the densities of the parts:

$$\rho_g = \sum_i \rho_g^{(i)} \quad (13.24)$$

Each component contributes a partial pressure to the total gas pressure. Only noncondensable gas components make significant contributions. By modeling all components as ideal gases, the total pressure can be approximated by the sum of the partial pressures:

$$p_g = \sum_i p_g^{(i)} \quad (13.25)$$

This then allows a connection to be made between the concentrations of gas-phase components with their liquid-phase concentrations through Henry's law.

13.3.6.3 Henry's law

Noncondensable gas solubility in the liquid phase may be expressed in terms of Henry's law, which gives a relationship between the partial pressure of a component in the gas phase and its molar fraction in the liquid (e.g., see Perry et al. [31]). This can be expressed by:

$$p_g^{(i)} = K_H^{(i)} \frac{X_\ell^{(i)}/M^{(i)}}{\left(X_\ell^{(1)}/M_w + \sum_{i \geq 2} X_\ell^{(i)}/M^{(i)}\right)}$$

where component 1 is water and $M^{(i)}$ is the molecular weight of component i . For single components at small concentration, the relationship is almost linear:

$$p_g^{(i)} = K_H^{(i)} X_\ell^{(i)} \frac{M_w}{M^{(i)}} \quad (13.26)$$

Here, $K_H^{(i)}$ is Henry's constant for component i in pure water; generally it is a function of temperature T . At high concentrations, the relationship is nonlinear; however, as mentioned at the outset, geothermal systems contain mainly water, with other components in relatively small quantities, and Eq. (13.26) serves as a reasonable approximation even when there are several minor components.

13.3.7 Boundary Conditions

To close the mathematical problem, boundary conditions are normally stated in terms of thermodynamic state variables, or in terms of mass and/or heat fluxes. Prescription of temperatures or pressures implies knowledge of heat or fluid reservoirs at the boundary that are unaffected in properties by fluid outflow or recharge. Examples include surface water at atmospheric conditions, or recharge fluid available in groundwater aquifers adjacent to a geothermal system. Impermeable boundaries may be modeled by specifying that the normal mass flux is zero, while nonzero mass flows may be controlled by boundary system pressures relative to a specified local exterior pressure.

13.4 Steady One-Dimensional Flows

Some of the main features of geothermal two-phase flows may be illustrated by considering two special cases. In horizontal flows, gravity has negligible effect and the motion is driven only by horizontal pressure gradients, while gravitational effects are important for vertical flows. It is assumed in both cases that capillary effects are negligible; the latter means that the pressures in the gas and liquid phases are assumed to be the same, see Eq. (13.16).

13.4.1 Horizontal Flows: Total Viscosity and Flowing Enthalpy

13.4.1.1 Total, or effective viscosity

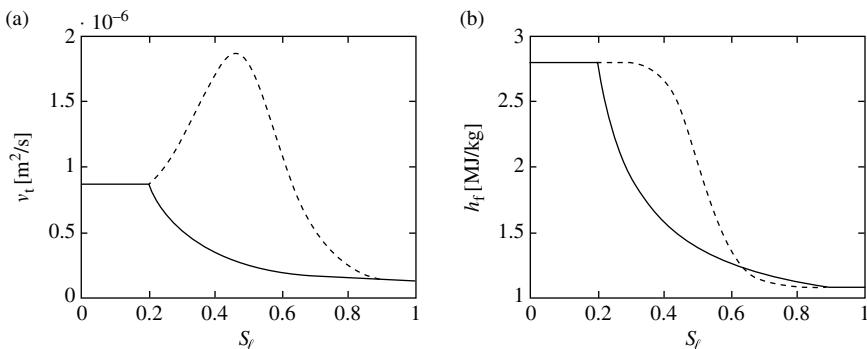
If capillary effects are neglected, then for horizontal flows with liquid and gas pressures equal, use of Eqs. (13.5a,b) for the phase mass fluxes (all proportional to the horizontal pressure gradient $\nabla_h p$) gives the total horizontal specific mass flux Q_{mh} in the form

$$Q_{mh} = \left[\frac{k_{r\ell}}{\nu_\ell} + \frac{k_{rg}}{\nu_g} \right] k_h (-\nabla_h p) \quad (13.27)$$

By comparison with the equation for horizontal flow of a single-phase fluid, an equivalent viscosity ν_t , called the total or effective kinematic viscosity, is defined by

$$\frac{1}{\nu_t} = \frac{k_{r\ell}}{\nu_\ell} + \frac{k_{rg}}{\nu_g} \quad (13.28)$$

Since the relative permeabilities are functions of liquid saturation S_ℓ , the effective viscosity itself depends on the relative proportions of liquid and gas present in the pores of the matrix.

**FIGURE 13.2**

Variation of (a) effective viscosity v_t and (b) flowing enthalpy h_f with liquid saturation S_ℓ for horizontal convection of two-phase water at $T = 250^\circ\text{C}$. The relative permeability functions have residual saturations $S_{\ell r} = 0.2$, $S_{gr} = 0.1$: — straight line functions (Eq. [13.14a]), - - - Corey curves (Eq. [13.14b]).

The dependence of v_t on S_ℓ is shown in Figure 13.2(a) for the case where $T = 250^\circ\text{C}$ and for both sets of relative permeability functions described in Eqs. (13.14a,b) with residual saturations $S_{\ell r} = 0.2$ and $S_{gr} = 0.1$. For $S_\ell \leq S_{\ell r} = 0.2$, v_t takes the gas value v_g , while for $S_g \leq S_{gr}$ ($S_\ell \geq 1 - S_{gr} = 0.9$), $v_t = v_\ell$. For intermediate values, the dependence on the form of the relative permeability functions is clear and shows the sensitivity of the calculated results to the choice of those functions.

13.4.1.2 Flowing enthalpy

The total specific energy flux is expressed by Eq. (13.10). If diffusive effects are neglected, then for steady horizontal flows with liquid and gas pressures equal, the total horizontal specific energy flux \mathbf{Q}_{eh} is given by

$$\mathbf{Q}_{eh} = \left[\frac{k_{r\ell} h_\ell}{v_\ell} + \frac{k_{rg} h_g}{v_g} \right] k_h (-\nabla_h p) \quad (13.29)$$

A fluid-averaged enthalpy value h_f , termed the flowing enthalpy, is found by dividing the magnitude of the total specific energy flux \mathbf{Q}_{eh} by that of the total convected specific mass flux \mathbf{Q}_{mh} given in Eq. (13.27). This averaged value is of the form:

$$h_f = \frac{h_\ell (k_{r\ell}/v_\ell) + h_g (k_{rg}/v_g)}{(k_{r\ell}/v_\ell + k_{rg}/v_g)} = \left[h_\ell \frac{k_{r\ell}}{v_\ell} + h_g \frac{k_{rg}}{v_g} \right] v_t \quad (13.30)$$

after using Eq. (13.28). For single-phase liquid conditions, $S_\ell = 1$ and $k_{rg} = 0$, leading to $h_f = h_\ell$ as expected, while single-phase gas conditions lead to $h_f = h_g$. The dependence of h_f on S_ℓ is shown in Figure 13.2(b) for the same

case as that for v_t in Figure 13.2(a). Comments similar to those for the behavior of v_t are pertinent (see earlier).

13.4.2 Steady Vertical Flows: Heat Pipes

Since heat flow within a large portion of the central region of natural geothermal systems is predominantly in the upward direction and exceeds that which could ensue from conduction only, transfer of energy from deep regions to the surface by convective processes is important. Within two-phase regions, a phenomenon known as a heat pipe can take effect. Upward mass flux of the gas phase, with its relatively high specific enthalpy, is balanced by a downward counterflow of liquid at a similar mass flow rate, but with smaller specific enthalpy. The effect is a small net mass transfer with a large upward heat flux.

The process can be modeled by considering the steady-state, one-dimensional vertical flow equations, with no internal sources. To simplify the demonstration, it will be assumed that the fluids are pure water (note: no diffusive flux in the gas phase), although a model that includes a noncondensable gas has been investigated by McKibbin and Pruess [27]. In a rectangular (Cartesian) coordinate system (x, y, z) where $\mathbf{g} = (0, 0, -g)$, the specific mass flux is of the form $\mathbf{Q}_m = (0, 0, Q_{mv})$. Then Eq. (13.3) requires that $dQ_{mv}/dz = 0$, that is Q_{mv} is independent of vertical position.

Assuming that the liquid and vapor pressures are the same, Eqs. (13.5a,b) give the separate vertical liquid and vapor mass flows to be:

$$(Q_{m\ell})_v = k_v \frac{k_{r\ell} \rho_\ell}{\mu_\ell} \left[-\frac{dp}{dz} - \rho_\ell g \right] \quad (13.31a)$$

$$(Q_{mg})_v = k_v \frac{k_{rg} \rho_g}{\mu_g} \left[-\frac{dp}{dz} - \rho_g g \right] \quad (13.31b)$$

where k_v is the vertical permeability and the net vertical mass flux is then given by $Q_{mv} = (Q_{m\ell})_v + (Q_{mg})_v$. In general, the pressure decreases with height (increases with depth) in a geothermal system, so $dp/dz < 0$ [$-dp/dz = dp/d(-z) > 0$].

There are two special cases of interest. The case:

$$-\frac{dp}{dz} = \rho_\ell g \quad (13.32)$$

is called the hydrostatic, or liquid-static gradient and occurs when there is no vertical movement of liquid; it is the vertical pressure gradient that occurs in a stationary single-phase warm water reservoir. The second special case is

$$-\frac{dp}{dz} = \rho_g g \quad (13.33)$$

which is called vapor-static, or steam-static. It should be noted that $\rho_g < \rho_\ell$ and these two special cases separate three flow situations:

1.

$$\rho_\ell g < -\frac{dp}{dz}$$

This means that the pressure gradients are steeper than liquid-static and, from Eqs. (13.31a,b), both phases move upward. For smaller pressure gradients:

2.

$$\rho_g g < -\frac{dp}{dz} < \rho_\ell g$$

In this case the pressure gradient lies between liquid-static and vapor-static. Liquid moves downward while vapor moves upward; this is called *counterflow*.

3. When the pressure change with depth is small enough,

$$-\frac{dp}{dz} < \rho_g g$$

and both liquid and steam fall.

While it is possible to set $Q_{mv} \neq 0$, corresponding to a net vertical mass throughout (e.g., see McGuinness [32]), here the net mass flux is taken to be zero. Then the downward liquid mass flux is equal to the upward steam mass flux:

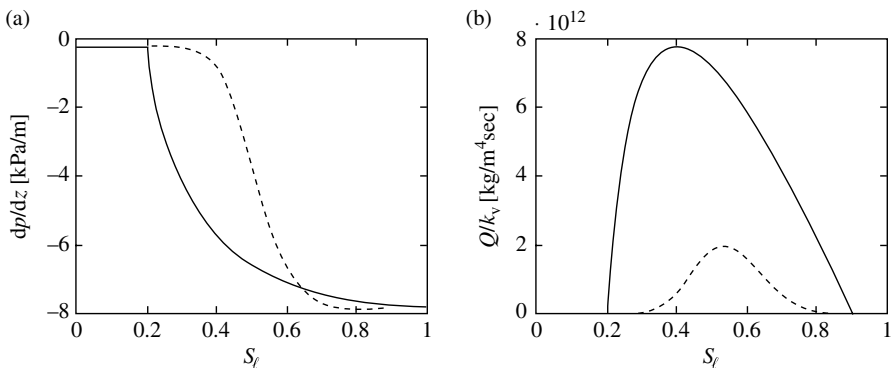
$$(Q_{m\ell})_v = -(Q_{mg})_v \quad (13.34)$$

The pressure gradient may then be determined explicitly from Eqs. (13.31a,b):

$$\frac{dp}{dz} = -\frac{(k_{r\ell}/v_\ell)\rho_\ell + (k_{rg}/v_g)\rho_g}{(k_{r\ell}/v_\ell + k_{rg}/v_g)} g$$

that lies between the liquid-static ($S_\ell = 1$) and the vapour-static ($S_\ell = 0$) pressure gradients given in Eqs. (13.32) and (13.33) respectively (see Figure 13.3[a]). Note that the pressure gradient so found is independent of the vertical permeability k_v . The vertical specific energy flux is then found from Eq. (13.10):

$$Q_{ev} = (Q_{mg})_v(h_g - h_\ell) - K \frac{dT}{dz} \quad (13.35)$$

**FIGURE 13.3**

Variation of (a) the vertical pressure gradient dp/dz and (b) the ratio of the advected vertical specific energy flux to vertical permeability, $(Q_{ev})_{adv}/k_v$, with liquid saturation S_l for vertical counterflow of two-phase water at $T = 250^\circ\text{C}$. The relative permeability functions have residual saturations $S_{lr} = 0.2$, $S_{gr} = 0.1$: — straight line functions (Eq. [13.14a]), - - - Corey curves (Eq. [13.14b]).

This shows that counterflow with zero net mass flux can transport considerable amounts of energy, even when no mass is moved, since the latent heat of vaporization $h_{lg} = h_g - h_\ell$ is large (about 1800 kJ/kg) for water at typical reservoir temperatures.

The advected vertical specific energy flux is represented by the first term on the right-hand side of Eq. (13.35): $(Q_{ev})_{adv} = (Q_{mg})_v(h_g - h_\ell)$. For a given temperature, this depends on the liquid saturation S_l and is directly proportional to permeability k_v .

The dependence on S_l of the vertical pressure gradient dp/dz and the ratio $(Q_{ev})_{adv}/k_v$ is shown in Figure 13.3 for the case where $T = 250^\circ\text{C}$ and for both sets of relative permeability functions defined in Eqs. (13.14a,b) with residual saturations $S_{lr} = 0.2$ and $S_{gr} = 0.1$ (conditions the same as in Figure 13.2). The choice of relative permeability functions has a marked effect on the calculated values, especially for the advected heat transfer. Note that for $S_l \leq S_{lr}$, the liquid relative permeability $k_{rl} = 0$. The pressure gradient is vapor-static and the gas phase does not move. Equation (13.35) indicates that the heat transfer is then conductive only. Similar remarks apply for the liquid-static case where $S_g \leq S_{gr}$ ($S_l \geq 1 - S_{gr}$).

13.5 Numerical Simulation

Several numerical simulation computer packages have been developed for solving the equations derived from conservation principles. In all techniques, the total formation region of interest is partitioned into a finite number N_{VE}

of discrete, nonoverlapping subregions, or volume elements. Algorithms are then based on discretized forms of the nonlinear differential equations, using finite-difference, finite element (finite volume) or integrated finite-difference techniques. The last is exemplified by the SHAFT–MULKOM–TOUGH sequence developed by Pruess and coworkers [7,8,30,33]. It is also a method that is conceptually closely allied to the intuitive method of dividing the system region to be simulated into subblocks that are chosen to reflect the detail required from the computed results.

In the integrated finite-difference scheme, which is the technique that also most closely models the REV formulation used to derive the continuum equations described earlier in this work, thermodynamic conditions are assigned a uniform average value within each element. For any volume element V_n , $n = 1, 2, \dots, N_{VE}$, the conservation of mass for component i is encapsulated in the integro-differential equation:

$$\frac{d}{dt} \int_{V_n} A_m^{(i)} dV = - \int_{S_n} Q_m^{(i)} \cdot \mathbf{n} dS + \int_{V_n} q_m^{(i)} dV \quad (13.36)$$

where S_n is the boundary surface to the volume element and \mathbf{n} is the outward-pointing normal to S_n , while $A_m^{(i)}$ is defined in Eq. (13.2), $Q_m^{(i)}$ in Eq. (13.7) and other parameters have already been defined. (Note that this equation may be reduced to Eq. [13.1] by standard calculus techniques.) Introduction of appropriate volume averages allows the mass accumulation for component i in volume element n , the first volume integral in Eq. (13.36), to be written:

$$\int_{V_n} A_m^{(i)} dV = V_n M_n^{(i)} \quad (13.37)$$

where $M_n^{(i)}$, a function of time t , is the average value of $A_m^{(i)}$ over V_n .

The surface integrals are approximated by a sum of average fluxes between an element and its neighbors:

$$- \int_{S_n} Q_m^{(i)} \cdot \mathbf{n} dS = \sum_j S_{nj} Q_{mnj}^{(i)} \quad (13.38)$$

where S_{nj} is the surface area between element n and neighboring element j . The areally averaged mass flux $Q_{mnj}^{(i)}$ across surface S_{nj} from element j into element n is obtained from the discretized form of Eqs. (13.5) to (13.7), and

may be expressed as:

$$\begin{aligned} Q_{mnj}^{(i)} = & k_{nj} \left\{ X_{\ell nj}^{(i)} \left(\frac{k_{r\ell} \rho_\ell}{\mu_\ell} \right)_{nj} \left[\frac{p_{\ell i} - p_{\ell n}}{d_{nj}} + \rho_{\ell nj} g_{nj} \right] \right. \\ & + X_{g nj}^{(i)} \left(\frac{k_{rg} \rho_g}{\mu_g} \right)_{nj} \left[\frac{p_{g j} - p_{g n}}{d_{nj}} + \rho_{g nj} g_{nj} \right] \left. \right\} \\ & + D_{wnj}^{(i)} \rho_{gnj} \frac{X_{gj}^{(i)} X_{gn}^{(i)}}{d_{nj}} \end{aligned} \quad (13.39)$$

The subscripts (*nj*) indicate that the quantity is to be evaluated at the interface between elements *n* and *j*, based on average values within V_n and V_j . Various weighting procedures are used to ensure stability. The distance d_{nj} between the nodal centers of elements *n* and *j* is used in calculation of gradients of pressure and mass fraction.

The conservation of energy within volume element *n* is given by:

$$\frac{d}{dt} \int_{V_n} A_e dV = - \int_{S_n} \mathbf{Q}_e \cdot \mathbf{n} dS + \int_{V_n} q_e dV \quad (13.40)$$

where A_e is defined in Eq. (13.9), \mathbf{Q}_e in Eq. (13.10) and all the other parameters have already been defined. (Again, this may be reduced to Eq. [13.8] by standard calculus methods.) Analogously to the mass term above, the energy accumulation in volume element *n* is approximated by

$$\int_{V_n} A_e dV = V_n E_n \quad (13.41)$$

The discretized form of the areally averaged energy flux from element *j* into element *n* may be deduced from Eq. (13.10) and the forms of Eqs. (13.38) and (13.39).

For each of the N_{VE} volume elements, the mass accumulation terms $M_n^{(i)}$ for each of the N fluid components as well as the energy accumulation term E_n must be evaluated. These depend, through thermodynamic relationships, on a set of primary variables that may be chosen according to the problem and the phase composition. A common set is $\{T_n, p_n, X_n^{(1)}, X_n^{(2)}, \dots, X_n^{(N)}\}$ when single-phase conditions exist in the element, or $\{T_n, S_{ln}, p_{gn}^{(1)}, p_{gn}^{(2)}, \dots, p_{gn}^{(N)}\}$ when two phases are present. There is therefore a total of $(N + 1) \times N_{VE}$ primary variable quantities to be calculated from the same number of the discretized forms of the mass and energy balance equations. An implicit time-stepping procedure is used to ensure stability, and the problem is reduced to a set of coupled algebraic equations in the set of derived unknown quantities $\{(E_n, M_n^{(1)}, M_n^{(2)}, \dots, M_n^{(N)}), n = 1, 2, \dots, N_{VE}\}$, all of which are functions of the primary variables. Fast algorithms for solving large sets of sparse

linear equations are used, see Pruess [30,33]. Because the derived quantities are nonlinear functions of the primary variables, Newton–Raphson iteration techniques are used to speed up the convergence at each time step.

There is much literature dealing with geothermal reservoir simulation, both from the theoretical viewpoint and as case studies. The latter are often contained in technical reports to companies or government agencies that need to know the possible effects of exploitation of a resource. An excellent summary article is provided by O’Sullivan et al. [9].

Theoretical studies are based on the sciences (physical chemistry, classical physics, geophysics, geology, thermodynamics, mathematics, statistics, computational methods) and establish commonality with other similar processes. An extensive list of references would take too much space here and therefore only a few published works are referred to here. The reader can work from the reference lists provided therein [7,8,11–16,28–30,33].

13.6 Some Current Research Efforts

As mathematical modeling of geothermal systems at subcritical conditions has advanced, so more attention is now being focused on modeling the deeper regions that supply some fluid and most of the heat to the base of geothermal reservoirs. The deep temperatures and pressures constitute conditions that may be regarded as supercritical for pure water, but since the deep fluids carry solutes and gases released from magma sources, such components need to be included in any model of mass and heat flows at depth. The thermodynamic state-space (phase-space) for such mixtures is not as simple as that for pure water.

Very deep wells have not yet been drilled to sample fluids much below the bottom of geothermal reservoirs. However, geochemical evidence from nearer-surface fluid samples, as well as the chemical characteristics of surface discharge features of geothermal systems, indicate that the main dissolved salt is NaCl (perhaps 80% of total solutes) and the main noncondensable gas component is CO₂.

An attempt at constructing models of deep flows has first been made by McKibbin and McNabb [19,20], with fluid properties based on a H₂O–NaCl–CO₂ system. Since system conditions involving a brine saturated with respect to chloride cannot be ruled out, contributions from the solid chloride precipitate phase are explicitly included in the mass and energy accumulation terms, and there are no internal mass or energy sources or sinks.

The model is built by regarding the noncondensable gas as an effective component added to the brine, the properties of which are determined by the mass fractions of water and chloride relative to their own total mass, rather than to the total mass of water plus chloride plus noncondensable gas. In this

regard, the basic fluid is brine, rather than pure water as in the model already described in the earlier sections for geothermal systems. The brine is then treated as one “component” of the mixture, but is itself characterized by the overall mass fraction X of chloride in the brine. It is assumed that the water and any noncondensable gas reside only in the fluid phases.

Rock properties are based on a stationary rock matrix. However, at near-magma depths, this assumption is probably not correct since the rock is not crystalized, and the model would then not apply. Otherwise, in regions where the solid matrix assumption does apply, it is assumed that any solute deposition does not alter the effective permeability. Improvements to the model would require some dependence of permeability on voidage to be included, and/or rock stress analysis to describe dilation of the formation as deposition continues.

Fluid properties are the focus of recent attention; see, for example, Kissling [29] and White and Kissling [34]. Correlations for NaCl brine properties for the liquid phase at lower temperatures have been extended to the regions of the p - T - X state-space for a H₂O-NaCl brine mixture that would apply in deep systems [24–26]. The p - T - X state-space itself is complicated, and mass flows in such a brine system trace state-paths through the space. Addition of a noncondensable gas [20,23,27] completes the essential ingredients of deep high-pressure high-temperature systems.

13.7 Summary

An overview of some currently used mathematical models for geothermal heat and mass transport processes has been given. The sets of partial differential equations that describe the principles of conservation of mass, momentum, and energy of such multiphase multicomponent systems are further complicated by complex dependence of the various formation and fluid parameters on thermodynamic variables. The implementation of physical and thermodynamical modeling through numerical simulation has produced some nice challenges in optimal system discretization and solution of the resulting large sets of algebraic equations.

While little has been said here about the related disciplines of geology, geophysics, geochemistry, and reservoir engineering, these disciplines use scientific methods to deduce the formation parameters for geothermal reservoirs, and also provide information about reservoir extent and likely boundary conditions for simulations. Without such a multidisciplinary approach, interaction and feedback about conceptual and mathematical models would not be possible.

There are few analytical solution methods that produce useful results, although some provide insights on a local scale. Numerical procedures are successful in producing solutions to the governing equations, but, as

mentioned above, require sophisticated discretization and matrix inversion methods.

Recent efforts are focused more on deeper heat and mass flows in regions below geothermal reservoirs, in order to provide better understanding of the processes that transfer heat and chemicals from deep magmatic sources to the base of reservoirs and to surface discharge features. These investigations may also eventually prove useful in modeling ore formation and other deposition processes.

References

1. J.W. Lund and D.H. Freeston. World-Wide Direct Uses of Geothermal Energy 2000. *Proc. World Geothermal Congr.* 2000, Kyushu-Tohoku, Japan, 2000, pp. 1–21.
2. G.W. Huttner. The Status of World Geothermal Power Generation 1995–2000. *Proc. World Geothermal Congr.* 2000, Kyushu-Tohoku, Japan, 2000, pp. 23–37.
3. J. Bear. *Dynamics of Fluids in Porous Media*. New York: Dover, 1972.
4. J. Bear and Y. Bachmat. *Introduction to Modeling of Transport Phenomena in Porous Media*. Dordrecht: Kluwer, 1991.
5. D.A. Nield and A. Bejan. *Convection in Porous Media*. 2nd edn. New York: Springer-Verlag, 1999.
6. I.W. Farmer. *Engineering Properties of Rocks*. London: Spon, 1968.
7. K. Pruess (ed.). *TOUGH Workshop*. Report LBL-29710, Lawrence Berkeley Laboratory, Berkeley, CA, 1990.
8. K. Pruess (ed.). *Proc. TOUGH Workshop '95*. Report LBL-37200, Lawrence Berkeley Laboratory, Berkeley, CA, 1995.
9. M.J. O'Sullivan, K. Pruess, and M.J. Lippman. Geothermal Reservoir Simulation: The State-of-Practice and Emerging Trends. *Proc. World Geothermal Congr.* 2000, Kyushu-Tohoku, Japan, 2000, pp. 4065–4070.
10. M.J. O'Sullivan and R. McKibbin. Geothermal Reservoir Engineering: A Manual for Geothermal Reservoir Engineering Courses, 2nd edn. Geothermal Institute, The University of Auckland, New Zealand, 1988.
11. Proceedings of the Workshop on Geothermal Reservoir Engineering. Stanford Geothermal Program, Stanford University, Stanford, CA, 1976–.
12. Proceedings of the New Zealand Geothermal Workshop, presented by the University of Auckland. Geothermal Institute in conjunction with the Centre for Continuing Education. The Centre for Continuing Education, The University of Auckland, Auckland, New Zealand, 1979–.
13. Geothermics. Oxford: Elsevier-Pergamon, 1972–.
14. M.A. Grant, I.G. Donaldson, and P.F. Bixley. *Geothermal Reservoir Engineering*. New York: Academic, 1982.
15. Proceedings of the World Geothermal Congress, Florence, May 1995. International Geothermal Association, 1995.
16. Proceedings of the World Geothermal Congress 2000, Kyushu-Tohoku, Japan, May 2000. International Geothermal Association, 2000.
17. M. Kaviany. *Principles of Heat Transfer in Porous Media*. New York: Springer-Verlag, 1991.

18. A.T. Corey. The interrelation between gas and oil relative permeabilities. *Producers Monthly*, 19: 38–41, 1954.
19. R. McKibbin and A. McNabb. From Magma to Groundwater: The Brine Connection. *Proc. World Geothermal Congr.*, Florence, 1995, pp. 1125–1130.
20. R. McKibbin and A. McNabb. Deep hydrothermal systems: mathematical modelling of hot dense brines containing non-condensable gases. *J. Porous Media*, 2: 107–126, 1999.
21. S. White and E. Mroczek. Permeability changes during the evolution of a geothermal field due to the dissolution and deposition of quartz. *Transp. Porous Media*, 33: 88–101, 1998.
22. G.F.C. Rogers and Y.R. Mayhew. *Thermodynamic and Transport Properties of Fluids*. 3rd edn. Great Britain: Blackwell, 1983.
23. M.J. O'Sullivan, G.S. Bodvarsson, K. Pruess, and M.R. Blakeley. Fluid and heat flow in gas-rich geothermal reservoirs. *Soc. Pet. Engineers J.*, 215–226, April 1985.
24. C.C. Palliser and R. McKibbin. A model for deep geothermal brines, I: $T-p-X$ state-space description. *Transp. Porous Media*, 33: 65–80, 1998.
25. C.C. Palliser and R. McKibbin. A model for deep geothermal brines, II: thermodynamic properties — density. *Transp. Porous Media*, 33: 129–154, 1998.
26. C.C. Palliser and R. McKibbin. A model for deep geothermal brines, III: thermodynamic properties — enthalpy and viscosity. *Transp. Porous Media*, 33: 155–171, 1998.
27. R. McKibbin and K. Pruess. Some effects of non-condensable gas in geothermal reservoirs with steam-water counterflow. *Geothermics*, 18: 367–375, 1989.
28. K. Pruess. Numerical Simulation of Water Injection into Vapor-Dominated Reservoirs. *Proc. World Geothermal Congr.*, Florence, 1995, pp. 1673–1679.
29. W.M. Kissling. Extending MULKOM to Supercritical Temperatures and Pressures. *Proc. World Geothermal Congr.*, Florence, 1995, pp. 1687–1690.
30. K. Pruess. Development of the General Purpose Simulator MULKOM. Earth Sciences Division Annual Report 1982, Report LBL-15500, Lawrence Berkeley Laboratory, Berkeley, CA, 1983.
31. R.H. Perry, D.W. Green, and J.O. Maloney. *Perry's Chemical Engineers' Handbook*. 6th edn. Singapore: McGraw-Hill, 1984.
32. M. McGuinness. Heat Pipes and Through-Flows in Geothermal Reservoirs. *Proc. 18th New Zealand Geothermal Workshop 1996*, The University of Auckland, 1996, pp. 285–290.
33. K. Pruess. TOUGH2 — A General Purpose Numerical Simulator for Multiphase Fluid and Heat Flow. Lawrence Berkeley Laboratory Report LBL-29400, Lawrence Berkeley Laboratory, Berkeley, CA, 1991.
34. S.P. White and W.M. Kissling. Including chloride and CO₂ chemistry in large-scale reservoir models. *Proc. 18th New Zealand Geothermal Workshop 1996*, The University of Auckland, 1996, pp. 295–300.

14

Transport Phenomena in Liquid Composites Molding Processes and their Roles in Process Control and Optimization

Suresh G. Advani and Kuang-Ting Hsiao

CONTENTS

14.1	Introduction	573
14.1.1	The Liquid Composite Molding (LCM) Processes	573
14.1.2	The Physics in LCM	576
14.1.3	LCM Simulations for Optimization and Control.....	577
14.2	Modeling and Experiments	579
14.2.1	Flow in LCM.....	579
14.2.2	Heat Transfer in LCM	580
14.2.3	Chemical Reaction	585
14.3	Process Control and Optimization	588
14.3.1	Injection Gates and Vents and Flow Distribution Network Optimization.....	589
14.3.2	Online Permeability Characterization	593
14.3.3	Flow Control.....	595
14.3.4	Temperature and Resin Cure Cycle Optimization	597
14.4	Conclusions and Outlook	599
Acknowledgment.....	601	
Nomenclature	601	
References	602	

14.1 Introduction

14.1.1 The Liquid Composite Molding (LCM) Processes

Polymer composite structures are fabricated using fibers as reinforcements held in position with a polymer matrix. There are a variety of processes to

manufacture composites, depending upon the type of applications, number of parts to be made, the geometry of the parts and the performance desired. For an introduction to this, readers may refer to the following texts on composite manufacturing [1–4].

Liquid composite molding (LCM) represents a class of composite manufacturing processes in which the fiber preforms are placed in a closed mold and the liquid polymer is impregnated to saturate the empty spaces between the fibers to create the composite structure. The reinforcing fiber preforms are usually fabrics formed from continuous strands or tows of a few hundred to 48,000 glass fibers, carbon fibers, or aramid fibers (such as Kevlar) by stitching, knitting, or weaving them as shown in Figure 14.1. The ability to tailor fiber directions allows the designer to build the structure for desired mechanical properties. The polymer matrix used to bind the framework of fabrics can be either thermoplastic or thermoset resin. Thermoplastic resins are usually in solid phase at room temperature but at elevated temperatures they melt into viscous liquids with viscosities of the order of about a million times higher than that of water. It is very difficult to impregnate the tiny empty spaces between and within the fiber preforms with the thermoplastic resin. Hence, thermoplastic resins are rarely used for LCM processes. On the other hand, most thermoset resins are in liquid phase at room temperature. The viscosities of the thermoset resins are about 50 to 300 times higher than water and relatively easier to saturate the fiber preform. However, thermoset resins undergo an exothermal chemical reaction and cross-link, and hence are difficult to recycle.

Thermoset resins are used for LCM processes mostly due to their low viscosities, which enable them to infiltrate into the small spaces between the fibers. The thermosets used are usually epoxies, vinyl esters, or polyesters with desired chemical or environmental resistance. In this chapter, we will focus on a class of manufacturing processes for long fibers/thermoset resin composites called liquid composite molding (LCM). LCM includes resin transfer molding (RTM), vacuum assisted resin transfer molding (VARTM), and structure reaction injection molding (SRIM). These processing techniques are widely used because they lend themselves to automation, readily reducing

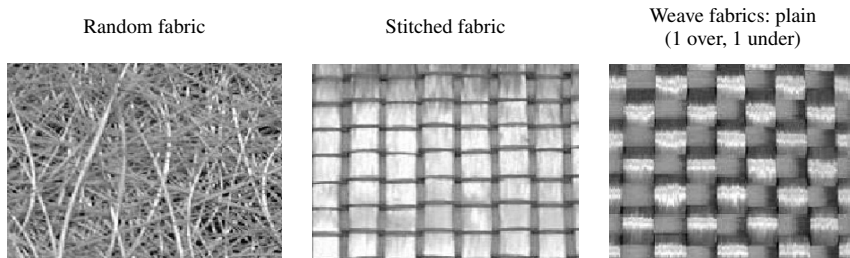
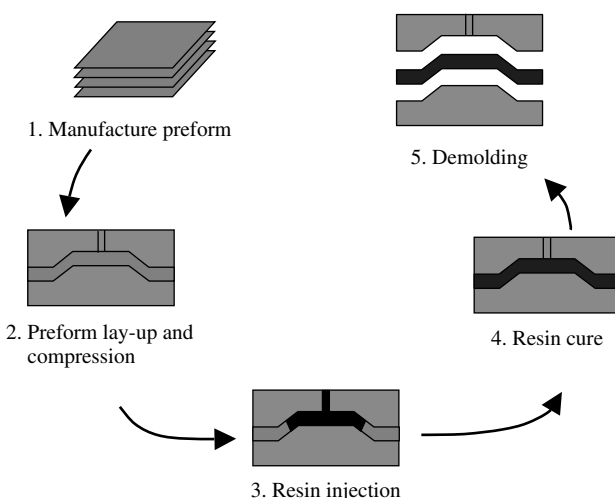


FIGURE 14.1
Different types of fiber preforms.

cost and time, and allows one to produce the nearly net-shaped composite parts. Different industries may have different expectations on LCM processes. For example, the automotive industry emphasizes the potential of high volume manufacturing and good surface finish. On the other hand, the requirement in the defense and aerospace industry [5–7] is to produce light, high quality, complex composite structures. Civil or transportation applications, such as composite bridge decks, ship hulls, and wind turbine blades, are usually large structures; hence the key constraints pertaining to them are to reduce the mold tooling cost and enable resin infusion into the fabric structure within reasonable time. The LCM process is versatile and flexible enough to accommodate these needs and constraints. Thus, over the last decade researchers have focused on gaining a scientific understanding of this process. Many mathematical models and simulations of the process have been developed to create a virtual manufacturing environment as this would help reduce the prototype development cost and time.

One of the representative LCM processes is the RTM, which can loosely be divided into five steps, as illustrated in Figure 14.2. The first step is to manufacture the fiber preform from glass, carbon, or Kevlar in a form as shown in Figure 14.1. The second step is to stack the preforms in the mold cavity. The mold is then closed, which compresses the fiber preforms into the designed thickness and fiber volume fraction. This stationary compacted fiber preform is a fibrous porous medium. The third step is to inject a thermoset resin into the mold cavity and impregnate the fibrous porous medium with a low viscosity thermoset resin. The fourth step is to initiate and accelerate the cure process of the thermoset resin either by adding a catalyst or by heating the resin that has saturated the empty pores between the fibers of the preform

**FIGURE 14.2**

Manufacturing steps for a typical RTM process.

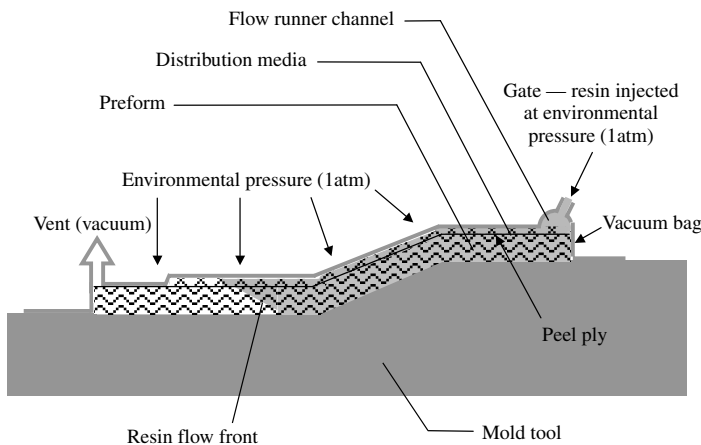


FIGURE 14.3
Schematic of VARTM process.

and then cooling the solidified composite to room temperature. The last step is to demold the net shaped composite part from the mold.

One of the limitations of RTM was that the cost of tooling and injection machinery went up exponentially as the part size increased. VARTM was invented to overcome this limitation. In the VARTM process, the preform is placed on a flat tool surface and enveloped with a plastic bag. A vacuum is applied to compact the preform and draw the resin from a reservoir at atmospheric pressure into the mold cavity to saturate the preform as shown in Figure 14.3. Thus, VARTM uses low pressures and one-sided tools to make large composite structures. To reduce the infusion time of the resin into the preform, flow channels and the distribution media are used to accelerate the flow infusion process. The flow in the channels and/or the distribution media makes the flow of resin in the anisotropic fibrous porous media truly three-dimensional.

14.1.2 The Physics in LCM

This chapter will focus on addressing the transport phenomena in LCM processes such as RTM and VARTM. The heat and mass transfer phenomena dominate the resin impregnation and cure during the LCM process [3]. Because of the presence of the fiber preform, the system can be treated as nonisothermal reactive flow through fibrous porous media. However, in many cases, the process of resin impregnation into the fiber preforms is isothermal. For such cases, the key parameter is the history of filling the mold with resin, which will allow one to understand the resin impregnation process.

In this chapter, we will first review the models and experiments that address the essential heat and mass transfer phenomena associated with LCM. Next,

we will discuss the need for numerical simulations of these models and how these simulations can be used for optimization and control of the filling process. The heat and mass transfer in LCM process is described by transport theories for flow through porous media. The mold filling process is modeled as flow through fibrous porous media using Darcy's law to predict the location of the resin front and the fluid pressure as it impregnates the fibrous preforms [8–16]. The RTM composite parts are usually shell-like structures about 3 to 10 mm thick as compared to being metered in length and width. Hence the velocity in the thickness direction is averaged and the pressure and the flow front motion are solved only in the in-plane direction. However, the three-dimensional flow modeling is crucial for the VARTM process due to the presence of flow enhancement network such as the flow runners and flow distribution layers to accelerate the resin infiltration. For such cases, the resin first flows through the flow runners and flow distribution layers due to their higher permeability than the fiber preform and then impregnates the fiber preform through the thickness requiring one to solve for flow through the thickness direction as well.

The flow modeling issue can be addressed by solving a linear set of equations; however, to predict the temperature field is more complex and involved since the heat transfer is strongly coupled with the local velocity field. Heat dispersion, which is known to be associated with pore-scale heat convection in porous media, has to be considered in heat transfer modeling. Furthermore, the heat transfer in the thickness direction is not negligible in the modeling since the thickness of a composite part is usually smaller than its other dimensions. In some cases, the viscosity varies significantly with the temperature change and will influence the flow solution.

Another important issue to be addressed is the exothermic chemical reactions that the resins undergo during the LCM process. As the resin cures and cross-links during the process, it becomes more viscous and continuously releases heat as its degree of curing increases. The viscosity change and heat generation of the curing resin will influence the velocity and thermal fields. In general, one has to couple the flow, heat transfer, and the chemical reactions for the LCM simulations unless one can clearly separate their dominant time frames and show that there is very little overlap between the filling and curing fields. This can be established by a simple scaling argument [4]. The process models, once they are validated and established, are incorporated into numerical simulations to aid in manufacturing with LCM.

14.1.3 LCM Simulations for Optimization and Control

One of the reasons to develop process simulations is for the enhancement of the process design and manufacturing of composites with LCM. Simulations allow one to investigate the best locations to inject resin into the mold. Such simulations can be combined with optimization algorithms such as Genetic

Algorithm (GA) [17,18] and Branch and Bound Search methods to optimize the injection gate(s) and vent(s) locations [19] and curing methodology for thick composite parts [20]. From the point of view of saving simulation cost, artificial neural network (ANN), with enough training from filling simulation, may be used to predict the LCM filling process and coupled with GAs to optimize the gate location [21]. In addition to gate optimization, a recent research showed that the methodology of coupling simulations and GAs was effective and superior than the conventional trial-and-error experimental approach in optimizing the flow runners and flow distribution media in VARTM [22].

In LCM, control of the filling process is necessary because during the pre-form placement stage, imperfect fits between the preform edges and the mold walls will cause the resin to flow faster in these regions as shown in Figure 14.4. These flow disturbances, whose locations may be repeatable but the strengths

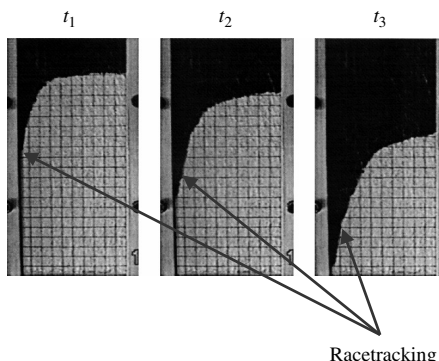


FIGURE 14.4

Racetracking in RTM: the imperfect fits between the preform edges and the mold walls that cause the fluid to race along the edges.

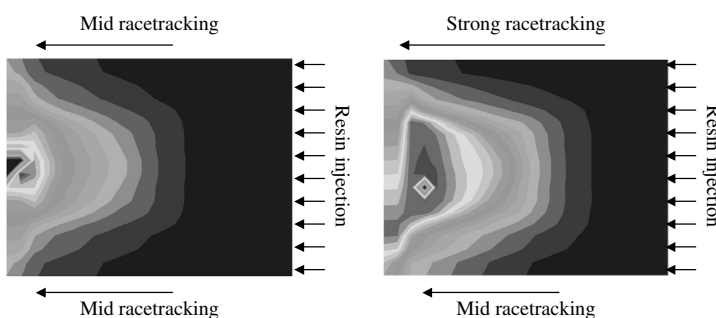


FIGURE 14.5

Flow front histories in the same mold due to different strengths of disturbances along the mold edges.

are not, can cause very different flow histories during the filling stage as shown in [Figure 14.5](#).

The most prominent flow disturbance is racetracking [23] and it arises because the local permeability along the mold edges will vary from one part to the next and will be a function of the preform type, the cutting method, and fiber preform placement into the mold cavity. As shown in [Figure 14.4](#), the imperfect fits between the mold walls and the fiber preform edges may create different sizes of flow channels and yield different resin filling patterns [24]. Hence, characterization of the permeability along the edges and control of the resin flow infiltration during the mold filling process become very important. This chapter will review several recent advances that used the simulations as a tool for sensing and characterizing such flow disturbances and the control approaches to address them in LCM processes.

14.2 Modeling and Experiments

To model the LCM process, we consider the fiber preform as fibrous porous media. The transport phenomena such as flow, heat, and mass transfer in porous media are influenced by the microstructure of the porous media. In practice, one uses volume-averaged properties to represent the macroscopic behavior of the porous system as shown in [Figure 14.6](#).

14.2.1 Flow in LCM

Tucker and Dessenberger [25] have derived and summarized the governing equations for the LCM processes using the volume averaging technique. Here we will just state them. The local volume-averaged continuity equation is

$$\nabla \cdot (\langle \mathbf{u}_f \rangle) = 0 \quad (14.1)$$

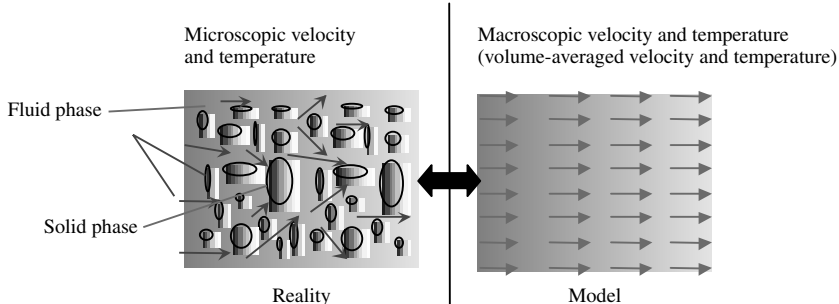


FIGURE 14.6

Microscopic and macroscopic velocity and temperature in porous media.

The operator $\langle * \rangle := \int_V * dV$ is the volume average operator. \mathbf{u}_f is the velocity of the fluid phase. The momentum equation is Darcy's law.

$$\langle \mathbf{u}_f \rangle = -\frac{1}{\mu} \mathbf{S} \cdot \nabla \langle P_f \rangle^f \quad (14.2)$$

here \mathbf{S} is the permeability tensor. P_f is a modified fluid pressure, defined as

$$P_f := p_f + \rho_f g z \quad (14.3)$$

where p_f is the pressure in the fluid, g is the acceleration due to gravity, and z is the height above a reference point.

14.2.2 Heat Transfer in LCM

Conventionally, the local thermal equilibrium volume-averaged energy equation [26] was widely used by modeling the heat transfer in LCM [25,26,28,29]. The important characteristic of the local thermal equilibrium model is its simplicity, which comes from the local thermal equilibrium assumption. This assumption states that the fluid phase-averaged temperature, the solid phase-averaged temperature, and the volume-averaged temperature are equivalent locally. Though the local thermal equilibrium simplifies the energy equation, some researchers do question its validity. Amiri and Vafai [30,31] discussed the validity of the local thermal equilibrium model. The local thermal equilibrium volume-averaged energy equation is given by:

$$\left\{ \sum_{i=s,f} (\rho c_p)_i \varepsilon_i \right\} \frac{\partial \langle T \rangle}{\partial t} + (\rho c_p)_f \langle \mathbf{u}_f \rangle \cdot \nabla \langle T \rangle = \nabla \cdot [(\mathbf{k}_e + \mathbf{K}_D) \cdot \nabla \langle T \rangle] + \sum_{i=s,f} \langle \dot{s}_i \rangle$$

where $\langle \mathbf{u}_f \rangle$ is the Darcy velocity and $\langle T \rangle$ is the volume-averaged temperature. The subscript s and f represent the solid phase and the fluid phase, respectively. \mathbf{k}_e and \mathbf{K}_D are the effective thermal conductivity tensor and the thermal dispersion [32–34] tensor, respectively. $\langle \dot{s} \rangle$ is the volume-averaged heat source term that can be used to describe the cure kinetics of the resin.

Another approach that deviates from the local thermal equilibrium model is the two-medium treatment [35–38]. By relaxing the local thermal equilibrium assumption, they allow the fluid phase-averaged temperature to be different from the solid phase-averaged temperature. Thus, this model requires one to solve two coupled phase-averaged energy equations [30,31]. For example,

the fluid phase-averaged energy equation [39] is given as:

$$\begin{aligned} \varepsilon_f(\rho c_p)_f \frac{\partial \langle T_f \rangle^f}{\partial t} + \varepsilon_f(\rho c_p)_f \langle \mathbf{u}_f \rangle^f \cdot \nabla \langle T_f \rangle^f - \mathbf{u}_{ff} \cdot \nabla \langle T_f \rangle^f - \mathbf{u}_{fs} \cdot \nabla \langle T_s \rangle^s \\ = \nabla \cdot (\mathbf{K}_{ff} \cdot \nabla \langle T_f \rangle^f + \mathbf{K}_{fs} \cdot \nabla \langle T_s \rangle^s) - a_v h (\langle T_f \rangle^f - \langle T_s \rangle^s) + \langle \dot{s}_f \rangle \end{aligned}$$

where a_v is the interfacial area per unit volume, h is the film heat transfer coefficient, and \mathbf{u}_{ff} , \mathbf{u}_{fs} are transfer coefficients in the fluid phase-averaged energy equation, respectively. \mathbf{K}_{ff} and \mathbf{K}_{fs} are the total effective thermal conductivity tensors in the fluid and the solid phase-averaged energy equation, respectively. Note that the solid phase-averaged energy equation can be written in the same way.

Most researchers expected the two-medium treatment to provide more accurate results than the local thermal equilibrium model. However, the complexity of the two-phase model makes it difficult to apply it to the LCM process. In order to use the two-phase model, one will have to measure and determine many additional coefficients and there are no standard approaches to collect such information. Second, the coupled two-energy equations require extensive computational effort. In spite of the challenges, some attempts to use the two-phase treatment to predict the heat transfer during mold filling in LCM have been made [11,40]. One cannot validate the model experimentally in LCM as the thermocouple measures only one temperature instead of measuring the fluid phase temperature and solid phase temperature separately. Hence it makes more sense to assume some sort of average of the fluid and solid temperatures at a spatial location rather than solve them separately and then average them.

To gain both simplicity and accuracy, one may want to use only one volume-averaged temperature as the governing variable. Moreover, as the mold filling stage of LCM involves the moving nonisothermal boundary of resin in the fibrous porous media, one may need an energy equation that can be used in the moving observation frame of the resin flow front. Since both the local thermal equilibrium model and the two-phase model are derived in the stationary frame and not in the moving frame with resin flow front, a generalized volume-averaged energy equation [41] that relaxes the local thermal equilibrium can be used in any Newtonian frame and is given as:

$$\begin{aligned} \left\{ \sum_{i=s,f} (\rho c_p)_i \varepsilon_i \right\} \frac{\partial \langle T \rangle}{\partial t} + \mathbf{c}_{hc} \cdot \frac{\partial (\nabla \langle T \rangle)}{\partial t} + \left\{ \sum_{i=s,f} (\rho c_p)_i \langle \mathbf{u}_i \rangle \right\} \cdot \nabla \langle T \rangle \\ = \nabla \cdot [\mathbf{K} \cdot \nabla \langle T \rangle + (\mathbf{k}_{2d} \cdot \nabla) \nabla \langle T \rangle] + \sum_{i=s,f} \langle \dot{s}_i \rangle \end{aligned} \quad (14.4)$$

The solid forming the porous matrix (preform) and fluid (resin) values are indexed with an "s" and "f," respectively. Two assumptions have been made

to differentiate volume-averaged values from microscopic values:

$$\mathbf{u}_i = \langle \mathbf{u} \rangle + \hat{\mathbf{u}}_i \quad (14.5)$$

where $\langle \mathbf{u} \rangle$ is Darcy's velocity and

$$T_i = \langle T \rangle + \mathbf{b}_i \cdot \nabla \langle T \rangle \quad (14.6)$$

here $\langle T \rangle$ is the volume-averaged temperature. The temperature deviation vector, \mathbf{b}_i , which maps $T_i - \langle T \rangle$ onto $\nabla \langle T \rangle$ is periodic for a periodic porous medium and is a function of the geometry of the unit cell, thermal properties of the materials, and the velocity field. The thermal capacity correction vector, which characterizes the sum of the difference between the volumetric heat capacity of the solid and the fluid and the difference between phase-averaged temperatures of the solid and the fluid phase, is expressed as

$$\mathbf{c}_{hc} = \sum_{i=s,f} (\rho c_p)_i \langle \mathbf{b}_i \rangle \quad (14.7)$$

The thermal diffusive correction vector, which characterizes the sum of the difference between the heat conductivities of the solid and the fluid and the difference between phase-averaged temperatures of the solid and the fluid phase, is expressed as

$$\mathbf{k}_{2d} = \sum_{i=s,f} k_i \langle \mathbf{b}_i \rangle \quad (14.8)$$

In this theory, the total effective thermal conductivity, \mathbf{K} , is expressed as the sum of three terms

$$\mathbf{K} = \mathbf{k}_e + \mathbf{K}_D + \mathbf{C}_{mc} \quad (14.9)$$

The contribution from the thermal conduction (the effective thermal conductivity of the fluid saturated porous media) is given by

$$\mathbf{k}_e = \sum_{i=s,f} k_i \left(\varepsilon_i \mathbf{I} + \frac{1}{V} \int_{S_i} \mathbf{n} \mathbf{b}_i \, dS \right) \quad (14.10)$$

Here k_s and k_f refer to the thermal conductivity of the solid and the fluid, and ε_s and ε_f refer to the volume fraction of the solid and the fluid, respectively. If the porous medium is isotropic, we have $\mathbf{k}_e \equiv k_e \mathbf{I}$. Torquato [42] suggested that the value of k_e be bounded by

$$\frac{k_f k_s}{\varepsilon_s k_f + \varepsilon_f k_s} \leq k_e \leq \varepsilon_s k_s + \varepsilon_f k_f \quad (14.11)$$

The second contribution to heat dispersion is due to the difference in the local velocity and the averaged velocity that can be best explained by [Figure 14.6](#) and is given by

$$\mathbf{K}_D = \sum_{i=s,f} -\frac{(\rho c_p)_i}{V} \int_{V_i} \hat{\mathbf{u}}_i \mathbf{b}_i dV \quad (14.12)$$

Finally, the contribution from the macroconvection along with local thermal nonequilibrium that can be lumped into effective thermal conductivity can be expressed as

$$\mathbf{C}_{mc} = -\langle \mathbf{u} \rangle \mathbf{c}_{hc} \quad (14.13)$$

Note that if the local thermal equilibrium is assumed, that is,

$$\langle T_s \rangle^s = \langle T_f \rangle^f = \langle T \rangle \Rightarrow \langle \mathbf{b}_s \rangle = \langle \mathbf{b}_f \rangle = \mathbf{0} \quad (14.14)$$

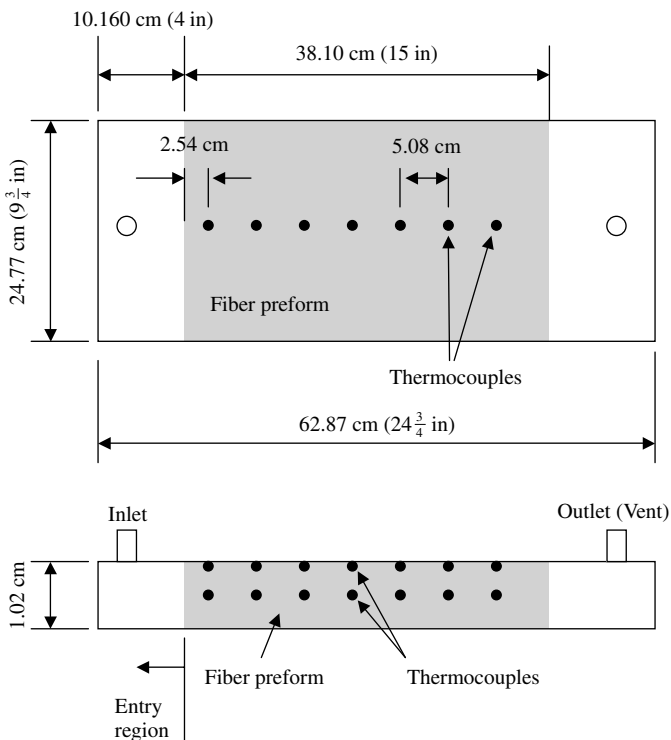
then \mathbf{c}_{hc} , \mathbf{k}_{2d} , and \mathbf{C}_{mc} will be zero. Therefore, the generalized model simplifies to the local thermal equilibrium model [25]. Note that if the fluid and solid have equal thermophysical properties, that is, $(\rho c_p)_f = (\rho c_p)_s$ and $k_f = k_s$, \mathbf{c}_{hc} , \mathbf{C}_{mc} , and \mathbf{k}_{2d} will be zero even if the local thermal equilibrium is not assumed [43]. This is because

$$\langle \mathbf{b}_s \rangle + \langle \mathbf{b}_f \rangle = \langle \mathbf{b} \rangle = \mathbf{0} \quad (14.15)$$

The volume-averaged heat flow from the general theory can be derived using Fourier's law.

$$\langle \mathbf{q}_{total} \rangle = \left\{ \sum_{i=s,f} (\rho c_p)_i \langle \mathbf{u}_i \rangle \right\} \langle T \rangle - \mathbf{K} \cdot \nabla \langle T \rangle - (\mathbf{k}_{2d} \cdot \nabla) \nabla \langle T \rangle \quad (14.16)$$

In order to assess the role of each term of the generalized volume-averaged energy balance model in RTM, Hsiao et al. [44] conducted an experimental investigation (see [Figure 14.7](#) and [Table 14.1](#)) and adjusted the value of each volume-averaging coefficient to match the thermocouple measurement. In this study, a cold nonreactive viscous liquid was pumped through the fibrous porous bed with a constant mold wall temperature. In this steady-state heat transfer analysis, the heat conduction in the inflow direction (x -direction) was neglected because the thickness (y -direction) of the mold cavity was much smaller than its width and length. Furthermore, they assumed that the temperature field was antisymmetric to the centerline along the flow direction of the unit cell and obtained $c_{hcy} = 0$ and $k_{2dy} = 0$. By analyzing the thermocouple measurements, they found that through the thickness, total effective conductivity K_{yy} increases as the Darcy's velocity (Péclet number) increases

**FIGURE 14.7**

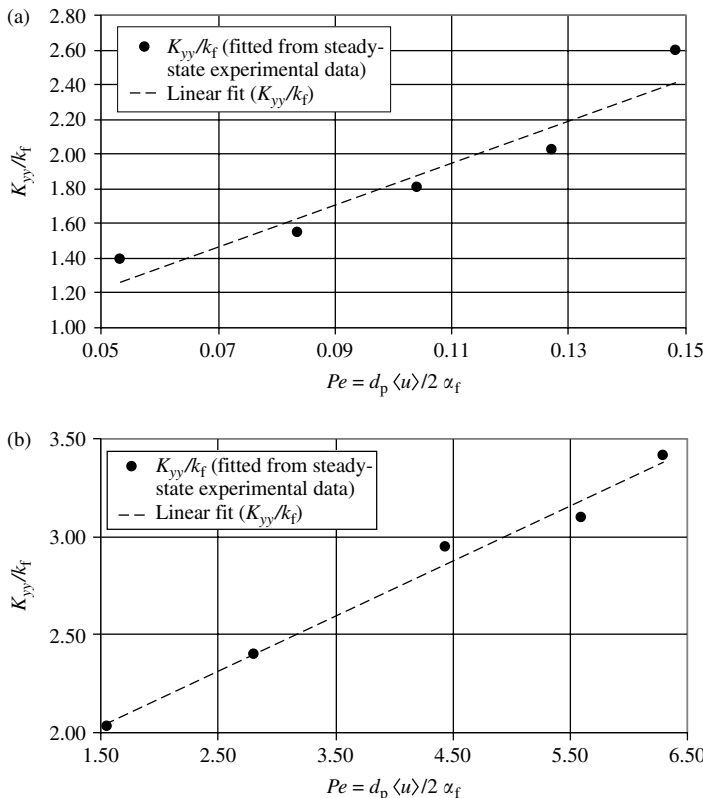
Dimensions of the mold cavity and the locations of thermocouples.

TABLE 14.1

Thermal Material Properties

Material	ρ (kg/m ³)	c_p (J/kg°C)	k (W/m K)	d_p (m)
Carbon fiber	1180	712	7.8	8.0×10^{-6}
E-Glass fibers	2560	670	0.417	1.4×10^{-4}
1/3 ethylene glycol + 2/3 glycerin	1202	2500	0.276	—

(see Figure 14.8 and Figure 14.9), and their relationship is approximately linear in the typical RTM Péclet number range. Since $K_{yy} = k_{eyy} + K_{Dyy}$, they compared the values of k_{eyy} with several models and found that the series arrangement model and the homogenization model provided by Chang [45,46] predict k_{eyy} reasonably well (see Table 14.2). After characterizing the steady-state experiment, several transient experiments were conducted by injecting cold liquid into the preheated porous bed with constant mold wall temperature. By combining the history of thermocouple measurement and order of magnitude analysis, it was justified that one can neglect all the

**FIGURE 14.8**

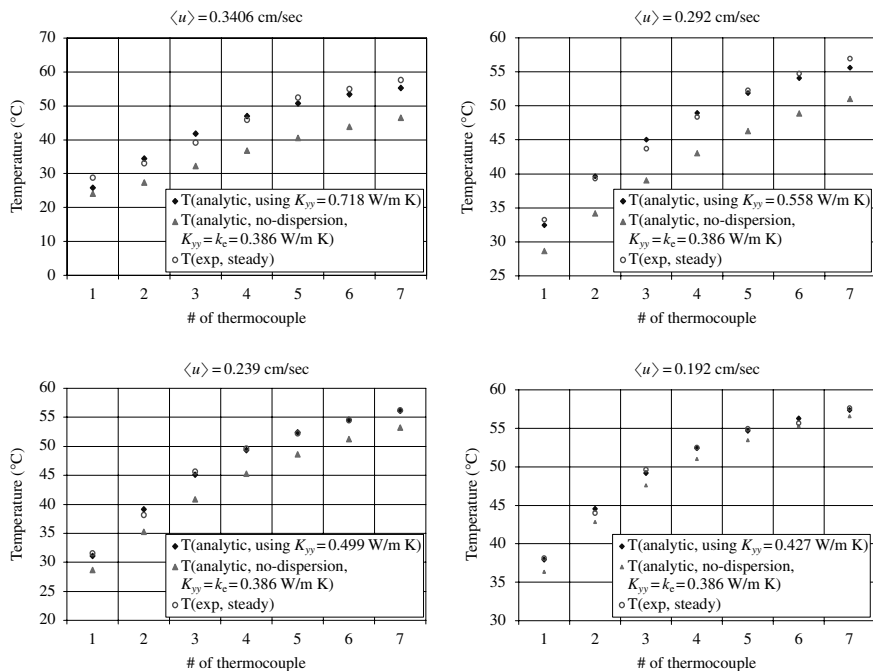
The K_{yy} versus Péclet number: (a) for the experiments in which the porous medium was carbon biweave preform with fiber volume fraction of 43%; (b) for the experiments with fibrous porous media of random fiberglass with fiber volume fraction of 22%.

complex terms (\mathbf{c}_{hc} , \mathbf{k}_{2d} , \mathbf{C}_{mc}) introduced by nonlocal thermal equilibrium for the low Darcy's velocity in typical RTM. By using the K_{yy} measured in the steady-state experiments, it is possible to predict the temperature history fairly well as validated by the experimental data in Figure 14.10.

14.2.3 Chemical Reaction

It is possible to include the transport phenomena of the conversion of chemical species in porous media. However, to simplify the analysis, many researchers [11,25,40,47] assumed that the mass diffusion and dispersion can be neglected since the mass diffusivity is very small compared with the convection and transient terms. Hence, the reaction equation can be expressed as

$$\varepsilon_f \frac{\partial \langle c_f \rangle^f}{\partial t} + \langle \mathbf{u}_f \rangle \cdot \nabla \langle c_f \rangle^f = \varepsilon_f R_c \left\{ \langle c_f \rangle^f, \langle T_f \rangle^f \right\} \quad (14.17)$$

**FIGURE 14.9**

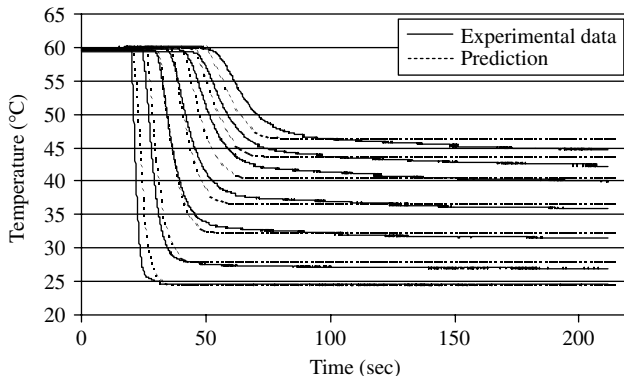
The significance of heat dispersion for the steady-state temperature predictions for four different Darcy's velocities; the dependence of K_{yy} on the Darcy's velocity must be considered to match the experimental data from the carbon biweave cases.

TABLE 14.2

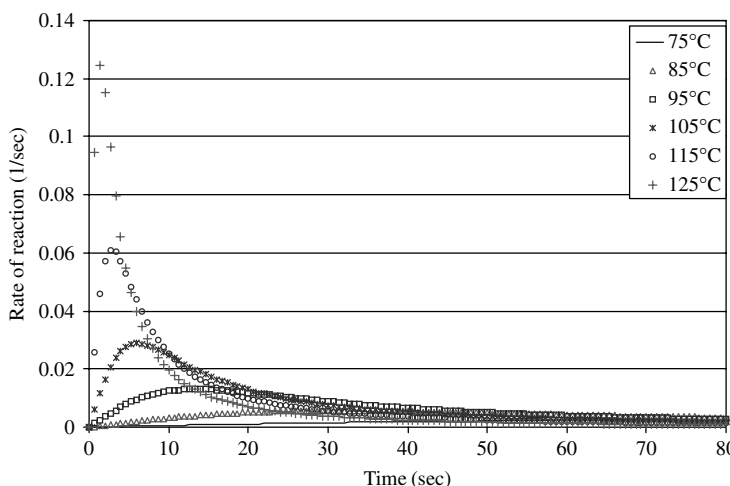
Comparison of Various Prediction of k_e for Carbon Biweave (The Models were Collected by M. Kaviany. *Principles of Heat Transfer in Porous Media*. New York: Springer-Verlag, 1995. With permission.)

Model	Formula	k_e (W/m K)	k_e/k_f
Parallel arrangement	$k_e = k_f \varepsilon_f + k_s \varepsilon_s$	3.59	13.01
Series arrangement	$k_e = \frac{k_f k_s}{k_f \varepsilon_f + k_s \varepsilon_f}$	0.47	1.71
Geometric mean	$k_e = (k_f)^{\varepsilon_f} (k_s)^{\varepsilon_s}$	1.17	4.24
Homogenization of diffusion equation (Chang, 1982) (two-dimensional periodic unit cell)	$\frac{k_e}{k_f} = \frac{(2 - \varepsilon_f) k_s / k_f + 1}{2 - \varepsilon_f + k_s / k_f}$	0.39	1.40

Note: For the carbon biweave experiments, we have $\varepsilon_f = 57\%$, $0.385 \leq K_{yy} \leq 0.718 \text{ (W/m K)}$, that is, $1.39 \leq K_{yy}/k_f \leq 2.60$.

**FIGURE 14.10**

The centerline temperature history at seven locations as shown in Figure 14.7; random fiberglass, $\varepsilon_s = 22\%$, $\langle u \rangle_x = 0.826 \text{ cm/sec}$, $Pe = d_p \langle u \rangle / 2\alpha_f = 6.28$, $K_{yy} = 0.94 \text{ W/m K} = 3.41 k_f$.

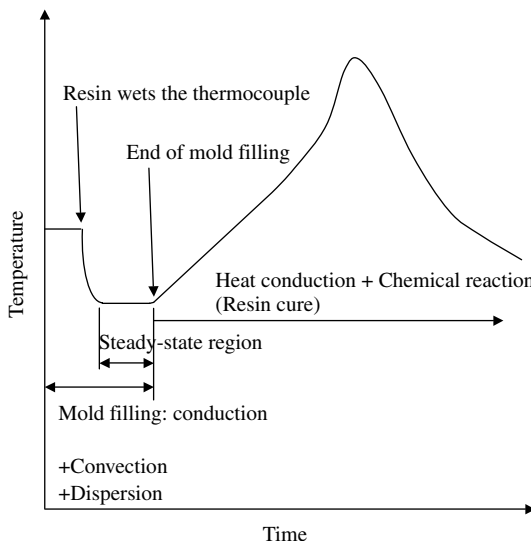
**FIGURE 14.11**

Rate of reaction of resin depends on the various resin temperature. (Taken from Antonucci et al. *Int. J. Heat Mass Transfer* 45: 1675–1684, 2002. With permission.)

here R_c is the reaction rate, which depends on the conversion of the chemical reaction $\langle c_f \rangle^f$ and the fluid phase-averaged temperature $\langle T_f \rangle^f$. A typical relationship between the temperature and reaction rate history of stationary resin is shown in Figure 14.11 [48].

The viscosity of the resin depends on the conversion of the chemical reaction $\langle c_f \rangle^f$ and the fluid phase-averaged temperature $\langle T_f \rangle^f$. Hence, we have

$$\mu = \mu \left\{ \langle c_f \rangle^f, \langle T_f \rangle^f \right\} \quad (14.18)$$

**FIGURE 14.12**

Typical temperature history for a thermocouple located at the mid-plane of the mold and embedded in the random fiberglass preform during RTM process.

Note that when the conversion approaches the gel point, the viscosity of a thermosetting resin will approach infinity.

The chemical reaction, which contributes to the thermoset resin consolidation and viscosity, is very important for process control in LCM. In typical LCM design, it is better to separate the resin injection stage and chemical reaction stage to gain better control of the process. A temperature history of typical RTM design is illustrated in Figure 14.12.

14.3 Process Control and Optimization

With the capabilities to model the LCM processes, it is natural to extend the process simulations for control and optimization. The LCM has been developed for over two decades and the process design tasks rely mainly on experienced molders. Process simulations are being used mainly to verify the trial-and-error approach, which is still prevalent in the manufacturing industry. However, as the composite structures being manufactured by LCM become larger and more complex, use of process simulation will (i) aid in improving the process design and (ii) increase the yield by counterbalancing any unforeseen disturbances that may arise during the impregnation phase if employed together with the methodologies for process optimization and flow control. However, this would require one to (i) couple the flow through fibrous porous media simulation with search techniques and

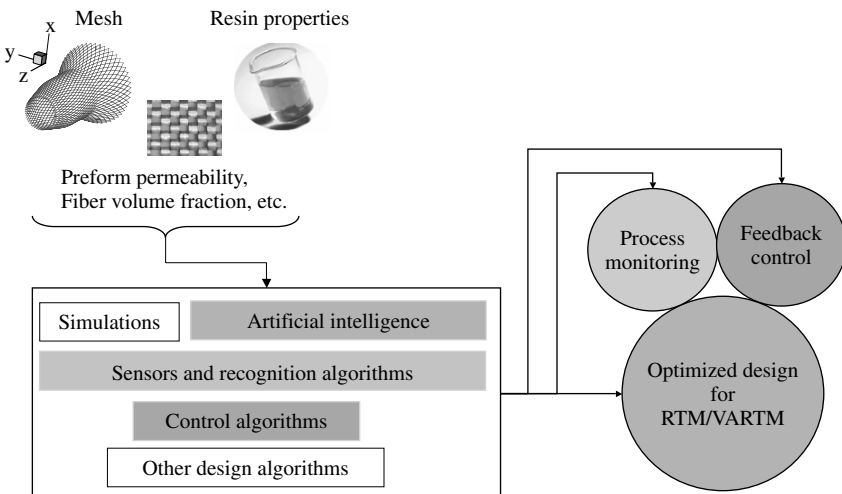


FIGURE 14.13
Philosophy of Simulation-based Liquid Injection Control.

optimization algorithms, (ii) develop various statistically different scenarios due to forecasted disturbances in the permeability of the preform along the mold walls, (iii) formulate methodologies to integrate sensors in the mold to detect these scenarios, and (iv) suggest control actions to redirect the flow with the help of auxiliary actuators to save a part that otherwise would have to be rejected due to the disturbance. Figure 14.13 schematically exhibits the philosophy of optimization and control. In the following sections, we summarize the recent developments toward these endeavors.

14.3.1 Injection Gates and Vents and Flow Distribution Network Optimization

An injection gate is a location through which the resin is impregnated in a closed mold. A vent is a location through which the air is displaced. An optimal selection of resin injection gate and vent locations is very essential for successful resin impregnation in LCM. For simple geometry, analytical solution may serve as a good rule of thumb for design practice. For example, a simplified analytical VARTM flow model [49] has been derived from Darcy's law and continuity equation and experimentally validated [50]. It has been used by the industry for easy estimation of the fill time and to assess the optimal sequential injection line and gate locations. However, for complex geometries, researchers tend to combine flow simulations with selected search algorithms, such as Simulated Annealing [51], GAs [17,18,21,52], and Branch and Bound Search [19] to systematically locate optimal resin injection regions for the geometry under consideration. The objective function that one must

usually maximize or minimize to optimize for the best gate location is usually a combination of void content (dry spot), mold fill time, and sometimes advanced features such as cost of equipment [52].

In addition to optimization of gate location, which focuses on finding a node that will deliver the lowest cost function, recent LCM development desires a methodology to optimize the flow distribution network, such as the flow runners and flow distribution media. The need to be able to optimize the flow distribution network to accelerate resin impregnation and reduce dry spot becomes more and more noticeable when the composite part becomes larger and more complex and contains inserts or internal features such as ribs. For example, many large structures have ribs to support the skin as shown in Figure 14.14. In such cases, the cocure VARTM process will be used. Contrary to traditional LCM geometries, the arrangement of the distribution network for such cocure VARTM process is very difficult to design by trial-and-error approach even for a simple geometry as shown in Figure 14.14. The complexity of this problem includes the variation in the fiber volume fraction under the rib held in place using a compaction force and the three-dimensional resin flow due to the presence of the distribution media. This requires one to optimize regions of porous media rather than a single node for a selected cost function. To simulate the three-dimensional flow in VARTM, Simacek et al. [53] utilized the one- and two-dimensional elements to represent the flow runner channels and the flow distribution media attached on the fiber preform, which is represented by three-dimensional elements. Recently, Hsiao et al. [22] attempted to optimize the flow distribution network by combining GA for optimization and LCM flow simulations. The concept is illustrated in Figure 14.15 and Figure 14.16.

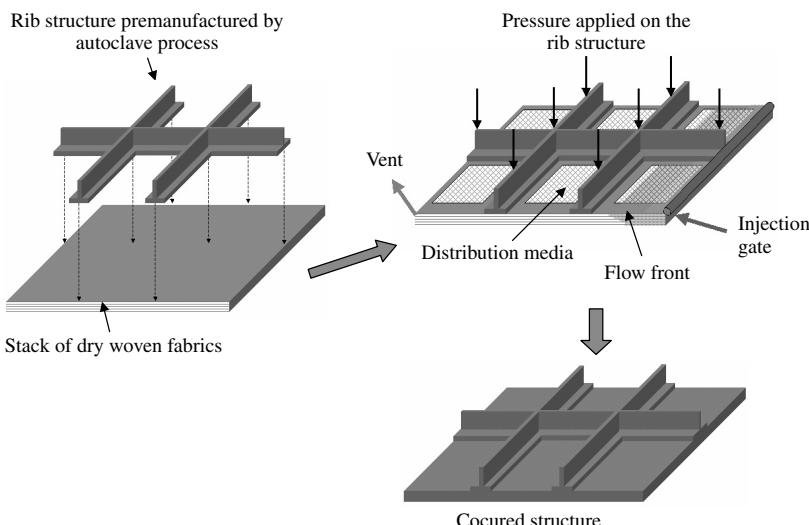
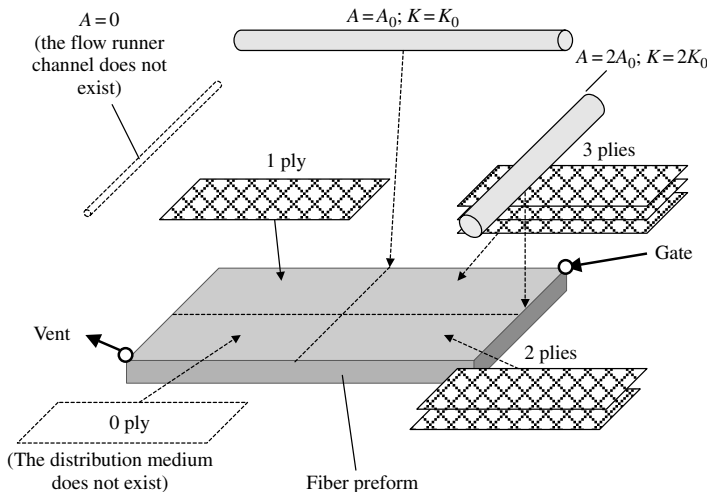
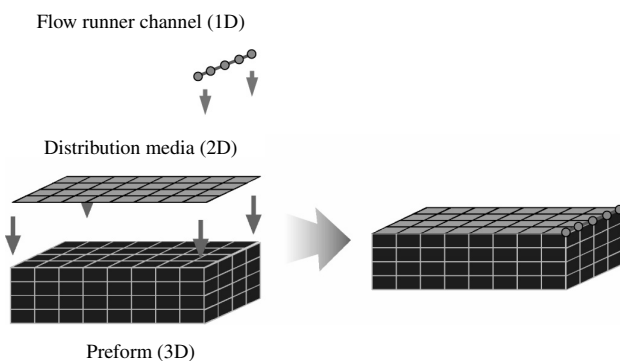


FIGURE 14.14

Schematic of the steps in manufacturing the cocured rib structure.

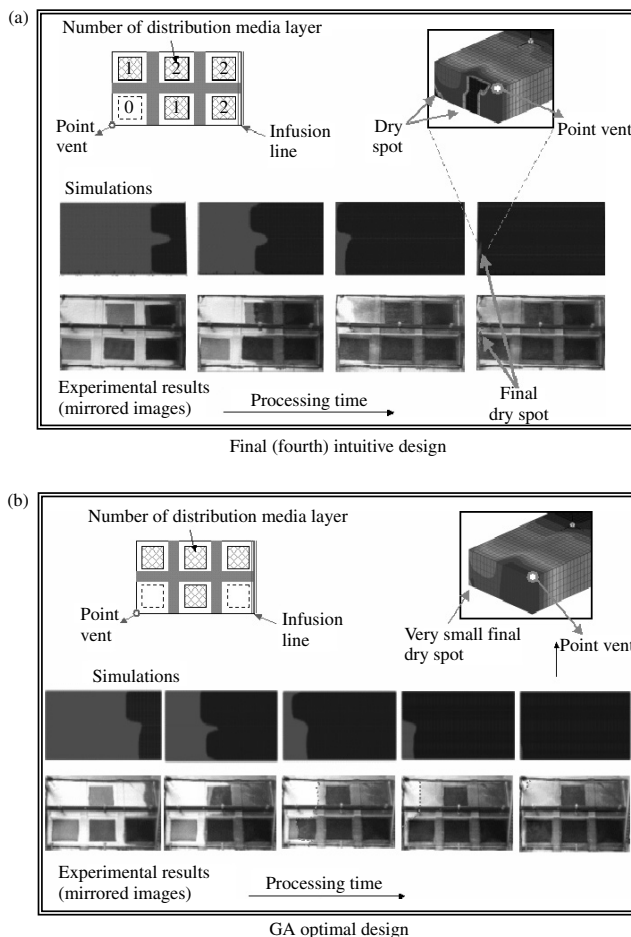
**FIGURE 14.15**

The number of plies of distribution media and the cross-section areas of the flow runner channels are the design parameters for flow distribution network optimization. (Taken from K.T. Hsiao, M. Devillard, and S.G. Advani. Simulation based flow distribution network optimization for vacuum assisted resin transfer molding process. *Modeling Simulation Mat. Sci. Eng.* 12(3): S175–S190, 2004. With permission.)

**FIGURE 14.16**

The distribution media and the flow runner channels can be modeled as two-dimensional elements and one-dimensional elements and attached to the three-dimensional model that represents the preform. (Taken from P. Simacek, D. Modi, and S.G. Advani. Proceedings of the 10th US-Japan Conference on Composite Materials at Stanford, CA, 2002, pp. 475–486. With permission.)

As shown in Figure 14.17, the combination of GA and LCM simulations suggested a nonintuitive arrangement of the flow distribution network, which was better than the trial-and-error intuitive design approach. Table 14.3 compares the results from the trial-and-error intuitive design and the GA/simulation-based design and clearly shows that the GA/simulation-based design provides better performance.

**FIGURE 14.17**

Flow simulations and experimental results from the final intuitive design and the GA optimal design for the cocured VARTM part. (Taken from K.T. Hsiao, M. Devillard, and S.G. Advani. Simulation based flow distribution network optimization for vacuum assisted resin transfer molding process. *Modeling Simulation Mat. Sci. Eng.* 12(3): S175–S190, 2004. With permission.)

TABLE 14.3

Comparison Between the Trial-and-Error Intuitive Design and GA Simulation-Based Design (Taken from K.T. Hsiao, M. Devillard, and S.G. Advani. Simulation based flow distribution network optimization for vacuum assisted resin transfer molding process. *Modeling Simulation Mat. Sci. Eng.* 12(3): S175–S190, 2004. With permission.)

	Dry spot content (%)	Fill time (min)	Number of experiments
Trial-and-error intuitive design	0.851	10.87	4
GA/simulation-based design (SLIC)	0.034	13.05	1

14.3.2 Online Permeability Characterization

The LCM flow simulations are based on Darcy's law and continuity equation. In order to gain accurate numerical results, the correct input of material properties, such as resin viscosity and preform permeability, is very critical. The in-plane preform permeability can be characterized by a one-dimensional experiment or by a radial experiment as shown in Figure 14.18. The location of the resin front with time is recorded with a camera through a transparent acrylic mold to calculate the permeability of the preform. This method is valid for characterizing most of the preform bulk permeability. However, many things can go wrong when an operator cuts and places the preform in a mold cavity and closes the mold. For example, the permeability and fiber

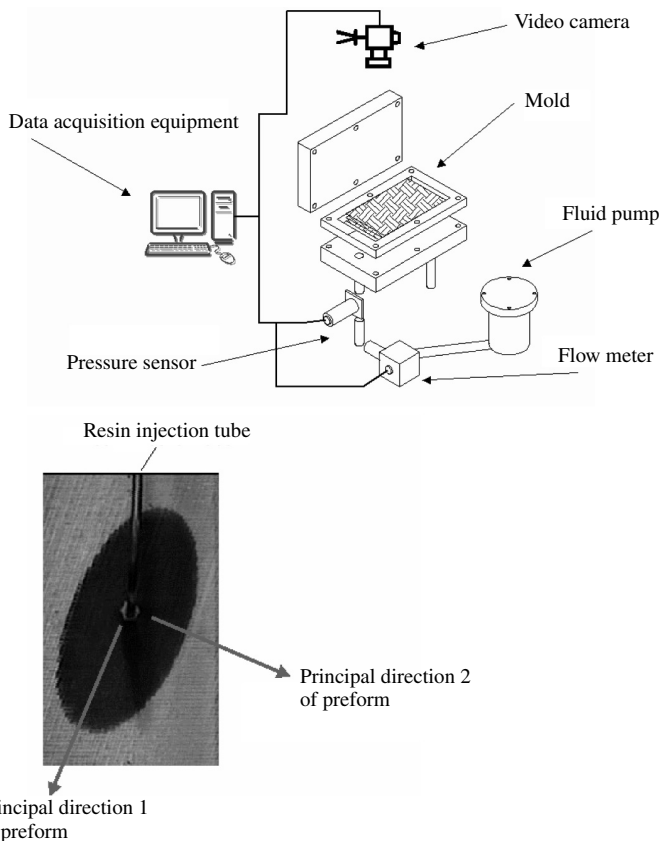
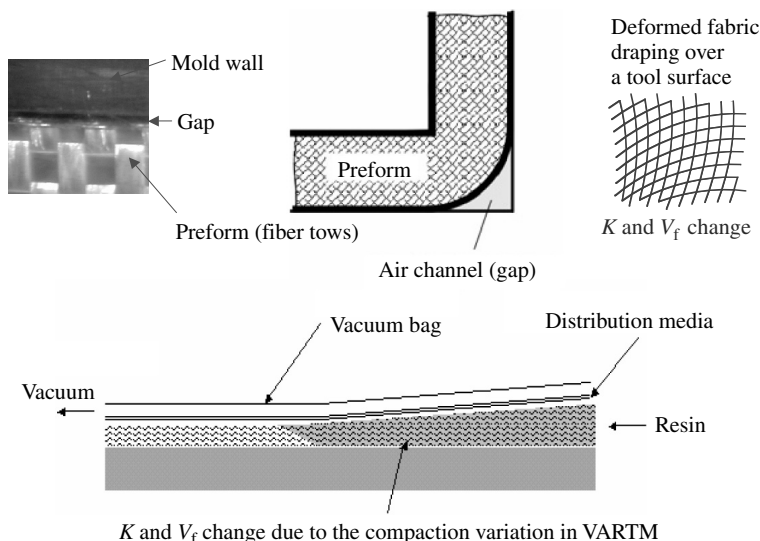


FIGURE 14.18

On the left is a schematic of linear injection for permeability characterization. Equipment includes a fluid flow meter, pressure sensor, and a video camera to record the experiment. On the right, one can see the resin movement for radial injection. (Taken from J. Slade, M. Sozer, and S. Advani, *J. Reinforced Plastics Composites* 19: 552–568, 2000; G. Estrada and S.G. Advani, *J. Composite Mater.* 36(19): 2297–2310, 2002. With permission.)

**FIGURE 14.19**

Local permeability and fiber volume fraction variation due to: edge effects, corner, draping, and compaction.

volume fraction may vary locally at preform edges due to the low stiffness of the acrylic mold, or due to preform draping [54] and compaction [55,56] as shown in Figure 14.19. These local disturbances in permeability and fiber volume fraction are difficult to characterize by classic permeability measurement techniques and sometimes result in different mold filling patterns as shown in Figure 14.4. Hence, it is very important to be able to accurately characterize the preform properties before one can use flow simulations to help the design of the LCM process.

To characterize the local permeability variation in real time, it is necessary to use the flow simulations with embedded flow sensors in the mold and a mold filling pattern recognition algorithm. This methodology has been suggested by using a dimensionless time vector system [52] defined as:

$$\bar{t}_k = \frac{t_k - t_0}{\sum_{j=0}^{N_{DS}-1} (t_j - t_0)}, \quad \text{for } k = 0, 1, 2, 3, \dots, N_{DS} - 1 \quad (14.19)$$

where N_{DS} is the number of flow detection sensors ($k = 0, 1, 2, 3, \dots, N_{DS} - 1$) in the mold cavity. Each flow sensor will be triggered when the resin covers it and will record the resin arrival time. Using this dimensionless time vector \bar{t}_k , one will obtain the same dimensionless time vector values even if the injection pressure and the resin viscosity are different from one experiment to the next. Another irregular but important feature of this dimensionless time vector definition is that it uses the sum of all resin arrival time, which are offset

by "sensor 0" as the base value to create the dimensionless vector because it is designed to characterize the local permeability variation during the mold filling stage and allows the appropriate active flow control to be launched if necessary.

This approach has also been experimentally verified and used to handle several difficult permeability measurements, such as racetracking at the preform edges [57] and distribution media permeability characterization [22]. Another use of this dimensionless time vector is to detect the flow disturbance during the mold filling stage and allow the process control computer (or operator) to select and launch suitable flow control action to avoid dry spot and reduce the part rejection rate.

14.3.3 Flow Control

Flow disturbance such as racetracking at preform edges can yield very different mold filling patterns and dry spot formation as shown in Figure 14.20. The flow disturbance is inevitable and not repeatable. Hence, it requires flow control techniques to amend the scenario if flow disturbance is detected during the mold filling stage.

If we examine Darcy's law and given the predetermined preform permeability and resin viscosity, we find we can actuate the flow system by either controlling the injection flow rate or the injection pressure or even the vent pressure. Thus, one can control either the pressure or the flow

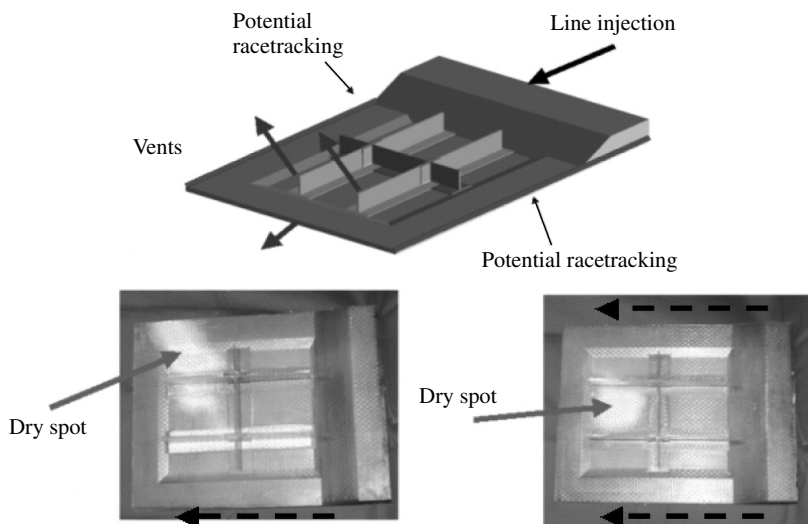


FIGURE 14.20

Two composite parts in which different dry spot sizes and locations resulted from the identical RTM tool and same processing conditions. The broken lines indicate possible racetracking channels.

rate of the resin delivery auxiliary sources. From literature review, it was found that several different flow control systems have been investigated by researchers. The flow rate control using multiple gates has been proven to be effective for steering flow during the mold filling stage [51,58–62]. The neural network process model, which was trained with off-line flow simulations in advance, was reported to be useful for optimizing the flow control decisions during the RTM filling stage [51,58,59,62]. Recently, Nielsen and Pitchumani [62] developed a close-loop flow control methodology, which uses the on-the-fly finite-difference-based numerical solution to optimize the injection flow rates using multiple gates in real time. Sozer et al. [63] and Bickerton et al. [60] investigated the concept of strategic flow rate control for manipulating the resin flow to compensate for the disturbances due to imperfect fits between mold and preform edges. In their work, the authors used flow detection sensors to register the arrival of resin at several discrete locations. In their approach, one must first specify where the disturbances are likely to occur and also specify the strength of disturbances. Next, numerical simulations are run for all possible permutations of scenarios. From the results, locations for resin arrivals are selected to effectively identify and distinguish between various scenarios based on the sequence of resin arrival at these locations. This information is stored in a database. By comparing the sensor triggering sequence during the experiment with the stored database, the manufacturing control computer will distinguish the corresponding flow disturbance mode online. After the disturbance mode is detected, the flow rates at the preselected auxiliary gates can be changed to steer the resin flow toward the vents. Recently, Lawrence et al. [64] used flow simulations and GA to optimize the flow rates at the auxiliary gates as well. These approaches were found to be useful for manufacturing complex composite parts.

Though the flow rate control has been proven useful in counteracting the flow disturbance, its effectiveness strongly depends on the relative locations of the control gates and the resin flow front. It was observed that a gate loses its controllability when the flow front moves far away from it and the sequential logic control was proposed to open and close the injection gates and vents sequentially during the filling process in order to adjust filling patterns [65]. Another disadvantage of the flow rate control is the complexity and cost associated with the flow rate control equipment. In order to control the flow rate of each individual gate, a flow rate controllable injection pump must be connected to only one gate. As a complex LCM mold requires many injection gates, to install and maintain so many pumps could soon make the system out of reach for most molding operations. Hence, the on-off logic control proposed by Berker et al. [65], which potentially allows the resin to be driven by a single constant pressure pump, is relatively cost-effective compared with the flow rate control setup.

The preliminary approach to control the flow in LCM successfully demonstrated the feasibility and advantages of using active flow control.

However, to design such an intelligent flow sensing-control system in LCM, the challenge is to find where to place the sensors, injection gates, vents, and the gates/vents control logic based on the sensors feedback for different flow disturbance scenarios in addition to developing robust hardware of auxiliary gates, embedded sensors, and computer controlled values to open and close gates and vents. Theoretically, simulations and control methodologies can be combined to develop such a system. Recently, Hsiao and Advani [52] have developed and demonstrated the design algorithm, which uses flow simulations, mold fill pattern recognition algorithm, and GAs in optimizing the strategic flow actuation installation (locations of gates/vents/sensors and selection of pumps) and control logistics (the timing to open/close gates/vents) for a given set of flow disturbance scenarios (or modes). This system also allows the user to expand the database of flow disturbance scenarios and has the potential to learn/self-improve from its experience. In this design algorithm, all physical items and events are translated to several sequences of numbers with a binary format. The rules of the physical manufacturing process are implemented as constraints to the sequences. Each set of sequences represents a design of intelligent LCM and can be conducted virtually and evaluated with flow simulations. A multitier GA was used to construct the set of design sequences that search for the best performance. A reliability study further demonstrated that an intelligent RTM initially designed based on only a few disturbance scenarios can address expended disturbance scenarios reasonably well if these are bounded by the initial disturbance design domain. In the numerical case study, Hsiao and Advani observed that the mold filling success rate, which is the rate at which parts with dry spot content is less than 1% by volume, increased from 27 to 70% with active flow control and a reasonable forecasting of the permeability disturbances along the edges. An experimental streamlined design-manufacture system [66,67] was achieved by transferring the process design files to a process control computer to automatically implement and operate the auxiliary flow control based on the feedback from the embedded sensors. The experimental results [67] showed that this approach was effective in reducing LCM filling failure from unexpected flow disturbances such as racetracking.

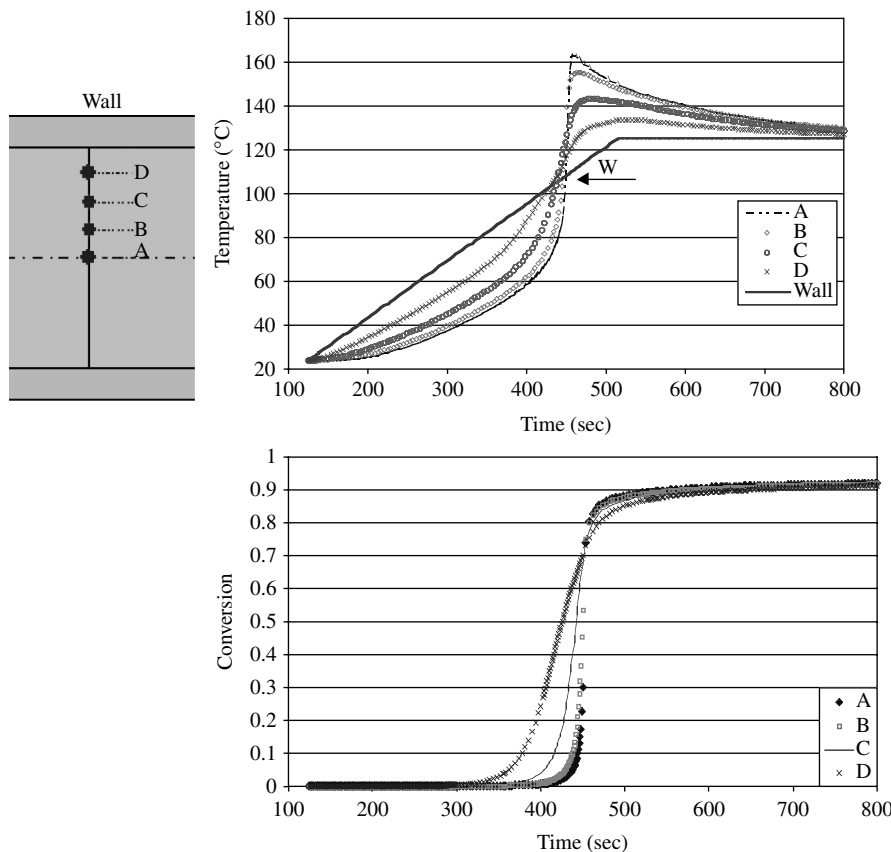
14.3.4 Temperature and Resin Cure Cycle Optimization

A typical LCM process involves the mold filling stage and the consolidation stage. In most cases, the preferred process is to fill the mold with the resin and then initiate cure because once the resin starts to cross-link, its viscosity will increase rapidly and it will become increasingly difficult to push the resin into spaces between the fibers, which will create a network of undesirable voids in the composite. In the previous sections, the modeling

of resin heating and curing and the experimental results were presented. However, research into optimizing and controlling the heat transfer during the filling stage has not arrived at any significant results though it is possible to numerically predict the temperature history for simple RTM cases [28,29,44,68–70]. There are several reasons why not much research has been carried out in this direction: (i) the nonisotropic heat dispersion tensor is very difficult to characterize if one considers a very complex preform and variations in resin flow direction from one experiment to the next; (ii) in most of the manufacturing situations, the resin is injected under isothermal conditions; and (iii) the error in prediction of material parameters is higher than the error in prediction of the temperature of the resin during mold filling.

However, there is an interest in optimizing the cure cycle after the mold is saturated with the resin as one would like to minimize the time for which the composite structure sits in the mold. Cure cycle optimization is a continuous and general research topic for all types of thermoset polymer composite manufacturing processes as the cure and thermal history essentially influences the mechanical properties of the composite materials. The cure cycle and the temperature history of the composite can be controlled and managed by designing and optimizing the temperature profile applied to the mold walls. Integrated use of process modeling and numerical simulations, experimental validation, and advanced sensors serve as useful tools to achieve this goal [71–73]. In recent years, to acquire real-time information about the process, sensors that monitor both the filling and the curing have been developed. These sensor systems are based on different operating principles, such as frequency dependent electromagnetic sensors [71], fiber optic systems [72], and conductive filament grids [73]. The ability to monitor temperature and cure will allow the possibility of control by modifying the boundary conditions (the mold wall temperatures) during the curing stage.

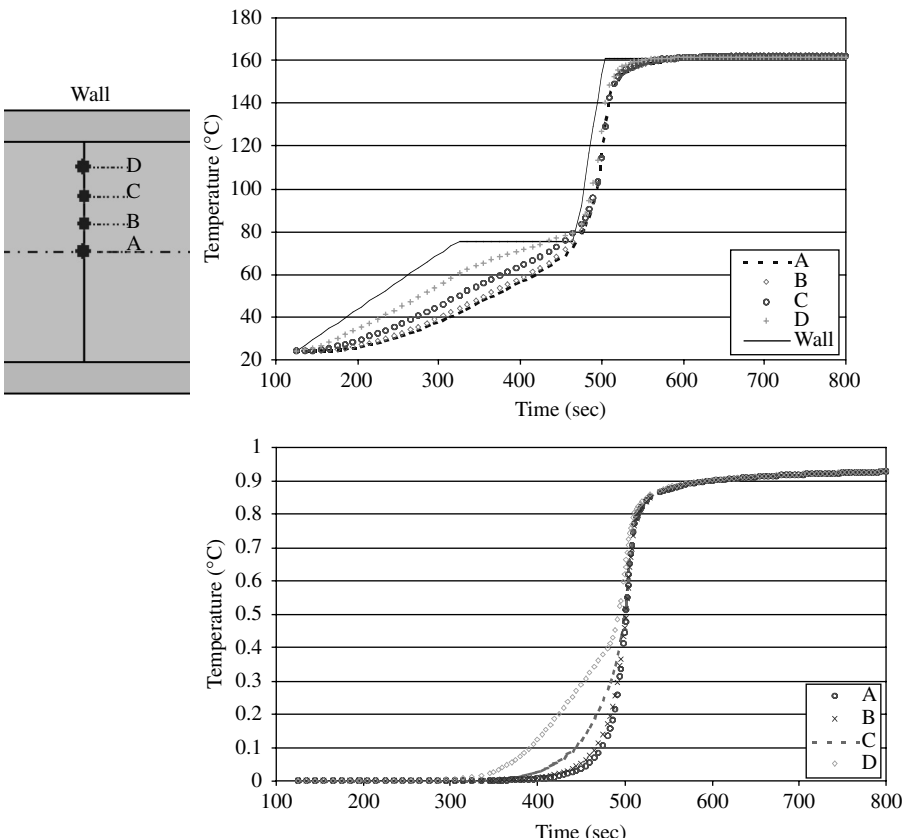
The modeling of the cure cycle usually involves a transient heat conduction equation and a source term for chemical reaction. The objectives are to minimize the cycle time, the local gradients of degree of cure and temperature that will reduce the thermal stress and strain in the composite [74], and maximize the final degree of cure. Yu and Young [75] employed GA to numerically optimize the cure cycle by analyzing the optimal mold wall temperature profile with respect to cycle time. Michaud et al. [76,77] developed an in-site cure sensing technique to identify the cure model parameters in RTM and applied adaptive control based on the simulated optimal cure cycle for thick-section RTM composite panels. Antonucci et al. [48] used the dimensionless arguments and the enthalpy of the resin reaction as a baseline to numerically minimize the gradients of temperature, the degree of cure, and the final cure temperature of the RTM process. The improvement of the uniformity of temperature and degree of cure can be found in [Figure 14.21](#) and [Figure 14.22](#).

**FIGURE 14.21**

History of temperature and conversion (degree of cure) in a nonoptimized cure cycle. (Taken from V. Antonucci et al. *Int. J. Heat Mass Transfer* 45: 1675–1684, 2002. With permission.)

14.4 Conclusions and Outlook

The LCM can be generally described as a nonisothermal reactive liquid (resin) flow through nonhomogeneous and nonisotropic porous media (fiber preform). This process involves simultaneous mass, momentum, and heat transfer in an anisotropic porous media. Fortunately, in LCM processes, not all the phenomena are simultaneously equally important, which allows one to decouple the flow and heat transfer equations and develop simulations that can be used to address the issues in case of unforeseen variability in the permeability of the porous media by introducing optimization and control. The engineering approach for this problem is to simplify the model to the level at which we can characterize and simulate flow using Darcy's law and the volume-averaging method. Based on these volume-averaged

**FIGURE 14.22**

History of temperature and conversion (degree of cure) in an optimized cure cycle. (Taken from V. Antonucci et al. *Int. J. Heat Mass Transfer* 45: 1675–1684, 2002. With permission.)

governing equations, the flow/thermal/chemical behaviors can be explained, predicted, and verified. For simple geometry and well-conditioned experiments, the numerical solutions predict the results reasonably well. During the last decade, researchers have started to use numerical simulations to optimize the LCM design and have been achieving satisfactory advancement in the LCM process. However, many uncertainties (or process instability) during LCM have also been identified when researchers compared the simulated results with the experiments. To address this disturbance induced by the uncertainties, one has to monitor the process and introduce active control if necessary. Recent efforts toward process sensing, control, and automation have achieved some success in enhancing quality and yield over traditional experience/trial-and-error based process development approaches in LCM. Modeling flow through porous media and creating a virtual manufacturing platform to address the needs of the process continue to fuel the science based manufacturing of composite molding processes.

Acknowledgment

The authors gratefully acknowledge the financial support by Office of Naval Research (Grant Number: N00014-02-1-0811) for the "Advanced Materials Intelligent Processing Center" at the University of Delaware.

Nomenclature

b	closure vector function (m)
<i>c</i>	conversion of chemical reaction
c_{hc}	thermal capacity correction vector (J/m ² K)
<i>c_p</i>	specific heat (J/kg K)
C_{mc}	correction of macro-convection (W/m K)
<i>d_p</i>	particle diameter (m)
e	unit vector
<i>g</i>	gravitational constant (m/sec ²)
<i>Gz</i>	Graetz number
<i>h_c</i>	heat transfer coefficient (W/m ² K)
<i>h_d</i>	half height of the two-dimensional unit cell (m)
I	identity tensor
<i>k_f</i>	thermal conductivity of the fluid (W/m K)
k_e	effective thermal conductivity of the fluid saturated porous media (W/m K)
k_{2d}	thermal diffusive correction vector (W/K)
K	total effective thermal conductivity tensor (W/m K)
K_D	effective thermal conductivity for dispersion effect (W/m K)
<i>l</i>	length of the two-dimensional unit cell (m)
<i>N_{DS}</i>	Number of resin flow front detection sensors
n	normal vector
<i>n</i>	normal direction or integer
<i>P</i>	pressure (Pa)
<i>Pe</i>	Pécelt number
<i>Pr</i>	Prandtl number
<i>q</i>	heat flux (W/m ²)
q	heat flux vector (W/m ²)
<i>R_c</i>	reaction rate (sec ⁻¹)
<i>S</i>	surface (m ²)
S	permeability tensor (m ²)
<i>s</i>	heat source (W/m ³)
<i>t</i>	time (sec)
<i>T</i>	temperature (K)
<i>T₀</i>	initial temperature (K)

u	velocity vector (m/sec)
u_D	magnitude of Darcy's velocity (m/sec)
\mathbf{u}_{pcf}	the reference velocity of the pure conduction frame (m/sec)
V	representative volume (m^3)
x, y, z	Cartesian coordinates
x_c, z_c	characteristic length (m)

Greek Letters

ΔT	temperature difference (K)
ε	volume fraction
θ	transformation of temperature
μ	dynamic viscosity (Pa/sec)
ρ	density (kg/m^3)

Subscripts

f	fluid phase
i	material index
pcf	pure conduction frame
s	solid phase

Superscripts

f	fluid phase
i	material index
s	solid phase
\wedge	deviation

Other

$\langle \rangle$	local volume-averaging operator
-------------------	---------------------------------

References

1. B.T. Åström. *Manufacturing of Polymer Composites*. 1st edn. London: Chapman & Hall, 1997.
2. T. Gutowski. *Advanced Composites Manufacturing*. New York: John Wiley & Sons, 1997.
3. S.G. Advani (ed.). *Flow and Rheology in Polymer Composites Manufacturing*. New York: Elsevier Science, 1994.
4. S.G. Advani and M. Sozer. *Process Modeling in Composite Manufacturing*. New York: Marcel Dekker Inc., 2002.

5. R. Cochran, C. Matson, S. Thoman, and D. Wong. *Advanced Composite Processes for Aerospace Applications*. 42nd International SAMPE Symposium, Long Beach, CA, 1997, pp. 635–640.
6. Lockheed Martin. F-22 RAPTOR: Air dominance for the 21st century. *Adv. Mater. Process.* 5: 23–26, 1998.
7. Simacek, Pavel and S.G. Advani Desirable Features in Mold Filling Simulations for Liquid Molding Processes, *Polym. Composites* 25: 355–367, 2004.
8. M.V. Bruschke and S.G. Advani. A finite element/control volume approach to mold filling in anisotropic porous media. *Polym. Composites* 11: 398–405, 1990.
9. M.V. Bruschke and S.G. Advani. A numerical approach to model non-isothermal viscous flow through fibrous media with free surface. *Int. J. Numer. Meth. Fluids* 19: 575–603, 1994.
10. Y.F. Chen, K.A. Stelson, and V.R. Voller. Prediction of filling time and vent locations for resin transfer molds. *J. Composite Mater.* 31(11): 1141–1161, 1997.
11. R. Lin, L.J. Lee, and M. Liou. Non-isothermal mold filling and curing simulation in thin cavities with preplaced fiber mats. *Int. Polym. Process.* 6(4): 356–369, 1991.
12. F. Trochu, J.F. Boudreault, D.M. Gao, and R. Gauvin. Three-dimensional flow simulations for the resin transfer molding process. *Mater. Manuf. Process.* 10(1): 21–26, 1995.
13. C.D. Rudd and K.N. Kendall. *Modeling Non-isothermal Liquid Moulding Processes*. Proceedings of 3rd International Conference on Automated Composites, The Hague, The Netherlands, 1991, pp. 30/1–30/5.
14. F.R. Phelan Jr. Simulation of the injection process in resin transfer molding. *Polym. Composites* 18(4): 460–476, 1997.
15. H. Aoyagi, M. Uenoyama, and S.I. Guceri. Analysis and simulation of structural reaction injection molding (SRIM). *Int. Polym. Process.* 7: 71–83, 1992.
16. M.I. Youssef and G.S. Springer. Interactive simulation of resin transfer molding. *J. Composite Mater.* 31(10): 954–980, 1997.
17. W.B. Young. Gate location optimization in liquid composite molding using genetic algorithms. *J. Composite Mater.* 28(12): 1098–1113, 1994.
18. R. Mathur, B.K. Fink, and S.G. Advani. Use of genetic algorithms to optimize gate and vent locations for the resin transfer molding process. *Polym. Composites* 20(2): 167–178, 1999.
19. A. Gokce, K.T. Hsiao, and S.G. Advani. Branch and bound search to optimize injection gate locations in liquid composites molding processes. *Composites Part A: Appl. Sci. Manuf.* 33(9): 1263–1272, 2002.
20. M.H. Chang, C.L. Chen, and W.B. Young. Optimal design of the cure cycle for consolidation of thick composite laminates. *Polym. Composites* 17(5): 743–750, 1996.
21. J. Luo, Z. Liang, C. Zhang, and B. Wang. Optimum tooling design for resin transfer molding with virtual manufacturing and artificial intelligence. *Composites Part A: Appl. Sci. Manuf.* 32(6): 877–888, 2001.
22. K.T. Hsiao, M. Devillard, and S.G. Advani. Simulation based flow distribution network optimization for vacuum assisted resin transfer molding process. *Modeling Simulation Mat. Sci. Eng.* 12(3): S175–S190, 2004.
23. C.J. Wu, L.W. Hourng, and J.C. Liao. Numerical and experimental study on the edge effect of resin transfer molding. *J. Reinforced Plast. Composites* 14: 694–719, 1995.

24. S. Bickerton and S.G. Advani. Characterization and modeling of race-tracking in liquid composite molding processes. *Composites Sci. Technol.* 59(15): 2215–2229, 1999.
25. C.L. Tucker III and R.B. Dessenberger. Governing equations for flow and heat transfer in stationary fiber beds. In S.G. Advani, ed., *Flow and Rheology in Polymer Composites Manufacturing*, Chapter 8. New York: Elsevier Science, 1994, pp. 257–323.
26. R.G. Carbonell and S. Whitaker. Dispersion in pulsed systems-II. Theoretical developments for passive dispersion in porous media. *Chem. Eng. Sci.* 38: 1795–1802, 1983.
27. A. Eidsath, R.G. Carbonell, S. Whitaker, and L.R. Herman. Dispersion in pulsed system-III. Comparison between theory and experiment for packed Beds. *Chem. Eng. Sci.* 38: 1803–1816, 1983.
28. R.B. Dessenberger and C.L. Tucker III. Thermal dispersion in resin transfer molding. *Polym Composites* 16(6): 495–506, 1995.
29. O. Mal, A. Couniot, and F. Dupret. Non-isothermal simulation of the resin transfer moulding process. *Composite Part A* 29A: 189–198, 1998.
30. A. Amiri and K. Vafai. Analysis of dispersion effects and non-isothermal equilibrium, no-Darcian, variable porosity, incompressible flow through porous media. *Int. J. Heat Mass Transfer* 37: 939–954, 1994.
31. A. Amiri and K. Vafai. Transient analysis of incompressible flow through a packed bed. *Int. J. Heat Mass Transfer* 41: 4259–4279, 1998.
32. J.J. Fried and M.A. Combarnous. Dispersion in porous media. *Adv. Hydrosci.* 7: 169–282, 1971.
33. G.I. Taylor. Condition under which dispersion of a solute in a stream of solvent can be used to measure molecular diffusion. *Proc. Roy. Soc. (London) A* 225: 473–477, 1954.
34. G.I. Taylor. Dispersion of soluble matter in solvent flowing slowly through a tube. *Proc. Roy. Soc. (London) A* 219: 186–203, 1953.
35. F. Zanotti and R.G. Carbonell. Development of transport equations for multiphase system I–III. *Chem. Eng. Sci.* 39: 263–311, 1984.
36. M. Quintard and S. Whitaker. One and two equation models for transient diffusion processes in two phase systems. *Advan. Heat Transfer* 23: 269–464, 1993.
37. S. Whitaker. *The Method of Volume Averaging*. Dordrecht: Kluwer, 1999.
38. A.V. Kuznetsov. Thermal nonequilibrium forced convection in porous media. In D.B. Ingham and I. Pop, eds., *Transport Phenomena in Porous Media*. Amsterdam: Elsevier, 1998, pp. 103–129.
39. M. Quintard, M. Kaviany, and S. Whitaker. Two-medium treatment of heat transfer in porous media: numerical results for effective properties. *Adv. Water Resour.* 20: 77–94, 1997.
40. H.T. Chiu, S.C. Chen, and L.J. Lee. *Analysis of Heat Transfer and Resin Reaction in Liquid Composite Molding*. SPE ANTEC Conference, Toronto, 1997, pp. 2424–2429.
41. K.T. Hsiao and S.G. Advani. A theory to describe heat transfer during laminar incompressible flow of a fluid in periodic porous media. *Phys. Fluids* 11(7): 1738–1748, 1999.
42. S. Torquato. Random heterogeneous media: microstructure and improved bounds on effective properties. *Appl. Mech. Rev.* 44: 37–76, 1991.

43. D.L. Koch, R.G. Cox, H. Brenner, and J.F. Brady. The effect of order on dispersion in porous media. *J. Fluid Mech.* 200: 173–188, 1989.
44. K.T. Hsiao, H. Laudorn, and S.G. Advani. Heat dispersion due to impregnation of heated fibrous porous media with viscous fluids in composites processing. *ASME J. Heat Transfer* 123(1): 178–187, 2001.
45. H.C. Chang. Multi-scale analysis of effective transport in periodic heterogeneous media. *Chem. Eng. Comm.* 15: 83–91, 1982.
46. M. Kaviany. *Principles of Heat Transfer in Porous Media*. New York: Springer-Verlag, 1995.
47. C.L. Tucker III. Heat transfer and reaction issues in liquid composite molding. *Polym. Composites* 17(1): 60–72, 1996.
48. V. Antonucci, M. Giordano, K.T. Hsiao, and S.G. Advani. A methodology to reduce thermal gradients due to the exothermic reactions in composites processing. *Int. J. Heat Mass Transfer* 45: 1675–1684, 2002.
49. K.T. Hsiao, R. Mathur, J.W. Gillespie Jr., B.K. Fink, and S.G. Advani. A close form solution to describe fully developed through thickness resin flow in vacuum assisted resin transfer molding (VARTM). *ASME J. Manuf. Sci. Eng.* 122(3): 463–475, 2000.
50. R. Mathur, D. Heider, C. Hoffmann, J.W. Gillespie Jr., S.G. Advani, and B.K. Fink. Flow front measurements and model validation in the vacuum assisted resin transfer molding process. *Polym. Composites* 22(4): 477–490, 2001.
51. D. Nielsen and R. Pitchumani. Intelligent model-based control of preform permeation in liquid composite molding processes, with online optimization. *Composites Part A: Appl. Sci. Manuf.* 32(12): 1789–1803, 2001.
52. K.T. Hsiao and S.G. Advani. Flow sensing and control strategies to address race-tracking disturbances in resin transfer molding — Part I: design and algorithm development. *Composites Part A: Appl. Sci. Manuf.* 35(10): 1149–1159, 2004.
53. P. Simacek, D. Modi, and S.G. Advani. *Numerical Issues in Mold Filling Simulations of Liquid Composites Processing*. Proceedings of the 10th US–Japan Conference on Composite Materials at Stanford, CA, 2002, pp. 475–486.
54. J. Slade, M. Sozer, and S. Advani. Effect of shear deformation on permeability of fiber preforms. *J. Reinforced Plastics Composites* 19: 552–568, 2000.
55. C. Baoxing, E.J. Lang, and T.W. Chou. Experimental and theoretical studies of fabric compaction behavior in resin transfer molding. *Mater. Sci. Eng.* 317(1–2): 188–196, 2001.
56. G. Estrada and S.G. Advani. Experimental characterization of the influence of tackifier material on preform permeability. *J. Composite Mater.* 36(19): 2297–2310, 2002.
57. M. Devillard, K.T. Hsiao, A. Gokce, and S.G. Advani. On-line characterization of bulk permeability and race-tracking during the filling stage in resin transfer molding process. *J. Composite Mater.* 37(17): 1525–1541, 2003.
58. H.H. Demirci and J.P. Coulter. Neural network based control of molding processes. *J. Mater. Process. Manuf. Sci.* 2: 335–354, 1994.
59. H.H. Demirci, J.P. Coulter, and S.I. Guceri. Numerical and experimental investigation of neural network-based intelligent control of molding processes. *ASME J. Manuf. Sci. Eng.* 119(1): 88–94, 1997.
60. S. Bickerton, H.C. Stadtfeld, K.V. Steiner, and S.G. Advani. Design and application of actively controlled injection schemes for resin-transfer molding. *Composites Sci. Technol.* 61: 1625–1637, 2001.

61. P. Barooah, B. Berker, and J.Q. Sun. Integrated switching and feedback control for mold filling in resin transfer molding. *ASME J. Manuf. Sci. Eng.* 123: 240–247, 2001.
62. D. Nielsen and R. Pitchumani. Closed-loop flow control in resin transfer molding using real-time numerical process simulations. *Composites Sci. Technol.* 62(2): 283–298, 2002.
63. E.M. Sozer, S. Bickerton, and S.G. Advani. On-line strategic control of liquid composite mould filling process. *Composites Part A: Appl. Sci. Manuf.* 31(12): 1383–1394, 2000.
64. J.M. Lawrence, K.T. Hsiao, R.C. Don, P. Simacek, G. Estrada, E.M. Sozer, H.C. Stadtfeld, and S.G. Advani. An approach to couple mold design and on-line control to manufacture complex composite parts by resin transfer molding. *Composites Part A: Appl. Sci. Manuf.* 33(7): 981–990, 2002.
65. B. Berker, P. Barooah, and J.Q. Sun. Sequential logic control of liquid injection molding with automatic vents and vent-to-gate converters. *J. Mater. Process. Manuf. Sci.* 6(2): 81–103, 1997.
66. K.T. Hsiao, M. Devillard, and S.G. Advani. *Streamlined Intelligent RTM Processing: From Design to Automation*. Proceedings of 47th International SAMPE Symposium and Exhibition, Long Beach, CA, 2002, pp. 454–465.
67. Jeffrey M. Lawrence, Mathieu Devillard, and Suresh G. Advani, Design and Testing of a New Injection Approach for Liquid Composite Molding. *Journal of Reinforced Plastics and Composites*, 23(15): 1625–1638, 2004.
68. D.M. Gao, F. Trochu, and R. Gauvin. Heat transfer analysis of non-isothermal resin transfer molding by the finite element method. *Mater. Manuf. Process.* 10(1): 57–64, 1995.
69. G. Lebrun and R. Gauvin. Heat transfer analysis in a heated mold during the impregnation phase of the resin transfer molding process. *J. Mater. Process. Manuf. Sci.* 4: 81–104, 1995.
70. B. Liu and S.G. Advani. Operator splitting scheme for 3-D temperature solution based on 2-D flow approximation. *Computational Mech.* 38: 74–82, 1995.
71. D.E. Kranbuehl, P. Kingsley, S. Hart, G. Hasko, B. Dexter, and A.C. Loos. In situ sensor monitoring and intelligent control of the resin transfer molding process. *Polym. Composites* 15: 299–305, 1994.
72. S.H. Ahn, W.I. Lee, and G.S. Springer. Measurement of the three-dimensional permeability of fiber preforms using embedded fiber optic sensors. *J. Composite Mater.* 29: 714, 1995.
73. B.K. Fink, S.M. Shawn, D.C. DeSchepper, J.W. Gillespie Jr., R.L. McCullough, R.C. Don, and B.J. Waibel. Advances in resin transfer molding flow monitoring using smart weave sensors. *ASME Proc.* 69: 999–1015, 1995.
74. T.A. Bogetti and J.W. Gillespie Jr. Process-induced stress and deformation in thick-section thermoset composite laminates. *J. Composite Mater.* 26: 626–660, 1992.
75. H.W. Yu and W.B. Young. Optimal design of process parameters for resin transfer molding. *J. Composites Mater.* 31(11): 1113–1140, 1997.
76. D.J. Michaud, A.N. Beris, and P.S. Dhurjati. Thick-sectioned RTM composite manufacturing: Part I — In situ cure model parameter identification and sensing. *J. Composite Mater.* 36(10): 1175–1200, 2002.
77. D.J. Michaud, A.N. Beris, and P.S. Dhurjati. Thick-sectioned RTM composite manufacturing, Part II. Robust cure cycle optimization and control. *J. Composite Mater.* 36(10): 1201–1232, 2002.

15

Combustion and Heat Transfer in Inert Porous Media

Raymond Viskanta

CONTENTS

15.1	Introduction	607
15.2	Physical and Mathematical Description of Combustion in a PIM ...	610
15.2.1	Physical Description.....	610
15.2.2	Mathematical Description	613
15.3	Heat Transfer in Porous Media	615
15.3.1	Effective Thermal Conductivity	615
15.3.1.1	Packed beds	615
15.3.1.2	Consolidated porous media	616
15.3.2	Convective Heat Transfer Coefficient.....	617
15.3.2.1	Packed beds	617
15.3.2.2	Consolidated porous media	618
15.3.3	Radiation Characteristics	619
15.3.3.1	Radiation characteristics of packed beds	620
15.3.3.2	Radiation characteristics of open-celled materials ..	621
15.4	Overview of Porous Medium Based Combustors	622
15.5	Premixed Porous Medium Combustors	624
15.6	Porous Medium Combustor–Radiant Heater	628
15.7	Premixed Porous Medium Combustors–Heaters.....	634
15.8	Concluding Remarks	637
	Nomenclature	639
	References	640

15.1 Introduction

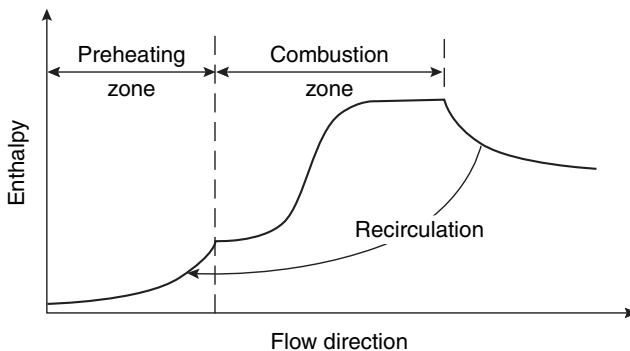
Combustion processes in porous media are of great practical importance and are encountered in numerous technological applications and systems such

as VOCs oxidation, packed bed incinerators, regenerative-type combustors, porous radiant burners, catalytic reactors and converters, direct energy gas conversion devices and systems, *in situ* coal gasification, high-temperature materials synthesis processing, smoldering of foam and cellulosic materials, combustion of wood and agricultural waste, cigarette burning, and many others. Numerous applications of the porous burner technology in energy and thermal-engineering and processing industries have been identified which are based on stabilized combustion in porous media [1–3]. When exothermic chemical reactions release sufficient energy, continuous chemical reactions can be sustained in porous media. Depending on the physical and chemical nature of the porous materials, combustion in porous media can be classified into three main types: (a) inert, (b) catalytic, and (c) combustible [4]. The classification is somewhat arbitrary but it reflects the wide range of current technological applications. The discussion in this chapter of the handbook focuses exclusively on combustion in porous inert media (PIM).

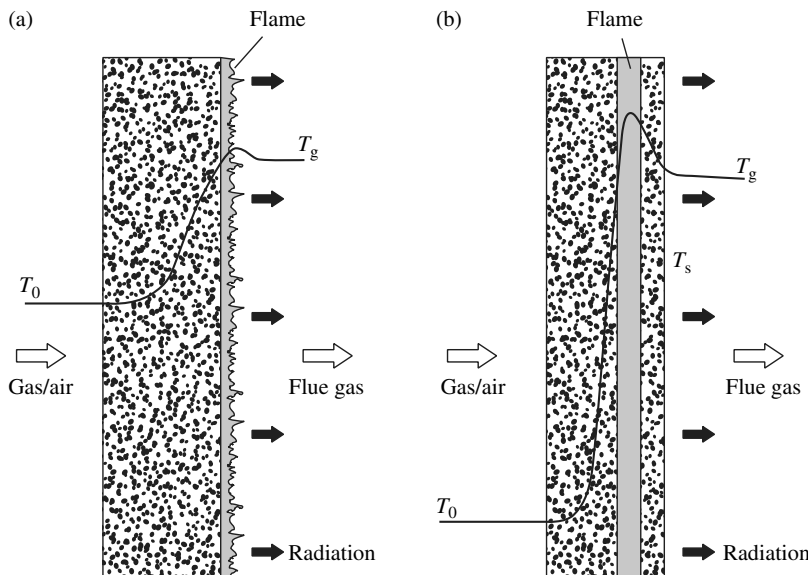
Combustion of a gas mixture within the voids of a porous medium has characteristics that are different from those observed in other (i.e., gas phase only) systems. This is owing to the fact that the thermophysical properties of the solid and gas phases are vastly different, and there is enhanced conduction heat transfer in the solid matrix. The “long range” radiation heat exchange between the surface elements of the solid phase and the large interfacial surface area per unit volume contribute to effective heat transfer between the gas and the solid phases. The energy release during the chemical reactions is intimately coupled to heat transfer (i.e., extraction or addition to the flame) as well as advective energy transport, and flammability limits as well as stability ranges that are different from those encountered in conventional designs.

Combustion in a PIM-based system can be characterized as a heat recirculating device in which the reactants or combustion air alone are preheated using heat “borrowed” from beyond the flame zone without mixing the two streams [5,6]. The concept of heat recirculation is illustrated schematically in [Figure 15.1](#) for an adiabatic combustion system. A variety of such systems has been identified by Weinberg [5] and the comprehensive review has been updated [6]. Combustion systems of this kind which take advantage of heat recirculation are sometimes being referred as “excesses enthalpy,” “super-adiabatic flame temperature” or “filtration” combustion. Although the principle of heat recirculation is straightforward, the consequences of its application can be far reaching concerning the process efficiency, fuel conservation, combustion intensity, and pollutant emissions.

In the absence of conclusive observations, the consensus of opinion is that four types of combustion are possible in inert porous media: (1) free combustion takes place when a flame forms (say, above the porous burner surface) that consists of small multiple flames; (2) surface combustion occurs when the flame is “anchored” at the surface with some chemical reactions occurring within the pores, and the combustion occurs when the flow rate of the reactant mixture is set such that the gases reach their ignition temperature inside the medium and the mixture burns just under the surface; (3) buried

**FIGURE 15.1**

Enthalpy versus distance in heat-recirculating adiabatic burner.

**FIGURE 15.2**

Schematic illustration of surface (a) and embedded (b) porous burners.

(embedded) combustion occurs within the medium in a stable fashion when the mixture velocity is equal to the flame speed for the local temperature and heat loss conditions; and (4) unstable combustion (i.e., flashback) occurs when the flame speed exceeds the mixture velocity. The difference between a surface and embedded (buried) porous burners is highlighted schematically in Figure 15.2. As illustrated in Figure 15.2(a), the fuel-oxidant mixture passes through the PIM and then combusts partly near/or entirely in the downstream gas phase in the vicinity of the PIM. Actually, the buried flame

combustion shown in [Figure 15.2\(b\)](#) is also corrugated and is discontinuous like the surface flame in [Figure 15.2\(a\)](#).

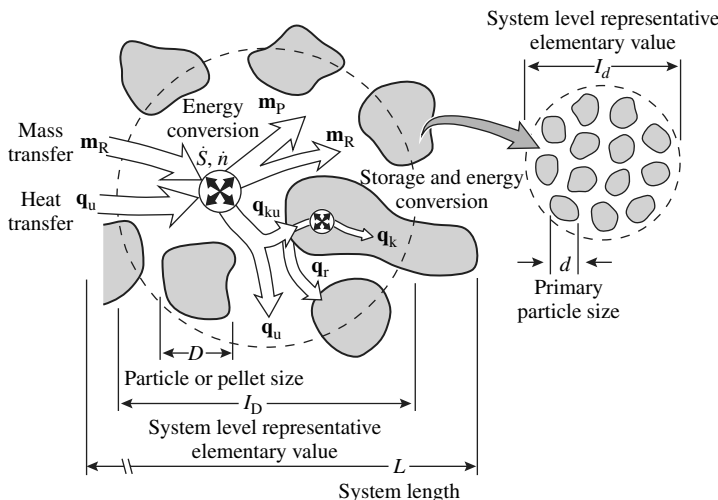
Porous burners operate on the combustion stabilization principle, which allows stable operation of the premixed combustion process in the porous matrix. The most important criterion which determines whether or not combustion can take place inside the porous structure is the critical pore size. If the size of the pores is smaller than this critical dimension, flame propagation inside the porous structure cannot be sustained; the flame is always quenched. The experiments of Babkin et al. [7] established the limiting condition in terms of the modified Pélet number, $Pe = S_L d_m \rho c_p / k > 65$, where S_L is the laminar flame speed, d_m is the equivalent pore diameter, and c_p , ρ , and k are the specific heat, density, and thermal conductivity of the gas mixture, respectively. If $Pe \leq 65$ flame quenching occurs since heat is transferred to the porous matrix at a higher rate than is generated due to the chemical reactions.

Premixed combustion with the flame stabilized in a PIM is a new and innovative technology that is promising for a variety of applications but which has not been discussed in textbooks [8] or reference books [9]. Recent accounts [1,4,10] provide excellent overviews of combustion in porous media, along with extensive citations to the current literature. It is difficult, in a limited space, to provide the reader with a fair and complete account of fundamentals and applications of combustion in porous media, particularly when the field is developing actively around the world. The best that can be hoped for is that this chapter will serve as a useful source of references and background information for both the students and practicing engineers working in the fields of combustion and thermal engineering. As already alluded to, the field of combustion in porous media is very broad and wide ranging; therefore, the discussion and scope in the chapter is exclusively focused only on stable combustion with the reaction zone embedded in the PIM.

15.2 Physical and Mathematical Description of Combustion in a PIM

15.2.1 Physical Description

A porous medium is formed by a solid phase and one or more fluid phases. The solid may have a regular (i.e., packed bed) or random (i.e., heterogeneous) structure, and each phase may be continuous or dispersed [11]. The characteristic sizes of the geometric heterogeneities may span a large range of length scales ([Figure 15.3](#)). A variety of different porous media are being used to support combustion of gaseous and liquid fuels and include the following: (1) bed of ceramic particles, (2) open-cell ceramic foams (reticulated ceramics), (3) metal and ceramic fiber mats, (4) bundles of small diameter tubes, (5) ported metals or ceramics (i.e., monolithic materials containing a large number

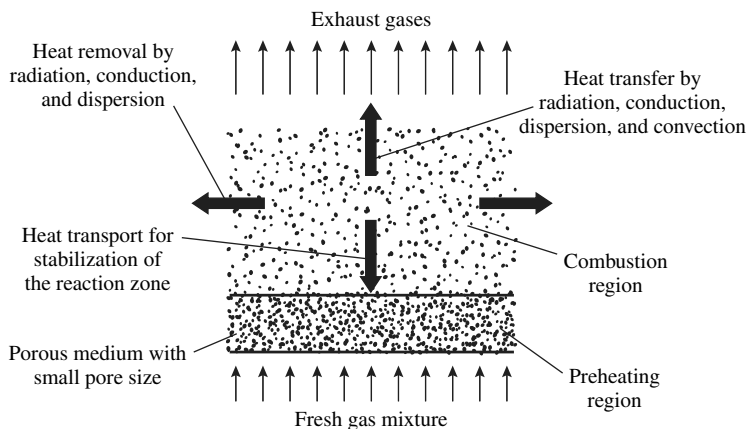
**FIGURE 15.3**

Schematic illustration of physicochemical processes in a porous buried flame burner depicting microscale processes in a PIM. (Reprinted from A.A. Oliveira and M. Kavany, *Prog. Energ. Combust. Sci.* 27:523–545, 2001. With permission from Elsevier.)

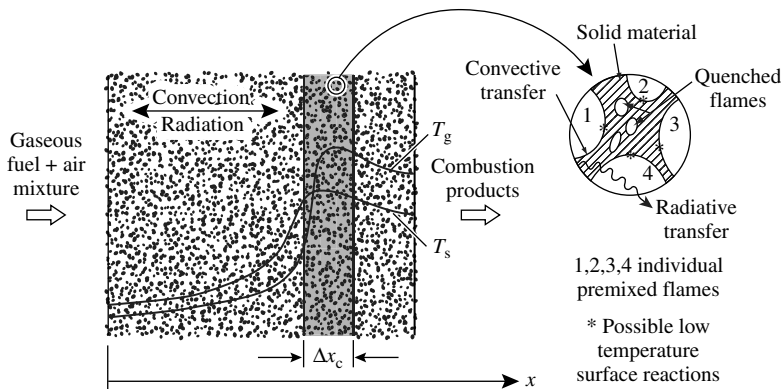
of small passages, (6) metal-alloy wire mesh, (7) C/SiC lamellas, and others [2,4]. The length scales can differ by orders of magnitude.

The heat and mass transfer processes taking place in the voids and at the interfaces are identified in Figure 15.3. The heat fluxes include heat conduction (q_k), interface surface convection (q_{ku}), radiation (q_r), and intraphase convection (q_u); the mass fluxes include reactants (m_R) and products (m_P). In addition to the heat and mass fluxes, the energy release (\dot{q}) and mass conversion (\dot{m}) describe the transport and chemical reactions during combustion in porous media. All porous materials have pore sizes, including small ones, in which the flames may quench. In this case, the unburnt fuel from such pores will be ignited downstream by products of combustion. Within the larger pores premixed gas phase flames are stabilized. The solid surface may also be at sufficiently high temperatures to support surface reactions. Furthermore, since the gas phase and solid surface reactions are at low temperature, formation of NO_x is suppressed. However, due to the low temperature reactions, some amount of nitrous oxide (N_2O) may be formed. In summary, the physicochemical processes occurring during combustion of a hydrocarbon fuel in a porous medium are more complex than those taking place in free flames [8].

Figure 15.4 provides a schematic representation of a premixed porous medium burner with a preheating region and a combustion region where the chemical reactions take place. Depending on the particular application, an additional region may be included in the design where the heat of combustion is transferred to some type of a load (i.e., heat sink). As a concrete example, consider a schematic of a one-dimensional (planar) porous medium

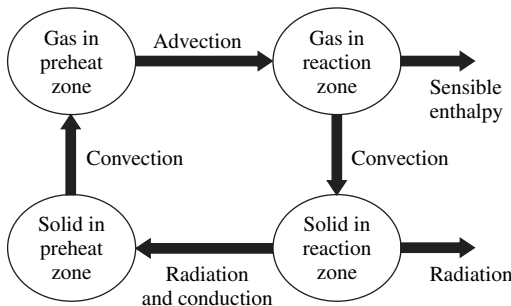
**FIGURE 15.4**

Schematic of a premixed porous inert medium based burner identifying transport processes in the combustion region. (Reprinted from D. Trimis, AIAA Paper 2000-2298. Roston, VA: AIAA, 2000. With permission from AIAA.)

**FIGURE 15.5**

Schematic representation of physical/chemical process in an embedded flame porous burner.

based buried flame burner shown in Figure 15.5. A homogeneous mixture of natural gas and air enters the inert porous medium at the left face ($x = 0$). In the preheat zone the solid matrix is at a higher temperature than the fuel-air mixture due to the conduction and radiation heat transfer within the solid. Heat is transferred to the gas mixture by convection. When the gas mixture is heated to a sufficiently high temperature the chemical reactions take place in the combustion region (Δx_c), and heat is liberated in the exothermic process. In a large part of the combustion zone and to the right of the zone the gas has a higher temperature than the solid matrix in which heat is transferred by convection. The combustion is controlled inside the porous medium by adjusting the mass flow rate of the fuel-air mixture and the flame speed so

**FIGURE 15.6**

Schematic illustration of physicochemical processes during combustion in a PIM.

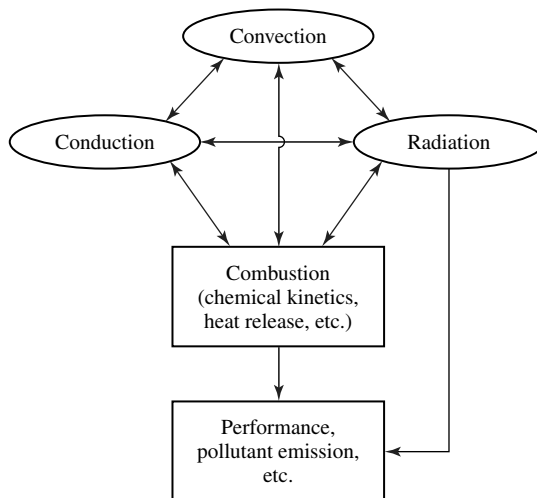
that flashback or blow off is prevented. Part of the heat of combustion is transferred from the gas phase to the porous medium by convection.

Combustion of hydrocarbon fuels in a PIM involves strong interaction of chemical reactions with heat transfer, and this is illustrated schematically in Figure 15.6. The porous medium that supports combustion of premixed reactants and in which combustion takes place can be considered as a heat exchanger. Such exchangers are designed to incorporate a high degree of heat recirculation (from burnt products to cold reactants) in the combustion process for the purpose of making the burners more efficient. Heat recirculation also extends the range of flame stability of lower heating value fuels and leaner mixtures. The principle of recirculating heat from hot combustion products to cold reactants by heat exchange without intermixing the reactants has been the subject of many studies, and excellent reviews of the scheme are available [5,6,12].

Irrespective of PIMs being used in a combustion device, the detailed design of the system and the operating conditions, premixed porous media based burners are characterized by strong interaction between heat transfer and combustion (Figure 15.7). Results of calculations show that advection, conduction and radiation as well as convective heat exchange between the gas and the solid matrix are of about the same order of magnitude in the combustion zone of the embedded flame porous burner, but these rates are somewhat smaller than the chemical heat release rate. This suggests that all modes of heat transfer need to be considered in any theoretical combustion–heat transfer model.

15.2.2 Mathematical Description

It is beyond the scope of this account to present a derivation and discussion of the conservation equations for a porous medium which are needed for the mathematical modeling of transport and combustion processes in a porous medium. The theoretical developments and derivation of the transport equations in porous media at the macroscopic level in the absence and in the

**FIGURE 15.7**

Schematic representation of combustion interaction of and heat transfer in an embedded flame burner.

presence of heat transfer are well in hand [11,13–17]. On the microscopic level the transport processes which occur in porous media are less understood, but they are clearly very important during combustion [10]. The macroscopic and microscopic level transport processes which occur during the combustion of liquid and gaseous hydrocarbon fuels in porous inert media must be coupled. This coupling is affected through closure relations, and, in the case of heat transfer, is accomplished by introducing a volume heat source/sink term in the conservation of energy equations to account for convective heat transfer between the two phases (i.e., gaseous fuel-air mixture and solid matrix).

In modeling combustion in porous media the gas and solid phases cannot be treated as a “mixture” and separate energy equations must be written for the gas and the solid phases, because the chemical reactions occur predominantly in the gas and the chemical energy liberated is transferred by convection to the solid matrix. This fact has been well recognized and accepted for modeling heat transfer in porous media [4,12]. The governing conservation equations for mass, momentum, and species transport in porous media are standard [11,16,18]. The volume averaged conservation of energy equations for the gas and the solid matrix are given, respectively, by

$$\begin{aligned} \phi \frac{\partial(\rho_g h_g)}{\partial t} + \nabla \cdot (\rho_g \mathbf{u} h_g) &= \nabla \cdot (k_{\text{eff},g} \nabla T_g) - \sum_{i=1}^N \rho_g Y_i c_{pi} \mathbf{V}_i \cdot \nabla T_g \\ &\quad - \sum_{i=1}^N h_i \dot{\omega}_i W_i - h_v (T_g - T_s) \end{aligned} \quad (15.1)$$

and

$$(1 - \phi)\rho_s c_s \frac{\partial T_s}{\partial t} = \nabla(k_{\text{eff},s} \nabla T_s) - \nabla \cdot \mathbf{F} - h_v(T_s - T_g) \quad (15.2)$$

The first term on the right-hand side of Eq. (15.1) accounts for heat conduction, the second for species interdiffusion, the third for chemical energy release during the N reactions, and the fourth for convective heat transfer between the gas and solid phases. In writing this equation it was assumed that the opacity of the gas is negligible in comparison to the solid, and, therefore, radiative transfer has been neglected. The first term on the right-hand side of Eq. (15.2) accounts for heat conduction, the second for radiative transfer, and the third for convective heat transfer. Note that inside the porous medium the porosity ϕ is less than unity and outside the medium ϕ is equal to one. Hence, the two-energy equation model can handle not only buried flame but also surface burners if a radiation flux divergence term is added to the conservation of energy Eq. (15.1).

15.3 Heat Transfer in Porous Media

Mathematical modeling (simulation) of combustion processes and prediction of system performance requires phenomenological and/or empirical description of conduction, convection, and radiation heat transfer on macroscale in all devices which employ PIMs to support combustion. Owing to the very complex geometrical and mechanical structure of PIMs it is very difficult to develop models based on first principles to predict the coefficients and/or closure relations needed in the volume-averaged conservation equations reviewed in the preceding section. The discussion in this section is limited to thermal characteristics (i.e., effective thermal conductivity, heat transfer coefficient and radiation absorption, and extinction coefficients) and is restricted to packed beds comprised of particles and open-cell materials which are typically employed as porous media in premixed combustion systems.

15.3.1 Effective Thermal Conductivity

15.3.1.1 Packed beds

Effective thermal conductivity of packed beds has received considerable research attention and reviews of earlier models are available [19–21]. More recent accounts [22,23] include assessment of radiation contributions at high temperatures. The effective thermal conductivity of a porous medium can be calculated under the assumptions that the medium is a continuum, and the temperature of the gas and the solid matrix are equal locally. The following

expression can be employed for the effective thermal conductivity [23]:

$$k_{\text{eff}} = k_{\text{con}} + k_{\text{dis}} + k_{\text{rad}} \quad (15.3)$$

where the effective thermal conductivity is the sum of the conductivities due to gas and solid matrix conduction (k_{con}), dispersion (k_{dis}) (if the fluid is not stagnant), and radiation (k_{rad}). The last contribution is included in the concept only if radiation is considered to be a diffusion process. If radiation transfer is treated as a "long range" process, radiative transfer theory can be used and the radiation characteristics of porous media will be needed. Recommendations for the choice of the appropriate effective thermal conductivity models in stagnant porous media [22,23], and the dispersion contributions in the axial and radial directions [23] are available.

15.3.1.2 Consolidated porous media

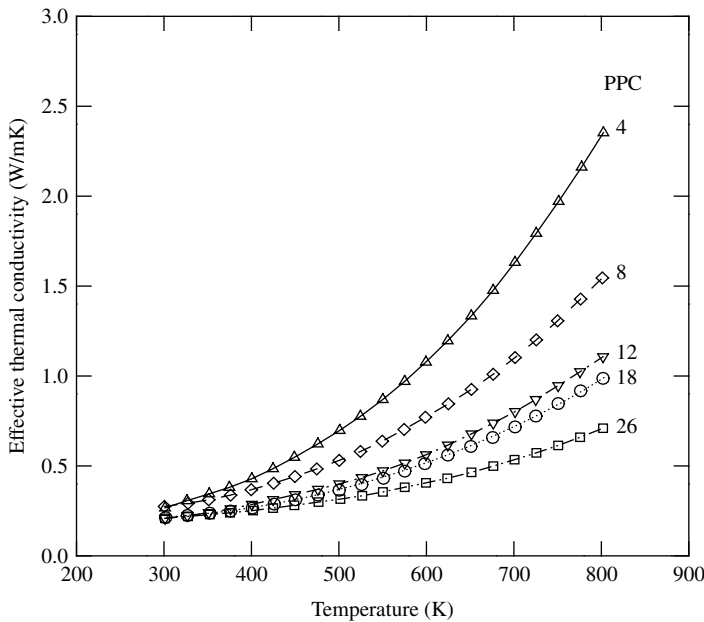
Understanding of heat conduction in consolidated porous media such as open-cell metal and ceramic foams, lamellae, etc. which are of interest in combustion systems is incomplete, and discussion of available models and experimental results is limited [1]. No general models or empirical correlations which are capable of predicting separate conduction, dispersion, and radiation contributions for consolidated materials of different mechanical structures as a function of temperature are available.

The effective thermal conductivity of partially stabilized zirconia (PSZ) open-cell foams at elevated temperatures (290 to 890 K) was measured by Hsu and Howell [24]. Measurements were made in a hot-plate apparatus for sample pore sizes of 4 to 26 PPC (pores per centimeter) (or 10 to 65 pores per inch). Negligible temperature dependence of the thermal conductivity of PSZ was observed, and a correlation of the data as a function of pore size is of the form

$$k_s = 0.188 - 0.0175\bar{d} \text{ (in W/m K)} \quad (15.4)$$

where \bar{d} is the actual mean pore diameter in millimeter. The correlation is limited to the temperature range noted and to pore diameters in the range of $0.3 < \bar{d} < 1.5$ mm. The variation of the experimentally determined effective thermal conductivity of PSZ as a function of the mean layer temperature is illustrated in [Figure 15.8](#). The results show the expected trends that as the temperature increases, the radiation contribution to the effective thermal conductivity, see Eq. (15.3), also increases.

Dul'nev's cubic cell thermal conductivity model [25] has been extended by Kamiuto [26] to account for the radiation contribution in open-cell porous media. The model was validated by comparing its predictions with the experimental data [24] for an open-cell partially stabilized Zirconia (ZrO_2) layer. Kamiuto has concluded that the Dul'nev's model can be used to accurately predict the conduction-radiation heat transfer characteristics of a porous cellular layer in the absence of gas flow.

**FIGURE 15.8**

Dependence of the effective thermal conductivity of open-cell partially stabilized zirconia on temperature. (Reprinted from P.-F. Hsu and J.R. Howell, *Exp. Heat Transfer* 5:293–313, 1992. With permission from Taylor & Francis.)

15.3.2 Convective Heat Transfer Coefficient

15.3.2.1 Packed beds

Convective heat (mass) transfer in unconsolidated porous media (i.e., packed beds comprised of spherical, granular, etc. particles) has received considerable experimental research attention and organization. The early work has been summarized by Wakao and Kaguei [19]. Most of the heat (mass) transfer studies have used relatively large (deep) bed packings. The heat (mass) transfer correlations in porous media are based on empirical data mainly for $Re > 10$. For example, Wakao and Kaguei [19] found that the dimensionless correlation for heat (mass) transfer coefficients for an isolated sphere can be represented by

$$Nu(Sh) = 2.0 + 1.1Re^{0.6}Pr^{1/3}(Sc^{13}) \quad (15.5)$$

Achenbach [27] extended the lower and higher Reynolds number ranges and deduced the following empirical correlation for the Nusselt number,

$$Nu = \left\{ (1.18Re^{0.58})^4 + \left[(0.23(Re/\phi)^{0.75}) \right]^4 \right\}^{1/4} \quad (15.6)$$

This correlation is appropriate for air ($Pr = 0.71$), $\phi = 0.387$ and $1 < Re/\phi < 7.7 \times 10^5$. It should be noted that most experiments have been carried out in deep beds. Hence, the bed thickness does not appear as a correlating parameter in the equation. Also, the particle diameter has been used as the characteristic length in both the Reynolds and Nusselt (Sherwood) numbers.

Various heat (mass) transfer studies have established that even for packed beds comprised of spherical particles the theoretically derived limiting value of 2 for $Nu(Sh)$ is not valid as the Reynolds number decreases. The regression formula, Eq. (15.6), is consistent with experimental data only in the turbulent flow regime ($Re > 100$). For $Re < 200$, Eq. (15.6), predicts lower Nusselt numbers than Eq. (15.5). There is some controversy among the various investigators concerning the discrepancy between different correlations at low Reynolds numbers, and alternate models have been proposed to explain the discrepancy. A comparison of accepted heat transfer correlations has been made [28] and it has been found that there is a large discrepancy between the published results, particularly for $Re < 10$.

15.3.2.2 Consolidated porous media

Understanding of convective heat transfer in consolidated porous media is much more limited. The earlier experimental and theoretical studies on dense, intermediate, and low density materials have been reviewed [28]. Here, only the low density ($\phi > 0.6$) PIMs are discussed since they are employed in combustion systems [1]. Because the structures are too complex for theoretical analysis, the practical needs are met by experimentation. The results are typically presented in terms of a volumetric heat transfer coefficient, $h_v (= a_v h)$, where h is the conventional convective heat transfer coefficient and a_v is the surface area per unit volume of the porous matrix.

There is no unique way to define a characteristic length needed for the Reynolds and Nusselt numbers. The mean pore diameter, hydraulic diameter, strut diameter, and other lengths have been used to correlate the experimental data [29]. Volumetric heat transfer coefficients were determined for several different reticulated ceramics having a range of PPC and the data were correlated in terms of the mean pore diameter d_m ,

$$d_m = \sqrt{\phi/\pi}/\text{PPC} \quad (15.7)$$

as the characteristic length. The volumetric heat transfer coefficient data are expressed in an empirical equation,

$$Nu_v = \frac{h_v d_m^2}{k} = [0.0426 + 1.236/(L/d_m)]Re_{d_m} \quad (15.8)$$

where L is the thickness of the porous layer. The correlation is based on data for air ($Pr = 0.71$) and covers a Reynolds number range of $2 \leq Re_{d_m} < 836$. In an earlier study [30] it was found that the Reynolds number exponent instead

of being unity as given in Eq. (15.8) depended on the specimen thickness L to the mean pore diameter d_m ratio L/d_m .

More recent studies [31,32] have provided additional experimental volumetric heat transfer coefficient data. Ichimiya [31] utilized a steady-state experimental method and correlated the results in terms of a mean pore diameter as a characteristic length, whereas Kamiuto et al. [32] employed a transient method and correlated the data in terms of a strut diameter. As a consequence, the empirical correlations obtained are different, but so far the available experimental results have not been generalized.

15.3.3 Radiation Characteristics

There are essentially two distinct approaches for treating radiative transfer in porous media [33,34]: (1) discrete or discontinuous models and (2) continuous or pseudocontinuous models. In the discontinuous approach the medium is considered to be an array of unit cells of given idealized geometry. Radiative transfer in each cell is computed by macroscopic methods such as ray tracing, Monte Carlo, radiosity, or hybrid. Discrete formulations are appropriate for porous media that have large characteristics lengths (i.e., particle or void diameter, etc.) such as packed beds, foams, and cellular materials. The continuous approach is based on the principle of radiant energy conservation on an elementary control volume which is much larger than the wavelength of radiation. In general, the assumptions of continuity, homogeneity, and randomness are implied in the formulation, although they are not mandatory. Homogeneity is essential for the medium to be treated as a continuum. A porous medium may be considered homogeneous if the "particle" dimensions are much smaller than some characteristic length of the system. The pseudocontinuous model is a combination of the discrete and continuous formulations. The absorption and scattering characteristics of the medium are modeled as a random distribution of "particles" which are calculated based on the discrete formulation. These radiation characteristics are then used in the radiative transfer equations based on continuous formulation.

Since only the continuum formulation of radiative transfer in terms of the integro-differential radiative transfer equation (RTE) is compatible with the continuum formulation for chemically reacting flows, only this model is discussed. Assuming that the opacity of the gas (void) phase is negligible in comparison to that of the solid phase and averaging the RTE over a small control volume which contains both phases results the local volume-averaged RTE for the radiatively participating medium [34]. The spectral and total (on the gray basis) absorption, scattering the extinction coefficients for porous media needed as inputs in the volume-averaged RTE have been thoroughly reviewed and extensive, up-to-date discussions are available [33–38].

The issue of independent and dependent scattering needs to be considered for porous media in closed packed arrangements [39]. Independent scattering implies that particles, say, in a packed bed, are assumed to interact

with radiation incident upon them as if uninfluenced by the presence of neighboring particles. Dependent scattering suggests that far-field effects resulting from interference between the waves scattered by the particles with phase differences and near-field effects resulting from multiple scattering in an elementary volume, in which absorption and scattering characteristics of a particle are affected by the proximity of the particle, need to be considered. Tien and Drolen [39] have analyzed the experimental data and delineated the independent and dependent scattering regimes in a plot relating the particle size parameter versus the particle void fraction. They used the interparticle particle clearance c to wavelength λ ratio c/λ to delineate the independent and dependent scattering for different porous media. Other investigators have established different criteria for independent and dependent scattering in packed and fluidized beds, fibrous media, fibrous composites, foams, and reticulated ceramics. Reference is made to comprehensive discussions of the theoretical and experimental approaches and results for radiation characteristics of porous media [37,38].

15.3.3.1 Radiation characteristics of packed beds

Kamiuto [40] proposed a heuristic correlated scattering theory which attempts to calculate the dependent radiation characteristics of a packed bed consisting of large particles from the independent characteristics. The extinction coefficient β and single scattering albedo ω are scaled as

$$\beta = \gamma \beta_{\text{ind}} = 2\gamma_2 \left(\frac{\pi}{4} d_p^2 n_p \right) \quad (15.9)$$

and

$$\omega = 1 - (1 - \omega_{\text{ind}})/\gamma_2 \quad (15.10)$$

where

$$\gamma_2 = 1 + 1.5(1 - \phi) - 0.75(1 - \phi)^2 \quad \text{for } \phi < 0.921 \quad (15.11)$$

In these equations d_p denotes the mean particle diameter, n_p is the particle number density, and γ_2 is the extinction enhancement factor. The subscript "ind" refers to independent scattering. According to Eq. (15.9) the extinction coefficient of a randomly packed bed of spheres ($\phi = 0.39$) is greater than that predicted by the Mie theory by a factor of 3.27. The single scattering albedo and the scattering phase function could not be derived theoretically; therefore, a heuristic model is required. The validity of this theory for predicting the extinction coefficients has been examined experimentally [40]. Reasonably good agreement between model predictions and data has been obtained for opaque spheres, but the model is not satisfactory for predicting the radiation characteristics of packed beds of transparent or semitransparent spheres.

The validity of various analytical models for predicting global quantities (i.e., transmittance) have been assessed [23,34,35,41]. For example, Singh and Kaviany [41] have calculated the transmittance through a bed of specularly reflecting opaque spherical particles as well as of transparent and semitransparent particles. They compared their results based on the Monte Carlo and on the dependence-included discrete ordinates methods with the results of Kamiuto [42] and found that his correlated theory for opaque particles overpredicts the transmittance and for transparent particles underpredicts the transmittance. However, the advantage of the simple correlated theory results over Monte Carlo or dependence-included discrete ordinate results for analysis and design calculations is undeniable. Also, contrary to the findings of Kamiuto and Yee [23] for radiative transfer based on their dependent scattering theory, the predicted transmittance of a packed bed of glass spheres based on the independent theory was found to be in good agreement with experimental data [43].

15.3.3.2 Radiation characteristics of open-celled materials

The radiation characteristics of open, reticulated ceramics have been determined on total and spectral basis, and reviews of published data are available [1,37,38]. For example, Mital et al. [44] measured total radiation emerging from isothermal reticulated ceramics specimen and with an aid of a two-flux approximation determined (recovered) the total extinction coefficient and single scattering albedo of several materials (YZA, mullite, silicon carbide, and cordierite).

Detailed experimental spectral extinction and scattering coefficients as well as spectral phase function measurements of open-cell ceramics have been reported [45] for 4, 8, and 26 PPC (nominal) materials. This is probably the most detailed study, of such materials, that has been published. The spectral transmittance and reflectance data were used in an inverse procedure to determine the spectral radiation characteristics of interest. The spectral scattering phase distribution function has also been determined.

The radiation characteristics of foams can be estimated from the geometric optics limit [39]. If the porous material can be represented as a monodisperse assembly of independently scattering voids ("particles") for large values of the size parameter, the absorption and scattering coefficients are given by the following relations

$$\kappa = \varepsilon(3/2d)(1 - \phi) \quad (15.12)$$

and

$$\sigma = (2 - \varepsilon)(3/2d)(1 - \phi) \quad (15.13)$$

where d is the mean void (pore) diameter, ε is the emissivity, and ϕ is the porosity. Therefore, the extinction coefficient can be expressed as

$$\beta = \kappa + \sigma = (3/d)(1 - \phi) \quad (15.14)$$

Comparison of experimental data with predictions based on the geometrical optics theory, Eq. (15.14), reveals that the theory underpredicts the extinction coefficients [45]. Instead of the coefficient being equal to 3, the range from 4.4 to 4.8 yields a better correspondence between the data and the model. Best-fit empirical correlation for the extinction coefficient of PSZ has been determined [24] to be

$$\beta = 1340 - 1540d + 527d^2 \quad (15.15)$$

where β is in m^{-1} and d is in mm. The above correlation is valid for the following conditions: $0.3 < d < 1.5$ mm, $0.85 < \phi < 0.87$, $290 < T < 890$ K, and $3 < \lambda < 5 \mu\text{m}$. A comparison of Eq. (15.15) with experimental extinction coefficient data for other open-cell materials is available [1]. More comprehensive discussions of the radiation characteristics of open-cell materials can be found in recent reviews [37,38].

Owing to the complex and irregular geometry of the open-cell porous media the absorption and extinction coefficients cannot be quantified theoretically using simple physical descriptions. The Monte Carlo method, weighted with some probabilistic distribution of the pore geometry to characterize the porous system, may present an option for calculating the coefficients.

15.4 Overview of Porous Medium Based Combustors

Porous media based combustors have been designed to burn both gaseous and liquid fuels. However, the past research and development has been primarily directed to premixed combustors burning gaseous fuels, and the early work is discussed in the literature [1–4,12]. But, in the more recent past there have been a number of studies reporting on combustion of liquid fuels in PIMs [46–50], and references cited therein just to provide a few examples. In spite of this interest, this account focuses exclusively on premixed porous medium combustors, burning gaseous fuels because of the imposed space limitations for this chapter of the handbook. The interested reader can refer to Howell et al. [1] for the discussion of the early work and to the references cited for recent developments.

A gaseous premixed porous medium combustor (PPMC) (burner) in which the flame is stabilized in the PIM is a promising technology for

a variety of applications owing to low pollutant emissions and ability to burn low heating value fuels [1–4,12,51]. Essentially, there are three types of devices which take advantage of PIMs to support combustion of the fuel: (1) combustors (burners), (2) burners–radiant heaters, and (3) combustors–heaters. A combustor is a device which converts the chemical energy of the fuel to the thermal energy of the product stream with minimum of unavoidable heat losses. Examples of such combustion systems include burners for destroying hazardous volatile organic compounds (VOCs), for incinerating chlorohydrocarbons, and for converting chemical energy of the fuel to thermal energy with minimum heat losses from the device. The function of the porous burner–radiant heater is to convert the chemical energy of fuel stream into the product stream enthalpy and eventually into thermal radiation directed to the target (load). Such burners–infrared radiant heaters are widely used for materials processing and manufacturing operations, human comfort and numerous other applications [1,2,51]. The function of the combustor–heater (with an integrated heat exchanger) is to convert the chemical energy of the fuel to the thermal energy of a working fluid being circulated through the exchanger. Examples of such devices include fluid heaters, steam generators, gasifiers, household appliances, etc. [2,3].

There is a great variety of PPMC devices used for various functions which employ different porous materials to support stable combustion of gaseous fuels under a wide range of operating conditions. The scope and space limitations of this chapter do not allow one to be comprehensive. Before discussing some specific devices based on combustion in porous media it is desirable to compare the operating characteristics/features of these type of systems against conventional combustion processes with free flames. Some, but not all, of the advantages of PIM stabilized combustion systems are the following [1–3]:

1. Intense heat transfer inside the porous structure allows for high power density operation, with the combustion zone being about a factor of ten smaller in volume than the corresponding conventional burners for comparable thermal loads.
2. Wide variation in turndown ratio of 1:20 compared to conventional premixed burners which have a turndown ratio of 1:3.
3. Stable combustion for equivalence ratios of 0.9 to 0.53 for methane–air mixtures.
4. Low pollutant emissions (<7 mg/kWh of CO and <25 mg/kWh of NO_x) over the complete thermal input range, due to reduction of the gas temperature in the reaction zone.
5. High combustion stability owing to the large heat capacity of the PIM.
6. Great flexibility in the choice of the burner geometry (i.e., cross-section) which allows for easy adaption of heat transfer device to demands of the application.

In summary, the main advantages of premixed combustion of gaseous fuels in porous inert media are the following:

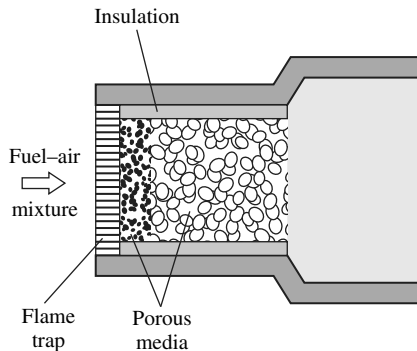
1. The large specific surface area per unit volume of the PIM enlarges the reaction zone and results in high heat transfer rates between the gas and solid phases.
2. The excellent heat transfer characteristics of the PIM result in higher combustion velocities and cool the reaction zone.
3. The high heat capacity of the PIM enhances combustion stability against changes in the excess-air ratio and in thermal load.

In what is to follow, three combustion systems, starting with the simplest and ending with the most complicated one, are discussed. The experimental and mathematical modeling details cannot be included because of space constraints, and the interested reader can refer to the original literature for the developments.

15.5 Premixed Porous Medium Combustors

A PPMC or burner is a device designed to convert chemical energy of the gaseous fuel into enthalpy of the product stream, to destroy hazardous VOCs, to incinerate (pyrolysis or oxidation) chlorohydrocarbons, and others. A PPMC in which a premixed flame is stabilized within the solid matrix is a promising technology. The main characteristics of this technology are the high burning rates, increased flame stability at low combustion temperatures which lead to low emission of key pollutants. Motivated by these advantages and a wide range of applications, porous medium burners have received, during the last two decades, increased interest and research and development attention, and comprehensive accounts are available [1,4,12].

A PPMC usually consists of two or more porous materials having desirable physical (geometrical), flow and heat transfer characteristics. A PIM-based burner can be oriented vertically (with upward or downward flow) or horizontally. A schematic diagram of a typical burner is illustrated in [Figure 15.9](#). Different porous media (i.e., ceramic spherical particles and saddles, ceramic foams, metal wire meshes, metallic foils, etc.) are used as porous media in the different sections of the unit which serve different functions. The fuel–oxidizer mixture flows through a flame trap, followed by a preheating region which consists of small size porous material (particles or ceramic foam) with $Pe < 65$. Chemical reactions take place in the combustion region which consists of larger pore size porous material with $Pe > 65$. High-temperature insulation is placed between the porous material and the combustor housing. Water or air cooling can be provided at selected location for flame stabilization. In order to stabilize the flame in the PIM and achieve the necessary preheating of the

**FIGURE 15.9**

Schematic of a premixed porous medium combustor (PPMC).

fuel-air mixture the porous media need to be properly selected for their flow and heat transfer characteristics.

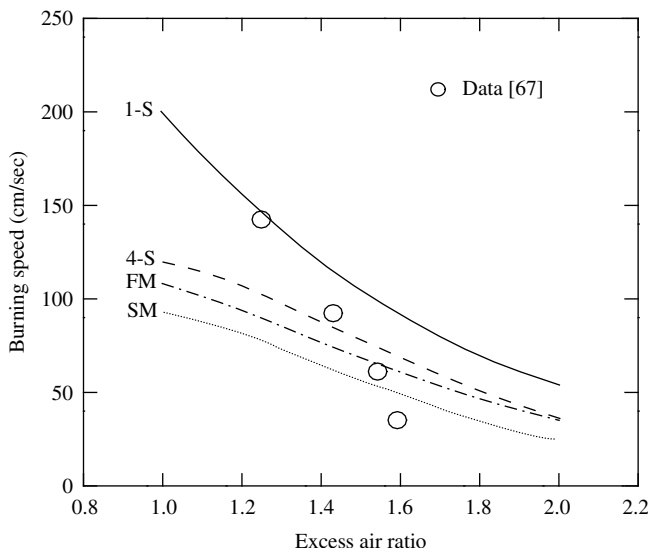
Essentially, there are three types of approaches for simulating combustion and heat transfer in matrix stabilized combustion systems: (1) pseudohomogeneous thermal equilibrium model [52,53], (2) volume-averaged models [54–56], and (3) direct simulation [57]. In the pseudohomogeneous thermal equilibrium approach the fluid and solid phases present locally are treated as an artificial unique phase which is described by a single thermal energy equation. Heat transfer between the gas and the solid phases is very effective, and the two phases are essentially in thermal equilibrium. In the volume-averaged approach the fluid and the solid phases are considered, and separate thermal energy equations are written for each phase, and the two phases are coupled through the volumetric convective heat transfer rate term. A direct simulation of premixed combustion allows for the study of the effect of the pore-level fluid flow as well as heat and mass transfer processes on the flame structure and speed. The approach is not necessarily more accurate, because it is difficult to transfer a three-dimensional unordered structure into a two-dimensional regular one. Although such direct simulations provide useful hints about the thermal structure, flame speed, and interfacial heat transfer, they are incapable of predicting the effects of the transport processes in the flame.

Chemical reactions in the PPMCs have been modeled mathematically. The flow field is considered to be non-Darcian with inertia, boundary, and buoyancy effects modeled by the Forchheimer and Brinkman extensions of the Darcy's equation [11,16,17]. Since the gas is not in thermal equilibrium with the solid matrix (i.e., the local volumetric convective heat transfer rate is not infinite but finite), a two-energy equation model for the porous medium must be used in the combustion zone [18], see Eqs. (15.1) and (15.2). The model equations are not presented here but can be found in the literature [52–54]. Suffice it to note that submodels are needed for flow in the porous media (i.e.,

permeability K and inertial coefficient F), formation and destruction of species due to chemical reactions as a source/sink term $\dot{\omega}_k$ in the species transport equation, the volumetric heat transfer h_v which couples the gas and the solid phase thermal energy equations, and extinction coefficient as well as scattering albedo of the PIM for the radiative transfer equation [1,33,34]. These submodels are specific to the combustion system, PIM used, and problem considered and cannot be described generically. For example, one-step [56] and detailed (consisting of 20 species and 164 reactions) [58] chemical reaction mechanisms have been considered in modeling combustor-heaters. Radiative transfer in two- or three-dimensional porous combustors is treated approximately using the Rosseland diffusion approximation [54] or solving the radiative transfer equation on the gray basis [59]. Detailed mathematical description of the PPMC is not given here because of space limitations, but it is available in the original literature [53,54,58,59]. A one-dimensional porous burner-radiant heater is described in detail in the section to follow.

Both experimental [60,61] and computational [53,62] studies have been undertaken to adapt different porous media and burner geometries to new applications. Most of the earlier studies were one-dimensional and used simple one-step chemical kinetics models [12,63]. Hsu and Matthews [64] found that one-step kinetics models lead to overprediction of peak flame temperatures. Consequently, more detailed models have been used to calculate the chemical reactions and temperature distributions in PPMS [65,66]. For example, Zhu and Pereira [66] used 27 species and 73 reactions in order to study formation and destruction of pollutants (CO, NO) in a porous matrix stabilized burner. More recently, two-dimensional models with single-step and multiple-step chemical kinetics have been used to model combustion in porous media, and detailed accounts citing numerous relevant references are available [53].

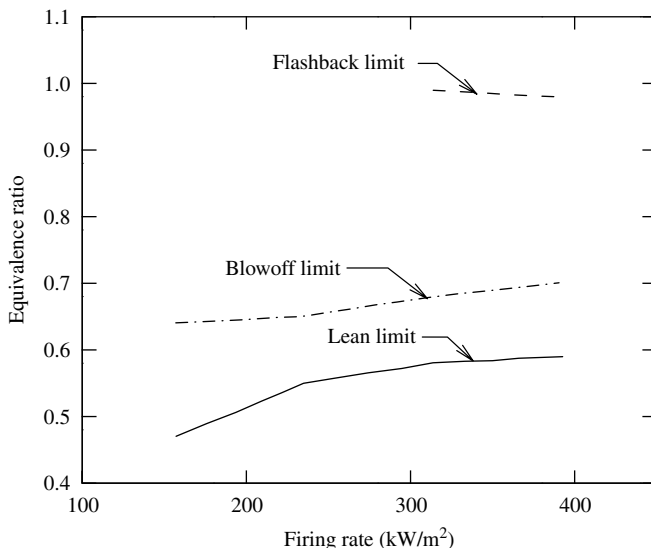
One-dimensional methane-air combustion in a two-layer PIM burner has been modeled [66] and compared with experimental data of Hsu and Matthews [64]. Four combustion models: full mechanism (FM, 49 species and 227 elemental reactions), skeletal mechanism (SM, 26 species and 77 elemental reactions), four-step reduced mechanism (4RM, 9 species), and one-step global mechanism (1GM) have been employed. A comparison between predictions and available experimental data for the burning speed are shown in [Figure 15.10](#). The results of Hsu and Matthews [64] calculated with a multiple kinetics mechanism for the same conditions fall between those of the FM and the SM but are not included in the figure for the sake of clarity. It is evident that none of these four models and the published calculations [64] predicts satisfactorily the burning speed. This discrepancy may be due to limited understanding of the transport processes in open-cell porous media and the uncertainties in some of the model parameters (i.e., effective thermal conductivity of the solid matrix, volumetric convective heat transfer coefficient which couples the gas and the solid phases, and the extinction coefficient as well as the single scattering albedo of the solid). A more comprehensive discussion of earlier studies on flame speed in PPMS is available [1].

**FIGURE 15.10**

Comparison of burning speeds predicted using different models with experimental data of Chaffin et al. [67] for methane–air combustion in a bilayer open-cell porous medium. (Reprinted from X.Y. Zhou and J.C.F. Pereira, *Fire Mat.* 22:187–197, 1998. With permission from Wiley Interscience.)

The stability ranges of different burners have been determined and discussed [1,44]. Figure 15.11 is an example of a stability range plot for a representative burner studied by Mital et al. [68]. As shown in the figure, the stability limit was generally between an equivalence ratio of 0.6 and 0.7. Lift off occurred first from the edges of the burner because of the higher heat losses in this region, which reduce the flame speed compared to the central region of the burner. With further decrease in the equivalence ratio the entire flame lifted off and resulted in complete extinction. The lean limit was between an equivalence ratio of about 0.5 to 0.6, depending on the firing rate. There was no flashback below a firing rate of 300 kW/m^2 for any porous burner studied [68]; however, above this firing rate, the burners showed flashback (Figure 15.11) at equivalence ratios close to stoichiometric.

Experiments have shown that pollutant emissions can be reduced in PIM-based burners with air staging [61,69]. The methane–air mixtures of different equivalence ratios were burned in two separate porous ceramic (PSZ) sections. A comparison of the two stage results with those obtained by burning the entire mixture in a single state showed that the emissions of NO and CO from the two stage burner were lower than those from the single stage burner [69]. Multiple staged combustion experiments of methane–air mixtures in alumina oxide and silicon carbide foams as porous media have been carried out for different equivalence and turndown ratios. The experimental results show that staging further homogenizes the temperature distribution in the burner

**FIGURE 15.11**

Stability range of a bilayer porous medium burner-radiant heater. (Reprinted from R. Mital et al., *Combust. Flame* 111:175–184, 1997. With permission from the Combustion Institute.)

and reduces NO_x emission by 30 to 40% compared to the cleanest unstaged porous medium burners [61].

A discussion of velocity measurements in packed beds and open-celled (reticulated) ceramics typical of ceramic burners is available [1]. The published data suggest that the flow passes from being essentially laminar at low flow rates to a fully developed turbulence at high flow rates. The transition from laminar to turbulent flow occurs at Reynolds number of approximately 150. However, it has not yet been conclusively established that what has been attributed as turbulence in small pores is not dispersion coupled to flow expansion in small size pores. There continues [70–72] to be a debate about the existence of turbulence in porous media even in the absence of combustion as the media are not accessible to any type of probes for experimentation.

15.6 Porous Medium Combustor–Radiant Heater

The function of a porous burner–radiant heater is to convert the chemical energy of the fuel stream into product stream enthalpy and eventually into directed radiation. In this type of a device combustion takes place in a flame anchored at the surface (Figure 15.2[a]) or embedded in the porous medium (Figure 15.2[b]) as shown schematically in Figure 15.2. In the embedded (buried) mode of operation higher combustion radiation

intensities can be achieved than with the surface-combustion mode. In addition, higher conversion of thermal energy to radiant energy is possible due to a combination of much higher opacities of the porous medium but somewhat lower temperatures. Embedded flame porous burners-radiant heaters have received considerable research and development attention and recent accounts are available [1,51,73].

Porous burners-radiant heaters usually consist of one, two, or more layers of PIMs having appropriate physical flow and heat transfer characteristics. A schematic diagram and coordinate system of a bilayer unit is shown in Figure 15.12. We consider premixed combustion stabilized inside a PIM with each layer being homogeneous and noncatalytic. The gas is not in thermal equilibrium with the solid, and thermal energy equations are written separately for each phase. The main assumptions used in the one-dimensional mathematical description of combustion and heat transfer are as follows: (1) the Dufour, Soret, and viscous heat dissipation effects, "bulk" viscosity and body forces are negligible; (2) the porous medium emits, absorbs, and scatters thermal radiation as a gray homogeneous medium, but gaseous radiation is considered to be negligible in comparison with the solid radiation; (3) potential catalytic effects of the high temperature solid are neglected as fundamental understanding and needed data are not available; (4) the flame is one-dimensional and neither stretch nor turbulence are induced by the flow through the PIM, but thermal dispersion effects are accounted for; and (5) a

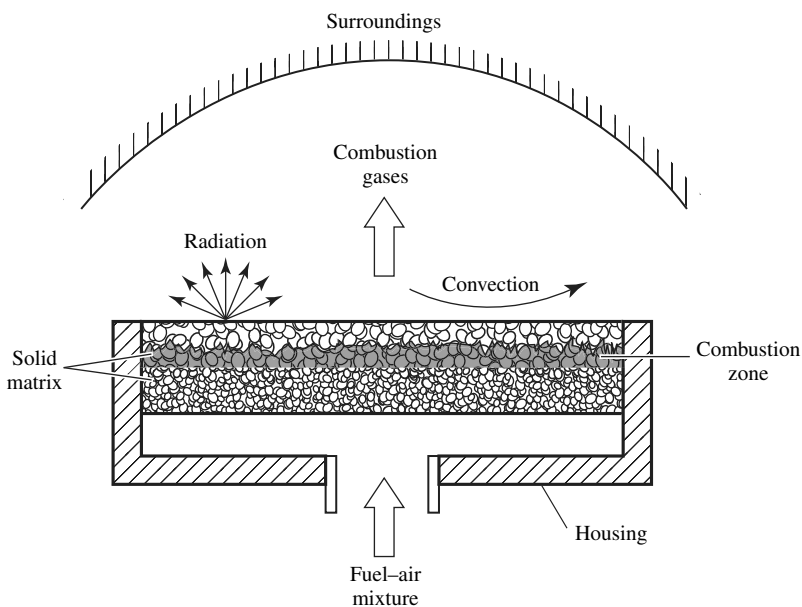


FIGURE 15.12

Schematic and coordinate system of a porous burner-radiant heater with the flame embedded in the burner.

model based on two-energy equations for the two phases is used to couple the gas phase to the solid matrix through a volumetric heat transfer coefficient.

With the assumptions listed the conservation equations for the reacting gas mixture and the porous matrix are as follows:

Governing equations for gas mixture

Conservation of mass (continuity) equation:

$$\frac{\partial(\phi\rho_g)}{\partial t} + \frac{\partial(\phi\rho_g u)}{\partial x} = 0 \quad (15.16)$$

Conservation of momentum equation:

$$\rho_g \left(\phi \frac{\partial u}{\partial t} + \phi u \frac{\partial u}{\partial x} \right) = -\frac{\partial p}{\partial x} + \frac{\partial}{\partial x} \left(\mu_e \frac{\partial u}{\partial x} \right) - \left(\frac{\mu_e}{K} + \frac{F\phi}{\sqrt{K}} |u| \right) u \quad (15.17)$$

Conservation of species equation:

$$\rho_g \left(\phi \frac{\partial Y_k}{\partial t} + \phi u \frac{\partial Y_k}{\partial x} \right) = \frac{\partial}{\partial x} \left(\rho_g D_{km} \frac{\partial Y_k}{\partial x} \right) + \dot{\omega}_k W_k, \quad k = 1, 2, \dots, K \quad (15.18)$$

Conservation of energy equation:

$$\begin{aligned} & \rho_g \left(\frac{\partial(\phi h_g)}{\partial t} + \frac{\partial(\phi u h_g)}{\partial x} \right) \\ &= \left[\frac{\partial}{\partial x} \left(k_g \frac{\partial T_g}{\partial x} \right) - \sum_{k=1}^K \phi h_k \dot{\omega}_k W_k - \sum_{k=1}^K \phi \rho_g Y_k V_k c_{pk} \frac{\partial T}{\partial x} \right] + h_v(T_s - T_g) \end{aligned} \quad (15.19)$$

Equation of state:

$$\rho_g = p \bar{W} / \mathcal{R} T_g \quad (15.20)$$

Solid matrix

Conservation of thermal energy:

$$(1 - \phi) \rho_s c_s \frac{\partial T_s}{\partial t} = \frac{\partial}{\partial x} \left(k_{eff,s} \frac{\partial T_s}{\partial x} \right) - \frac{\partial \mathcal{F}}{\partial x} - h_v(T_s - T_g) \quad (15.21)$$

Note that inside the porous medium the porosity ϕ is less than unity and outside the medium ϕ is equal to one. Hence, the model Eqs. (15.16) to (15.19) and (15.21) can handle not only submerged flame but also surface burners if the radiation flux divergence term ($\partial \mathcal{F} / \partial x$) is added to the conservation of energy equation, Eq. (15.17), in the gas phase and the burner is extended to

account for the flame/products region ahead of the solid matrix where the flame is anchored.

Appropriate initial conditions can be specified for both the gas mixture and the solid matrix if one desires to predict the transient response of the burner. At the faces of the PIM continuity of fluxes is enforced for the species mass fractions and the energy. At the inlet ($x = 0$) to the burner,

$$u = u_{g,o}, \quad T_g = T_{g,o}, \quad Y_k = Y_{k,o}, \quad k = 1, 2, \dots, K \quad (15.22)$$

An energy balance on solid matrix which accounts for convection and radiation yields

$$-(1 - \phi)k_s \frac{\partial T_s}{\partial x} = (1 - \phi)h_o(T_s - T_g) - (1 - \phi)\varepsilon\sigma(T_s^4 - T_{sur,i}^4) \quad (15.23)$$

At the outlet face of the burner ($x = L$),

$$\frac{\partial u}{\partial x} = \frac{\partial Y_k}{\partial x} = 0, \quad k = 1, 2, \dots, K \quad (15.24)$$

and the energy balance at the out face of the burner is

$$(1 - \phi)k_s \frac{\partial T_s}{\partial x} = (1 - \phi)h_e(T_s - T_g) + (1 - \phi)\varepsilon\sigma(T_s^4 - T_{sur,e}^4) \quad (15.25)$$

Note that in writing Eq. (15.25) absorption of radiation emerging from the solid matrix emitted by the gases as well as emission and self-absorption of radiation by the combustion products upstream of the outlet has been neglected. Of course, this neglect would lead to underprediction of the solid matrix temperature. The disregard is justified on the basis that the matrix is effectively opaque, and radiation emerging from it is much more intense than that radiated by the optically thin gases (CO_2 and H_2O) at a lower temperature than the matrix. Therefore, because of the uncertainties in the model input parameters, the small opacity of the combustion products and the additional complications of the analysis, the heating of the solid matrix has been neglected. Any heating of the right face of the solid matrix (at $x = L$) by the exhaust gases can be simulated by arbitrarily increasing the effective surroundings temperature $T_{sur,e}$.

Submodels describing the flow in porous media, chemical reactions, conduction, and convection heat transfer as well as radiative transfer are needed to complete the model description. These models are specific to the burner design, PIMs used, and operating conditions. Suffice it to mention that one-step [74–76] and detailed multiple chemical kinetics [64–66,73,77] models for methane oxidation have been used. Probably the most comprehensive simulations of premixed combustion in submerged porous burners–radiant heaters has been reported by Diamantis et al. [73] and Leonardi et al. [77]. They used GRI 2.11 mechanism (49 species and 249 reactions) to model the chemical

kinetics of methane–air combustion in ceramic foam [73] and in metal fiber mat [77] burners–radiant heaters. In all other major respects their models were similar except that the different materials used for the burner pads had different mechanical–structural and thermophysical characteristics as well as radiative transfer models. The former authors used thicker (~30 mm) and the latter much thinner (=2 mm) thick porous media layers for supporting submerged combustion. Radiative transfer has been modeled using discrete ordinates method [77] and integral formulation [73]. Both absorption and scattering of radiation by the solid matrix have been accounted for. The presence of fuel–combustion products on radiative transfer in the PIM has been neglected in comparison to that of the solid matrix as the pores are of small size, and the opacity of the gases is negligible to that of the matrix.

Figure 15.13 illustrates the gas temperature measured in the flame (within the flame support layer) as a function of position with a reticulated ceramic at the center of the pore for different firing rates of the radiant burner [68]. In spite of the fact that the thermocouple readings have been corrected for conduction and radiation errors, the authors believe that the measured temperatures to the left of the peak are too high. This is due to the fact that conduction along the probe and catalytic effects ignite the incoming mixture. When the firing rate is increased from 157 to 315 kW/m², the peak flame temperature location moves closer to the burner face. This is caused by an increase in the advective velocity of the mixture beyond the burner flame speed at the lower firing rate. At the new location, the heat transfer rate from the flame to the matrix

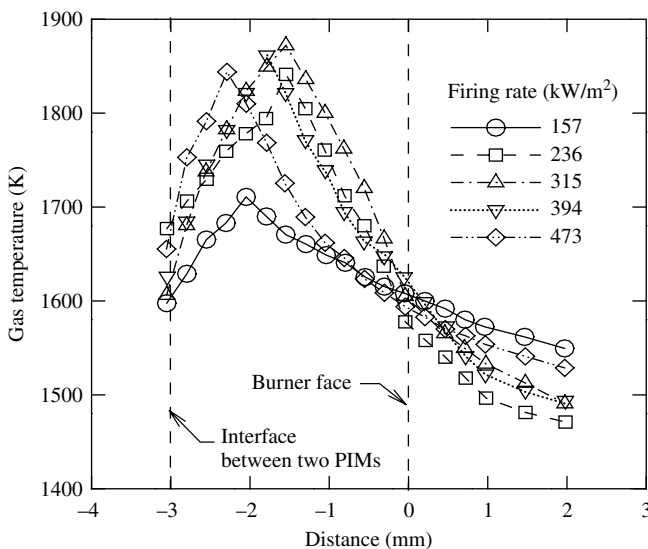
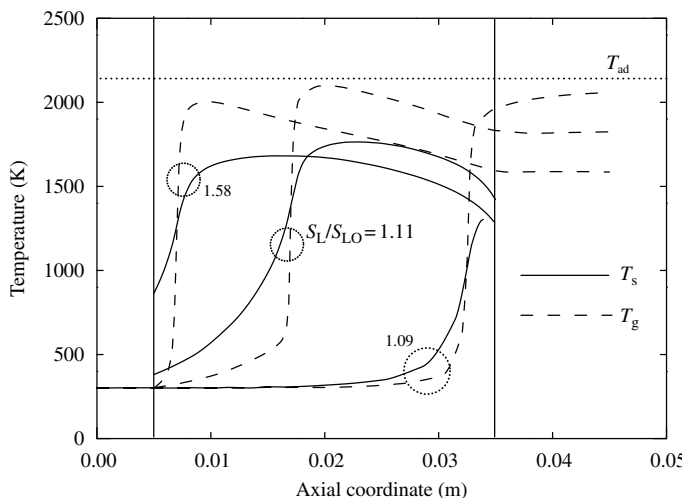


FIGURE 15.13

Temperature distribution in a flame support layer of a bilayer reticulated ceramic radiant heater. (Reprinted from R. Mital et al., *Combust. Flame* 111:175–184, 1997. With permission from the Combustion Institute.)

**FIGURE 15.14**

Effect of firing rate on local gas temperature in a porous, double-layer radiant burner at an equivalence ratio of 0.9. (Reprinted from D.J. Diamantidis et al., *Combust. Theory Model.* 6:383–411, 2002. With permission from Institute of Physics.)

is reduced leading to flame stabilization at higher mixture velocities. This is consistent with the conventional knowledge of laminar free flames [8]. For higher firing rates (beyond 315 kW/m^2) the flame moves further upstream in the flame support layer. An additional increase in the firing rate results in flashback, thereby limiting the operation of the burner.

Figure 15.14 shows typical temperature distributions calculated in the gas and solid phases at an equivalence ratio of 0.9. For burning velocity ratios, $S_L/S_{LO} \geq 1.09$, with S_{LO} being the laminar burning velocity of a free flame at the same equivalence ratio, the flames are submerged in the porous matrix. But, for a velocity ratio of 1.58 the flame is anchored at the front face of the burner. The maximum flame temperature is below the adiabatic flame temperature T_{ad} which is shown in the figure. The results do not reveal superadiabatic combustion which is evident for an equivalence ratio of 0.5 [73]. Upstream of the flame the solid is at a higher temperature than the gas. The solid becomes colder than the gas downstream of the reaction zone in a 3-cm-thick porous ceramic. Similar results have been obtained for different dimensionless flame speeds (S_L/S_{LO}), but with the flame position at different locations in the PIM. The results show that lean submerged flames can have burning velocities up to 2.5 times higher than laminar burning velocities.

The comprehensive models for flames in embedded porous media reproduce most experimental trends observed and reported in the literature. In this mode of combustion the reaction zone is located fully inside the porous medium and the flame temperature is below the adiabatic flame temperature. If the PIM is not sufficiently thick combustion is completed at the burner exit [76]. Energy considerations in the gas-phase equation suggest that these

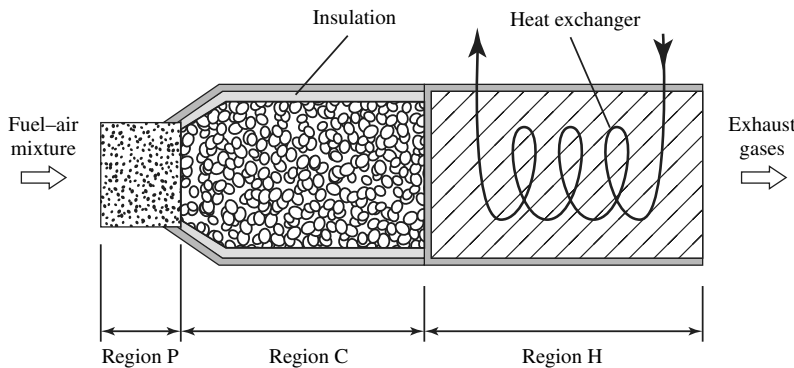
flames have a structure similar to those of freely propagating flames with preheated reactants. The local heat transfer rate from the gases to the solid matrix is a small part of the chemical energy released. The inability of the models to quantitatively agree with the experiments is due to both the experimental difficulties in making local measurements in the porous matrix and the uncertainties in the thermophysical and radiation characteristics of the matrices used for the burners.

The predictions are in quantitative agreement with the data concerning the gas outlet temperatures, pollutant emissions, and radiation efficiencies [51,73,77]. The thermal performance predictions of the submerged flame burners is sensitive to the convective heat transfer characteristics, the opacity of the PIM (i.e., the thickness extinction coefficient product), and the operating conditions such as the firing rate and the equivalence ratio influence the radiation efficiency of the burner–radiant heater. It has been observed that the burners with the thicker flame support layer [51,68,76] have higher radiation efficiency than their thinner counterparts at the same operating conditions. This performance increase is owing to a combination of two factors: a longer gas mixture residence time in the high-temperature region resulting in more complete combustion and an effective increase in pad volume allowing for a large fraction of thermal radiation emission not only from within the PIM but also from the solid of the burner face.

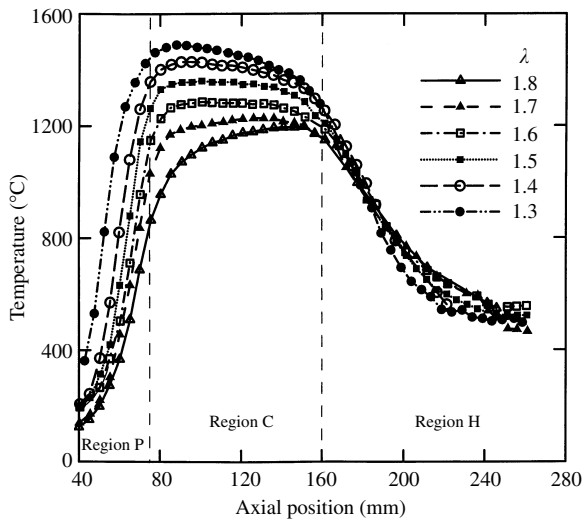
15.7 Premixed Porous Medium Combustors–Heaters

Porous inert media based burners–heaters with integral heat exchangers, either in the PIM [52,54,79–81] or in the postcombustion region [58,59,82], have potential applications in industrial fluid heating, household appliances, etc. and have received considerable experimental and theoretical research and development attention during the last decade. PPMC heaters usually consist of two or more different solid matrices having appropriate physical (geometrical), flow, and heat transfer characteristics. The combustor can be located vertically (with upward or downward flow) or horizontally. A schematic diagram of a combustor is shown in [Figure 15.15](#). A heat exchanger (i.e., tubes through which a working fluid is circulated) is placed in the exhaust stream of the postcombustion zone. The water vapor in the combustion products is condensed and gives its latent heat to the heat exchanger. Mounting of the burner vertically facilitates the gas flows from top to bottom and enables the condensed water to flow out of the burner [82].

PPMC heaters have received both experimental and theoretical research attention [58,59], and additional studies are cited in these references. As shown in Figure 15.15 a typical PPMC unit with an integral heat exchanger consists of three main regions: a preheat zone (P), a combustion zone (C), and a heat exchanger zone (H). The preheating zone is composed of ceramic

**FIGURE 15.15**

Schematic diagram of a PPMC with heat exchanger in the exhaust stream.

**FIGURE 15.16**

Effect of excess air ratio λ on the temperature distribution in the porous matrix for 16 mm Al_2O_3 balls in region C. (Reprinted from D. Trimis and F. Durst, *Combust. Sci. Technol.* 121:153–168, 1996. With permission from Taylor & Francis.)

(i.e., Al_2O_3) particles, and the combustion zone consists of ceramic particles, open-cell ceramic (i.e., SiC) foams having different number of pores per unit length and other porous materials. The burner walls are water cooled, but the combustion region is insulated from the cold walls by a ceramic cylinder (liner) in order to ensure stable combustion.

Temperature measurements made inside the porous matrix [82] using type S thermocouples are illustrated in Figure 15.16. The porous matrix in the combustion zone C was comprised of 16 mm diameter Al_2O_3 particles. Methane–air mixtures of different compositions were burned in two different

sections of the PPMC of the type discussed in this section. The results of the figure show that the basic features of the flame stabilization and heat transfer are satisfied.

Probably the most detailed analysis from the chemical kinetics point of view is that of Brenner et al. [58]. They used a pseudohomogeneous thermal equilibrium model for porous media to simulate a two-dimensional methane–air combustor connected to a finned tube heat exchanger located past the burner exit. A water cooling jacket was placed around the combustion region which contained the porous medium comprised of either Al_2O_3 or SiC lamellae structure. The chemical kinetics model accounted for 20 species and 164 reactions. Radiative transfer in the porous media was treated empirically through the Rosseland diffusion approximation, and the dispersion effects were accounted for using an anisotropic effective thermal conductivity. The two-dimensional temperature and species concentration distributions were calculated for premixed methane–air combustion in burner with rectangular cross-section geometry. A comparison of predicted and measured maximum temperatures for different equivalence ratios and two firing rates is given in Figure 15.17. The measured temperatures were corrected for errors, which at the centerline of the burner were approximately 100 K. The experimental and computational results show that the model is capable of simulating the overall trends, which included the equivalence ratio, specific firing rate and thermophysical characteristics of the PIMs used.

PPMC heaters with heat exchangers embedded directly in the porous matrix have the potential of greater compactness and higher thermal efficiency, lower solid matrix temperatures and reduced pollutant emissions, but their

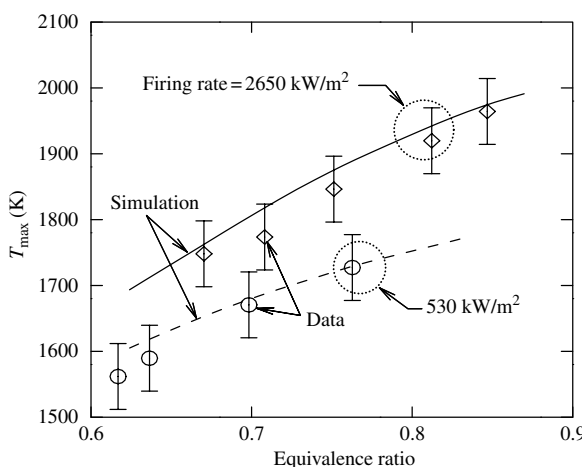


FIGURE 15.17

Comparison of measured and predicted maximum temperatures for various equivalence ratios and firing rates. (Reprinted from G. Brenner et al., *Combust. Flame* 123:201–213, 2000. With permission from the Combustion Institute.)

development is not as far advanced as the combustors-heaters mentioned in the preceding paragraphs. As already discussed, in PPMCs without heat extraction in the solid matrix there is usually an extended range of stable flame speed which can be achieved at an equivalence ratio to maintain stable combustion. At a particular equivalence ratio, when the velocity of the fuel-air mixture in the solid matrix is higher than the corresponding stable flame speed, the reaction zone is pushed downstream closer to the embedded heat exchanger tubes. With the flame closer to the tubes, a large fraction of heat released is extracted by the coolant, and the heat feedback needed to preheat the fuel-air mixture is reduced. If this process continues, eventually either the flame stabilizes in the gas-phase (i.e., becomes anchored at the front face of the solid matrix) or blowout occurs. If, on the other hand, the velocity of the fuel-air mixture is lower than the stable flame speed, the process discussed is reversed and the flame moves out of the porous material and remains in the gas-phase upstream of the porous matrix.

Two-dimensional numerical simulations of a PPMC heater stabilized in a packed bed of alumina (Al_2O_3) particles has been reported [52,54,80]. Either horizontal [52,54] or vertical [80] tubes were embedded in the bed for extracting the heat of combustion. One-step chemical kinetics model was employed for the premixed methane-air combustion. Radiation was treated as a diffusion process, and effects of dispersion were accounted for in the effective thermal conductivity model. The emphasis in the calculations was on the flame location, temperature distribution in the bed, pressure drop, and thermal efficiency. The effects of excess air, firing rate, particle diameter, activation energy, and thermal conductivity were investigated. Model predictions were compared with available experimental data for a similar system, and the predictions were found to agree with the available data within the experimental uncertainty. It was found that there is a significant difference between the predictions based on the thermal equilibrium [52] and the nonequilibrium [54] models for larger particle diameters.

In spite of the fact that PPMC devices with the heater embedded in the porous matrix have potential for improved thermal performance and reduced pollutant emissions, the unstable combustion observed in experiments [79,81] appears to have held back development. Means have to be found to overcome design and operational problems to maintain stable combustion under fuel-lean conditions with the equivalence ratio lower than the flammability of free-burning systems.

15.8 Concluding Remarks

There are diverse technologies and fields of application of hydrocarbon fuel (gaseous and liquid) combustion within porous inert material that stabilize reactions in the pore structure of the matrix. Premixed fuel and air enters the

porous matrix where it is convectively heated as it passes through the interstitial voids of the matrix upstream of the reaction zone. The porous material upstream of the reaction zone is heated by conduction and radiation. The preheated fuel-air mixture then passes through the combustion zone where chemical reactions occur and heat release takes place. The nonadiabatic combustion taking place in the voids of the porous matrix is intimately coupled to heat transfer by convection, conduction, and radiation in the porous material.

Significant progress has been made in the development and application of the innovative porous media combustion technology and reviews are available [1–4,8,12]. Reference is made to these accounts for detailed discussion of research issues and specific applications of the technology. Briefly, the problems needing research attention include improved understanding of conductive, convective, and radiative heat transfer in unconsolidated and consolidated porous media, establishment of chemical kinetics parameters for nonadiabatic combustion in porous media, flame quenching in small pores, development and validation of more realistic transport-combustion models, establishment of combustion regimes in different porous media, and their stability limits. Most of all, the effect of chemical reactions and combustion product expansion on flow and turbulence in porous media has not been adequately studied and is not understood.

PPMC devices have been shown to maintain stable combustion under fuel-lean conditions with an equivalence ratio lower than the flammability of free-flame burning systems. The flame speed of a porous burner has been found to be significantly higher than in free-burning systems. The combustion within a porous matrix exhibits the characteristics of low flame temperature, extended chemical reaction zone, high preheating fuel-air mixture, and low NO_x and CO emissions. In summary, a properly designed and operated PPMC has the potential of greatly improved thermal and combustion performance as well as reduced pollutant emissions. However, significant research and development issues remain to be resolved before the innovative technology, with its special niche, can find greater acceptance and a wider range of applications.

The use of pseudohomogeneous and heterogeneous volume-averaged models requires the quantification of numerous parameters that have to be specified *a posteriori* using experiments. A more rigorous approach of quantifying these parameters can be performed *a priori* using the lattice Boltzmann method (LBM). Such an innovative approach to predict the flow structure in a packed bed has been used by Brenner et al. [53], but so far combustion and heat transfer in a packed bed has not been simulated. This may be an area of future research direction since knowledge of structural details of a bed may allow LBM to be used efficiently to analyze porous media and extract important characteristics of bulk flow, direction dependent dispersion coefficients, and other parameters needed to simulate combustion and heat transfer or for incorporation in pseudohomogeneous models.

The solid matrix limits access by optical and mechanical probes for experimental measurements of flame structure in porous media. This presents

a great challenge and identifies the need for experimental and theoretical research of combustion phenomena and for determination of thermophysical, transport, and radiation characteristics of porous media. The lack of reliable information on the characteristics leads to discrepancies between model calculations and the experimental data that need to be overcome in the future.

Nomenclature

a_v	surface area per unit volume
c_p	specific heat at constant pressure
c_s	specific heat of solid
D	diffusion coefficient
d	diameter of pore or of particle
F	Forchheimer factor
\mathcal{F}	radiative flux in the x -direction
\mathbf{f}	radiation flux vector
h	enthalpy or convective heat transfer coefficient
h_v	volumetric heat transfer coefficient ($=ha_v$)
K	permeability of porous medium
k	thermal conductivity
L	thickness
Nu	Nusselt number
p	pressure
R	universal gas constant
Re	Reynolds number
Sc	Schmidt number
Sh	Sherwood number
T	temperature
u	velocity in the x -direction
\mathbf{u}	velocity vector
Y_i	mass fraction of species i
W_i	molecular weight of species i
β	extinction coefficient ($=\kappa + \sigma$)
ε	emissivity
κ	absorption coefficient
λ	excess air ratio
μ	dynamic viscosity
ρ	density
σ	scattering coefficient or Stefan–Boltzmann constant
ϕ	porosity
$\dot{\omega}_i$	generation rate of species i

Subscripts

con	refers to conduction
dis	refers to dispersion
eff	refers to effective
g	refers to gas
i	refers to inlet (entrance)
m	refers to mean
o	refers to exit (outlet)
rad	refers to radiation
s	refers to solid
sur	refers to surroundings

References

1. J.R. Howell, M.J. Hall, and J.L. Ellzey. Combustion of hydrocarbon fuels within porous inert media. *Prog. Energ. Combust. Sci.* 22:121–145, 1996.
2. D. Trimis. Stabilized combustion in porous media — applications of the porous burner technology in energy- and heat engineering. AIAA Paper 2000-2298. Reston, VA: AIAA, 2000.
3. S. Mössbauer, O. Pickenäcker, K. Pickenäcker, and D. Trimis. Applications of the porous burner technology in energy- and heat engineering. *Clean Air* 3:183–198, 2002.
4. R. Viskanta. Interaction of combustion and heat transfer in porous inert media. In: S.H. Chan, Ed., *Transport Phenomena in Combustion*. Washington: Taylor & Francis, 1996, Vol. 1, pp. 64–87.
5. F.J. Weinberg. Combustion in heat-recirculating burners. In: F.J. Weinberg, Ed., *Advanced Combustion Methods*. London: Academic Press, 1986, pp. 184–236.
6. F. Weinberg. Heat-recirculating burners: principles and some recent developments. *Combust. Sci. Technol.* 121:3–22, 1996.
7. V.S. Babkin, A.A. Korzhavin, and V.A. Bunev. Propagation of premixed explosion flames in porous media. *Combust. Flame* 87:182–190, 1991.
8. S.R. Turns. *An Introduction to Combustion*. 2nd edn. Boston: McGraw-Hill, 2000.
9. C.E. Baukal, Jr., V.Y. Gershtein, and X. Li. *Computational Fluid Dynamics in Industrial Combustion*. Boca Raton, FL: CRC Press, 2001.
10. A.A. Oliveira and M. Kaviani. Nonequilibrium in the transport of heat and reactants in combustion in porous media. *Prog. Energ. Combust. Sci.* 27:523–545, 2001.
11. M. Kaviani. *Principles of Heat Transfer in Porous Media*. 2nd edn. Berlin: Springer, 1999.
12. R. Echigo. Radiation enhanced/controlled phenomena of heat and mass transfer in porous media. In: J.R. Lloyd and Y. Kurosaki, Eds., *Proceedings of the Third ASME/JSME Thermal Engineering Joint Conference*. New York: ASME, 1991, Vol. 1, pp. xxi–xxxii.
13. J.H. Cushman. *The Physics of Fluids in Hierarchical Porous Media: Angstroms to Miles*. Dordrecht: Kluwer, 1997.

14. S. Whitaker. Volume averaging of transport equations. In: J.P. DuPlessis, Ed., *Flow in Porous Media*. Southampton, UK: Computational Mechanics Publications, 1997, chapter 1.
15. S. Whitaker. Coupled transport in multiphase systems: a theory of drying. In: *Advances in Heat Transfer*. New York: Academic Press, 1998, Vol. 31, pp. 1–104.
16. S. Whitaker. *The Method of Volume Averaging*. Dordrecht: Kluwer, 1999.
17. M. Quintard and S. Whitaker. Theoretical analysis of transport in porous media. In: K. Vafai, Ed., *Handbook of Porous Media*. New York: Marcel Dekker, 2000, pp. 1–52.
18. R. Viskanta. Modeling transport phenomena in porous media using two-energy equation model. In: L.S. Fletcher and T. Aiahara, Eds., *Proceedings of the Fourth ASME/JSME Thermal Engineering Joint Conference*. New York: ASME, 1995, Vol. 3, pp. 11–22.
19. N. Wakao and S. Kaguei. *Heat and Mass Transfer in Packed Beds*. London: Gordon and Breach, 1982.
20. E. Tsotsas and H. Martin. Thermal conductivity of packed beds: a review. *Chem. Eng. Process.* 22:19–37, 1987.
21. E.-U. Schlünder and E. Tsotsas. *Wärmeübertragung in Festbetten, durchmischten Schüttungen und Wirbelschichten*. Stuttgart: Georg Thieme Verlag, 1988.
22. K. Nasr, R. Viskanta, and S. Ramadhyani. An experimental evaluation of the effective thermal conductivities of packed beds at high temperature. *J. Heat Transfer* 116:829–837, 1994.
23. K. Kamiuto and S.S. Yee. Elementary transport processes in packed beds. *Trends Heat Mass Moment. Transfer* 7:19–42, 2001.
24. P.-F. Hsu and J.R. Howell. Measurements of thermal conductivity and optical properties of partially stabilized zirconia. *Exp. Heat Transfer* 5:293–313, 1992.
25. G.N. Dul'nev. Heat transfer through solid disperse systems. *J. Eng. Phys.* 9:275–279, 1965.
26. K. Kamiuto. Study of Dul'nev's model for the thermal and radiative properties of open-cellular porous materials. *JSME Int. J.* 40:577–582, 1997.
27. E. Achenbach. Heat and fluid flow characteristics in packed beds. *Exp. Thermal Fluid Sci.* 10:17–21, 1995.
28. R. Viskanta. Convective heat transfer in consolidated porous materials: a perspective. *Symposium on Thermal Science and Engineering in Honor of Chancellor Chang-Lin Tien*. Urbana, IL: University of Illinois at Urbana — Champaign, 1995, pp. 43–50.
29. X. Fu, R. Viskanta, and J.P. Gore. Measurements of volumetric heat transfer coefficient of cellular ceramic. *Exp. Thermal Fluid Sci.* 17:285–293, 1998.
30. L.B. Younis and R. Viskanta. Experimental determination of the volumetric heat transfer coefficient between stream of air and ceramic foam. *Int. J. Heat Mass Transfer* 36:1425–1434, 1993.
31. K. Ichimiya. A new method for evaluation of heat transfer between solid materials and fluid in a porous solid. *J. Heat Transfer* 121:978–983, 1999.
32. K. Kamiuto, S.Y. Yee, and K. Matsuda. Experimental determination of the heat transfer and fluid flow characteristics of open-cellular porous materials. In: J.A. Taine, Ed., *Heat Transfer 2002 — Proceedings of the Twelfth International Conference*. Paris: Editions Scientifiques et Medicales Elsevier, 2002, Vol. 1, pp. 815–820.
33. R. Viskanta and M.P. Menguç. Radiative transfer in dispersed media. *Appl. Mech. Rev.* 42:241–259, 1989.

34. M. Kaviany and B.P. Singh. Radiative heat transfer in porous media. In: J.P. Hartnett, T.F. Irvine, Jr., and Y.I. Cho, Eds., *Advances in Heat Transfer*. San Diego: Academic Press, 1993, Vol. 23, pp. 133–186.
35. C.L. Tien. Thermal radiation in packed beds. *J. Heat Transfer* 110:1230–1242, 1988.
36. L.A. Dombrovsky. *Radiation Heat Transfer in Disperse Systems*. New York: Begell House, 1996.
37. D. Baillis and J.-F. Sacadura. Thermal radiation properties of dispersed media: theoretical predictions and experimental characterization. *J. Quant. Spectrosc. Radiative Transfer* 67:327–363, 2000.
38. J.R. Howell. Radiative transfer in porous media. In: K. Vafai, Ed., *Handbook of Porous Media*. New York: Marcel Dekker, 2000, pp. 663–698.
39. C.L. Tien and B.L. Drolen. Thermal radiation in particulate media with dependent and independent scattering. In: T.C. Chawla, Ed., *Annual Reviews of Numerical Fluid Mechanics and Heat Transfer*. Washington: Hemisphere, 1987, Vol. 1, pp. 1–34.
40. K. Kamiuto. Study of scattering regime diagrams. *J. Thermophys. Heat Transfer* 4:432–435, 1990.
41. B.P. Singh and M. Kaviany. Modeling radiative heat transfer in packed beds. *Int. J. Heat Mass Transfer* 35:1397–1405, 1992.
42. K. Kamiuto. Correlated radiative transfer in packed bed-sphere systems. *J. Quant. Spectrosc. Radiative Transfer* 43:39–43, 1990.
43. K. Kamiuto, M. Iwamoto, T. Nishimura, and M. Sato. Albedoes and assymetry factors of the phase function for packed sphere systems. *J. Quant. Spectrosc. Radiative Transfer* 46:309–316, 1991.
44. R. Mital, J.P. Gore, and R. Viskanta. Measurements of extinction coefficient and single scattering albedo of reticulated porous ceramics at high temperature. *J. Thermophys. Heat Transfer* 19:33–38, 1996.
45. T.J. Hendricks and J.R. Howell. Absorption/scattering coefficients and scattering phase functions in reticulated porous ceramics. *J. Heat Transfer* 118:79–87, 1996.
46. C.J. Tseng and J.R. Howell. Combustion of liquid fuels in a porous radiant burner. *Combust. Sci. Technol.* 112:141–161, 1996.
47. H. Takami, T. Suzuki, Y. Itaya, and M. Hasatani. Performance of flammability of kerosene and NO_x emission in the porous burner. *Fuel* 77:165–171, 1998.
48. S. Jugjai, N. Wonganit, T. Laoketkan, and S. Nokkaew. The combustion of liquid fuels using a porous medium. *Exp. Thermal Fluid Sci.* 26:15–23, 2002.
49. C.-W. Park and M. Kaviany. Evaporation-combustion affected by in-cylinder reciprocating porous regenerator. *J. Heat Transfer* 124:184–197, 2002.
50. S. Jugjai and N. Polmart. Enhancement of evaporation and combustion of liquid fuels through porous media. *Exp. Thermal Fluid Sci.* 27:901–909, 2003.
51. R. Viskanta and J.P. Gore. Overview of cellular ceramics based porous radiant burners for supporting combustion. *Env. Combust. Technol.* 1:167–203, 2000.
52. A.A. Mohamad, S. Ramadhyani, and R. Viskanta. Modeling of combustion and heat transfer in a packed bed with embedded coolant tubes. *Int. J. Heat Mass Transfer* 37:1181–1191, 1994.
53. G. Brenner, T. Zeiser, T. Weber, and F. Durst. Flow in porous media: applications and methods of analysis. In: R. Bennaur and A.A. Mohamad, Eds., *Proceedings of APM 2002—1st International Conference on Applications of Porous Media*. Jerba, Tunisia: Tunisia Press, 2002, pp. 675–690.

54. A.A. Mohamad, R. Viskanta, and S. Ramadhyani. Numerical predictions of combustion and heat transfer in a packed bed with embedded coolant tubes. *Combust. Sci. Technol.* 96:387–407, 1994.
55. G.J. Rørveit, K. Zepter, Ø. Skreiberg, M. Fossum, and J.E. Hustad. A comparison of low- NO_x burners for combustion of methane and hydrogen mixtures. *Proc. Combust. Inst.* 29:1123–1129, 2002.
56. W.M. Mathis, Jr. and J.L. Ellzey. Flame stabilization, operating range, and emissions force methane/air porous burner. *Combust. Sci. Technol.* 175:825–839, 2003.
57. M. Saharaoui and M. Kaviany. Direct simulation versus volume-averaged treatment of adiabatic, premixed flame in porous media. *Int. J. Heat Mass Transfer* 37:2817–2834, 1994.
58. G. Brenner, K. Pickenäcker, O. Pickenäcker, D. Trimis, K. Wawrzinck, and T. Weber. Numerical and experimental investigation of matrix-stabilized methane/air combustion in porous inert media. *Combust. Flame* 123:201–213, 2000.
59. I. Malico, X.Y. Zhu, and J.F. Pereira. Two-dimensional numerical study of combustion and pollutant formation in porous burners. *Combust. Sci. Technol.* 152:57–79, 2000.
60. J.G. Hoffmann, R. Echigo, S. Tada, and H. Yoshida. Analytical study of flammable limits of reciprocating superadiabatic combustion in porous media. In: S.H. Chan, Ed., *Transport Phenomena in Combustion*. Washington: Taylor & Francis, 1996, Vol. 2, pp. 1430–1440.
61. O. Pickenäcker and D. Trimis. Experimental study of a staged methane/air burner based on combustion in a porous inert medium. *J. Porous Media* 4:197–213, 2001.
62. J.G. Hoffmann, R. Echigo, H. Yoshida, and S. Tada. Experimental study on combustion in porous media with a reciprocating flow system. *Combust. Flame* 111:32–46, 1997.
63. Y. Yoshizawa, K. Sasaki, and R. Echigo. Analytical study of the structure of radiation controlled flame. *Int. J. Heat Mass Transfer* 31:311–319, 1988.
64. P.-F. Hsu and R.D. Matthews. The necessity of detailed kinetics in models for premixed combustion in porous media. *Combust. Flame* 93:457–466, 1993.
65. P.-F. Hsu, W.D. Evans, and J.R. Howell. Experimental and numerical study of premixed combustion within nonhomogeneous porous ceramics. *Combust. Sci. Technol.* 90:149–172, 1993.
66. X.Y. Zhu and J.C.F. Pereira. Comparison of four combustion models for simulating the premixed combustion in inert porous media. *Fire Mat.* 22:187–197, 1998.
67. C. Chaffin, M. Koenig, M.M. Koeroghlian, R.D. Matthews, M.J. Hall, S.P. Nichols, and I.-G. Lim. Experimental investigation of premixed combustion within highly porous media. In: J.R. Lloyd and Y. Kurosaki, Eds., *Proceedings of the ASME/JISME Joint Engineering Conference*. New York: ASME, 1991, Vol. 4, pp. 219–224.
68. R. Mital, J.P. Gore, and R. Viskanta. A study of submerged reaction zone in porous ceramic radiant burners. *Combust. Flame* 111:175–184, 1997.
69. J.L. Ellzey and R. Goel. Emissions of CO and NO from a two stage porous media burner. *Combust. Sci. Technol.* 107:81–91, 1999.
70. V. Tvarkin and I. Catton. A two-equation model for turbulent flow and heat transfer in a porous layer. *J. Fluids Eng.* 117:181–188, 1995.

71. Y. Takatsu and T. Masuoka. Turbulent phenomena in flow through porous media. *J. Porous Media* 1:243–251, 1998.
72. N. Nakayama and F. Kuwahara. A macroscopic turbulence model for flow in a porous medium. *J. Fluids Eng.* 121:427–433, 1999.
73. D.J. Diamantis, E. Mastorakos, and D.A. Goussis. Simulations of premixed combustion in porous media. *Combust. Theory Model* 6:383–411, 2002.
74. S.W. Baek. The premixed flame in a radiatively active porous medium. *Combust. Sci. Technol.* 64:277–287, 1989.
75. S.B. Sathe, M.R. Kulharni, R.E. Peck, and T.W. Tong. An experimental and theoretical study of porous radiant burner performance. *Twenty-Third Symposium (International) on Combustion*. Pittsburgh: The Combustion Institute, 1990, pp. 1011–1018.
76. Y.L. Lee, Y.D. Shin, and S.W. Baek. Experimental and numerical premixed flame stabilized inside a honeycomb ceramic. *Combust. Sci. Technol.* 112:75–93, 1996.
77. S.A. Leonardi, R. Viskanta, and J.P. Gore. Analytical and experimental study of combustion and heat transfer in submerged flame metal fiber burners/heaters. *J. Heat Transfer* 125:118–125, 2003.
78. S.A. Leonardi, R. Viskanta, and J.P. Gore. Radiation and thermal performance measurements of metal fibre burner. *J. Quant. Spectrosc. Radiative Transfer* 73:491–501, 2002.
79. T.-Y. Xiong and R. Viskanta. A basic study of a porous matrix combustor-heater. In: R. Ruiz, Ed., *Fossil Fuels Combustion*. New York: ASME, 1992, PD-Vol. 39, pp. 31–39.
80. Y. Xuan and R. Viskanta. Numerical investigation of porous matrix combustor-heater. *Numer. Heat Transfer (Part A)* 36:359–374, 1999.
81. J. Rabovitser, Y. Chudnovsky, K. Matsui, R. Viskanta, and A. Fedorov. Development of compact, high-efficiency low-emissions surface combustor-burner. *Proceedings of the 1998 International Gas Research Conference*. Chicago: Gas Research Institute, 1998, pp. 197–208.
82. D. Trimis and F. Durst. Combustion in a porous medium — advances and applications. *Combust. Sci. Technol.* 121:153–168, 1996.

16

Modeling Bioconvection in Porous Media

A.V. Kuznetsov

CONTENTS

16.1	Introduction	646
16.2	Stability of a Suspension of Gyrotactic Microorganisms in a Fluid Saturated Porous Medium	648
16.2.1	Stability Analysis under the Assumption that a Porous Matrix does not Absorb Microorganisms	648
16.2.1.1	General linear stability analysis	648
16.2.1.2	Investigation of stability under the assumption that the principle of exchange of stabilities is satisfied	655
16.2.2	Stability Analysis Accounting for the Absorption of Microorganisms by the Porous Matrix and the Reduction of its Permeability	656
16.2.3	Stability Analysis of Bioconvection of Gyrotactic Microorganisms in a Layer of Final Depth.....	659
16.3	Stability of a Suspension of Oxytactic Microorganisms in a Fluid Saturated Porous Medium and Analysis of a Bioconvection Plume Caused by these Microorganisms	664
16.3.1	Stability of a Shallow Layer	664
16.3.2	Self-Similarity Solution for a Falling Plume in Bioconvection of Oxytactic Bacteria in a Deep Fluid Saturated Porous Layer	672
	Acknowledgment.....	682
	Nomenclature	682
	References	685

Bioconvection is a new area of fluid mechanics, which has been developed during the last few decades. The term “bioconvection” refers to macroscopic convection induced in water by the collective motion of a large number of self-propelled motile microorganisms. This convection is usually characterized by

regular fluid circulation patterns. Bioconvection is induced not by momentum generated as a result of the swimming of individual microorganisms, but rather by a density gradient, which occurs when a large number of these microorganisms (which are heavier than water) accumulate in a certain region of the fluid.

This chapter concentrates on the theory of bioconvection in porous media. By using porous media with different permeabilities, it is possible to have either a stable suspension (this happens if permeability is small) or unstable suspension (this happens if permeability is large), in which case bioconvection plumes will develop. Utilizing porous plugs in composite porous/fluid domains makes it possible to control and, if necessary, suppress bioconvection.

In this chapter, the stability criteria for bioconvection of gyrotactic microorganisms in porous media are derived. It is established that there is a critical permeability of a porous medium. If permeability is larger than critical, bioconvection develops; if it is smaller than critical, it is suppressed. Critical permeability is determined as a function of parameters of upswimming microorganisms through a linear stability analysis of governing equations. The effect of cell deposition and resuspension as well as the effect of fouling of porous media on the critical permeability is investigated.

The chapter also presents a theory of bioconvection plume in a suspension of oxytactic bacteria in a deep chamber filled with a fluid-saturated porous medium. The plume transports oxygen from the upper boundary layer, which is rich in cells and oxygen, to the lower part of the chamber, which is depleted of both cells and oxygen. A similarity solution of full governing equations (without utilizing the boundary layer approximation) that describe fluid flow as well as oxygen and cell transport in the plume is obtained. The resulting ordinary differential equations are singular when the similarity variable approaches zero; therefore, a series solution of these ordinary differential equations, which is valid for small values of the similarity variable, is obtained. This series solution is used as a starting point for a numerical solution that makes it possible to investigate the plume for the whole range of values of the similarity variable.

16.1 Introduction

Many living microorganisms (many species of bacteria and algae) can propel themselves by rotating flagella, which are driven by reversible molecular motors that are embedded in the cell wall. These microorganisms are generally heavier than water (the algae are approximately 5% denser than water, whereas the bacteria are nearly 10% denser than water); therefore, the fluid regions with a higher number density of motile cells become heavier than the fluid regions with a smaller number density of the cells. Since the cells

tend to swim in a particular direction in response to certain stimuli such as gravity (gravitaxis), light (phototaxis), or chemical gradients (e.g., oxygen gradient), they concentrate in certain regions of the fluid domain. This causes density gradients in the fluid that may result in the development of convection instability. This instability leads to a spontaneous pattern formation in suspensions of motile microorganisms, which is called bioconvection [1]. In the case of upswimming microorganisms, the mechanism of development of bioconvection is somewhat similar to the mechanism of the Rayleigh–Bénard convection instability, yet, the development of bioconvection does not require the vertical temperature gradient [2–4].

Most of the significant results in the area of bioconvection were obtained over the last two decades [5–8]. A model for bioconvection depends on the orientation of cell swimming, which depends on the species of microorganisms. A typical behavior in algal suspensions is gyrotaxis. The direction of swimming of gyrotactic microorganisms is determined by the balance of two torques. The first one is the viscous torque that acts on a body placed in a shear flow. The second torque is generated by gravity because the center of mass of a typical microorganism is displaced from its center of buoyancy. If microorganisms are heavier than the fluid, gyrotactic behavior results in their swimming toward the regions of most rapid downflow. Therefore, the regions of downflow become denser than the regions of upflow. Buoyancy increases the upward velocity in the regions of upflow and downward velocity in the regions of downflow, thus enhancing the velocity fluctuations [5,6,9]. The formation of almost regular patterns and gyrotactic plumes in algal suspensions is documented in numerous experimental papers [3,10–12].

Although there is a large number of publications on bioconvection in suspensions of gyrotactic microorganisms, very little has been done concerning the problem of separation of living and dead cells in these suspensions. One possible approach is to suppress bioconvection so that living cells would concentrate at the top of the fluid layer and dead cells would concentrate at the bottom. This idea is based on the pioneering work by Kessler [13] who suggested the utilization of upswimming of algal cells to concentrate the cells, to purify cultures, and to separate vigorously swimming subpopulations. For these applications, bioconvection is undesirable, because it would prevent upswimming cells from concentrating near the surface of the culture. To suppress bioconvection, Kessler [13] suggested the use of a porous medium (a surgical cotton wool), which must be sufficiently permeable to allow cells to swim through it but sufficiently tight to prevent the development of bioconvection instability. For practical purposes, it is desirable to have the permeability of the porous medium as high as possible. This would ensure that the cells can swim through it without cutting their tails off, and this will also maximize the flux of the cells in the upward direction. Numerical results by Kuznetsov and Jiang [14,15] and an analytical investigation by Kuznetsov and Avramenko [16] suggest that there is a critical value of the permeability of a porous medium. If the permeability is smaller than this

critical value, bioconvection does not occur and microorganisms simply swim in the upward direction; if it is larger than critical, bioconvection instability develops.

16.2 Stability of a Suspension of Gyrotactic Microorganisms in a Fluid Saturated Porous Medium

16.2.1 Stability Analysis under the Assumption that a Porous Matrix does not Absorb Microorganisms

16.2.1.1 General linear stability analysis

A powerful analytical result can be obtained under the assumption that the porous matrix does not absorb microorganisms [16,17]. It is also assumed that the suspension is dilute ($n_b\theta \ll 1$), where θ is the average volume of the microorganism and n_b is the number density of microorganisms in the basic state. Governing equations for a three-dimensional unsteady flow in a porous medium are obtained by volume averaging the equations in the Pedley et al. [5] model. The volume-averaging procedure is described in detail in Whitaker [18]. This procedure results in the replacement of the Laplacian viscous terms with the Darcian terms that describe viscous resistance in a porous medium [19].

The resulting governing equations are given below:

$$c_a \rho_0 \frac{\partial u}{\partial t} = -\frac{\partial p}{\partial x} - \frac{\mu u}{K} \quad (16.1)$$

$$c_a \rho_0 \frac{\partial v}{\partial t} = -\frac{\partial p}{\partial y} - \frac{\mu v}{K} \quad (16.2)$$

$$c_a \rho_0 \frac{\partial w}{\partial t} = -\frac{\partial p}{\partial z} - \frac{\mu w}{K} - n_s \theta \Delta \rho g \quad (16.3)$$

$$\frac{\partial u}{\partial x} + \frac{\partial v}{\partial y} + \frac{\partial w}{\partial z} = 0 \quad (16.4)$$

$$\frac{\partial n_s}{\partial t} = -\text{div}(n_s \mathbf{v} + n_s W_c \hat{\mathbf{p}} - D_n \nabla n_s) \quad (16.5)$$

where c_a is the acceleration coefficient introduced in Nield and Bejan [19]; D_n is the diffusivity of the microorganisms (this assumes that all random motions of the microorganisms can be approximated by a diffusive process); g is the gravitational acceleration; K is the permeability of the porous medium; n_s the number density of suspended motile microorganisms; p is the excess pressure (above hydrostatic); $\hat{\mathbf{p}}$ is the unit vector indicating the direction of swimming of microorganisms; t is the time; u , v , and w are the x -, y -, and z -velocity components, respectively; \mathbf{v} is the velocity vector, (u, v, w) ; $W_c \hat{\mathbf{p}}$ is the vector of average swimming velocity relative to the fluid (W_c is assumed

to be constant); x , y , and z are the Cartesian coordinates (z is the vertical coordinate); $\Delta\rho$ is the density difference, $\rho_{\text{cell}} - \rho_0$; μ is the dynamic viscosity, assumed to be approximately the same as that of water; and ρ_0 is the density of water.

Equation (16.5) is a simplified form of a more general cell conservation equation for porous media, which can be presented as:

$$\varphi \frac{\partial n_s}{\partial t} = -\text{div}(n_s \mathbf{v} + n_s (W_c)_{\text{eff}} \hat{\mathbf{p}} - D_{n,\text{eff}} \nabla n_s) \quad (16.5a)$$

Porosity φ is involved in the term on the left-hand side of Eq. (16.5a) because in the porous medium, the number density of cells (unlike the heat) is advected/convected with the intrinsic velocity (not the Darcy filtration velocity) since the cells cannot pass through the solid phase. Extra factor φ has been incorporated into the effective transport coefficients for the porous medium, $(W_c)_{\text{eff}}$ and $D_{n,\text{eff}}$, in Eq. (16.5a). In a pioneering investigation, it is desirable to keep things as simple as possible, also, there are no experimental measurements for $(W_c)_{\text{eff}}$ and $D_{n,\text{eff}}$. Therefore, Eq. (16.5a) is reduced to Eq. (16.5) by assuming that $(W_c)_{\text{eff}} = W_c$ and $D_{n,\text{eff}} = D_n$. It is also assumed that φ is sufficiently close to unity (otherwise bioconvection cannot develop).

To determine critical permeability, stability of the following basic state is investigated. A uniform suspension of microorganisms, with number density n_0 , in an infinite region occupied by an isotropic fluid-saturated porous medium of uniform porosity is considered. In the basic state, no macroscopic motion of the fluid occurs. All microorganisms are swimming vertically upwards; however, because of the infinite size of the domain, this upswimming does not change the cell concentration or the fluid density.

The perturbations in this system are introduced as follows:

$$n_s(t, x, y, z) = n_b + \varepsilon n'_s(t, x, y, z) \quad (16.6)$$

$$u(t, x, y, z) = \varepsilon u'(t, x, y, z) \quad (16.7)$$

$$v(t, x, y, z) = \varepsilon v'(t, x, y, z) \quad (16.8)$$

$$w(t, x, y, z) = \varepsilon w'(t, x, y, z) \quad (16.9)$$

$$p(t, x, y, z) = p_b(z) + \varepsilon p'(t, x, y, z) \quad (16.10)$$

$$\hat{\mathbf{p}}(t, x, y, z) = \hat{\mathbf{k}} + \varepsilon \hat{\mathbf{p}}'(t, x, y, z) \quad (16.11)$$

where $p_b(z)$ is the unperturbed excess pressure ($\partial p_b / \partial z = -n_b \theta \Delta \rho g$ from Eq. (16.3)), $\hat{\mathbf{k}}$ is the unit vector in the vertically upward z -direction, a prime denotes a perturbation quantity, and ε is the small perturbation amplitude. Substituting Eqs. (16.6) to (16.11) into the governing equations (16.1) to (16.5)

and linearizing gives the following equations for perturbation quantities:

$$c_a \rho_0 \frac{\partial u'}{\partial t} = -\frac{\partial p'}{\partial x} - \frac{\mu u'}{K} \quad (16.12)$$

$$c_a \rho_0 \frac{\partial v'}{\partial t} = -\frac{\partial p'}{\partial y} - \frac{\mu v'}{K} \quad (16.13)$$

$$c_a \rho_0 \frac{\partial w'}{\partial t} = -\frac{\partial p'}{\partial z} - \frac{\mu w'}{K} - n'_s \theta \Delta \rho g \quad (16.14)$$

$$\frac{\partial u'}{\partial x} + \frac{\partial v'}{\partial y} + \frac{\partial w'}{\partial z} = 0 \quad (16.15)$$

$$\frac{\partial n'_s}{\partial t} = -\operatorname{div} \left[n_b (\mathbf{v}' + W_c \hat{\mathbf{p}}') + n'_s W_c \hat{\mathbf{k}} - D_n \nabla n'_s \right] \quad (16.16)$$

where \mathbf{v}' is the vector composed of perturbations of the corresponding velocity components, (u', v', w') .

By analyzing the effect of gyrotaxes on orientation of swimming, Pedley et al. [5] obtained the following equation for the perturbation of a unit vector indicating the direction of swimming of microorganisms:

$$\hat{\mathbf{p}}' = B \tilde{\eta} \hat{\mathbf{i}} - B \tilde{\xi} \hat{\mathbf{j}} + 0 \hat{\mathbf{k}} \quad (16.17)$$

where $\hat{\mathbf{i}}$ and $\hat{\mathbf{j}}$ are the unit vectors in the x - and y -directions, respectively.

In Eq. (16.17), B is the timescale for the reorientation of the microorganisms by the gravitational torque against viscous resistance. In Pedley and Kessler [7] this parameter is called the “gyrotactic orientation parameter.” It can be expressed as:

$$B = \frac{\alpha_{\perp} \mu}{2 h \rho_0 g} \quad (16.18)$$

where α_{\perp} is a dimensionless constant, relating viscous torque to the relative angular velocity of the cell, and h is the displacement of the center of mass of the cell from its center of buoyancy.

The parameters $\tilde{\eta}$ and $\tilde{\xi}$ in the x - and y -components of vector $\hat{\mathbf{p}}'$ in Eq. (16.17) are:

$$\tilde{\eta} = -(1 - \alpha_0) \frac{\partial w'}{\partial x} + (1 + \alpha_0) \frac{\partial u'}{\partial z} \quad (16.19)$$

$$\tilde{\xi} = (1 - \alpha_0) \frac{\partial w'}{\partial y} - (1 + \alpha_0) \frac{\partial v'}{\partial z} \quad (16.20)$$

In Eqs. (16.19) and (16.20) α_0 is a measure of the cell eccentricity, which is given by the following equation:

$$\alpha_0 = \frac{a^2 - b^2}{a^2 + b^2} \quad (16.21)$$

where a and b are the semi-major and semi-minor axes of the spheroidal cell.

The substitution of Eq. (16.17) into Eq. (16.16) results in the following equation for the perturbation of the number density of the cells:

$$\frac{\partial n'_s}{\partial t} + W_c \frac{\partial n'_s}{\partial z} + W_c B n_0 \left(\frac{\partial \tilde{\eta}}{\partial x} - \frac{\partial \tilde{\xi}}{\partial y} \right) = D_n \nabla^2 n'_s \quad (16.22)$$

where $\tilde{\eta}$ and $\tilde{\xi}$ are given by Eqs. (16.19) and (16.20).

The governing equations for the perturbation quantities, (16.12) to (16.15) and (16.22), are linear and therefore, the stability of their solutions can be examined in terms of individual Fourier modes. Following Pedley et al. [5], perturbation quantities are introduced in the following form:

$$u'(t, x, y, z) = U \exp[\sigma t + i(kx + ly + mz)] \quad (16.23)$$

$$v'(t, x, y, z) = V \exp[\sigma t + i(kx + ly + mz)] \quad (16.24)$$

$$w'(t, x, y, z) = W \exp[\sigma t + i(kx + ly + mz)] \quad (16.25)$$

$$p'(t, x, y, z) = P \exp[\sigma t + i(kx + ly + mz)] \quad (16.26)$$

$$n'_s(t, x, y, z) = N_s \exp[\sigma t + i(kx + ly + mz)] \quad (16.27)$$

where k , l , and m are the wavenumbers in the x , y , and z directions, respectively; and σ is the dispersion parameter characterizing the growth rate of perturbations.

Substituting Eqs. (16.23) to (16.27) into Eqs. (16.12) to (16.15) and (16.22) and accounting for Eqs. (16.19) and (16.20), the following equations for the amplitudes (U , V , W , P , and N_s) are obtained:

$$kU + lV + mW = 0 \quad (16.28)$$

$$kKP - iU(\mu + c_a \rho_0 K \sigma) = 0 \quad (16.29)$$

$$lKP - iV(\mu + c_a \rho_0 K \sigma) = 0 \quad (16.30)$$

$$mKP - iW(\mu + c_a \rho_0 K \sigma) - igN_s K \Delta \rho \theta = 0 \quad (16.31)$$

$$D_n \kappa^2 N_s + B n_b W W_c (k^2 + l^2) (1 - \alpha_0) \\ - m W_c [-i N_s + B n_b (kU + lV) (1 + \alpha_0)] + N_s \sigma = 0 \quad (16.32)$$

where $\kappa^2 = k^2 + l^2 + m^2$. The elimination of amplitudes (U, V, W, P , and N_s) from Eqs. (16.28) to (16.32) leads to the following dispersion relation:

$$\begin{aligned} & \kappa^2(D_n\kappa^2 + imW_c + \sigma)(\mu + c_a\rho_0K\sigma) \\ &= Bn_bgKW_c\Delta\rho\theta(k^2 + l^2)[m^2(1 + \alpha_0) + (k^2 + l^2)(1 - \alpha_0)] \end{aligned} \quad (16.33)$$

Equation (16.33) can be solved for the growth rate parameter, σ . This results in two roots:

$$\begin{aligned} \sigma = & -\frac{c_a\rho_0K(D_n\kappa^2 + imW_c) + \mu}{2c_a\rho_0K} \\ & \pm \left\{ 4Bc_a\rho_0n_bgK^2(k^2 + l^2)W_c\Delta\rho\theta[m^2(1 + \alpha_0) + (k^2 + l^2)(1 - \alpha_0)] \right. \\ & \left. + \kappa^2[\mu - c_a\rho_0K(D_n\kappa^2 + imW_c)]^2 \right\}^{1/2} / (2c_a\rho_0K\kappa) \end{aligned} \quad (16.34)$$

Instability appears when the real part of σ has a positive sign. Since the root with a positive sign in front of the second term has the greater real part, further analysis is concentrated on this root.

When the permeability is small, the system is expected to be stable because of the large resistance that the porous medium creates to the flow. It is expected that the increase of permeability will make the system unstable. The permeability value corresponding to this transition is called the *critical permeability*. It is assumed that the critical permeability value is small. In this case, the solution for σ , given by Eq. (16.34) can be expended in Taylor series about the point $K = 0$. Neglecting quadratic and higher order terms, this expansion results in:

$$\begin{aligned} \sigma = & -\left(D_n\kappa^2 + imW_c\right) \\ & + \frac{(k^2 + l^2)Bn_bgW_c\Delta\rho\theta[m^2(1 + \alpha_0) + (k^2 + l^2)(1 - \alpha_0)]}{\kappa^2\mu}K + O(K^2) \end{aligned} \quad (16.35)$$

Thus for $K = 0$ the real part of σ has a negative real part $-\kappa^2D_n$, and the system is stable (unless the diffusivity of microorganisms, D_n , equals zero). This illuminates the role of diffusion in the stability of bioconvection in porous media. The diffusion stabilizes bioconvection, because it eliminates cell concentration gradients and, consequently, density gradients.

To find the value of the critical permeability it is necessary to find the value of K when the real part of σ changes its sign. To do this, it is necessary to solve the equation $\text{Re}(\sigma) = 0$. Taking the real part of Eq. (16.35) and equating it to

zero results in:

$$(k^2 + l^2)Bn_{bg}W_c\Delta\rho\theta[m^2(1 + \alpha_0) + (k^2 + l^2)(1 - \alpha_0)]\hat{K} - D_n\kappa^4\mu = 0 \quad (16.36)$$

where \hat{K} denotes the value of K for which the real part of σ equals to zero.

Solving this equation for \hat{K} and replacing $k^2 + l^2$ with $\kappa^2 - m^2$ results in:

$$\hat{K}(\kappa, m) = \frac{\kappa^4}{(\kappa^2 - m^2)[m^2(1 + \alpha_0) + (\kappa^2 - m^2)(1 - \alpha_0)]} \frac{D_n\mu}{Bn_{bg}W_c\Delta\rho\theta} \quad (16.37)$$

To find the critical permeability value, it is necessary to find the minimum value of \hat{K} for all wavenumbers. The investigation of function $\hat{K}(\kappa, m)$ for extremum gives two equations:

$$\frac{\partial \hat{K}}{\partial \kappa} = \frac{2m^2\kappa^3(4m^2\alpha_0 + (1 - 3\alpha_0)\kappa^2)}{(\kappa^2 - m^2)^2(2m^2\alpha_0 + (1 - \alpha_0)\kappa^2)^2} \frac{D_n\mu}{Bn_{bg}W_c\Delta\rho\theta} = 0 \quad (16.38)$$

and

$$\frac{\partial \hat{K}}{\partial m} = -\frac{2m\kappa^4(4m^2\alpha_0 + (1 - 3\alpha_0)\kappa^2)}{(\kappa^2 - m^2)^2(2m^2\alpha_0 + (1 - \alpha_0)\kappa^2)^2} \frac{D_n\mu}{Bn_{bg}W_c\Delta\rho\theta} = 0 \quad (16.39)$$

Both Eqs. (16.38) and (16.39) result in the same equation that relates κ and m :

$$4m^2\alpha_0 + (1 - 3\alpha_0)\kappa^2 = 0 \quad (16.40)$$

Solving Eq. (16.40) for κ gives the following:

$$\kappa = \pm 2m\sqrt{\frac{\alpha_0}{3\alpha_0 - 1}} \quad (16.41)$$

Of the two roots given by Eq. (16.41), only the positive one is relevant. Substituting it in Eq. (16.37) results in:

$$K_{\text{crit}} = \frac{8\alpha_0}{(1 + \alpha_0)^2} \frac{D_n\mu}{Bn_{bg}W_c\Delta\rho\theta} \quad (16.42)$$

Equation (16.42) is valid only if the expression under the square root in Eq. (16.41) is larger or equal to zero, which gives:

$$\alpha_0 \geq \frac{1}{3} \quad (16.43)$$

By definition of α_0 , it may change between zero and unity. According to condition (16.43), Eq. (16.42) for critical permeability can be used only for $\frac{1}{3} \leq \alpha_0 \leq 1$.

If $\alpha_0 \leq \frac{1}{3}$, the function $\hat{K}(\kappa, m)$ defined by Eq. (16.37) does not possess an extremum. In this case its minimum value occurs at the boundary of the domain, at $m=0$, which physically corresponds to the case of no vertical disturbances.

Substituting $m = 0$ into Eq. (16.37) gives the following critical permeability for the case of $\alpha_0 \leq \frac{1}{3}$:

$$K_{\text{crit}} = \frac{1}{(1 - \alpha_0)} \frac{D_n \mu}{B n_b g W_c \Delta \rho \theta} \quad (16.44)$$

Equations (16.42) and (16.44) match at $\alpha_0 = \frac{1}{3}$. These equations for the critical permeability are obtained assuming that its value is small, so that only the linear terms in the Taylor expansion for σ must be retained. From Eqs. (16.42) and (16.44), it follows that this is a good approximation if the diffusivity of cells, D_n , is small.

Equations (16.42) and (16.44) reveal that increasing cell diffusivity increases the critical permeability, which means that it makes the system more stable. This is because diffusion eliminates concentration gradients and makes it more difficult for the instability to develop. Increasing the fluid viscosity also makes the system more stable. Increasing the number density of the cells in the basic state, volume of the cell, density difference, and gravitational acceleration decreases K_{crit} , which means that the system becomes less stable. This is because increasing these parameters increases the buoyancy force on a fluid particle, and thus stimulates the growth of the disturbances. Increasing the average swimming velocity of the cells decreases K_{crit} as well.

Following Pedley et al. [5], the following parameter is introduced:

$$\gamma = \left(\frac{B n_b g W_c \Delta \rho \theta}{D_n \mu} \right)^{1/2} \quad (16.45)$$

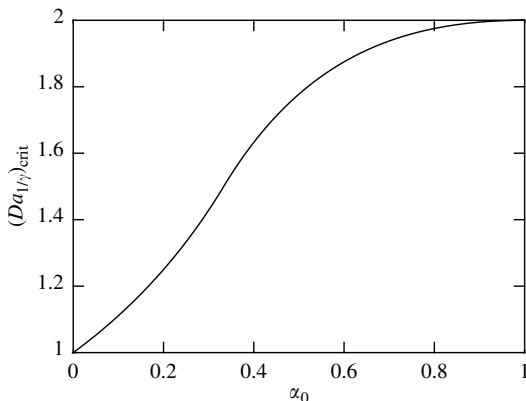
The parameter γ has the dimension $1/m$. This suggests that $1/\gamma$ be used as a length-scale and the introduction of a critical Darcy number defined as:

$$(Da_{1/\gamma})_{\text{crit}} = K_{\text{crit}} \gamma^2 \quad (16.46)$$

In this case Eqs. (16.44) and (16.42) can be recast as:

$$(Da_{1/\gamma})_{\text{crit}} = \begin{cases} 1/(1 - \alpha_0) & \text{for } 0 \leq \alpha_0 \leq \frac{1}{3} \\ 8\alpha_0/(1 + \alpha_0)^2 & \text{for } \frac{1}{3} \leq \alpha_0 \leq 1 \end{cases} \quad (16.47)$$

[Figure 16.1](#) displays the dependence of the critical Darcy number on α_0 . It shows that the transition between the two regions defined in (16.47) is smooth

**FIGURE 16.1**

Dependence of the critical Darcy number on cell eccentricity. (Taken from Kuznetsov and Avramenko, *Transp. Porous Media* 53: 95–104, 2003. With permission.)

and that $(Da_{1/\gamma})_{crit}$ monotonically increases from unity to two as α_0 increases from zero to unity.

16.2.1.2 Investigation of stability under the assumption that the principle of exchange of stabilities is satisfied

If the principle of exchange of stabilities is satisfied, that is, σ is real and the marginal states are characterized by $\sigma = 0$, the analysis can be simplified dramatically. In this case, time derivatives in equations for disturbances (16.12) to (16.15), and (16.22) can be neglected. The substitution of Eqs. (16.23) to (16.27) into these simplified steady equations and subsequent elimination of amplitudes results in the following dispersion relation:

$$\begin{aligned} \kappa^2 \mu \left(D\kappa^2 + imW_c \right) &= Bn_b g KW_c \Delta\rho \theta (\kappa^2 - m^2) \\ &\times [m^2(1 + \alpha_0) + (\kappa^2 - m^2)(1 - \alpha_0)] \end{aligned} \quad (16.48)$$

In Eq. (16.48), there is an imaginary term, imW_c . Therefore, Eq. (16.48) predicts a complex value of critical permeability unless $m = 0$. This proves that the principle of exchange of stabilities is invalid for this system unless the minimum of the function $\hat{K}(\kappa, m)$, which is defined by Eq. (16.37), occurs at $m = 0$. In other words, if m is not zero, then there is a wave motion in the z -direction which means that the system exhibits oscillatory convection. This conclusion is consistent with the analysis carried out in Hill et al. [20] who found regions of overstability for the case of gyrotactic microorganisms suspended in a clear fluid layer of finite depth.

16.2.2 Stability Analysis Accounting for the Absorption of Microorganisms by the Porous Matrix and the Reduction of its Permeability

If a porous matrix absorbs microorganisms, mathematical modeling becomes more involved. In addition to the number density of the suspended motile microorganisms, n_s , there is also the number density of microorganisms captured by the porous matrix, n_c . In addition, absorption of microorganisms by the porous matrix results in biofilm accumulation and thus leads to the decrease of permeability of the porous media. Under these assumptions Eqs. (16.1) to (16.4) still hold, but permeability of the porous medium, K , is no more constant, but is a function of the number density of captured cells. To calculate permeability in Eqs. (16.1) to (16.3) the Carman-Kozeny equation [19] is utilized as:

$$K = \frac{d^2 \varphi^3}{180(1 - \varphi)^2} \quad (16.49)$$

and porosity, φ , is connected to the number density of captured cells, n_c , as:

$$\varphi = \varphi_0 - n_c \theta \quad (16.50)$$

where d is the effective average diameter of a particle or a fiber that compose porous matrix (this is a constant value in this model), n_c is the number density of captured microorganisms, φ is the porosity, and φ_0 is the initial porosity (when there are no captured cells and all cells are suspended cells). The objective of this research is to find a critical value of the initial porosity (φ_0)_{crit}, which determines the boundary between the stable and unstable regimes for this system.

In place of Eq. (16.5) now there are two cell conservation equations, for the suspended and captured cells, respectively:

$$\frac{\partial n_s}{\partial t} = -\text{div}(n_s \mathbf{v} + n_s W_c \hat{\mathbf{p}} - D_n \nabla n_s) - R_a \quad (16.51)$$

$$\frac{\partial n_c}{\partial t} = R_a \quad (16.52)$$

where k_{dep} is the rate of cell deposition, k_{decl} is the rate of cell resuspension (declogging), n_c is the number density of captured microorganisms, and R_a is the net cell deposition rate per unit volume given by the following equation:

$$R_a = k_{\text{dep}} n_s - k_{\text{decl}} n_c \quad (16.53)$$

This model assumes that once the cell is absorbed (captured) by the porous matrix, it can still escape and become a suspended cell again. According to Eq. (16.53), volume rates of cell deposition and resuspension are proportional to number densities of suspended and captured cells, respectively.

As in the previous case, a uniform suspension of microorganisms in an infinite region occupied by an isotropic fluid saturated porous medium of uniform porosity is considered. It is assumed that in the basic state the number density of suspended cells is n_b and the number density of captured cells is $(k_{\text{dep}}/k_{\text{decl}})n_b$.

The perturbations are introduced according to Eqs. (16.6)–(16.11). Additionally, the perturbation of the number density of captured cells is introduced as:

$$n_c(t, x, y, z) = (k_{\text{dep}}/k_{\text{decl}})n_b + \varepsilon n'_c(t, x, y, z) \quad (16.54)$$

Substituting Eqs. (16.6)–(16.11) and (16.54) into the governing equations (16.1)–(16.4) and (16.51)–(16.53) and linearizing gives equations for perturbation quantities. Four of these equations are identical to Eqs. (16.12)–(16.15), however, since permeability now depends on the number density of captured cells, the following Taylor expansion for $1/K$ must be used in Eqs. (16.12)–(16.14):

$$\begin{aligned} \frac{1}{K} &= \frac{180k_{\text{decl}}(k_{\text{decl}} + k_{\text{dep}}n_b\theta - k_{\text{decl}}\varphi_0)^2}{d^2(-k_{\text{dep}}n_b\theta + k_{\text{decl}}\varphi_0)^3} \\ &+ \frac{180k_{\text{decl}}^2\theta(k_{\text{dep}}n_b\theta - k_{\text{decl}}(-3 + \varphi_0))(k_{\text{decl}} + k_{\text{dep}}n_b\theta - k_{\text{decl}}\varphi_0)n'_c}{d^2(k_{\text{dep}}n_b\theta - k_{\text{decl}}\varphi_0)^4}\varepsilon \end{aligned} \quad (16.55)$$

The following two equations hold in place of Eq. (16.16):

$$\frac{\partial n'_s}{\partial t} = -\text{div}[n_b(\mathbf{v}' + W_c \hat{\mathbf{p}}') + n' W_c \hat{\mathbf{k}} - D_n \nabla n'] - (k_{\text{dep}}n'_s - k_{\text{decl}}n'_c) \quad (16.56)$$

$$\frac{\partial n'_c}{\partial t} = k_{\text{dep}}n'_s - k_{\text{decl}}n'_c \quad (16.57)$$

Equations (16.17) to (16.20) for the perturbation of a unit vector indicating the direction of swimming of microorganisms, $\hat{\mathbf{p}}'$, still hold.

The substitution of Eq. (16.17) into Eq. (16.56) results in the following equation for the perturbation of the number density of the suspended cells:

$$\frac{\partial n'_s}{\partial t} + W_c \frac{\partial n'_s}{\partial z} + W_c B n_b \left(\frac{\partial \tilde{\eta}}{\partial x} - \frac{\partial \tilde{\xi}}{\partial y} \right) = D_n \nabla^2 n'_s - (k_{\text{dep}}n'_s - k_{\text{decl}}n'_c) \quad (16.58)$$

where $\tilde{\eta}$ and $\tilde{\xi}$ are still given by Eqs. (16.19) and (16.20).

The governing equations for the perturbation quantities, (16.12)–(16.15), (16.57), and (16.58) are still linear, and therefore, the stability of their solutions can be examined in terms of individual Fourier modes. Perturbation quantities are introduced by Eqs. (16.23)–(16.27). Additionally, the perturbation of

the number density of captured cells is introduced as:

$$n'_c(t, x, y, z) = N_c \exp[\sigma t + i(kx + ly + mz)] \quad (16.59)$$

Substituting Eqs. (16.23)–(16.27) and (16.59) into Eqs. (16.12)–(16.15), (16.57), and (16.58) and accounting for Eqs. (16.19) and (16.20), equations for the amplitudes (U, V, W, P, N_c , and N_s) are obtained. The first of these equations coincides with Eq. (16.28), and the following five equations hold in place of Eqs. (16.29)–(16.32):

$$ikP + U \left(c_a \rho_0 \sigma + \frac{180k_{\text{decl}}\mu(k_{\text{decl}} + k_{\text{dep}}n_b\theta - k_{\text{decl}}\varphi_0)^2}{d^2(-k_{\text{dep}}n_b\theta + k_{\text{decl}}\varphi_0)^3} \right) = 0 \quad (16.60)$$

$$ilP + V \left(c_a \rho_0 \sigma + \frac{180k_{\text{decl}}\mu(k_{\text{decl}} + k_{\text{dep}}n_b\theta - k_{\text{decl}}\varphi_0)^2}{d^2(-k_{\text{dep}}n_b\theta + k_{\text{decl}}\varphi_0)^3} \right) = 0 \quad (16.61)$$

$$imP + gN_s \Delta\rho\theta + c_a W \rho_0 \sigma + \frac{180k_{\text{decl}}\mu(k_{\text{decl}} + k_{\text{dep}}n_b\theta - k_{\text{decl}}\varphi_0)^2}{d^2(-k_{\text{dep}}n_b\theta + k_{\text{decl}}\varphi_0)^3} W = 0 \quad (16.62)$$

$$\begin{aligned} k_{\text{dep}}N_s - k_{\text{decl}}N_c + D_n\kappa^2N_s + Bn_0WW_c(\kappa^2 - m^2)(1 - \alpha_0) \\ - mW_c[-iN_s + Bn_b(kU + lV)(1 + \alpha_0)] + N_s\sigma = 0 \end{aligned} \quad (16.63)$$

$$k_{\text{dep}}N_s - (k_{\text{decl}} + \sigma)N_c = 0 \quad (16.64)$$

The elimination of amplitudes (U, V, W, P, N_c , and N_s) from Eqs. (16.28), (16.60)–(16.64) leads to the following cubic equation for the growth rate σ :

$$\begin{aligned} & -Bn_bgW_c\Delta\rho\theta(\kappa^2 - m^2)[-m^2(1 + \alpha_0) + (\kappa^2 - m^2)(-1 + \alpha_0)](k_{\text{decl}} + \sigma) \\ & - (\mu/K_b)\kappa^2 \left\{ D_n\kappa^2(k_{\text{decl}} + \sigma) + k_{\text{decl}}(imW_c + \sigma) + \sigma(k_{\text{dep}} + imW_c + \sigma) \right\} \\ & - c_a \rho_0 \sigma \kappa^2 \left\{ D_n\kappa^2(k_{\text{decl}} + \sigma) + k_{\text{decl}}(imW_c + \sigma) + \sigma(k_{\text{dep}} + imW_c + \sigma) \right\} = 0 \end{aligned} \quad (16.65)$$

where K_b is the permeability of the porous matrix in the basic state, which is different from the initial permeability of the porous matrix (the permeability of the porous matrix when no cells are attached to it). Because the number density of captured microorganisms in the basic state is $n_b(k_{\text{dep}}/k_{\text{decl}})\theta$, K_b can be calculated as:

$$K_b = \frac{d^2(\varphi_0 - n_b(k_{\text{dep}}/k_{\text{decl}})\theta)^3}{180[1 - (\varphi_0 - n_b(k_{\text{dep}}/k_{\text{decl}})\theta)]^2} \quad (16.66)$$

As a cubic equation, Eq. (16.65) has three roots. To find the critical permeability value, it is necessary to solve the equation $\text{Re}(\sigma_1) = 0$, where σ_1 is the root with the greatest real part. Because permeability is not constant (it depends on the number density of cells absorbed by the porous matrix, n_c), it is possible to talk either about critical *initial permeability* (when no cells are yet attached to the porous matrix) or about *critical permeability in the basic state*, $(K_b)_{\text{crit}}$. Because K_b is naturally present in the dispersion relation (Eq. (16.65)), it is more convenient to solve for $(K_b)_{\text{crit}}$. It is also more convenient to present the results in the dimensionless form to minimize the number of parameters involved. Using $1/\gamma$ as a length-scale (parameter γ is defined in Eq. (16.45)), the critical permeability in the basic state, $(K_b)_{\text{crit}}$, can be used to define the following critical Darcy number:

$$(Da_{1/\gamma})_{\text{crit}} = (K_b)_{\text{crit}} \gamma^2 \quad (16.67)$$

The analysis of Eq. (16.65) (for details of the numerical analysis see Kuznetsov and Avramenko [21]) shows that $(Da_{1/\gamma})_{\text{crit}}$ defined by Eq. (16.66) does not depend on the rates of cell deposition and resuspension, but only depends on cell eccentricity and can be computed utilizing Eq. (16.47).

Once $(Da_{1/\gamma})_{\text{crit}}$ is calculated according to Eq. (16.47), the critical initial porosity $(\varphi_0)_{\text{crit}}$ can be calculated by solving the following equation:

$$\frac{((\varphi_0)_{\text{crit}} - (k_{\text{dep}}/k_{\text{decl}})(n_b \theta))^3}{180[1 - ((\varphi_0)_{\text{crit}} - (k_{\text{dep}}/k_{\text{decl}})(n_b \theta))]^2} = \frac{(Da_{1/\gamma})_{\text{crit}}}{(\gamma d)^2} \quad (16.68)$$

and the critical initial permeability can be calculated by substituting the obtained value of $(\varphi_0)_{\text{crit}}$ into Eq. (16.49).

16.2.3 Stability Analysis of Bioconvection of Gyrotactic Microorganisms in a Layer of Final Depth

This problem was analyzed in Nield et al. [22]. For this analysis, it is assumed that the porous matrix does not absorb microorganisms. Further, it is assumed that the pores are large compared with the microorganisms so that the permeability of the medium is not changed by the presence of microorganisms. Governing equations for this problem are given by Eqs. (16.1) to (16.5).

A horizontal layer of porous medium of depth H is considered. Cartesian axes with the vertical z -axis are chosen, so that the layer is confined between $z = 0$ and $z = H$. The layer is unbounded in the x and y directions. The equation of continuity admits a steady-state solution where n_b , the number density of the microorganisms in the basic state and P_b , the pressure distribution in the basic state are functions of z only, while all components of the velocity are zero.

Under this assumption Eq. (16.5) can be solved to give

$$n_b(z) = \nu \exp\left(\frac{W_c z}{D_n}\right) \quad (16.69)$$

The integration constant ν , which represents the value of the basic number density at the bottom of the layer, is related to the average concentration of suspended microorganisms, \bar{n}_s , by

$$\nu = \frac{\hat{n}_s Q}{\exp(Q) - 1} \quad (16.70)$$

where

$$\hat{n}_s = \frac{1}{H} \int_0^H n_b(z) dz \quad (16.71)$$

and the Péclet number for bioconvection caused by gyrotactic microorganisms, Q , is defined by

$$Q = \frac{W_c H}{D_n} \quad (16.72)$$

The perturbations are introduced by Eqs. (16.7)–(16.11), and the perturbation of the number density of suspended cells is introduced by the following equation:

$$n_s(t, x, y, z) = n_b(z) + \varepsilon n'(t, x, y, z) \quad (16.73)$$

where $n_b(z)$ is given by Eq. (16.69). Substituting Eqs. (16.7)–(16.11) and (16.69) into Eqs. (16.1)–(16.5) and linearizing results in the following equations for perturbations, four of which coincide with Eqs. (16.12)–(16.15), and the following equation replaces Eq. (16.16):

$$\frac{\partial n'_s}{\partial t} = -\text{div} \left[n_b (\mathbf{v}' + W_c \hat{\mathbf{p}}') + n'_s W_c \hat{\mathbf{k}} - D_n \nabla n'_s \right] \quad (16.74)$$

Equations (16.17)–(16.20) for the vector $\hat{\mathbf{p}}'$ still hold and Eq. (16.74) can be rewritten as follows

$$\frac{\partial n'_s}{\partial t} = -w' \frac{\partial n_b}{\partial z} - W_c \frac{\partial n'_s}{\partial z} - W_c B n_0 \left(\frac{\partial \tilde{\eta}}{\partial x} - \frac{\partial \tilde{\xi}}{\partial y} \right) + D_n \nabla^2 n'_s \quad (16.75)$$

A normal mode expansion is introduced in the following form:

$$[u', v', w', p', n'] = [U(z), V(z), W(z), P(z), N(z)] f(x, y) \exp(\sigma t) \quad (16.76)$$

Substituting Eq. (16.76) into Eqs. (16.17)–(16.20) and (16.75), the following equations for the amplitudes U , V , W , P , and N are obtained:

$$U \frac{\partial f}{\partial x} + V \frac{\partial f}{\partial y} + \frac{dW}{dz} f = 0 \quad (16.77)$$

$$KP \frac{\partial f}{\partial x} + U(\mu + c_a \rho_0 K \sigma) f = 0 \quad (16.78)$$

$$KP \frac{\partial f}{\partial y} + V(\mu + c_a \rho_0 K \sigma) f = 0 \quad (16.79)$$

$$K \frac{dP}{dz} + W(\mu + c_a \rho_0 K \sigma) + g K \Delta \rho \theta N = 0 \quad (16.80)$$

In order to separate the variables, the horizontal wavenumber m is introduced as a separation constant, so that

$$\frac{\partial^2 f}{\partial x^2} + \frac{\partial^2 f}{\partial y^2} = -m^2 f \quad (16.81)$$

Eliminating P , U , and V from Eqs. (16.77)–(16.80), these equations are reduced to the following two equations for $W(z)$ and $N(z)$:

$$(\mu + c_a \rho_0 K \sigma) \left[\frac{d^2}{dz^2} - m^2 \right] W = m^2 g K \Delta \rho \theta N \quad (16.82)$$

and

$$\begin{aligned} & \left[D_n \frac{d^2}{dz^2} - W_c \frac{d}{dz} - (D_n m^2 + \sigma) \right] N \\ &= \left[\frac{dn_0}{dz} + B n_0 W_c \left(m^2 (1 - \alpha_0) - (1 + \alpha_0) \frac{d^2}{dz^2} \right) \right] W \end{aligned} \quad (16.83)$$

To recast Eqs. (16.82) and (16.83) in nondimensional form, the following scalings are introduced:

$$\bar{z} = \frac{z}{H}, \quad a = mH, \quad \bar{W} = \left(\frac{v\theta W_c H^2}{D_n^2} \right) W, \quad \bar{N} = N\theta \quad (16.84)$$

The dimensionless Rayleigh number R and the gyrotaxis number G are introduced as:

$$R = \frac{v\theta g K H^2 W_c \Delta \rho}{\mu D_n^2}, \quad G = \frac{\alpha_\perp D_n \mu}{2ghH^2 \rho_0} \quad (16.85)$$

According to Eq. (16.85), R is the product of a regular Rayleigh–Darcy number $gKH\Delta\rho/(\mu D_n)$, the Péclet number Q , and a microorganism number $\nu\theta$, while $G = D_n B/H^2$.

As indicated in Nield et al. [22], there is no restoring mechanism here which can cause oscillatory instability, and hence the principle of exchange of stabilities [23] can be invoked and σ can be set to zero for the onset of instability. (Hill et al. [20] confirmed by numerical calculation that, in the case of a clear fluid, oscillatory convection could not occur unless vorticity was produced as a result of a no-slip condition at a rigid boundary, and clearly this effect is absent here.) Equations (16.82) and (16.83) then reduce to

$$\left[\frac{d^2}{d\bar{z}^2} - a^2 \right] \bar{W} = a^2 R \bar{N} \quad (16.86)$$

$$\left[\frac{d^2}{d\bar{z}^2} - Q \frac{d}{d\bar{z}} - a^2 \right] \bar{N} = \exp(Q\bar{z}) \left[1 + G \left(a^2(1 - \alpha_0) - (1 + \alpha_0) \frac{d^2}{d\bar{z}^2} \right) \right] \bar{W} \quad (16.87)$$

Equations (16.86) and (16.87) constitute a fourth-order differential equation system. They must be solved subject to four boundary conditions, which in the case of boundaries that are impermeable to both the fluid and the swimming organisms, are

$$\bar{W} = \frac{d\bar{N}}{d\bar{z}} - Q\bar{N} = 0 \quad \text{at} \quad \bar{z} = 0 \quad \text{and} \quad \bar{z} = 1 \quad (16.88)$$

For the solution of this system, a simple Galerkin method is utilized. Suitable trial functions (satisfying the boundary conditions) are

$$\bar{W}_1 = \bar{z} - \bar{z}^2 \quad (16.89)$$

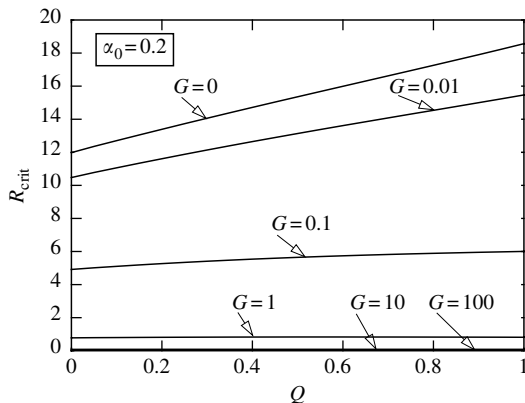
$$\bar{N}_1 = 2 - Q(1 - 2\bar{z}) - Q^2(\bar{z} - \bar{z}^2) \quad (16.90)$$

The standard procedure [24] leads to

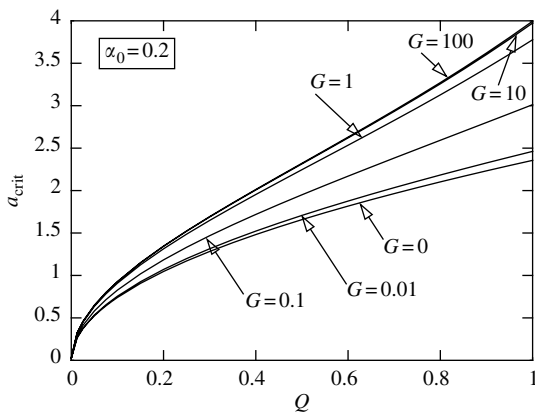
$$\begin{aligned} R_{\text{crit}} &= \min_a \\ &\frac{(10 + a^2)Q^3[a^2(120 - 10Q^2 + Q^4) + 10Q^4]}{\{30a^2(10 - Q^2)16 - a^2G(4 + Q)^2(-1 + \alpha_0) + Q(8 + Q(1 - 4G(1 + \alpha_0))) \\ &+ e^Q[-16 + a^2G(-4 + Q)^2(-1 + \alpha_0) + Q(8 + Q(-1 + 4G(1 + \alpha_0)))]\}} \end{aligned} \quad (16.91)$$

Equation (16.91) corrects a typo in Eq. (41) of ref. [22].

The fact that there exists a critical value of the bioconvection Rayleigh number defined in Eq. (16.91) shows that a critical value K_{crit} of the permeability K

**FIGURE 16.2**

Plots of critical bioconvection Rayleigh number R_{crit} versus bioconvection Péclet number Q , for various values of the gyrotaxis number G , for cell eccentricity $\alpha_0 = 0.2$. (Taken from Nield et al., *Transp. Porous Media* 54: 335–344, 2004. With permission.)

**FIGURE 16.3**

Plots of critical wavenumber a_{crit} versus bioconvection Péclet number Q , for various values of the gyrotaxis number G , for cell eccentricity $\alpha_0 = 0.2$. (Taken from Nield et al., *Transp. Porous Media* 54: 335–344, 2004. With permission.)

must be exceeded for bioconvection to occur in a porous medium, namely

$$K_c = \frac{\mu D_n^2}{R_c v \theta g H^2 W_c \Delta \rho} \quad (16.92)$$

In Figure 16.2 and Figure 16.3, the critical bioconvection Rayleigh number R_{crit} and the corresponding critical wave number a_{crit} , respectively, are plotted against the bioconvection Péclet number Q for various values of the gyrotaxis

number G , for a typical value ($\alpha_0 = 0.2$) of the measure of cell eccentricity. It is seen that both R_{crit} and a_{crit} increase as Q increases, and decrease as G increases. For large G , R_{crit} is approximately inversely proportional to G .

16.3 Stability of a Suspension of Oxytactic Microorganisms in a Fluid Saturated Porous Medium and Analysis of a Bioconvection Plume Caused by these Microorganisms

16.3.1 Stability of a Shallow Layer

Many bacterial species swim up the oxygen gradients. This behavior is called oxytaxis. Bioconvection in suspensions of oxytactic bacteria is investigated in Hillesdon et al. [25], Hillesdon and Pedley [26], and Metcalfe and Pedley [27, 28].

Oxytactic bacteria require oxygen for their metabolism and swim up the oxygen gradients. They require a minimum oxygen concentration, C_{\min} , in order to be active. Since this chapter deals with a shallow layer, it is assumed that even at the bottom of the layer the oxygen concentration is larger than the minimum concentration. In this case, the average swimming velocity of a bacterium can be approximated as

$$\mathbf{V} = bW_c \hat{H}(\bar{C}) \nabla \bar{C} \quad (16.93)$$

where

$$\bar{C} = (C - C_{\min}) / (C_0 - C_{\min}) \quad (16.94)$$

is the dimensionless oxygen concentration, C is the dimensional oxygen concentration, C_0 is the free-surface oxygen concentration, b has dimensions of length, and W_c has dimensions of velocity (the product bW_c is assumed to be constant). Since for the shallow layer $\bar{C} > 0$ throughout the layer thickness, the Heaviside step function, $\hat{H}(\bar{C})$, equals to unity. The layer is of depth H and is assumed to be infinitely large in the horizontal dimensions.

The governing equations for this problem can be presented as follows. The momentum equation is

$$c_a \rho \frac{\partial \mathbf{U}}{\partial t} = -\nabla p_e - \frac{\mu}{K} \mathbf{U} + n_s \theta \Delta \rho g \mathbf{k} \quad (16.95)$$

where c_a is the acceleration coefficient; g is the gravity; \mathbf{k} is the vertically downward unit vector; K is the permeability of the porous medium; n_s is the number density of oxytactic cells; p_e is the excess pressure (above hydrostatic); t is the time; \mathbf{U} is the fluid filtration velocity whose components are (u, v, w) ; x, y , and z are the Cartesian coordinates (z is the vertically downward

coordinate); $\Delta\rho$ is the density difference, $\rho_{\text{cell}} - \rho$; μ is the dynamic viscosity, assumed to be approximately the same as that of water; θ is the average volume of the bacterium; and ρ is the density of water.

The continuity equation is

$$\frac{\partial u}{\partial x} + \frac{\partial v}{\partial y} + \frac{\partial w}{\partial z} = 0 \quad (16.96)$$

The equation expressing the conservation of cells is

$$\frac{\partial n_s}{\partial t} = -\nabla \cdot (n_s \mathbf{U} + n_s b W_c \hat{H}(\bar{C}) \nabla \bar{C} - D_n \nabla n_s) \quad (16.97)$$

where D_n is the cell diffusivity (the diffusion term models the random aspects of cell swimming). The equation expressing the conservation of oxygen is

$$\frac{\partial \bar{C}}{\partial t} = -\nabla \cdot (\bar{C} \mathbf{U} - D_C \nabla \bar{C}) - \frac{\tilde{\gamma} n_s}{\Delta C} \quad (16.98)$$

where D_C is the oxygen diffusivity, the term $-\tilde{\gamma} n_s$ describes the consumption of oxygen by the bacteria, and ΔC equals $C_0 - C_{\min}$.

Similar to Eqs. (16.5) and (16.5a), Eqs. (16.97) and (16.98) are the simplified forms of the following more general equations:

$$\varphi \frac{\partial n_s}{\partial t} = -\nabla \cdot (n_s \mathbf{U} + n_s (b W_c)_{\text{eff}} \hat{H}(\bar{C}) \nabla \bar{C} - D_{n,\text{eff}} \nabla n_s) \quad (16.97a)$$

$$\varphi \frac{\partial \bar{C}}{\partial t} = -\nabla \cdot (\bar{C} \mathbf{U} - D_{C,\text{eff}} \nabla \bar{C}) - \frac{\tilde{\gamma}_{\text{eff}} n_s}{\Delta C} \quad (16.98a)$$

Equations (16.97a) and (16.98a) take into account that in the porous medium, the concentrations of cells and oxygen are advected/convected with the intrinsic velocity since the cells and oxygen cannot pass through the solid phase. Utilizing assumptions similar to those made for the transformation of Eq. (16.5a) to Eq. (16.5), Eqs. (16.97a) and (16.98a) can be reduced to Eqs. (16.97) and (16.98), respectively.

Governing equations (16.95) to (16.98) must be solved subject to the following boundary conditions:

$$\text{At } z = 0: \bar{C} = 1, \quad n_s b W_c \frac{\partial \bar{C}}{\partial z} - D_n \frac{\partial n_s}{\partial z} = 0, \quad w = 0 \quad (16.99)$$

where the second equation in (16.99) means no cell flux through the free surface.

$$\text{At } z = H: \frac{\partial \bar{C}}{\partial z} = 0, \quad n_s b W_c \frac{\partial \bar{C}}{\partial z} - D_n \frac{\partial n_s}{\partial z} = 0, \quad w = 0 \quad (16.100)$$

Initially, the fluid is assumed to be well-stirred and motionless:

$$\text{At } t = 0: \bar{C} = 1, \quad n_s = n_0, \quad u = v = w = 0 \quad (16.101)$$

Dimensionless variables are introduced as follows:

$$\begin{aligned} \bar{n} &= n_s/n_0, \quad [\bar{x}, \bar{y}, \bar{z}] = [x, y, z]/H, \quad \bar{t} = \left(\frac{D_n}{H^2}\right)t \\ [\bar{u}, \bar{v}, \bar{w}] &= \left(\frac{H}{D_n}\right)[u, v, w], \quad \bar{p}_e = \left(\frac{H^2}{\mu D_n}\right)p_e \end{aligned} \quad (16.102)$$

Dimensionless constants are defined as

$$\begin{aligned} \delta &= D_C/D_n, \quad Pe = bW_c/D_n, \quad \beta = (\tilde{\gamma}n_0H^2)/(D_C\Delta C) \\ Da &= K/H^2, \quad Sc = \mu/(c_a\rho D_n), \quad Ra = \frac{\Delta\rho\theta n_0 g}{\mu D_n} H^3 \end{aligned} \quad (16.103)$$

where Ra is the Rayleigh number and Sc is the Schmidt number. Ra characterizes the ratio of the rate of oxygen consumption to the rate of oxygen diffusion, it can be regarded as a depth parameter [26]. Pe can be regarded as a ratio of characteristic velocity due to oxytactic swimming to characteristic velocity due to random, diffusive swimming.

In Cartesian coordinates the dimensionless governing equations can be presented as:

$$\frac{Da}{Sc} \frac{\partial \bar{u}}{\partial \bar{t}} = -Da \frac{\partial \bar{p}_e}{\partial \bar{x}} - \bar{u} \quad (16.104)$$

$$\frac{Da}{Sc} \frac{\partial \bar{v}}{\partial \bar{t}} = -Da \frac{\partial \bar{p}_e}{\partial \bar{y}} - \bar{v} \quad (16.105)$$

$$\frac{Da}{Sc} \frac{\partial \bar{w}}{\partial \bar{t}} = -Da \frac{\partial \bar{p}_e}{\partial \bar{z}} - \bar{w} + Ra Da \bar{n} \quad (16.106)$$

$$\frac{\partial \bar{u}}{\partial \bar{x}} + \frac{\partial \bar{v}}{\partial \bar{y}} + \frac{\partial \bar{w}}{\partial \bar{z}} = 0 \quad (16.107)$$

$$\begin{aligned} \frac{\partial \bar{n}}{\partial \bar{t}} + \left(\bar{u} + Pe \frac{\partial \bar{C}}{\partial \bar{x}}\right) \frac{\partial \bar{n}}{\partial \bar{x}} + \left(\bar{v} + Pe \frac{\partial \bar{C}}{\partial \bar{y}}\right) \frac{\partial \bar{n}}{\partial \bar{y}} + \left(\bar{w} + Pe \frac{\partial \bar{C}}{\partial \bar{z}}\right) \frac{\partial \bar{n}}{\partial \bar{z}} \\ + Pe \bar{n} \left(\frac{\partial^2 \bar{C}}{\partial \bar{x}^2} + \frac{\partial^2 \bar{C}}{\partial \bar{y}^2} + \frac{\partial^2 \bar{C}}{\partial \bar{z}^2}\right) = \frac{\partial^2 \bar{n}}{\partial \bar{x}^2} + \frac{\partial^2 \bar{n}}{\partial \bar{y}^2} + \frac{\partial^2 \bar{n}}{\partial \bar{z}^2} \end{aligned} \quad (16.108)$$

$$\frac{\partial \bar{C}}{\partial \bar{t}} + \bar{u} \frac{\partial \bar{C}}{\partial \bar{x}} + \bar{v} \frac{\partial \bar{C}}{\partial \bar{y}} + \bar{w} \frac{\partial \bar{C}}{\partial \bar{z}} = \delta \left(\frac{\partial^2 \bar{C}}{\partial \bar{x}^2} + \frac{\partial^2 \bar{C}}{\partial \bar{y}^2} + \frac{\partial^2 \bar{C}}{\partial \bar{z}^2}\right) - \beta \delta \bar{n} \quad (16.109)$$

Dimensionless boundary and initial conditions are:

$$\text{At } \bar{z} = 0: \bar{C} = 1, \quad Pe \bar{n} \frac{\partial \bar{C}}{\partial \bar{z}} - \frac{\partial \bar{n}}{\partial \bar{z}} = 0, \quad \bar{w} = 0 \quad (16.110\text{a-c})$$

$$\text{At } \bar{z} = 1: \frac{\partial \bar{C}}{\partial \bar{z}} = 0, \quad Pe \bar{n} \frac{\partial \bar{C}}{\partial \bar{z}} - \frac{\partial \bar{n}}{\partial \bar{z}} = 0, \quad \bar{w} = 0 \quad (16.111\text{a-c})$$

$$\text{At } \bar{t} = 0: \bar{C} = 1, \quad \bar{n} = 1, \quad \bar{u} = \bar{v} = \bar{w} = 0 \quad (16.112\text{a-c})$$

In the basic state the fluid is motionless and the cell and oxygen concentrations change in the z -direction only. Dimensionless equations for the basic state are:

$$\frac{d\bar{C}_b}{d\bar{z}} \frac{d\bar{n}_b}{d\bar{z}} + \bar{n}_b \frac{d^2\bar{C}_b}{d\bar{z}^2} = \frac{1}{Pe} \frac{d^2\bar{n}_b}{d\bar{z}^2} \quad (16.113)$$

$$\frac{d^2\bar{C}_b}{d\bar{z}^2} - \beta \bar{n}_b = 0 \quad (16.114)$$

where subscript b denotes the steady-state solution for the basic state.

Equations (16.113) and (16.114) must be solved subject to boundary conditions (16.110a,b) and (16.111a,b). In addition, the following integral constraint must be satisfied:

$$\int_0^1 \bar{n}_b d\bar{z} = 1 \quad (16.115)$$

Solution of this problem is found in Hillesdon et al. [25] as:

$$\bar{C}_b(\bar{z}) = 1 - \frac{2}{Pe} \ln \left(\frac{\cos\{A_1(1-\bar{z})/2\}}{\cos\{A_1/2\}} \right) \quad (16.116)$$

$$\bar{n}_b(\bar{z}) = \frac{A_1^2}{2Pe\beta} \sec^2 \left(\frac{A_1}{2}(1-\bar{z}) \right) \quad (16.117)$$

where constant A_1 is found as:

$$\tan(A_1/2) = Pe \beta / A_1 \quad (16.118)$$

The solution for the basic state given by Eqs. (16.116) to (16.118) is valid as long as the oxygen concentration is positive throughout the layer. In Hillesdon and Pedley [26], it is shown that this condition holds as long as

$$Pe \beta \leq 2\phi \tan^{-1} \phi \quad (16.119)$$

where $\phi^2 = \exp(Pe) - 1$.

Perturbations to the basic state are introduced as follows:

$$\bar{\mathbf{u}}(\bar{t}, \bar{x}, \bar{y}, \bar{z}) = \varepsilon \bar{\mathbf{u}}'(\bar{t}, \bar{x}, \bar{y}, \bar{z}) \quad (16.120)$$

$$\bar{n}(\bar{t}, \bar{x}, \bar{y}, \bar{z}) = \bar{n}_b(\bar{z}) + \varepsilon \bar{n}'(\bar{t}, \bar{x}, \bar{y}, \bar{z}) \quad (16.121)$$

$$\bar{C}(\bar{t}, \bar{x}, \bar{y}, \bar{z}) = \bar{C}_b(\bar{z}) + \varepsilon \bar{C}'(\bar{t}, \bar{x}, \bar{y}, \bar{z}) \quad (16.122)$$

$$\bar{p}_e(\bar{t}, \bar{x}, \bar{y}, \bar{z}) = \bar{p}_{e,b}(\bar{z}) + \varepsilon \bar{p}'_e(\bar{t}, \bar{x}, \bar{y}, \bar{z}) \quad (16.123)$$

where primes denote the perturbation quantities; the components of $\bar{\mathbf{u}}$ and $\bar{\mathbf{u}}'$ are $(\bar{u}, \bar{v}, \bar{w})$ and $(\bar{u}', \bar{v}', \bar{w}')$, respectively; ε is a small perturbation amplitude; $\bar{C}_b(\bar{z})$ and $\bar{n}_b(\bar{z})$ are the steady-state solutions in the basic state which are given by Eqs. (16.116) and (16.117); and $d\bar{p}_{e,b}/d\bar{z} = Ra \bar{n}_b(\bar{z})$ from Eq. (16.106).

Upon substituting Eqs. (16.120)–(16.123) into dimensionless governing equations (16.104)–(16.109), the following equations for perturbation quantities are obtained:

$$\frac{Da}{Sc} \frac{\partial \bar{u}'}{\partial \bar{t}} = -Da \frac{\partial \bar{p}'_e}{\partial \bar{x}} - \bar{u}' \quad (16.124)$$

$$\frac{Da}{Sc} \frac{\partial \bar{v}'}{\partial \bar{t}} = -Da \frac{\partial \bar{p}'_e}{\partial \bar{y}} - \bar{v}' \quad (16.125)$$

$$\frac{Da}{Sc} \frac{\partial \bar{w}'}{\partial \bar{t}} = -Da \frac{\partial \bar{p}'_e}{\partial \bar{z}} - \bar{w}' + Ra Da \bar{n}' \quad (16.126)$$

$$\frac{\partial \bar{u}'}{\partial x} + \frac{\partial \bar{v}'}{\partial y} + \frac{\partial \bar{w}'}{\partial z} = 0 \quad (16.127)$$

$$\begin{aligned} \frac{\partial \bar{n}'}{\partial \bar{t}} + \bar{w}' \frac{d\bar{n}_b(\bar{z})}{d\bar{z}} + Pe \bar{n}' \frac{d^2 \bar{C}_b(\bar{z})}{d\bar{z}^2} + Pe \frac{d\bar{n}_b(\bar{z})}{d\bar{z}} \frac{\partial \bar{C}'}{\partial \bar{z}} + Pe \frac{d\bar{C}_b(\bar{z})}{d\bar{z}} \frac{\partial \bar{n}'}{\partial \bar{z}} \\ + Pe \bar{n}_b(\bar{z}) \left(\frac{\partial^2 \bar{C}'}{\partial \bar{x}^2} + \frac{\partial^2 \bar{C}'}{\partial \bar{y}^2} + \frac{\partial^2 \bar{C}'}{\partial \bar{z}^2} \right) = \frac{\partial^2 \bar{n}'}{\partial \bar{x}^2} + \frac{\partial^2 \bar{n}'}{\partial \bar{y}^2} + \frac{\partial^2 \bar{n}'}{\partial \bar{z}^2} \end{aligned} \quad (16.128)$$

$$\frac{\partial \bar{C}'}{\partial \bar{t}} + \bar{w}' \frac{d\bar{C}_b(\bar{z})}{d\bar{z}} = \delta \left(\frac{\partial^2 \bar{C}'}{\partial \bar{x}^2} + \frac{\partial^2 \bar{C}'}{\partial \bar{y}^2} + \frac{\partial^2 \bar{C}'}{\partial \bar{z}^2} \right) - \beta \delta \bar{n}' \quad (16.129)$$

From Eqs. (16.124)–(16.127) it follows that

$$-\left(\frac{\partial^2 \bar{p}'_e}{\partial \bar{x}^2} + \frac{\partial^2 \bar{p}'_e}{\partial \bar{y}^2} + \frac{\partial^2 \bar{p}'_e}{\partial \bar{z}^2} \right) + Ra \frac{\partial \bar{n}'}{\partial \bar{z}} = 0 \quad (16.130)$$

Thus \bar{u}' and \bar{v}' are eliminated, and Eqs. (16.126) and (16.128)–(16.130) contain \bar{p}'_e , \bar{w}' , \bar{n}' , and \bar{C}' only. From Eq. (16.126) the following is obtained:

$$\begin{aligned} \frac{Da}{Sc} \frac{\partial}{\partial \bar{t}} & \left(\frac{\partial^2 \bar{w}'}{\partial \bar{x}^2} + \frac{\partial^2 \bar{w}'}{\partial \bar{y}^2} + \frac{\partial^2 \bar{w}'}{\partial \bar{z}^2} \right) \\ & = -Da \frac{\partial}{\partial \bar{z}} \left(\frac{\partial^2 \bar{p}'_e}{\partial \bar{x}^2} + \frac{\partial^2 \bar{p}'_e}{\partial \bar{y}^2} + \frac{\partial^2 \bar{p}'_e}{\partial \bar{z}^2} \right) - \left(\frac{\partial^2 \bar{w}'}{\partial \bar{x}^2} + \frac{\partial^2 \bar{w}'}{\partial \bar{y}^2} + \frac{\partial^2 \bar{w}'}{\partial \bar{z}^2} \right) \\ & \quad + Ra Da \left(\frac{\partial^2 \bar{n}'}{\partial \bar{x}^2} + \frac{\partial^2 \bar{n}'}{\partial \bar{y}^2} + \frac{\partial^2 \bar{n}'}{\partial \bar{z}^2} \right) \end{aligned} \quad (16.131)$$

Substituting $\nabla^2 \bar{p}'_e$ from Eq. (16.130) into Eq. (16.131), the following is obtained:

$$\begin{aligned} \frac{Da}{Sc} \frac{\partial}{\partial \bar{t}} \left(\frac{\partial^2 \bar{w}'}{\partial \bar{x}^2} + \frac{\partial^2 \bar{w}'}{\partial \bar{y}^2} + \frac{\partial^2 \bar{w}'}{\partial \bar{z}^2} \right) & = Ra Da \left(\frac{\partial^2 \bar{n}'}{\partial \bar{x}^2} + \frac{\partial^2 \bar{n}'}{\partial \bar{y}^2} \right) \\ & \quad - \left(\frac{\partial^2 \bar{w}'}{\partial \bar{x}^2} + \frac{\partial^2 \bar{w}'}{\partial \bar{y}^2} + \frac{\partial^2 \bar{w}'}{\partial \bar{z}^2} \right) \end{aligned} \quad (16.132)$$

Thus \bar{p}'_e is also eliminated, Eqs. (16.128), (16.129), and (16.132) are expressed in terms of \bar{w}' , \bar{n}' , and \bar{C}' only. Decomposing \bar{w}' , \bar{n}' , and \bar{C}' into normal modes as

$$[\bar{w}', \bar{n}', \bar{C}'] = [W(\bar{z}), N(\bar{z}), \Xi(\bar{z})] f(\bar{x}, \bar{y}) \exp(\sigma \bar{t}) \quad (16.133)$$

where $W(\bar{z})$, $N(\bar{z})$, and $\Xi(\bar{z})$ are the amplitudes of perturbed values and f is the horizontal planform function, which satisfies the following equation:

$$\frac{\partial^2 f}{\partial \bar{x}^2} + \frac{\partial^2 f}{\partial \bar{y}^2} = -\bar{k}^2 f \quad (16.134)$$

In Eq. (16.134), k is a constant dimensionless wavenumber which is defined as

$$\bar{k} = kH \quad (16.135)$$

and which corresponds to the dimensionless wavelength $\bar{\lambda} = 2\pi/\bar{k}$.

Substituting Eqs. (16.133) into Eqs. (16.128), (16.129), and (16.132) results in the following equations for the amplitudes $W(\bar{z})$, $N(\bar{z})$, and $\Xi(\bar{z})$:

$$\begin{aligned} Pe \frac{d\bar{C}_b(\bar{z})}{d\bar{z}} \frac{dN(\bar{z})}{d\bar{z}} + \frac{d\bar{n}_b(\bar{z})}{d\bar{z}} \left\{ W(\bar{z}) + Pe \frac{d\Xi(\bar{z})}{d\bar{z}} \right\} + N(\bar{z}) \left(\bar{k}^2 + \sigma + Pe \frac{d^2\bar{C}_b(\bar{z})}{d\bar{z}^2} \right) \\ - \frac{d^2N(\bar{z})}{d\bar{z}^2} + Pe \bar{n}_b(\bar{z}) \left\{ -\bar{k}^2 \Xi(\bar{z}) + \frac{d^2\Xi(\bar{z})}{d\bar{z}^2} \right\} = 0 \end{aligned} \quad (16.136)$$

$$\beta \delta N(\bar{z}) + (\bar{k}^2 \delta + \sigma) \Xi(\bar{z}) + W(\bar{z}) \frac{d\bar{C}_b(\bar{z})}{d\bar{z}} - \delta \frac{d^2\Xi(\bar{z})}{d\bar{z}^2} = 0 \quad (16.137)$$

$$Da \bar{k}^2 Ra Sc N(\bar{z}) - (Sc + Da \sigma) \left\{ \bar{k}^2 W(\bar{z}) - \frac{d^2W(\bar{z})}{d\bar{z}^2} \right\} = 0 \quad (16.138)$$

where steady-state solutions for the basic state, $\bar{C}_b(\bar{z})$ and $\bar{n}_b(\bar{z})$, are given by Eqs. (16.116) and (16.117), respectively.

Equations (16.136) to (16.138) represent a sixth-order system of ordinary differential equations that must be solved subject to the following boundary conditions:

$$\text{At } \bar{z} = 0: \Xi = 0, \quad Pe \left(\bar{n}_b|_{\bar{z}=0} \frac{d\Xi}{d\bar{z}} + \frac{d\bar{C}_b}{d\bar{z}} \Big|_{\bar{z}=0} N \right) - \frac{dN}{d\bar{z}} = 0, \quad W = 0 \quad (16.139)$$

$$\text{At } \bar{z} = 1: \frac{d\Xi}{d\bar{z}} = 0, \quad \frac{dN}{d\bar{z}} = 0, \quad W = 0 \quad (16.140)$$

For an oscillatory instability to occur, there must be two competing physical mechanisms at work, one destabilizing and one stabilizing. According to Hillesdon and Pedley [26], double-diffusive convection itself cannot provide the second (stabilizing) mechanism in this case because one of the diffusing species (oxygen) does not contribute to buoyancy. Hillesdon and Pedley [26] have shown that in the case of a deep layer there are indeed two mechanisms, the destabilizing mechanism obviously comes from the unstable density stratification in the upper region while the stabilizing mechanism comes from the stable density stratification in the lower region (the region where the oxygen concentration is so low that the bacteria become inactive). For the case of a shallow layer there is no lower region because the oxygen concentration is larger than the minimum concentration throughout the layer; therefore, only the destabilizing mechanism is present. For this reason, it is logical to assume that the principle of exchange of stabilities [23] applies to this problem, the instability is stationary, and σ can be set to zero for the onset of instability.

Solution of Eqs. (16.136) to (16.138) (once σ is set to zero) depends on four dimensionless parameters: δ , β , Pe , and $Da Ra$. For the solution of this system,

a simple Galerkin method is utilized. Suitable trial functions (satisfying the boundary conditions [16.139] and [16.140]) are

$$W = \bar{z} - \bar{z}^2, \quad \Xi = \bar{z} - \frac{1}{2}\bar{z}^2, \quad N = 1 + v(\bar{z} - \frac{1}{2}\bar{z}^2) \quad (16.141)$$

where

$$v = \frac{A_1(A_1 - \beta \sin A_1)}{\beta(1 + \cos A_1)} \quad (16.142)$$

Following the standard procedure [24], the following equation for the critical value of $Ra Da$ is obtained [29]:

$$(Ra Da)_{\text{crit}} = \min_b \frac{8(10 + b)Pe \beta \delta \{(I_4 + b\{2 + (4v/3) + (4v^2/15)\})(5 + 2b) + A_1^3 I_3(5 + 2v)\}}{A_1^3 b(20 + 7v)\{15A_1 I_1 I_3 + 2I_2(5 + 2b)(1 + \delta)\}} \quad (16.143)$$

where $b = \bar{k}^2$ and

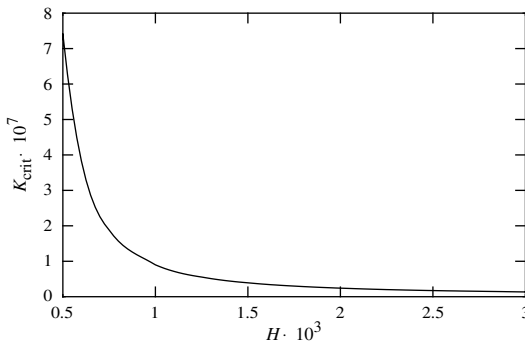
$$\begin{aligned} I_1 &= \int_0^1 (\bar{z} - 2)(\bar{z} - 1)\bar{z}^2 \tan \left\{ \frac{1}{2}A_1(1 - \bar{z}) \right\} d\bar{z} \\ I_2 &= \int_0^1 \bar{z}F(\bar{z})d\bar{z}, \quad I_3 = \int_0^1 F(\bar{z})d\bar{z} \end{aligned} \quad (16.144)$$

$$F(\bar{z}) = (\bar{z} - 1) \left(1 - \frac{1}{2}(\bar{z} - 2)\bar{z}v \right) \sec^2 \left\{ \frac{1}{2}A_1(\bar{z} - 1) \right\} \tan \left(\frac{1}{2}A_1(\bar{z} - 1) \right) \quad (16.145)$$

$$\begin{aligned} I_4 &= \int_0^1 \left(1 - \frac{1}{2}(\bar{z} - 2)\bar{z}v \right) \left[2v + A_1^2\{2 - (\bar{z} - 2)\bar{z}v\} \sec^2 \left\{ \frac{1}{2}A_1(\bar{z} - 1) \right\} \right. \\ &\quad \left. + 2A_1(\bar{z} - 1)v \tan \left(\frac{1}{2}A_1(1 - \bar{z}) \right) \right] d\bar{z} \end{aligned} \quad (16.146)$$

One of the objectives of this chapter is to investigate whether bioconvection of oxytactic bacteria can develop in porous media at all. From the linear stability analysis presented above, it follows that there is a critical value of permeability; if permeability is larger than critical, bioconvection develops, if it is smaller than critical, the basic state remains stable. In the analysis that follows the critical permeability is calculated as a function of the depth of the layer.

According to Hillesdon and Pedley [26] who investigated bioconvection of oxytactic bacteria *Bacillus subtilis*, dimensionless parameters relevant to this

**FIGURE 16.4**

The effect of the layer depth, H (m), on the critical permeability, K_{crit} (m^2). (Taken from Kuznetsov and Avramenko, *Int. Comm. Heat Mass Transfer* 30: 593–602, 2003. With permission.)

problem can be estimated as follows:

$$\delta = 16, \quad \beta = 7 \times 10^6 H^2, \quad Pe = 1.5 \times 10^4 H, \quad Ra = 10^{12} H^3 \quad (16.147)$$

where H is measured in meters.

Figure 16.4 displays the effect of the depth of the layer on the critical permeability value, which is computed as $K_{\text{crit}} = Da_{\text{crit}}H^2 = (RaDa)_{\text{crit}}H^2/Ra$, where $(RaDa)_{\text{crit}}$ is computed according to Eq. (16.143). Figure 16.4 shows that the critical permeability decreases from 7.4×10^{-7} to $1.3 \times 10^{-8} \text{ m}^2$ as the depth of the layer increases from 0.5×10^{-3} to 3×10^{-3} m. This means that in a deeper layer bioconvection can develop at smaller permeability of the porous medium than in a layer of smaller depth. Nield et al. [30] reported that some porous aluminum forms exhibit permeability up to $8 \times 10^{-6} \text{ m}^2$, which is much larger than the critical permeability displayed in Figure 16.4.

16.3.2 Self-Similarity Solution for a Falling Plume in Bioconvection of Oxytactic Bacteria in a Deep Fluid Saturated Porous Layer

Hillesdon et al. [25] and Kessler et al. [31] describe experiments that show the formation of falling plumes in a deep chamber (7 to 8 mm in depth) that contains a suspension of oxytactic bacteria *B. subtilis*. These bacteria consume oxygen and swim up the oxygen gradient as they require a certain minimum concentration of oxygen to be active. Since the diffusivity of oxygen in water is very small, sufficient amounts of oxygen can penetrate by diffusion only in the upper portion of the fluid layer. In the lower part of the chamber, the bacteria consume all the oxygen keeping the oxygen concentration very low; therefore, the bacteria in this region become inactive. The chamber is thus divided into two regions, the upper cell-rich boundary layer, which contains actively swimming cells, and the lower region of the chamber, where the

concentration of oxygen is smaller than the minimum concentration and the cells are therefore inactive. Since the bacteria are heavier than water, the upper cell-rich boundary layer becomes unstable, which results in the formation of falling plumes that carry cells and oxygen into the lower part of the chamber. The plumes provide for an additional convective transport mechanism into the depth of the chamber which is more efficient than the diffusion transport mechanism. The oxygen transported by falling plumes resuscitates some of the inactive cells in the lower part of the chamber.

Once bioconvection instability has developed, the falling plumes will eventually deplete the upper boundary layer of oxygen and bacteria. However, the timescale for the development of bioconvection plumes is much smaller than that for the depletion of the upper boundary layer. Therefore, the plume can be assumed to be quasi-steady and concentrations of oxygen and bacteria at the free surface can be assumed to be constant. Utilizing these assumptions, Metcalfe and Pedley [28] obtained a similarity solution for a falling plume in a suspension of oxytactic bacteria in a clear (of solid material) fluid. In Kuznetsov et al. [32,33], a similarity solution for a falling plume in a suspension of oxytactic bacteria in a fluid saturated porous medium is obtained. Becker et al. [34] obtained a numerical solution for a falling plume in a porous layer.

A schematic diagram of the problem is displayed in Figure 16.5, which shows a falling bioconvection plume emerging from the upper boundary layer that is rich in cells and oxygen. The dimensionless oxygen concentration, \bar{C} , is again defined by Eq. (16.94) and the bacterial swimming velocity, V , is defined by Eq. (16.93).

As in Metcalfe and Pedley [28], Kuznetsov et al. [32,33] investigated a steady-state (more precisely, a quasi-steady) axisymmetric falling plume.

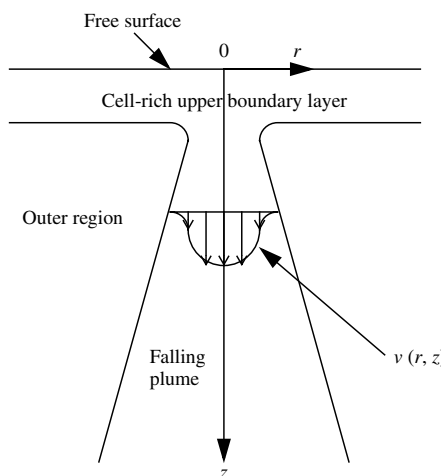


FIGURE 16.5

Schematic diagram of falling bioconvection plume in a fluid saturated porous medium. (Taken from Kuznetsov et al., *Int. J. Eng. Sci.* 42: 557–569, 2004. With permission.)

Governing equations for this problem can be presented as follows. The steady-state conservation of cells equation can be presented as:

$$\operatorname{div}(\mathbf{J}) = 0 \quad (16.148)$$

where \mathbf{J} is the volume-average cell flux given by the following equation [5]:

$$\mathbf{J} = n_s \mathbf{U} + \varphi n_s \mathbf{V} - \varphi D_n \nabla n_s \quad (16.149)$$

where n_s is the concentration of cells (n_s is understood as a volume-average property), \mathbf{U} is the filtration velocity vector, $D_n = D_{n0}H(\bar{C})$ is the cell diffusivity in the fluid, and D_{n0} is a constant. The first term on the right-hand side of Eq. (16.149) corresponds to cell flux due to advection by the bulk fluid filtration flow, the second term corresponds to cell flux due to cells swimming up the oxygen gradient, and the third term corresponds to cell flux by diffusion. It is assumed that random aspects of cell motion such as cell-to-cell interactions, Brownian motion, and distribution of swimming velocity can be modeled through a diffusion process.

Substituting Eq. (16.149) into Eq. (16.148), the following equation of conservation of cells is obtained:

$$\nabla \cdot (n_s \mathbf{U} + n_s (bW_c)_{\text{eff}} \hat{H}(\bar{C}) \nabla \bar{C}) = \nabla (D_{n,\text{eff}} \nabla n_s) \quad (16.150)$$

Note that extra factors φ have been incorporated into $(bW_c)_{\text{eff}}$ and $D_{n,\text{eff}}$. For simplicity, the subscript eff is dropped in further analysis. The plume in the upper part of the chamber, where the oxygen concentration is larger than C_{\min} and all bacteria are actively swimming, is considered. In this part of the chamber $\bar{C} > 0$; therefore, the step function, $H(\bar{C})$, is identically equal to unity and Eq. (16.150) can be recast as:

$$\begin{aligned} & \left(v + bW_c \frac{\partial \bar{C}}{\partial z} \right) \frac{\partial n_s}{\partial z} + \left(u + bW_c \frac{\partial \bar{C}}{\partial r} \right) \frac{\partial n_s}{\partial r} + bW_c n_s \left(\frac{\partial^2 \bar{C}}{\partial z^2} + \frac{\partial^2 \bar{C}}{\partial r^2} + \frac{1}{r} \frac{\partial \bar{C}}{\partial r} \right) \\ &= D_n \left(\frac{\partial^2 n_s}{\partial z^2} + \frac{\partial^2 n_s}{\partial r^2} + \frac{1}{r} \frac{\partial n_s}{\partial r} \right) \end{aligned} \quad (16.151)$$

where r is the radial coordinate, z is the vertically downward coordinate, u is the radial velocity component, and v is the vertical velocity component.

Oxygen flux is due either to advection by the bulk flow or diffusion of oxygen in water. Also, bacteria consume oxygen to remain active; therefore, the equation of conservation of oxygen must include a term describing a sink of oxygen due to bacterial consumption. This results in the following form of oxygen conservation equation:

$$\nabla \cdot (C \mathbf{U}) = D_{C,\text{eff}} \nabla^2 C - \gamma_{\text{eff}} n_s \quad (16.152)$$

where $D_{C,\text{eff}}$ is the effective oxygen diffusivity in the porous medium and the term $-\gamma_{\text{eff}}n_s$ describes the consumption of oxygen by the bacteria. To account for the reduction of cell activity in the lower part of the chamber, where cell concentration is smaller than in the upper layer, it is assumed that $\gamma_{\text{eff}} = \gamma_0(n_s/n_{fs})H(\bar{C})$, where n_{fs} is the concentration of bacteria at the free surface (assumed to be constant) and γ_0 is a constant characterizing the rate of oxygen consumption by the bacteria. Again the subscript eff is dropped in further analysis.

For axisymmetric plume, Eq. (16.152) can be recast as:

$$v \frac{\partial \bar{C}}{\partial z} + u \frac{\partial \bar{C}}{\partial r} = D_C \left(\frac{\partial^2 \bar{C}}{\partial z^2} + \frac{\partial^2 \bar{C}}{\partial r^2} + \frac{1}{r} \frac{\partial \bar{C}}{\partial r} \right) - \frac{\gamma n_s}{\Delta C} \quad (16.153)$$

where $\Delta C = C_0 - C_{\min}$.

The suspension is assumed to be dilute and Darcy's law is assumed to be valid. Utilizing the Boussinesq approximation, the z -momentum equation can be presented as:

$$\frac{\partial p}{\partial z} + \frac{\mu}{K} v - n_s \theta \Delta \rho g = 0 \quad (16.154)$$

where p is the pressure; K is the permeability of the porous medium; θ is the average volume of the bacterium; $\Delta \rho$ is the density difference, $\rho_{\text{cell}} - \rho_0$; μ is the dynamic viscosity, assumed to be approximately the same as that of water; and ρ_0 is the density of water. The last term on the left-hand side of Eq. (16.154) is the buoyancy term that represents the increase of density in the control volume as more bacteria enter the control volume (because bacteria are heavier than water).

Utilizing Darcy's law, the r -momentum equation can be presented as:

$$\frac{\partial p}{\partial r} + \frac{\mu}{K} u = 0 \quad (16.155)$$

The suspension is assumed to be incompressible; therefore, the continuity equation is simply $\nabla \cdot \mathbf{U} = 0$, or

$$\frac{1}{r} \frac{\partial(ru)}{\partial r} + \frac{\partial(v)}{\partial z} = 0 \quad (16.156)$$

Eliminating the pressure from Eqs. (16.154) and (16.155) results in:

$$\frac{\mu}{K} \left(\frac{\partial v}{\partial r} - \frac{\partial u}{\partial z} \right) - \frac{\partial n_s}{\partial r} \theta \Delta \rho g = 0 \quad (16.157)$$

Equations (16.151), (16.153), (16.156), and (16.157) must be solved subject to the following boundary conditions. Utilizing symmetry of the plume about

$r = 0$, the following boundary conditions are imposed at $r = 0$:

$$\frac{\partial n_s}{\partial r} = 0, \quad \frac{\partial \bar{C}}{\partial r} = 0, \quad u = 0, \quad \frac{\partial v}{\partial r} = 0 \quad (16.158)$$

At $r \rightarrow \infty$ the following boundary conditions are imposed:

$$n_s \rightarrow 0, \quad \frac{\partial \bar{C}}{\partial r} \rightarrow 0, \quad v \rightarrow 0 \quad (16.159)$$

The following self-similar transformation is utilized. The similarity variable η is defined as:

$$\eta = \frac{r}{z} \quad (16.160)$$

and the new dimensionless functions $N(\eta)$, $G(\eta)$, and $F(\eta)$ are defined as:

$$\begin{aligned} n_s &= \frac{K^{1/2}}{\theta} z^{-1} N(\eta), \quad \bar{C} = G(\eta), \quad \psi = \frac{\mu}{\rho} z F(\eta) \\ u &= \frac{\mu}{\rho} z^{-1} \left[F'(\eta) - \frac{F(\eta)}{\eta} \right], \quad v = \frac{\mu}{\rho} \frac{z^{-1}}{\eta} F'(\eta) \end{aligned} \quad (16.161)$$

where the streamfunction is defined as $\partial\psi/\partial r = vr$ and $\partial\psi/\partial z = -ur$.

The continuity equation (16.156) is automatically satisfied. Substituting Eqs. (16.160) and (16.161) into Eqs. (16.151), (16.153), and (16.157), the following equations for the dimensionless functions $N(\eta)$, $G(\eta)$, and $F(\eta)$ are obtained:

$$\begin{aligned} (1 + \eta^2)N'' + \left[4\eta + \frac{1}{\eta}(1 + Sc F) - Pe G'(1 + \eta^2) \right] N' \\ + \left[2 + \frac{Sc F'}{\eta} - Pe \frac{1}{\eta} G' - Pe G''(1 + \eta^2) - 3\eta Pe G' \right] N = 0 \end{aligned} \quad (16.162)$$

$$(1 + \eta^2)G'' + \left(\frac{1}{\eta} + \frac{Sc}{\eta} \frac{D_n}{D_C} F + 2\eta \right) G' - \beta N^2 = 0 \quad (16.163)$$

$$(1 + \eta^2)F'' - \frac{F'}{\eta} - Ar\eta N' = 0 \quad (16.164)$$

where prime denotes the derivative with respect to η and

$$Pe = \frac{W_c b}{D_n}, \quad Sc = \frac{\mu}{\rho D_n}, \quad Ar = \frac{g K^{3/2} \rho \Delta \rho}{\mu^2}, \quad \beta = \frac{K \gamma_0}{D_C n_{fs} \Delta C \theta^2} \quad (16.165)$$

In Eqs. (16.165), Pe is the Péclet number, Sc is the Schmidt number, Ar is the Archimedes number, and β is the dimensionless parameter that represents the strength of oxygen consumption relative to its diffusion.

Equations (16.162) to (16.164) must be solved subject to the following boundary conditions that are obtained by transforming the boundary conditions given by Eqs. (16.158) and (16.159)

$$\text{At } \eta = 0: N' = 0, \quad G' = 0, \quad F' - \frac{F}{\eta} = 0, \quad \frac{F''}{\eta} - \frac{F'}{\eta^2} = 0 \quad (16.166)$$

$$\text{As } \eta \rightarrow \infty: N = 0, \quad G' = 0, \quad \frac{F'}{\eta} = 0 \quad (16.167)$$

An additional condition that the solution must obey can be obtained from Eq. (16.151). Integrating this equation with respect to r from zero to infinity and rearranging, the following is obtained:

$$\begin{aligned} & \int_0^\infty \frac{\partial}{\partial r} \left[run + rbW_c n \frac{\partial C}{\partial r} - rD_n \frac{\partial n}{\partial r} \right] dr \\ & + \int_0^\infty \frac{\partial}{\partial z} \left[rvn + rbW_c n \frac{\partial C}{\partial z} - rD_n \frac{\partial n}{\partial z} \right] dr = 0 \end{aligned} \quad (16.168)$$

The first integral identically equals zero due to boundary conditions (16.166) and (16.167).

From Eq. (16.168) it follows that the integral given below is a constant (takes on the same value at any cross-section independent of z):

$$Q = 2\pi \int_0^\infty \left[rvn + rbW_c n \frac{\partial C}{\partial z} - rD_n \frac{\partial n}{\partial z} \right] dr = \text{constant} \quad (16.169)$$

This integral characterizes the flux of the cells in the plume in the z -direction due to advection by the bulk flow (the first term in this integral), due to the cells swimming up the oxygen gradient (the second term), and due to cell diffusion (the third term). Thus, Eq. (16.169) means that the total flux of the cells in the z -direction due to these three factors is the same in any cross-section of the plume for any value of z .

Equation (16.169) can be recast in the dimensionless form as

$$\bar{Q} = \frac{Q\theta\rho}{2\pi\mu K^{1/2}} = \int_0^\infty [NF' - Pe Sc^{-1} \eta^2 NG' + Sc^{-1} \eta(N + N'\eta)] d\eta = \text{constant} \quad (16.170)$$

where \bar{Q} is the dimensionless flux of cells in the z -direction.

Equations (16.162) to (16.164) as well as boundary conditions (16.166) are singular at $\eta = 0$. To initiate the numerical solution a series solution must

be obtained for small η . The following series expansions are assumed for functions $N(\eta)$, $G'(\eta)$, and $F(\eta)$:

$$N(\eta) = \sum_{i=0}^6 n_i \eta^i, \quad G'(\eta) = \sum_{i=0}^6 g_i \eta^i, \quad F(\eta) = \sum_{i=0}^6 f_i \eta^i \quad (16.171)$$

Boundary conditions at $\eta = 0$ given by Eqs. (16.166) yield the following relations:

$$n_1 = g_0 = f_0 = f_1 = f_3 = 0 \quad (16.172)$$

It is assumed that $n_0 \neq 0$ and $f_2 \neq 0$ to provide for nonzero concentration of bacteria and nonzero axial fluid velocity in the center of the plume. The solution is obtained in terms of n_0 and f_2 as:

$$\begin{aligned} N(\eta) = & n_0 + \frac{1}{4} n_0 (-2 - 2f_2 Sc + n_0^2 Pe\beta) \eta^2 \\ & + \frac{1}{64D_C} (2D_C n_0 (12 + Sc(Ar n_0 + f_2(18 + 4f_2 Sc + Ar n_0 Sc))) \\ & - n_0^3 Pe (2D_n f_2 Sc + D_C (18 + 12f_2 Sc + Ar n_0 Sc))\beta + 4D_C n_0^5 Pe^2 \beta^2) \eta^4 \\ & + \frac{1}{2304D_C^2} (-2D_C^2 n_0 (360 + Sc(24f_2^3 Sc^2 + Ar n_0 [66 + Ar n_0 Sc]) \\ & + 2f_2^2 Sc (126 + 11Ar n_0 Sc) + f_2 [660 + Ar n_0 Sc (90 + Ar n_0 Sc)])) \\ & + n_0^3 Pe \{8D_n^2 f_2^2 Sc^2 + 2D_C D_n Sc [2Ar n_0 + f_2 (62 + 26f_2 Sc + 3Ar n_0 Sc)] \\ & + D_C^2 (660 + Sc(176f_2^2 Sc + Ar n_0 [94 + Ar n_0 Sc] + f_2 [760 + 52Ar n_0 Sc]))\}\beta \\ & - D_C n_0^5 Pe^2 \{2D_n (15f_2 + Ar n_0) Sc + D_C (254 + 148f_2 Sc + 15Ar n_0 Sc)\}\beta^2 \\ & + 36D_C^2 n_0^7 Pe^3 \beta^3) \eta^6 \end{aligned} \quad (16.173)$$

$$\begin{aligned} G'(\eta) = & \frac{1}{2} n_0^2 \beta \eta + \frac{n_0^2 \beta}{8D_C} [-D_n f_2 Sc + D_C (-5 - 2f_2 Sc + n_0^2 Pe\beta)] \eta^3 \\ & + \frac{1}{192D_C^2} [n_0^2 \beta (4D_n^2 f_2^2 Sc^2 + D_C D_n Sc (2Ar n_0 + 2f_2 (22 + 4f_2 Sc + Ar n_0 Sc)) \\ & - n_0^2 (6f_2 + Ar n_0) Pe\beta + D_C^2 (132 + 2Sc(Ar n_0 + f_2 (46 + 8f_2 Sc + Ar n_0 Sc))) \\ & - n_0^2 Pe (46 + 20f_2 Sc + Ar n_0 Sc)\beta + 6n_0^4 Pe^2 \beta^2)] \eta^5 \end{aligned} \quad (16.174)$$

$$\begin{aligned}
 F(\eta) = & f_2\eta^2 + \frac{1}{16}[-2f_2(2 + Ar n_0 Sc) + Ar n_0(-2 + n_0^2 Pe\beta)]\eta^4 \\
 & + \frac{1}{384D_C}[2D_C\{24(f_2 + Ar n_0) + Ar n_0(30f_2 + Ar n_0)Sc \\
 & + Ar f_2 n_0(4f_2 + Ar n_0)Sc^2\} - Ar n_0^3 Pe\{2D_n f_2 Sc \\
 & + D_C(30 + 12f_2 Sc + Ar n_0 Sc)\}\beta + 4ArD_C n_0^5 Pe^2 \beta^2]\eta^6
 \end{aligned} \quad (16.175)$$

For computational results displayed in Figures 16.6 to 16.8, the following parameter values are utilized: $Ar = 1$, $D_n/D_C = 1$, $Pe = 10$, $Sc = 20$, and $\beta = 10^6$. Since Eqs. (16.162)–(16.164) and boundary conditions (16.166) are singular at $\eta = 0$, to initiate numerical solution a series solution given by Eqs. (16.173)–(16.175) is used. The utilization of this series solution requires an assumption concerning the values of n_0 and f_2 that are present as parameters in this series solution. Values of n_0 and f_2 are initially guessed and then their values are iteratively improved by the Shooting Method until the boundary conditions at $\eta \rightarrow \infty$ and the integral condition given by Eq. (16.170) are satisfied. Utilizing this series solution, computations are performed up to $\eta = 0.01$. At $\eta = 0.01$, values of $N(\eta)$, $N'(\eta)$, $G'(\eta)$, $F(\eta)$, and $F'(\eta)$ are evaluated utilizing the series solution. These values are used as the initial condition for the numerical solution. For $\eta > 0.01$, Eqs. (16.162)–(16.164) are solved numerically utilizing RKF45 ordinary differential equation solver.

Figure 16.6 displays the dimensionless cell concentration, $N(\eta)$, for different values of the dimensionless cell flux in z -direction, \bar{Q} . The increase of \bar{Q} corresponds to larger concentration of cells, as expected. The width of the plume slightly decreases with the increase of \bar{Q} .

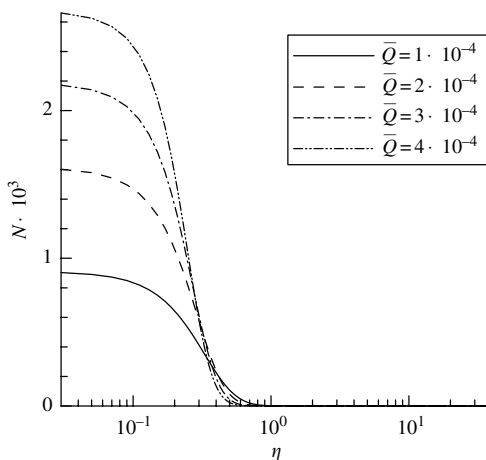
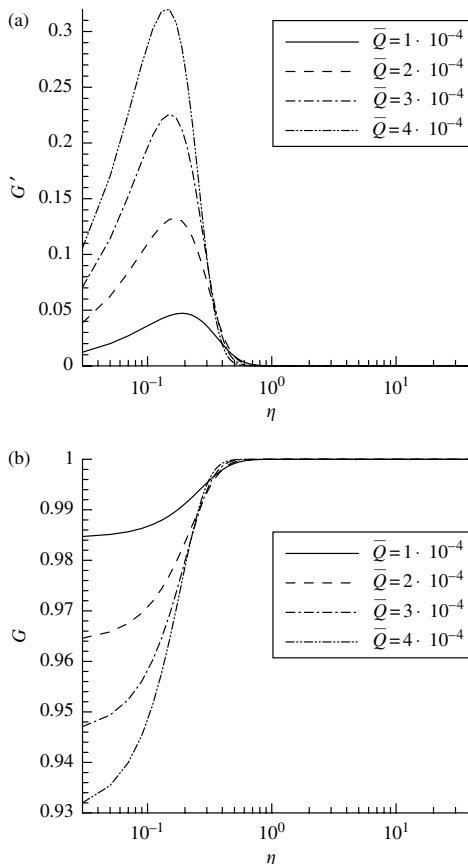


FIGURE 16.6

Similarity solution: dimensionless cell concentration, $N(\eta)$. (Taken from Kuznetsov et al., *Int. J. Eng. Sci.* 42: 557–569, 2004. With permission.)

**FIGURE 16.7**

Similarity solution: (a) dimensionless rate of change of oxygen concentration, $G'(\eta)$; (b) dimensionless oxygen concentration, $G(\eta)$, computed assuming that $G(\infty) = 1$. (Taken from Kuznetsov et al., *Int. J. Eng. Sci.* 42: 557–569, 2004. With permission.)

Figure 16.7(a) displays the dimensionless rate of change of oxygen concentration, $G'(\eta)$, and Figure 16.7(b) displays the dimensionless oxygen concentration, $G(\eta)$, which is computed by integrating $G'(\eta)$ assuming that $G(\infty) = 1$. The oxygen concentration decreases toward the center of the plume. This happens because the center of the plume has the largest concentration of cells (cf. Figure 16.6) that consume oxygen. This result is in agreement with the clear fluid results obtained in Metcalfe and Pedley [28]. The increase of \bar{Q} increases the number of the cells in the plume which increases the rate of oxygen consumption; therefore, the increase of \bar{Q} leads to a smaller oxygen concentration in the center of the plume. It should be noted that the proposed model is valid only as long as $\bar{C} > 0$ (or $C > C_{\min}$), which is true only in the upper part of the plume, where oxygen concentration around the plume is relatively high. In the lower part of the chamber, the oxygen

concentration in the bulk of the fluid is smaller than C_{\min} , and the plume will provide the convective mechanism for the oxygen and cell transport into the lower part of the chamber. However, the solution obtained in this chapter is valid only as long as $C > C_{\min}$, and this explains why the oxygen concentration in the center of the plume is a little smaller than at its edges.

Figure 16.8(a) displays the dimensionless streamfunction, $F(\eta)$, while Figure 16.8(b) displays the dimensionless downward fluid filtration velocity, $F'(\eta)/\eta$. The downward fluid velocity increases as \bar{Q} increases, as expected; the axial velocity takes its maximum value in the center of the plume and decreases to zero at the edge of the plume.

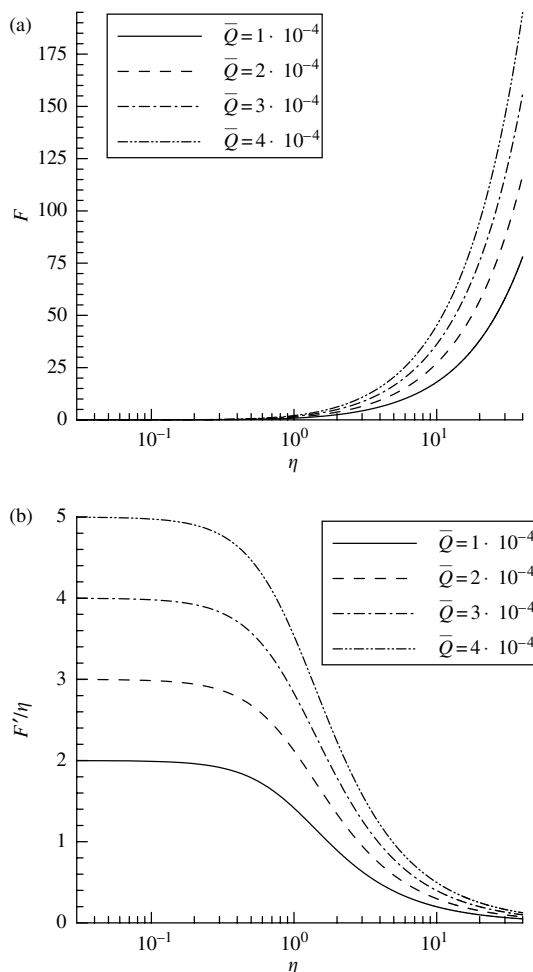


FIGURE 16.8

Similarity solution: (a) dimensionless streamfunction, $F(\eta)$; (b) dimensionless downward fluid filtration velocity, $F'(\eta)/\eta$. (Taken from Kuznetsov et al., *Int. J. Eng. Sci.* 42: 557–569, 2004. With permission.)

Further experimental research is needed to verify theoretical models reported in this chapter. Magnetic Resonance Imaging (MRI) [35,36] is one of the promising techniques for this type of investigation.

Acknowledgment

The author gratefully acknowledges the grant # NAG3-2706 awarded to him by NASA Office of Biological and Physical Research, Physical Sciences Division. Critical comments of Prof. D.A. Nield and Dr. A.A. Avramenko are greatly appreciated.

Nomenclature

Roman Letters

<i>a</i>	semi-major axis of the spheroidal cell, m
<i>A</i> ₁	parameter defined by Eq. (16.118)
<i>b</i>	semi-minor axis of the spheroidal cell, m
<i>B</i>	gyrotactic orientation parameter, $\alpha_{\perp}\mu/(2h\rho_0g)$, sec
<i>c</i> _a	acceleration coefficient
<i>C</i>	oxygen concentration, molecules/m ³
<i>C</i> _{min}	minimum oxygen concentration that oxytactic bacteria require to be active, molecules/m ³
\bar{C}	dimensionless oxygen concentration, $(C - C_{\min})/(C_0 - C_{\min})$
\bar{C}_b	dimensionless steady-state oxygen concentration for the basic state
<i>d</i>	average diameter of a particle or a fiber that compose the porous matrix, m
<i>D</i> _C	diffusivity of oxygen, m ² /sec
<i>D</i> _n	diffusivity of microorganisms, m ² /sec
<i>Da</i>	Darcy number for bioconvection caused by oxytactic microorganisms, K/H ²
$\hat{D}a_{1/\gamma}(\kappa, m)$	Darcy number based on γ^{-1} as a length-scale for bioconvection caused by gyrotactic microorganisms, $\hat{K}(\kappa, m)\gamma^2$
$(Da_{1/\gamma})_{\text{crit}}$	critical Darcy number based on γ^{-1} as a length-scale for bioconvection caused by gyrotactic microorganisms, $K_{\text{crit}}\gamma^2$
<i>g</i>	gravitational acceleration, m/sec ²
<i>G</i>	gyrotaxis number defined by Eq. (16.85)
<i>h</i>	displacement of the center of mass of the microorganism from its center of buoyancy, m
<i>H</i>	depth of a horizontal layer, m
\hat{H}	Heaviside step function

$\hat{\mathbf{i}}$	unit vector in the x -direction
$\hat{\mathbf{j}}$	unit vector in the y -direction
k	wavenumber in the x -direction, m^{-1}
k_{dep}	rate of cell deposition, sec^{-1}
k_{decl}	rate of cell resuspension (declogging), sec^{-1}
$\hat{\mathbf{k}}$	unit vector in the vertically upward z -direction
K	permeability of the porous medium, m^2
K_b	permeability in the basic state for the case when the porous matrix can absorb microorganisms, defined by Eq. (16.66), m^2
\hat{K}	permeability value for which the real part of the dispersion parameter σ equals zero, m^2
K_{crit}	critical permeability, m^2
l	wavenumber in the y -direction, m^{-1}
m	wavenumber in the z -direction, m^{-1}
\bar{m}	dimensionless wavenumber in the z -direction, mD_n/W_c
n_b	number density of suspended microorganisms in the basic state, cells/m^3
n_0	initial uniform number density of oxytactic bacteria, cells/m^3
n_c	number density of captured microorganisms, cells/m^3
n_s	number density of suspended motile microorganisms, cells/m^3
\hat{n}_s	average number density of suspended microorganisms in a layer of final depth, given by Eq. (16.71), cells/m^3
\bar{n}	dimensionless number density of suspended oxytactic microorganisms
p	excess pressure (above hydrostatic), Pa
$p_b(z)$	unperturbed excess pressure in the basic state, Pa
\bar{p}_e	dimensionless excess pressure, $H^2 p_e / (\mu D_n)$
$\hat{\mathbf{p}}$	unit vector indicating the swimming direction of microorganisms
Pe	Péclet number for bioconvection caused by oxytactic microorganisms, $W_c b / D_n$
Q	Péclet number for bioconvection caused by gyrotactic microorganisms, $W_c H / D_n$
r	radial coordinate, m
R	Rayleigh number for bioconvection caused by gyrotactic microorganisms, defined by Eq. (16.85)
R_{crit}	critical Rayleigh number for bioconvection caused by gyrotactic microorganisms
R_a	net rate of cell deposition per unit volume, $\text{m}^{-3}/\text{sec}^{-1}$
Ra	Rayleigh number for bioconvection caused by oxytactic microorganisms, defined by Eq. (16.103)
Sc	Schmidt number, $\mu / (c_a \rho D_n)$
t	time, sec
\bar{t}	dimensionless time, $D_n t / H^2$
u	x -velocity component, m/sec
\bar{u}	dimensionless x -velocity component, $H u / D_n$
v	y -velocity component, m/sec

\bar{v}	dimensionless y -velocity component, Hv/D_n
\mathbf{v}	velocity vector, (u, v, w) , m/sec
\mathbf{v}'	vector composed of perturbations of the corresponding velocity components, (u', v', w') , m/sec
\mathbf{V}	average swimming velocity of an oxytactic bacterium, defined by Eq. (16.93)
w	z -velocity components, m/sec
\bar{w}	dimensionless z -velocity component, Hw/D_n
$W_c \hat{\mathbf{p}}$	vector of average swimming velocity of a gyrotactic microorganism relative to the fluid, m/sec
x	Cartesian coordinate, m
\bar{x}	dimensionless coordinate, x/H
y	Cartesian coordinate, m
\bar{y}	dimensionless coordinate, y/H
z	Cartesian (vertically upward) coordinate, m
\bar{z}	dimensionless upward coordinate, z/H

Greek Letters

α_0	measure of the cell eccentricity, $(a^2 - b^2)/(a^2 + b^2)$
α_{\perp}	dimensionless constant relating viscous torque to the relative angular velocity of the cell
β	dimensionless parameter defined by Eq. (16.103), $(\tilde{\gamma} n_0 H^2)/(D_C \Delta C)$
γ	parameter defined by Eq. (16.45) (inverse to characteristic length-scale), m^{-1}
$\tilde{\gamma}$	parameter characterizing the rate of oxygen consumption by microorganisms, molecules/(cell sec)
δ	dimensionless parameter defined by Eq. (16.103), D_C/D_n
$\Delta\rho$	density difference, $\rho_{\text{cell}} - \rho_0$, kg/m ³
ε	small perturbation amplitude
η	similarity variable defined by Eq. (16.160), r/z
$\tilde{\eta}$	parameter defined by Eq. (16.19), sec ⁻¹
θ	average volume of the microorganism, m ³
κ	combination of wavenumbers, $(k^2 + l^2 + m^2)^{1/2}$, m ⁻¹
$\bar{\kappa}$	dimensionless form of parameter κ , $\kappa D_n/W_c$
μ	dynamic viscosity of suspension (assumed to be approximately the same as that of water), kg/(m sec)
ν	integration constant defined by Eq. (16.70), m ⁻³
$\tilde{\xi}$	parameter defined by Eq. (16.20), sec ⁻¹
ρ_{cell}	density of microorganisms, kg/m ³
ρ_0	density of water, kg/m ³
σ	dispersion parameter characterizing the growth rate of perturbations, sec ⁻¹
ν	dimensionless parameter defined by Eq. (16.142)
φ	porosity
φ_0	initial porosity (when there are no deposited cells)

References

1. T.J. Pedley and J.O. Kessler. Hydrodynamic phenomena in suspensions of swimming microorganisms. *Ann. Rev. Fluid Mech.* 24:313–358, 1992.
2. M.A. Bees and N.A. Hill. Wavelengths of bioconvection patterns. *J. Exp. Biol.* 200:1515–1526, 1997.
3. J.O. Kessler, G.D. Burnett, and K.E. Remick. Mutual dynamics of swimming microorganisms and their fluid habitat. In: P.L. Christiansen, M.P. Sorensen, and A.C. Scott, eds., *Nonlinear Science at the Dawn of the 21st Century*. New York: Springer, 2000, pp. 409–426.
4. A. Harashima, M. Watanabe, and I. Fujishiro. Evolution of bioconvection patterns in a culture of motile flagellates. *Phys. Fluids* 31:764–775, 1988.
5. T.J. Pedley, N.A. Hill, and J.O. Kessler. The growth of bioconvection patterns in a uniform suspension of gyrotactic microorganisms. *J. Fluid Mech.* 195:223–338, 1988.
6. S. Ghorai and N.A. Hill. Development and stability of gyrotactic plumes in bioconvection. *J. Fluid Mech.* 400:1–31, 1999.
7. T.J. Pedley and J.O. Kessler. The orientation of spheroidal microorganisms swimming in a flow field. *Proc. R. Soc. Lond. B* 231:47–70, 1987.
8. T.J. Pedley and J.O. Kessler. A new continuum model for suspensions of gyrotactic microorganisms. *J. Fluid Mech.* 212:155–182, 1990.
9. S. Ghorai and N.A. Hill. Periodic arrays of gyrotactic plumes in bioconvection. *Phys. Fluids* 12:5–22, 2000.
10. J.O. Kessler. Hydrodynamic focusing of motile algal cells. *Nature* 313:218–220, 1985.
11. J.O. Kessler. Cooperative and concentrative phenomena of swimming microorganisms. *Contemp. Phys.* 26:147–166, 1985.
12. J.O. Kessler, D.A. Wiseley, K.E. Remick, and D.E. Marthaler. Individual and collective dynamics of swimming bacteria. In: M. Schreckenberg and D.E. Wolf, eds., *Proceedings of the Workshop “Traffic and Granular Flow 97.”* New York: Springer, 1997, pp. 37–51.
13. J.O. Kessler. The external dynamics of swimming micro-organisms. In: F.E. Round and D.J. Chapman, eds., *Progress in Phycological Research*, Vol. 4. Bristol: Biopress, 1986, pp. 257–307.
14. A.V. Kuznetsov and N. Jiang. Numerical investigation of bioconvection of gravitactic microorganisms in an isotropic porous medium. *Int. Commun. Heat Mass Transfer* 28:877–886, 2001.
15. A.V. Kuznetsov and N. Jiang. Bioconvection of negatively geotactic microorganisms in a porous medium: the effect of cell deposition and resuspension. *Int. J. Numer. Meth. Heat Fluid Flow* 13:341–364, 2003.
16. A.V. Kuznetsov and A.A. Avramenko. A 2D analysis of bioconvection in a fluid saturated porous medium — estimation of the critical permeability value. *Int. Commun. Heat Mass Transfer* 29:175–184, 2002.
17. A.V. Kuznetsov and A.A. Avramenko. Stability analysis of bioconvection of gyrotactic motile microorganisms in a fluid saturated porous medium. *Transp. Porous Media* 53:95–104, 2003.
18. S. Whitaker. *The Method of Volume Averaging*. Dordrecht: Kluwer, 1999.

19. D.A. Nield and A. Bejan. *Convection in Porous Media*, 2nd edn. New York: Springer, 1999.
20. N.A. Hill, T.J. Pedley, and J.O. Kessler. Growth of bioconvection patterns in a suspension of gyrotactic micro-organisms in a layer of finite depth. *J. Fluid Mech.* 208:509–543, 1989.
21. A.V. Kuznetsov and A.A. Avramenko. The effect of deposition and declogging on the critical permeability in bioconvection in a porous medium. *Acta Mech.* 160:113–125, 2003.
22. D.A. Nield, A.V. Kuznetsov, and A.A. Avramenko. The onset of bioconvection in a horizontal porous-medium layer. *Transp. Porous Media* 54:335–344, 2004.
23. S. Chandrasekhar. *Hydrodynamic and Hydromagnetic Stability*. Oxford: Oxford University Press, 1961.
24. B.A. Finlayson. *The Method of Weighted Residuals and Variational Principles*, Chapter 6. New York: Academic Press, 1972.
25. A.J. Hillesdon, T.J. Pedley, and J.O. Kessler. The development of concentration gradients in a suspension of chemotactic bacteria. *Bull. Math. Biol.* 57:299–344, 1995.
26. A.J. Hillesdon and T.J. Pedley. Bioconvection in suspensions of oxytactic bacteria: linear theory. *J. Fluid Mech.* 324:223–259, 1996.
27. A.M. Metcalfe and T.J. Pedley. Bacterial bioconvection: weakly nonlinear theory for pattern selection. *J. Fluid Mech.* 370:249–270, 1998.
28. A.M. Metcalfe and T.J. Pedley. Falling plumes in bacterial bioconvection. *J. Fluid Mech.* 445:121–149, 2001.
29. A.V. Kuznetsov and A.A. Avramenko. Analysis of stability of bioconvection of motile oxytactic bacteria in a horizontal fluid saturated porous layer. *Int. Commun. Heat Mass Transfer* 30:593–602, 2003.
30. D.A. Nield, S.L.M. Junqueira, and J.L. Lage. Forced convection in a fluid-saturated porous-medium channel with isothermal or isoflux boundaries. *J. Fluid Mech.* 322:201–214, 1996.
31. J.O. Kessler, M.A. Hoelzer, T.J. Pedley, and N.A. Hill. Functional patterns of swimming bacteria. In: L. Maddock, Q. Bone, and J.M.V. Rayner, eds., *Mechanics and Physiology of Animal Swimming*. Cambridge: Cambridge University Press, 1994, pp. 3–12.
32. A.V. Kuznetsov, A.A. Avramenko, and P. Geng. A. similarity solution for a falling plume in bioconvection of oxytactic bacteria in a porous medium. *Int. Commun. Heat Mass Transfer* 30:37–46, 2003.
33. A.V. Kuznetsov, A.A. Avramenko, and P. Geng. Analytical investigation of a falling plume caused by bioconvection of oxytactic bacteria in a fluid saturated porous medium. *Int. J. Eng. Sci.* 42:557–569, 2004.
34. S.M. Becker, A.V. Kuznetsov, and A.A. Avramenko. Numerical modeling of a falling bioconvection plume in a porous medium. *Fluid Dynamics Research* 33:323–339, 2004.
35. A.-R.A. Khaled and K. Vafai. The role of porous media in modeling flow and heat transfer in biological tissues. *Int. J. Heat Mass Transfer* 46:4989–5003, 2003.
36. K. Khanafer, K. Vafai, and A. Kangarlu. Water diffusion in biomedical systems as related to magnetic resonance imaging. *Magn. Reson. Imag.* J. 21:175–184, 2003.

17

Parameter Identification within a Porous Medium using Genetic Algorithms

S.D. Harris and D.B. Ingham

CONTENTS

Summary	688
17.1 Introduction	689
17.2 Fluid Flow Equations	693
17.2.1 Multiphase Fluid Systems in Porous Media	693
17.2.2 Single-Phase Flow	694
17.2.3 Multiphase Flow	695
17.3 Introduction to Genetic Algorithms	699
17.3.1 What are Genetic Algorithms?	699
17.3.2 Advantages of Using Genetic Algorithms	700
17.3.3 Components of a Genetic Algorithm	702
17.3.3.1 Binary encoding of individuals	702
17.3.3.2 Selection operators	702
17.3.3.3 Crossover operators.....	703
17.3.3.4 Mutation operators	704
17.3.3.5 Further genetic algorithm techniques	704
17.3.4 A Theoretical Basis for the Genetic Algorithm Approach....	705
17.3.5 Details and Example of the Genetic Algorithm Technique Employed in this Chapter	706
17.4 Parameter Identification within Rock Samples	710
17.4.1 Introduction	710
17.4.2 Experimental Method	713
17.4.3 Mathematical Formulation	714
17.4.3.1 The governing equation	714
17.4.3.2 Boundary conditions	715
17.4.3.3 Direct solution for the homogeneous case.....	716
17.4.4 Inverse Problem Formulation.....	716
17.4.5 Sensitivity Coefficients	717

17.4.6 The Homogeneous Hydraulic Conductivity Case, $k(x) = k_0 = \text{constant}$	718
17.4.7 Linear Hydraulic Conductivity, $k(x) = k_0 + k_1x$	719
17.4.8 Quadratic Hydraulic Conductivity, $k(x) = k_0 + k_1x + k_2x^2$...	719
17.4.9 Simultaneous Retrieval of Constant Hydraulic Conductivity and Constant Specific Storage.....	719
17.5 Hydraulic Conductivity Measurements in Composite	
Homogeneous Rocks	720
17.5.1 Experimental Setup and Limitations.....	721
17.5.2 Mathematical Formulation	721
17.5.3 Steady-State Mathematical Analysis	722
17.5.4 The Composite Homogeneous Situation	723
17.5.5 Retrieval of the Hydraulic Conductivities	723
17.5.6 Simultaneous Retrieval of the Compressive Storage of the Upstream Reservoir and the Specific Storages of the Samples	724
17.5.7 Comparison with Experimental Data.....	725
17.6 Hydraulic Conductivity Measurements in	
Anisotropic Rocks	726
17.6.1 Introduction	726
17.6.2 Mathematical Formulation	727
17.6.3 Inverse Problem Formulation	729
17.6.4 Numerical Results	730
17.7 Hydraulic Conductivity Measurements in Composite	
Anisotropic Rocks	730
17.7.1 Mathematical Formulation	730
17.7.2 Inverse Problem Formulation.....	731
17.7.3 Numerical Results and Discussion	731
17.7.3.1 The case when the fault is perpendicular to the x -axis of the sample, $x_t^f = x_b^f$	731
17.7.3.2 The case when the fault is inclined to the x -axis of the sample, $x_t^f \neq x_b^f$	734
17.8 Comparison of Methods.....	734
17.9 Conclusions	736
Acknowledgments	737
References	737

Summary

This chapter is concerned with the inverse problem of the identification of the hydraulic properties of porous materials in the context of petroleum, civil, and mining engineering. The applicability of the novel technique of genetic algorithms (GAs), which attempt to imitate the principles of biological evolution in the construction of optimization strategies and have led to

the development of a powerful and efficient optimization tool, is studied for such purposes.

First, we model a one-dimensional hydraulic pump-flow permeability test and formulate an inversion technique in order to retrieve homogeneous or spacewise dependent material property coefficients, with the extension in the homogeneous situation to the case of layered materials. The direct problem is solved using the finite-difference method (FDM) while the recovery of the material parameters is achieved through a GA approach. Both exact and simulated noisy data are incorporated at optimally selected instants in time through the test, the data measurements used being consistent with a sensitivity analysis of each problem. Second, both steady-state and transient experiments are modeled for the case of anisotropic materials. The direct solution procedures are based on the boundary element method for the steady-state situation while the FDM is chosen for the transient case. Surface measurements, by means of simulated ports along the sealed boundaries of the materials, serve as information to the GA-based optimization procedure, hence enabling a modified least-squares functional to minimize the difference between the observed and the numerically predicted boundary pressure and/or average hydraulic flux measurements under current hydraulic conductivity tensor and specific storage estimates. Composite anisotropic materials, that is, with the incorporation of faults, are also studied.

Parameter identifiability in inverse problems is numerically investigated and the results are found to provide an accurate means of recovering the required material properties. A comparison on the performance of the inversion highlights the advantages that a GA-based optimization approach offers in comparison to a traditional gradient-based optimization procedure.

17.1 Introduction

One of the basic tasks of engineering and science is the extraction of information from data. In this respect, parameter estimation is a discipline that provides tools for the efficient use of data in the estimation of physical properties that appear in mathematical models, and for assisting in obtaining a better model of the phenomena under investigation.

Parameter estimation can be regarded as a study of inverse problems. In general, in the solution of a partial differential equation we seek a solution in a domain knowing both the boundary and initial conditions as well as any of the constants or parameters involved. In the inverse problem, not all of these parameters are known. Instead, discrete measurements of the dependent variable(s), or its (their) derivatives, must be used to estimate the values of such unknown parameters.

In experiments we can often measure the *states* (independent variables) directly, but not the *parameters* (dependent variables). Approximate values, or *estimates*, of the parameters are inferred from state measurements.

This chapter deals with the identification of the hydraulic properties of porous materials in the context of petroleum, civil, and mining engineering. Two main categories of models have been used in the field of petroleum engineering, namely analog models and physical models. The most common analog models are the electrical models; see [1] for a comprehensive description of such models. Physical models can be classified into two categories, namely, scaled models and elemental models. In a scaled laboratory model, the reservoir dimensions and the fluid and rock properties are scaled so that the ratio of the various forces in the reservoir and in the model are the same. Such a model would provide results that can be directly applied to the field. However, full-scale models are difficult, sometimes impossible, to construct [2]. In an elemental model, the experiments are conducted with actual (or simulated) rocks and fluids. While the results of such a model cannot be applied directly to the field, they can provide some important information about the reservoir mechanics. Numerical reservoir models can also be verified, or even improved, by using the results of the physical models, and then used to predict the field performance.

The optimal design of experiments to obtain the “best” parameter estimates is a problem that is closely related to the notion of *sensitivity coefficients*. Such sensitivity coefficients are important because they indicate the magnitude of the change of the dependent variable due to perturbations in the values of the parameters, therefore providing indicators of how well an experiment is designed. In general, sensitivity coefficients are desired to be uncorrelated.

Although traditional, gradient-based, optimization procedures can be applied, in this chapter we focus on the use of the GA to design experiments and develop estimation methodologies for the determination of the hydraulic properties. The suitability of the GA approach in the optimization and design of experiments for parameter estimation in the related context of heat transfer has been confirmed; see, for example, [3–5].

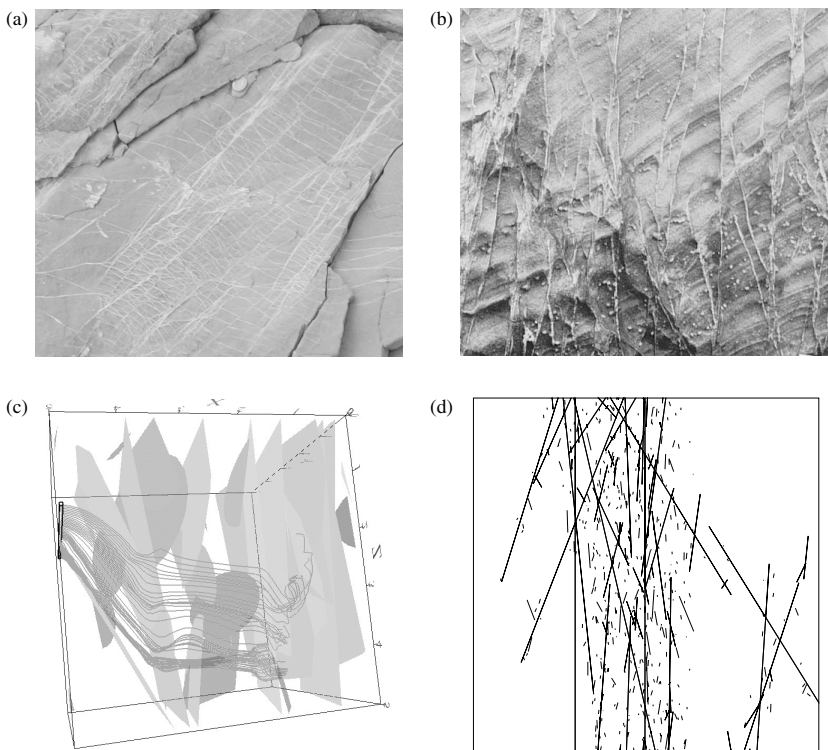
The attempt to imitate the principles of biological evolution in the construction of optimization strategies has led to the development of the powerful and efficient process of GAs, also known as *evolution strategies*. GAs have been successfully applied to nonlinear optimization problems in many dimensions, where more traditional methods are often found to fail. Moreover, deterministic, gradient-based optimization methods do not search the entire parameter space and can tend to converge toward local extrema of the function to be optimized (or fitness function), which is clearly unsatisfactory for problems where the fitness varies nonmonotonically with the parameters. On the other hand, GAs are able to depart from local optima due to the variability of the parameters within the “gene pool” and the element of randomness inherent within the methods. Furthermore, GAs do not require knowledge of the gradient of the fitness functions, which makes them particularly suited to optimization problems for which an analytical expression for the fitness function is not known. A complete description of the GA technique has been provided by several authors; see, for example, [6,7].

A GA performs a multidirectional search. It starts with a randomly initialized population of candidate solutions and implements a probabilistic, parallel search in the solution space using domain-independent “genetic operators” to form a new population of candidate solutions. The population undergoes a simulated evolution process. At each generation the relatively “good” solutions reproduce, while the relatively “bad” solutions die. To distinguish between different solutions we use an objective (evaluation) function that plays the role of an environment. There are unary transformations (mutation type) which create new individuals by small changes in single individuals, and higher-order transformations (crossover type) which create new individuals by combining parts from several (two or more) individuals. Crossover and mutation produce new areas of the solution space to explore.

The central theme of research on GAs has been related to its *robustness*, the balance between efficiency and efficacy necessary for survival in many different environments. GAs are a class of general purpose search methods that strike a remarkable balance between exploration and exploitation of the search space. They have been successfully applied to many optimization problems, such as wire routing, scheduling, adaptive control, game playing, cognitive modeling, transportation problems, traveling salesman problems, and optimal control problems; see, for example, [6] and the references therein.

The inverse problem of recovering the hydraulic properties of materials, for example, the spatially dependent hydraulic conductivity of an isotropic rock, has been considered by several researchers; see also [8,9] in the related field of heat transfer. In the study [10], the authors have been concerned with the simultaneous estimation of the linearly varying thermal conductivity and heat capacity, which are the analog heat paradigms for hydraulic conductivity and specific storage. However, these studies used multiple internal spatial and temporal measurements made during the transient process, whereas the main approach here is to use as little information as possible at the boundaries, thus reducing the damage to the samples to be tested which can cause associated changes in the hydraulic properties. The restriction of using boundary measurements solely was first taken into account in [11] during a study of “slightly” heterogeneous materials with linear and exponential spatially varying properties.

The problem of accurately quantifying the flow properties of faults is central to groundwater simulations and the modeling of hydrocarbon reservoirs [12]. An individual fault is a break or planar surface in a rock across which there is observable displacement, that is, the cohesion of the material is lost, and they may be seen in any rock exposure. There exists a large range of heterogeneities that are created by both the stratigraphic and fault architectures, and thus local flow conduits, baffles, or barriers can be formed; see, for example, [13]. Depending on the stress history, temperature, stratigraphy, etc., some fault surfaces contain relatively coarse rock fragments that can act as a conduit for migrating oil or gas, whereas the surface of other faults are smeared with impermeable clays or crushed grains that can act as a fault seal. Single large-scale faults observed from seismic surveys are in reality

**FIGURE 17.1**

Outcrop-scale images of complex regions of faulting from (a) the Moab fault zone, Utah, USA, and (b) the ninety-fathom fault, Whitley Bay, UK, which provide analogs for reservoir-scale flow simulations. (c) Flow pathways across, and (d) a planar slice through, a three-dimensional stochastically generated fault zone.

composed of many millions of smaller faults, samples of which can be found within cores through fault zones. The accurate modeling of these “damage zones” is a topic currently being studied by many research groups and oil companies. Figure 17.1 shows some natural examples of the complexity that is encountered when studying fault zone architectures and their fluid flow properties, together with some recent examples of geometric and flow models for such systems [14–16]. The limitations of upscaling detailed geological information has often led to such systems being modeled as a single fault with an applied “multiplier,” from which the fluxes are calculated as a function of the transmissibility between pairs of grid blocks [17]. The inclusion of multiphase fault rock properties is now being recognized to be crucial in providing more accurate models for production forecasting. The production of hydrocarbons from a reservoir is modeled through saturation-dependent relative permeability and capillary pressure (the pressure needed for oil to enter a rock) functions, which have a major influence on the predictions of phase-specific cross-fault flow [18]. The success of the future predictions of the fluid flow behavior will depend upon the ability to upscale from local

observations, as well as being able to interpret detailed rock properties and behavior from large-scale flow measurements.

After providing an introduction to the basic fluid flow equations for single-phase and multiphase flow, with reference to models in petroleum reservoir simulation, in Section 17.2 and the class of nonclassical optimization procedures known as GAs in Section 17.3, we consider some models of hydraulic pump-flow tests for determining the permeabilities of rock samples. Section 17.4 provides a finite-difference model of a one-dimensional hydraulic pump-flow test, as developed by Clennell [19] for the permeability estimation of tight (low permeability) rocks. The inverse analysis that is performed makes use of the GA approach for various spatial dependencies of the hydraulic properties of the sample. Section 17.5 extends this finite-difference forward model and GA-based inverse model to deal with the case of faulted rocks or geological discontinuities due to the sedimentary layering. The situation where the location of the discontinuity is unknown, but where the hydraulic conductivity is known, has been investigated in [20]. The case of unknown piecewise homogeneous hydraulic conductivity, but with a known discontinuity location, has been briefly investigated numerically in [21]. A thorough comparison with experimental results is undertaken, highlighting the flaws in the model, and thus the direction of improvements in the experimental design.

Section 17.6 introduces the same problem of the identification of the hydraulic parameters, but for the case of anisotropic materials where the hydraulic conductivity is represented by a symmetric tensor. A classical boundary integral equation method, see, for example, [22,23], is used in order to solve the direct well-posed problem. Since all the numerical approximations take place only at the boundaries, the dimensionality of the problem is reduced by one and a smaller system of equations is obtained in comparison with those achieved through finite-difference and finite element methods. Section 17.7 extends this formulation to deal with composite and anisotropic materials. The mathematical model developed is for the case of two such anisotropic materials that are butted together and the hydraulic experiment is performed over the whole of the linked material. Methods of identifying the components of the hydraulic conductivity tensors and the fault position(s) are devised by employing the GA technique.

In Section 17.8 the relevance of the GA technique is discussed by means of a comparison with a more traditional, gradient-based technique. The results are compared with the ones presented in [24,25] and a further investigation into the comparative performance of the approaches is undertaken for one of the problems investigated in Section 17.7.

17.2 Fluid Flow Equations

17.2.1 Multiphase Fluid Systems in Porous Media

Sand, sandstone, soil, fissured rocks, ceramic, foam rubber, industrial filters, wicks, bread, and lungs are examples of porous materials encountered in

practice. Common to all of them is the presence of both a persistent *solid matrix* and a persistent *void space*. The latter is occupied by one or more fluid phases. A *phase* is defined as a portion of space, whether connected or non-interconnected, that is separated from other such portions by a well-defined surface, referred to as an *interface*, or *interphase boundary*. A phase is characterized by the fact that its behavior at all points within it can be described by the same set of state variables. There can be only a single gaseous phase in the void space, as all gaseous phases are completely *miscible* and do not maintain a distinct interface between each other. However, we may have a number of liquid phases, each occupying a well-defined portion of the void space. We often regard certain liquids as *immiscible*, even when certain components contained in them do cross interphase boundaries in small quantities and thus diffuse in both phases, as long as a distinct sharp interface is maintained.

The concept of a continuum is a great convenience because it permits a description of the physical behavior of the fluid by the use of differential expressions. However, this concept cannot be extended to immiscible fluids that are separated by interfaces across which pressure discontinuities exist. In this case it is necessary to consider each individual phase as a separate continuum.

When two or more fluids exist within the pore space, they are separated by boundaries, called *interfaces*, across which discontinuities in density and pressure exist. The existence of the interfaces is characteristic of what are called *immiscible* fluids. In the case of miscible fluids there is no distinct boundary, at least on the microscopic scale, for example, in a groundwater aquifer into which salt water has intruded. Then, on a macroscopic scale it is possible to find distinct regions of salt and fresh water, but on a microscopic scale there is no interface.

The concept of different "phases" implies that interfaces exist. An interface is made possible by the existence of forces called "interfacial forces" that act only at boundaries between separate phases and these forces act tangentially to the boundaries between the different phases. When these boundaries are curved, the tangential interfacial forces produce pressure discontinuities at the interfaces. Each phase may consist of a number of chemical constituents, but they are assumed to be homogeneous within themselves and to constitute physical continua to which the mathematical methods of fluid mechanics can be applied.

17.2.2 Single-Phase Flow

Consider the three-dimensional flow of a fluid of density ρ (single-phase and single component) in a porous medium. The law of mass conservation can be written as

$$-\nabla \cdot (\rho \mathbf{u}) = \frac{\partial}{\partial t}(\rho \phi) + \tilde{q} \quad (17.1)$$

where \mathbf{u} is the fluid velocity vector, ϕ is the porosity, and mass accumulates due to a sink of strength \tilde{q} . In addition, we require a linear momentum conservation equation that relates the fluid flow rate and the pressure gradient in each phase. This could be Darcy's law discovered in 1856, see, for example, [26], which has the following differential form:

$$\mathbf{u} = -\frac{\mathbf{K}}{\mu} \left(\nabla p - \rho \frac{\mathbf{g}}{g_c} \right) \quad (17.2)$$

where \mathbf{K} is the absolute permeability tensor of the porous medium that must be determined experimentally, μ is the fluid viscosity, \mathbf{g} is the gravitational acceleration vector, g_c is a conversion constant, and the z -axis is oriented in the vertically downward direction. In some practical problems it is possible (or sometimes necessary) to assume that \mathbf{K} is a diagonal tensor given by

$$\mathbf{K} = \begin{bmatrix} K_x & 0 & 0 \\ 0 & K_y & 0 \\ 0 & 0 & K_z \end{bmatrix} \quad (17.3)$$

If $K_x = K_y = K_z$ then the medium is called isotropic, otherwise it is orthotropic. If off-diagonal terms exist then \mathbf{K} is anisotropic.

Based upon measuring z vertically downward, we can write

$$\rho \frac{\mathbf{g}}{g_c} = \rho \frac{\mathbf{g}}{g_c} \nabla z = \gamma \nabla z \quad (17.4)$$

and with the above definition of $\gamma = \rho g / g_c$ we can rewrite Darcy's law as follows:

$$\mathbf{u} = -\frac{\mathbf{K}}{\mu} (\nabla p - \gamma \nabla z) \quad (17.5)$$

Finally, Eq. (17.5) can be substituted into Eq. (17.1) to obtain

$$\nabla \cdot \left[\frac{\rho \mathbf{K}}{\mu} (\nabla p - \gamma \nabla z) \right] = \frac{\partial}{\partial t} (\rho \phi) + \tilde{q} \quad (17.6)$$

17.2.3 Multiphase Flow

The mass conservation equations can be generalized, if we consider several phases, as follows:

$$-\nabla \cdot \dot{\mathbf{m}}_l = \frac{\partial m_l}{\partial t} + \tilde{q}_l \quad (17.7)$$

where m_l is the mass of the phase l in a unit volume of the medium, \dot{m}_l is the mass flux of the phase l , and $\nabla \cdot \dot{m}_l$ is the rate of mass efflux per unit volume.

There are two important mathematical models that are frequently used in a petroleum reservoir simulation, namely, multiphase or single-phase flow when more than two hydrocarbon components are considered, and multiphase flow when the hydrocarbon system can be approximated by two components, a nonvolatile component (black oil) and a volatile one (gas) that is soluble in the oil phase. The latter model is called the β -model or *black-oil model* [27].

In the β -model it is assumed that there are at most three distinct phases, namely oil, water, and gas. Usually water is the wetting phase, oil has an intermediate wettability, and gas is the nonwetting phase, where water and oil are assumed to be immiscible and they do not exchange mass or change phase. Gas is assumed to be soluble in oil but usually not in water. If we assume that the solubility of gas is zero at stock tank (or standard) conditions (STC) then reservoir oil may be considered to be a solution of two components, namely stock tank oil and gas at standard conditions. Furthermore, we can consider the fluids to be at a constant temperature and in thermodynamic equilibrium throughout the reservoir. Under these conditions, the pressure–volume–temperature behavior of the system can be expressed by the formation of the volume factors as follows:

$$B_o = \frac{[V_o + V_{dg}]_{RC}}{[V_o]_{STC}} = f_o(p_o) \quad (17.8)$$

$$B_w = \frac{[V_w]_{RC}}{[V_w]_{STC}} = f_w(p_w) \quad (17.9)$$

$$B_g = \frac{[V_g]_{RC}}{[V_g]_{STC}} = f_g(p_g) \quad (17.10)$$

where the subscripts o, w, and g refer to the oil, water, and gas phases, respectively, RC to the reservoir conditions, STC to the stock tank (or standard) conditions, and dg to the dissolved gas.

For fluids that can be approximated by the isothermal β -model, formation volume factors and viscosities are functions of the pressure only and should be determined at the reservoir temperature. It should be noted that B_g is related to the gas compressibility (as expressed by the perfect gas law). The mass transfer between the oil and gas phases is described by the solution gas to oil ratio, namely

$$R_s = \left[\frac{V_{dg}}{V_o} \right]_{STC} \quad (17.11)$$

which gives the amount of gas dissolved in the oil as a function of the oil-phase pressure. The densities of the three phases at reservoir conditions are related

to those at the STC as follows:

$$\rho_o = \frac{\rho_{o,STC} + R_s \rho_{g,STC}}{B_o} \quad (17.12)$$

$$\rho_w = \frac{\rho_{w,STC}}{B_w} \quad (17.13)$$

$$\rho_g = \frac{\rho_{g,STC}}{B_g} \quad (17.14)$$

The density of the oil phase may also be expressed in the following form:

$$\rho_o = \bar{\rho}_o + \bar{\rho}_{dg}, \quad \bar{\rho}_o = \frac{\rho_{o,STC}}{B_o}, \quad \bar{\rho}_{dg} = \frac{R_s}{B_o} \rho_{g,STC} \quad (17.15)$$

where $\bar{\rho}_o$ and $\bar{\rho}_{dg}$ are the densities of the two oil components.

Before considering multiphase flow we must introduce the concept of saturation. The saturation S_l of the phase l is the part of the pore volume occupied by phase l , and clearly we have $\sum_l S_l = 1$. The equation of mass conservation can be written by considering Eq. (17.7) for each phase and, in particular, for the oil component we have

$$\dot{\mathbf{m}}_o = \bar{\rho}_o \mathbf{u}_o \quad (17.16)$$

$$m_o = \bar{\rho}_o \phi S_o \quad (17.17)$$

Substituting Eqs. (17.16) and (17.17) into Eq. (17.7) and dividing both sides of the resulting equation by $\rho_{o,STC}$, we obtain

$$-\nabla \cdot \left[\frac{1}{B_o} \mathbf{u}_o \right] = \frac{\partial}{\partial t} \left[\frac{1}{B_o} \phi S_o \right] + q_o \quad (17.18)$$

where $q_o = \tilde{q}_o / \rho_{o,STC}$. The mass conservation equation for water is obtained in a similar way, while that for the gas component is more complicated since it exists in both the gas phase and in solution in the oil phase.

Darcy's law may be extended to describe simultaneously the fluid flow of more than one fluid phase as follows, see, for example, [26]:

$$\mathbf{u}_l = - \frac{K \mathbf{K}_{rl}}{\mu_l} \left(\nabla p_l + \rho_l \frac{\mathbf{g}}{g_c} \right) \quad (17.19)$$

where \mathbf{K}_{rl} is the relative permeability tensor of phase l and K is the permeability of a single phase based upon an isotropic situation. Darcy's law may be substituted into the mass conservation equation for each phase to obtain the

fluid flow equations as follows:

$$\nabla \cdot [\mathbf{k}_o(\nabla p_o - \gamma_o \nabla z)] = \frac{\partial}{\partial t} \left[\frac{\phi S_o}{B_o} \right] + q_o \quad (17.20)$$

$$\nabla \cdot [\mathbf{k}_w(\nabla p_w - \gamma_w \nabla z)] = \frac{\partial}{\partial t} \left[\frac{\phi S_w}{B_w} \right] + q_w \quad (17.21)$$

$$\nabla \cdot [R_s \mathbf{k}_o(\nabla p_o - \gamma_o \nabla z) + \mathbf{k}_g(\nabla p_g - \gamma_g \nabla z)] = \frac{\partial}{\partial t} \left[\phi \left(\frac{R_s}{B_o} S_o + \frac{S_g}{B_g} \right) \right] + R_s q_o + q_{fg} \quad (17.22)$$

where the transmissibility tensors \mathbf{k}_l with $l \in \{o, w, g\}$ are defined by

$$\mathbf{k}_l = \frac{\mathbf{K}_{rl}}{\mu_l B_l} K \quad (17.23)$$

and the subscript fg denotes free gas. While the conservation equation is sufficient to describe single-phase flow, the only dependent variable being p , this is not the case for multiphase flow and Eqs. (17.20) to (17.22) contain six dependent variables. To complete the description of multiphase flow we need three additional conditions that relate capillary pressures, P_c , and the saturations in the following form:

$$S_o + S_w + S_g = 1 \quad (17.24)$$

$$P_{c,ow} = p_o - p_w = f_{ow}(S_w, S_g) \quad (17.25)$$

$$P_{c,og} = p_g - p_o = f_{og}(S_w, S_g) \quad (17.26)$$

where the relationships between the capillary pressures and the saturations are usually given empirically. In a first approximation, capillary pressure can be considered to be a function of the reservoir rock only. Capillarity depends on the saturation of the wetting fluid and the direction of saturation change, called a drainage or imbibition curve [27]. Leverett and Lewis [28] first investigated the functions defined in Eqs. (17.25) and (17.26) and found some justification for the following assumptions:

$$P_{c,ow} = f_{ow}(S_w), \quad P_{c,og} = f_{og}(S_g) \quad (17.27)$$

which are still generally used.

The mathematical model for the fluid flow is not complete without the necessary boundary and initial conditions. The reservoir being simulated interacts with its surroundings through the conditions specified at the boundaries. It is essential that the boundary conditions be formulated and approximated so that the desired interaction of the reservoir with its surroundings takes place.

Usually, the initial condition of a reservoir, first treated in the literature in [29], is the state of static equilibrium at which the velocities of all phases are zero.

17.3 Introduction to Genetic Algorithms

17.3.1 What are Genetic Algorithms?

There is a large class of interesting and challenging problems for which no reasonably fast algorithms have been developed and many of these problems are optimization problems that arise frequently in practical applications. For some difficult optimization problems we can use probabilistic algorithms which, although they do not guarantee the optimum value, rely on randomly choosing sufficiently many “witnesses,” and then the probability of the error may be made as small as we wish to specify.

There are many important practical optimization problems for which high quality algorithms have become available, for example, simulated annealing for wire routing or the traveling salesman problem; see [30] for more details. Moreover, many other large-scale combinatorial optimization problems can be solved approximately by using Monte Carlo techniques. In general, any problem to be solved can be perceived as a search through a space of potential solutions. Since we seek “the best” solution for the problem, we can view this search as an optimization process. For small search spaces the classical optimization methods usually suffice, whereas for larger spaces such methods frequently fail. In the latter case special artificial intelligence techniques can be employed.

Genetic algorithms use a vocabulary borrowed from natural genetics. We may talk about *individuals* in a *population* and often refer to these individuals as *strings* of *chromosomes*. This might be a little misleading since each cell of every organism of a given species carries a certain number of chromosomes. However, we consider only one-chromosome individuals, which are composed of *genes* arranged in linear succession, each gene controlling the inheritance of one or more characteristics, for example, the color of hair. Any characteristic of an individual can manifest itself differently; the states in which the gene can occur are called *alleles* (feature values). Each genotype represents a potential solution to a problem and a particular chromosome is interpreted externally by an encoding. An evolution process run on a population of chromosomes corresponds to a search through a space of potential solutions to the corresponding optimization problem.

A GA performs a multidirectional search. Given a population of candidate solutions, it implements a probabilistic, parallel search in the solution space using domain-independent “genetic operators” that simulate evolution processes. At each generation the relatively “good” solutions reproduce, while the relatively “bad” solutions die. A predefined objective (evaluation)

function allows the “fitness” of potential solutions to be determined, and this function plays the role of an environment. The individuals undergo a process of *selection* in which the chromosomes of the *fittest* individuals of every *generation* are most likely to survive and produce *children* for the next generation. Genetic information is exchanged by the process of *recombination* to form children and some random *mutations* occur, thereby producing new areas of the solution space to explore.

In summary, a GA must have the following components:

1. A genetic representation for potential solutions to the problem.
2. A method for creating an initial population of potential solutions.
3. An evaluation function that plays the role of the environment, rating solutions in terms of their “fitness.”
4. Genetic operators that alter the composition of subsequent “generations” of a population of individuals.
5. Values for various parameters that the GA uses, for instance, the population size and the probabilities of applying genetic operators.

Genetic algorithms have been developed by John Holland, his colleagues, and his students at the University of Michigan since 1962. Since then several authors have investigated their applications in many fields of research such as biology [31,32], computer science [33], engineering and operations research [34,35], hybrid techniques [36], image processing and pattern recognition [37], physical sciences [38], social sciences [39], but also in the development of the GA technique, for example, the work of [6,40], and further ideas in [7,41–44]. GAs have been applied with much success to many optimization problems such as wire routing, scheduling, adaptive control, game playing, cognitive modeling, transportation problems, traveling salesman problems [6], optimal control problems, and database query optimization.

17.3.2 Advantages of Using Genetic Algorithms

Genetic algorithms are perhaps the most widely known type of evolutionary algorithms in the field of evolutionary computation, which also includes evolution strategies and evolutionary programming [45]. By imitating genetic and selection mechanisms of nature, GAs are easily programmed and are neither bound to assumptions regarding continuity nor limited by required prerequisites, citing [6], “GAs are blind.”

A search in the space of potential solutions requires balancing two objectives, namely, exploitation of the best solutions and exploration of the search space. This is referred to as the *robustness* of the search technique. The method of *hillclimbing* is an example of a strategy that exploits the best solution for possible improvement; on the other hand, it neglects exploration of the search

space. Hillclimbing methods provide *local* optimum values only, depending crucially on the selection of the starting point, and no information on the relative error of the solution found. *Random search*, which chooses the new point at random from the search space if the new point provides a better value than the current one, is a typical example of a strategy that explores the search space ignoring its promising regions. The *simulated annealing technique*, see, for example, [46], inspired from the formation of crystals in solids during cooling, eliminates most of the disadvantages of hillclimbing methods. In this approach solutions no longer depend on the starting point and are, usually, close to the optimum point. The *Monte Carlo* method [47], provides approximate solutions to a variety of mathematical problems by performing statistical sampling experiments on a computer, and is applicable to problems with absolutely no probabilistic content. Among all numerical methods that rely on n -point evaluations in m dimensions, the Monte Carlo technique has an absolute error of estimate that decreases as $n^{-1/2}$ whereas, in the absence of an exploitable structure, all others have errors that decrease as $n^{-1/m}$ at best. This property gives the Monte Carlo method a considerable advantage in computational efficiency as m , the size of the problem, increases.

The use of GAs over conventional optimization methods actually finds its justification for problems where the search space is large, multimodal and noisy, and fraught with discontinuities. The ergodicity of the evolution operators makes GAs potentially effective at performing global searches (in probability). GAs have been successfully applied to multidimensional nonlinear optimization problems in many dimensions, where traditional methods frequently fail. Moreover, deterministic, gradient-based optimization techniques tend to converge toward local extrema of the objective function, which is clearly unsatisfactory for problems where the objective function varies nonmonotonously with the parameters. While it is likely to be more expensive in computing time, the GA approach undertakes a more complete search of the parameter space.

In summary, GAs are different from other optimization and search procedures in the following ways:

1. GAs work with a coding of the parameter set and not the parameters themselves.
2. They search through a population of points and not a single point.
3. They use information based only upon an objective function rather than its derivatives or other auxiliary knowledge.
4. They use probabilistic transition rules, not deterministic rules, to guide their search.

However, the use of probability does not suggest that the method is some simple random search. GAs use randomized operators as a tool to guide a search toward promising regions of the solution space. These differences

contribute to the robustness of a GA and its resulting advantage over other more commonly used techniques.

17.3.3 Components of a Genetic Algorithm

The mechanics of a basic GA are surprisingly simple, involving nothing more complex than copying fixed-length binary strings and swapping partial strings. An explanation of why this simple process works is given in Section 17.3.4.

In a simple GA, the process of *evaluation* assigns each candidate (potential) solution in a population an associated fitness value which measures the candidate's survivability. A GA does its search through an iterative process in which this population evolves at each generation according to the three operations of selection, crossover, and mutation. Given an initial population, usually randomly assigned, selection probabilistically chooses better candidates for a new generation, while crossover and mutation manipulate candidate solutions to generate new individuals for the selection procedure to process again.

17.3.3.1 *Binary encoding of individuals*

Suppose we wish to maximize a function of k variables, $f(x_1, \dots, x_k) : \mathbb{R}^k \rightarrow \mathbb{R}$. Further, suppose that each variable x_i can take values from a domain $\mathcal{D}_i = [a_i, b_i] \subseteq \mathbb{R}$, for $i = 1, \dots, k$. A precision of d_i decimal places for the i th parameter can be specified by employing an n_i digit binary representation, where n_i is the least positive integer such that $(b_i - a_i)10^{d_i} \leq 2^{n_i} - 1$.

Now, each chromosome, as a potential solution, is represented by a binary string of length $n = \sum_{i=1}^k n_i$. The first n_1 bits define a gene that maps into a value from the range $[a_1, b_1]$, the next group of n_2 bits map into a value from the range $[a_2, b_2]$, and so on until the last group of n_k bits that map into a value from the range $[a_k, b_k]$.

17.3.3.2 *Selection operators*

Selection is a process in which individual strings are copied according to their objective function values or *fitness*. The higher the fitness, the more likely an individual is to be selected. The process of selection or sampling must be considered at two separate stages of the GA procedure, namely, the selection of parents of the next generation from the individuals of the previous population and the selection of the individuals of the next generation from the parents and children derived from the previous population.

Selection processes are, of course, an artificial version of natural selection, a Darwinian survival of the fittest among strings. There are several selection methods available, but probably the simplest one is the *roulette wheel selection* in which a biased roulette wheel is defined such that each current string

in the population has a slot sized in proportion to its fitness. The selection procedure is based upon spinning the roulette wheel and selecting a single chromosome. Thus, the individuals with the highest fitness have a better chance of being selected relative to the less-fit individuals and also fitter individuals may be selected more than once, which is in accordance with the Schema theorem (see [Section 17.3.4](#)). However, due to its large stochastic errors, the roulette wheel selection does not guarantee that high-fitness candidate solutions propagate to the next generation. To overcome this, several researchers have investigated a number of alternative selection schemes. The first recognized work is due to De Jong [48] who, in his doctoral dissertation, considered several variations of the simple selection procedure. One such approach, named the *elitist model*, preserves the best chromosome out of the old population and transfers it directly into the new population. Other methods were proposed by Brindle [42] in his doctoral thesis, namely *deterministic sampling*, *remainder stochastic sampling without replacement*, *tournament selection*, and *remainder stochastic sampling with replacement*. Baker [44] presented an improved version of selection called *stochastic universal sampling*. The method uses a single wheel spin of the roulette wheel with exactly N_{pop} equally spaced markers as opposed to N_{pop} repetitions of the random positioning of a single marker.

Other methods to sample a population are based on introducing artificial weights. The chromosomes are selected proportionally to their rank rather than actual function evaluation values. These methods are based on the belief that premature convergence is caused by the presence of high-fitness *super individuals* that have a large number of offspring and prevent other individuals from contributing any offspring. In a few generations a super individual can eliminate desirable chromosome material and cause rapid convergence to some (possibly) local optimum.

The *k-tournament selection* method utilizes the idea of ranking. This method (in a single iteration) randomly selects some number k of individuals from the population and, from this pool of individuals, one member is selected as a parent for the next generation. The selection of one member of the pool of k individuals begins by ranking them according to their fitness. The highest ranking individual is then selected with some probability p_t , the *tournament probability*. If this individual is not selected then the second-ranking individual is selected with the probability $p_t(1 - p_t)$. This process is repeated until we have a successful selection or until we have reached the end of the pool, in which case the lowest ranking individual is selected, and this occurs with probability $(1 - p_t)^{k-1}$. It is clear that large values of k increase the selection process. A typical value for many applications is $k = 2$, where the parameter k is called the *tournament size*.

17.3.3.3 Crossover operators

Crossover is the mating process that allows information exchange during the creation of N_{child} children from the population of N_{pop} parents. The most

simple crossover operator is *one-point crossover*. One of the parameters of a genetic system is the probability that a chromosome will undergo crossover, p_c . For each pair of coupled chromosomes selected for crossover we mate them by choosing a random crossing point and exchanging bits beyond this location, thereby producing a pair of offspring.

If the crossover probability p_c is close to unity, then highly fit individuals mate more and are discarded faster than selection can produce improvements. On the other hand, if the crossover rate is close to zero, then the search might stagnate for lack of exploration. Usually p_c lies between 0.5 and 1.

The extension to *N-point crossover* is achieved by cutting the parents in the specified number of places, with locations chosen at random, and creating offspring by splicing. Various kinds of improved crossover techniques are available, for example, *segmented crossover* and *shuffle crossover* [49,50]. A further generalization of multipoint crossover is *uniform crossover* [51], which, for each position, randomly chooses between the bits from each parent with a certain probability. This kind of crossover can combine features regardless of their relative location and for some problems this ability prevents the destruction of the “building blocks,” see [Section 17.3.4](#).

17.3.3.4 *Mutation operators*

The mutation operator is performed on a bit-by-bit basis, that is, changes in one or several bits of the chromosome. Another parameter of the genetic system is the probability of mutating an individual bit, p_m . Every bit has an equal chance to undergo mutation, that is, change from 0 to 1, or vice versa.

17.3.3.5 *Further genetic algorithm techniques*

Genetic algorithm theory provides some explanation as to why, for a given problem formulation, we may obtain the convergence to some desired optimal point. Unfortunately, practical applications do not always follow the theory. Under certain conditions, GAs fail to determine the optimal solution due to premature convergence to some local optimum, which is a common problem in many other optimization algorithms. If convergence occurs too rapidly, then the valuable information developed in part of the population is often lost. There are several strategies to prevent premature convergence, including a mating strategy called *incest prevention*, the use of *uniform crossover*, and the detection of duplicates in the population’s strings. Another direction in fighting premature convergence is trying to fix the function itself by introducing a scaling mechanism [6].

It is also important to specify a termination condition to be used in the algorithm. The simplest one would check the current generation number and end the search if the total number of generations exceeds a prescribed constant. In many versions of evolution programs, not all individuals need to be reevaluated when passing from one generation to another without alteration. If the number of function evaluations that are necessary is monitored,

then the algorithm search can be terminated when the chance for significant improvements is small. Other categories of termination conditions use the characteristics of the search for making termination decisions [6].

17.3.4 A Theoretical Basis for the Genetic Algorithm Approach

Section 17.3.3 portrayed an accurate, but somewhat crude, picture of GAs and their mechanisms and power. The theoretical foundations of GAs rely on a binary string representation of solutions and on the notion of *schemata*, templates allowing exploration of similarities among chromosomes.

A schema is built by introducing the “wildcard” symbol (*) in the binary alphabet of genes. A schema represents all strings (a hyperplane or a subset of the search space) which match it on all positions other than “*”. The *order* of a schema S , denoted by $o(S)$, is defined as the number of fixed positions within the chromosome, that is, those specified as 0 and 1, and this notion defines the speciality of a certain schema. The *defining length* of a schema S , denoted by $\delta(S)$, is the distance between the first and the last fixed positions in the template and it defines the compactness of information contained in a schema. These two notions are useful in calculating survival probabilities of a certain schema under the operations of mutation and crossover, respectively.

Let us assume that, at a given time step t , there are ξ representatives of a particular schema S in the population. The growth equation for the number of this schema can be estimated as follows [7]:

$$\xi(S, t+1) \geq \xi(S, t) \frac{f(S)}{\bar{f}} \left[1 - p_c \frac{\delta(S)}{n-1} - o(S)p_m \right] \quad (17.28)$$

where the three terms in the bracket represent contributions due to reproductive, crossover, and mutation operations, respectively. Thus, schemata with both above-average performance and a short defining length will be sampled at exponentially increasing rates. This final growth equation (17.28) can be interpreted as the Schema theorem.

Schema theorem *Short, low-order, above-average schemata receive exponentially increasing trials in subsequent generations of a GA.*

An immediate result of this theorem is that GAs explore the search space by short, low-order schemata which are used subsequently for information exchange during crossover.

Building block hypothesis *A GA seeks near-optimal performance through the juxtaposition of short, low-order, high-performance schemata, called the building blocks.*

Although some research [52] has been done to prove this hypothesis, for most nontrivial applications we rely mainly on empirical results. Numerous GA applications were developed supporting the building block hypothesis

in many different problems. Nevertheless, this hypothesis suggests that the problem of coding for a GA is critical for its performance and that such a coding should satisfy the idea of short building blocks.

17.3.5 Details and Example of the Genetic Algorithm Technique Employed in this Chapter

When applying a GA approach to an optimization problem, the details of the optimization procedure strongly depends on the problem under consideration. In the scheme that we use, the population evolves through a sequence of generations and the details of the scheme are as described below. These concepts are most easily explained through an illustrative example, for which we have chosen to maximize the following function of two variables over the domain \mathcal{D} with $(x, y) \in \mathcal{D} = [2, 3] \times [-1, 3]$:

$$f(x, y) = (x - 1.5)^2 \sin(8\pi x) + (y + 0.5)(y - 2.5)^2 \sin(7\pi y) + 21.5 \quad (17.29)$$

This function has multiple peaks (local optimum values) on its domain of definition and is illustrated in Figure 17.2. The maximum value of the function over \mathcal{D} is 28.3076 and this occurs at the point for which $x = 2.8149$ and $y = -0.9345$.

For our example, we wish to maximize the function (17.29) of two variables. Let us suppose that a precision of four decimal places is required for each of the variables x and y . Then, as in Section 17.2.3.1, we must employ n_x digit and n_y digit binary representations for x and y , respectively, where n_x

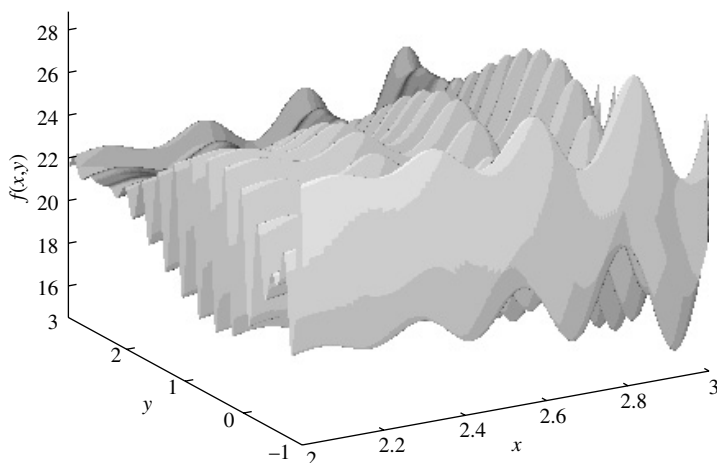


FIGURE 17.2
The function of two variables presented in Eq. (17.29).

and n_y are the least positive integers such that $(3 - 2) \times 10^4 \leq 2^{n_x} - 1$ and $(3 - (-1)) \times 10^4 \leq 2^{n_y} - 1$. Thus, we choose $n_x = 14$ and $n_y = 16$ and each chromosome is represented by a binary string of length $n = 14 + 16$, where the first $n_x = 14$ bits define a gene which maps into a value x from the range $[2, 3]$ and the next $n_y = 16$ bits map into a value y from the range $[-1, 3]$.

The GA algorithm now proceeds as follows:

1. *Initialization of the population*

We randomly construct an initial population of N_{pop} chromosomes, each of which characterizes an estimate to the solution of the problem through its separate genes, which represent encodings of all the unknown parameters over some specified ranges.

For our example, we choose $N_{\text{pop}} = 50$. Each of the 50 chromosomes consists of 30 bits and to initialize the population we set each of these 50×30 bits randomly as either 0 or 1. An example pair of chromosomes would be as follows:

$$\begin{aligned} C_1 &= (01100011100101 \mid 1101000101110101) \\ C_2 &= (11110001000011 \mid 0001011100111001) \end{aligned} \quad (17.30)$$

where the symbol “|” indicates the division of the chromosome into its separate genes. As binary numbers, the two genes in C_1 equate to 6,373 and 53,621. Therefore, C_1 represents the coordinates $(2.3890, 2.2728)$ and its “fitness” value, namely the value of the function (17.29), is $f = 21.1875$.

2. *Selection of the parents for the next generation*

Using k -tournament selection and some value for the probability p_t , we can choose a single parent for the next generation from the old population of individuals based upon a fitness evaluation function.

For our example, we choose $k = 2$ and $p_t = 0.8$ and follow the description in Section 17.3.3.2. Thus, we randomly choose two individuals from the population and rank them according to their fitness value. We want to choose one of these two individuals to be a parent for the next population. The first, higher-fitness individual is chosen with a probability $p_t = 0.8$ and the second is chosen with a probability $1 - p_t = 0.2$. This process is repeated and the two chosen parents will be used to produce offspring.

3. *Construction of children from a pair of parents*

Using two-point crossover with some probability p_c of crossover occurring, we produce two child chromosomes from the given two parent chromosomes. For every child produced, each bit within the chromosome is selected for mutation with a probability p_m .

For our example, we choose $p_c = 0.65$ and $p_m = 0.02$. Suppose that we have selected two parents, P_1 and P_2 , and they are the chromosomes given in Eq. (17.30). Further, suppose that we have randomly

chosen to apply two-point crossover (with probability p_c), rather than simply retaining the parent chromosomes. We then randomly choose two locations (indicated below by the symbol “|”) along the chromosome pair and interchange the bits of the parents between these locations to produce the chromosomes O_1 and O_2 . Finally, the mutation process takes each of the 30 bits of each child chromosome and randomly changes it from 0 to 1, or vice versa, with probability p_m . The resulting chromosomes O_1 and O_2 are now two of the children, or “offspring,” of the generation. This process can be represented as follows:

$$\begin{aligned}
 P_1 &= (011000111 | 00101110100010111 | 0101) \\
 &\quad \Downarrow \\
 P_2 &= (111100010 | 00011000101110011 | 1001) \\
 \text{Two-point crossover} &\implies \\
 O_1 &= (011000111 | 00011000101110011 | 0101) \tag{17.31} \\
 O_2 &= (111100010 | 00101110100010111 | 1001) \\
 \text{Mutation} &\implies \\
 O_1 &= (\mathbf{011000011}000110001011100110101) \\
 O_2 &= (111100010001011101000101111101)
 \end{aligned}$$

where the two mutated bits are indicated in bold type.

4. Construction of the next generation

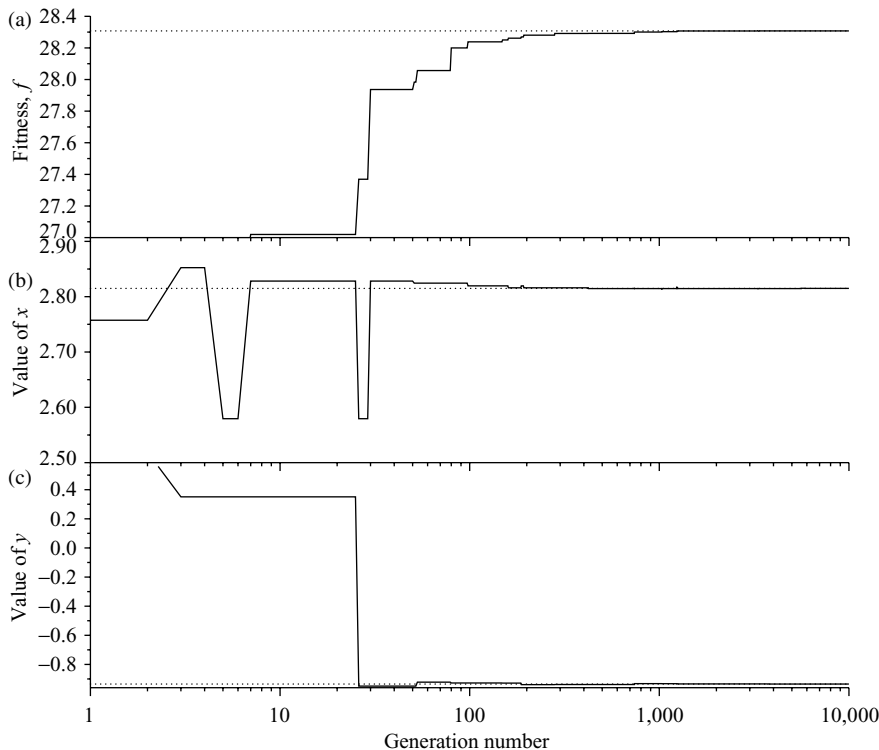
By repeating the steps of parent selection, crossover, and mutation we can generate a pool of offspring of size N_{child} . By merging the parents and offspring we can construct the next generation of N_{pop} individuals. The n_e fittest (elitist model) individuals from the parent population are first copied into the next generation. The children are then ranked and the fittest (unique) chromosomes used to complete the next generation.

For our example, we produce $N_{\text{child}} = 60$ children and merge the parent and child populations, under an elitist model with $n_e = 2$, to produce the next population of $N_{\text{pop}} = 50$ individuals.

5. Evolution of generations

The steps 2 to 4 are repeated until a specified number of generations has been performed.

The above procedure was applied to the maximization of the function (17.29) and 10,000 generations were performed. In a typical run of this optimization process, the maximum value of the function (17.29) was predicted to occur at $(x, y) = (2.8149, -0.9348)$, where $f = 28.3074$, and clearly these results are in excellent agreement with the known optimal solution. [Figure 17.3](#) demonstrates how the values of x , y , and the fitness f each evolve with the generation number,

**FIGURE 17.3**

The evolution of (a) the fitness f , see Eq. (17.29), (b) the coordinate x , and (c) the coordinate y , as a function of the generation number. The value plotted at each generation represents the current fittest individual and the dotted line indicates the known optimal solution.

where the value plotted at each generation represents the current fittest individual. Clearly, the required accuracy of solutions can be viewed in relation to the number of generations prescribed, and such considerations are important in the design of parameter inversion routines when the evaluation of the fitness of an individual is computationally expensive. In our example, a fitness of $f = 28.3004$ has been achieved after 1,000 generations, and the predicted optimum solution is $x = 2.8146$ and $y = -0.9321$. Such a solution may be considered to be “sufficiently” accurate according to the problem under investigation.

In this section a basic introduction to the GA concept has been presented. Much more could have been reviewed, including numerous different applications and many different theoretical approaches. However, the intention here was to show that GAs are on their way to becoming another powerful approach for solving optimization problems. In the following sections we

study the applicability of the GA approach to the field of inverse problems, especially in the determination of the hydraulic properties of porous media.

17.4 Parameter Identification within Rock Samples

17.4.1 Introduction

Transient flow analyses have numerous geophysical and geotechnical applications and they are necessary for the understanding and development of laboratory measurement techniques in rock and soil mechanics, particularly in the determination of the permeability of substances. In petroleum reservoirs and aquifers the flow rate and pressures throughout the system are continually changing in response to the withdrawal or injection of fluids within boreholes, in accordance with known poroelastic phenomenon that couple the stress and displacement fields of the fluids and rocks [53]. Clearly, the hydraulic properties are *transient* and can be described in terms of the propagation of perturbations through a diffusive system. The topic of well test analysis relies on an understanding of these transients in order to recover hydraulic properties [54]. Transient methods have been used to determine the hydraulic conductivity of rocks [55], and their storage properties [56–59], using boundary measurements alone. By changing the applied boundary conditions, a variety of other methods have been proposed for probing the internal structure of the rock sample [60,61]. In this section we investigate the identification of the hydraulic properties of rocks using boundary measurements in time of the pressure and/or hydraulic flux in transient hydraulic experiments; see [24,62–64] for more details.

The fluid flow within petroleum reservoirs is strongly dependent upon both the heterogeneity and/or the anisotropy of the rock structure. However, any attempt to accommodate both in an approach that retrieves internal information on the physical properties of the rock from boundary measurements alone is highly complex and, at the moment, very difficult to achieve. Viewed from the fluid flow, anisotropy and heterogeneity are closely related properties and can be presented by a single approach if one views the hydraulic conductivity as a tensor whose principal directions are functions of the space coordinates. Clearly what is required is a detailed knowledge of this tensor and the question is whether, and how well, information from laboratory small-scale experiments and numerical calculations from mathematical models can help to achieve this kind of knowledge. One of the main problems is that experiments, simply by their laboratory-modified constraints, for example, the sides of the sample being confined within an impermeable material, make the scaling-up of any of the results obtained very difficult.

It is known that the flow pattern in a rectangular rock sample is significantly changed if the no-fluid-flow condition is imposed on the side walls of the rock

sample, according to both the orientation of the sample axis with respect to the principal directions of the hydraulic conductivity tensor and the ratio of the principal values of the hydraulic conductivity. Hence, in discussing any one-dimensional model of the fluid flow in a rock, its limitations in any scale-up prediction have to be understood. A mathematical model needs to be initially validated by experiments and it has to be subject to the same restrictions as the experiments.

In general, laboratory permeability tests are performed using the following techniques:

1. *Constant head testing*

A pressure gradient is imposed suddenly across opposite faces of a saturated rock or soil sample. If there are no compressibility or inertial effects, then the flow is established in the steady-state condition in accordance with Darcy's law, see Al-Dhahir and Tan [65] who plotted a graph of the outflow rate against the square root of time to show when a steady-state flow rate had been reached.

2. *Transient (pulse decay)*

See [55,56,66]; Brace et al. [55] showed that the permeability of a small and rigid sample can be calculated from the decay constant of the exponential pressure function. The decay constant is the slope of the curve of the natural logarithm of the pressure plotted as a function of time and the permeability is calculated from a formula involving this constant as well as the system compliance, which is a small number representing the volume of water required to change the pressure (or head) by a unit amount, and this quantity can be measured.

3. *Constant flow rate (pump–flow)*

See [67,68]; this method is fully discussed and taken into consideration in this chapter.

The above-mentioned articles provide analytical solutions assuming that the specimen is homogeneous; it is the purpose of this section to provide numerical solutions for heterogeneous rock samples.

In a hydraulic pump–flow test, a cylindrical rock sample is placed in a sealed pressure cell and the permeability is measured by injecting fluid at a constant rate into the inflow end of the rock sample using the "syringe infusion pump–flow method" [69,70]. The pressure across the sample builds up to a steady-state value, which, if the sample is homogeneous, can be used to calculate the effective permeability of the whole sample through the application of Darcy's law. After the pressure has reached its steady-state value, or even before that, the pump may be switched off. The technique has the advantage of an easy setup and computer control, a high level of accuracy at low permeabilities, and, in general, short testing times, that is, a short transient period before the steady state is reached. In real time the pressure is easy to measure very accurately using electron transducers. However, if the sample

is heterogeneous then there is little information that can be deduced about the permeability structure from the steady-state pressure response. The initial, transient part of the pressure response that follows the onset of pumping, and the pressure decay that follows the cessation of pumping, can be used to obtain information about the permeability and storage properties of the sample [67].

In the studies [67,71], a constant hydraulic flux at the upstream face of the sample (rock) is prescribed. However, the constant hydraulic flux boundary condition is not physically achievable in a real experiment as the upstream storage of an upstream reservoir, which is maintained in hydraulic contact with the sample, is never zero. The approach in [67] is strictly valid for the case when the specific storage of the sample dominates the compressibility of the system, as in the case of large soil samples, and not for small samples or rigid rock specimens that are investigated here.

In this section we make use of the experimental setup designed by Clennell [19], shown schematically in Figure 17.4(a), and the numerical results of Lesnic et al. [24], who investigated the case of the spatial dependence of the properties of the material (rock sample) using a constrained optimization NAG routine. This requires the calculation of the gradient of a least-squares functional using finite differences and, in addition, it may be dependent upon the choice of initial guess, so that the search for the global optimum may become trapped in a local optimum region. In order to overcome such

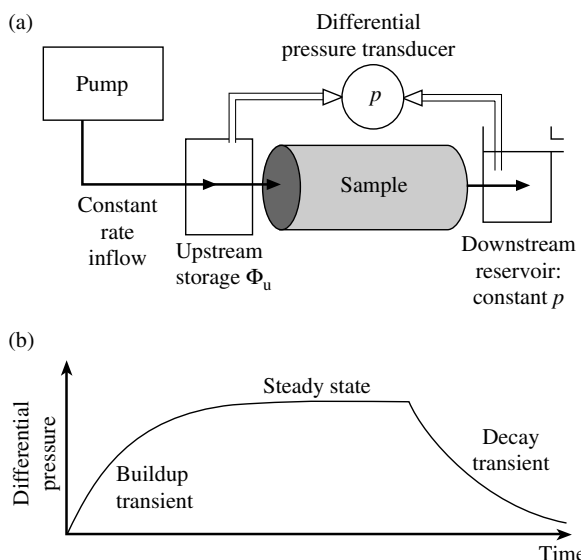


FIGURE 17.4

(a) Schematic representation of the pump–flow experiment designed by Clennell [19], and (b) a typical differential pressure response within the sample during a pump–flow experiment. This type of experimental setup is used throughout this chapter.

restrictions, we use a GA-based optimization procedure which does not depend on the initial guess and, moreover, does not require any gradient calculations. A typical pressure response within the sample as a function of time is shown in [Figure 17.4\(b\)](#), where the pressure buildup, the steady state, and the decay response can be observed.

17.4.2 Experimental Method

Samples to be tested are first saturated fully in the chosen permeant solution by immersion in de-aired water under vacuum for several hours. Cylindrical samples (2.5–5.5 cm in diameter and 2–10 cm in length) are mounted in a close-fitting polypropylene sleeve and placed in a stainless steel sample holder, and the experimental setup is similar to that shown later in [Figure 17.6](#). The confining pressure is set to a constant value of 100 kPa and maintained at this value by a servo pump. A constant back pressure of 300 kPa is employed in order to ensure that the sample is fully saturated and this is provided via a second pressure generator. Flow rates between 1.2×10^{-7} and 0.3 cm/sec can be set via a computer control system and this may be changed at any time during the test. An inflow of fluid mass is applied at an upstream reservoir that is in hydraulic contact with the rock sample. The pressure drop induced across the sample by the flow of permeant is measured with an accurate differential pressure transducer. The flow rate of the pump is chosen so that the equilibrium pressure lies between 10 and 120 kPa. The readings for the differential pressure during the test are accurate to within 0.1 kPa.

In general, the temperature affects the pressure readings as water expands and contracts in the pipes. However, all the experiments are performed for samples with a permeability that is greater than 10^{-13} cm² and under such circumstances the obtained results are essentially unaffected by temperature changes.

Using the above description of the equipment and procedures it is possible to measure permeabilities over a wide range of values, namely 10^{-16} to 10^{-8} cm². The upper limit of this range is set by the syringe volume and the tendency of the flow to be non-Darcian, that is, at high flow rates the fluid flow enters the Forchheimer regime and inertial effects become important. In contrast, the lower limit is imposed by the temperature variation in the laboratory, but this can be overcome by performing the experiments in a sealed, air-conditioned environment.

The time taken to reach equilibrium, that is, when no further increase in the pressure distribution across the sample is observed, and the timescales of all the transient phenomena are largely dictated by the elastic compliance of the system to fluid pressure changes. Short testing times are obtained by minimizing this compliance and this can be achieved by the design having short, rigid lengths of thick-walled stainless steel tubing and a small upstream dead volume in the sample holder. The upstream compliance is a system constant and can be measured by replacing the sample with a steel blank and pumping

permeant into the upstream tubing and dead volume at a constant rate, while the pressure is monitored. The downstream compliance of the system that we take into consideration is infinite as the back pressure is buffered at a constant value with an air line.

While the compliance of the system is quite small, the samples are generally small in size and have low porosity, so that the measured transient response and the overall elastic storage of the system are dominated by the upstream compliance of the apparatus. This means that, while the permeability can be measured with great accuracy, the exact value of the sample elastic storage coefficient, and consequently the specific storage of the rock, cannot be measured accurately. So we assume the value of sample storage Φ to be small and known and all the meaningful remaining storage is ascribed to the storage coefficient Φ_u , termed the compressive storage of the upstream reservoir and comprising the dead volume including the syringe and tubing at the injection end of the system; see Figure 17.4(a). However, the pump-flow mathematical model, which is developed in Section 17.4.3, provides numerical justification for the fact that the pressure measurements at the upstream face of the sample are found to be insensitive to values of Φ , while being sensitive to the value of Φ_u because of the rate of fluid flow that is supplied at the entrance of the upstream reservoir [24].

17.4.3 Mathematical Formulation

17.4.3.1 The governing equation

By ignoring the influence of gravity and in the absence of any source terms, the governing equation (17.6) has the following form:

$$\nabla \cdot (\mathbf{k} \nabla p) = \frac{\partial}{\partial t} \left[\frac{\phi}{B} \right] \quad (17.32)$$

after dividing by ρ_{STC} and using the definitions of the formation volume factor $B = [V]_{RC}/[V]_{STC}$ and the hydraulic conductivity $\mathbf{k} = (1/\mu B)\mathbf{K}$. Since de-aired water is used in the experiments, a simplified form for the equation of state for the pore fluid can be assumed, namely

$$\rho = \rho^0 \exp(c_f(p - p^0)) \quad (17.33)$$

where ρ^0 is the fluid density at some reference pressure p^0 and c_f is the fluid compressibility. This is considered to be a good description of the isothermal flow of most fluids of constant and small compressibility. If B^0 is the formation volume factor at p^0 then

$$\frac{\rho}{\rho^0} = \frac{B^0}{B} \approx 1 + c_f(p - p_0) \quad \text{or} \quad \frac{1}{B} = \frac{1}{B^0}[1 + c_f(p - p_0)] \quad (17.34)$$

since c_f is sufficiently small (around 10^{-5} to 10^{-6}) for terms of $O(c_f^2)$ to be neglected. If the rock porosity is assumed to be constant, then Eq. (17.32) may be recast in the following form:

$$\nabla \cdot (\mathbf{k} \nabla p) = \phi \frac{c_f}{B^0} \frac{\partial p}{\partial t} \quad (17.35)$$

Here the reference pressure is considered to be the back pressure in the experimental device. Since the observed pressure rise throughout the sample, in time, is one or two orders of magnitude lower than the back pressure and c_f is a small quantity, Eq. (17.34) indicates that B and B^0 can be assumed constant and equal. If we consider the flow to be one-dimensional along a sample of length L , then Eq. (17.35) may be recast in the form of a one-dimensional partial differential equation with spacewise dependent coefficients, that is,

$$\frac{\partial}{\partial x} \left(k(x) \frac{\partial p}{\partial x} \right) = \Phi(x) \frac{\partial p}{\partial t} \quad \text{for } (x, t) \in (0, L) \times (0, \infty) \quad (17.36)$$

where $\Phi(x) = c_f \phi(x)/B^0$ is the sample specific storage and $k(x)$ is the hydraulic conductivity of the rock.

17.4.3.2 Boundary conditions

In order to complete the mathematical model, we require some boundary conditions which are derived from the pump-flow experiment [19]. At the start of the experiment, the pressure distribution in the sample (rock) is taken to be zero, that is,

$$p(x, 0) = 0 \quad \text{for } x \in [0, L] \quad (17.37)$$

The downstream face of the sample, $x = L$, is maintained at its initial pressure value, namely

$$p(L, t) = 0 \quad \text{for } t \in (0, t_\infty] \quad (17.38)$$

where t_∞ represents the time at which the pump is switched off, which is usually a time at which the flow is in a steady state.

The third boundary condition is obtained by applying the mass conservation law at the sample-reservoir interface and applying Darcy's law, to give

$$\Phi_u \frac{\partial p}{\partial t}(0, t) = k(0)A \frac{\partial p}{\partial x}(0, t) + Q_u \quad \text{for } t \in (0, \infty] \quad (17.39)$$

where A is the cross-sectional area of the sample, Q_u is the inflow rate at the entrance of the upstream reservoir, and $\Phi_u = \gamma_w c_f V_u$ is the compressive storage of the upstream reservoir of volume V_u [24].

17.4.3.3 Direct solution for the homogeneous case

The first step in the inverse analysis of identifying the hydraulic properties of the rock is the development of the corresponding direct solution technique. The numerical method adopted is a time-weighted average FDM, using a Galerkin weight factor $\delta \in [0, 1]$, and uniform space and time grids.

A set of experiments were used to validate this model for samples of medium and large dimensions subjected to various inflow rates. Figure 17.5 shows examples of the numerical simulated data and the experimental data as a function of time at the upstream face of the sample, $x = 0$, for two different inflow rates. The sample has a length of $L = 3$ cm, a cross-sectional area of $A = 22.6 \text{ cm}^2$ and a measured hydraulic conductivity of $k = 1.35 \times 10^{-6} \text{ cm/sec}$. The specific and compressive storages of the sample were taken to be $\Phi = 10^{-9} \text{ cm}^{-1}$ and $\Phi_u = 0.75 \times 10^{-4} \text{ cm}^2$, respectively. This study has also been thoroughly validated in [24,63].

17.4.4 Inverse Problem Formulation

The inverse analysis requires the determination of both the spatially varying hydraulic conductivity and specific storage. Although uniqueness conditions for this inverse problem are difficult to prove, it is to be expected that strong additional information should be provided in order to render a unique solution. In initial cases for which only the hydraulic conductivity needs to be identified, an *a priori* estimate of the specific storage is provided. The first

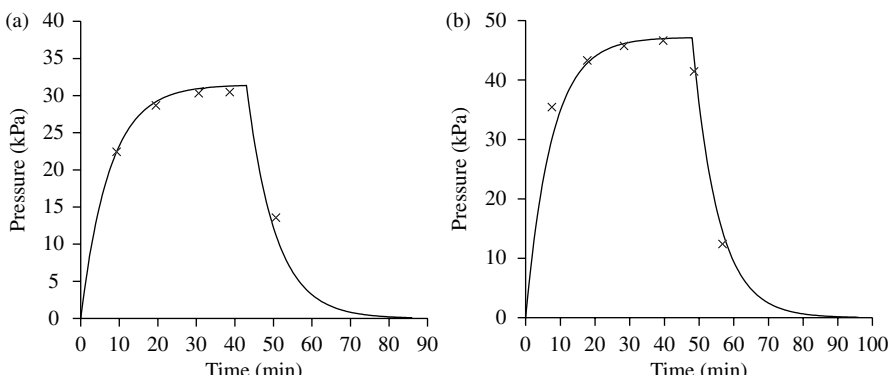


FIGURE 17.5

Numerical solutions (solid lines) and experimental values (\times symbols) for the pressure at the upstream face of the sample, $p(0, t)$, when $L = 3$ cm and $k = 1.35 \times 10^{-6} \text{ cm/sec}$, for (a) $Q_u = 3.2 \times 10^{-3} \text{ cm}^3/\text{sec}$ and (b) $Q_u = 4.8 \times 10^{-3} \text{ cm}^3/\text{sec}$.

case that we study is the particular situation when the unknown hydraulic conductivity $k(x)$ belongs to the space of at most quadratic polynomials, that is,

$$k(x) = k_0 + k_1x + k_2x^2 \quad \text{for } k_0, k_1, k_2 \in \mathbb{R} \text{ and } x \in [0, 1] \quad (17.40)$$

Our approach is simple but rational, namely we start with one to three unknowns, that is, the coefficients for constant, linear, and quadratic space-wise dependencies of the hydraulic conductivity, to be retrieved from the same number, namely one to three, of time measurements of available information, that is, pressure and hydraulic flux, which is the minimal necessary condition for identifiability. In all cases, the same mean hydraulic conductivity $k^* = \int_0^L k(x) dx/L$ is maintained.

In general, only boundary measurements are available if we are not to damage the sample. Therefore, in practice, possible reliable measurements involve the temporal pressure values at the upstream face of the sample $x = 0$, that is, $p(0, t)$, and values for the hydraulic fluxes at both ends of the sample, that is, $q_0(t) = q(0, t) = k(0)\partial p/\partial x(0, t)$ and $q_1(t) = q(1, t) = k(1)\partial p/\partial x(1, t)$. We consider a modified least-squares fitness functional and maximize it using the GA-based optimization technique described in Section 17.3.5.

Using values derived from the hydraulic experiments, simulated pressure buildup curves are produced at the upstream face of the sample. After the equilibrium in pressure has been reached, the supply of the inflow mass of fluid is closed and the simulated decay curve is also recorded. In the direct problem the mean hydraulic conductivity of the sample is taken to be $k^* = 1.48 \times 10^{-8}$ cm/sec and the specific storage of the sample is $\Phi = 10^{-9}$ cm $^{-1}$. A very low constant inflow rate of $Q_u = 3.33 \times 10^{-5}$ cm 3 /sec is supplied at the upstream reservoir, the length of the sample is $L = 3.42$ cm, and the pump is switched off after $t_\infty = 20,000$ sec with a corresponding pressure value of $p_\infty = 96$ kPa. The compressive storage of the upstream reservoir was measured to be $\Phi_u = 2 \times 10^{-4}$ cm 2 .

17.4.5 Sensitivity Coefficients

Once the mathematical model has been validated, prior to performing the inverse analysis, it is useful to undertake a sensitivity analysis of the boundary data with respect to the unknown parameters. In general it is desired that the sensitivity coefficients are uncorrelated, that is, they are linearly independent [72]. The degree of uncorrelation of these coefficients can then be illustrated by the departure of ratios of sensitivity coefficients from a constant value. Based on this criterion we can determine the values of the time measurements to be imposed and recorded in order to reduce the ill-posedness of the inverse-formulated problem. Therefore, a study of the sensitivity coefficients, prior to performing experiments, can lead to better experimental designs. The (normalized) sensitivity coefficients, as a function of the time t ,

are calculated using forward finite differences, that is,

$$\text{Sens}(T; k_i) = k_i \frac{\partial T}{\partial k_i} = k_i \left(\frac{T(k_i + h) - T(k_i)}{h} \right) \quad \text{for } i = 0, 1, \text{ and } 2 \quad (17.41)$$

where h is a small perturbation of the hydraulic conductivity coefficients and T is a measured value.

17.4.6 The Homogeneous Hydraulic Conductivity Case, $k(x) = k_0 = \text{constant}$

A single time measurement of the pressure has been found to be sufficient in order to retrieve the value of the unknown parameter k_0 [24]. We aim to choose a time instant so that the sensitivity coefficient has its maximum absolute value, and a time instant close to the moment when the pump is switched off gives a high sensitivity coefficient. Therefore, the pressure measurement was recorded at $t = 18,600$ sec. The range in which we search for the unknown parameter, namely the constant hydraulic conductivity k_0 , is given by the domain $\mathcal{D} = [0.5, 2.5] \times 10^{-8}$ cm/sec which encloses the expected value to be retrieved, namely $k_0 = 1.48 \times 10^{-8}$ cm/sec. These limits on the domain \mathcal{D} ensure a sufficiently large variation for the simulated steady-state values of the pressure at $x = 0$ within the range of values $32 \text{ kPa} \leq p(0, \infty) \leq 162 \text{ kPa}$, so that good agreement with the experimental data may be achieved.

As there are no general guidelines as to how to choose the values of the GA parameters, a study was made in [63,64] of the effect of changes in the evolution parameters on the convergence to the optimal solution. As a result, the evolution parameters $N_{\text{pop}} = 50$, $N_{\text{child}} = 60$, $k = 2$, $p_t = 0.8$, $n_e = 2$, $N_{\text{gen}} = 150$, $p_m = 0.02$, and $p_c = 0.65$ were chosen for the GA description given in Section 17.3.5. These are typical values of the evolution parameters that have been used for different purposes by other authors [7].

Even in this simple problem, the GA proves its ability to perform an effective search in the given domain, which is in contrast with the results obtained using the procedure in [24] for the same type of information in the inversion. A typical recovered value for the constant hydraulic conductivity was the highly accurate $k_0 = 1.4799954 \times 10^{-8}$ cm/sec; see [62–64] for further details.

When incorporating normally distributed (zero mean) noise into the inversion process, the error can be decreased as soon as an overspecified situation is prescribed. When increasing the number of measurements the effect of noise is canceled out. This leads to the situation in which the best fit to the noisy data is a curve that resembles the “exact” one, producing, in turn, a very good approximate value for the constant hydraulic conductivity k_0 . For example, when using all the available information for one case of 1% (of the mean pressure) generated noise, an error of 0.02% in the predicted value of k_0 was achieved.

17.4.7 Linear Hydraulic Conductivity, $k(x) = k_0 + k_1 x$

For the heterogeneous linear hydraulic conductivity, the values of the constants k_0 and k_1 that are to be retrieved are chosen to maintain the mean hydraulic conductivity measurement $k^* = 1.48 \times 10^{-8}$ cm/sec so that, for example, we choose $k_0 = 3k^*/4 = 1.11 \times 10^{-8}$ cm/sec and $k_1 = k^*/2L = 2.164 \times 10^{-9}$ cm/sec. As argued in [24], and due to the near correlation of the corresponding sensitivity coefficients, boundary pressure measurements alone do not contain sufficient information for the identification of both constants k_0 and k_1 , and therefore flux measurements at the upstream face $x = 0$ of the sample have to be considered. Also, the sensitivity coefficients of the hydraulic fluxes at $x = L$ appear to be correlated, while the hydraulic fluxes at $x = 0$ are uncorrelated and therefore identifiability is expected for both parameters. Hence, we consider measurements of differential pressures and hydraulic fluxes at the upstream face of the sample, and the time instant at which the sample measurements are recorded is chosen according to the sensitivity analysis to be $t = 12,000$ sec. Again, the boundary values were input as exact or noisy measurements. Typical retrieved values were accurate to within about 0.005% of the “exact” values for the coefficients, and this high accuracy was maintained with the introduction of random noisy measurements [62–64].

17.4.8 Quadratic Hydraulic Conductivity, $k(x) = k_0 + k_1 x + k_2 x^2$

The constant values for the coefficients of the quadratic hydraulic conductivity, namely, $k_0 = k^*/7$, $k_1 = 6k^*/7L$, and $k_2 = 9k^*/7L^2$, to be retrieved are again a choice that maintains the mean hydraulic conductivity k^* . In order to retrieve these coefficients a sensitivity analysis shows that sufficient information is provided by one measurement of each of the differential pressure and the hydraulic flux measurements at both ends of the sample [24,62–64], and also indicates the optimal time instants at which these measurements should be taken. As for the constant and linear hydraulic conductivity problems, accurate results for the prediction of the unknown parameters are achieved for both exact and noisy simulated measurement data.

17.4.9 Simultaneous Retrieval of Constant Hydraulic Conductivity and Constant Specific Storage

The problem considered in Section 17.4.6 can be extended by additionally retrieving the constant specific storage of the sample. As suggested by the sensitivity analysis, we can recover accurate values for both parameters based upon differential pressure measurements at $x = 0$ and hydraulic flux values at $x = L$, using either the minimum amount of information, adding redundant information (all measurements in time), or by incorporating noisy measurements [62–64].

17.5 Hydraulic Conductivity Measurements in Composite Homogeneous Rocks

A transient hydraulic experiment, similar to that performed in the single homogeneous rock case, has been performed for composite rocks, namely homogeneous rocks butted together and representing a faulted rock sample. The experimental setup and apparatus in [70] is updated and improved, and new specimens are tested. Unlike the previous single-sample experiment in Section 17.4, in which boundary data alone was sufficient to retrieve a constant, linear, or quadratic variation of $k(x)$, preliminary numerical investigations performed in [25] indicate that internal pressure measurements within the sample might be necessary for a successful retrieval of a discontinuous hydraulic conductivity. Therefore, the previous pump–flow experimental setup in [19] is improved by a new data acquisition and control system and the Rock Deformation Research transient permeameter, see [73] and Figure 17.6, which allows for internal pressure measurements to be made at “ports” along the sample. For at most two rocks butted together, a mathematical analysis of the steady-state situation enables the hydraulic conductivities and the fault location to be determined. For the unsteady case, the FDM direct procedure used for the single-sample situation is extended and combined with a GA-based optimization technique in order to retrieve the unknown hydraulic parameters; see [62–64] for further details.

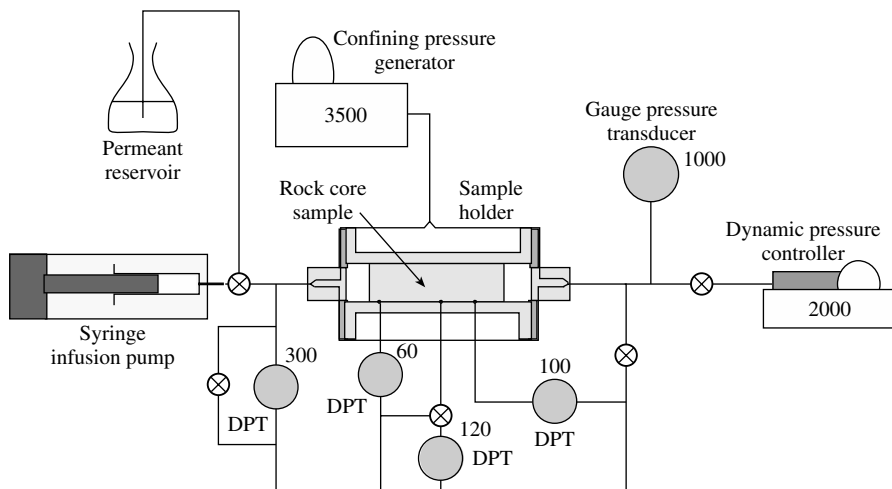


FIGURE 17.6

Data acquisition and control system and the Rock Deformation Research transient permeameter. The pressure values indicated are measured in kPa, and DPT denotes a differential pressure transducer.

17.5.1 Experimental Setup and Limitations

We aim to test tight rocks, that is, rocks with low permeabilities, and we again consider the pump–flow method, using an extension of the experimental setup designed by Clennell [19]. The new setup is designed for the simultaneous determination of both the specific storage and the hydraulic conductivity of the specimen. The new design shown in Figure 17.6 is based around a 5 cm diameter custom steel sample holder that accepts cores of up to 13 cm long. There is an extra pump to regulate the pressure on the downstream end ($x = L$) of the samples to within 0.5 kPa, and this enables the volume of fluid leaving the sample at $x = L$ to be measured to a precision of 1 μl . Transient interior pressure measurements within the specimen are now available, to a precision of three significant figures, by the provision of a holder of the “Hassler” type with three internal pressure ports in a polymer confining sleeve. However, the internal pressure measurements change the transient behavior of both the boundary pressure and the flux because the storage associated with the transducer is quite large in comparison with that of the sample.

17.5.2 Mathematical Formulation

The formulation given by Eqs. (17.36) to (17.39) for the single-sample case is again appropriate for describing the flow through the composite specimen. For composite homogeneous rocks the hydraulic conductivity is assumed to be piecewise constant, that is, for N_f layers of homogeneous materials that are butted together we have

$$k(x) = k_i, \quad \Phi(x) = \Phi_i \quad \text{for } x \in [x_{i-1}^f, x_i^f] \quad \text{and} \quad i = \overline{1, N_f} \quad (17.42)$$

where $x_0^f = 0$, $x_{N_f}^f = L$, and x_i^f for $i = \overline{1, (N_f - 1)}$ are the discontinuity locations at which the pressure and the hydraulic flux are assumed to be continuous; see Figure 17.7. The inverse problem requires the determination of the piecewise homogeneous values k_i for the hydraulic conductivities, the piecewise constant values Φ_i for the specific storages, the constant specific storage Φ_u

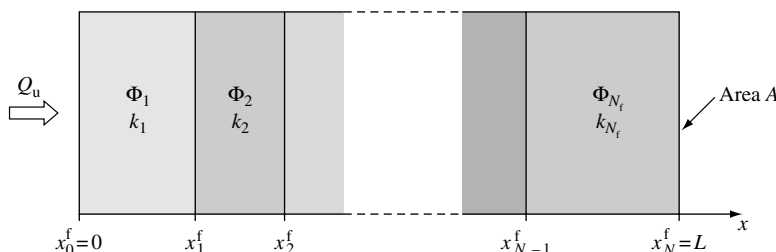


FIGURE 17.7

A composite homogeneous rock sample, comprising N_f different layers.

of the upstream reservoir, and the fault locations. The lack of information is compensated for by additional pressure readings within the linked sample. A necessary condition for identifiability is that the number of conditions to be imposed has to be greater than or equal to the number of unknowns.

For the case of no faults, that is, $N_f = 1$, numerical FDM and boundary element methods (BEM) have produced reasonable agreement with the experimental data, as presented in Section 17.4 for the homogeneous case, or see [24].

17.5.3 Steady-State Mathematical Analysis

A steady-state analysis shows that the pressure distribution inside the i th part of the sample as $t \rightarrow \infty$ is given by

$$p(x, \infty) = \frac{Q_u}{A} \left[-\frac{x}{k_i} + \frac{L}{k_{N_f}} + \sum_{j=i}^{N_f-1} x_j^f \left(\frac{1}{k_j} - \frac{1}{k_{j+1}} \right) \right] \quad (17.43)$$

see Figure 17.7. If we make use of a single steady-state pressure reading within each layer, combined with the steady-state pressure at $x = 0$, then we can retrieve the hydraulic conductivities and the positions of each fault if and only if the number of layers is either one or two [25].

For the case of two homogeneous rocks that are butted together, we provide one reading for the steady-state pressures $p(x_T, \infty) = p_T$ and $p(x_M, \infty) = p_M$ within each rock at the ports x_T and x_M , respectively, combined with the reading of the steady-state pressure $p(0, \infty) = p_\infty$ at the upstream surface of the linked sample. Thus, the hydraulic conductivities and the position of the fault can be recovered as follows:

$$k_1 = \frac{Q_u x_T}{A(p_\infty - p_T)}, \quad k_2 = \frac{Q_u(L - x_M)}{A p_M}, \quad x_1^f = \frac{p_\infty x_T (L - x_M) - p_M x_T L}{(p_\infty - p_T)(L - x_M) - p_M x_T} \quad (17.44)$$

The estimation of the hydraulic conductivity in either sample is very sensitive to small errors in these steady-state pressure measurements when its value is of $O(10^{-5})$ cm/min in comparison to the case when it is of $O(10^{-6})$ cm/min. However, there are a few drawbacks when using the steady-state approach, as given below:

1. The values of Φ_i , for $i = \overline{1, N_f}$, and Φ_u may be required.
2. The steady state may not exist, or it may take a long time to reach, which is practically expensive.
3. Insufficient internal measurements of the static pressure may be available.

4. The transient pressure distribution may also be required.
5. The number of faults may be greater than two and then the steady-state analysis cannot be utilized.

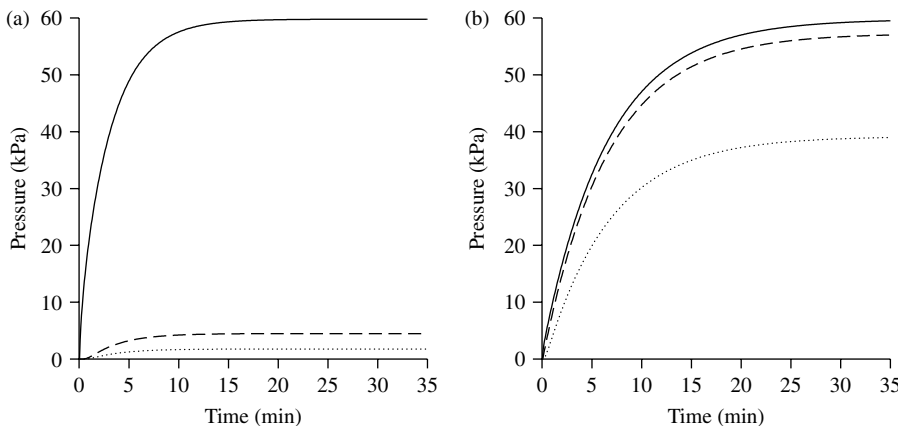
Therefore, in order to deal with such potential practical difficulties, the transient case must be considered. In the unsteady case, analytical and semi-analytical solutions for the pressure were obtained in [20,74–77], but only for the semi-infinite strip and the radially symmetric and radially asymmetric cases in aquifers. However, for realistic finite porous samples there is, as yet, no analytical study, and therefore we numerically investigate the recovery of the hydraulic conductivities based upon data measurements from the transient process. Numerous runs of the GA-based optimization were performed in an attempt to recover all the unknown parameters, namely the sample hydraulic conductivities, the sample specific storages, the compressive storage of the upstream reservoir and the position of the fault, using only additional transient pressure readings at ports along the specimen. Although none of these were successful, the insight gained from these calculations led to a possible scenario from which a successful retrieval of the required parameters can be achieved.

17.5.4 The Composite Homogeneous Situation

We consider two cylindrical homogeneous samples “X” (a Darley Dale sandstone) and “Y” of lengths 2.4 and 4.3 cm, respectively, and cross-sectional area $A = 20.5 \text{ cm}^2$, which are butted together to give a total length of $L = 6.7 \text{ cm}$. The compressive storage of the upstream reservoir $\Phi_u = 1.2 \times 10^{-5} \text{ cm}^2$ and the constant inflow rate of $Q_u = 10.02 \times 10^{-3} \text{ cm}^3/\text{min}$ mean that the steady-state pressure is encountered at $t_\infty = 25 \text{ min}$. Following individual tests on each sample, X was found to be approximately 20 times less permeable than Y, namely $k_X = 2.121 \times 10^{-6} \text{ cm}/\text{min}$ and $k_Y = 4.68 \times 10^{-5} \text{ cm}/\text{min}$. The corresponding specific storages are $\Phi_X = 10^{-6} \text{ cm}^{-1}$ and $\Phi_Y = 2 \times 10^{-6} \text{ cm}^{-1}$. The configurations “XY” and “YX” are both considered, that is, X followed by Y, and Y followed by X, respectively, and for both configurations additional pressure readings are recorded at the two ports $x_T = 2.4 \text{ cm}$ and $x_M = 5.05 \text{ cm}$. The corresponding pressure transients at the ports and the upstream face are shown in [Figure 17.8](#). In the configuration “XY” the steady-state pressure measurements are $p_T = 4.41 \text{ kPa}$ and $p_M = 1.69 \text{ kPa}$, while in the second configuration “YX” we have $p_T = 56.20 \text{ kPa}$ and $p_M = 37.30 \text{ kPa}$. The steady-state pressure at the active boundary $x = 0$ is $p_\infty = 58.66 \text{ kPa}$, regardless of the configuration being considered.

17.5.5 Retrieval of the Hydraulic Conductivities

The identification of the hydraulic conductivities, as well as the position of a single fault, has been investigated fully by Lesnic et al. [25] using pressure readings at the upstream face of the linked sample and one port

**FIGURE 17.8**

Buildup of the pressure curves for the configurations (a) "XY," and (b) "YX," at the upstream face (solid line), the port x_T (dashed line), and the port x_M (dotted line).

location within each sample. The direct solver made use of the BEM, and an inverse minimization technique based on a least-squares approach was solved using the NAG routine E04UCF. Here we consider a GA-based optimization procedure and a FDM direct solver, which is most easily applied if the fault position is first calculated from the steady-state analysis.

Using the steady-state pressure measurements from the configuration "XY," Eq. (17.44) accurately defines the position of the fault to be $x_1^f = 2.4$ cm. A sensitivity analysis shows that only pressure measurements in time at the upstream face of the linked sample are required to retrieve the hydraulic conductivities of the two samples, and that small times are the most optimal ones for reducing the degree of ill-posedness of the problem. Typical recovered values for the hydraulic conductivities were $k_X = 2.12099 \times 10^{-6}$ cm/min and $k_Y = 4.68130 \times 10^{-5}$ cm/min, and therefore the hydraulic conductivities were recovered to a high degree of accuracy [63,64]. If x_1^f is additionally assumed to be unknown, then transient pressure measurements from both ports are needed to retrieve accurate values of the hydraulic conductivities of each sample together with the fault locations [64].

17.5.6 Simultaneous Retrieval of the Compressive Storage of the Upstream Reservoir and the Specific Storages of the Samples

The sample hydraulic conductivities k_X and k_Y and the fault position x_1^f are assumed to have been calculated precisely from the steady-state analysis, and we investigate the simultaneous retrieval of the compressive storage of the upstream reservoir, Φ_u , and the two specific storages of the samples, Φ_X and Φ_Y , using the pressure variation in time at the upstream face of the

TABLE 17.1

Results Obtained from the Three-Step GA Retrieval of Φ_X , Φ_Y , and Φ_u , using Pressure Measurements at the Upstream Face of the Linked Samples

Configuration	Time (min)	$\Phi_X (\times 10^{-6} \text{ cm}^{-1})$	$\Phi_Y (\times 10^{-6} \text{ cm}^{-1})$	$\Phi_u (\times 10^{-5} \text{ cm}^2)$
"XY"	2.4, 4.8, 7.1	0.2182	1.9997	1.4407
"YX"	2.4, 4.8, 7.1	0.9996	1.5601	1.3383
"XY"	7.1	0.9996	1.9997	1.2000
Known values		1.0	2.0	1.2

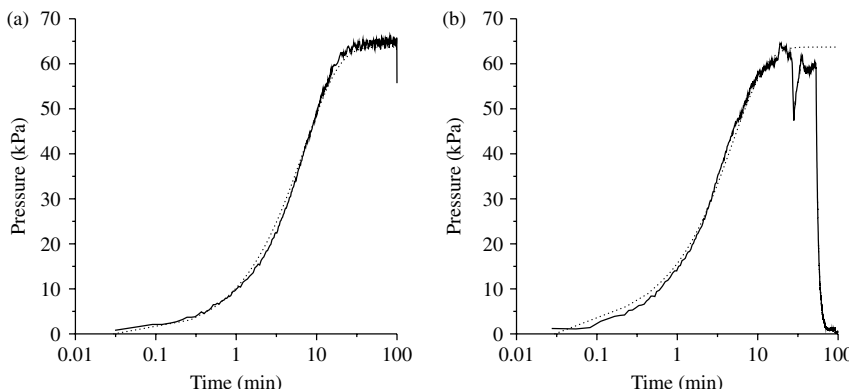
Notes: Italicized values indicate those parameters which are not expected to be retrieved at that step, and are therefore not accurate. In the third step Φ_X and Φ_Y are fixed (indicated by bold values) at their values determined from the first two steps.

linked samples. A sensitivity analysis shows that the sensitivity coefficients for Φ_u and the specific storage of the first sample are always correlated, while those for the other two hydraulic parameter pairings are always uncorrelated. Therefore only the retrieval of the specific storage of the second sample for either configuration is possible and we must study both configurations. An inverse analysis of the configurations "XY" and "YX" separately, specifying upstream pressure values at three small time instants, defines accurate values for Φ_Y and Φ_X , respectively. Fixing these values, we obtain Φ_u from an inverse analysis of either configuration using a single upstream pressure measurement.

As an example, pressure transients were simulated for $\Phi_X = 10^{-6} \text{ cm}^{-1}$, $\Phi_Y = 2 \times 10^{-6} \text{ cm}^{-1}$, and $\Phi_u = 1.2 \times 10^{-5} \text{ cm}^2$, and we consider the three time instants $t = 2.4, 4.8$, and 7.1 min . The results presented in Table 17.1 show that the required hydraulic parameters can be recovered accurately. Further details, including examples with noisy data and for which the hydraulic parameters can again be recovered accurately, are given in [62–64].

17.5.7 Comparison with Experimental Data

Figure 17.9 shows results obtained from an attempt to match experimental data from a hydraulic test performed on two, assumed homogeneous, rock samples [63,64]. The fault position was assumed to be known and the hydraulic conductivities of each sample were determined from a steady-state analysis based on pressure measurements at $x = 0$ and one port. As was found with this initial experimental data, difficulties may be encountered in estimating the sample storativities and the compressive storativity of the upstream reservoir if the experiments are conducted with ports connected and the compliance of the transducers is not very small. Therefore, another set of experiments was performed with no transducers connected to measure only the upstream pressure. Utilizing the experimental data for times less than $t = 10 \text{ min}$, and repeating the inversion process presented in Section 17.5.6,

**FIGURE 17.9**

Numerically simulated pressure curves (dotted lines) compared with the experimental data (solid lines) for the configurations (a) "XY," and (b) "YX," at the upstream face of the sample.

the retrieved values for Φ_X , Φ_Y , and Φ_u generated a good graphical agreement over the transient regime, as can be observed in Figure 17.9.

17.6 Hydraulic Conductivity Measurements in Anisotropic Rocks

17.6.1 Introduction

The production of gas and oil in many reservoirs is seriously affected by their highly heterogeneous and/or anisotropic structure. The origin of anisotropy in rocks was discussed in [78] from the transport properties point of view. One conclusion is that the directionality of the pore structure, namely the preferred orientation of the micro-cracks or of nonspherical grains, can only produce moderate hydraulic conductivity anisotropy (experimental evidence was given in [79]). Strong hydraulic conductivity anisotropy is more likely to originate from fine-scale heterogeneities in, for example, sand-shale sequences, aeolian deposits, and jointed or fractured rock masses. As a consequence, anisotropy, like heterogeneity, is scale dependent [80]. The scaling-up of the hydraulic conductivity from the centimeter scale, as in cores or well logs, to the scale of hundreds of meters, such as grid blocks in large-scale numerical simulations, is a problem that is frequently encountered by reservoir engineers. Many techniques have been proposed to perform this task, more commonly known as determining grid block effective hydraulic conductivities. However, difficulties are often encountered, especially in the case of multiphase flow [81].

A number of methods have been proposed to measure the full hydraulic conductivity tensor in rocks or soils. In one approach, two flow

measurements were simultaneously performed on a prepared soil, with the fluid outlets aligned with the assumed principal directions, and then the ratio of the principal hydraulic conductivities was determined [82]. The magnitudes of the principal hydraulic conductivities were measured separately. In another experimental procedure, the streamlines were forced to be straight lines parallel to the sample axis [83]. However, this method involves the reshaping, by trial and error, of the sample, and so is difficult to implement in practice. All these methods assume that the sample axis can be oriented parallel, or perpendicular, to one of the principal directions. This is not as serious a restriction as it might appear since, in many cases, at least one of the principal directions can be deduced from, for example, the bedding planes or the preferred orientation of the micro-cracks. The commonly used concept of horizontal and vertical hydraulic conductivities implicitly assumes that the principal hydraulic conductivity directions *in situ* are likewise, but this is not always the case. However, samples can be taken in directions parallel and perpendicular to the bedding planes when they are visible, instead of the usual practice of sampling parallel and perpendicular to the axis of the core.

If the principal directions cannot be estimated then a different method becomes necessary. The best solution would be to measure the full hydraulic conductivity tensor in one single sample by imposing periodic boundary conditions [84–87]. While this can be achieved, it is rather difficult to implement in practice. Alternatively, it may be possible to perform a suite of independent flow measurements, each one with a different set of Neumann and Dirichlet boundary conditions. As this is perfectly possible in laboratory measurements, this method may yield enough information to allow one to infer the full hydraulic conductivity tensor [88,89].

17.6.2 Mathematical Formulation

As in Section 17.4.3, the governing equation for single-phase flow in a two-dimensional anisotropic, homogeneous, porous medium can be derived as follows:

$$\nabla \cdot (\mathbf{k} \nabla p) \equiv k_{11} \frac{\partial^2 p}{\partial x^2} + 2k_{12} \frac{\partial^2 p}{\partial x \partial y} + k_{22} \frac{\partial^2 p}{\partial y^2} = \Phi \frac{\partial p}{\partial t} \quad (17.45)$$

where the hydraulic conductivity tensor \mathbf{k} has components k_{11} , $k_{12} = k_{21}$, and k_{22} in the reference frame x, y . In the principal-axes frame we use k_1 and k_2 to denote the principal hydraulic conductivities, with the convention that $k_1 > k_2$. For a single homogeneous sample, sufficient information [63], can be gained from the steady-state flow ($\partial p / \partial t = 0$ in Eq. [17.45]) in order to retrieve all three components of the hydraulic conductivity tensor.

The most significant quantity to characterize the anisotropy of the medium is the determinant of the hydraulic conductivity coefficients, that is, $|k_{ij}| = k_{11}k_{22} - k_{12}^2$. The smaller the value of $|k_{ij}|$, the more asymmetrical are the

pressure field and the hydraulic flux vectors. Since the criterion $|k_{ij}| > 0$ determines the type of differential equation, parabolic for transient problems and elliptic for steady problems, the smaller the value of $|k_{ij}|$ the more difficult are the numerical calculations.

In conventional laboratory measurements, rock samples are shaped into cylinders with circular cross-sections. In two dimensions, they can simply be represented as a rectangle or, for simplicity, a square, whose dimension we take to be L . A steady-state flow is forced through the sample by applying the constant pressures p_0 and $p_0 - \delta p_0$ on opposite faces, while the sides of the plug are jacketed with impermeable material. Thus, the boundary conditions are as follows:

$$p|_{x=0} = p_0, \quad p|_{x=L} = p_0 - \delta p_0, \quad \mathbf{q} \cdot \mathbf{n}|_{y=0} = \mathbf{q} \cdot \mathbf{n}|_{y=L} = 0 \quad (17.46)$$

where $\mathbf{q} = -\mathbf{k}\nabla p$ is the fluid velocity, \mathbf{n} is the normal to the face ($\mathbf{n} = -\mathbf{j}$ and $+\mathbf{j}$ on $y = 0$ and L , respectively) and the final equation expresses the no-flow conditions along the sides of the sample.

The solution of this direct, well-posed problem is obtained by employing a classical BEM approach [22,23], and a full description of the implementation and validation of this technique is given in [63,90].

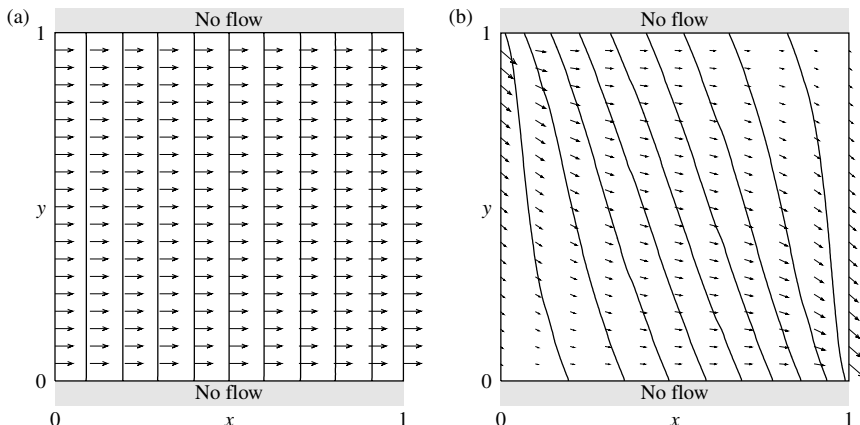
Before performing the numerical calculations, the steady-state form of the governing equation (17.45) and the boundary conditions (17.46) are nondimensionalized according to

$$\bar{x} = \frac{x}{L}, \quad \bar{y} = \frac{y}{L}, \quad \bar{p} = \frac{p - (p_0 - \delta p_0)}{\delta p_0}, \quad \bar{k}_{ij} = \frac{k_{ij}}{k^*} \quad (17.47)$$

where k^* is a representative value of the hydraulic conductivity. Then, after dropping the bars for simplicity, we have the following boundary-value problem:

$$\begin{aligned} k_{11} \frac{\partial^2 p}{\partial x^2} + 2k_{12} \frac{\partial^2 p}{\partial x \partial y} + k_{22} \frac{\partial^2 p}{\partial y^2} &= 0 \\ p|_{x=0} = 1, \quad p|_{x=1} = 0, \quad \left(k_{12} \frac{\partial p}{\partial x} + k_{22} \frac{\partial p}{\partial y} \right) \Big|_{y=0} &= \left(k_{12} \frac{\partial p}{\partial x} + k_{22} \frac{\partial p}{\partial y} \right) \Big|_{y=1} = 0 \end{aligned} \quad (17.48)$$

Rather than providing the coefficients of the hydraulic conductivity tensor, we provide the magnitudes of the principal hydraulic conductivities and the angle of inclination θ of the x -axis of the sample with the larger principal direction, that is, the direction of k_1 . Figure 17.10 shows the pressure and velocity fields when $\theta = 0^\circ$ and 60° , and the nondimensional values for the principal hydraulic conductivities are $k_1 = 5$ and $k_2 = 1$. It should be noted that if the applied (global) pressure gradient does not lie in one of the

**FIGURE 17.10**

The pressure contours and velocity field within the sample when $k_1 = 5$, $k_2 = 1$, and (a) $\theta = 0^\circ$ and (b) $\theta = 60^\circ$. Note that uniform pressures of $p = 1$ and $p = 0$ have been applied to the faces $x = 0$ and $x = 1$, respectively. The pressure contours are at intervals of 0.1.

principal directions of the hydraulic conductivity tensor then the local fluid flux is not simply perpendicular to the local pressure gradient (i.e., not normal to the pressure contours). Also, if θ is not close to 0° or 90° then the pressure field is strongly distorted due to the presence of the impermeable jacket.

17.6.3 Inverse Problem Formulation

The inverse analysis requires the identification of the values of the principal hydraulic conductivities k_1 and k_2 and the angle θ only from local measurements of the pressure and/or average (rather than pointwise) hydraulic flux on the boundary of the rock sample. Therefore, in practice, possible reliable measurements involve pressure readings along the sides of the sample and total flux readings at the downstream or upstream faces of the rock sample, which will be equal in the steady-state case. The GA-based optimization technique is employed to search in an *a priori* specified range for each of the parameters k_1 , k_2 , and θ .

A sensitivity analysis for measurements of the pressure along the sides of the sample shows that this information is insufficient to fully retrieve the unknown values of k_1 , k_2 , and θ , and that only the ratio of k_1/k_2 and the angle θ can be determined [63,90]. This observation can be argued from the mathematical formulation (17.48), since, on dividing the governing equation and the boundary conditions on $y = 0$ and 1 by k_{22} , we obtain an equivalent problem that is dependent upon only two parameters, namely k_{11}/k_{22} and k_{12}/k_{22} , or, in our case, k_1/k_2 and θ . In addition, when measuring the average hydraulic flux, the sensitivity coefficients for k_1 and k_2 are correlated, whereas the other two remaining pairings of sensitivity coefficients are uncorrelated.

17.6.4 Numerical Results

The approach proposed in [63,90] was to consider a two-step inversion process and provide information in the form of three pressure readings and the average hydraulic flux. The problem considered was simulated experimental data for the case of $k_1 = 5$, $k_2 = 1$, and $\theta = 10^\circ$. Pressure readings alone will not provide sufficient information to fully retrieve k_1 , k_2 , and θ , and only the ratio k_1/k_2 and θ can be found. By employing a method in which the search space of the GA was gradually reduced, accurate values of $k_1/k_2 = 5.00$ and $\theta = 9.99^\circ$ were achieved. Having found the ratio k_1/k_2 and the angle θ , the inversion was continued by fixing θ and providing the average hydraulic flux at the downstream face of the sample. Typical estimates for the principal permeabilities were $k_1 = 5.003$ and $k_2 = 0.990$.

This problem was also considered in [91] in the context of the related heat conduction problem of determining the thermal conductivity tensor of anisotropic heat conductors using measurements provided by heat flow experiments. Using a FDM direct solver and a GA-based inversion technique, the components of a spatially dependent (linear) conductivity tensor have also been successfully retrieved in the situations of an orthotropic thermal conductivity [91] and an anisotropic hydraulic conductivity [63,92].

17.7 Hydraulic Conductivity Measurements in Composite Anisotropic Rocks

The formulation of Section 17.6 can be extended to deal with the identification of the hydraulic properties of composite anisotropic materials, namely, the case in which two rocks are butted together and a steady-state flow is forced through the linked sample by the application of the constant pressures p_0 and $p_0 - \delta p_0$, where $\delta p_0 > 0$, on two opposite faces.

17.7.1 Mathematical Formulation

The boundary-value problem is essentially the same as in the case of a single piece of anisotropic material, namely Eq. (17.48), except that we take the total nondimensional length of the butted sample to be 2. A straight fault is located within the linked sample, namely between samples X (at the upstream face in the initial "XY" configuration) and Y (at the downstream face in the initial "XY" configuration), and it is defined by the straight line joining the coordinates $(x_b^f, 0)$ and $(x_t^f, 1)$, the subscripts "b" and "t" denoting locations along the bottom and top no-flow boundaries, respectively. The fault is again considered to provide a perfect discontinuity in the hydraulic properties of the materials, while, clearly, the pressure and hydraulic flux must remain continuous across this interface. The BEM formulation of Section 17.6 can be readily extended to this situation [63].

In the parameter identification problems that we consider, we look at the following two situations:

1. *Fault perpendicular to the x-axis of the sample, $x_t^f = x_b^f$*

We let sample X have a nondimensional length of 1.33 and suppose that the magnitudes of the principal hydraulic conductivities are given by $k_1^X = 5$ and $k_2^X = 1$, with $\theta^X = 30^\circ$. The remainder of the linked sample, Y, has a nondimensional length of 0.67 and the hydraulic properties are defined by $k_1^Y = 5$, $k_2^Y = 1$, and $\theta^Y = 60^\circ$. The pressure contours and the velocity field within the linked sample are shown in Figure 17.11(a).

2. *Fault inclined to the x-axis of the sample, $x_t^f \neq x_b^f$*

The hydraulic properties remain the same as in (1), but the fault is now determined by $x_t^f = 1.42$ and $x_b^f = 1.23$. The pressure contours and the velocity field within the linked sample are shown in Figure 17.11(b). Clearly, the fault has a significant influence on the flow field locally, but otherwise the fluid pressure and velocity is similar to the case shown in Figure 17.11(a). Figure 17.11(c), in which the hydraulic properties of sample Y have been modified to $k_1^Y = 7$, $k_2^Y = 2$, and $\theta^Y = -45^\circ$, shows a situation in which the preferred direction for flow (the larger of the two principal directions) is very different in sample Y in comparison with sample X. The fluid flow across the fault is focused around the portion near the x-axis and the surrounding flow pattern is influenced to a greater extent than in Figures 17.11(a,b).

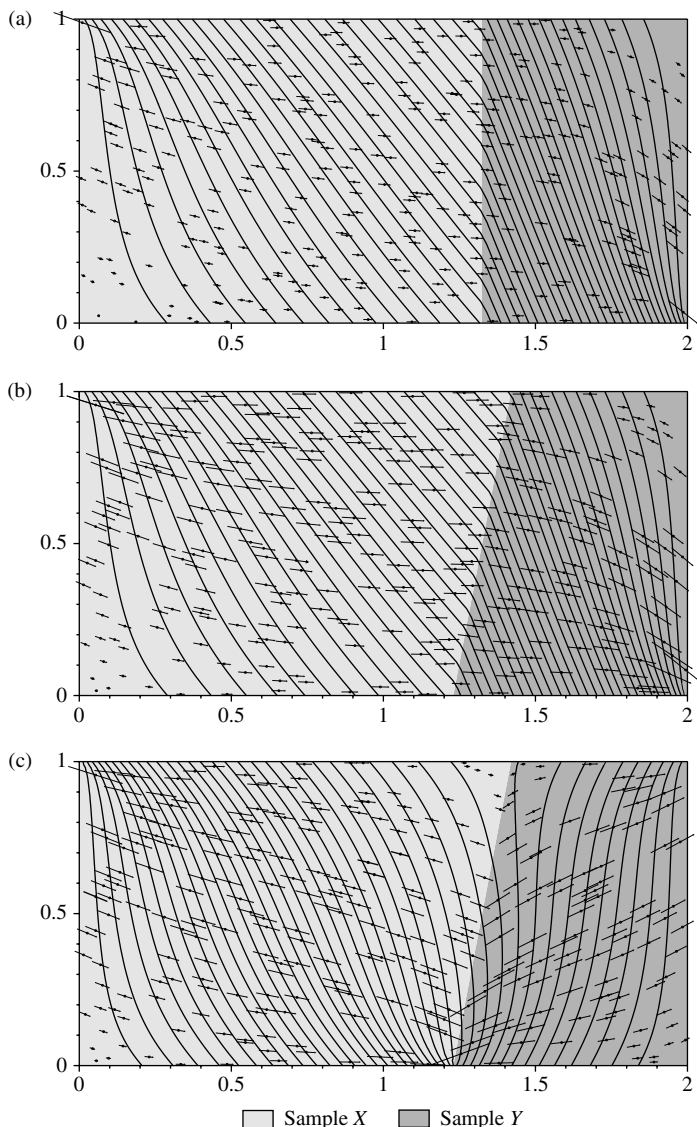
17.7.2 Inverse Problem Formulation

The inverse analysis requires the identification of the values of the principal hydraulic conductivities and the angles θ within each sample together with the fault location, defined by a further one or two parameters, respectively, according to whether the fault is perpendicular or inclined to the x-axis. The only (simulated) experimental data provided is in the form of local pressure measurements from ports situated on the bottom and top no-flow boundaries and average hydraulic flux values at either end of the linked sample. As stated in Section 17.6.3, pressure alone does not provide sufficient information for a successful retrieval of the hydraulic parameters.

17.7.3 Numerical Results and Discussion

17.7.3.1 *The case when the fault is perpendicular to the x-axis of the sample, $x_t^f = x_b^f$*

Through a detailed investigation of this situation, it was shown in [63] that measurements from pressure ports must be taken within both samples simply to retrieve the fault location. Moreover, a minimum of seven

**FIGURE 17.11**

The pressure contours and velocity field within the linked sample when $k_1^X = 5$, $k_2^X = 1$, and $\theta^X = 30^\circ$. In (a) the fault is vertical (at $x = 1.33$) and in (b) the fault is inclined between the coordinate points $(1.23, 0)$ and $(1.42, 1)$. Sample Y has the hydraulic properties (a,b) $k_1^Y = 5$, $k_2^Y = 1$, and $\theta^Y = 60^\circ$, and (c) $k_1^Y = 7$, $k_2^Y = 2$, and $\theta^Y = -45^\circ$. Note that uniform pressures of $p = 1$ and $p = 0$ have been applied to the faces $x = 0$ and $x = 1$, respectively, while the top and bottom surfaces of the sample are no-flow boundaries. The pressure contours are at intervals of 0.025, while the dots indicate the locations at which the velocity vectors apply.

independent measurements, namely pressure readings from six ports located along the top and bottom no-flow boundaries together with the average flux at the inflow face, are required to successfully retrieve the fault location and the hydraulic conductivity tensor within each sample.

In the first approach, the ports at which the simulated experimental data was taken had the coordinate positions $(0.35, 0)$, $(0.65, 0)$, $(1.55, 0)$, and $(1.85, 0)$ on the bottom no-flow face and $(0.55, 1)$ and $(1.75, 1)$ on the top no-flow face, so that three ports lie within each sample. Typical retrieved parameter values were accurate to within 1%, namely $(k_1^X, k_2^X, \theta^X) = (5.0156, 1.0015, 29.9717)$, $(k_1^Y, k_2^Y, \theta^Y) = (4.9804, 1.0000, 59.9843)$, and $x_b^f = x_t^f = 1.3292$.

Another technique, utilizing three separate steps for the inversion process, was proposed to improve on this accuracy. In the first step and starting with the configuration "XY," the ports are all moved to lie within sample X only with the coordinate positions $(0.25, 0)$, $(0.35, 0)$, $(0.45, 0)$, $(0.25, 1)$, $(0.35, 1)$, and $(0.45, 1)$. When this information is coupled with the average flux value at the inflow face, it is expected that there will be insufficient information to determine the fault location or the hydraulic conductivity tensor in sample Y, while the determination of the hydraulic conductivity parameters k_1^X , k_2^X , and θ^X in sample X constitutes an overspecified problem. In the second step, after switching the samples around, namely considering the configuration "YX," the same information is expected to allow the retrieval of k_1^Y , k_2^Y , and θ^Y . Typical results from each of these two steps are provided in Table 17.2, and the hydraulic parameters which were sought at each step were retrieved accurately. With the hydraulic conductivity tensors accurately obtained from the first two steps of the inversion, the final step of imposing pressure readings in both samples allows the fault location to be obtained accurately. For the chosen example and the configuration "XY" these pressure readings were taken on the bottom no-flow boundary at $(0.35, 0)$ and $(1.65, 0)$.

TABLE 17.2

Numerical Results for the GA Simultaneous Recovery of the Sample Hydraulic Conductivities and the Fault Position when the Inversion is Performed in Three Steps

Parameter	Exact value	Step 1	Step 2	Step 3
k_1^X	5	4.9919	5.3656	4.9919
k_2^X	1	0.9986	0.9797	0.9986
θ^X	30°	29.9825	23.6439	29.9825
k_1^Y	5	5.4287	4.9921	4.9921
k_2^Y	1	0.7973	0.9917	0.9917
θ^Y	60°	69.3777	60.0307	60.0307
$x_b^f = x_t^f$	1.33	1.6277	0.8613	1.3298

Notes: Italicized values indicate those parameters which are not expected to be retrieved at that step, and are therefore not accurate. Bold values indicate those parameters which are specified for the final step of the inversion.

TABLE 17.3

Numerical Results for the GA Simultaneous Recovery of the Sample Hydraulic Conductivities and the Fault Position when the Inversion is Performed in Three Steps and for Different Numbers of Ports for the Pressure Measurements

Parameter	Exact	Six ports	Eight ports	Nine ports
k_1^X	5	5.1891	5.0783	5.0531
k_2^X	1	1.0391	1.0146	1.0131
θ^X	30°	31.2898	30.4689	30.2750
k_1^Y	5	4.5788	4.7918	5.0525
k_2^Y	1	1.0316	1.1139	1.0624
θ^Y	60°	58.2246	61.4308	61.8755
x_b^f	1.23	1.1524	1.0616	1.1494
x_t^f	1.42	1.3891	1.4374	1.4574

A typical value retrieved for the position of the fault was $x_b^f = x_t^f = 1.3299$. The relatively large number of measurements that are taken from ports makes this approach quite expensive from a practical point of view.

17.7.3.2 *The case when the fault is inclined to the x-axis of the sample, $x_t^f \neq x_b^f$*

Applying the same three-step inversion process as described for the case $x_t^f = x_b^f$, the retrieved parameters are no longer as accurate as for the case considered in Section 17.7.3.1 [63]. The inversion process was carried out for varying numbers of ports. As can be seen from Table 17.3, as the number of ports is increased there is a general improvement in the accuracy of the retrieved parameters. However, for a reasonable number of ports, we do not reach a similar accuracy of retrieval as for the case when the fault was perpendicular to the x-axis of the sample.

17.8 Comparison of Methods

In this section, by means of a comparison with the more traditional, gradient-based, optimization techniques, we discuss the relevance of the GA technique to some of the problems that we have studied in previous sections.

In Section 17.4 we applied for the first time our GA optimization scheme to the inverse problem of determining the heterogeneous hydraulic conductivity of a rock from a transient hydraulic experiment, and we compared the results with those from Lesnic et al. [24]. All these numerical simulations were fully specified situations, namely a certain number of unknown parameters

to be retrieved from at least the same number of independent boundary information items. However, the sophisticated NAG routine E04UCF that was used in [24] for solving the constrained minimization problem produced, for the same type and amount of information, about the same level of accuracy as the GA optimization scheme. For the composite sample situation, the GA results were again equally as good as the ones produced by the same NAG routine [25].

We now perform a more detailed comparative study by referring to the particular problem presented in Section 17.7.3.1, namely the identifiability of the components of the hydraulic conductivity tensors and the fault position (perpendicular to the x -axis) for a butted sample composed of two anisotropic rocks. The iterative NAG routine that we use, namely E04KCF, is a quasi-Newton algorithm for finding the minimum of a function of several variables subjected to fixed upper and lower bounds on the independent variables when the first derivatives are available. The function that we consider is the least-squares functional that minimizes the difference between the observed and the BEM-predicted boundary pressure and average hydraulic flux measurements at the inflow face. Initially, (i) a single port in each sample was used at $(0.35, 0)$ and $(1.55, 0)$, and then the number of ports was gradually increased by adding ports at (ii) $(0.55, 1)$, (iii) $(1.75, 1)$, (iv) $(0.65, 0)$, and (v) $(1.85, 0)$, the latter case being the fully specified situation when pressure measurements are provided from three ports within each sample, as in Section 17.7.3.1. It should be stated that in each of the cases the average flux value at the inflow face of the sample was also prescribed in the inversion. The results of the NAG inversion are presented in Table 17.4. As can be observed from these results, as we move toward the fully specified situation the errors in the estimates decrease, the numerical technique producing very accurate results in the final case (v). It should be mentioned that whenever an underspecified situation is encountered, the results obtained, while providing a very good match to the data, are not the optimal ones. This is due to the nonuniqueness

TABLE 17.4

Numerical Results of the Inversion Process when using the NAG Routine and the Information (i)–(v) Described in the Text

Parameter	Exact	(i)	(ii)	(iii)	(iv)	(v)
k_1^X	5	4.5001	4.5001	5.5000	5.0081	5.0000
k_2^X	1	0.7638	0.8290	1.1325	1.0032	1.0000
θ^X	30°	20.0001	23.3569	34.6067	30.0737	30.0000
k_1^Y	5	4.5000	4.5000	4.5000	4.5001	5.0000
k_2^Y	1	0.9750	0.8612	0.9816	0.9848	1.0000
θ^Y	60°	57.7295	50.0000	58.2044	58.2645	60.0000
$x_b^f = x_t^f$	1.33	1.1863	1.1304	1.3532	1.3226	1.3300

that the underspecification produces, a situation that was also encountered in the case of the GA optimization. However, in such cases, in order to produce better results, we can provide good initial guesses for the NAG routine as results from the GA optimization. Then, despite the underspecification of the situation it is possible to achieve results close to their optimal values [63].

If we now consider the fully specified situation encountered in the three-step inversion of Section 17.7.3.1, then, unless an initial guess close to the optimum is prescribed, the NAG routine does not retrieve the correct solution. This is due to the fact that such a situation implies a degree of underspecification for the second sample. However, the GA optimization procedure does not encounter such problems as it effectively combines the information in the same domain of search to produce close-to-optimal solutions for the first sample.

Clearly, there is a strong relationship between the fitness function and the degree of specification of the unknowns. When an underspecified situation is prescribed, then a detailed investigation of the "landscape" of the fitness function reveals the presence of more than one peak. Thus, for such cases, the results of the NAG inversion, while providing a very good match to the data imposed in the inversion, are not the optimal ones. A traditional hillclimbing technique might find this misleading, especially when the initial guess is taken far from the solution. The results presented in [Table 17.4](#) possess a high GA fitness, yet they reach such values in areas around local "peaks" as opposed to the area around the peak of the "optimal" solution. This is something which can be overcome by employing the GA procedure since it uses the entire search space to produce a multitude of possibilities as candidate solutions. However, where there is a fully specified situation, or an overspecified one, the "landscape" of the fitness function has usually just one sharp peak and therefore, provided that an initial guess does not fall in a very "flat" region, the hillclimbing approach will converge faster than the GA procedure.

In conclusion, in the case of a fully specified situation the NAG optimization technique behaves, for this particular problem, better than the GA optimization. However, whenever some degree of underspecification is encountered the GA usually produces better results. A method of producing good results when an underspecified and realistic situation is encountered is to combine the GA with the NAG optimization technique.

17.9 Conclusions

In this chapter we have studied the applicability of the GA approach to the inverse parameter identification problem of identifying the hydraulic properties of porous materials.

For one-dimensional problems, a hydraulic pump-flow test has been directly and inversely mathematically modeled and the investigations were performed for both experiments based upon a single sample and a composite

sample. The sensitivity analysis provided indicators of which measurements should be recorded for the inversion to be successful. In contrast with other inverse formulations that lack physical motivation, see, for example, [10], only boundary pressure and hydraulic flux values were used as available information due to both laboratory and real-life difficulties that would be encountered when considering internal measurements. For the various spatial dependencies of the hydraulic parameters considered, accurate estimates were obtained by the GA parameter identification process for both exact and noisy (simulated) experimental measurements.

The same techniques were then successfully extended to the case of anisotropic materials, for which the hydraulic conductivity is represented by a symmetric tensor. Again, the sides of the sample were jacketed with impermeable material and a pressure gradient was applied to drive the fluid flow. The situations of both a single sample and a composite sample, namely two samples butted together at a planar fault (simply considered to be a discontinuity in the hydraulic properties), were considered.

A comparison with a traditional gradient-based optimization technique has been performed for the particular case when the fault between the two anisotropic materials is perpendicular to the sample horizontal axis. While a fully specified situation produced better results than the GA approach, whenever some degree of underspecification was encountered the GA usually produced superior results. However, in underspecified situations, which can commonly be encountered in practice, a combination of the GA with a traditional optimization technique is thought to produce good results.

Acknowledgments

The authors wish to particularly thank Dr R. Mustata for his significant contribution to some of the work described in this chapter. We would also like to express our thanks to Drs M.B. Clennell, L. Elliott, and D. Lesnic and Professor I. Pop. One of the authors, D.B. Ingham, would like to thank the Royal Society for their support of some of the work presented.

References

1. W.J. Karplus. *Analog Simulation Solution of Field Problems*. New York: McGraw-Hill, 1958.
2. A.L. Pozzi and R.J. Blackwell. Design of laboratory models for study of miscible displacement. *Trans. SPE AIME*, 228:28–40, 1963.
3. S. Garcia and P.E. Scott. Use of genetic algorithms in thermal property estimation: Part 1 — experimental design optimization. *Num. Heat. Transfer A*, 33:135–147, 1998.

4. S. Garcia, J. Guynn, and P.E. Scott. Use of genetic algorithms in thermal property estimation: Part 2 — simultaneous estimation of thermal properties. *Num. Heat Transfer A*, 33:149–168, 1998.
5. Y.T. Huang, P.M. Wong, and T.D. Gedeon. Prediction of reservoir permeability using genetic algorithms. *AI Appl.*, 12:67–75, 1998.
6. D.E. Goldberg. *Genetic Algorithms in Search, Optimization and Machine Learning*. New York: Addison-Wesley, 1984.
7. Z. Michalewicz. *Genetic Algorithms + Data Structures = Evolution Programs*. Berlin: Springer-Verlag, 1996.
8. W.H. Chen and J.H. Seinfeld. Estimation of spatially varying parameters in partial differential equations. *Int. J. Control*, 15:487–495, 1972.
9. S. Kitamura and S. Nakagiri. Identifiability of spatially-varying and constant parameters in distributed systems of parabolic type. *J. Control Optimiz.*, 15:785–802, 1977.
10. C.H. Huang and M.N. Özışık. A direct approach for simultaneously estimating spatially varying thermal conductivity and heat capacity. *Int. J. Heat Fluid Flow*, 11:262–268, 1990.
11. M. Ciampi, W. Grassi, and G. Tuoni. The flash method and the measure of thermal diffusivity of nonhomogeneous samples. *Termotecnica*, 37:43–48, 1983.
12. P.R. King. Rescaling of flow parameters using renormalisation. In: J.O. Aasen, E. Berg, A.T. Buller, O. Hjelmeland, and R.M. Holt, eds. *North Sea Oil and Gas Reservoirs III. Proc. Third North Sea Oil Gas Reservoirs Conf.*, Norwegian Institute of Technology, Trondheim, Norway. Dordrecht: Kluwer, 1994, pp. 265–271.
13. R.J. Knipe, Q.J. Fisher, G. Jones, M.B. Clennell, A.B. Farmer, A. Harrison, B. Kidd, E. McAllister, J.R. Porter, and E.A. White. Fault seal analysis: Successful methodologies, application and future directions. In: P. Møller-Pedersen and A.G. Koestler, eds. *Hydrocarbon Seals: Importance for Exploration and Production*. Norwegian Petroleum Society (NPF). Special publications 7. Singapore: Elsevier, 1997, pp. 15–40.
14. S.D. Harris, E. McAllister, R.J. Knipe, L. Elliott, and D.B. Ingham. Scaling of fluid flow associated with flow through complex geological structures. *Proc. Fifth Annu. Conf. of the Int. Assoc. for Mathematical Geol.*, August 6–11, Trondheim, Norway, 1999, pp. 711–716.
15. S.D. Harris, E. McAllister, R.J. Knipe, and N.E. Odling. Predicting the three-dimensional population characteristics of fault zones: a study using stochastic models. *J. Struct. Geol.*, 25:1281–1299, 2003.
16. N.E. Odling, S.D. Harris, and R.J. Knipe. Permeability scaling properties of fault damage zones in siliciclastic rocks. *J. Struct. Geol.*, 26:1727–1747, 2004.
17. T. Manzocchi, J.J. Walsh, P.A.R. Nell, and G. Yielding. Fault transmissibility multipliers for flow simulation models. *Pet. Geoscience*, 5:53–63, 1999.
18. T. Manzocchi, A.E. Heath, J.J. Walsh, and C. Childs. The representation of two-phase fault rock properties in flow simulation models. *Pet. Geoscience*, 8:119–132, 2002.
19. M.B. Clennell. *Fluid flow transients in the petrophysical characterisation of reservoir rocks*. Internal report for Rock Deformation Research, Department of Earth Sciences, University of Leeds, 1997.
20. J.R. Cannon. Determination of certain parameters in heat conduction problems. *J. Math. Anal. Appl.*, 8:188–201, 1964.

21. J.V. Carrera and S.P. Neuman. Estimation of aquifer parameters under transient and steady state conditions: 2. Uniqueness, stability and solution algorithms. *Water Resour. Res.*, 22:211–227, 1986.
22. G.T. Symm and R.A. Pitfield. Solution of Laplace's equation in two dimensions. *NPL report, NAC 44*, 1974.
23. C.A. Brebbia, J.C.F. Telles, and L.C. Wrobel. *Boundary Element Techniques: Theory and Application in Engineering*. Berlin: Springer-Verlag, 1984.
24. D. Lesnic, L. Elliott, D.B. Ingham, and R.J. Knipe. A mathematical model and numerical investigation for determining the hydraulic conductivity of rocks. *Int. J. Rock Mech. Min. Sci.*, 34:741–759, 1997.
25. D. Lesnic, L. Elliott, D.B. Ingham, R.J. Knipe, and M.B. Clennell. An inverse problem to determine the piecewise homogeneous hydraulic conductivity within rocks. In: G. Jones, Q.J. Fisher, and R.J. Knipe, eds. *Faulting, Fault Sealing and Fluid Flow in Hydrocarbon Reservoirs*. Geological Society, London. Special publications 147, 1998, pp. 261–268.
26. J. Bear. *Dynamics of Fluids in Porous Media*. New York: Elsevier, 1972.
27. K. Aziz and A. Settari. *Petroleum Reservoir Simulations*. London: Applied Science Publishers, 1979.
28. M.C. Leverett and W.B. Lewis. Steady flow of gas–oil–water mixtures through unconsolidated sands. *Trans. SPE AIME*, 18:624–636, 1966.
29. M. Muskat. *Physical Principles of Oil Production*. New York: McGraw-Hill, 1949.
30. L. Davis. *Genetic Algorithms and Simulated Annealing*. San Mateo: Morgan Kaufmann, 1987.
31. P.B. Grosso. *Computer simulation of genetic adaptation: Parallel subcomponent interaction in a multilocus model*. PhD thesis, University of Michigan, MI, 1985.
32. A.V. Sannier and E.D. Goodman. Genetic learning procedures in distributed environments. In: J.J. Grefenstette, ed. *Genetic Algorithms and Their Applications. Proc. Second Int. Conf. on Genetic Algorithms*. Hillsdale: Lawrence Erlbaum, 1987, pp. 162–169.
33. M.D. Gordon. *Adaptive subject indexing in document retrieval*. PhD thesis, University of Michigan, MI, 1984.
34. D.E. Goldberg and M.P. Samtani. Engineering optimization via genetic algorithms. *Proc. Ninth Conf. on Electronic Computation*, University of Alabama, 1986, pp. 471–482.
35. K.A. De Jong and W.M. Spears. Using genetic algorithms to solve NP-complete problems. In: J. Schaefer, ed. *Proc. Third Int. Conf. on Genetic Algorithms*. San Mateo: Morgan Kaufmann, 1989, pp. 124–132.
36. C.G. Shaefer. The ARGOT strategy: Adaptive representation genetic optimizer technique. In: J.J. Grefenstette, ed. *Genetic Algorithms and Their Applications. Proc. Second Int. Conf. on Genetic Algorithms*. Hillsdale: Lawrence Erlbaum, 1987, pp. 50–58.
37. D.J. Cavicchio. Reproductive adaptive plans. *Proc. ACM 1972 Annu. Conf.*, 1972, pp. 1–11.
38. C.G. Shaefer. Multiple objective optimization with vector evaluated genetic algorithms. In: J.J. Grefenstette, ed. *Genetic Algorithms and Their Applications. Proc. First Int. Conf. on Genetic Algorithms*. Hillsdale: Lawrence Erlbaum, 1985, pp. 93–100.
39. T. Smith and K.A. de Jong. Genetic algorithms applied to the calibration of information driven models of US migration patterns. *Proc. Twelfth Annu. Pittsburgh Conf. on Modelling Simulation*, 1981, pp. 955–959.

40. J.H. Holland. *Adaptation in Natural and Artificial Systems*. Ann Arbor: University of Michigan Press, 1975.
41. D.E. Goldberg. Messy genetic algorithms; motivation, analysis and first results. *Complex Systems*, 3:493–530, 1990.
42. A. Brindle. *Genetic algorithms for function optimization*. PhD thesis, University of Michigan, MI, 1982.
43. J.E. Baker. Adaptive selection methods for genetic algorithms. In: J.J. Grefenstette, ed. *Genetic Algorithms and Their Applications. Proc. First Int. Conf. on Genetic Algorithms*. Hillsdale: Lawrence Erlbaum, 1985, pp. 101–111.
44. J.E. Baker. Reducing bias and inefficiency in the selection algorithm. In: J.J. Grefenstette, ed. *Genetic Algorithms and Their Applications. Proc. Second Int. Conf. on Genetic Algorithms*. Hillsdale: Lawrence Erlbaum, 1987, pp. 14–21.
45. T. Bäck, F. Hoffmeister, and H.P. Schwefel. A survey of evolution strategies. In: R. Belew and L. Booker, eds. *Proc. Fourth Int. Conf. on Genetic Algorithms*. San Mateo: Morgan Kaufmann, 1991, pp. 2–9.
46. E.H.L. Aarts and J. Korst. *Simulated Annealing and Boltzmann Machines*. Chichester: Wiley, 1989.
47. G.S. Fishman. *Monte Carlo: Concepts, Algorithms and Applications*. New York: Springer-Verlag, 1996.
48. K.A. De Jong. *An analysis of the behavior of a class of genetic adaptive systems*. PhD thesis, University of Michigan, MI, 1975.
49. L.J. Eshelman, R.A. Caruana, and J.D. Schaffer. Biases in crossover landscape. In: J. Schaefer, ed. *Proc. Third Int. Conf. on Genetic Algorithms*. San Mateo: Morgan Kaufmann, 1989, pp. 10–19.
50. J.D. Schaffer and A. Morishima. An adaptive crossover distribution mechanism for genetic algorithms. In: J.J. Grefenstette, ed. *Genetic Algorithms and Their Applications. Proc. Second Int. Conf. on Genetic Algorithms*. Hillsdale: Lawrence Erlbaum, 1987, pp. 36–40.
51. G. Syswerda. Uniform crossover in genetic algorithms. In: J. Schaefer, ed. *Proc. Third Int. Conf. on Genetic Algorithms*. San Mateo: Morgan Kaufmann, 1989, pp. 2–9.
52. A.D. Bethke. *Genetic algorithms as function optimizers*. PhD thesis, University of Michigan, MI, 1980.
53. H.F. Wang. *Linear Poroelasticity*. Princeton, NJ: Princeton University Press, 2000.
54. R.N. Horne. *Modern Well Test Analysis*. Palo Alto: Petroway, 2000.
55. W.F. Brace, J.B. Walsh, and W.T. Frangos. Permeability of granite under high pressure. *J. Geophys. Res.*, 73:2225–2236, 1968.
56. P.A. Hsieh, J.V. Tracy, C.E. Neuzil, J.D. Bredehoeft, and S.E. Silliman. A transient laboratory method for determining the hydraulic properties of 'tight' rocks — I. Theory. *Int. J. Rock Mech. Mining Sci. Geomech. Abstr.*, 18:242–252, 1981.
57. F.A. Donath, J.T. Holder, and L.S. Fruth. Simultaneous hydraulic/physical parameter measurement on rock specimens subjected to triaxial conditions. In: R.T. Donahe, R.C. Chaney, and M.L. Silver, eds. *Advanced Triaxial Testing of Soil and Rock*. Philadelphia: ASTM STP 977, 1988, pp. 143–154.
58. R.L. Kranz, J.S. Saltzman, and J.D. Blacic. Hydraulic diffusivity measurements on laboratory rock samples using an oscillating pore pressure method. *Int. J. Rock Mech. Mining Sci. Geomech. Abstr.*, 27:345–352, 1990.
59. G.J. Fischer and M.S. Paterson. Measurement of permeability and storage capacity of rocks during high deformation at high temperature and pressure.

- In: T. Evans and T. Weng, eds. *Fault Mechanics and Transport Properties of Rocks*. New York: Blackwell, 1992, pp. 213–252.
- 60. J. Kamath, R.E. Boyer, and F.M. Nakagawa. Characterization of core-scale heterogeneities using laboratory pressure transients. SPE paper 20575, 1990.
 - 61. P. Rigord, Y. Caristan, and J.P. Hulin. Analysis of porous media heterogeneities using the diffusion of pressure waves. *J. Geophys. Res.*, 98:9781–9791, 1993.
 - 62. R. Mustata, S.D. Harris, L. Elliott, D.B. Ingham, and D. Lesnic. Parameter investigation in a boundary element model of a hydraulic pump–flow test. In: M.H. Aliabadi, ed. *Boundary Element Techniques*. London: Queen Mary College, 1999, pp. 331–341.
 - 63. R. Mustata. *Parameter identification within a porous medium using genetic algorithms*. PhD thesis, University of Leeds, Leeds, UK, 2000.
 - 64. D. Lesnic, R. Mustata, L. Elliott, D.B. Ingham, M.B. Clennell, and S.D. Harris. Genetic algorithm to identify the hydraulic properties of heterogeneous rocks from laboratory flow–pump experiments. *Hybrid Methods Eng.*, 4:1–26, 2002.
 - 65. Z.A. Al-Dhahir and D.C. Tan. A note on one-dimensional constant-head permeability tests. *Geotechn.,* 18:499–505, 1968.
 - 66. C.E. Neuzil, C. Cooley, S.E. Silliman, J.D. Bredehoeft, and P.A. Hsieh. A transient laboratory method for determining the hydraulic properties of ‘tight’ rocks — II. Application. *Int. J. Rock Mech. Mining Sci. Geomech. Abstr.*, 18: 253–258, 1981.
 - 67. R.H. Morin and H.W. Olsen. Theoretical analysis of the transient pressure response from a constant flow rate hydraulic conductivity test. *Water Resour. Res.*, 23:1461–1470, 1987.
 - 68. M. Zhang, M. Takahashi, R.H. Morin, and T. Esaki. Evaluation and application of the transient-pulse technique for determining the hydraulic properties of low-permeability rocks. Part 1. Theoretical evaluation. *Geotech. Testing J.*, 23:83–90, 2000.
 - 69. R.E. Olson and D.E. Daniel. Measurement of the hydraulic conductivity of fine grained soils. In: T.F. Zimmie and C.O. Riggs, eds. *Permeability and Groundwater Contaminant Transport*. Philadelphia: ASTM STP 746, 1981, pp. 18–64.
 - 70. H.W. Olsen, J.D. Gill, J.D. Wilden, and K.R. Nelson. Innovations in hydraulic conductivity measurements. *Proc. Transportation Research Board*, 70th Annual Meeting, Washington, 1991, Paper No. 910367.
 - 71. H.W. Olsen, R.H. Morin, and R.W. Nichols. Flow pump applications in triaxial testing. In: R.T. Donaghe, R.C. Chaney, and M.L. Silver, eds. *Advanced Triaxial Testing of Soil and Rock*. Philadelphia: ASTM STP 977, 1988, pp. 68–81.
 - 72. J.V. Beck and K.J. Arnold. *Parameter Estimation in Engineering and Science*. New York: Wiley, 1977.
 - 73. M.B. Clennell. Transient flow in reservoir rocks and seals: laboratory experiments and forward numerical models. Programme with Abstracts, Second IMA Congress on Modelling Permeable Rocks, Cambridge, Institute of Mathematics and Its Applications, 1998.
 - 74. J.J. Butler, Jr. Pumping tests in non-uniform aquifers — the radially-symmetric case. *J. Hydrol.*, 101:15–30, 1988.
 - 75. J.J. Butler, Jr. and C.D. McElwee. Variable-rate pumping tests for radially-symmetric non-uniform aquifers. *Water Resour. Res.*, 26:291–306, 1990.
 - 76. J.J. Butler, Jr. and W.Z. Liu. Pumping tests in non-uniform aquifers — the linear strip case. *J. Hydrol.*, 128:69–99, 1991.

77. J.J. Butler, Jr. and W.Z. Liu. Pumping tests in non-uniform aquifers — the radially-asymmetric case. *Water Resour. Res.*, 29:259–269, 1993.
78. L.W. Lake. The origins of anisotropy. *J. Pet. Tech.*, 40:395–396, 1988.
79. P.A. Rice, D.J. Fontugne, R.G. Latini, and A.J. Barduhn. Anisotropic permeability in porous media. *Ind. Eng. Chem.*, 62:23–31, 1970.
80. G. Dagan. Statistical theory of groundwater flow and transport: Pore to laboratory, laboratory to formation and formation to regional scale. *Water Resour. Res.* 22:120S–134S, 1986.
81. T.A. Hewett and R.A. Behrens. Considerations affecting the scaling of displacements in heterogeneous permeability distributions. SPE paper 20739, 1993.
82. D.J. Fontugne. *Permeability measurement in anisotropic media*. PhD thesis, Syracuse University, NY, 1969.
83. W.D. Rose. New method to measure directional permeability. *J. Pet. Tech.*, 34:1142–1144, 1970.
84. M. Quintard and S. Whitaker. Ecoulement monophasique en milieu poreux: Effet des heterogeneites locales (in French). *J. Meca Theor. Appl.*, 6:691–726, 1987.
85. L.J. Durlofsky and E.Y. Chung. Effective permeability of heterogeneous reservoir regions. In: D. Guerillot and O. Guillon, eds. *Second European Conf. on the Mathematics of Oil Recovery*. Paris: Éditions Technip, 1989, pp. 57–64.
86. A.E. Saez, C.J. Otero, and I. Rusinek. The effective homogeneous behavior of heterogeneous porous media. *Transp. Porous Media*, 4:213–238, 1989.
87. C.C. Mei and J.L. Auriault. Mechanics of heterogeneous porous media with several spatial scales. *Proc. R. Soc. London A*, 426:391–423, 1989.
88. C.D. White and R.N. Horne. Computing absolute transmissibility in the presence of fine-scale heterogeneity. SPE paper 16001, 1987.
89. Y. Bernabe. On the measurement of permeability in anisotropic rocks. In: B. Evans and T.-F. Wong, eds. *Fault Mechanics and Transport Properties of Rocks*. London: Academic Press, 1992, pp. 147–167.
90. R. Mustata, S.D. Harris, L. Elliott, D.B. Ingham, and D. Lesnic. An inverse boundary element method for determining the hydraulic conductivity in anisotropic rocks. *Comput. Modelling Eng. Sci.*, 1:95–104, 2000.
91. R. Mustata, S.D. Harris, L. Elliott, D. Lesnic, D.B. Ingham, R.A. Khachfe, and Y. Jarny. The determination of the properties of orthotropic heat conductors. In: D. Petit, D.B. Ingham, Y. Jarny, and F. Plourde, eds. *Inverse Problems and Experimental Design in Thermal and Mechanical Engineering*. Proc. Eurotherm Seminar 68, March 5–7, Poitiers, 2001, pp. 325–333.
92. R. Mustata, S.D. Harris, L. Elliott, D.B. Ingham, and D. Lesnic. Retrieval of spacewise dependent hydraulic properties of anisotropic rocks from transient flow experiments. *Transp. Porous Media*, 48:79–99, 2002.